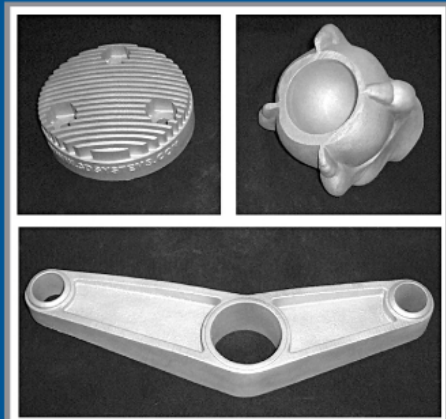


WOODHEAD PUBLISHING IN MATERIALS



Fundamentals of aluminium metallurgy

Production, processing
and applications

Edited by Roger Lumley

WP
WOODHEAD
PUBLISHING

Fundamentals of aluminium metallurgy

Related titles:

Titanium alloys: modelling of microstructure, properties and applications
(ISBN 978-1-84569-375-6)

Computer-based modelling of material properties and microstructure is a fast-growing area of research and the use of titanium is also growing rapidly in many applications. The book links the modelling of microstructure and properties to titanium. The first part of the book reviews experimental techniques for modelling the microstructure and properties of titanium. A second group of chapters looks in depth at the physical models and a third group examines neural network models. The final section covers surface engineering products.

Friction stir welding: from basics to applications
(ISBN 978-1-84569-450-0)

Friction stir welding (FSW) is a solid-state welding process that is gaining wide acceptance in industry, especially the shipbuilding, aerospace, mass transportation and automotive industries. FSW is particularly suited to those industries that use aluminium and its alloys. This authoritative book provides a comprehensive review of the subject of friction stir welding and covers topics such as process basics, equipment, modelling, inspection and quality control and applications.

Hydrometallurgy: principles and applications
(ISBN 978-1-84569-407-4)

The book is concerned with the theoretical principles of hydrometallurgical processes and engineering aspects. The hydrometallurgical processes of production of copper are discussed and leaching of chalcopryite as the main sulphide mineral of copper processed in industry is used as an example. The book is suitable as a university textbook for students of metallurgy.

Details of these and other Woodhead Publishing books can be obtained by:

- visiting our web site at www.woodheadpublishing.com
- contacting Customer Services (e-mail: sales@woodheadpublishing.com; fax: +44 (0) 1223 893694; tel.: +44 (0) 1223 891358 ext. 130; address: Woodhead Publishing Limited, Abington Hall, Granta Park, Great Abington, Cambridge CB21 6AH, UK)

If you would like to receive information on forthcoming titles, please send your address details to: Francis Dodds (address, tel. and fax as above; e-mail: francis.dodds@woodheadpublishing.com). Please confirm which subject areas you are interested in.

Fundamentals of aluminium metallurgy

Production, processing and applications

Edited by
Roger Lumley



Oxford Cambridge Philadelphia New Delhi

Published by Woodhead Publishing Limited, Abington Hall, Granta Park, Great Abington, Cambridge CB21 6AH, UK
www.woodheadpublishing.com

Woodhead Publishing, 525 South 4th Street #241, Philadelphia, PA 19147, USA

Woodhead Publishing India Private Limited, G-2, Vardaan House, 7/28 Ansari Road, Daryaganj, New Delhi – 110002, India
www.woodheadpublishingindia.com

First published 2011, Woodhead Publishing Limited
© Woodhead Publishing Limited, 2011
The authors have asserted their moral rights.

This book contains information obtained from authentic and highly regarded sources. Reprinted material is quoted with permission, and sources are indicated. Reasonable efforts have been made to publish reliable data and information, but the authors and the publisher cannot assume responsibility for the validity of all materials. Neither the authors nor the publisher, nor anyone else associated with this publication, shall be liable for any loss, damage or liability directly or indirectly caused or alleged to be caused by this book.

Neither this book nor any part may be reproduced or transmitted in any form or by any means, electronic or mechanical, including photocopying, microfilming and recording, or by any information storage or retrieval system, without permission in writing from Woodhead Publishing Limited.

The consent of Woodhead Publishing Limited does not extend to copying for general distribution, for promotion, for creating new works, or for resale. Specific permission must be obtained in writing from Woodhead Publishing Limited for such copying.

Trademark notice: Product or corporate names may be trademarks or registered trademarks, and are used only for identification and explanation, without intent to infringe.

British Library Cataloguing in Publication Data
A catalogue record for this book is available from the British Library.

ISBN 978-1-84569-654-2 (print)
ISBN 978-0-85709-025-6 (online)

The publisher's policy is to use permanent paper from mills that operate a sustainable forestry policy, and which has been manufactured from pulp which is processed using acid-free and elemental chlorine-free practices. Furthermore, the publisher ensures that the text paper and cover board used have met acceptable environmental accreditation standards.

Typeset by RefineCatch Limited, Bungay, Suffolk, UK
Printed by TJI Digital, Padstow, Cornwall, UK

Contents

<i>Contributor contact details</i>	<i>xiii</i>
1 Introduction to aluminium metallurgy R.N. LUMLEY, CSIRO Light Metals Flagship, Australia	1
1.1 Aluminium as an engineering material	1
1.2 The development of aluminium alloys	2
1.3 Cast aluminium alloys	5
1.4 Wrought aluminium alloys	7
1.5 Production of aluminium	8
1.6 Uses of aluminium	8
1.7 Conclusion	17
1.8 References	18
Part I Production and casting of aluminium and its alloys	21
2 Production of alumina J. METSON, The University of Auckland, New Zealand	23
2.1 Introduction to the aluminium oxides	23
2.2 Al minerals – mining and processing	24
2.3 Alumina production processes	27
2.4 The Bayer alumina refinery	30
2.5 Alumina microstructure	38
2.6 Impurities	40
2.7 Production of speciality aluminas	42
2.8 Alumina production trends	43
2.9 Acknowledgements	44
2.10 References	44
3 Production of primary aluminium H. KVANDÉ, Qatar University, Qatar	49
3.1 Introduction	49
3.2 Raw materials used in the aluminium production process	51

3.3	Energy efficiency in the utilisation of carbon anodes	52
3.4	The carbon anodes	52
3.5	Electrolyte materials	54
3.6	The cathode and cathode materials	56
3.7	Current efficiency	57
3.8	Cell amperage increase	60
3.9	Cell lines	61
3.10	Health, environment and safety (HES)	63
3.11	Inert anodes	65
3.12	The past, present and future of primary aluminium production	67
3.13	Acknowledgements	69
3.14	References	69
4	Production of secondary aluminium G. WALLACE, Sims Aluminium Pty Limited, Australia	70
4.1	History of secondary aluminium	70
4.2	Sources of raw materials	73
4.3	Processing	78
4.4	Cost drivers	81
4.5	Future trends	81
4.6	Further reading	82
4.7	Reference	82
5	Ingot casting and casthouse metallurgy of aluminium and its alloys J.F. GRANDFIELD, Grandfield Technology Pty Ltd, Australia	83
5.1	Direct chill casting	83
5.2	Heat flow and solidification	86
5.3	Macrosegregation	97
5.4	Typical surface defects	98
5.5	Gas pressurised extrusion billet casting	105
5.6	Rolling slab technology	107
5.7	Special variants of DC casting	108
5.8	DC casting safety	108
5.9	Chain conveyor casting	108
5.10	Melt treatment	110
5.11	Conclusion	123
5.12	Notes	124
5.13	References	124
6	Casting of aluminium alloys S. OTARAWANNA, National Metal and Materials Technology Center (MTEC), Thailand and A.K. DAHLE, The University of Queensland, Australia	141
6.1	Introduction	141

6.2	Aluminium casting alloys	141
6.3	Microstructure control in aluminium foundry alloys	142
6.4	Filling the casting	143
6.5	Feeding and porosity	144
6.6	Casting processes	144
6.7	Summary	153
6.8	References	153
7	Quality issues in aluminum castings G.K. SIGWORTH, GKS Engineering Services, USA	155
7.1	Introduction	155
7.2	Standard molds	156
7.3	Effect of solidification time	162
7.4	Theoretical basis for the quality index	164
7.5	Effect of inclusions and porosity on quality	167
7.6	Fatigue failure	169
7.7	Sources of casting defects	174
7.8	Effect of metal treatment and transfer on quality	177
7.9	Possible improvements in fatigue life	180
7.10	Conclusion	182
7.11	References	182
8	Case studies in aluminium casting alloys J.A. TAYLOR and D.H. STJOHN, CAST CRC, The University of Queensland, Australia and M.A. EASTON, CAST CRC, Monash University, Australia	185
8.1	Introduction	185
8.2	The effect of the alloy specification range on microstructure and properties	186
8.3	An impurity that reduces castability and increases casting defects	190
8.4	The effect of grain refinement on defect formation	195
8.5	The effect of excess titanium on foundry alloys	202
8.6	Selecting the right master alloy for grain refinement in terms of effectiveness and cost optimisation	207
8.7	Selecting the right master alloy for eutectic modification in terms of effectiveness and cost optimisation	208
8.8	Summary	214
8.9	References	214
9	High pressure die casting of aluminium and its alloys M.T. MURRAY, M Murray & Associates Pty Ltd, Australia	217
9.1	History of high pressure die casting	217
9.2	The die casting process	221
9.3	Aluminium alloys used in die casting	232
9.4	Defects in die casting	235

viii	Contents	
9.5	Conclusion	257
9.6	References	259
10	Progress on the heat treatment of high pressure die castings	262
	R.N. LUMLEY, CSIRO Light Metals Flagship, Australia	
10.1	Introduction	262
10.2	Role of alloying elements during solution treatment	271
10.3	Role of alloying elements during age hardening	279
10.4	Application to industrially produced parts and commercial heat treatment facilities	291
10.5	Implications for redesign of high pressure die castings	299
10.6	Conclusion	300
10.7	Notes	302
10.8	References	302
Part II	Metallurgical properties of aluminium and its alloys	305
11	Work hardening in aluminium alloys	307
	W.J. POOLE and J.D. EMBURY, The University of British Columbia, Canada and D.J. LLOYD, Novelis Global Technology Centre, Canada	
11.1	Introduction	307
11.2	Fundamentals of work hardening	308
11.3	Models of work hardening	312
11.4	Applications of work hardening models to industrial alloys	325
11.5	Commercial aspects of work hardening	332
11.6	Conclusion and future trends	338
11.7	Acknowledgements	339
11.8	Notes	339
11.9	References	339
12	Precipitation and solute clustering in aluminium: advanced characterisation techniques	345
	G. SHA, R.K.W. MARCEAU and S.P. RINGER, The University of Sydney, Australia	
12.1	Introduction	345
12.2	Al-Cu based alloys	347
12.3	Al-Cu-Mg based alloys	349
12.4	Al-Mg-Si based alloys	354
12.5	Al-Zn-Mg-(Cu) based alloys	356
12.6	Precipitation in Al alloys under severe plastic deformation	359
12.7	Conclusion	361
12.8	Acknowledgements	362
12.9	References	362

13	Solute partitioning to enhance mechanical properties of aged aluminium alloys I.J. POLMEAR, Monash University, Australia	367
13.1	Introduction	367
13.2	Solute partitioning through compositional change	368
13.3	Studies of underaged alloys	371
13.4	Secondary precipitation	379
13.5	Conclusion	381
13.6	Acknowledgments	382
13.7	References	383
14	Vacancies in aluminium and solute-vacancy interactions in aluminium alloys A. SOMOZA, Universidad Nacional del Centro de la Provincia de Buenos Aires and Comisión de Investigaciones Científicas de la Provincia de Buenos Aires, Argentina and A. DUPASQUIER, Politecnico di Milano, Italy	386
14.1	Introduction	386
14.2	Experimental studies of vacancies and solute-vacancy interactions	388
14.3	Modelling	408
14.4	Conclusion	415
14.5	Acknowledgements	416
14.6	References	416
15	Modeling the kinetics of precipitation processes in aluminium alloys C.R. HUTCHINSON, Monash University, Australia	422
15.1	Introduction	422
15.2	Physical processes controlling precipitation	425
15.3	Current approaches to modeling precipitation kinetics	426
15.4	Coupling precipitation and plastic deformation	458
15.5	Future trends and perspectives	461
15.6	References	462
16	Ultrafine-grained aluminium alloys: processes, structural features and properties Y. ESTRIN, Monash University and CSIRO Process Science and Engineering, Australia and M. MURASHKIN and R. VALIEV, Ufa State Aviation Technical University, Russia	468
16.1	Introduction	468
16.2	Severe plastic deformation techniques used in processing of Al alloys	469
16.3	Producing ultrafine-grained aluminium alloys by means of SPD techniques	473

16.4	Mechanical properties of UFG Al alloys at room temperature	480
16.5	Innovation potential of UFG Al alloys	494
16.6	Conclusion	497
16.7	Acknowledgements	497
16.8	References	497
17	Design for fatigue crack growth resistance in aluminum alloys D.A. LADOS, Worcester Polytechnic Institute, USA	504
17.1	Introduction	504
17.2	Background and current state of knowledge	505
17.3	Materials, processing, mechanical properties and fatigue crack growth testing	507
17.4	Fatigue crack propagation in the near-threshold regime	510
17.5	Fatigue crack propagation mechanisms in Regions II and III of crack growth	520
17.6	K_{\max} and stress ratio effects on fatigue crack growth	526
17.7	A dual parameter ΔK - K_{\max} approach to fatigue crack growth	529
17.8	K_{\max} sensitivity and data normalization for generating design curves	530
17.9	Conclusion	532
17.10	References	532
18	Fracture resistance in aluminium J.F. KNOTT, The University of Birmingham, UK	538
18.1	Introduction	538
18.2	Fracture in uni-axial tension	539
18.3	Fracture in thin sheet: stretching and deep-drawing operations	544
18.4	Fracture in aluminium alloy castings	548
18.5	Fracture in high strength wrought alloys: fracture toughness	551
18.6	The fracture toughness of aluminium alloys: micro-structural aspects	557
18.7	Fracture in aluminium particulate metal-matrix composites	563
18.8	Effects of serrated yielding (dynamic strain-aging) on fracture	565
18.9	Future trends: optimised properties versus 'fitness for purpose'	569
18.10	References	571
19	Corrosion and corrosion protection of aluminium N. BIRBILIS and B. HINTON, Monash University, Australia	574
19.1	Introduction	574
19.2	General, galvanic and pitting corrosion	575
19.3	Localised corrosion: intergranular and exfoliation	582
19.4	Environmentally assisted cracking	584

19.5	Corrosion protection in the aircraft structure	590
19.6	Summary case study: corrosion of a C-130J Hercules aircraft wing trailing edge strip	593
19.7	Acknowledgements	601
19.8	References	601
Part III Processing and applications of aluminium and its alloys		605
20	Joining of aluminium and its alloys S. LATHABAI, CSIRO Process Science and Engineering, Australia	607
20.1	Introduction	607
20.2	Mechanical joining	609
20.3	Fusion welding	618
20.4	Solid state welding	630
20.5	Brazing	643
20.6	Adhesive bonding	647
20.7	Conclusion	650
20.8	References	650
21	Aluminium powder metallurgy S.H. HUO, M. QIAN and G.B. SCHAFFER, The University of Queensland, Australia and E. CROSSIN, The University of Queensland, Australia and RMIT University, Australia	655
21.1	Introduction	655
21.2	The press and sinter powder metallurgy process	655
21.3	Sintering fundamentals	658
21.4	Sintering of aluminium	678
21.5	PM aluminium alloys and their applications	688
21.6	Future trends	692
21.7	Acknowledgements	694
21.8	References	694
22	Laser sintering and rapid prototyping of aluminium T.B. SERCOMBE, The University of Western Australia, Australia	702
22.1	Introduction	702
22.2	The skeleton	705
22.3	Infiltration	711
22.4	Dimensional changes	713
22.5	Conclusion	714
22.6	Acknowledgements	715
22.7	References	715

xii	Contents	
23	Aluminium sheet fabrication and processing J. HIRSCH, Hydro Aluminium Deutschland GmbH, Germany	719
23.1	Introduction	719
23.2	Aluminium alloys and specifications	721
23.3	The aluminium sheet fabrication processing route and microstructure evolution	725
23.4	Parameters and metallurgical effects in Al alloy sheet processing	741
23.5	Integrated material and through-process modelling	743
23.6	Conclusion	744
23.7	Acknowledgements	745
23.8	References	745
24	Application of modern aluminium alloys to aircraft E.A. STARKE, JR and J.T. STALEY, Consultant, University of Virginia, USA	747
24.1	Introduction	747
24.2	Drivers for materials selection and aluminum alloy product development for aircraft	749
24.3	Performance criteria and property requirements for primary structure of subsonic aircraft	751
24.4	Structure–property relationships	754
24.5	New products and recent manufacturing technologies	775
24.6	Conclusion	780
24.7	References	780
25	Materials selection and substitution using aluminium alloys M. LEARY, RMIT University, Australia	784
25.1	Introduction	784
25.2	Fundamental material selection strategies	785
25.3	Material selection for specific scenarios	791
25.4	Non-stationary fatigue-limited application	803
25.5	Multi-objective problems and numeric optimisation	804
25.6	Multiple objective material selection	811
25.7	Environmental consequence of material selection	816
25.8	Conclusion	822
25.9	Acknowledgements	824
25.10	Notes	824
25.11	References	824
	<i>Index</i>	828

Contributor contact details

(* = main contact)

Editor and chapters 1 and 10

Roger Lumley
Principal Research Scientist
CSIRO Light Metals Flagship
Private Bag 33
Clayton South MDC
Melbourne
Victoria 3169
Australia
E-mail: Roger.Lumley@csiro.au

Chapter 2

James Metson
Department of Chemistry and Light
Metals Research Centre
The University of Auckland
Private Bag 92019
Auckland, 1142
New Zealand
E-mail: j.metson@auckland.ac.nz

Chapter 3

Halvor Kvande
Professor of Chemical Engineering
Department of Chemical
Engineering
Qatar University
P.O. Box 2713
Doha
Qatar
E-mail: halvorkvande@qu.edu.qa;
halvor.kvande@hydro.com

Chapter 4

Graeme Wallace
Trading Manager
Sims Aluminium Pty Limited
P.O. Box 602 Sunshine VIC 3187
Australia
E-mail: graeme.wallace@simsmm.com

Chapter 5

John F. Grandfield
Grandfield Technology Pty Ltd
37 Mattingley Cr
Brunswick West
Victoria 3055
Australia
E-mail: grandfieldtechnology@gmail.com

Chapter 6

Somboon Otarawanna
Researcher/National Metal and
Materials Technology Center
(MTEC)
Thailand

Arne K Dahle*
Professor of Materials Engineering
The University of Queensland
Australia
E-mail: A.Dahle@uq.edu.au

Chapter 7

Geoffrey K. Sigworth
GKS Engineering Services
1710 Douglas Ave
Dunedin
FI 34698
USA
E-mail: gksigworth@gmail.com

Chapter 8

J.A. Taylor*
D.H. StJohn
CAST Cooperative Research Centre
The University of Queensland
St Lucia
Queensland 4072
Australia
E-mail: john.taylor@uq.edu.au;
d.stjohn@uq.edu.au

M.A. Easton
CAST Cooperative Research Centre
Monash University
Clayton
Victoria 3069
Australia
E-mail: mark.easton@eng.monash.edu.au

Chapter 9

Morris T Murray
M Murray & Associates Pty Ltd
51 Teal Lane
Briar Hill
Victoria 3088
Australia
E-mail: mmaa@bigpond.net.au

Chapter 11

W.J. Poole* and J.D. Embury
Department of Materials
Engineering
The University of British Columbia
309-6350 Stores Road
Vancouver
BC, V6T 1Z4
Canada
E-mail: warren.poole@ubc.ca

D.J. Lloyd
Novelis Global Technology Centre
P.O. Box 8400
945 Princess Street
Kingston
Ontario
K7L 5L9
Canada

Chapter 12

G. Sha*, R.K.W. Marceau and
S.P. Ringer
Australian Key Centre for
Microscopy and Microanalysis
Madsen Building F09
The University of Sydney
New South Wales 2006
Australia
E-mail: s.ringer@usyd.edu.au;
g.sha@usyd.edu.au

Chapter 13

I.J. Polmear
Professor Emeritus
Department of Materials
Engineering
Monash University
Melbourne 3800
Australia
E-mail: ian.polmear@eng.monash.
edu.au

Chapter 14

Alberto Somoza*
Instituto de Física de Materiales
Tandil – IFIMAT
Universidad Nacional del Centro de
la Provincia de Buenos Aires and
Comisión de Investigaciones
Científicas de la Provincia de
Buenos Aires
Pinto 399
B7000GHG Tandil
Argentina
E-mail: asomoza@exa.unicen.edu.ar

Alfredo Dupasquier
Department of Physics
LNESS
Politecnico di Milano
via Anzani 42
I-22100 Como
Italy

Chapter 15

Christopher R. Hutchinson
Department of Materials
Engineering
Monash University
Clayton Campus
Clayton
Victoria 3800
Australia
E-mail: christopher.hutchinson@
monash.edu

Chapter 16

Yuri Estrin*
ARC Centre of Excellence for
Design in Light Alloys
Department of Materials
Engineering
Monash University, Clayton
3800 VIC
Australia
E-mail: yuri.estrin@eng.monash.edu.au

and

CSIRO Division of Process Science
and Engineering
Clayton South
3169 VIC
Australia

Maxim Murashkin and Ruslan
Valiev
Institute of Physics of Advanced
Materials
Ufa State Aviation Technical
University
12 K. Marx st.
Ufa, 450000
Russia
E-mail: maxmur@mail.rb.ru;
RZValiev@mail.rb.ru

Chapter 17

Diana A. Lados
Department of Mechanical
Engineering
Integrative Materials Design Center
Worcester Polytechnic Institute
Washburn Building
100 Institute Road
Worcester
Massachusetts 01609
USA
E-mail: lados@wpi.edu

Chapter 18

John F. Knott
School of Metallurgy and Materials
The University of Birmingham
Elms Road
Edgbaston
Birmingham B15 2TT
UK
E-mail: J.F.Knott@bham.ac.uk

Chapter 19

Nick Birbilis*
Monash University
Australia
E-mail: nick.birbilis@eng.monash.
edu.au

Bruce Hinton
Monash University
Australia
E-mail: bruce.hinton@eng.monash.edu.au

Chapter 20

S. Lathabai
Principal Research Scientist
CSIRO Process Science and
Engineering
Private Bag 33, Clayton South MDC
Victoria 3169
Australia
E-mail: sri.lathabai@csiro.au

Chapter 21

S.H. Huo*, Ma Qian and G.B.
Schaffer
The University of Queensland
School of Mechanical and Mining
Engineering
CAST CRC
Brisbane
QLD 4072
Australia
E-mail: Shuhai.huo@uq.edu.au

E. Crossin
The University of Queensland
School of Mechanical and Mining
Engineering
CAST CRC
Brisbane
QLD 4072
Australia
E-mail: enda.crossin@rmit.edu.au

and

Centre for Design
RMIT University
Melbourne
VIC 3000
Australia
E-mail: enda.crossin@rmit.edu.au

Chapter 22

T.B. Sercombe
School of Mechanical Engineering
The University of Western Australia
MDBP MO50
35 Stirling Highway
Crawley WA 6009
Australia
E-mail: tim.sercombe@uwa.edu.au

Chapter 23

Juergen Hirsch
Hydro Aluminium Deutschland
GmbH, R&D Bonn
P.O. Box 2468
D-53104 Bonn
Germany
E-mail: juergen.hirsch@hydro.com

Chapter 24

E.A. Starke, Jr*
University of Virginia
Charlottesville, VA 22904, USA
E-mail: eas1o@cms.mail.virginia.edu

James T. Staley, Consultant
58 Forest at Duke Drive
Durham, NC, USA

Chapter 25

Martin Leary
RMIT University, Australia
School of Aerospace, Mechanical
and Manufacturing Engineering
P.O. Box 71 Bundoora
Victoria 3083
Australia
E-mail: martin.leary@rmit.edu.au

Introduction to aluminium metallurgy

R.N. LUMLEY, CSIRO Light Metals Flagship, Australia

Abstract: This chapter provides the introduction to the book and gives a brief overview of the history and growth of the global aluminium industry up to the present day, including some of the significant achievements, breakthroughs and challenges. It also discusses the future avenues of growth and where the global industry may be headed over the next 20 years.

Key words: aluminium industry, aluminium alloys, primary aluminium, secondary aluminium.

1.1 Aluminium as an engineering material

Aluminium is the third most abundant element in the earth's crust, and the most abundant metallic element. For the last 50 years, it has been second only to iron in its industrial use. Aluminium does not occur in an elemental state; rather it is always combined in a chemical compound. Its existence was not recognized until 1808, when an impure form was identified by Sir Humphry Davy in Britain. In 1825, Hans Christian Oersted of Denmark produced minute quantities of the metal, and two years later Freidrich Wöhler of Germany described a process for producing aluminium as a powder by reacting potassium with anhydrous aluminium chloride. In 1845, he determined its specific gravity thereby establishing it as a low-density metal. The first commercial process for producing aluminium was developed by Henri Sainte-Claire Deville in 1854, using an improved version of Wöhler's process. The metal was, however, still very expensive, and during the next 30–40 years numerous attempts were made to develop more economic processes whereby costs could be reduced. Developments during this period are described in an interesting book by Aldophe Minet (1902, 1905) published first in German in 1902 and then English in 1905.

The development of the present electrolytic process occurred almost simultaneously in 1886 by Charles Martin Hall in the United States and Paul L.T Héroult of France (i.e. the Hall–Héroult process). This represented a major advance, since it opened the way for the economical production of aluminium, which began in about 1890. One essential stage in the process was the extraction of alumina (Al_2O_3) from the ore bauxite, and an efficient method to do this was developed by Karl Joseph Bayer in 1888. A further essential factor was the availability since the early 1870s of generators capable of supplying electricity on the large scales required for electrolysis. To this day, the Bayer and the Hall–Héroult processes have remained the most economical methods for the production of commercial quantities of aluminium, and are the mainstay of the primary aluminium industry.

1.2 The development of aluminium alloys

It is interesting to note that the potential for aluminium alloys as engineering materials was recognized well before it became an industrial metal. In early 1886, it had been stated that: 'It has been generally held that the most useful field for this metal would be found in its alloys, many of which are possessed of valuable properties; but we incline to the opinion that the metal itself, should it become possible to produce it cheaply enough to enable it to compete in price with tin or copper for example, would find innumerable applications' (*The Manufacturer and Builder*, 1886). Due to its very high cost, the early applications of aluminium were often limited to small- or high-value items made of alloys such as Al-Ag which were used in the manufacture of instruments for marine observations (such as sextants) and balance beams where light weight was highly advantageous. Various other high-value domestic items were also produced such as tablespoons, which were reported in 1879 to cost (US) \$20/dozen or close to a month's wages for a labourer of the time (*The Manufacturer and Builder*, 1879).

Well before the Hall-Héroult process was known publicly, the compositions of several engineering alloys had been investigated, including those of aluminium with varying contents of Fe, Cu, Zn, Sn, Au and Ag (e.g. *The Manufacturer and Builder*, 1877). As early as the 1870s, alloys containing between five per cent and ten per cent Cu were reported as being suitable for castings as well as for working into sheet, wire and other wrought products (e.g. Lange, 1873). One particular composition within this range, which was known as alloy 12 (Al-8Cu), was used extensively at least until the late 1930s for castings in automotive, consumer and aerospace applications, including the engine of the Wright Flyer 1 in 1903 (for a photograph of Wright engine #17 from 1910, see Armistej, 2006). By the time the book by Minet (1902, 1905) was published, the mechanical properties of a range of aluminium alloys and processes employed for working them had been examined in greater detail. Even at this early stage, their potential use for castings and wrought body structures for the transport industry had been recognized. For example, the Paris exposition of 1900 featured a wide range of aluminium alloy castings including a number produced for the then fledgling automotive industry (Minet, 1902, 1905). Wrought sheet of an alloy Al-3Cu-0.8Sn, known as 'partinium' (Minet, 1902, 1905), had also been used extensively in the electric vehicle named '*La Jamais Contente*' built by Rothschild Coach Builders. Driven by Camille Jenatzy of Belgium, this vehicle attained the first world speed record greater than 100 km/h (105.9 km/h) in 1899 (e.g. Furet, 2008).

In 1906, four years after the publication of Minet's book, Alfred Wilm of Germany discovered the basic procedure by which some aluminium alloys (i.e. the Al-3.5Cu-0.5Mg-0.5Mn alloy that became known as Duralumin) could be heat treated. These techniques which involved precipitation (age) hardening are still used today, for strengthening a wide range of automotive and aerospace components (Cahn, 1984; Wilm, 1911). The basic technique developed by Wilm

(a high-temperature solution treatment followed by quenching) was similar to that used previously for aluminium bronzes (Cu with 5–10% Al), as a way of softening the alloy so that it was easier to work at ambient temperature (*The Manufacturer and Builder*, 1881). The discovery of age hardening by Wilm is reported to be an extension of earlier patents related to the heating and quenching of aluminium (Cahn, 1984). Duralumin was instrumental in the development of the airship and aircraft industries and related Al-Cu-Mg alloys are still produced today. Examples of current wrought and cast aluminium alloys, and whether or not they are heat treatable, are shown in Table 1.1. Similarly, a wide array of procedures for heat treatment and thermomechanical processing has been developed, which are summarized in Table 1.2.

Table 1.1 The Aluminum Association alloy designation system*

Wrought alloys		
Series	Major alloying elements	Heat treatable
1XXX	Al \geq 99%	N
2XXX	Al-Cu-(Mg)	Y
3XXX	Al-Mn	N
4XXX	Al-Si	N (some alloys are heat treatable e.g. 4032)
5XXX	Al-Mg	N
6XXX	Al-Mg-Si	Y
7XXX	Al-Zn-(Mg)-(Cu)	Y
8XXX	Al-(other elements)	N/Y (some alloys are heat treatable e.g. 8090)
9XXX	Unused series	
Cast alloys		
Series	Major alloying elements	Heat treatable (note many are used as cast)
1XX.X	Al \geq 99%	N
2XX.X	Al-Cu	Y
3XX.X	Al-Si (+Cu or Mg)	Y
4XX.X	Al-Si	N
5XX.X	Al-Mg	N
6XX.X	Unused series	
7XX.X	Al-Zn-(Mg)-(Cu)	Y
8XX.X	Al-Sn	N
9XX.X	Al-(other elements)	

Note: *While the Aluminum Association wrought alloy designations are very widely used, there are no universal casting alloy designations in wide use. However, for any casting alloy, there are usually equivalent alloy designations from each different region.

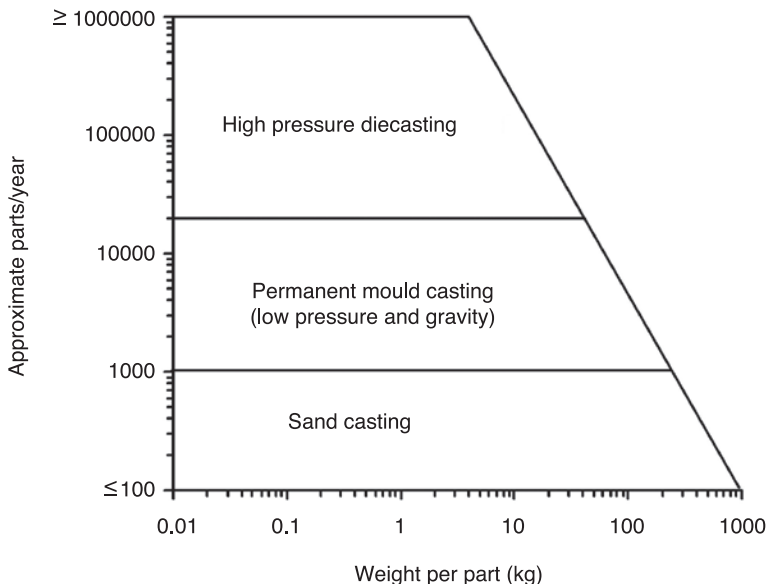
Table 1.2 Registered temper designations for aluminium alloys

Suffix letter indicates basic treatment or condition	First digit	Second digit	Other nomenclature
F As fabricated			
O Annealed: wrought products only			
	1 Cold worked only	2 [1/4 Hard]	
	2 Cold worked and partially annealed	4 [1/2 Hard]	HXX1: Strain hardened less than the amount for the HXX temper.
H Cold worked (strain hardened)	3 Cold worked and stabilized	6 [3/4 Hard]	HXX3: For high Mg products resistant to stress corrosion cracking
		8 [Hard]	
		9 [Extra hard]	
	1 Partial solution plus natural ageing	T79: Very slight overageing	TX2 requires heat treatment by the user
	2 Annealed cast products only	T78: As T79 (T4 aged first)	TX51: Stress relieved by stretching 1–3%
	3 Solution plus cold work	T77: Retrogression and reageing	TX510: No straightening after stretching
	4 Solution plus natural ageing	T76: As T79 but heavier overageing for corrosion resistance while maintaining strength	TX511: Minor straightening after stretching
	5 Artificially aged only	T75: Also used for some casting alloys	TX52: Stress relieved by compressing nominal 2.5%
T Heat treated	6 Solution plus artificial ageing	T74: As T76 but better corrosion resistance and lower strength.	TX53: Stress relieved by thermal treatment
	7 Solution plus stabilizing (overageing)	T73: Maximum corrosion resistance.	
	8 Solution plus cold work plus artificial ageing		
	9 Solution plus artificial ageing plus cold work.	Amount of cold work may be shown by a second digit, e.g. T83 means 3% cold work.	

1.3 Cast aluminium alloys

For many years, the casting of aluminium presented problems. Although it was relatively easy to produce useful shapes, it was rare for the castings to be free of visual porosity or other defects. By 1892, it had been recognized that: ‘It requires some experience and expertness on the part of the founder to master the peculiarities of the metal, before perfectly sound castings can be made. The aluminium should not be heated very much beyond the melting point; otherwise it seems to absorb gases, which remain in the metal, preventing sound casting’ (*The Manufacturer and Builder*, 1892). Although it was realized that this problem was associated with gas pickup, it was some years before it was fully understood (e.g. Eastwood, 1946 and references therein). Meanwhile, although the properties of parts being produced were usually adequate for service, it is also to be expected that the reject rates were likely to have been unacceptably high by today’s standards.

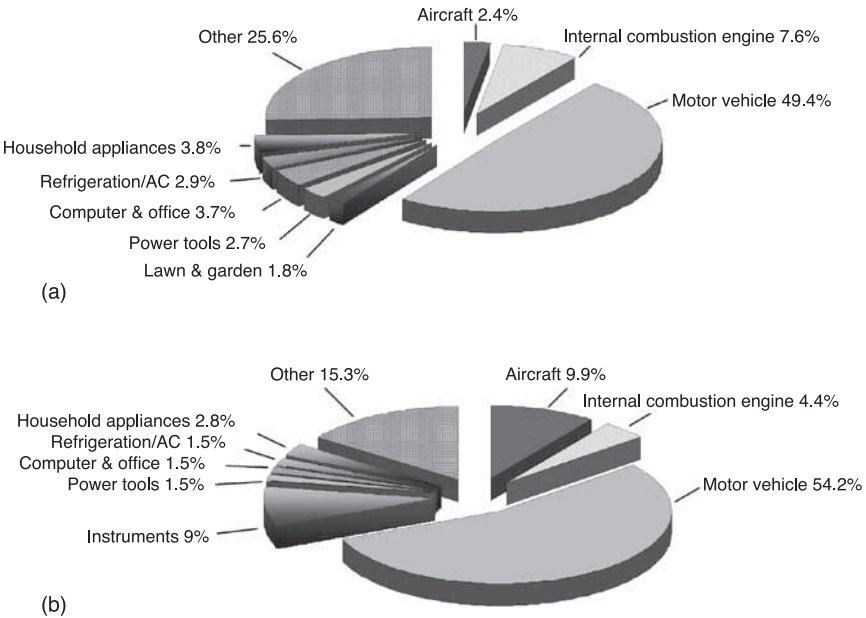
Today, the technology of aluminium casting has advanced significantly along many different paths. Porosity in aluminium castings still poses an array of issues to the casting engineer, but techniques for minimizing or eliminating porosity



1.1 The (approximate) relationship between part size, production rate and casting process used for cast aluminium components (where sand cores are not required) (Bonollo et al., 2005). Note that high volumes for permanent mold and sand cast components similar to that of high pressure die castings are common where sand cores are needed (e.g. cylinder heads).

through improved melt-handling procedures, design (including solidification modelling), degassing and filtration are now common in industry. Nevertheless they remain a topic for ongoing research.

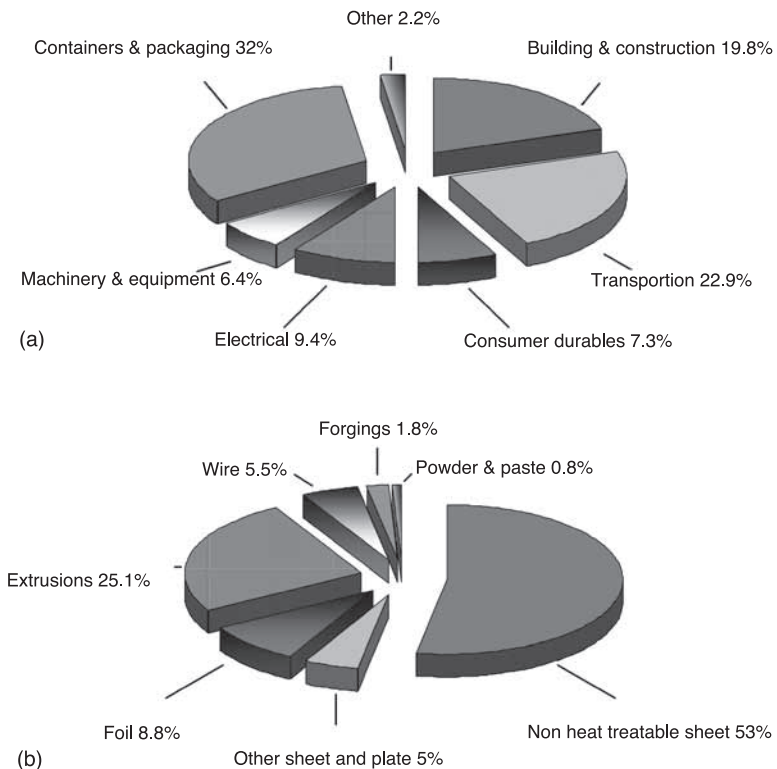
Castings now dominate the use of aluminium in the transport sector and are widely used in applications including engine blocks, cylinder heads, pistons, wheels and suspension components, to name some notable examples. Choice of the method of casting typically depends on the size, design and number of parts to be cast, and an approximate representation of this relationship is shown in Fig. 1.1. Of these methods, high pressure diecasting accounts for over 50% of all aluminium castings produced as well as for about 57% of the aluminium currently used in each passenger vehicle (Kirgin, 2009). Permanent mould and sand casting is more often used for thick wall products or for those requiring internal hollow sections where sand cores are necessary and high-pressure diecasting cannot be used (e.g. cylinder heads). Permanent mould casting is also currently the preferred technique for the production of wheels, steering knuckles and suspension components, to name a few examples. The applications and relative percentages of high pressure diecastings are shown in Fig. 1.2(a), and the same information for permanent mould and sand casting is presented in Fig. 1.2(b).



1.2 The distribution of cast aluminium products made (a) by high pressure diecasting, and (b) permanent mould and sand casting. Currently, high pressure die castings comprise over 50% of all aluminium castings produced (Kirgin, 2009).

1.4 Wrought aluminium alloys

Many of the very first applications of aluminium involved wrought products (e.g. Lange, 1873; *The Manufacturer and Builder*, 1879), and the high workability of the metal in both pure and alloyed states has always been one of the greatest attractions for its use. Today, around two-thirds of aluminium produced is used in wrought forms and includes plate, sheet, extrusions, forgings, stampings, foil and wire. Summaries of the aluminium mill products manufactured in North America in 2007 and their end uses are provided in Fig. 1.3. Non-heat treatable sheet is the most common form due, in part, to its extensive use in packaging (e.g. beverage cans), the transport industry (e.g. radiators) and construction industries (e.g. siding or panelling). Extrusions are the second most common product form, and a large proportion of these are now used in the construction industry (e.g. window frames) as well as the transport industry (e.g. structural sections and heat exchangers). Most wrought aluminium products are alloyed to give them desirable



1.3 The distribution of aluminium mill products in North America in 2007 by (a) end use market, and (b), by product type (Adams and Sattlenthight, 2008).

combinations of properties, but near-to-pure aluminium used in foil and electrical cable still comprises a substantial proportion of the products manufactured.

1.5 Production of aluminium

As a general rule, four tons of dried bauxite is required to produce two tons of alumina, from which 1 ton of aluminium is extracted. The global mine production and the industry reported reserve base for bauxite is shown in Fig. 1.4. Total bauxite resources are estimated to be 55–75 billion tons, which is located in Africa (33%), Oceania (24%), South America and the Caribbean (22%), Asia (15%) and elsewhere (6%) (Bray, 2009a).

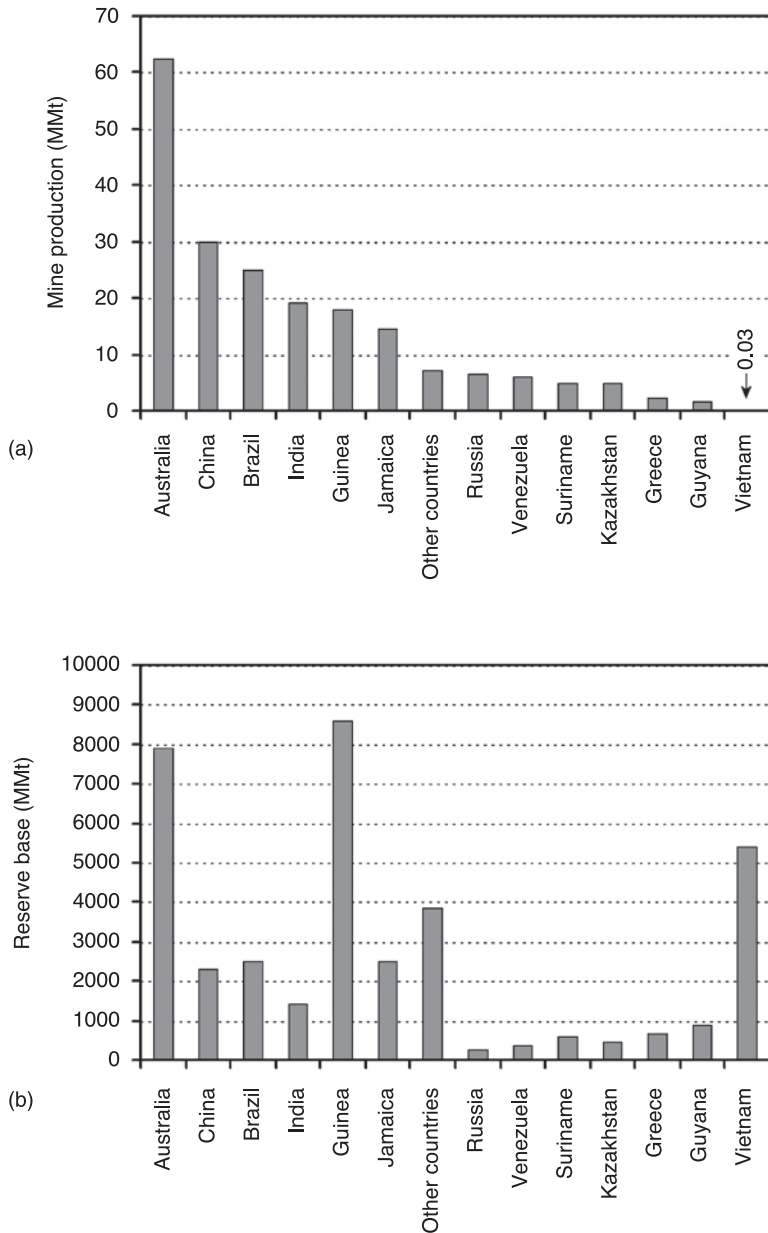
The worldwide production of aluminium has risen dramatically in the past 100 years, and Fig. 1.5 shows the worldwide output of primary aluminium over the period from 1900 to 2007. In 1900, 6800 metric tons were produced. This figure rose to 45 000 tons by 1910, and to 125 000 tons by 1920. Annual production first reached 1 million tons in 1941, and then doubled approximately every 10 years until around 1970 (10 million tons). By 1996, the total had doubled again to reach 20 million tons, and by 2007, it was nearly 38 million tons. Primary aluminium smelter production by country for 2007 is shown in Fig. 1.6.

Figure 1.7 shows the relative price (USD/metric ton) of aluminium metal from 1900 until 2007, normalized to the 1998 value. Although there have been fluctuations, the average price has steadily decreased as the volume of metal and production efficiency have increased.

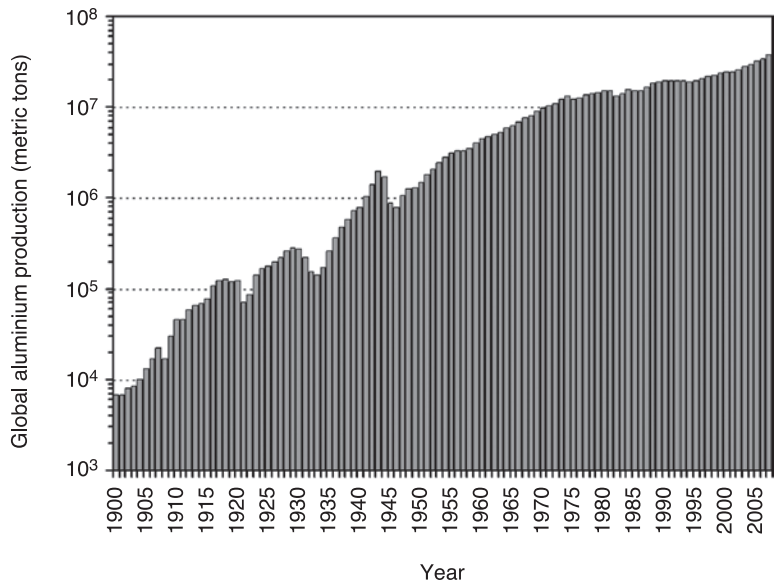
It is also important to consider the relative importance of primary versus secondary aluminium. Secondary aluminium is termed as ‘old scrap’ where the metal has been recovered from post-consumer material, and as ‘new scrap’ if the metal is recovered from industrial fabrication processes. Comparative (US) production of primary versus secondary metal is shown in Fig. 1.8. Based on 2007 figures, secondary aluminium accounted for around 60% of the metal produced in North America of which 42% of the metal was old scrap and 58% new scrap. Worldwide, reported figures show a similar trend although it is estimated that the amount of secondary aluminium is less, accounting for around 40% of total production.

1.6 Uses of aluminium

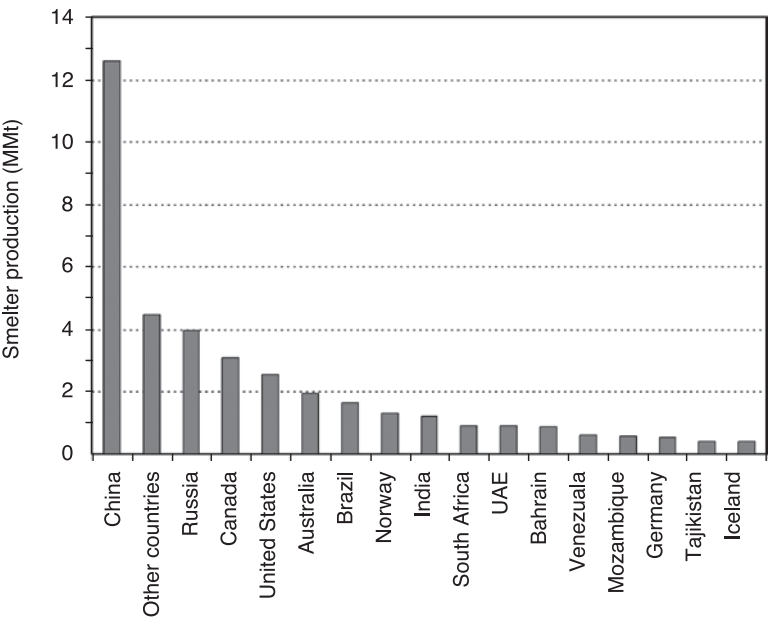
Aluminium has many useful properties. It is light, being only one-third the density of steel, and like copper, it has a high conductivity for heat and electricity, excellent corrosion resistance in most environments, and can be readily cast or fabricated into a wide range of consumer goods. It is highly valued for recycling because the remelting of scrap requires only five per cent of the total energy needed to extract the same amount of primary metal from bauxite ore. Characteristics of aluminium alloys and their relative importance for different products are shown in Table 1.3.



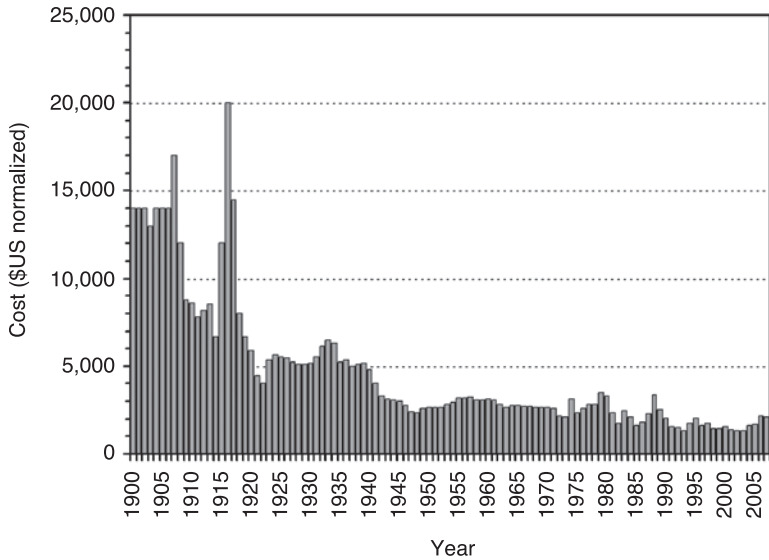
1.4 (a) 2007 mine production of bauxite by region, and (b) bauxite reserve base. The reserve base includes those resources that are currently classed as economic reserves, marginally economic reserves, and some of those that are currently sub-economic resources. Current economic reserves make up 71% of the total reserve base (Bray, 2009a). Units are millions of metric tons.



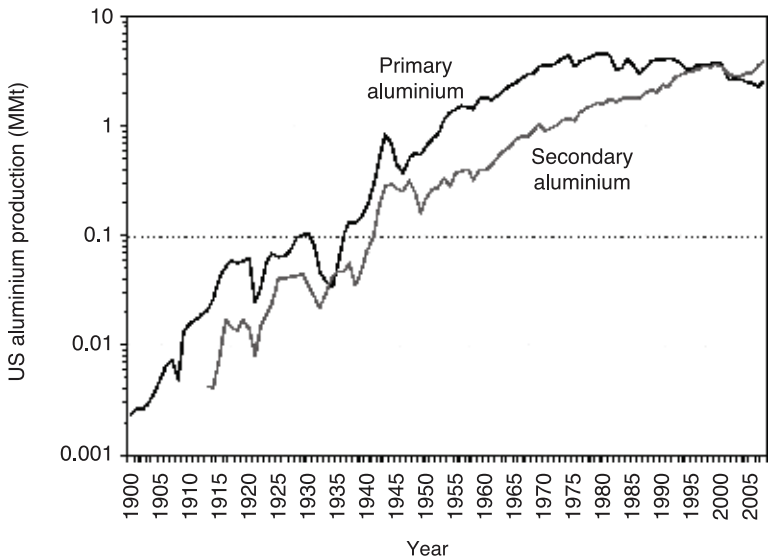
1.5 Worldwide production of primary aluminium from 1900–2007 (Buckingham et. al., 2008).



1.6 Primary aluminium production by country for 2007 (Bray, 2009b). Units are millions of metric tons.



1.7 Cost of aluminium (per metric ton) from 1900–2007 normalized to the 1998 value (Buckingham et. al., 2008).

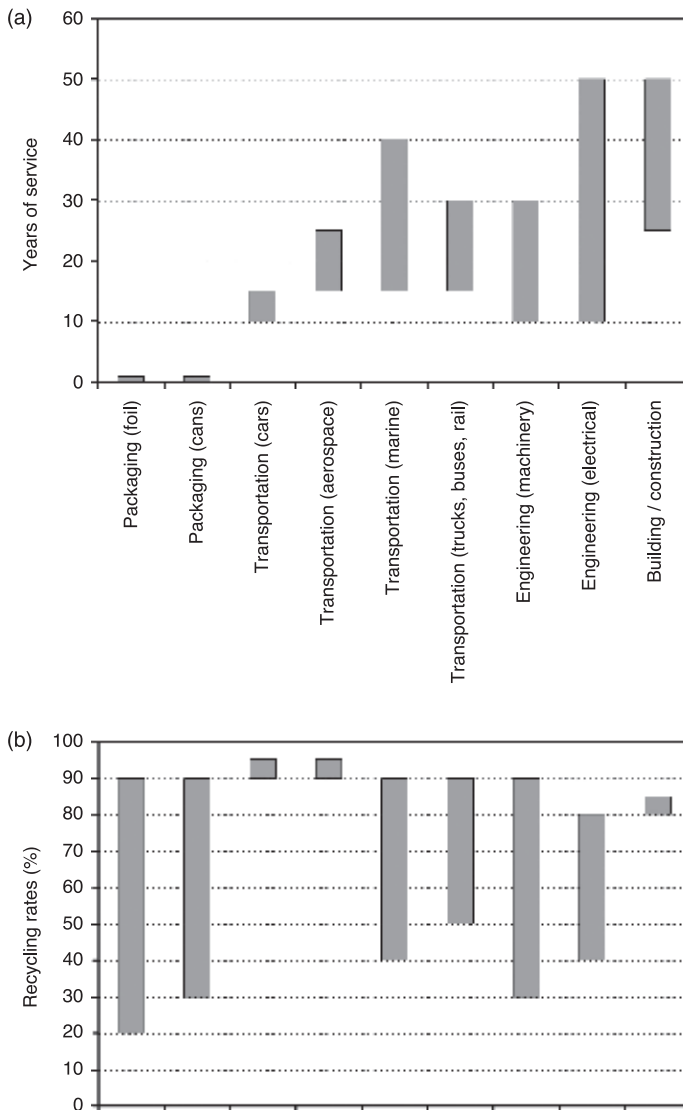


1.8 US production of primary and secondary aluminium from 1900 to 2007 (Buckingham et. al., 2008). Units are millions of metric tons.

Table 1.3 Some characteristics of aluminium and relative importance in different products

Characteristics		Type of product									
		Use	Density	Conductivity	Corrosion resistance	Decorative	Castings	Forgings	Sheet	Extrusions	Cable
Transport Machinery Building Household Chemicals and Food		↑↑↑	↑↑	↑↑↑	↑↑↑	↑↑↑	↑↑↑	↑↑	↑↑	—	—
		↑↑↑	↑↑	↑↑	↑↑	↑	↑↑↑	↑↑	↑	—	—
		↑↑	—	—	↑	↑↑↑	—	↑↑	↑↑	—	—
		↑↑	↑↑↑	↑↑↑	↑↑↑	↑↑	—	↑	—	—	↑
		↑↑	↑↑	↑↑↑	↑↑↑	↑	↑	↑	↑	—	↑
Packaging Electrical		↑	↑	↑↑↑	↑↑↑	↑↑↑	—	—	—	—	↑
		↑	↑↑↑	↑↑↑	↑	—	↑	↑	↑	↑	↑

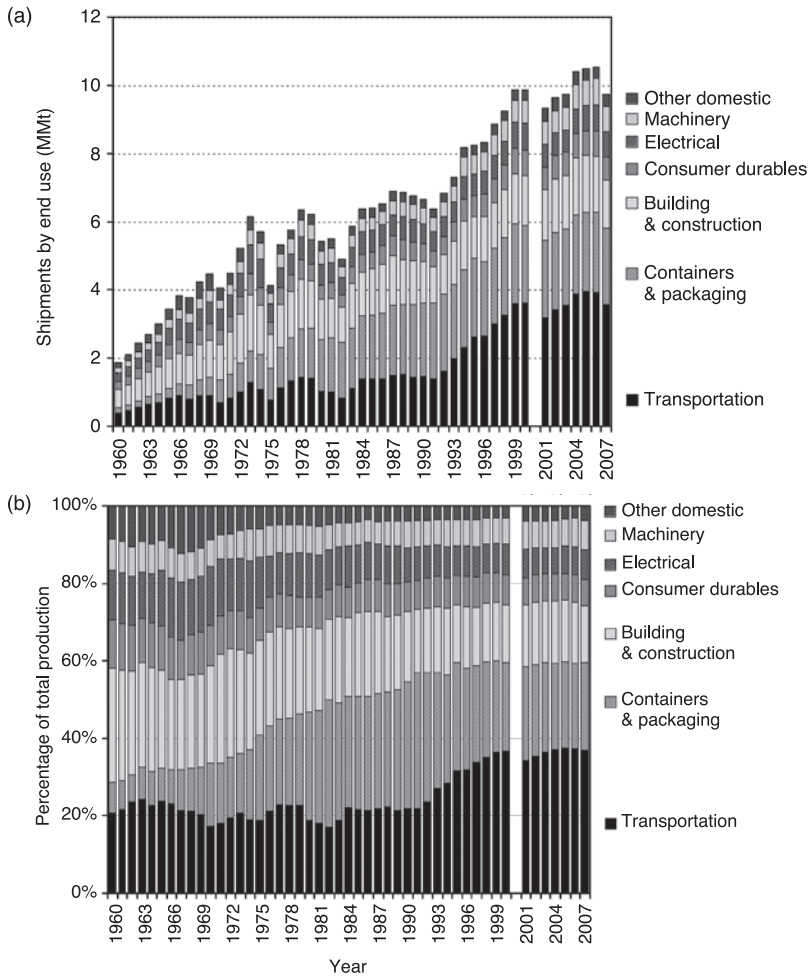
Because of its durability, aluminium has a relatively long lifecycle for around 75% of manufactured products and Fig. 1.9 shows some typical lifetimes. With the exception of packaging applications, components may be in service for years or decades before there is a need to recycle. It is of interest to note that packaging



1.9 Typical lifecycles of aluminium products by (a) end use, and (b) typical recycling rates (Polmear, 2006). Note that the data shown (i.e. years of service) may not accurately reflect the re-use rate of aluminium components in some markets such as automotive transportation.

has relatively low rates of recycling (~55% global average), whereas transport and construction applications are usually much higher.

Shipments of aluminium for the period from 1960 until 2007 in North America (as a representative large market sample) and the end use percentages are provided in Fig. 1.10. From this information, it is also interesting to note the applications where greatest increases have occurred as well as the time when this happened. In the period from around 1960 until about 1980, all applications of aluminium increased, the most notable being in the area of containers and packaging. This



1.10 Shipments by market in North America, 1960–2007, (a) in tons, and (b), as a percentage of total (Adams and Sattlethight, 2008). Units in (a) are millions of metric tons. Note that pre-2001 is US only, post-2001 is both the US and the Canada.

would seem to coincide with the introduction of the all-aluminium can in 1964 by the Royal Crown Cola Company and its subsequent rapid acceptance across the beverages market.

What is also clear from the data presented in Fig. 1.10 is that, during the period from 1990 until 2000, aluminium shipments for the transport industries in the United States rose by approximately 160% from around 1.4 million tons in 1990 to 3.6 million tons in 2000. This increase comprised shipments of ingot for casting in the transport sector, which trebled from a quantity of just over 700 000 tons to almost 2.1 million tons, and shipments of mill products (including extrusions, forgings, plate, sheet, rod etc.), which doubled from around 750 000 tons to just over 1.5 million tons. For the most part, these increases reflect changes in demand within the automotive industry.

Since the total number of new vehicles manufactured in the US over this period increased by only 31%, from 9.77 to 12.77 million vehicles (RITA, 2009), these figures clearly show the increased use of aluminium for automotive components. This trend was also reflected in other regions of the world, such as in Europe, where the amount of aluminium used per car increased from 50 kg in 1990 to 132 kg in 2005, and is forecast to rise to around 157 kg by 2010 (EAA, 2008).

It should also be noted that there are other factors that will cause the aluminium usage in vehicles to increase in the next 5–20 years. In western countries, this is in part due to the combination of the recent European Union directive mandating 130 g CO₂/km by 2012 for passenger vehicles, and the more recent US Energy Bill mandating an average fleet economy of 35 mpg (42 mpg for passenger vehicles and 26.6 mpg for light commercial vehicles) by 2020. Put simply, replacement of iron and steel with lower weight aluminium is now an accepted strategy for decreasing mass, such that fuel economy is improved and CO₂ emissions are reduced. In this regard, 100 kg of weight reduction in a vehicle translates to a decrease of 0.35 litres of fuel/100 km or 9 g CO₂/km (EAA, 2008). Hybrid and electric vehicle drivetrains, emissions control technology, alternate fuels, fuel cells and lightweight materials will all contribute to reaching these goals.

The high recyclability of aluminium is also expected to play a significant role in its future applications. For example, by 2015 both the EU and Japan will have regulations requiring 95% recycling of the total material used in new vehicles. The implications of this are that many lightweight materials that are not easy to recycle, or which have low intrinsic value, are likely to be eliminated or minimized in favour of highly recyclable alternatives.

In other regions of the world, particularly Asia, the growth in the transport sector, at least in the period up until 2030, is forecast to be extraordinary. It has been widely stated that during the next 20 years, there will be more vehicles manufactured in the world than there have been in the entire previous history of the automotive industry. In this regard, the number of operational vehicles

today worldwide is estimated at close to 800 million, whereas this figure may rise to as many as 2 billion by 2030 with most of this growth occurring in Asia (ISEE, 2009). Annual production of vehicles globally will more than double from around 73 million vehicles per year (2007) (OICA, 2008) to a value expected to be more than 160 million vehicles per year by 2030.

When this manuscript was compiled in 2009, it seemed clear that the general use of aluminium worldwide would continue to increase, despite the many major economic challenges facing both the aluminium industry, and the manufacturers who buy the metal. An examination of the per capita usage can provide a glimpse of the future of aluminium as an engineering material, and its prospects. In 2009, the global usage of aluminium is estimated at 6 kg per capita, whereas by 2030, this value based on perceived demand has been predicted to double (Greenland Development Inc., 2009). In the same time frame, the global population is predicted to rise by approximately 1.3 billion people to reach 8.1 billion (United Nations, 1999). Table 1.4 gives some indications as to where the greatest capacity for growth in aluminium may reside. Although it is a common perception that recent growth in aluminium consumption for many western countries has not been as rapid as for developing countries, trends do show that substantial increases have occurred in many western countries (e.g. Belgium, the Netherlands). Further significant increases are also possible for others (e.g. Ireland, Greece, France and Australia). However, the greatest future growth will be in developing regions where demand is high, such as in India, elsewhere in Asia and in Africa (note current consumption figures for Africa are not available, but have been estimated at less than 1 kg per capita (Equity Master, 2008)). As an example, on recent growth figures, the per capita usage of aluminium in China has doubled approximately every 5 years since about 1994, to the 2007 value of 9.7 kg per capita (Adams and Sattlethight, 2008). On this basis, it could be predicted that consumption in China will rise to at least 20 kg per capita by 2030 (i.e. a total of around 32 million tons).

Production of (primary) aluminium in China is forecast to exceed 30 million tons by 2030, which represents an increase of around 150% above the 2007 value of 12 million tons (Finnimore, 2007). During the same period, production in India is forecast to rise from around 1 million tons in 2007 to around 7–8 million tons by 2030, and it is to be expected that per capita consumption will also grow. Globally, it has been predicted that primary aluminium production will rise from its current level at around 38 million tons to over 80 million tons by 2030, close to 10 kg per capita (Finnimore, 2007). What is also clearly important in meeting the future demand is the role of secondary aluminium during the next 20 years and beyond. Inevitably, the economics of producing primary aluminium is strongly tied to the price of energy, and as a result, it is to be expected that secondary aluminium will also display levels of growth which closely parallel that of the primary metal.

Table 1.4 The 2002–2007 kg per capita usage of aluminium from a selection of 33 countries (Adams and Sattlethight, 2008)

	2002	2003	2004	2005	2006	2007
Australia	20.5	23.1	23.3	20.6	21	–
Austria	33.8	39.9	34.2	26.2	–	–
Belgium	19.3	19.2	33.9	33.4	33.8	40.2
Bulgaria	N/A	N/A	5.3	6.9	9	9.1
Brazil	4.1	3.8	4.1	4.4	4.6	5
Canada	30.1	29.3	31.1	30.2	30.6	28.6
China	3.8	4.8	5.6	6.5	7.3	9.7
Denmark	23.5	25	29.2	27.6	25.8	23.2
Estonia	–	–	8	9.2	15.6	10.4
Finland	16	15.3	17.6	17.3	19.8	21.8
France	22.2	21.9	21.9	20	20.4	21.5
Germany	30.6	30.4	34.7	34.5	38	39
Greece	14.6	15	16.9	16.3	16	17
India	0.7	0.4	0.4	0.5	0.5	0.6
Ireland	13.2	14	10.8	14.2	13.4	13
Italy	28.5	30.3	30.3	29.7	30.9	32
Japan	28	30.9	32.3	34.3	33.3	33
Republic of Korea	21	21.3	23.4	25	26.3	26.6
Latvia	–	–	1.1	2.1	2.5	2.4
Lithuania	–	–	2	2.3	3.1	3.5
Mexico	5	7.5	8	7.6	7.7	8
The Netherlands	24.6	24.3	30.6	43.5	53.1	45.6
Norway	27.2	27.8	19.3	24	–	–
Philippines	0.9	0.9	0.8	0.8	0.7	2
Slovenia	22	30.9	46.8	33.6	42.5	39
South Africa	4.7	4.2	3.7	4.3	4.5	4.6
Spain	20.3	21.7	28.4	28.4	29	30.5
Sweden	29.1	29.1	26.6	28	28.9	36.5
Switzerland	20.7	21.6	24.7	24.3	–	–
Turkey	3.6	4.3	5.3	5.8	6.3	7.3
United Kingdom	18.3	24.3	21.1	17.6	25.7	25.5
United States	32.7	32.3	34.4	34.3	34	31.3
Venezuela	5	5.4	5.4	5.3	6.8	–

1.7 Conclusion

This book, *Fundamentals of Aluminium Metallurgy*, has been compiled on topics related to this metal and its alloys by engineers and scientists from academia and industry who are eminent and active in this field. The chapters have been structured to present specific topics related to the metallurgy of aluminium, its production and uses. Special attention has been given to new advances in technology and understanding that have been developed so as to further the utilization of this metal and its alloys. The book is not an exhaustive account of metallurgy as applied to aluminium and its alloys (to do so would require several volumes!).

Rather the aim is to provide an overview of many of the recent advances that may contribute to the long-term future of this industry.

1.8 References

- Adams, N. & Sattlethight, H. (2008), *Aluminum Statistical Review for 2007*, The Aluminum Association, Arlington, VA, USA
- Armistej, (2006), 'Wright Brothers', available from: http://en.wikipedia.org/wiki/Wright_brothers (accessed May 2009)
- Bonollo, F., Urban, J., Bonatto, B. & Botter, M. (2005), Gravity and Low Pressure diecasting of Aluminium Alloys: a Technical and Economical Benchmark, *La Metallurgia Italiana*, 6: 23–32
- Bray, E.L. (2009a), US Geological Survey, Mineral Commodity Summaries, January 2009, p. 29, available from: <http://minerals.usgs.gov/minerals/pubs/commodity/bauxite/mcs-2009-bauxi.pdf> (accessed May 2009)
- Bray, E.L. (2009b), U.S. Geological Survey, Mineral Commodity Summaries, January 2009 pp. 18–19, available from: <http://minerals.usgs.gov/minerals/pubs/commodity/aluminum/mcs-2009-alumi.pdf> (accessed May 2009)
- Buckingham, D.A., Plunkert, P.A. and Bray, E.L. (2008), Historical Statistics for Mineral and Material Commodities in the United States US Geological Survey, available from: <http://minerals.usgs.gov/ds/2005/140/aluminum.xls> (accessed May 2009)
- Cahn, J.W. (1984), Erratum: Age Hardening of Aluminium Alloy, *Bulletin of Alloy Phase Diagrams / Journal of Phase Equilibria*, 5(1): 21
- Eastwood, L.W. (1946), *Gas in Light Alloys*, New York: John Wiley and Sons
- Equity Master (2008), 'Aluminium', available from: <http://www.equitymaster.com/research-it/sector-info/aluminium/> (accessed May 2009)
- European Aluminium Association (EAA) (2008), 'Aluminium in Cars', available from: http://www.eaa.net/upl/4/en/doc/Aluminium_in_cars_Sept2008.pdf (accessed May 2009)
- Finnimore, P. (2007), 'UC Rusal, Chinese and Russian Aluminium Industries Partnering for the Future', available from: http://www.rustocks.com/put.phtml/rual_083007.pdf (accessed May 2009)
- Furet, G. (2008), 'EDF Electric Transportation Newsletter, number 85', available from: <http://www.challengebibendum.com/challengeBib/document.DocumentRepositoryServlet?codeDocument=6279&codeRepository=MICHA&codeRubrique=SRM2008> (accessed May 2009)
- Greenland Development Inc. (2009), 'The Global Demand for Aluminium', available from: http://www.aluminium.gl/content/us/about_the_project/aluminum/the_global_demand_for_aluminium (accessed May 2009)
- International Organisation of Motor Vehicle Manufacturers (OICA) 2007 Statistics (2008), available from: <http://oica.net/category/production-statistics/2007-statistics/> (accessed May 2009)
- International Sustainable Energy Exchange (ISEE) (2009), 'Global challenges /Transportation Growth / Automotive', available from: <http://www.hartisee.com/index.php?page=world-transport-growth> (accessed May 2009)
- Kirgin, K. (2009), Feeling the Domino Effect, *Modern Casting*, 99(3): 34–36.
- Lange, F.A. (1873), Improvement in the Manufacture of Springs for Watches and Other Time Pieces of Aluminium Compounds, US Patent 139678

- The Manufacturer and Builder* (1877), Alloys of Aluminium, 9(9): 201. Western and Company, New York (H.N. Black, publisher, W.H. Wahl, editor), available from: http://cdl.library.cornell.edu/moa/moa_browse.html
- The Manufacturer and Builder* (1879), Cost of Aluminium, 11(5): 120. Western and Company, New York (H.N. Black, publisher, W.H. Wahl, editor), available from: http://cdl.library.cornell.edu/moa/moa_browse.html
- The Manufacturer and Builder* (1881), Alloys of Aluminium, 13(11): 254–255, Western and Company, New York (H.N. Black, publisher, W.H. Wahl, editor), available from: http://cdl.library.cornell.edu/moa/moa_browse.html
- The Manufacturer and Builder* (1886), Properties of Aluminium, 18(1): 13. Western and Company, New York (H.N. Black, publisher, W.H. Wahl, editor), available from: http://cdl.library.cornell.edu/moa/moa_browse.html
- The Manufacturer and Builder* (1892), The Uses of Aluminium, 21(6): 132–133 (summary of the lecture given to the Franklin Institute by Capt. A.E. Hunt of Pittsburgh), Western and Company, New York (H.N. Black, publisher, W.H. Wahl, editor), available from: http://cdl.library.cornell.edu/moa/moa_browse.html
- Minet, A. (1902, 1905), *The Production of Aluminium and its Industrial Use*, 1st ed., 1905, New York, J. Wiley and Sons., Chapman and Hall, London, translated to English by Leonard Waldo, from the German text ‘*Die Gewinnung des Aluminiums und dessen Bedeutung für Handel und Industrie*’, 1902. available from: <http://www.archive.org/details/productionofalum00minerich>
- Polmear, I.J. (2006), *Light Alloys: From Traditional Alloys to Nanocrystals*, 4th ed., Butterworth Heinemann, p. 12
- Research and Innovative Technology Association (RITA) (2009), US Department of Transportation, Bureau of Transportation Statistics, available from: http://www.bts.gov/publications/national_transportation_statistics/html/table_01_17.html (accessed May 2009)
- United Nations (1999), Population Division, Department of Economic and Social Affairs, United Nations Secretariat, The World at Six Billion, available from: <http://www.un.org/esa/population/publications/sixbillion/sixbillion.htm> (accessed July 2009)
- Wilm, A. (1911), Physical-Metallurgical Experiments on Aluminium Alloys Containing Magnesium, *Metallurgie* 8: 223. (Translated to English). In: Martin, J.W. (1968) *Precipitation Hardening*, 22: 103–111, Pergamon Press, Oxford

J. METSON, The University of Auckland, New Zealand

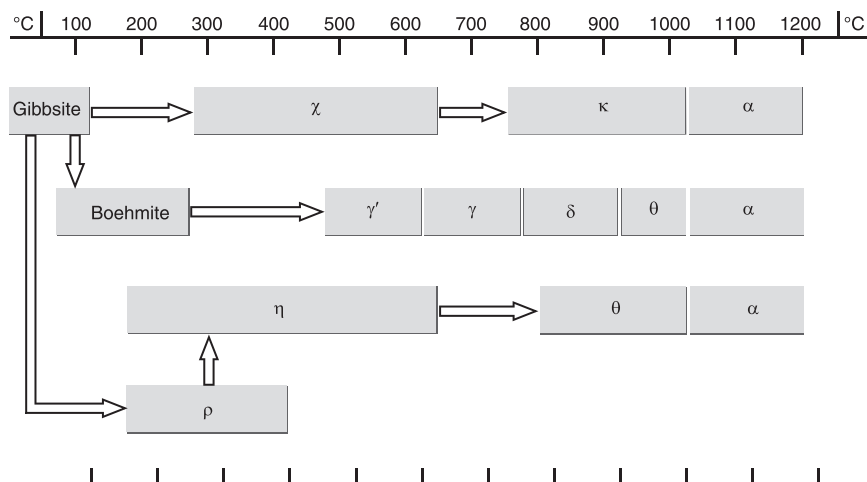
Abstract: Aluminium minerals are abundant in the earth's crust with equatorial lateritic bauxites the dominant Al bearing resource used as the raw material for alumina production. The Bayer process, essentially unchanged for more than 100 years, accounts for much of this production. The process involves ore digestion in a hot caustic soda solution, the clarification of a sodium aluminate solution and the precipitation of aluminium hydroxide, subsequently calcined to produce alumina. Refinery operation and particularly the processes of gibbsite precipitation and calcination have a profound effect on the properties of the product alumina, and its use in the production of aluminium metal in the Hall-Héroult process. Although around 95% of alumina production is used in primary metal production, there are also increasing specialist markets for alumina in applications as diverse as catalysis, in microelectronics and as an absorbent.

Key words: alumina, bauxite, Bayer process, calcination, microstructure, catalysis.

2.1 Introduction to the aluminium oxides

Aluminium is the most abundant metallic element in the earth's crust, with its oxides, hydroxides and aluminosilicates ubiquitous in the terrestrial environment. Aluminium is a light element with a dominant formal oxidation state of three and it might be expected that the oxide chemistry would be relatively straightforward. However, a large diversity of phases or 'forms' of the oxide of stoichiometry Al_2O_3 is known. Commercially these are prepared in pure form by the calcination of gibbsite $[\text{Al}(\text{OH})_3]$ or boehmite (AlOOH) . The structural richness of the oxides is highlighted in a series of transition aluminas; here transitional means that they are thermodynamically unstable intermediates on a pathway, as a function of temperature, to the thermodynamically stable alpha alumina structure as shown in Fig. 2.1. However, the transition aluminas are important in their own right and indeed dominate the commercial production of aluminas, including metallurgical grade aluminas used as a feedstock for the production of aluminium metal. The most authoritative description of the interrelationship of the alumina phases or 'forms' as a function of calcination temperature is provided by Wefers and Misra (1987).

Although the bulk oxide chemistry of aluminium is dominated by the forms of Al_2O_3 , suboxides of aluminium, in particular Al_2O and AlO , have been reported at the interface between the metal and surface oxide films, however the literature in this area is contentious. There is limited evidence for these phases in the solid state (MacKenzie, 1968), but there is strong evidence for suboxides at the



2.1 The relationship of alumina phases, or forms, arising from the calcination of Gibbsite, to calcination temperature (diagram adapted from Wefers and Misra (1987)).

metal/oxide interface. This can be interpreted as oxygen penetration into the metal lattice at the interface (Eberhardt and Kunz, 1978). The cohesion, stability and strength of interfacial bonding of the protective oxide layer on aluminium metal are indeed critical to the utility of the metal. The metal is sufficiently reactive that when exposed it reacts strongly with air, thus the metal is never found naturally in its native state.

2.2 Al minerals – mining and processing

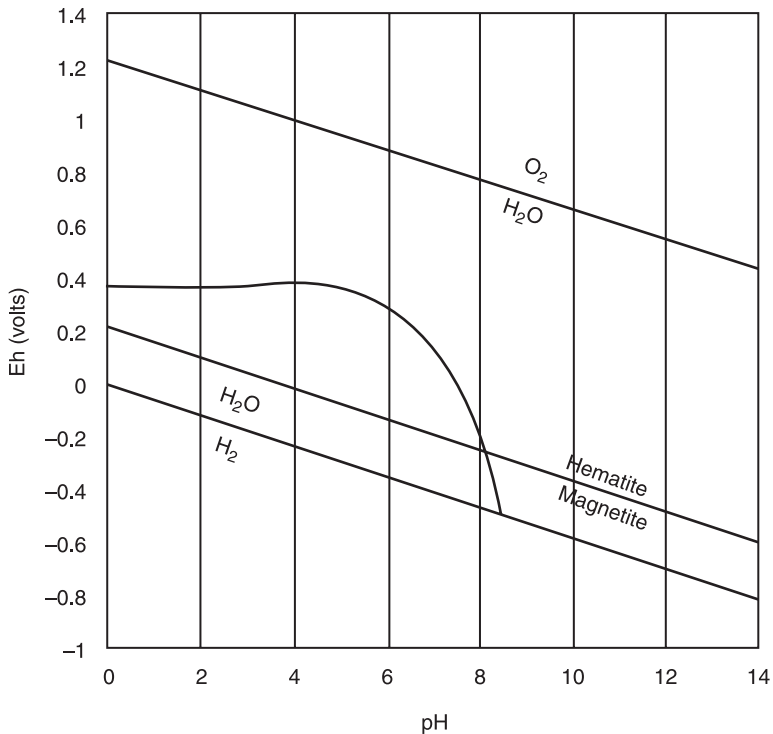
Calculated as an oxide, aluminium constitutes around 15.3 wt% of the non-water content of the earth's crust (Weast, 1974). The primary ore of relevance to the aluminium industry is bauxite, a mixture of aluminium hydroxides and oxyhydroxides, accompanied by varying amounts of iron oxides, silicates and other impurities. In 1821, Pierre Bertier offered the first description of such reddish brown deposits found near a village in southern France named Les Baux-de-Provence, from which the name bauxite originates. Such deposits are classified as aluminous laterites (Hancock and Skinner, 2000), with gibbsite, aluminium hydroxide, as the prevailing aluminium containing phase. The economically important deposits are now the tropical silicate bauxites which are formed by weathering at the surface of various silicate rock formations such as granites, gneisses, basalts, syenites, clays and shales.

The mechanism of formation of such deposits defines their equatorial location. Warm and mildly acidic rainfall acts to leach and alter primary minerals, gradually removing predominantly silicates. The zones with highest Al contents are

frequently located below an iron rich surface layer and are due to downward leaching and reprecipitation of aluminium which is more soluble than iron under oxidising conditions (Costa, 1997; Kogel et al., 2006). This process is illustrated in Fig. 2.2. The economically important bauxite deposits are thus concentrated on areas of high rainfall, generally on large continental land masses close to the equator. Significant deposits of such lateritic bauxites are found in Australia, Brazil, Guinea and India together with Guyana, Suriname and Venezuela.

The known reserves of bauxites are estimated to be 55–75 billion tons, located in Africa (33%), Oceania (24%), South America and Caribbean (22%), Asia (15%) and elsewhere (6%) (USGS, 2009). This compares with ≈ 190 M tons mined in 2007. Such bauxitic ores currently provide the lowest cost pathway to the production of high-purity aluminium oxides.

Between 93% and 95% of the total alumina production is used as a feedstock for metal production (International Aluminium Institute, 2008). The balance is



2.2 The Eh-pH diagram at 25°C mapping the weathering conditions generating pathways to bauxite deposits, adapted from Norton 1973. In the shaded area Al minerals are more soluble than Fe minerals, while in the lighter area above the H_2/H_2O boundary, the Fe minerals are more soluble.

used across a wide range of applications, with this diversity strongly related to the structures and properties of the various forms of the oxide. Diversity of application is well illustrated by the high temperature, thermodynamically stable oxide Alpha alumina. In its impure form, it is widely used as corundum in industrial abrasives, however it also occurs naturally as a gemstone, in its ruby and sapphire polymorphs. Melt growth single crystal sapphire is also widely used in microelectronics as a substrate for the growth of semiconductor materials, for example as the substrate in the fabrication of GaN-based blue diodes (Nakamura et al., 1994; Nanjo et al., 2009). The balance of alpha alumina production is used primarily in ceramics, refractories and abrasives. The excellent dielectric properties of thin films of the oxide give rise to applications in capacitors and other electronic devices. The anodic growth of such films, both for electronic and surface protection and decorative applications, is a mature technology.

The production of aluminas is dominated by variations on the process patented by Karl Josef Bayer. Laterite-type ores are dissolved in hot caustic soda while iron oxides and silica are insoluble in this pH range and are separated out as a red mud residue. Gibbsite $[\text{Al}(\text{OH})_3]$ is precipitated from the decanted and clarified sodium aluminate liquor. The bulk of the filtered gibbsite product from precipitation is then calcined to yield a range of target alumina phases. The overwhelming proportion of this industrial alumina is then transported to smelters of the electrolytic production of aluminium metal. There is also a significant market for gibbsite itself, industrially known as ‘trihydrate’. For example, this is used as a fire retardant in fabrics and in mixing with acrylic resins to produce a range of hard, wear resistant and fire retardant composites used widely in construction for interior surfaces (Dando et al., 1996; Horn, 1998). The trihydrate terminology arises from the common (mis)representation of gibbsite as a hydrated oxide of aluminium:



Partial calcination is also used to produce a range of speciality aluminas for example for catalyst and absorbent applications.

In the laterite ores described above, three minerals are of primary importance in the viability of alumina production: the hydroxide gibbsite $[\text{Al}(\text{OH})_3]$, and the two oxyhydroxides (AlOOH), boehmite and diaspore. Deposits rich in these minerals are generally recovered using opencast strip mining and the classified product sent to the Bayer refinery. The oxyhydroxides and particularly the high pressure polymorph diaspore require higher digestion temperatures, which makes them less attractive resources for the Bayer process. Such deposits are however becoming increasingly important in regions of the world such as China, which lack gibbsitic ores. Current estimates suggest 98% of Chinese bauxite is of this diasporic type (Zhao et al., 2005). Hard rock minerals such as nepheline $(\text{Na}_3\text{KAl}_4\text{Si}_4\text{O}_{16})$ have also been historically exploited as alumina resources for similar reasons (Liu et al., 2009; Vinograd et al., 2009).

For alumina production, the quality and viability of bauxite deposits is largely determined by the Al:Fe and Al:Si ratios, and the speciation of the Al-containing minerals as described above. The speciation of the Si (e.g. quartz vs aluminosilicates) is critical in determining the reactive silica – which is susceptible to digestion in the Bayer process. A highly reactive Si limits the kinetics of the digestion process as a holding time is needed for desilication – the precipitation of a desilication product – and incorporation of sodium in the product results in excess consumption of caustic soda. This imposes a practical upper limit in Western refineries of around six per cent to seven per cent in reactive silica in the bauxite feed. Impurities, including organic material, are the other critical determinant in the viability of processing and quality of product.

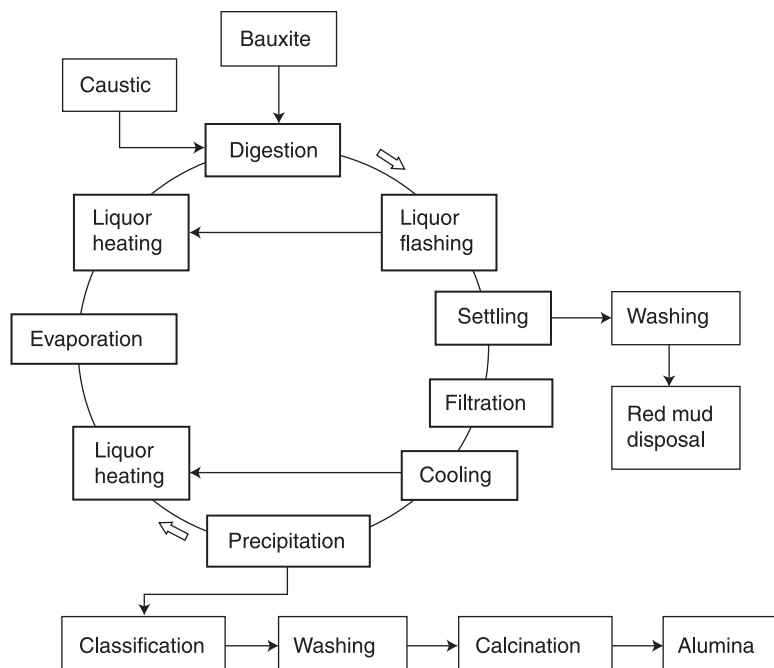
Bayer plants have historically been located in countries where the aluminium was produced, exemplified by the refineries on the US Gulf Coast. However, the volume of bauxite transported, over half of which eventually ends as waste, means that more recent plants are primarily located proximal to the bauxite deposits that provide the raw materials for processing. Trucks, belt conveyors or slurry pipelines, some over considerable distances, are then to be used to transport raw material from mine to refinery (Sant'Ana et al. 2008).

As with the Hall-Héroult process for metal production, alumina production has grown steadily with minimal change to the Bayer process, driven by a steadily increasing demand for the metal, and in lesser quantities, for specialty oxides. For every tonne of primary metal, 1.92 tonnes of alumina are required. Thus, the tonnage of alumina produced rises at approximately twice the rate of growth in metal production.

2.3 Alumina production processes

The process described in the patent of Karl Bayer in 1887 proved pivotal in completing the production cycle for aluminium, by providing an inexpensive route to the large-scale production of the primary raw material, alumina. Ironically, Bayer's interest was in the supply of alumina to the textile industry where it was used as a fixing agent in the dyeing of cotton. Bayer's discovery was that gibbsite $[\text{Al}(\text{OH})_3]$ precipitated in a more useful crystalline form from alkaline solution than it did from the neutralisation of acid solutions. Thus, the digestion of bauxite in hot caustic solutions, the separation from the undissolved red mud containing most of the iron and silica, and the filtration and calcination of the precipitated gibbsite rapidly became the standard alumina production method. A schematic of this process is shown in Fig. 2.3, and it remains largely unchanged from Bayer's original concept.

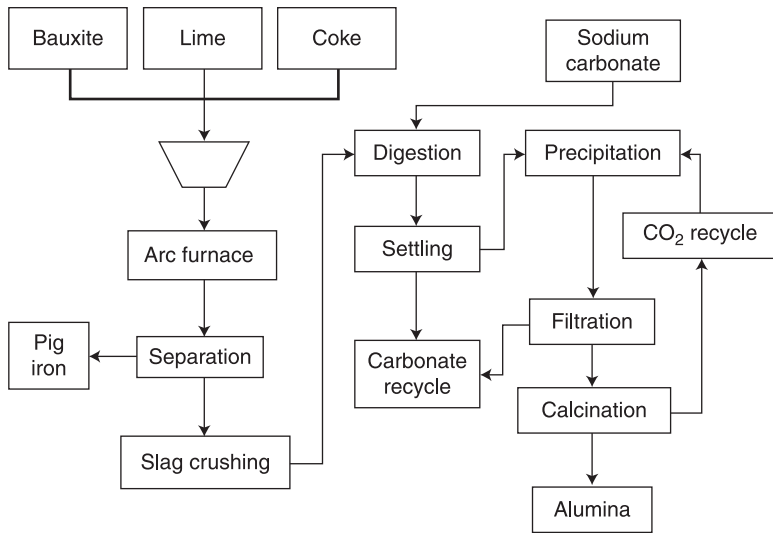
Accommodating lower grade, and especially diasporic (AlOOH) , ores has introduced variants on treatment before and after digestion, with combined processes such as presintering with lime and the Lime-Bayer process increasingly used in China. Other processes have been used on a small scale to process



2.3 A flowsheet of the Bayer process for alumina production. The liquor circulates in the direction of the arrows and steam is transferred across the circuit to preheat the spent liquor before recycle into digestion.

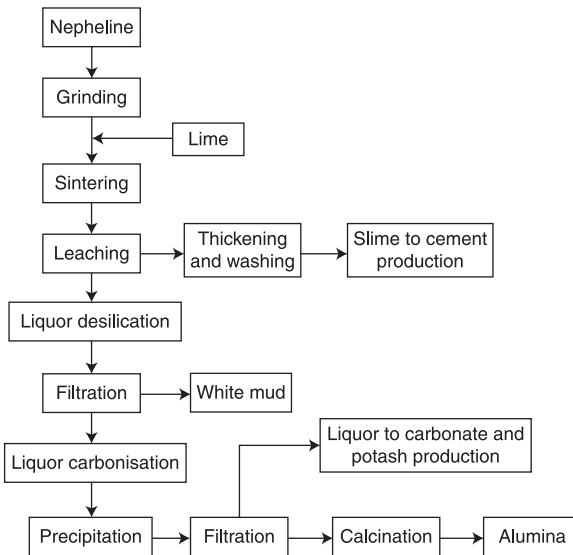
particular bauxitic ores. The Pedersen Process (Miller and Irgens, 1974; Nielsen, 1978) is based on the processing of laterite ores of a lower $\text{Al}_2\text{O}_3:\text{Fe}_2\text{O}_3$ ratio than typical bauxites. The smelting of such ores with lime and coke produces a pig iron product and a calcium aluminate slag (Fig. 2.4). The slag, which disintegrates on cooling due to a particularly favourable volume expanding phase change, is then leached with sodium carbonate to generate a sodium aluminate liquor. Gibbsite is then produced by the injection of carbon dioxide into this liquor stream. The simplicity of the process and the value of the iron by-product have made this option of interest for iron rich ores and such a plant was operated on a small scale in Norway for over 40 years. From time to time, high steel prices prompt a re-examination of the viability of the process, but this currently remains non-competitive with the conventional Bayer process.

The processing of nepheline $(\text{Na,K})\text{AlSiO}_4$ has also been used for alumina production, particularly in Russia (Smirnov, 1996). The mineral concentrate is sintered with limestone and following alkali tube digestion and further processing, the resulting liquor is autoclaved and the resulting filter cake calcined to produce alumina (Fig. 2.5). Key to the economics of this process is again the value of the by-product streams. The residue from tube digestion is fed to a cement kiln, while



2.4 A flowsheet for the production of alumina using the Petersen process.

the liquor from alumina filtration is also processed to yield high purity potassium and sodium carbonates. Stepanov and Stepanov (1998) estimate that the processing of 3.9–4.2 mt of nepheline ore yields 1 mt of Al_2O_3 , 0.6–0.8 mt of soda, 0.2–0.3 mt of potash and 9–10 mt of Portland cement.



2.5 Flowsheet for alumina production based on the sintering of nepheline.

2.4 The Bayer alumina refinery

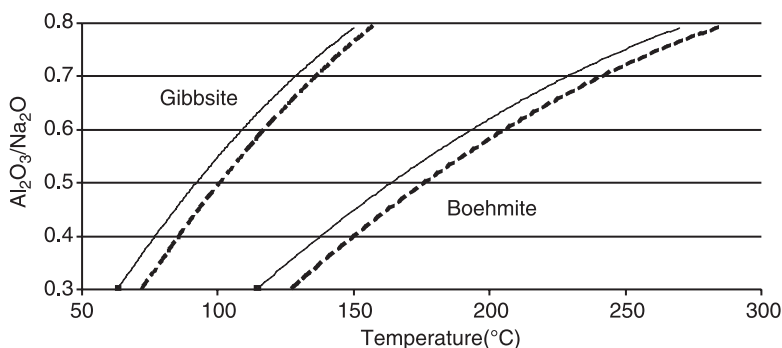
The Bayer process, illustrated in Fig. 2.3, currently dominates world alumina production and remains little changed from the original concepts of Karl Bayer. Starting with a gibbsite rich bauxite feed, there are four distinct stages to this process:

- Digestion
- Clarification
- Precipitation
- Calcination.

Refinery configurations are similar with variation primarily in digestion to optimise temperature for the particular ores being processed or to allow pre-treatment – e.g. sintering with lime, to again aid digestion. The alumina product for the dominant smelter or metallurgical grade market is also increasingly similar as the requirements of the smelting process are increasingly tightly prescribed.

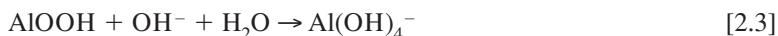
2.4.1 Digestion

In the first stage, the ground bauxite is mixed with recirculating hot caustic liquor and passed into a digestion vessel. Dissolution of the aluminium containing minerals, oxides, hydroxides and silicates occurs at temperatures which are customised according to the nature of the ore. Gibbsitic ores can be processed at relatively low temperatures, indeed in isolated cases at atmospheric pressure, while boehmitic and diasporic ores are digested at temperatures up to 250°C (Fig. 2.6).



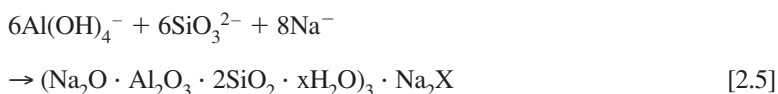
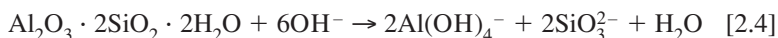
2.6 The temperatures needed for bauxite digestion. The solid line is calculated for a caustic concentration of $2.36 \text{ M l}^{-1} (\text{Na}_2\text{O})$, while the dashed line is for 1.9 M l^{-1} . Recalculated from the diagram of Den Hond et. al. (2007).

The basic reaction of digestion can be represented as:



The sodium aluminate, red mud mixture is then passed through a series of pressure-reducing tanks called blow-off tanks, where the solution is flashed to atmospheric pressure, the steam recovered being used to heat the spent liquor being returned into the digestion circuit (Fig. 2.3).

The digestion of aluminosilicate minerals also occurs during digestion of the ore, however silicate ions are subsequently unstable in the pH range of the Bayer solution and precipitate as a desilication product. This process can be represented by the dissolution of kaolinite:



where X can be a range of anions, but is typically carbonate or sulphate.

Desilication product is then settled out during the clarification of the digestion liquor and exits with the red mud. The optimisation of this process is critical to the efficient operation of the digestion circuit as the process is significantly slower than digestion itself, but is important in both lowering dissolved silica in the liquor stream and in the co-precipitation of a number of major impurities. A pre-desilication process is thus sometimes used, where the caustic is mixed with the incoming ground ore and held before feeding into the main digestion circuit. The desilication process also contributes to some of the more persistent plant maintenance issues, causing scaling in heat exchangers and vessels in the digestion train.

The objective of the digestion process is to achieve the best compromise between a high dissolved alumina burden in the pregnant liquor (high sodium aluminate concentration) and the highest possible extraction efficiency from the ore being processed. Increasingly, this optimisation also includes minimising losses of potential alumina yield through, for example, the premature precipitation of gibbsite during digestion, and loss into the red mud residue. This limits the total yield in extraction and thus the alumina to caustic ratio in the pregnant liquor. Thus, while Den Hond et al. (2007) calculate a theoretical maximum yield of 675 g l⁻¹ in digestion and 160 g l⁻¹ in precipitation, as pointed out most plants operate little higher than half these numbers, certainly for the latter quantity.

In most plants digestion is the most energy intensive part of the Bayer process. Overall energy consumption in alumina production is quoted between 9.6 GJ t⁻¹ for a near pure gibbsite ore and double this number for a mixed gibbsite and boehmite/diaspore ore (Liu et al., 2006). This compares with up to 50 GJ t⁻¹ when a highly

diasporic ore is processed in a combined sinter process. Thus, overall energy demand is driven primarily by the nature of the ore and the digestion temperatures required (Fig. 2.6). To limit energy consumption, there is considerable emphasis on energy recovery from the flash train and on processes such as sweetening. In sweetening, high grade, easily digested, gibbsitic bauxite is added late in the digestion circuit, at temperatures of 150–180°C, to push up the alumina to caustic ratio in the pregnant liquor. The speed of digestion, and the lack of opportunity for further desilication, means this process requires a particularly high-grade ore.

2.4.2 Clarification

The red mud, containing the iron oxides, desilication product and quartz, is then settled out of the slurry in large settling tanks. The addition of flocculating and dewatering agents is critical in the productivity of this step and in limiting the carryover of impurities. The supersaturated sodium aluminate containing liquor overflows the settlers and is filtered for final clarification before passing to the precipitation circuit.

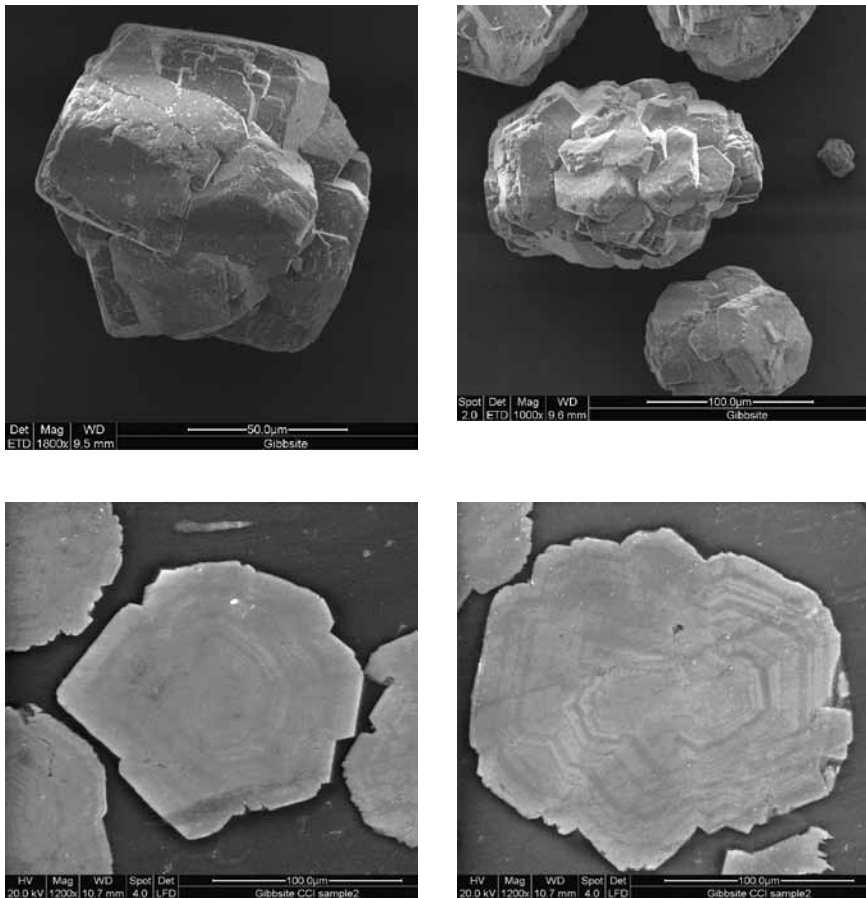
The solids from the settlers are washed in several stages of countercurrent washing to maximise caustic recovery. This is important not only to raw materials costs, but in the ease of neutralisation and disposal of the red mud residue. The mud is then generally treated in a number of ways – for example neutralisation by mixing with seawater and sent to tailings ponds. Given that more than half of the incoming bauxite feed may end up in red mud disposal, this disposal is a large and persistent problem. Uses for this material have been limited to date (Nunn, 1998; Pilurzu et al., 1999), and rehabilitation of the red mud disposal areas is the widely practised alternative.

2.4.3 Precipitation

The supersaturated sodium aluminate liquor is quite stable and is seeded, typically in several stages, with fine and then coarser gibbsite to initiate and sustain particle growth and agglomeration. As particles grow, the solution, containing an increasing burden of gibbsite crystals, is passed through a series of tanks with increasing solids content, decreasing alumina to caustic ratio, and decreasing temperature forcing higher supersaturation. The growth of particles in the precipitation tanks is generally the rate limiting step in the productivity of the alumina refinery, and is driven by the degree of supersaturation of the incoming liquor and the temperature drop across the chain of precipitation tanks. Increasing tank volumes and thus holding times, to further push the yield of precipitated gibbsite, is countered by the capital cost of these large stirred tank reaction vessels.

Current generation Hall-Héroult reduction cells are typically point feed and require a so-called ‘sandy’ alumina for adequate feed control (Grjotheim and Welch, 1988). Such aluminas must meet specified limits for per cent (by weight)

of fine and coarse particles, as discussed below. In gibbsite precipitation, agglomeration of particles is a much more effective route to producing sufficiently large particles than waiting for the growth of individual particles. These agglomerated particles are also considered somewhat stronger in accommodating the shrinkage of the lattice during the calcination process (see Section 2.4.4). Thus, the initial fine seeding is optimised to encourage agglomeration, while a coarser seed is subsequently added to maximise the available surface for particle growth on bigger particles. Optimising yield, while maintaining a sufficiently large particle size distribution, is a delicate balancing act for the refinery (Garner et al., 1999). When sufficiently large, the resulting agglomerated particles (see Fig. 2.7) are cyclone classified, recovered on a pan filter and washed prior to calcination.

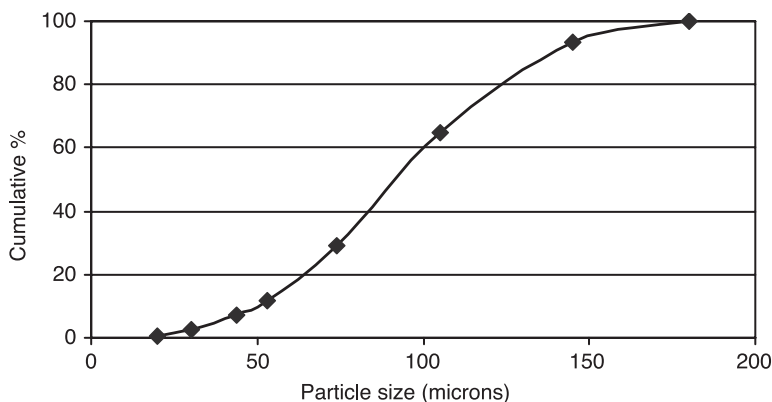


2.7 Scanning electron microscope images of agglomerated gibbsite particles from precipitation (upper images), and in cross-section (lower images).

The slow rate of gibbsite growth (typically a few $\mu\text{m hr}^{-1}$) at typical supersaturations (Misra and White, 1971; White and Bateman, 1988) means the volumes of liquor held in the circuit are high and a typical particle may pass through the circuit several times to grow to recoverable size. In cross-section, the internal microstructure of the gibbsite particle reveals several growth morphologies, frequently displaying a tree-ring like growth morphology (Fig. 2.7). The rings reflect variations in composition with the changing alumina to caustic ratio as the particle moves from tank to tank and cycles through the circuit. There are several complications which can limit growth in real circuits, such as the role of organics in constraining growth through adsorption on growing crystal faces (Bouchard et al., 2005) and the holding times which are practical in terms of tank capacity in the precipitation circuit.

The total temperature drop across the precipitation circuit typically ranges from 10 to 20°C, often aided by several stages of heat exchanger cooling between tanks. The temperature drop is limited by the compromise between forcing the maximum degree of supersaturation, and the slowing kinetics of particle growth as the liquor temperature drops. Thus, the yield from the equivalent total dissolved alumina in the pregnant liquor may reach only 50%, the balance being returned with the spent liquor to digestion.

Particle size requirements are typically expressed in a specification of the maximum per cent of the sample above a limit ($\% > 150 \mu\text{m}$) and below a minimum size ($\% < 40 \mu\text{m}$ or also $\% < 20 \mu\text{m}$). Thus, an example of particle size distribution from such a specification sheet is shown in Fig. 2.8. What must be remembered is that distribution by weight differs very significantly to distribution by particle number. To meet these size specifications, the initial particle size distribution of the precipitated gibbsite needs to be weighted to slightly higher particle sizes to allow for attrition during calcination and handling.



2.8 A particle size distribution measure for a typical Bayer process smelter alumina.

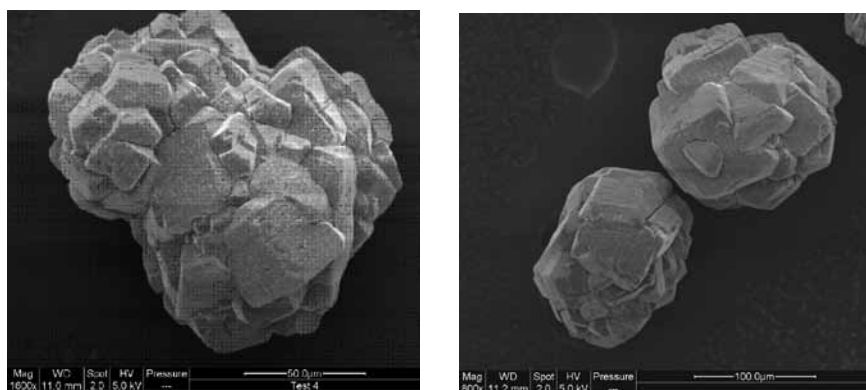
2.4.4 Calcination

Gibbsite from the precipitation circuit is recovered on a pan filter, following particle classification. The washed gibbsite is then fed into a calciner and heated to temperatures around 1000°C to produce the product alumina. Calcination is achieved in either rotary kilns or more commonly stationary calciners based on Recirculating Fluid Bed or Gas Suspension Technology.

Exposure to high temperatures induces a series of phase and structural changes as the hydroxide is converted to the oxide, as shown in Fig. 2.1. In gibbsite $[\text{Al}(\text{OH})_3]$ aluminium ions occupy two-thirds of the octahedral positions, with hydroxyl groups octahedrally coordinated in double layers. Upon heating, the hydroxyls are progressively lost through structural channels formed between the octahedral layers. Proton exchange between neighbouring hydroxyls gives rise to a water molecule which is then lost from the lattice (Lippens and de Boer, 1964; Rouquerol et al., 1975, 1979).

As the long range ordering in gibbsite is progressively lost, between 250°C and 300°C, boehmite (AlOOH) and the amorphous transition aluminas begin to appear. This is accompanied by the structural rearrangement of the crystal lattice, inducing a pseudomorphic transformation (i.e. the original crystal habit of the gibbsite structure is retained) with a little change in the external dimensions (see Fig. 2.9). As a consequence of the loss of structural hydroxides (as water), significant internal porosity develops. This internal porosity is critical in a range of applications of specialty aluminas in adsorption and catalysis, and in the use of metallurgical grade aluminas in gas cleaning in aluminium smelter dry-scrubbers (Gillespie et al., 1999; Grjotheim and Welch, 1988).

With increasing temperature, the phase sequence moves from the hexagonal gibbsite, $\text{Al}(\text{OH})_3$, through the oxyhydroxide boehmite, AlOOH , into the cubic



2.9 Scanning electron microscope images of typical agglomerated smelter grade alumina particles. Note the comparison with the morphology of the gibbsite particles shown in Fig. 2.7.

system represented by the spinel structured gamma alumina (Lippens and de Boer, 1964). Neutron diffraction studies indicate that the face centred cubic oxygen sublattice in the spinel-based transition aluminas tends to be highly ordered in these materials, the aluminium ions however are quite disordered, leading to the broadened lines typically observed in the powder X-ray diffraction (XRD) patterns of these materials (Zhou and Snyder, 1991). In these spinel structures, aluminium occupies both octahedral and tetrahedral sites. The proportion of tetrahedral sites occupied increases with temperature with 25–30% of the octahedral sites occupied for gamma-alumina until the transition to largely octahedral coordination in theta-alumina (Lee et al., 1997; Wefers and Misra, 1987; Wolverson and Hass, 2001). Whittington and Ilievski (2004) have studied this transition under conditions relevant to Bayer refineries.

The net reaction can be represented as:



The industry routinely uses the terminology of ‘trihydrate’ or $\text{Al}_2\text{O}_3 \cdot 3\text{H}_2\text{O}$ to represent gibbsite, and thus the calcination process is often erroneously referred to as dehydration, or loss of waters of crystallisation, from trihydrate, rather than the progressive removal of the hydroxide groups. The process of calcination initially involves proton captured by an adjacent hydroxyl, resulting in a water molecule which subsequently diffuses out of the structure. Complete calcination, involving the removal of all the hydroxyls and conversion to alpha alumina, is thus difficult and requires extended times at temperatures above 1000°C.

For smelter use, the incomplete removal of the hydroxides, and the microstructure this generates, is key to several critical aspects of smelter performance:

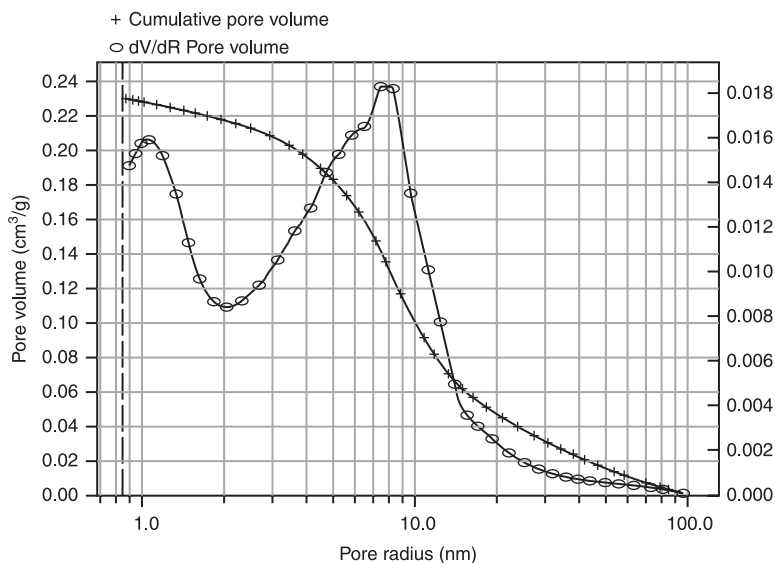
- The effective dissolution of the alumina in molten cryolite (Lillebuen, 2009). In dissolution, the break-up and rapid dispersion of alumina, when fed to the electrolyte, is critical to rapid dissolution and sludge minimisation. This is aided by the explosive release of residual moisture in the transition aluminas.
- The role of alumina as a gas cleaning medium in the dry-scrubbing of pot gases (Gillespie et al., 1999). In almost all smelters, the feed alumina is used first as the dry-scrubbing medium for cleaning cell gases before exhaust to atmosphere. The primary gaseous pollutant of interest is HF, and contact with alumina provides almost quantitative removal of HF from the process gas. It is less effective in the removal of other acid gases including SO_2 (Hay et al., 2004).
- The role of alumina, mixed with crushed electrolyte, as the cell cover material. This cover provides thermal insulation to the top of the cell, which acts as a primary gas containment and cleaning system, and limits the ingress of air, thus restricting air burning of the anodes.

The requirements outlined above are suited to a material of typical surface area in the 60–80 m^2g^{-1} range. In the transition aluminas, these surface areas are

associated with a network of pores in the nm range and their formation requires incomplete loss of the structural hydroxides of the original gibbsite. The pore-size distribution is readily measured and an example is shown in Fig. 2.10. During the initial formation of the transition aluminas, early in the calcination reaction, the mean pore size is less than 2 nm, and the specific surface area is very high, peaking at $350 \text{ m}^2\text{g}^{-1}$ and above (Grjotheim and Welch 1988). Upon further heating the migration of hydrogen and aluminium atoms and the loss of water will result in an expansion of the pore size and a progressive loss of this surface area.

Historical calciner technology has centred on rotary kilns, many of which are still in operation. In more modern plants, these have been displaced by stationary calciners using fluid bed or gas suspension technology (Reh, 1995). The capacity of such individual reactors now exceeds 4000 ton d^{-1} and energy consumption is quoted below 3 GJ t^{-1} alumina. This compares with a theoretical limit for a gibbsite of 5–10% residual moisture of around 2.5 GJ t^{-1} . The energy efficiency of calciners is now largely dictated by the efficiency of energy recovery in recycling waste heat to pre-heat the incoming feed.

Along with precipitation, calcination technology clearly plays a major role in the morphology, microstructure and phase composition of the product alumina (Perander et al. 2008, 2009). Metallurgical grade aluminas consist of a range of alumina phases or 'forms' dominated by the transition aluminas. Under the operational conditions of stationary calciners where heat transfer to the alumina particles is rapid, a continuum



2.10 The pore size distribution of a fluid bed calcined smelter alumina of surface area $70 \text{ m}^2 \text{ g}^{-1}$. Note the bimodal pore size distribution, with a dominant pore radius around 7 nm.

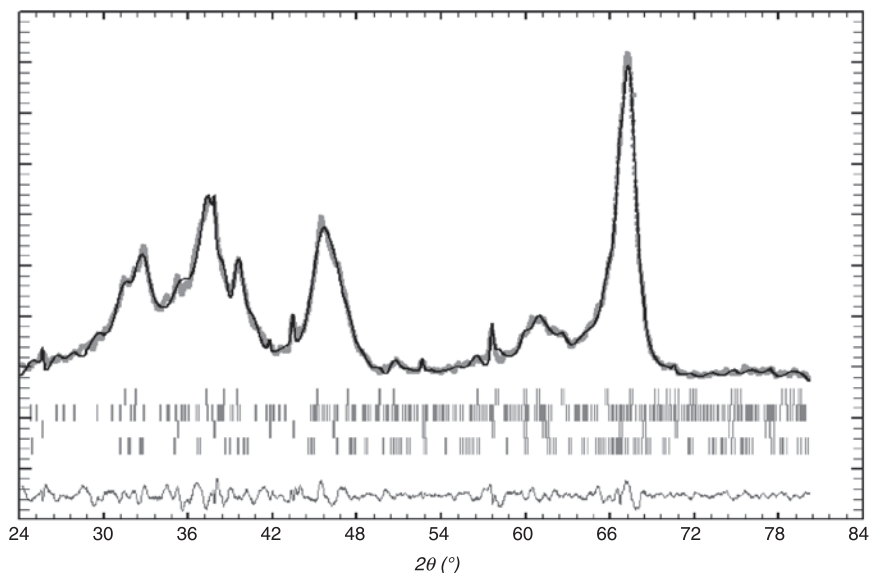
of phases is observed spanning the transition aluminas. Thermodynamically stable alpha alumina is typically less than 10% of the final product from this process. Calciner geometries that recirculate fines tend to over calcine fine particles, increasing alpha content in this fraction, while those that use high gas velocities are susceptible to by-pass, leading to the appearance of fine undercalcined gibbsite particles in the product alumina (Perander et al., 2008). Thus, fine particles are rarely of similar phase composition to the bulk alumina in which they appear.

2.5 Alumina microstructure

The thermodynamically stable alpha alumina is based on a hexagonal close packed array of oxygen ions, with aluminium ions occupying two-thirds of the octahedral sites. The transition aluminas dominant in metallurgical aluminas are defected spinels with structures indexed in the cubic system. As discussed above, in these materials the aluminium ions are distributed across both octahedral and tetrahedral sites (Wefers and Misra, 1987; Ashida et al., 2004), and indeed in MGAs the rapid calcination conditions cause a portion of these aluminums to be located in interstitial sites. The distribution of aluminums in different coordination geometries gives rise to a range of environments for the bonding of oxygen and hydroxyl groups important in the use of aluminas in catalysis – see Section 2.7.

A distinctive aspect of aluminas is the extensive discussion of the subtleties of the structures of the transition aluminas. The most extensive literature is available for gamma alumina, due to its importance as a catalyst and catalyst support. However, even gamma has several accepted structures involving slightly different indexing of the lattice. Indeed, the use of the gamma prime variant introduced by Paglia et al. (2004, 2006) measurably improves the refinement and interpretation of phase structure of the metallurgical grade aluminas. Ashida et al. (2004) have developed a model for the Rietveld refinement of metallurgical grade aluminas based on the gamma, gamma prime, theta and alpha phases which typically dominate this material. An example of such a spectral fit, and the accompanying phase analysis, is shown in Fig. 2.11. Such a phase analysis is complex and although useful in a comparative sense, over-interprets the importance of steps along what is essentially a continuous rearrangement of the structure through these transition aluminas. This is particularly so for metallurgical aluminas where the speed of the modern calcination process, together with the variation of particle size, velocity and residence time, inevitably produces a far from equilibrium phase distribution both between and within individual alumina grains. Such a model can be at best self-consistent, but is useful, for example in assessing the relative degree of calcination.

Solid state ^{27}Al Magic Angle Spinning–Nuclear Magnetic Resonance (MAS–NMR) studies can also provide considerable insight into Al occupancy in these structures. NMR chemical shift ranges for aluminium in different coordinations with oxygen (or hydroxyls) are typically 10–20 ppm for octahedrally coordinated aluminium (AlO_6), 30–40 ppm for pentahedrally coordinated aluminium (AlO_5)



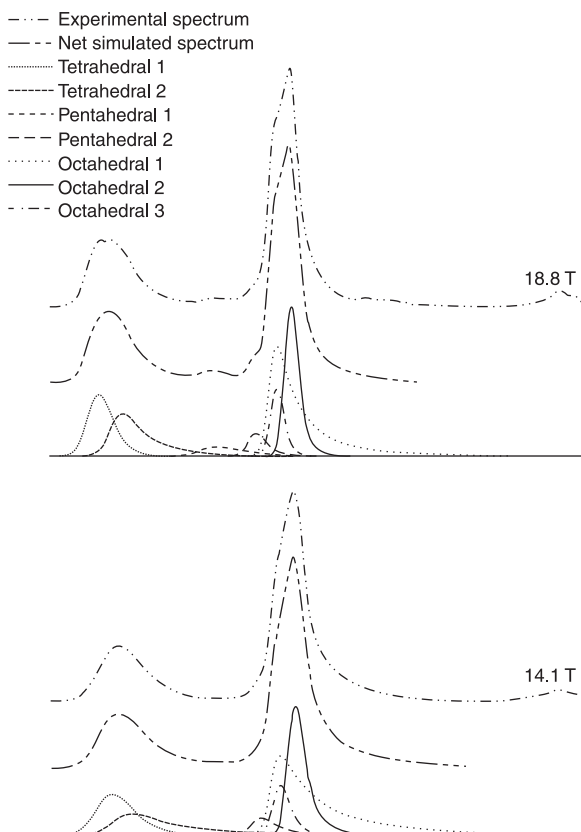
2.11 Rietveld refinement from the X-ray diffraction pattern of a typical stationary calciner produced alumina. The labelled line represents the fitted simulation and the lower trace indicates the residual deviation between the experimental and fitted data.

and 50–80 ppm for tetrahedrally coordinated aluminium (AlO_4) (John et al., 1983; Slade et al., 1991; Smith, 1993; Kunath-Fandrei et al., 1995).

The variation in the reported ranges for the chemical shift reflects the range of possible Al–O bond lengths and angles, and next-nearest-neighbour species. Several ^{27}Al studies have made use of the high sensitivity and the relatively minor contribution of particle and crystallite size effects of this technique to explore the transition aluminas (Lee et al., 1997; MacKenzie and Smith, 2002). MAS–NMR has also been very useful in defining onset temperatures of the transition reactions in the conversion of gibbsite into the transition aluminas as it does not require the development of sufficient size or long-range order needed for XRD detection of the phase.

In the NMR spectrum, second-order quadrupolar interaction is particularly problematic for aluminium, causing significant spectral broadening (MacKenzie and Smith 2002). This interaction dominates the central transition and has an angular dependence that is only partially averaged by conventional MAS. The interaction scales inversely with the applied magnetic field, so that high-magnetic fields are particularly advantageous for the examination of Al, as illustrated in Fig. 2.12. Increasing access to higher field instruments is steadily improving the usefulness of this approach in examining aluminas (Perander et al. 2007).

X-ray absorption near edge spectroscopy is another method sensitive to the chemical environment of all aluminiums and thus well suited to the poorly crystalline metallurgical grade aluminas. Studies of the Al K edge in transition



2.12 Comparison of high field ^{27}Al MAS NMR spectra of a commercial metallurgical alumina at two magnetic field strengths. The upper spectrum obtained on an 800 MHz spectrometer (18.8T) demonstrates the ability to resolve at least three distinct octahedral sites and two tetrahedral sites, indicative of different transition alumina phases. The small bump around 35 ppm suggests the presence of a small amount of Al in pentahedral coordination. By comparison, the same sample examined at lower fields typical of a 300 MHz instrument provides very limited structural detail (spectra courtesy of Professor Mark Smith, University of Warwick and Dr Zoran Zujovic, University of Auckland).

aluminas have been reported by Kato et al. (2001), however this approach has been limited to date.

2.6 Impurities

Bauxite deposits invariably contain a range of impurities, ranging from organic material to trace elements such as Ga, Zn, Pb, P and Be. Table 2.1 shows typical compositions of a range of smelter aluminas. In the Bayer process, many impurities

Table 2.1 Properties and analyses of a range of commercial metallurgical aluminas

Alumina	A	B	C	D	E	F	G	H
Na ₂ O ppm	3900	3700	3700	4300	3500	3800	4400	4700
SiO ₂	100	90	70	170	90	90	110	160
CaO	310	80	140	110	120	100	360	580
Fe ₂ O ₃	130	190	80	80	160	90	150	160
TiO ₂	40	40	20	10	30	40	40	20
Ga ₂ O ₃	140	130	100		100		150	
P ₂ O ₅	10	30	10	10	10	10	10	12
LOI (%)*	0.8	0.53	0.8	0.88	0.66	0.65	0.8	0.95
BET (m ² /g)†	72	68	76	80	72	70	70	72
Alpha %	9	2.8	2.9		5		5	5

Notes:

* Loss on ignition – the weight loss measured on heating from 300°C to 1000°C.

† Specific surface area measured by the BET method.

are at least partially soluble in the caustic digestion liquor and may be carried over into precipitation if they are not removed in the desilication product. The addition of lime is widely used to control some of these impurities, particularly phosphorus, by precipitation as their calcium salts. Certain impurities are of concern to the smelter, especially if high-purity grades of metal are being produced. Bath accumulation is also observed for some elements, calcium, phosphorus and occasionally beryllium being of ongoing interest. Phosphorus has been associated with losses in current efficiency (Haugland et al., 2001). Sturm and Wedde (1998) suggest a one per cent reduction in current efficiency in the reduction cell, per 100 ppm increase of P₂O₅ in the electrolyte. Surveys of aluminium smelter perceptions of alumina quality inevitably rank impurity content, along with particle size distribution, as of particular importance (Chandrashakar et al. 2005).

With respect to impurities, the capability of the refinery is significantly constrained by its bauxite source. The seeding of the sodium aluminate liquor and the growth and aggregation of gibbsite particles produce a material with varying levels of incorporated sodium, and other significant impurities, particularly calcium, silicon and iron, that will be carried through the process.

Sodium and calcium both have reduction potentials larger than aluminium and therefore accumulate in the electrolyte. The sodium specification in the input alumina is thus a key parameter in the scheduling of aluminium fluoride additions to the electrolyte to maintain a stable chemistry. Levels typically range between 0.25 and 0.5%. Almost all modern smelters target an acidic bath composition rather than pure Na₃AlF₆ (3NaF + AlF₃) with around 10% excess AlF₃. Soda additions with the alumina thus consume AlF₃. However, requirements also depend on the age and size of the reduction cells being used, and thus finding optimal soda levels can be a challenge for large alumina plants supplying a number of smelters.

Metallic impurities with lesser reduction potentials than Al largely report to the metal. Thus, their primary impacts are in metal quality and they may ultimately constrain capability in terms of the grades of metal a smelter is able to produce (Lindsay 2005, Dorion and Lindsay 2009). Most of these enter the process with the alumina; however several, such as Ni and V, enter predominantly with the petroleum coke and coal tar pitch used in anode manufacture (Metson and Hyland, 2001). It is notable that process improvements in Bayer plants have progressively been able to reduce impurity burdens in alumina, while the progressive move to the processing of increasingly sour crude oils has increased the impurity burden associated with petroleum cokes used in electrode manufacture (Vogt et al. 2004, Edwards et al. 2007).

2.7 Production of speciality aluminas

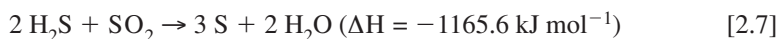
Although around 93% of alumina production is subsequently used as the feedstock in the smelting of the metal, there is a significant market for specialty aluminas. These markets lie in ceramics, particularly insulators and refractories, abrasives, catalysts, catalyst supports and absorbents. Some 4538 kT of such materials was produced for such markets in 2008 (International Aluminium Association, 2009).

Pure alpha alumina (corundum) has a Mohs hardness of 9.0, second only to diamond. The melting point of 2040°C for the pure material makes this useful for high temperature, high strength ceramics (Morrell 1987). Although an electrical insulator, it has a relatively high thermal conductivity ($40 \text{ W m}^{-1} \text{ K}^{-1}$) for a ceramic material, making it particularly useful in electrical insulators. The fabrication of such ceramics requires extended calcination of the green body at temperatures above 1300°C to complete conversion from the transition aluminas. Alpha alumina also occurs naturally as the gemstones ruby and sapphire, the colour depending on the nature of impurity substitutions in the lattice.

Outside of natural gemstones and the use of synthetic single crystal sapphire as a semiconductor substrate, the highest value uses, and the widest reported literature amongst the aluminas, are involved with the transition aluminas. The defect structure, surface acidity and high surface areas make these materials, and particularly gamma alumina, widely useful as absorbents, catalysts and catalyst supports. The surfaces exhibit both electron acceptor (Lewis acid acidity) and some proton donor (Bronsted acidity) behaviour. Peri (1960, 1965) derived the structural configurations of five possible surface hydroxyl groups in γ -alumina, explaining the Lewis acid acidity in relation to the range of sites observed in infrared spectroscopic studies. The model was further developed by Knoezinger and Ratnasamy (1978) to account for the range of coordination of the aluminiums (octahedral and tetrahedral) to which the hydroxyl groups can be bound.

The critical stage in the customising of γ -alumina as a catalyst lies in the control of surface area (Paglia et al. 2004), and the distribution and activity of these hydroxyl groups, several of which are frequently involved in the catalytic steps in

a given reaction (Ghorbel et al., 1973, 1974). Activity is thus dictated by a combination of calcination conditions and subsequent treatments of the catalysts. For example in the Claus process for the desulphurisation of natural gas in gas plants and refineries, sulphur is removed from the process stream by reaction over an activated alumina catalyst (Eq. 2.7).



Alpha alumina is fully dehydroxylated, has only geometrical surface area, and is not active in this sense, although its thermal stability makes it an ideal catalyst support in applications such as reforming (Moreno et al. 2009; Pompeo et al. 2009).

The particular properties of γ -alumina have also prompted a range of approaches to its synthesis in increasingly exotic morphologies. Nanorods (Shen et al., 2007), nanobelts (Peng et al., 2002; Gao et al., 2005), nanotubes (Pu et al., 2001; Zhang et al., 2002) and nanoflowers (Ma and Zhu, 2009) are amongst many reported morphologies, synthesised by electrochemical, sol-gel, etching and evaporation techniques.

2.8 Alumina production trends

As seen in production figures discussed earlier, alumina is used primarily as a feedstock in making aluminium metal. As demand for the metal continues to increase, this is the primary driver in the anticipated growth of alumina production. The Bayer process continues to dominate this production, although rapidly increasing capacity in China has introduced a number of variants on this process largely to accommodate more difficult bauxites high in diasporite. As with many high volume mineral resources, the ongoing challenge lies in the utilisation of progressively poorer deposits with rising processing costs, particularly in energy consumption. The increasing capacity of Bayer plants is also limited by environmental constraints, especially in red mud disposal and 'licence to operate' issues such as odours from the destruction of organics.

Most projections based on historical consumption patterns place the long-term growth in aluminium demand between 3 and 4% per year. There is a strong correlation between use of the metal and growth in gross domestic product (GDP) and thus projections in the latter, in the developing countries particularly, give a broad estimate of growth in Al demand. The implication is that given the dependence on Bayer process alumina, and the Hall-Héroult smelting process for primary metal production, alumina capacity must grow at twice this rate of growth in metal demand. This requirement will far outstrip growth in specialty applications of alumina and has significant flow on effects.

One such issue is that growth in aluminium smelting capacity occurring in regions such as the Middle East, Russia and China continues to be located in most cases large distances from the corresponding growth in alumina production. The

exception is China where much of this capacity growth will be internal, but will be based on more difficult, diaspora rich, mineral resources. The long and increasingly fluid alumina supply lines provide considerable impetus to the further improvement and global standardisation of alumina specifications. This also prompts the need to look at the step-change potential in radically altering the current geographically and resource-inefficient approach to alumina production.

2.9 Acknowledgements

The author would like to acknowledge the assistance of a number of colleagues at the Light Metals Research Centre, The University of Auckland, in particular Linus Perander, Margaret Hyland, Tania Groutso and Zoran Zujovic. The expertise of the solid state NMR group at the University of Warwick, led by Mark Smith, and the access to facilities at the Australian Synchrotron has also been extremely helpful.

2.10 References

- Ashida T., Metson J.B. and Hyland M.M. (2004) New Approaches to Phase Analysis of Smelter Grade Aluminas. *Light Metals*. A. Tabereaux Ed. The Metals Minerals and Materials Society, Warrendale, PA. pp. 93–97.
- Bayer, K.J. (1888) Studium über die Gewinnung reiner Tonerde. *Chem. Zeitung*, 12, p. 1209. *Ibid.*, 14, p. 736, 1890.
- Bouchard N.-A., Breault R., Picard F., Chouinard Y. and Menard H. (2005) Dynamic Adsorption Isotherm for Some Hydrate Active Organics and Selected Degradation Products with Implication for Gibbsite Precipitation Yields. *Light Metals*. H Kvande Ed. Minerals, Metals & Materials Society, Warrendale, PA. pp. 197–202.
- Chandrasekhar S., Jackson D. and Kisler J. (2005) Alumina Fines' Journey From Cradle To Grave. *Proceedings of the 7th Alumina Quality Workshop*. AQW Inc. pp. 5–9.
- Costa M.L. (1997) Lateritization as a Major Process of Ore Deposit Formation in the Amazon Region. *Exploration and Mining Geology*, 6(1): 79–104.
- Dando N.R., Clever T.R., Kolek P.L., Person A. and Martin E.S. (1996) Aluminium Trihydroxide as a Filler for Polymer Composites: Comparative Evaluation of Precipitation and Grinding on Thermal Stability and Dehydration Kinetics. *Proceedings of the SPIE/CI 51st Annual Conference*. Session 19A, pp. 1–9.
- Den Hond R., Hiralal I. and Rijkeboer A. (2007) Alumina Yield in the Bayer Process Past, Present and Prospects. *Light Metals*. M. Sørli Ed. Minerals, Metals & Materials Society, Warrendale, PA. pp. 37–42.
- Doiron P. and Lindsay S.J. (2009) Pure Metal Production And Methodology: The Alcoa Deschambault Experience *Light Metals*. G. Bearne Ed. Minerals, Metals & Materials Society, Warrendale, PA. pp. 499–503.
- Eardley-Wilmot V.L. (1926) *Can. Dept. Mines Bull.* 675, p. 51.
- Eberhardt W. and Kunz C. (1978) Oxidation of Aluminum Single Crystal Surfaces by Exposure to Oxygen and Water. *Surface Science*, 75, pp. 709–714.
- Edwards L.C., Neyrey K.J. and Lossius L.P. (2007) A Review Of Coke And Anode Desulfurization. *Light Metals*. M. Sørli Ed. Minerals, Metals & Materials Society, Warrendale, PA. pp. 895–900.

- Gao P., Xie Y., Chen Y., Ye L.N. and Guo Q.X. (2005) Large-Area Synthesis of Single-Crystal Boehmite Nanobelts with High Luminescent Properties. *Journal of Crystal Growth*, 285: 555–560.
- Garner B., Cristol B. and Soirat A. (1999) Precipitation Particle size Control. *Light Metals*. CE Eckert Ed. Minerals, Metals & Materials Society, Warrendale, PA. pp. 71–76.
- Ghorbel A., Van-Hoang C. and Teicher S.J. (1973) Catalytic Activity of Amorphous Alumina Prepared in Aqueous Media. I. Catalytic Activity in Isomerization of 1-Butene. *Journal of Catalysis*, 30: 298–308.
- Ghorbel A., Van-Hoang C. and Teicher S.J. (1974) Catalytic Activity of Amorphous Alumina Prepared in Aqueous Media. II. Nature of Active Sites in the Isomerization of 1-Butene. *Journal of Catalysis*, 33: 123–132.
- Gillespie A.R., Hyland M.M. and Metson J.B. (1999) Irreversible Adsorption of Hydrogen Fluoride in the Dry Scrubbing Process. *Journal of Metals*, 51(5): 30–34.
- Grjotheim K. and Welch B.J. (1988) *Aluminium Smelting Technology*. 2nd edn. Aluminium Verlag, Düsseldorf.
- Hancock P. and Skinner B. (2000) ‘Laterites,’ in *The Oxford Companion to the Earth*. Oxford University Press.
- Haugland E., Haarberg G.M., Thisted E., and Thonstad J. (2001) The Behaviour of Phosphorus Impurities in Aluminium Electrolysis Cells. *Light Metals*, JL Anjier Ed. Minerals, Metals & Materials Society, Warrendale, PA. pp. 549–553.
- Hay S.J., Metson J.B. and Hyland M.M. (2004) Sulfur Speciation in Aluminium Smelting Anodes. *Industrial and Engineering Chemical Research*, 43(7): 1690–1700.
- Horn W.E., Jr. (1998) *Recent Advances in Flame Retardancy of Polymeric Materials*, 9, pp. 286–299. See also Greenaway P.A., Schreiber B., Schmidt R., *Light Metals*. BJ Welch Ed. Minerals, Metals & Materials Society, Warrendale, PA. pp. 199–203.
- International Aluminium Institute statistics (2008), Available at: <http://stats.world-aluminium.org/iai/>
- International Aluminium Institute (2009) data at <http://www.world-aluminium.org/Statistics/Current+statistics>, accessed December 12th 2009.
- Kato Y., Shimizu K.-I., Matsushita N., Yoshida T., Yoshida H., Satsuma A. and Hattori T. (2001) Quantification of Aluminium Coordinations in Alumina and Silica-Alumina by Al K-edge XANES. *Physical Chemistry Chemical Physics*, 3(10), pp. 1925–1929.
- Knoezinger H. and Ratnasamy P. (1978) Catalytic Aluminas: Surface Models and Characterization of Surface Sites. *Catalysis Review – Science and Engineering*, 17: 31.
- Kogel J.E., Trivedi N., Barker J.M. and Krukowski S.T. (2006) *Industrial Minerals and Rocks*. Society for Mining, Metallurgy and Exploration. (SME), Littleton, CO.
- Lee M H, Cheng C-F, Heine V and Klinowski J. (1997) Distribution of Tetrahedral and Octahedral Al Sites in Gamma Alumina. *Chemical Physics Letters*, 265(6), pp. 673–676.
- Lillebuen B. Bugge M. and Høie H. Alumina Dissolution And Current Efficiency In Hall-Heroult Cells. *Light Metals*. G Bearne Ed. Minerals, Metals & Materials Society, Warrendale, PA. pp. 389–394.
- Lindsay S. (2005) SGA Properties and Value Stream Requirements. *Proceedings of the 7th Alumina Quality Workshop*, pp. 6–21.
- Lippens, B.C. and de Boer J.H. (1964) Study of Phase Transformations During Calcination of Aluminium Hydroxides by Selected Area Electron Diffraction. *Acta Crystallographica*, 17(10), pp. 1312–1321.
- Liu L., Aye L., Lu Z. and Zhang P. (2006) Analysis of the Overall Energy Intensity of Alumina Refinery Process Using Unit Process Energy Intensity and Product Ratio Method. *Energy*, 31: 1167–1176.

- Liu Z., Li W., Chen W. and Liu B. (2009) The Application of Nepheline in Alumina Industry. *Light Metals 2009*, G Bearne Ed. Minerals, Metals & Materials Society, Warrendale, PA. pp. 125–130.
- Ma M.G. and Zhu J.-F. (2009) A Facile Solvothermal Route to Synthesis of γ -alumina with Bundle-like and Flower-like Morphologies. *Materials Letters*, 63: 881–883.
- MacKenzie K.J.D. (1968) Oxides of Aluminum Other Than Al_2O_3 [alumina]. *Journal of the British Ceramic Society*, 5(2): 363–367.
- MacKenzie K.J.D. (2002) *Multinuclear Solid-State Nuclear Magnetic Resonance of Inorganic Materials*. Pergamon, New York.
- MacKenzie K.J.D., Temuujin J. and Okada K. (1999) Thermal decomposition of mechanically activated gibbsite. *Thermochimica Acta*, 327(1–2): 103–108.
- Metson J.B. and Hyland M.M. (2001) Sulfur in Anodes – Future Issues and Challenges, *Proceedings Seventh Australasian Aluminium Smelting Technology Conference and Workshops*. M. Gustafsson, J. Metson, M. Skyllas-Kazacos and BJ Welch Eds.
- Miller J. and Irgens A. (1974) *Alumina Production and the Pedersen Process – History and Future*. AIME paper, pp. 72–74.
- Misra C. and White E.T. (1971) Crystallisation of Bayer Aluminium Hydroxide. *Journal of Crystal Growth*, 8: 172–178.
- Moreno M.S., Wang F., Malac M., Kasama T., Gigola C.E., Costilla I. and Sanchez M.D. (2009) Electron Microscopy Study of $\text{CeOx-Pd}/\gamma\text{-Al}_2\text{O}_3$ Catalysts for Methane Dry Reforming. *Journal of Applied Physics*, 105: 083531.
- Morrell R. (1987) *Handbook of Properties of Technical and Engineering Ceramics*. Part 2, Section 1. High Alumina Ceramics. HSO, London.
- Nakamura S., Mukai T. and Senoh M. (1994) Candela-class High-Brightness InGaN/AlGaN Double-Heterostructure Blue-Light-Emitting Diodes. *Applied Physics Letters*, 64: 1687–1689.
- Nanjo T., Suita M., Oishi T., Abe Y., Yagyu E., Yoshiara K. and Tokuda Y. (2009) Comparison of Characteristics of AlGaN Channel HEMTs Formed on SiC and Sapphire Substrates. *Electronics Letters*, 45(8): 424–426.
- Nielsen K. (1978) The Pedersen process – An Old Process in a New Light. *Erzmetall*, 31: 523–525.
- Norton, S.A. (1973) Laterite and bauxite formation. *Economic Geology and the Bulletin of the Society of Economic Geologists*, 68(3): 353–361.
- Nunn R.F. (1998) Advances in Red Mud Dewatering and Disposal Technologies. *Light Metals 1998*. BJ Welch Ed. Minerals, Metals & Materials Society, Warrendale, PA. pp. 107–113.
- Paglia G., Bozin E.S. and Billinge S.J.L. (2006) Fine-Scale Nanostructure in $\gamma\text{-Al}_2\text{O}_3$. *Chemistry of Materials*, 18(14): 3242–3248.
- Paglia G., Buckley C.E., Rohl A.L., Hart R.D., Winter K., Studer A.J., Hunter B.A. and Hanna J.V. (2004) Boehmite Derived γ -Alumina System. 1. Structural Evolution with Temperature, with the Identification and Structural Determination of a New Transition Phase, γ' -Alumina. *Chemistry of Materials*, 16(2): 220–236.
- Paglia G., Buckley C.E., Rohl A.L., Hunter B.A., Hart R.D., Hanna J.V. and Byrne L.T. (2003) Tetragonal Structure Model for Boehmite Derived γ -alumina. *Physical Review B*, 68 144110.
- Paglia G., Buckley C.E., Udovic T.J., Rohl A.L., Jones F., Maitland C.F. and Connolly J. (2004). Boehmite Derived γ -Alumina System. 2: Consideration of Hydrogen and Surface Effects. *Chemistry of Materials*, 16: 1914–1923.
- Peng, X.S., Zhang L.D., Meng G.W., Wang X.F., Wang Y.W., Wang C.Z., and Wu G.S.

- (2002), Photoluminescence and Infrared Properties of γ - Al_2O_3 Nanowires and Nanobelts. *Journal of Physical Chemistry B*, 106(43): 11163–11167.
- Perander L.M., Zujovic Z.D., Groutso T., Hyland M.M., Smith M.E., O'Dell L.A. and Metson J.B. (2007) Characterization of Metallurgical Grade Aluminas and their Precursors by ^{27}Al NMR and XRD. *Canadian Journal of Chemistry*, 85: 889–897.
- Perander L., Klett C., Wijayarathne H., Hyland M., Stroeder M. and Metson J. (2008) Impact of Calciner Technologies on Smelter grade Alumina Microstructure and Properties. *Proceedings of the 8th International Alumina Quality Workshop*, AQW Inc. pp. 103–108.
- Perander L.M., Zujovic Z.D., Kemp T.F., Smith M.E., Metson J.B. (2009) The Nature and Impacts of Fines in Smelter Grade Alumina. *Journal of the Minerals, Metals and Materials Society*, 61(11): 33–39.
- Peri J.B. (1965) Infrared and Gravimetric Study of the Surface Hydration of γ -Alumina. *Journal of Physical Chemistry*, 69(1): 211.
- Peri J.B. and Hannan R.B. (1960) Surface Hydroxyl Groups on γ -Alumina. *Journal Of Physical Chemistry*, 64: 1526
- Pilurzu S., Cucca L., Tore G. and Ullu F. (1999) *Proceedings of REWAS '99 Global Symposium on Recycling, Waste Treatment and Clean Technology*, Gaballah I., Hager J., and Solozabal R. Minerals Eds. Metals & Materials Society, Warrendale, PA. pp. 471–480.
- Pompeo F., Gazzoli D. and Nichio N. (2009) Characterization of γ - Al_2O_3 Supports Modified with CeO_2 and ZrO_2 . *Materials Letters*, 63: 477–479.
- Pu L., Bao X., Zou J. and Feng D. (2001), Individual Alumina Nanotubes. *Angewandte Chemie*, International edition, 40(8): 1490–1493.
- Reh L. (1995) New and Efficient High-Temperature Processes with Recirculating Fluid Bed Reactors. *Chemical Engineering Technology*, 18: 75–89.
- Rouquerol J., Rouquerol F., and Ganteaume M., (1975) Thermal Decomposition of Gibbsite under Low Pressures. I: Formation of the Boehmitic Phase. *Journal of Catalysis*, 36(1): 99–110.
- Rouquerol J., Rouquerol F. and Ganteaume M. (1979) Thermal Decomposition of Gibbsite under Low Pressures. II. Formation of Microporous Alumina. *Journal of Catalysis*, 57(2): 222–230.
- Sant'Ana M., Morales J., Prader R., Kappel J. and Heinzle M. (2008) Hyperbaric Bauxite Filtration: New ways in Bauxite Transportation. *Proceedings of the 8th Alumina Quality Workshop*. AQW Inc. pp. 292–294.
- Shen S.C., Chen Q., Chow P.S., Tan G.H., Zeng X.T. and Wang Z. (2007) Steam-Assisted Solid Wet-Gel Synthesis of High-Quality Nanorods of Boehmite and Alumina. *Journal of Physical Chemistry, C* 111(2): 700–707.
- Slade R.C.T., Southern J.C. and Thompson I.M. (1991) Aluminum-27 Nuclear Magnetic Resonance Spectroscopy Investigation of Thermal Transformation Sequences of Alumina Hydrates. I. *Journal of Materials Chemistry*, 1(4): 563–568.
- Smirnov V. (1996) Alumina Production in Russia Part I. Historical Background. *Journal of Physical Chemistry*, 48(8): 24–26.
- Smith M.E. (1993) Application of Aluminum-27 NMR Techniques to Structure Determination in Solids. *Applied Magnetic Resonance*, 4(1–2): 1–64.
- Stepanov V.S. and Stepanov S.V. (1998) Energy Efficiencies and Environmental Impacts of Complex Industrial Technologies. *Energy*, 23(12): 1083–1088.
- Sturm E. and Wedde G. (1998) Removing Impurities from the Aluminium Electrolysis Process. *Light Metals*, BJ Welch Ed. Minerals, Metals & Materials Society, Warrendale, PA. pp. 235–240.

- United States Geological Survey (USGS) (2009) *Mineral Commodity Summaries*, U.S. Department of the Interior, U.S. Geological Survey.
- Vinogradov S.A. and Sizyakov V.M. (2009) Improved Quality of Raw-Material Mixture for Comprehensive Processing of Nepheline Ore and Concentrates by Sintering at the Achinsk Integrated Alumina Plant. *Metallurgist*, 53(3–4): 242–247.
- Vogt F., Tonti R., Hunt M. and Edwards L. (2004) A Preview Of Anode Coke Quality in 2007. *Light Metals*, AT Tabereaux Ed. Minerals, Metals & Materials Society, Warrendale, PA. pp. 489–493.
- Weast R.C. (1974) *CRC Handbook of Chemistry and Physics*. 55th edn. CRC Press, Cleveland, OH.
- Wefers K. and Misra C. (1987) *Oxides and Hydroxides of Aluminum*. Alcoa Technical Paper No. 19. Aluminum Company of America: Pittsburgh, PA.
- White E.T. and Bateman S.H. (1988) Effect of Caustic Concentration on the growth Rate of $\text{Al}(\text{OH})_3$ Particles. *Light Metals 1988*, L.C. Boxall Ed. Minerals, Metals & Materials Society, Warrendale, PA. pp. 157–162.
- Whittington B. and Ilievski D. (2004) Determination of the Gibbsite Dehydration Reaction Pathway at Conditions Relevant to Bayer Refineries. *Chemical Engineering Journal*, 98: 89–97.
- Wolverton C. and Hass K.C. (2001) Phase Stability and Structure of Spinel-based Transition Aluminas. *Physical Review B: Condensed Matter and Materials Physics*, 63(2): 024102/1–024102/16.
- Zhang, Y., Liu, J., He R., Zhang Q., Zhang X. and Zhu J. (2002), Synthesis of Alumina Nanotubes using Carbon Nanotubes as Templates. *Chemical Physics Letters*, 360(5–6): 579–584.
- Zhao Q., Yang Q., Qi L., Chen Q., Yin Z. and Zhang L. (2005) Fundamental Research in Alumina Production of the Future. *Light Metals*, H Kvande Ed. Minerals, Metals & Materials Society, Warrendale, PA. pp. 29–32.
- Zhou R.S. and Snyder, R.L. (1991) Structures and Transformation Mechanisms of the η , γ and θ Transition Aluminas. *Acta Crystallographica, Section B: Structural Science*, 47(5): 617–630.

Production of primary aluminium

H. KVANDE, Qatar University, Qatar

Abstract: This chapter describes the industrial production of primary aluminium in Hall-Héroult electrolysis cells, where alumina (Al_2O_3) is dissolved in a molten fluoride-containing electrolyte consisting mainly of cryolite (Na_3AlF_6) at about 960°C . The chapter then discusses health, environment and safety (HES), and workers' health and safety are now an integrated part of the primary aluminium industry. The chapter finally discusses the past, present and future of the primary aluminium production process.

Key words: primary aluminium production, Hall-Héroult electrolysis cells, cryolite-containing electrolyte, prebaked carbon anodes.

3.1 Introduction

Primary aluminium production involves two independent energy-intensive processes to transform the ore, which is bauxite, to the metal. These are the Bayer process (1888), which makes alumina from bauxite, and the Hall-Héroult process (1886), in which molten aluminium is produced by electrolytic reduction of alumina dissolved in a molten salt electrolyte consisting mainly of cryolite.

3.1.1 Alumina production

In an alumina refinery bauxite is processed into pure aluminium oxide (alumina, or Al_2O_3), which is the main raw material required for production of primary aluminium. The Bayer process extracts alumina by caustic digestion of crushed bauxite at high temperature and pressure in an autoclave, followed by clarification, precipitation, washing and finally calcination to produce pure anhydrous alumina. Some aluminium producers own, or partly own, alumina refineries. Many companies also purchase alumina on the open market. The alumina is then shipped directly to the aluminium smelters.

Alumina is a white powder that looks like table salt. It has a very high melting point, above 2050°C , and is chemically a very stable compound. This is why we need to use so much energy to produce aluminium from alumina.

3.1.2 Aluminium production

The overall electrochemical reaction of dissolved alumina with solid carbon to form molten aluminium and gaseous carbon dioxide may be written as:



The alumina raw material in the Hall-Héroult process is consumed according to the stoichiometric ratio predicted from Eq. 3.1. This consumption theoretically amounts to 1.89 kg of Al_2O_3 per kg Al produced and it should then react with 0.33 kg of carbon producing 1.22 kg of carbon dioxide. In practice the typical values are 1.93 kg of Al_2O_3 per kg Al and 0.40–0.45 kg C per kg Al, which produces about 1.5 kg of CO_2 .

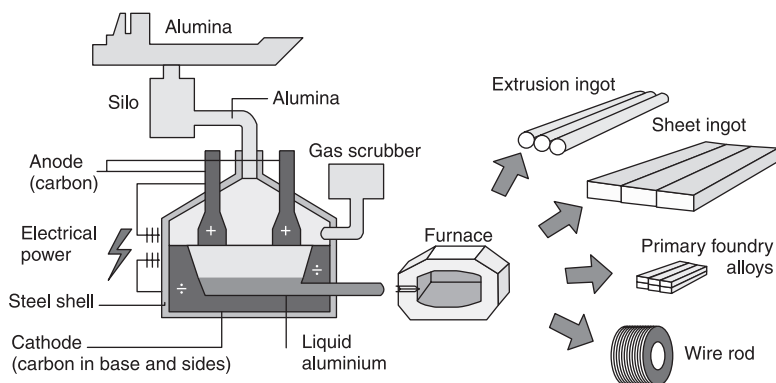
While older electrolysis cell designs had large and infrequent additions of alumina, modern cells are equipped with special automatic so-called point feeders. The alumina is supplied from an overhead bin or hopper, which is built into the superstructure of the cell. Two to five volumetric feeders then successively add about 1 kg of alumina every minute or so. The small additions enhance the ability for the alumina to dissolve and mix rapidly with the electrolyte. The alumina content in the electrolyte is usually maintained within the limited range of 2–3 wt. % Al_2O_3 . Higher alumina contents may lead to the formation of excessive amounts of undissolved alumina sludge collecting underneath the metal pad. Lower alumina contents risk a change in the anode process, which leads to a so-called anode effect.

An anode effect causes a very high cell voltage, up to 30–40 V, by forming an electrically insulating gas layer underneath the anodes. The anode gas composition then changes to contain mainly CO (g) , but also two gaseous perfluorocarbon compounds, $\text{CF}_4 \text{ (g)}$ and smaller amounts of $\text{C}_2\text{F}_6 \text{ (g)}$, which are emitted to the atmosphere. The amounts of these gases can be recalculated to CO_2 equivalents. The perfluorocarbons are particularly harmful to the environment because of their high global warming potential, and they have therefore received considerable attention in recent years. The formation of these gases can be reduced by reducing the anode effect frequency (number of anode effects per cell per day) and the anode effect duration (given in minutes), and most aluminium producers have now made significant progress in this regard.

In addition to being the raw material, alumina also acts as a thermal insulator when placed on top of the self-formed frozen crust above the electrolyte. This conserves heat in the cell. Covering the top of the anodes with alumina, or blends of alumina and crushed solid electrolyte, conserves heat and minimises air-burning of anode carbon.

The third major role fulfilled by alumina is capturing of fluoride emissions from the cells by anode gas cleaning, using the so-called dry scrubbing method. Alumina powder is used to adsorb the hydrogen fluoride gas evolved, and also to entrap fluoride condensates, mainly particulate sodium tetrafluoroaluminate, NaAlF_4 . The resulting secondary alumina is then used as the feed material to the cells, while the cleaned exhaust gas containing carbon dioxide is discharged to the atmosphere. Figure 3.1 shows a flow sheet of the Hall-Héroult process.

Aluminium production



3.1 Flow sheet of the Hall-Héroult process.

3.2 Raw materials used in the aluminium production process

3.2.1 Bauxite

Aluminium is the third most abundant element, and the most abundant metallic element (8 wt.%), in the earth's crust. Because the aluminium compounds are chemically very stable, aluminium is never found as a metal in nature. Thus, all aluminium metal that exists in the world today is man-made.

Aluminium is found in nature in a wide variety of minerals combined with oxygen, silicon and other metals, but it is mainly bauxite that is used as raw material for the aluminium industry. The name comes from the small French town of Les Baux, where the ore was discovered for the first time. Bauxite deposits are mainly found in a wide belt around the Equator. It lies relatively close to the surface and is normally strip-mined. Bauxite contains typically 40–60% aluminium oxide (alumina) in the form of several hydrous alumina phases (gibbsite, $\text{Al}(\text{OH})_3$, boehmite (AlOOH) and diaspore (AlOOH), and with smaller amounts of iron, silicon and titanium compounds as well as other trace impurities.

Much more extensive information about bauxite and alumina is given in Chapter 2 of this book.

3.2.2 Electric power

A large amount of energy and high temperature is required to reduce aluminium oxide to aluminium. This explains why aluminium became a commercial product only about 150 years ago, while for example iron, copper, bronze and lead have been used for over 3000 years.

Modern aluminium smelters need close to 13 kilowatt-hours to produce 1 kg of aluminium. About 50% of the world's aluminium is presently produced from renewable hydroelectric power, while the major other electric energy sources are coal (30%), natural gas (15%) and nuclear energy (less than five per cent). Energy is typically accounting for roughly 30% of the aluminium production cost. Energy consumption has decreased in recent years by means of technological improvements. However, with the global demand for energy increasing steadily, energy savings in all parts of the production process will be an important task for aluminium smelters in the coming years.

3.3 Energy efficiency in the utilisation of carbon anodes

The amount of electrical energy required in Hall-Héroult cells is reduced by use of consumable carbon anodes. Thus, the thermal energy content of carbon saves electrical energy. Let us therefore look at the energetic efficiency with which carbon is utilised:



This reaction has a standard Gibbs energy corresponding to 1.03 V, which is the standard electromotive force (emf) of a reversible fuel cell burning carbon to CO_2 . This represents the depolarisation due to the carbon anode. In the present cells about half of it is lost by the overpotential on the carbon anode, but it still leaves 50% energy efficiency in the utilisation of carbon. This is much higher than the efficiency that can be achieved in a thermal, coal-fired power station. If we consider the fact that the overpotential generates heat that is necessary to balance the heat losses of the electrochemical process, the energy efficiency of the carbon anode will be about 80%.

3.4 The carbon anodes

Prebaked anodes. One may also consider carbon as a raw material in aluminium production, because carbon is consumed by the anode reaction. The main constituent of prebaked carbon anodes is calcined petroleum coke, which is produced from the heavy residual fractions of crude oil by a process known as delayed coking. Thus, coking is used to upgrade waste products from oil refineries that would otherwise have to be sold as low-value fuels. In addition the anodes contain 13–16 wt.% coal tar pitch as a binder material, binding the coke particles together. Pitch is liquid hydrocarbon with more than 90% carbon. It is distilled from the coal tar evolved when coke for the steel industry is made from coking of bituminous coal. Before they can be used the anodes are prebaked in special anode baking furnaces. Because 0.40–0.45 kg of anode material is consumed for each kilogram of aluminium produced, this represents the major carbon

requirement. It gives a carbon mass consumption efficiency of 70–80%. In the industrial electrowinning of aluminium, part of the energy for reducing alumina is supplied as electricity and part comes from the consumption of the carbon anode.

Because the ash from the carbon will contaminate either the aluminium produced or the electrolyte, high-purity carbon is desirable. Certain impurities, such as vanadium, are particularly harmful in that they catalyse air burning of the carbon. Other impurities, such as phosphorus, accumulate in the electrolyte and undergo cyclic red-ox reactions (partial reduction followed by reoxidation), consuming electric current without producing any product.

The coke residue from petroleum refining is quite pure, and therefore it has been the major source of carbon for anodes. The structure of petroleum coke varies depending on the nature of the petroleum feedstock used at the refinery, the refinery flowstream and the coking conditions used. This coke produced at about 500°C requires calcining at about 1200°C to remove volatile constituents and increase its density before it is being blended into the anode mix. After calcination, the coke and recycled anode material are crushed and sieved into fractions, which are then blended to obtain an optimum particle size composition. This blend is mixed with sufficient coal-tar pitch to allow moulding into anode blocks by pressing or by vibrating. They are baked in separate anode baking furnaces at about 1150–1200°C, causing the pitch to carbonise, and forming strong carbon anode blocks.

To provide electrical contact and physical support an aluminium or copper rod with an iron yoke and iron stubs is attached to the anode. The stubs are placed into two to six cavities in the top of the carbon anode and are attached by applying cast iron or rammed paste around the stubs.

A salient feature of the Hall-Héroult process is the use of consumable anodes. There are two basic anode designs, prebaked anodes, and monolithic, continuous, self-baking Söderberg anodes. The prebaked anodes have been described above and here is a short description of Söderberg anodes.

Söderberg anode. This anode is made from a similar mix of petroleum coke and coal tar pitch, but the mix here typically contains between 25 and 28 wt.% pitch, whereas the mix used for making prebaked anodes usually contains between 13 and 16 wt.% pitch, as mentioned before. Briquettes of Söderberg anode paste are added on top of the Söderberg anode. While the paste passes slowly downwards through a rectangular steel casing, it is baked into an electrically conducting solid composite by pyrolysis of the pitch by the waste heat generated in the electrolyte and in the anode itself.

The baked portion extends past the casing and into the molten electrolyte. Baked mix replaces anode being consumed at the bottom surface. Electric current usually enters the Söderberg anode through vertical spikes or studs connected to the anode beam, although in some older Söderberg cells side-entry horizontal studs are still being used. These spikes are pulled and reset to a higher level as they approach the lower surface. Söderberg anodes have an electrical resistivity about 30% higher than that of prebaked anodes. Because of the resulting lower

power efficiency and the greater difficulty in collecting and disposing of baking fumes, Söderberg anodes are gradually being replaced by prebaked anodes, even though the former save the capital, labour and energy required to manufacture the latter. In recent years many Söderberg potlines have been shut down because they cannot cope with the stringent new emission requirements.

3.5 Electrolyte materials

Cryolite usually comprises more than 75 wt.% of the electrolyte, which typically also contains excess aluminium fluoride (6–13%), calcium fluoride (4–7%) and alumina (2–4%). Sometimes lithium fluoride (2–4%) and magnesium fluoride (2–5%) are added in the form of lithium carbonate and magnesium oxide. These additives lower the melting point as well as the operating temperature, and they increase the current efficiency of the process.

Cryolite. The mineral cryolite is a double fluoride of sodium and aluminium and has a stoichiometry very near the formula Na_3AlF_6 and a melting point of about 1010°C. It has been found in substantial quantities only in Greenland, and was mined extensively there in the early twentieth century, but the mine is now essentially exhausted. Synthetic cryolite can be produced by reacting hydrofluoric acid with an alkaline sodium aluminate solution:



Cryolite also can be recovered from used cell linings. The lining is then crushed and treated with dilute sodium hydroxide solution to dissolve fluorides. After being filtered, the solution is neutralised with carbon dioxide to precipitate the cryolite. Cryolite is produced directly in reduction cells by reaction of the soda impurity in the feed alumina with added aluminium fluoride:



Electrolyte generated by Eq. 3.4 must be tapped from the cells periodically. In modern smelters with dry scrubbing equipment for fume treatment and cell lives greater than 3 years, cryolite is a by-product rather than a raw material in the production of aluminium.

Aluminium fluoride. Aluminium fluoride, AlF_3 , may comprise as much as 12–13 wt.% of the electrolyte when it is recorded in excess of the amount represented by the cryolite composition. Aluminium fluoride is consumed during normal operation by three major mechanisms. First, losses of aluminium fluoride by vaporisation are appreciable; the most volatile species present in the electrolyte is sodium tetrafluoroaluminate, NaAlF_4 , having a partial pressure of 200–600 Pa over the operating electrolyte, depending on composition and temperature. Second, aluminium fluoride is depleted by hydrolysis due to moisture:



Fume capture and scrubbing efficiencies have been improved in aluminium smelters. Fluoride previously lost by vaporisation of NaAlF_4 and hydrolysis of bath is now almost completely recycled to the cells.

Finally, aluminium fluoride is consumed by reaction with the soda present in the feed alumina (Eq. 3.4) and this is the main reason why most cells need an addition of about 20–30 kg of aluminium fluoride per ton of aluminium produced.

Aluminium fluoride lowers solubility of reduced species and lowers surface tension, viscosity and density of the melt. It has the undesirable effects of decreasing alumina solubility and electrical conductivity and also increasing vapour pressure. Aluminium fluoride acts as a Lewis acid, with sodium fluoride acting as a Lewis base. Neutrality has been defined arbitrarily in this chemical system as a molar ratio of sodium fluoride to aluminium fluoride of 3: 1, corresponding to the cryolite composition.

Calcium fluoride is seldom added intentionally. Because of the small amount of calcium oxide impurity in the alumina (typically 0.035 wt.%), it attains a steady-state concentration of 4–7% in the melt. At this level calcium is codeposited into the aluminium and is emitted in the off-gas at a rate equal to its rate of introduction. Calcium fluoride, in addition to lowering the liquidus temperature, decreases vapour pressure and solubility of reduced species in the electrolyte for better current efficiency. Detrimentally, it lowers alumina solubility and electrical conductivity and increases density, viscosity and surface tension of the electrolyte.

Lithium fluoride, in addition to lowering the melting point, decreases the vapour pressure, density, reduced species solubility and viscosity, and it also increases electrical conductivity. The only negative effect appears to be lowered alumina solubility. Its high cost, however, requires that its benefits are outweighed by the price. Lithium fluoride is a slightly weaker Lewis base than sodium fluoride. Magnesium fluoride and calcium fluoride on the other hand are weak Lewis acids.

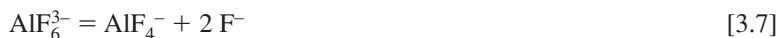
Magnesium fluoride accumulates to 0.1–0.3 wt.% in the electrolyte by the same mechanism as calcium fluoride. Some operators add up to 5 wt.% MgF_2 because it expels carbon dust from the electrolyte by decreasing the ability of the electrolyte to wet carbon.

3.5.1 Ionic structure of the melt

There is general agreement that molten cryolite is completely ionised to sodium ions and hexafluoroaluminate ions:



Also it is well established that the hexafluoroaluminate anion dissociates further:



At the cryolite composition the anion AlF_6^{3-} is about 30% dissociated. Raman spectroscopy has shown that the dissociation increases with increasing aluminium fluoride content.

The nature of the species formed when alumina is added is not so well established. Combination of results of cryoscopic measurements, Raman spectrographic data, equilibrium studies and vapour pressure measurements has led to the conclusion that $\text{Al}_2\text{O}_2\text{F}_4^{2-}$ and $\text{Al}_2\text{OF}_6^{2-}$ are the two major oxygen-containing ions in the melt. Possible reactions for their formation are:



and



3.5.2 The electrolyte – mainly cryolite with fluoride additives

The electrolyte may be regarded as the heart of the process. Cryolite is the dominant electrolyte constituent because of its unique capacity to dissolve alumina. The electrolyte is not consumed during the electrolysis process, but some losses do occur through vaporisation, hydrolysis, and also by penetration into the cathode lining, as mentioned before. During normal cell operation the electrolyte typically has a density lower than that of liquid aluminium (2.1 compared to 2.3 kg/dm³), floating on top of it. The temperature is usually between 955°C and 965°C, and the melting temperature may be 5°C to 10°C lower. This temperature difference between the electrolyte temperature and its melting temperature is called superheat. The superheat has received greatly increased attention in the last decade or so, because it was realised that it controls the thickness of the solid side ledge that protects the sidewall material against the corrosive action of the electrolyte. Modern cells may contain between four and six tonnes of molten electrolyte, corresponding to an electrolyte height of about 20 cm.

The four main functions of the electrolyte are:

- to pass electricity from the anode to the cathode;
- to be a solvent for alumina to enable its electrolytic decomposition, forming aluminium and carbon dioxide;
- to provide a physical separation between the cathodically produced aluminium metal and the anodically evolved carbon dioxide gas; and
- to provide a heat-generating resistor that allows the cell to be self-heating.

3.6 The cathode and cathode materials

The electrolyte and the aluminium are contained in a preformed carbon lining, which has refractory and thermally insulating materials inside a steel shell. Anthracite has been the major constituent in the cell *cathode* blocks, although

graphitic and semi-graphitised materials are now used extensively. Although the word cathode is used in the aluminium industry to describe the whole container of metal and electrolyte, the real acting cathode from an electrochemical point of view is the top surface of the liquid aluminium pool (metal pad). Thus, aluminium is formed from aluminium-containing anions that are reduced at the electrolyte-aluminium interface.

The materials used are prebaked carbon cathode blocks, SiC sidewall bricks, and carbonaceous ramming paste. The cathode blocks and sidewall materials are shaped and baked by manufacturers, while the ramming paste is formed directly in the cathode by ramming and is baked when the cathode is preheated and the cell is put into operation.

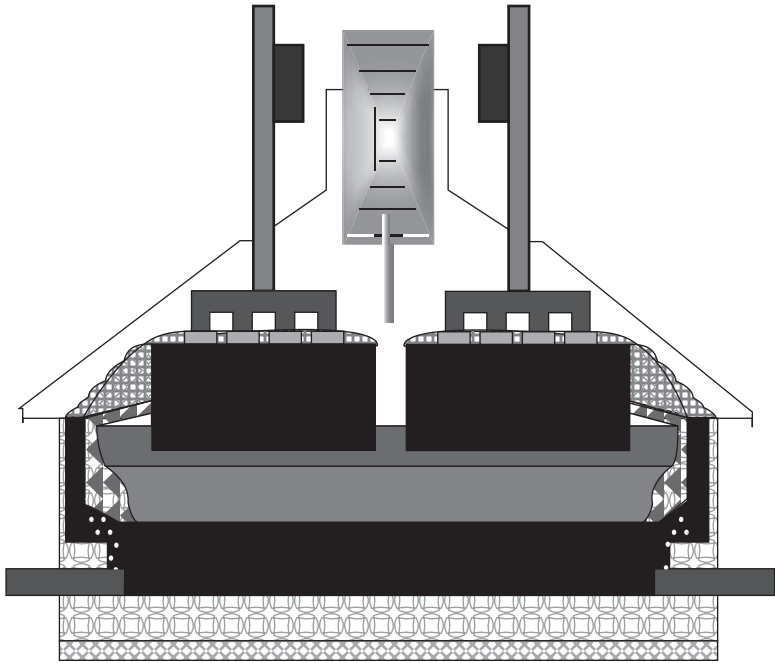
To insulate the cathode, insulation bricks are used. These are porous and vulnerable to penetration of electrolyte components. The insulation materials are protected by using refractory bricks and also sometimes a barrier material made of steel and/or glass is added. Refractory bricks also have some insulating effect, so that the temperature in the insulation materials does not become too high. There is often a compromise between the wanted insulation and the protection of the insulation materials.

Electric current deposits aluminium into a pool of molten aluminium, resting under the electrolyte in the carbon-lined cavity of the cell. Oxygen from the alumina deposits electrolytically onto the carbon anode dipping into the electrolyte and reacts with (burns) the anode. Cells are typically sized from 9 to 14 m in length, 3 to 5 m in width and 1 to 1.5 m in depth. The depth of the operating cavity is only 0.4 to 0.5 m, however.

Thermal insulation surrounds the carbon lining of the cell to control heat losses. Although carbon is the material known to withstand best the combined corrosive action of molten fluorides and molten aluminium, even carbon would have a very limited life in contact with the electrolyte at the sides of the cell were it not protected by a layer of frozen electrolyte. The thermal insulation is adjusted carefully to maintain a protective coating on the sidewalls but not on the bottom, which must remain substantially bare for electrical contact. Steel collector bars in the carbon cathode conduct electric current from the cell. These bars are inserted into holes that have been sized precisely so that thermal expansion forms a tight electrical contact, or they are cemented in place with carbonaceous cement containing metal particles, or bonded in place with cast iron. Figure 3.2 shows a drawing of an electrolysis cell.

3.7 Current efficiency

According to Faraday's first law, 1 kAh of electric current should produce 0.335 kg of aluminium, but only 85–95% of this amount is obtained. This loss in metal production is typical for electrolytic processes. To account for these losses and to measure the electrochemical efficiency of the process, the concept of



3.2 Schematic drawing of an aluminium electrolysis cell.

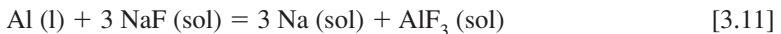
current efficiency (CE) is introduced as the ratio between measured and theoretical production rates:

$$CE = p/p_o \times 100\% \quad [3.10]$$

Here, p is measured production rate (kg Al/hour) and p_o is theoretical production rate (kg Al/hour).

One may then say that current efficiency is that part of the current that is used to produce aluminium, according to Faraday's first law. The principal loss mechanism is recombination of anodic and cathodic products. Reduced species go into solution in the electrolyte at the aluminium-electrolyte interface.

Disagreement exists over whether the dissolved species is metallic sodium, subvalent sodium, monovalent aluminium, colloidal aluminium or a combination of these species. For instance, Eq. 3.11 below defines a thermodynamic activity of sodium in the melt:



There are several mechanisms accounting for additional minor losses in current efficiency. New cell linings absorb sodium. Fortunately, the cell lining becomes saturated early in the cell's life but until this occurs, the current efficiency is low.

When a metal dissolves in a molten salt it usually imparts electronic conductivity to the melt, thereby lowering current efficiency. Some investigators have found a small electronic conductance for cryolite-based melts in contact with aluminium, while others have not. Such elements as phosphorus and vanadium, which can be reduced partially at the cathode and then reoxidised at the anode, can lower the current efficiency.

The solubility of aluminium in industrial electrolytes is small, between 0.03 and 0.06 wt.%. Recent studies have indicated that aluminium may dissolve in the melt in the form of AlF_2^- ions:



Metal going into solution must first diffuse through the metal-electrolyte boundary layer. The metal is then transported by convection to the vicinity of the anode. Here it can react with carbon dioxide. Chemical reactions appear to be fast compared to mass transport. The rate-controlling step was previously assumed to be diffusion of dissolved metal through the boundary layer at the metal-electrolyte interface. However, recent studies indicate that mixed control with diffusion, both at the aluminium-electrolyte interface and at the bubble-electrolyte interface, may be important.

It is possible that this AlF_2^- ion is the one that supplies aluminium ions to the cathode and thus is the source for the aluminium produced. But how can negative ions (anions) participate in reactions at the negative cathode? Anions can be reduced at the cathode if they contain an element whose oxidation state can be lowered in the stability range of the melt. Aluminium is such an element, and in the species AlF_2^- aluminium is monovalent. Thus, the reactions forming aluminium at the cathode may be written:



3.7.1 Energy consumption and energy efficiency

The specific energy consumption (EC) in kilowatt-hours per kilogram of aluminium produced can be calculated by the simple equation:

$$\text{EC (kWh/kg Al)} = 2.9806 \times V/\text{CE} \quad [3.15]$$

Here the current efficiency CE is given as a fraction and V is the cell voltage given in Volts. The so-called energy efficiency may be described as that part of the electrical energy added to the cell, which is used to produce aluminium. Electrical energy is here the product of amperage and voltage. Typical values for the energy efficiency are 45–50%, and the rest of the energy input produces heat that is lost from the cell to the surroundings.

3.7.2 Heat balance

Heat balance considerations are important in designing and operating a cell at the optimum temperature. Calculation is complicated by simultaneous heat flow and heat generation in conductors that carry electric current into and out of the cell. More than 50% of the heat loss may occur through the anodes and the top crust. It is extremely important that the sidewalls must be protected from erosion by a ledge of frozen electrolyte maintained by extracting the exact amount of heat required for the desired ledge thickness. The complex geometry and the interaction between heat flow and electrical flow generally require a computer program using either a finite element or finite difference technique for heat balances.

3.8 Cell amperage increase

In the last 10–20 years many aluminium producers have increased the amperage in their cells. Based on the experience gained from this work the most important technical item with respect to amperage increase is to combine this increase with reduced cell voltage to keep a nearly constant heat input to the cells. It is really surprising how much has been achieved here, and for some cell lines it has been possible to increase amperage by more than 30–40%.

The limit for amperage increase in a given cell will occur when the cell voltage cannot be reduced any more. In this case the anodes get too close to the aluminium cathode, and the back reaction between aluminium and carbon dioxide will reduce the current efficiency significantly. Then it will not be possible to maintain a constant energy input to the cell any longer. If the voltage is not decreased accordingly, the cell may become too hot and production will suffer.

3.8.1 Magneto hydrodynamics

The large electric currents used in modern cells generate relatively strong magnetic fields within the cell. These magnetic fields interact with the high electric currents and exert Lorentz forces, producing movement of liquid conductors.

Three types of magnetic disturbances have been observed:

1. a vertical or static displacement of the metal pad;
2. a circulating flow within the metal pad at velocities that may be as high as 20 cm/s; and
3. wave motion in the metal pad.

The last type of disturbance is probably the most harmful, because waves may lead to electrical short circuiting. The magnetic stirring of the metal may give rise to high metal velocities, metal height variations and instabilities. To minimise the adverse consequences of these effects it is desirable to compensate for the magnetic forces by a special arrangement of the interconnecting electrical busbar system.

Calculation of the magnetic fields and electric current flow patterns is complicated. Computer programs have been designed to make these calculations and describe the fluid-dynamic consequences. These calculations have been refined to the point where cells with amperages over 350 000 A have been designed and operated with high current efficiency. Natural convection caused by temperature gradients or composition differences in the electrolyte are insignificant compared with the movement induced by magnetic forces and gas bubbles. Gas bubbles produce significant stirring in the electrolyte and are the dominant force in electrolyte movement, whereas electromagnetic forces predominate in metal pad movement.

3.9 Cell lines

In an aluminium plant anything from 150 and up to about 300 cells are arranged in series, with the cathode of one cell electrically connected to the anode of the next cell, to form a cell line (which is commonly called a potline). A photograph of a modern cell line is shown in Fig. 3.3.

Series connection allows the use of high-voltage rectifiers, and for modern cell lines the maximum voltage now may be up to 1500 V. While the current through the cell lines is kept constant, the cells have individual voltage adjustments to satisfy special requirements, such as heat balance, operating conditions and the age and condition of the cathode.



3.3 (a) and (b) Photographs of modern cell lines with high-amperage side-by-side prebake cells. Two cell lines are here located in one cell room. A tapping vehicle is shown in the photograph (b) on page 62.

(b)



3.3 Continued.

Cell lines with prebaked anodes now typically have amperages from about 175 kA and up to the largest cells that are now operated at about 380 kA. These cells are placed side-by-side to reduce the adverse magnetic effects of the high electrical currents, and also to reduce the heat loss from the cells. Older cells, which can be below 100 kA, are often placed end-to-end, but not always. Retrofitting and modernisation of 150 kA end-to-end cells have made it possible to operate some of these at above 200 kA. Some end-to-end cell lines have now even reached 220 kA.

3.9.1 Cell operation

The following operational procedures are performed regularly, although at different time intervals:

- Alumina feeding
- Anode change
- Metal tapping
- Addition of aluminium fluoride
- Rack raising

Since alumina feeding now is done automatically, it is anode changing and metal tapping that are the two main and most labour-intensive manual routine operations. Prebaked anodes must be replaced at regular intervals when they have reacted down to about one fourth of their original size, which usually occurs after 22–30 days. Because the cells may have between 16 and 40 prebaked anodes, this means

that one anode is changed approximately each day in every cell. Modern potlines are equipped with sophisticated overhead cranes that allow the operator to stay in an air-conditioned cab and perform the anode changing operation by manipulating robotic arms. The use of anode-changing vehicles is also common in many plants.

Anode changing causes the largest operating disturbance in cells with prebaked anodes. When a new, cold anode is inserted, a layer of solid electrolyte freezes on the underside of the anode, and it can take up to 24 hours to melt this layer completely. This reduces the temperature of the electrolyte locally, as the new anode then draws very little current during this remelting process. It also disturbs the anodic current distribution in the cell. Several aluminium plants are now changing two anodes simultaneously, and this introduces an even larger thermal and electrical disturbance in the cell. Spent anodes, called butts, are cleaned outside the cell in a separate butts-cleaning station. The cleaned butts are crushed and are reused as raw material in the manufacture of new anodes. The adhering electrolyte removed in the cleaning operation is also recycled to the cells.

Extraction of molten aluminium from the cells is called tapping. The spout of a vacuum ladle or crucible is dipped into the metal pad in the cell and the metal is then siphoned into the crucible by the suction from an air ejector system. The molten metal is then weighed and transported to an open-hearth furnace in the cast house. While overhead cranes are usually used to assist the manual tapping work practices, specially constructed motorised vehicles can also be used. Otherwise the tapping procedures are the same as for crane tapping.

Addition of aluminium fluoride is performed automatically in modern cells. One or more silos for aluminium fluoride are built into the superstructure of the cell, and the addition is made through the hole in the crust made by the point feeder breakers for alumina addition.

The last manual routine operation is rack raising or anode beam raising. Because the anodes are consumed, the anode beam is gradually lowered downwards into the cell to maintain a constant interpolar distance. Ultimately the position of the anode beam becomes so low that it may reach an electronic or physical stopping device. The beam then has to be raised by a special anode-beam raising machine (called a rig) carried by the overhead crane. All anodes are first connected electrically to this machine and are held in position in the electrolyte while the anode clamps are loosened and the anodes are electrically disconnected from the anode beam. The beam is then raised to its upper position, the anodes are refastened in their correct position and the machine is finally removed from the top of the cell superstructure. This operation is carried out every two to three weeks for each cell, raising the anode beam by about 20 cm.

3.10 Health, environment and safety (HES)

These areas have received considerable attention in recent decades, and rightly so. Every company would like to be a world leader in industrial safety, which is a key

element in modern management philosophy. Protection of the employees is critical. Workers' health and safety are an integral part of the business. A good working environment is crucial, and good housekeeping is a prerequisite. The goal to eliminate accidents with lost-time injuries will be approached in the future. In principle, all accidents at work can be avoided. The expression 'Accidents don't happen; they are caused' is a good philosophy.

During the last 15 years or so, the industry has realised that the perfluorocarbon gases formed during so-called anode effects (CF_4 and to a smaller extent C_2F_6) are strong and harmful greenhouse gases. These were previously considered innocuous, since they are non-toxic to humans, animals and plant life, they do not affect the ozone layer and they are present only at very low contents in the atmosphere (5 million times lower than CO_2). Fundamental research has shown how these gases are formed during anode effects in laboratory cells, and measurements in industrial cells have produced data for calculation of their emissions and for comparison of results from different smelters. However, there may still be something to be learned about anode effects. Marks et al. (2000) suggested that low-level perfluorocarbon emissions may be produced even without a defined anode effect occurring. Previously, it was categorically claimed that these emissions occur only during anode effects, i.e., for cell voltages above 8 or 10 V. This new finding may cause some doubt on whether we now fully understand what we are dealing with here.

These perfluorocarbon gas emissions have been reduced significantly in recent years, largely due to a decrease in the number of anode-effect minutes brought about by improved operating practices. Modern prebake cells can now be operated for many months without an anode effect, and the obvious target here must be zero anode effects. For Söderberg cells, work should be undertaken to determine the minimum possible anode effect frequency without negative and harmful operational consequences. It is probable that all cell types can be operated with less than 0.1 anode effects per cell-day, and the time required to terminate anode effects can be reduced.

Aluminium companies in many countries entered into voluntary agreements with their national environmental protection authorities to reduce the 1990 perfluorocarbon gas emissions level by at least 50% by 2005. Most smelters have succeeded in achieving this goal. The Voluntary Objective of the Industrial Aluminium Institute (IAI) is now an 80% reduction in PFC gas emission per tonne of aluminium produced for the industry as a whole by 2010 versus 1990 levels. Still further efforts are needed in the coming years. IAI has suggested that the next step towards the eventual elimination of PFC emissions will be at least a two-thirds cut in the 2005 PFC emissions per tonne of aluminium by 2020.

Technological improvements are needed to continue to lower production cost, but also to improve the environmental impact. Modern electrolysis cell technology has set a new standard in the aluminium industry, not the least in terms of

environmental criteria. It reduces external emissions significantly and improves the indoor potroom environment, thereby contributing to a safer and better working environment.

3.11 Inert anodes

3.11.1 Introduction

Inert anodes for aluminium electrolysis are not a new idea. It was suggested first by Charles Martin Hall, one of the inventors of the process, in 1886. The copper anodes that Hall suggested did not work in practice, however, and he had to give up his idea. Carbon anodes have since then been the only possible practical solution for alumina reduction cells.

What do we mean by an inert anode? The word inert means non-reactive, and an inert anode will therefore not react chemically or electrochemically in the process. This means that it would ideally not be consumed by the anode reaction. Therefore, an inert anode may have many names such as dimensionally stable anode, non-consumable anode, passive anode and non-reactive anode. With inert anodes in the electrolysis cell, the total cell reaction will be:



Here oxygen is formed at the anode, which environmentally is a very favourable gas, compared to CO_2 , which is an unwanted greenhouse gas.

All materials have finite solubility in the very corrosive cryolitic melts, so a totally inert anode will in all probability not exist in these electrolytes. Thus, what one really is looking for is a slowly consumable anode. How slow a consumption rate can we tolerate? There are two issues here: the anode material should survive sufficiently long in the electrolyte, and the metal produced must be of adequate purity. A wear rate of the order of 10 mm/year may be sufficient, but lower values would certainly be beneficial.

There are three principal potential advantages in favour of developing cell technology with inert anodes:

1. *Cost reduction.* All costs associated with the consumable carbon anode will then be eliminated, including the capital saving and raw materials costs by eliminating the need for the carbon anode fabrication, baking and rodding plant. These cost savings may be significant. In addition, it has been indicated that there might be 25–30% lower capital costs for a new cell line with inert anode cell technology.
2. *Environmental friendliness.* A usual reason for wanting inert anode cells relates to saving fossil carbon consumption by producing oxygen instead of carbon dioxide. Inert anodes would eliminate all greenhouse gas generation and emissions from the electrolysis cells. Smelters would no longer generate carbon dioxide, carbon monoxide, sulphurous gases and perfluorocarbon

gases (CF_4 and C_2F_6), because carbon would no longer be used as the anode material. Furthermore, there will be no PAH gas emissions from the cells. In addition, the fluoride and dust emissions during anode change will be nearly eliminated. Carbon residues (butts) will also be eliminated. It should also be noted that all emissions associated with the present carbon anode baking furnaces would be eliminated.

3. *Improved occupational health issues.* Inert anodes would reduce the heavy work practices associated with the present prebaked carbon anode change. This is presently the operational procedure on prebake cells that causes the most severe heat stress for the operators, as well as causing the largest thermal disturbance of the cells. The frequency of anode changes will be drastically reduced with inert anodes. Working conditions in the cell rooms would also be improved by avoiding all anode effects.

There are two main challenges in the development of inert anode materials:

1. *The wear rate of the anodes.* The anode material should have low solubility and reactivity in the electrolyte and also show good chemical resistance to the anodically produced oxygen. There will be extreme requirements for keeping the wear rates of these anodes low. It should be noted that short-term electrolysis tests of a few hours' duration may give a rather poor basis for reliable estimates of wear rates given in millimetres per year. In addition, the anode material should be physically stable at the operating temperature, mechanically robust and resistant to thermal shock. The latter may require that the anodes must be preheated before they are inserted into the electrolyte.
2. *The impurity metal content in the aluminium.* The need for making pure aluminium will become more stringent in coming years. The corrosion products formed by the dissolution of the anode oxide materials into the electrolyte report predominantly to the aluminium contaminating the metal produced. Hence, the anode corrosion should be low enough to give impurity contents meeting specifications for smelter grade aluminium.

In the last 40 years many aluminium producers and research institutions have worked on developing inert anodes. In most cases this has been done in laboratory-scale cells, with amperages between 10 and 100 A, but people have also worked with pilot-scale sized cells with 2 and up to 20 kA. Two paths have emerged, the ceramic and cermet conducting electrodes, which have been championed by Alcoa, and the so-called 'metal anodes' developed by Moltech. Both groups can claim they appear to have conquered the materials science with respect to the primary criteria, and both have reported larger scale trials retrofitting conventional cell design. In reality these two types of the electrodes become extremely similar at the anode-electrolyte interface, because this electroactive surface necessarily has to be an oxide, irrespectively of what material the substrate is made of, see Welch (2009).

3.11.2 Present conclusion on inert anodes

Several companies and research institutions in recent years have studied inert anode materials actively. There is no doubt that substantial progress has been made in inert anode development during the last few years, particularly regarding the two main challenges: *anode wear* and *metal purity* in inert anode cells. Galasiu et al. (2007) have written a book that gives a very good overview of the work that has been done on inert anodes so far.

The commercial aspects have not yet been proven. At present a number of engineering problems remain to be solved, and the operation of inert-anode cells will certainly be very challenging. Cell retrofitting may not be the preferred development path in the future. It is impossible to say when, or even if, this may be a proven technology. Welch (2009) concluded that it will take dedication, time – one or two decades – and many millions of dollars before the issues mentioned above will be solved satisfactorily.

3.12 The past, present and future of primary aluminium production

What will happen to the Hall-Héroult process in the next 10–20 years? Generally, predictions about future technological development are very difficult, as we all know, and the area of primary aluminium production is no exception. Sometimes one may be tempted to be very optimistic and foresee revolutionary inventions that may give dramatic improvements of the process, while in other situations one may be rather conservative and expect little technological change and progress. One way of trying to make predictions about the next 20 years is to look back 20 years and see what happened in that period. Then one may assume that the development will continue at about the same pace in the years to come.

Thonstad et al. (2001) made an attempt to forecast operational performance data for the best Hall-Héroult cells in 2020. Their data are given in Table 3.1.

Table 3.1 The state-of-the-art Hall-Héroult cell technology parameters from 1980 to 2000 and an attempted forecast made for the year 2020

Cell parameter	Year 1980	Year 2000	Year 2020
Line current (kA)	225	325	500–600
Cell voltage (V)	4.1	4.1	3.9–4.0
Current efficiency (%)	94.0	96.0	96.5–97.0
Energy consumption (kWh/kg Al)	13.0	12.8	12.0
Cell life (days)	1500	2000–2800	3000
Anodic current density (A/cm ²)	0.80	0.85	0.95

Source: Thonstad et al. (2001)

Certainly the list could have been made longer, but it will suffice here to illustrate the achievements that have been made and the progress that may be expected.

The previous industrial advances were led by magnetic compensation and computerised process control coupled with improved alumina feeding. Surprisingly, the rate of progress has been rather slow with respect to optimisation of the electrolyte composition. The present electrolyte composition of 10–12 wt.% excess AlF_3 was used already in the best cells about 30 years ago. Many high-amperage cells are operated with the same electrolyte composition today.

There are some areas where changes and improvements obviously have to come. With the higher alumina throughput caused by increasing cell amperage there will be more focus on consistency of the alumina and less tolerance of 'difficult' aluminas, which may cause operational disturbances and more dust in the working environment in the cell rooms. Apart from perceivable technological breakthroughs, the process has long been characterised by incremental improvements. We may need to break away from the approach of incremental engineering. However, small but significant improvements in fundamental knowledge and its application to improve the operation of industrial cells are still possible and worth striving for. These will not only remove false concepts that may have existed and thereby improve the Hall-Héroult process, but will also strengthen the competitiveness of aluminium against other metals and plastics.

The outlook of the primary aluminium industry may now be summarised as follows:

- A mature industry that presently suffers severely from low aluminium prices and a very challenging market situation.
- Several Greenfield smelters are presently planned or under construction.
- There are opportunities for incremental improvements if they can be justified economically.
- There will be an ever-increasing pressure on health, safety and environmental control.
- The intense focus on cost reductions will continue.
- There is no break-through technology on the near horizon.

Aluminium may become an even 'greener' metal than today. Technically, the aluminium production process can be close to a zero greenhouse gas producer. The first step, which is actually ongoing, is to focus on lower specific energy consumption, and also to eliminate the occurrence of anode effects. A natural second step is related to the recovery of energy from the main heat loss sources of the cells, like cathode sidewalls and gas exhaust systems. A third step may be CO_2 gas cleaning related to the electric power generation, and finally collection and cleaning of the CO_2 from the electrolysis process itself may be a technical possible future scenario.

3.13 Acknowledgements

The author acknowledges the valuable comments on the content of this chapter by Professor emeritus Jomar Thonstad at the Norwegian University of Science and Technology in Trondheim.

3.14 References

- Galasiu, I., Galasiu, R. and Thonstad, J. (2007), *Inert Anodes for Aluminium Electrolysis*, 1st edn. Düsseldorf: Aluminium-Verlag, Marketing & Kommunikation GmbH, 207 pages.
- Marks, J., Roberts, R., Bakshi, R.V. and Dolin, E. (2000), 'Perfluorocarbon (PFC) generation during primary aluminium production', in *Light Metals* 2000, 365–71.
- Thonstad, J., Fellner, P., Haarberg, G.M., Hives, J., Kvande, H. and Sterten, Å. (2001), *Aluminium Electrolysis – Fundamentals of the Hall-Héroult Process*, 3rd edn. Düsseldorf: Aluminium-Verlag, Marketing and Kommunikation GmbH, 359 pages.
- Welch, B. (2009), 'Inert anodes – The status of the materials science, the opportunities they present and the challenges that need resolving before commercial implementation', in *Light Metals* 2009, 971–8.

Production of secondary aluminium

G. WALLACE, Sims Aluminium Pty Limited, Australia

Abstract: The term ‘secondary aluminium’ refers to aluminium that is produced from recycled aluminium originating from various forms of aluminium scrap including new production off-cuts, machining swarf, drosses or obsolete end-of-life aluminium products. This chapter will give some background on the development of this important industry. It will cover the various sources of raw materials and their characteristics and the important pre-processing techniques employed to efficiently recover aluminium and convert it to a usable alloy and form. The major cost drivers will be discussed, followed by a brief comment on the likely future directions of the secondary aluminium industry.

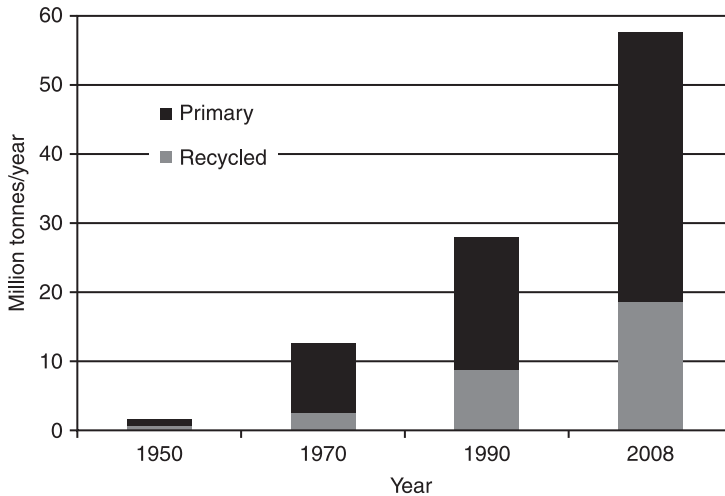
Key words: secondary aluminium, recycling, casting alloys, scrap, ISRI.

4.1 History of secondary aluminium

Aluminium has been recycled since it was first commercially produced and today secondary aluminium accounts for about one-third of world aluminium consumption. The initial reasons for recycling were commercial as well as environmental. There are significant energy savings in recycled aluminium, using some 5% of the energy required to produce primary aluminium. In the western world recycling rates are high, ranging from 60% for used beverage cans (UBCs) to 85% in building and construction and 95% in transportation. Aluminium quality is not impaired by recycling – it can be repeatedly recycled and hence aluminium retains a high scrap value. Almost 100% of the scrap arising from manufacturing of aluminium products is recycled.

The predominant use (approx 70%) of recycled aluminium is in the production of aluminium-silicon casting alloys mostly used in the automotive industry, with the balance converted to wrought alloys for re-use in sheet or extruded form, with a small proportion being converted to de-oxidant for the steel industry.

World aluminium production in 1990 was around 28 million tonnes, of which some 8 million tonnes, was recycled from scrap. Today the total is around 56 million tonnes, of which some 18 million tonnes is recycled from scrap (Fig. 4.1). By 2020 metal demand is projected to have increased these levels to 96 million tonnes (with around 31 million tonnes recycled from scrap). Today, around 50% of the scrap is old scrap (i.e. scrap from end-of-life products). Since the 1940s both Europe and North America have generated sufficient aluminium scrap to permit the development of a strong aluminium recycling industry. Following the energy crisis in the 1970s, Japan ceased domestic



4.1 Global aluminium usage 1950–2008, showing proportions of primary and recycled aluminium.

primary aluminium production and switched to aluminium recycling in the 1980s. In the past 20 years there has been strong development of an aluminium recycling industry in Russia, India and in particular China. Their low labour rates have made them highly competitive and in recent times this has created strong and increasing scrap flows from North America and Europe to these countries.

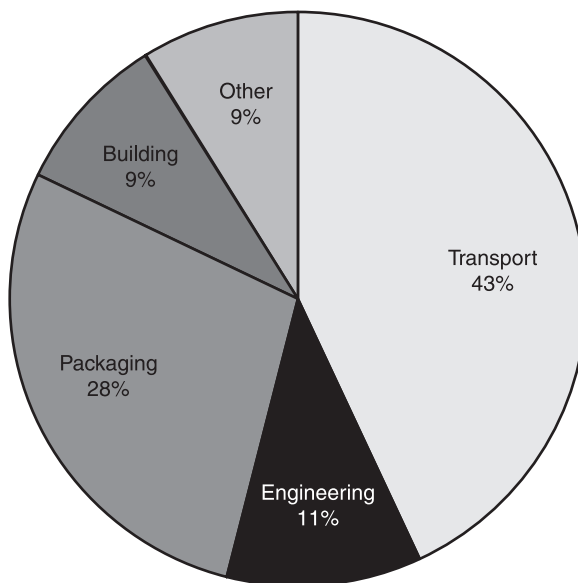
For most countries, there is a well-established market for recycled aluminium with firmly defined distribution chains. There are two types of secondary producers – refiners and remelters. The refiners produce casting alloys and deoxidation aluminium from old and new scrap and supply them in ingot or molten form. In addition to alloying to required specification, the refiners will flux the metal to improve quality through removal of oxides and intermetallics plus at times remove elements such as magnesium and calcium. The remelters produce wrought alloys mostly from clean and sorted wrought alloy scrap and supply them in the form of rolling slab, extrusion billets or master alloys. Alloys are supplied according to international standard and/or customer specifications.

The number of companies involved in secondary aluminium is significant compared with the relatively low number of primary producers. This has occurred in part as a result of localised requirements for recycling and the fact that a secondary refiner can be economically run on reasonably low volumes. There are still many secondary refiners with a capacity of less than 10,000 tpa, although the increasing pressures from environmental legislation and the high capital cost of more efficient technologies are impacting heavily on this low margin industry. In recent years there have been a number of plant closures and consolidations.

Figure 4.2 shows the distribution of recycled scrap by source market. Whilst the value of aluminium scrap has been known for many years, the first major impetus to the growth of recycling was through the humble aluminium can. The aluminium can has really been the face of aluminium recycling since the 1970s. The intensive marketing of can collection by the general public gave awareness to the real value of aluminium scrap and this has been carried on by governments and local communities alike in their drive to reduce landfill and create a sustainable environment. Packaging, whilst only accounting for about 12% of aluminium consumption, has long been important for recycling due to the relatively short life span of packaging items. New packaging developments such as the screw top wine closure are creating new volumes in recycling aluminium.

Transport is the most important industry for aluminium applications. In 2007 almost 30% of wrought and casting alloys went into transport, cars, trains, ships, aircraft, etc. The refiners in particular rely on the automotive industry for around 70% of their volume and the pressure from governments for lower emission vehicles has been significant in the growth of secondary aluminium as automotive producers strive for lighter weight. Aluminium has been increasingly used for some 40 years in automotive drive-train components and with cars averaging a 12 year life this area of scrap is very important to the recycling industry.

The building industry accounts for some 25% of aluminium consumption, but with a relatively long life of 35–40 years, it has only in the last 10 years become an important source of scrap.



4.2 Global recycled scrap by market.

4.2 Sources of raw materials

Secondary aluminium scrap sources include new production off-cuts, used aluminium products, machining swarf and drosses generated in the melting process. The chemical composition of each category of scrap will determine the sector of industry where it will ultimately be used. The silicon-containing aluminium casting alloys can accommodate a greater variety of scraps as their impurity limits are broader than the wrought alloys. The casting alloys are lower value added than the wrought alloys however and therefore the use of some scraps needs to be limited not because of composition but on the basis of cost. For example, all aluminium-silicon casting alloys could be produced solely from extrusion scrap plus alloying additives such as silicon, copper, etc., however the lower sales value of casting alloys makes this unviable. A large proportion of scrap recycled by remelters is in-house scrap from the initial billet and slab production. All scrap collected by the metal merchants is sorted, processed and graded into the various scrap categories for sale to refiners or remelters either locally or to export destinations. Scraps are traded to international specifications. There are about 40 grades of aluminium scraps specified by the Institute of Scrap Recycling Industries (ISRI, 2007).

The important factors which define the value of scrap are:

- Is the scrap a single known alloy? – This allows the user to know exactly what the composition will be when melted.
- Is the scrap free of contaminants? – Metallic contaminations will change the chemical composition of the recovered molten alloy and may render it ‘out of specification’. Non-metallic contaminants may have environmental impacts and will decrease the yield attainable.
- Does it contain dangerous items such as sealed containers which may result in an explosion and potential loss of life?
- Is it suitable for direct charge to a furnace or is some form of pre-processing required?

4.2.1 New production off-cuts

The advantage of new production off-cuts is that they can easily be segregated into their various alloys, they generally don’t contain attachments which may be a contamination and they require minimal labour to pre-process prior to melting. In many cases the scrap is uncoated and therefore will have a higher possible metal yield. Likely pre-processing will include baling, shearing and in the more high-tech plants de-coating if lacquered or painted. Also included in this category of scrap is casting trim or rejects. A couple of typical ISRI specifications for new production off-cuts are:

Tough – mixed new aluminium alloy clippings and solids

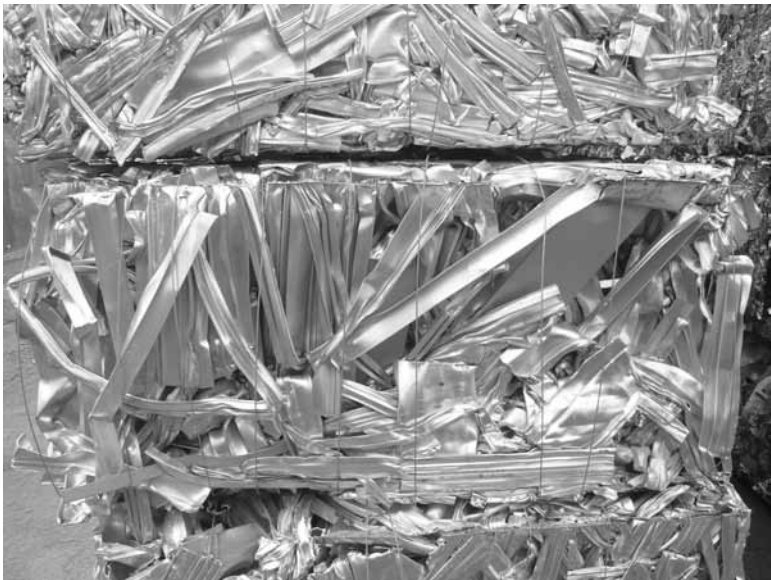
Shall consist of new, clean, uncoated and unpainted aluminium scrap of two or more alloys with a minimum thickness of .015" (.38 mm) and to be free of hair wire, wire screen, dirt and other non-metallic items. Oil and grease are not to total more than 1%. Also free from punchings less than ½" (1.27 mm) in size.

Tata – new production aluminium extrusions

Shall consist of one alloy (typically 6063). Material may contain 'butt ends' from the extrusion process but must be free of any foreign contamination. Anodized material is acceptable. Painted material or alloys other than 6063 must be agreed upon by the buyer and seller. An example of baled Tata is shown in Fig. 4.3.

4.2.2 Post consumer scrap

This category will include products that may have had a life as short as a few weeks in the case of UBCs to around 12 years for automotive sources or even 30 years plus in the case of construction materials. They will have been collected from a vast range of sources and will generally require sorting prior to any further pre-processing for melting. They will invariably be contaminated with one or more of paint, lacquer coatings, dirt, plastic, oil, grease and various metallic and non-metallic attachments. For effective use this category may require more



4.3 Tata.

sophisticated methods of pre-processing including shredding and magnetic, eddy current or heavy media separation. The most common ISRI specifications are:

Taint/tabor – clean mixed old alloy sheet aluminium

Shall consist of clean old alloy aluminium sheet of two or more alloys, free of oil, venetian blinds, castings, hair wire, screen wire, food beverage containers, radiator shells, airplane sheet, bottle caps, plastic, dirt and other non-metallic items. Oil and grease is not to total more than 1%. Up to 10% of *Tale* permitted (painted siding). Figure 4.4 shows an example of clean mixed old alloy sheet aluminium (Taint/tabor).

Tense – mixed aluminium castings

Shall consist of clean aluminium castings which may contain auto and airplane castings but no ingots, and to be free of iron, brass, dirt and other non-metallic items. Oil and grease are not to total more than 2%. Mixed aluminium castings (Tense) are shown in Fig. 4.5.

Taldon – baled aluminium UBC scrap

Shall have a minimum density of 14 pounds per cubic foot (225 kg/m^3 for unflattened UBC and 22 pounds per cubic foot (353 kg/m^3) for flattened UBC.



4.4 Taint/tabor.



4.5 Tense.

Size: Minimum 30 cubic feet (.85m³) with bale range dimensions of 24" to 40" (61 to 100 cm) by 30" to 52" (76 to 132 cm) by 40" to 84" (102 to 213 cm). The only acceptable tying method shall be as follows: four to six 5/8" (1.6 cm) × .020" (5cm) steel bands, or six to ten #13 gauge steel wires (aluminium bands or wires are acceptable in equivalent strength and number). Use of skids and/or support sheets of any material is not acceptable. Must be magnetically separated material and free of steel, lead, bottle caps, plastic cans and other plastic, glass, wood, dirt, grease, trash and other foreign substances. Any free lead is basis for rejection. Any and all aluminium items, other than UBCs are not acceptable. Baled aluminium UBC (Taldon) is shown in Fig. 4.6.

4.2.3 Swarf

Mostly generated from machining of castings or wrought bar-stock, swarf will contain significant oil and moisture which must be removed prior to melting for clean efficient recovery. In recent years plants with large swarf generation have installed briquetting machines to recover and recycle the expensive cutting fluids. This has led to strong pricing for the resultant briquettes which attract lower freight costs and virtually no pre-processing for melting. The downside is that any free iron present is retained in the briquette. Loose swarf must be dried to remove moisture and burn-off hydrocarbons to ensure maximum recovery and then passed over a magnet to remove any iron contamination. The advantage of swarf is that in many cases it will be of single known alloy type. Mixed swarf on the other hand



4.6 Taldon.

can be quite a minefield for the remelter, as it may contain a range of wrought and casting alloys or even zinc alloys – it is not easy to tell the difference. The ISRI specification is:

Telic – mixed aluminium borings and turnings

Shall consist of clean, uncorroded aluminium borings and turnings of two or more alloys and subject to deductions for fines in excess of 3% through a 20 mesh screen and dirt, free iron, oil, moisture and all other non-metallic items. Material containing iron in excess of 10% and/or free magnesium or stainless steel or containing highly flammable cutting compounds will not constitute good delivery. To avoid dispute, material should be sold on the basis of definite maximum zinc, tin and magnesium content.

4.2.4 Dross

Aluminium dross (see Fig. 4.7) is generated during the melting process and essentially consists of metallic aluminium and aluminium oxide. Processing of aluminium dross is a specialised industry. Dross is classified as hazardous and if exposed to water will give off ammonia and other gases. The technique for processing and melting is significantly different to that of other scraps. The secondary aluminium industry processes significant volumes of dross generated in the primary industry and in fact there are plants which exist solely to recover



4.7 Aluminium dross.

metal from primary dross. In most cases this is done on a fee for service basis and the recovered metal returned to the primary smelter.

4.3 Processing

In order to maximise the yield of the different scraps melted, they must be pre-processed to get them in the best state for handling, charging and melting. It is important to be able to charge the scrap to the furnace at a rate greater than the melt rate of the furnace. There are a number of processing techniques that can be employed to present the scrap in the most suitable form. Some scraps may require several processes.

4.3.1 Sorting

At the point of receipt all scraps will be inspected for possible contaminations and may be quarantined awaiting hand sorting. The inspection will also be looking for potentially dangerous items such as sealed containers. It is also the point at which a claim on quality or a correction to price can be made. Subsequent sorting may involve removal of free contaminants, both metallic and non-metallic, or simply segregation of different scrap types to upgrade the various qualities.

Specialised methods of separation include magnetic separation, heavy media separation and eddy current separation. A significant source of aluminium scrap today is from car-shedders. A major byproduct is a material known as Zorba

which consists of approx 60% aluminium together with various other non-magnetic metals including lead, zinc, stainless steel and magnesium plus some non-metallics. Large volumes are shipped to China, where the labour cost is low, and the material is tipped out onto large tables surrounded by many operators and hand sorted. A mechanised method for this process is separation using heavy media plants where the metal is segregated based on its density. The mixed solids are placed in a liquid denser than one metal and less dense than the others. The denser material sinks whilst the less dense floats.

Eddy current separation is used for separation of plastic and paper from UBCs emanating from kerbside collection of containers.

4.3.2 Baling and shearing

The oldest forms of pre-processing are shearing to reduce length and baling to improve density and handling. Early baling was in small bales around a foot square, producing a dense product which can be stacked on pallets for transporting, however today the most common form is large bales approx 1 m × 1 m × 1.5 m. This highly automated process produces bales that stack well, removes the need for pallets and provides much faster baling rates so that large volumes can be processed economically.

4.3.3 Shredding

The shredding process produces a free flowing material ideally suited to subsequent pre-melting processes such as magnetic separation, heavy media separation or de-coating. Clean scrap may also be shredded to facilitate charging and melting direct into a molten bath to improve yield.

4.3.4 Drying and de-coating

Aluminium swarf contains oil and moisture which must be removed to maximise metal recovery. Drying may involve centrifuging and/or passing swarf through a barrel drier where the oils are burnt off. Once dried the swarf is then passed over a magnetic separator. In the past decade many large generators of swarf have installed equipment to briquette the swarf and in the process recover valuable cutting fluids for re-use. The briquettes do not require drying, however they will contain any free iron which is generally present in swarf to a small degree from tool wear. This may be critical for the end user if the swarf is from automotive wheels and is used back in the same alloy (e.g. A356), which has a tight iron limit of 0.2% maximum (note as well A356.1 has a limit of 0.15Fe and A356.2 has a limit of 0.12Fe).

De-coating involves the removal of paints and lacquers using pyrolysis, a form of incineration that chemically decomposes organic materials by heat in the

absence of oxygen. By controlling furnace temperature and atmosphere to a level that will decompose the organics but below the melting point of the scrap, improved yields are obtained in the subsequent melting process.

4.3.5 Milling and screening

Drosses are frequently milled and/or screened to concentrate the recoverable metal and therefore reduce the volume of waste produced. The resultant fines may still contain some metallic aluminium, but at a concentration too low to economically recover in the melting process. The fines can however be re-directed to other industries for re-use, thus significantly reducing the amount of waste going to landfill.

4.3.6 Melting and alloying

The secondary aluminium industry employs a range of furnaces, however the most common is oil or gas fired reverberatory furnaces ranging from 5 to 90 tonnes capacity and rotary furnaces of 2–20 tonnes capacity. Modern plants will utilise efficient oxygen enriched burners for faster melting rates.

Reverberatory furnaces are box shaped and ideally suited to the melting of high yield solid scraps. More sophisticated types may be fitted with magnetic stirrers or electro magnetic pumps to improve melt rates and in large plants. Those used for casting rolling slab will also tilt for rapid pouring whilst ingot casters are usually static. Whilst reverbs, as they are commonly known, are frequently used as primary melting furnaces they are almost always used as the final alloying and casting furnace. When used as a primary melter they may be fitted with stage burners that permit the pyrolysis of the scrap to burn off the paints and lacquers prior to getting to melting temperatures thus increasing metal yield. The final alloying and casting furnace will be fitted with fluxing and degassing equipment to clean the melt prior to casting.

Rotary furnaces can also be used to melt the high yield scraps, however their real forte is for melting of dross and low yield scraps under a flux cover of sodium chloride and/or potassium chloride. The flux is added to protect the scrap from oxidation and to remove the unwanted oxides. Early rotary furnaces were single pass, fixed axis furnaces where the flux was wet. Today the tilting axis double pass rotary is more common, where less flux is used and the flux is dry. The waste slag resulting from the use of salt fluxes will contain a small percentage of aluminium plus oxides and salt. Special plants exist to process this waste which in many countries is now banned from being sent to landfill. These plants recover the aluminium, salt and oxides for re-use.

Other furnaces which may be used include refractory crucible and induction furnaces although these are usually for specific niche applications such as master alloys production. Sweat furnaces are also employed for recovery of aluminium

from scrap that is heavily contaminated with iron. Modern plants now have furnaces with accurate temperature control which often permits the melting of moderately iron contaminated scraps with nil dissolution of the iron.

4.4 Cost drivers

The principal aim of all secondary plants is to achieve the lowest possible raw material cost. As a general rule, raw material accounts for some 85% of the ultimate selling price. Ensuring that the scrap purchased meets the plant's quality and price requirements is of course important, but if the alloy maker does not then select the best scrap mix or the furnace operator does not achieve the best yield, then it will be difficult to make a satisfactory return. Computer programs are used to select the range of scraps that will most economically produce the desired metal composition at the lowest possible cost. Materials are then charged to the appropriate furnace and melted efficiently. Investment in modern technology will improve metal yield, but the capital cost can be expensive and the smaller plants will be disadvantaged, making it difficult in the western world for the smaller plants to remain viable.

Secondary aluminium plants operate in countries with diverse economies. Therefore there is a large range in labour costs, and yet the resultant aluminium products are traded globally at competitive rates. In the western world labour costs are high and hence the smaller plants which are not growing in volume or investing in modern technology are increasingly becoming unviable and eventually closing.

The secondary aluminium industry has been for some time working on reducing waste disposal costs through seeking new outlets for the ultimate waste. Governments in many countries are now restricting the wastes which can be landfilled or at least escalating the fees, forcing recyclers to develop strategies to minimise waste generation or find alternative applications where the waste can be a resource.

4.5 Future trends

Aluminium recycling is here to stay. It will have a natural increase in line with the increase in the use of primary aluminium. The fact that recycling consumes only 5% of the energy used for primary production means that aluminium can be re-used repeatedly without loss of properties for generations to come. However, for many of the recyclers to remain viable there needs to be development of new recycling methods to recover the still significant amount of post consumer aluminium that ends in landfill. Increased recycling rates are essential for sustainable development. Further improved techniques for obtaining the best possible metal yield are required to ensure the viability of recyclers. For example, a 1% yield improvement for a recycler with a 100 ktpa capacity translates to

approx \$A2 million improvement in bottom line performance. The strong growth in countries like China and India will continue to place pressure on the viability of smaller plants in the western world and as a consequence further consolidation must occur.

4.6 Further reading

1. Australian Aluminium Council – *Sustainability Report 2007*.
2. International Aluminium Institute – *Global Aluminium Recycling: A Cornerstone of Sustainable Development*.

4.7 Reference

Institute of Scrap Recycling Industries (ISRI), 2007. *Scrap Specifications Circular*. Washington, DC: ISRI.

Ingot casting and casthouse metallurgy of aluminium and its alloys

J.F. GRANDFIELD, Grandfield Technology Pty Ltd, Australia

Abstract: The key casting processes used in primary and secondary aluminium cast houses are described, i.e. direct chill casting of wrought alloy products and open mould conveyor casting of remelt ingots. The process economics and product quality are determined by the heat and fluid flow behaviour during casting. The current state of the art for control of melt impurities (sodium, inclusions and hydrogen) using melt refining technology is given. Process physics is linked to optimisation of these processes.

Key words: direct chill casting, water cooling, ingot conveyor casting, cracking, hot tearing, melt refining, degassing, filtration, inclusions, sodium removal.

5.1 Direct chill casting

Direct chill (DC) casting is used in the aluminium industry's primary and secondary aluminium smelter cast houses to produce millions of tonnes per annum of wrought alloy products for rolling and extrusion and also remelt ingots used to make shape castings. DC casting process technology has been well reviewed (Emley, 1976; Granger, 1989; Katgerman, 1991; Grandfield and McGlade, 1996; Grandfield, 1997; Schneider, 2002) and the recent book by Eskin (2008) discusses the physical metallurgy of aluminium DC casting in detail with an emphasis on defect formation and control. In addition to DC casting and chain conveyor ingot casting, other processes can be and are used to produce aluminium ingot products; notably wheel and belt casting and sow casting. Twin roll casting is also an important process for direct casting of flat wrought alloy products.

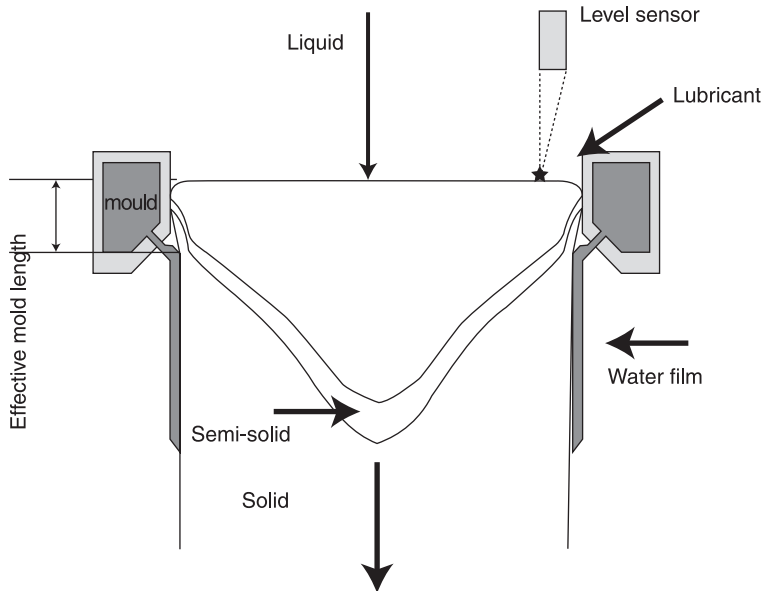
Precursor continuous casting processes included that of Junghaus (1933) involving continuous withdrawal of an ingot from a water cooled mould, but no direct water quenches on the ingot; see Lippert (1944) for a comparison of these early processes. DC casting was developed independently in the 1930s in Germany (Roth, 1936; Zunkel, 1939), and the USA (Ennor, 1942) as a continuous casting alternative to the practice of casting extrusion and rolling ingots in permanent moulds. Russian work on DC casting quickly followed (Dobatkin, 1948).

The higher cooling rates, elimination of shrinkage cavities, better productivity and yields of DC continuous casting led to its rapid adoption over permanent mould ingot casting. The DC casting process was used at an early stage for magnesium and is currently applied to aluminium, magnesium, zinc and copper alloys in a variety of configurations. Early cooling configurations included direct

immersion of the ingot as it emerged from the mould into a water bath, pipes spraying water onto the emerging product below the mould and alternatively holes or slots at the base of the mould plenum to create a DC water jet; the latter becoming the standard configuration used today.

In one early version of the process a single strand was cast, sometimes fully continuously with a saw below the mould cutting the ingots to the desired length. These early processes were all vertical, and vertical DC (VDC) casting remains the most common version as opposed to horizontal DC (HDC) casting.

The DC process used today is essentially the same as the early process but significantly different in detail (Fig. 5.1). In the case of VDC, a starting head is in place in the mould when liquid is first poured into the mould. Once some solid is formed, the starting head or 'dummy' is lowered either on a platen on a hydraulic ram or a suspended platen into a pit in the ground up to 11 m. The lowering rate sets the casting speed. The emerging ingot is chilled by water jets spraying directly onto the emerging ingot. The water then forms a falling film down the ingot. Liquid metal is continually fed to the liquid pool in the mould to maintain a set level. Mould lubrication is essential to stop the ingot shell sticking to the mould. Early embodiments used fat or grease applied to the mould before the start of casting. Modern configurations use continuous lubricant feed of oils



5.1 Schematic of open top vertical direct chill casting. Liquid is supplied to the mould via a refractory downspout. The level may be controlled by a refractory float at the tip of the downspout or by an actuated pin in the downspout which is adjusted according to the measured metal level.

such as castor or rapeseed. Early mould designs were simple tubes that suffered distortion. Modern moulds tend to have a box construction with interior baffles for rigidity and ease of control of the water cooling. Mould technology is discussed in more detail below and several variants have been used over the years, some of which like electromagnetic casting (EMC) have been superseded.

A variety of products can be produced by DC casting; extrusion billet, rolling slab, forging performs, T-bar shapes and hollow sections. Sizes range from 50 mm to 1.1 m diameter and up to 3 m wide, 10 m long rolling slab. The technology for DC casting rolling slab and extrusion billet has diverged considerably. Modern extrusion billet VDC casting consists of casting up to 100 strands depending on diameter, through a flooded table gas pressurised hot top mould into a 10 m pit. Typical capacities of up to 100 000 tpa are achieved for each unit. State-of-the-art slab casting for ingots of up to $1600 \times 3000 \text{ mm}^2$ is usually undertaken with open moulds using automated level control for typically five or six slabs cast at once. Casting speed depends on alloy and ingot size and varies from 50 to 1000 mm/min.

HDC casting was developed in France during the 1960s (Angleys, 1960, 1964), for making aluminium busbar rectangular sections sized from $120 \times 20 \text{ mm}^2$ up to $700 \times 200 \text{ mm}^2$. Casting speeds up to 1000 mm/min were used for the small sections. This early process used a water-cooled metal mould with a porous graphite insert through which lubricant was supplied. Later, metal only mould technology was also used. Two rolls were used as the drive mechanism to pull the product out of the mould.

HDC casting gradually gained more acceptance in the aluminium industry, being adopted for remelt ingot, rolling slab and billet production. Several companies developed their own versions of the process which differ mainly in mould design, including:

- Reynolds (Simonson et al., 1963; Wuetig, 1975)
- Wagstaff (Wagstaff, 1975)
- Gautchi (Anonymous, 1963)
- Kaiser (Spaulding, 1975)
- Alcoa (Spear and Brondyke, 1971; Powers, 1975).

Continuous mould lubrication is essential to avoid surface tears in HDC because of the long run times. Lubricant can be added via an oil plate (Kaiser) (Spaulding, 1975), a permeable refractory gasket (Gautchi; Anonymous, 1963), positioned between the mould face and the refractory orifice plate or permeable graphite. In the case of Reynolds, casting would continue for 30 m without lubricant (or flying saw) and then stop, relying only on the self-lubricating properties of graphite. A version of the HDC process was developed by VAW to cast wide strip $10 \times 1000 \text{ mm}^2$ (Moritz and Dietz, 1979). Toward the end of the last century and early this century, HDC became popular for production of small remelt ingots and in extrusion plants for reprocessing internal scrap because of the low capital cost and

small incremental capacity (Zeillinger and Beevis, 1997; Niedermair, 2001) as well as for T-bar sections (Garipey et al., 2005) and small diameter forging stock (Yoh, 1989).

The evolution of DC casting process technology has been driven by the downstream customer requirements. For remelt ingots, as long as the ingot is of the correct composition, sound and free from porosity and of the correct dimensions then the internal microstructure is of no concern since the ingot is remelted. Extrusion billets need to be within certain straightness and diameter tolerances and correctly homogenised before extrusion. The surface zone microstructure is of importance because it determines the size of the butt discard left after direct extrusion. Thus, much of the mould technology evolution has taken place to reduce the size of this surface zone. Similarly, with rolling slab the surface zone must be scalped before rolling and the smaller the zone the less scalping losses. Shape requirements for rolling slab are more stringent than billet with rolling face flatness, twist, bow, straightness, and butt thickness being important.

5.2 Heat flow and solidification

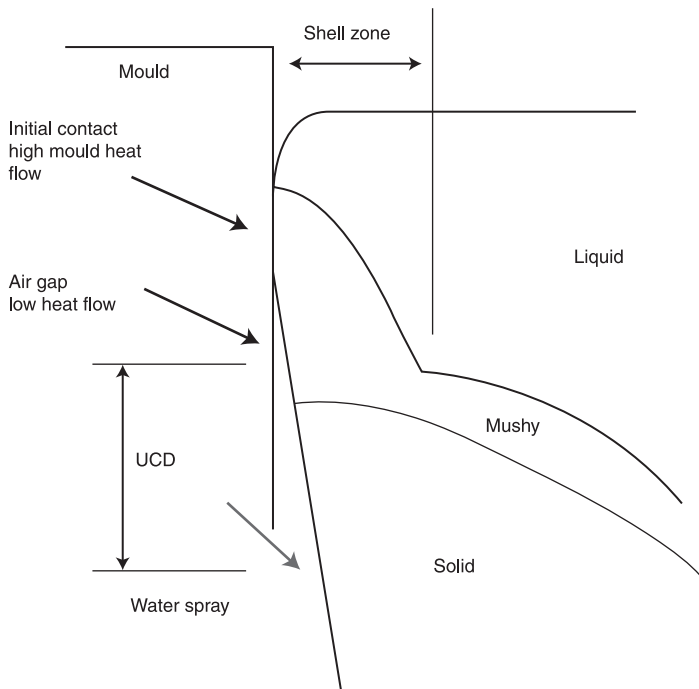
DC casting heat flow is generally considered in two phases; the start of the process when the temperature field is changing and the steady state phase where the temperature distribution is relatively stable when the heat input is balanced by the heat extraction. The process heat flow determines the temperature distribution and controls the solidification rate, solidification defects, and stress development which determines slab deformation, final shape and the formation of cracks. It is thus essential to have a good understanding of the heat flow to minimise scrap and control ingot microstructural quality.

Experimental methods, reviewed by Grandfield (2000), such as thermocouple implant temperature measurements and liquid doping etc. have revealed that a liquid pool forms during casting (Fig. 5.2). Where the metal first touches the mould, mould cooling causes solidification of a thin shell. The water spray has an upstream cooling effect into the mould and a thicker region of solid forms near the mould exit. In VDC castings the length of solid formed above the water spray is often known as the 'upstream conduction distance' (Groce, 1971; Devadas and Grandfield, 1991; Flood et al., 1995; Grandfield, Goodall et al., 1997).

It is important to appreciate that there are two components of the total pool depth when examining the effects of variables on the temperature distribution and resulting pool shape. The first is the shell length, which is defined by the distance between the point where metal first contacts the mould and the water spray impact point (Fig. 5.3). The second is the vertical distance from the water spray impact point to the lowest point of the pool, labelled here as the 'water spray pool depth'. For example, in the case where two metal levels are used, with all other conditions the same, the total pool depth changes, but the water spray pool depth does not



5.2 Pool shape in 155 mm diameter 6063 alloy billet casting obtained by adding AlCu liquid during casting and then sectioning and etching.



5.3 Schematic of shell formation in an open top mould. Contraction of the ingot below the mould pulls the shell away from the mould forming an air gap.

change. The solid in the mould consists of two components; the thin shell formed by the mould cooling, and the solid formed by the upstream effect of the water spray. In the case of a refractory hot top mould the physical mould length differs from the shell length due to the meniscus determining the first point of metal contact and the water spray impact point is not exactly at the end of the mould. The spray is angled and the metal has contracted away from the mould at that point.

The temperature distribution during the steady state part of the cast is determined by a balance between the convective heat input (determined by casting speed V , density ρ , ingot size R , specific heat C_p and latent heat L), heat extraction by diffusion (determined by diffusion path length i.e. the ingot size R and thermal conductivity k) and convection cooling (described by the heat transfer coefficient h). For example, as the casting speed or ingot size is increased or the thermal conductivity of the alloy decreases then the pool depth increases. Two non-dimensional numbers have been used to characterise the heat balance (Flood et al., 1995; Hakonsen, 1995; Grandfield, Goodall et al., 1997): the Peclet number, $Pe = \rho C_p VR/k$ (the ratio of convective to diffusive heat flow) and the Biot number $Bi = hR/k$ (the ratio of resistance to heat flow from conduction to that from surface convection).

The water spray in DC casting results in intense cooling [$\sim 6 \text{ M/Wm}^2$ (Jensen et al., 1986; Grandfield and Baker, 1987)] and high Biot numbers. Approximately 90–95% of the heat is typically extracted by the direct water spray (Grandfield and Baker, 1987; Hakonsen and Mortensen, 1995) with the remainder going into the mould. Much work has been conducted to characterise the water spray heat transfer coefficients as a function of the boiling mode and spray parameters of the cooling water, such as impact velocity, jet angle and water composition (Weckman and Niessen, 1982; Jensen et al., 1986; Grandfield and Baker, 1987; Fjaer et al., 1992; Grandfield, Goodall et al., 1997; Grandfield, Hoadley et al. 1997). Water cooling is further discussed below.

Typical non-dimensional number values for commercial aluminium VDC casting are: $1.8 < Pe < 4.5$ and $2 < Bi < 60$ (Flood et al., 1995). It can be observed that diffusion and convection are both strong in this process. In contrast, continuous casting of steel has much higher casting speeds and lower thermal conductivity values, giving larger Peclet numbers. The diffusive heat flow in the casting direction is very small compared to convection in the case of steel, resulting in large pool depths for given ingot dimensions and little axial heat flow. The low Pe for aluminium also explains why the pool depth is relatively small; typically the order of the diameter or width of the ingot.

Early studies (Roth and Weisse, 1942; Dobatkin, 1948; Adenis et al., 1962–1963) showed that pool depths in both aluminium and magnesium increase linearly with casting speed. The normalised pool depth Δ_{ss} (absolute pool depth divided by radius) was found to be linear with Peclet number in a modelling study by Flood et al. (1995) i.e.

$$\Delta_{ss} = (a_1 + b_1 Pe) (c_1 + Bi^{-d_1}) \quad [5.1]$$

where a_1 , b_1 , c_1 and d_1 are constants. This was later confirmed experimentally (Grandfield, Goodall et al., 1997).

One tends to find that casting speeds used (often set empirically) for a given billet diameter and alloy tend to follow an inverse relationship, i.e.

$$V_c = \frac{F}{R}$$

where V_c is the casting speed, R the radius and F some alloy dependent factor. If one casts too fast then the ingot develops internal cracks. Although it has been known since the 1940s (Wilkinson and Hirst, 1952–1953) that slower speeds must be used for larger diameter billet to prevent cracking, it is perhaps not widely appreciated within the industry that the speed at which cracking starts for a given alloy is also found to follow an inverse relationship with diameter.

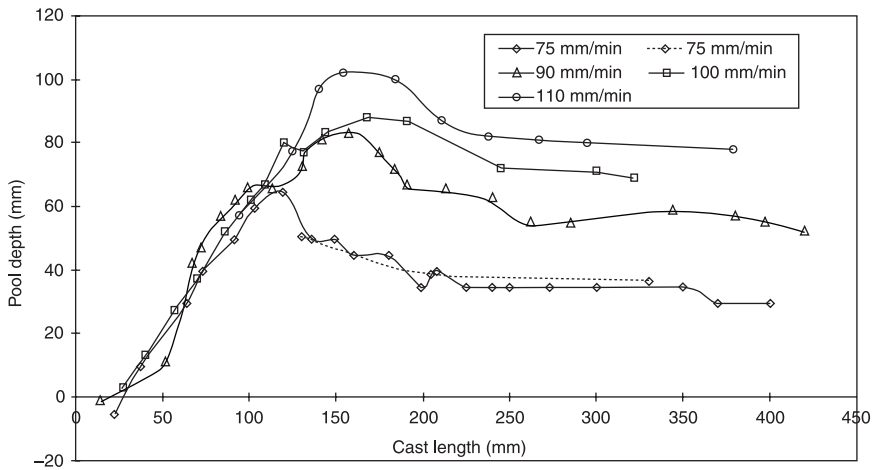
Cooling rates at the solidification front affect the size of the dendrite arm spacing (DAS) and grain size. Small ingots naturally have higher cooling rates than large ingots. Typical DC cooling rates are in the order of 1–10°C/s. The cooling rate is also higher near the surface of the ingot and drops toward the centre as a function of the pool shape and casting speed.

At cast start, the stable temperature distribution has not been established. Initially, when the mould is filled and the starter bar is in place but not moving more heat leaves the system than comes in and a solid base builds up. Once the platen starts to descend and the ingot emerges into the water cooling, the liquid pool starts to develop. Because there is a delay for the water-cooling effect to act in the centre of the ingot there tends to be an overshoot of the pool depth before it reverts to the steady state pool depth if a constant cast start speed is used (Fig. 5.4). Hot tear defects can often occur at this time (Jensen and Schneider, 1990; Schneider and Jensen, 1990).

In practice, two methods are used to avoid the overshoot of the pool depth and the possible occurrence of hot tears (Grandfield and Wang, 2004):

1. using an initial slow casting speed which is then ramped up to the desired run speed after the stage of pool overshoot, or
2. having a raised central section in the starting head.

The mould chill zone region has an unacceptable microstructure with surface segregation and a coarse grain region. If the size of this zone is minimised it allows smaller butt discard during extrusion and smaller scalping losses in the case of rolling ingot. Much of the evolution of DC mould technology has been driven by the intention of eliminating the shell reheating by reducing mould cooling (Emley, 1976; Grandfield and McGlade, 1996). The length of the upstream conduction distance is found to vary inversely with casting speed and alloy thermal conductivity (Groce, 1971; Flood et al., 1995; Grandfield, Goodall et al.,



5.4 Development of pool depth measured by dip rod as a function of cast speed for 228 mm diameter 6061 alloy billet (from Grandfield et al. 1997a). The pool depth goes through a maximum before reaching equilibrium.

1997) and is generally around 10–20 mm. Surface defect formation is further discussed below.

Fluid flow has an important influence on the heat flow and temperature distribution and on macrosegregation and has been widely studied (Davidson and Flood, 1994; Hakonsen and Mortensen, 1995; Reese, 1997; Jones Jr et al., 1998). Flow patterns have been found to affect the temperature distribution within the liquid pool, pool profile and shell temperature (Raffourt et al., 1990; Brochu et al., 1993).

Natural convection becomes stronger with increased superheat, i.e. greater casting temperature. Natural convection becomes much stronger with larger ingots and is the main driver for macrosegregation in VDC casting due to crystal transport and flow of interdendritic liquid (Yu and Granger, 1984; Chu and Jacoby, 1990; Davidson and Flood, 1994; Reddy and Beckermann, 1997).

Despite DC casting having been a subject of scientific study since its inception in the 1930s, many technical challenges remain the subject of active research; about a third of this work is of a fundamental nature, including mathematical modelling of the process. A full review of mathematical modelling is beyond the scope of this work, but a short overview is given here. Roth made early thermal calculations (Roth, 1943) but the problem is not solvable with analytical solutions except if the boundary conditions are simplified using an assumption of constant ingot temperature on the water cooled surface. Heat flow in DC casting was first modelled with a digital computer and numerical methods in the 1960s (Adenis et al., 1962–1963). Weckman reviewed mathematical modelling of DC casting in 1984 (Weckman and Niessen, 1984) but the field has seen rapid development

since then, and fully coupled heat and fluid flow stress analysis models are available (Gruen and Schneider, 1996; Gruen et al., 2000; Mhamdi et al., 2000; M'Hamdi and Mo, 2002; M'Hamdi et al., 2002a, 2002b; M'Hamdi, Benum et al. 2003; M'Hamdi and Hakonsen, 2003; M'Hamdi et al., 2004; M'Hamdi and Mo, 2005; M'Hamdi et al., 2006; M'Hamdi and Mo, 2008; Mortensen et al., 2008). These have been extensively verified against experimental measurements. These models also include macrosegregation, defect and microstructure prediction (Drezet et al., 1995; Drezet and Rappaz, 1996, 1997). Prediction of strains and ingot deformation have been well verified but residual stress measurement has been difficult. Residual stresses in DC cast product were measured by removing successive inner layers from round ingots while measuring the displacement in the diameter and length (Roth et al., 1942). These results were used for comparison with a stress model (Bohmer and Jordan, 1995). The hole drilling strain gauge method often used to measure residual stresses in welds has also been used to measure residual stresses in DC product (Inoue et al., 1989). Residual stresses in a 126 mm diameter billet were also measured using X-rays (Moriceau, 1975). Displacements and final ingot shape are easier to measure than stresses and have been used more widely to verify predictions from stress/strain models. Measurements of the displacement of the butt of the ingot at cast start have been made (Droste and Schneider, 1990).

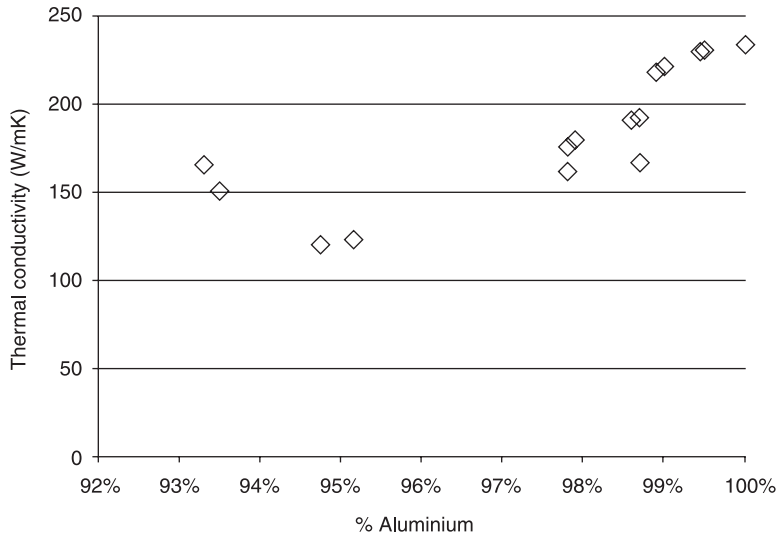
The flatness of rolling ingot can be measured using the mould as a reference after casting (Drezet et al., 1995). The displacement of the shell in the mould and the air gap formation was confirmed experimentally in the same study. The amount of contraction between the final ingot size and the mould opening varies according to ingot size. It is greater than the linear thermal contraction.

5.2.1 Effect of alloy type on heat flow, stresses and microstructures

The alloy composition has a profound effect on the alloy properties, both the thermal properties which determine the temperature field, and also the mechanical properties which influence the response of the material to the strains generated by the thermal field i.e. the stresses generated and whether cracks form or not.

As alloy content increases the thermal conductivity drops (Fig. 5.5). Specific heat and latent heat stay relatively unaffected although specific heat for some high silicon alloys can be slightly higher than for pure aluminium. Density also varies with alloy thus having a slight effect on heat flow. Liquidus temperature and freezing range are also affected by alloy composition and these in turn influence macrosegregation and other defects. In practice, a super heat of around 40–50°C is used so that alloys with a lower liquidus temperature are cast at a lower casting temperature.

In general, as alloy content increases the resulting drop in thermal conductivity gives rise to deeper liquid pools and greater thermal stresses for the same casting



5.5 Variation in alloy thermal conductivity with aluminium content (data from *ASM Metals Handbook V2 1990* for selected alloys).

speed. One finds that as a consequence, casting speeds need to be lower, the higher the alloy content, to avoid cracking and in practice casting speed tends to vary inversely with thermal conductivity.

There have been a great many studies on the DC cast microstructure of particular alloys. A full review of these is beyond the scope of the chapter. A few key issues are touched on here.

DC casting ingots destined for extrusion and rolling are nearly always grain refined with titanium and titanium diboride to achieve an equiaxed grain structure. This is primarily done to reduce the chance of cracking during casting (the columnar grain structure being more crack prone). However, it also eliminates any as cast crystallographic texture (Granger, 1989). The titanium diboride acts as a nucleant for crystal formation and the titanium suppresses grain growth so that more nucleants activate as the melt cools (Easton and St John, 1999a, 1999b). An understanding of the grain refining mechanisms can allow cost reduction in the Ti and TiB_2 additions by tailoring the amounts for different alloys (Easton et al., 2004). Some 1xxx alloys destined for fine foil applications are not grain refined as they are less crack prone and the grain refiner can introduce inclusions. Some 5xxx alloys with high magnesium content tend to have some issues with reaction between TiB_2 and magnesium oxides causing surface defects which lead to cracking. These alloys are then grain refined with titanium carbide.

Grain sizes (generally around 100–500 μm) also depend on the cooling rate, which is primarily a function of the ingot size since casting speed is reduced with size. Because the cooling rate reduces toward the centre of the ingot the grains

here are coarser. Dendrite arm spacing also becomes finer as cooling rate increases and shows a similar variation as grain size throughout the ingot section. The surface region can often show a coarse DAS/grain size area associated with the shell formation. This is discussed further below.

Given the solidification rates in DC casting of 1–20°C/s, there is microsegregation or ‘coring’ within the as cast structure which tends to approach a Scheil-Guliver solidification path i.e. zero diffusion in the solid. Thus, non-equilibrium eutectic phases form between the grains. Homogenisation heat treatments are then used to adjust the phase type, particle size and morphology.

Because of the cooling rate variation within the ingots different intermetallics phases can form in different parts of the ingot. One well-known example of this is the so-called ‘Fir tree’ structure observed in 1xxx series Al–Fe–Si alloys, and some 5xxx alloys where variation in cooling rate during casting gives rise to a zone of AlFe (Si) phases which appears like a fir tree (Westengen, 1982a, 1982b; Skjerpe, 1987; Skjerpe et al., 1987; Maggs et al., 1995; Allen et al., 1997; Aliravci et al., 1998; Allen et al., 1998a, 1998b; Chen, 1998).

Another undesirable ingot structure is twin grain growth known as ‘feathery crystals’ due to their columnar structure where high melt temperatures, presence of certain elements and low grain refiner addition can promote a twinned mode of crystal growth (Dobatkina, 1948; Henry et al., 2004; Turchin et al., 2005, 2007; Salgado-Ordorica and Rappaz, 2008; Li et al., 2009).

5.2.2 Mould cooling

DC mould cooling determines the formation of the initial ingot shell and has a large effect on surface microstructure and surface defects. When the liquid metal first touches the mould the degree of contact is high and the measured heat transfer coefficients are of the order of several 1000 W/m²K and a solid shell rapidly starts to form. However, because the ingot below the mould experiences thermal contraction due to the cooling of the water sprays, the shell inside the mould is pulled away from the mould once it is sufficiently strong. Thus, an air gap forms with a correspondingly low heat transfer rate causing reheating of the shell to the extent it becomes semi-solid.

The range of typical mould heat transfer coefficient values (Ho and Pehlke, 1985), for both aluminium and magnesium, are around 1000–2000 W/m²K during mould contact and 100–500 W/m²K for the air gap (Adenis et al., 1962–1963; Jensen, 1984; Weckman and Niessen, 1984; Baker and Grandfield, 1987). The exact values for the contact region are thought to depend on the pressure between the metal and mould, the lubrication conditions and the mould roughness. As with air gap formation in permanent mould casting, the size of the gap and the thermal conductivity of the gas in the gap are believed to control the heat transfer (Ho and Pehlke, 1985; Nishida et al., 1986; Muojekwu et al., 1995). In permanent moulds with rapeseed oil lubricant, the gas has been shown to be a mixture of lubricant

decomposition and combustion products, i.e. water vapour, methane and air (Muojekwu et al., 1995). The size of the air gap during DC casting was measured by Drezet and Rappaz (1997) using displacement sensors and shown to be 1.5 mm at the mould exit for a 510 mm thick 3004 alloy rolling ingot. Recently, shell temperature measurements inside the mould have been made showing that as mould heat flux increases, the shell temperature drops and vice versa (Bainbridge and Grandfield, 2007).

The reheating gives rise to exudation out of the surface of the solute rich liquid in the semi-solid shell region under the driving force of the metallostatic head pressure giving rise to compositional variation at the surface and surface bumps. The reheating can give rise to periodic behaviour in shell temperatures as the shell becomes weak on reheating and the metallostatic head pushes it back against the mould causing cooling. The details of formation of this mould chill zone region are discussed in a number of studies (Bachowski and Spear, 1975; Buxmann, 1982; Ohm and Engler, 1989). The air gap causes a reduced solidification rate, remelting of the shell and formation of a coarse DAS region below the surface. Under the influence of the metallostatic head pressure, the solute rich liquid exudes out of the surface (Mo et al., 1997). This exudate can appear as raised areas of the order of 1–10 mm diameter or as sweat bands, depending on the alloy. Oscillatory behaviour can arise due to the shell reheating causing loss of shell strength and collapse back against the mould. This has been observed in mould temperature measurements (Bakken and Bergstrom, 1986; Fjaer et al., 2000) and periodic composition variation on the ingot surface in the casting direction (Siebel et al., 1953).

An interesting early comment by Roth and Weisse (1942) is that surface exudation is reduced by using an inwardly tapered mould (0.5–1% of diameter over the length of the mould) to reduce air gap formation. The mechanism proposed for this improvement was that the reheating of the shell can be limited by limiting the air gap width, thus reducing exudation. Tapered moulds are not used in non-ferrous DC casting, possibly because tearing problems are largely controlled by good lubrication practice. However, it is common practice in ferrous continuous casting.

Mould temperature measurements at various points within open top moulds (Muto et al., 1996; Hamadaiid, 2004) and hot top moulds have been made (Jensen, 1984; Instone et al., 2003; Bainbridge and Grandfield, 2007) showing the effects of casting speed, mould lubrication and alloy composition on mould heat fluxes. The gas pressurised hot top moulds show much reduced heat fluxes. Mould heat transfer coefficients and the formation of the air gap have been inferred from mould temperature measurements.

Lubrication type, application practice and mould material have significant effects on mould heat flow and shell and surface defect formation. This is discussed in Section 5.4.

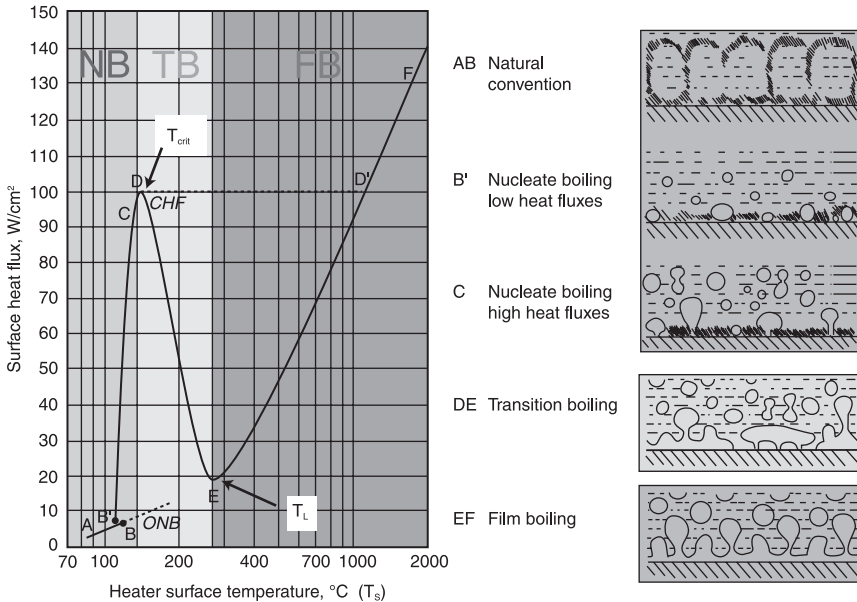
There has been a great deal of development of the mould technology to control mould heat flow and there are many variants. These are discussed in Section 5.5.

Gas pressurised extrusion billet casting including the important breakthrough of gas pressurised hot top casting.

5.2.3 Water cooling

The DC water cooling has a profound effect on the process. The DC water spray results in a high heat flux of the order of 2–10 MW/m². The heat flux depends on the water boiling mode on the surface of the ingot. As with other water-cooling processes, nucleate, unstable film and film boiling can occur in DC casting. Ingot surface temperature, water composition, water temperature and the physical characteristics of the water jet and falling film (velocity flow rate per perimeter, angle of the jet) all affect the boiling mode and the heat-transfer coefficients.

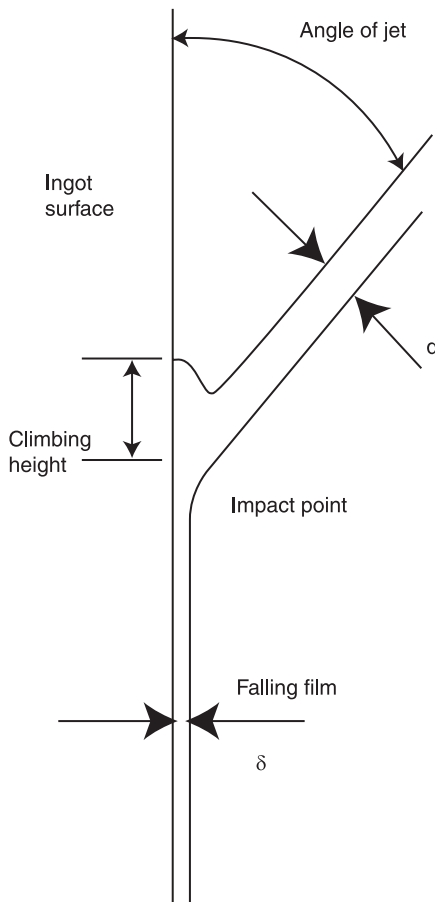
The boiling regimes are best described in terms of a boiling curve (Fig. 5.6) showing heat flux or heat transfer coefficient as a function of ingot surface temperature. Below ~100°C convection cooling occurs, above that nucleate boiling takes place where steam bubbles nucleate in non-wetted crevices on the ingot surface. The release of these bubbles into the water generates stirring in the water and reduction of the boundary layer and a high heat flux. These bubbles collapse in the water. If the ingot surface temperature is higher than some critical temperature there are so many steam bubbles that they start to



5.6 Boiling curve and boiling modes. The heat transfer coefficient and heat flux depend on the ingot surface temperature and the resulting boiling mode.

agglomerate and form a periodically collapsing steam layer on the ingot. This boiling regime is known as unstable film boiling where the heat flux is reduced by the low thermal conductivity of the steam layer. At temperatures above the Leidenfrost temperature the steam layers become stable and fully stable film boiling occurs.

The water cooling can be divided into the impingement zone, where the water jet first impacts the ingot and the falling film below the impingement zone (Fig. 5.7). Typically, there is some unstable film boiling in the impingement zone where ingot surface temperatures are around 350°C but the ingot surface temperature drops rapidly below the critical temperature and nucleate boiling occurs in the falling film. The surface temperatures drop rapidly and most of the falling film cools by convection cooling.



5.7 Detail of direct chill water spray showing water impingement zone and falling film zone.

Many studies of DC casting water cooling have been made (Fjaer and Mo, 1990). Rappaz et al. (1995), by freezing in thermocouples and using inverse calculation, found that the peak heat flux in the water spray was 4 MW/m^2 similar to other published values. Tarapore (1989) modelled casting of 2024 alloy 396 mm diameter billets, and found that to get the best fit with measured frozen in thermocouples, the peak htc was 20 kW/m with values of $1.25\text{--}1.68 \text{ kW/m}^2$ in the convection cooled region.

Grandfield and Baker (1987) found that under normal water flows for a 150-mm ingot (resulting in an impact velocity of 2 m/s) the surface temperature at the impact point was around $250\text{--}300^\circ\text{C}$, and nucleate boiling occurred with a peak htc of 40 kW/m below a critical temperature of around 150°C . If the impact velocity was reduced to 1 m/s by increasing the outlet area of the water slot (flow rate per perimeter kept constant) film boiling occurred.

In most cases, nucleate boiling is the desired boiling regime but there are cases where film boiling is deliberately induced to achieve a lower cooling rate. For example, at the start of slab casting the initial butt formed lifts up at the ends due to thermal stresses causing cracking at cast start. This can also cause problems with liquid break outs and/or the ingot can jam in the mould resulting in mould damage or catastrophic release of the ingot from the mould. It has been found that by reducing the intensity of water cooling at the start of the process by inducing film boiling the amount of butt curl can be reduced. Film boiling can be induced by dissolving CO_2 in the water (Yu, 1985), pulsing the water on and off so the surface temperature stays above the Lidenfrost temperature (Bryson, 1969), and using a low water flow rate.

Because most plants use recycled evaporative cooling water systems the water composition varies over time. The water lost during evaporation must be made up with fresh water. The dissolved salts build up in the water also due to evaporation, and water is periodically dumped to control the total dissolved solids concentration. The higher the total dissolved solids level i.e. the harder the water, the higher the Lidenfrost temperature (Grandfield, Hoadley et al., 1997) thus variation in water-cooling behaviour can arise due to composition variation in the water. Casting lubricant also finds its way into the water system and must be removed both for environmental reasons and because it encourages film boiling. In practice, well run DC casting installations pay careful attention to management of the water-cooling system and water-composition variation.

5.3 Macrosegregation

In addition to macrosegregation in the surface region of the ingot (discussed in the section on surface defects), there can be significant compositional variation from centre to surface particularly in large DC castings. Macrosegregation can occur whenever differential movement of the liquid or the solid within the partially solidified regions occurs. In many cases, this macrosegregation is not a significant problem, however in some final applications it can give rise to unacceptable

property variation, for example where aircraft wing components are machined from thick plate.

Typical macrosegregation patterns for eutectic elements show a high concentration on the surface of a corresponding depleted zone below the surface, a higher than nominal concentration in the rest of the ingot apart from the centre which is again below nominal. The peritectic elements such as titanium and chromium show the reverse pattern. See Eskin (2008) for a full discussion of the literature and mechanisms of macrosegregation in DC casting. The bulk macrosegregation pattern is generally thought to arise due to two main mechanisms:

1. Solidification shrinkage gives rise to liquid of original composition flowing into the mushy region, and since this region is bigger toward the centre of the ingot the affect varies across the ingot section (Reddy and Beckermann, 1997).
2. Transport of free floating solid grains which are of more pure composition than nominal; the main driver is the strong natural convection flow of cold liquid flowing down the solidification front into the centre of the ingot.

Several other affects are also thought to play a role:

1. Melt flow in the semi-solid region caused by the metallostatic head pressure. This is more important in the surface region.
2. Melt flow caused by deformation of the mushy zone; tensile thermal stresses are imposed on the semi-solid in the centre of the ingot which tend to suck liquid into the semi-solid region.

The transport of free floating solid grains is supported by observations of a duplex DAS structure, where large grains with large DAS are observed mixed in with finer grains with significantly smaller DAS in the centre of the ingots (Nadella et al., 2007; Chu and Jacoby, 1990).

The natural convection driven flows in the sump increase with ingot size which increases the temperature gradients. Thus, macrosegregation tends to be a bigger problem with larger ingots >400 mm particularly highly alloyed rolling ingots. However, macrosegregation is observable in smaller 200 mm diameter billets (Nadella et al., 2006). Faster casting speed leads to wider semi-solid regions which in turn gives rise to greater macrosegregation (Eskin, Zuidema et al., 2004). Grain refinement tends to increase macrosegregation (Gariépy and Caron, 1990) although it depends on the type of grain refiner.

The flow pattern due to the liquid metal distributor system also influences the crystal transport and resulting macrosegregation (Gariépy and Caron, 1990).

5.4 Typical surface defects

A variety of defects can form on the surface of DC castings depending on the mould technology, casting practice and alloy.

Cold folding defects form when the meniscus is frozen, then pulled down and new liquid laps over the previously frozen material. They may be eliminated by increasing casting speed and/or using gas pressurised or electromagnetic moulds which push the liquid meniscus away from the mould.

In 1954, Porro and Lombardi discussed cold folding of aluminium during DC casting (Porro and Lombardi, 1954). Waters conducted tests with aluminium, copper, zinc and lead in 1953 and found that the surface quality was improved as casting speed increased (Waters, 1954). The cold fold spacing was found to decrease as casting speed increased. These experiments were performed with 1 inch diameter unlubricated moulds, one of which was a Pyrex mould to enable visual recording and direct observation of the meniscus freezing. The cold fold spacing for the different metals at a constant cast speed was also successfully related to the surface tension to density ratio of the metals. Surface tension to density ratio determines the height of the meniscus.

In the early 1970s, Bergmann (1970, 1973, 1975) showed clearly that for the case of VDC casting, the mechanism of cold folding involves these steps:

1. the meniscus freezes;
2. it is pulled away from the refractory in the casting direction;
3. solidification proceeds into the ingot and then opposite to the casting direction until;
4. the diffusion path is too long and liquid breaks through to fill the gap; and
5. the cycle repeats.

Similar behaviour was found during HDC casting (Weckman and Niessen, 1984). The cyclic nature of the folding process was evident in the cycling of orifice plate temperature due to liquid periodically contacting the refractory. Formation of folds was found to be controlled by the mould heat transfer, the casting speed and the geometry of the refractory overhang. Weckman and Niessen (1984) confirmed the previous VDC result that the cold fold spacing becomes smaller as casting speed increased in HDC casting of Al, Zn and Pb. As the heat input increases with increasing casting speed, the solidification front does not move as far along the meniscus before the thermal diffusion path length becomes too long, allowing the liquid to flood against the mould again. The ratio of the rate of the solidification front movement perpendicular to the mould and the casting speed sets the angle of the cold fold relative to the mould face. Weckman and Niessen (1984) assumed that the growth rate is initially interface-controlled (a good assumption given the Biot number), and were then able to calculate the mould heat transfer coefficient from the angle of the fold and the casting speed.

Weckman and Niessen (1983) also modelled the effect of changes in the mould heat transfer coefficient. The results showed that an increased mould heat transfer enables the solidification front to extend further into the product, resulting in deeper cold folding. Both Bergmann (1970) and Weckman and Niessen (1984) studied the effect of metal head. The severity of cold folds increased as the head

was increased and the mould heat transfer increased as the head was increased, and it was proposed that this was caused by a greater degree of contact between the hot semisolid shell and the mould (Weckman and Niessen, 1984). It was further proposed that the friction with the mould also increased with metal head, sometimes causing tearing of the shell. This is one reason that HDC casting can be prone to cold folding and surface tears compared to VDC as the metal head pressures are higher (usually about 400–500 mm for HDC compared to 100–200 mm for vertical hot top DC casting).

Weckman proposed that not only does the metal head affect the mould heat transfer but that the fold also collapses sooner as the head is increased. The differential pressure across the material at the final stage of the fold development was proposed to be important, i.e. the head pressure minus the pressure in the void. The pressure in the void is influenced by the amount of gas evolved due to lubricant decomposition and whether gas is injected into the mould as in the gas-pressurised processes. Therefore, the lubricant supply pressure should be greater than the metallostatic head pressure to reduce cold fold formation. Other defects such as gas bubbles under the surface can occur in this case.

Weckman and Niessen (1984) found experimentally that cold folds are eliminated if the overhang is essentially zero but that there is the risk of solidifying material into the refractory and causing tears. Also, if the refractory is not flush with the mould and recessed behind the mould face, solid can form on the lip and cause tearing.

Bergmann (1973) found that graphite as a mould material reduced cold folding compared to a metallic mould. This is probably because of the lower thermal conductivity of graphite. Conduction of heat through the mould is generally not the controlling heat flow resistance with a metallic mould, but it may become the controlling factor when the conductivity is low. For example, with a carbon mould the cold folds do not penetrate as deep.

Cold folds may cause shell tearing if the cold folding is extensive because the solid formed may jam inside the mould (Weckman and Niessen, 1984). In addition, the interface between the folds may cause a weak spot in the shell where surface tearing could initiate.

Surface tearing of the shell and subsequent liquid break out is well known to practitioners of aluminium DC casting and an important problem as it reduces productivity causing scrap and in some cases casting must be stopped. It is also a potential safety hazard when the molten metal escapes. The thickness and strength of the solidifying shell within the mould will control the load it can bear before rupture. These surface cracks, transverse to the casting direction, are generally believed to occur when the shell tears open as some part of the shell remains stuck in the mould while the product is pulled out.

The high temperature mushy zone mechanical properties of the alloy being cast, have been found to influence the point at which the shell contracts. Pure aluminium was found to pull away quickly while less rigid wide freezing range

alloys such as 5182 and 7075 maintain contact with the mould for longer periods (Bachowski and Spear, 1975). It has been concluded that wide freezing range alloys are more prone to tearing because their shells maintain contact with the mould longer than dilute alloys, resulting in greater friction forces acting on the shell (Emley, 1976; Ohm and Engler, 1989). It was further argued that the more dilute alloys obtain sufficient strength at higher temperatures and are able to pull away from the mould at a higher shell temperature. It was also concluded that higher casting speeds not only increased friction on the shell, but also increased the shell temperature and reduced its strength. Lubrication theory also suggests that higher speeds will generate greater friction forces (Grandfield, 2001). In HDC casting, there may be differences in forces acting on the top and bottom shell due to the difference in metal head pressure but also if the mould is not correctly positioned vertically there is a misalignment between the emerging ingot held in place by the press down roller on the conveyor and there may be difference forces on each shell. If the mould is positioned too high, the bottom shell would be forced against the mould base. If positioned too low, a pressure will be applied to the top shell. The metallostatic pressure will be applied to the shell, regardless of mould position. If the shell is hot and weak then it is pushed against the mould. In this case, friction might be expected to be affected by metal head pressure. Some measurements of friction loads between the shell and the mould have been published for DC casting (Donnerburg and Engler, 2000). The load was 10–100 N on a 156 mm diameter VDC cast billet and found to decrease with increasing oil flow rate and to be dependent on the type of lubricant used.

Friction load data are in fact rare for all types of continuous casting. Yao and Fang (1996) calculated friction loads during continuous casting of steel by measuring the power on the motor oscillating the mould. Loads were around 4 kN, however, no friction coefficients were calculated. The coefficient of friction between hot copper and steel (to simulate the friction between a steel shell and mould in continuous casting of steel) was found to be 0.4 with rapeseed oil as the lubricant (Sorimachi and Nabeshima, 1998). Friction loads for leaded gunmetal on a carbon mould have been measured at around 0.5–2 kN (Thomson et al., 1969). A value of 280–560 kPa is given for interfacial stresses for continuously casting of aluminium, in an unlubricated graphite mould, without a DC spray (Thomson and Ellwood, 1972).

Friction and inadequate lubrication certainly plays a role in surface tear formation and all DC casting is practiced with some form of lubricant in order to prevent tearing. Drag marks may appear along the product in the casting direction if there is insufficient lubrication where local welding takes place between the ingot and the mould. If casting continues with insufficient lubrication, then shell tearing eventually occurs (Ohm and Engler, 1989; Laemmle and Bohaychick, 1992).

Laemmle and Bohaychick (1992) examined the viscosity index and thermal stability of various lubricants. They argued that castor oil performs well

because it maintains a high viscosity at high temperature enabling the lubricant film to remain continuous. They also reported that oil vaporisation caused deposition of varnish-like deposits which presumably increase friction, and may therefore result in tearing. This was also reported by Jacoby et al. (1986). The varnish-like deposits are attributed to fatty esters including triglycerides present in castor oil.

Weckman (1987) discussed the requirements mould lubrication and compared a number of lubricants including castor oil, rapeseed oil and some synthetic oils. The main requirements are a high viscosity and high viscosity index (i.e. low sensitivity of viscosity to temperature). He also examined the defects that occur with either too little or too much lubricant. With insufficient lubricant, sticking, tears and heavy cold folding occur. With too much lubricant, a so-called 'Chevron' defect formed (i.e. a bent half moon type shape) on the top surface and ripples formed on the bottom surface of HDC casting. The lubricant is presumed to act as a parting agent and prevent direct metal/mould contact. Direct contact would cause an increased heat-transfer rate since heat flow would be directly through the metal rather than through the oil and oil vapour.

Waters (1952) examined the effect of alloy composition on shell tearing propensity, relating increased alloy freezing range to an increased probability of tearing. Waters suggested that both mechanical grabbing and poor lubrication contributed to tearing. Langerweger (1981) ascribed formation of 'transverse surface cracks', i.e. tears in aluminium VDC casting, to the presence of oxides combined with salt particles which stick to the mould wall. Nofal (1992) also suggested inclusions caused tearing. The importance of lubrication to prevent tearing is emphasised throughout the papers on HDC casting. Formation of lubricant tar deposits on the mould was reported to cause tearing and the mechanism was described by the lubricant deposits being 'detrimental to the thermal transfer' (Spear and Brondyke, 1971). Presumably, a thinner, weaker shell was in the mind of these researchers. An alternative analysis is that sticking and tearing occurred, as a result of high friction forces. In VDC casting, the cast times are short (<2 hours) and the moulds are cleaned between casts. In contrast, HDC casting can run for many days before a mould is changed. Tar build-up is therefore more likely to be a problem in HDC casting. Aitchison and Kondic (1953) discussed at length mould lubrication for continuous casting.

5.4.1 Cracking

The cooling of the ingot during DC casting generates thermal stresses due to the differential cooling rate for different parts of the casting. For example, the surface cools quickly due to the high heat fluxes from the water spray and thus is driven to contract rapidly, however the interior of the ingot is cooled more slowly at a later stage and thus the different contraction rates in centre and surface result in tension in the interior and compression on the surface.

DC casting cracks can be divided into hot tears occurring above the solidus, i.e. in the semi-solid region and hot cracks occurring below the solidus. For most common alloys in the 1000, 3000, 5000 and 6000 series ranges, hot tearing is the usual type of cracking while hot cracks tend to occur for the high strength, low-thermal conductivity, low ductility 2000 and 7000 series alloys.

Hot tearing in DC casting is an area of ongoing research (Eskin, Suyitno et al., 2004), however the main mechanism is generally agreed upon. Hot cracks in DC casting form due to the semi-solid material in the solidification front being subjected to tensile strains generated by thermal contraction of the cooling solid. Different parts of the casting cool at different rates and consequently contract at different rates. The solid at the base of the liquid pool in the centre of the ingot is driven to contract after the solid at the surface has already cooled; consequently tension is generated in the mushy material at the base of the liquid pool in the centre of the ingot due to constrained thermal contraction. This tension causes dilation of the mushy material. If the liquid is unable to feed the imposed strain, crack-shaped voids appear between the grains. These are intergranular and show fracture surfaces that look like shrinkage porosity i.e. evidently liquid was present during failure.

Eskin (2008) gives a full review of hot tearing in DC casting. Hot tearing at the start of billet casting is discussed below in detail being one of the more important manifestations of the problem.

Schneider and Jensen (Jensen and Schneider, 1990; Schneider and Jensen, 1990) examined cracking at the start of extrusion billet casting and proposed the concept of using pool depth as a cracking criterion, i.e. above a critical pool depth cracks would form. This is consistent with recently developed hot cracking theories based around feeding models (Rappaz et al., 1999). As the pool gets deeper, it is expected that so too does the width of the mushy zone. Consequently, the feeding pressures increase and cracks are more likely to form. Also, the increase in pool depth reflects an increase in strain rate as the differential cooling and contraction rate between the centre and the surface of the billet increase. Schneider and Jensen (Jensen and Schneider, 1990; Schneider and Jensen, 1990) also revealed the phenomenon of pool depth over-shoot. If one starts with a constant casting speed, then the pool depth goes through a maximum before reaching and maintaining a constant steady state value. Flood et al. (1995) successfully modelled this phenomenon in non-dimensionalised heat flow models and this was also verified experimentally by Grandfield, Goodall et al. (1997). This effect occurs due to the time delay before the cooling effect of the DC water spray is felt in the centre of the billet while the billet is being lowered.

Two schemes are generally used in the industry to control start cast cracks:

1. use an initial slow start speed and then ramp up the speed later;
2. use dummy blocks with a centrally raised section (truncated cone or dome).

With a ramped cast start speed the cast starts at slower speed than the usual run speed, so that when the pool depth goes through its maximum it is at a lower level than that which causes cracking. The speed is then increased to the run speed. In the case of the dummy with a centrally raised section, the pool in the centre is higher at the start. When the effect of the water cooling has penetrated into the centre of the ingot the pool is at a higher position. The difficulty in practice is to know exactly what dummy height or ramp conditions to use for a given alloy and diameter.

Casters know well that certain alloys are more crack prone than others (Jacoby, 1995). Alloy composition and variation of minor elements are known to affect hot tearing tendency. For example, copper has been shown to increase cracking in alloy 6060 (Later, 2001). Additionally, the grain size and morphology also affect hot tearing. This is the main reason grain refiner is added during DC casting to prevent hot tearing.

Hot cracks tend to be intragranular rather than intergranular as with hot tears. Trouser or J cracks can be formed during DC slab casting of high-strength alloys. These cracks can occur after casting is completed upon cooling or when the product is sawn. There is a large amount of energy in the residual stresses and the failure can be quite dangerous; throwing large masses of material some distance.

Alloys, which have high plasticity at high temperature such as pure alloys, tend to not to cold crack as they yield plastically without cracking, however, the high-strength alloys such as 7xxx series have low plasticity at high temperature and combined with high strength. This allows the thermal stresses to accumulate during casting and then cracking failure occurs; sometimes during casting but sometimes after casting. The high alloy content of the high-strength alloys also results in a low thermal conductivity, this makes the temperature gradient difference and resulting thermal stresses greater when casting these alloys than more pure alloys.

Chang and Kang (1999) measured mechanical properties for alloy 7050 at high temperature and modelled stress evolution during DC casting. The predicted stresses increased as casting progressed. High-stress regions in the mid and quarter positions were predicted as well as at the water quench point and the corners of the slab. Stress at the corner is a function of the increased water cooling in that region. Increasing casting speed was predicted to reduce butt curl stresses, but made no difference to the internal high-stress regions.

A solution to cold cracking problems in high-strength aluminium alloys which has been widely adopted is the use of wipes to remove the falling water film at some point below the mould. This practice results in reheating of the surface while the centre cools thus reducing the differential in contraction between the surface and the centre. Zeigler (1952) first patented the use of wipers or air jets to remove the falling film of water. The optimum position of the wipes and the degree of reheating to be achieved as function of casting speed and alloy type

need to be determined by modelling and experiment, and the exact implementation of wipe technology tends to be closely guarded within the industry. Both rubber wipes and air jets (Taylor et al., 1957) have been used. Behr et al. (1973) used the idea of using a second spray at some point after the dry zone below the wipes is revealed. Gervais and Chollet (1975) offered further refinement of the wipe idea by controlling the position of the wipe to achieve higher casting speeds without cracks. This patent is targeted at small diameter 5 inch zinc DC casting. Zinniger (1980) disclosed the idea of using inflatable wipers so that the butt of the ingot can easily pass through at cast start. Measurements of the surface temperature showed that the surface does reheat when wipers are used.

In order to predict hot crack occurrence, a cracking criterion is needed. A simple criterion is that the strength has been exceeded, however the difficulty is to compare uniaxial tension and compression strength data with the tri-axial stress state of the material during DC casting. Boender and Burghardt (2004) discuss failure criteria with respect to high strength 2000 and 7000 series aluminium alloys and suggest that von Mises stress is not appropriate, but if the maximum principle stress exceeds the uniaxial tensile strength or uniaxial compressive strength failure is likely.

In practice, cracking tends to occur at lower predicted stresses than the strength of the material. A fracture mechanics explanation that small defects can reduce the stress needed for failure can be invoked (Boender and Burghardt, 2004; Ludwig et al., 2006). Even without cracking criteria, mathematical models can be used to find optimum casting conditions which minimise the internal stresses.

5.5 Gas pressurised extrusion billet casting

Up until the late 1970s billet casting was carried out using either float and spout open top moulds or level pour flooded table hot top moulds (Emley, 1976). The later provided better metal delivery in terms of reduce dross generation and greater productivity and reduced cost in terms of less manning and consumables per tonne of product.

With the open top moulds the metal level was controlled by a float in the case of billet casting. This necessitated relative high metal levels in the mould which in turn leads to a large degree of shell reheating and poor surface quality. It was well known that if a low metal level was used then a smaller mould chill zone and less surface segregation resulted as the initial metal contact point approached the extent of the upstream water-cooling effect. However, these low levels cause difficulties at cast start, and it is not possible to change the level with a float technology (one system moved the whole mould table up on screws during casting to lower the metal level in the mould). An alternative approach is to use a hot top mould where a refractory top determines the point of initial metal contact against the mould. These moulds produced substantially better surface quality than open top moulds.

Initially, hot top moulds were simple open top moulds with a refractory liner (Moritz, 1961) still with a float but later the refractory became an integral part of the mould and was used to deliver the liquid metal via a refractory pan on top of a water box containing the moulds (Furness and Harvey, 1975). This allowed level pour delivery from a tilting furnace with reduced dross generation. These systems have relatively high metal head pressures of 100–200 mm head, and this results in the metal being pushed into the corner below the refractory and some cold folding as the meniscus freezes.

In the late 1970s, Showa Aluminium substantially improved the performance of hot top moulds with the invention of the gas pressurised hot top mould (Mitamura et al., 1978; Mitamura and Itoh, 1979; Yanagimoto and Mitamura, 1984). In the Showa configuration, air was injected through small grooves on a metal plate just below the refractory at a pressure equal to the metallostatic head pressure resulting in a larger more stable meniscus, low mould heat fluxes and elimination of shell reheating. The gas pressurised moulds produce billets with very smooth surfaces and almost no surface segregation.

Many other companies followed the Showa Aluminium development with variants having air injected at different points and via different delivery systems e.g. through porous graphite mould liners along with continuous lubricant delivery (Wagstaff and Wagstaff, 1986; Steen et al., 1997; Apostolou and Armaos, 1988; Schneider and Kramer, 1994; Bainbridge et al., 2005).

There have been some different views on the mechanism whereby the gas pressurised moulds work. Direct observation of the meniscus has shown it to be of the same size as an open top mould meniscus with no metal head when the air pressure balances the metal head pressure (Ekenes and Peterson, 1990) and can be readily predicted (Baker and Grandfield, 2001). The mould heat flow is very low for gas pressurised moulds compared to hot top moulds without gas pressure (Baker and Grandfield, 1987; Bainbridge and Grandfield, 2007) due to the fact that the gas pressure moves the base of the meniscus to the point where the solid shell formed by the water spray is being pulled away from the mould. Some suggestions of an air bearing have been made, but the essential mechanism is that the meniscus is stabilised whereby the base is near the point where the shell formed by the water spray is being pulled away from the mould. There is, thus, essentially no metal-mould contact, and therefore very little mould heat flow and the shell reheating mechanism which normally gives rise to macrosegregation are eliminated. Some inverse segregation can still occur (Benum et al., 1999).

It is important to realise that the mould length of a gas pressurised hot top mould is a key factor to the performance of the mould (Bainbridge and Grandfield, 2007). If the mould is too long then gas pressurised mode cannot be obtained at normal casting speed and if too short, cold folding will occur at normal casting speeds. The gas pressurised hot top technology has continued to evolve with the relative recent adoption of improved automatic gas pressure control systems acting on each mould.

5.6 Rolling slab technology

Rolling slab casting mould technology evolution has followed a different path to billet casting technology. In order to get better metal level control during casting to achieve smaller mould chill zones and scalping losses, float level control was superseded by the use of a downspout coming from a trough over the moulds with a pin inside the spout. The pin position was controlled by a lever arrangement with a refractory float on the melt. This 'steady eddy' system enables manual adjustment of the level during casting via positioning of a counter weight on the lever. It is also essential to use a flow distribution system in the metal pool for slab casting to ensure an even melt temperature distribution. The short sides being further from the inlet are otherwise too cold and the long sides too hot. In practice, a fibreglass permeable cloth distributor system is used. Designs vary enormously from plant to plant and optimum distributor design for rolling slab casting is the subject of ongoing research (Tremblay and Lapointe, 2002; Hasan and Ragel, 2009).

Conversion of slab moulds to hot top casting has been done using the simple refractory liner system, but a flooded table hot top system has not been adopted due to practical difficulties, for example the large amount of butt curl at the start of casting can drive the slab up into and destroy the refractory hot top.

Another approach, developed in Samara, Russia, to reduce mould cooling and get better cast surfaces was EMC (Getselev et al., 1969). A high-frequency AC current is passed through the mould creating induced currents in the melt and a levitating force balancing the metallostatic head pressure to hold the liquid away from the mould. In this configuration, all heat flows to the water spray and there is no shell-reheating effect. Excellent cast surface quality is obtained with EMC casting. Several companies developed variants of EMC (Pritchett, 1973; Bergmann, 1975; Dunn, 1979; Nagae et al., 1988; Hudault et al. 1989; Goodrich and Tarapore, 1991). One issue with EMC was the fact that the final ingot dimensions depended on the balance between the EM forces and the metal level. Thus, if the level rose during casting the ingot became thicker. In order to get good dimensional control, automatic level control systems began to be developed using capacitance metal level sensors.

Considerable modelling and fundamental work was carried out on EMC casting (Drezet and Plata, 1995; Drezet et al., 1995a, 1995b; Prasso, Evans et al., 1995; Kageyama and Evans, 1996; Xu et al., 1998a, 1998b, 1998c; Evans and Jones Jr, 2002; Zhao et al., 2007a, 2007b; Zhu et al., 2008a, 2008b 2008c; Zuo et al., 2008; Pang et al., 2009; Zhu et al., 2009).

EMC casting has gradually been phased out of the industry due to its high capital cost and ironically the quality improvement of conventional open top casting due to the application of the enabling technology of automatic level control first developed for EMC. Modern open top casting systems for slab casting use laser level control and fully automatic hands free operation. Low

metal levels are easily programmed as a function of alloy and casting speed to get small chill zones. The use of carbon lined low level moulds allows lubrication usage to be minimised (Wagstaff and Bowles, 1995).

5.7 Special variants of DC casting

DC casting can be used to produce shapes and hollows from small to large diameter (Nawata et al., 1991); 1.1 m external diameter with 100 mm wall thickness have been cast at the Samara plant in Russia. Hollow sections were cast at a very early stage of the development of DC casting (Roth, 1949). A common variant to round or rectangular shapes is the production of T-Bar shapes for remelt ingots. The T-Bar is sawn to short lengths and is easily handled with a forklift. T-Bar can be cast vertically or horizontally (Garipey et al., 2005). More complicated shapes have also been cast which are then sawn into forging performs (Anderson et al., 2001). Small diameter <100 mm DC casting is also carried out to produce forging pre-forms (Sekiguchi et al., 1981; Bergsma and Kassner, 1997). Another recent development is the DC casting of a clad product using two metal streams of different composition to cast and outer cladding of one alloy around an inner core of another alloy (Gupta et al., 2007).

5.8 DC casting safety

The main danger with DC casting is the chance of a liquid breakout and subsequent possible molten metal steam explosion (Richter and Ekenes, 2005). The risk of an explosion can be substantially minimised by the use of special coatings on the casting pit (Roberts and Lowery, 2009). Explosion mechanisms have been extensively investigated by the industry. The use of automation also allows personnel to be safely removed from close proximity to the casting machine in the event of an explosion (Austen and Swain, 1997).

5.9 Chain conveyor casting

Chain conveyor casting machines are used to produce over 10 million tonnes per annum of aluminium ingots. A typical primary smelter machine configuration is a machine capable of 20–25 tonnes per hour production rate of 22–23 kg trapezoid ingots, with an annual capacity of over 100 000 tpa. A variety of smaller formats down to 5 kg ingots are produced on smaller machines. In concept, the machine is simple with open moulds on a conveyor filled at one end and the solidified ingots rejected at the other end, stacked and bundled. Generally, the large capacity machines are water cooled. Two machine configurations are used; in one case the ingots are filled before the moulds enter the water-cooling bath, in the other they are filled while in the water bath.

Many new smelter cast houses are being installed solely with conveyor lines. In the last decade, the process has seen considerable improvement in technology (Jones and Clough, 1999; Grandfield et al., 2001, 2003; Meadows, 2003; Whiteley, 2003; Grandfield et al., 2004, 2005; Meadows, 2005; Grandfield et al., 2006, 2007, 2008).

Filling systems vary but generally a rotating wheel system is used where the liquid metal is fed to a wheel with spouts that are synchronised to the passing ingots on the conveyor. The metal flows through the spouts filling each mould as the pass. Recent modelling and development work (Grandfield et al., 2003, 2004; Grandfield et al., 2005; Prakash et al., 2006, 2007; Grandfield et al., 2008) has gone into optimising the wheel filling design to reduce dross so that skimming is not needed even at high production rates (short filling times).

Since most of the costs associated with running ingot casting machines are fixed costs, any increase in the productivity of these machines results in a reduction in conversion costs. Ingot chain conveyor line speed is set such that the ingots are solid when they reach the end of a ~20 m conveyor, where they are knocked out and stacked into bundles. The maximum production rate is therefore given by

$$P = \frac{WL}{I_s t_s} \quad [5.2]$$

where, W is the ingot mass, P is the productivity, I_s is the mould spacing on the line, L is the line length and t_s is the ingot solidification time. The ingot weight is set by the customer and the mould spacing by the ingot dimensions. Longer machines are one way to increase productivity and there has been a trend in recent times to lengthen casting machines from 20 to 40 m, but this adds to machine capital and associated building costs. Reducing solidification time offers a potentially cost effective alternative.

Studies of mould heat flow and deformation (Clausen and Whan, 2001; Grandfield et al., 2001; Sztur et al., 2001; Grandfield et al., 2006) have shown that at first the metal in the mould is liquid and without any strength and there is good contact between the ingot and the mould and as a consequence the mould heats rapidly and consequently expands outward while the ingot starts to solidify. The first solid that forms will be weak and thus stays close to the expanding mould under the weight of the ingot. Once the shell becomes sufficiently rigid (~50–60 seconds after filling), the mould and ingot part, forming the air gap. The low thermal conductivity air gap then reduces heat flow to the mould, and the water cooling causes mould temperature to fall and the mould contracts inward toward the ingot. As more solid forms, however, the ingot contracts at a faster rate than the mould and shrinks away from the mould increasing the air gap dimension, except for those points such as the centre ridge where it rests.

Mould design is important to both solidification time and mould life. If the mould is too thin then film boiling can occur with a reduced heat transfer and the

resulting high mould temperatures increase stress and reduce mould life and the ingot has a longer solidification time (Nguyen et al., 2009).

Casting temperature and ingot weight have been shown to affect solidification time and productivity. Every 1 kg extra of ingot weight adds ~13 seconds to the solidification time for 99.85% A1 alloy and every 10°C extra of melt temperature adds 3 seconds. Water-cooling parameters (water level, flow rate, temperature) have also been shown to affect solidification time (Grandfield et al., 2008).

5.10 Melt treatment

Before casting, the melt must be alloyed but also impurity levels may need to be reduced depending on the final product and application. The main impurities that have major effects on the performance of casthouse products in subsequent processing and final service are hydrogen, alkali earth metals and inclusions. The trace metallic elements can also cause problems depending on the alloy (Grandfield and Taylor, 2009). Peritectics, for example, are removed by reaction with aluminium boride and settling of the resulting metal borides in the case of production of electrical conductor grade alloy. Iron levels are restricted in some alloys but there is no commercial mass production iron removal method. Very high purity metal can be produced in small amounts by specialist techniques for exotic applications such as capacitor foil.

Primary aluminium produced from the Hall–Héroult electrolysis cells has a range of impurity species present. Their concentration depends on cell operation, the composition of the cell feed materials and the cell materials of construction that the metal comes in contact with (Grjotheim, Krohn et al., 1982). The solid inclusions in primary metal can be borides, carbides, nitrides, oxides or halides. The solid particles cause problematic defects and die wear during extrusion, pin holes in foil and sometimes failure in service of castings. Carbon in solution normally precipitates as aluminium carbide when the liquid metal cools (Rødseth et al., 2002). Chlorides can be present downstream where either chlorine gas or magnesium/potassium chloride additions are used for sodium removal and melt cleaning, respectively (Table 5.1).

Recycled material has a somewhat different impurity profile. Sodium levels are low due to removal at the primary stage and evaporation on remelting. However, calcium pickup for example from dirt contamination can occur in recycled material. Hydrogen remains an issue for secondary material as the melt re-absorbs hydrogen from the atmosphere upon remelting.

There are several possible changes to impurity concentration and interventions at each stage before casting (Table 5.2; see Schneider, 1998; Waite, 2002; Le Brun, 2008 for reviews). Casthouses strive to achieve the required quality at the lowest processing cost while meeting environmental and safety requirements and there are now many melt treatment technologies to choose from with various advantages and disadvantages. Typical technology and practice used to control

Table 5.1 Concentration ranges of impurity elements in primary aluminum metal

Element	Concentration range (ppm)
Iron	400–3000
Silicon	200–1500
Copper	5–100
Magnesium	5–60
Zinc	10–200
Nickel	1–80
Titanium	10–100
Vanadium	10–200
Sodium	<1–500
Boron	<2–60 (as borides)
Calcium	<1–50
Lithium	1–10
Oxygen	1–100 (as oxides)
Nitrogen	1–60 (as nitrides)
Carbon	<1–100 (as carbides)
Barium	<1–10
Bismuth	0–10
Chromium	2–50
Lanthanum	<1–10
Lead	1–50
Manganese	5–50
Phosphorus	1–30
Sulphur	<1–20
Tin	<1–30
Zirconium	10–40

Source: Grjotheim (1982), Simensen (1985) and Taylor (1995)

Table 5.2 Melt processing steps, changes in impurities and possible interventions

Processing stage	Impurities	Possible interventions
Tapping	Na, cryolite, dross, borides, carbides, hydrogen	Bath detection
Crucible transport	Na evaporation	Crucible treatment system (eg TAC & RAM) to remove Na & Li, Crucible alloying
Furnace charging	Na evaporation, dross generation	Siphoning
Furnace	Al_2MgO_4 from Mg alloying, Inclusions from other alloy hardeners, dross generation, hydrogen pickup	Furnace cleaning, alloying, fluxing with inert gas-chlorine gas mixtures, fluxing with salt fluxes, stirring
Melt transfer	Dross generation	Level pour system
In line treatments	Possible agglomeration of inclusions, pickup from grain refiner	Ceramic foam, deep bed and rigid media filters, degassers, grain refiner additions
Casting process	Oxide generation	Controlled flow, skim dams

impurities are described. A more comprehensive review of melt treatment principles is too large to encompass here.

Melt refining generally involves the dispersion of a 'getter' phase within the melt which collects the impurity of interest and is then removed with the getter phase. For example, argon can be injected to collect dissolved hydrogen and remove it from the melt as the injected gas phase leaves the melt. In some cases, the injected phase reacts with the impurity in the melt, e.g. MgCl_2 reacts with dissolved sodium in the melt producing NaCl which rises to the dross layer where it can be skimmed away. In all these processes, the efficiency of the operation is generally kinetically controlled rather than equilibrium controlled (Sigworth and Engh, 1982; Kulunk and Guthrie, 1992; Sigworth, 1999, 2000), i.e. reaction rates and efficiencies depend on the surface area of the dispersed phase (as set by its droplet/particle/bubble size). The residence time within the melt of the purge phase also determines the rate of removal of the impurity. Thus, deeper baths tend to be more efficient. Lastly, a higher degree of dispersion and mixing within the melt also increases efficiencies. Poor removal efficiency occurs if the dispersed phase is segregated to just one part of the furnace or reactor and the melt is not mixed through that reaction zone. For further detail on the principles of melt refining, the reader is referred to Engh (1992).

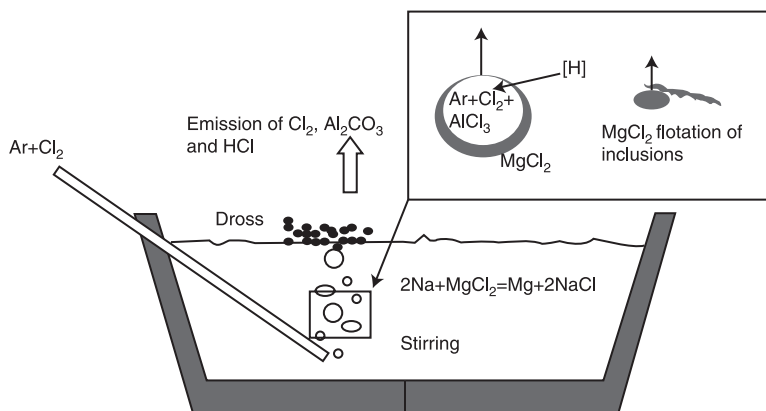
5.10.1 Impurity measurement

Over the past three decades, there has been steady improvement in the technology used to treat the melt driven by the need to increase throughput, reduce costs and improve emissions but also enabled by the development and application of methods for measuring inclusions and dissolved hydrogen. Sodium is easily measured using conventional spectrographic techniques. See Poynton et al. (2009) for a recent review of inclusion measurement technology, and Fergus (2005) for a general review of melt characterisation. The two main inclusion measurement techniques used commercially are a molten metal Coulter Counter [for example SICOTM (Simensen, 1993) and LiMCATM unit (Doutre et al., 1985)] or filtration of a melt sample and examination of the captured inclusions on a fine pore filter. Two popular embodiments of the later method are the PodFaTM and the LaisTM units [see (Rinderer et al., 2005) for a comparison of the two filtration techniques]. The LiMCATM gives inclusion size distribution and concentration data but does not differentiate particle type. LiMCA cannot distinguish between small gas bubbles and particles (Cooksey et al., 2001; Ware et al., 2001; Hakonsen et al., 2004). It can be used in an online mode and can be easily used to track variation in inclusion levels over time or before and after an in-line filter for example. The filtration methods give an overall inclusion concentration measure but also importantly allow identification of inclusion types either under optical or scanning electron microscope thus enabling the source of inclusions to be determined.

Many methods are available to measure hydrogen concentration in aluminium (Ray, 1991; Chen et al., 1994). These can be used either on solid samples or in the melt. Hot subfusion vacuum extraction of hydrogen from solid samples is considered the reference method, however, it is expensive and slow and producers need fast results at the time of casting thus the need for units measuring hydrogen in the liquid. Nitrogen carrier fusion method is also conducted on solid samples e.g. the LECOTM units, which is quicker and less expensive than vacuum extraction. A long-used commercial method is to measure the hydrogen partial pressure by collecting hydrogen in a gas stream and measuring the thermal conductivity of the gas versus a reference gas. Two popular units using this principle are TelegasTM and AlscanTM. The recent work (Gansemer et al., 2007; Badowski and Droste, 2009) has shown the importance of seal materials to ensure no pickup of hydrogen from water vapour in the atmosphere during measurement with these instruments. Another method using calcium zirconate as a reference electrode material has also emerged (Yajima et al., 1995) and two commercial embodiments are available; NotorpTM (Martin et al., 1989) and ALSPEKTM (Hills et al., 2009). This method tends to have a faster response time than the partial pressure units (Badowski and Droste, 2009).

5.10.2 Use of chlorine

Chlorine was used in furnace treatment of melts either as 100% Cl₂ or in combination with Ar or N₂. The Cl₂ gas reacts with the melt to produce MgCl₂, AlCl₂ and AlCl₃ salts that then react with sodium and also can float out inclusions such as oxides (Kulunk and Guthrie, 1992; Fig. 5.8). The aluminium and magnesium chlorides remove alkali earth metals by reacting with the dissolved sodium or lithium in the melt to produce NaCl or LiCl which rise into the dross layer (Guthrie



5.8 Schematic of phenomena taking place during fluxing with argon containing chlorine gas.

and Nilmani, 1993). Magnesium can also be removed if the chlorine is in excess of that needed to react with the alkali earth metals. For many years, the idea persisted that chlorine removed hydrogen by producing HCl. This has been shown to be untrue. HCl droplets can be produced by the reaction of magnesium or aluminium chlorides with water vapour. Hydrogen simply transfers to the gas phase and is carried away. There is some evidence that the interfacial transfer rate of H_2 into the mixed gas purge bubbles increases with Cl_2 addition and that the maximum occurs at around 10% Cl_2 in a N_2 – Cl_2 mix (Sigworth and Engh, 1982). Inclusions are also removed by the chloride salts. The inclusions adhere to the salts and float into the dross layer. In recent years, as the role of chlorine has become better understood it has been realised that rather than injecting chlorine gas the same effects can be obtained more safely by injecting $MgCl_2$.

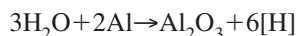
The use of high concentrations of chlorine gas in melt refining once common, has become a contentious practice from the point of view of effectiveness, safety and environment. The presence of chlorine gas handling systems on site presents a risk and there are undesirable emissions from using chlorine. The aluminium chlorides are vapours at normal melt temperatures. Emissions consist of unreacted Cl_2 , and Al_2O_3 dust and HCl fume are produced through reaction of volatile $AlCl_3$ with water vapour in the air (DeYoung and Levesque, 2005).

The development of the technology has been driven by the need to get faster treatment of the melt and to reduce emissions. Two approaches have emerged: improvement of Cl_2 gas mixture injection technology to allow much lower concentrations of chlorine gas, and introduction of halide fluxes in preference to using Cl_2 . These are discussed in Section 5.10.4 on sodium removal.

Emission monitoring systems such as FTIR-CEM (Fourier Transform Infrared Continuous Emissions Monitor) can be used to control chlorine level in fluxing gas so that as the alkali earth concentration drops excess chlorine is reduced (Williams, 2001). Chlorine represents a safety risk and a cost; the industry is moving to eliminate chlorine from site (Rasool et al., 2007).

5.10.3 Hydrogen removal

Water vapour in the atmosphere over the melt reacts with the melt to put hydrogen into solution in liquid aluminium according to



Because the liquid aluminium hydrogen solubility is higher than the solid solubility, hydrogen comes out of solution during solidification, causing the formation of porosity. Porosity reduces strength and causes failure and leakages in castings, and hydrogen needs to be removed from wrought and cast alloy products. Tolerable levels of hydrogen depend on the product application and also on the cooling rate during solidification, which affects the porosity characteristics. Generally, the target aimed for is <0.2 ppm.

Hydrogen is easily removed by purging with another gas; generally argon. Although nitrogen can be used it produces aluminium nitrides and tends to create more dross with a higher metal content. The degassing process has been found to be a first-order diffusion controlled reaction (Engh and Pedersen, 1984; Sigworth et al., 2008) (except at low concentrations levels less than 0.1 ppm^1) so the purge gas bubbles are usually not fully saturated with hydrogen and thus the greater the bubble surface area the faster the hydrogen pickup and removal. Therefore, much effort has gone into reducing the bubble size of the purge gas, and the industry has progressed from lances to diffusers and then to spinning rotor units for purge gas deliver into the melt. The later allows the metal to be degassed in-line immediately before casting so there is little re-introduction of hydrogen into the melt unlike furnace degassing. Much effort has gone into optimising rotor design and flow conditions to reduce bubble sizes. This also helps reduce the usage of expensive argon.

For many years, the practice was to inject a bigas (N_2/Cl_2) with high levels of Cl_2 into furnace melts. Often the gas was injected through a simple steel tube of 1–2" diameter creating a large bubble size, a lot of turbulence and dross. The method has been refined in recent years by using better gas injection methods and lower Cl_2 concentrations in the gas.

The various means of creating smaller bubble sizes in their general order of effectiveness are:

1. improved lances, e.g. graphite with small holes;
2. diffusers; and
3. spinning nozzles.

There are many papers (e.g. Grandfield et al., 1990; Fang et al., 2002) comparing different lances, diffuser and rotor designs using de-oxygenation in water physical modelling and melt trials. Some care is needed when extrapolating from water models to the melt system due to the differences in the transfer of the gas phase on the top surface (Johansen et al., 1998).

Diffusers can be made of porous graphite or ceramics and may be in a wand configuration or used as plugs in the base of a furnace. These systems can encounter problems sometimes with blockage of the plugs. The hydrogen levels achieved are generally higher than that achieved with inline degassers but can be sufficient for certain products. However, because gas flow is maintained through the plugs they tend to keep any inclusions suspended.

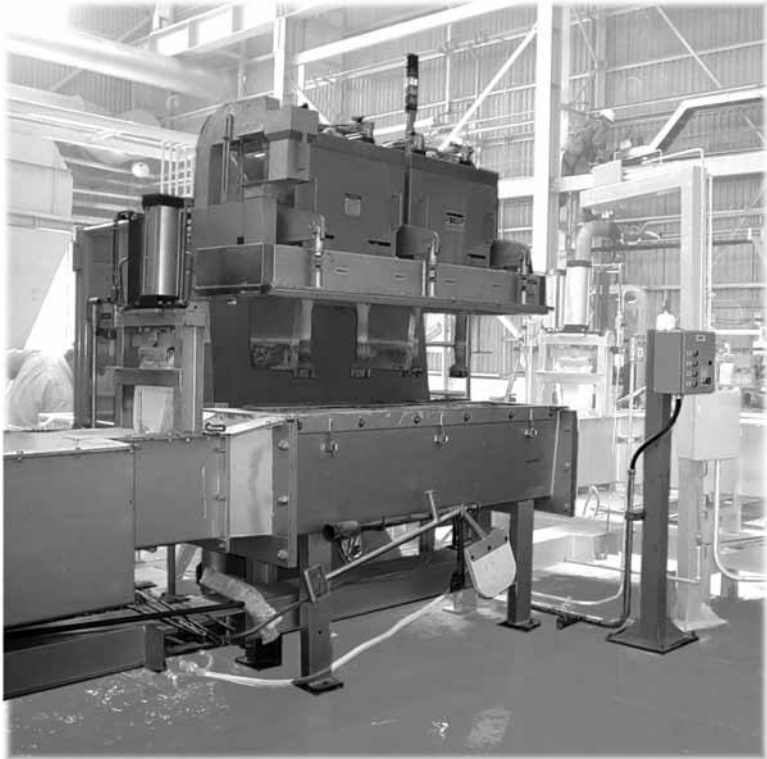
Spinning nozzles can be introduced at an angle through a furnace door (e.g. RGI system) or through the roof in the case of the IRMA system (Le Brun and Mathis, 2004). The improved gas injection systems have been found to meet the U.S. Secondary MACT (Maximum Achievable Control Technology) standards, and rotary gas injection was found to give lower particulate and HCl levels but higher Cl_2 levels than rotary flux injection.

A comparison of lances, porous plugs and spinning rotor gas injection systems (Williams, 2001) showed that the rotor based system was the most efficient at

removing sodium when using chlorine in the gas mixture, however the inclusion levels were higher than for the porous plug system.

In-line spinning nozzles units are widely used because they remove hydrogen at the last stage before casting so there is no time for further hydrogen pickup before solidification. Early units were typically a heated box configuration (e.g. Alpur™, SNIF™, Alcoa 622™) with one or two spinning nozzles. These units could cause problems with met temperature control and also with alloy changes the metal in the box had to be cast out to a sow. A solution to this problem is to use the launder system as the reaction vessel. The Alcan Compact Degasser pioneered this approach (Fig. 5.9). The low depth in the launder compared to a treatment ladle requires that multiple spinning nozzles be used (Waite, 1998).

Gas injection through jets has also been used for degassing units; both in a conical ladle unit, and an inline trough unit (Le Roy et al., 2006). A lesser known hydrogen removal method is vacuum degassing (Alker, 1974; Ellebrecht and



5.9 Alcan Compact Degasser which uses the transfer trough as the reaction vessel for degassing by argon injection, showing four rotors in the raised position for maintenance and cleaning between casts (photograph courtesy of STAS).

Richly, 1974; Aarflot and Patak, 1976; Winterhager and Koch, 1978; Kaestner et al., 1979). Molten metal is transferred into a furnace under vacuum and the hydrogen evaporates from the melt. Although vacuum degassing was commercially used on a large scale in Norway and Russia it is not commonly used elsewhere, due to the issue of hydrogen pickup during transfer to casting and the cost of the more sophisticated furnace technology. One of the in-line spinning rotor degassing units HYCAST™ uses a partial vacuum over the melt to achieve increased hydrogen removal efficiencies (Maeland et al., 2002). This unit drains between casts.

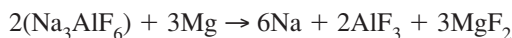
Spray degassing whereby the melt is injected and atomised into small droplets into a chamber with the inert carrier gas has also been investigated (Wu et al., 2007). This method of droplets of melt in gas offers the possibility of a greater reaction surface area than the inverse case of bubbles of gas in the melt and thus faster reaction rates and lower gas consumption. Additionally, the issue with consumable rotors and moving parts is eliminated. At this stage, the method is not commercially available.

5.10.4 Sodium removal

Sodium causes problems in wrought alloys containing magnesium. Magnesium containing 5000 series alloys can experience edge cracking during rolling if the sodium levels are above even 1 or 2 ppm. Sodium is present in metal produced by reduction cells and can be up to 200 ppm when tapped.

Some sodium is naturally lost through evaporation during the transfer of melt from the reduction cells to the furnaces however there is a major incentive to remove sodium as soon as possible after tapping because sodium is known to increase oxidation rates and dross generation. A 23% reduction in casthouse dross generation was reported in one plant after the installation of a crucible treatment sodium removal system (Leinum and Rasch, 2001) which saved several hundred thousand US\$ p.a. The size of the reduction in dross will normally depend on the type of transfer used from the hot metal crucible to the furnace. If siphoning is used then there is less dross generated and the effect of removing sodium before the transfer will be less than if a cascade transfer is used where large amounts of dross are generated.

An additional incentive for crucible treatment is control of bath carryover. Some cryolite from reduction cells inevitably finds its way into the hot metal crucible during tapping. This causes several problems; such as reducing crucible and furnace capacity as it builds up on the walls. Also during the preparation of magnesium containing alloys, magnesium in the melt can react with the bath releasing additional sodium which must be subsequently removed. The reaction is



Crucible treatment systems (e.g. TAC™ and RAM™ are two such commercial systems) involve bringing the crucible to a treatment station where a rotor is

lowered into the melt and either Ar-Cl_2 gas or AlF_3 powder are injected for a short time of 5–10 (Fig. 5.10).

As discussed above, sodium can also be removed by fluxing with chlorine gas. Rather than using Cl_2 gas which has attendant health and safety issues, to produce the MgCl_2 , which reacts with sodium in the melt and floats out inclusions, it is possible to inject MgCl_2 directly into the melt. In practice, the flux mixtures used often also contain other halides salts such as KCl , NaCl , CaF_2 and Na_3AlF_6 (DeYoung, 2001). These can be useful in lowering the melting point of the flux so that it is a liquid and more easily dispersed into small droplets at the melt temperature. The carrier gas for the flux also serves to remove hydrogen.

Salt fluxes have long been used for furnace fluxing and added in simple ways such as manually using bags. One of the main drivers was to produce a dross with a lower metal content, but salt fluxes were also known to affect alkali and alkali earth metal levels. In recent times, the pressures on emissions with respect to inert



5.10 TAC crucible treatment system for skimming bath and removal of sodium by injection of aluminium fluoride. The rotor stirrer is shown. The hot metal crucible is not shown (photograph courtesy of STAS).

gas/chlorine mixtures hastened the development of improved flux injection systems as an alternate means of fluxing.

Stirring with rotors increases the mass transfer and reaction rates and commercial systems are available (Beland et al., 1998; Flisakowski et al., 2001). These can be mobile or mounted on the side of a furnace for in furnace treatment (Fig. 5.11) or used in-line (Leboeuf et al., 2007). These systems perform far better than fluxing with Ar-Cl_2 or $\text{N}_2\text{-Cl}_2$ gas through a pipe. They use less Cl_2 gas (total and %), produce less dross, have faster removal of hydrogen and alkali and alkali earth metals, and produce far fewer emissions. Large furnaces may require more than one rotor.

A significant problem with MgCl_2 is that it readily reacts with moisture in the air transforming to various hydrated forms and can become liquid at room temperature. Additionally, the hydrated form if added to the melt has the potential to cause an explosion, produce HCl emissions and reduce the useful amount of MgCl_2 thus reducing efficiency. This means the MgCl_2 must be kept separate from the atmosphere. There are some downsides with the use of fluxes in that oxide/flux agglomerates tend to be quite difficult to remove using filters that rely on density difference with the melt (Eady et al., 1986).



5.11 Rotary Flux Injector furnace treatment system for injecting magnesium chloride to remove sodium (photograph courtesy of STAS).

5.10.5 Inclusion removal

Solid inclusions such as oxides cause a variety of defects such as extrusion tears, extrusion die wear, pinholes in foil and cans etc. Inclusions arise due to a variety of sources such as carbides from cell operations, aluminium oxides generated in transfer operations, aluminium magnesium spinels produced during magnesium alloying, borides from grain refiner additions and various halide salts such as cryolite from the cells and chlorides and fluorides from added fluxes. The technology is available to make extremely clean material with less than <0.01 ppm particulate but the cost of the treatment, the price of the product and the quality standard needed for each application dictate that only essential inclusion removal is carried out. For example, rolling slab destined for thin <6 mm foil requires much lower inclusion levels than typical extrusion billet product.

Commercial inclusion removal techniques can be divided into:

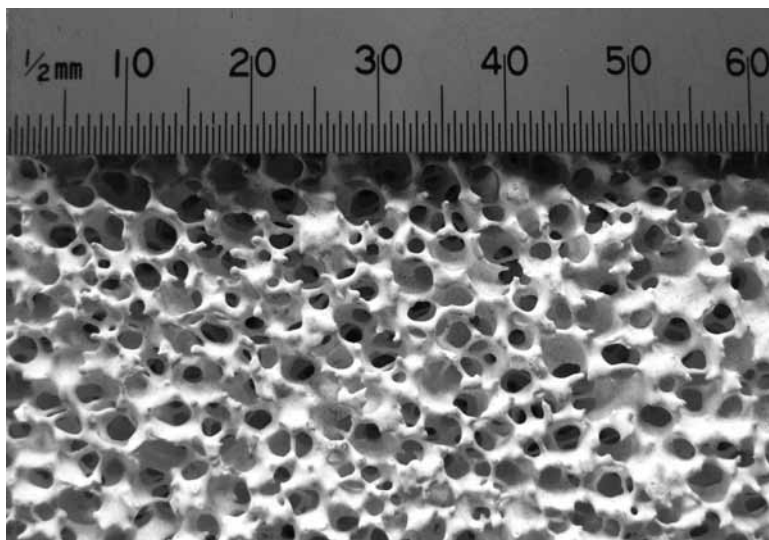
1. Settling
2. Flotation
3. Filtration.

Inclusion settling rates can be relatively fast depending on the concentration, size and density of the inclusions i.e. within 20 minutes a significant fraction (a third to a half) has settled out. Stokes law settling calculation is not applicable due to the significant natural convection currents in the melt, however, the drop in concentration is well described as a first-order reaction i.e. the concentration drops exponentially with time. Lately, further detailed flow modelling has been carried out (Instone et al., 2008). Care must be taken not to empty all the metal from the furnace thereby releasing all the particles at the end of casting from the furnace.

During gas purging for sodium and hydrogen removal, particles can also be removed by flotation. The non-wetted particles adhere to the gas bubbles and are taken to the melt surface dross layer. In line degassing units generally achieve around 50% inclusion removal (Le Brun, 2008) but depending on size and concentration of inclusions, and the purge gas composition can be up to 90% (Hakonsen et al., 2004; Sigworth et al., 2008).

Inclusions are also removed using a variety of filtration technology. Some fibreglass cloth socks are used in the feeding troughs for very large particles >1 mm, but the simplest useful molten metal filter is a disposable ceramic foam filter (CFF) tile (Fig. 5.12). These are produced by coating polyurethane foam with an alumina based slurry and then firing them to produce a ceramic foam structure. They are generally 50-mm thick and up to ~ 600 mm square. The pore size varies from 1 to 10 mm. The usual configuration is an almost horizontal tile with the metal flowing into the top and out the bottom side of the filter. CFF were first developed in the 1970s (Aubrey and Dore, 1993) by Selee corporation.

The capture mechanisms of CFF filters have been extensively studied (Gauckler et al., 1985; Grandfield et al., 1990; Smith et al., 1998; Lai et al., 2006;



5.12 Structure of ceramic foam filter tile. Tiles are usually 50 mm thick and up to $\sim 580 \times 580 \text{ mm}^2$.

Zhang et al., 2008; Duval et al., 2009). Some early studies indicated these filters acted as cake filters with inclusions deposited in a cake on the top surface of the filter (Apelian et al., 1985). However, given the large pore size relative to the inclusion dimensions and typical industrial concentrations of $<10 \text{ ppm}$ of inclusions, cake filtration does not occur in normal practice. If cake filtration occurs due to unusually high particle concentrations then the filter cake tends to block the flow of metal (Aubrey and Dore, 1993). Used filters show inclusions deposited throughout the filter and a concentration gradient of particles from the inlet side to the outlet side (Duval et al., 2009) corresponding to depth filtration. Although many capture mechanisms are possible, the two main depth filtration capture mechanisms considered important are sedimentation and peripheral interception within the pores. Good correspondence was found with this theory although for larger particles some agglomeration also needed to be accounted for. Heavy boride particles have been shown to have an effect on filtration efficiency by encouraging cascading of particles through the body of the filter (Towsey et al., 2002; Instone et al., 2005a, 2005b).

The main factors affecting filter efficiency are the melt velocity (set by the filter tile area, porosity and the metal flow rate), the particle size and density and the filter pore size and thickness. By using two filters in series in a dual stage configuration, one effectively doubles the filter thickness thus increasing efficiency. Smaller pore sizes give higher efficiencies and also less variation in efficiency (Duval et al., 2009).

CFFs have a limited capacity and as the concentration of particles builds up within the filter the chance of particle release from the filter increases. In practice, they are used to treat around 60 tonnes of metal and then discarded. Any flow disturbance such as a sudden change in metal level can also cause release of particles (Dupuis and Dumont, 1993).

Deep bed filters are widely used to achieve removal efficiencies generally greater than 90% compared to the lower efficiencies of CFFs (Dupuis and Dumont, 1993). Consisting of beds of filter media (usually alumina balls) in a heated box (Fig. 5.13; Clement, 1995) these units are more expensive and are



5.13 Deep bed filter box for inline filtration of inclusions from the melt (photograph courtesy of STAS).

generally applied to higher quality products such as rolling ingot destined for thin foil production. Because of the depth and area of the filter bed these filters are highly efficient. The melt velocity within the bed is low because of the large area increasing probability of particle capture and the depth of the bed increases the number of possible capture events.

Rigid media filters (RMF) are generally made of bonded silicon carbide or alumina and have finer pore sizes than CFFs and thus high efficiency, and are often applied to the filtration of metal for thin foil where particles $<10\text{ }\mu\text{m}$ need to be removed (Kakimoto et al., 1993), however they can be prone to blocking if the metal inclusion concentration is high (Hoshino et al., 1996). Thus, they are often used with a CFF upstream as a coarse filter and can achieve 90% or higher efficiencies in this configuration (Keegan et al., 1997). They can consist of a cartridge of porous tubes or a 'top Hat' configuration (Neff and Stankiewicz, 1986). The long contact times of the melt with the rigid media filters can produce reactions within the filter between the melt and the deposited particles which cause blockages and reduce filter life (Hane et al., 1997; Mabry et al., 1997).

There are current attempts to use centrifugal force for inclusion removal in the form of a molten metal cyclone (Courtenay and Reusch, 2009) but as yet the technique is not commercially available. Another method which has been investigated is the application of an electromagnetic field to push the non-conducting inclusions out of the metal stream (Frisvold et al., 1991; Patel and El-Kaddah, 1997; Shu et al., 1999; Cao et al., 2002).

5.11 Conclusion

The science and technology for producing aluminium ingots for further processing into castings or wrought alloy products has shown steady development, and now constitutes a considerable body of knowledge. The application of this knowledge has led to improved product quality, process efficiency and new technology. By understanding the physical phenomena taking place in these processes, operations become more competitive. This chapter has given a brief review of these phenomena which should assist casting process operators in achieving improved performance.

DC casting process productivity (set by scrap rates) largely depends on heat and fluid flow, and how they generate stresses, strains and cracking defects. By using mathematical models and sophisticated experimental techniques, control of many of these defects has been made possible, and the resultant metal quality is greatly improved. Examination of open mould conveyor ingot casting heat flow and deformation has led to new improved mould designs and hence improved operations. Filtration and other particle removal mechanisms for molten aluminium are now quite well understood and enable careful maximisation of quality while minimising particle removal costs.

5.12 Notes

- 1 Degassing can become equilibrium controlled at low gas levels with well-dispersed small bubbles. In this case, the bubbles rapidly become fully saturated with hydrogen, and the removal rate solely depends on the amount of gas flow rather than the rate at which hydrogen transfers to the bubbles.

5.13 References

- Aarflot, A. and F. Patak (1976). Dynamic vacuum treatment of molten aluminium and its alloys. *Light Metals 1976*, The Metallurgical Society of the AIME: 389–399.
- Adenis, D.J.P., K.H. Coats, et al. (1962–1963). ‘An analysis of the direct chill casting process by numerical methods’, *Journal of the Institute of Metals*, 91: 395–403.
- Aitchison, L. and V. Kondic (1953). *The Casting of Non-Ferrous Ingots*, London, Macdonald & Evans Ltd.
- Aliravci, C.A., J.E. Gruzleski, et al. (1998). Thermodynamic study of metastable Al-Fe phase formation in direct chill (DC)-cast aluminum alloy ingots. *Light Metals: Proceedings of Sessions, TMS Annual Meeting (Warrendale, Pennsylvania)*. B.J. Welch. San Antonio, TX, USA, Minerals, Metals & Materials Soc (TMS): 1381–1389.
- Alker, K. (1974). ‘Vacuum degassing of aluminum casting alloys’, *Vakuumentgasung Von Aluminium-Gusslegierungen*, 61(23): 693–696.
- Allen, C.M., K.A.Q. O’Reilly, et al. (1997). ‘Heterogeneous nucleation of solidification of equilibrium and metastable phases in melt-spun Al-Fe-Si alloys’, *Materials Science and Engineering: A*, 226–228: 784–788.
- Allen, C.M., K.A.Q. O’Reilly, et al. (1998a). ‘Intermetallic phase selection in 1XXX Al alloys’, *Progress in Materials Science*, 43(2): 89–170.
- Allen, C.M., K.A.Q. O’Reilly, et al. (1998b). Calorimetric evaluation of the role of impurities in the nucleation of secondary phases in 1xxx Al alloys. *Materials Research Society Symposium – Proceedings*. Boston, MA, USA., 481: 3–14.
- Anderson, M., R. Bruski, et al. (2001). Netcast shape casting technology: A technological breakthrough that enhances the cost effectiveness of aluminum forgings. *Light Metals: Proceedings of Sessions, TMS Annual Meeting (Warrendale, Pennsylvania)*. J. Anjier. New Orleans, LA: 847–853.
- Angleys, P. (1960). ‘Ugine Venhth process’, *Journal of Metals*: 42.
- Angleys, P. (1964). ‘Horizontal continuous casting process’, *Modern metals*, 20: 46–48.
- Anonymous (1963). ‘Bell Bay aluminium plant makes its own busbar’, *Castings*: 34–35.
- Apelian, D., C.E. Eckert, et al. (1985). ‘Refining of molten aluminum by filtration technology’, in *Refining and Alloying of Liquid Aluminum and Ferro-Alloys*, Aluminum-Verlag, Düsseldorf, Germany, pp. 123–143.
- Apostolou, G. and S. Armaos (1988). ‘Process and apparatus for top feed casting of metals’, Aluminium Pechiney, US Patent 4732209.
- Aubrey, L.S. and J.E. Dore (1993). Ceramic foam: A deep bed or caking filter in aluminum cast shop operations. *Light Metals: Proceedings of Sessions, TMS Annual Meeting (Warrendale, Pennsylvania)*. Denver, CO, USA, Minerals, Metals & Materials Soc (TMS): 1009–1020.
- Austen, P.R. and E.J. Swain (1997). Automation and upgrading of VDC4 at Comalco (Bell Bay) Limited post implementation operating performance. *Proceedings of the Australasian Asian Pacific Conference on Aluminium Cast House Technology*. Gold Coast, Aust, Minerals, Metals & Materials Soc (TMS): 339–350.

- Bachowski, R. and R. E. Spear (1975). 'Ingot shell formation', *Light Metals*: 111–118.
- Badowski, M. and W. Droste (2009). *Hydrogen measurement practices in liquid aluminium at low hydrogen levels*. TMS Annual Meeting.
- Bainbridge, I.F., J.F. Grandfield, et al. (2005). Meniscus shape and direct chill cast hot top mould design. *Proceedings of the Australasian Conference and Exhibition – Aluminium Cast House Technology*. Melbourne. 2005: 93–100.
- Bainbridge, I.F. and J.F. Grandfield (2007). Measurement of hot top direct chill casting mould ingot shell temperatures. *Aluminium Cast House Technology 2007, 10th Australasian conference and exhibition*. 5–8 August 2007, Sydney, CAST Consult Pty Ltd: 81–88.
- Baker, P.W. and J.F. Grandfield (1987). Mould wall heat transfer in air-assisted DC casting. *Solidification Processing 1987*, The Institute of Metals: 257–259.
- Baker, P.W. and J.F. Grandfield, (2001). The role of surface tension forces in gas pressurized VDC casting. *Seventh Australian Asian Pacific Conference Aluminium Cast House Technology*. Hobart, Tasmania, TMS: 195–204.
- Bakken, J.A. and T. Bergstrom (1986). Heat transfer measurements during DC casting of aluminum. I. Measurement Technique. *Light Metals 1986*, The Metallurgical Society/AIME: 883–889.
- Behr, R.D., S.L. Couling, et al. (1973). Direct chill casting method. USA, Dow chemical corporation.
- Beland, G., C. Dupuis, et al. (1998). Rotary flux injection: Chlorine-free technique for furnace preparation. *Light Metals: Proceedings of Sessions, TMS Annual Meeting (Warrendale, Pennsylvania)*. B.J. Welch. San Antonio, TX, USA, Minerals, Metals & Materials Soc (TMS): 843–847.
- Benum, S., A. Hakonsen, et al. (1999). Mechanisms of surface formation during direct chill (DC) casting of extrusion ingots. *Light Metals: Proceedings of Sessions, TMS Annual Meeting (Warrendale, Pennsylvania)*. San Diego, CA, USA, Minerals, Metals & Materials Soc (TMS): 737–742.
- Bergmann, W.J. (1970). 'Solidification in continuous casting of aluminium', *Metallurgical Transactions*, 1: 3361–3364.
- Bergmann, W.J. (1973). 'Surface structures of continuously cast aluminium', *Journal of Metals*: 23–27.
- Bergmann, W.J. (1975). 'Aluminium ingot surface improvement by advanced continuous casting technology', *Aluminium*, 51(5): 336–339.
- Bergsma, S.C. and M.E. Kassner (1997). 'Comparison of unextruded air slip direct chill cast 6061 ingot with bar stock extruded from conventional direct chill cast 6061 ingot', *Journal of Materials Engineering and Performance*, 6(4): 469–472.
- Boender, W., A and A. Burghardt (2004). Numerical simulation of DC casting; interpreting the results of a thermo-mechanical model. *Light Metals*. Carlotte, NC, TMS.
- Bohmer, J.R. and M. Jordan (1995). Verification of a mathematical model for continuous billet casting with a temperature and load history approach. *Modeling of Casting, Welding and Advanced Solidification Processes VII*, TMS: 809–816.
- Brochu, C., A. Larouche, et al. (1993). Study of shell zone formation in lithographic and anodizing quality aluminum alloys: Experimental and numerical approach. *Light Metals*, The Minerals, Metals Materials Society: 961–67.
- Bryson, N.B. (1969). 'Casting of Aluminium Ingots', Alcan, U.S. Patent 3411079.
- Buxmann, K. (1982). 'Solification conditions and microstructure in continuously cast aluminum', *Journal of Metals*.

- Cao, Z.Q., Q.M. Zhang, et al. (2002). 'Research on electromagnetic separation efficiency of nonmetallic inclusions from aluminum melts', *Dalian Ligong Daxue Xuebao/ Journal of Dalian University of Technology*, 42(4): 441–445, 455.
- Chang, K.M. and B. Kang (1999). 'Cracking control in dc casting of high-strength aluminum alloys', *Journal of the Chinese Institute of Engineers, Transactions of the Chinese Institute of Engineers, Series A/Chung-kuo Kung Ch'eng Hsueh K'an*, 22(1): 27–42.
- Chen, X.G. (1998). Growth mechanisms of intermetallic phases in DC cast AA1xxx alloys. *Light Metals: Proceedings of Sessions, TMS Annual Meeting (Warrendale, Pennsylvania)*, San Antonio, TX, USA, Minerals, Metals & Materials Soc (TMS).
- Chen, X.-G., F.-J. Klinkenberg, et al. (1994). 'Comparing hydrogen testing methods for wrought aluminum', *JOM*, 46(8): 34–38.
- Chu, M. and J. Jacoby (1990). Macrosegregation characteristics of commercial size aluminum alloy ingot cast by the direct chill method. *Light Metals*. Anaheim, CA, USA, Minerals, Metals & Materials Soc (TMS): 925–930.
- Clausen, P. and G. Whan (2001). An assessment of the design of a Gautschi mould using finite element analysis. *Proceedings of the Australian Asian Pacific Conference on Aluminium Cast House Technology*: 247–252.
- Clement, G. (1995). Pechiney deep bed filter: technology and performance. *Light Metals: Proceedings of Sessions, TMS Annual Meeting (Warrendale, Pennsylvania)*. Las Vegas, NV, USA, Minerals, Metals & Materials Soc (TMS): 1253–1262.
- Cooksey, M., T. Ware, et al. (2001). Effect of pressure cycle and extension probe on LiMCA measurement of inclusions. *Light Metals: Proceedings of Sessions, TMS Annual Meeting (Warrendale, Pennsylvania)*. J. Anjier. New Orleans, LA: 965–971.
- Courtenay, J.H. and F. Reusch (2009). Trial results with an improved system of filtration of molten aluminium based on a three stage reactor employing a cyclone as its final stage. *TMS Annual Meeting*: 773–776.
- Davidson, P.A. and S.C. Flood (1994). 'Natural convection in an aluminum ingot: A mathematical model', *Metallurgical Transactions: B*, 25(2): 293–302.
- Devadas, C. and J.F. Grandfield (1991). Experiences with modelling DC casting of aluminum. *Light Metals*. New Orleans, LA, Minerals, Metals & Materials Soc (TMS): 883–892.
- DeYoung, D.H. (2001). Salt fluxes for alkali and alkaline earth element removal from molten aluminium. *Aluminium cast house technology, 7th Australian Asian Pacific Conference*, TMS: 99–113.
- DeYoung, D.H. and R. Levesque (2005). Air Emissions from Rotary Gas And Rotary Salt Injection Furnace Fluxing Processes. *9th Aluminium Casthouse Technology Conference*. Melbourne, CAST consult Pty Ltd: 7–16.
- Dobatkina, V.I. (1948). *Continuous Casting and Casting Properties of Alloys*. Moscow: Oborongiz.
- Donnerburg, F. and S. Engler (2000). *Influence of Different Lubricants on the Friction Between the Solidifying Shell and the Mould During DC Casting of AlMgSi0.5*. Weinheim, Wiley-VCH: 47.
- Doutre, D., B. Garipey, et al. (1985). Aluminium cleanliness monitoring: methods and applications in process development and quality control. *Light Metals: Proceedings of Sessions, AIME Annual Meeting (Warrendale, Pennsylvania)*. H. O. Bohner. New York, NY, USA, Metallurgical Soc of AIME: 1179–1195.
- Drezet, J.M. and M. Plata (1995). Thermomechanical effects during direct chill and electromagnetic casting of aluminum alloys, part I: Experimental investigation. *Light*

- Metals: Proceedings of Sessions, TMS Annual Meeting (Warrendale, Pennsylvania)*. Las Vegas, NV, USA, Minerals, Metals & Materials Soc (TMS): 931–940.
- Drezet, J.M. and M. Rappaz (1996). ‘Modeling of ingot distortions during direct chill casting of aluminum alloys’, *Metallurgical and Materials Transactions A: Physical Metallurgy and Materials Science*, 27(10): 3214–3225.
- Drezet, J.M. M. Rappaz, et al. (1995a). ‘Experimental investigation of thermomechanical effects during direct chill and electromagnetic casting of aluminum alloys’, *Metallurgical and Materials Transactions: B*, 26(4): 821–829.
- Drezet, J.M. M. Rappaz, et al. (1995b). Thermomechanical effects during direct chill and electromagnetic casting of aluminum alloys, part II: Numerical simulation. *Light Metals: Proceedings of Sessions, TMS Annual Meeting (Warrendale, Pennsylvania)*. Las Vegas, NV, USA, Minerals, Metals & Materials Soc (TMS): 941–950.
- Drezet, J.M. and M. Rappaz (1997). Direct chill casting of aluminum alloys: Ingot distortions and mold design optimization. *Light Metals: Proceedings of Sessions, TMS Annual Meeting (Warrendale, Pennsylvania)*. Orlando, FL, USA, Minerals, Metals & Materials Soc (TMS): 1071–1080.
- Droste, W. and W. Schneider (1990). Laboratory investigations about the influence of starting conditions on butt curl and swell of DC cast sheet ingots. *Light Metals 1991*. New Orleans, LA, USA, Minerals, Metals & Materials Soc (TMS): 945–951.
- Dunn, E.M. (1979). ‘Metallurgical structure of electromagnetically cast extrusion billet’. *Light Metals*, ed. W.S. Peterson (Warrendale, Pennsylvania). *Hutnicke Listy*, USA, TMS: 671–782.
- Dupuis, C. and R. Dumont (1993). Impact of LIMCA technology on the optimization of metal cleanliness. *Light Metals: Proceedings of Sessions, TMS Annual Meeting (Warrendale, Pennsylvania)*. Denver, CO, USA, Minerals, Metals & Materials Soc (TMS): 997–1002.
- Duval, H., C. Riviere, et al. (2009). ‘Pilot-scale investigation of liquid aluminum filtration through ceramic foam filters: Comparison between coulter counter measurements and metallographic analysis of spent filters’, *Metallurgical and Materials Transactions B: Process Metallurgy and Materials Processing Science*, 40(2): 233–246.
- Eady, J.A., D.M. Smith, et al. (1986). ‘Filtration of aluminium melts’, *Journal of the Institute of Metals*: 93–100.
- Easton, M. and D. St John (1999a). ‘Grain refinement of aluminum alloys: Part I. The nucleant and solute paradigms – a review of the literature’, *Metallurgical and Materials Transactions A: Physical Metallurgy and Materials Science*, 30(6): 1613–1623.
- Easton, M. and D. St John (1999b). ‘Grain refinement of aluminum alloys, part II: Confirmation of, and a mechanism for, the solute paradigm’, *Metallurgical and Materials Transactions A: Physical Metallurgy and Materials Science*, 30(6): 1625–1633.
- Easton, M., D. St John, et al. (2004). Reducing the cost of grain refiner additions to DC casting. *TMS Light Metals*. A. T. Tabereaux. Charlotte, NC: 827–831.
- Ekenes, J. and W. Peterson (1990). Visual observations inside an Airslip™ mold during casting. *Light Metals*. Anaheim, CA, USA, Minerals, Metals & Materials Soc (TMS): 957–961.
- Ellebrecht, C. and O. Richly (1974). ‘Equipment for vacuum treatment of molten metals, especially aluminum and aluminum alloys’, *Vorrichtungen zur Vakuumbehandlung von Metallschmelzen, insbesondere Aluminium und seinen Legierungen*, 61(23): 697–699.
- Emley, E.F. (1976). ‘Continuous Casting of Aluminium’, *International Metals Reviews*, 21: 75–115.

- Engh, T.A. (1992). *Principles of metal refining*. Oxford, Oxford Scientific.
- Engh, T.A. and T. Pedersen (1984). Removal of hydrogen from molten aluminum by gas purging. *Light Metals: Proceedings of Sessions, AIME Annual Meeting (Warrendale, Pennsylvania)*. Los Angeles, CA, USA, Metallurgical Soc of AIME: 1329–1344.
- Ennor, W.T. (1942). *Method of Casting*. USA.
- Eskin, D. (2008). *Physical Metallurgy of Direct Chill Casting of Aluminium Alloys*, CRC Press.
- Eskin, D.G., Suyitno, et al. (2004). ‘Mechanical properties in the semi-solid state and hot tearing of aluminium alloys’, *Progress in Materials Science*, 49(5): 629–711.
- Eskin, D.G., J. Zuidema, et al. (2004). ‘Structure formation and macrosegregation under different process conditions during DC casting’, *Materials Science and Engineering A*, 384(1–2): 232–244.
- Evans, J.W. and W.K. Jones Jr (2002). Mathematical modeling in aluminum casting and molten metal treatment. *Light Metals: Proceedings of Sessions, TMS Annual Meeting (Warrendale, Pennsylvania)*. R. Peterson. Seattle, WA: 669–678.
- Fang, W.B., Y.H. Geng, et al. (2002). ‘Simulation on flow process of filtered molten metals’, *Transactions of Nonferrous Metals Society of China (English Edition)*, 12(1): 102–104.
- Fergus, J.W. (2005). ‘Sensors for monitoring the quality of molten aluminum during casting’, *Journal of Materials Engineering and Performance*, 14(2): 267–275.
- Fjaer, H. and A. Mo (1990). Mathematical modelling of thermal stresses during D.C. casting of aluminum billets. *Light Metals*. Anaheim, CA, USA: Minerals, Metals & Materials Soc (TMS): 945–950.
- Fjaer, H.G., E. K. Jensen, et al. (1992). Mathematical modeling of heat transfer and thermal stresses in aluminium billet casting. Influence of the direct water cooling conditions. *5th International Aluminum Extrusion Technology Seminar*, The Aluminum Association: 113–20.
- Fjaer, H.G., A. Buchholz, et al. (2000). Investigations of the primary cooling in sheet ingot casting. *Continuous Casting*. Weinheim, Wiley-VCH: 131–137.
- Flisakowski, P., J.M. McCollum, et al. (2001). Improvements in cast shop processing using Pyrotek’s HD-2000 and PHD-50 Rotary injector system. *Light Metals*, TMS: 1041–1047.
- Flood, S.C., P.A. Davidson, et al. (1995). A scaling analysis for the heat flow, solidification and convection in continuous casting of aluminium. *Modeling of Casting, Welding and Advanced Solidification Processes VII* (Warrendale, Pennsylvania 15086), USA, Minerals, Metals and Materials Society/AIME: 801–808.
- Frisvold, F., T.A. Engh, et al. (1991). Removal of inclusions – A survey and comparison of principles. *Light Metals*, San Diego, CA, USA, Minerals, Metals & Materials Soc (TMS).
- Furness, A.G. and J.D. Harvey (1975). *Mould assembly and method for continuous or semi-continuous casting UK*, British Aluminium.
- Gansemer, T.M., B.C. Reynolds, et al. (2007). Improvement in hydrogen measurement technique for molten aluminum. *Light Metals 2007*. Orlando, FL, Minerals, Metals & Materials Soc (TMS): 685–689.
- Gariepy, B. and Y. Caron (1990). Investigation in the effects of casting parameters on the extent of centerline macrosegregation in DC cast sheet ingots. *Light Metals 1991*. New Orleans, LA, USA, Minerals, Metals & Materials Soc (TMS): 961–971.
- Gariepy, B., D. Mazerolle, et al. (2005). Alcan HDC casting experience at Dubuc and Alma plants for the production of busbar, pure and foundry T ingots. *Aluminium Cast House Technology*. Melbourne, Cast Consult Pty Ltd: 93–102.

- Gauckler, L.J., M.M. Waerber, et al. (1985). 'Ceramic foam for molten metal filtration', *Journal of Metals*, 37(9): 47–50.
- Gervais, H.L. and P. Chollet (1975). *Method for the continuous casting of metal ingots or strips*. USA, Noranda Mines.
- Getselev, Z.N., G.A. Balakhontsev, et al. (1969). *Method of Continuous and Semicontinuous Casting of Metals and a Plant for Same*. USSR, KMPO (Kuibyshev Metallurgical Works): US 3467166.
- Goodrich, D. and E. Tarapore (1991). Comparison of ingot structures for aluminum ingots produced by direct-chill and electromagnetic casting. *Light Metals 1992*. San Diego, CA, USA, Minerals, Metals & Materials Soc (TMS): 1371–1377.
- Grandfield, J.F. (1997). DC casting of aluminium: a short review of process development. *Proceedings of the Australasian Asian Pacific Conference on Aluminium Cast House Technology*. Gold Coast, Australia, Minerals, Metals & Materials Soc (TMS): 231–243.
- Grandfield, J.F. (2000). 'Experimental methods for direct chill casting, including new techniques for magnesium horizontal direct chill casting', *Aluminium Transactions*, 3(1): 41–51.
- Grandfield, J.F. (2001). *Hot tear defect formation during horizontal direct chill casting of magnesium*. PhD thesis, Brisbane, University of Queensland.
- Grandfield, J.F. and P.W. Baker (1987). Variation of heat transfer rates in direct chill water spray of aluminium continuous casting. *Solidification Processing, The Institute of Metals*: 260–263.
- Grandfield, J.F., P. Cleary, et al. (2003). Mathematical modelling of ingot caster filling systems. *Proceedings of the Australian Asian Pacific Conference on Aluminium Cast House Technology*. P.R. Whiteley. Brisbane, QLD: 271–276.
- Grandfield, J.F., P. Cleary, et al. (2004). Mathematical modeling of ingot caster filling systems. *TMS Light Metals*. A. T. Tabereaux. Charlotte, NC: 661–666.
- Grandfield, J.F., Goodall, K., Misic, P. and Zhang, X. et al., (1997). Water cooling in direct chill casting: Part 2, effect on billet heat flow and solidification. *Light Metals: Proceedings of Sessions, TMS Annual Meeting (Warrendale, Pennsylvania)*. Orlando, FL, USA, Minerals, Metals & Materials Soc (TMS): 1081–1090.
- Grandfield, J.F., Hoadley, A. and Instone, S., et al., (1997). Water cooling in direct chill casting: Part 1, boiling theory and control. *Light Metals: Proceedings of Sessions, TMS Annual Meeting (Warrendale, Pennsylvania)*. Orlando, FL, USA, Minerals, Metals & Materials Soc (TMS): 691–699.
- Grandfield, J.F., D.W. Irwin, et al. (1990). Mathematical and physical modelling of melt treatment processes. *Light Metals 1990*. Anaheim, CA, USA, Minerals, Metals & Materials Soc (TMS): 737–745.
- Grandfield, J.F. and McGlade P.T. (1996). DC casting of aluminium: Process behaviour and technology. *Materials Forum*, 20: 29–51.
- Grandfield, J.F., D. Mortensen, et al. (2006). Remelt ingot mold heat flow and deformation. *TMS Light Metals*. San Antonio, TX: 869–876.
- Grandfield, J.F., T.T. Nguyen, et al. (2001). Aspects of heat transfer during production of remelt ingot using chain casters. *Proceedings of the Australian Asian Pacific Conference on Aluminium Cast House Technology*: 263–271.
- Grandfield, J.F., V. Nguyen, et al. (2007). Ingot caster productivity improvement through examination of mould heat flow and deformation. *Proceedings of the Australasian Conference and Exhibition – Aluminium Cast House Technology 2007*. Sydney: 147–154.

- Grandfield, J.F., V. Nguyen, et al. (2008). Chain conveyor remelt ingot casting improvement. *TMS Light Metals*. New Orleans, LA: 671–677.
- Grandfield, J.F., P. Rohan, et al. (2005). Development of an ingot caster filling system. *Proceedings of the Australasian Conference and Exhibition – Aluminium Cast House Technology*. Melbourne. 2005: 145–152.
- Grandfield, J.F. and J.A. Taylor (2009). The downstream consequences of rising ni and v concentrations in smelter grade metal and potential control strategies. *Light Metals*: 1007–1011.
- Grandfield, J.F. and L. Wang (2004). Application of mathematical models to optimization of cast start practice for DC cast extrusion billets. *TMS Light Metals*. A.T. Tabereaux. Charlotte, NC: 685–690.
- Granger, D.A. (1989). Ingot casting in the aluminium industry. *Treatise on Material Science and Technology*, Academic press 31: 109–135.
- Grjotheim, K., Krohn, C., Malinovsky, M., Matiasovsky, K., Thonstad, J. (1982). *Aluminium Electrolysis: Fundamentals of the Hall-Heroult Process*, Aluminium Verlag.
- Groce, T.E.H.D.G. (1971). Control of Heat Transfer in Continuous Casting of AL and Mg Ingots, Kaiser.
- Gruen, G.U., A. Buchholz, et al. (2000). 3-D modeling of fluid flow and heat transfer during the DC casting process – Influence of flow modeling approach. *Light Metals: Proceedings of Sessions*, TMS Annual Meeting (Warrendale, Pennsylvania), Nashville, TN.
- Gruen, G.U. and W. Schneider (1996). 3-D Modeling of the start-up phase of DC casting of sheet ingots. *Light Metals: Proceedings of Sessions*, TMS Annual Meeting (Warrendale, Pennsylvania), Anaheim, CA, USA, Minerals, Metals & Materials Soc (TMS).
- Gupta, A., S.T. Lee, et al. (2007). ‘Direct chill casting of aluminium-manganese against aluminium-silicon layer via Novelis fusion process’, *Materials Technology*, 22(2): 71–75.
- Guthrie, R.I.L. and M. Nilmani (1993). Impurity sources and control—general principles of melt treatment. *Aluminum Cast House Technology: Theory & Practice*, Melbourne University: 85–104.
- Hakonsen, A., G. Maeland, et al. (2004). The pick-up of micro bubbles during LiMCA II measurements post an inline gas fluxing unit. *TMS Light Metals*. A.T. Tabereaux. Charlotte, NC: 749–754.
- Hakonsen, A. and D. Mortensen (1995). FEM model for the calculation of heat and fluid flows in DC casting of aluminum slabs. *Modeling of Casting, Welding and Advanced Solidification Processes*. Cross, M. and Campbell, J. London, UK: Minerals, Metals & Materials Soc (TMS): 763–770.
- Hakonsen, A.M. (1995). ‘Dimensionless diagrams for the temperature distribution in direct-chill continuous casting’, *Cast Metals*, 8(3): 147–157.
- Hamadaid, A. (2004). *The Role of Casting/Mould Interface on the Heat Transfer and Solidification in Aluminium Die-Casting*. I.F. Bainbridge: PhD literature review.
- Hane, A., T. Nishizaka, et al. (1997). Influence of Al-Ti grain refiner on filter life. *Light Metals: Proceedings of Sessions*, TMS Annual Meeting (Warrendale, Pennsylvania). Orlando, FL, USA, Minerals, Metals & Materials Soc (TMS): 991–996.
- Hasan, M. and K.R. Ragel (2009). Advanced cfd modeling of DC casting of aluminum alloys. *TMS Annual Meeting*: 805–810.
- Henry, S., G.U. Gruen, et al. (2004). ‘Influence of convection on feathery grain formation in aluminum alloys’, *Metallurgical and Materials Transactions A: Physical Metallurgy and Materials Science*, 35(8): 2495–2501.

- Hills, M.P., C. Thompson, et al. (2009). Accurate measurement of hydrogen in molten aluminium using current reversal mode. *TMS Annual Meeting*: 707–712.
- Ho, K. and R.D. Pehlke (1985). 'Metal/Mould interfacial heat transfer', *Metallurgical Transactions B*, 16(3): 585–94.
- Hoshino, K., T. Nishizaka, et al. (1996). Filtration of molten 1XXX series aluminum alloys with rigid media tube filter. *Light Metals: Proceedings of Sessions, TMS Annual Meeting (Warrendale, Pennsylvania)*. Anaheim, CA, USA, Minerals, Metals & Materials Soc (TMS): 833–838.
- Hudault, G., D. Cheve, et al. (1989). First experience of commercial operation with the CREM process. *Light Metals: Proceedings of Sessions, AIME Annual Meeting (Warrendale, Pennsylvania)*. Las Vegas, NV, USA, Metallurgical Soc of AIME: 769–775.
- Inoue, T., D.Y. Ju, et al. (1989). Temperature and viscoplastic stresses during vertical semi-continuous direct chill casting of aluminum alloy. *International Conference on Residual Stress. ICRS 2*, Elsevier Applied Scien: 523–528.
- Instone, S., M. Badowski, et al. (2005a). Development of molten metal filtration technology for aluminium. *TMS Light Metals*. San Francisco, CA: 933–938.
- Instone, S., M. Badowski, et al. (2005b). XC filter – A filter technology for increased filtration performance. *Proceedings of the Australasian Conference and Exhibition – Aluminium Cast House Technology*. Melbourne. 2005: 267–275.
- Instone, S., A. Buchholz, et al. (2008). Inclusion transport phenomena in casting furnaces. *TMS Light Metals*. New Orleans, LA: 811–816.
- Instone, S., W. Schneider, et al. (2003). Improved VDC billet casting mould for Al-Sn alloys. *Light Metals*, San Diego, TMS, USA.
- Jacoby, J. (1995). Direct chill casting defects. *Aluminium cast house technology, 5th Australian Asian Pacific Conference*.
- Jacoby, J. E., J. T. Laemmle, et al. (1986). *Lithium Alloy Casting*. USA, Aluminum Company of America.
- Jensen, E.K. (1984). Mould temperatures during DC casting of 8 In. Dia. Extrusion Ingots in Alloy 6063. *Light Metals*, The Metallurgical Society/AIME: 1159–75.
- Jensen, E.K., T. Bergstrom, et al. (1986). Heat transfer measurements during DC casting of aluminium, part II: Results and verification for extrusion ingots. *Light Metals (Warrendale, Pennsylvania 15086)*, USA: The Metallurgical Society/AIME: 891–896.
- Jensen, E.K. and W. Schneider (1990). Investigations about starting cracks in DC-Casting of 6063-Type billets. II. Modelling results. *Light Metals*, The Minerals, Metals & Materials Society: 937–943.
- Johansen, S.T., S. Graadahl, et al. (1998). Can rotor-based refining units be developed and optimised based on water model experiments? *Light Metals 1998*, TMS: 805–810.
- Jones, D. and S. Clough (1999). Foundry ingot casting upgrade at comalco bell bay. *Proceedings of the Australian Asian Pacific Conference on Aluminium Cast House Technology*. Whiteley, P.R. and Grandfield, J.F.: 297–305.
- Jones Jr, W.K., D. Xu, et al. (1998). Physical modeling of the effects of non-symmetric placement of flow control bags used in semi-continuous casting of aluminum. *Light Metals 1998*, Minerals, Metals and Materials Society/AIME: 1051–1057.
- Junghaus, S. (1933). *Apparatus for the continuous casting of metal rods*. USA.
- Kaestner, S., J. Krueger, et al. (1979). 'Current status of aluminum vacuum degassing in the foundry', *Aluminium-Vakuumgussung in der Giesserei – Stand der Technik*, 66(3): 56–62.

- Kageyama, R. and J.W. Evans (1996). Instability of a liquid metal surface in an electromagnetic field and relevance to EMC. *Light Metals: Proceedings of Sessions, TMS Annual Meeting (Warrendale, Pennsylvania)*. Anaheim, CA, USA, Minerals, Metals & Materials Soc (TMS): 899–904.
- Kakimoto, K., E. Takahashi, et al. (1993). Filtration of molten aluminum. *Light Metals: Proceedings of Sessions, TMS Annual Meeting (Warrendale, Pennsylvania)*. Denver, CO, USA, Minerals, Metals & Materials Soc (TMS): 1021–1028.
- Katgerman, L. (1991). ‘Developments in continuous casting of aluminium alloys’, *Cast Metals*, 4(3): 133–139.
- Keegan, N.J., W. Schneider, et al. (1997). Evaluation of the efficiency of in-line filtration systems. *Proceedings of the Australasian Asian Pacific Conference on Aluminium Cast House Technology*, Gold Coast, Aust, Minerals, Metals & Materials Soc (TMS).
- Kulunk, B. and R. Guthrie (1992). On the kinetics of removal of sodium from aluminum and aluminum–magnesium alloys. *Light Metals 1992*, TMS: 963–975.
- Laemmlle, J.T. and J. Bohaychick (1992). ‘Mold lubricants for casting aluminum and its alloys’, *Lubrication Engineering*, 48(11): 858–863.
- Lai, E., H. Duval, et al. (2006). Experimental and numerical study of ceramic foam filtration. *TMS Light Metals*. San Antonio, TX. 2006: 753–758.
- Langerweger, J. (1981). Nonmetallic particles as the cause of structural porosity, heterogeneous cell structure and surface cracks in DC cast aluminum products. *Light Metals 1981*, Metallurgical Society AIME: 685–705.
- Later, D. (2001). Optimising pit recoveries on 6xxx extrusion billet. *7th Aluminium Cast House Technology conference*, Minerals, Metals and Materials Society/AIME: 213–222.
- Le Brun, P. (2008). Melt treatment – Evolution and perspectives. *TMS Light Metals*, New Orleans, LA.
- Le Brun, P. and A. Mathis (2004). Improved molten metal quality at the outlet of the furnace through the IRMA treatment. *TMS Light Metals*, Charlotte, NC.
- Le Roy, G., J.M. Chateau, et al. (2006). ‘In-plant evaluation of jetcleaner metal cleaning efficiency’, *Light Metals 2006*, TMS: 749–752.
- Leboeuf, S., C. Dupuis, et al. (2007). *Inline salt fluxing process: The solution to chlorine gas utilization in casthouses*. TMS Light Metals, Orlando, FL.
- Leinum, T. and B. Rasch (2001). Crucible fluxing of potroom metal in a Norsk Hydro cast shop effect on dross reduction and increased metal recovery. *Light Metals 2001*, TMS: 1049–1052.
- Li, L., Y. Zhang, et al. (2009). ‘Formation of feathery grains with the application of a static magnetic field during direct chill casting of Al-9.8wt%Zn alloy’, *Journal of Materials Science*, 44(4): 1063–1068.
- Lippert, T.W. (1944). ‘Continuous casting’, *The Iron Age*, 153(8): 48–146.
- Ludwig, O., J.M. Drezet, et al. (2006). Modelling of internal stresses in DC casting and sawing of high strength aluminum alloys slabs. *Modeling of Casting, Welding and Advanced Solidification Processes – XI*. Opio. 1: 185–192.
- M’Hamdi, M., S. Benum, et al. (2003). ‘The importance of viscoplastic strain rate in the formation of center cracks during the start-up phase of direct-chill cast aluminum extrusion ingots’, *Metallurgical and Materials Transactions A: Physical Metallurgy and Materials Science*, 34 A(9): 1941–1952.
- M’Hamdi, M., H.G. Fjaer, et al. (2004). A new two-phase thermo-mechanical model and its application to the study of hot tearing formation during the start-up phase of DC cast ingots. *Solidification of Aluminum Alloys*. M.G. Chu, D.A. Granger and Q. Han. Charlotte, NC: 191–200.

- M'Hamdi, M. and A. Hakonsen (2003). Experimental and numerical study of surface macrosegregation in DC casting of aluminium sheet ingots. *Modeling of Casting, Welding and Advanced Solidification Processes*. M. Stefanescu D, J.A. Warren, M.R. Jolly et al. Destin, FL: 505–512.
- M'Hamdi, M. and A. Mo (2002). Microporosity and other mushy zone phenomena associated with hot tearing. *Light Metals: Proceedings of Sessions, TMS Annual Meeting (Warrendale, Pennsylvania)*. Seattle, WA: 709–716.
- M'Hamdi, M. and A. Mo (2005). 'On modelling the interplay between microporosity formation and hot tearing in aluminium direct-chill casting', *Materials Science and Engineering A*, 413–414: 105–108.
- M'Hamdi, M., A. Mo, et al. (2002a). 'Two-phase modeling directed toward hot tearing formation in aluminum direct chill casting', *Metallurgical and Materials Transactions A: Physical Metallurgy and Materials Science*, 33(7): 2081–2093.
- M'Hamdi, M., A. Mo, et al. (2002b). 'Modelling of air gap development and associated surface macrosegregation in DC casting of aluminium sheet ingots', *Light Metals*.
- M'Hamdi, M., A. Mo, et al. (2006). 'TearSim: A two-phase model addressing hot tearing formation during aluminum direct chill casting', *Metallurgical and Materials Transactions A: Physical Metallurgy and Materials Science*, 37(10): 3069–3083.
- M'Hamdi, M. and A. Mo (2008). Modeling the mechanics of solidification defects in aluminum DC casting. *TMS Light Metals*. New Orleans, LA: 765–771.
- M'Hamdi, M., A. Mo, et al. (2000). 'Mathematical modelling of surface segregation in DC casting of multicomponent aluminium alloys', *Modelling of Casting, Welding and Advanced Solidification Processes – IX*: 656–663.
- Mabry, G., J. Kaems, et al. (1997). Characteristics of particulate captured by a rigid tube filter. *Light Metals: Proceedings of Sessions, TMS Annual Meeting (Warrendale, Pennsylvania)*, Orlando, FL, USA, Minerals, Metals & Materials Soc (TMS).
- Maeland, G., E. Myrbostad, et al. (2002). Hycast I-60 SIR – A new generation inline melt refining system. *Light Metals: Proceedings of Sessions, TMS Annual Meeting (Warrendale, Pennsylvania)*. R. Peterson. Seattle, WA: 855–859.
- Maggs, S.J., R. F. Cochrane, et al. (1995). Effect of trace elements on intermetallic phase selection in simulated DC castings. *Light Metals: Proceedings of Sessions, TMS Annual Meeting (Warrendale, Pennsylvania)*. Las Vegas, NV, USA, Minerals, Metals & Materials Soc (TMS): 1039–1047.
- Martin, J.P., F. Tremblay, et al. (1989). HyDRAL: A new and simple technique for in-line analysis of hydrogen in aluminum alloys. *Light Metals: Proceedings of Sessions, AIME Annual Meeting (Warrendale, Pennsylvania)*, Las Vegas, NV, USA, Metallurgical Soc of AIME.
- Meadows, L. (2003). 23 kg Remelt Ingot Productivity, the aspects of Mould Life and Heat Transfer. *Proceedings of the Australian Asian Pacific Conference on Aluminium Cast House Technology*. Brisbane, QLD: 313–324.
- Meadows, L. (2005). Ingot line productivity. *Proceedings of the Australasian Conference and Exhibition – Aluminium Cast House Technology*. Melbourne. 2005: 127–136.
- Mitamura, R. and T. Itoh (1979). Process for direct chill casting of metals, Showa Denko Kabushiki Kaisha. US Patent 4157728.
- Mitamura, R.I., T.Y. Takahashi, et al. (1978). New hot top continuous casting method featuring application of air pressure to mold. *Light Metals*, TMS: 281–291.
- Mo, A., T. Rusten, et al. (1997). Modelling of surface segregation development during DC casting of rolling slab ingots. *Light Metals 1997: Proceedings of Sessions, TMS Annual*

- Meeting (Warrendale, Pennsylvania)*. Orlando, FL, USA, Minerals, Metals & Materials Soc (TMS): 667–674.
- Moriceau, J. (1975). Thermal stresses in continuous DC casting of Al alloys. *Light Metals 1975*, TMS-AIME: 119.
- Moritz, G.E. (1961). *Metal Casting System*, Reynolds Metals Company.
- Moritz, D. and W. Dietz (1979). 'Horizontal strip casting of aluminum using a new stationary mold [Horizontales Bandgiessen Von Aluminium Mit Einer Stationaeren Kokille]', *Aluminium*, 55(6): 395–397.
- Mortensen, D., B.R. Henriksen, et al. (2008). Coupled modelling of air-gap formation and surface exudation during extrusion ingot DC-casting. *TMS Light Metals*. New Orleans, LA: 773–779.
- Muojekwu, C.A., I.V. Samarasekera, et al. (1995). 'Heat transfer and microstructure during the early stages of metal solidification', *Metallurgical and Materials Transactions B*, 26(2): 361–382.
- Muto, N., N. Hayashi, et al. (1996). 'Analysis of Solidification Process in Aluminium SemiContinuous Casting Slab by Monitoring the Mould Temperature', *Sumitomo Light Metals Technical Reports*, 37(3, 4): 180–184.
- Nadella, R., D. Eskin, et al. (2006). Role of grain refining in macrosegregation upon direct chill casting of AA 2024 round billet. *Materials Science Forum*. Vancouver. 519–521: 1841–1846.
- Nadella, R., D. Eskin, et al. (2007). Effect of grain refining on defect formation in DC cast Al-Zn-Mg-Cu alloy billet. *TMS Light Metals*. Orlando, FL: 727–732.
- Nagae, K., N. Hayashi, et al. (1988). 'Effect of some factors on the meniscus shape in electromagnetic Casting', *Sumitomo Keikin-zoku Gihō/Sumitomo Light Metal Technical Reports*, 29(3): 1–8.
- Nawata, S., K. Ichikawa, et al. (1991). DC Casting of Aluminium Alloy Hollow Ingots. *Science and Engineering of Light Metals*. RASELM '91. Tokyo; Japan, RASELM: 1053–1057.
- Neff, D.V. and E.P. Stankiewicz (1986). *Multicast Filtration System*, New Orleans, LA, USA, Metallurgical Soc of AIME.
- Nguyen, V., B. Todd, et al. (2009). Safety enhancement in ingot casting at Tomago Aluminium. *Aluminium Cast House Technology 2009*. Gold Coast Queensland, Materials Science forum: 235–242.
- Niedermair, F. (2001). Horizontal Direct Chilled (HDC) casting technology for aluminium and requirements to metal cleanliness. *Proceedings of the Australian Asian Pacific Conference on Aluminium Cast House Technology*: 253–262.
- Nishida, Y., W. Droste, et al. (1986). 'The air-gap formation process at the casting/mould interface and the heat transfer mechanism through the gap', *Metallurgical Transactions B*, 17(4): 833–844.
- Nofal, A.A. (1992). Surface defect formation in the DC-Cast aluminium products. *Advances in Continuous Casting: Research and Technology*. Abington Hall, Abington, Cambridge, Woodhead: 205–218.
- Ohm, L. and S. Engler (1989). 'Driving forces of surface segregation of non-ferrous DC-casting', *Metall*, 43(6): 520–524.
- Ohm, L. and S. Engler (1989). 'Mechanical properties of solidifying shells' *Metall*, 43(6): 539–43.
- Pang, L., X.G. Zhang, et al. (2009). 'Effects of medium-frequency electromagnetic field on solidification process of semi-continuous casting AZ31 magnesium alloy', *Materials Research Innovations*, 13(2): 107–111.

- Patel, A.D. and N. El-Kaddah (1997). Kinetics of inclusion removal from molten aluminum under an applied alternating magnetic field. *Light Metals: Proceedings of Sessions, TMS Annual Meeting (Warrendale, Pennsylvania)*, Orlando, FL, USA, Minerals, Metals & Materials Soc (TMS).
- Porro, G. and P. Lombardi (1954). 'Studio Sulla Colata Continua e Calcoli Empirici Delle Velocità Di Abbassamento Nella Colata Di Lingotti Di Leghe Leggere', *Aluminio*, 23: 23–24.
- Powers, R.B. (1975). 'The Alcoa horizontal continuous casting process', *Light Metal Age*: 5–7.
- Poynton, S., M. Brandt, et al. (2009). A review of inclusion detection methods in molten aluminium. *TMS Annual Meeting*.
- Prakash, M., P.W. Cleary, et al. (2006). Design optimization of ingot casting wheels using smoothed particle hydrodynamic modelling and experiments. *Modeling of Casting, Welding and Advanced Solidification Processes – XI*. Opio. 1: 79–86.
- Prakash, M., P.W. Cleary, et al. (2007). Optimisation of ingot casting wheel design using SPH simulations. *Progress in Computational Fluid Dynamics*, 7: 101–110.
- Prasso, D.C., J.W. Evans, et al. (1995). 'Heat transport and solidification in the electromagnetic casting of aluminum alloys: Part II, development of a mathematical model and comparison with experimental results', *Metallurgical and Materials Transactions B: Process Metallurgy and Materials Processing Science*, 26(6): 1281–1288.
- Pritchett, T.R. (1973). 'Application of electromagnetism to aluminum metallurgy', *Light Metal Age*, 31(11–12): 21–24.
- Raffourt, C., Y. Fautrelle, et al. (1990). Liquid metal distribution in a slab DC casting: Experiments and modelling approach. *Light Metals 1991*. New Orleans, LA, USA, Publ by Minerals, Metals & Materials Soc (TMS): 877–882.
- Rappaz, M., J. M. Drezet, et al. (1999). 'A new hot-tearing criterion', *Metallurgical and Materials Transactions A: Physical Metallurgy and Materials Science*, 30A(2): 449–455.
- Rasool, A., S. Chatterjee, et al. (2007). Elimination of chlorine at the Aluminium Bahrain cast house. *Aluminium Cast House Technology 2007: 10th Australasian Conference and Exhibition*: 25–30.
- Ray, L. (1991). Comparative assessment of quantitative hydrogen analyzers commonly used in the aluminum industry. *Light Metals 1992*, San Diego, CA, USA, Minerals, Metals & Materials Soc (TMS).
- Reddy, A.V. and C. Beckermann (1997). 'Modeling of macrosegregation due to thermosolutal convection and contraction-driven flow in direct chill continuous casting of an Al-Cu round ingot', *Metallurgical and Materials Transactions B: Process Metallurgy and Materials Processing Science*, 28(3): 479–489.
- Reese, J.M. (1997). 'Characterization of the flow in the molten metal sump during direct chill aluminum casting', *Metallurgical and Materials Transactions B: Process Metallurgy and Materials Processing Science*, 28(3).
- Richter, R.T. and J.M. Ekenes (2005). Cause and prevention of explosions involving DC casting of aluminum sheet ingot. *TMS Light Metals*. H. Kvande. San Francisco, CA: 819–824.
- Rinderer, B., N. Danilova, et al. (2005). A comparison of LAIS and PoDFA analysis of metal cleanliness. *Proceedings of the Australasian Conference and Exhibition – Aluminium Cast House Technology*, Melbourne.
- Roberts, J. and A. Lowery (2009). Safety coatings to prevent molten aluminum-water explosions. *Light Metals 2009*, TMS: 667.

- Rødseth, J., B. Rasch, et al. (2002). Solubility of carbon in aluminium and its effect upon the casting process. *Light Metals: Proceedings of Sessions, TMS Annual Meeting (Warrendale, Pennsylvania)*. R. Peterson. Seattle, WA: 883–887.
- Roth, W. (1936). *Verfahren zum Giessen von Metallblocken mit Ausnahme solcher aus Leichtmetall*. Germany.
- Roth, W. (1943). 'Ueber die Abkühlung des Stranges beim "Wasserguss"', *Aluminium*, 25: 283.
- Roth, W. (1949). 'Strangiessen von Leichtmetall nach dem Wassergiessverfahren', *Zeitschrift fuer Metallkunde*, 40(12): 445–460.
- Roth, W. and E. Weisse (1942). 'Strangeissen von Magnesiumlegierungen, insbesondere nach dem Wassergiessfahren', *Aluminium*, 26(7/8): 134–36.
- Roth, W., M. Welsch, et al. (1942). 'Über die Eigenspannungen in Strangguss-Blocken aus einer eutektischen Al-Si-Legierung', *Aluminium*, 24: 206.
- Salgado-Ordorica, M.A. and M. Rappaz (2008). 'Twinned dendrite growth in binary aluminum alloys', *Acta Materialia*, 56(19): 5708–5718.
- Schneider, W. (1998). Melt Processing Strategies and Measures to Improve Quality. *2nd International Melt Processing Technology Workshop*. Dublin, Foseco Aluminium & VAW Aluminium: 11.
- Schneider, W. (2002). D.C. casting of aluminium alloys-past, present and future. *Light Metals: Proceedings of Sessions, TMS Annual Meeting (Warrendale, Pennsylvania)*. Seattle, WA: 953–960.
- Schneider, W. and E.K. Jensen (1990). Investigations about starting cracks in dc casting of 6063 type billets. Part I: Experimental results. *Light Metals 1990*. Anaheim, CA, USA, Minerals, Metals & Materials Soc (TMS): 931–936.
- Schneider, W. and K. Kramer (1994). Method and apparatus for continuous casting, VAW AG (Vereinigte Aluminium-Werke Aktiengesellschaft): W.Schneider, K. Kramer, 28 Jun 93, 05 Jul 94 VAW AG; US5325910.
- Sekiguchi, T., R. Mitamura, et al. (1981). Forgeability of cast bar made by new hot top continuous casting process. *Light Metals 1981*, TMS 1981: 871–883.
- Shu, D., B. D. Sun, et al. (1999). 'Study of electromagnetic separation of nonmetallic inclusions from aluminum melt', *Metallurgical and Materials Transactions A: Physical Metallurgy and Materials Science*, 30(11): 2979–2988.
- Siebel, G., D. Altenpohl, et al. (1953). 'Periodische Seigerungen bei Reinaluminium-Strangguss', *Zeitschrift fuer Metallkunde*, 44: 173.
- Sigworth, G.K. (1999). Gas fluxing of molten aluminum, part 1: Hydrogen removal. *Light Metals: Proceedings of Sessions, TMS Annual Meeting (Warrendale, Pennsylvania)*: 641–648.
- Sigworth, G.K. (2000). Gas fluxing of molten aluminum, part 2: Removal of alkali metals. *Light Metals: Proceedings of Sessions, TMS Annual Meeting (Warrendale, Pennsylvania)*. R. Peterson. Nashville, TN: 773–778.
- Sigworth, G.K. and T.A. Engh (1982). 'Chemical and kinetic factors related to hydrogen removal from aluminium', *Metallurgical Transactions B*, 13(3): 447–460.
- Sigworth, G.K., E.M. Williams, et al. (2008). *Gas fluxing of molten aluminum: An overview*. TMS Light Metals.
- Simensen, C.J. (1985). Sampling and analysis of impurities in aluminium. *International Seminar on refining and Alloying of Liquid aluminium and Ferro-Alloys*. Trondheim, Norway, Aluminium Verlag.

- Simensen, C.J. (1993). 'Analyses of inclusions in molten aluminium by electrical resistivity measurements', *Zeitschrift fuer Metallkunde/Materials Research and Advanced Techniques*, 84(10): 730–733.
- Simonson, L., C. Wieman, et al. (1963). *Graphite Mould Casting System*. USA, Reynolds Metals Company, assignee.
- Skjerpe, P. (1987). 'Intermetallic phases formed during DC-casting', *Metallurgical Transactions A*, 18(3): 189–200.
- Skjerpe, P., J. Gjnnnes, et al. (1987). 'Solidification structure and primary Al-Fe-Si particles in direct-chilled-cast aluminium alloys', *Ultramicroscopy*, 22(1–4): 239–249.
- Smith, D.D., L.S. Aubrey, et al. (1998). LiMCA II evaluation of the performance characteristics of single element and staged ceramic foam filtration. *Light Metals: Proceedings of Sessions, TMS Annual Meeting (Warrendale, Pennsylvania)*, San Antonio, TX, USA, Minerals, Metals & Materials Soc (TMS).
- Sorimachi, K. and S. Nabeshima (1998). 'Lubrication And Friction Between Mould and Solidified Shell in Continuous Casting of Steel', *Tetsu to Hagane-Journal of the Iron and Steel Institute Japan*, 84(2): 103–108.
- Spaulding, H.S. (1975). 'The Kaiser Aluminium process for horizontal continuous casting aluminium ingot', *Light Metal Age*: 8–11.
- Spear, R.E. and K.J. Brondyke (1971). 'Continuous casting of aluminium', *Journal of Metals*, 23: 36–39.
- Steen, I.K., B. Heggset, et al. (1997). Casting equipment. USA, Norsk Hydro A.S.
- Sztur, C., L. Maenner, et al. (2001). Thermal modelling of ingot chain production. *TMS Light Metals*. J.L. Anjier: 1099–1105.
- Taylor, A.T., D.H. Thompson, et al. (1957). 'Direct chill casting of large aluminium ingots', *Metal Progress*, 72: 70–74.
- Taylor, J.A. (1995). 'Metal related castability effects in aluminium foundry alloys', *Cast Metals*, 8(4): 225–252.
- Thomson, R., F. Mojab, et al. (1969). 'Experiments on continuous casting', *The British Foundryman*, 62: 73–80.
- Thomson, R. and E.C. Ellwood (1972). 'Closed-head continuous casting: Part II – Mould billet interactions', *The British Foundryman*, 65: 186–97.
- Towsey, N., W. Schneider, et al. (2002). The effects of rod grain refiners with differing Ti/B ratio on ceramic foam filtration. *Light Metals: Proceedings of Sessions, TMS Annual Meeting (Warrendale, Pennsylvania)*, Seattle, WA.
- Tremblay, S.P. and M. Lapointe (2002). The manufacturing, design and use of a new reusable molten metal distributor for sheet ingot casting. *Light Metals: Proceedings of Sessions, TMS Annual Meeting (Warrendale, Pennsylvania)*. Seattle, WA: 961–965.
- Turchin, A.N., D.G. Eskin, et al. (2005). 'Effect of melt flow on macro- and microstructure evolution during solidification of an Al-4.5%Cu alloy', *Materials Science and Engineering A*, 413–414: 98–104.
- Turchin, A.N., M. Zuijderwijk, et al. (2007). 'Feathery grain growth during solidification under forced flow conditions', *Acta Materialia*, 55(11): 3795–3801.
- Wagstaff, F.E. and W.G. Wagstaff and Richard J. Collins (1986). *Direct Chill Metal Casting Apparatus and Technique*. US, Wagstaff Engineering Inc.
- Wagstaff, R.B. and K.D. Bowles (1995). Practical low head casting (LHC) mold for aluminum ingot casting. *Light Metals: Proceedings of Sessions, TMS Annual Meeting (Warrendale, Pennsylvania)*. Las Vegas, NV, USA, Minerals, Metals & Materials Soc (TMS): 1071–1075.

- Wagstaff, W.G. (1975). 'The Wagstaff horizontal casting machine', *Light Metal Age*: 28.
- Waite, P.D. (1998). Improved metallurgical understanding of the Alcan compact degasser after two years of industrial implementation in aluminum casting plants. *Light Metals: Proceedings of Sessions, TMS Annual Meeting (Warrendale, Pennsylvania)*, San Antonio, TX, USA, Minerals, Metals & Materials Soc (TMS).
- Waite, P. (2002). A technical perspective on molten aluminum processing. *Light Metals: Proceedings of Sessions, TMS Annual Meeting (Warrendale, Pennsylvania)*. Seattle, WA: 841–848.
- Ware, T.N., M. Cooksey, et al. (2001). Measurement of the performance of in-line processes using LiMCA. *Proceedings of the Australian Asian Pacific Conference on Aluminium Cast House Technology*.
- Waters, B.H.C. (1952). 'Continuous casting of non-ferrous metals: Part III factors controlling permissible speed of casting', *Metal Treatment and Drop Forging*, 19: 527.
- Waters, B.H.C. (1954). 'Continuous casting of non-ferrous metals: Part V surface appearance', *Metal Treatment and Drop Forging*, 20: 79–84.
- Weckman, D.C. (1987). 'Horizontal direct-chill continuous casting of non-ferrous alloy rods', *Zeitschrift fuer Metallkunde/Materials Research and Advanced Techniques*, 78(12): 880–886.
- Weckman, D.C. and P. Niessen (1982). 'A numerical simulation of the D.C. continuous casting process including nucleate boiling heat transfer', *Metallurgical Transactions B*, 13(4): 593–602.
- Weckman, D.C. and P. Niessen (1983). 'Optimum mould length design for the D. C. continuous casting of non-ferrous alloy rods', *Zeitschrift fuer Metallkunde/Materials Research and Advanced Techniques*, 74(11): 709–715.
- Weckman, D.C. and P. Niessen (1984a). 'Heat-transfer conditions in hot-top mould and cold-shut formation mechanism on Dc continuously cast non-ferrous alloy rods', *Metals Technology*, 11(pt 11): 497–503.
- Weckman, D.C. and P. Niessen (1984b). 'Mathematical models of the DC continuous casting process', *Canadian Metallurgical Quarterly*, 23(2): 209–216.
- Weckman, D.C. and P. Niessen (1984c). 'The mechanism of cold shut formation on D.C. direct-chill', *Zeitschrift fuer Metallkunde*, 75(5): 332–40.
- Weckman, D.C. and P. Niessen (1984d). 'Mechanism of cold shut formation on DC continuously cast non-ferrous alloy products II The influences of oxidation, metallostatic head and mould insert geometry', *Zeitschrift fuer Metallkunde/Materials Research and Advanced Techniques*, 75(6): 414–422.
- Westengen, H. (1982a). 'Formation of intermetallic compounds during DC casting of a commercial purity AL-FE-Si alloy', *Zeitschrift fuer Metallkunde/Materials Research and Advanced Techniques*, 73(6): 360–368.
- Westengen, H. (1982b). 'Structure inhomogeneities in direct chill cast sheet ingots of commercial purity aluminium', *Aluminium Dusseldorf*, 58(7): 398–401.
- Whiteley, P. (2003). Recent technological developments. *Proceedings of the Australian Asian Pacific Conference on Aluminium Cast House Technology*. P. R. Whiteley. Brisbane, QLD: 17–22.
- Wilkinson, R.G. and S.B. Hirst (1952–1953). 'The control of quality in melting and casting magnesium alloys for hot working', *Journal of the Institute of Metals*, 81: 393–400.
- Williams, E.M. (2001). Alkali removal and reduced chlorine use during furnace fluxing. *Light Metals: Proceedings of Sessions, TMS Annual Meeting (Warrendale, Pennsylvania)*, New Orleans, LA.

- Winterhager, H. and M. Koch (1978). 'Investigations of vacuum degassing of aluminum melts', *Untersuchungen zur Vakuumentgasung von Aluminium-Schmelzen*, 65(19): 505–510.
- Wu, R., Z. Qu, et al. (2007). 'Spray degassing as a method for hydrogen removal in aluminum melts', *Materials Transactions*, 48(5): 1029–1033.
- Wuetig, F.L. (1975). 'The reynolds horizontal casting process', *Light Metal Age* 22–23.
- Xu, D., W.K. Jones Jr, et al. (1998a). 'Mathematical and physical modeling of systems for metal delivery in the continuous casting of steel and DC casting of aluminum', *Applied Mathematical Modelling*, 22(11): 883–893.
- Xu, D., W.K. Jones Jr, et al. (1998b). 'The use of particle image velocimetry in the physical modeling of flow in electromagnetic or direct-chill casting of aluminum: Part I, development of the physical model', *Metallurgical and Materials Transactions B: Process Metallurgy and Materials Processing Science*, 29(6): 1281–1288.
- Xu, D., W.K. Jones Jr, et al. (1998c). 'The use of particle image velocimetry in the physical modeling of flow in electromagnetic or direct-chill casting of aluminum: Part II. Results of the physical model, including bag geometry, blockage, and nozzle placement', *Metallurgical and Materials Transactions B: Process Metallurgy and Materials Processing Science*, 29(6): 1289–1295.
- Yajima, T., K. Koide, et al. (1995). 'Application of hydrogen sensor using proton conductive ceramics as a solid electrolyte to aluminum casting industries', *Solid State Ionics*, 79(C): 333–337.
- Yanagimoto, S. and R. Mitamura (1984). Application of new hot top process to production of extrusion and forging billet. *ET'84: Extrusion Productivity Through Automation*, The Aluminum Assoc: 247–56.
- Yao, M. and D.C. Fang (1996). 'On line measuring method for mould friction in continuous casting', *Ironmaking and Steelmaking*, 23(6): 522–27.
- Yoh, I. (1989). HDC process for small diameter ingot. *Light Metals: Proceedings of Sessions, AIME Annual Meeting (Warrendale, Pennsylvania)*. Las Vegas, NV, USA, Metallurgical Soc of AIME: 673–679.
- Yu, H. (1985). *Light Metals 1985*, TMS: 1331–1347.
- Yu, H. and D.A. Granger (1984). Macrosegregation in aluminum alloy ingot cast by the semicontinuous direct chill method. *NASA Conference Publication*. Cleveland, OH, USA, NASA, Scientific & Technical Information Branch: 157–168.
- Zeigler, P.P. (1952). *Method of continuous casting*. United States of America.
- Zeillinger, H. and A. Beevis (1997). 'Universal continuous horizontal caster for ingot, billet or bar', *Light Metal Age*, 55(5–6).
- Zhang, L., L. N. W. Damoah, et al. (2008). Mechanisms of inclusion removal from aluminum through filtration. *TMS Light Metals*, New Orleans, LA.
- Zhao, Z., J. Cui, et al. (2007a). 'Effect of low-frequency magnetic field on microstructures and macrosegregation of horizontal direct chill casting 7075 aluminum alloy', *Journal of Materials Processing Technology*, 182(1–3): 185–190.
- Zhao, Z., J. Cui, et al. (2007b). Low-frequency electromagnetic field influencing horizontal direct chill casting of aluminum alloy rods. *Materials Science Forum*. Beijing. 546–549: 691–696.
- Zhu, Q. F., Z. H. Zhao, et al. (2008a). 'Effect of low-frequency electromagnetic field on the as-casting microstructures and mechanical properties of HDC 2024 aluminum alloy', *Acta Metallurgica Sinica (English Letters)*, 21(3): 205–210.

- Zhu, Q.F., Z. H. Zhao, et al. (2008b). 'Effect of combined application of electromagnetic fields on horizontal direct chill casting of 7050 aluminium alloy', *Materials Science and Technology*, 24(5): 560–566.
- Zhu, Q.F., Z. H. Zhao, et al. (2008c). 'Effect of out-phase electromagnetic field on the as-casting structure of HDC casting 2024 aluminum alloy', *Cailiao Kexue yu Gongyi/ Material Science and Technology*, 16(SUPPL. 1): 91–94.
- Zhu, Q., Z. Zhao, et al. (2009). Effect of application of out-of-phase electromagnetic field on horizontal direct chill casting of 7075 aluminum alloy. *TMS Annual Meeting*: 843–848.
- Zinniger, T.C. (1980). *Direct chill cating method with coolant removal*. USA, Kaiser Aluminium & Chemical Corporation.
- Zunkel, B. (1939). *Giessvorrichtung zum ununterbrochen Giessen von Blocken und ähnlichen Werkstücken aus Leichtmetall oder Leichtmetalllegierungen*. Germany.
- Zuo, Y., H. Nagaumi, et al. (2008). 'Study on the sump and temperature field during low frequency electromagnetic casting a superhigh strength Al-Zn-Mg-Cu alloy', *Journal of Materials Processing Technology*, 197(1–3): 109–115.

Casting of aluminium alloys

S. OTARAWANNA, National Metal and Materials Technology Center (MTEC), Thailand and A.K. DAHLE, The University of Queensland, Australia

Abstract: Casting is one of the main routes for producing aluminium-alloy parts. Good castability for foundry alloys includes a relatively high fluidity, low melting point, short casting cycles, relatively low tendency for hot cracking, good as-cast surface finish and chemical stability. In hypoeutectic alloys, it is common to refine the size of the aluminium crystals by grain refinement for applications requiring good mechanical properties. In Al-Si alloys, a treatment called eutectic modification is often used to change the eutectic silicon from coarse platelike into fine fibrous morphology, which is less harmful to mechanical performance. Main shape casting processes include high-pressure die casting, low-pressure die casting, permanent mould casting and sand casting. Each process has its own strategy for filling the alloy into the mould/die and feeding the solidification shrinkage.

Key words: aluminium alloys, casting, solidification, microstructure control, grain refinement, eutectic modification.

6.1 Introduction

On average, the production of aluminium castings counts for approximately 20–25% of the annual world aluminium production, and die castings would be approximately 60% of that production. Aluminium castings can be produced by virtually all casting processes, generating products with a wide variety of useful engineering properties. High-pressure die casting (HPDC) is the preferred production process for large production volumes and this process has been improved so much in recent years that it can now be used to reliably produce castings with high integrity, and that are heat treatable. For smaller production volumes, low-pressure die casting, permanent mould casting and sand casting can be used. Investment casting is also used in the production of some aluminium components.

This chapter first provides an overview of the typical aluminium casting alloys, essential microstructural features, typical microstructural control strategies, a brief introduction about filling and feeding, followed by an overview of the main casting processes.

6.2 Aluminium casting alloys

Aluminium casting alloys offer a range of advantages, particularly a good castability. This includes a relatively high fluidity, low melting point, short casting

Table 6.1 Aluminum Association designation system for aluminium casting alloys

Series	Alloys
1XX	>99.0% Al
2XX	Al-Cu
3XX	Al-Si-Mg, Al-Si-Cu, Al-Si-Cu-Mg
4XX	Al-Si
5XX	Al-Mg
7XX	Al-Zn
8XX	Al-Sn

cycles, relatively low tendency for hot cracking, good as-cast surface finish and chemical stability. In addition, advantages are gained by the specific alloy chosen. There is no world-wide alloy designation system for aluminium casting alloys, and many countries have their own system. The system from the Aluminum Association is described in Table 6.1.

Whilst Table 6.1 provides the main alloying element, most commercial alloys have strict limitations on a range of different elements which affect the properties. For example, in HPDCs, Fe and Mn are controlled in order to control die soldering properties. Often, Mg is also strictly controlled because of its hardening effect. Certain trace elements must also be monitored due to a strong impact on castability.

Commercial casting alloys include both heat treatable and non-heat treatable alloys. Therefore, the standard aluminium temper designation system is also applicable to aluminium castings. The O, T4, T5, T6 and T7 tempers are normally used for aluminium castings. Die castings traditionally had a problem with blistering on heat treatment, but new alloys and processes now allow such castings to be heat treated to T6 and T7 tempers. Some developments in this area are presented elsewhere in this book.

Amongst the aluminium castings alloys, the Al-Si alloys are by far the most widely used, particularly for automotive applications. Silicon provides good castability, and a wide variety of properties can be obtained by alloys from this alloy system. Most are of the eutectic or hypoeutectic compositions (i.e. near eutectic), but hypereutectic alloys are also popular for certain applications which require elevated temperature strength, low thermal expansion and wear resistance.

6.3 Microstructure control in aluminium foundry alloys

The typical microstructure of as-cast aluminium alloys depends on the alloy composition, but in most cases it comprises primary aluminium crystals surrounded by a eutectic mixture. However, in hypereutectic Al-Si alloys, primary silicon crystals may form before the eutectic. The composition of the eutectic

depends on which alloy system is cast. In hypoeutectic alloys it is common to refine the size of the aluminium crystals by grain refinement for applications requiring good mechanical properties.

6.3.1 Grain refinement

Whilst grain refinement is done virtually 100% for wrought aluminium alloys, it is not always required in aluminium castings. However, in premium castings grain refinement is usually used. The grain refiners used in foundry alloys are the same as used in wrought alloys. The most popular grain refiners are based on the Al-Ti-B system, with a range of compositions, with Al-5wt%Ti-1wt%B being the most common. Additions are usually made in rod or waffle form, and addition levels can be around 1 kg/tonne or more. These grain refiners typically contain small hexagonal TiB_2 and particles, and coarse Al_3Ti needles in an aluminium matrix. Both particles can theoretically be expected to nucleate aluminium, but Al_3Ti is expected to dissolve in the molten metal so that nucleation is expected to occur on TiB_2 particles. There has been a lot of debate about the exact nucleation mechanism, and this is discussed in detail in a separate chapter in this book.

6.3.2 Eutectic modification

In sand and permanent mould cast Al-Si alloys it is often common to use a treatment called eutectic modification to change the eutectic silicon from coarse platelike into fine fibrous morphology. This is commonly done by trace additions (<400 ppm) of certain elements. These additions are usually made in the form of master alloys, that is rods or waffle, or canisters. Industrially, strontium has become the most popular modifier because it is more durable and longer lasting than the other common modifier – Na. Modification treatments improve strength, ductility, pressure tightness and machinability.

6.4 Filling the casting

Most castings need to contain a running and gating system to transport the molten alloy from the point where it is first filled into the mould. The metal needs to be effectively distributed to the whole casting before the alloy has lost too much of its superheat. In the past decade, much emphasis has been placed on the importance of avoiding turbulence during filling of the casting and to have a smooth, laminar flow front of the molten metal. The reason is that aluminium readily oxidises in contact with air and therefore is always covered in a very thin oxide layer at the surface. With turbulent flow, these oxide films can become mixed into the bulk of the metal where they represent porosity initiation sites in the casting during solidification. Such bifilms are considered to have a dry side which formed in contact with air and a wet side which was in contact with the molten metals. These

bifilms may become folded onto themselves during turbulent flow. Campbell has shown that for aluminium alloys, turbulence can be avoided if the metal flow rate is kept below 0.5 m/s. Many aluminium foundries now use computer software to design their running and gating systems.

6.5 Feeding and porosity

A challenge with most aluminium casting alloys is that they contract about 3–6% on solidification. Unless this shrinkage is properly compensated by the provision of extra feed liquid, porosity may be present within the casting or at the surface. This porosity can significantly reduce the mechanical properties, pressure tightness, machinability and general appearance of the casting. Feeders are therefore carefully and strategically designed as part of the casting to provide liquid to the last regions to solidify.

Hydrogen is the only gas with significant solubility in molten aluminium. On solidification, it can also create porosity because it has a very low solubility in the solid. Thus, for high integrity applications it may be necessary to degas the molten metal either by bubbling inert gas through the molten metal, or by adding certain tablets that can either react with or remove the hydrogen from the molten metal.

6.6 Casting processes

6.6.1 High-pressure die casting (HPDC)

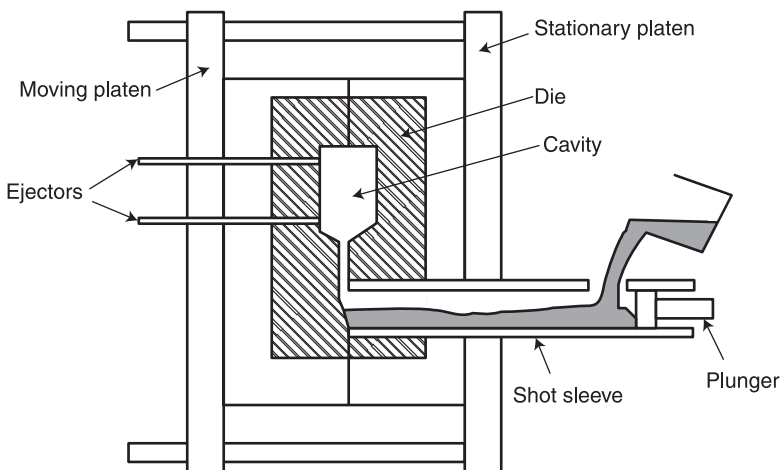
The HPDC process is a fast and highly automated near-net shape manufacturing method for making thin-walled, complex castings. It involves high-velocity injection of molten metal into metal dies and solidification of the alloy under high pressure¹. The cycle time is relatively short, typically a few seconds for relatively small castings and less than a minute for large parts². HPDC dies are not coated with refractory materials since high cooling rate is desired to cool the casting quickly and achieve fast cycle time. However, the die must be sprayed between each shot with a lubricant to avoid die sticking. Dimensional accuracy and surface finish of the casting are good so subsequent machining processes are minimised or even eliminated. HPDC is widely used to cast the alloys of aluminium, magnesium, zinc, lead and brass, and the applications are widespread, including automotive, electrical, electronic and household. The commonly used HPDC alloys, such as A380 (AlSi8CuFe) and 384 (AlSi10Cu2Fe), contain 8–10% Si and 2–4% Cu with around 1% Fe.

The capacity of HPDC machines is described by their locking force, typically in the range 100–2000 tonnes. The maximum size of casting produced by a machine is determined by the machine's locking force. To ensure good casting quality, HPDC dies are required to be carefully designed and optimised. Also process parameters have to be optimised and well-controlled. HPDC dies are

costly but they can last for more than 100,000 shots. The initial cost for the machine and die set is high, but the operating cost is relatively cheap. Therefore, the process is suitable for high volume production.

Aluminium alloys are cast in cold-chamber (cc) HPDC machines where the metal injection system is in contact with the melt for only a short time. Molten alloy is held in a separate holding furnace and is transferred to the shot sleeve for each casting cycle as illustrated in Fig. 6.1. The injection of molten alloy in cc HPDC is performed by moving the plunger horizontally forward.

In conventional HPDC processes, alloy at $\sim 50\text{--}100^\circ\text{C}$ superheat is poured into the shot sleeve in cc HPDC. In cc HPDC, the alloy is left in the sleeve for a period, so-called delay time, of a few seconds to create more quiescent liquid. The shot sleeve walls, injection plunger and die are maintained at $\sim 200\text{--}300^\circ\text{C}$. The heat transfer coefficient at the sleeve wall was measured to be of the order $10^3 \text{ W m}^{-2}\text{K}^{-1}$ for alloy A356³. Cooling rates in the shot sleeve are typically of the order 10°C/s ⁴. The alloy is pushed forward up until the gate in the slow shot phase of around $1\text{--}7 \text{ s}$ ⁵. After that, the plunger is accelerated to inject the alloy at very high velocity (velocity at the gate around 50 m/s ^{6–8} corresponding to a shear rate of around $10^4/\text{s}$ ⁸ to fill the cavity within $0.01\text{--}0.3 \text{ s}$ ⁵). Once the alloy touches the die surface, the initial heat flux from the die cavity is very high, with reported values of heat transfer coefficient in the range $10^4\text{--}10^5 \text{ W m}^{-2}\text{K}^{-1}$ ^{9–12}. Air gap formation between the shrinking and contracting alloy and the die wall decreases heat transfer considerably. After the cavity is completely filled, a pressure (intensification pressure) of up to $\sim 120 \text{ MPa}$ ¹³ is typically applied to the casting to assist feeding and prevent solidification shrinkage as the casting continues to solidify. In addition to this mechanical effect, the applied pressure increases the heat transfer coefficient at the die-alloy interface and therefore increases the



6.1 Schematic diagram of a cold chamber HPDC machine.

cooling rate. A range of cooling rates therefore exist during in-cavity solidification, reportedly in the range $100\text{--}1000^\circ\text{C/D}^{14-16}$.

One of the major defects in conventional HPDC parts is porosity which largely results from air entrapment during die filling and solidification shrinkage. The presence of porosity has an adverse effect on mechanical properties and pressure tightness of components. Furthermore, it can cause other defects, such as blistering during subsequent heat treatment¹⁷. This has so far limited the extent of HPDC applications in structural components requiring strength and ductility properties.

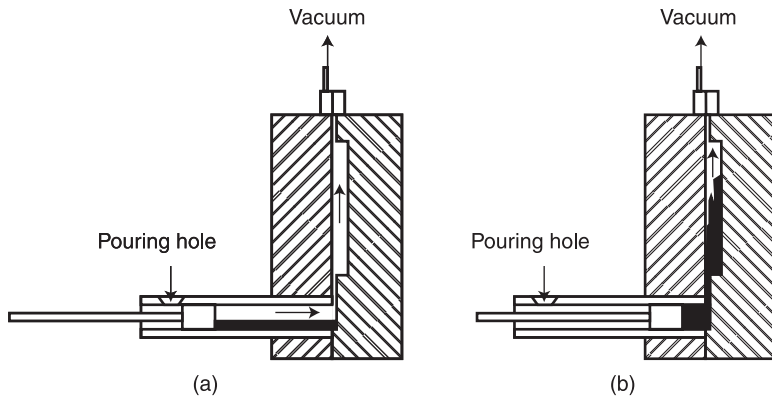
High integrity HPDC processes

In the past decades, there has been a keen interest and R&D into producing structural automotive components, such as chassis parts by HPDC. Castings are therefore required to be sound, reliable and capable of conventional solution heat treatment without blistering. A number of high integrity HPDC processes have been developed to meet these requirements. At present no one process meets all requirements, so it is important to understand both the advantages and limitations of these 'potential' high integrity HPDC processes. For high integrity HPDC processes, both investment and production costs are generally higher than for their conventional counterparts. This is due to the requirements of using primary alloy, uncontaminated melt and special process controls.

Vacuum-assisted techniques

The strategy of vacuum-assisted HPDC is to eliminate the entrapped air from the source which is the atmosphere in the shot sleeve, runner system and die cavity. The benefits of vacuum-assisted HPDC are not only reducing entrapped air. Some significant degree of vacuum also assist die filling of material and air venting from the cavity. The vacuum in the system is typically achieved by a vacuum pumping system attached to the die cavity (Fig. 6.2). To produce castings that can be fully heat-treated to a conventional T6 temper without blistering, a vacuum level of 100 mbar or less is required¹⁸. This is obtained by the combination of particularly high quality sealing, certain water-based lubricants and a well-controlled venting system. Well-sealed contacts between moving parts and between mating die surfaces help to retain the high vacuum level. Water-based lubricants releasing a relatively low level of gases are used to minimise gas evolution in the cavity. Precise control of the vacuum pumping system attached to the vent is essential to control the vacuum level in the system.

In the open literature there are only two systems reported to be capable of consistently producing heat-treated HPDC parts¹⁸: the Vacural method and the BDW/Alcan High-Q-Cast method. In the Vacural method, vacuum is very strong and applied relatively early. The melt is drawn from the furnace into the shot



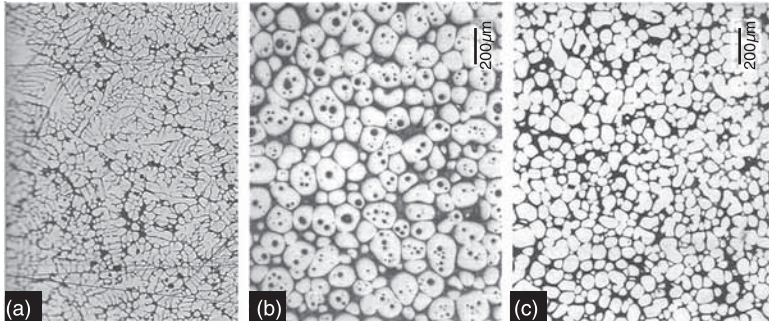
6.2 (a) and (b) Schematic illustration showing the principle of a vacuum-assisted die casting technique [19].

sleeve by the aid of vacuum in the die cavity. With extremely high vacuum applied early, sufficiently high vacuum in the cavity can be sustained although the vacuum valve is shut before the cavity is completely filled to avoid the invasion of alloy into the vacuum system. In the High-Q-Cast method, the high vacuum level is kept throughout the process by keeping the vacuum valve open until the very end of the die filling stage. The valve movement is controlled by a piezo electric controller which is ~ 12 times faster than a conventional hydraulic controller¹⁸. Apart from these two high vacuum techniques, a number of techniques have also been developed to obtain partial vacuum in the die cavity. For simplicity of the system, a tortuous vent path which can shut off metal flow due to metal solidification, a so-called chill vent, is often used to replace the vacuum valve. Although heat-treatable parts cannot be manufactured by these partial vacuum techniques, the performance of castings is significantly improved.

Semi-solid metal processing (SSP)

SSP is a type of die casting process wherein a partially solid metal, typically solid fraction (f_s) of ~ 0.5 ¹⁸, is intentionally prepared and injected into a die cavity. The semi-solid material is prepared to have globular primary phase morphology (Fig. 6.3a) which exhibits thixotropic behaviour and therefore is more 'castable' than a dendritic material (Fig. 6.3b–c)²⁰. This can be obtained by either stirring (typically mechanical stirring or electromagnetic stirring) or grain refinement and thermal history control¹⁸.

Despite the fact that there are numerous techniques for SSP, they can be categorised by the processing route into two groups: (1) thixocasting, and



6.3 Comparison of different A356 microstructures obtained from: (a) above-liquidus casting, (b) thixocasting and (c) rheocasting [18] (courtesy of North America Die Casting Association). Note that the thixocast microstructure contains eutectic entrapped within the primary (Al) globules whilst the rheocast does not.

(2) rheocasting. In the thixocasting route, a billet containing globular microstructure is prepared by a billet manufacturer. Upon reheating, the billet is ready to be placed into the shot sleeve of an HPDC-like machine and injected into the die cavity. For rheocasting, the thixotropic slurry is prepared on-site before subsequently being transferred into a pressure casting machine. Thixocasting billets are sold at a premium price, up to twice the ingot-alloy price, and cannot be reused by the die-caster. A material loss of 8–10% during reheating has been reported²¹. This billet-cost issue leads to a global trend to develop and use the rheocasting processes.

With more viscous injected alloy and lower injection velocity compared to conventional HPDC, SSP provides a more stable flow front and therefore less entrapped air during die filling. As the injected alloy already contains a substantial f_s , subsequent solidification shrinkage is clearly less than in conventional HPDC. Die life is normally longer due to lower alloy temperature. Due to the fact that rheological properties of semi solid alloy are a function of f_s , only some alloys (with clearly defined eutectic point and f_s is not a strong function of temperature in the working f_s range) are suitable for SSP and good control of temperature is also required.

Indirect squeeze casting

There are two types of squeeze casting, direct and indirect. Direct squeeze casting is also known as liquid-metal forging because it resembles a forging process. Molten metal is poured into the bottom half of the pre-heated die, the upper die half is lowered towards the bottom die causing the melt to fill the mould cavity and a pressure typically in the range 70–140 MPa or more¹⁸ is applied over the entire cavity during solidification. As the direct squeeze casting process is not considered as a variant of the HPDC process, its details are not reviewed here.

Indirect squeeze casting process is akin to HPDC. The melt is transferred into the shot sleeve of an indirect squeeze casting machine, which can be vertical or horizontal type. After that, the alloy is injected into the die cavity through relatively thick gates (typically 6–35 mm¹⁸) at relatively lower gate velocity compared to those in conventional HPDC processes. The cavity filling time is typically 2–5 s¹⁸. The relatively slow filling velocity promotes non-turbulent filling. The amount of entrapped air during die filling is therefore reduced. Furthermore, entrapped air and folded oxide films can be further reduced by carefully pouring the alloy onto the side wall of a tilted shot sleeve in vertical-typed machines. This pouring technique promotes more quiescent flow of molten metal.

The minimum casting thickness allowed to be manufactured by this process is ~5 mm¹⁸. Relatively thick gates delay gate solidification and therefore promote the transfer of intensification pressure through the gate to the casting. Due to the relatively thick gating system, the yield of material in this process is relatively low. The die life is shorter than conventional HPDC processes due to higher melt temperature and longer dwell time in the die cavity.

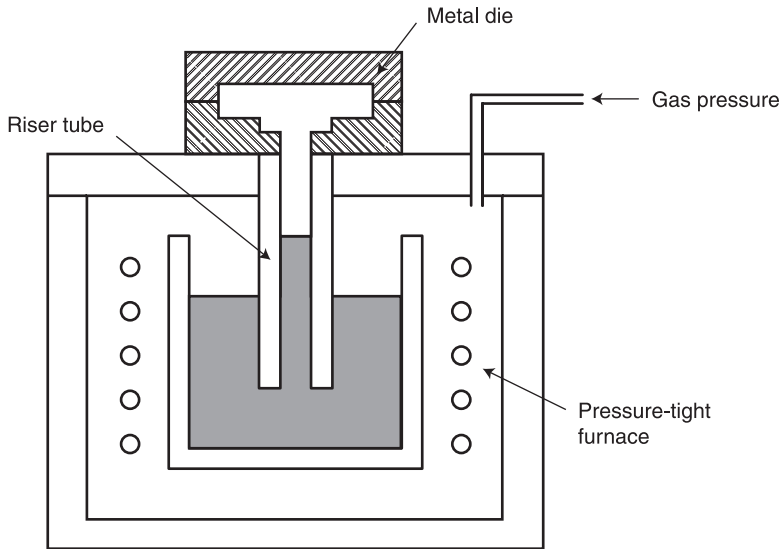
Melt flow technique

Advanced thixotropic metallurgy (ATM) technique is a runner design concept developed by a group at CSIRO, Australia²². The technique employs a flow restriction section, a so-called melt pre-conditioner (MPC), in the runner. The MPC is aimed to shear and accelerate the flowing material before it reaches the gate. In HPDC, there are some equiaxed crystals, so called externally solidified crystals (ESCs), solidified in the shot sleeve prior to being injected into the die cavity. The shearing of partially solid alloy containing ESCs is believed to make ESCs smaller and more globular, and disperse porosity in the final microstructure. Due to smaller ESC size and more disperse porosity, ATM castings often show better mechanical properties than conventional ones.

Smaller and more globular ESCs decrease viscosity of the suspension and therefore reduce the tendency for cold shuts. This allows a lower gate speed than that in conventional HPDC to be used with the ATM design. Die erosion problem associated with high gate speeds can be reduced. Additional time gained from lower filling velocity enhances gas venting from the cavity. The ATM runner system is typically smaller than the conventional design, leading to better material yield and energy saving.

6.6.2 Low-pressure die casting (LPDC)

The LPDC process is illustrated schematically in Fig. 6.4. A metal die is mounted above a sealed furnace containing molten metal. A riser tube, so-called the stalk, connects the bottom of the die to the molten metal bath. During the process, molten metal is transferred upwards from a sealed furnace via a riser tube to a



6.4 Schematic showing the LPDC process.

metal die. The upwards movement of the melt is assisted by air or inert-gas pressure of around 15–100 kPa²³ in the chamber containing the holding furnace. After the metal in the die has solidified, the chamber pressure is released allowing the molten metal in the riser tube to fall back into the furnace. Generally, the furnace is capable of making around 10 castings before refilling is necessary.

The die filling in this process is relatively slow to minimise turbulence and air entrapment. In order to obtain a well-fed casting, the die system needs to be designed and controlled to promote directional solidification from the end of the cavity back to the riser tube. The process is capable of producing castings with a relatively low amount of porosity. Good dimensional accuracy and surface finish can be obtained and sand cores can be used. The die is typically coated with refractory coating to ease the casting ejection, control heat transfer from the metal to the die and prolong the die life. To prevent Fe dissolution into molten aluminium, the coating is required for the riser tube which has prolonged contact with molten aluminium. The cycle time is similar to that in gravity die casting, typically around 5–15 minutes. One of the major applications of LPDC is in aluminium automotive parts such as wheels and cylinder heads. The alloys frequently used for LPDC are 319 (AlSi5Cu3), 413 (AlSi12) and A356 (AlSi7Mg).

Vacuum permanent mould casting

There is another variant of LPDC which is known as vacuum permanent mould casting. It is similar to LPDC, but a vacuum is used instead of a pressure to draw

the melt to fill the mould. Since vacuum is used instead, the purity of the metal is maintained by lowering the amount of dissolved gases in the molten metal. Therefore, all of the advantages of LPDC are still retained whilst melt cleanliness is even better. However, the weight of casting is limited to about 0.2 to 5 kg.

6.6.3 Permanent mould casting

Like HPDC and LPDC, permanent mould casting uses a metal die which can be reused. In permanent mould casting, molten metal is poured under gravity into a metal die so it is often referred to as gravity die casting. Like LPDC dies, the dies used for permanent mould casting are typically coated with a refractory material. Cores can be used and made from high alloy steels or resin bonded sands. Permanent mould casting is typically used for high-volume production of simple metal parts with uniform wall thickness. The minimum wall thickness that can be permanent mould cast is approximately 4 mm because of the limited ability of metal to run into thin sections. The process is used for the volume production ranging from 1000 to more than 100 000 per year. Common permanent mould parts include gears, automotive pistons and car wheels. The alloys commonly cast by permanent mould casting include 319 (AlSi5Cu3), 413 (AlSi12) and A356 (AlSi7Mg).

The casting operation ranges from manually operated (hand-operated die sets) to automatically operated (carousel machines having several dies automatically operated and the melt is automatically poured). It typically takes around 4–10 minutes before the casting can be taken out from the die so the process is relatively slow. If higher production rates are required, multiple die sets have to be employed.

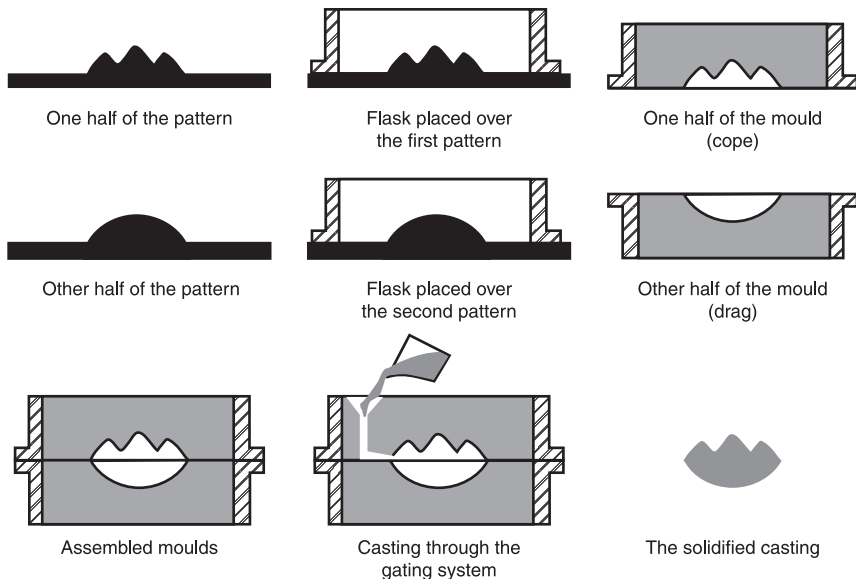
6.6.4 Sand casting

Sand casting is a process where molten metal is cast in a mould made from a sand mixture. In the past, the process was cost effective only for small volume production. But nowadays it is also suitable for high volume production thanks to automated equipment for making sand moulds. Sand castings generally have a rough surface sometimes with surface impurities, and surface variations. Medium to large parts such as valve bodies, crankshafts and engine blocks are typically manufactured by this process. The dimensional accuracy and surface finish of the casting depend on the type of sand and the moulding process. There are two main types of sand used for moulding: green sand and dry sand. Green sand consists of silica sand, clay, moisture and other additives. Dry sand is a mixture of sand and fast curing adhesive. When dry sand is used, it is often referred to as no bake mould casting or air set sand casting. Castings made from coarse green sand typically have a rough surface whilst air-set moulds can produce castings with much smoother surfaces.

A schematic diagram for the sand casting process is shown in Fig. 6.5. A pattern is made in the shape of the desired part, but enlarged to account for shrinkage and machining allowances in the final casting. The pattern is typically made from wood or plastic, and can be reused to produce new sand moulds. Sand cores can be used to form the inside shape of hollow parts of the casting. A metal box (the flask) is used for making the sand mould. It typically consists of two halves to form the top and bottom parts of the mould, termed cope and drag respectively. The pattern is placed in the flask, and then packed with sand mixture forming a mould cavity. If necessary, a temporary plug is placed to form a channel for pouring the cast metal (so-called a sprue). After that, the pattern and channel plug are removed leaving the mould cavity and pouring channel. The cope and drag are prepared separately and assembled afterwards to form a mould. The molten metal is poured into the mould through a sprue, which transmits the molten metal via runners into the mould cavity. After the cast metal has solidified and cooled, the casting is taken out from the sand mould. Generally, no mould release agent is used and the sand mould is destroyed in the removal process. Green sand can be reused after adjusting its composition by compensating the lost moisture and additives.

6.6.5 The Cosworth process

The Cosworth process is a precision sand casting process. It was developed in 1978 initially for manufacturing aluminium alloy castings to be used in the



6.5 Schematic showing the sand casting process.

Cosworth engine. The mould making method is similar to conventional sand casting, but zircon sand is used instead of silica sand. Zircon sand has a more uniform and lower thermal expansion rate than silica sand, so dimensional accuracy can be improved. The chilling effect of zircon also promotes fine-grained casting structures. Zircon sand is relatively expensive, but can be reused. The main feature of this process is that a liquid metal pump is employed to fill the mould from below with minimum turbulence, through a simplified gating system, in a similar manner to LPDC. The holding furnace is maintained under an inert atmosphere to limit the amount of oxidation in the molten aluminium.

In the original Cosworth process, productivity is low because the mould is kept in place on the casting machine until the casting has solidified. A later development introduced a turnover type of casting machine, allowing the casting rate to be increased. This is done by taking out a filled mould with an unfilled one before the casting has solidified. By inversion of the filled mould, hot feed metal is above the cooler casting and that assists the feeding.

6.7 Summary

The major aspects of aluminium alloy casting have been discussed in this chapter. To manufacture aluminium cast parts for a given application, there can be more than one combination of alloy composition and casting process which suit the requirements. Other factors such as expertise and facilities of the caster are also considered to decide on how to make aluminium castings.

6.8 References

1. Street, A.C., 1994. *The die casting book*. 2nd ed. Redhill: Portcullis Press.
2. Jorstad, J.L., 2003. *High integrity die casting process variations*, in AFS international conference on structural aluminum castings, 2–4 November. Orlando, FL, pp. 137–148.
3. Helenius, R., Lohne, O., Arnberg, L., and Laukli, H.I., 2005. The heat transfer during filling of a high-pressure die-casting shot sleeve. *Materials Science and Engineering: A*. 413: 52–5.
4. Gourlay, C.M., 2006. *Rheology of solidifying alloys containing 0–50% solid and the formation of dilatant shear bands*. Thesis (PhD). The University of Queensland: Brisbane, Australia.
5. Laukli, H.I., 2004. High pressure die casting of aluminium and magnesium alloys – grain structure and segregation characteristics. Dr. Ing Thesis. Norwegian University of Science and Technology: Trondheim, Norway.
6. Ghomaschi, M.R., 1995. High-pressure die casting: Effect of fluid flow on the microstructure of LM24 die-casting alloy. *Journal of Materials Processing Technology*. 52: 193–206.
7. Chen, Z.W., 2003. Skin solidification during high pressure die casting of Al-11Si-2Cu-1Fe alloy. *Materials Science and Engineering: A*, 348: 145–153.
8. Niu, X.P., Tong, K.K., Hu, B.H., and Pinwill, I., 1998. Cavity pressure sensor study of the gate freezing behaviour in aluminium high pressure die casting. *International Journal of Cast Metals Research*. 11: 105–112.

9. Sannes, S., Gjestland, H., Westengen, H., Laukli, H.I., and Lohne, O., 2003. *Die casting of magnesium alloys – The importance of controlled die filling and solidification*, in Society of Automotive Engineers (SAE) Exposition. Detroit, MI, pp. 1–9.
10. El-Mahallawy, N.A., Taha, M.A., Pokora, E., and Klein, F., 1998. On the influence of process variables on the thermal conditions and properties of high pressure die-cast magnesium alloys. *Journal of Materials Processing Technology*. 73: 125–138.
11. Dour, G., Dargusch, M.S., Davidson, C.J., and Nef, A., 2005. Development of a non-intrusive heat transfer coefficient gauge and its application to high pressure die casting: Effect of the process parameters. *Journal of Materials Processing Technology*. 169: 223–233.
12. Schnorf, T., Gabathuler, J.-P., and Imwinkelried, T., 2003. *Heat transfer coefficients for pressure die-casting and semi-solid forming*, in Modeling of casting, welding and advanced solidification processes X. TMS, Warrendale, PA, pp. 717–724.
13. Beeley, P., 1999. *Foundry technology*. 2nd ed. Oxford: Butterworth-Heinemann.
14. Avedesian, M.M., and Baker, H., 1999. *Magnesium and magnesium alloys*. Materials Park, OH: ASM International.
15. Gjestland, H., Sannes, S., Svaestuen, J., and Westengen, H., 2006. Optimizing the magnesium die casting process to achieve reliability in automotive applications. *SAE Transactions: Journal of Materials & Manufacturing*. 114: 67–73.
16. Ghomaschi, M.R., and Chadwick, G.A., 1986. Cold chamber die casting of aluminium alloys. *Metals and Materials*. 2: 477–481.
17. Vinarcik, E.J., 2003. *High integrity die casting processes*. New York: John Wiley & Sons.
18. Jorstad, J.L., and Apelian, D., 2008. *High integrity die castings (sound, reliable & heat treatable)*. Wheeling, IL: North American Die Casting Association.
19. Niu, X.P., Hu, B.H., Pinwill, I., and Li, H., 2000. Vacuum assisted high pressure die casting of aluminium alloys. *Journal of Materials Processing Technology*. 105: 119–127.
20. Spencer, D.B., Mehrabian, R., and Flemings, M.C., 1972. Rheological behaviour of Sn-15% Pb in crystallization range. *Metallurgical Transactions*. 3: 1925–1932.
21. Kaufmann, H., and Uggowitzer, P.J., 2007. *Metallurgy and processing of high-integrity light metal pressure castings*. Berlin: Schiele & Schon.
22. Gunasegaram, D.R., Givord, M., O'Donnell, R.G., and Finnin, B.R., 2008. Improved quality and reduced cost through ATM high pressure die casting. *Die Casting Engineer*. 52(1): 42–46.
23. Brown, J.R., 1999. *Foseco non-ferrous foundryman's handbook*. 11th ed. Oxford: Butterworth-Heinemann.

Quality issues in aluminum castings

G.K. SIGWORTH, GKS Engineering Services, USA

Abstract: The concept of metal quality has been pervasive, yet elusive. Everyone uses the term, but few are able to offer a precise definition for it. One approach has been to use a 'standard' mold to evaluate metal quality. The two most commonly used in North America are the ASTM B108 test bar, and a 'step' casting proposed by the Aluminum Association (AA). Some results with these molds are given for A356-T6 alloy. It is seen that better degassing practices have resulted in significant improvements in casting quality over the last 30 years. Iron is shown to be detrimental to quality. A numerical index is proposed to define the quality of castings, which describes the combinations of strength and elongation possible in heat-treated castings. This quality index is considered in detail, and equations are presented which give the mechanical properties of castings as a function of defect concentration. An estimate is also given of quality in 'defect free' castings. When considering tensile properties in commercial aerospace castings, solidification rate is found to be especially important, because it determines the size and amount of microporosity (and brittle phases) in the casting. Mechanical property data are presented and rationalized in the form of casting quality plots for different casting and heat treatment conditions. The role of porosity on fatigue properties and the use of Weibull statistics to evaluate quality are also considered.

Key words: aluminum castings, casting quality, degassing, defects, melt treatment, oxides, porosity, fatigue life.

7.1 Introduction

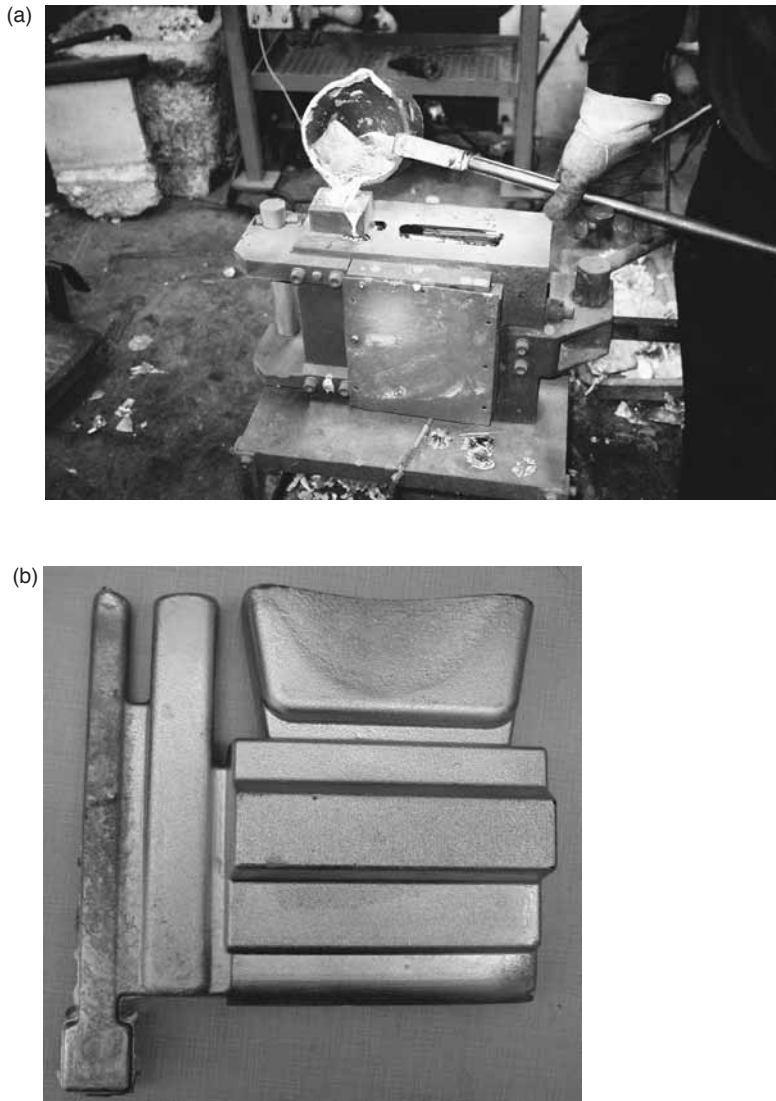
When one talks with buyers of castings, it is common to hear the following story. A cast component is obtained from foundry 'A' with good results. However, after some time the purchase agent puts out the part for bid and foundry 'X' comes in with a lower price. The order is awarded to 'X', but the mechanical properties are found to be significantly lower when castings are delivered. What has caused this change? We are using the same alloy. We might even be using the same tooling. Why are the material properties different? This story illustrates why net-shaped castings sometimes have a poor reputation compared to wrought products. It also illustrates why most handbook values for mechanical properties should be taken with a 'grain of salt', since little is said about the casting process or melt treatment used.

Considering this problem, how can we develop better engineering information for casting users? And how do we get the best quality? One approach is to use a test casting. This may be a production casting with a great deal of past history. It may also be a 'standardized' casting using a specified mold design.

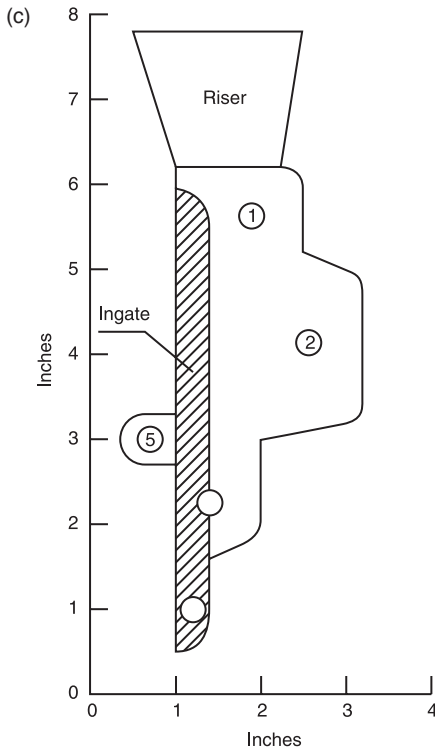
7.2 Standard molds

7.2.1 Aluminum Association Casting

The Aluminum Association (AA) mold was introduced almost 30 years ago (Miguelucci 1985). The mold and the resulting casting are shown in Fig. 7.1. This



7.1 (a)-(c) Aluminum Association permanent mold test casting (location of tensile test samples is shown in (c)).



7.1 Continued.

mold was used by the Aluminum Association to develop property data in six different alloys. Tensile test samples were taken from five areas, each having a different solidification rate and section thickness. Section 4 has the fastest solidification rate. The available tensile property data may be found in a report published by the Aluminum Association (AA 1990). The data tabulated for A356-T62 alloy castings is given in Table 7.1, together with properties for separately cast test bars. The dendrite arm spacing (DAS) observed at each of the five locations is also given. This DAS has been used to estimate the local solidification times from published correlations (Cáceres and Wang 1996). It is readily seen that the elongation and UTS decrease as the solidification time increases.

It should be emphasized that these are *average* values obtained when the same mold was sent to a number of different foundries. It is useful to consider the range of alloy compositions used and tensile properties obtained. Table 7.2 shows the maximum and minimum values recorded.

Some foundries evidently had much better practices than the others. There was a significant difference in tensile properties, especially elongation. This variability

Table 7.1 Average tensile properties of A356-T62 alloy in the AA mold

Location (thickness)	UTS (MPa)	Yield (MPa)	Elongation (%)	Dendrite arm spacing		Solidification time (sec)
				Inches	Microns	
1 (1–3/8")	246	216	2.7	0.0020	51	100
2 (2")	252	221	3.0	0.0018	46	63
3 (7/8")	274	230	4.6	0.0015	38	36
5 (3/8")	274	229	4.9	0.0013	33	25
4 (1/2")	288	233	6.5	0.0010	25	11
Test bars	294	242	4.8	0.0012	30	20

Source: AA, 1990; reproduced courtesy of the Aluminum Association

in quality is a good example of the problem one faces when mechanical property data lacks the proper ‘pedigree’ regarding melting and casting practices. There is no information about the degassing process used, if any, in the AA report. Likewise, other important treatments are unknown, such as filtration, grain refinement and modification. These all have an influence on mechanical properties.

The above information is interesting, but what does it really mean? Is it possible to do better? To find out it will be useful to compare these results with castings having a better ‘pedigree’.

We first consider castings produced by Ken Whaler (1995) at Stahl Specialty Company. A heat of A356 alloy with 0.07% Fe, 0.36% Mg and 0.08% Ti was melted in a double chamber dry hearth furnace. The metal in the dip out well was degassed by porous plugs and maintained at a low gas level, as determined by reduced pressure samples taken every 30 minutes. A filter crucible was placed in the furnace dip out well and all metal was ladled from this crucible. The metal temperature inside the crucible was held between 1350 and 1380 F (730°C to 750°C). The metal was modified with strontium and grain refined with small additions of 5Ti-1B rod. Thermal analysis samples were taken every 30 minutes to ensure that the grain refinement and modification were not lost.

Table 7.2 Minimum/maximum values for A356-T62 alloy in AA study

% Si	% Fe	% Mg	UTS (MPa)	YS (MPa)	Elongation (%)	Location
6.8/7.45	0.12/0.18	0.28/0.40	235/276	166/242	1.8/4	1
			231/283	166/242	1.5/4.5	2
			252/297	173/162	3/7.7	3
			248/293	173/162	3/7.5	5
			259/314	166/269	3.5/9.5	4

Source: AA, 1990; reproduced courtesy of the Aluminum Association

The resulting castings were solution heat treated for six hours at 1000 F (538°C) and water quenched. After a 24 hour hold at room temperature the castings were aged for six hours at 310 F (160°C). The resulting mechanical property data are given in Table 7.3. The tensile properties were considerably improved over those found in the AA study.

Values of quality index were calculated and shown in Table 7.3. This index will be considered in more detail later. We only note here that the index was proposed by Drouzy et al. (1980) and is defined by the formula:

$$Q = UTS + 150 \log E \quad [7.1]$$

where Q and UTS are given in MPa and the elongation to fracture, E, is in percent. The quality index drops by about 20% (100 MPa) at longer solidification times. It should be noted that the properties of the AA castings in Table 7.1 had a significantly lower overall level of quality index. (The best value was 380 MPa; the worst was 293 MPa.)

More recently, casting trials with the AA mold were conducted by Alcoa at Littlestown Hardware and Foundry (Sigworth and Kuhn 2009). The chemistry of the base alloy used is given in Table 7.4. The dissolved Ti level was varied between 0.01 and 0.15 wt. % by adding Al-6% Ti rod and waiting half an hour for the Ti to dissolve. Further grain refiner additions were either not made, or made as Al-3Ti-1B rod at an addition level of 20 ppm B. The melt was degassed 30 minutes with a rotary impeller degasser. Gas samples were taken at the beginning and end of each cast with a copper Ransley mold and analyzed for hydrogen by a LECO analyzer. The measured

Table 7.3 Tensile properties of A356-T6 alloy

Location (thickness)	UTS (MPa)	Yield (MPa)	Elongation (%)	DAS (microns)	Quality index (MPa)
1 (1–3/8")	270	193	6.2	51	389
2 (2")	269	197	6.2	46	388
3 (7/8")	292	197	12.3	38	455
5 (3/8")	290	198	10.1	33	440
4 (1/2")	308	210	14.3	25	481

Source: Ken Whaler (1995)

Table 7.4 Chemistry of base A356 alloy

Si	Fe	Mn	Cu	Mg	Ti	Sr	V
7.13	0.07	0.001	0.009	0.34	0.01	0.012	0.007

Source: Sigworth and Kuhn (2009)

gas content of all the melt samples was between 0.08 and 0.14 cc/100 grams. Castings were solution heat treated for six hours at 540°C, quenched into 60°C water, held eight to nine hours at room temperature, and aged six hours at 155°C.

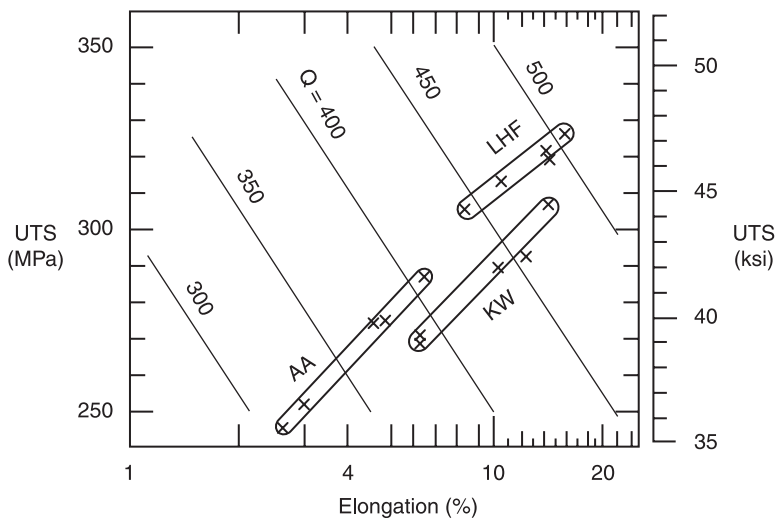
An analysis of the resulting tensile data showed that the dissolved Ti content and the boron addition had no significant effect on casting quality. The average values (56 samples for each location) and the 1 σ deviation of the tensile properties are given in Table 7.5.

The three sets of tensile property data (from Tables 7.1, 7.3 and 7.5) have been plotted in Fig. 7.2. The elongation is shown on a logarithmic scale, so that constant values of quality (in MPa, as defined by Eq. 7.1) appear as diagonal straight lines. The results from the AA report (Table 7.1) are labeled 'AA'. Ken Whaler's data (Table 7.3) is labeled 'KW' and the most recent results from castings poured at Littlestown Hardware and Foundry (Table 7.5) are labeled 'LHF'.

Table 7.5 A356-T6 alloy tensile properties in AA mold

Location	Yield (MPa)	UTS (MPa)	Elongation (%)	Quality index (MPa)
1	236.3 \pm 4.2	304.3 \pm 10.9	7.9 \pm 2.2	433.3 \pm 31.8
2	235.4 \pm 3.1	312.1 \pm 5.9	10.7 \pm 1.9	463.8 \pm 18.3
3	236.3 \pm 3.7	318.8 \pm 4.0	14.3 \pm 1.7	491.1 \pm 10.8
5	238.5 \pm 3.6	321.7 \pm 3.4	14.3 \pm 1.5	494.2 \pm 8.8
4	240.2 \pm 3.6	325.2 \pm 3.4	15.5 \pm 2.0	502.9 \pm 10.9

Source: Sigworth and Kuhn (2009)



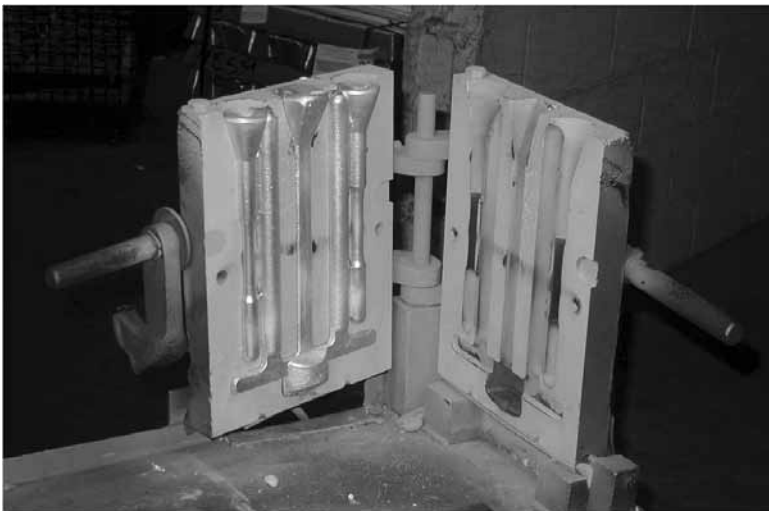
7.2 A356-T6 alloy tensile properties in AA test casting.

The important effect of melt treatment on casting quality should be obvious from this plot. The 'AA' data is for castings produced 25–30 years ago, when degassing was a haphazard affair and the need for melt treatment was not widely known. At this time many foundrymen melted ingot and poured the metal into the mold without any treatment. Many shops did not even do a chemical analysis. The castings produced at Stahl Specialty by Ken Whaler ('KW') were filtered and degassed, and showed a significant improvement in properties. However, Stahl Specialty used only a short degassing treatment with a porous plug. The most recent experiments ('LHF') used a 30 minute treatment with a rotary impeller degasser. Very low gas contents were found in this metal and the highest mechanical properties were obtained.

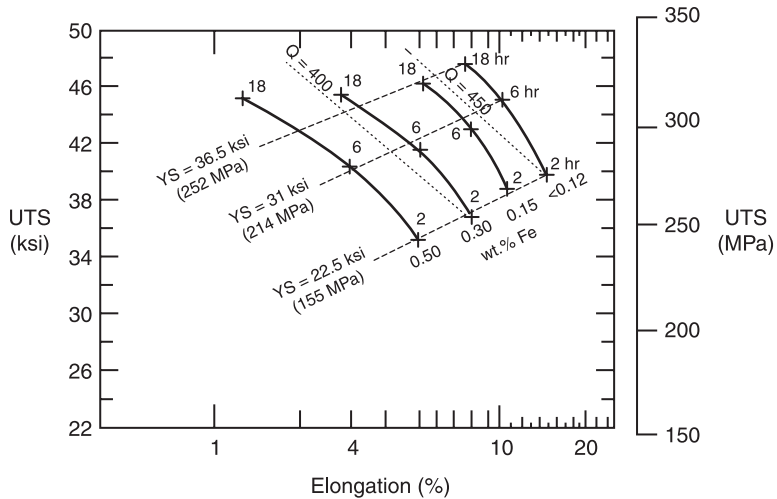
7.2.2 ASTM B108 test bar

Another standard mold commonly used in North America is specified in ASTM B108. This is a gravity-fed permanent mold casting. (Fig. 7.3.) An example will show how this mold may be used to evaluate metal quality. Experimental data was kindly supplied by Ken Whaler (2003). An A356 alloy containing 7.0% Si, 0.03% Fe, 0.36% Mg, 0.02% Zn, 0.08% Ti and 0.0002% P was melted in a reverberatory furnace, degassed, and filtered. The Cu and Mn in this alloy were below the limits of detection. The alloy was modified with 0.012% strontium and grain refined with a 5Ti-1B master alloy. Duplicate heats were made by adding small amounts of iron to the base alloy.

All test bar castings were given a solution heat treatment (eight hours at 1000 F, 538°C), water quenched, pre-aged 24 hours and aged for times between 2 and



7.3 ASTM B108 test bar mold.



7.4 Mechanical properties of 356 alloy containing various iron levels, and aged 2, 6 and 18 hours at 310 F (155°C) (Ken Whaler, 1995).

18 hours at 310 F (155°C). The tensile properties obtained are plotted in Fig. 7.4. The iron content of the alloy and the aging time used are indicated in the figure. The diagonal dotted lines show values of the quality index (Q), and the diagonal dashed lines indicate the yield strength (YS) of the material.

Figure 7.4 shows how aging time determines the trade-off between strength and elongation. The loss of elongation and strength that occurs with increased iron is also evident. This is the reason why the maximum specified for A356 alloy ingot is 0.12% Fe. These results also show how the heat treatment process may be changed to produce the desired strength in a casting alloy.

In general, there are four factors which have an important influence on the tensile properties of a casting:

- melt treatment and pouring procedures,
- heat treatment,
- alloy composition, and
- solidification time, or freezing rate.

The first three were considered in the results shown above for the two 'standard' molds. We now consider the effect of solidification rate.

7.3 Effect of solidification time

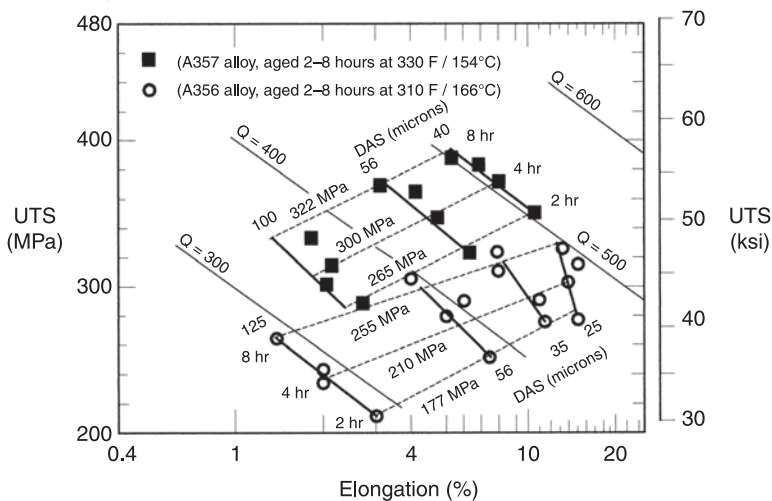
Many studies have shown that the rate of solidification has a significant influence on the properties of castings. Castings that freeze quickly can tolerate quite high contents of gas. Slowly cooled castings, however, easily form significant amounts of porosity. The freezing rate also determines the relative size of silicon particles

and iron intermetallics that form during freezing. The practical implication is simple: Casting quality depends strongly on solidification time.

This is best seen by considering data tabulated in an extensive study of aerospace castings by Oswalt and Misra (1980). They cut test bar samples from A356 (0.35% Mg and 0.11% Fe) and A357 (0.56% Mg, 0.14% Fe and 0.04% Be) alloy castings. Sample locations were selected from areas having different section thickness to determine the effect of freezing rate on tensile properties. The DAS was used to characterize the solidification rate of each sample. Different aging times (two, four and eight hours) were employed to obtain different strength levels in each alloy. The resulting tensile properties are plotted in Fig. 7.5.

There are several features of this plot worth noting. Following Drouzy et al. (1980), a logarithmic scale has been used for the elongation. As a consequence, the values of both constant quality index and yield strength appear as diagonal, straight lines. This type of plot is extremely valuable. It shows all of the important tensile properties (yield strength, ultimate tensile strength and elongation) as well as the quality index of the casting. This figure also shows the combined effect of three important variables: heat treatment, alloy composition and solidification rate. Once this plot is understood, you will know how the alloy used, the heat treatment and the casting process can be controlled to provide the mechanical properties desired for any particular application.

In practice, one may strengthen a casting by increasing the aging time or adding magnesium, or by doing both. (The primary difference between these two alloys is the fact that A357 has more magnesium.) By adjusting the magnesium level and the aging time it is possible to obtain a yield strength anywhere between 170 and



7.5 Tensile strength and quality of A356-T6 and A357-T6 alloy castings.

320 MPa (24–46 ksi) and a UTS (for rapid solidification rates) between 260 and 400 MPa (38–58 ksi).

The solidification rate is indicated in Fig. 7.5 by the numerical values for the secondary DAS. For A356 alloy the smallest DAS was 25 microns, which corresponds to a local solidification time of about 20 seconds and produced a quality index of 475–500 MPa. The largest DAS was 125 microns, which corresponds to a freezing time of 20 minutes. This produced a casting quality just under 300 MPa. The important effect of freezing rate on elongation and tensile strength is clearly seen from these results.

It may be worth noting again the results shown in Fig. 7.2 for the AA test casting. The freezing rates in this casting varied from 20 seconds to 2 minutes. Of course, better degassing practices helped to limit the loss of quality observed in the thick sections of this casting. In this regard, one should note that the data in Fig. 7.5 was for aerospace castings produced nearly 30 years ago. It would be interesting to repeat this study now, to see if improved degassing practices would reduce the loss in casting quality observed with slow solidification.

We now consider some of the theoretical underpinnings of casting quality.

7.4 Theoretical basis for the quality index

There are a number of ways to define the quality of net-shaped castings, but the one most commonly used was first proposed by French foundrymen (Drouzy et al., 1980). They studied the effects of casting conditions, metal composition and aging time on the mechanical properties of Al-Si-Mg (356 type) alloys. As they analyzed the aging process, they noticed that for a given ‘quality’ of casting, as determined by freezing rate (DAS), porosity and iron content, the T6 aging process produced tensile properties that followed a straight line on a certain type of plot. Figures 7.4 and 7.5 gave examples of the French quality plot, where the ultimate tensile strength was plotted versus the logarithm of the elongation to fracture. Equation 7.1 is the formula developed empirically by Drouzy, Jacob and Richard to calculate the quality index. It can be seen that the change of tensile properties versus aging time in Fig. 7.4 and 7.5 follow closely lines of constant quality index.

This result has important ramifications:

- The quality index describes the relative trade-off between strength and elongation. If we need to increase the strength or the elongation in a casting, this behavior allows us to change the heat treatment accordingly. (The same effect may also be obtained by increasing or decreasing the Mg content.)
- The quality index allows us to compare two different castings, which may have received different heat treatments or whose chemical composition (especially %Mg) are different.
- The quality index gives an indication of improvements that might be made in any particular casting.

- The iso-quality and iso-yield strength contours appear as straight lines in the quality plots developed by the French. Thus, the quality plot shows all important tensile properties.

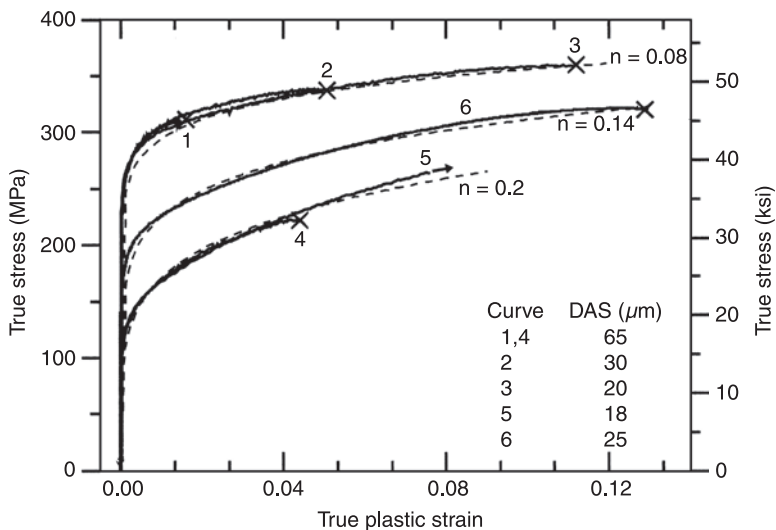
Cáceres (1998, 2000) has developed a more general framework for the concept of quality index, based on the notion that the maximum attainable ductility and strength of a tensile bar are determined by the onset of necking. The onset of necking thus represents the maximum theoretical quality for any given alloy and temper. He began with the equation:

$$\sigma = K \varepsilon^n \quad [7.2]$$

which relates the true stress (σ) and true strain (ε) observed during a tensile test. K is a material constant, and n is the strain hardening coefficient:

$$n = \frac{\varepsilon}{\sigma} \frac{d\sigma}{d\varepsilon} \quad [7.3]$$

Equation 7.2 represents the experimental curves reasonably well. A single value of K is used, and n is varied to represent different heat treatments. Examples of experimental flow curves are given in Fig. 7.6 for an Al-7%Si-0.4%Mg alloy. Curves 4 and 5 in Fig. 7.6 are for T4 bars; Curve 6 is for a casting aged one hour at 170°C; and Curves 1–3 are for samples aged six hours at 170°C (a traditional T6 treatment). Dashed lines were calculated with $K = 430$ MPa and the values of n as indicated in the figure. Note that the solidification rate (or DAS) controls the elongation in these castings for each temper, but does not affect the yield strength or the strain hardening rate.



7.6 True stress–true strain curves for an Al-7%Si-0.4%Mg alloy (Cáceres, 1998; reproduced with permission of Maney Publishing, www.maney.co.uk/journals/ijcmr).

In the castings having the highest ductility, tensile failure involves necking. Necking will occur when the Considère criterion is met; or when

$$\frac{1}{\sigma} \frac{d\sigma}{d\varepsilon} = 1 \quad [7.4]$$

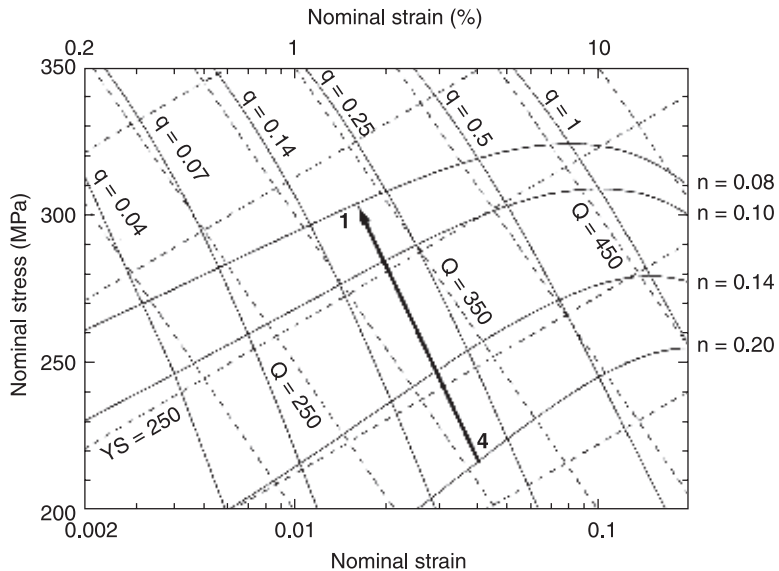
Comparing Eqs. 7.3 and 7.4, it is obvious that necking will occur when $\varepsilon = n$. In other words, the strain hardening exponent, n , determines the maximum uniform strain possible in the tensile sample.

The condition where $\varepsilon = n$ represents the maximum ductility. This is the best quality possible. Samples failing earlier have a lower ductility and quality. Cáceres consequently defined a relative quality factor by the relationship:

$$q = \frac{\varepsilon}{n} \cong \frac{E_f}{n} \quad [7.5]$$

where the \cong indicates that the difference between true and nominal strain has been ignored. Considering the level of ductility found in most casting alloys, this is an excellent approximation. Equations 7.2 and 7.5 were used by Cáceres to generate the quality curves shown by solid lines in Fig. 7.7, for a value of K equal to 430 MPa. The dashed lines in Fig. 7.7 show the lines of constant quality and yield strength originally proposed by Drouzy, Richard and Jacobs. The theoretical curves are seen to correspond closely to the empirical lines established by the French.

Cáceres (2000) also showed that the maximum possible quality for a material (when $q = 1$) occurs when Q is numerically equal to $1.11 K$. For Al-Si-Mg casting



7.7 The quality index map proposed by Cáceres (Cáceres, 1998; reproduced with permission of Maney Publishing, www.maney.co.uk/journals/ijcmr).

alloys $1.11K \cong (1.11 \times 430 \cong 477 \text{ MPa})$. From the results shown above, this value is very close to what is found empirically in the best quality castings ($Q = 480\text{--}500 \text{ MPa}$). Another indication of relative quality is the elongation to fracture. When this is equal to n , the elongation to fracture is 100% of that theoretically possible.

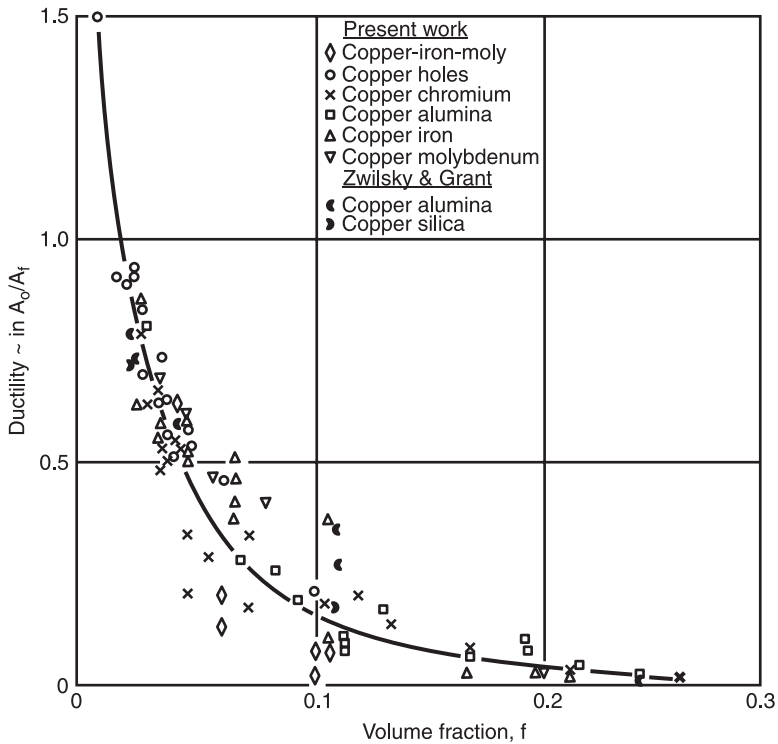
This theoretical approach to quality is important, because it allows a foundry engineer or casting user to establish the absolute quality of a casting, which is imposed by the onset of necking, and to determine whether further improvements are possible. It also allows us to understand better, from a scientific point of view, what microstructural features determine casting quality.

7.5 Effect of inclusions and porosity on quality

A detailed study of the tensile properties of copper containing second phase particles and porosity defects was presented by Edelson and Baldwin (1962). Controlled amounts of porosity (and other defects) were introduced into copper-based alloys, produced by sintering metal powders. A detailed analysis of their results showed that the volume fraction of defects was the governing variable. The size or the shape of defects was not important. Furthermore, the most sensitive indicator of defect concentration was the elongation to fracture in tensile specimens. A figure from their study is reproduced in Fig. 7.8. It shows the relative loss in ductility as a function of the volume fraction of defects. The ductility was determined from the reduction in area of the tensile specimen, and compared to a standard sample having a one per cent concentration of defects (i.e. $f = 0.01$).

This result shows that the elongation to fracture (and quality) is extremely sensitive to the presence of defects, but it suffers from two limitations. First, the form of the plot does not allow us to estimate accurately the quality of relatively 'defect free' material. Second, it is not clear that this result applies to high quality, net-shaped castings. Cáceres and Selling (1996) have shown that the tensile properties of castings do not correlate well with measurements of volumetric porosity content. In commercial castings the distribution of porosity and other defects is non uniform, and tensile failure occurs at the weakest spot. As a consequence, the concentration of defects found on the fracture surface may be three to twenty times the average volumetric concentration. Another approach is needed.

Cáceres and Selling presented a model for the growth of a plastic instability inside a tensile specimen, when a certain area fraction (f) of porosity was present on a planar section of an otherwise defect-free material. An equation was derived for the loss of elongation and strength caused by these defects. Their equation correlated well with experimental measurements of the elongation to fracture and the area fraction of defects found *on the fracture surface* of Al-Si-Mg alloy samples. These results were later extended by Sigworth and Cáceres (2004) who derived the equation:



7.8 Loss of elongation associated with defects (Edelson and Baldwin, 1962; reprinted with permission of ASM International®, all rights reserved, www.asminternational.org).

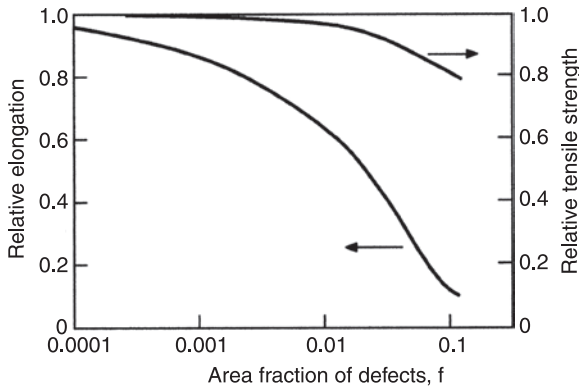
$$(1-f) = q^n e^{n(1-q)} \quad [7.6]$$

This equation relates the relative loss in ductility of a tensile sample (value of q) to the area fraction of defects present, f . Considering Eq. 7.2, the resulting loss in tensile strength is equal to:

$$\frac{\sigma}{\sigma_{\max}} = q^n \quad [7.7]$$

Figure 7.9 shows a plot of these two equations for A356-T6 alloy (i.e. for a value of n equal to 0.1). Note that even very small amounts of defects in a material have a significant effect on elongation. The ultimate tensile strength is affected much less. For example, a concentration of defects of only 0.1% ($f = 0.001$) results in a loss of 15% in elongation, while the reduction in UTS is hardly measurable. With 1% area fraction of defects ($f = 0.01$) the elongation is reduced by 40%, but the ultimate tensile strength is decreased by only five per cent.

Unfortunately, this plot has limited predictive value, since the area fraction of defects on the fracture surface is only a post mortem value. However, it shows



7.9 Effect of defect concentration in the fracture surface on elongation and UTS (Eq. 7.6–7.7).

foundrymen the dangers of even small amounts of porosity; and it informs us as to the metal cleanliness needed to produce the highest quality castings. It also shows clearly that elongation to fracture is the most sensitive indicator for the presence of porosity or other defects in castings.

7.6 Fatigue failure

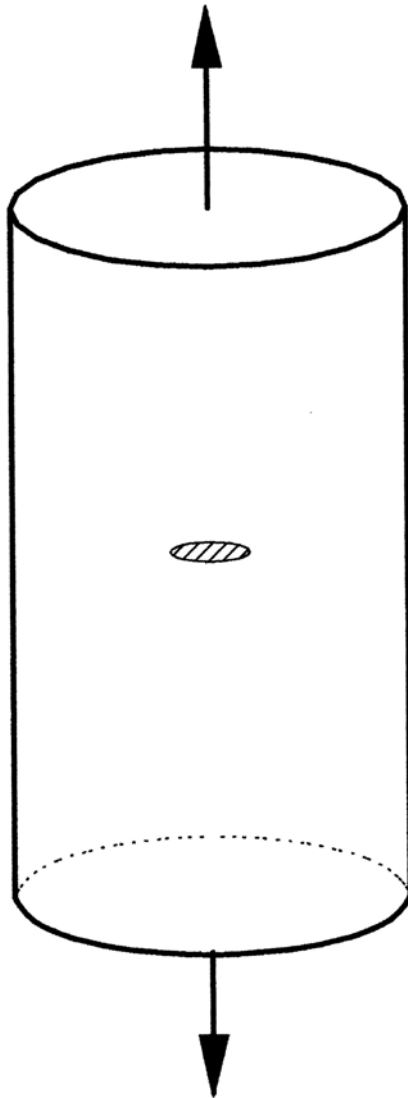
Aluminum castings are often used in structural components subject to cycles of applied stress. Over their commercial lifetime millions of stress cycles may occur. In these applications it is important to characterize their fatigue life. This is especially true for safety critical applications, such as automotive suspension components. The commercial importance of fatigue has provided the motivation for extensive studies by automotive and university researchers. What follows is, by necessity, a simplified approach to the problem of fatigue failure. The intention is to offer practical guidelines for design engineers, so they know what to look and ask for in a casting.

We consider a simple case, illustrated in Fig. 7.10. This shows a piece of material subjected to a tensile stress in the vertical direction (arrows). In the center is a circular-shaped crack. Because the crack provides no mechanical strength, stress accumulates there. The stress intensity parameter is:

$$K = 2\sigma \left(\frac{a}{\pi} \right)^{1/2} \quad [7.8]$$

where a is the crack radius and σ is the applied stress. When the load is applied cyclically to the material, the crack grows a little bit each time the load is applied. We want to know how fast the crack grows, and how long it will take for failure to occur. The growth of the crack with each cycle is usually represented by this equation:

$$\frac{da}{dN} = C(\Delta K)^n \quad [7.9]$$



7.10 Schematic view of a crack in fatigue failure.

where N represents the number of times the stress has been applied and C is an empirical constant. Equation 7.9 applies to the intermediate region (Stage II) of crack growth, and is called the Paris Equation. For aluminum alloys the exponent (n) is very nearly equal to four, which means that:

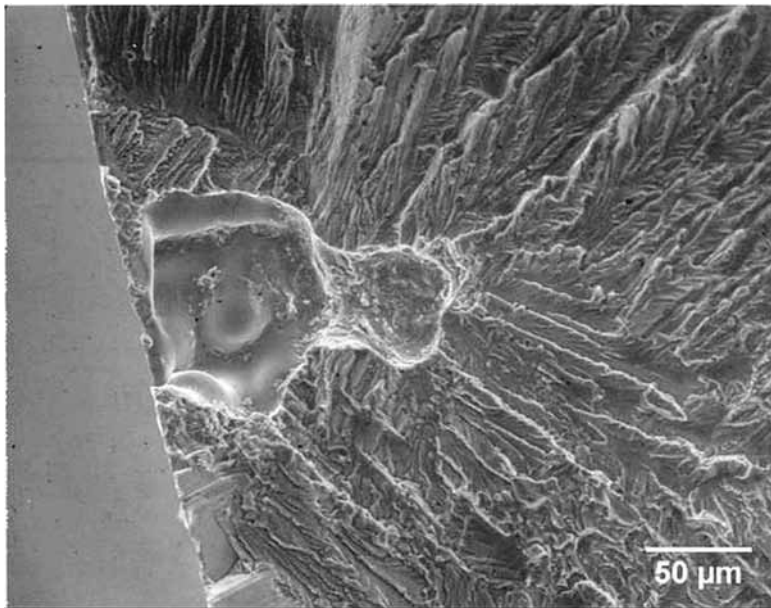
$$\frac{da}{dN} \cong C' (a)^2 \quad [7.10]$$

In other words, the crack growth rate is proportional to the square of the radius, or to the area of the crack.

Now suppose we have two cracks present in the material. The larger crack is twice as large as the smaller one. From Eq. 7.10 we find that the larger crack will grow four times as fast as the smaller crack. And as it becomes larger with each fatigue cycle, it continues to grow faster and faster. The practical implication is obvious: Fatigue life is controlled by the largest ‘crack’. In most commercial castings, this is the largest pore. For all practical purposes, large pores are built-in cracks. An example of how a pore may nucleate a fatigue failure is shown in Fig. 7.11.

The effect of pore size on fatigue has been shown clearly in several recent studies. Fatigue tests were made with A356-T6 alloy at a stress ratio $R = -1$. Several types of castings were studied: two gravity poured castings, a squeeze casting and a semi-solid metal (SSM) casting. These castings exhibited a range of defect sizes; the high pressure die cast (squeeze and SMM) components having the smallest size of pores. The fracture surface of all specimens was examined under a microscope, to determine the size of the defect initiating fatigue crack growth. The measured fatigue life, N_f , the stress amplitude (maximum applied stress), σ_a , and the defect area, A_i , are related by the equation:

$$\sigma_a^m N_f A_i^{(m-2)/4} = B \quad [7.11]$$



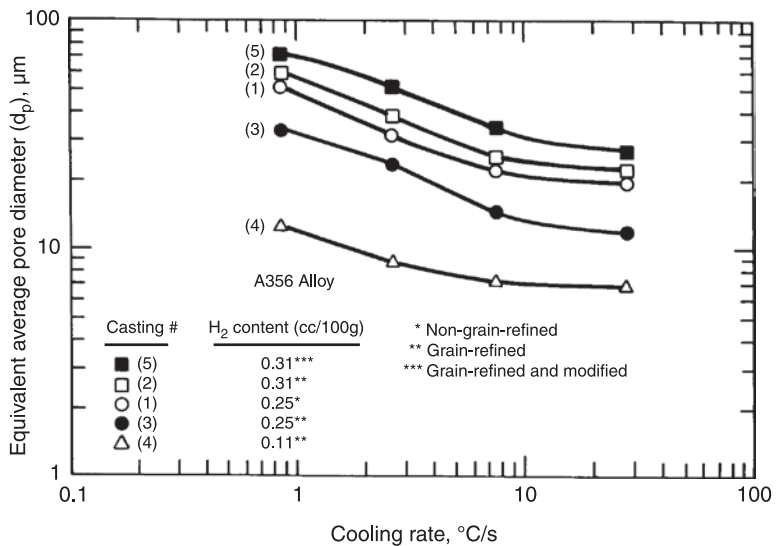
7.11 Fracture surface of A356 alloy fatigue specimen, showing incipient pore (Wang et al., 2001; reproduced courtesy of the Minerals, Metals & Materials Society).

where m is equal to 4.2 and $\log B$ is about 16 when one uses units of MPa, μm^2 and cycles for stress, defect area and fatigue life, respectively (Davidson et al., 2000; Griffiths, 2003; Wang et al., 2005).

The relationship given in Eq. 7.11 appears to have a wide range of validity. For example, in the study by Couper et al. (1990), several different heat treatments were applied to vary the strength. This had no significant effect on the fatigue life. The size of defects controlled fatigue life in all conditions. Similar results were found when the solution time was changed (Davidson et al., 2002). There are also recent studies of commercial grade automotive castings (Boileau and Allison, 2003). The largest defect was almost always a pore, which controlled the rate of fatigue failure.

Above we considered the effect of solidification rate on the tensile properties. It will now be useful to consider the effect of freezing rate on pore size and fatigue strength. Looking at the data from the study by Fang and Granger (1989), we find the results in Fig. 7.12. Pore diameter is reduced by rapid solidification. Also, by comparing Curves (1) and (3), we see that grain refinement reduces the pore size. Reducing gas content also produces smaller pores. (Compare Curves 2, 3 and 4.) Hence, good degassing, grain refinement and rapid solidification contribute to smaller pores and an improved fatigue life.

These considerations have been confirmed experimentally. Figure 7.13 gives an example of how fatigue life relates to pore size, and to the solidification rate in a casting.



7.12 Pore sizes in directionally solidified Al-7Si-0.3Mg (A356) alloy castings (Fang and Granger, 1989; reproduced courtesy of the American Foundry Society).

Equation 7.11 and the results plotted in Fig. 7.13 were obtained from failed fatigue specimens. That is, the size of the pore initiating fatigue failure was measured on the fracture surface. (As shown in Fig. 7.11.) Unfortunately, determining the size of the ‘largest pore’ by standard metallographic examination is not straightforward. As noted above, the distribution of porosity in commercial castings is non uniform. This problem was considered by Wang and Jones (2007) who offered a solution provided by the use of extreme value statistics.

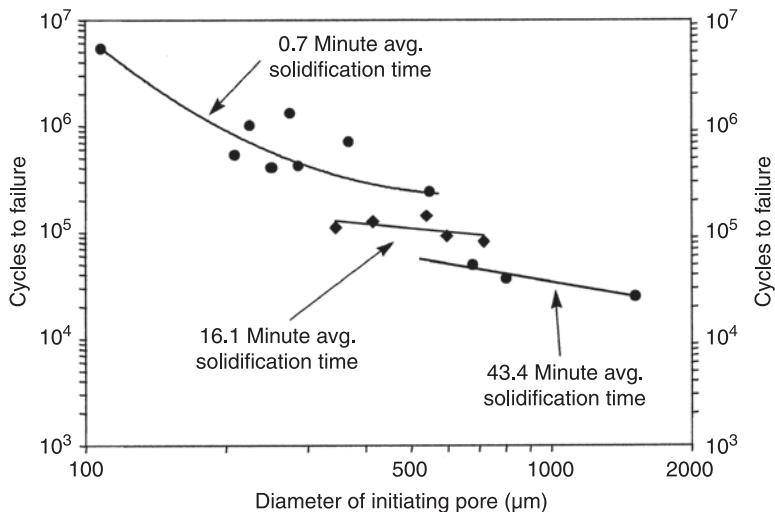
From a practical point of view, however, the implications are clear. Control of porosity is the single most important factor in obtaining good fatigue life in net-shaped castings. Compared to porosity, the strength level of the alloy (as determined by heat treatment or alloy composition) is less important. This means that best results are obtained by:

- good degassing and melt treatment,
- effective grain refinement,
- proper modification practice, and
- rapid solidification.

Also, some new casting processes apply pressure to solidifying castings to reduce the amount of porosity and the size of the resulting pores.

It is also possible to reduce porosity in castings by the use of Hot Isostatic Pressure treatment (HIPping). Numerous studies have shown that fatigue life can be improved in this way.

It will now be instructive to consider the sources of casting defects.



7.13 Measured fatigue life of W319 alloy at alternating stress of 96.5 MPa (Boileau and Allison, 2003; reproduced with kind permission of Springer Science and Media).

7.7 Sources of casting defects

In Fig. 7.4 we saw that iron in Al-7Si-0.3Mg alloy castings resulted in a significant loss in elongation and tensile strength. Iron has low solubility in solid aluminum, so most of the iron in the liquid metal forms brittle intermetallic compounds. In Al-Si casting alloys Al_5FeSi plates are found. These act as defects. Because of the stoichiometry of the compound, and the results shown in Fig. 7.9, even small amounts of iron have a significant effect: At 0.3% Fe one-half of the elongation is lost. Thus, iron contents must be held to low levels for best quality.

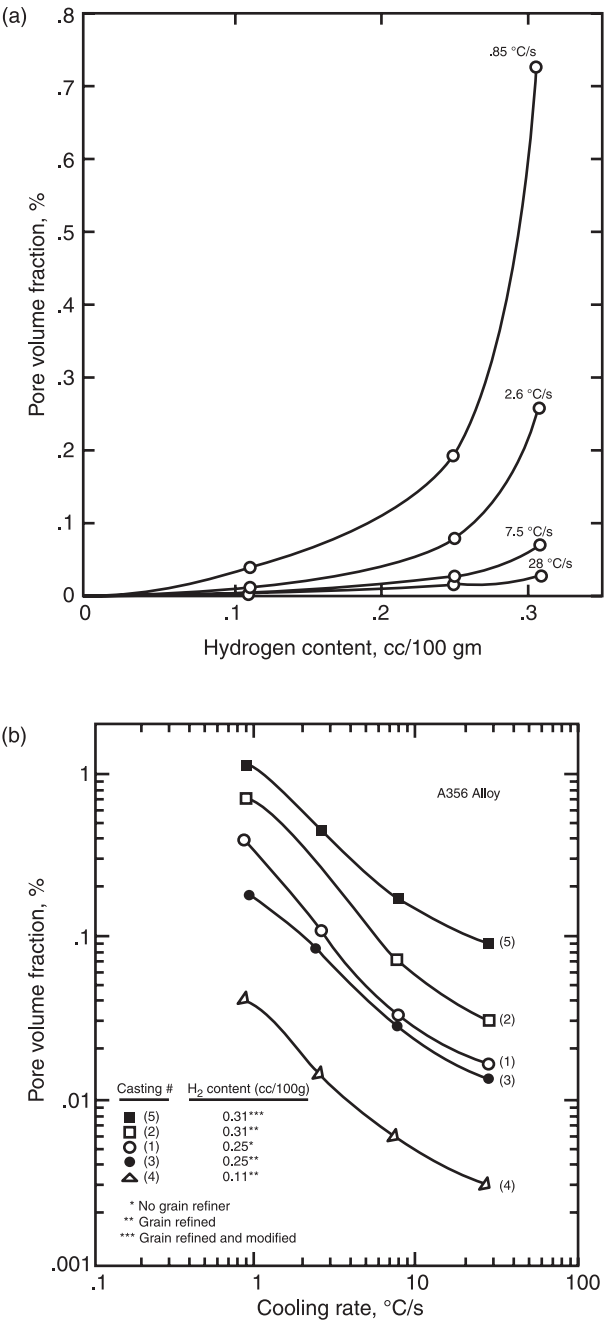
Silicon may also form large, brittle flakes in Al-Si-based casting alloys. This is especially true in large, slowly cooled castings. When best elongation and highest strength are desired, one must change the shape and size of the silicon phase. This may be accomplished by heat treatment, and/or by small additions of Na or Sr, which ‘modify’ the morphology of the silicon in the eutectic phase. Modification is a fascinating, complex subject; one that is extremely important for best quality in Al-Si casting alloys. Modification has also been the subject of an extensive literature review (Sigworth 2008).

The most serious problem facing foundrymen is usually porosity. For this reason, it is worth while considering in some detail. The amount of porosity in a casting depends on several factors. Listed roughly in order of importance they are:

- solidification rate,
- gas content,
- metal cleanliness,
- pressure in the casting,
- modification, and
- grain refinement.

Four of the above factors were studied by Fang and Granger (1989). Their castings had a water-cooled chill at one end and were solidified directionally, so feeding was more than adequate to prevent shrinkage. The amount of porosity and the average size of the pores were measured by quantitative metallography at various distances from the chill. The solidification rate at these locations was determined by thermocouples in the mold. The amount of porosity formed in their castings is plotted in Fig. 7.14.

Oxide films are also an important source of casting defects. A thin oxide film forms on the surface as soon as liquid aluminum comes in contact with air. If the liquid is quiescent, this oxide stays on the surface and does not affect metal quality. But if there is any turbulence or splashing, the oxide film is mixed (or folded) into the melt; and the quality of the casting suffers. The generation of oxide films has been studied in great detail by John Campbell and his associates. An excellent review of their research has been published and is highly



7.14 (a) and (b) Volume fraction porosity in directionally solidified Al-7Si-0.3Mg (A356) alloy castings (Fang and Granger, 1989; reproduced courtesy of the American Foundry Society).

recommended (Campbell, 2006). This work clearly establishes the importance of 'folded in' oxides, which have aptly been called 'bi-films'.

One important practical implication on metal quality is that oxide films assist in porosity formation.

Aluminum readily picks up hydrogen gas from humidity in the atmosphere. Hydrogen has low solubility in solid metal – only six per cent of the gas soluble in the liquid – so any gas in liquid metal tends to form dispersed micro-pores during solidification. Because of the high surface tension of liquid metal, it is not possible for pores to nucleate homogeneously, so gas pores form on oxide films in the melt. In fact, if the metal is filtered carefully, no porosity will form, even if significant amounts of gas are dissolved in the metal. This phenomenon was first documented by Brondyke and Hess (1964) and Rooy and Fischer (1963). If one looks carefully at pores found in aluminum castings under a microscope, one usually sees remnants of an oxide film. An example of an oxide in contact with a pore is shown in Fig. 7.15. In this case, it is clear that an oxide on the surface of the metal was 'folded into' the bath, by excessive metal turbulence and/or splashing.

To sum up the preceding discussion, not only do oxide films act as defects in their own right, but they also are a necessary precursor for the formation of porosity. In both cases, they have a significant deleterious effect on quality.

With these concepts firmly in mind, it will be instructive to consider how practices in the foundry determine casting quality.



7.15 Pore nucleating on a folded oxide film in A356 alloy.

7.8 Effect of metal treatment and transfer on quality

In many foundries it is possible to see this sequence of operations. Metal is pumped into a crucible. The crucible is then transferred by fork lift or crane, whereupon the metal is poured into a holding furnace. Then a ladle is used to dip out of the holding furnace, and to pour metal into the mold. Each transfer of liquid metal produces an aluminum 'waterfall'. The resulting splashing generates a great deal of oxide films, which are folded into the liquid and carried into the casting.

In contrast to the above, a level-pour transfer has been employed for many years by primary aluminum suppliers. A launder (or trough) carries liquid metal from the melting furnace to the casting pit. Once the launder is filled, the metal flows in the lower part of the channel, and the surface is quiescent. Because the transfer is level, there are no 'waterfalls', and oxide films are not 'folded into' the melt. Normally the metal also passes through an in-line degasser and a filter box. As a result of these metal transfer and treatment practices, it is possible to produce castings which are very low in gas, and nearly free from oxide films or other inclusions.

A good example of the quality produced in this way is can stock. Can producers take large 3xxx alloy slabs and roll them into thin sheet, which is drawn into shapes needed for the can body. If you crush an empty aluminum can, you will quickly appreciate how thin the body of the can has become. If there are inclusions in the cast metal, they cause pin-holes in the wall of the can. Each can is tested for holes before filling with a beverage. When I first came into the aluminum industry, the 'standard' reject rate for can stock was one in 10 000. Now it is closer to 20 ppm. The level-pour transfer system (and the associated melt treatment) is the main reason for the high level of quality associated with wrought aluminum products.

This suggests that improved metal handling in the foundry would significantly improve aluminum castings; and moreover, produce a consistency of quality and reliability normally associated with wrought alloys. Unfortunately, before realizing this improvement, there is one last hurdle to clear. The metal must enter and fill the mold in a way that does not produce additional oxides, or other defects. The importance of quiescent metal flow was demonstrated clearly by the pioneering research of Runyoro et al. (1992) who established that the metal gate velocity must be less than a critical value (0.5 m/sec) to avoid the formation of oxide films. Subsequent studies demonstrated the importance of runner design on tensile and fatigue properties of aluminum castings (Green and Campbell, 1994; Nyahuma et al., 1998). In a sense, this problem represents the 'last frontier' for aluminum foundrymen. Solving it would allow us to produce oxide-free, net-shaped castings having the same reliability as forgings and machined wrought alloy components.

This objective is probably best accomplished when the metal transfer/treatment system and the casting process are considered and designed together, to avoid the problem of oxide film generation. One example is the Cosworth low-pressure sand

casting process (Campbell and Wilkins, 1982), designed to eliminate metal turbulence during mold filling. Metal is transferred via an electromagnetic pump into the bottom of the mold, minimizing the generation and entrapment of oxides caused by falling metal. Very low porosity and a high casting quality are obtained. This process was used for many years by Cosworth to produce Formula 1 and CART racing engines. It was later adapted by Ford to produce engine blocks. Another approach is a level pour transfer system with in-line degassing and filtration stations. This type of metal delivery system is now being used by a number of foundries (Kennedy 2001). But most cast shops have not completely solved the challenge of filling the mold without generating oxides. It is common practice to place a holding furnace with a dip-out well at the end of the launder, and ladle metal into the mold with a robot. The ladling operation will generate some oxide films. One solution, adapted at Littlestown Hardware and Foundry (Anon 2003), is to use a molten metal pump. It is also possible to place a dosing furnace at the end of the level pour transfer system. This approach was used by Nemak (Cardoso et al. 2005).

It will now be instructive to consider examples of how metal transfer and mold design affect the casting quality. What follows is taken from the 1994 study of Green and Campbell. They made simple round bar castings having a diameter of 12 mm. These were poured from a heat of Al-7Si-0.42Mg (356) alloy containing 0.30% Fe and 0.17% Mn. They poured sand castings under four different conditions:

1. Top poured and unfiltered: 12 mm bars were poured from the top of the mold, using a pour cup, down sprue and no filtration in the mold. In this casting, the fall of metal was in excess of 150 mm. So, the theoretical maximum metal velocity was 1.7 m/sec. This was in excess of the critical flow velocity of 0.5 m/sec, so there was potential for metal turbulence and oxide production.
2. Bottom filled and unfiltered: These castings were bottom filled, but no precautions were taken to eliminate turbulence, and no filters were used in the mold.
3. Bottom filled and filtered: A filter was placed in the runner. This ensured that the metal flow into the mold was not turbulent. This was confirmed by real time, high speed radiography of the mold during filling.
4. Bottom filled, filtered and Sr modified: This condition was the same as (3) above, except the melt was modified with Sr.

The quality of each casting was determined by calculating the Weibull modulus associated with the distribution of ultimate tensile strength of the bars. The modulus is determined by using the equation:

$$F_x = 1 - \exp \left[- \left(\frac{X}{\sigma} \right)^m \right] \quad [7.12]$$

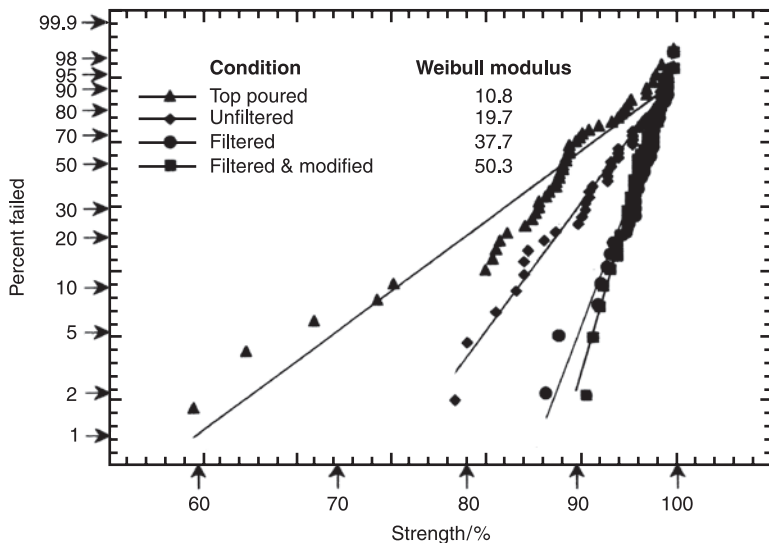
where, F_x is the cumulative fraction of tensile failures that occurred, X is a specific value of the mechanical property under consideration (in this case, tensile strength), σ is the value of X at which 37% ($1-1/e$) of the samples survive, and m

is a material constant, which determines the width (or spread) of values. This is called the modulus.

The results obtained for the four different designs of the casting are plotted in Fig. 7.16.

In many respects the Weibull modulus is a better measure of material reliability than conventional statistics (Campbell, 2003). In the latter a Gaussian distribution is assumed, and variation about the mean is determined. This is the approach commonly taken by automotive companies, who specify minimum properties using $\pm 3\sigma$. However, the distribution of mechanical properties is not really Gaussian. It is skewed. On one side we have the 'maximum' quality possible, associated with defect-free areas. On the other side there are areas (or volumes) of material which contain flaws. The Weibull analysis has been used for many years to describe the probability of fracture in ceramics, considering the distribution and size of flaws in the material. Taking the same approach in castings appears to offer several benefits. First, Weibull plots clearly establish the quality of each casting process. Also, with the Weibull modulus it is easier to predict the probability of failure at some reduced level of stress. The modulus is also a way to compare components made by different processes. For example, the best casting design shown in Fig. 7.16 had a Weibull modulus of 50, which is close to values reported for aerospace forgings (Green and Campbell, 1994).

As noted above, and shown in Fig. 7.8–7.9, the elongation to fracture is a more sensitive indicator of casting quality. So, calculating the Weibull modulus for the



7.16 Weibull plot of normalized tensile data (Green and Campbell, 1994; reproduced courtesy of the American Foundry Society).

elongation to fracture is probably the best way to determine material quality for safety critical applications.

7.9 Possible improvements in fatigue life

In the preceding text we found that good melt treatment (especially degassing) and pouring practices and optimum mold design can produce castings having tensile properties close to a theoretically predicted 'maximum' value ($Q \cong 480\text{--}500$ MPa). But what about fatigue life? Are we reasonably close to a 'maximum' theoretical value? Or is significant progress still possible?

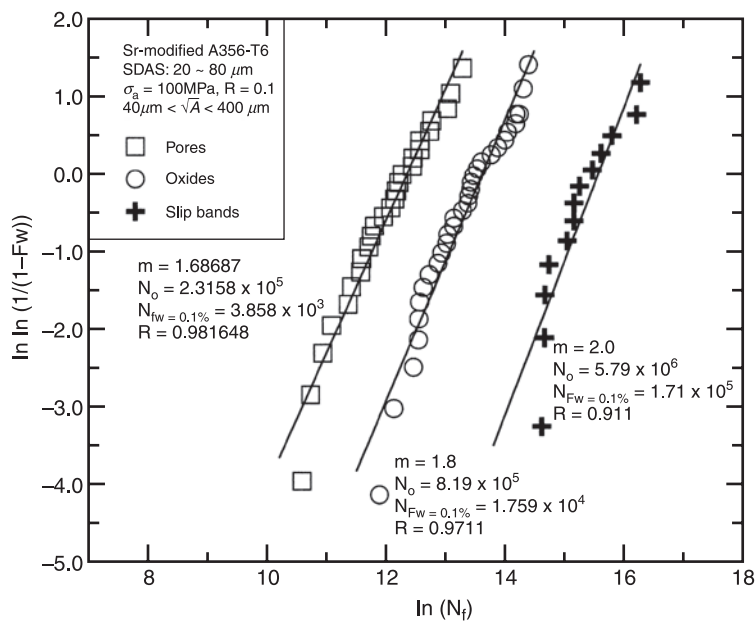
We showed how the fatigue life in commercial castings may be controlled by pore size (Eq. 7.11). But the amount of porosity and the size of the pores can be reduced by rapid solidification and good degassing. It is also possible to HIP a casting after solidification. In practice, however, it may be sufficient to reduce the maximum pore size to a reasonably small value, probably less than about 25–50 microns equivalent diameter.

Now, once pores have been removed as a source of fatigue cracks, we are left with the seemingly ubiquitous oxide films. These take over as the largest flaw in the metal. Can these be removed? The answer is: 'Yes.' Careful filtration of the metal is possible. Certain fluxing practices are also efficient at removing oxides. So fatigue life can be improved still further. What happens when we do this? Fatigue cracks then form on slip bands, which accumulate at the surface of the metal during application of cyclic stresses. This case presumably represents the 'ultimate' fatigue strength of cast aluminum.

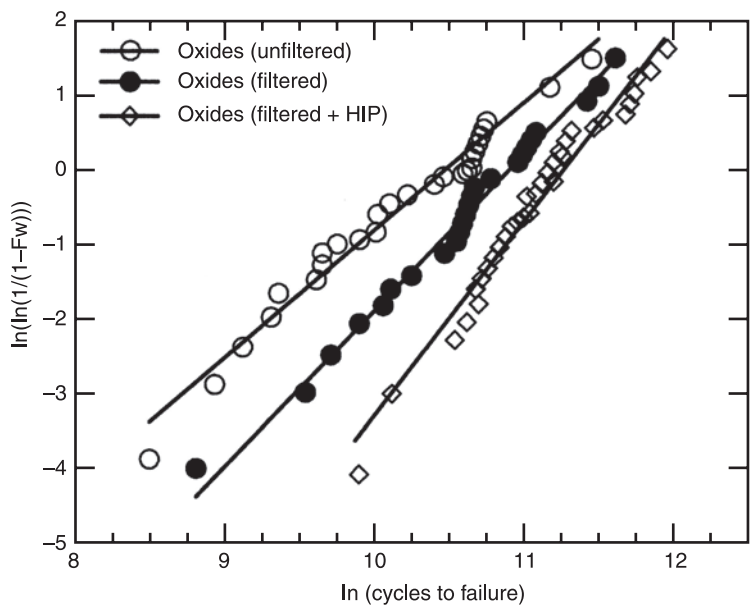
A recent study (Wang et al., 2001) measured how different defects in the metal determine fatigue life in Sr-modified A356-T6 alloy castings. Figure 7.17 shows a Weibull plot of the measured fatigue life for three cases: crack initiation on pores, crack initiation on oxides and crack formation on slip bands. It can be seen that removing porosity in a casting increases the fatigue life by about six times. Removing the oxides increased it further by almost ten times. In other words, the fatigue life of 'average' commercial castings may be improved by as much as 50 times.

Another example of the improvement possible with better casting practices is given in the study by Nyahumwa et al. (2001) who tested the fatigue properties of the bottom filled (non-modified) bar castings whose tensile strengths were plotted in Fig. 7.16. Their results are shown in Fig. 7.18 using the Weibull format. As expected, filtering the metal gave a significant improvement in fatigue life. They also HIPed unfiltered castings, which gave the best fatigue resistance.

There is also an interesting study by Wang et al. (2002) at General Motors and their colleagues at Nemak. They presented a case study of the successful pilot plant development of an engine block, which experienced quality problems after it went into production. A detailed investigation then began, and changes were made to the melting and casting practices in order to realize an improvement in fatigue strength.



7.17 Weibull plot for fatigue life of Sr-modified A356 alloy containing different defects (Wang et al., 2001; reproduced courtesy of the Minerals, Metals & Materials Society).



7.18 Weibull plot for fatigue life of 356 alloy castings (maximum applied stress was 240 MPa, $R = 0.1$; Nyahumwa et al., 2001; reproduced with kind permission of Springer Science and Media).

7.10 Conclusion

In this chapter we have tried to establish a scientific basis to evaluate the quality of net-shaped castings. This approach to quality is important, because it allows a foundry engineer or casting user to establish a value for the absolute or relative quality of a casting, and to know whether further improvements are possible.

Experimental information and equations provided show that even small quantities of defects result in a significant loss of ductility and tensile strength. This observation places a special emphasis on maintaining the highest metal quality in order to reduce the presence of oxide films, porosity and brittle intermetallic phases in castings.

The fatigue life of a casting is also strongly affected by the presence of defects. A number of excellent studies have shown that in commercial aluminum castings the fatigue life is usually controlled primarily by the size of the largest pore, or sometimes by the largest oxide film. Significant improvements in fatigue life appear to be possible with improved melt treatment and casting practices.

Solidification rate has an overwhelming effect on the amount and distribution of porosity in a casting, and a significant effect on pore size. This is the primary reason why the fatigue and tensile properties of aluminum alloy castings depend so strongly on freezing rate. Proper grain refinement and modification and good degassing also improve mechanical properties.

It should be noted that the focus of this chapter has been the deleterious effect of defects on casting quality, with the objective of better understanding the melt treatment, metal handling and casting procedures that must be undertaken to produce the highest quality castings. In other words, this analysis was primarily intended to develop a strong scientific case for improving our foundry practices.

Our intent was not to provide an in-depth analysis of the failure mechanisms of metals, or of metal fatigue. The analyses presented were by necessity somewhat simplified. For example, it should be noted that others have taken a different approach to establishing a scientific basis for quality (Tiryakioglu et al., 2009). It is possible that one of these approaches may eventually provide a better understanding of metal failure mechanisms, and how we might reach an 'ultimate' level of casting quality.

And finally, the use of Weibull statistics appears to be an extremely powerful and valuable tool to help us evaluate the quality of castings produced by a specific combination of foundry practices and mold design. Further studies along these lines are strongly encouraged.

7.11 References

- AA, 1990. *Special report on the mechanical properties of permanent mold aluminum alloy test castings*. Washington, DC: Jobbing Foundry Division of the Aluminum Association.
- Anon., 2003. 'The best of matchplate molding,' *Modern Casting*, 93(8): 28–32.

- Boileau, J.M. and Allison, J.E. 2003. 'The effect of solidification time and heat treatment on the fatigue properties of Cast 319 alloy,' *Metallurgical and Materials Transactions A*, 34: 1807–1820.
- Brondyke, K.J. and Hess, P.D., 1964. 'Interpretation of vacuum gas test results for aluminum alloys,' *Transactions of AIME*, 230, 1542–1546.
- Cáceres C.H. and Selling, B.I., 1996. 'Casting defects and tensile properties of an Al-Si-Mg alloy,' *Materials Science and Engineering A*, 220: 109–116.
- Cáceres, C.H. and Wang, Q.G., 1996. 'Dendrite cell size and ductility of Al-Si-Mg casting alloys: Spear and Gardner revisited,' *International Journal of Cast Metals Research*, 9: 157–162.
- Cáceres, C.H., 1998. 'A rational for the quality index of Al-Si-Mg casting alloys,' *International Journal of Cast Metals Research*, 10: 293–299.
- Cáceres, C.H., 2000. 'A phenomenological approach to the quality index,' *International Journal of Cast Metals Research*, 12: 367–375.
- Campbell, J. and Wilkins, P.S.A., 1982. 'New developments in light alloy founding,' Institute of British Foundrymen, 79th Annual Conference, Brighton, 17–18 June 1982, 250–253.
- Campbell, J., 2003. *Castings*, 2nd edn, pp. 301–305. Oxford: Elsevier Butterworth-Heinemann.
- Campbell, J., 2006. 'Entrainment defects,' *Materials Science and Technology*, 22: 127–145.
- Cardoso, M.I. *et al.*, 2005. *A rational approach to casting – Building quality into the process*. Shape Casting: The John Campbell Symposium of TMS (The Minerals, Metals & Materials Society), Edited by Murat Tiryakioğlu and Paul N. Crepeau, pp. 337–346.
- Couper, M.J., Neeson, A.E. and Griffiths, J.R., 1990. 'Casting defects and the fatigue behavior of an aluminum casting alloy,' *Fatigue & Fracture of Engineering Materials & Structures*, 13(3): 213–227.
- Davidson, C.J., Griffiths, J.R., Badiali, M. and Zanada, A., 2000. 'Fatigue properties of a semi-solid cast Al-7Si-0.3Mg-T6 alloy,' *Metallurgical Science Technology*, 18(2): 27–31.
- Davidson, C.J., Griffiths, J.R. and Machin, A.S., 2002. 'The effect of solution treatment time on the fatigue properties of an Al-Si-Mg Casting alloy,' *Fatigue & Fracture of Engineering Materials & Structures*, 25: 223–230.
- Drouzy, M., Jacob, S. and Richard, M., 1980. 'Interpretation of tensile results by means of a quality index,' *AFS International Cast Metals Journal*, 5: 43–50.
- Edelson, B.I. and Baldwin, W.M., 1962. 'The effect of second phases on the mechanical properties of alloys,' *Transactions of the ASM*, 55, 230–250.
- Fang, Q.T. and Granger, D.A., 1989. 'Porosity formation in modified and unmodified A356 alloy castings,' *AFS Transactions*, 97: 989–1000.
- Green, N.R. and Campbell, J., 1994. 'Influence of oxide film filling defects on the strength of Al-7Si-Mg alloys castings,' *AFS Transactions*, 102: 341–347.
- Griffiths, J.R., 2003. CSIRO, Kenmore, Australia, private communication, 2003.
- Kennedy, S., 2001. *Aluminum melting and metal quality processing technology for continuous high quality castings*. 6th International Conference on Molten Aluminum Processing of the American Foundry Society, Des Plaines, IL, pp. 2–17.
- Miguelucci, E.W., 1985. 'The Aluminum Association cast alloy test program: Interim report,' *AFS Transactions*, 93: 913–916.
- Nyahumwa, C., Green, N.R. and Campbell, J., 1998. 'Effect of mold-filling turbulence on the fatigue properties of cast aluminum alloys,' *AFS Transactions*, 106: 215–223.

- Nyahumwa, C, Green, N.R. and Campbell, J., 2001. 'Influence of casting technique and hot isostatic pressing on the fatigue of an Al-7Si-Mg alloy,' *Metallurgical and Materials Transactions A*, 32: 349–358.
- Oswalt, K.J. and Misra, M.S., 1980. 'Dendrite Arm Spacing (DAS): A nondestructive test to evaluate tensile properties of premium quality aluminum alloy (Al-Si-Mg) castings,' *AFS Transactions*, 88: 845–862.
- Rooy, E.L. and Fischer, E.F., 1963. 'Control of aluminum casting quality by vacuum solidification tests,' *AFS Transactions*, 76: 237–240.
- Runyoro, J.S., Boutorabi, S.M.A. and Campbell, J., 1992. 'Critical gate velocities for film forming alloys,' *AFS Transactions*, 100: 225–243.
- Sigworth, G.K. and Cáceres, C.H., 2004. 'Quality issues in aluminum net shape castings,' *AFS Transactions*, 112: 373–386.
- Sigworth, G.K., 2008. 'The modification of Al-Si casting alloys: Important practical and theoretical aspects,' *International Journal of Metalcasting*, 2(2), 19–41 (2008); also in *AFS Transactions*, 116: 115–139.
- Sigworth, G.K. and Kuhn, T.A., 2009. 'Use of "standard" molds to evaluate metal quality and alloy properties,' *AFS Transactions*, 117: 55–62.
- Tiryakioglu, M., Campbell, J. and Alexopoulos, N., 2009. 'Quality indices for aluminum alloy castings: A critical review,' *Metallurgical and Materials Transactions A*, 40 (6): 802–811.
- Wang, Q. G., Apelian, D. and Lados, D.A. 2001. 'Fatigue Behavior of A356-T6 Aluminum Cast Alloys – Part 1: Effect of Casting Defects,' *Journal of Light Metals*, 1: 73–84.
- Wang, Q.G., Crepeau, P.N., Gloria, D. and Valtierra, S. 2002. *Improvement of fatigue strength in aluminum castings*. Proceeding from the 2nd International Aluminum Casting Technology Symposium of the ASM International, 7–9 October 2002, Columbus, OH, pp. 209–218.
- Wang, Q.G., Crepeau, P.N., Griffiths J.R. and Davidson, C.J., 2005. *The effect of oxide films and porosity on fatigue of cast aluminum alloys*. Shape Casting: The John Campbell Symposium of The Metals Society, Warrendale, PA, pp. 205–214.
- Wang, Q.G. and Jones, P.E., 2007. 'Prediction of Fatigue Performance in Aluminum Shape Castings Containing Defects,' *Metallurgical and Materials Transaction B*, 38: 615–621.
- Whaler, K.R., 1995. Stahl Specialty Company, Kingsville, Missouri, private communication.
- Whaler, K.R., 2003. Stahl Specialty Company, Kingsville, Missouri, private communication.

Case studies in aluminium casting alloys

J.A. TAYLOR and D.H. StJOHN, CAST CRC, The University of Queensland, Australia and M.A. EASTON, CAST CRC, Monash University, Australia

Abstract: The case studies presented in this chapter are examples where fundamental knowledge is applied to solve casting problems or to improve understanding of the behaviour of aluminium casting alloys when used in commercial casting processes. Each case study was initiated by an alloy producer, master alloy supplier or caster of aluminium components. The case studies illustrate the impact of a range of factors on casting quality and include the effect of: alloy specification range on microstructure and tensile properties; impurities such as iron on microstructure, defects and properties; grain refinement on defect formation; and excess titanium on foundry alloys.

Key words: aluminium, casting alloys, grain refinement, modification, alloy specification, casting defects.

8.1 Introduction

The issues associated with the casting of aluminium casting alloys to produce complex shaped castings or direct chill cast products, such as extrusion billet, are related to the effect of casting process parameters, casting design and alloy chemistry on the quality of the castings produced. Quality is defined by the reliability of the mechanical and physical properties achieved, and these properties are controlled by the microstructure, including the amount, size and distribution of secondary phases, intermetallics and defects, such as porosity and hot tears, and post-processing, such as heat treatment.

The case studies described in this chapter have been selected to illustrate the impact of a range of factors on casting quality. The factors addressed are as follows:

- The effect of the alloy specification range on microstructure and tensile properties.
- The effect of impurities such as iron on microstructure, defects and properties.
- The effect of grain refinement on defect formation.
- The effect of excess titanium on the grain refinement and properties of foundry alloys.
- Selecting the right master alloy for modification and grain refinement in terms of effectiveness and cost optimisation.

It will be shown that one size does not fit all for the range of aluminium alloys and casting conditions that can be used. Often it is a case of selecting casting

parameters to achieve the best compromise and one case study provides a good example of compromise in dealing with the interaction between alloy chemistry and casting conditions.

8.2 The effect of the alloy specification range on microstructure and properties

This case study arose due to the desire of a major metal producer to understand the effect of changes in alloy chemistry within the specification limits. Alloys are typically designated by codes with particular specifications that describe the acceptable content ranges (minimum and maximum) of each alloying element (major and minor) and the acceptable upper limits for various impurity elements. These codes vary according to country of origin, although they tend to be similar, though not always identical, within particular alloy types and families. For example, US Aluminum Association alloy A356 (nominally Al-7%Si-0.3%Mg) is essentially identical to Australian alloy code AA601 and British Standard designation LM25. In this case, the composition specifications are quite tight and the alloys are often made of primary sourced ingot with low impurity levels. Some other work-horse casting alloys, such as US Aluminum Association A380 (nominally around Al-8.5%Si-3.5%Cu; equivalent to Australian alloy CA313 and British Standard LM24) have wider composition specifications and much higher acceptable impurity levels and are usually made from secondary/recycled alloy sources.

Once alloy composition windows are broadened, it opens up the possibility for a considerable range of actual compositions to be produced which still meet the specification. However, there is a trade-off that occurs in such instances, namely the processability, properties and performance of the alloy can also vary along with this composition variability. The following examples illustrate this.

8.2.1 Primary sourced alloys for high performance castings

Alloys of the A356 and A357 types (US Aluminum Association codes; both containing approximately seven per cent Si but with 357 richer in Mg than 356) are age hardenable and are typically employed to make castings with superior mechanical properties, such as automotive wheels. These alloy codes, however, have several sub-types that tend to vary in terms of either the acceptable iron (Fe) impurity level or the type of eutectic modifier added.

For critical applications, it is important for an alloy to reliably meet minimum property levels. However, a detailed study (Taylor et al., 2000) of the effect of varying the Mg content from 0.3% to 0.7% (i.e. covering the whole 356/357 alloy range) and the Fe content from 0.05% to 0.20% (a broad primary metal range) demonstrated that considerable variability in mechanical properties is possible.

Firstly, it should be noted that for any given heat treatment regime and solidification rate (controlling SDAS – Secondary Dendrite Arm Spacing), the effect of increasing Mg content is to:

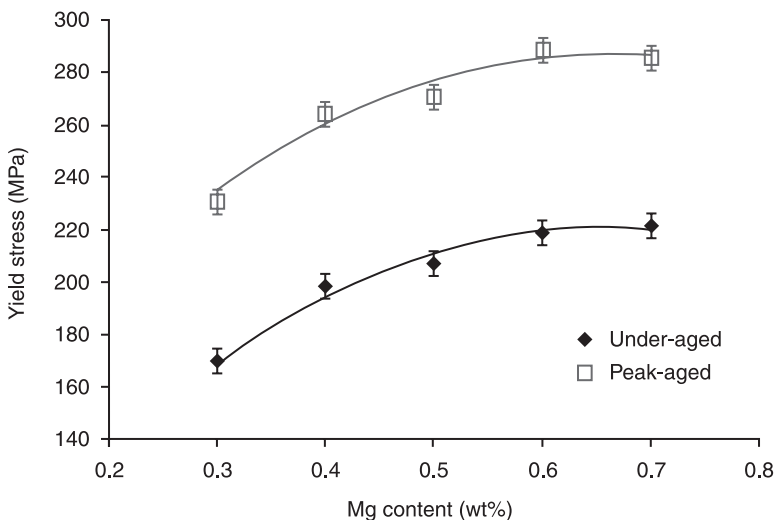
1. raise the yield strength (YS) and
2. increase the work hardening rate, following yielding.

While the effect of increasing Fe content (at any given Mg content) is to:

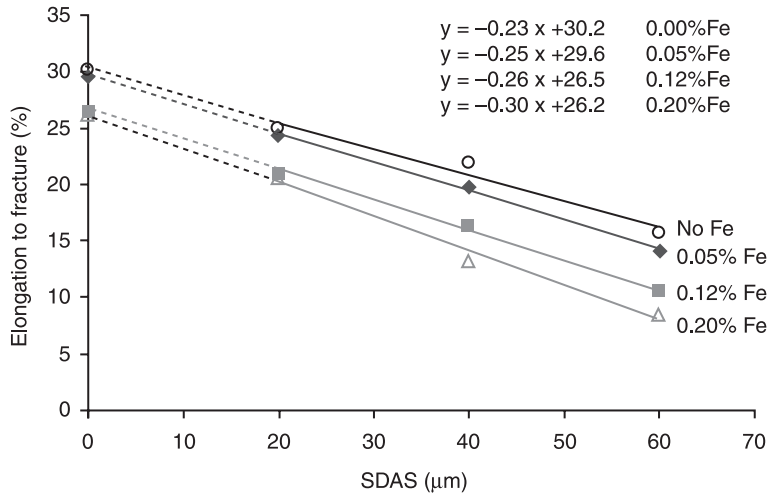
3. decrease the ductility or elongation to fracture, E or s_p , and as a consequence of a fixed work-hardening rate, also to decrease the ultimate tensile strength (UTS).

Effects 1 and 3 are represented in Fig. 8.1 and 8.2, respectively. The data points for YS (Fig. 8.1) are the mean values for a large number of tensile tests for each condition, while the data points for elongation (Fig. 8.2) are the best performing samples from each particular condition (e.g. 0.3% Mg, under aged).

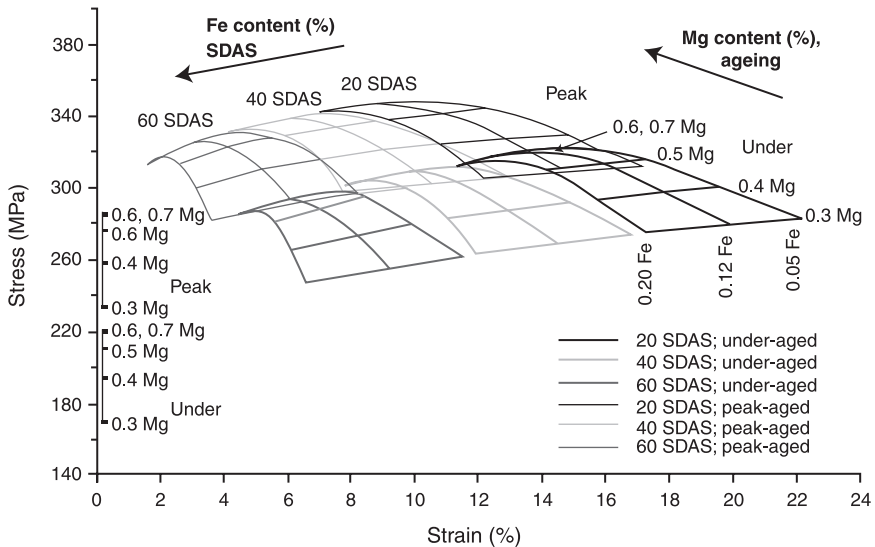
Considering the full test data set, the best fits for each condition (as for examples shown in Fig. 8.1 and Fig. 8.2) can be determined. Those determinations can then be used to develop a predictive matrix for best case expectations (Fig. 8.3). Of course, it must always be borne in mind that the actual behaviour of any individual test bar (or an individual casting for that matter) is strongly affected by other factors such as the presence of casting defects, for example oxide inclusions, porosity, shrinkage defects and hot tears, each of these tending to reduce ductility and UTS, sometimes to the point of fracturing before yielding occurs.



8.1 Mean tensile yield stress versus Mg content of A356/357 alloy samples for two different ageing conditions (Taylor et al., 2000).



8.2 Best examples of elongation to fracture of A356 alloy samples (0.3% Mg content) versus SDAS for an under-aged condition (Taylor et al., 2000).



8.3 Graphical plot showing predicted values of yield stress (two scales at left) and the fracture points (UTS and s_r , represented by the six grid sets) for various SDAS and heat treatment conditions (see legend). All grids are indexed in the same manner as the heavy dark line grid (20 μm SDAS, under-aged) at the right hand side. Note that the predicted curves for the 0.6% and 0.7% Mg alloys are almost identical and therefore inseparable at this scale (Taylor et al., 2000).

So, if a particular set of tensile properties is required, Fig. 8.3 can be used to predict the best expected mechanical properties for both peak-aged and under-aged alloys when minimal casting defects are present. The plot only applies to Al-7% Si alloys with a 0.3–0.7% Mg range, 20–60 μm SDAS range and Fe content varying from 0.05% to 0.20%.

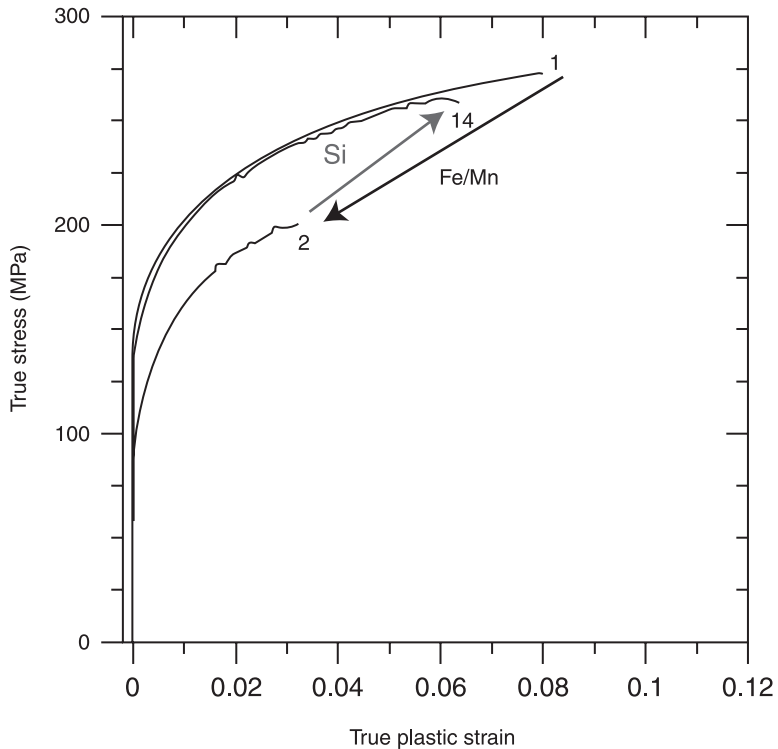
8.2.2 Secondary sourced alloys for general casting applications

Widely used alloys of the US Aluminum Association A319/A380 types contain highly variable levels of Si, Cu and Mg (common alloying elements) and Fe, Mn, Cr, Ni, Zn, Sn and Pb (typical impurity elements). The impurities arise from the secondary/recycled metal supply chain. In general, though not always, the cost of aluminium alloy ingot decreases as the level of these impurities increases; certainly there is a cost differential between primary-based alloys and secondary-based alloys. Thus, there is a cost driver in foundries to be able to use lower grade alloys if possible, providing property specifications can still be met for the castings.

It would be convenient if we could assume that as Fe, for example, is increased that performance always decreased. However, as will be shown below, this is not always the case.

In the Al-Si-Cu-Mg type of alloys, it has been observed (Cáceres et al., 2003; Cáceres and Taylor, 2006) that a low Si alloy (say 4.5% Si) containing both Cu and Mg and with a low Fe content, $\sim 0.2\%$ Fe, exhibits reasonably good mechanical properties, i.e. YS, ductility and tensile strength, as well as Quality Index (QI) (Drouzy et al., 1980) (an empirical combination of ultimate tensile strength and ductility/elongation to fracture, $\text{QI} = \text{UTS} + 150 \log E$; the principles behind the QI are explained in more detail in Chapter 7). This is indicated by curve/point 1 in Fig. 8.4 and 8.5. If the Fe content of this alloy is then increased to 0.5%, even with 0.25% Mn present, an element typically added to negate the deleterious effects of Fe, the mechanical properties of the alloy drop severely, as demonstrated by curve/point 2 in Fig. 8.4 and 8.5. However, if this second alloy then has its Si content increased to nine per cent (while keeping other elements, including Fe and Mn, the same) the properties return to almost those of the original low Si, low Fe alloy. See curve/point 14 in Fig. 8.4 and 8.5.

This ductility recovery phenomenon is remarkable, and has significant ramifications for broad specification complex alloys, such as A319 and A380, where the acceptable Si content range can often be as wide as two per cent, e.g. 7.5–9.5% for A380.1. What is the implication of this? Take, for example, a situation in which there is a higher than normal Fe content but lower than normal Si content in the incoming ingot stock. In this case, there is room for an upward Si adjustment (while still complying with the chemical specification), and therefore improved mechanical properties in the final product may be achievable.

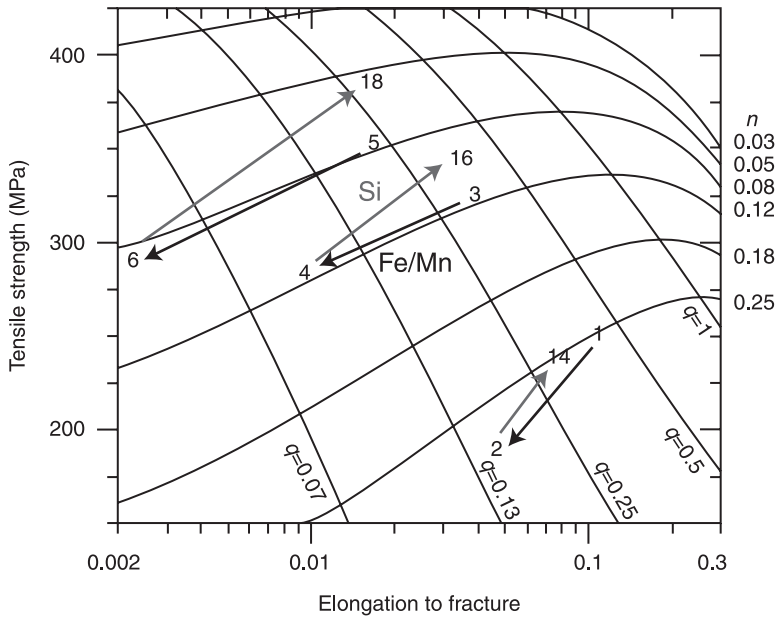


8.4 Example of tensile flow curves for three alloy compositions:
 1 – Al-4.5Si-1Cu-0.1Mg-0.2Fe; 2 – as for 1 but with 0.5Fe, 0.25Mn;
 14 – as for 2 but with 9Si (after Cáceres et al., 2003).

The metallurgical reasons for this ductility recovery phenomenon are not yet fully clear, but considerable research work has gone into understanding it so far. It appears that in the presence of significant Cu content (at least one per cent), increasing the Si content creates a situation in the solidifying casting where the final pools of liquid to solidify (highly enriched in Cu, Fe and Mn) are more dispersed and fragmented than those that form in lower Si alloys (which instead tend to be more connected and continuous). This solidification situation leads to a refinement and dispersal of the brittle intermetallic phases, e.g. Al_2Cu , $\beta\text{-Al}_5\text{FeSi}$ and $\alpha\text{-Al}_{15}(\text{Fe,Mn})_3\text{Si}_2$, in the higher Si alloy, that would otherwise contribute to poor ductility.

8.3 An impurity that reduces castability and increases casting defects

From time to time, foundries encounter casting problems where a particular batch of metal (e.g. a bundle of ingots) appears to be the culprit despite the batch being

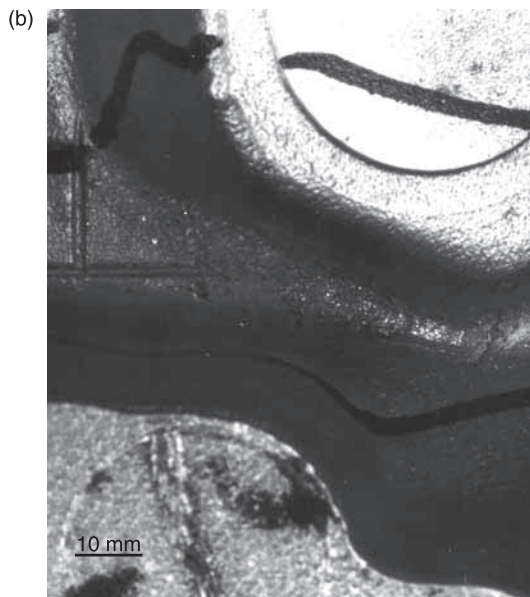
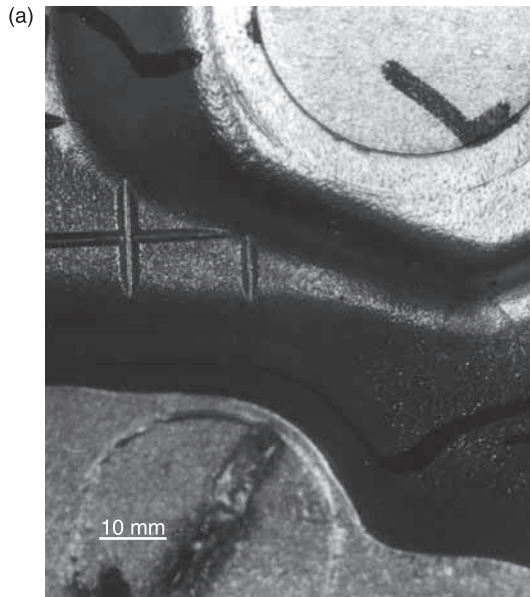


8.5 Pseudo-Quality Index chart in which three similar alloy sets with different Si, Cu and Mg levels (including set shown in Fig. 8.4) show the same recovery of ductility obtained by increased Si content at high Fe. Note that q is a normalised measure of QI and $q = 1$ is the ideal case where samples neck before fracture (after Cáceres et al., 2003).

within the required alloy specification. In such cases, it is not easy to determine which alloying element(s) or impurities are actually responsible for the problem. One such rogue element is now known to be iron (Fe). This element adversely affects shrinkage porosity defects. However, the level at which Fe starts to present problems in practice is both alloy dependent and product dependent. It should be noted that contrary to the above, Fe is actually acceptable at quite high levels (less than one per cent) in high pressure die cast alloys and products.

An interesting situation arose several years ago at an Australian casting plant when it experienced two separate outbreaks of excessive porosity and shrinkage defects on the low pressure die casting (LPDC) production line of automotive cylinder heads, using an A355 type alloy (nominally Al-5%Si-1.2%Cu-0.5%Mg with max. 0.55% Fe). The first instance occurred across the entire casting line and the second from only one casting machine. In both cases, reject rates for 'leakers' (i.e. fluid leak paths created by continuously connected porosity throughout the casting thickness usually occurring at known problem locations) increased by more than an order of magnitude. In this particular product, the leaker defect was evidenced by a 'sink' on the surface between two thicker regions (Fig. 8.6).

In the first instance, a new batch of secondary alloy ingot (with 0.52% Fe content) had been added to the main furnace immediately prior to the defect



8.6 Defect prone region of the cylinder head: (a) without shrinkage defect present, and (b) with shrinkage defect present. In (a), the surface cross-hatching is complete near the valve stem boss, whereas in (b) the cross-hatching is incomplete (images courtesy of J.A. Taylor).

outbreak across several casting machines as they required refilling. This batch was suspected as being the main cause, despite the chemical analysis being within the A355 alloy specification (i.e. 0.55% Fe max.). Since the normal melt mix ratio used by the company had been 45% primary ingot, 45% secondary ingot and ten per cent in-house returns, cylinder heads were rarely produced with iron levels as high as these maximum secondary metal levels. Primary metal with iron levels of typically 0.1–0.2% acted to dilute the secondary metal and this resulted in overall iron levels in the melt of approximately 0.3%. The suspect molten charge was removed from the melting furnace and the holding pots. A new charge was prepared with another batch of secondary ingots from the same supplier (containing 0.38% Fe content). When cylinder heads were cast using this new alloy charge, the problem defects no longer occurred. The remaining stock of suspect secondary metal ingots were later added to another furnace charge, casting of cylinder heads resumed and the ‘leaker’ defects immediately returned, causing high-product reject rates.

At another time, the same type of casting defect was observed on the cylinder heads being produced from a single LPDC machine. After checking the process conditions on this occasion, it was discovered that severe erosion of the cast iron riser stalk in the casting furnace had occurred. This had resulted in an increased iron level in the melt. Iron levels for the product typically averaged between 0.25% and 0.35%. In this particular case, the iron level had risen steadily up to a maximum of 0.54% (close to the 0.55% upper limit for secondary ingot). After the degraded riser stalk had been replaced, casting of the cylinder heads resumed. As the cast progressed, the high-Fe metal was gradually diluted with additions of known low-Fe metal. As the dilution progressed (back to normal iron levels of approximately 0.35%), it was observed that the reject rate for the defect gradually returned to the normal low level.

These two observations strongly suggested that increased Fe content in the alloy was the primary cause of the defects and high reject rates; however, this appeared to make little sense. It was well known from other manufacturers that other alloys of the Al-Si-Cu-Mg family (e.g. A319 alloy) used to cast automotive cylinder heads did not show the same propensity to form serious shrinkage defects at these Fe levels. In fact, they appeared to tolerate Fe at considerably higher levels than the A355 alloy.

A detailed laboratory-based investigation (Taylor et al., 1999a, 1999b) ensued to explore the effect of iron on castability and porosity formation. At the conclusion of this study, it was found that increasing Fe levels did indeed contribute towards increased shrinkage porosity but that this deleterious effect was strongly dependent on the Si content of the alloy, and that it was more prone in poorly fed regions of castings, i.e. hot-spots.

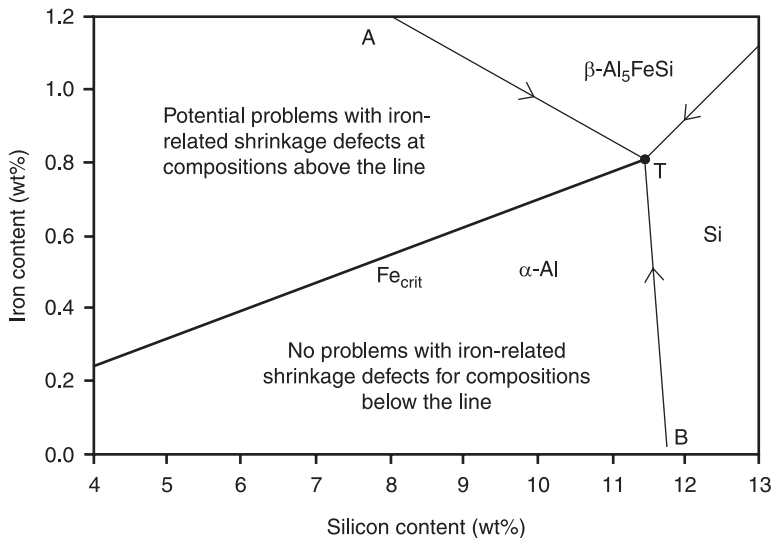
It had long been suspected that increasing the β -Al₅FeSi phases (occurring as platelets but appearing as needles in 2D images) was problematic for castability as well as being bad for mechanical properties; however, it was not clear whether

number, size, amount or location of these intermetallic particles was the most important factor.

The case study presented in this chapter provided a vital clue to the puzzle. It enabled the identification of an alloy-dependent critical iron level, Fe_{crit} , that was based on the Si content and which could be readily determined from the ternary Al-Si-Fe phase diagram (Fig. 8.7). The critical iron content for a given alloy's Si content was found to be that which resulted in solidification (assuming Scheilian behaviour; i.e. no diffusion in the solid, full diffusion in the liquid) proceeding directly from primary α -Al solidification to the formation of ternary eutectic (Al-Al₅FeSi-Si) at the ternary eutectic point, T (the bold line in Fig. 8.7). Any Fe content above Fe_{crit} would therefore result in the formation of coarser Al₅FeSi as solidification was forced to proceed along the binary Al-Al₅FeSi eutectic valley (line AT) before arriving at point T.

For the case of A355 alloy (approximately five per cent Si) used by our example foundry, the critical Fe content is approximately 0.35%, thus explaining quite clearly why problems were encountered as Fe contents rose above that level.

It was observed that below the critical iron content, Fe_{crit} , overall porosity levels were largely restricted, even in hot spots of castings, however, once Fe_{crit} is



8.7 A simplified liquidus projection of the Al-Fe-Si ternary phase diagram showing the calculated line (bold) that defines the compositions at which the solidification sequence, according to the Scheil equation, proceeds directly from α -Al to the ternary eutectic formation (at point T) without travelling along one of the binary eutectic troughs (either AT or BT). To ensure that serious iron-related shrinkage porosity defects do not occur, compositions below the bold line are best (Taylor et al., 1999b).

exceeded the frequency and intensities of shrinkage-related defects/porosity in hot spot areas increased dramatically. In some cases, minimum levels of porosity/defects were observed at Fe_{crit} . These shrinkage defects can, in thinner cross-sections, easily extend from internal to external surfaces, thus allowing fluid leakage pathways to develop, and the incidence of 'leaker' defects to increase. Remediation of this type of problem can be addressed in various ways:

1. Reduce the iron level below Fe_{crit} .
2. Redesign the casting to minimise the hot spot effect.
3. Increase the content of Fe-neutralising elements, such as Mn, which reduce the amount of coarse $\beta-Al_5FeSi$ phases that form.

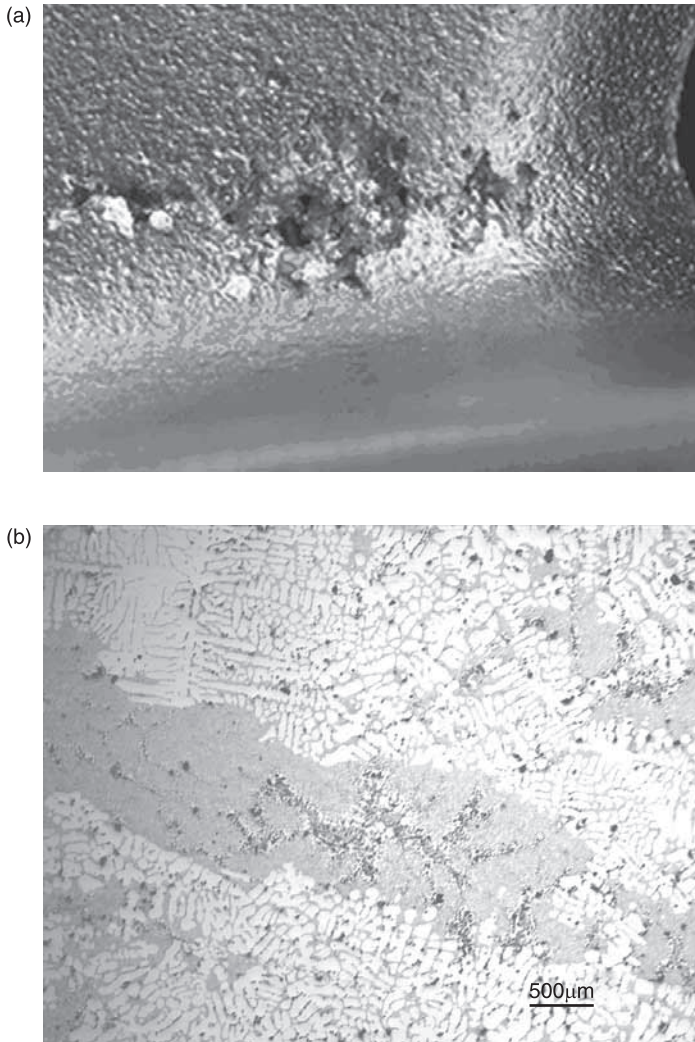
It should be noted that the effect of exceeding Fe_{crit} can be less marked and even masked in alloys containing higher levels of Cu and/or Mn than A355. Hence, some alloys may appear tolerant of high Fe levels. However, as a general rule-of-thumb, keeping Fe content below the Fe_{crit} level for that particular Si level is a prudent measure to employ in order to ensure optimum castability.

8.4 The effect of grain refinement on defect formation

Grain refinement is generally accepted to be important for obtaining a high-quality casting (Sigworth and Wang, 1993). Fine grain sizes are known to reduce hot tearing susceptibility, improve mechanical properties, disperse and refine porosity (Roy et al., 1996a, 1996b; Tynelius et al., 1993) and improve feeding by delaying dendrite coherency (Chai et al., 1995). Presented here is a contrary example where grain refining was found to increase the reject rate of wheel castings produced by an after-market wheel manufacturer (Easton and StJohn, 2000). It was thought that the defects (excessive porosity in the spoke-rim junction) were caused by the alloy ingot supplied to them by the alloy producer. The alloy supplier engaged our research team to determine what was actually causing the porosity defects.

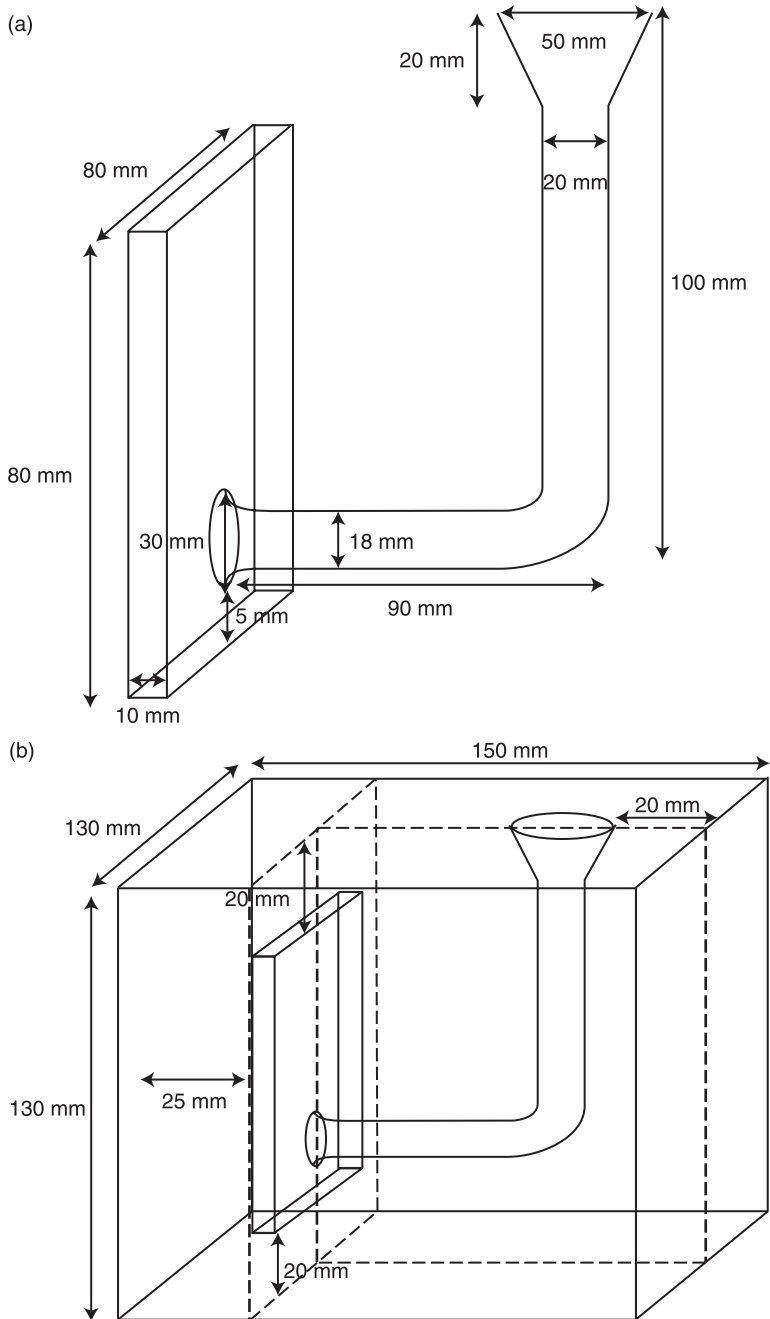
The wheels were cast from alloy A356 (Al-7Si-0.3Mg) and it was found that the addition of Ti and more dramatically, the addition of grain refining master alloy, Al-5Ti-1B, increased the amount of porosity near the spoke-rim junction. This porosity was found to often come to the surface (Fig. 8.8) increasing the likelihood of a loss of pressure tightness. An interesting observation in the castings where no grain refiner addition was made resulting in a large grain size was a large region or channel of segregated eutectic in the centre of the runners. This segregation of eutectic was not observed in the grain refined castings.

To investigate this phenomenon more closely a laboratory scale mould was developed to simulate the spoke rim-junction in an industrial casting. It was based on a runner feeding a vertical plate (Fig. 8.9), so that feeding through a solidifying channel at various grain refiner additions could be assessed. The casting was designed using MAGMASOFT® and various casting parameters were trialled.

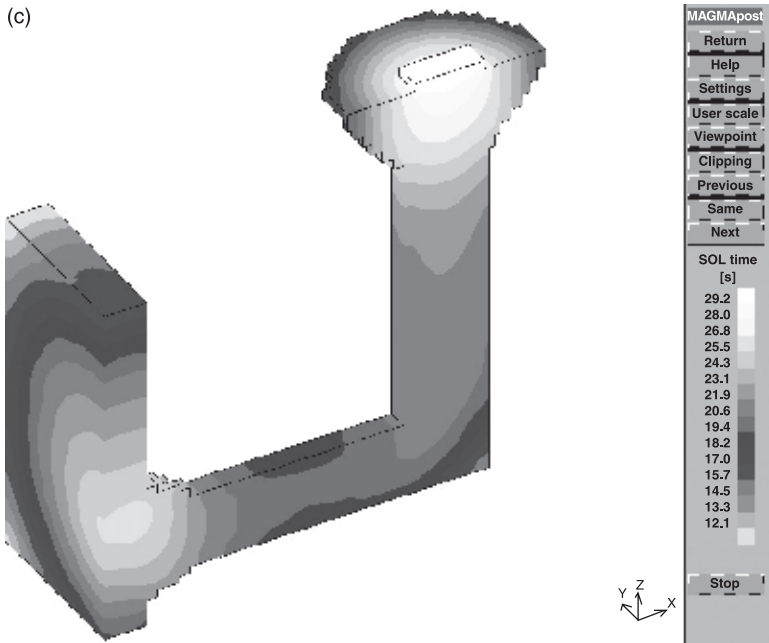


8.8 (a) Interconnected macro-porosity at the spoke-rim junction, the most common cause of rejection directly after casting for a grain refined wheel casting produced industrially. (b) Segregated eutectic in the centre of a spoke for an alloy that is not grain refined (Easton and StJohn, 2000).

Although the wheel spoke cross-sections were closer to a semi-ellipse than a circle, a cylinder of approximately the same cross-sectional area was used to model the spoke. The vertical plate was of a thickness similar to the rim of the wheel casting. The runner (simulating the spoke) was designed to enter the plate (simulating the rim) through a small tapered region near the bottom of the plate. The runner was fed by a down sprue which was flared out at the top. The runner



8.9 Schematics of the mould design: (a) the dimensions of the internal cavity; (b) the dimensions of the die; (c) MAGMASOFT® modelling showing the solidification time contours during solidification (Easton and StJohn, 2000).

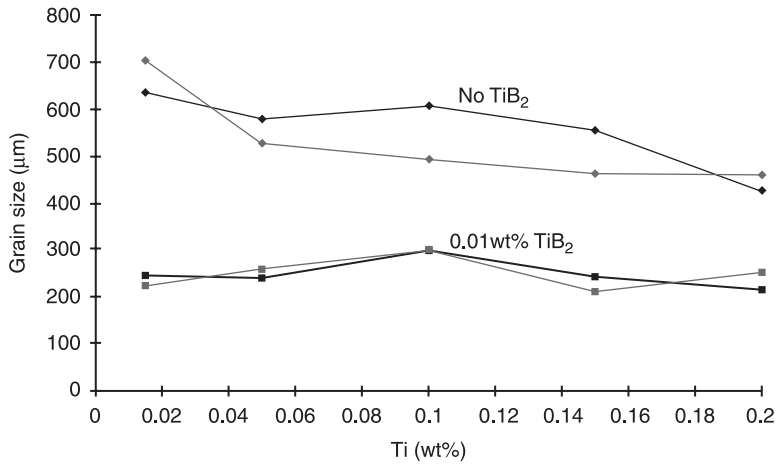


8.9 Continued.

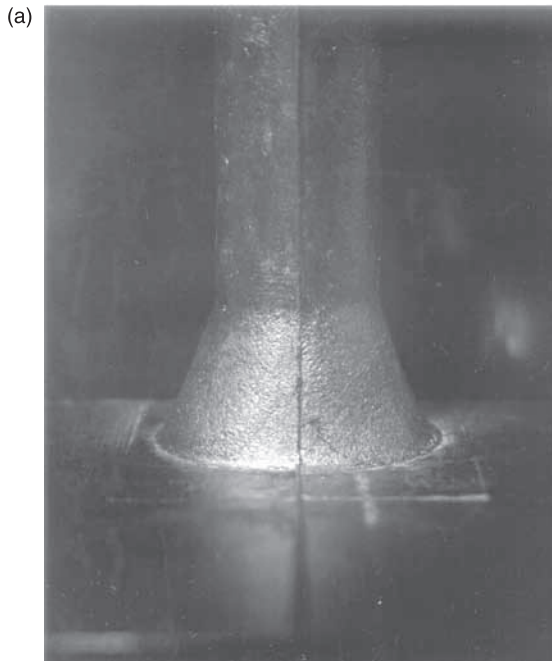
was designed to enter the casting so that it would move the hot spot from the centre of the plate to this junction. The size of the runner and the dimensions of the tapered section were critical for this to occur. The design did not contain a riser as the industrial wheel casting did not. Figure 8.9(c) shows the solidification times that are predicted by the MAGMASOFT® solidification package for the experimental die showing a hot spot in the tapered region of the casting.

Alloy 356.1 (6.8Si, 0.067Fe, 0.35Mg, 0.016Ti) was cast into the die with and without the addition of 0.01 wt% TiB_2 particles via an Al-3TiB₂ master alloy and with Ti additions up to 0.2% via an Al-6Ti master alloy to generate a range of grain sizes. Interestingly, it was found that the addition of Ti had very little effect on the grain size while the addition of the TiB_2 particles refined the grain size substantially (Fig. 8.10). This will be discussed further in the next section.

Grain refinement was found to have a number of effects on the casting quality. Grain refinement appeared to reduce the fluidity of the alloy, as the top of the plate was not as well filled. Positively, it reduced the propensity of fine cracks (hot tears) where the runner was joined to the plate. However, the most interesting observation was that when grain refined there was a large amount of slumping near the spoke-rim junction (Fig. 8.11). As observed in the industrial castings, a segregated eutectic region was not found down the centre of the spoke. Hence, it appeared that the main reason for slumping in the grain refined castings was that it was more difficult to feed a hot spot through a grain refined mushy zone than one with large grain sizes and consequently larger feeding channels.

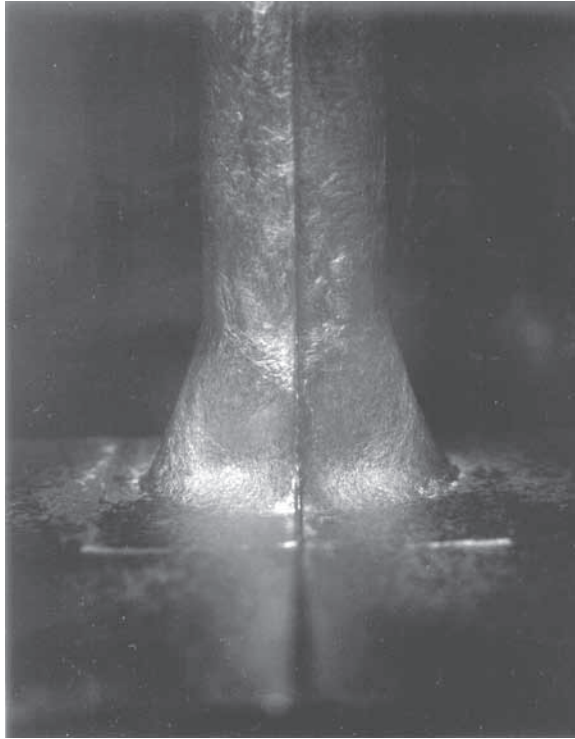


8.10 A comparison of the grain sizes observed in the experimental die (taper and runner) for various grain refiner additions to A356.1 (Easton and StJohn, 2000).



8.11 (a) The tapered region in an A356 casting without the addition of grain refiner. (b) The tapered region for the alloy of composition 356-0.01TiB₂-0.2Ti, showing external shrinkage (slumping of the surface) (Easton and StJohn, 2000).

(b)

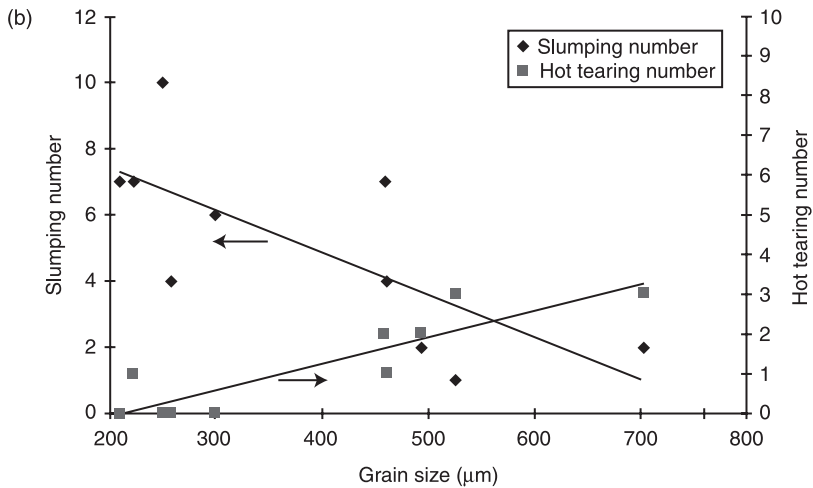
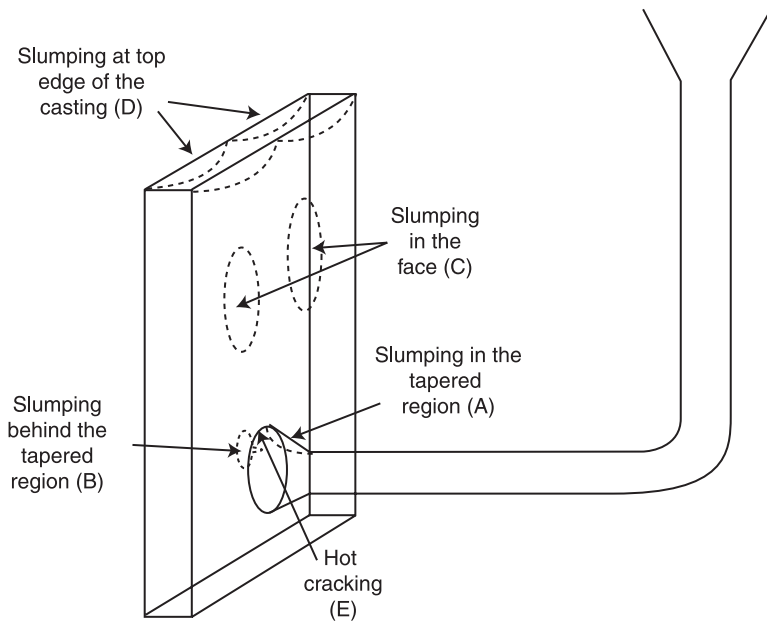


8.11 Continued.

At four points on the castings, the slumping was assessed and given a rating between 0 and 3 (Fig. 8.12a) where 0 meant that there was no observable slumping and 3 meant severe slumping. These were summed to give a rating for the external slumping for the casting. Hot tearing was also given a rating between 0 and 3. The ratings for slumping and hot tearing are plotted against the grain size in Fig. 8.12(b). It is observed that increasing the grain size reduces the amount of slumping but increases the amount of hot tearing in the castings. Hence, there is a trade-off between the grain size and which defect is more prominent.

In the actual wheel castings, slumping was not observed but rather the formation of porosity in the region of the spoke-rim junction. To improve the simulation accuracy of the laboratory casting the molten metal was poured through a coarse gauze as was done in the foundry. This method would introduce additional oxide films entrained in the melt. Interestingly, when the melt was poured through the gauze no surface slumping occurred and instead there was a substantial amount of internal porosity and an increase in the amount of hot tearing observed. Hence, even with relatively turbulent pouring conditions, the alloy did not nucleate porosity as easily as when oxides are artificially generated. This result showed

(a) Defects



8.12 (a) The location of the defects that were observed in the experimental castings. Slumping indicates the locations where external shrinkage occurs. (b) Graphical representation of grain size versus the severity of external shrinkage and hot tearing observed in the experimental castings (Easton and StJohn, 2000).

that oxides are definitely associated with porosity formation, but the observation indicates that fresh oxides may be more problematic than old oxide films (Campbell, 1996). Also, it is surprising that turbulent pouring without the gauze did not generate sufficient fresh oxide films to cause the formation of porosity in the constrained feeding condition of the hot spot. The foundry's casting conditions and those used in these simulation experiments are well outside John Campbell's rules for ensuring a high-quality casting (Campbell, 1997).

This case study showed that grain refinement does not always lead to a reduction in the reject rate of a casting. When feeding into an isolated hot spot, it appears that grain refining the alloy makes the feeding channels much more tortuous leading to a reduction in the ability of the eutectic liquid to feed the hot spot. This leads to a shrinkage defect of some sort. If freshly formed oxides are not present then surface slumping is observed. If fresh oxides are generated during casting then internal porosity is generated. However, a large grain size leads to an increase in the hot tearing susceptibility of the alloy requiring a compromise to ensure acceptable casting quality is achieved. This example, as much as anything, shows how important it is to design castings to minimise the size and severity of hot spots in order to obtain a good quality casting.

8.5 The effect of excess titanium on foundry alloys

This study picks up a theme from the previous case study where Fig. 8.10 shows that the addition of Ti solute has little effect on the grain size, while the addition of TiB_2 particles caused a substantial decrease in grain size. There have been numerous studies in Al-Si foundry alloys to support this observation that the addition of Ti solute has little effect on the grain size while the addition of boride-containing particles refines the grain size substantially (Easton and StJohn, 2000; Easton and StJohn, 2001b; Guzowski et al., 1987; Johnsson, 1994; Sigworth et al., 2007; Sigworth and Guzowski, 1985; Spittle et al., 1997; Spittle and Keeble, 1999; Tøndel et al., 1993; Wu et al., 1981). In fact, there is a family of grain refiners that have been developed, especially for Al-Si alloys, based on this understanding (Bondhus et al., 1999; Sigworth and Guzowski, 1985; Tøndel et al., 1993).

Despite the development of special grain refiners, Ti additions up to 0.2% are routinely made to Al-Si foundry alloys probably because, in the past, it has been thought that it was needed to grain refine these alloys (Sigworth et al., 2007). Since Ti additions are expensive (0.2Ti can increase the cost of the alloy by above \$10/tonne Al depending upon the cost of Ti at any one time; Easton and StJohn, 2007), significant savings to the cost of the alloys can be made if it is removed. A metal supplier wanted the role of excess titanium to be clearly established so that foundries would have confidence in using low titanium alloys. There are two issues that need consideration: one is how low can the Ti addition go as there is some anecdotal evidence (Pearson and Cooper, 1999) and a little experimental

evidence (Young et al., 1991) that the boride-based grain refiners require some Ti solute in the alloy to work effectively. The other issue is whether decreasing the Ti additions affects the properties of the alloy.

It has been observed in wrought alloys that a Ti:B (wt:wt) ratio of less than 2.2 (i.e. there is excess B in the alloy above that required to form TiB_2) leads to a large grain size (Easton and StJohn, 2001a), and it is when Ti is added in excess of that required to form TiB_2 that effective grain refinement occurs. An explanation is that the excess boron combines with other elements in the melt to coat the TiB_2 particles with phases that are less effective nucleant substrates. While B additions have been found to grain refine alloys with low Ti contents, it may be that this grain refinement is inconsistent and depends upon the other alloying elements that may be present in the melt.

To investigate this, three Al-7Si-0.3Mg alloys with different impurity contents and vanadium contents were chosen for the experiments. One was a commercial alloy (A356CM), one was alloyed from commercial purity aluminium, A170 (A356CP), and one was alloyed from high-purity 99.95% aluminium (A356HP). The alloy compositions are given in Table 8.1.

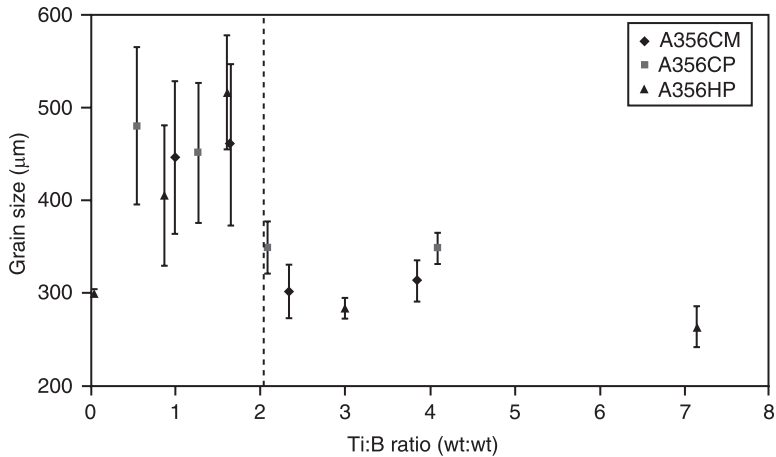
Boron additions were made using Al-4B waffle master alloy to a level of approximately 0.012% B. Four titanium additions were then made using Al-2Ti master alloy made from commercial purity aluminium and 75% Ti AlTab™ tablet to vary the Ti:B ratio.

Figure 8.13 shows that there was a difference in grain size for alloys above and below the Ti:B ratio of two. In general, the grain size was significantly smaller above a ratio of two. Therefore, for a consistent fine grain size to be achieved a Ti:B ratio of greater than two is required. This ratio provides a lower bound on the useful amount of Ti in the alloys. However, if grain refiners with Ti:B ratios close to stoichiometry or with a slight excess of Ti are used then no Ti needs to be added to an alloy for grain refinement purposes.

To determine the effects of Ti and TiB_2 additions on alloy properties alloy A356 with and without the addition of 0.005 wt% Ti of Al-5Ti-1B master alloy and up to 0.12% Ti were sand cast into a die with a chill (Smith et al., 2004). The grain size of the alloys without the addition of the Al-5Ti-1B grain refiner ranged from approximately 800 μm to 600 μm at 0.12Ti. The grain size for all the alloys containing the Al-5Ti-1B grain refiner was around 400 μm .

Table 8.1 Compositions (wt%) of the three Al-7Si-0.3Mg type alloys measured by inductively couple plasma – atomic emission spectroscopy (ICP-AES)

Alloy	Si	Fe	Mg	Zn	Ti	V	B
A356CM	6.67	0.07	0.35	0.04	0.016	0.004	<0.001
A356CP	6.96	0.08	0.36	<0.005	0.007	0.013	<0.001
A356HP	6.22	0.03	0.32	<0.005	<0.005	<0.002	<0.001

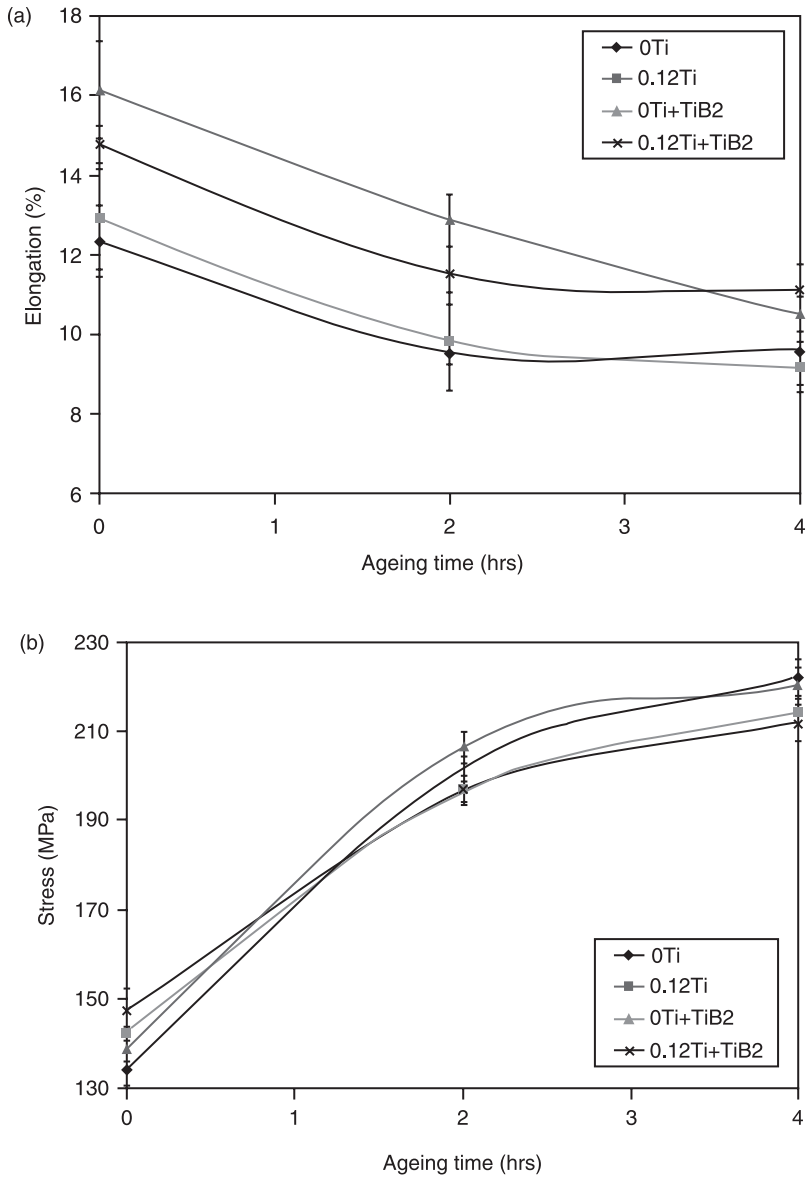


8.13 The grain size plotted against the Ti:B ratio (wt:wt) for each of the A356 alloys. All alloys contain an addition of 0.012%B via an Al-4B master alloy.

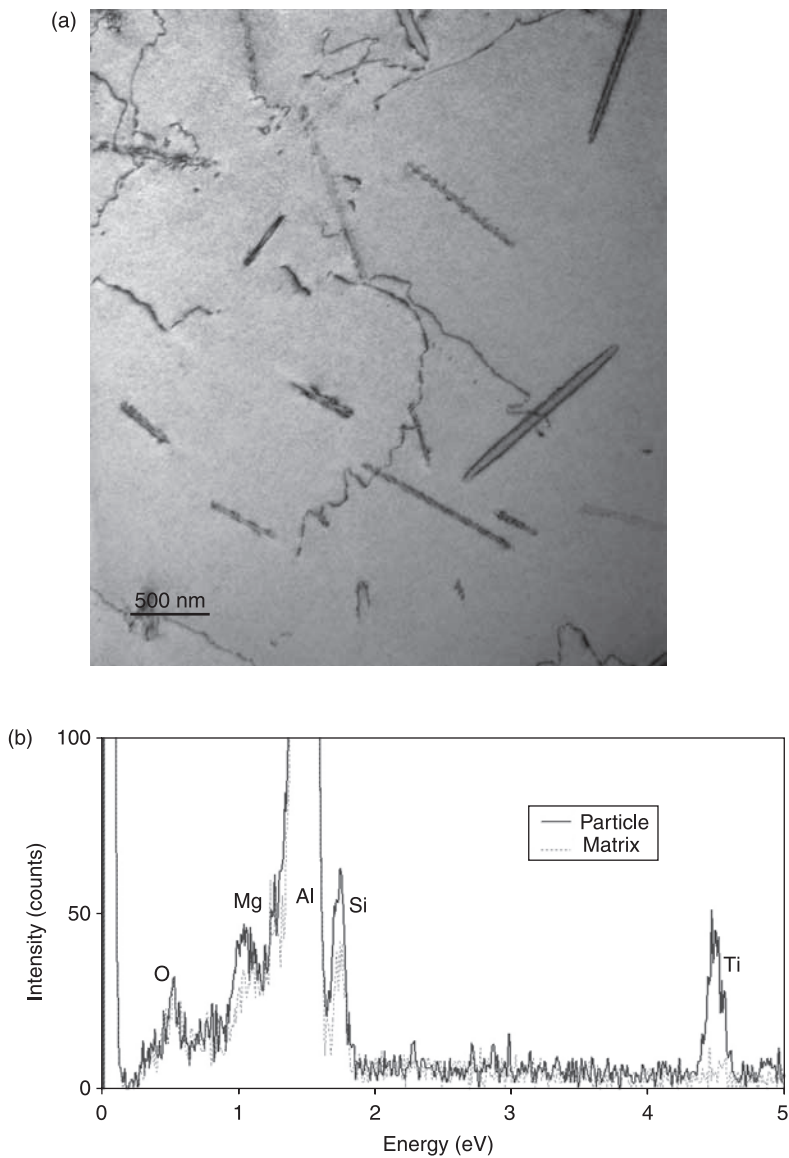
The alloys were solution treated at 540°C for six hours and then quenched in hot water, before ageing. It was found that the alloys containing 0.12Ti had a reduced age hardening response compared to the alloys without Ti (Fig. 8.14a). They also had a reduced elongation at short ageing times, although grain refinement appeared to be more important than a reduction in Ti content to the measured elongation (Fig. 8.14 b).

Transmission electron microscopy (TEM) was used to determine the location of the Ti atoms in the microstructure. Clouds of long needle precipitates which were often hundreds of nanometres in length were unevenly distributed within the α -Al phase (Fig. 8.15a). The EDX spectrum (Fig. 8.15b) showed them to be rich in Ti but also having above background levels of Si and possibly Mg (later unpublished work has suggested that the precipitates only contain Al, Si and Ti). These precipitates may be the reason for the lower age hardening response as they reduce the amount of Si available to form magnesium silicide which is the main strengthening phase formed during age hardening. It is also possible that these precipitates could reduce the elongation in the larger grain size samples at short ageing times although it has not been substantiated directly.

Therefore, the addition of Ti to Al-Si foundry alloys is an unnecessary cost with little benefit in reducing the grain size, although sometimes moderate grain size reductions can be achieved (Pasciak and Sigworth, 2001) probably due to the presence of low levels of Ti-containing nucleant particles in Ti-containing master alloys. The grain size is better controlled by boride-containing master alloys. However, it is important to make sure that there is excess Ti present over that required to form the borides, because excess boron in the alloy may lead to poisoning and a consequent reduction of the grain size.



8.14 Variation in (a) 0.2% yield strength, and (b) elongation to fracture as a function of ageing time at 160°C (Smith et al., 2004).



8.15 (a) Transmission electron micrograph showing rod-shaped particles in 0.12Ti-containing A356 alloy aged four hours at 160°C, and (b) energy dispersive X-ray spectra recorded from a rod-shaped particle and the adjacent matrix phase (Smith et al., 2004).

8.6 Selecting the right master alloy for grain refinement in terms of effectiveness and cost optimisation

To optimise grain refinement there are a number of considerations. The quality and effectiveness of individual grain refiners varies between suppliers (Vainik, 2007), although this will not be commented upon here. However, there are a number of important considerations that guide a high-quality and relatively low-cost grain refining treatment. This study was initiated to determine the scope of potential cost savings from manipulating the make-up of grain refining master alloy additions.

It was shown in the previous section that the addition of Ti solute to foundry alloys has little effect on the grain size and hence is an unnecessary expense. In contrast, low solute wrought alloys can be effectively grain refined by Ti additions (Easton and StJohn, 1999; Easton and StJohn, 2001b; Maxwell and Hellawell, 1975) and substantial cost savings can be obtained by using solute Ti additions to off-set the more expensive rod grain refiner additions (Bäckerud and Vainik, 2001; Easton et al., 2004; Vatne, 1999). This is possible because Ti has a very large growth restriction factor, Q , per unit of solute, i.e. ~ 245 , compared with most other alloying elements which are below ten (Johnsson and Bäckerud, 1996). The most cost-effective combination will depend upon the relative cost of Ti metal and Al-Ti-B grain refiner at the time, but this technique can generally save a significant amount of money in lower solute alloys such as 1000 series, 3000 series and the soft 6000 series alloys (see Table 8.2 and Fig. 8.16) (Easton et al., 2004). The Q values for a particular alloy can be simply calculated using simple parameters from phase diagrams, i.e.

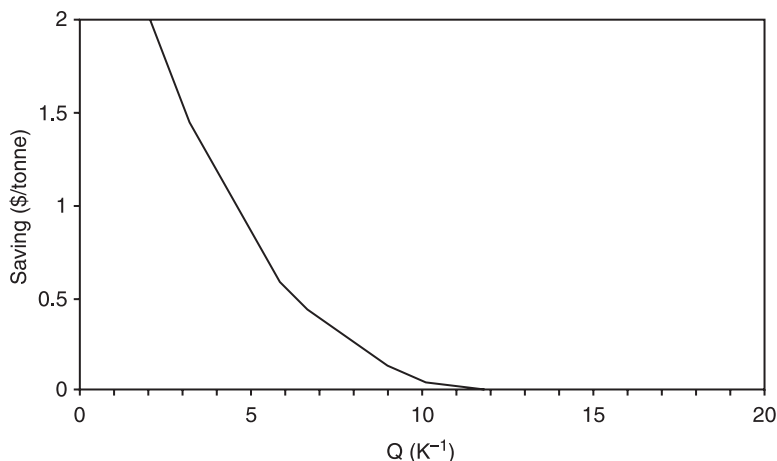
$$Q = \sum_i m_{l,i} c_{0,i} (k_i - 1)$$

where m_l is the liquidus gradient, c_0 is the composition and k is the partition coefficient for each element i in the alloy.

The benefits shown in Fig. 8.16 are from an optimisation algorithm (Easton et al., 2003, 2004) where a relationship was developed between the grain size, the solute content and the nucleant particle addition rate (Easton and StJohn, 2005) for a particular set of casting conditions. Another approach is to add Ti up to a

Table 8.2 Typical Q values for a range of wrought alloy compositions

Alloy	Q
1050	1.96–2.17
2014	21.1–22.7
3003	5.43–5.59
5083	15.93–16.35
6060	4.46–4.70
6061	7.52–7.82



8.16 Calculated potential savings plotted against the Q value of an alloy for prices of Ti and Al-5Ti-1B grain refiner in the year 2004 assuming a 0.005 wt% Ti addition as Al-5Ti-1B (Easton et al, 2004).

Q value of approximately 15 to obtain the maximum effect of Ti solute and then add nucleant particles to the appropriate content (Bäckerud and Vainik, 2001).

As well as making Ti additions there are a few other considerations with regard to grain refinement. In casting of secondary metal and operations where in-house scrap is recycled there may be different residual grain refiner contents in the melt. This means that there is already residual grain refining inherent in the melt before casting. This can be taken into account to reduce the cost of grain refinement on a cast-by-cast basis if desired (Bäckerud and Vainik, 2001).

Another key factor that needs to be considered is whether there are elements present that poison grain refinement by Al-Ti-B based grain refiners, e.g. Zr, and consequently there are many 7000 series alloys where Al-Ti-C based grain refiners can be used instead. Also, there have been some advances in the design of Al-Ti-B grain refiners where aspects such as the size distribution of the TiB_2 particles have been optimised to improve the effectiveness of the grain refiner (Quested and Greer, 2004).

8.7 Selecting the right master alloy for eutectic modification in terms of effectiveness and cost optimisation

Strontium is deliberately added to Al-Si casting alloys to modify the eutectic silicon structure from an acicular to a fibrous morphology (Gruzleski, 1992; Sigworth, 2008) and results in improved ductility, more rapid spheroidisation of silicon during solution treatment (Apelian et al., 1990) and redistribution of porosity from localised macro-shrinkage to dispersed microporosity (Sigworth,

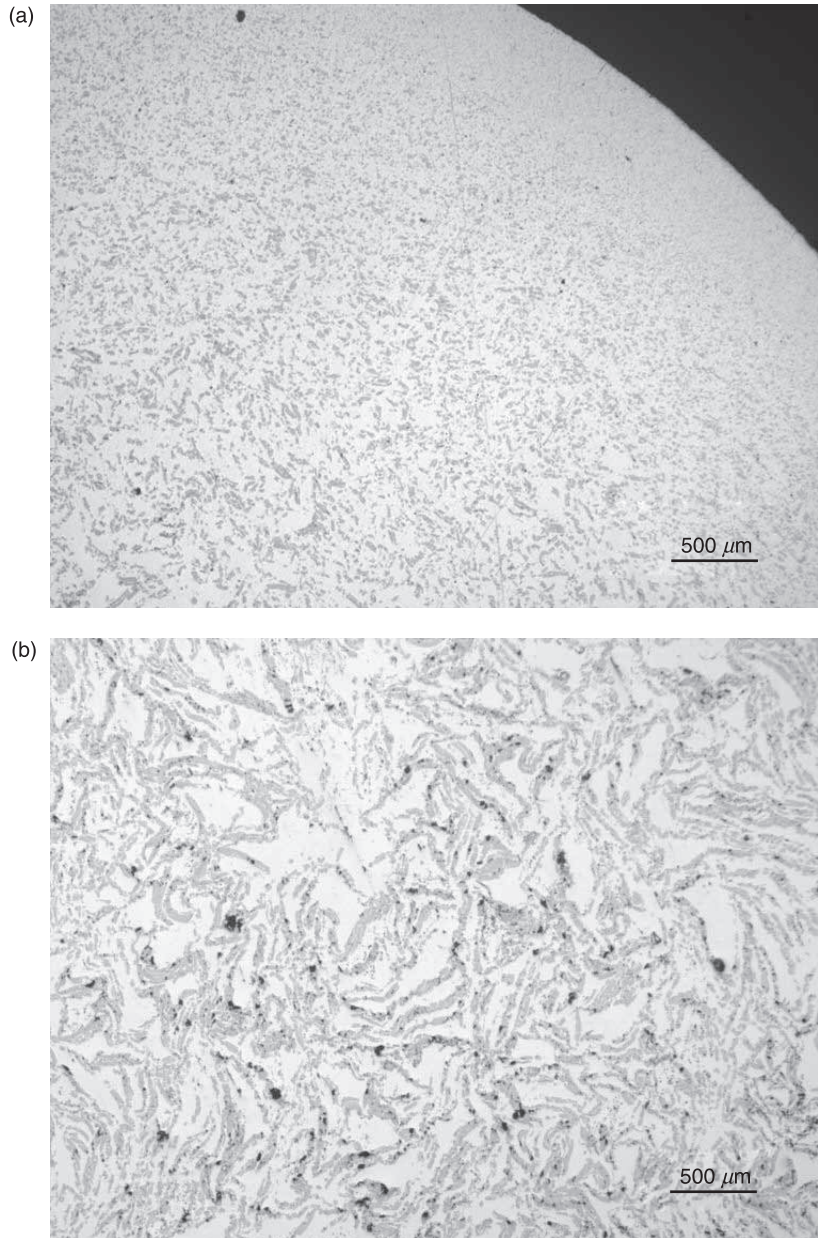
2008). This addition practice is commonplace in the foundry industry but the choice of Al-Sr master alloy can sometimes be difficult. Master alloys are available in various product forms, with different Sr contents and at different costs. This case study arose from the request of a master alloy producer and supplier for an independent study to compare the effectiveness of various forms of silicon modification master alloy additions.

Strontium master alloys display more predictable elemental recovery than sodium (the main alternative eutectic modifier), but are still susceptible to some elemental losses during the addition process and from prolonged melt holding. The ability of a foundry to reliably hit and maintain a target Sr level with minimal losses is important in keeping production costs down. Information on the relative performances of the different products can assist in this task but it is not easy to find since it is necessary to rely on suppliers' marketing-focused information.

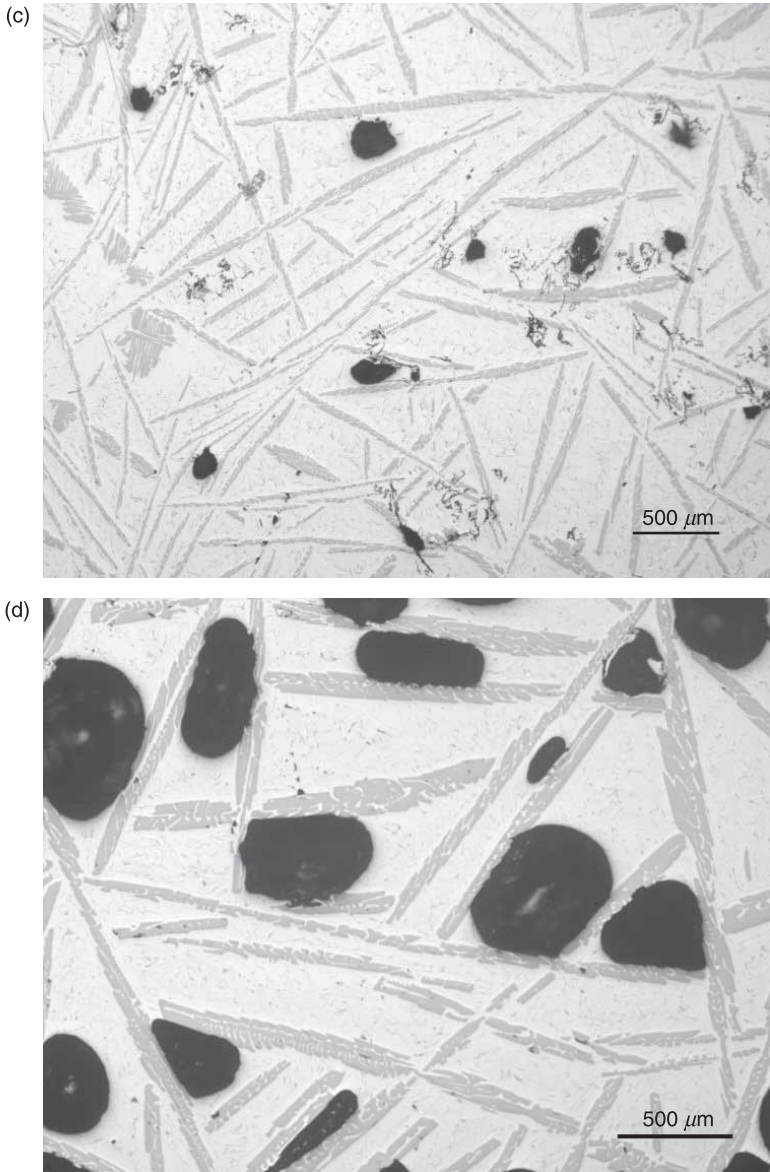
The Al-Sr alloy system exhibits two eutectics and the master alloys are based on these. The more dilute eutectic at 4.1 wt% Sr (654°C) forms the basis for the most popular and commonly used master alloys containing between 5% and 20% Sr (typically 10% or 15%). They contain primary Al_4Sr particles in a matrix of Al-Al₄Sr eutectic and undergo classical dissolution with dissolution rate increasing with melt temperature (Pekguleryuz and Gruzleski, 1989). The other eutectic at 88% Sr (560°C) is the basis of a more specialised master alloy typically marketed with 90% Sr. This form contains primary Sr phase in an Al-AlSr eutectic and behaves differently, undergoing exothermic dissolution with the dissolution rate increasing with decreasing temperature.

The more common dilute Al-Sr master alloys are produced in various forms. The two most common forms are waffle (a type of cast flat rectangular ingot with 'waffle-like' protrusions and gullies, typically weighing a few kg) and small diameter (~10 mm) rod supplied as a coil and produced by a continuous Properzi-type casting process. Master alloys are also supplied in larger cross-section bars/rods (e.g. ~20 mm Ø, or ~40 mm × 40 mm) produced by continuous casting and/or extrusion processes. These various product forms display quite different internal microstructures. Examples of a few types are shown in Fig. 8.17. In each of these, the primary Al_4Sr intermetallic is the darker grey phase, the Al-Al₄Sr eutectic (usually difficult to resolve) is the lighter phase and the black regions are porosity. What is quite evident is that the amount and the size of primary intermetallic vary greatly. This has ramifications for use in the foundry as will be demonstrated by the research work (Taylor et al., 2005) described below.

To assess these modifiers, melts of unmodified, non-grain refined Al-7Si-0.55Mg alloy were prepared and held in an open bath at various temperatures. Most trials were conducted at 710°C and some were carried out at 670°C, 690°C, 740°C and 770°C. For each melt, one of 16 different master alloys (including some identical product types but from different producers and/or differing batches) was chosen and weighed to give a target Sr concentration of 200 ppm. Following addition of a master alloy, the melts were sampled, and then sampled again after various holding



8.17 Optical micrographs showing typical microstructures of several different Al-Sr master alloys: (a) 10% Sr small diameter (10 mm) rod; (b) 10% Sr large diameter (20 mm) cast-extruded rod; (c) 10% Sr waffle; (d) 15% Sr waffle (Taylor et al., 2005).



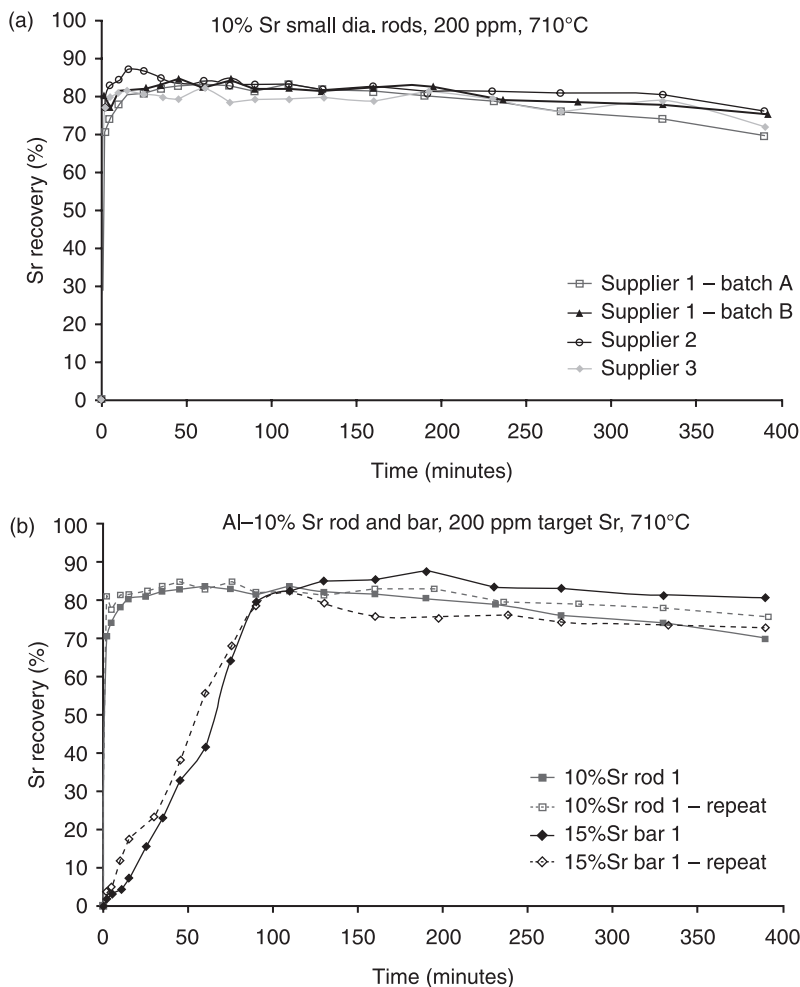
8.17 Continued.

times subsequently, from 2 minutes to 390 minutes after addition. The collected samples were chemically analysed by optical emission spectroscopy (OES).

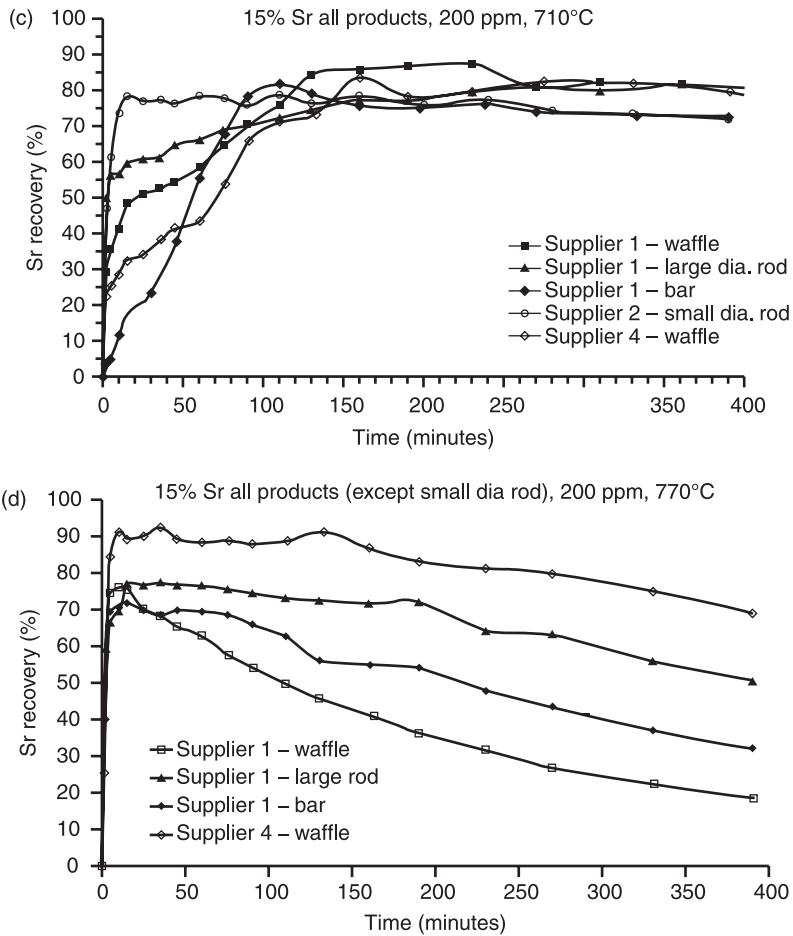
The gathered data showed various trends in terms of rate of dissolution and elemental recovery, the maximum recovery achieved and the rate of fade of Sr after the maximum level was reached. Some of this data are presented in Fig. 8.18

(more complete data can be found in Taylor et al., 2005). Some of the key observations were the following:

1. The rate of dissolution/elemental pickup for similar products are similar (e.g. small diameter ten per cent Sr rods, regardless of manufacturer or batch), see Fig. 8.18(a).
2. The rate of dissolution is faster for ten per cent Sr alloys than for 15% alloys (Fig. 8.18b).



8.18 Graphs showing the variation of Sr content with time for constant Sr addition level (200 ppm target) using various master alloy forms and melt temperatures: (a) 10% Sr small diameter rods at 710°C; (b) repeatability of trials with two different products at 710°C; (c) a range of 15% Sr products at 710°C; and (d) a range of 15% Sr products at 770°C (Taylor et al., 2005).



8.18 Continued.

3. The rate of dissolution for a given master alloy increases as the melt temperature increases (compare Fig. 8.18c with 8.18d).
4. The rate of dissolution is dependent on the master alloy form, particularly at lower melt temperatures, i.e. fine-scale microstructure products generally dissolve faster than coarse-scale products (see Fig. 8.18c, and consider in light of Fig. 8.17).
5. Most master alloy additions eventually achieve ~80–90% Sr recovery regardless of the time taken to achieve maximum Sr level. This is more evident at lower melt temperatures (Fig. 8.18a and 8.18c). At higher melt temperatures, recovery levels tend to be more variable (Fig. 8.18d).
6. The rate of Sr fade is largely independent of the original master alloy form, but it does depend strongly on melt holding temperature (compare Fig. 8.18d at 770°C with Fig. 8.18a–c at 710°C).

These results suggest a number of measures that foundries may find useful when using Sr as a modifier for Al-Si based alloys. Care should be exercised when contemplating a process change from a low Sr content master alloy to a high one, even if cost per Sr unit is lower. Dissolution rates are generally slower for high Sr product but this can be compensated for by increasing the melt temperature. However, high temperatures may lead to Sr loss rates several times faster than loss rates at lower temperatures. The use of a high dissolution temperature followed by a reduced holding temperature may be a workable solution. It appears that changing master alloy supplier may have little effect on recovery and fade behaviour, at least where Al-10% Sr small diameter rod products are used. However, there may be considerable differences in performance when other product forms are used, even if the Sr content remains unchanged. It is clear, therefore, that although master alloy cost is an important factor to consider for any foundry, productivity issues must also be considered before any decisions on master alloy changes are made.

8.8 Summary

The case studies presented in this chapter illustrate the difficulties that industry has in applying the knowledge developed through scientific enquiry. By its nature, scientific studies simplify and control particular casting parameters and conditions in an ideal way. To do otherwise would not result in the understanding we have today. In contrast, industry needs to know more than they can gain from a textbook. Their own industrial processes often create additional uncontrolled variables. Also, the alloys and alloy additions they purchase vary in their effectiveness and the knowledge related to why these variations in performance occur is not easy to find, thus relying on trial and error and/or supplier information. The case studies presented here illustrate how our scientific and engineering knowledge can be used to evaluate a range of effects and to explain the formation of defects and as a consequence identify methods that can be used to control them.

8.9 References

- Apelian, D., Shivkumar, S. & Sigworth, G. (1990) Fundamental aspects of heat treatment of cast Al-Si-Mg alloys. *Transactions of the American Foundryman's Society*, 97: 727–742.
- Bäckcrud, L. & Vainik, R. (2001) Method for optimised aluminum grain refinement. In Anjier, J.L. (Ed.), *Light Metals 2001*. Warrendale, PA: The Minerals, Metals & Materials Society.
- Bondhus, E., Sagstad, T. & Dahle, N. (1999) Grain refinement of hypoeutectic Al-Si foundry alloys with TiB₂. In Eckert, C.E. (Ed.), *Light Metals 1999* (pp. 693–697). San Diego, CA: The Minerals, Metals & Materials Society.
- Cáceres, C.H., Svensson, I.L. & Taylor, J.A. (2003) Strength-ductility behaviour of Al-Si-Cu-Mg casting alloys in T6 temper. *International Journal of Cast Metals Research*, 15: 531–543.
- Cáceres, C.H. & Taylor, J.A. (2006) Enhanced ductility of Al-Si-Cu-Mg foundry alloys with high Si content. *Metallurgical and Materials Transactions B*, 37B: 897–903.

- Campbell, J. (1996) The origin of porosity in castings. In Lakeland, K. (Ed.), *Proceedings of the Fourth Asian Foundry Congress* (pp. 33–50). Gold Coast, Australia: Australian Foundry Institute.
- Campbell, J. (1997) *Castings*. Oxford: Butterworth-Heinemann.
- Chai, G., Bäckerud, L. & Arnberg, L. (1995) Relation between grain size and coherency parameters in aluminium alloys. *Materials Science and Technology*, 11: 1099–1103.
- Drouzy, M., Jacob, S. & Richard, M. (1980) Interpretation of tensile results by means of quality index and probable yield strength. *AFS International Cast Metals Journal*, 5: 43–50.
- Easton, M.A. & StJohn, D.H. (1999) Grain refinement of aluminium alloys. Part 1: The nucleant and solute paradigms – a review of the literature. *Metallurgical and Materials Transactions A*, 30A: 1613–1623.
- Easton, M.A. & StJohn, D.H. (2000) The effect of grain refinement on the formation of casting defects in alloy 356 castings. *International Journal of Cast Metals Research*, 12: 393–408.
- Easton, M.A. & StJohn, D.H. (2001a) The effect of alloy content on the grain refinement of aluminium alloys. In Anjier, J.L. (Ed.), *Light Metals 2001*. Warrendale, PA: The Minerals, Metals & Materials Society.
- Easton, M.A. & StJohn, D.H. (2001b) A model of grain refinement incorporating the alloy constitution and the potency of nucleation sites. *Acta Materialia*, 49: 1867–1878.
- Easton, M.A. & StJohn, D.H. (2005) An analysis of the relationship between grain size, solute content and the potency and content of nucleant particles. *Metallurgical and Materials Transactions A*, 36A: 1911–1920.
- Easton, M.A., StJohn, D.H. & Sweet, E. (2004) Reducing the cost of grain refiner additions to DC casting. In Tabereaux, A. (Ed.) *Light Metals 2004*. Charlotte, NC/Warrendale, PA: The Minerals, Metals & Materials Society.
- Easton, M.A., StJohn, D.H., Sweet, L. & Couper, M.J. (2003) Optimising the cost of grain refinement by separate TiB_2 and Ti additions to wrought aluminium alloys. In Whiteley, P.R. (Ed.) *8th Australasian Conference on Aluminium Casthouse Technology* (pp. 153–165). Brisbane: The Minerals, Metals & Materials Society.
- Gruzleski, J.E. (1992) The art and science of modification: 25 years of progress. *Transactions of the American Foundryman's Society*, 100: 673–683.
- Guzowski, M., Sigworth, G. & Sentner, D. (1987) The role of boron in the grain refinement of aluminium with titanium. *Metallurgical Transactions A*, 18A: 603–619.
- Johnsson, M. (1994) Influence of Si and Fe on the grain refinement of aluminium. *Zeitschrift für Metallkunde*, 85: 781–785.
- Johnsson, M. & Bäckerud, L. (1996) The influence of composition on equiaxed crystal growth mechanisms and grain size in Al alloys. *Zeitschrift für Metallkunde*, 87: 216–220.
- Maxwell, I. & Hellawell, A. (1975) A simple model for grain refinement during solidification. *Acta Metallurgica*, 23: 229–237.
- Pasciak, K.J. & Sigworth, G.K. (2001) Role of alloy composition in grain refining of 319 alloy. *AFS Transactions*, 109: 567–577.
- Pearson, J. & Cooper, P. (1999) A review of the basics of grain refining. In Whiteley, P.R. & Grandfield, J. (Eds.) *6th Australian Asian Pacific Conference on Aluminium Cast House Technology* (p. 109). Sydney, Australia: The Minerals, Metals and Materials Society.
- Pekguleryuz, M.O. & Gruzleski, J.E. (1989) Dissolution of non-reactive strontium containing master alloys in liquid aluminum and A356 melts. *Canadian Metallurgical Quarterly*, 28: 55–65.
- Quested, T.E. & Greer, A.L. (2004) The effect of the size distribution of inoculant particles on as-cast grain size in aluminium alloys. *Acta Materialia*, 52: 3859–3868.

- Roy, N., Samuel, A. & Samuel, F. (1996a) Porosity formation in Al-9wt pct Si-3wt pct Cu alloy systems: Metallographic observations. *Metallurgical and Materials Transactions A*, 27A: 415–429.
- Roy, N., Zhang, L., Louchez, P. & Samuel, F. (1996b) Porosity formation in Al-9wt%Si-3wt%Cu-X alloy systems: Measurements of porosity. *Journal of Materials Science*, 31: 1243–1254.
- Sigworth, G.K. (2008) The modification of Al-Si casting alloys: Important practical and theoretical aspects. *International Journal of Metalcasting*, 2: 19–40.
- Sigworth, G.K. & Guzowski, M. (1985) Grain refining of hypoeutectic Al-Si alloys. *AFS Transactions*, 172: 907–912.
- Sigworth, G.K., Smith, C., Easton, M.A., Barresi, J. & Kuhn, T.A. (2007) The grain refinement of Al-Si casting alloys. In Sorlie, M. (Ed.) *Light Metals 2007*. Warrendale, PA: The Metals, Minerals & Materials Society.
- Sigworth, G.K. & Wang, C. (1993) Mechanisms of porosity formation during solidification: A theoretical analysis. *Metallurgical and Materials Transactions B*, 24B: 349–363.
- Smith, C., Easton, M.A., Nie, J.F., Zhang, X. & Couper, M.J. (2004) The effect of Ti content on the mechanical properties of an Al7Si0.35Mg alloy. *Materials Forum*, 28: 1222–1228.
- Spittle, J.A. & Keeble, J.M. (1999) The grain refinement of Al7Si alloys with boron containing refiners. In Eckert, C.E. (Ed.) *Light Metals 1999*. Warrendale, PA: The Minerals, Metals & Materials Society.
- Spittle, J.A., Keeble, J.M. & Al Meshhedani, M. (1997) The grain refinement of Al-Si foundry alloys. *Light Metals 1997*. Warrendale, PA: The Minerals, Metals & Materials Society.
- Taylor, J.A., Couper, M.J., Smith, C.L. & Singh, D.P.K. (2005) Behaviour of Al-Sr master alloys in Al-7Si-0.5Mg alloy melts. *9th Australasian Conference on Aluminium Casthouse Technology*, Melbourne, Australia.
- Taylor, J.A., Schaffer, G.B. & StJohn, D.H. (1999a) The role of iron in porosity formation in Al-Si-Cu based casting alloys. Part I: Initial experimental observations. *Metallurgical and Materials Transactions*, 30A: 1643–1650.
- Taylor, J.A., Schaffer, G.B. & StJohn, D.H. (1999b) The role of iron in porosity formation in Al-Si-Cu based casting alloys. Part II: A phase diagram approach. *Metallurgical and Materials Transactions*, 30A: 1651–1655.
- Taylor, J.A., StJohn, D.H., Barresi, J. & Couper, M.J. (2000) An empirical analysis of trends in mechanical properties of T6 heat treated Al-Si-Mg casting alloys. *International Journal of Cast Metals Research*, 12: 419–430.
- Tøndel, P., Halvosen, G. & Arnberg, L. (1993) Grain refinement of hypoeutectic Al-Si foundry alloys by addition of boron containing silicon metal. In Das, K. (Ed.) *Light Metals 1993*. Warrendale: The Minerals, Metals & Materials Society.
- Tynelius, K., Major, J. & Apelian, D. (1993) A parametric study of microporosity in the A356 casting alloy system. *AFS Transactions*, 101: 401–413.
- Vainik, R. (2007) Variations in aluminium grain refiner performance and the impact on addition optimization. In Deyoung, D.H. (Ed.) *Light Metals 2008*. New Orleans, LA/Warrendale, PA: The Minerals, Metals & Materials Society.
- Vatne, H.E. (1999) Efficient grain refinement of ingots of commercial wrought aluminium alloys. Part II: Industrial applications. *Aluminium*, 75: 200–203.
- Wu, H., Wang, L. & Kung, S. (1981) Grain refining in A356 alloys. *Journal of Chinese Foundryman's Association*, 29: 10–18.
- Young, D., Dunville, B., Setzer, W. & Koch, F. (1991) A survey of grain refiners for hypoeutectic Al-Si alloys. In Rooy, E. (Ed.) *Light Metals 1991*. Warrendale, PA: The Minerals, Metals & Materials Society.

High pressure die casting of aluminium and its alloys

M.T. MURRAY, M Murray & Associates Pty Ltd, Australia

Abstract: High pressure die casting is an established process that produces high quality castings with close dimensional tolerances. This chapter covers the history of high pressure die casting from its humble beginnings in 1849 up to the present. It also details the most common aluminium alloys, the defects that can occur and typical microstructures.

Key words: high pressure diecasting, aluminium silicon alloys, secondary aluminium, diecasting defects, metal velocity.

9.1 History of high pressure die casting

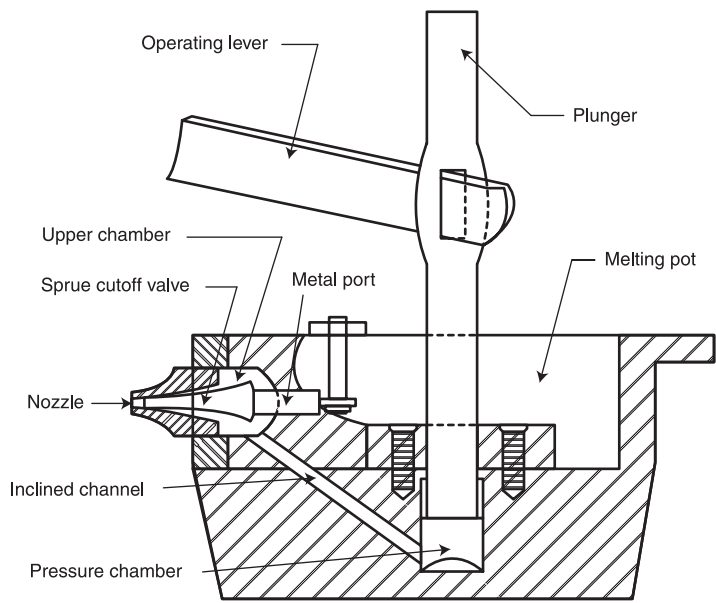
Casting has been around for millennia. Superb castings of pots, water containers and theatrical masks that are thousands of years old have been found in Europe and China. One of the first metal mould applications was in China in about 2000 BC, where a bronze mould was used to cast 22 circular coins. Metal moulds were used extensively in the 1800s to cast complex and repeatable parts. The moulds were generally based on two halves with a sand core to make any inside cavities. These were typically used in the making of cups and vases or lamp bases.

Every founder knows that you need extra pressure to make thin-walled castings with good surface detail. This was achieved by increasing the height of the mould so that the extra head of metal applied pressure to the metal in the cavity. This approach was however limited as there was only a reasonable height that could be achieved.

The invention of the printing press brought forward the need for higher detail, as the letters used in the printing process were formed by lead 'type'. In order to produce smaller font, it was necessary to cast smaller letters. This proved quite difficult with gravity casting, as the metal would not flow into the fine details of each letter. Metal dies helped in producing accurate and reproducible shapes, but the surface tension of the lead alloys inhibited the detail being formed.

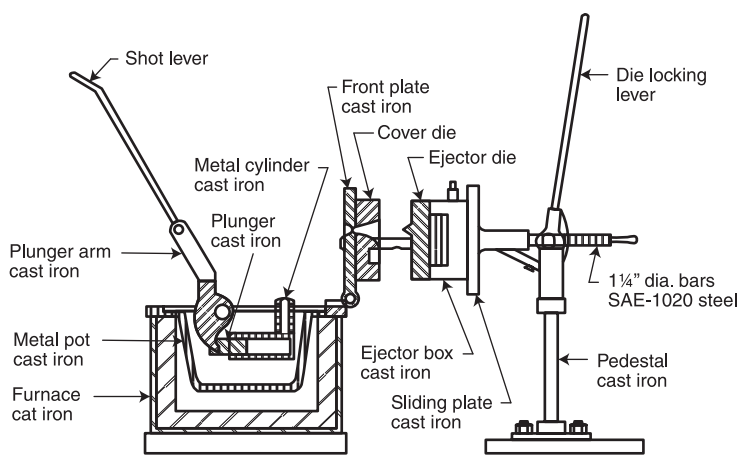
The obvious solution was to push the metal into the die using a piston and cylinder. This enabled much higher pressures to be achieved, but obviously required the use of metal moulds that could withstand the extra pressure. The first patent awarded for a die casting machine was to Sturges in 1849 (Fig. 9.1) (Barnard, 1925). His was the first manually operated machine for die casting print type using lead.

Other applications followed 20 years later with the making of phonograph parts. These required the uniting of both decorative and engineering features into the one product. This gave rise to a new machine that was operated by two people, which



9.1 Sturges (1849) die casting machine patent (Barnard, 1925).

involved swinging the whole machine by 90 degrees (Doehler, 1951). A typical machine is shown in Fig. 9.2. This type of machine was used to cast magneto housings, carburettors and other automotive parts during the early days of the automotive industry right up until 1915 (Vinarcik, 2003). It could only cast zinc, tin and lead alloys.



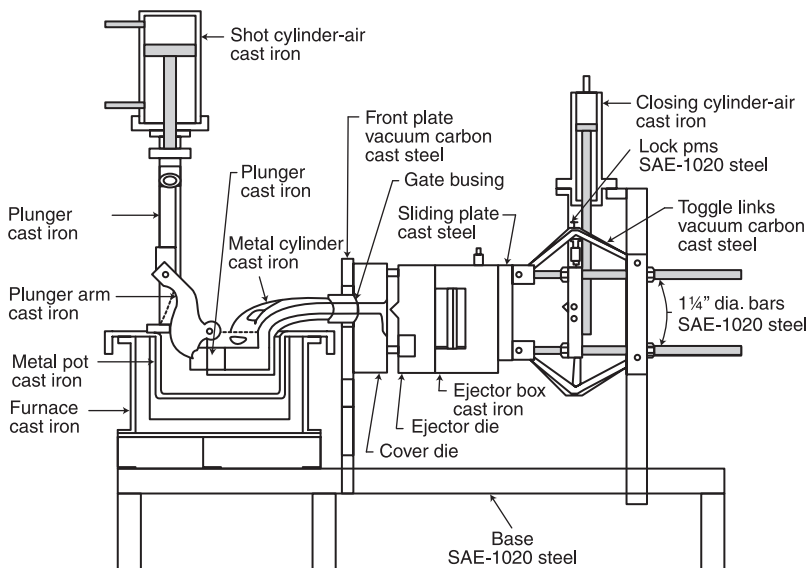
9.2 Early die casting machine that required two people to operate (Doehler, 1951).

A later machine used pneumatics to push the piston and to open and close the dies (Fig. 9.3). This reduced the manual effort needed to cast the parts and resulted in more uniform quality. The other advantage of this type of machine was that higher metal pressures could be used which meant that thinner castings with better surface detail could be produced.

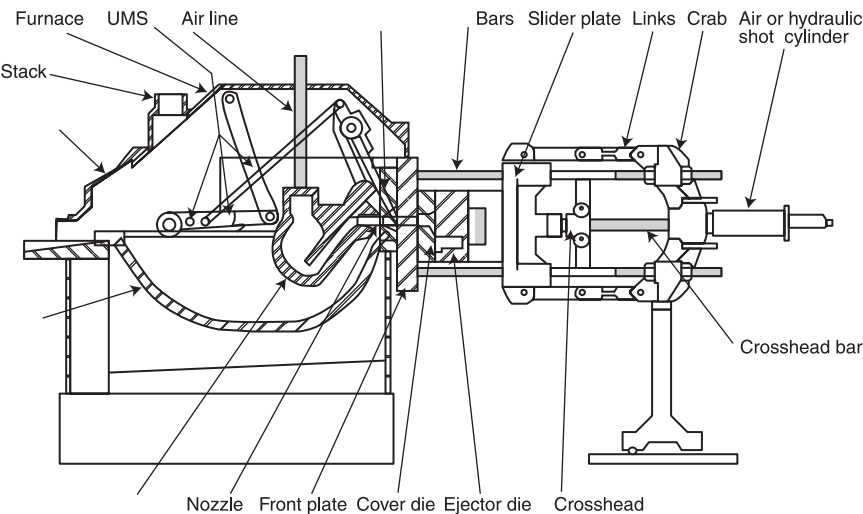
The first aluminium machine was developed in 1915 (Doehler, 1951). This machine temporarily submerged the piston/cylinder arrangement in a bath of molten aluminium. The cylinder was filled with aluminium and then it was raised and the piston pushed forward. An early aluminium die casting machine is shown in Fig. 9.4.

The main market for die cast parts has always been the automotive industry, from the Model T Ford era right through to the present. In the 1950s and 1960s die castings were used extensively for large amounts of chrome decal used on the inside and outside of cars, but were also used for gearboxes, windscreen wiper motors, starter motors and differential covers. To service this industry, though, the die casting machines needed to be more repeatable and consistent.

The die casting machine quickly changed to the form used today where a horizontal cylinder with a piston is pushed by hydraulics. The molten aluminium was poured into the cylinder and the hydraulics pushed the metal into the die. This is called the 'cold chamber' die casting machine. The modern cold chamber die casting machine was used extensively during World War 2 to manufacture lightweight aluminium parts for aeroplanes as well as for automotive applications. In this form the power is provided by hydraulics (Fig. 9.5). This allowed very high pressures to be applied



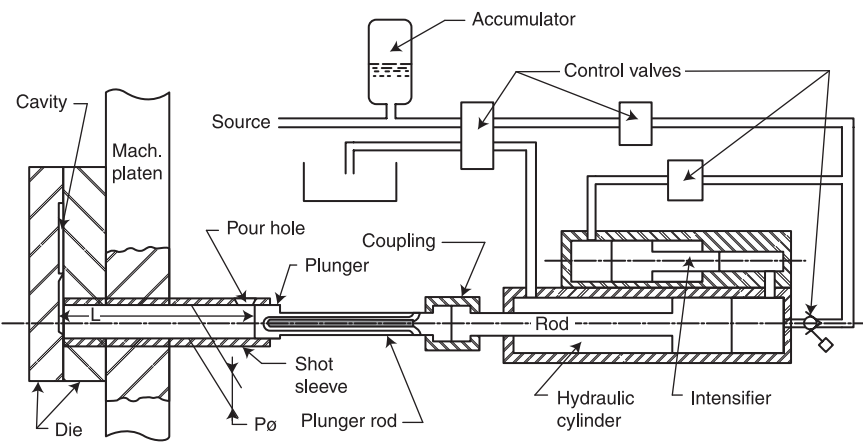
9.3 Pneumatic machine that enabled more consistent product (Doehler, 1951).



9.4 Early aluminium die casting machine (Doehler, 1951).

with close control of the whole process. Hydraulics are very rigid and can apply pressure rapidly, whereas pneumatics always have a high springiness.

Today, the automotive industry consumes approximately 60% of all die castings produced, and, as cars have improved, there has been a requirement for more complex, thinner walled castings, with higher quality. High pressure die casting is now used to produce an immense range of products ranging from magnesium laptop cases (0.6 mm thickness) through to automotive gearboxes and engine blocks which must withstand very high stresses. Very small parts can be made, such as zipper



9.5 Hydraulic systems are used to push the metal in a modern die casting machine (Herman, 1991).



9.6 Typical high pressure die castings demonstrating their complex shape and high dimensional accuracy.

parts, as well as much larger components, such as automotive instrument panels (Lin et al., 2005). Hence, high pressure die cast parts can range from purely decorative through to high strength structural parts. An example of some complex high pressure die castings is shown in Fig. 9.6.

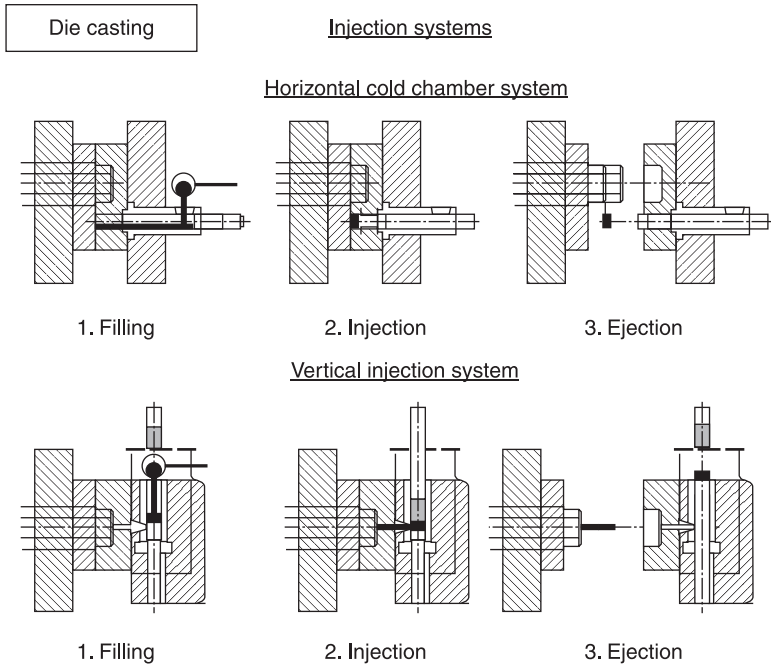
9.2 The die casting process

9.2.1 Defining the high pressure die casting process

The die casting process for aluminium is relatively simple in concept. A piston and cylinder arrangement pushes molten aluminium into a die and then applies a high pressure. However, it is easier to understand if the processing steps are detailed (Fig. 9.7).

The molten aluminium is melted in a furnace and then transported to the holding furnace. This holding furnace usually holds the metal at a temperature between 650°C and 700°C. Either an automated ladling system or a dosing furnace then presents the metal to the die casting machine. Dosing furnaces use air pressure to push the metal along a heated pipe.

Near the holding furnace is the shot end of the die casting machine. This comprises a cylinder, called the shot sleeve, and a piston, called the plunger. The plunger is pushed forward by a relatively large hydraulic cylinder. There is an opening at the top of the shot sleeve that allows the molten aluminium to be poured in. The hydraulic system is controlled via a computer that carefully synchronises the speed and force when the plunger is moved forward.

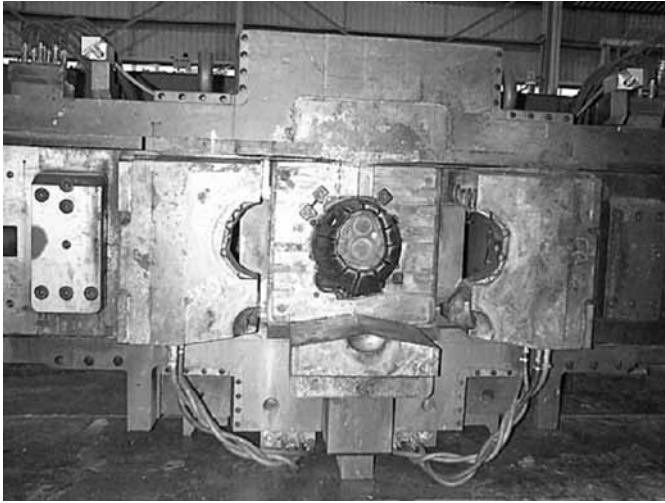


9.7 Steps in the die casting process (Takach, 1993).

The locking region of the machine comprises a series of platens that hold the two halves of the die. These dies have the actual casting shape machined into them. The dies are made of special steel that can withstand the high temperatures and pressures (e.g. see Fig. 9.8). The dies are forced together by the locking end of the machine. This locking force defines the size of part that can be made. The range of locking force on machines is from 1 tonne up to 5000 tonnes. Typically, the locking force for most machines internationally is between 250 tonnes and 2400 tonnes.

9.2.2 Typical process conditions

The dies are pushed together and a force applied (Fig. 9.7). The dies are maintained at a temperature of between 120°C and 280°C depending on the part being made. Metal at a temperature of 650–700°C is poured into the shot sleeve. The plunger then moves forward and pushes the metal into the die area. The molten metal flows along runners in the die and then through a narrow channel, called a gate, and then into the cavity or casting shape (Fig. 9.7). In aluminium die casting, high pressure of 40–160 MPa is applied and the molten metal is cooled by the die until it freezes. The dies are separated and the casting pushed out of one die by rods in the dies, called ejector pins. The dies are then sprayed with a water/oil emulsion



9.8 Typical die casting die set made of high strength tool steel (Nissan Casting Australia).

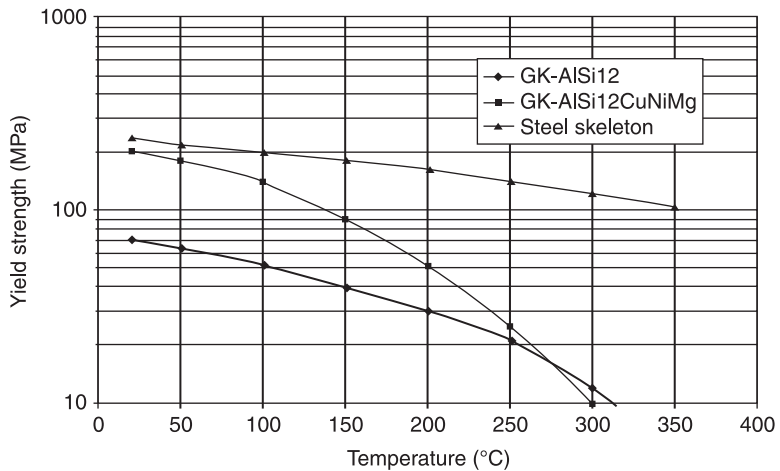
that cools the dies and provides lubrication. The dies are then moved together again and the process repeated.

Usually, there are drilled holes machined through the die and either water or oil is passed through. These are carefully placed so that the die and thence the casting is cooled both to reduce the resident time needed in the die and to cool the part to ejection temperature. It is necessary to cool the aluminium parts to a relatively low temperature prior to ejection so that the aluminium is strong enough to withstand the ejection forces. The strength of normal die cast aluminium alloys is relatively low until the temperature is below 300°C (Fig. 9.9).

9.2.3 Behaviour of molten aluminium at high speeds

Molten metal was initially believed to flow into the die like a normal gravity die casting, that is, the metal fills from the bottom of the die until the cavity is filled. Frommer (1925) found that metal actually flowed at a high speed from the gate and impacted the die surface opposite the gate (Fig. 9.10).

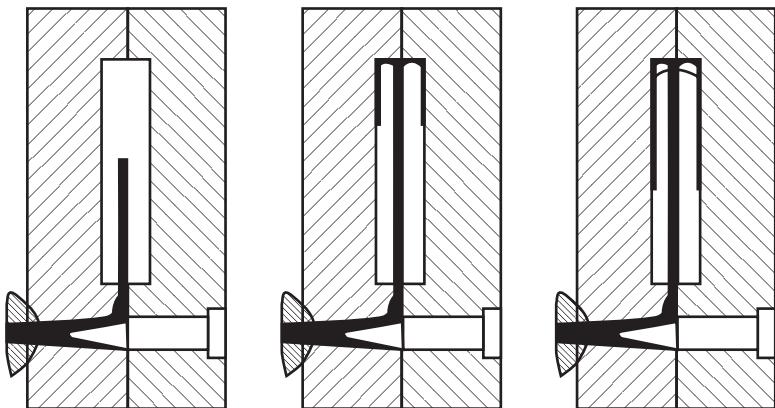
The plunger moves forward and pushes the molten metal through the narrow gate and into the die. It is important to fill the cavity with molten metal very rapidly (10–150 milliseconds depending on the part size and alloy being cast). To achieve a good surface finish, it is also important to have the molten aluminium entering the die at a high speed. Typically, the molten metal is travelling through the gate at 20–50 m/s for aluminium. When casting magnesium, these gate speeds can be up to 120–150 m/s (400–500 kph).



9.9 Strength of typical cast aluminium alloys with temperature, also showing that a steel reinforcement makes the composite much stronger at higher temperatures (Witt, 2009). GK-AlSi12 is a primary aluminum (very corrosion resistant). GK-AlSi12CuNiMg is an alloy from scrap (not corrosion resistant).

It is believed that the metal forms into small drops (atomisation) as it exits the gate and passes into the cavity (Herman, 1985). These droplets then impact the inside of the cavity and rapidly freeze, forming a skin of metal on the cavity face. This skin layer can make up 30–60% of the overall casting thickness.

Because the metal is travelling so fast, the flow in the cavity is turbulent and chaotic. It does not fill the cavity slowly, such as in normal sand casting. Instead, the metal impacts on the various die parts and results in small vortices that trap air in the



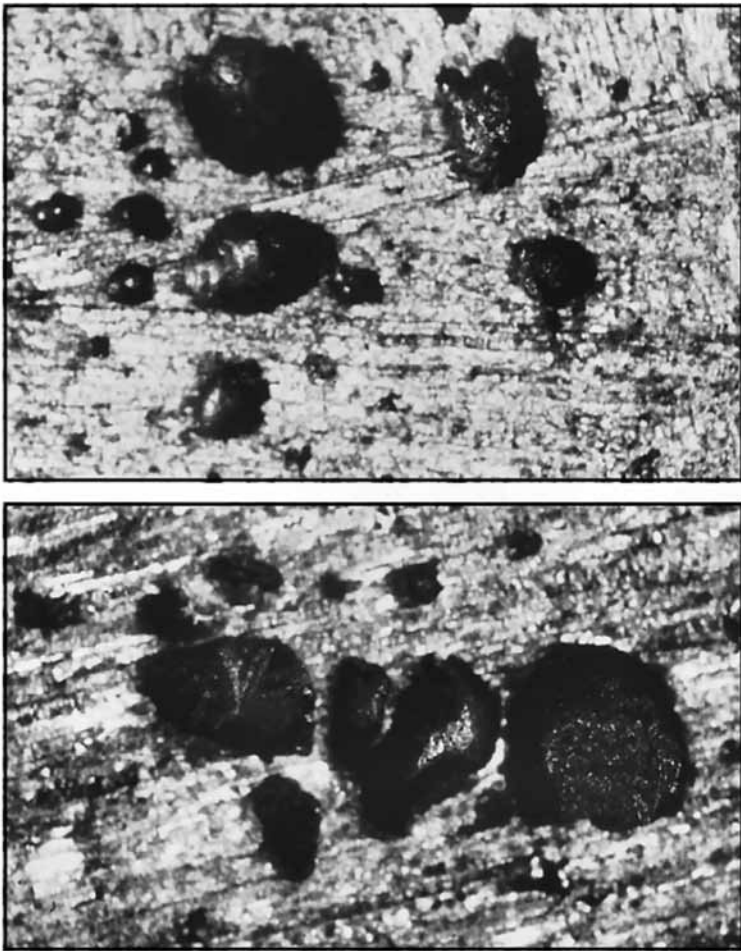
9.10 Flow travels from the gate to the opposite side of the cavity (Frommer, 1925).

liquid aluminium. As a result, normal high pressure die cast aluminium parts contain approximately 1–2% of air in the form of small bubbles or gas pores (Fig. 9.11).

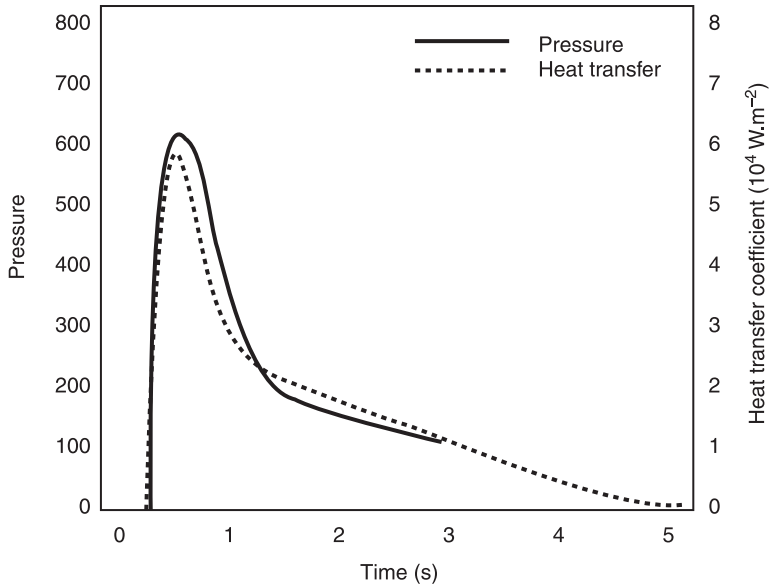
9.2.4 The role of the die and pressure in heat transfer

The molten metal fills the die and then a high pressure is applied. This forces the molten metal against the die and provides a very good heat transfer. Hence, the casting freezes rapidly due to the heat being transferred into the die.

The heat transfer is not constant. As the metal freezes it does so from the skin through to the centre of the part. As the casting progressively freezes it shrinks and hence reduces the pressure of the metal against the die. This reduces the heat transfer. Dour et al. (2003) measured the pressure applied by the metal by installing



9.11 Typical gas porosity found in most die castings (Walkington, 2004).



9.12 Pressure on the metal and heat transfer for aluminium alloys (Dour et al., 2003).

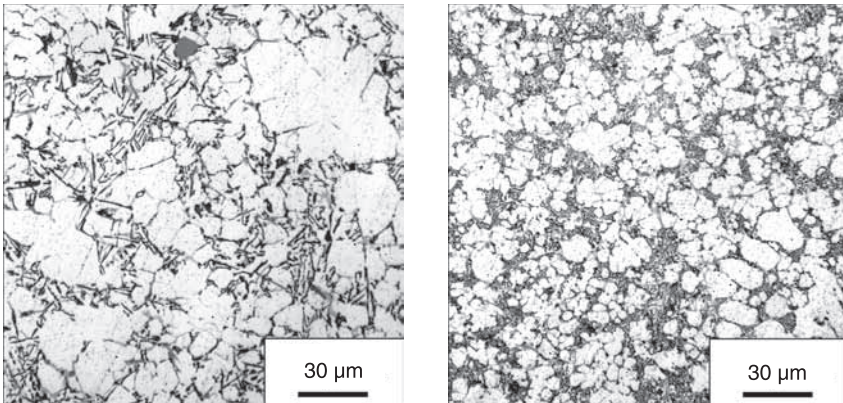
a pressure transducer in the die (Fig. 9.12). They also used a series of thermocouples in the die set at different distances from the cavity to measure the heat flux through the die, and hence the heat transfer.

They found that the heat flux density peaked at 10^5 W/m^2 at the point where the pressure is first applied and then reduced to $5 \times 10^3 \text{ W/m}^2$ after four seconds. Hence, it is common to have a very fine microstructure on the surface or skin of the casting and then a coarse dendritic/eutectic structure in the centre.

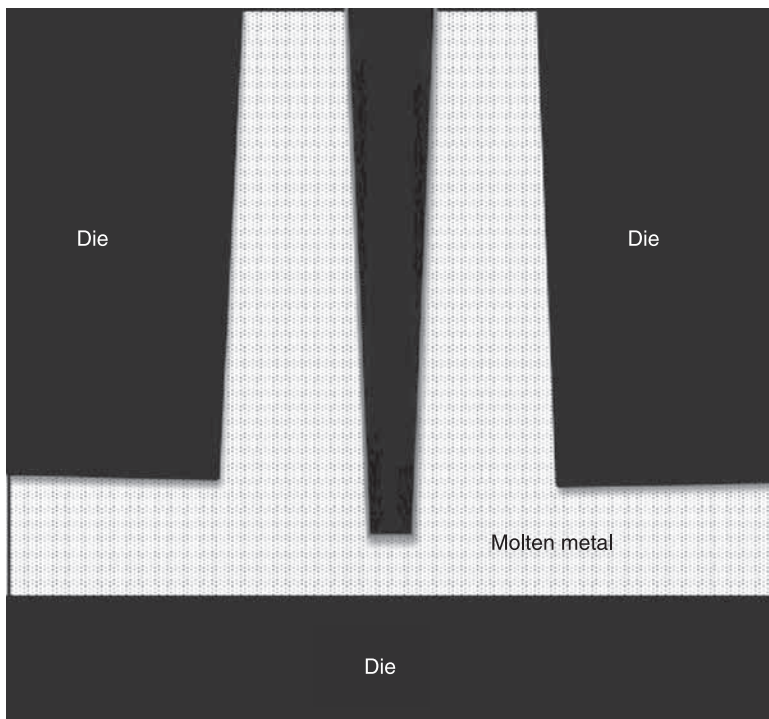
This has a major effect on the resultant microstructure in the part. The high initial heat flux causes rapid solidification and hence produces fine dendrites with a small secondary dendrite arm spacing. As the casting starts to solidify, the heat flux drops rapidly. Hence the dendrites become coarser with a larger dendrite arm spacing (Fig. 9.13). This is particularly true for thicker castings of 6 mm or more.

It is common in high pressure die casting to have steel cores in the die so that complex parts can be made. This results in a long rod of steel being surrounded by molten aluminium (Fig. 9.14). These rods or cores cannot conduct the heat away except through the small base. Hence, they rapidly reach very high temperatures. The thermal energy these cores can absorb is limited. Hence, it is common to get an initial chill or skin layer around the core, but then the core heats up and accepts no further heat. This results in slow solidification and hence large dendrites with large secondary dendrite arm spacings.

These cores can reach sufficiently high temperatures such that the aluminium surrounding the cores does not solidify for some time. Aharonov et al. (1999) and



9.13 Changes in grain size across a die casting in A380 alloy showing (left) the centre of the casting and (right) the skin region (micrographs courtesy R.N. Lumley, CSIRO).



9.14 Drawing of the thin steel section of the die surrounded by molten metal.

Jahedi and Fraser (2001) have shown that this leads to the aluminium reacting with the steel of the core. As a result, intermetallics of Al-Fe are formed on the surface of the core (Fig. 9.15). This can lead to the casting sticking to the core and makes retraction of the core from the casting difficult. This is called soldering. To overcome this die casters can either coat the cores with a PVD layer (Physical Vapour Deposition) or surface diffuse a hard layer onto the core (e.g. CrN).

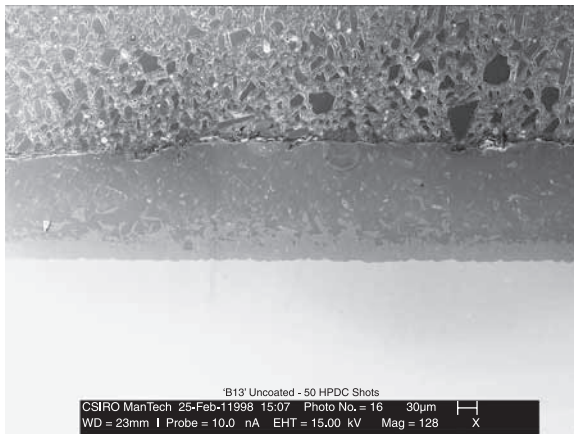
9.2.5 Partial solidification prior to entering the cavity

The molten aluminium starts off in the furnace as fully molten. However, throughout the process it is in contact with steel that is relatively cold. For example, when the molten aluminium is poured into the relatively cold shot sleeve it is held there for a few seconds before the plunger starts to move. Gershenzon et al. (1999) showed that a skin is formed in the aluminium next to the shot sleeve wall (Fig. 9.16). As the plunger moves forward this skin is broken into small flakes that then flow into the cavity.

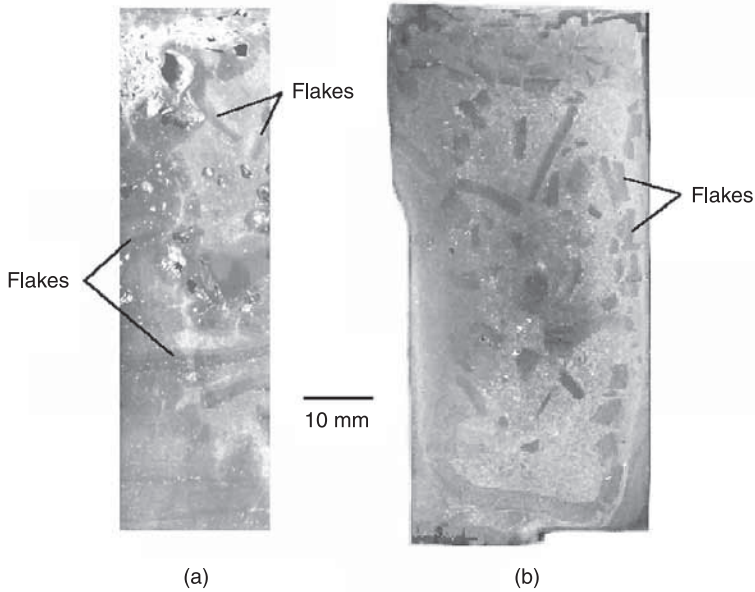
Wang et al. (2004) also carried out simulation of the temperature of the metal in the shot sleeve during the movement of the plunger (Fig. 9.17). They noted that there was a cool spot at the bottom of the melt where solidification should occur.

As the molten metal is forced along the runners the metal can also freeze as a skin. Due to the high metal speed, Murray (1979) showed, for zinc alloys, that the dendrites growing from the wall break off. As these dendrite fragments move through the gate, the very high velocity and shearing action breaks up these fragments into even smaller solid particles. These produce a cascade of nuclei into the cavity. Hence, the die temperature and gate velocity can have a large effect on the resultant grain structure in the casting.

Finally, it has been noted that some solidification can occur simply because the overall metal temperature drops below the liquidus temperature. This produces



9.15 Soldering layer over the tool steel (Gulizia, 2008).



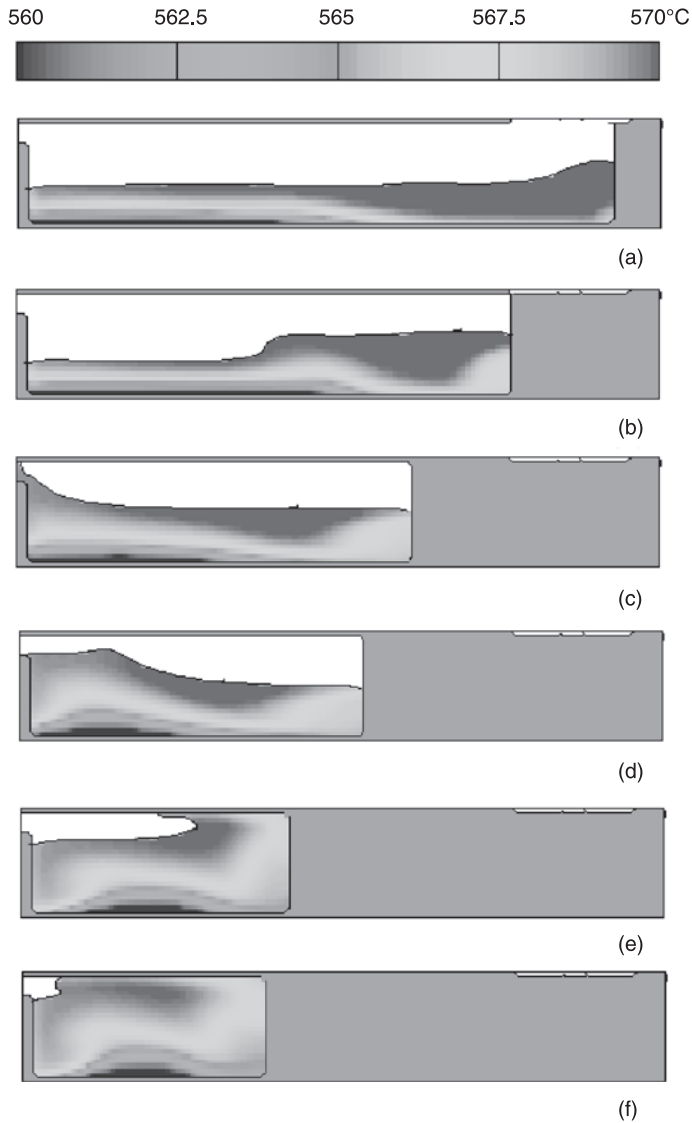
9.16 (a) and (b) Flakes observed in the shot sleeve (Gershenzon et al., 1999).

grains that have grown slowly, such as during the residence time in the shot sleeve. Hence, in the final casting, microstructure can be mainly small, fine grained dendrites but with a few larger secondary dendrite arm spacing grains. These have been called PSGs by Sequeira et al. (1996) (Fig. 9.18).

9.2.6 Hydrogen in die casting

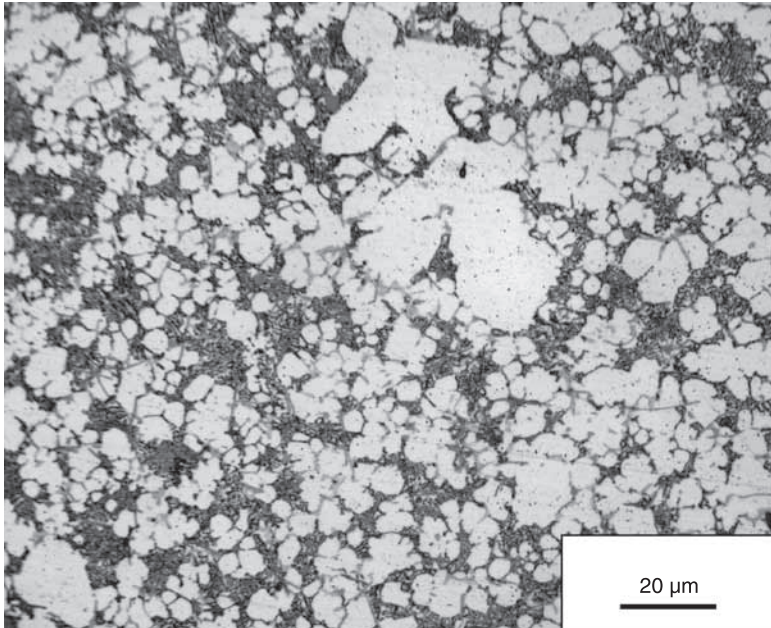
In most casting operations, the presence of hydrogen in the metal can lead to gross porosity. Hydrogen has a reasonable solubility in liquid aluminium and a low solubility in the solid (Fig. 9.19). Hence, hydrogen can form scattered porosity throughout the part. The role of hydrogen in porosity in high pressure die casting is more uncertain. Many practitioners have found that hydrogen has very limited effect on porosity. Others have found that hydrogen plays a key role in the development of porosity (Fig. 9.20). Many die casters degas their metal prior to casting.

There is some reason for the difference between these two findings. If the die caster is manufacturing thin-walled castings, then the pressure can be applied to the solidifying metal during most of the solidification. In this case the hydrogen may stay in solution or form as small, high pressure bubbles. If large castings are made, especially ones with large bosses, then the thick sections can solidify over a number of seconds especially after the neighbouring region has solidified. Hence, the boss section could solidify with no, or minimal, external pressure and hence be similar to gravity casting. This would result in hydrogen porosity.

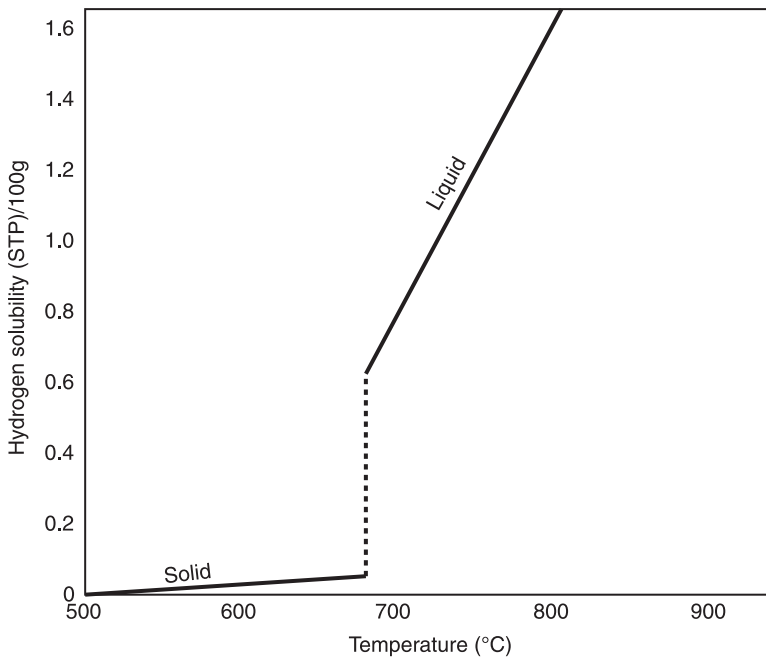


9.17 (a)–(f) Simulation of the temperature profile in the melt (Wang et al., 2004).

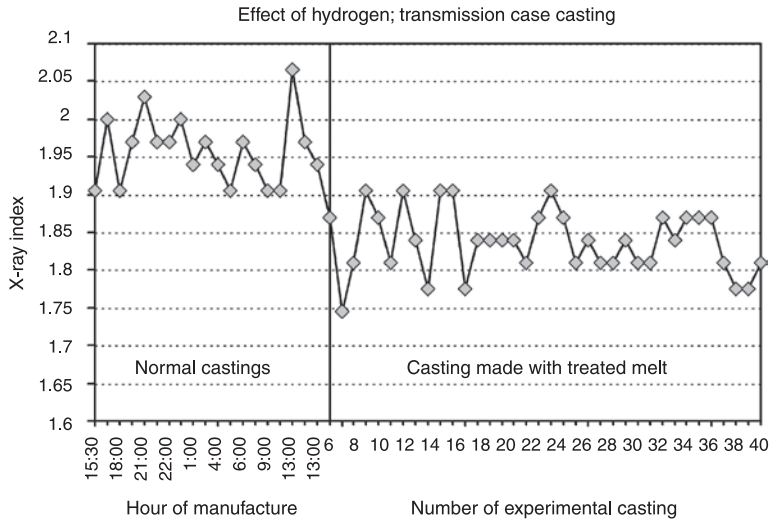
SPX Contech stated in their presentation at the NADCA Conference in 2006 that hydrogen should be continuously removed if ultra-high quality castings are required (Brown et al., 2006). They also stated that hydrogen could also be picked up from the humidity left in the die after spraying with the oil/water emulsion (die spray). They evaluated various die sprays to determine which resulted in the least hydrogen pick up.



9.18 Micrograph showing bimodal grain size with large grains formed in the shot sleeve (micrograph courtesy R.N. Lumley, CSIRO).



9.19 Hydrogen solubility in aluminium metal (La-Orchan, 1994).



9.20 Effect of hydrogen on reject rate (Tian, 2001).

9.3 Aluminium alloys used in die casting

9.3.1 Defining the alloys

There are two basic alloy groups used in high pressure die casting. These are based on Al-9Si and Al-12Si. These make up the majority of high pressure die casting alloys. There are many other alloys but these make up a much smaller percentage of the overall market. A range of alloys can be observed in many of the metal data sheets (e.g. Aluminium Standards and Data, 1997).

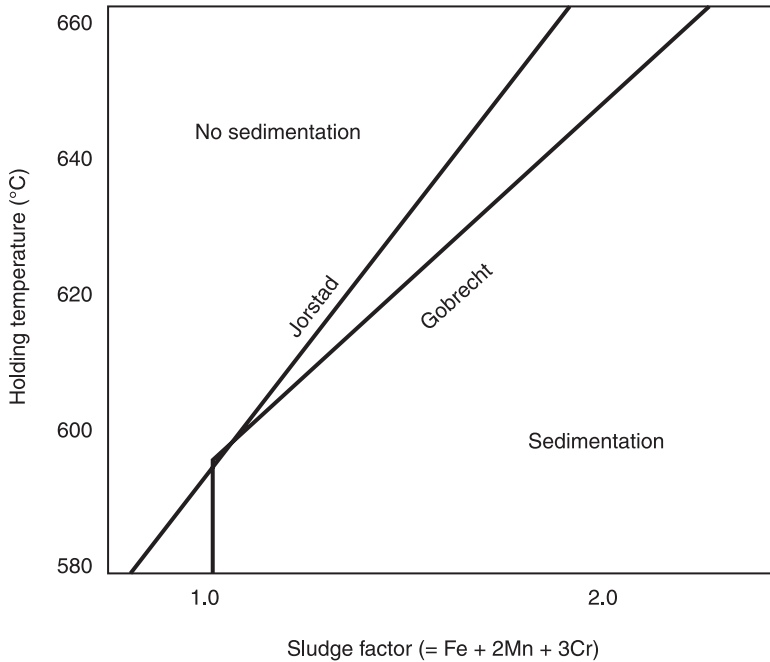
Typical alloys in each of the groups are:

- Al-9Si – LM24, A380, ADC8, CA313, AlSi8Cu3Fe
- Al-12Si – LM6, A413, LM2, ADC12, AC3A, AlSi12

High pressure die casting alloys tend to be secondary alloys, that is, they are made from recycled metal. Hence, it is common for the alloys to contain a number of additional elements that range from advantageous to tramp.

- Silicon – aids fluidity and makes the alloy more castable.
- Iron – reduces the rate of attack of the dies by the aluminium (Makhlouf and Apelian, 2002).
- Copper – increases the hardness of the casting. Excess can result in increased cracking.
- Magnesium – increases hardness.

A combination of elements can result in the formation of large intermetallics called sludge (Makhlouf et al., 2001; Fig. 9.21). Hence, for die casting alloys, there is a Sludging Factor which is defined as:



9.21 Sludge factor with holding temperature (Makhlouf et al., 2001).

$$\text{Sludge Factor} = (\% \text{Fe}) + 2 (\% \text{Mn}) + 3 \times (\% \text{Cr})$$

The factor depends on the temperature that the metal is held. However, if the sludge factor goes above critical then either small intermetallics are formed in the casting, or large chunks are formed in the furnace. These sludge particles are very hard and can cause premature failure of any machining tools when the casting is machined.

9.3.2 Microstructure of typical alloys

The microstructures of typical high pressure die casting alloys are complex because:

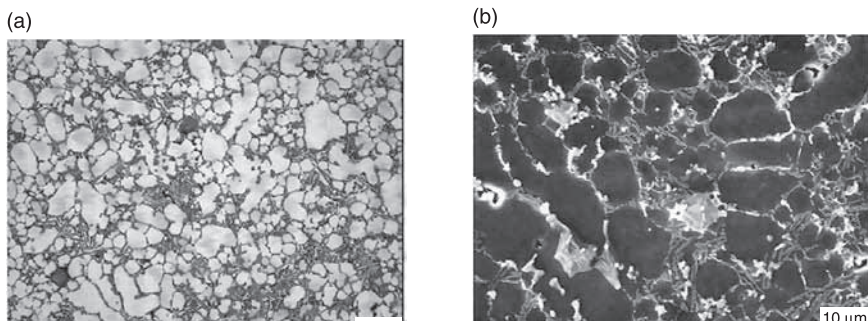
- They are usually a secondary alloy and hence have a large number of elements that can form complex phases and intermetallics. They are not a simple binary alloy.
- The solidification is not solely within the cavity. The metal often begins to solidify via dendrite formation in the shot sleeve. This is a relatively slow growth rate and hence large dendrites are formed with relatively large dendrite arm spacing. The metal then finishes this solidification within the cavity where the growth rate is much higher. Hence, small dendrites are formed in the cavity with relatively fine dendrite arm spacing.

- The solidification does not proceed within a quiescent melt. During injection the metal is travelling at 20–50 m/s and hence concentration gradients typical of equilibrium solidification are not evident.

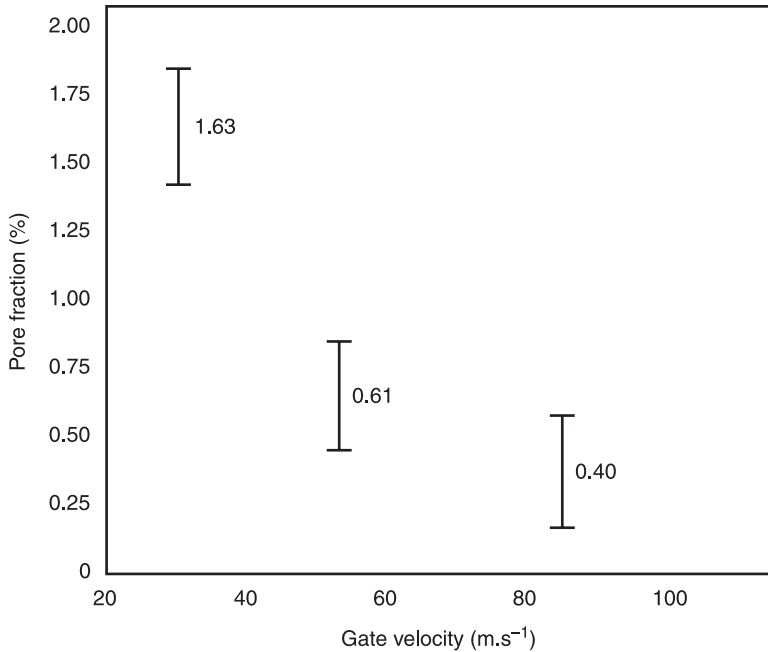
The study of the microstructure of die casting alloys has been going on since at least 1929 (Dix and Keller, 1929). An excellent review of data on the microstructure of Al-Si die casting alloys is given in the book by Makhoul et al. (1998). An example of typical microstructures of an A380/LM24 alloy is presented in Fig. 9.22.

As can be seen in Fig. 9.18, the dendrite sizes are bimodal with larger dendrites that are formed in the shot sleeve and the smaller dendrites which are formed in the cavity. The ratio of the two depends on the percentage of solidification that occurs in the shot sleeve. In small machines (around 250 tonnes locking force or less) the amount of metal poured into the shot sleeve is small compared to the mass of the shot sleeve. The high surface area relative to the mass of the metal poured means that the aluminium will rapidly lose heat. With larger machines (1200 tonne locking force or more) the amount of aluminium poured is a much larger ratio and hence the metal loses only a small amount of heat. The temperature of the shot sleeve and the metal poured into it are also important in determining the ratio of pre-solidified dendrites in the final casting. If the shot sleeve is relatively warm (300°C according to Gershenzon et al., 1999) then virtually no solidification occurs in the shot sleeve. The effect of molten metal temperature is less important, as usually the metal is between 650°C and 680°C. If the molten aluminium is hotter than 700°C then the amount of dissolved hydrogen becomes excessive, the level of magnesium in the melt tends to reduce and the growth rate of dross or oxides accelerates.

The microstructure comprises silicon cuboids and eutectic silicon phases embedded in an α -aluminium matrix (Suarez-Pena et al., 2007). Intermetallic needles of β -phase Al_5FeSi , common in Al-Si alloys, are also present. Fe-bearing Chinese script with a composition similar to α -phase $\text{Al}_{15}(\text{Fe},\text{Mn})_3\text{Si}_2$ is also often present (Makhoul et al., 1998). Acicular and polyhedral sludge particles of α -phase are nearly always present.



9.22 (a) and (b) Typical microstructure of an A380/LM24 alloy (Makhoul et al., 1998).



9.23 Pore fraction with changes in gate velocity (Gunasegaram et al., 2007).

The morphology of the dendrites also depends on the processing parameters. Gunasegaram et al. (2007) produced tensile samples in a high pressure die casting machine using different gate velocities. They found that at higher gate velocities the dendrites decreased in size. Similarly, they noted that the porosity size and pore area fraction decreased with increasing gate velocity (Fig. 9.23). This combination led to an improvement in the yield strength (Hall-Petch equation) and the UTS (maximum defect size).

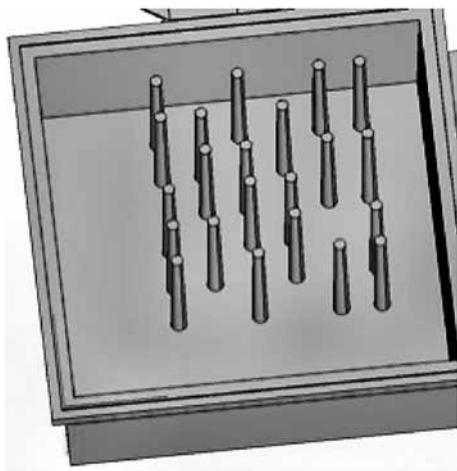
9.4 Defects in die casting

9.4.1 Flow and cold flow defects

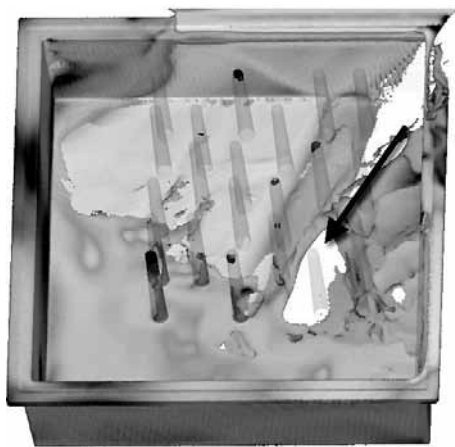
The molten metal entering the cavity already contains some solids due to solidification in the shot sleeve and in the runner. These dendrites have relatively large arm spacings due to their slow growth.

Two fronts meeting

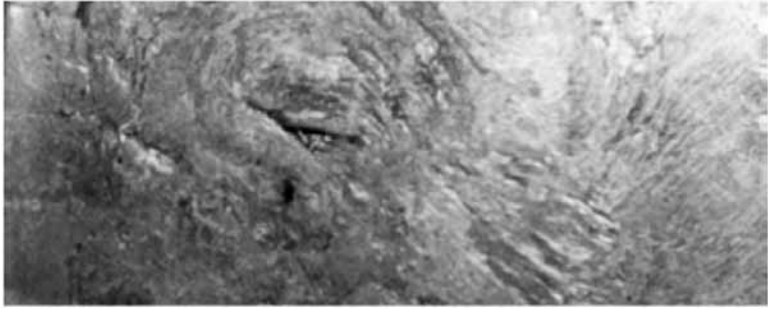
As stated, the molten metal enters the cavity at a high speed of 30–40 m/s. This causes the metal to impact on the die walls and produces a number of micro vortices as well



9.24 Typical case where micro vortices and impacting counter flows occur. A simulation was carried out using Flow3D and it demonstrates the two types of impacting flow.



9.25 Simulation showing two major fronts meeting.



9.26 Typical cold flow marks.

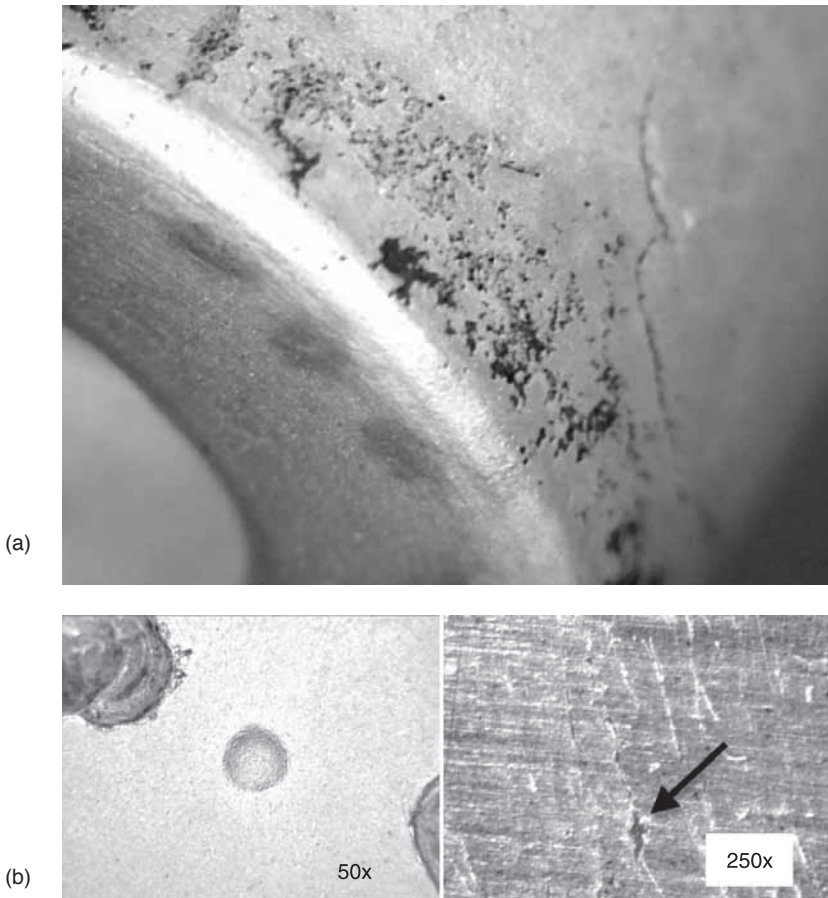
as flow fronts that impact together from near-opposite directions. These vortices and impacting flows result in semi-solid flow fronts meeting. If the solid content is too high, then the flow fronts will not weld together. Also, if there is air trapped between the fronts then welding cannot occur. A typical example of flow fronts meeting is in a casting with bosses (Fig. 9.24). The runner used in this example produces a large major flow that results in a secondary back flow. These meet within the casting.

These fronts meet and often cause a cold flow mark to occur. This cold flow may arise from the metal being too cold to weld together or, as demonstrated in Fig. 9.25, the trapped air within the two fronts cannot be vented away. Hence, the air is trapped between the fronts and results in the two fronts being kept apart during solidification. A typical cold flow is shown in Fig. 9.26.

These cold flow marks can cause significant problems in post processes such as powder coating and plating. The gap left between the two faces may be only 10–50 mm across on the surface but this may lead to a significantly larger cavern inside the casting. The narrow gap inhibits any surface cleaners entering the cold flow during the cleaning of the castings prior to painting or plating. Hence, any die lubricant can be trapped inside the cold flow mark. During the painting process the casting is sprayed with powder and then heated to approximately 200°C. This results in the air in the cold flow defect expanding, as well as any die spray oils vaporising, which results in a blister in the paint. In plating, the air will expand during the plating process and any oils can leach out of the defect and contaminate the surface. This can lead to either blisters or black marks on the plated surface (Fig. 9.27).

Micro vortices

The simulation shown in Fig. 9.25 also demonstrates micro vortices. The flow up the narrow and long bosses is often along one side of the boss. This flow is forced back when it reaches the top and hence produces a micro vortex a short distance down from the tip of the boss.

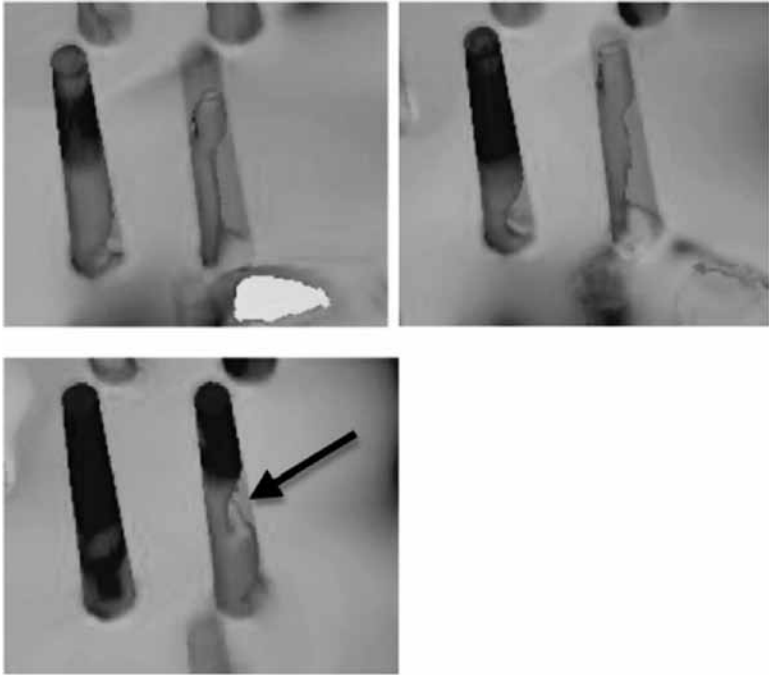


9.27 (a) Oil marks on the plated surface due to die spray oils leaching out of the cold flow defect during plating. (b) Blister on a plated casting, which was linked to a small cold flow mark on the surface of the casting.

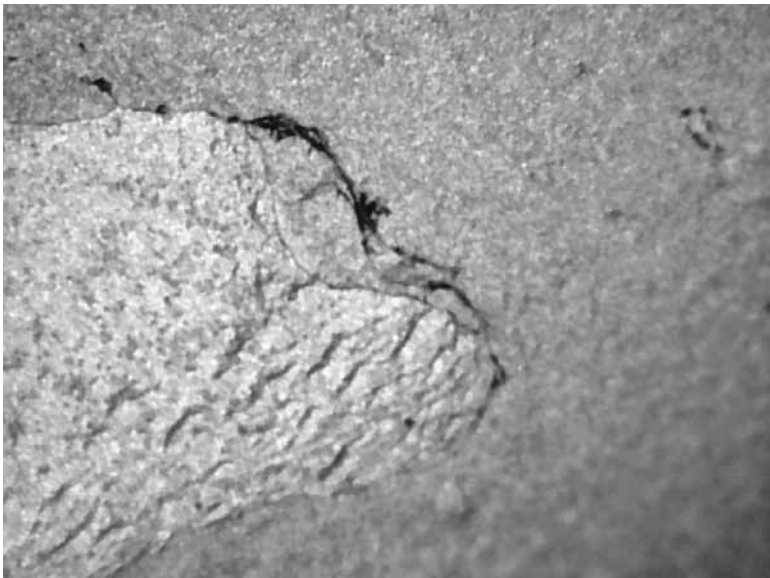
The flow shown in Fig. 9.28 clearly shows the difficulty in filling these long, narrow bosses. The flow can proceed up on side of the boss and then during back flow cause two fronts to meet and/or air to be trapped. This flow often results in a poor surface finish and in porosity within the boss (Fig. 9.29).

Sheared metals as they freeze

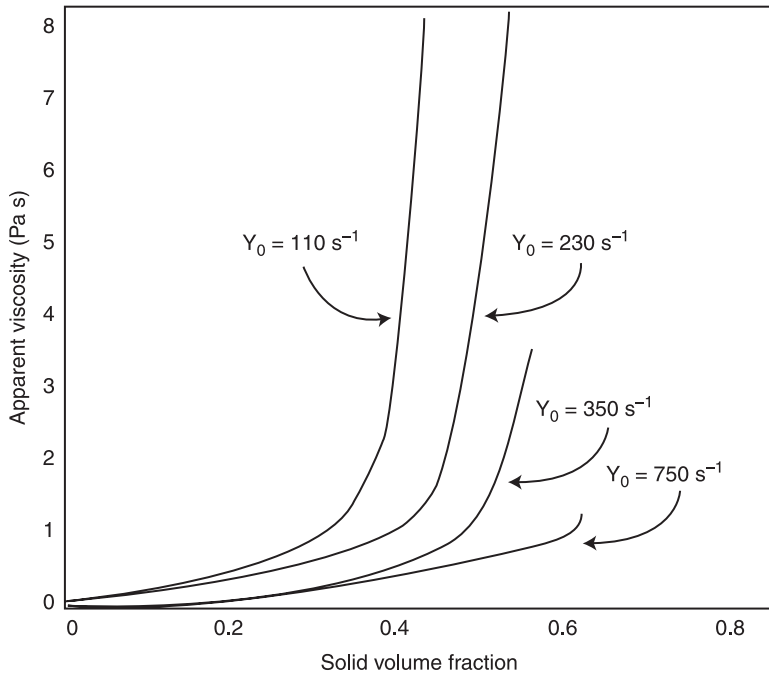
Flemings et al. (1977) was one of the first to study semi-solid flow. He showed that the viscosity of metals increases as the solids increase (see Fig. 9.30). Since then there has been a large number of studies on metals that solidify while being sheared.



9.28 Flow up the long, narrow boss results in micro vortices and trapped air (kind permission granted by Hansen, 2009).



9.29 Typical poor surface when micro vortices occur in long, narrow bosses.



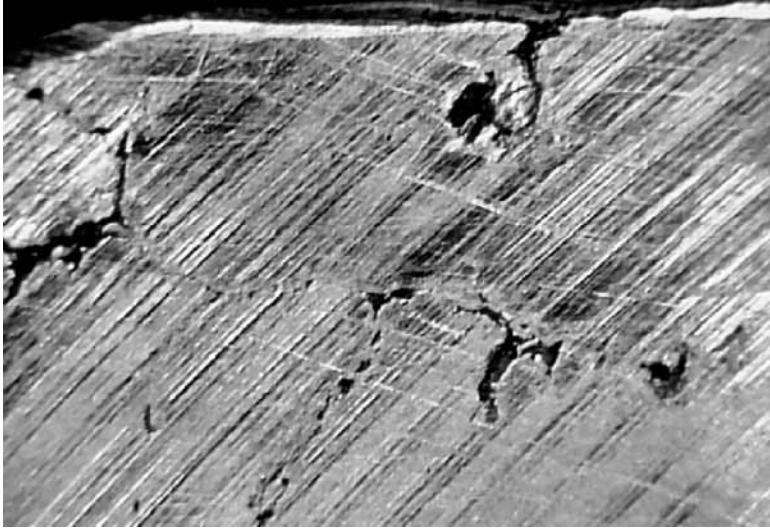
9.30 Viscosity with solid fraction for various shear rates (Fan, 2002).

Within die casting, the metal is being pushed into the die at approximately 40 m/s. This produces a high stirring or shearing action within the die. Since the die temperature is significantly cooler than the molten metal, the aluminium starts to freeze during die filling. As the percentage of solids rises the viscosity increases. This results in the metal behaving more like toothpaste than water.

The result is that the semi-solid metal reaches a high viscosity and hence the metal stops. Then hotter metal can flow around the stopped flow and cause a cold flow. Similarly, the front can stop and a flow from the opposite direction then meets up with the semi-solid, stopped front and cannot weld together. This can then appear as a series of flows that have intersected, see for example Fig. 9.31.

The obvious solution is to stop the metal solidifying to such an extent. This can be achieved by a number of ways:

- 1 Heat up the die – The heat transfer from the molten metal to the die is simply related to the difference in temperature between the molten metal and the die. By increasing the die temperature the heat loss from the metal to the die would decrease. This is the normal approach and is often successful. However, by increasing the die temperature there is an increased rate of attack of the aluminium on the die steels. This attack takes the form of dissolving the Fe and forming Al-Fe intermetallics. This is called soldering. Many workers have



9.31 Cold flow region showing a number of fronts that have met.

shown that soldering is very dependent on the die temperature (e.g. Jahedi and Fraser, 2001 or Han and Viswanathan, 2003). Hence, it is not advisable to increase the die temperature excessively.

- 2 Heat up the molten metal – Increasing the temperature of the molten metal will mean that the aluminium has a higher superheat and hence energy level. However, increasing the molten metal temperature also increases the solubility of hydrogen in the melt, results in higher oxidation and hence dross formation and can cause the loss of important elements (e.g. Mg). Therefore, this is usually not advisable. Fig. 9.32 shows some problem defects and their causes, and it will be seen that the majority are related to casting temperature and die temperature.
- 3 Change the casting parameters – By injecting the molten metal into the die at a higher flow rate, the metal will fill the cavity faster and will have less time to lose heat. Hence, the percentage of solids will reduce and so will the viscosity. This will inhibit the flows reaching the critical solid content and hence the viscosity that results in stoppage of the flow front. Also, the hotter metal fronts will have a higher propensity to weld when they meet. This increase in flow rate can be achieved by increasing the plunger speed during the filling of the cavity or by increasing the diameter of the plunger. The higher plunger area will sweep a larger volume of metal into the die cavity for each millimetre of movement. Hence, at the same plunger speed, a larger plunger will have a higher flow rate. It is important to calculate the gate velocity during this change. If the gate velocity is increased to more than 40 m/s then the metal can erode both the gate and some die features within the cavity. It may be necessary to increase the gate thickness so that the gate area is increased, and hence the gate velocity

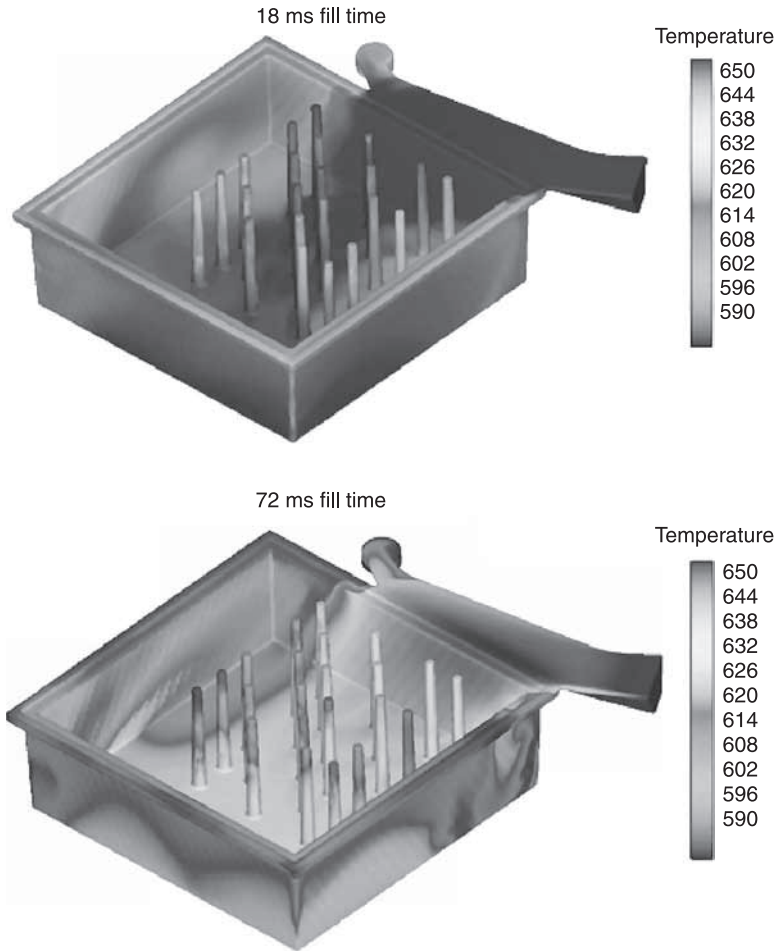
Analysis type	Die casting problem															
	Process								Casting							
	Bolt breaking	Die cracking	Erosion	Flash	Heat checking	Soldering	Sticking	Tearing	Dimensions	Drags	Gas porosity	Galls	Poor fill	Seams	Shrink porosity	Thin wall
Casting temperature																
Die temperature																
Solidification																
Cavity fill																
Casting distortion																

Traditional
 Unique to die casting

9.32 Defect problem and some causes (Mehta et al., 2003).

decreased. Examples of the differences in metal temperature when filling the die in different timeframes are provided in Fig. 9.33.

- 4 Changing the flow pattern within the cavity – As has been shown before, the flow within the cavity can either cause air to be trapped or result in micro or macro vortices. By changing the flow pattern within the die these vortices or swirls can be eradicated. The die caster will very carefully consider the flow within the cavity. This can be carried out either based on experience, or by ‘short shots’ or simulations. ‘Short shots’ are produced by only partly filling the die with molten metal and then observing the resultant partly filled casting. This can be achieved by either stopping the plunger part way through filling the cavity or by placing insufficient metal into the shot sleeve, thus producing only part of the casting. The results are very useful and give a general idea of the flow pattern within the cavity. However, molten metal is being pushed into the cavity at 40 m/s. Even though the plunger is stopped part way through filling the cavity, the inertia of the molten metal will carry the metal beyond the position at the time when the plunger stopped. Hence, there is some interpretation needed when viewing the resultant semi-filled casting. Examples of short shots used for examining the flow pattern within the cavity are shown in Fig. 9.34.



9.33 Differences in metal temperature when filling the die in 18 milliseconds and 72 milliseconds (Hansen, 2009).

9.4.2 Shrinkage porosity

Shrinkage porosity is known in all forms of casting. In its simplest form it is a cavity formed due to the solidification of metal that is not fed from a supply. Many metals shrink when they freeze. If there is a set volume of liquid in a die and the gate freezes, then the resultant casting must be smaller than the cavity shape due to solidification shrinkage. Hence, the metal can either shrink away from the wall of the die or form a cavity within the casting. Therefore, a section of casting that is divorced from the gate will usually form shrinkage voids or pores. Typical shrinkage porosity in a casting is shown in Fig. 9.35.



9.34 Series of short shots showing the filling of a door handle.



9.35 Typical shrinkage porosity in a casting.

In high pressure die casting it is not that simple. Firstly, the molten metal entering the cavity is doing so at a high velocity. This impacts on the die surfaces and usually entrains air within the casting. At the end of cavity fill, a pressure is applied to the molten metal by the plunger in the shot sleeve. This pressure, of between 300 bar and 1200 bar, contracts the pores.

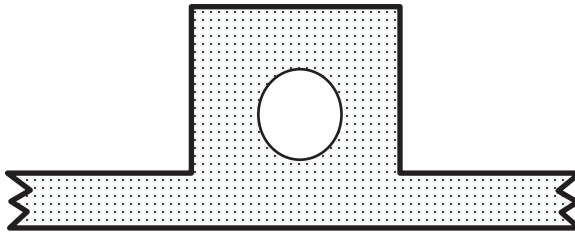
As shown in Fig. 9.36, the gas pore can be trapped in a thick boss. The surrounding, thinner casting solidifies sooner, leaving a pool of molten or semi-molten metal within the boss. The liquid in the boss area is now divorced from the gate and hence must solidify without any feed metal.

Initially, the gas pore is under a high pressure, but as the boss metal progressively freezes the overall volume of metal shrinks. This causes the gas bubble to expand and effectively feeds the shrinkage. However, if the overall shrinkage volume is excessive, then the pore cannot expand sufficiently. This results in the last part of the shrinkage process causing a traditional shrinkage pore to form off the gas pore. Therefore, a pore in a boss can be a combination of both gas and shrinkage, see for example Fig. 9.37.

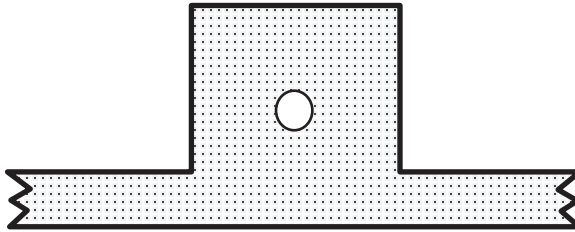
In some cases, a small amount of gas porosity is very useful in reducing shrinkage. This is common to other casting methods and gravity casters will sometimes increase the hydrogen level purposefully so that it 'feeds' the shrinkage. In high pressure die casting, it is usual to change other things, such as the shot velocity and/or profile, to increase the air entrapped.

Thermal control

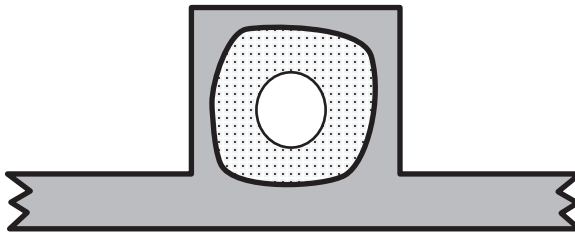
The best way of reducing shrinkage porosity is to control the cooling in the die so that the thicker areas solidify before the surrounding thinner areas. In that way they are fed with molten metal during solidification. Figure 9.38 shows examples of thermal images of a die runner and cavities in an eight-cavity die.



Gas bubble in a boss during metal fill

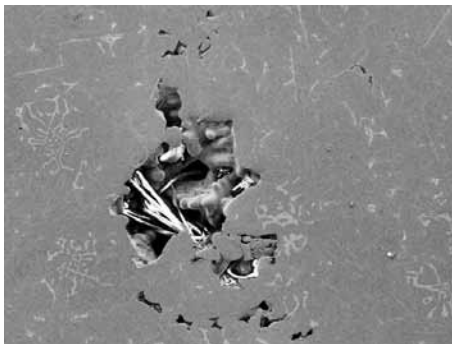


When pressure applied gas bubble shrinks

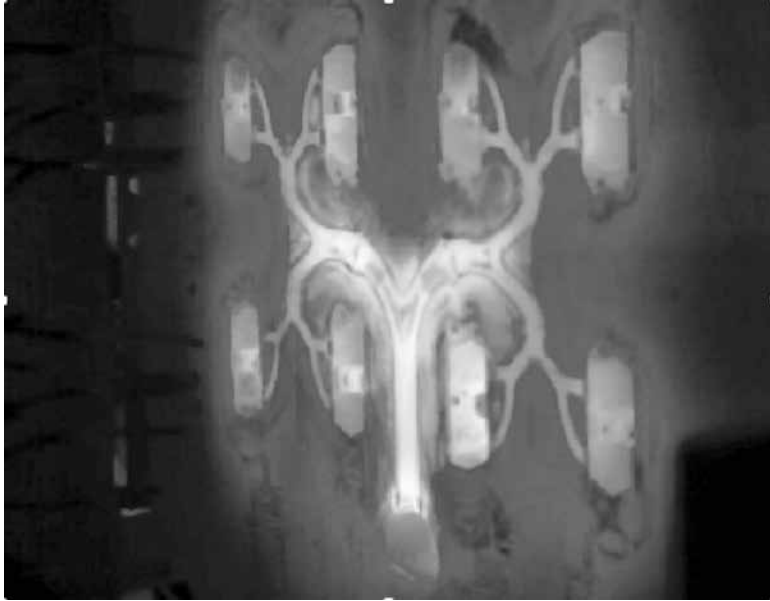


Surrounding area freezes leaving boss area unfed

9.36 Schematic of a gas pore expanding during solidification.



9.37 A gas and shrinkage pore combined.



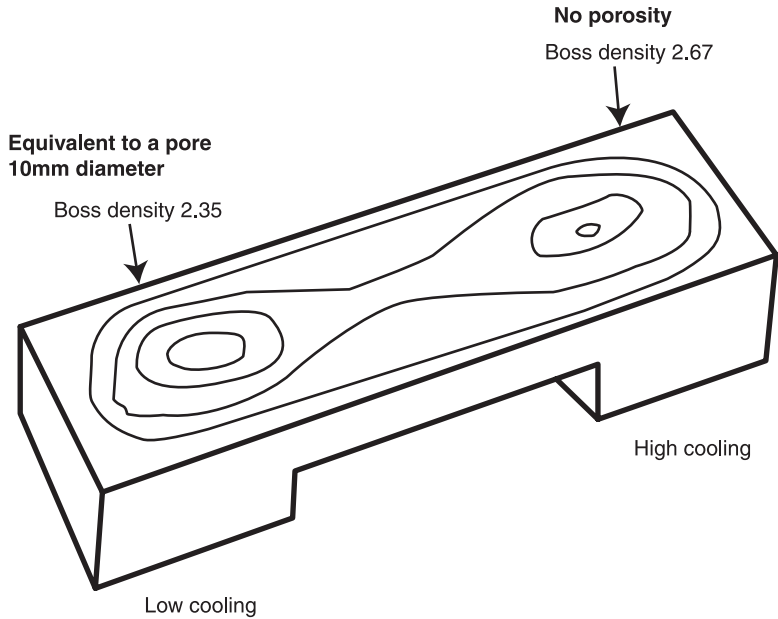
9.38 Thermal picture of the die showing hot regions at the runner and cavity. Thicker sections appear hotter.

There are a number of ways of controlling the solidification sequence during high pressure die casting. The usual is either to add water cooling channels in the die near the thicker areas or to add electric heaters or oil heating channels in the thinner areas. It is usually not possible to have directional solidification from the furthest part from the gate right along to the gate area, since the casting is often too complex. However, it is possible to freeze critical areas that require minimal porosity before uncritical areas.

Wang et al. (1999) showed that it was possible to move the porosity from one large boss into a surrounding boss via a thin section of casting (Fig. 9.39). Cooling one boss aggressively resulted in the boss freezing before the thin section or the other boss. Hence, all the shrinkage was transferred into one boss. The cooled boss had a density of 2.67 g/cm^3 (close to theoretical density for this alloy) while the other had a density of 2.35 g/cm^3 (12% porosity). Similar results were shown by Bailey et al. (1997).

Pressure control

The molten metal can be forced through the dendrite network if the molten metal pressure is sufficiently high. Savage et al. (2001) showed that increasing the metal pressure during solidification resulted in a decrease in the porosity size. This was determined by X-raying the castings and then rejecting any parts that had a pore size beyond a predetermined limit. Hence, by plotting reject rate against metal pressure



9.39 Drawing of the cooling experiment from Wang et al. (1999).

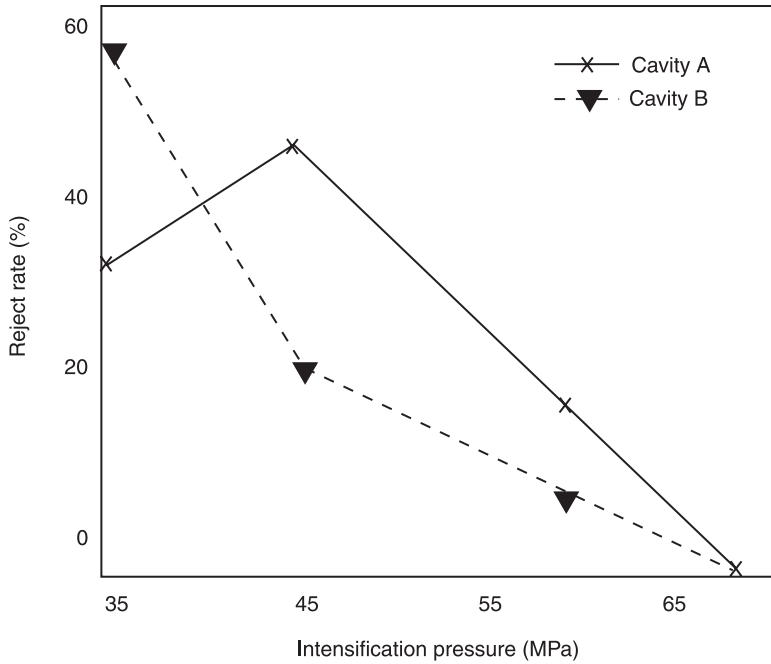
it is possible to view the affect of metal pressure. As can be seen in Fig. 9.40, the reject rate decreased progressively when the metal pressure was increased.

Similarly, Raji and Khan (2006) found that, in squeeze casting, the density increased progressively when the pressure was increased (Fig. 9.41). Since there are a lot of similarities between high pressure die casting and squeeze casting this data is also of interest.

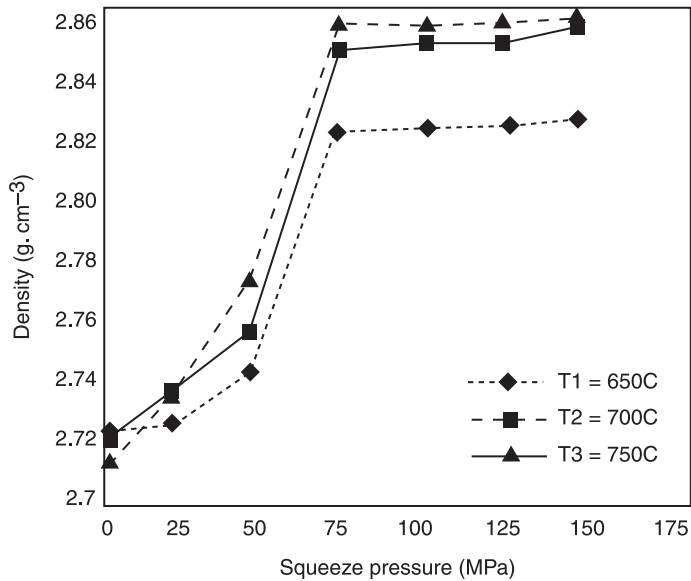
However, there may be a negative side to using pressure. Laukli et al. (2004) showed that the high pressure can lead to a banded structure (Fig. 9.42). This is believed, by some, to occur due to the semi-solid dendritic network being fractured leaving a channel from the gate into the casting.

Elemental additions control

Sigworth (2008) showed that the shrinkage porosity level in gravity die casting could be modified by adding Sr or Na (Fig. 9.43). Various foundries have tried adding Sr or TiB to the melt and have had mixed results. Laukli et al. (2005) added AlTi5B and Ti to A356 alloy (Al-7Si-Mn-Fe). They found that the microstructure produced in the shot sleeve was heavily affected by the addition of grain refiners. There were some changes to the microstructure in the casting but, again, this was limited to the large dendrites formed in the shot sleeve. It is usually believed that the solidification rate in high pressure die casting is sufficiently rapid to render grain refining or the addition of Sr ineffective.



9.40 Variation in reject rate with increased metal pressure (Savage et al., 2001).



9.41 Effect of squeeze pressure on density for an Al-8Si alloy squeeze cast (Raji and Khan, 2006).



Metal freezes but is still hot and hence weak



Pressure fractures eutectic and produces a channel

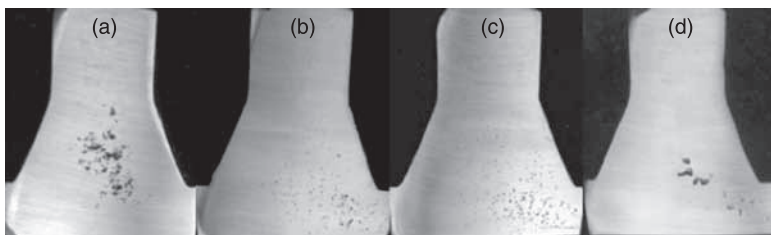
9.42 Segregation band due to pressure.

9.4.3 Gas porosity

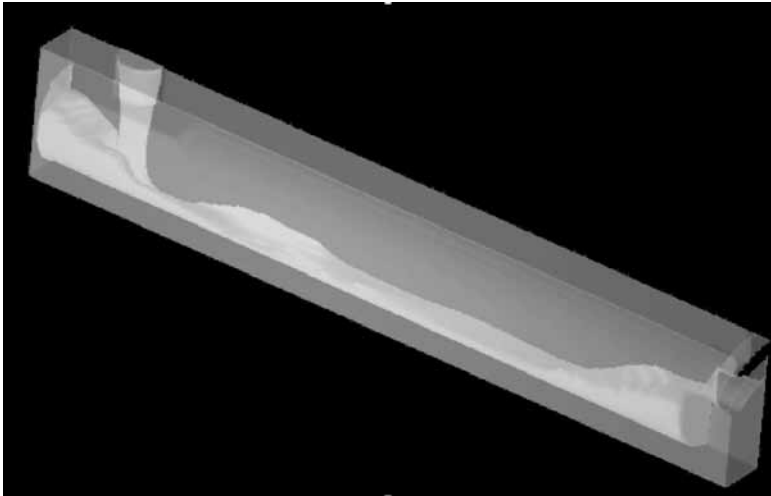
Gas porosity is one of the biggest problems in die casting. Over the years the allowed level of porosity has continually decreased. This has been partly due to the changes in gasket material in automotive components. In the 1960s the gasket was either a cork or paper gasket. Due to the compliance of the gasket material, the castings were only rough machined and this tended to cover up any small-to-medium pores. Now, the gasket material is often sprayed on to the two mating surfaces as a thin layer. This is cheaper and easier to apply, but requires a fine machined surface finish. This near-mirror finish easily shows up any minor defects within the casting.

The other reason for reduction in pore size is the improvements in X-ray radiography. The new fine screen systems can easily see pores that were invisible a decade ago. It has been an interesting phenomenon to watch companies that upgrade their radiography systems. Suddenly they are very concerned that the castings they are receiving are ‘full of gas pores’, yet they could not see them with the old system. The casting quality often has not changed, just their ability to see it. The casting is still fit for service.

So, what causes gas porosity and how do you fix it? It turns out that almost every phase of the process can produce gas porosity!



9.43 Effect of Sr and Na on the porosity level in an Al-10Si-Mg casting, with (a) unmodified, (b) 50 ppm Sr, (c) 100 ppm Sr, and (d) Na-modified (Sigworth, 2008).



9.44 Wave motion in shot sleeve due to pouring action (Lukezic, 2008).

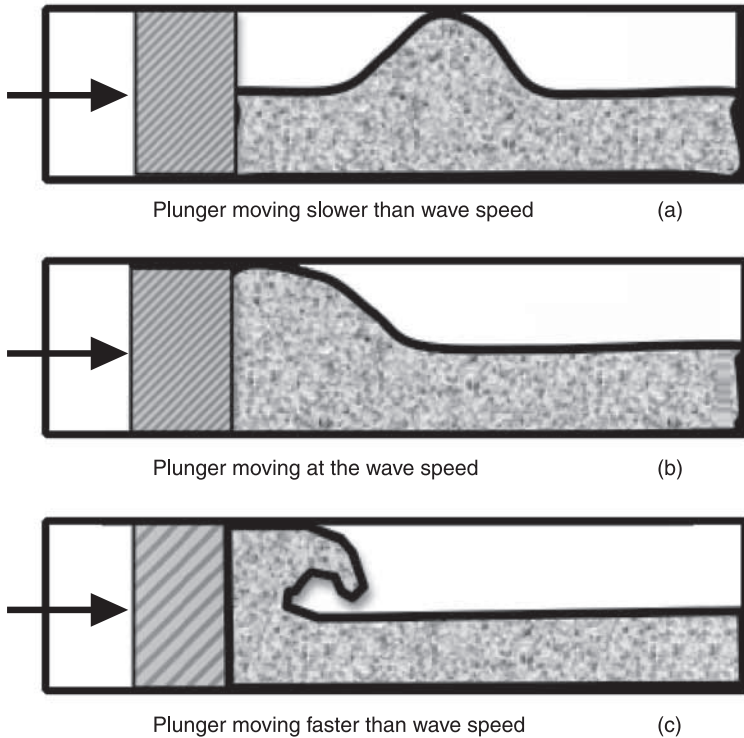
Shot sleeve

The metal is poured into the shot sleeve through a slot or channel in the top of the shot sleeve. This usually causes a wave to form that can splash into the runner and partly block the runner. This blockage can lead to excessive turbulence that, in turn, causes air entrainment in the flowing molten metal. The wave motion in a shot sleeve due to pouring is shown in Fig. 9.44.

You can also form a wave in the shot sleeve due to the motion of the plunger (Mobley et al., 2003). The molten metal wave forms in the shot sleeve due to it being a constrained channel that is partly filled. The wave moves with a velocity that depends on the diameter of the channel (shot sleeve) and the amount of molten metal (percentage fill). If the plunger is moving slower than this wave velocity then the wave will continue ahead faster than the plunger. This can leave an air gap behind the wave which can be entrained into the flowing molten metal (see Fig. 9.45a). If the plunger moves faster than the wave velocity then the wave breaks similar to a wave on the beach. This also traps air (see Fig. 9.45c). If the plunger moves at the same speed as the wave then the wave can push the air out in front of the flow, thus reducing the air entrainment (see Fig. 9.45b).

The runner

It must be remembered that the molten metal is travelling at a high speed throughout the flow system in the die. The runner takes the metal from the shot sleeve up to the part cavity. It is usually a channel cut into the die (Fig. 9.46).



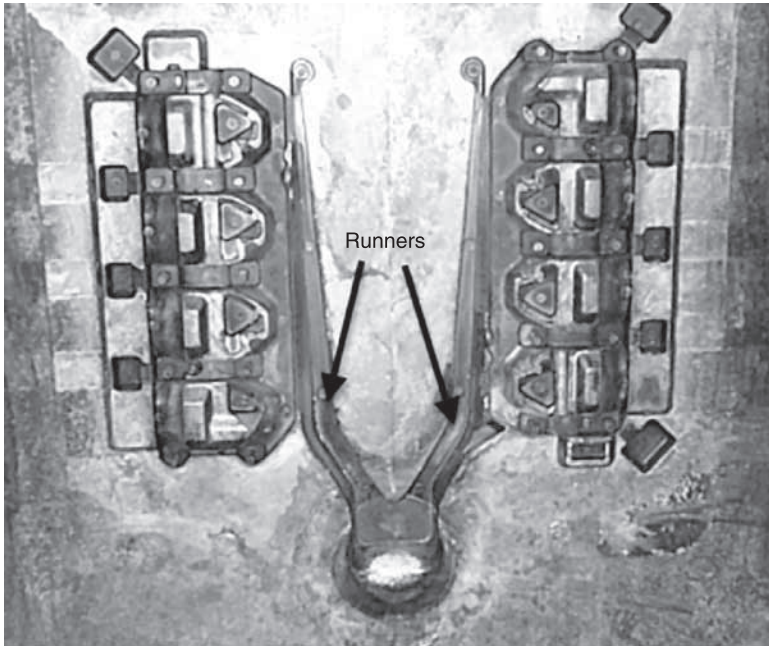
9.45 (a)-(c) Changes in wave with plunger speed.

It has been shown by many researchers that this high velocity flow can be fragmented easily. This fragmentation usually results in the entrainment of air into the molten metal. Recent simulations show this in the best form, for example Fig. 9.47.

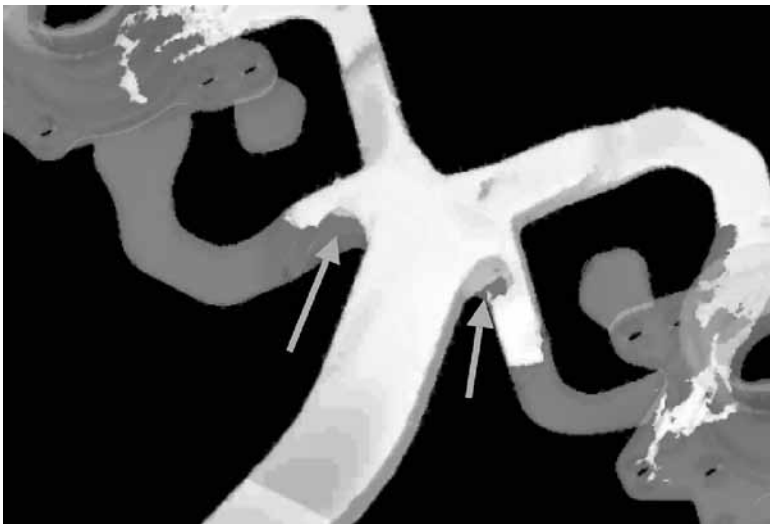
Therefore, it is good practice to have gradual changes in direction so that the molten metal front is kept unbroken. Hence, any bends in the runner are usually required to have a reasonable radius. Murray (2006) recommends that the bend has an internal radius of twice the width of the runner (Fig. 9.48).

Flow in the cavity

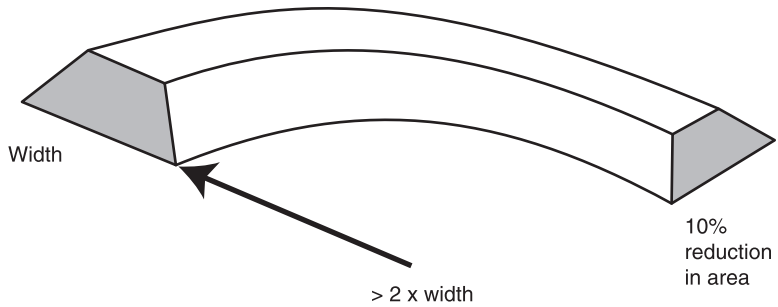
As stated previously, the flow in the cavity can trap air between major flows, within the centre of vortices or in long bosses where the flow progresses up on one side of the boss and back along the other side. When the porosity is formed in these flow areas it is common to see a particular elongated shape rather than a traditional round morphology. As can be seen in Fig. 9.49, the gas porosity has been elongated by the flow proceeding out of the boss. This is typical of gas related porosity. When the flow in the cavity is grossly incorrect, it is possible to



9.46 Runners in a two-cavity die.



9.47 Fragmentation of the flow due to runner changes (Lukezic, 2008).

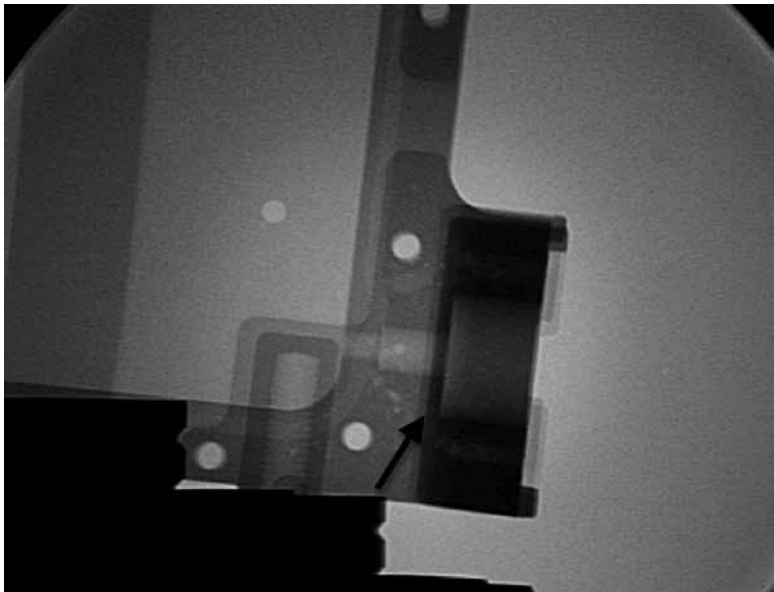


9.48 Suggested minimum radius of curvature for bends in the runner (Murray, 2006).

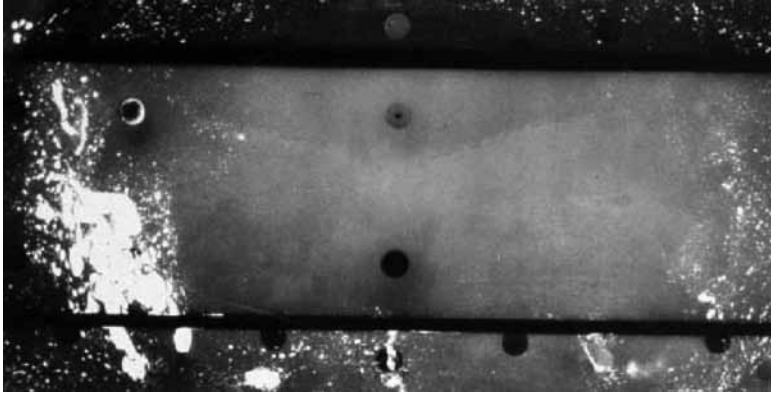
determine the vortices within the flow from the porosity. The gas pores have a comet-like tail due to the vortices formed (Fig. 9.50).

Venting the gas in the cavity

The die is full of air before the molten metal is injected. This is both the air in the runners and the cavity. This air must be removed during cavity filling or else it will be trapped in the cavity and result in gas porosity. There are two ways of removing this air. The first is to place thin channels around the cavity that are



9.49 Radiograph of porosity in a casting showing the elongated shape typical of flow-type gas porosity.



9.50 Gas porosity in a casting evident in a radiograph; this part had very poor molten metal flow.

typically 10 mm wide and 0.15 mm deep. These allow the air to escape but inhibit the molten aluminium from travelling along the channels, see Fig. 9.51.

The second is to use a vacuum to suck the air out of the cavity. This requires some extra technology as the vacuum channels need to be large so that the maximum amount of air can be removed. However, these large channels can then



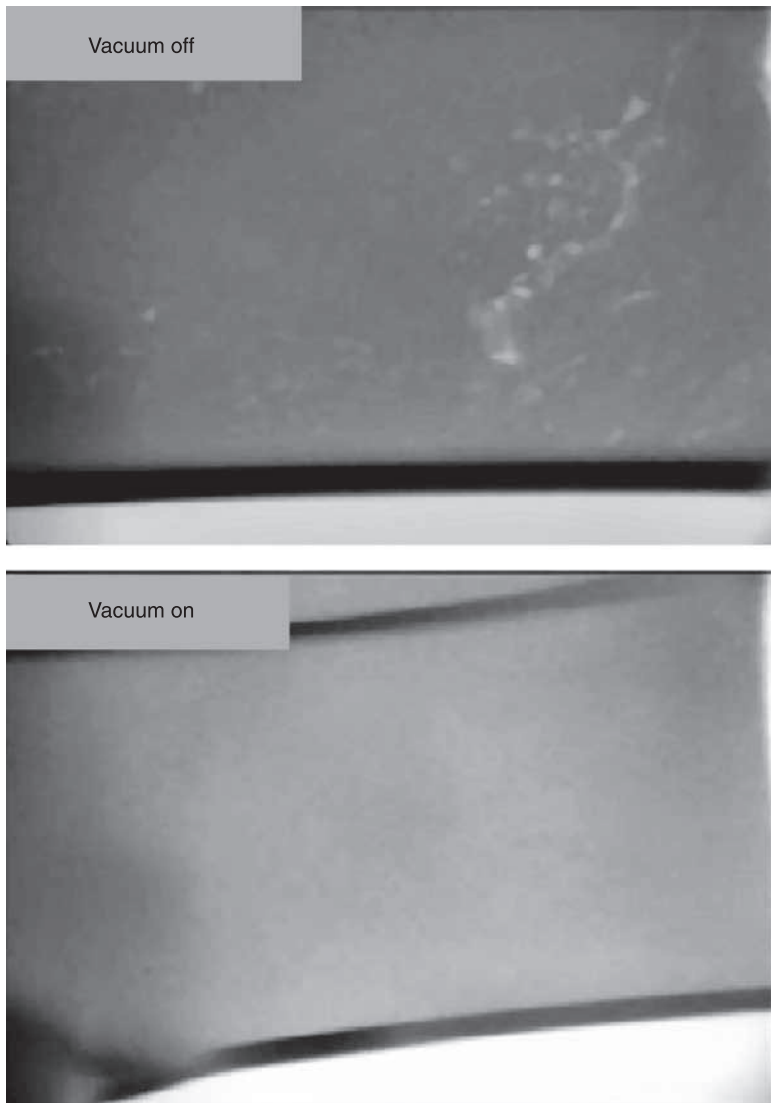
9.51 Typical vents machined into the die.



9.52 The Fondarex vacuum valve.

allow molten aluminium to be ejected from the die. Hence, there is usually a valve or similar attachment to the die that enables air to be removed but inhibits aluminium egression.

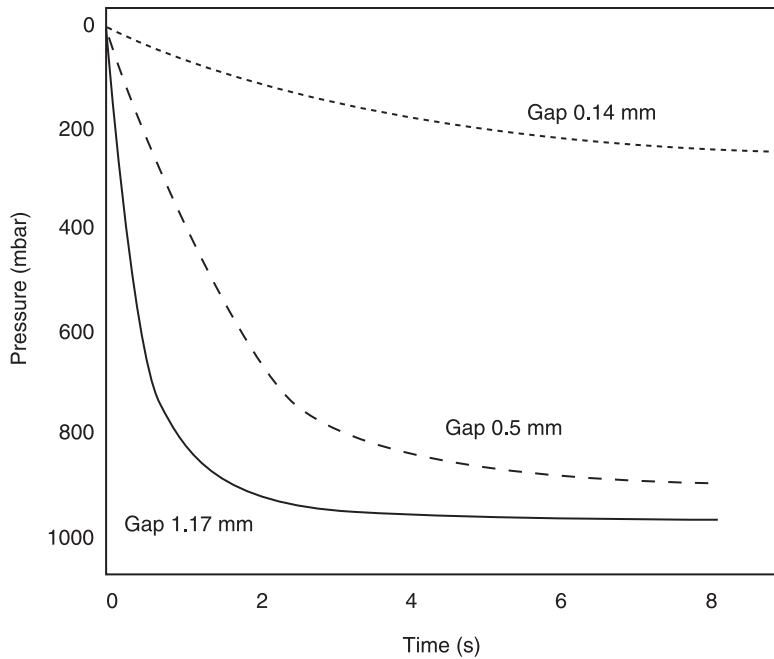
A typical vacuum valve is shown in Fig. 9.52. Brown et al. (2007) measured the effect of using vacuum on ultra-high quality die castings. They found that substantial improvement could be made with the correct application of vacuum (Fig. 9.53). This is also borne out by the experiences in many die casting companies. Wang et al. (2007) used a chill vent to act as the vacuum valve. This is a series of flats in a washboard pattern that are cooled, so that the metal freezes before ejecting from the die. They found that the channel gap was critical in achieving a reasonable vacuum within two seconds (Fig. 9.54).



9.53 Effect of vacuum application to a cavity on the porosity (Brown et al., 2007).

9.5 Conclusion

High pressure die casting of aluminium alloys involves the control of metals travelling at high speed, being subjected to high pressures and high solidification rates. The requirements of the current customers for the components being



9.54 Level of vacuum achieved in the cavity using a chill vent of different thicknesses (Wang et al., 2007).

manufactured are typically to achieve very high integrity with no visible porosity and very high dimensional accuracy, and with a very low reject rate.

As has been shown, there are a number of variables whose changes can result in shrinkage porosity, gas porosity, cold flow or a number of other defects that have not been mentioned.

The fact that die casting can and does produce high strength parts at a competitive price attests to the long history of die casting research that has been carried out within die casting and machine manufacturing companies as well as research centres. This data has been dissimulated through a number of venues, but none stands out more than the North American Die Casting Association. As can be seen from the references, most of the practical research results are spoken about in their conferences.

High pressure die casting has come a long way since Sturges' patent in 1849. With the aid of computer simulation and new algorithms, the future understanding of the process is even brighter for the die caster.

It will never be easy. Better processes mean higher expectations from the customer, which will put added pressure on the die caster. There will always be die casters competing for the market and this is healthy.

9.6 References

- Aharonov, R.R., Chellapilla, S., Janoss, B., Shivpuri, R. and Lakare, A. (1999) 'An investigation of the corrosion of H13 steel coated with CrN in molten aluminum alloys: Effect of steel surface preparation and coating thickness', *NADCA Transactions*, Cleveland, T99-113.
- Aluminium Standards and Data. (1997) *Ingots and Castings*. The Australian Aluminium Council, Dickson.
- Bailey, G., Taylor, G.A., Bounds, S.M., Moran, G. and Cross, M. (1997) 'PHYSICA: A Multiphysics Computational Framework and its application to casting simulation', *International Conference on CFD in Mineral and Metal Processing and Power Generation*, CSIRO, Australia.
- Barnard, N.C., (1925) 'Die casting – 1', *Machinery Forum*, Feb 5, 1925.
- Brown, Z., Bigelow, J., Ryder, R. and Dasgupta, R., (2006) 'Advancements in high pressure die casting processes', *NADCA Transactions*, Paper T06-021.
- Brown, Z., Szymanowski, B., Musser, M., Saha, D. and Seaver, S., (2007) 'Manufacturing of thin wall structural automotive components through high vacuum die casting technology', *NADCA Transactions*, Paper T07-022.
- Dix, E.H. and Keller, J.F. (1929) 'Microscopic analysis of specimens of die casting alloys', *ASTM Proceedings*, Vol. 29, Pt. 1, pp. 215–228.
- Doehler, H.H., (1951) *Die Casting*, McGraw-Hill, New York.
- Dour, G., Dargusch, M., Davidson, C., Nel, A. and St John, D. (2003) 'Development of a non intrusive heat transfer coefficient gauge and its application to high pressure die casting', *Proceedings of the First International Light Metals Technical Conference*, Brisbane, Australia, pp. 155–160.
- Fan, Z. (2002) 'Semisolid metal processing', *International Metal Review*, 47 (2), pp. 49–85.
- Flemings, M.C., Young, K.P. and Riek, R.G. (1977) 'Thixocasting of steel', *Journal of SDCE 9th International Congress*, Paper G-T77-092.
- Frommer, L. (1925) 'Der Spritzguss und Seine Aufgaben fur die Metallkunde', *Zeitschrift für Metallkunde*, August and September, 1925.
- Gershenson, M., Rohan, P.W. and Murray, M.T. (1999) 'Formation of cold flakes in aluminium high pressure die casting', *Transactions of North American Die Casting Association*, Paper T99-085.
- Gulizia, S. (2008) *Soldering in High Pressure Die Casting (HPDC): Performance Evaluation and Characterisation of Physical Vapour Deposition (PVD) Coatings*, Masters Thesis, 2008, Swinburne University of Technology, Melbourne, Australia.
- Gunasegaram, D.R., Finnin, B.R. and Polivka, F.B. (2007) 'Melt flow velocity in high pressure die casting: Its effect on microstructure and mechanical properties in an Al–Si Alloy', *Materials Science and Technology*, Vol. 23, Number 7, pp. 847–856.
- Han, Q. and Viswanathan, S., (2003) 'Analysis of the mechanism of die soldering in aluminum die casting', *Metallurgical and Materials Transactions A*, 34: 139–146.
- Hansen, L.F. (2009) Private communication, 4c-technologies, Copenhagen, Denmark.
- Herman, E.A. (1985) *Die Casting Dies: Designing*, NADCA publication No. ECDS 506.
- Herman, E.A. (1991) *Die Casting Process Engineering and Control*, NADCA Publication E410, North American Die Casting Association, Chicago, USA.
- Jahedi, M.Z. and Fraser, D.T. (2001) 'Prevention of soldering in high pressure die casting dies using aluminium and iron oxide surface treatments', *NADCA Transactions*, Paper T01-112.

- La-Orchan, W. (1994) *Quantification of the Reduced Pressure Test*, PhD Thesis, McGill University, P2.
- Laukli, H.I., Gourlay, C.H. and Dahle, A.K. (2004) 'Segregation Band Formation in Al-Si Die Castings', *Metallurgical Transactions A*, Vol. 35, Number 9, September 2004, pp. 2881–2891(11).
- Laukli, H.I., Arnberg, L. and Lohne, O. (2005) 'Effects of grain refiner additions on the grain structures in HPDC A356 castings', *International Journal of Cast Metals Research*, 18 (2): 65–72(8).
- Lin, J.Z., Lanka S. and Ruden T. (2005) *Physical and Virtual Prototyping of Magnesium Instrument Panel Structures*, SAE Technical Paper 2005-01-0726.
- Lukezic, B. (2008), Private communication, Flow Science, USA.
- Makhlouf, M.M. and Apelian, D. (2002) *Casting Characteristics of Aluminum Die Casting Alloys*, US Department of Energy Report DEFC07-99ID13716, Final Report Feb 5.
- Makhlouf, M.M., Apelian, D. and Wang, L. (1998) *Microstructures and Properties of Aluminum Die Casting Alloys*, North American Die Casting Association Publication No. 215.
- Makhlouf, M.M., Apelian, D. and Wang, L. (2001) 'Sludge formation tendency of selected aluminum die casting alloys', *NADCA Transactions*, T01-083.
- Mehta, K.B., Akay, H.U., Walkington, W.G. and Holland, R. (2003) 'A case study for simulation-based improvements in dimensional accuracy of die cast parts', *NADCA Transactions*, Paper T03-017.
- Mobley, C., Sahai, Y. and Brevicek, J. (2003) *The Effects of Externally Solidified Product on Wave Celerity and Quality of Die Cast Products*, US Department of Energy Grant/Contract No. DE-FC07-99ID13844, OSURF Project No. 739694, Report Period: 07-03-2000 through 07-02-2003.
- Murray, M.T. (2006) *'Runner Design' Training Manuals*. Australia: M Murray & Associates.
- Murray, M.T. (1979) *Fracture of a Zinc Diecasting Alloy*, Master's Thesis, Monash University, Clayton, Victoria, Australia.
- Raji, A. and Khan, R.H., (2006) 'Effects of pouring temperature and squeeze pressure on Al-8%Si alloy squeeze cast parts', *AU.J.T.*, 9 (4): 229–237.
- Savage, G., Gershenzon, M. and Rogers K.J. (2001) 'The role of pressure in high pressure die casting', *NADCA Transactions*, Paper T01-053.
- Sequeira, W.P., Dunlop, G.L. and Murray, M.T. (1996) 'Effect of section thickness microstructure and mechanical properties of high pressure die casting magnesium alloy AZ91D', *Proceedings of the Third International Magnesium Conference*. Manchester, UK.
- Sigworth, G.K. (2008) 'Modification of Al-Si casting alloys: Important practical and theoretical aspects', *AFS Transactions*, Schaumburg, IL, Paper 08-019(02).pdf, pp. 1–25.
- Suarez-Pena, B., Asensio-Lozano, J., Verdeja-González, J.I. and Pero-Sanz Elorz, J.A. (2007) 'Microstructural characterization and process selection by attributive analysis of eutectic and quasi-eutectic Al-Si alloys for pressure die casting', *Revista de Metalurgia*, 43 (4), pp. 310–317.
- Takach, B.V. (1993) *Pressure Die Casting Knowledge*, Australian Die Casting Association, Australia.
- Tian, C. (2001) unpublished research.
- Vinarcik, E.J., (2003) *High Integrity Die Casting Processes*, John Wiley & Sons, New York.

- Walkington, W. (2004) *Defects in Die Casting*, North American Die Casting Association.
- Wang, L., Gershenzon, M., Nguyen, V. and Savage, G. (2007) 'Air evacuation and metal solidification with varied profiles of chill surfaces', *NADCA Transactions*, Paper T07-111.
- Wang, L., Rohan, P. and Murray, M. (1999) 'Porosity redistribution by molten metal transport due to variations in die cooling', *NADCA Transactions*, Paper T99-074.
- Wang, L., Nguyen, T., Law, J. and Luxford, G. (2004) 'Wave control in the Shot Sleeve of High Pressure Die Casting Process', *Proceedings of the Australian Diecasting Conference*, P13.
- Witt, H. (2009) *Advantages & Disadvantages of Different Aluminum Impeller Designs*. Available online at: www.wittfan.de/english/techinf_alublade.php (accessed December 2009).

Progress on the heat treatment of high pressure die castings

R.N. LUMLEY, CSIRO Light Metals Flagship, Australia

Abstract: This chapter discusses the development of heat treatment procedures for high pressure die castings, the role of alloy chemistry, development of microstructure, and application to industrially produced products. The discovery that conventional high pressure die castings can be heat treated by a newly developed procedure now means that consideration can be given to designing HPDC alloys specifically for heat treatment, while retaining high castability.

Key words: high pressure die casting, HPDC, heat treatment, alloy design.

10.1 Introduction

Aluminium alloys used for high pressure die casting are mostly those based on the alloying systems Al-Si-Mg and Al-Si-Cu and composition ranges of some of the more common alloys used worldwide are shown in Table 10.1. Two important features of conventionally produced HPDCs are: (i) the high turbulence experienced by the shot of molten metal as it is forced at high speed into a die and (ii) the very rapid rate at which it then solidifies. Because of this, castings often contain internal pores comprising entrapped gases, such as air, hydrogen or vapours, formed by the decomposition of organic lubricants. The gas content inside high pressure die cast parts varies between 10 and 50 cc/100 g (normalised to ambient temperature and pressure) (Badini et al., 2002). Moreover, the gas volume is compressed by up to 1000 times during intensification under a metal pressure of 100 MPa during the casting process. Metal shrinkage during solidification and planar defects such as oxide skins or cold shuts may also result in porosity. The rapid rate of solidification also means that the microstructures developed within a high pressure die casting are usually inhomogeneous. The 'skin' layer of metal is typically much finer and of higher integrity when compared to the internal structure of the casting. Examples of the skin and interior microstructures from a common A380 HPDC casting are shown in Fig. 10.1.

While some level of porosity in die castings is normal (e.g. Fig. 10.2), the existence of internal pores containing gases under pressure does present a significant disadvantage because components made from HPDC alloys that are age hardenable cannot be solution treated under the same conditions used for other casting alloys (e.g. at 540°C for eight hours). The gas-containing pores trapped within the

Table 10.1 HPDC alloys from different world regions that are amenable to heat treatment*

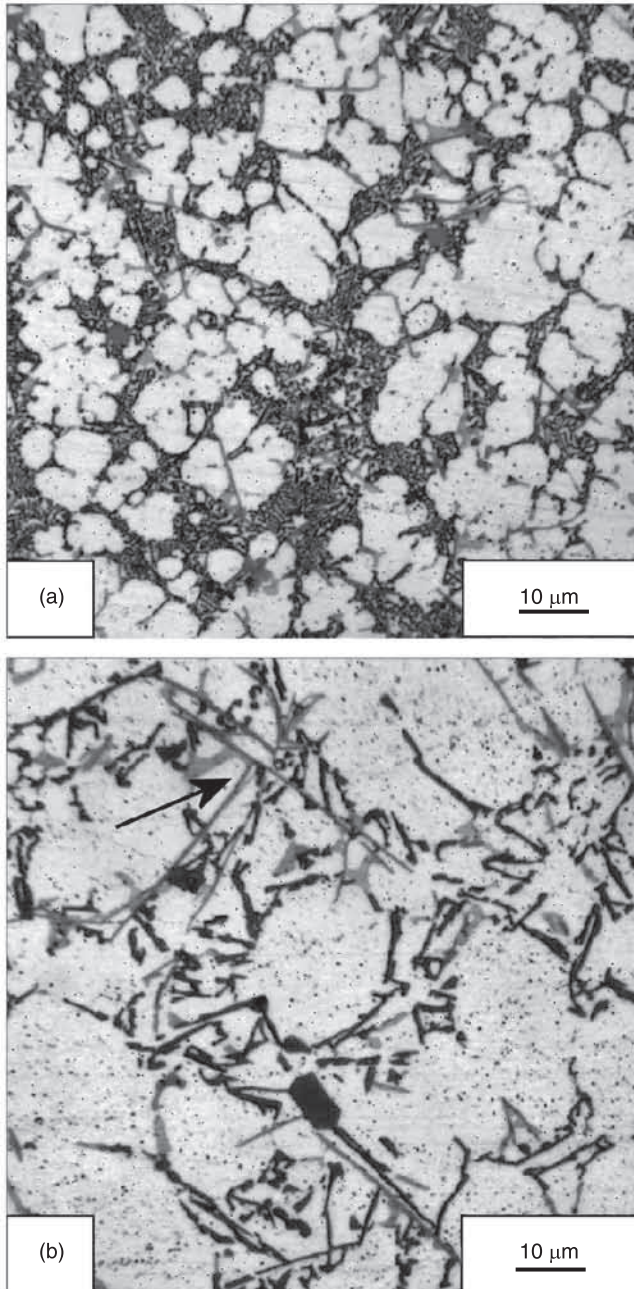
Alloy/wt% (Al bal)	Si	Fe	Cu	Mn	Mg	Ni	Zn	Pb	Sn	Ti	Other total
CA313 (Aus)**	7.5–9.5	1.3	3.0–4.0	0.5	0.3	0.5	3	0.35	0.25	0.2	0.2
A380 (US)	7.5–9.5	1.3	3.0–4.0	0.5	0.1	0.5	3		0.35		0.5
C380 (US)	7.5–9.5	1.3	3.0–4.0	0.5	0.1–0.3	0.5	3		0.35		0.5
A383 (US)	9.5–11.5	1.3	2.0–3.0	0.5	0.1–0.3	0.5	3		0.15		0.5
383 (US)	9.5–11.5	1.3	2.0–3.0	0.5	0.1	0.5	3		0.15		0.5
A384 (US)	10.5–12.0	1.3	3.0–4.5	0.5	0.1	0.5	1		0.35		0.5
B384 (US)	10.5–12.0	1.3	3.0–4.5	0.5	0.1–0.3	0.5	1		0.35		0.5
390 (US)	16.0–18.0	1.3	4.0–5.0	0.5	0.45–0.65	0.1	1.5		0.35	0.1	0.2
ADC10 (JIS)	7.5–9.5	1.3	2.0–4.0	0.5	0.3	0.5	1		0.3		
ADC12 (JIS)***	9.6–12.0	1.3	1.5–3.5	0.5	0.3	0.5	1		0.3		
AlSi8Cu3(Fe) (ISO)	7.5–9.5	1.3	2.5–4.0	0.6	0.3	0.5	1.2	0.3	0.2	0.2	0.5 (each)
AlSi9Cu3(Fe) (DIN 226)	8.0–11.0	1.2	2.0–3.5	0.1–0.5	0.1–0.5	0.3	1.2	0.2	0.1	0.15	0.15
SC84R (Canada)	7.5–9.5	0.7–1.2	3.0–4.0	0.5	0.45–0.75		0.7–1.2			0.1	0.15
LM2 (UK)	9–11.5	1.0	0.7–2.5	0.5	0.3	0.5	2	0.3	0.2	0.2	0.05
A360 (US)	9.0–10.0	1.3	0.6	0.35	0.4–0.6	0.5	0.5		0.15		0.25
AlSi10Mg (DIN 239B)	9.0–11.0	0.8	0.8	0.4	0.2–0.5		0.1			0.15	0.15
AK9 (CIS)	8.0–11.0	0.8	1	0.2–0.5	0.2–0.8	0.5	0.5				2.4
AK9M2 (CIS)	7.5–10.0	0.9	0.5–2.0	0.1–0.4	0.2–0.8	0.5	1.2	Pb+Sn	0.3	0.05–0.2	2.5

Notes:

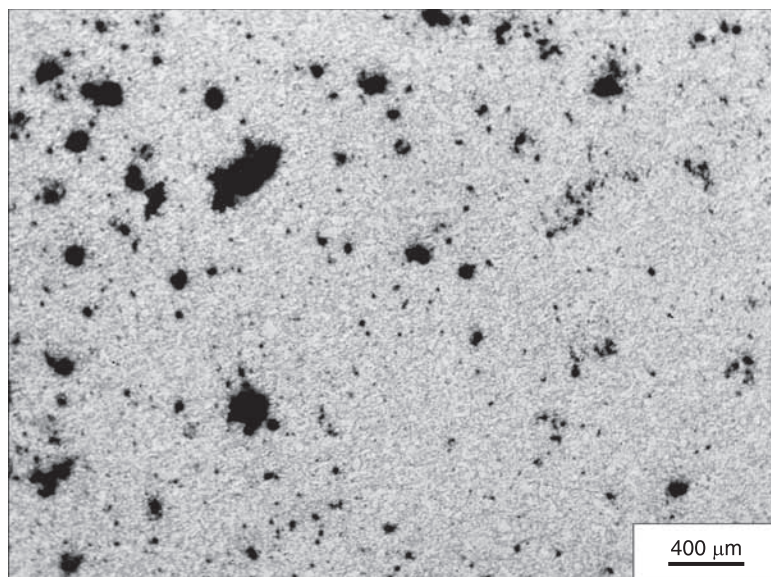
* Elements are maximums unless presented as ranges.

** May contain up to 0.1 Cr.

*** ADC12Z contains up to 3% Zn.



10.1 Optical microstructures of an A380 alloy as-cast (a) in the 'skin' region of the casting and (b) the internal microstructure, showing the size and morphology of the solidified eutectic. Fe-bearing needles of the β (Al_5FeSi) phase are arrowed in (b) (Lumley et al., 2008a).

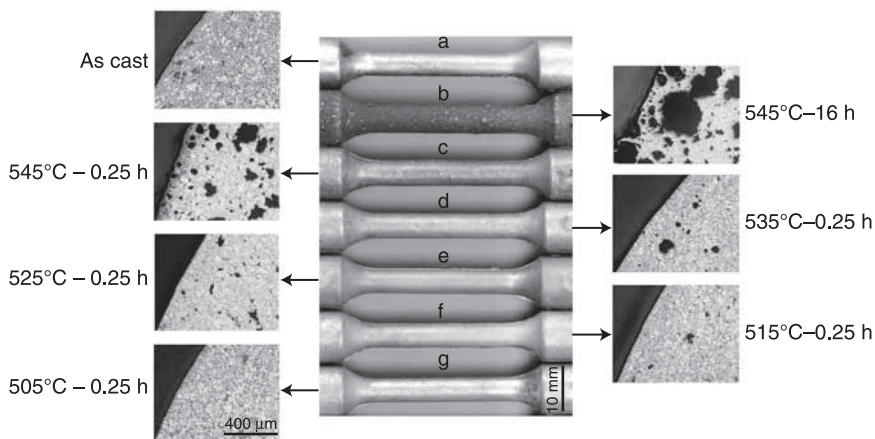


10.2 HPDC alloy in the as-cast condition showing porosity. The alloy was C380. Note that the microstructure is a mixture of shrinkage and gaseous porosity. The top left hand corner is towards the centre of the casting whereas the bottom right is towards the edge of the casting (Lumley et al., 2005).

microstructure expand resulting in unacceptable surface blistering. Swelling may also occur that changes the dimensions of the die cast parts, and can adversely affect mechanical properties. However, it has been shown recently that significant responses to age hardening are still possible if solution treatment temperatures and times are reduced (e.g. Lumley et al., 2005, 2006, 2007a, 2007b). As a result, the mechanical properties of the common HPDC alloys can be substantially improved.

Figure 10.3 shows specimens of A360 alloy (Al-9Si-0.7Fe-0.6Mg-0.3Cu-0.1Mn-0.2Zn), where an as-cast specimen (a) is compared with specimens that were heat treated using various solution treatment times and temperatures. Comparison of the as-cast specimen with the one that has been solution treated for 16 hours at 545°C (b) reveals that the latter has suffered severe surface blistering and discolouration. Swelling has also occurred so that the specimen has become dimensionally unstable in both axial and longitudinal directions. When the solution treatment time was reduced to 15 minutes (c) (note references to solution treatment time include that required to heat up), and the temperature was lowered, (d–g), both blistering and dimensional change were significantly reduced. At temperatures of 515°C and below (f and g), blistering is eliminated.

Included in Fig. 10.3 are representative micrographs of sections prepared from the same components and the internal appearance of the castings corresponds to



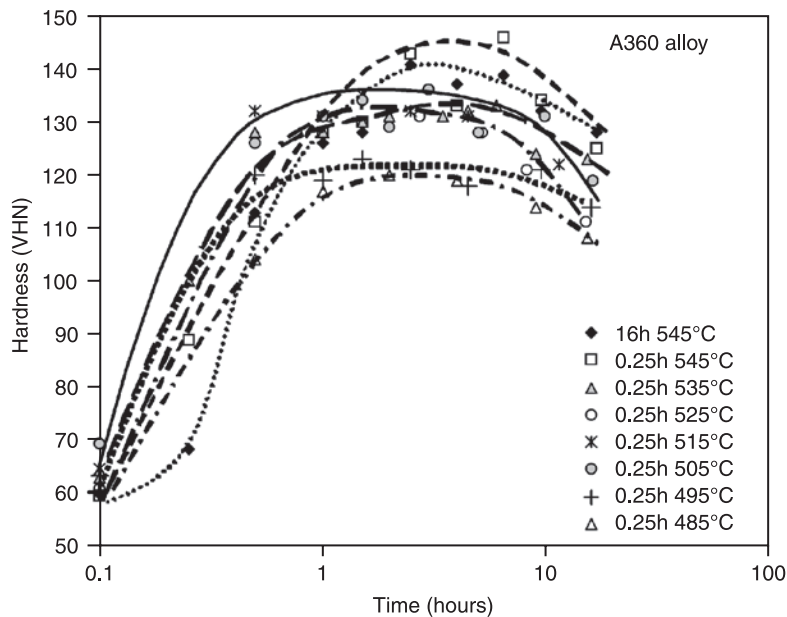
10.3 Comparisons of the surfaces and internal microstructures of an A360 alloy solution treated under different conditions (Lumley et al., 2007b).

the blistering present on the sample surface. Based on Fig. 10.3, it is clear there may be a thermal cycle within which the alloys can be at least partially solution treated. Subsequently, it was confirmed that alloy A360 retained a relatively high response to age hardening at 180°C even though the solution treatment was only 15 minutes and temperatures were progressively lowered from 540°C to 485°C (Fig. 10.4). In each case, the alloy aged rapidly at 180°C and peak hardness was achieved after about two hours.

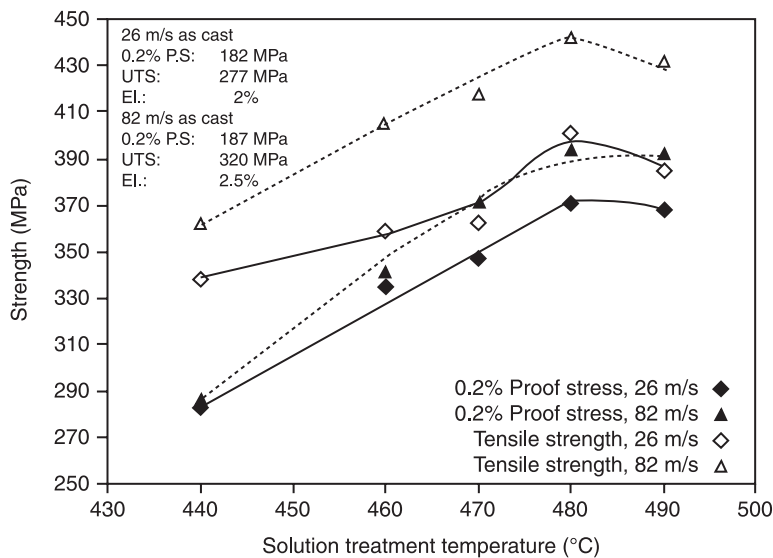
Further investigations on the effect of solution treatment temperature were conducted on a different alloy having the composition Al-8.8Si-0.86Fe-3Cu-0.2Mn-0.22Mg-0.59Zn (<0.2 other) which corresponded to alloy C380 in Table 10.1 (Lumley et al., 2007a). In this case, substantial responses to age hardening were achieved over the range of 440°C up to 490°C, with solution treatment of 15 minutes immersion, followed by water quenching and ageing at 150°C. The times to reach peak hardness for each solution treatment temperature were similar, although the actual peak hardness values and tensile properties decreased as the solution treatment temperature was reduced (Fig. 10.5) (Lumley et al., 2007b).

Figure 10.5 also shows the influence of melt velocity (at the gate) on the tensile properties in the T6 treated HPDCs. At solution treatment temperatures of 470°C and above, the samples produced at a melt velocity (at the gate) of 82 m/s have 0.2% proof strength values approximately 25 MPa above those for which a lower melt velocity of 26 m/s was used. For tensile strengths, the difference was as high as 56 MPa. At lower solution treatment temperatures, melt velocity still had a significant effect on tensile strengths, but not on values of 0.2% proof stress.

A wider range of alloy compositions have since been examined to determine their respective responses to heat treatment (e.g. Lumley et al., 2007, 2008a, 2009,



10.4 The hardening responses for A360 alloy aged at 180°C, following different solution treatment procedures (Lumley et al., 2007a).

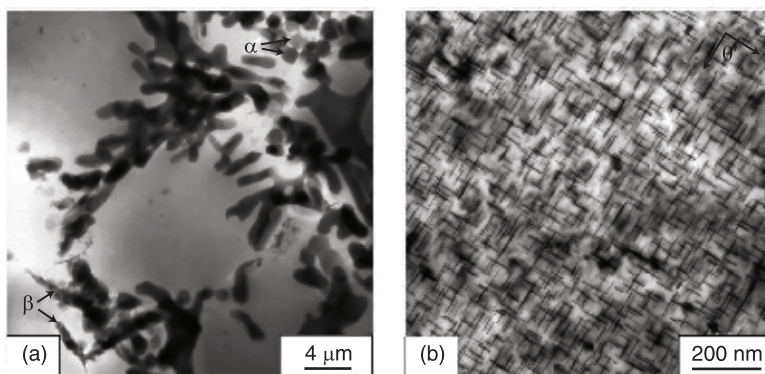


10.5 The effects of solution treatment temperature on tensile properties of HPDC alloy C380. Note that tensile elongations for all results shown in Fig. 10.5 were between one per cent and two per cent. Five samples per condition were tested. Alloy specimens for tensile testing were flat specimens 70 mm long, 14 mm wide and 3 mm thick with a central gauge length of 30 mm and width of 5.65 mm (Lumley et al., 2007b).

2009a, 2009b, 2009c). Of particular interest were the roles of the potent age-hardening elements Cu, Mg, Si and Zn. As discussed in other chapters, for heat-treated aluminium alloys containing these elements, strengthening precipitate phases such as θ' (Al_2Cu), S (Al_2CuMg) β' ($\text{Al}_3(\text{MgSi})^1$) and Q' ($\text{Al}_5\text{Cu}_2\text{Mg}_8\text{Si}_6$) form within the aluminium grains. It is these precipitates that provide an impediment to the process of crystallographic slip, thereby increasing mechanical strength. Although up to three per cent Zn is permissible in some HPDC alloy variants, there is usually insufficient Mg present to form significant quantities of η' precipitates, (MgZn_2).

In the HPDC alloys containing high levels of Si, the contributions precipitation hardening may make to strengthening are additional to those arising from the presence of the Al-Si eutectic (Fig. 10.6). In this regard, an interesting comparison may be made between binary wrought Al-4Cu alloy and a HPDC composition containing a similar atomic percentage of Cu (Table 10.2). Within the aluminium grains, both alloys display a similar precipitate structure containing the θ' phase. For the binary Al-Cu alloy, the 0.2% proof stress is 236 MPa, whereas for the more complex microstructure in the HPDC composition, the 0.2% proof stress is 379 MPa.

As shown with reference to Table 10.3 and Fig. 10.7, compositional differences in Al-Si-Cu die castings may cause large variations in mechanical properties after age hardening. In this example, nine different alloys were prepared in as-cast, as solution treated, T4 treated, or T6 treated conditions. Solution treatment was standardised at 490°C for 15 minutes total immersion time in a circulating air furnace, followed by water quenching (Lumley et al., 2005, 2006, 2007a, 2007b). Specimens for the T6 tempers were subsequently aged in oil at 150°C for 24 hours and those for T4 tempers were aged at 25°C for 14 days. As solution treated and



10.6 TEM micrographs of an A380 alloy aged to a T6 temper, showing the various features within the heat treated microstructure: (a) shows grains within the solidified microstructure (also showing silicon, and α or β intermetallic Fe-bearing particles, arrowed) and (b) shows the precipitate structure present within the aluminium grains (Lumley et al., 2008a).

Table 10.2 Comparison of properties developed from either the binary Al-Cu alloy or the more complex HPDC alloy, displaying a similar Al:Cu ratio

Product form	Alloy (wt%)	Alloy (at%)	Atomic ratio Al:Cu	0.2% Proof stress (MPa)	Tensile strength (MPa)	Elongation (%)
Wrought T6	Al-4Cu	Al-1.74Cu	56.5:1	236	325	5
HPDC T6 (Alloy 4)	Al-8.6Si-3.6Cu-0.93Fe-0.1Mg-0.53Zn-0.18Mn	Al-8.54Si-1.58Cu-0.46Fe-0.11Mg-0.23Zn-0.09Mn	56.3:1	379	457	2.7

Source: Lumley et al. (2008a)

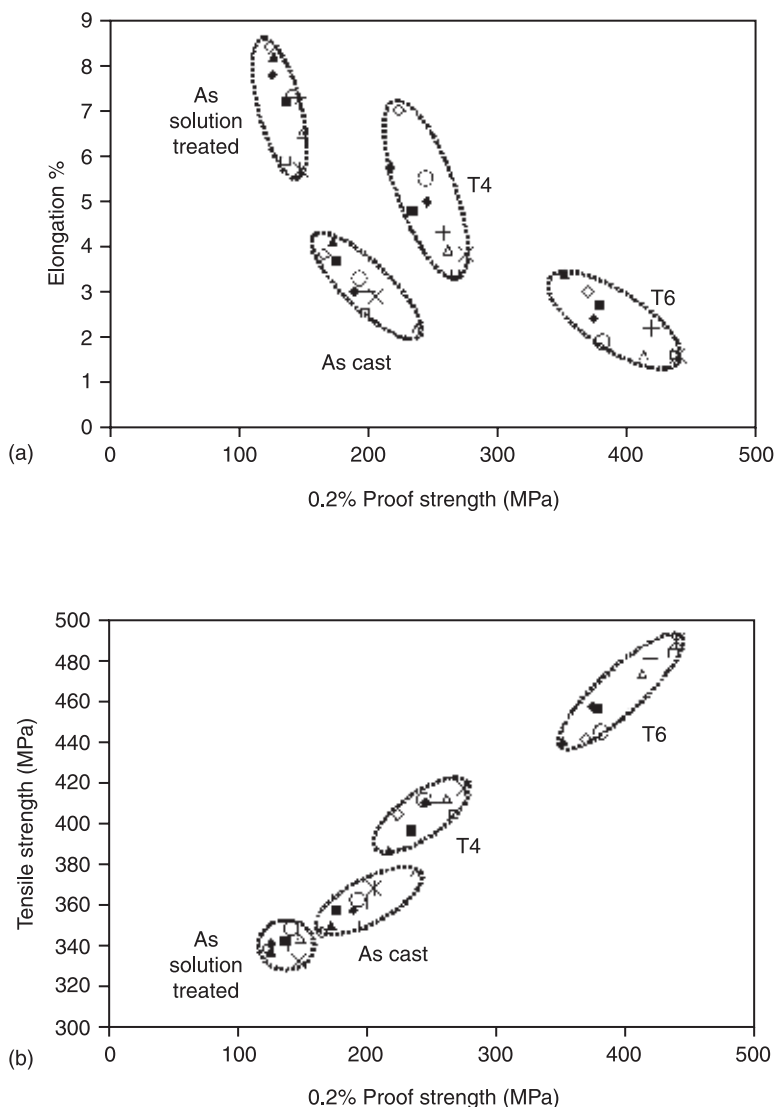
quenched specimens were also prepared and the tensile properties were determined immediately following quenching.

Typically, the as solution treated and quenched specimens displayed an approximate 30% decrease in 0.2% proof stress compared to the as-cast condition, although elongation was increased. Ageing to the T4 temper raised the 0.2% proof stress to about 30% above that for the as-cast condition with values ranging between 217 MPa and 275 MPa, and in most cases, there was a simultaneous increase in tensile elongation. Ageing to the T6 temper typically raised the 0.2% proof stress by 100% or more. For Alloy 1, which contained lower Cu and Mg contents, the 0.2% proof stress in the T6 temper was 352 MPa whereas for Alloy 5 which contained higher Cu and Mg content, the 0.2% proof stress value was as

Table 10.3 Compositions of nine alloys examined

Alloy	Figure 10.7 legend	Al	Si	Cu	Mg	Zn	Fe	Mn	other
1 (base)	▲	Balance	9	3.1	0.1	0.53	0.86	0.16	<0.2
2	◆	Balance	9.1	3.18	0.29	0.6	0.86	0.14	<0.2
3	◇	Balance	9.2	3.11	0.09	2.9	0.9	0.16	<0.2
4	■	Balance	8.6	3.6	0.1	0.53	0.93	0.18	<0.2
5	+	Balance	8.6	3.6	0.3	0.53	1.0	0.2	<0.2
6	○	Balance	8.5	4.9	0.1	0.51	0.97	0.2	<0.2
7	*	Balance	8.7	4.9	0.27	0.51	1.0	0.21	<0.2
8	□	Balance	9.1	4.2	0.22	1.2	1.3	0.2	<0.2
9	△	Balance	8.8	4.0	0.7	0.56	1.1	0.19	<0.2

Source: Lumley et al. (2007)



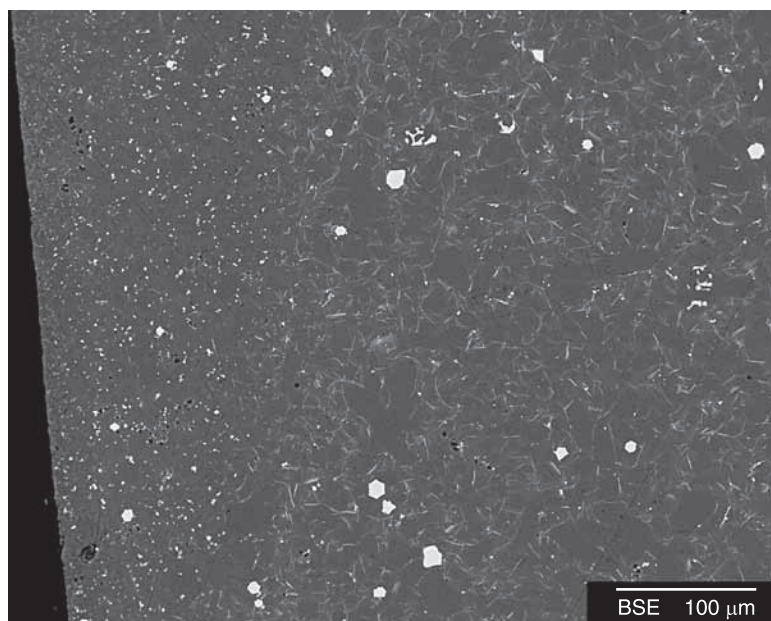
10.7 The mechanical properties of HPDC alloys based on Al-Si-Cu showing: (a) elongation as a function of average 0.2% proof strength and (b) tensile strength as a function of average 0.2% proof strength for the as-cast, as-solution treated, T4 and T6 tempers (Lumley et al., 2007c; see Table 10.3 for legend. Five samples per condition were tested. Alloy specimens for tensile testing were cylindrical and had a total length of 100 mm with a central parallel gauge length 33 mm long and a diameter of 5.55 ± 0.1 mm).

high as 419 MPa. There was little additional benefit in adding more than 3.6% Cu to the alloys, since the increases were more moderate (e.g. compare Alloys 7 and 8 with Alloy 5). Likewise, there was no observed benefit by raising the Mg content above 0.3%. For example, Alloy 9 showed values of 0.2% proof stress similar to those for Alloy 5, despite having elevated contents of both Mg and Cu.

10.2 Role of alloying elements during solution treatment

10.2.1 Silicon

Silicon is present in casting alloys to improve castability, to form a eutectic and to promote the formation of strengthening precipitates (in conjunction with other elements) through the decomposition of the saturated solid solution in which Si is retained from casting. Silicon also forms hard intermetallic particles when combined with Fe and Mn in the melt (e.g. β -Al₅FeSi), often referred to as ‘sludge’ (Jorstad, 1986) (see, e.g., Fig. 10.1 and 10.8). These elements are essential in HPDC alloys, as it is due to their presence that problems associated with die



10.8 Backscattered electron image of a T7 treated HPDC alloy Al-9.37 Si-0.73Cu-0.41Mg-0.31Zn-0.79Fe-0.21Mn-(<0.2 other), showing the distribution of Fe-bearing intermetallic particles, at the edge (left side) and interior of the casting. The polyhedral particles and script-like phases present are the α phase Al₁₅(Fe,Mn)₃Si₂ and the needle-shaped particles are the β phase, Al₅FeSi (image courtesy Colin MacRae, CSIRO).

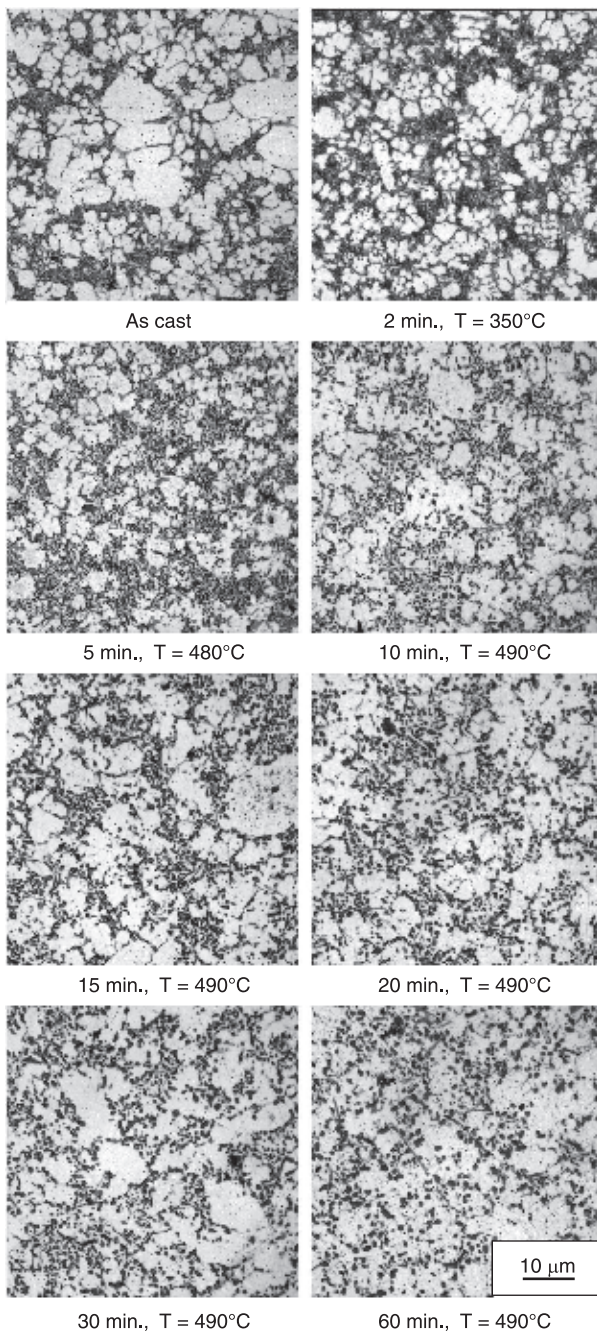
sticking and soldering are reduced or eliminated. The sludge particles also influence machinability, hardness, high temperature strength and fracture resistance.

As shown in Fig. 10.1, Si plate size in HPDC alloys can vary greatly between the edge and the centre of a part. During heating to the solution treatment temperature, the Si plates rapidly fragment and then become spheroidised. These microstructural changes are demonstrated for silicon particles at the edge of samples in Fig. 10.9 and are quantified in Fig. 10.10. Here it should be noted that similar effects also occur at the centre of a casting, but the changes are less pronounced. As shown by Fig. 10.9, when the alloy has reached 480°C (corresponding to a time of immersion of five minutes), a large quantity of fine, spheroidised Si has already formed within the microstructure. After a further five minutes the Si has begun to grow in size by a process of Ostwald Ripening and the number of particles present has begun to decrease. These changes are largely complete in less than 20 minutes after which little additional change occurs. Here it is also interesting to note that surface blistering was found to begin at the same time, i.e. 20 minutes.

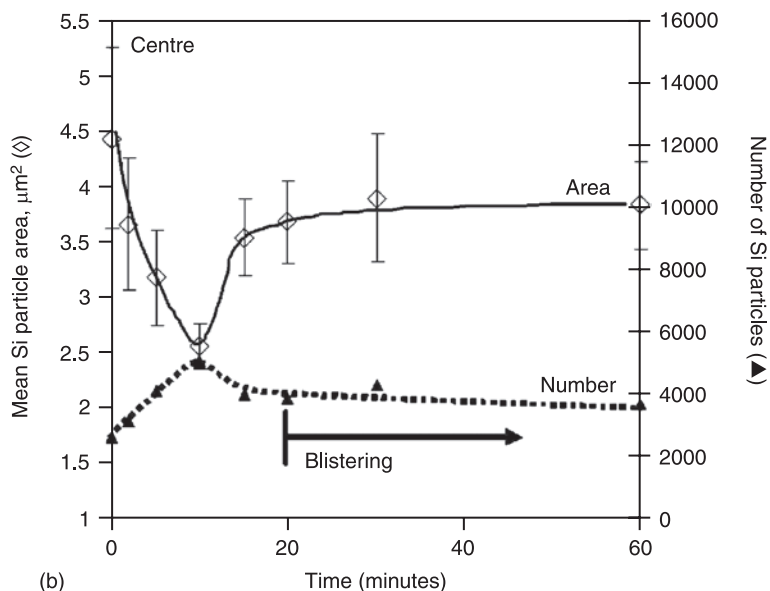
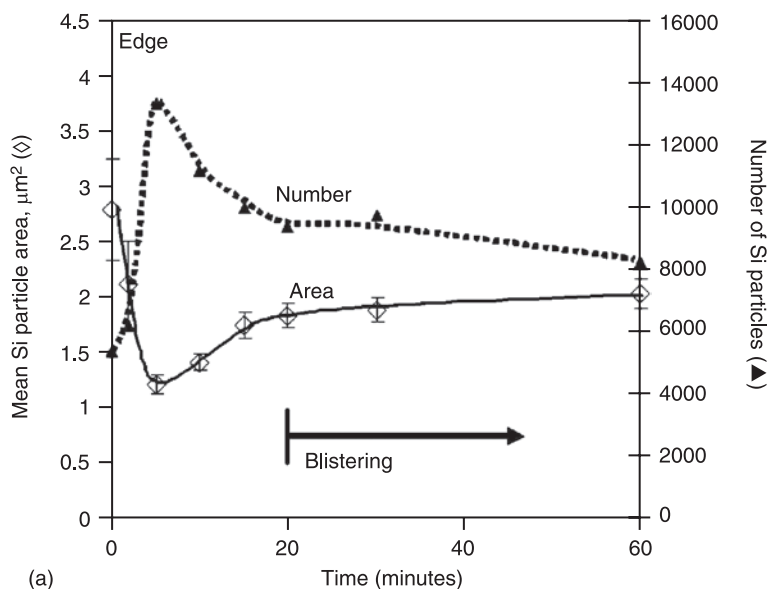
Figure 10.11 shows the microstructure of a sub-surface region of a HPDC in which a blister is in the process of being formed. In addition, what has been identified as an unexpanded blister (i.e. a thin, laminar defect) decorated with small Si particles is arrowed. Although the changes to the Si present within the microstructure and their correlation to the onset of blistering may be coincidence, it seems quite possible that the presence of particles of this size and their distribution has had a direct influence on pinning the defect, thereby preventing or delaying its expansion into an actual blister. Features such as these have been observed to be discontinuous defects displaying only partial metallurgical bonding across their interfaces, and would appear to be responsible for a significant proportion of blisters that are generated during the solution treatment process, as shown in Fig. 10.3(b) and 10.3(c). One explanation is that small pockets of gas entrapped at high pressure in these laminar defects cause them to expand to form small cracks, which then extend and coalesce with adjacent cracks forming from other gas pockets. These laminar defects then continue to coalesce and grow, eventually producing large surface blisters. Analysis has revealed that these defects may be readily detected using high resolution laboratory X-ray imaging. As shown in Fig. 10.12, they appear essentially as a two-dimensional feature, not unlike 'froth', rather than as a discrete, spherical gas pore (e.g. see Fig. 10.2). A diagrammatical representation of the proposed progression of blister formation from laminar features in the microstructure is shown in Fig. 10.13 which is based on these observations of blistering phenomena.

10.2.2 Copper

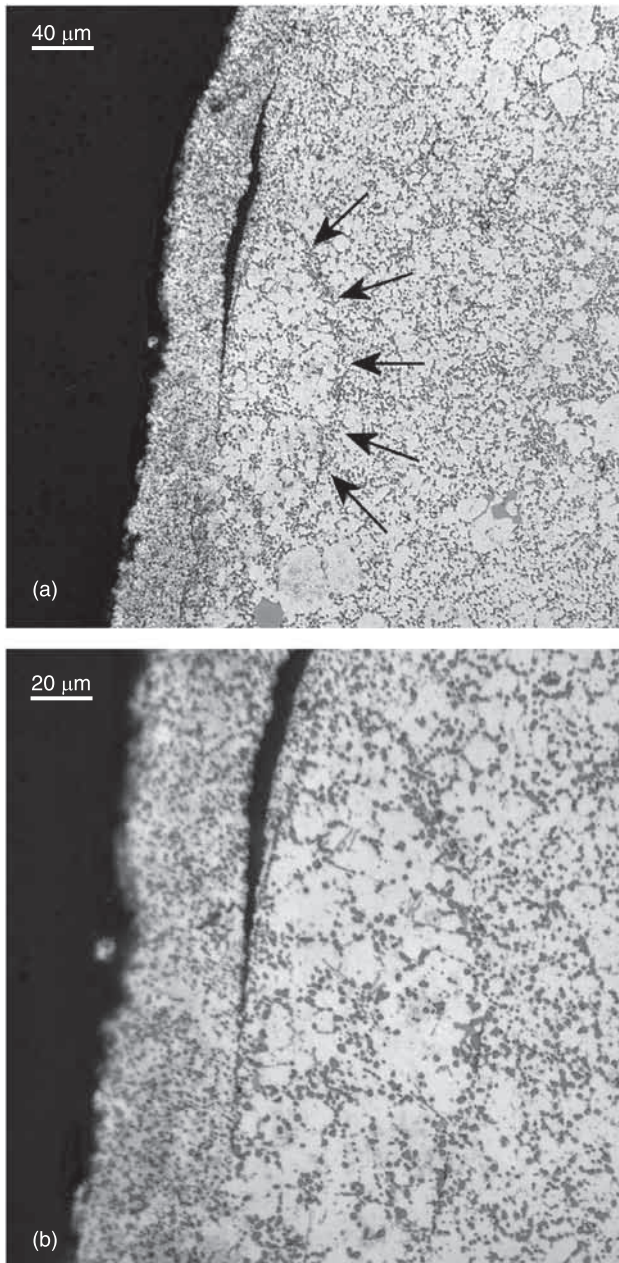
The homogenisation of cast aluminium alloys containing copper normally requires a long time because of the relatively slow rate of diffusion of Cu in Al. The rate of dissolution of the Cu-containing particles present in any casting would appear to be determined largely by the size and morphology of the Cu-bearing phases



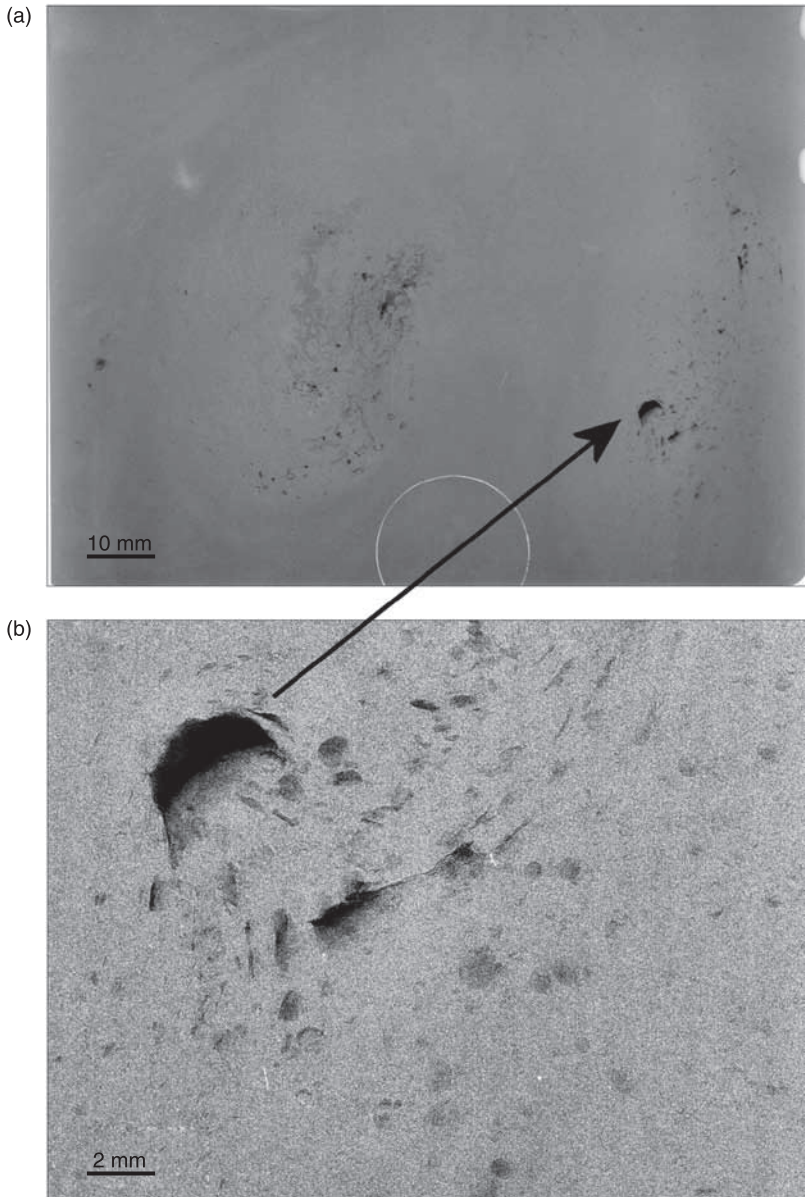
10.9 The refinement of silicon particles during heating to 490°C and then holding at temperature. Note that blisters form at times of ≥ 20 minutes (Lumley et al., 2009a; see also Fig. 10.10 for quantification).



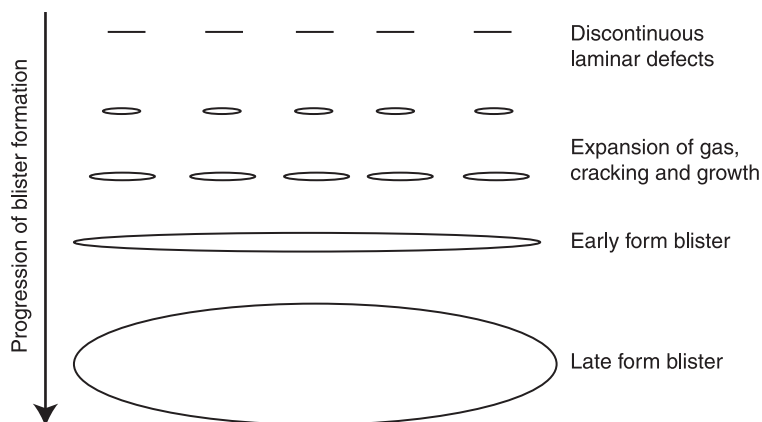
10.10 Quantification of the changes to silicon particle size (diamonds) and number (triangles), for (a) edge and (b) centre regions of the die castings. Total area examined for each data point is $\sim 122000 \mu\text{m}^2$. The silicon particles fragment and spheroidise, then undergo Ostwald ripening, decreasing their number (Lumley et al., 2009a).



10.11 A laminar defect leading to blistering in an A380 alloy, (a) solution treated 20 minutes at 490°C. A similar, unexpanded laminar defect is also shown arrowed and at higher magnification in (b). Note the distribution of pinning silicon particles along the defect length (Lumley et al., 2008a).



10.12 High resolution X-ray images showing (a) regions of variable density in a high pressure die cast plate (casting was 70 mm × 60 mm × 2 mm), including porosity (black). Fine, laminar, nearly two-dimensional defects can be detected within the image (b) either parallel to, or perpendicular to the surface. Both of the large defect clusters shown in (a) are defects containing high amounts of gaseous porosity, and would become large blisters once the alloy was heated to elevated temperature (images courtesy Andrew Stevenson, CSIRO).



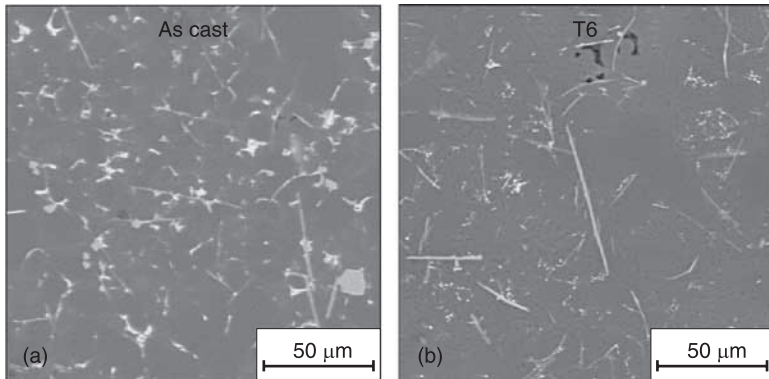
10.13 Representation of the progression of blister formation from small laminar defects containing high quantities of entrapped gas under pressure.

(e.g. equilibrium θ , Al_2Cu). Generally, a time of up to 48 hours is reported (Campbell, 1991) to facilitate complete homogenisation of Cu in Al (Singh et al., 1970), although most aluminium casting alloys that are heat treated are solution treated for 12 hours or less. For HPDCs it is certainly the case that some of the Cu present will be retained in the solid solution from cooling after casting. However, much of the Cu is retained as intermetallic particles and fine, solidified eutectic present in the microstructure. It has also been shown in sintered Al-Cu alloys that the time of dissolution and homogenisation is related largely to the size of the (elemental) Cu particles within the alloy. That is, as the Cu particle size decreases, the time of dissolution and homogenisation also decreases (Lumley and Schaffer, 1996). For HPDCs what this means is that a reduced duration of solution treatment is made possible, at least in part, by the much finer distribution of phases. The rapid cooling rate found in the high pressure die casting process refines the size of the Cu-bearing phases and distributes them more thoroughly within the microstructure.

Figures 10.14(a) and 10.14(b) show backscattered SEM images of unetched polished HPDC sections in which silicon particles are not distinguished but Cu-rich and Fe-rich particles appear bright. The Fe-containing particles were either needle-like ($\beta\text{-Al}_5\text{FeSi}$) or polyhedral $\alpha\text{-Al}_{15}(\text{Fe,Mn})_3\text{Si}_2$ where Mn was present. Only the Fe-containing particles remain after the T6 treatment, which clearly demonstrated that the dissolution of Cu has occurred during a solution treatment of only 15 minutes duration.

10.2.3 Magnesium

Solution treatment of other types of cast Al-Si alloys (e.g. permanent mould and sand castings) has been studied in some detail and, although times up to 16 hours



10.14 Backscattered SEM images of sections from (a) as-cast and (b) solution treated and T6 aged alloy. Cu-bearing phases are white, and Fe-bearing phases are light grey (Lumley et al., 2008b).

are often utilised, the use of much shorter times has been investigated (e.g. Li et al., 1989; Ohnishi et al., 1995; Parker et al., 1982; Rometsch et al., 1999; Taylor et al., 2001a, 2001b; Zhang et al., 1996, 1998). Studies of both cast and wrought aluminium alloys have revealed that homogenisation in Al-Si-Mg alloys will be mostly complete by the time the alloy reaches the temperature of solution treatment (e.g. Ohnishi et al., 1995), with mechanical properties being improved by subsequent quenching and then ageing heat treatments. For HPDCs the improved T5 heat treatment response attainable in HPDC alloys containing higher levels of Mg suggests much of the Mg present in the alloys is actually retained in the solid solution following casting (Dunn and Dickert, 1975). As a result, the major effect of solution treatment is the dissolution of any Mg-containing precipitates that do form in the aluminium matrix during solidification and cooling, or during subsequent natural ageing at ambient temperature (most natural ageing following casting is complete in around seven days).

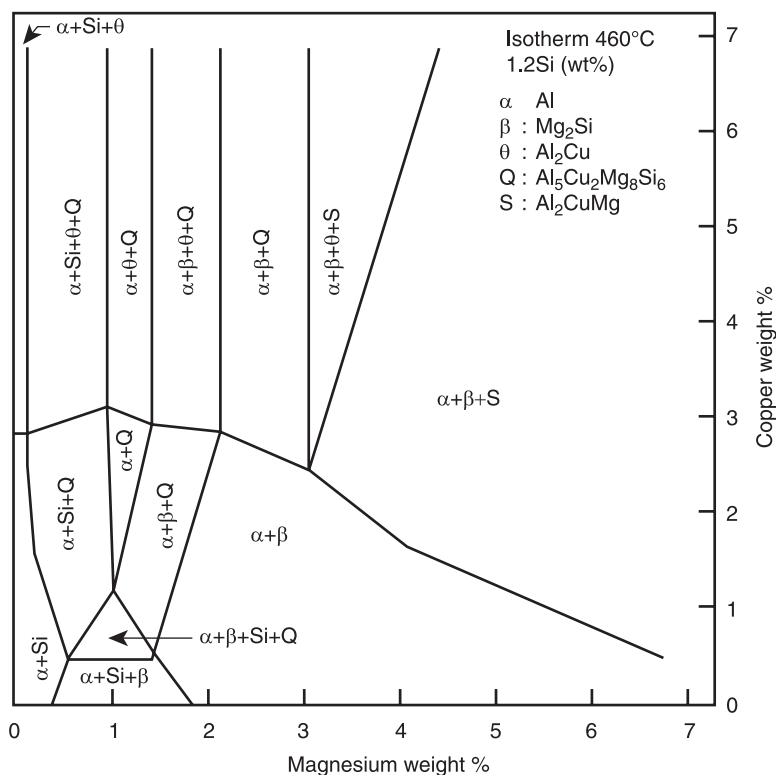
10.2.4 Zinc

Zinc is normally added to HPDC alloys to improve castability, machinability and corrosion resistance (Wang et al., 1995). As with the Mg present in HPDC alloys, Zn would also appear to be largely retained in solid solution in the Al grains during solidification after casting. One potential complication to the use of the high Zn-containing alloys, however, is that eutectics containing Zn form at low temperatures (e.g. the binary Al-Zn eutectic temperature is 381°C). This means that if residual Zn-rich eutectic was present, incipient melting could occur well below the solution treatment temperature. This is particularly the case where thick wall sections are present and solute may segregate towards the centre of thick sections. However, this effect has not so far been observed for high Zn-containing alloys in castings up to >5 kg with wall thicknesses up to 20 mm.

10.3 Role of alloying elements during age hardening

10.3.1 Silicon

The role of Si on precipitation processes during the age hardening of many Al-Si-Cu-(Mg) HPDCs is largely confined to its effects on the complex Q' phase, $\text{Al}_5\text{Cu}_2\text{Mg}_8\text{Si}_6$, or, for low-Cu high-Mg alloys, precipitation of the β'' phase. If the alloy compositions shown in Tables 10.1 and 10.3 are considered with reference to the 460°C isotherm of the quaternary Al-Si-Cu-Mg phase diagram shown in Fig. 10.15, it is evident that the majority fall within one of six different phase domains (in regard to the assumed composition of the aluminium grains following solution treatment). These are $\alpha + \text{Si}$, $\alpha + \text{Si} + \theta$, $\alpha + \text{Si} + \theta + \text{Q}$, $\alpha + \text{Si} + \text{Q}$, $\alpha + \text{Si} + \beta$ and $\alpha + \text{Si} + \beta + \text{Q}$. This assumption was tested by microanalysis of approximately 100 α -Al grains of an alloy Al-9.37Si-0.73Cu-0.41Mg-0.31Zn-0.79Fe-0.21Mn-(<0.2 other) which had been solution treated at 505°C, quenched, then heavily overaged to a T7 temper. Results are presented in Table 10.4. Here it will be seen that the levels of Mg, Cu and Zn detected in the grains correspond



10.15 Isotherm of the quaternary phase diagram for Al-Si-Cu-Mg at 460°C, assuming a constant 1.2%Si (Lumley et al., 2009).

Table 10.4 Quantitative analysis of solute content for aluminium grains within a T7 treated HPDC composition solution treated at 505°C, quenched and overaged at 180°C

Elements	Alloy composition wt% (measured) ♦	Aluminium grain composition wt% (measured)*	Aluminium grain composition at% (measured)*
Al	Balance	Balance	Balance
Si	9.37	1.411 ± 0.226	1.364 ± 0.218
Cu	0.73	0.799 ± 0.127	0.341 ± 0.054
Mg	0.41	0.42 ± 0.024	0.47 ± 0.027
Zn	0.31	0.362 ± 0.02	0.15 ± 0.008
Fe	0.79	0.056 ± 0.031	0.027 ± 0.015
Mn	0.21	0.059 ± 0.019	0.029 ± 0.009
Other elements	<0.2 total	Not measured	Not measured

Notes:

♦ Spectrographic analysis for alloy composition courtesy Stephen Gear, Universal Testing Company Inc.

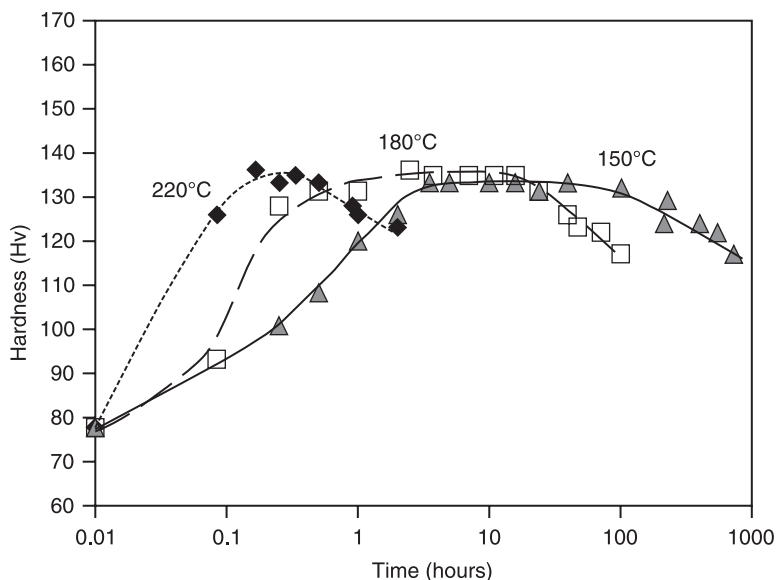
* Electron probe data for grain composition courtesy Colin MacRae, CSIRO.

closely with those present in the original composition of the alloy. One other significant result was that the level of Si present in the grains (1.4 ± 0.23 wt%) is higher than expected for a solution treatment temperature of 505°C. The increased amount for the (Si) composition suggests that some supersaturation of Si may be retained from higher temperatures and then precipitated during cooling from solidification after casting. The alloy presented in Table 10.4 is of particular interest for heat treatment, as it displays rapid hardening behaviour without substantial loss of properties when aged at higher temperatures such as 220°C for times as short as 15 minutes (e.g. Fig. 10.16).

Other evidence for the above assumption that the phase diagram provides a good representation of precipitate phase formation was obtained by examining the microstructures of three other alloys having differing compositions, all of which fell within Q-forming regions of the phase diagram. The results are shown in Fig. 10.17. When aged to peak strength at 150°C, all microstructures contained large amounts of the (Q' precursor) phase L (Lumley et al., 2009). Moreover, the Q' phase became dominant when the alloys were aged to peak strength at 220°C. With alloy A360 shown in Fig. 10.17(f) and aged at 220°C, the microstructure consists of both the Q' and β'' phases. Here it should be noted that these precipitates are easily distinguished by the presence, or absence, of strain contrast for the β'' or Q' phases, respectively.

10.3.2 Copper

Copper is a critical element in facilitating age hardening of HPDCs, particularly when Mg and Si are also present. The strengthening that Cu additions provide

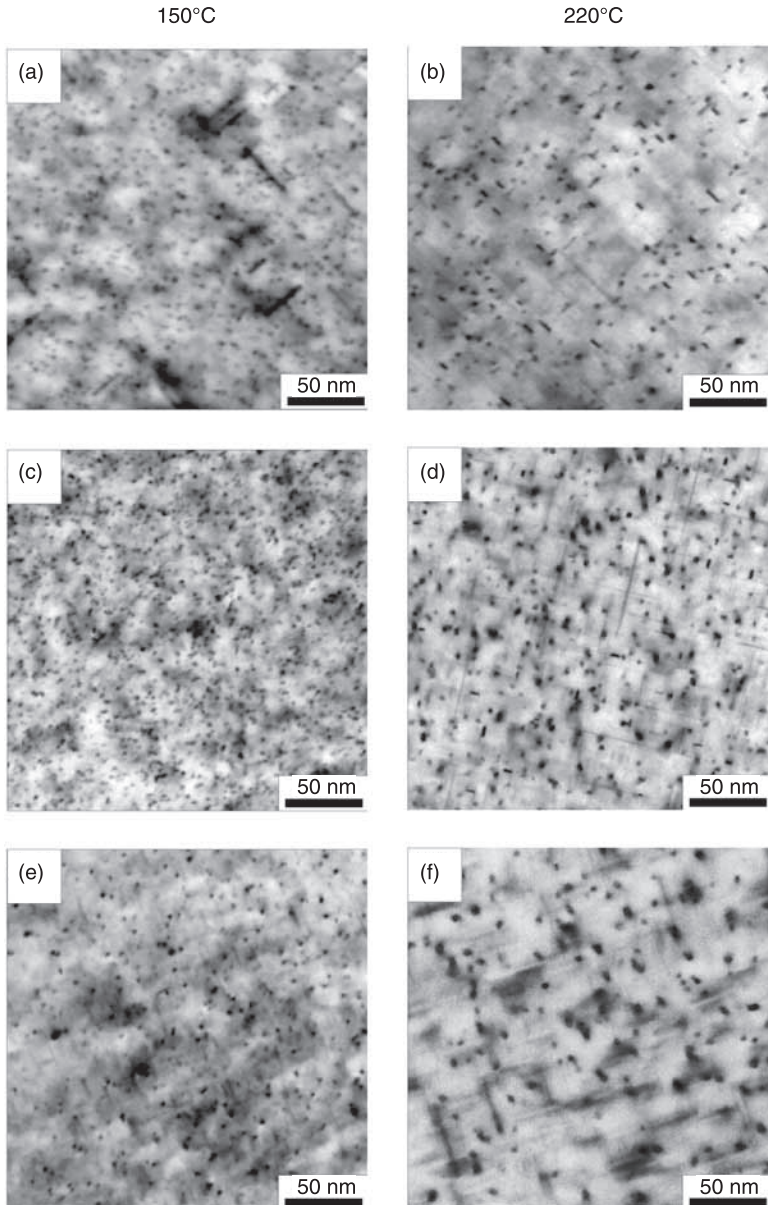


10.16 The age-hardening responses for the alloy Al-9.37Si-0.73Cu-0.41Mg-0.31Zn-0.79Fe-0.21Mn-(<0.2 other) aged at 150°C, 180°C and 220°C following solution treatment at 505°C for 15 minutes and quenching (Lumley et al., 2009).

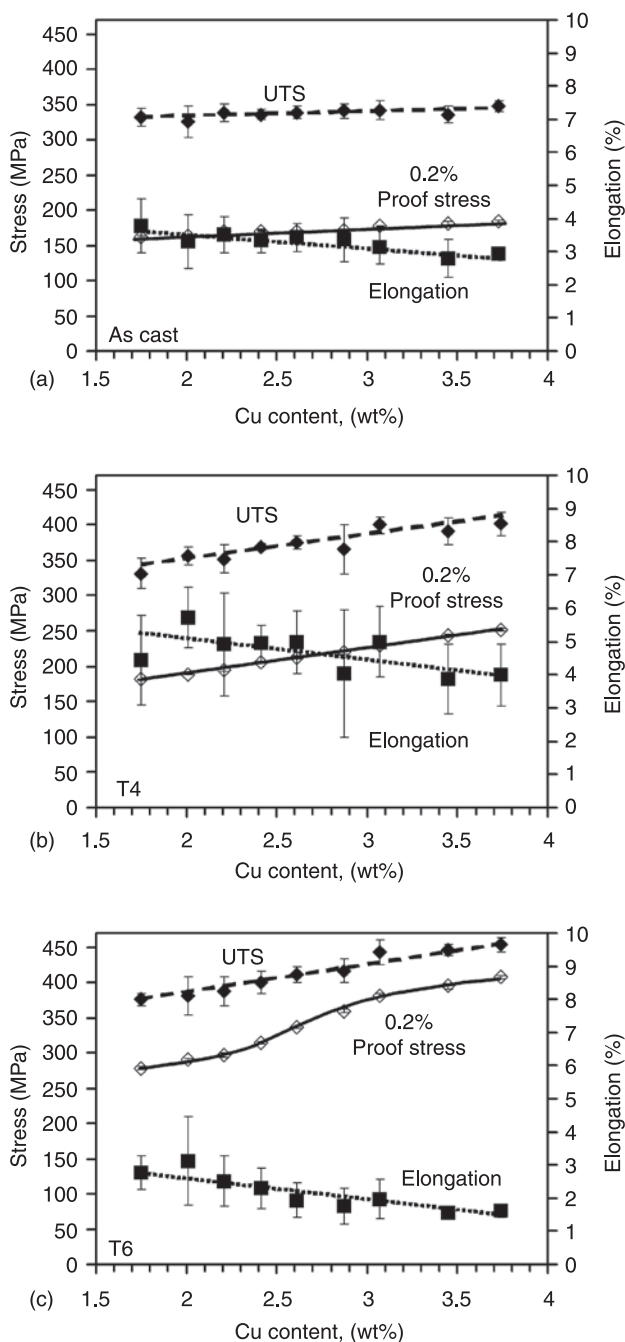
arises from precipitation of Cu-rich clusters and fine Guinier-Preston (GP) zones when aged to the T4 condition, and other phases such as θ' (Al_2Cu) or Q' ($\text{Al}_5\text{Cu}_2\text{Mg}_8\text{Si}_6$) that form during elevated temperature ageing. Ageing the alloy A380 to peak strength and hardness at 150°C results in precipitation of high levels of the θ' (precipitate within the aluminium grains (Fig. 10.6). It is also important to note that this alloy falls within the narrow phase region for Al + Si + θ corresponding to the presence of approximately 0.1 wt% Mg as shown in Fig. 10.15. If the Mg content is raised slightly to 0.2 wt%, the alloys are microstructurally similar but now fall within the Al+Si+ θ +Q phase region so significant amounts of the Q' phase, or its precursor L, form in addition to the θ' (Lumley et al., 2009).

To examine the role of Cu in greater detail, a series of alloys with compositions of Al-(10.4–10.6)Si-(X)Cu-(0.71–0.91)Fe-(0.16–0.2)Mn-(0.2–0.25)Mg-(0.74–0.76)Zn-(<0.2 other) were prepared, where small but progressively increasing amounts of Cu were added to the melt so that contents were raised from 1.75% up to 3.74% Cu. Mg content was not altered. HPDC samples of 11 alloy compositions were prepared, and the results of tensile tests for the as-cast, T4 and T6 tempers, are summarised in Fig. 10.18.

It will be seen that increasing Cu content steadily improves the strength properties in each of the as-cast, T4 or T6 heat treated conditions. For the as-cast alloys, the 0.2% proof stress and UTS increased linearly between 1.75 wt% and 3.74 wt% Cu whereas elongation decreased slightly from approximately four per cent to three per



10.17 (a and b) ADC10 alloy, Al-9.1Si-2.04Cu-0.26Mg-0.53Zn-0.79Fe-0.15Mn-<0.2 other; (c and d) AK9M2 alloy, Al-8.6Si-1.32Cu-0.46Mg-0.41Zn-0.62Fe-0.22Mn-<0.2 other; (e and f) A360 alloy, Al-9.3Si-0.59Cu-0.58Mg-0.49Zn-0.79Fe-0.19Mn-<0.2 other. When aged at 150°C, the ADC10 alloy forms L phase with a small amount of θ' present on prior dislocations (a). At 220°C it forms only Q' phase (b). Alloy AK9M2 forms only L phase when aged at 150°C (c) and Q' when aged at 220°C (d). Alloy A360 forms a combination of L and β'' when aged at 150°C (e) or Q' and β'' when aged at 220°C (f) (Lumley et al., 2009).



10.18 Effects of progressive increases of Cu for the (a) as-cast, (b) T4 and (c) T6, conditions in alloy: Al-(10.4-10.6)Si-(X)Cu-(0.71-0.91)Fe-(0.16-0.2)Mn-(0.2-0.25)Mg-(0.74-0.76)Zn-<0.2 other.

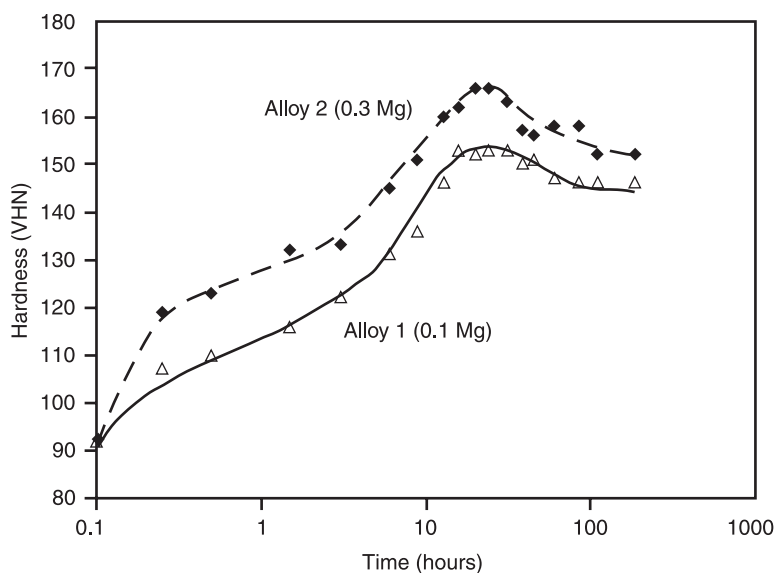
cent. For the T4 temper, the tensile properties followed similar trends although respective values for 0.2% proof stress, UTS and elongation were all higher.

Alloys aged to a T6 temper showed the highest strength levels. Values for 0.2% proof stress increased non-linearly with Cu content from 279 MPa up to 407 MPa, while the tensile strength rose linearly over the same composition ranges. It is interesting to note that, in contrast to the as-cast and T4 conditions, the 0.2% proof stress exhibited a gradual inflection centred at around 2.7% Cu. This Cu level is close to the phase boundary between the Al + Si + Q and Al + Si + θ + Q phase domains shown in Fig. 10.15.

10.3.3 Magnesium

When present in combination with Cu and/or Si, Mg is a very efficient alloying addition for promoting age hardening in aluminium alloys. Even small amounts can have a profound effect. For example, there are significant differences in response to age hardening at 150°C between alloys containing 0.1% Mg and those containing higher levels such as 0.2–0.3 wt%, Fig. 10.19. However, as shown by comparing tensile results for alloys 5 and 9 in Fig. 10.7, no further changes occur if the Mg content is raised to 0.7%. The ageing curve for Alloy 2 in Fig. 10.19 indicates that raising the Mg content from 0.1% to 0.3% initiates the phenomenon of rapid early hardening, which is discussed elsewhere in this book. However, whereas rapid early hardening is often attributed to a process of solute clustering, in HPDC alloys it has been linked to the rapid formation of the L phase, which is a precursor to the higher order precipitate Q' (Lumley et al., 2009). Other differences between the alloys containing ~0.1% Mg and those containing ~0.3% Mg have been shown to be a function of the precipitate type that forms during artificial ageing (Lumley et al., 2009). As may be determined from the phase diagram shown in Fig. 10.15, the alloys with 0.1% Mg would appear to be within the Al + Si + θ phase domain (e.g. see Fig. 10.6), whereas those containing 0.3% Mg are within the Al + Si + θ + Q domain. In the case of the alloys containing 0.3% Mg, when aged to a T6 temper at 150°C, large quantities of the L phase were found together with the θ' phase (Lumley et al., 2009). These microstructural differences were more pronounced at higher ageing temperatures such as 220°C, where the higher Mg alloy displays a microstructure containing almost entirely the Q' phase.

The role of Mg contents ranging from 0.005% up to 0.22% was investigated further using an experimental 383/A383/ADC12 alloy, based on Al-10Si-2.2Cu that was developed to improve ductility (Lumley et al., 2009a, 2009c). The actual compositions of these alloys are shown in Table 10.5. It should be noted that these alloys do not contain Zn, the presence of which could have complicated the effect Mg may have upon ageing processes. The higher levels of ductility were achieved by controlling the Fe and Mn contents so that formation of the β -Al₃FeSi phase was minimised or eliminated during solidification (Lumley et al., 2009b). This issue is discussed later in this chapter. For these experiments, a small amount of



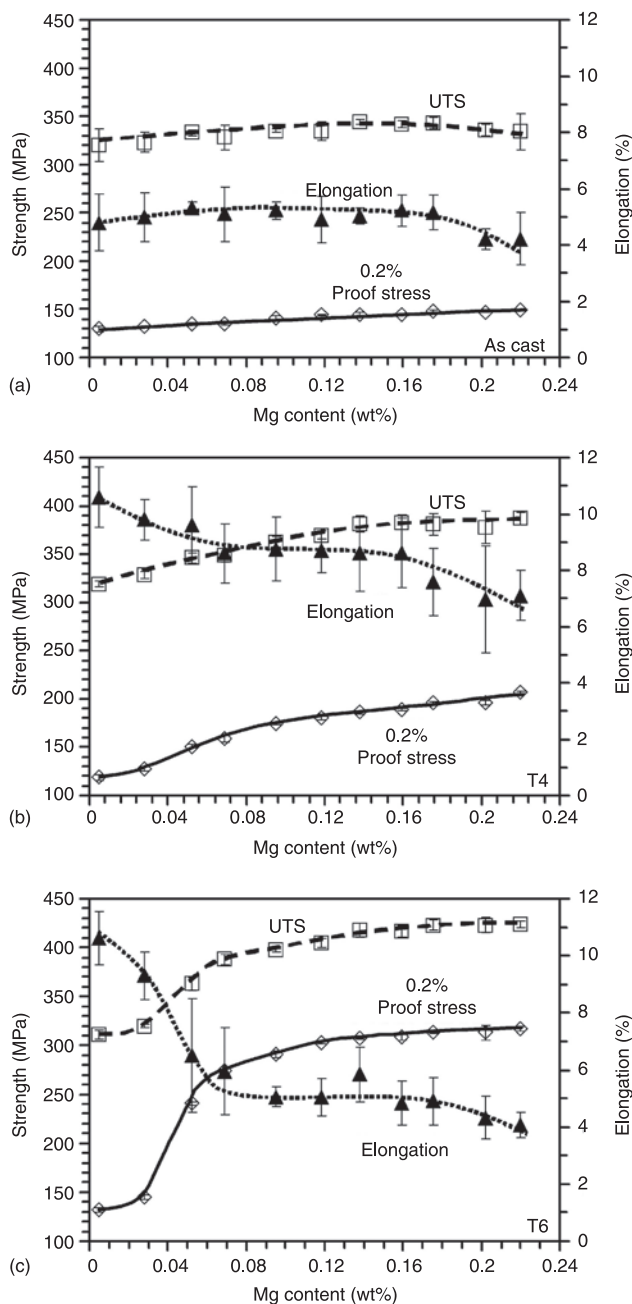
10.19 A comparison of 380-type alloys containing either 0.1% Mg or 0.3% Mg. Alloys 1 and 2 correspond to the compositions shown in Table 9.3 (Lumley et al., 2006).

Mg was progressively added to the molten aluminium alloy at predetermined intervals during casting, and samples were produced at each composition. The results of tensile testing for these compositions are shown for as-cast, T4 and T6 tempers, in Fig. 10.20.

Table 10.5 High ductility HPDC compositions examined to determine the effect of Mg in Al-Si-Cu alloy

Alloy	Composition
A	Al-10.22Si-0.25Fe-2.2Cu-0.48Mn-0.005Mg-(<0.2 other total)
B	Al-10.25Si-0.25Fe-2.19Cu-0.48Mn-0.028Mg-(<0.2 other total)
C	Al-10.05Si-0.24Fe-2.14Cu-0.47Mn-0.052Mg-(<0.2 other total)
D	Al-10.07Si-0.24Fe-2.11Cu-0.47Mn-0.069Mg-(<0.2 other total)
E	Al-10.19Si-0.25Fe-2.16Cu-0.49Mn-0.095Mg-(<0.2 other total)
F	Al-10.18Si-0.25Fe-2.22Cu-0.48Mn-0.118Mg-(<0.2 other total)
G	Al-10.19Si-0.25Fe-2.21Cu-0.48Mn-0.138Mg-(<0.2 other total)
H	Al-10.29Si-0.25Fe-2.2Cu-0.47Mn-0.159Mg-(<0.2 other total)
I	Al-10.26Si-0.25Fe-2.23Cu-0.46Mn-0.175Mg-(<0.2 other total)
J	Al-10.38Si-0.25Fe-2.28Cu-0.48Mn-0.202Mg-(<0.2 other total)
K	Al-10.40Si-0.25Fe-2.25Cu-0.47Mn-0.220Mg-(<0.2 other total)

Source: Lumley et al. (2009c)



10.20 (a)-(c) The effect of Mg content in 383/A383 alloys containing ~2.2% Cu (Lumley et al., 2009a).

In the as-cast condition, the 0.2% proof stress increased moderately with Mg contents up to 0.22% Mg. Tensile strength was maximised between 0.14% and 0.175% Mg, before then decreasing slightly at 0.2% and 0.22% Mg. Elongation values recorded for these alloy specimens did not vary significantly for compositions up to 0.175% Mg, after which they decreased.

For T4 tempers, progressive increases in the Mg content had a far greater effect on mechanical properties. At 0.005% Mg, the 0.2% proof stress was 119 MPa which is 11 MPa less than the values for the as-cast condition. This suggests that the natural ageing response has been suppressed at the very low Mg concentration. At 0.028% Mg the 0.2% proof stress was similar to that recorded for the as-cast condition. For both alloys, the elongation was effectively doubled, from an average of close to five per cent to an average of close to ten per cent after T4 ageing. As the Mg level was raised to 0.095%, the 0.2% proof stress increased 47% above the alloy containing 0.005% Mg. It was then increased further to 74% above the 0.005% Mg alloy, when the Mg level was raised to 0.22%. Tensile strength followed a similar trend to the 0.2% proof stress. The T4 elongation values of the alloys in general followed an inverse relationship to the 0.2% proof stress.

For the 11 alloys treated to a T6 temper, progressive increases in Mg content had large effects. Similarly to the T4 temper, the alloy containing 0.005% Mg displayed no age-hardening response and its 0.2% proof stress was only 2 MPa higher (132 MPa) than the as-cast condition. At 0.028% Mg, 0.2% proof stress was improved only ten per cent, but when Mg content was increased to 0.052%, the 0.2% proof stress increased 83% above the 0.005% Mg alloy. At 0.118% Mg, the 0.2% proof stress was 130% higher than the T6 values achieved for the alloy containing only 0.005% Mg. Less significant changes were then observed up to Mg levels of 0.22%. Tensile strength followed a similar trend to the 0.2% proof stress. Ductility changes were more significant for the T6 treated alloys, again displaying an inverse relationship to the 0.2% proof stress. At 0.005% Mg, the average elongation was 10.6%, which decreased to approximately five per cent at 0.07% Mg, after which it remained effectively unchanged up to ~0.18% Mg. The elongation then decreased to an average of four per cent at 0.22% Mg.

The apparent sensitivity of these compositions to Mg content shown in Fig. 10.20 and the lack of heat treatment response for the low Mg alloys are somewhat surprising because they should be heat treatable due to the levels of Cu present. However, the current results are consistent with results for sand-cast 319 variant alloys with different Mg contents (Al-7.5Si-3.5Cu-XMg) (Zindel et al., 2006). It appears that Mg only commences to stimulate enhanced hardening in these HPDC alloys if the levels increase beyond about 0.04 wt%. At 0.1%, precipitation is still dominated by the θ' phase, but it is the L and Q' phases that become favoured at higher levels of Mg. It is these phases that promote higher strengths and lower ductility. One hypothesis is that L, which is the precursor to Q', and exists as laths with a $\{100\}_\alpha$ habit plane as well as an orientation

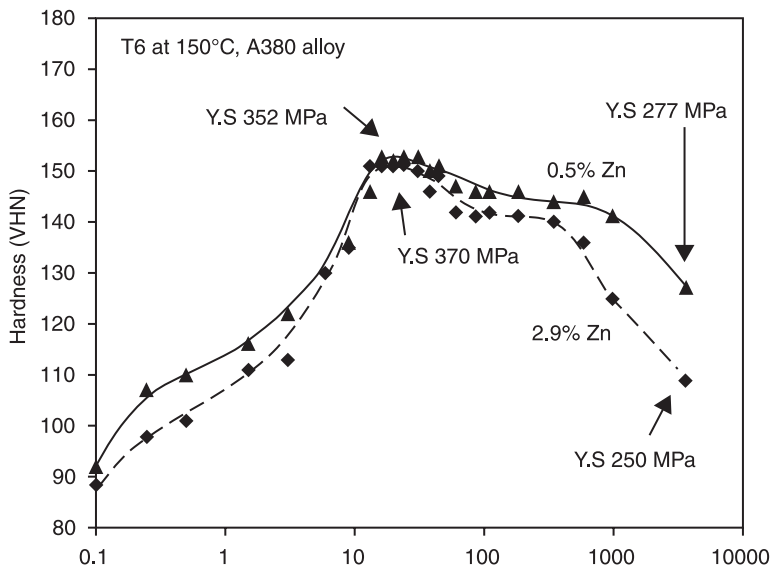
relationship $[100]_L/[100]_\alpha$ and $[010]_L/[010]_\alpha$, may have the ability to nucleate different precipitating phases depending on the composition of the residual α -aluminium solid solution.

10.3.4 Zinc

Whereas Zn and Mg together can cause significant age hardening through the precipitation of $MgZn_2$ in many aluminium alloys, the levels of Mg in most HPDC alloys are generally low and the effect on tensile properties is negligible. The increase in tensile properties that is facilitated by increasing Zn content in low Mg HPDC alloys is therefore considered to arise from solution strengthening rather than from precipitation. High additions (i.e. approximately three per cent) of Zn do however appear to increase softening during overageing (Fig. 10.21). The mechanism of this effect is not currently understood.

10.3.5 Tin

Tin may be present in HPDC alloys due to the use of secondary metal, so HPDC specifications worldwide include varying allowances for this element, up to 0.35%. However, Sn may cause severe flashing, die sticking and hot tearing, resulting in reduced productivity, increased die wear and high reject rates.

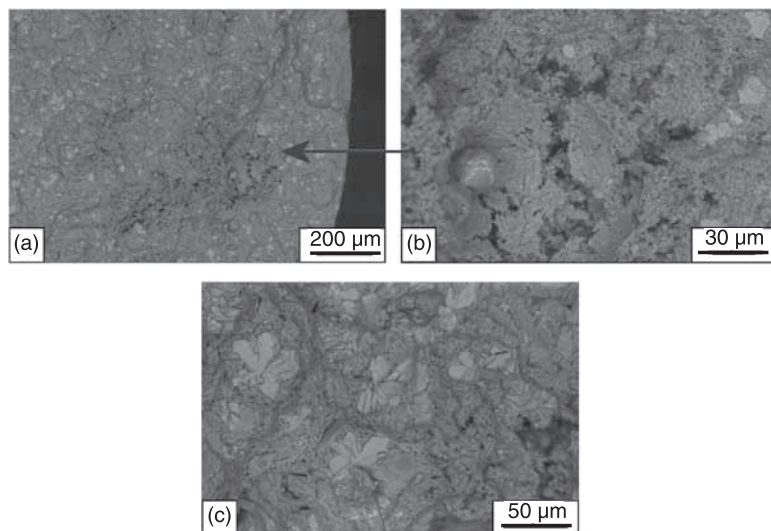


10.21 The role of Zn on overageing in Al-Si-Cu alloys. Higher levels of Zn appear to increase the rate at which overageing occurs. Yield stress (YS) is 0.2% offset (Lumley et al., 2008a).

Corrosion may also be adversely affected (Wang et al., 1995). Furthermore, Sn modifies the form and dispersion of the Fe-bearing phases (Lumley et al., 2008a), producing large rosette-shaped particles (Fig. 10.22) that are detrimental to fracture resistance. Although it is well known that trace amounts of Sn (e.g. 0.05%) may be beneficial in stimulating age hardening in binary Al-Cu alloys (e.g. Hardy, 1950–1951), a recent study has revealed that additions of up to 0.08% Sn have no effect on the ageing of HPDC 380 alloys (Lumley et al., 2008a). It may be concluded therefore that Sn levels in HPDCs should be kept as low as possible for the reasons discussed above.

10.3.6 Transition metal elements (Fe, Mn, Cr)

Fe and Mn are present in HPDC alloys to minimise die soldering so that die life is increased and productivity improved. These elements have no discernable effect on response to heat treatment because they form stable intermetallic compounds such as the needle-shaped β -Al₅FeSi. As these phases (e.g. Fig. 10.22) tend to be brittle, their size and shape can have a profound effect on the fracture properties of HPDCs. The morphology of these particles is strongly influenced by the Fe:Mn:Cr ratio. For that reason, Mn and Cr, and to a lesser extent Co, Ni, V and Sr, serve as so-called Fe correctors. Their role is to reduce

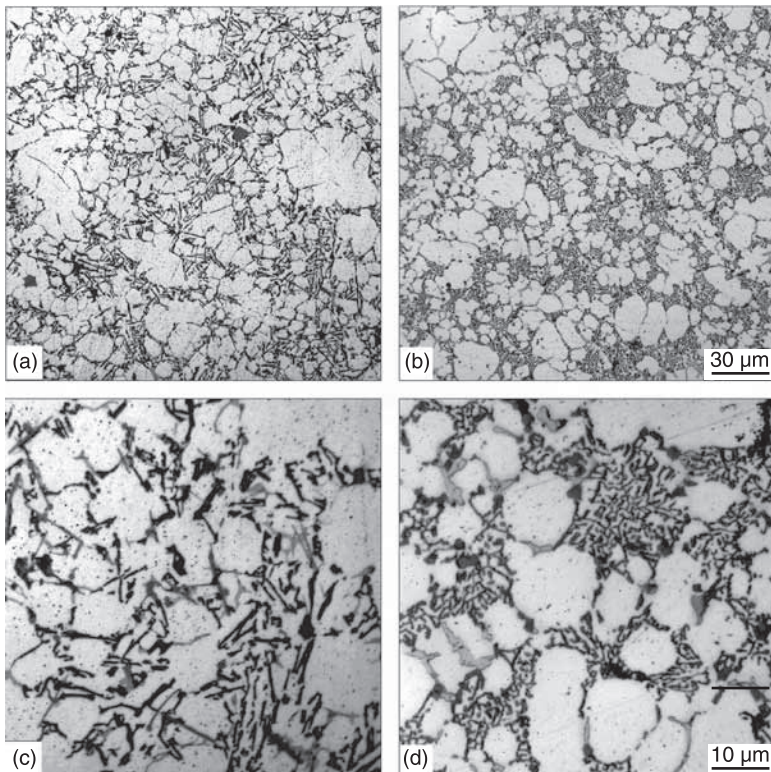


10.22 Fractography of a HPDC Al-Si-Cu-(Fe) alloy containing 0.08 wt% Sn. Examples of hot tearing are shown in (a) and (b). Sn also causes the formation of rosette-shaped Fe-bearing particles (c), which are brittle and therefore preferred crack propagation sites. In (a), all the bright phases seen are the rosette-shaped Fe-bearing particles. Backscattered SEM (Lumley et al., 2008a).

the proportion of the needle-shaped β -Al₅FeSi and encourage the phases to adopt more innocuous shapes (i.e. Chinese script, blocky or polyhedral particles, see e.g. Fig. 10.8).

Effects of altered Fe to Mn ratios on heat treated tensile and fracture properties

As part of a wider investigation on the role of the Fe and Mn, a comparison was made of the effects of these elements on the microstructure and mechanical properties of two alloys. Alloy 1 (A380) from Table 10.3 which contains 0.86% Fe and 0.16% Mn was compared with an alloy having a composition of Al-7.6Si-0.27Fe-2.74Cu-0.48Mn-0.43Zn-(<0.2 other) (hereafter termed ADC10M). Both were produced as HPDC cylindrical test bars and their optical microstructures at two magnifications are shown in Fig. 10.23. Samples were taken from similar locations in the interior of the cylindrical sample head ($\phi = 12$ mm). The first



10.23 Comparative optical microstructures of Alloy 1 (a and c) and Alloy ADC10M (b and d) as-cast. (c) and (d) are higher magnification images of (a) and (b). Samples etched in 0.5% HF solution (Lumley et al., 2009b).

important difference observed was in the morphology of the solidified eutectic Si. This effect was not attributable to chemical modification by the effect of Sr, Na, Ca or P, rather it arose due to an altered solidification sequence for the ADC10M alloy (Lumley et al., 2009b).

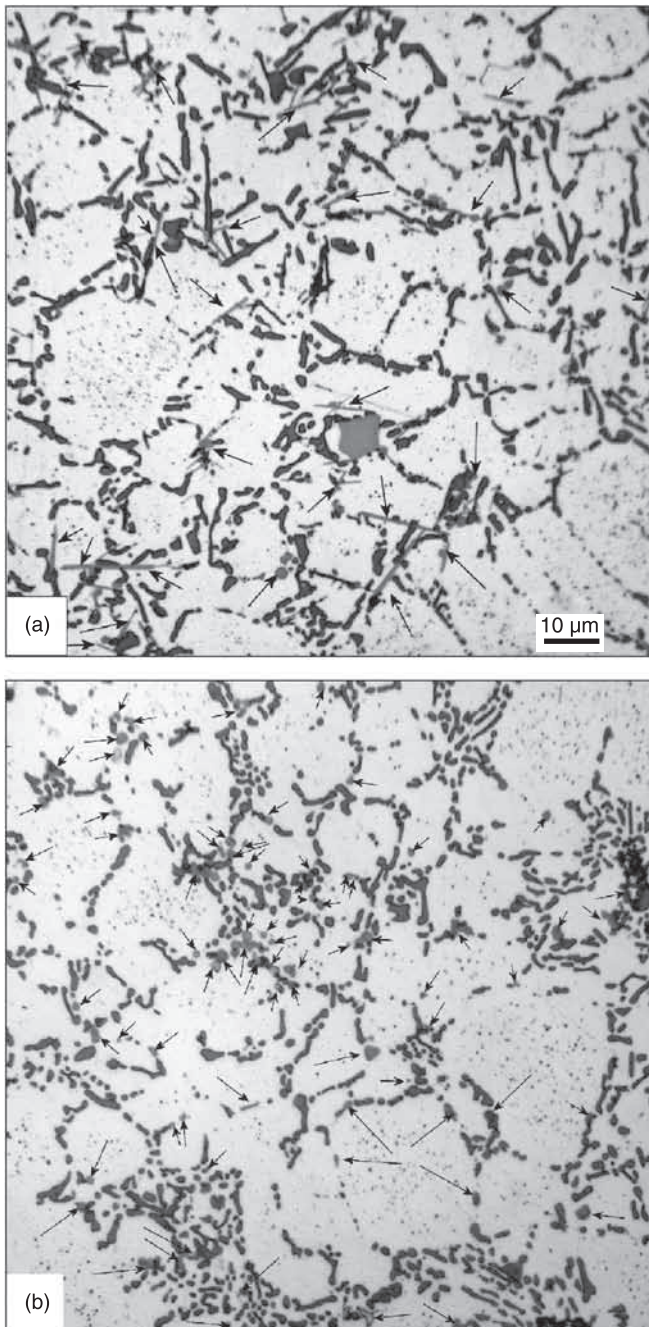
Because of these differences in Si morphology between the alloys in the as-cast condition, the ADC10M alloy also retained finer, spheroidised particles of Si after heat treatment than were present in Alloy 1 (Fig. 10.24). Moreover, whereas Alloy 1 contained both the needle-shaped, Fe-bearing β -phase (Al_3FeSi) along with some polyhedral particles of α -phase $\text{Al}_{15}(\text{Fe,Mn})_3\text{Si}_2$, only the α -phase was observed in the alloy ADC10M. This α -phase is present as fine, dispersed polyhedral particles similar in size and morphology to the spheroidised Si particles. That the changes to microstructure should improve fracture properties was confirmed by tear test measurements (ASTM B871), the results of which are summarised in Fig. 10.25 (Lumley et al., 2009b, 2009c; Lumley and Griffiths, 2008).

10.4 Application to industrially produced parts and commercial heat treatment facilities

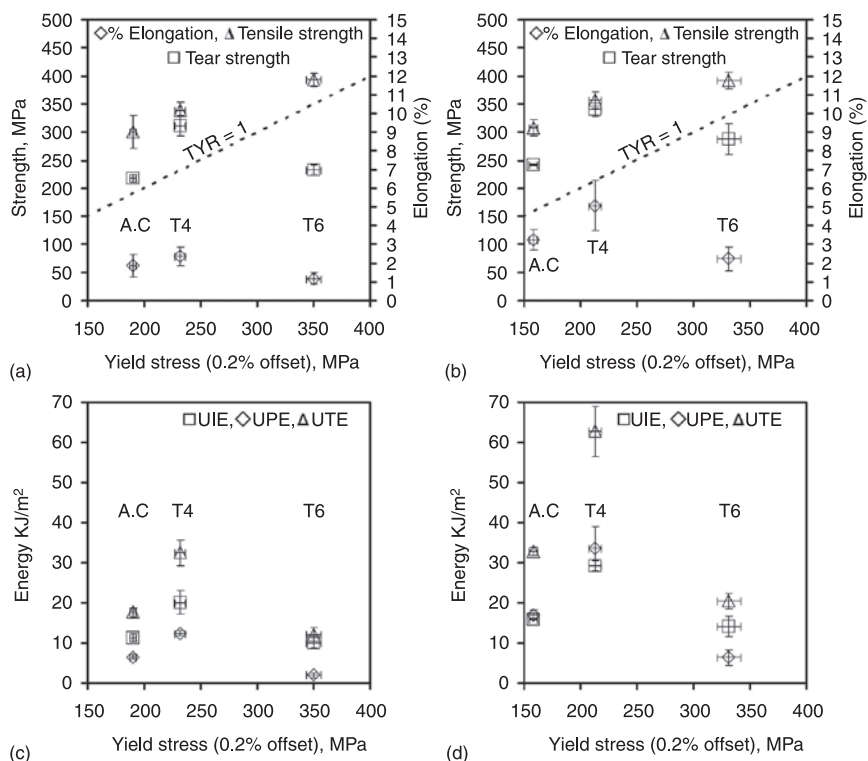
Twenty commercially manufactured HPDC components were selected to cover a wide range of size and complexity. Parts ranging from ~50 g up to >30 kg were investigated (Table 10.6), and heat treatment procedures were developed in each case. In addition, 250 test samples of a ring-shaped component were produced from alloy 380 to enable the solution treatment operation to be carried out on an industrial scale using a fluidised bed facility (Fig. 10.26). These samples were made in a Toshiba horizontal cold chamber die casting machine with a 250 tonne locking force, a shot sleeve with an internal diameter of 50 mm and a length of 400 mm. This particular part characteristically contained high levels of both gas and shrinkage porosity, weighed ~400 g, had wall thickness between 10 mm and 20 mm and an internal diameter of 88 mm. The samples were made from three different batches of alloy 380, and therefore displayed some small variation in composition within the specified range. For heat treatment, two separate trials were conducted on 50 kg batches using approximately equal numbers of parts from each separate casting run. In addition to the total weight of the test samples, the furnace basket into which the parts were placed weighed 60 kg. To assess variability of properties, each of the 250 test samples was Vickers hardness tested a minimum of three times after the full T6 ageing treatment.

10.4.1 Development of heat treatment procedures

Appropriate procedures were developed for heat treatment of each of the parts shown in Table 10.6, which took into account part size, complexity and porosity content. The temperatures found suitable for solution treatment of the specific parts



10.24 Comparative microstructures of (a) Alloy 1 and (b) Alloy ADC10M heat treated to a T6 temper. Fe-bearing phases are arrowed in both images. Samples etched in 0.5% HF solution (Lumley et al., 2009b).



10.25 Effects of heat treatment on the tensile and fracture properties of alloy A380 (Alloy 1) compared to the alloy ADC10M for as-cast (AC), T4 and T6 conditions. Fracture energy and tear strength results are for tear tests according to standard ASTM B871. (a) and (c) are for A380, (b) and (d) are for ADC10M. In (a) and (b), the line for a tear-to-yield ratio (TYR) = 1 is shown. In (c) and (d), UIE is the unit (crack) initiation energy, UPE is the unit (crack) propagation energy, and UTE is the unit total energy (Lumley et al., 2009b, 2009c; Lumley and Griffiths, 2008).

are shown in Table 10.7. The total immersion time during solution treatment was maintained at below 20 minutes in all cases and the time at maximum temperature, which was typically less than 10 minutes, was monitored using thermocouples embedded in the interiors of representative parts. Casting quality and entrapped gas content varied from part to part, and were determined by X-ray fluoroscopy prior to heat treatment. From this information, the maximum solution treatment temperature selected for each specific part varied. Furthermore, because part size, mass and surface area were diverse, the actual thermal cycles (time and temperature) used for components 1–20 were also different. In general, however, the aim was to achieve the highest temperature possible during solution treatment, in significant numbers of parts, while still avoiding blistering. What was most important was that the metal temperature reached the desired maximum temperature for solution

Table 10.6 Description of parts sourced for development of heat treatment procedures

Part number	Description	Alloy	Approximate weight	Minimum thickness	Maximum thickness	Shape complexity	Structural Y/N
1	Washer	380	49 g	1.5 mm	7 mm	Low	Y
2	Casing	380	53 g	1.4 mm	4.3 mm	Medium	N
3	Non-structural automotive	380	430 g	2 mm	6.4 mm	High	N
4	Structural automotive	360	514 g	8.2 mm	16 mm	Low	Y
5	Structural automotive	360	547 g	8 mm	16 mm	Low	Y
6	Vacuum pump part	360	630 g	1.4 mm	8 mm	High	Y
7	Structural automotive	380	320 g	5.5 mm	32.1 mm	Medium	Y
8	Pulley	380	242 g	4.4 mm	6 mm	Low	Y
9	Pulley mount	383	191 g	1.9 mm	7.6 mm	Medium	Y
10	Pulley cover	383	132 g	2.5 mm	4 mm	Low	N
11	Structural automotive	AlSi9Cu3(Fe)	850 g	5 mm	23 mm	Low	Y
12	Engine component	380	94 g	2 mm	20.5 mm	Medium	Y
13	Bush	380	54 g	7 mm	7 mm	Low	Y
14	Bush	380	53 g	4 mm	6 mm	Low	Y
15	Bush	360	100 g	4.2 mm	14 mm	Low	Y
16	Bush	360	53 g	4 mm	6 mm	Low	Y
17	Housing	ADC12	682 g	4 mm	19 mm	Medium	Y
18	Marine part	380	1.2 kg	2.2 mm	9 mm	High	Y
19	Transmission case	ADC12	9 kg	4.3 mm	14.3 mm	High	Y
20	Engine block	380	>30 kg	4 mm	28 mm	High*	Y

Note: * Includes cast iron inserts.



10.26 Fluidised bed basket and loaded 50 kg batch of HPDC ring samples.

treatment, and that the parts spent an appropriate time (e.g. 10 minutes) within a specified temperature range (e.g. 440–490°C) (Lumley et al., 2005; Lumley and Tartaglia, 2007). The solution treatment procedures, even when non-isothermal, proved to be highly effective in dissolving the solute elements. Once solution treatment schedules were determined on small batches of parts, the same procedures were applied for the larger quantities required for accurate statistical analysis of the results. Following solution treatment parts were water quenched before artificial ageing, at 150°C or 180°C, to achieve peak T6 properties. Hardness of the different parts was measured and average values are shown in Table 10.7. Approximate values for the tensile properties of these products can be derived from Fig. 10.27.

10.4.2 Statistical analysis of heat treated parts

Porosity evolution and surface quality of components numbered 1–7 were evaluated, and rated according to NADCA guidelines (NADCA, 2006). For each casting design, between 70 and 100 parts were examined. All parts were X-rayed before and after heat treatment to assess possible changes to the internal porosity, if present. X-ray inspection before heat treatment revealed that high levels of porosity, ranging up to pore sizes of 10 mm, were present in all cases except part

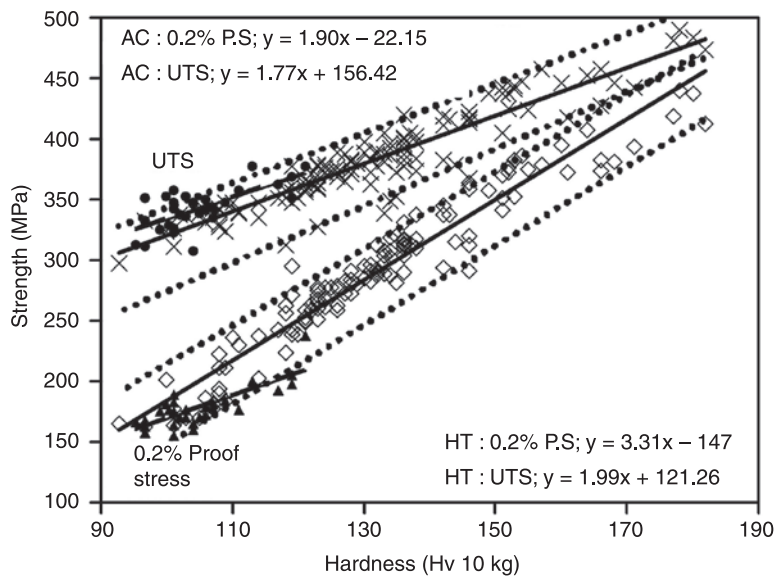
Table 10.7 Solution treatment temperatures and hardness following age hardening of HPDC parts

Part number	Temperature of solution treatment (°C)	Hardness after T6 treatment (VHN)
1	475	145
2	465	147
3	455	122
4	475	134
5	475	117
6	475	128
7	480	160
8	465	132
9	470	124
10	470	123
11	490	155
12	440	123
13	470	124
14	480	137
15	495	125
16	495	120
17	465	137
18	460	136
19	450	130
20	440	113

numbers 2 and 7 which were generally clear. An example of an X-ray taken from part number 5 is provided in Fig. 10.28. Nevertheless, reject rates due to blistering following heat treatment averaged only 1.2% despite the relatively high levels of porosity present (Table 10.8). This rate is similar to that arising from heat treatment for permanent mould and sand cast products, which also can distort during solution treatment and quenching. For these cast products, quench distortion is minimised by quenching into water at between 65°C and 90°C. No quench distortion was observed for any of the HPDC die castings examined, and there was no apparent difference between cold water quenching and hot water quenching. It should be noted, however, that for reasons of convenience, it is more practical to quench into hot water in an industrial setting.

10.4.3 Experiments using an industrial heat treatment facility

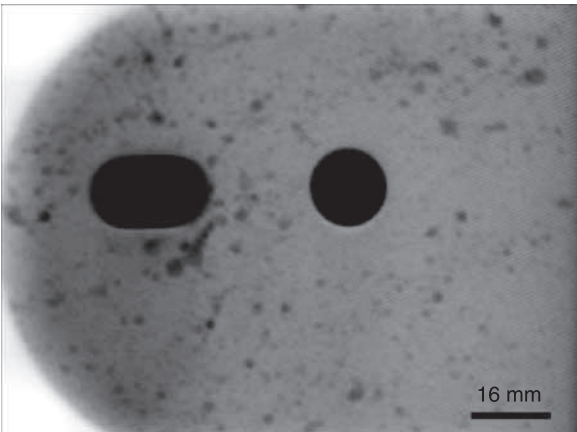
For the parts shown in Fig. 10.26, two 50 kg batches of the ring-shaped test samples were heat treated in an industrial fluidised bed facility. Prior to this, a suitable thermal cycle was established in a laboratory circulating air furnace using a sample in which a K-type thermocouple was embedded. Heat treatment of one sample included in the fluidised bed tests was also monitored in the same way. Comparative heating rate curves are shown in Fig. 10.29 and the aim was to attain



10.27 The relationships between hardness and tensile properties for the as-cast (AC, solid symbols) or heat treated (HT, open symbols) HPDCs. Each data point represents five or more tensile tests and three or more hardness tests. All heat treated samples were artificially aged. Equations approximating the line of best fit are also provided together with bands that enclose the results for the HT specimens.

a maximum temperature of 450–460°C in both furnaces. After water quenching, all samples were aged to peak strength and hardness in a circulating air furnace.

For the sample solution treated in the circulating air furnace, the maximum hardness in the T6 temper was 152 VHN. Following batch solution treatment in



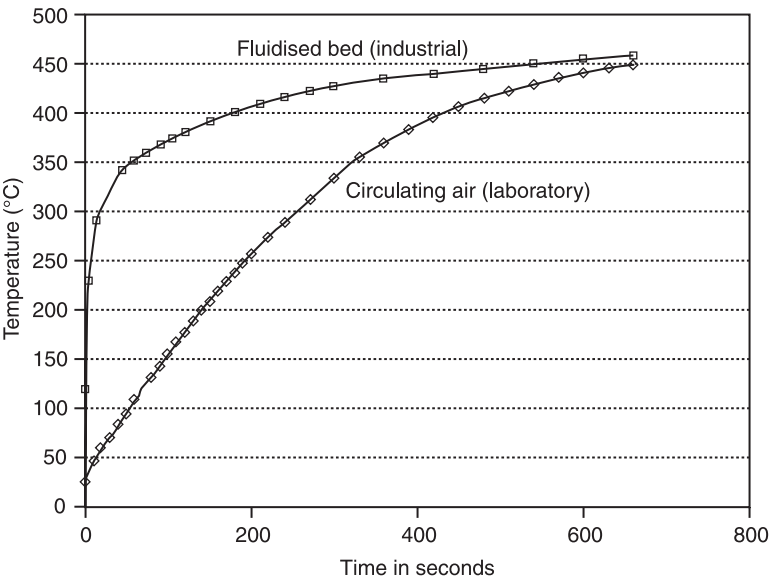
10.28 Typical X-ray from part number 5 showing internal porosity.

Table 10.8 Statistical analysis of heat treated HPDCs given a T6 ageing treatment

Part number	Number of parts treated	Surface rating	Parts rejected due to blistering	Reject rate (%)
1	100	Commercial grade 3	1	1
2	75	Consumer grade 4	1	0.75
3	100	Functional grade 2	2	2
4	100	Commercial grade 3	0	0
5	100	Commercial grade 3	1	1
6	100	Consumer grade 4	3*	3
7	70	Consumer grade 4	0	0
Total	645		8	1.2

Note: *Parts changed to a surface rating grade of 3.

the fluidised bed facility, quenching and T6 ageing, the hardness levels were found to be consistent across all 250 samples and average values ranged from 152 VHN to 155 VHN (Fig. 10.30). Thus, the results for samples solution treated in the two different furnaces were similar. The fluidised bed facility has an advantage of heating rates that are much faster and larger loads of components can be accommodated. However, because of the high throughput normally required in mass production, it is probable that the use of in-line processing could be preferred

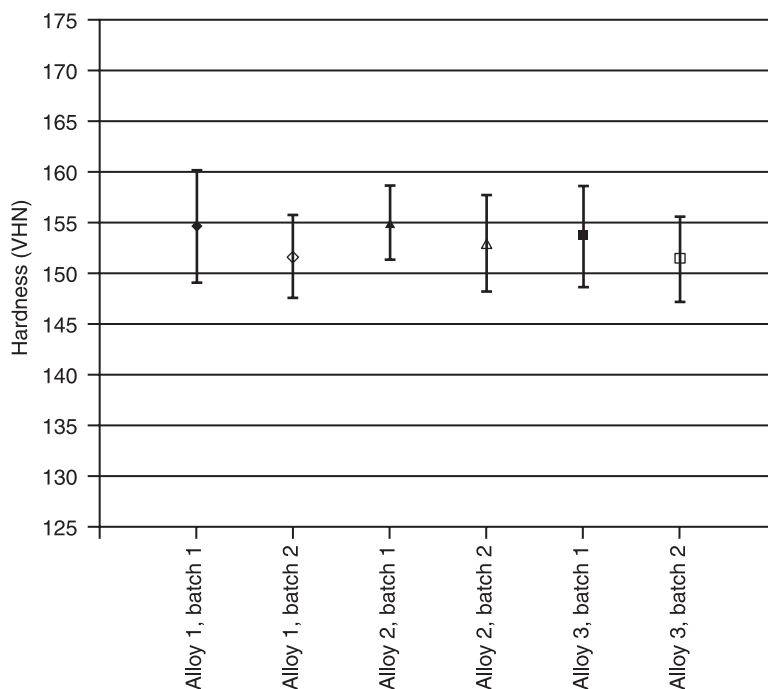


10.29 Heating rates to solution treatment temperature using embedded thermocouples either in a circulating air furnace or an industrial fluidised bed facility.

involving continuous furnaces or heat treatment systems. This approach would have the advantage of further reducing heat treatment costs.

10.5 Implications for redesign of high pressure die castings

The increases in mechanical properties that may be achieved by heat treating conventional HPDCs now mean that there is significant potential for component weight savings by redesign of parts as high strength, high pressure die castings. As a consequence of reducing weight, component cost reduces as well since less metal is used per part. In addition to the redesign of parts which are currently manufactured by the HPDC route, there is also an opportunity for the replacement of a wide range of permanent mould cast components, especially where sand cores for hollow sections are not required. The replacement of more expensive permanent mould cast components with cheaper, heat treated HPDCs is also therefore an attractive materials substitution scenario.



10.30 Hardness summary of 250 test samples across three different 380 alloys and two 50 kg heat treatment batches produced in an industrial fluidised bed heat treatment facility. Approximate tensile properties may be derived from Figure 10.27.

As may be appreciated, no single property is used in the design and utilisation of a component; rather a range of properties is required to obtain the optimum characteristics for any HPDC part. Yield stress, fatigue life, hardness and wear resistance, fracture resistance/energy absorption, thermal conductivity, corrosion resistance, damping capacity, recyclability, etc., are all important. In addition to the improvements to tensile properties discussed earlier, a range of other properties of HPDCs have also been found to be improved by heat treatment. These include fatigue resistance, thermal conductivity, hardness and wear resistance, as well as fracture resistance (for a summary, see Lumley, 2008). Corrosion resistance has not been observed to be affected. The implications on component design by improving the above-mentioned properties using the newly developed heat treatment procedures are shown in Table 10.9.

Inevitably, the cost of heat treatment is an added expense in component manufacture, but due to the reduced durations of the solution treatment cycle, heat treatment cost is reduced to about half of that which is usual for a permanent mould or sand cast component (Lumley and Tartaglia, 2007). As a result, it has been determined that a component weight reduction of eight per cent is required to offset the added cost of heat treatment (Lumley, 2009). However, due to the large improvements to mechanical properties that may be achieved by heat treating HPDCs, it would appear that weight reductions well in excess of eight per cent are practical in the majority of cases, resulting in a cost reduction per part.

10.6 Conclusion

1. Modified heat treatment procedures have been developed that may produce significant improvements in the 0.2% proof strength of conventionally produced HPDCs. The procedures involve the use of short solution treatment times at lower temperatures, followed by conventional quenching and ageing cycles. For some alloys, increases of more than 100% in 0.2% proof stress can be achieved over the as-cast values.
2. The ability to achieve significantly improved mechanical properties by heat treating HPDC aluminium alloys provides opportunities to achieve both weight reductions and simultaneous cost savings through the redesign of automotive and other components.
3. Now that it is known to be possible to heat treat conventionally produced HPDC aluminium alloy die castings, it has been desirable to examine the specific roles of the alloying elements. Optimisation of the compositions of these materials may lead to alloys tailored specifically for their application or function in service.
4. The new heat treatment procedures have been successfully applied to conventional, industrially produced HPDCs of a range of different sizes, complexities and weights without incurring problems with blistering or dimensional change. Components in batches of 50 kg have been successfully heat treated in an industrial facility with minimal variation in hardness properties developed.

Table 10.9 Some key design properties in automotive applications and implications of weight reduction via component redesign

Property	Implications of improvement to design	Design strategy for weight reduction	Additional benefits
Yield stress	The design stress is increased meaning a smaller or thinner walled component can manage service loads.	A rough guide is that three per cent component weight reduction for every ten per cent improvement in yield stress or design stress is feasible where the part is load limited.	Less metal per casting means reduced cost per part.
Fatigue life/fatigue limit	Improvements raise the usable design stress where fatigue limited meaning lighter, thinner walled components may be used.	Increase usable design stress, particularly, on rotating or moving components where the effect of weight reduction is multiplicative.	Less metal per casting means reduced cost per part; moving components have greater equivalent mass loss for fuel consumption/performance.
Fracture resistance/energy absorption	Improvements raise the energy absorbed during crack propagation (e.g. during fatigue), the tearing resistance and the capacity to absorb energy in impact.	Increase usable design stress through the relationship between fracture toughness, design stress and critical flaw size.	Many structural parts are fracture limited, rather than yield stress limited meaning fracture resistance may be more important than tensile properties.
Thermal conductivity	Improvements increase the rate at which heat is transferred to, or extracted from a part.	Removal or reduction of cooling fins, simplification of geometry.	Cost reduction in tooling, potential for reduction of fluid reservoir size.
Hardness (and wear resistance)	Improvements raise the durability of the part where wear or periodic minor impact damage occurs.	Loading may be increased in wear prone areas.	Potential for removal of cast iron inserts or liners.

Source: Lumley (2009)

5. As weight saving becomes more desirable due to the requirements of reducing fuel consumption and greenhouse gases, the ability to achieve this goal and also reduce costs makes the ability to heat treat conventionally produced HPDCs highly attractive to suppliers and manufacturers in the automotive industry.

10.7 Notes

1. Previously reported to be either Mg_2Si or MgSi , the composition of the β' and β'' phases have been shown to be $\text{Al}_3(\text{MgSi})$ where the ratio of $\text{Mg}:\text{Si}$ may vary widely (Buha et al., 2008).

10.8 References

- Badini, C., Bonollo, F., Cavatorta, M.P., La Vecchia, G.M., Panvini, A., Pola, A., Nicodemi, W., Vadani, M. (2002) 'Process Simulation of Microstructure and Relationship with Mechanical Properties in Diecastings', *Metallurgical Science and Technology*, 20(2):14–21.
- Buha, J., Lumley, R.N. and Crosky, A.J. (2008) 'Precipitation and solute distribution in an interrupted-aged Al-Mg-Si-Cu Alloy', *Philosophical Magazine*, 88(3): 373–390.
- Campbell, J. (1991) *Castings*, Butterworth Heinemann Ltd., Oxford, UK, pp. 273–275.
- Dunn, R.P and Dickert, W.Y. (1975) 'Magnesium effect on the strength of A380.0 and 383.0 aluminum die casting alloys', *Die Casting Engineer*, 19(2): 12–20.
- Hardy, H.K. (1951–1952) 'The ageing characteristics of ternary aluminium copper alloys with cadmium, indium, or tin', *Journal of the Institute of Metals*, 80: 483–492.
- Jorstad, J.L. (1986) 'Understanding sludge', *Die Casting Engineer*, 30(6): 30–36.
- Li, H.J., Shivkumar, S., Luo, X.J. and Apelian, D. (1989) 'Influence of modification on the solution heat-treatment response of cast Al-Si-Mg alloys', *Cast Metals*, 1(4): 227–234.
- Lumley, R.N. (2008) 'Technical data sheets for heat-treated aluminium high-pressure die castings', *Die Casting Engineer*, 52(5): 32–36.
- Lumley, R.N. (2009) *Weight Reduction from High Strength Aluminum Die-Castings*, Paper no. 2009-01-0553, SAE World Congress, Detroit, MI, USA.
- Lumley, R.N., Gershenzon, M. and Gunasegaram, D.R. (2009a) 'Alloy design for heat treatment of high pressure diecastings', *Materials Science Forum*, 618/619: 331–339.
- Lumley, R.N. Gershenzon, M., Gunasegaram, D.R., Davidson, C.J. and Yob, A.C. (2009b) 'Al-Si-Cu alloy design for enhanced fracture toughness in heat treated high pressure die-castings', *Proceedings of the 113th Metalcasting Congress Conference*, NADCA, T09-042.
- Lumley, R.N., Gershenzon, M., Gunasegaram, D.R. and Yob, A.C. (2009c) *International Patent Application, Improved Aluminium Based Casting Alloy*, PCT/AU2009/000532.
- Lumley, R.N. and Griffiths, J.R. (2008) 'Fatigue and fracture resistance of heat treated aluminium high pressure die-castings', *Proceedings of the 112th Metalcasting Congress Conference*, NADCA, T08-042.
- Lumley, R.N., Gunasegaram, D.R., Gershenzon, M. and O'Donnell, R.G. (2007) 'The effect of alloy composition on the heat treatment of aluminium high pressure diecastings', *Proceedings of the 111th Metalcasting Congress Conference*, NADCA, T07-013.
- Lumley, R.N., O'Donnell, R.G., Gunasegaram, D.R. and Givord, M. (2005) *Heat Treatment of High Pressure Diecasting Alloys*, International Patent Application PCT/2005/001909, WO2006/066314.

- Lumley, R.N., O'Donnell, R.G., Gunasegaram, D.R. and Givord, M. (2006) 'Blister free heat treatment of high pressure diecasting alloys', *Materials Science Forum*, 519/522: 351–359.
- Lumley, R.N., O'Donnell, R.G., Gunasegaram, D.R. and Givord, M. (2007a) 'Heat treatment of high pressure diecastings', *Metallurgical and Materials Transactions A*, 38A: 2564–2574.
- Lumley, R.N., O'Donnell, R.G., Gunasegaram, D.R. and Givord, M. (2007b) 'Development of heat treatments to strengthen high pressure diecastings', *Giessereiforschung*, 59(3): 8–13.
- Lumley, R.N., O'Donnell, R.G., Gunasegaram, D.R., Kittel-Sherri, T., Gershenzon, M., Yob, A.C. and Polmear, I.J. (2008a) 'The role of alloy composition in the heat treatment of aluminium high pressure die castings', *Metallurgical Science and Technology*, 26(2): 2–11.
- Lumley, R.N., Polmear, I.J., Groot, H. and Ferrier, J. (2008b) 'Thermal characteristics of heat treated aluminum high pressure die-castings', *Scripta Materialia*, 58: 1006–1009.
- Lumley, R.N., Polmear, I.J. and Curtis, P.R. (2009) 'Rapid heat treatment of aluminum high pressure diecastings', *Metallurgical and Materials Transactions A*, 40(7): 1716–1726.
- Lumley, R.N., and Schaffer, G.B. (1996) 'The effect of solubility and particle size on liquid phase sintering', *Scripta Materialia* 35(5): 589–595.
- Lumley, R.N. and Tartaglia, S. (2007) 'A new heat treatment process for aluminium high pressure diecastings – development of procedures for industrially produced components', *Proceedings of the 111th Metalcasting Congress Conference*, NADCA, T07-023.
- NADCA (2006) *Product Specification Standards for Die Castings* (Guideline g-6-6-06), 6th ed., North American Die Casting Association, Wheeling, IL.
- Ohnishi, N., Takaai, T., Nakayama, Y. and Ohmori, M. (1995) 'High temperature solutionizing of AC4CH aluminum casting alloy', *Journal of Japan Institute of Light Metals*, 45(8): 447–452.
- Parker, B.A., Saunders, D.S. and Griffiths, J.R. (1982) 'The quantitative evaluation of the microstructure of a strontium-modified Al-Si-Mg alloy following prolonged solution treatment', *Metals Forum*, 5(1): 48–53.
- Rometsch, P.A., Arnberg, L. and Zhang, D.L. (1999) 'Modelling dissolution of Mg₂Si and homogenisation in Al-Si-Mg casting alloys', *International Journal of Cast Metals Research*, 12: 1–8.
- Singh, S.N., Bardes, B.P. and Flemings, M.C. (1970) 'Solution treatment of cast Al-4.5pct Cu alloy', *Metallurgical Transactions*, 1: 1383–1388.
- Taylor, J.A., StJohn, D.H., Zheng, L.H., Edwards, G.A., Barresi, J. and Couper, M.J. (2001a) 'Solution treatment effects in Al-Si-Mg casting alloys. Part 1: Intermetallic phases', *Aluminum Transactions*, 4/5: 95–110.
- Taylor, J.A., StJohn, D.H. and Couper, M.J. (2001b) 'Solution treatment effects in Al-Si-Mg casting alloys. Part 2: Solid solution chemistry', *Aluminum Transactions*, 4/5: 111–124.
- Wang, L., Makhlof, M. and Apelian, D. (1995) 'Aluminum die casting alloys: Alloy composition, microstructure, and properties-performance relationships', *International Materials Reviews*, 40(6): 221–238.
- Zhang, D.L., Zheng, L.H. and StJohn, D.H. (1996) 'Heat treatment of Al-7wt%Si-Mg casting alloys', *Proceedings of the Conference on Materials Research* 96, 1: 25–28.
- Zhang, D.L., Zheng, L.H. and StJohn, D.H. (1998) 'Effect of a short solution treatment time on microstructure and mechanical properties of modified Al-7wt%Si-0.3wt%Mg alloy', *Materials Science and Technology*, 14: 619–625.
- Zindel, J.W., Kofeldt, K.A., Godlewski, L.A., Vijayaraghavan, R. and Donlon, W.T. (2006) *Rational Selection of Mg Concentration Specifications for 319-Type Alloys*, Paper no. 2006-01-0511, SAE World Congress, Detroit, MI, USA.

Work hardening in aluminium alloys

W.J. POOLE and J.D. EMBURY, The University of British Columbia, Canada and D.J. LLOYD, Novelis Global Technology Centre, Canada

Abstract: This chapter deals with the process of work hardening in aluminium and a number of its alloys. The approach taken is to develop a simple one parameter model based on dislocation density and modify this to try and describe the essential behaviour of a range of solid solution and precipitation hardening alloys. Attention is also given to large strain behaviour and its description. The basic framework for the description of work hardening is then related to formability and to the treatment of a number of commercial aluminium alloys.

Key words: work hardening, aluminium alloys, large strain deformation, dislocation accumulation, dynamic recovery, solute effects, grain size effects, precipitation effects, temperature effects, forming limit diagrams.

11.1 Introduction

The process of work hardening in Al alloys is important both from the fundamental viewpoint of understanding the microstructural evolution with imposed plastic strain and the practical consideration of optimising the formability of Al alloys for a wide variety of applications. In addition, work hardening is an effective method of strengthening aluminium alloys and it is important for understanding large strain forming processes such as cold extrusion, drawing and rolling.

The relationship between microstructural evolution and forming is not easily integrated because much of the work on microstructural evolution has been conducted using uniaxial tensile tests in which the range of strains is of order 0.01–0.4 whereas some forming operations require strains in the range 0.5–5.0 and the use of stress states other than uniaxial tension. In addition, the constitutive laws developed to describe the plasticity do not necessarily encompass descriptions of microstructural evolution or have the ability to describe changes in strain path.

In the present chapter, a brief review of the development of various constitutive laws will be given, prior to describing a general framework for work hardening based on the simultaneous processes of dislocation accumulation and annihilation by dynamic recovery processes (Kocks and Mecking, 2003). This model provides a simplified but general framework in which the role of a variety of microstructural features can be examined. Thus, for example, it is possible to explore the influence of grain size, or second phase particles or solute atoms on both the competing processes of dislocation accumulation and dynamic

recovery. It is also possible to ascertain whether these microstructural features influence the work hardening by contributing to kinematic hardening which is polarised with respect to the direction of imposed plastic strain, or isotropic hardening which is governed by the scalar quantity describing the global average dislocation density (Stout and Rollett, 1990). The model can also be interrogated to determine the influence of various microstructural features on the work hardening rate at large plastic strains that are appropriate to metal forming operations.

Prior to reviewing the basis of the model developed by Kocks–Mecking and other models, it is appropriate to emphasise that most microstructurally based models of work hardening are developed in terms of variables such as average dislocation density or a defined length scale of the microstructure, such as the dislocation cell size, and are compared with experiments performed in monotonic loading, thus they do not readily relate to complex strain paths or combined thermal and mechanical operations which are basic to many metal forming operations.

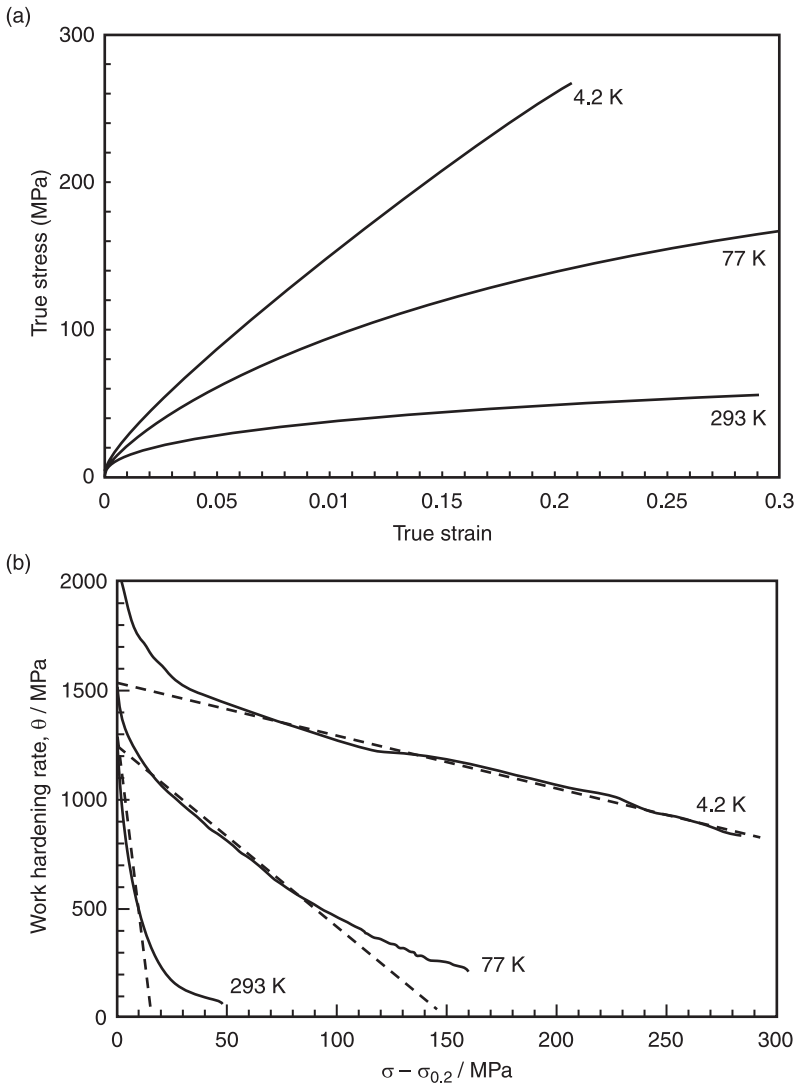
In addition, we need to consider work hardening in a more general context of the events which can occur due to imposed plastic strains. We can define a number of processes which limit the extent to which plastic deformation can be imposed or distributed including the uniformity of plastic flow, localisation of plasticity into intense shear bands and the occurrence of damage events, such as particle fracture, intergranular decohesion or decohesion at the interface of second phase particles and the matrix.

The scope of this review encompasses low temperature deformation of polycrystalline aluminium alloys (i.e. $T < 0.4 T_{MP}$, $T < 100^\circ\text{C}$), over strains of zero to five with a focus on microstructures typical of industrial alloys (grain sizes of 1–100 μm , several percentage of solid solution, nm precipitates, μm particles, constituent particles, two phase systems), i.e. not UFG aluminium which is considered elsewhere (e.g. the chapter by Estrin et al. in this book)

11.2 Fundamentals of work hardening

11.2.1 Phenomenology of work hardening in high-purity aluminium

Figure 11.1(a) shows results for the stress-strain curve of high-purity aluminium tested in uniaxial tension at temperatures of 4.2 K, 77 K and 293 K. By numerically differentiating the data shown in Fig. 11.1(a), the work hardening rate can then be plotted as a function of the flow stress as shown in Fig. 11.1(b). It will be shown that this type of plot, which is usually described as a Kocks–Mecking plot, provides a very useful way to interpret experimental data. From the stress-strain curves in Fig. 11.1(a), it can be observed that the yield stress is very low (less than 10 MPa) and it is almost independent of temperature, while the level



11.1 Tensile response of high-purity aluminium: (a) true stress vs. true strain and (b) work hardening rate, θ , vs. true stress. The work hardening rate in (b) was obtained by numerically differentiating the data in (a). The dashed lines correspond to the prediction of linear decrease in work hardening rate with stress in Stage III (experimental data courtesy of A. Deschamps and M. Niewczas).

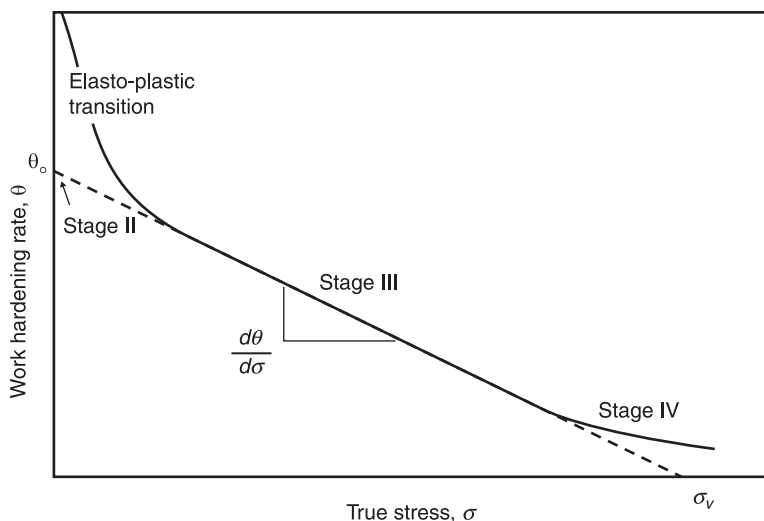
of work hardening is strongly dependent on strain and temperature. Traditionally, the phenomenology of work hardening for single crystals has been considered in terms of stages of deformation. Stage I corresponds to a low level of work hardening in single crystals oriented for glide on a single slip system (as we are

interested in polycrystalline deformation, this will not be considered further; see Gil Sevillano et al., 1981; Gil Sevillano, 1993; Kocks and Mecking, 2003 for details). Stage II corresponds to the highest rate of work hardening in high-purity FCC metals and is observed when single crystals begin slip on multiple slip systems or in polycrystalline samples after yielding (or more precisely when the elasto-plastic transition is complete). For polycrystalline FCC samples, the Stage II work hardening is approximately $\mu/20$ where μ is the shear modulus for the material, i.e. the initial plastic work hardening rate, θ_0 is approximately 1200–1500 MPa for aluminium at ambient temperature.

Plastic strain occurs by the motion of dislocations and the interaction and the multiplication of dislocations lead to an increase in the resistance to plastic flow. However, dislocations of opposite sign can be annihilated if they are sufficiently close together. This leads to a reduction in the dislocation density termed dynamic recovery which is a softening process occurring concurrently with plastic strain. The local transport process needed for dynamic recovery may involve either slip or diffusional processes. It should be noted that the rate of hardening in Stage II for pure metals is due to dislocation storage with no dynamic recovery. Higher rates of apparent work hardening are observed in the elasto-plastic transition as will be discussed later.

It is found that the Stage II hardening rate is rather insensitive to strain rate and temperature (after correction for the temperature dependence of the shear modulus) as can be observed in Fig. 11.1(b). Stage III of work hardening corresponds to the regime where the work hardening rate decreases linearly as the flow stress of the sample increases (see the dashed lines in Fig. 11.1b). At larger strains, there is a breakdown of the linear decrease in the work hardening rate with stress which is referred to as Stage IV. This can be observed in Fig. 11.1(b) for the tests at ambient temperature and at 77 K. For a test temperature of 4.2 K, one does not observe a Stage IV deviation. In tests at 4.2 K, there is negligible thermal activation and thus at low strains the work hardening rate is constant and of order $\mu/20$ in polycrystals. Further, tests at 4.2 K on copper single crystals suggest that in the absence of dynamic recovery, flow stresses of order $\mu/100$ can be obtained implying that the stored energy due to work hardening can attain values of five per cent to 10 per cent of the latent heat of fusion (Niewczas et al., 2004). At larger strains, dynamic recovery can occur even at 4.2 K by the annihilation of dislocations with separation of order 0.5 nm and thus the hardening rate is observed to decrease slightly but never approaches the Stage IV hardening rate.

The rate of work hardening in Stage IV is low (usually below 100 MPa at ambient temperature) but this can be very important for large strain processes such as extrusion, rolling or equal channel angular extrusion (ECAE). Figure 11.2 schematically summarises the three stages of work hardening (Stages II–IV) which can readily be observed from a Kocks–Mecking plot. Some researchers have further identified a final stage before the flow stress saturates where the work hardening rate is constant at a very low value, known as Stage V (Argon and



11.2 Schematic diagram illustrating the various stages of work hardening and the elasto-plastic transition. Note that the extrapolated scaling stress for the Voce equation, i.e. the linear decrease of work hardening rate with stress in Stage III is extrapolated to zero work hardening rate.

Haasen, 1993; Zehetbauer and Seumer, 1993; Estrin et al., 1998; Kocks and Mecking, 2003). Finally, it is assumed the flow stress must saturate at some point. In practice, this often occurs at very large strains and is therefore difficult to measure experimentally.

While the work hardening rate is clearly strongly dependent on temperature, as can be observed in Fig. 11.1, for temperatures below $0.4T_{MP}$ ($T < 100^\circ\text{C}$), the work hardening rate is relatively insensitive to strain rate, at least for conventional strain rates between 10^{-4} and 10^2 s^{-1} .

11.2.2 Physical basis of work hardening

Plastic deformation in high-purity aluminium at temperatures below $0.4 T_{MP}$ ($T < 100^\circ\text{C}$) is controlled by the motion of dislocations in the lattice, i.e. the strain rate can be related to mobile dislocation density and the average dislocation velocity:

$$\dot{\epsilon} = \rho_m b \bar{v} \quad [11.1]$$

where ρ_m is the mobile dislocation density, b is the Burgers vector and \bar{v} is the average dislocation velocity. As deformation proceeds, the density of dislocations increases in the crystal and the stress to continue deformation increases due to the interaction of the mobile dislocations with an increasingly dense network of

dislocations stored in the crystal due to plastic strain. As such, work hardening can be understood as a competition between the accumulation of dislocations in the crystal and the reduction in the number and total dislocation line length which is commonly referred to as dynamic recovery, i.e.

$$d\rho = d\rho_{\text{accumulation}} - d\rho_{\text{recovery}} \quad [11.2]$$

The accumulation of dislocations is geometrically driven due to the multiplication (e.g. Frank–Read sources and the nucleation of dislocation line length at sources such as grain boundaries) and the trapping of dislocations (sometimes referred to as debris). At its simplest level, the mechanism of dynamic recovery involves the annihilation of dislocations of opposite signs in the crystal which reduces the rate of increase of the dislocation density. At the saturation limit of the flow stress, the accumulation and recovery terms balance. At ambient temperatures it is often difficult to attain saturation of the flow stress.

The details of the mechanisms for dynamic recovery remain controversial. It is generally considered to involve thermally activated process such as cross-slip and possibly climb. The reader is referred to the excellent reviews of Gil Sevillano (1993), Nes (1997), Kocks and Mecking (2003) and Holmedal et al. (2006) for further details. The aforementioned strong dependence of the work hardening rate on temperature, but weak dependence on strain rate, arises as there are two separate thermally activated processes involved in the total work hardening process, i.e. one is associated with dislocation motion and interaction and the other is associated with dynamic recovery or annihilation of dislocations. This latter process is concurrent with plastic flow but much more temperature dependent.

11.3 Models of work hardening

11.3.1 Empirical models

The simplest model for work hardening is known as power law hardening (or Ludwik/Holloman) equation, i.e.

$$\sigma = K_1 \epsilon^n \quad [11.3]$$

where K_1 is known as the strength coefficient and n is the work hardening exponent. This equation is often used in industry although, as we shall see later, there are serious limitations in its utility for aluminium and its alloys. Note that n is a very useful parameter as it can be shown to be equivalent to the true strain at necking, i.e. the uniform elongation. Fundamentally, this equation suffers from four disadvantages: (1) it does not particularly well describe the entire stress-strain curve, (2) it predicts infinite strength, (3) the absence of a physical basis and (4) K and n are not independent variables. There are more complex empirical equations in the literature which fit the data to large plastic strains but also do not have a simple physical basis (e.g. Hockett and Sherby, 1975).

11.3.2 Dislocation-based models

Single parameter models

Single parameter models for work hardening start from the premise that the flow stress can be simply related to the average dislocation density using the Taylor equation:

$$\sigma = \alpha \mu b M \rho^{1/2} \quad [11.4]$$

where α is a geometric factor having a magnitude of 0.2–0.4 for FCC metals (Gil Sevillano, 1993), μ is the shear modulus, b is the magnitude of the Burgers vector, M is the Taylor factor (≈ 3)¹ and ρ is the dislocation density. Given Eq. 11.4, it is now necessary to develop a differential equation to describe the evolution of dislocation density with plastic strain. The most developed and commonly used single parameter model is the Kocks–Mecking model (Mecking and Kocks, 1981; Kocks and Mecking, 2003). For this model a single differential equation can be used to describe the evolution of dislocation density with plastic strain, ε_p , and is given by:

$$\frac{d\rho}{d\varepsilon_p} = (k_1 \rho^{1/2} - k_2 \rho) \quad [11.5]$$

where k_1 and k_2 are constants which describe the statistics of dislocation accumulation and dynamic recovery, respectively. The constant k_1 is a thermal and rate insensitive while k_2 is strongly temperature dependent and weakly rate dependent. The rate of accumulation of dislocations (i.e. term $k_1 \rho^{1/2}$) can be written as

$$\frac{d\rho}{d\varepsilon_p} = \frac{1}{bL} \quad [11.6]$$

where L is the mean free path and b is the magnitude of the Burgers vector, i.e. the line length of dislocation stored by unit strain is proportional to the mean free path between existing dislocations (Rollett and Kocks, 1994). Since the mean free path is proportional to the average dislocation spacing, $\rho^{-1/2}$, one obtains the first term in Eq. 11.5. It should be noted that in the case of high-purity aluminium dislocations are the only obstacles, thus there is only one mean free path. In more complex systems, one may need to consider more than one obstacle spacing.

The second term in Eq. 11.5 corresponds to the effect of dynamic recovery. Here, a simple assumption is made that the amount of dislocation line length lost per unit strain is proportional to the current dislocation density. This term is strongly temperature dependent but only weakly dependent on strain rate. Combining Eq. 11.5 with Eq. 11.4, the work hardening rate can be shown as:

$$\theta = \theta_0 \left(1 - \frac{\sigma}{\sigma_v}\right) \quad [11.7]$$

where θ_0 is the initial work hardening rate, σ_v is the scaling stress and σ is the flow stress; note that the introduction of the term scaling stress, σ_v , here is meant to emphasise the difference between the concepts of the saturation stress for the Voce equation (see Eq. 11.11) from the true physical saturation stress, Kocks et al. (1998). This can be seen schematically in Fig. 11.2, where one can observe that σ_v results from an extrapolation of the work hardening in Stage III to zero work hardening rate (i.e. Stage IV is ignored). The initial work hardening rate, θ_0 , and the scaling stress, σ_v , are related to k_1 and k_2 by:

$$\theta_0 = \frac{\alpha \mu b M k_1}{2} \quad [11.8]$$

and

$$\sigma_v = \frac{\alpha \mu b M k_1}{k_2} \quad [11.9]$$

In terms of Fig. 11.2, k_1 and k_2 have a clear physical basis, i.e. k_1 is related to the initial hardening rate, θ_0 , and k_2 is proportional to the slope of the θ vs. σ plot, i.e.

$$\frac{d\theta}{d\sigma} = -\frac{\theta_0}{\sigma_v} = -\frac{k_2}{2} \quad [11.10]$$

Figure 11.1(b) shows that to first approximation, k_1 is temperature independent and k_2 is strongly temperature dependent for high-purity aluminium (i.e. the ratio for the rate of dynamic recovery at ambient temperature to that at 4.2 K is ≈ 30).

Finally, integration of Eq. 11.5 gives the Voce equation:

$$\sigma = \sigma_s \left\{ 1 - \exp \left(\frac{\theta_0}{\sigma_v} \varepsilon_p \right) \right\} \quad [11.11]$$

An attractive feature of the Kocks–Mecking model is that only two fitting parameters are necessary to describe the work hardening behaviour at a given temperature. By accounting for the dependence of dynamic recovery on temperature and stacking fault energy the model can be extended to describe the temperature dependent work hardening behaviour.

Multiple parameter models

The single variable models such as Kocks–Mecking do not always capture the complexity of microstructure development, especially in cases of deformation at higher temperatures (e.g. typical of hot rolling), transient deformation, strain path changes and cyclic deformation (Mughrabi, 1983) or when models are needed that provide input into recovery/recrystallisation models (i.e. when the details on the local arrangements of the dislocation network are necessary). There are currently two major schools of thought on developing more complex work

hardening models, i.e. the microstructure metal plasticity model (MMP) by Nes and co-workers (Nes, 1997; Holmedal et al., 2006) and the 3 internal variable model (3IV) by Gottstein and co-workers (Roters et al., 2000; Goerdeler and Gottstein, 2001; Goerdeler et al., 2004). These models build on the early efforts of Prinz and Argon (1984), Nix et al. (1985) and Mughrabi (1983) who originally proposed multi-parameter models for work hardening.

The MMP model proposes that the dislocation structure can be described in terms of dislocation cells of size, δ , and the dislocation density within the interior of the cells, ρ_i (Nes, 1997). The flow stress at the slip system level can be described in terms of these two variables, i.e.

$$\tau = \tau_i + \alpha_1 \mu b \rho_i^{1/2} + \alpha_2 \mu b \left(\frac{1}{\delta} \right) \quad [11.12a]$$

or for polycrystals

$$\sigma = \sigma_i + \alpha_1 \mu b M \rho_i^{1/2} + \alpha_2 \mu b M \left(\frac{1}{\delta} \right) \quad [11.12b]$$

In this case, the description of the stress-strain behaviour requires that differential equations be developed to describe the evolution of ρ_i and δ as a function of strain, temperature and strain rate.

In contrast, the approach of Gottstein and co-workers (Roters et al., 2000) considers that three variables are required to describe the spatial distribution of dislocations. The three variables are the mobile dislocation density, ρ_m , the immobile dislocation density, ρ_i in the cell interior and the immobile dislocation density in the cell walls ρ_w . Furthermore, the volume fraction of the cell walls is defined as f and the resulting flow stress on the slip system level is given as

$$\tau = \tau_i + (1 - f) \alpha \mu b \rho_i^{1/2} + f \alpha \mu b \rho_{i0}^{1/2} \quad [11.13a]$$

or for polycrystals

$$\sigma = \sigma_i + (1 - f) \alpha \mu b M \rho_i^{1/2} + f \alpha \mu b M \rho_{i0}^{1/2} \quad [11.13b]$$

In this case, evolution laws for these internal variables must be derived, i.e. the processes of dislocation accumulation and dynamic recovery are modelled. For both the MMP and 3IV models, analytical solutions do not exist to describe the stress-strain curve and as such computer codes have been developed to implement the model. Through careful fitting of experimental measurements, these models give excellent descriptions of the work hardening behaviour and have been developed to include temperature deformation conditions typical of hot rolling or extrusion processes.

Stage IV behaviour

As can be seen in Fig. 11.1(b) for high-purity aluminium, at temperatures of 77 K and ambient temperature, there is a clear breakdown of the linearity between the

work hardening rate and the flow stress at higher flow stresses, i.e. the onset of Stage IV can be readily observed although it is worth emphasising that it is usually difficult to study experimentally since it falls in a strain range well beyond that attained in a tensile test. The physical basis for large strain work hardening in Stage IV remains unclear (Gil Sevillano, 1993; Estrin et al., 1998; Kocks and Mecking, 2003).

To account for this in a simple empirical manner, Tomé (Tomé et al., 2001) has modified the Voce law (Eq. 11.11) as follows²:

$$\sigma = (\sigma_v + \theta_v \varepsilon_p) \left\{ 1 - \exp \left(- \frac{\theta_0}{\sigma_v} \varepsilon_p \right) \right\} \quad [11.14]$$

In terms of the Kocks–Mecking, MMP and 3IV models, various approaches have been described in the literature to incorporate Stage IV (see Rollett and Kocks, 1994; Nes, 1997; Estrin et al., 1998; Kocks and Mecking, 2003; Holmedal et al., 2006).

Additional considerations

Prior to discussing the role of specific microstructural features on work hardening, it is appropriate to comment on the relationship of models for the evolution of various microstructural features, such as cell size, cell wall character, etc. Much of the knowledge of microstructure is based on transmission electron microscopy (TEM) and diffraction methods. However, plastic deformation also produces a high density of point defects and dislocation loop debris which is beyond the resolution of TEM and it is conceivable that these also play a role in dynamic recovery. Thus, in general, models exist which try to account for the observed mechanical response and are consistent with the observed microstructural evolution without providing a detailed physical description of the events pertaining to dynamic recovery.

11.3.3 Effect of microstructure

Grain size effects

The grain size of traditional industrial alloys falls in the range of 1–100 μm . For this range of grain sizes, grain boundaries affect the problem of work hardening in two ways. First, grain boundaries modify the accumulation of dislocations by acting as sources and storage sites for dislocations. Second, grain boundaries can provide sinks for dislocations thereby affecting dynamic recovery. Building on the seminal work of Ashby (1970), Estrin (1996) proposed a modification to the Kocks–Mecking model by the addition of a second dislocation accumulation term, k_D :

$$\frac{d\rho}{d\varepsilon_p} = \left(k_1 \rho^{1/2} - k_2 \rho + \frac{k_D}{bD} \right) \quad [11.15]$$

where D is the grain size of the alloy. A similar modification of the MMP approach has been suggested by Holmedal et al. (2006). The challenge with this modification is that by increasing the accumulation rate of dislocations one expects an acceleration of the work hardening as the grain size is reduced. While the model suggests a finer grain size should increase work hardening rate, experimental observations on aluminium alloys are not consistent with this prediction. Over the commercial range of grain sizes 15–50 μm , the Hall–Petch slope, for example, is independent of strain, even in 5000 series alloys where dynamic recovery is low (Lloyd and Court, 2003; Jin and Lloyd, 2004b). Further, for grain sizes below 5 μm , the work hardening rate is reduced and can be very low (Lloyd, 1980; Nijs et al., 2008). It has been argued that when the free slip distance is of the order of the grain size, dislocations may be absorbed in to the grain boundaries rather than stored within the grains. Recently, a first attempt to modify the Kocks–Mecking framework to include the effect of grain boundaries on dislocation accumulation and recovery has been made by Sinclair et al. (2006). This model extends Kocks–Mecking to include a kinematic hardening term and has so far been applied to other FCC metals but it appears promising as a means to describe results for aluminium alloys such as that reported by Lloyd (1980) and Nijs et al. (2008).

These models treat the grain size as an average variable. Recent modelling work has suggested that the grain size distribution can have important effects in some cases. In particular, when the grain size is below 5 μm , the width of the grain size distribution can significantly affect the yield stress and work hardening rate (Raeisinia et al., 2008; Raeisinia and Sinclair, 2009). One approach to incorporating this effect is to use a representative grain size (i.e. for different grain size distributions select a single grain size to represent the average behaviour, see Raeisinia and Sinclair, 2009 for details).

There has also been interest in developing materials with bimodal grain size distribution. For example, Jin and Lloyd (2004a) have shown that improved combinations of strength and ductility can be produced in 5xxx series alloys processed by asymmetric rolling and annealing to produce a bimodal grain size distribution. In recent years, several models have been presented which allow for the prediction of work hardening when bimodal grain size distributions are present (see Joshi et al., 2006; Berbenni et al., 2007; Raeisinia et al., 2008).

The role of bimodal grain size distributions introduces a second aspect of the work hardening process. If the two components of the grain size distribution are considered as materials which have a mechanical contrast due to a local difference in yield stress, the material now has the characteristic of a composite, i.e. for some period, the stronger material will be loaded *elastically* (e.g. see the model results of Raeisinia, 2008). This gives rise to an elasto-plastic transition in which the slope of the stress-strain curve, $d\sigma/d\varepsilon$, is dominated by the volume fraction of the harder component and the unrelaxed elastic strain. This applies to both materials with distributions of grain size and to systems with hard particles particularly

those with plates or rod/lathe-shaped precipitates. The important result is that the initial work hardening rates in these cases are much higher than that given by the Stage II work hardening rate. Thus, we have an important work hardening behaviour due to mechanical contrast in the microstructure and the resulting elasto-plastic transitions can extend to quite large plastic strain. It will also be seen that the presence of this complexity has important impact on strain path changes, for example as observed in tension followed by compression (Bauschinger tests).

Solid solution effects

In considering the role of solute and second phase particles (next section), it is useful to emphasise at the beginning that, in general, models for the yield stress are well developed (Brown and Stobbs, 1971a; Ardell, 1985; Martin, 1998; Polmear, 2006) and can be expressed in a variety of scaling laws. However, the influence of these features on dislocation accumulation and dynamic recovery is poorly understood and much of our current understanding is a rationalisation of experimental observations rather than the application of well-formulated scaling laws.

The addition of solute atoms to aluminium can be an effective method to increase the yield strength and also to improve the work hardening characteristics of alloys. For low temperature deformation of aluminium alloys, there are two cases to consider. First, the simpler case of solute atoms which remain stationary during deformation and the second case is when the solute atoms are mobile during deformation (Estrin, 1996). This latter case is particularly relevant for the commercially important case of Al-Mg alloys.

For the case of stationary solute atoms, these have been observed to have important effects on Stages III and IV of work hardening, i.e. the rate of dynamic recovery is reduced as the alloy level is increased (see Ryen et al., 2006a for a good summary on Mn and Mg additions). On the other hand, the accumulation of dislocations appears to be unaffected, or weakly affected, by the solute atoms (Marthinsen and Nes, 2001). As such, modifications of work hardening models have focused on the effect of solute on dynamic recovery. The mechanism by which solutes affect the rate of dynamic recovery is poorly understood but has been considered to derive from the effect of solute on local recovery events (Deschamps et al., 1996; Marthinsen and Nes, 2001) or on the stacking fault energy of the alloy (Estrin, 1996).

In terms of modelling, one approach taken is found in the work of Deschamps et al. (1996). They have modified the Kocks–Mecking model framework to account for the effect of solute pinning which makes the annihilation of dislocations more difficult (e.g. either by increasing the critical cross-slip distance or dipole collapse width). This model has been shown to provide a reasonable description for their data on Al-0.2wt%Cu and Al-0.4wt%Cu alloys. The MMP model of Nes

and co-workers explicitly includes solute effects in their recovery model and accounts for the effects of solute on dislocation glide and climb (Marthinsen and Nes, 2001; Holmedal et al., 2006).

Magnesium additions to aluminium alloys represent a particular challenge for modelling of work hardening due to the well-known high mobility of magnesium solute atoms in aluminium at ambient temperatures (McCormick, 1972). This creates a very complicated deformation mode due to dynamic strain ageing effects (also referred to as the Portevin LeChetelier (PLC) effect). The dynamic strain ageing can manifest itself at the microscopic level where the mean free path may be dictated by the dynamic pinning process resulting in high rate of dislocation storage and a change in the pattern of dislocation storage. At the macroscopic level, a variety of types of strain localisation can occur. Kang et al. (2006) have performed a very careful study to examine the inhomogeneity of deformation in Al-Mg alloys using digital image correlation. The propagation of PLC bands has also been modelled using the finite element method (Kok et al., 2002, 2003).

For most analysis, it appears that the complications of deformation at the local level can be ignored and the models such as Kocks–Mecking or the MMP can be applied. However, it is worth emphasising the limitations of these models for these cases when the deformation is much more complicated, i.e. deformation at the macroscopic level is heterogeneous. This includes cases where deformation proceeds by the propagation of Lüders bands on a variety of PLC bands and also cases where intense shear banding occurs at large strain (Deschamps et al., 1996). This points to the need for both microscopic and macroscopic views of plasticity to be combined for a number of cases.

Precipitate effects

The addition of precipitates further complicates the work hardening of aluminium alloys and can have very strong effects (see the seminal work of Byrne et al., 1961 for effects on Al-Cu single crystals). At the local level, precipitates can affect both the storage and recovery of dislocations in the aluminium matrix. The distribution of slip can also be modified and precipitates can modify the local storage of elastic energy. There are two limiting cases: shearable and non-shearable precipitates, although in general there is a need to consider a size distribution of precipitates where the smaller precipitates are shearable and the larger ones are non-shearable (Fazeli et al., 2008). Finally, there are cases of alloys where a mixture of different precipitates is observed (Gable et al., 2001).

Shearable precipitates

The literature on the effect of shearable precipitates on work hardening behaviour suggests that the overall work hardening rate is reduced in the presence of shearable precipitates. There are two important interrelated problems which make

the analysis of this problem complicated. First, the decomposition of the supersaturated solid solution produces precipitates on the glide plane which act as additional obstacles to dislocation motion and, second, the solute content of the matrix is reduced as a result of the precipitation process. If the first effect is considered one notes that when precipitates in aluminium alloys are very small (typically less than a few nm), the mobile dislocations will shear through the precipitate creating a step at the precipitate-matrix interface. As such, this would not be expected to greatly influence the storage and recovery of dislocations (although the difference in lattice parameters between the precipitate and aluminium may lead to the storage of misfit dislocations at the precipitate-matrix interface). However, an important question relates to whether local softening on the slip plane will lead to localisation of deformation on specific slip planes (Duva et al., 1988). Hornbogen and Gahr (1975) considered this situation and developed a simple model to examine this effect and, more recently, Estrin (1996) developed a model in the Kocks–Mecking framework to capture this effect on work hardening. These models are consistent with a reduction in the macroscopic work hardening rate. However, the experimental evidence for the localisation of slip is mixed in the literature and apparently depends on the alloy system. For Al–Li–Cu–Mg alloys TEM evidence exists for localisation on the slip plane (Blankenship et al., 1993) while the situation appears different in Al–Mg–Si–Cu alloys (Poole et al., 2005). In the case of the Al–Mg–Si–Cu alloys, Cheng et al. (2003) have argued that a careful consideration of the flow stress addition law for precipitate hardening and dislocation hardening can account for the experimental observations. On the other hand, the reduction in the average solute content in the matrix would be expected to increase the rate of dynamic recovery (see Section 11.3.3) thereby reducing the macroscopic work hardening rate. Simar et al. (2007) have emphasised this effect in their modelling work. Clearly, this is a complex problem which is most likely alloy sensitive and requires further investigation.

Non-shearable precipitates

As the precipitates grow and coarsen, a critical radius is usually observed where the mobile dislocations can no longer shear the precipitate and instead they bow around the precipitate and bypass the particle leaving a dislocation loop around the particle. The implications of these additional stored dislocations loops (sometimes referred to as geometrically necessary dislocations) have important impact on the macroscopic stress-strain response. In this case, the presence of non-shearable precipitates significantly increases the initial work hardening rate. There are two mechanisms which have been proposed to explain this increase in the initial work hardening rate. First, the role of these additional dislocation loops must be accounted for in the overall evolution law for the dislocation density both in terms of the accumulation of dislocations and their effect on dynamic recovery (Ashby, 1970, 1971). Second, the storage of loops around precipitates leads to the

development of local storage of elastic energy (see the seminal work of Brown and Stobbs, 1971a, 1971b). This second mechanism has particularly significant implications when strain path changes occur during deformation (we will return to this point later in this section). Finally, an additional important consideration that must be explicitly accounted for in these models is the precipitate shape (i.e. spheres, rods, laths or plates).

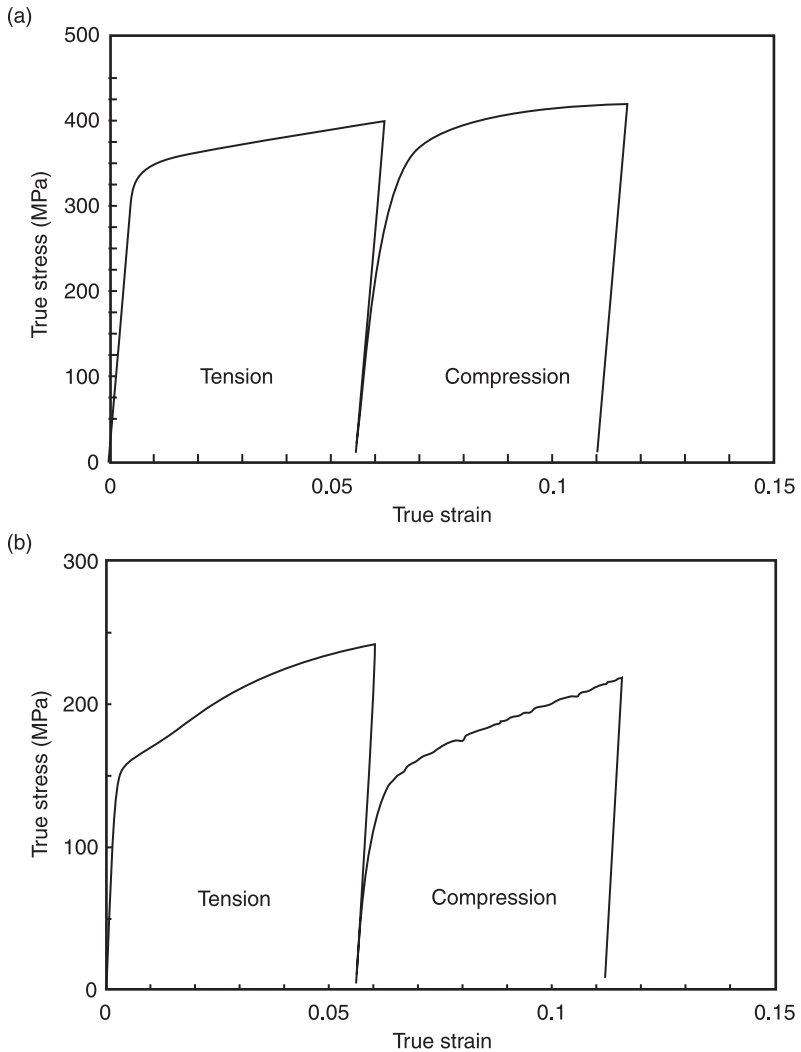
In terms of modelling, the effect of the additional dislocation loops stored during deformation has been considered in the Kocks–Mecking framework (Estrin, 1996; Cheng et al., 2003; Simar et al., 2007) and in terms of the MMP model (Holmedal et al., 2006) by adding an additional dislocation storage term. In the Kocks–Mecking framework, the evolution of the dislocation density can be written as:

$$\frac{d\rho}{d\varepsilon_p} = \left(k_1 \rho^{1/2} - f k_2 \rho + \frac{\alpha_{\text{ppt}}}{b L_{\text{ppt}}} \right) \quad [11.16]$$

where f is a factor to describe the effect of the precipitates (or change in dynamic recovery due to the decreased solid solution content) on dynamic recovery, α_{ppt} is a constant and L_{ppt} is the mean inter-precipitate spacing. In order to account for the development of local elastic energy storage or in terms of the earlier discussion, mechanical contrast in the microstructure (i.e. a plastic matrix and a non-shearable precipitate), models have been developed which build on the original Brown and Stobbs work (Proudhon and Poole, 2006; da Costa Teixeira et al., 2009).

In order to differentiate between the effect of the non-shearable precipitates on dislocation accumulation and local elastic energy storage, Bauschinger effect experiments have been conducted by a number of researchers (Moan and Embury, 1979; Proudhon and Poole, 2006; da Costa Teixeira et al., 2009). These tests involve uniaxial tension followed by compression for different levels of pre-strain. Figure 11.3 shows results from Bauschinger tests on a 6xxx series aluminium alloy at its peak strength and in the overaged conditions (i.e. a case with shearable and non-shearable precipitates, respectively). It can be observed that for the peak aged sample in Fig. 11.3(a), after a short transient of approximately 0.01 strain, the stress-strain behaviour returns to a similar level as would have been the case for monotonic loading. On the other hand, for the case of non-shearable precipitates shown in Fig. 11.3(b), there is a much larger difference between compressive stress-strain behaviour and what would have been the case for monotonic loading. Models such as those developed by Proudhon et al. (2008) and da Costa Teixeira et al. (2009) are able to make first order predictions for these sort of simple strain path changes.

Returning to the question of precipitate shape, a range of experimental data and models has been developed over the past several years. For spheres, Fazeli and co-workers have considered the Al-Mg-Sc system where spherical precipitates



11.3 Bauschinger tests (tension followed by compression) on AA6111 illustrating the difference in behaviour between (a) peak aged and (b) overaged samples. The samples were solution treated at 560°C for ten minutes and then artificial aged for seven hours at 180°C (peak aged) and seven days at 250°C (overaged). Note that the sign of the compressive stress has been reversed and the cumulative magnitude of strain has been plotted so that the stress-strain curve can be more easily compared to the initial tensile loading (see Proudhon et al., 2008 for details).

are observed (Fazeli et al., 2006, 2008). Spheres have the smallest effect on kinematic hardening. Proudhon and Poole (2006) have examined the effect of long lath precipitates while examinations on Al-Cu and Al-Mg-Cu have considered the effects of plates (da Costa Teixeira et al., 2009; Sharma et al., 2009). Finally, there

is a lack of knowledge for cases where different precipitates coexist in the microstructure.

Flow stress addition laws

The problem of describing plasticity in a system with a variety of obstacles is complex. Obstacles such as solute atoms may influence the flow stress but there may be different mechanisms which also alter the rate of dislocation accumulation and dynamic recovery. The influence of obstacles on the stress to move dislocations can often be described by simple scaling laws but the influence on hardening is more difficult to quantify. An additional question that must be considered when developing models for work hardening in complex systems is how one sums the different flow stress contributions. There are two limiting cases: (1) linear addition of flow stress contributions and (2) a Pythagorean (or root mean square) addition law (Koppelaar and Kuhlmann-Wilsdorf, 1964; Foreman et al., 1966; Brown and Ham, 1971; Kocks et al., 1975; Kocks, 1979; Ardell, 1985), i.e.

$$\sigma = \sigma_1 + \sigma_2 \quad [11.17]$$

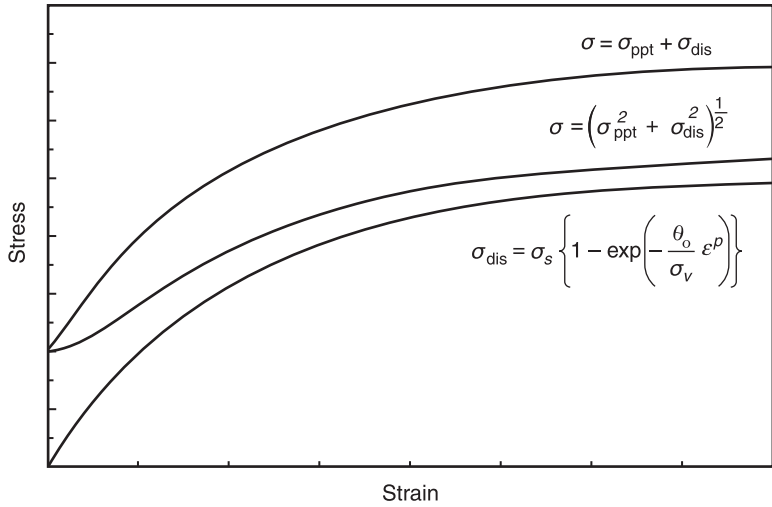
$$\sigma = (\sigma_1^2 + \sigma_2^2)^{1/2} \quad [11.18]$$

It is assumed that linear additions laws are appropriate to add terms when the length scale and obstacle strength of the mechanisms involved are very different, e.g. solid solution hardening and dislocation hardening would fall under this case since the typical spacing of solute atoms would be a few atomic spacings, while the dislocation spacings would usually be greater (tens of atomic spacing and much larger). Another example where this would be the case is solid solution and grain size hardening. On the other hand, if the spacing of obstacles and the strength of obstacles are similar, then the Pythagorean addition law would be appropriate. Here, an example would be hardening due to the dislocation network and non-shearable precipitates, i.e. each obstacle would be considered a strong obstacle and their spacings would be typically 10–100 nm. Clearly, there are cases which fall in-between these limits, i.e.:

$$\sigma = (\sigma_1^n + \sigma_2^n)^{1/n} \quad [11.19]$$

where n is a constant between 1 and 2. This is further complicated due to the fact that the relative length scales of the strengthening contributions will change either during heat treatment for the case of precipitates (the spacing increases during coarsening and the obstacle strength increases with precipitate size) or during deformation where the spacing between dislocations is significantly reduced.

The effect of the addition law on work hardening behaviour was considered by Kocks (1979) who showed that the use of Pythagorean addition law (i.e. $n = 2$)



11.4 Schematic diagram illustrating the difference in macroscopic work hardening rate for different flow stress addition laws. The dislocation hardening response was modelled with Eq. 11.11 in the text. The ratio of σ_v to σ_{ppt} was 0.4 (adapted from Kocks, 1979).

resulted in a substantial change in the macroscopic work hardening rate. The schematic diagram shown in Fig. 11.4 illustrates the effect of the addition law on the overall shape of the stress-strain curve. This example considers that dislocation hardening follows a Voce law (i.e. Eq. 11.11) and that there is a constant additional precipitation hardening contribution from precipitates which have similar obstacle strength as dislocation hardening. The limiting cases to consider are a linear addition law (i.e. $n = 1$) and a Pythagorean addition law (i.e. $n = 2$). It can readily be observed that for the case of the Pythagorean addition law, both the initial work hardening rate and the saturation stress are considerably lowered compared with the linear addition law. This can be seen in a more quantitative way by determining the work hardening rate by differentiating the Pythagorean addition law, i.e.

$$\frac{d\sigma}{d\varepsilon} = \frac{\sigma_{dis}}{\sqrt{\sigma_{dis}^2 + \sigma_{ppt}^2}} \frac{d\sigma_{dis}}{d\varepsilon} \quad [11.20]$$

where σ_{dis} is the strain dependent contribution from dislocation hardening and σ_{ppt} is a strain independent contribution from precipitation hardening. Note that the term $\sigma_{dis}/\sqrt{\sigma_{dis}^2 + \sigma_{ppt}^2}$ on the right hand of Eq. 11.20 in front of the work hardening contribution due to dislocation hardening will always be less than unity, i.e. the overall work hardening rate will be reduced when this addition law is employed (Poole et al., 2005). Cheng et al. (2003) have argued that this is a critical factor to be considered to understand the evolution of the work

hardening behaviour in commercial alloys (see also Poole et al., 2005). Poole and Lloyd (2004) have made a very simple approach to account for the transition of the addition law from a linear to a Pythagorean form in a continuous manner as the strength of precipitates as dislocation obstacles increases during ageing.

Other cases

There are a number of other cases which are of interest which have received some attention in the literature. First, the deformation of supersaturated solid solutions has been examined by a number of researchers (Kelly and Nicholson, 1963; Deschamps et al., 1999, 2003). There is strong evidence that precipitation can occur during deformation thereby producing a new set of obstacles as deformation proceeds. Second, there is some evidence that macroscopic work hardening behaviour is affected by solute clusters which form during natural ageing (Hutchinson et al., 2008; Serizawa et al., 2008). Third, a model for the work hardening of aluminium alloys after various levels of static recovery based on the Kocks–Mecking framework has been developed by Roumina and Sinclair (Roumina, 2009; Roumina and Sinclair, 2010). This is a challenging exercise and illustrates how the simple framework must be expanded to examine a complex problem such as this.

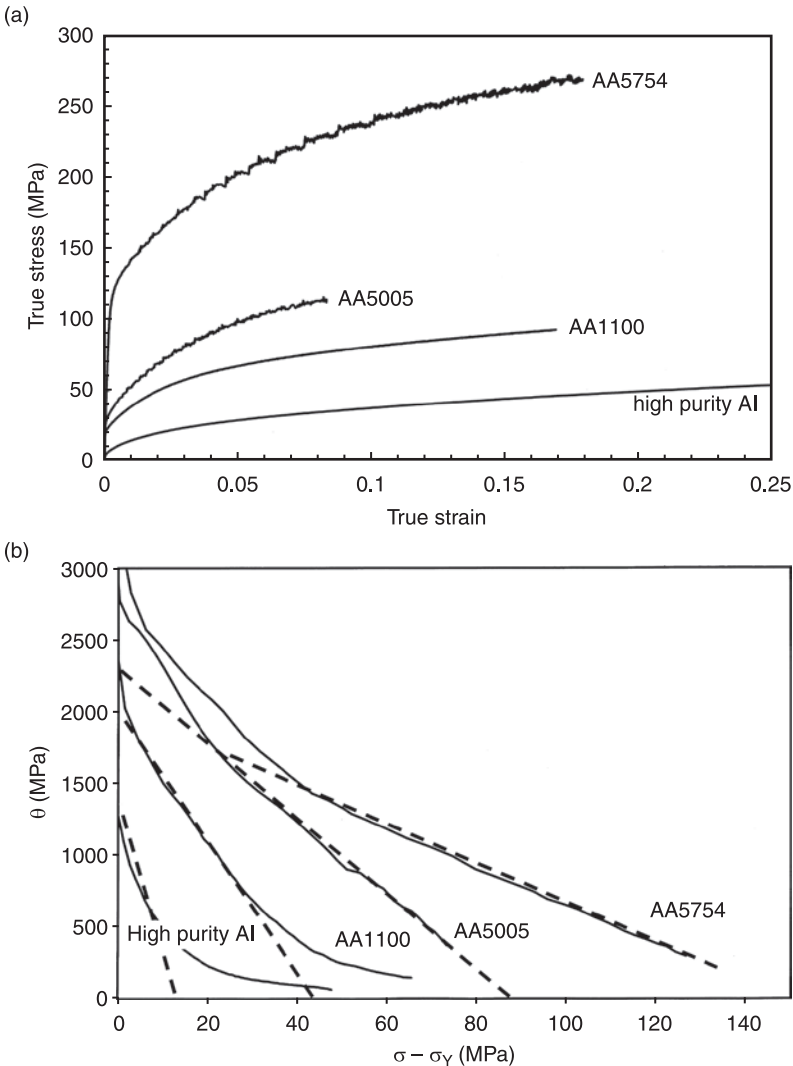
11.4 Applications of work hardening models to industrial alloys

This section will consider a brief overview with some examples of how the work hardening behaviour of commercial alloys fits with the work hardening models that were presented in the previous sections.

11.4.1 Non-heat treatable alloys (1xxx, 3xxx, 5xxx)

Aluminium alloys of the 1xxx, 3xxx and 5xxx families of alloys are strengthened by the addition of solute elements which typically do not exhibit classic precipitation hardening behaviour, i.e. combinations of Fe, Mn, Si and Mg. The microstructures generally consist of (1) aluminium grains with alloy additions in solution, (2) constituent particles of 1–5 μm which develop during solidification and homogenisation (Al(Fe,Mn)_6 , $\alpha\text{-Al(Mn,Fe)Si}$, etc.) (Mondolfo, 1976; Embury et al., 1989) and (3) dispersoids of 50–250 nm distributed in the aluminium grains. Figure 11.5(a) compares the stress-strain behaviour of high-purity aluminium, AA1100 (0.1 wt% Si, 0.05 wt% Mn, 0.3 wt% Fe), AA5005 (0.8 wt% Mg, 0.1 wt% Si, 0.5 wt% Fe) and AA5754 (3.2 wt% Mg, 0.1 wt% Si, 0.2 wt% Mn and 0.2 wt% Fe), tested at ambient temperature. Inspection of the stress-strain curves shows that as expected the yield stress increases with solute content. In

addition, it can be qualitatively observed that the work hardening behaviour is also strongly affected and that the alloys with Mg additions show serrated or PLC flow behaviour. Figure 11.5(b) plots the work hardening rate as a function of the flow stress for the four aluminium alloys (note that the stress-stress data were first smoothed and then numerically differentiated). Here the differences in the work hardening behaviour can be seen more clearly. The initial work hardening rate, θ_0 , is higher for the commercial alloys compared to high-purity aluminium, i.e. 2000–2500 MPa vs. 1200–1500 MPa, respectively. The slope of the $\theta - \sigma$ plot,

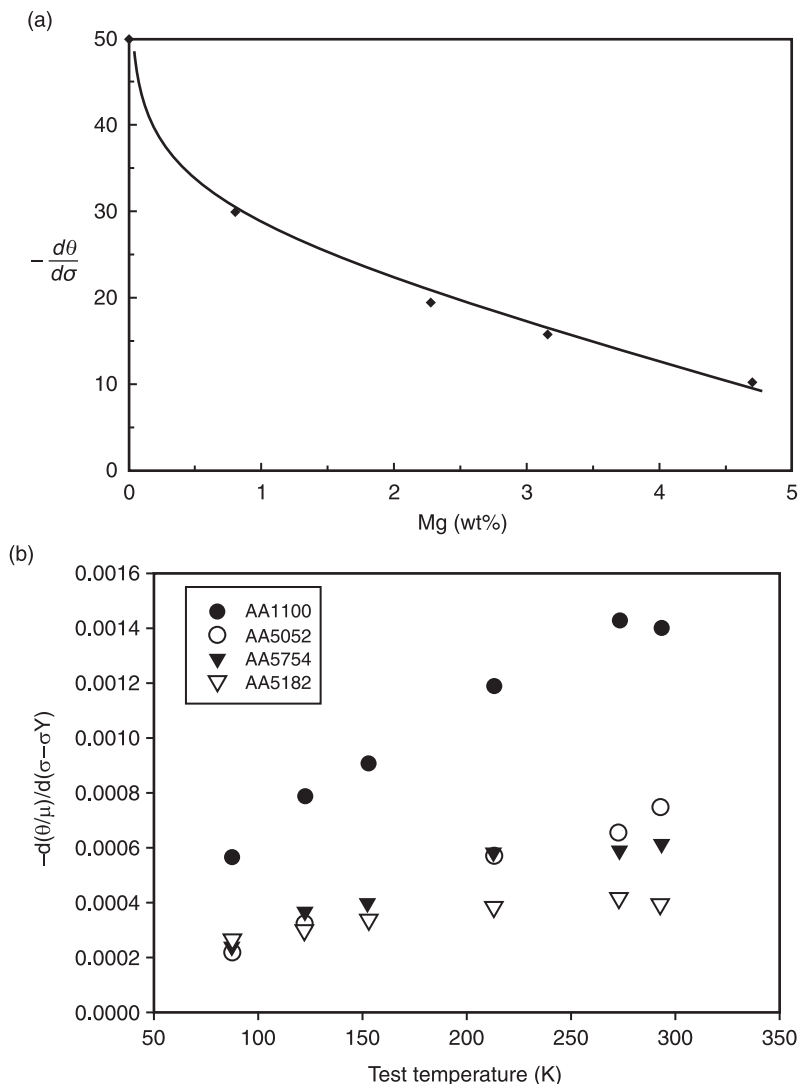


11.5 A comparison of (a) the stress-strain response and (b) the work hardening behaviour for a number of commercial solid solution alloys.

$d\theta/d\sigma$, which was discussed in Section 11.3.2 and can be interpreted as the rate of dynamic recovery in the Kocks–Mecking framework (see Single parameter models) is strongly dependent on alloy content. Finally, there are significant deviations from linearity of the $\theta - \sigma$ plot at low and high stresses. The deviations at low stress (i.e. near the yield stress) are not fully understood but can be related to multiple factors including (1) a more complex elasto-plastic transition due to the presence of a relatively large, non-deformable phase (constituent particles), (2) storage of additional dislocation line length around the fine scale dispersoids and (3) modification of the mean free path for the dislocation storage due to solute effects. Currently, there is a lack of high-quality data in the literature on high-purity solid solution alloys which could help to differentiate these effects.

The deviations in the $\theta - \sigma$ plot at large stresses is apparent in the high-purity aluminium and AA1100 alloy but not observed in the AA5xxx alloys. The deviation is related to Stage IV behaviour as described in the earlier section entitled ‘Stage IV behaviour’. The absence of this deviation for the AA5xxx should not be interpreted as evidence that Stage IV is not present but rather it likely results from the limitation in the level of uniform strain that can be measured in a tensile test. For example, the results of Lloyd and Kenny (1982) (torsion tests) or Ryen et al. (2006b) (compression and tension after rolling) have shown that Stage IV can readily be observed in Al-Mg alloys. Quantifying Stage IV is not simple as it is associated with large strain deformation. The approaches on which tensile tests are conducted on previously rolled material have the intrinsic problem that the structure developed by rolling is probed with a different loading path and strain rate. Also at large strains there may be textural effects (evolution of the Taylor factor, Kocks, 1987), the influence of redundant work (as in ECAP experiments), frictional effects and the localisation of deformation (e.g. the formation of shear bands). Also, as the dimensions of the material are reduced, the surface may have a direct influence on plasticity. This is exemplified in bending which is a process that is limited by fracture rather than plastic stability but where the fracture event develops from increasing surface roughness.

The effect of solute, particularly magnesium, on dynamic recovery is very important for commercial alloys as it allows for increased formability of these alloys. In Fig. 11.6(a), the data of Lloyd (2006) have been re-plotted in terms of the slope of the $\theta - \sigma$ plot, $d\theta/d\sigma$ (i.e. which may be interpreted as the rate of dynamic recovery) as a function of the Mg content in commercial alloys. Here, it can clearly be observed that the rate of dynamic recovery is dramatically reduced as the level of Mg addition increases. Further, Fig. 11.6(b) shows the temperature dependence for the dynamic recovery rate from 80 K to 300 K for AA1100 and several AA5xxx alloys (note that this data has been normalised by the temperature dependence of the shear modulus). Here the interesting observation can be made that the temperature dependence of dynamic recovery is reduced when Mg is added as an alloy addition. Further, results on the effect of temperature for AA5754 may be found in the work of Park and Niewczas (2008). In addition to



11.6 The change in the slope of the θ vs. σ plot as a function of (a) Mg content for tests at room temperature and (b) the test temperature for a range of commercial solid solution alloys (in this case the slope was normalised by the temperature dependence of the shear modulus). Note that the slope of the θ vs. σ plot, is proportional to the rate of dynamic recovery in the Kocks–Mecking framework.

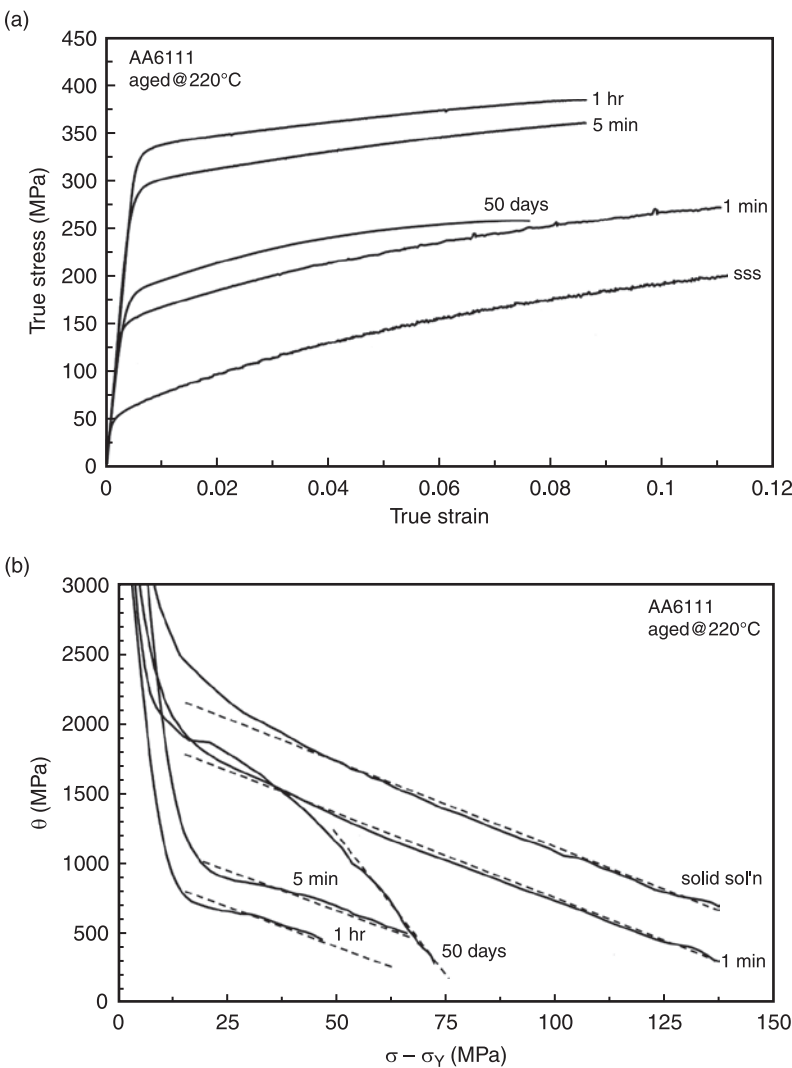
the effects of Mg in solution, Mn in solution has been shown to have important effects at ambient temperature (Ryen et al., 2006a) and although the solubility of Fe is very low, it may also have a significant influence (Diak et al., 1998; Marthinsen and Nes, 2001).

11.4.2 Heat treatable alloys (2xxx, 6xxx, 7xxx)

Work hardening in commercial precipitation hardening systems demonstrates the most complex behaviour of all aluminium alloys. The microstructures consist of the features found in non-heat treatable alloys described in the previous section (aluminium grains with solute atoms, dispersoids and constituent particles) and superimposed on these microstructural features is a fine distribution of nanometer precipitates (rods, laths, plates or spheres) in the grains which may be shearable or non-shearable to the mobile dislocations. As an example of the complexity one observes, Fig. 11.7(a) shows examples of the stress-strain curves for AA6111 aged at 220°C for a variety of times going from the as-quenched supersaturated solid solution to the peak aged condition (one hour) to massively overaged. The classic age-hardening response can be observed with the yield stress first increasing, reaching a peak and then decreasing. Qualitative observations from the stress-strain curves show that the overall level of work hardening decreases near the peak strength and then increases (at least the initial hardening rate) for the overaged sample. In addition, one can note that there is evidence of serrated flow in the supersaturated solid solution (sss) but this disappears as the ageing time is increased. The differences in the macroscopic work hardening behaviour can be more readily observed in the $\theta - \sigma$ plot illustrated in Fig. 11.7(b). To quantify these differences, the behaviour of the $\theta - \sigma$ plot can be characterised by the initial hardening rate after the elasto-plastic transition and the slope of the $\theta - \sigma$ plot, $d\theta/d\sigma$. In the case of the slope of the $\theta - \sigma$ plot, it is apparent that the overaged sample does not display a single linear region. In this case, Cheng et al. (2003) has proposed that the asymptotic slope as the work hardening rate approaches zero would be appropriate if one wants to characterise dynamic recovery in these systems (note that the dashed lines shown in Fig. 11.7b illustrate the slopes used in the present analysis).

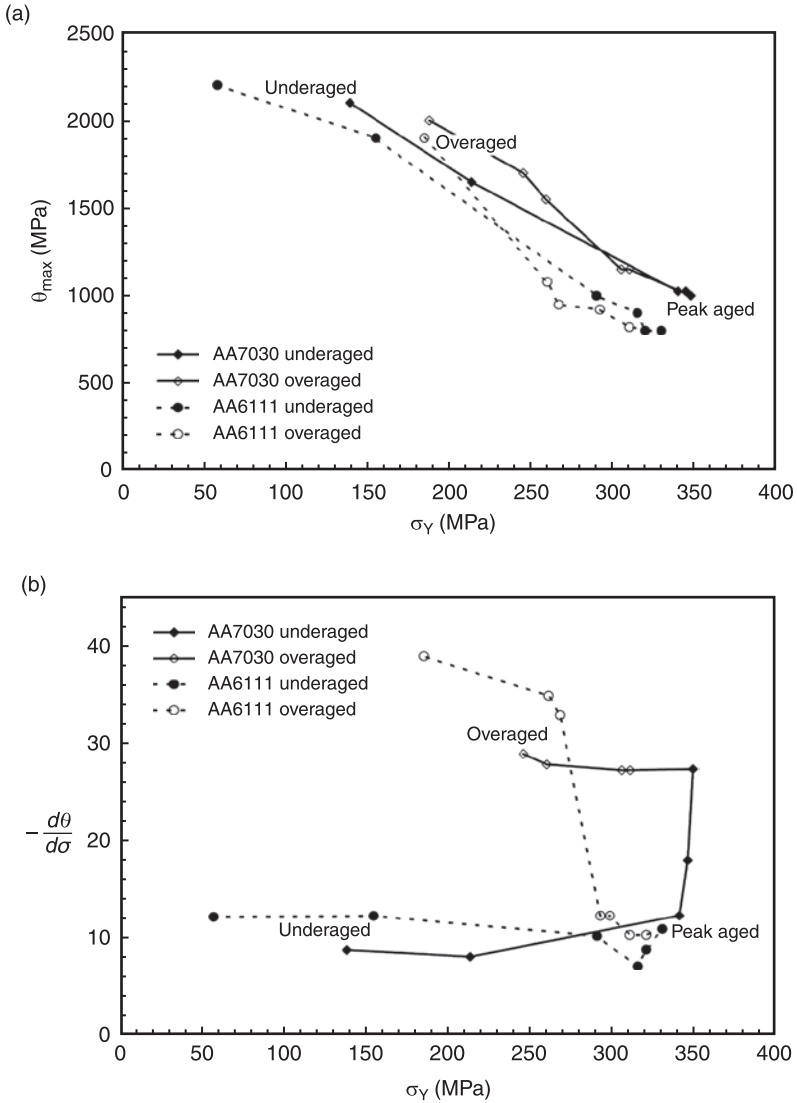
Figures 11.8(a) and 11.8(b) represent the results for the maximum hardening rate and the slope of the $\theta - \sigma$ plot as a function of the yield stress of the alloy for AA6111 and AA7030. Both alloys show a similar behaviour where the maximum initial work hardening rate decreases as the yield stress increases. The maximum initial hardening rate reaches a minimum around the peak strength and then starts to increase again as shown in Fig. 11.8(a). The slope of the $\theta - \sigma$ plot illustrated in Fig. 11.8(b) also has a similar behaviour for the two alloys. As the yield stress increases, little change is observed in $d\theta/d\sigma$. For AA7030, the magnitude of $d\theta/d\sigma$ increases dramatically at the peak stress while for AA6111 there is also a large increase but this occurs during overageing of the alloy (i.e. at an overaged yield stress of ≈ 300 MPa compared to the peak stress of 330 MPa). Similar observations have been reported in AA2219 (Sharma et al., 2009), AA6005 (Simar et al., 2007), AA2219 (Sharma et al., 2009) and AA7108 (Westermann et al., 2009).

The complexity of this behaviour makes the interpretation challenging. There is general agreement that the change in the initial work hardening rate and the



11.7 Experimental data illustrating (a) the stress-strain response and (b) work hardening behaviour of the precipitation hardened alloy, AA6111 as function of the ageing time at 220°C. Note that the dashed lines correspond to the ones used to characterise the slope of the θ vs. σ plot, shown in Figure 11.8(b).

magnitude of $d\theta/d\sigma$ near the peak strength are related to the shearable/non-shearable transition and this has been supported by detailed studies of slip behaviour and TEM studies for AA6xxx alloys (Poole et al., 2005). However, phenomenological models have emphasised different mechanisms to describe the



11.8 The characterisation of (a) the maximum work hardening rate after the elasto-plastic transition and (b) the θ vs. σ plot, as a function of the yield stress of the precipitation hardened aluminium alloys, AA6111 and AA7030. Note that the under-aged data have solid symbols and the overaged open symbols. The plot should be read by following the increases of the yield stress of the under-aged samples to the peak stress and then the subsequent decrease of the yield stress during overageing.

overall behaviour. For example, Poole and Lloyd (2004) have suggested that the change in the addition law (see Section 11.3.3) for summing the contributions from precipitation hardening and dislocation hardening is critical, while Simar et al. (2007) have stressed that the change in the residual solid solution content in the matrix is significant while da Costa Teixeira et al. (2009) has incorporated aspects of both mechanisms. Finally, in order to incorporate the macroscopic effect of cases where local mechanical contrast exists (i.e. a plastic matrix and non-shearable precipitates), Proudhon et al. (2008) and da Costa Teixeira et al. (2009) have incorporated models based on the seminal work of Brown et al. (1971a), to account for the unrelaxed plastic strain in the particles. These models allow for predictions to be made regarding kinematic hardening observed during strain path change experiments such as Bauschinger tests described in Section 11.3.3.

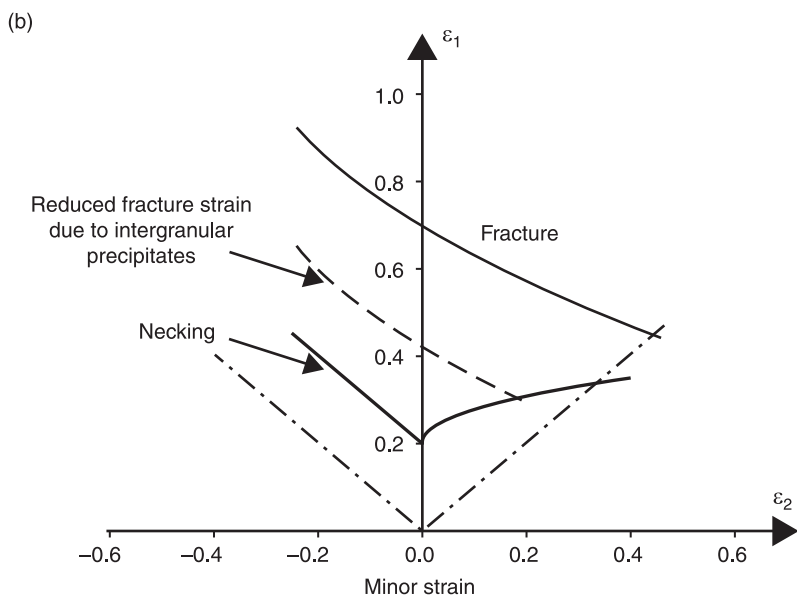
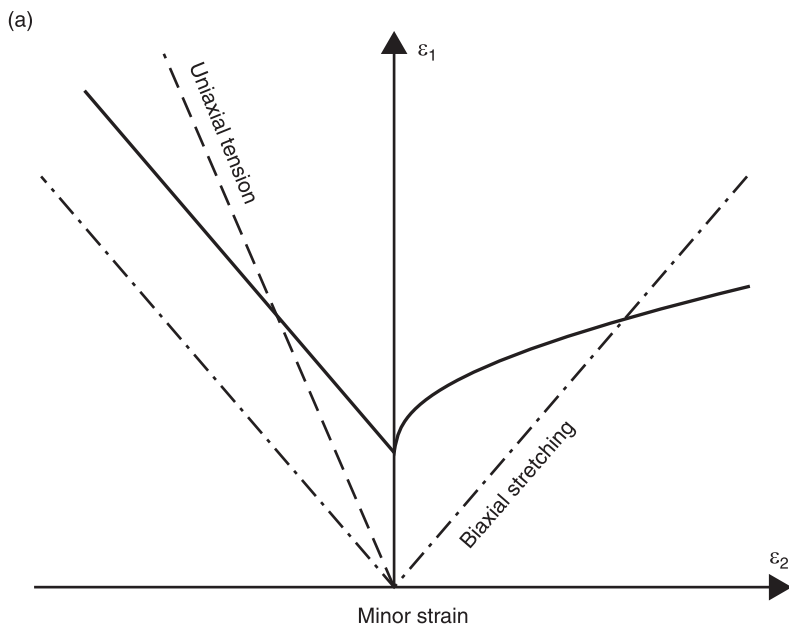
11.5 Commercial aspects of work hardening

From the commercial perspective, work hardening influences alloy applications in two main ways:

1. Its influence on formability, particularly for annealed and solution treated tempers.
2. Controlling the strength in strain hardened tempers.

11.5.1 Formability

Formability is a very broad topic but in the present context it is sheet forming that is most relevant, and in this case formability is usually represented in terms of the Forming Limit Diagram (FLD; Keeler, 1965; Hecker, 1975; Hosford and Caddell, 2007). The classic example of non-uniformity of plastic flow is the necking of a sample pulled in uniaxial tension. However, this concept can be extended in sheet samples to a variety of other stress states by use of a forming diagram usually expressed in strain co-ordinates as shown in Fig. 11.9(a). Some forming processes are limited not by strain localisation but by fracture events, as in small radius bending operations. Thus, there are examples where the concept of forming limit diagram can be extended to encompass fracture events in sheet materials and an example of this is shown in Fig. 11.9(b) (Embury and Duncan, 1981). The FLD plots the $\varepsilon_1\varepsilon_2$ strain at which a neck is formed following proportional straining along a series of different strain paths, where ε_1 is the major strain and ε_2 is the minor strain. Typically, the diagram has a maximum ε_1 along the tensile strain path, $\varepsilon_1/\varepsilon_2 = -2$, a minimum along the plane strain path, $\varepsilon_1/\varepsilon_2 = \infty$, and then increases again for balanced biaxial straining, $\varepsilon_1/\varepsilon_2 = 1$. This shape reflects the influence of strain path on work hardening and necking. For the tensile case a diffuse neck is nucleated at a strain for which $\theta = \sigma$, i.e. the Considère Criterion. This is a purely geometrical requirement and is an upper limit for the



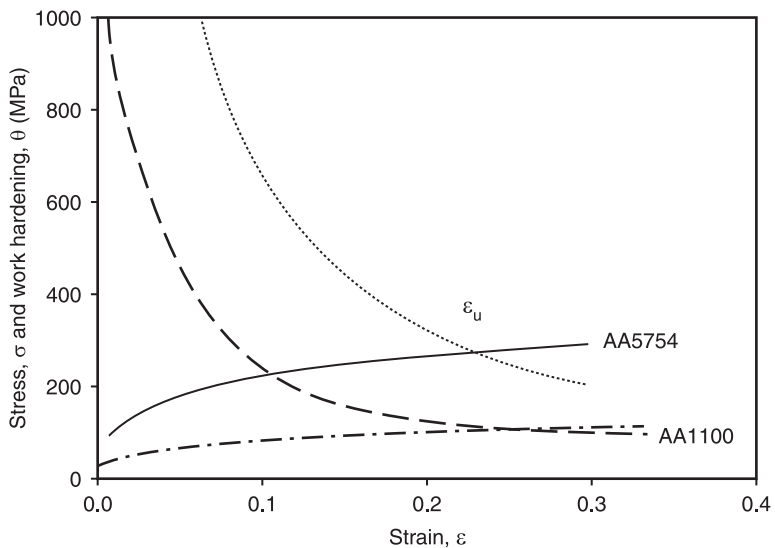
11.9 Schematic diagrams of forming limit diagrams (FLDs) illustrating (a) theoretical strains as the onset of the local necking in a sheet and (b) schematic forming limit (necking) and fracture strains in punch stretching tests of an aluminium-copper alloy (adapted from I. Dover 1979) showing the intervention of the necking and fracture lines on the FLD (adapted from Embury and Duncan, 1981).

strain to necking, ε_U , so any microstructural damage, such as voiding at particles, will reduce ε_U . For most commercial alloys extensive voiding does not occur until triaxial stresses are developed in the neck, so the geometrical criterion is generally valid. The neck formed in tension is referred to as a 'diffuse neck' because at its initiation it is truly diffuse and gradually grows into a well-defined neck. Neck growth leading to final fracture is dependent on the strain rate sensitivity, m , which can be described empirically by:

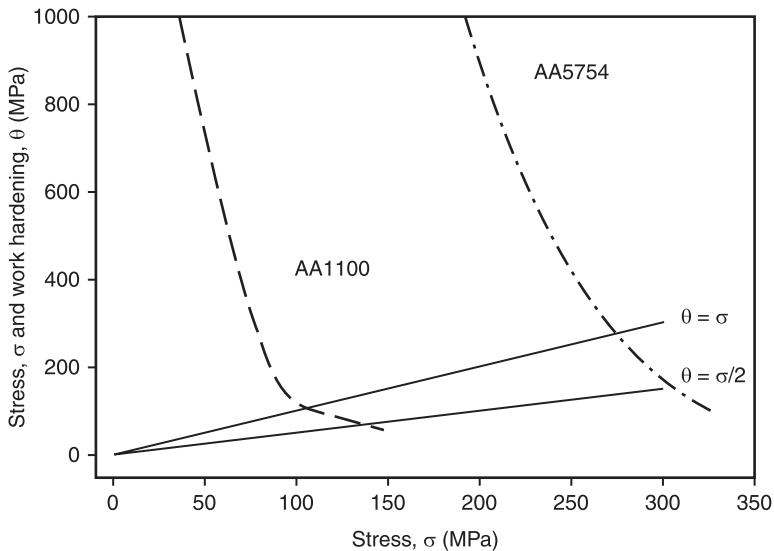
$$\sigma = K_2 \dot{\varepsilon}^m \quad [11.21]$$

where σ is the flow stress, K_2 is a constant and $\dot{\varepsilon}$ is the strain rate of the test (note that in Al alloys, deformed at room temperature, m is small, and in some cases negative, as in the Al-Mg 5000 series alloys, which results in the strain after necking begins being quite limited). In addition to diffuse necking, there is another type of necking that is referred to as 'local necking', which can occur in deformed sheet depending on the strain path. In local necking the sheet is deformed along a narrow band inclined at an angle to the major strain axis, and a local neck forms when $\theta = \sigma/2$. Comparing the two criteria, the strain for local necking is larger than that for a diffuse neck and localised necks predominate for biaxial deformation and heavily worked sheet (a detailed discussion on necking is given by Backofen, 1972 or Hosford and Caddell, 2007).

In strain space the nucleation of a diffuse neck occurs at the intersection of the $\theta - \varepsilon$ curve with the $\sigma - \varepsilon$ curve, as shown for AA 1100 and AA5754 in Fig. 11.10. The necking criteria can also be represented in stress space by the intersection of the $\theta - \sigma$ curve with the $\theta = \sigma$ and $\theta = \sigma/2$ lines, as shown in Fig. 11.11 for biaxial

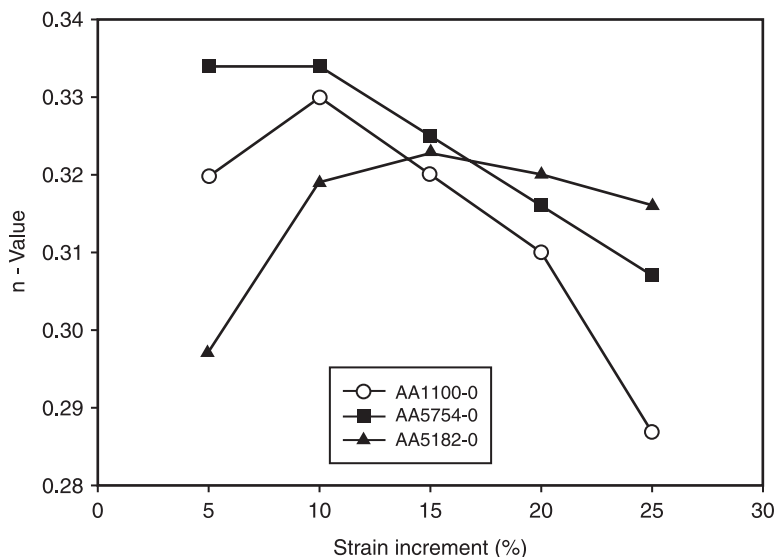


11.10 Necking instability plots in strain space for AA1100 and AA5754.



11.11 Necking instability plots in stress space for AA1100 and AA5754.

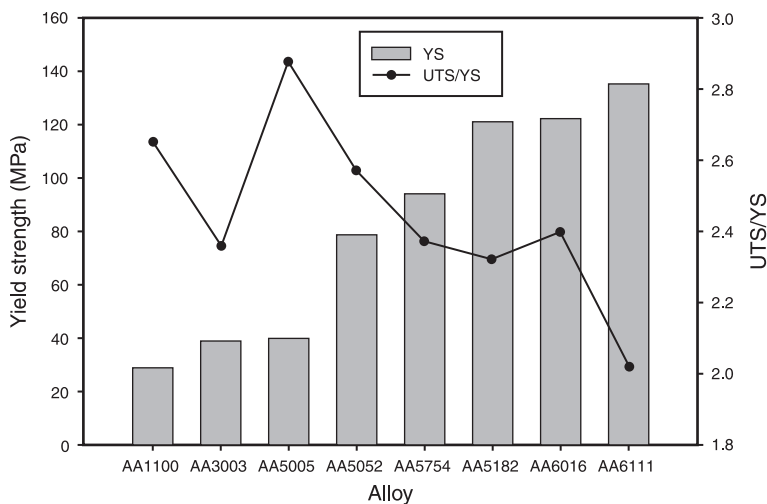
straining of AA1100 and AA5754. The stresses at the intersection of the plots correspond to the strain to necking. Obviously the strain dependence and degree of work hardening has a major influence on the necking strain. While the FLD and the corresponding necking instability analyses are used for assessing sheet formability, they require significant effort, and have the limitation that they are only valid for proportional strain paths, while real forming operation may involve complex strain paths. As a result more approximate methods are often used to reflect work hardening and necking. The most common is to measure the work hardening index, n , assuming the Power Law, $\sigma = K_1 \epsilon^n$, and n is the gradient of a $\log \sigma - \log \epsilon$ plot. It is straightforward to show that, for an alloy obeying the Power Law, the Considère Criterion is equivalent to the uniform elongation for a uniaxial tensile test, ϵ_U equalling the n -value. Unfortunately, most Al alloys do not obey the Power Law, and n varies with the strain increment over which it is measured, so $\epsilon_U \neq n$. Figure 11.12 shows the variation of n for different strain increments (0–5%, 0–10%, etc.) in hydraulic bulge tests of different alloys. Another approach is to consider the ratio σ_{UTS}/σ_{YS} as reflecting the work hardening potential. Some values of this ratio, along with the relevant yield stresses, are shown in Fig. 11.13. Typically, $\sigma_{UTS}/\sigma_{YS} \geq 2$ is considered necessary for good formability, but the problem with this approach is that it ignores the strain involved, and the key feature of most forming operations is maintaining a reasonable work hardening rate after extensive strain. This results in any highly strained region hardening sufficiently to spread the deformation to softer regions of the sheet, and hence avoid localisation and fracture. Finally, the details of the microstructure have



11.12 Variation of the work hardening exponent, n , with strain increment for different commercial alloys.

been shown to effect the formation of localised necks, e.g. the spatial grain orientation distribution has been shown to be significant (Wu et al., 2007).

One important forming operation that is not controlled by necking is bending. Bendability is limited not by plastic instability but by fracture (Lloyd, 2001). In

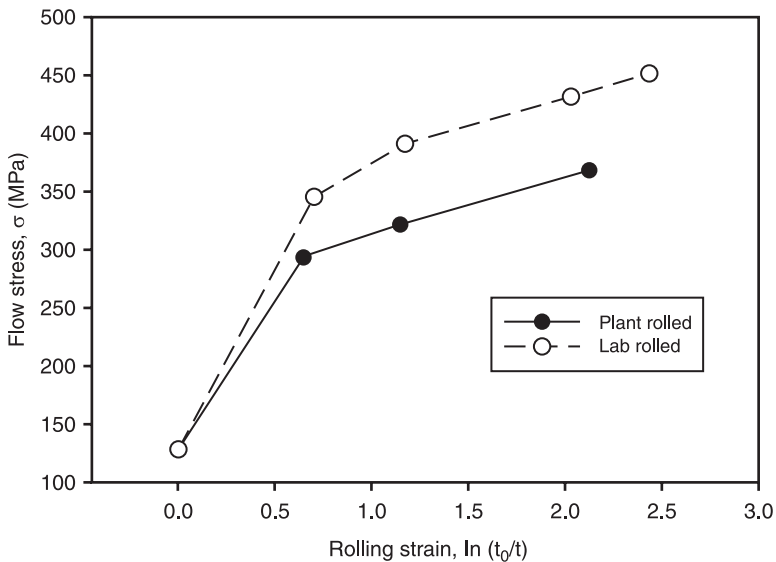


11.13 Yield stress and ultimate tensile strength to yield stress ratios for different commercial alloys.

this case, high work hardening rates are a disadvantage, particularly if accompanied by high yield strength. This is a result of fracture processes, such as particle fracture and interface voiding, being strongly dependent on the development of high local stress. In contrast to necking, the evolution of surface topology has been found to play an important role in bend failures.

11.5.2 Strain hardened tempers

A second aspect where work hardening is important is to develop high strength in strain hardened tempers. Many alloys are used in the strain hardened H-temper, such as 1000 series foil alloys, 3000 can-body stock and 5000 can-end stock. The objective in these applications is to achieve high strength levels by using the alloy in the cold rolled condition, or after cold rolling and partial annealing. Cold rolling achieves very high strains, which can be as high as six to seven in thin gauge foil rolling, and the strength attained relies on maintaining a level of work hardening even at high strains. So these applications ultimately rely on Stage IV work hardening. As we have seen the work hardening rate in Stage IV is low, but if the strains are sufficiently high, significant strengths can be achieved. Stage IV deformation involves very high levels of microstructural refinement, as discussed in foil alloys (Liu et al., 2002). This refinement and the continued accumulation of dislocations increase the strength, as shown in Fig. 11.14 for can-end AA5182. Consistent with Stage IV behaviour, the alloy has an essentially constant work



11.14 Flow stress as function of rolling strain for can-end alloy AA5182 after plant and laboratory cold rolling.

hardening rate beyond a strain of 0.5 of about 50 MPa, which is comparable with a work hardening rate of around 150 MPa just before fracture, and before a well-defined Stage IV has been established, in a hydraulic bulge test. However, it is important to appreciate that commercial cold rolling is rather different from laboratory tests; in the laboratory the strain rate is sufficiently low that the test is essentially isothermal, while there is considerable heating of the sheet due to the much higher strain rate in commercial rolling. As a result the flow stress for laboratory rolling lies above that of commercial rolling, as seen in Fig. 11.14. However, the terminal Stage IV work hardening rates are about the same, and the major difference is in Stage III behaviour, where the dynamic recovery rate is higher in plant rolled material. Because of the very high stored energy levels achieved in cold rolling, the dislocation structure can be thermally unstable, with the alloy sheet undergoing softening over time at room temperature. To avoid this, cold rolled sheet is often given a partial anneal at low temperature to produce some softening but with stabilisation of the strength.

11.6 Conclusion and future trends

The current review aims to give an overview of the process of work hardening and to show its relevance to some industrial processes. It is clear that a number of issues remain to be studied further in terms of clarifying basic mechanisms including the role of solute in dynamic recovery and the characterisation of aluminium alloys at large plastic strains. Also, most of the data have been obtained from tests at ambient temperature and there is much that can be gained from tests over a broader range of temperatures including the use of low temperature tests for multi-axial stress states. Also, many forming operations involve changes in strain path and these changes can affect both the stability of the microstructure and the overall flow of the process. Both experimental studies and modelling approaches are needed in this area.

It is important to also recognise that changes in technology may lead to new problems and opportunities in forming. For example, the development of the FUSION™ co-casting process enables non-uniform sheet materials with very ductile surface layers to be produced (Wagstaff et al., 2006). Thus, the work hardening, damage and fracture processes in architected or compositionally graded materials represent new challenges. The recycling of aluminium alloys also raises challenges as the level of Fe intermetallics is increased through recycling and the intermetallics can become limiting features in the large strain plasticity of aluminium products. On the other hand, new forming processes such as accumulated roll bonding are likely to bring new opportunities for aluminium alloys. Similarly, new local heat treatments based on laser annealing or joining processes, such as friction stir welding, will also challenge our ability to apply basic materials science to very heterogeneous processes in the future. In summary, work hardening in aluminium alloys presents many opportunities and challenges for future research and industrial applications.

11.7 Acknowledgements

The authors would like to gratefully acknowledge the valuable comments on the manuscript from Chad Sinclair and Roger Lumley. The support of Natural Sciences and Engineering Research Council of Canada is also greatly appreciated.

11.8 Notes

1. The Taylor factor accounts for the averaging of the grain orientations over all grains in the sample. For random textures, its value is bounded between the Sachs and Taylor solutions of 2.24 and 3.06. These values can be well estimated by polycrystal plasticity codes such as VPSC (Lebensohn et al., 1993; Kocks et al., 1998).
2. In the work of Tomé, the Voce law is written to describe the hardening on an individual slip system which is then incorporated in a polycrystal plasticity model. Equation 11.14 extends this concept to provide an analytical description of work hardening that can be used to model polycrystals.

11.9 References

- Ardell, A.J. (1985) Precipitation hardening. *Metallurgical and Materials Transactions A*, 16A(12): 2131–2165.
- Argon, A.S. and P. Haasen (1993) A new mechanism of work hardening in the late stages of large strain plastic flow in FCC and diamond cubic crystals. *Acta Metallurgica et Materialia*, 41(11): 3289–3306.
- Ashby, M.F. (1970) The deformation of plastically non-homogeneous materials. *Philosophical Magazine*, 21: 399–424.
- Ashby, M.F. (1971) The deformation of plastically non-homogeneous alloys. In *Strengthening methods in crystals*, ed. A. Kelly and R.B. Nicholson, 137–190. New York: J. Wiley and Sons.
- Backofen, W.A. (1972) *Deformation processing*. Reading, MA: Addison-Wesley.
- Berbenni, S., V. Favier and M. Berveiller (2007) Impact of the grain size distribution on the yield stress of heterogeneous materials. *International Journal of Plasticity*, 23: 114–142.
- Blankenship, C.P., E. Hornbogen and E.A. Starke (1993) Predicting slip behavior in alloys containing shearable and strong particles. *Materials Science and Engineering*, A169: 33–41.
- Brown, L.M. and R.K. Ham (1971) Dislocation-particle interactions. In *Strengthening methods in crystals*, ed. A. Kelly and R.B. Nicholson, 12–135. New York: Wiley and Sons.
- Brown, L.M. and W.M. Stobbs (1971a) ‘Work hardening of Cu-silica. Part 1: Model based on internal stresses with no plastic relaxation. *Philosophical Magazine*, 23(185): 1185–1199.
- Brown, L.M. and W.M. Stobbs (1971b) Work hardening of Cu-silica. Part 2: Role of plastic relaxation. *Philosophical Magazine*, 23(185): 1201–1233.
- Byrne, J.G., M.E. Fine and A. Kelly (1961) *Philosophical Magazine*, 6: 1119–1145.
- Cheng, L.M., W.J. Poole, J.D. Embury and D.J. Lloyd (2003) The influence of precipitation on the work hardening behavior of the aluminum alloys AA6111 and AA7030. *Metallurgical and Materials Transactions A*, 34A: 2473–2481.

- da Costa Teixeira, J., L. Bourgeois, C.W. Sinclair and C.R. Hutchinson (2009) The effect of shear-resistant, plate shaped precipitates on the work hardening of Al alloys: Towards a prediction of the strength-elongation correlation. *Acta Materialia*, 57: 6075–6089.
- Deschamps, A., F. Bley, F. Livet, D. Fabregue and L. David (2003) In-situ small-angle X-ray scattering study of dynamic precipitation in an Al-Zn-Mg-Cu alloy. *Philosophical Magazine*, 83(6): 677–692.
- Deschamps, A., Y. Brechet, C.J. Necker, S. Saimoto and J.D. Embury (1996) Study of large strain deformation of dilute solid solutions of Al-Cu using channel die compression. *Materials Science and Engineering*, A207: 143–152.
- Deschamps, A., M. Niewczas, F. Bley, Y. Brechet, J.D. Embury, L. Le Sinq, F. Livet and J.P. Simon (1999) Low-temperature dynamic precipitation in a supersaturated Al-Zn-Mg alloy and related strain hardening. *Philosophical Magazine*, 79(10): 2485–2504.
- Diak, B.J., K.R. Upadhyaya and S. Saimoto (1998) Characterization of thermodynamic response by materials testing. *Progress in Materials Science*, 43: 223–363.
- Dover, I. (1979) Microstructural influences on formability and fracture of Al alloys. M. Eng. Thesis. McMaster University, Hamilton, ON.
- Duva, J.M., M.A. Daeubler, E.A. Starke and G. Luetjering (1988) Large shearable particles lead to coarse slip in particle reinforced alloys. *Acta Metallurgica*, 36(3): 585–589.
- Embury, J.D. and J.L. Duncan (1981) Formability maps. *Annual Review of Materials Science*, 11: 505–521.
- Embury, J.D., D.J. Lloyd and T.R. Ramachandran (1989) Strengthening mechanisms in aluminum alloys. *Treatise on Materials Science and Technology*, 31: 579–601.
- Estrin, Y. (1996) Dislocation density related constitutive modelling. In *Unified constitutive laws of plastic deformation*, ed. A.S. Krausz and K. Krausz, 69–106. Orlando, FL: Academic Press.
- Estrin, Y., L.S. Toth, A. Molinari and Y. Brechet (1998) A dislocation-based model for all hardening stages in large strain deformation. *Acta Materialia*, 46: 5509–5522.
- Fazeli, F., W.J. Poole and C.W. Sinclair (2006) Work hardening behaviour of an Al-2.8Mg-0.16Sc alloy. *Materials Science Forum*, 519/521: 961–966.
- Fazeli, F., W.J. Poole and C.W. Sinclair (2008) Modeling the effect of Al₃Sc precipitates on the yield stress and work hardening of an Al-Mg-Sc alloy. *Acta Materialia*, 56: 1909–1918.
- Foreman, A.J.E. and M.J. Makin (1966) Dislocation movement through random arrays of obstacles. *Philosophical Magazine*, 14: 911–924.
- Gable, B.M., A.W. Zhu, A. Csontos and E.A. Starke (2001) The role of plastic deformation on the competitive microstructural evolution and mechanical properties of a novel Al-Li-Cu-X alloy. *Journal of Light Metals*, 1: 1–14.
- Gil Sevillano, J. (1993) Flow stress and work hardening. In *Materials science and technology: A comprehensive treatment*, ed. P. Haasen, R.W. Cahn, E.J. Kramer, Vol. 6, 19–88. Weinheim: VCH.
- Gil Sevillano, J., P. van Houtte and E. Aernoudt (1981) Large strain work hardening and textures. *Progress in Materials Science*, 25: 69–412.
- Goerdeler, A., M. Crumbach, M. Schneider, G. Gottstein, L. Neumann, H. Aretz and R. Kopp (2004) Dislocation density based modeling of work hardening in the context of integrative modeling of aluminum processing. *Materials Science and Engineering*, 387: 266–271.
- Goerdeler, M. and G. Gottstein (2001) A microstructural work hardening model based on three internal state variables. *Materials Science and Engineering*, A309/310: 377–381.

- Hecker, S.S. (1975) A simple technique for determining forming limit curves. *Sheet Metal Industries*, 52: 671–676.
- Hockett, J.E. and O.D. Sherby (1975) Large strain deformation of polycrystalline metals at low homologous temperatures. *Journal of the Mechanics and Physics of Solids*, 23: 87–98.
- Holmedal, B., E. Nes and K. Marthinsen (2006) Work hardening of aluminium alloys. In *Virtual fabrication of aluminium products*, ed. J. Hirsch, 129–155. Weinheim, Germany: Wiley-VCH Verlag GmbH & Co.
- Hornbogen, E. and K.H.Z. Gahr (1975) Distribution of plastic strain in alloys containing small particles. *Metallography*, 8: 181–202.
- Hosford, W.F. and R.M. Caddell (2007) *Metal forming: Mechanics and metallurgy*. Cambridge, UK: Cambridge University Press.
- Hutchinson, C.R., J. de Costa Teixeira and L. Bourgeois (2008) Responding microstructures: A means to simultaneously achieve high strength and high elongation in Al alloys. *11th International Conference on Aluminium Alloys*, Aachen, Germany: Wiley-VCH: 1647–1652.
- Jin, H. and D.J. Lloyd (2004a) Effect of a duplex grain size on the tensile ductility of an ultra-fine grained Al-Mg alloy, AA5754, produced by asymmetric rolling and annealing. *Scripta Materialia*, 50(10): 1319–1323.
- Jin, H. and D.J. Lloyd (2004b) The tensile response of a fine-grained AA5754 alloy produced by asymmetric rolling and annealing. *Metallurgical and Materials Transactions A*, 35: 997–1006.
- Joshi, S.P., K.T. Ramesh, B.Q. Han and E.J. Lavernia (2006) Modelling the constitutive response of bimodal metals. *Metallurgical and Materials Transactions A*, 37A: 2397–2404.
- Kang, J., D.S. Wilkinson, M. Jain, J.D. Embury, A.J. Beaudoin, S. Kim, R. Mishra and A.K. Sachdev (2006) On the sequence of inhomogeneous deformation processes occurring during tensile deformation of strip cast AA5754. *Acta Materialia*, 54: 209–218.
- Keeler, S.P. (1965) Determination of forming limits in automotive stampings. *Sheet Metal Industries*, 42: 683–691.
- Kelly, A. and R.B. Nicholson (1963) Precipitation hardening. *Progress in Materials Science*, 10: 312–315.
- Kocks, U.F. (1979) Superposition of alloy hardening, strain hardening and dynamic recovery. *5th International Conference on Strength of Metals and Alloys*, Cambridge, UK: 1661–1680.
- Kocks, U.F. (1987) Constitutive behavior based on crystal plasticity. In *Constitutive equations for creep and plasticity*, ed. A.K. Miller, 1–87. Amsterdam: Elsevier.
- Kocks, U.F., A.S. Argon and M.F. Ashby (1975) Thermodynamics and kinetics of slip. *Progress in Materials Science*, 19: 195–229.
- Kocks, U.F. and H. Mecking (2003) Physics and phenomenology of strain hardening: The FCC case. *Progress in Materials Science*, 48: 171–273.
- Kocks, U.F., C.N. Tome and H-R. Wenk (1998) *Texture and anisotropy: Preferred orientations in polycrystals and their effect on materials properties*. Cambridge, UK: Cambridge University Press.
- Kok, S., A.J. Beaudoin, D.A. Tortorelli and M. Lebyodkin (2002) A finite element model for the Portevin Le Chatelier effect based on polycrystal plasticity. *Modelling and Simulation in Materials Science and Engineering*, 10: 745–763.
- Kok, S., M.S. Bharathi, A.J. Beaudoin, C. Fressengeas, G. Ananthakrishna, L.P. Kubin and M. Lebyodkin (2003) Spatial coupling in jerky flow using polycrystal plasticity. *Acta Materialia*, 51: 3651–3662.

- Koppenaar, T.J. and D. Kuhlmann-Wilsdorf (1964) The effect of prestressing on the strength of neutron-irradiated copper single crystals. *Applied Physics Letters*, 4(3): 59–61.
- Lebensohn, R.A. and C.N. Tome (1993). “A self-consistent anisotropic approach for the simulation of plastic deformation and texture development of polycrystals: Application to zirconium alloys.” *Acta Metall. Mater.* 41(9): 2611–2624.
- Liu, Q., X. Huang, D.J. Lloyd and N. Hansen (2002) Microstructure and strength of commercial purity aluminum (AA1200) cold rolled to large strains. *Acta Materialia*, 50: 3789–3802.
- Lloyd, D.J. (1980) Deformation of fine grained aluminum alloys. *Metal Science*, 14: 193–198.
- Lloyd, D.J. (2001) *Bending in aluminum automotive alloys*. Metals Park, OH: ASM International.
- Lloyd, D.J. (2006) The work hardening of some commercial Al alloys. *Materials Science Forum*, 519/521: 55–62.
- Lloyd, D.J. and S.A. Court (2003) Influence of grain size on tensile properties of Al-Mg alloys. *Materials Science and Technology*, 19(10): 1349–1354.
- Lloyd, D.J. and D. Kenny (1982) The large strain deformation of some aluminum alloys. *Metallurgical and Materials Transaction A*, 13A: 1445–1452.
- Marthinsen, K. and E. Nes (2001) Modelling strain hardening and steady state deformation of Al-Mg alloys. *Materials Science and Technology*, 17: 376–388.
- Martin, J.W. (1998) *Precipitation hardening*. Oxford: Butterworth-Heinemann.
- McCormick, P.G. (1972) A model for the Portevin Le Chatelier effect in substitutional alloys. *Acta Metallurgica*, 20: 351–354.
- Mecking, H. and U.F. Kocks (1981) Kinetics of flow and strain hardening. *Acta Metallurgica*, 29: 1865–1875.
- Moan, G.D. and J.D. Embury (1979) A study of the Bauschinger effect in Al-Cu alloys. *Acta Metallurgica*, 27: 903–914.
- Mondolfo, L.F. (1976) *Aluminum alloys: Structure and properties*. London: Butterworths.
- Mughrabi, H. (1983) Dislocation wall and cell structures and long-range internal stresses in deformed metal crystals. *Acta Metallurgica*, 31: 1367–1379.
- Nes, E. (1997) Modelling of work hardening and stress saturation in FCC metals. *Progress in Materials Science*, 41(3): 129–194.
- Niewczas, M., O. Engler and J.D. Embury (2004) The recrystallization of copper single crystals deformed at 4.2K. *Acta Materialia*, 52: 539–552.
- Nijs, O., B. Holmedal, J. Friis and E. Nes (2008) Sub-structure strengthening and work hardening of an ultra-fine grained aluminium-magnesium alloy. *Materials Science and Engineering*, A483/484: 51–53.
- Nix, W.D., J.C. Gibeling and D.A. Hughes (1985) Time-dependent deformation of metals. *Metallurgical and Materials Transaction A*, 16A: 2215–2226.
- Park, D.Y. and M. Niewczas (2008) Plastic deformation of Al and AA5754 between 4.2K and 295K. *Materials Science and Engineering*, A491: 88–102.
- Polmear, I.J. (2006) *Light alloys: From traditional alloys to nanocrystals*. Oxford: Butterworth-Heinemann.
- Poole, W.J. and D.J. Lloyd (2004) *Modelling the stress-strain behaviour for aluminum alloy AA6111*. 9th International Conference on Aluminium Alloys, August 2–5, 2004, Brisbane, Australia 939–944.
- Poole, W.J., X. Wang, D.J. Lloyd and J.D. Embury (2005) The shearable/non-shearable transition in Al-Mg-Si-Cu precipitation hardening alloys: Implications on the distribution of slip, work hardening and fracture. *Philosophical Magazine*, 85(26/27): 3113–3135.

- Prinz, F.B. and A.S. Argon (1984) The evolution of plastic resistance in large strain plastic-flow of single-phase subgrain forming metals. *Acta Metallurgica*, 32: 1021–1028.
- Proudhon, H. and W.J. Poole (2006) *The Bauschinger effect in AA 6111*. 10th International Conference on Aluminum Alloys. Vancouver, BC, Canada: Trans-Tech., pp. 913–918.
- Proudhon, H., W.J. Poole, X. Wang and Y. Brechet (2008) The role of internal stresses on the plastic deformation of the Al–Mg–Si–Cu alloy AA6111. *Philosophical Magazine*, 88(5): 621–640.
- Raeisinia, B. (2008) Modelling the effect of grain size distribution on the mechanical response of metals. Ph.D. thesis Department of materials engineering. Vancouver, BC, Canada: The University of British Columbia.
- Raeisinia, B. and C.W. Sinclair (2009) A representative grain size for the mechanical response of polycrystals. *Materials Science and Engineering*, A525: 78–82.
- Raeisinia, B., C.W. Sinclair, W.J. Poole and C.N. Tome (2008) On the impact of grain size distribution on the plastic behaviour of polycrystalline metals. *Modelling and Simulations in Materials Science and Engineering*, 16(2): 15.
- Rollett, A.D. and U.F. Kocks (1994) A review of the stages of work hardening. *Solid State Phenomena*, 35/36: 1–18.
- Roters, F., D. Raabe and G. Gottstein (2000) Work hardening in heterogeneous alloys: A microstructural approach based on three internal state variables. *Acta Materialia*, 48: 4181–4189.
- Roumina, R. (2009) Mechanical properties of a recovered Al–Mg–Sc alloy. Ph.D. thesis Department of materials engineering. Vancouver, BC, Canada: The University of British Columbia.
- Roumina, R. and C.W. Sinclair (2010) Recovery kinetics in the presence of precipitates: The softening response of an Al–Mg–Sc alloy. *Acta Materialia*, 58(1): 111–121.
- Ryen, O., H.I. Laukli, B. Holmedal and E. Nes (2006b) Large strain work hardening of aluminum alloys and the effect of Mg in solid solution. *Metallurgical and Materials Transactions A*, 37A: 2007–2013.
- Ryen, O., O. Nijs., E. Sjolander, B. Holmedal, H.-E. Ekstrom and E. Nes (2006a) Strengthening mechanisms in solid solution aluminum alloys. *Metallurgical and Materials Transactions A*, 37A: 1999–2006.
- Serizawa, A., W.J. Poole and T. Sato (2008) *Nanocluster-dislocation interactions for two types of nanoclusters in Al–Mg–Si alloys*. 11th International Conference on Aluminium Alloys. Aachen, Germany: Wiley-VCH., pp. 698–704.
- Sharma, V.M.J., K.S. Kumar, B.N. Rao and S.D. Pathak (2009) Studies on work-hardening behaviour of AA2219 under different aging treatments. *Metallurgical and Materials Transactions A*, 40A: 3186–3195.
- Simar, A., Y. Bréchet, B. de Meester, A. Denquind and T. Pardoen (2007) Sequential modeling of local precipitation, strength and strain hardening in friction stir welds of an aluminum alloy 6005A–T6. *Acta Materialia*, 55(18): 6133–6143.
- Sinclair, C.W., W.J. Poole and Y. Brechet (2006) A model for the grain size dependent work hardening of copper. *Scripta Materialia*, 55(8): 739–742.
- Stout, M.G. and A.D. Rollett (1990) Large-strain Bauschinger effects in FCC metals and alloys. *Metallurgical and Materials Transaction A*, 21A: 3201–3213.
- Tome, C.N., P.J. Maudlin, R.A. Lebensohn and G.C. Kaschner (2001) Mechanical response of zirconium – I. Derivation of a polycrystal constitutive law and finite element analysis. *Acta Materialia*, 49: 3085–3096.
- Wagstaff, R.B., D.J. Lloyd and T.F. Bischoff (2006) Direct chill casting of CLAD ingot. *Materials Science Forum*, 519/521: 1809–1814.

- Westermann, I., O.S. Hopperstad, K. Marthinsen and B. Holmedal (2009) Ageing and work-hardening behaviour of commercial AA7108 aluminum alloy. *Materials Science and Engineering*, A524: 151–157.
- Wu, P.D., D.J. Lloyd, M. Jain, K.W. Neale and Y. Huang (2007) Effects of spatial grain orientation distribution and initial surface topography on sheet metal necking. *International Journal of Plasticity*, 23: 1084–1104.
- Zehetbauer, M. and V. Seumer (1993) Cold work hardening in stages IV and V of FCC metals. I: Experiments and interpretation. *Acta Metallurgica et Materialia*, 41(2): 577–588.

Precipitation and solute clustering in aluminium: advanced characterisation techniques

G. SHA, R.K.W. MARCEAU and S.P. RINGER,
The University of Sydney, Australia

Abstract: Recent development of characterisation techniques and computer simulation has extended our ability to access atomic scale information regarding materials microstructure evolution. New results from such techniques have significantly progressed our knowledge about solute behaviour during the earliest stages of decomposition of the solid solution. This chapter updates current understanding about solute clustering and discusses the effect of solute clustering and micro-alloying on precipitate microstructure evolution in aluminium alloys. In addition, a brief review is given on the effect of severe plastic deformation on precipitate evolution in Al alloys.

Key words: precipitation, solute clustering, micro-alloying, aluminium alloys, severe plastic deformation (SPD).

12.1 Introduction

Age hardening is one of the very important strengthening mechanisms employed in the design and development of medium and high strength wrought Al alloys for aerospace, automotive and engineering architecture applications. With the addition of alloying elements, 2xxx, 6xxx and 7xxx series wrought Al alloys are developed using precipitation strengthening. A series of heat treatments will be given to the alloys in order to control precipitation and improve alloy strength. Firstly, a solution treatment is conducted at a high temperature of above 450°C to dissolve major alloying elements into the Al matrix, which is then followed by water quenching to obtain a supersaturated solid solution at room temperature. Finally, ageing treatment will be conducted at a pre-selected elevated temperature, or room temperature, for a certain period of time to promote precipitation. For over a century, there have been huge research efforts to understand precipitation process in a variety of Al alloys. This chapter summarises current understanding about the precipitation in simple binary systems, ternary, quaternary and more complicated multi-component aluminium alloy systems.

Precipitation processes are complicated, involving formation of a range of metastable precipitation phases at different stages of ageing. A thorough review on microstructure evolution and age hardening in Al alloys can be found in the work of Ringer and Hono (2000). Guinier-Preston (GP) zones (Guinier, 1938; Preston, 1938) are usually formed during the initial ageing treatment, then a series

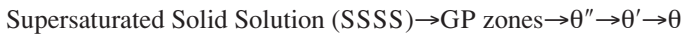
of intermediate metastable precipitates, such as θ'' and θ' in 2xxx series Al alloys and finally the equilibrium phase. Interestingly, metastable intermediate precipitates are often found to be more effective in producing a strengthening effect than the equilibrium precipitation phases. For example, metastable θ' , β'' and η' , rather than equilibrium θ , β and η are known to be responsible for the peak strength in 2xxx, 6xxx and 7xxx series Al alloys, respectively.

A wide range of microstructural characterisation techniques have been employed to characterise precipitate evolution. Some of them are direct observation techniques, such as optical microscopy, scanning electron microscopy (SEM), transmission electron microscopy (TEM), etc., but others are indirect observation techniques, such as differential scanning calorimetry (DSC) and measurement of electrical resistivity. X-ray diffraction analysis (XRD) and (both conventional and high resolution) TEM have made major contributions towards unveiling the crystallographic information of precipitation phases and establishing the orientation relationship between precipitates and the matrix. The crystal structure information of most equilibrium precipitate phases is well established from XRD characterisation. However, accessing the complete crystal structure information of metastable precipitates has proved to be challenging due to the small size of these precipitates embedded in the matrix. Energy dispersive X-ray spectroscopy (EDX) and electron energy loss spectroscopy (EELS) analysis can only give qualitative chemical information because of the difficulty in separating the signals from a metastable precipitate and its surrounding matrix. High resolution transmission electron microscopy (HRTEM) image simulation (Zandbergen et al., 1997; Li et al., 1999) and the first principles (*ab initio*) calculations (Wolverton, 2001) are extremely useful in revealing the complete crystal structure of metastable precipitates. The theoretical calculations, in particular, are informative to the thermodynamics regarding the precipitation of the metastable phase. Atom probe tomography (APT), on the other hand, as a powerful analytical technique, has greatly improved our understanding about early stage precipitation process in Al alloys (Ringer et al., 1995, 1997; Miller et al., 1996; Sha and Cerezo, 2004a). Owing to the significant development of APT over the last five years, a large volume containing several hundred millions of atoms can be inspected routinely with significant improvement on data statistics. Advanced atom probe data analysis algorithms (Miller et al., 1996; Hyde and English, 2000; Vaumousse et al., 2003; Moody et al., 2007a, 2007b) have been developed to analyse large data sets systematically in order to extract quantitative structural and chemical information of precipitation microstructure, including the size, spatial distribution, number density and morphology of precipitates and chemical composition of precipitates and matrix. Three-dimensional (3D) geometry information of the precipitates is very useful in uncovering the growth mechanism of the precipitates, whilst the combination of APT with atomistic kinetic Monte Carlo Simulation has proved to be effective in revealing the kinetic effects of precipitation processes (Sha and Cerezo, 2004a,

2005). With APT and atomistic modelling, we are gaining much deeper insight into solute clustering processes and the precise mechanisms for microalloying to improve the ageing response of Al alloys.

12.2 Al-Cu based alloys

The Al-Cu binary alloy is the most widely studied alloy system used to understand the age-hardening phenomenon. The precipitation sequence is well established, and is affected by many factors including the degree of supersaturation, ageing temperature and trace element addition. The typical decomposition sequence in this system may contain one or more of the following (Guinier, 1938; Preston, 1938; Murray, 1985; Wada et al., 1985; Hono et al., 1986; Karlik and Jouffrey, 1997):

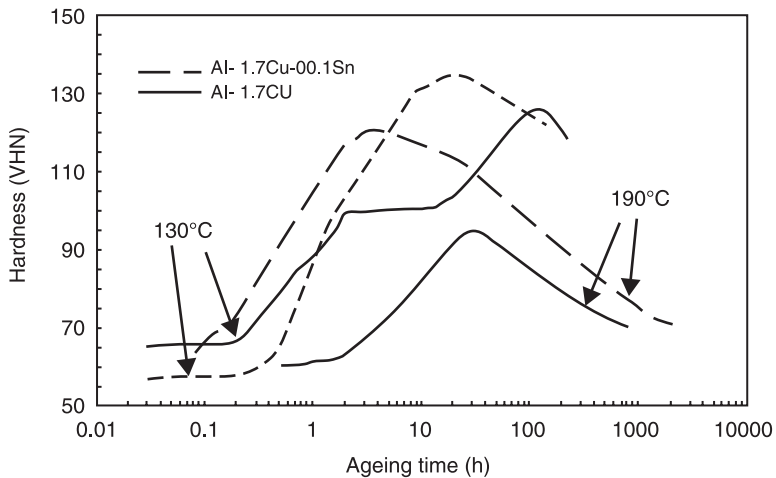


GP zones, θ'' and θ' , are metastable phases, but θ is the equilibrium phase in the binary system. Their crystal structure and orientation relationship with the matrix are listed in Table 12.1. The GP zone solvus is lower than that of metastable θ'' , and much lower than that of θ' (Murray, 1985). θ -phase has the highest solvus amongst all the precipitate phases. During ageing at a low temperature such as 130°C, Al-1.7 Cu (at%) alloy proceeds through the whole sequence of phase decomposition, and demonstrates a two-stage age-hardening response, as shown in Fig. 12.1. The first hardening stage corresponds to the formation of GP zones, whilst the second stage of hardening corresponds to θ'' precipitation. However, if aged at a higher temperature of 190°C, the decomposition will start with the precipitation of θ'' and demonstrate a single stage hardening curve, as seen in Fig. 12.1.

Trace element addition of Cd, In and Sn can have a significant effect on the decomposition sequence of Al-Cu alloy (Sully et al., 1949–1950; Polmear and Hardy, 1952–1953; Silcock et al., 1955). For example, the addition of Sn at 0.01 at% can effectively suppress the formation of GP zones and θ'' , but promote a finer and more uniform dispersion of the semi-coherent θ' . As a result, the hardness curve shows a single stage hardening response, as shown in Fig. 12.1. Two different mechanisms have been proposed to explain the refined precipitate dispersion. One mechanism is the absorption of trace elements at the θ' /matrix interface which lowers the interface energy for θ' precipitate nucleation. This mechanism was first proposed by Silcock et al. (1955) based on their XRD results, and was later supported from the calorimetric measurements by Boyd and Nicholson (1971), and from the TEM observations by Sankaren and Laird (1974). However, this mechanism is not supported by later one-dimensional atom probe (1DAP) analyses in which no Sn segregation at the θ' /matrix interfaces was observed (Ringer et al., 1995). Another mechanism is the heterogeneous nucleation of θ' at Sn (Cd or In)-rich particles (Suzuki et al., 1975; Kanno et al., 1979, 1980),

Table 12.1 Crystal structures of metastable and equilibrium phases in Al-Cu-Mg systems

Phase	Space group	Lattice parameter			Composition	Habit planes	References
		a (nm)	b (nm)	c (nm)			
GP zone					Single/ multi-layer Cu	$\{100\}_\alpha$	Guinier (1938); Preston (1938)
θ''					Two layers of Cu separated by three layer Al	$\{100\}_\alpha$	Hono et al. (1986)
θ'	body-centred tetragonal	0.404		0.58	Al ₂ Cu	$\{100\}_\alpha$	Silcock et al. (1953–1954)
θ	body-centred tetragonal	0.607		0.487	Al ₂ Cu	159 known orientations	Ringer and Hono (2000)
GPB zone					Rod-like features elongated along $<100>_\alpha$		Silcock (1960–1961); Bagaryatsky (1952)
S	base-centred orthorhombic	0.4	0.923	0.714	Al ₂ CuMg		Perlitz and Westgren (1943)
Ω	orthorhombic	0.496	0.859	8.48	Al ₂ Cu	$\{111\}_\alpha$	Knowles and Stobbs (1988).
σ	cubic	1.999			Al ₅ Cu ₆ Mg ₂		Lumley and Polmear (2004)
X'	hexagonal	0.496		1.375	similar to S	$\{111\}_\alpha$	Chopra et al. (1995)
Z	cubic	1.999					Chopra et al. (1996)
T	cubic	1.425			Al ₆ CuMg ₄		Ringer and Hono (2000)
T ₁	hexagonal				Al ₂ CuLi		Howe et al. (1988)



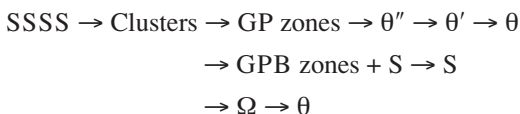
12.1 Hardness time plot for Al-1.7Cu alloy with and without addition of 0.01 Sn, aged at 130°C and 190°C (after Hardy, 1951–1952).

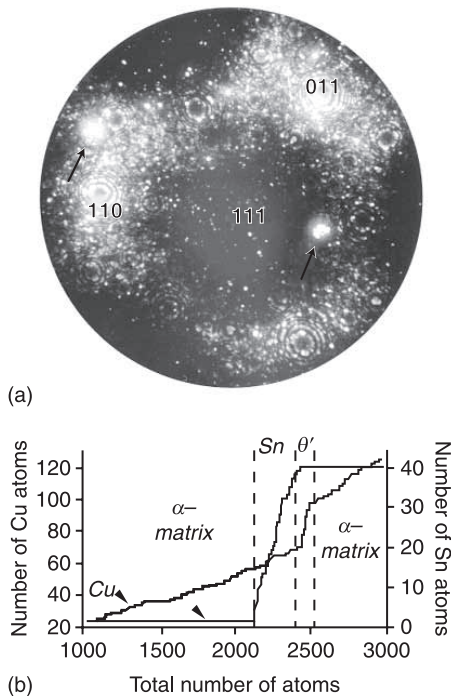
or indirectly at the dislocation loops present in the AQ microstructure (Van Nuyten, 1967).

Early 1DAP analyses give important clues about solute clustering behaviour in an Al-1.7Cu-0.01 Sn alloy. Both clusters of Sn, and occasionally Cu clusters, were observed in the as-quenched samples after solution treatment, but the two types of clusters are not spatially correlated with each other (Ringer et al., 1995). After ageing for three minutes at 190°C, 1DAP analysis on brightly imaged precipitates observed in He field ion microscopy (FIM) image, as shown in Fig. 12.2, confirmed that the Cu-rich θ' nuclei heterogeneously nucleated on Sn particles. Preferred Sn-vacancy interactions and fast diffusion of Sn in comparison with Cu in Al (at least two orders of magnitude; Ringer et al., 1995) have been considered to be responsible for the rapid clustering and precipitation of Sn in these alloys.

12.3 Al-Cu-Mg based alloys

Wrought Al-Cu-Mg alloys can cover a wide range of composition space and form different constituent phases in equilibrium conditions. Typical Al-Cu-Mg alloys frequently fall into one of the three phase fields, i.e. $\alpha + \theta$, $\alpha + S$ or $\alpha + S + T$, each having a different age-hardening response. The decompositions of the supersaturated solid solution (SSSS) of these alloys proceed as follows:

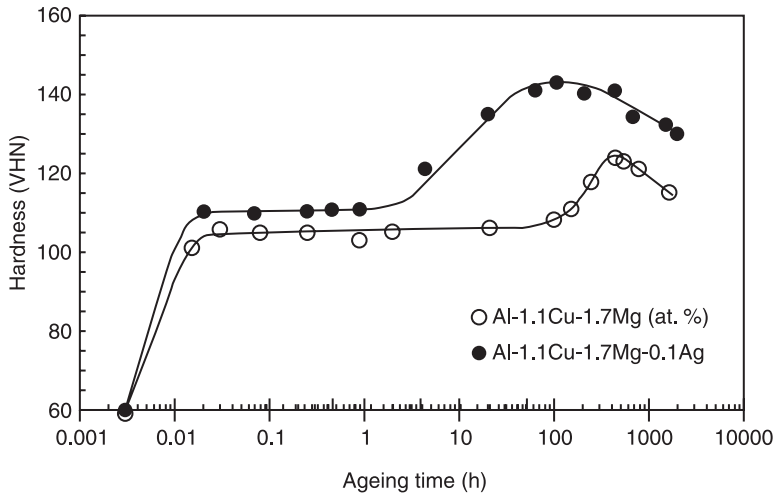




12.2 (a) Field ion micrograph (He) from the Al-1.7Cu-0.01Sn alloy aged at 190°C, three minutes. The 1DAP results in (b) indicate that the brightly imaging regions are Cu-rich nuclei, heterogeneously nucleated on Sn particles (after Ringer et al., 1995).

Al-1.7Cu-0.3Mg alloy is a typical alloy in the $\alpha + \theta$ phase field. The microstructure evolution of this alloy aged at 180°C is similar to that of the binary Al-Cu alloy. During short ageing at 180°C for just 30 seconds, solute of Cu and Mg demonstrates a preferred interaction (Ringer et al., 1996). The interaction is not evident in the as-quenched condition. The microstructure of the alloy aged at 180°C for 2.5 hours consists of a fine and uniform dispersion of θ' precipitates and GPB zones. The term GPB zones was introduced by Silcock (1960–1961) in recognition of the XRD work on these rod-shaped zones by Bagaryatsky (1952). Prolonged ageing at this temperature induces precipitation of equilibrium S phase (Cmcm; $a = 0.400$ nm, $b = 0.923$ nm, $c = 0.714$ nm) (Perlit and Westgren, 1943).

The $\alpha + S$ phase field alloys are the basis of 2xxx series Al alloys. The hardening response of Al-1.1Cu-1.7Mg alloy aged 150°C shows two-stage hardening phenomenon separated by a plateau, as shown in Fig. 12.3 (Ringer et al., 1997). The first stage, known as rapid hardening, occurs within 60 seconds and reaches 60% of the total hardening effect of the material. The second stage hardening was accomplished after a few hundred hours of ageing treatment. The rapidly hardening effect has attracted a large amount of research interest. Early



12.3 Hardness time plots for the Al-1.1Cu-1.7Mg alloy aged at 150°C, showing the effects of Ag additions (after Ringer et al., 1997).

research has suggested that the first stage hardening is due to the formation of GPB zones, and the second stage of hardening has been attributed to the formation of the S' or S phase (Silcock, 1960–1961; Vietz and Polmear, 1966). Recent experimental investigation on model alloys having nominal compositions of Al-1.1Cu-xMg, $0.2 < x < 1.7$ at% using APT has confirmed that solute clusters containing up to a couple of tens atoms are formed after short ageing at 150°C (Marceau et al., 2008, 2009). The Mg concentration of the alloys has a positive effect on the number density of Cu-Mg clusters formed during ageing treatment at 150°C. There are significantly less Cu-Mg clusters formed in an alloy containing 0.2 at% Mg with no rapid hardening (RH) response. In combination with microstructural characterisation using TEM and positron annihilation spectroscopy (PAS), this investigation concludes that the rapid hardening response is attributed to solute clustering. Not all solute clusters have the same hardening effect. It is the Cu-Mg type of clusters, rather than Cu-Cu, and Mg-Mg clusters, that correlate with the RH phenomenon. Cu-Mg clusters with a high Mg:Cu ratio (less than approximately two) and a size containing less than approximately three atoms are more potent in their strengthening effect.

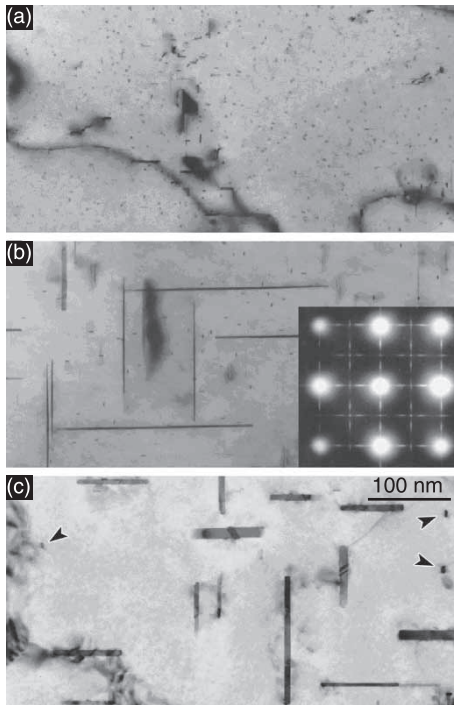
The $\alpha + S + T$ phase field alloys are less attractive since their tensile strengths are no greater than alloys containing less Mg, when tested at temperatures ranging from 150°C to 200°C. However, Ag additions have effectively enhanced their age-hardening response, which will be discussed later.

The addition of microalloying elements, such as Ag and Sn, can improve on the hardening response of Al-Cu-Mg alloys effectively. The addition of Ag at a level of 0.1 at% to $\alpha + \theta$ phase field alloys, such as Al-1.7Cu-0.3Mg, stimulates the

formation of a hexagonal-shaped precipitate phase, designated Ω , which habits on the $\{111\}$ planes of the Al matrix (Chester and Polmear, 1983; Taylor et al., 1978). The Ω phase has the same chemistry as θ , but different crystal structure, i.e. a face-centred orthorhombic structure, as listed in Table 12.1. Prolonged ageing at temperatures $\geq 250^\circ\text{C}$ results in the eventual replacement of Ω precipitates with the equilibrium θ (Ringer et al., 1994a). Ag modifies the precipitation process from the very earliest stages of the decomposition through a preferred Mg-Ag interaction according to AFIM characterisation (Hono et al., 1994; Ringer et al., 1994b) and 3DAP characterisation (Murayama and Hono, 1998; Reich et al., 1998). The Ag-Mg co-clusters containing 40–80 atoms are formed in the alloy with the addition of 0.2 at% Ag when aged at 180°C for 15 seconds. The initial co-clusters appear diffuse, but with subsequent ageing, Cu atoms aggregate to the clusters which exhibit a distinct disc- or plate-like shape, with habit plane $\{111\}_{\alpha-\text{Al}}$. Ω and θ' are evident in the microstructure after being aged 2.5 hours at 180°C . 3DAP analysis confirms that Ag and Mg atoms are absent from the interior of Ω precipitates, but are strongly segregated at the Ω/α interfaces. The formation of Mg-Ag co-clusters has been considered to act as potent nucleation sites for Ω phase (Ringer et al., 1994; Murayama and Hono, 1998). Recently, the observation of GP zones on $\{111\}_{\alpha-\text{Al}}$ planes has been reported in binary Al-Cu alloys (Karlik and Jouffrey, 1997). More Ω precipitates observed in ternary Al-Cu-Mg alloy with the addition of Ag may suggest that Mg-Ag co-clusters can stabilise the GP zone type features and transform into Ω precipitates with increasing ageing time.

The combined addition of Ag and Li to the Al-1.7Cu-0.3Mg alloy can produce a high level of hardening (Polmear and Chester, 1989). Additions of Li, at a relatively low level of <2.5 at%, only promote the formation of Ω phase, but higher Li additions of between 2.5 and 5 at% will promote the T_1 phase (Lee et al., 1994, 1995; Huang and Wang, 1998). Further, Li additions stimulate copious precipitation of $\delta'(\text{Al}_3\text{Li})$ phase. 1DAP (Ringer et al., 1994) and EDX (Lee et al., 1994) analyses confirm that Mg and Ag are associated with the T_1 precipitates, and segregate to the T_1/α interface. The uniform dispersion of the T_1 phase may be similar to that discussed for Ω phase.

The Ge addition into $\alpha + \theta$ phase field alloys, such as Al-1.7Cu-0.3Mg alloy, can effectively influence the precipitation microstructure by refining θ' precipitate dispersion after ageing at 200°C . Recent detailed TEM and HRTEM investigations revealed that lath-shaped Mg_2Ge precipitates are formed in an Al-1.7Cu-0.3Mg-0.1Ge alloy as the first decomposition product by ageing at 200°C , as shown in Fig. 12.4. (Ringer et al., 2008). They are stable up to 200 hours ageing at 200°C and are eventually replaced by FCC Mg_2Ge precipitates. Some Mg_2Ge -type precipitates, designated as K phase, with a hexagonal unit cell, are situated inside θ' precipitates, as seen in Fig. 12.4(c). The K phase grows coordinately with the associated θ' phase. The extralattice structures arising from the association of K phase are responsible for the thickening of θ' .



12.4 Bright-field transmission electron micrographs recorded near $\langle 001 \rangle_{\alpha}$ from the Al-Cu-Mg-Ge alloy after ageing at 200°C for (a) 15 minutes (b) 2 hours and (c) 200 hours. The $\{100\}_{\alpha-\text{Al}}$ type laths are visible in all ageing conditions reported and several are arrowed in (c). Inset in (b) is the corresponding selected area electron diffraction pattern (after Ringer et al., 2008).

The addition of Si has been shown to hinder the matrix Ω precipitation and stability in Al-4.0Cu-(0.1-0.4)Mg-(Ag) alloys. This effect has been considered to be due to the high binding energy between Si and Mg. Trace additions of Si have also been shown to stimulate matrix precipitation of θ' , S and σ . Careful investigation by Gable et al. (2004) demonstrated that trace amounts of Si, depending on the Mg content, were responsible for limiting Ω precipitation in both Al-Cu-Mg and Al-Cu-Mg-Ag base alloys. A Mg/Si ratio greater than approximately two is required for Ω nucleation. The sensitivity of Ω precipitation to the alloy Mg/Si ratio should be considered for designing the next generation of Al-Cu-Mg-(Ag) alloys.

The addition of Ag in Al-Cu-Mg alloys which are in $\alpha + \text{S}$ phase field promotes the formation of the X' precipitate on the $\{111\}_{\alpha-\text{Al}}$ habit plane (Chopra et al., 1995; Ringer et al., 1997). Ag is a constituent solute of the precipitation phase and partitions into the precipitate rather than segregating at $\Omega/\alpha\text{-Al}$ interfaces (Ringer et al., 1997). The addition of Ag into $\alpha + \text{S} + \text{T}$ phase field alloys can also promote the formation of Z (Chopra et al., 1996). The Z phase contains Al, Mg, Cu and Ag,

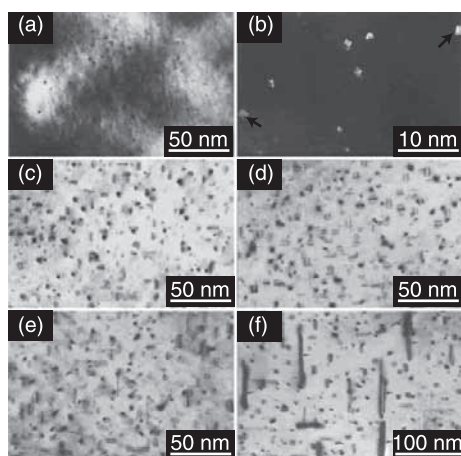
with a cubic structure (Federighi, 1958; Desorbo et al 1958; Nicholson et al 1958–1959; Philips, 1973; Rioja and Laughlin, 1977) as listed in Table 12.1.

12.4 Al-Mg-Si based alloys

The 6xxx series Al alloys are widely used as medium strength structural alloys for transportation and architecture applications. Owing to their application in automobile body panels, there have been huge research activities in Al-Mg-Si-(Cu) alloys over the last ten years. In car factories, the 6xxx Al sheets are shaped into car parts by stamping firstly. This stage requires the alloys to be easily deformable. After stamping, the car parts are painted and then undergo the paint baking treatment at $\sim 180^\circ\text{C}$ for 30 minutes, during which the precipitation of β'' takes place to produce precipitation hardening, called bake hardening. This process gives the material sufficient strength and stiffness for passenger protection. The early stage precipitation of these materials becomes a main focus of many research investigations. Typical β'' in commercial A6061 alloy are enriched with Mg, and Si, as shown in Fig. 12.5.

The ternary Al-Mg-Si alloys have their compositions in a three phase field consisting of the equilibrium phases: α -Al, β (Mg₂Si) and Si. Depending on the Mg/Si ratio of the alloy, they are classified as either a balanced alloy with a ratio of 1.73:1 (corresponding to the 2:1 stoichiometry for Mg₂Si), or an ‘excess Si’ alloy with the ratio <1.73 . The generic precipitation sequence in the ternary Al-Mg-Si alloys is generally considered as:

SSSS \rightarrow solute clusters \rightarrow GP zones (spherical) \rightarrow β'' (needle) \rightarrow β' (rod) \rightarrow β



12.5 TEM micrographs of precipitate dispersions at different stages of artificial ageing in A6061 alloy. (a) and (b), 10 mins at 175°C , (c) 0.5 h at 175°C , (d) 4 h at 175°C , (e) 72 h at 175°C , (f) 20 h at 200°C . After Edwards et al. (1998).

The actual precipitation sequence is considerably more complex than the generic sequence, which often involves a complex sequence of metastable phases forming under different conditions and affected by various parameters including ageing time, ageing temperature and alloy compositions.

Many metastable precipitates with different crystal structures and chemistry are reported. More details of these precipitate phases in the 6xxx Al alloys can be found in two recent review articles (Chakrabarti and Laughlin, 2004; Ravi and Wolverton, 2004). Experimental investigations have reported metastable precursor phases including GP zones (Thomas, 1961–1962; Matsuda et al., 1998; Marioara et al., 2001) and β'' (Lynch et al., 1982; Zandbergen et al., 1997; Edwards et al., 1998) having different Mg/Si ratios such as 5:6, 1:1 and 2:1. Atom probe characterisation indicates that Si and Mg form clusters during the early stage precipitation (Edwards et al., 1998; Murayama and Hono, 1999). Initial clusters are rich in Si due to the low solubility of Si in Al and its fast diffusion. Subsequently, Mg and more Si will diffuse into Si-rich clusters to increase their Mg concentration forming Mg-Si co-clusters (Murayama and Hono, 1999). GP zones are formed from these Mg-Si co-clusters. Atom probe characterisation has suggested that the Mg/Si ratio is about 1:1 for all precursor phases prior to β phase. However, Murayama and Hono (1999) suggest that the atomic ratio of Mg and Si in the GP zones and the β'' precipitates varies depending on the alloy compositions. Clusters formed during natural ageing have been found to be stable during later bake-hardening treatment and most of them are not effective for heterogeneous nucleation of β'' phases (Serizawa et al., 2008). A combination of 3DAP and DSC investigations suggested that two types of clusters are formed by ageing at different temperatures (Serizawa et al., 2008). The type-one clusters formed during natural ageing and the type two clusters formed during pre-ageing at 100°C can then easily be transformed into β'' during bake-hardening treatment.

Our understanding of the precursor metastable precipitates in 6xxx Al alloys has benefited from the recent computer modelling approach, by which we gain insight into phase stability and structural features of matrix-embedded hardening precipitates in Al-Mg-Si alloys (Ravi and Wolverton, 2004; Sandberg et al., 2007; van Huis et al., 2008). Early first principle calculations suggest that there may not be a single structure for GP zones of Al-Mg-Si alloys, but rather that the GP zone structure is likely to depend qualitatively on the Mg/Si ratio of the alloy (Ravi and Wolverton, 2004). For Si-rich alloys, GP zones with $(\text{Al} + \text{Mg})_5\text{Si}_6$ (Marioara et al., 2001) derivatives seem energetically likely to form whereas, for Mg-rich alloys, the L1_0 -type Mg_1Si_1 structure (Matsuda et al., 1998) is energetically more favourable. The Mg_1Si_1 GP zone structure has been further confirmed by Sandberg et al. (2007). Other recent first principle calculations show that for alloys with an Mg/Si ratio smaller than one, needle-type precipitates with Si pillars extending in the needle direction are energetically favourable (van Huis et al., 2008). For alloys with a Mg/Si ratio larger than one, platelet-type precipitates

consisting of stacked layers of Mg, Si and Al atoms are energetically favoured. By considering formation enthalpies and calculated lattice mismatch with the Al matrix, they suggested that the most favourable structures with high Al content are the needle-type initial- β'' $\text{Mg}_2\text{Si}_3\text{Al}_6$ structure and platelet-type structures $(\text{MgSi})_2\text{Al}_{10}$, $(\text{MgAl})_1\text{Al}_{10}$, $\text{Mg}_3\text{Si}_2\text{Al}_5$ and $\text{Mg}_2\text{Si}_1\text{Al}_3$. Because there are no entropy effects considered in the simulation which can be important during early stage precipitation, the calculation may not fully reflect what happens during real ageing treatment processes.

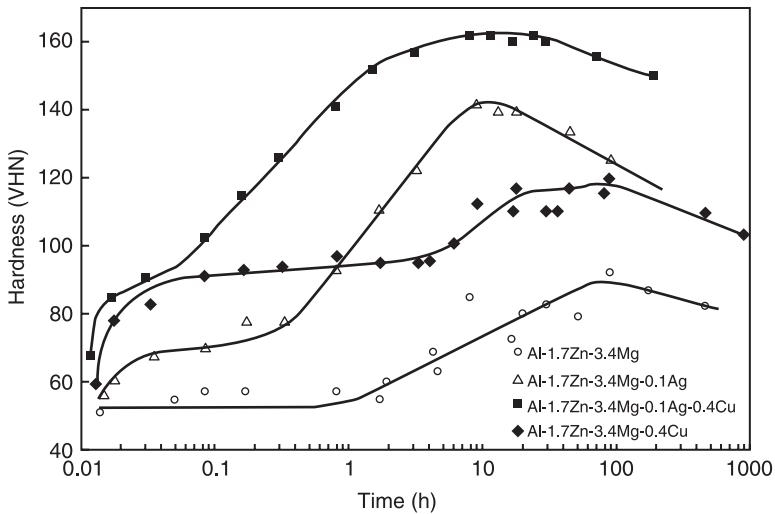
Many commercial 6xxx series Al alloys often contain Cu in varying amounts. The Cu-containing alloys fall into the quaternary Al-Mg-Si-Cu system which may exist either as 6xxx or 2xxx alloys. Q phase, a quaternary compound with various reported stoichiometry, often exists in these Al-Mg-Si-Cu alloys. Owing to the addition of Cu, precipitation sequences are more complicated and several other equilibrium phases coexist with β , including θ (Al_2Cu), S-phase (Al_2CuMg), T-phase and the quaternary intermediate Q-phase, all of which can precipitate during the ageing treatment. Q' is the metastable version of Q, and has the same crystal structure and lattice parameters as equilibrium Q and is coherent with the Al matrix along its long axis. Q' has a lath morphology with its long axis parallel to $\langle 100 \rangle_{\alpha\text{-Al}}$ and $\{150\}_{\alpha\text{-Al}}$ habit planes of the matrix. A thorough review about phase relations and precipitation in Al-Mg-Si alloys with Cu additions can be found in the work of Chakrabarti and Laughlin (2004).

12.5 Al-Zn-Mg-(Cu) based alloys

Al-Zn-Mg-(Cu) alloys have been widely used as high-strength structural materials. They have a high response to age hardening, as seen in Fig. 12.6. Under the peak hardening condition, these alloys suffer from susceptibility to stress corrosion cracking (SCC). As a result, they are used in the T73 temper. The precipitation sequence is generally considered as:



It has been proposed that the clustering of solute and possibly vacancies into vacancy-rich clusters (VRC) precede the formation of GP zones (Guinier, 1938; Preston, 1938). Small solute clusters with a size in the range of 10–30 atoms existing in as-quenched materials have been confirmed by 3DAP analysis and they are Mg rich (Sha and Cerezo, 2004a). Two types of GP zones, i.e. GPI and GPII exist in an artificially aged Al-Zn-Mg alloy according to HRTEM and selected area diffraction analysis (Li et al., 1999; Berg et al., 2001). GPI zones are coherent with the Al matrix, with internal ordering of Zn and Al/Mg on $\{001\}_{\alpha\text{-Al}}$ planes, and are formed over a wide temperature range, from room temperature (RT) to 140–150°C, independent of quenching temperature. GPII zones are zinc-rich layers on $\{111\}_{\alpha\text{-Al}}$ planes that are formed after quenching from temperatures above 450°C and ageing at temperatures above 70°C. Large GP zones have been



12.6 Hardness time plots for the Al-1.7Zn-3.4Mg alloy aged at 150°C, showing the effects of individual and combined Ag and Cu additions (after Caraher et al., 1998)).

found to have a Zn/Mg ratio of 1:1 (Sha and Cerezo, 2004), similar to the value predicted by first principles calculation (Wolverton, 2001).

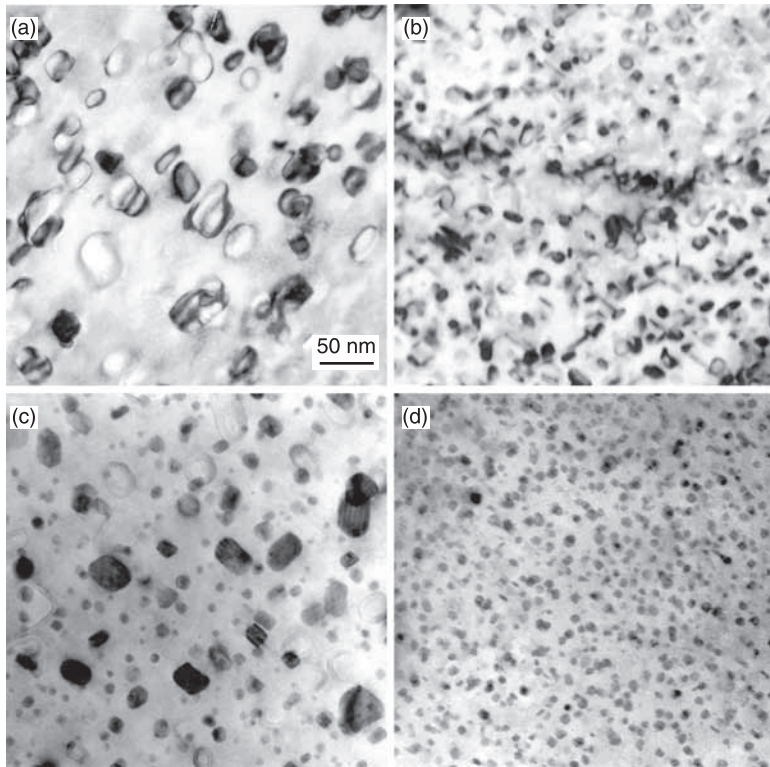
Metastable phase η' is the major strengthening phase in 7xxx Al alloys. Their Zn/Mg ratios are in the range of 1.2–1.4 depending on alloy compositions according to 3DAP measurements (Bigot et al., 1996; Maloney et al., 1999). Such ratios have been further supported by other 3DAP investigations (Sha and Cerezo, 2004b; Lefebvre et al., 2007). The Zn/Mg ratio obtained from atom probe measurement is much lower than the stoichiometries proposed for η' phase which have a value ≥ 2 . Several different crystal structures, including an orthorhombic structure and a hexagonal structure, have been proposed for η' phase. The orthorhombic structure with MgZn_2 stoichiometry was proposed by Gjønnes and Simensen (1970). However, the hexagonal structure with $a = 4.96 \text{ \AA}$ and $c = 14.02 \text{ \AA}$, with an approximate composition $\text{Mg}_4\text{Zn}_{11}\text{Al}$ proposed by Auld and Cousland (1974), has been well accepted in the literature.

More recently, Li et al. (1999) proposed a hexagonal model with a chemical composition of $\text{Mg}_2\text{Zn}_{5-x}\text{Al}_{2+x}$ based on their HRTEM investigation. First principles calculations have been employed to evaluate the energetics of each structure model for η' . Both the Gjønnes and Simensen model and Li et al. model are not favourable but calculations do support the crystal structure model proposed by Auld and Cousland which yields strongly negative formation enthalpies. By evaluating lattice misfit across the $\{111\}_{\alpha-\text{Al}}$ planes, Auld and Clousland's model is found to be more plausible due to yielding a low misfit greater than one per cent. The precipitation process is dominated by both kinetic and thermodynamic

effects. As a result, the actual precipitation process is much more complicated. It is likely due to the kinetic effect that a range of precipitate chemistries has been reported in similarly aged conditions. Even the equilibrium η phase formed in the T7 condition was measured to contain 8.45 ± 0.94 at% Al, with a Zn/Mg ratio of 1.82:1, which is less than the theoretical value of 2:1 in a Al-Zn-Mg alloy (Lefebvre et al., 2007). In Al-Zn-Mg-Cu alloys, η precipitates formed in the T6 condition were measured to contain 58 ± 9 at% Al, with Zn/Mg ratio of 1.2 ± 0.1 . In the overaged condition, and after ECAP at 200°C with up to eight passes, η contains 7.4–8 at% Al, 8.1–11% Cu and Zn/Mg ratio of 1.1–1.43 (Sha et al., 2009b).

A combination of atom probe characterisation and atomistic kinetic Monte Carlo simulation has been employed to gain insight into the detailed mechanisms dominating η' formation (Sha and Cerezo, 2004a, 2005). Careful quantitative evaluation of early stage precipitation microstructure evolution in three dimensions has gained insight into precipitate size, number density, chemistry and their spatial relationship, to form a clear picture on the formation of solute clusters, GP zones and η' precipitates. Small Mg-rich clusters are the first to form in a 7050 Al alloy during short ageing at 121°C, together with larger GPI zones with a Zn/Mg = 1:1. Zn-rich η' platelets formed mainly between 30 minutes and 240 minutes ageing and coexist with larger GPI zones. A significant fraction of $\langle 110 \rangle_{\alpha\text{-Al}}$ elongated clusters are observed over this period of ageing. Early η' precipitates are observed to be independent rather than attaching to large GP zones. The dominant mechanism for η' formation at this stage is by transformation of small GPI zones via the elongated clusters, and not by nucleation on larger GP zones. Kinetic Monte Carlo simulation successfully reproduces the main features of solute clusters observed by 3DAP, including early formed small cluster chemistry and coalescence for large GP zone growth. More importantly, it reveals that the growth of large GP zones is accompanied by an increase of Zn-rich medium-sized clusters, similar in chemistry to the elongated clusters observed by experimental investigation and having a chemistry close to η' . These small Zn-rich clusters serve as nuclei for formation of η' . This kinetic effect explains why small solute clusters that form later are effective in transformation into η' and the formation of η' is accompanied by the growth of larger GPI zones.

Most 7xxx Al alloys are in quaternary alloy systems that contain Cu or Ag. The addition of Cu (e.g. ~0.5 at%) is beneficial in both increasing tensile properties and decreasing susceptibility to SCC (Polmear, 1995). Similar effects are also observed in Al-Zn-Mg alloys containing small amounts (0.1 at%) of Ag. For ageing in the range of 100–235°C, Cu produces a very rapid hardening response. Despite the rapid hardening effect, Cu additions do not affect the second stage of hardening. Cu is partitioned into all precipitates that are formed in Cu-containing 7xxx alloys. As is apparent from Fig. 12.7, the effect of the addition of Cu and/or Ag is mostly to influence the dispersion of the precipitation rather than introduce new metastable precipitates (Caraher et al., 1998). The addition of Ag clearly



12.7 Peak hardness microstructures of the alloy series based on Al-1.7Zn-3.4Mg: (a) base alloy; (b) Al-1.7Zn-3.4Mg-0.1Ag; (c) Al-1.7Zn-3.4Mg-0.37Cu; (d) Al-1.7Zn-3.4Mg-0.1Ag-0.37Cu of the Al-1.7Zn-3.4Mg-0.1Ag alloy (after Caraher et al., 1998).

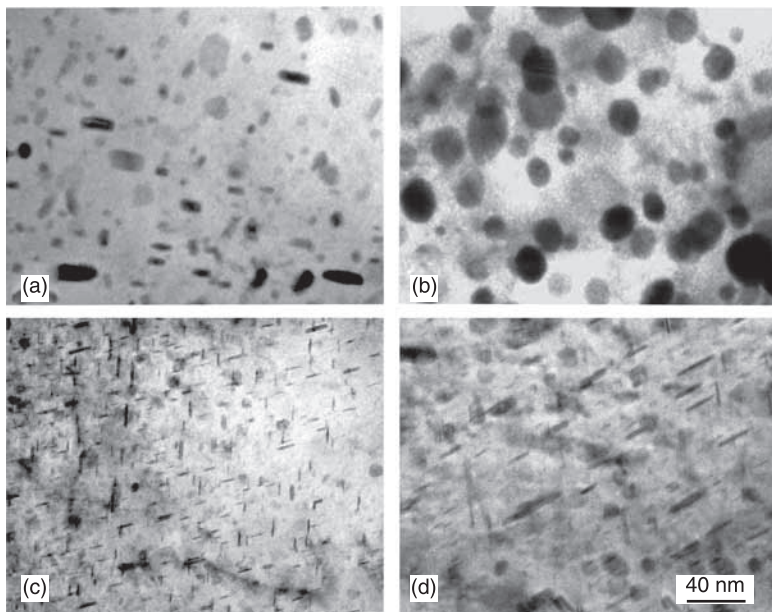
refines the precipitate dispersion as seen in Fig. 12.7. 3DAP characterisation shows that Ag is partitioned into the η' phase in the alloy. Because the addition of Ag reduces the PFZ width, it is thought that the quenched-in vacancies are retained from the solution treatment and that this accelerates subsequent diffusion and precipitation kinetics.

12.6 Precipitation in Al alloys under severe plastic deformation

Severe plastic deformation (SPD) is effective for producing metals and alloys having ultrafine grained (UFG) and/or nanocrystalline structures (Valiev et al., 2000; Valiev and Langdon, 2006; Zhilyaev and Langdon, 2008). Equal channel angular pressing (ECAP) and high pressure torsion (HPT) are two well-known SPD techniques having different capacities on grain refinement. ECAP can

refine the grain size of material to ~ 100 nm in Al alloys, whereas HPT can refine the grain size to a few ten nm. According to the Hall–Petch relationship (Hall, 1951; Petch, 1953), the grain refinement can cause significant strengthening of the material. Understanding grain refining effects and texture development under SPD has been a focus of many researchers, especially for single phase materials. More recently, there has been growing interest in understanding precipitation in order to control the precipitate microstructures of Al alloys and to achieve a combination of strengthening from both grain refinement and precipitation hardening (Murayama et al., 2001).

The evidence to date suggests that processing by SPD has a relatively complicated effect on precipitate microstructures. The precipitations under SPD are significantly different from those obtained by conventional ageing treatment, as shown in Fig. 12.8. The SPD processing has a marked effect on the size and morphology of precipitates. The large amount of shear deformation introduced by SPD will first initiate a rotation of pre-existing platelet or rod precipitates, as indicated by the arced reflection from precipitates in a circumferential direction, such as θ' in an Al–Cu–Mg alloy sample (Murayama et al., 2001) and η in an Al–Zn–Mg–Cu alloy sample (Sha et al., 2009a) processed after the first ECAP



12.8 TEM bright field images of Al–Zn–Mg–Cu alloy samples processed by ECAP at 200°C after one pass (a) and four passes (b) and samples only thermally aged at 200°C for 5 minutes (c) and 20 minutes (d) which are equivalent to the thermal durations of one pass and four passes ECAP processing, respectively.

pass. The shear deformation can further cause the fragmentation of pre-existing large precipitates and the formation of smaller spherical particles (Murayama et al., 2001; Xu et al., 2005). Careful TEM characterisation confirms that the SPD is effective in altering the orientation relationship between precipitates and the matrix (Murayama et al., 2001; Sha et al., 2009). As a result, the initial low energy interface associated with the preferential orientation relationship between the precipitate and the matrix will disappear. The higher surface energy at the interface between the precipitates and the matrix in the sample processed by SPD will promote the isotropic growth of the precipitates rather than anisotropic growth. The alternation of orientation relationship between precipitate and the matrix induced by SPD is responsible for the precipitates having lower aspect ratios or spherical morphology.

Temperature is another processing parameter affecting precipitation under SPD. SPD at room temperature generally suppresses precipitation in Al alloys. No precipitation was reported in as-quenched samples during ECAP (Zhao et al., 2004) and there was dissolution of pre-existing θ' precipitates in the matrix after eight passes of ECAP (Murayama et al., 2001). In contrast, when SPD is conducted at higher temperatures, such as 200°C, precipitation is promoted in an Al-Zn-Mg alloy (Sha et al., 2009b). A recent investigation on an Al-Zn-Mg-Cu alloy confirms that precipitation under ECAP accelerates the precipitation kinetics to about 50 times faster than that in conventional ageing treatments. SPD affects the precipitation thermodynamics by promoting isotropic growth and forming equiaxed η precipitates in the alloy. The high density of mobile dislocations produced by ECAP promotes the dissolution of small metastable precipitates and the formation of large η precipitates by coalescence.

Precipitation under SPD is a relatively new area, which demands more research to understand fundamentals. High volumes of grain boundaries are introduced into the materials due to the grain refinement under SPD. The segregation of solutes at grain boundaries can have a significant influence on the solute balance in the material (Sha et al., 2009a). Many basic questions regarding thermodynamics and kinetics of precipitation have yet to be answered in order to control the precipitation under SPD. For example, what is the phase equilibrium for each alloy system under SPD? How do mobile dislocations affect precipitation at different temperature? Better fundamental understanding will help to establish the threshold temperature at which precipitation can be activated under SPD.

12.7 Conclusion

Precipitation in Al alloys is a complicated process. Ageing temperature and time, alloy composition, trace element and microalloying additions all have a significant influence on the precipitation pathway. Atomistic experimental characterisation using modern analysis techniques, such as TEM and APT, combined with computer modelling are playing an important role in gaining deep

insights into the kinetics and thermodynamics of precipitation. New information from this kind of research has improved our understanding of the detailed precipitation mechanisms, revealing more about the early stage clustering processes and the effect that has on formation of metastable and equilibrium precipitates. It has also been seen that precipitation under extreme conditions, such as SPD, provides a new area for rich scientific research.

12.8 Acknowledgements

The authors are grateful for scientific and technical input and support from the Australian Microscopy & Microanalysis Research Facility (AMMRF) node at The University of Sydney.

12.9 References

- Auld J H and Cousland S Mck (1974), 'The structure of the metastable η' phase in aluminium–zinc–magnesium alloys', *J. Aust. Inst. Met.* 19, 194–201.
- Bagaryatsky Y A (1952), *Doklady Akad. Nauk SSSR* 87, 559–562.
- Berg L K, Gjønnes J, Hensen V, Li X Z, Knutson-Wedel M, Waterloo G, Schryvers D, and Wallenberg L R (2001), 'GP-zones in Al–Zn–Mg alloys and their role in artificial aging', *Acta Mater.* 49, 3443–3451.
- Bigot A, Danoix F, Auger P, Blavette D, and Reeves A (1996), 'Tomographic atom probe study of age hardening precipitation in industrial AlZnMgCu (7050) alloy', *Mater. Sci. Forum* 217/222, 695–700.
- Boyd J D and Nicholson R B (1971), 'A calorimetric determination of precipitate interfacial energies in two Al–Cu alloys', *Acta Metall.* 19, 1101–1109.
- Caraher S K, Polmear I J, and Ringer S P (1998), 'Effects of Cu and Ag on precipitation in Al–4Zn–3Mg (wt%)', in T Sato, S Kumai, T Kobayashi and Y Murakami (eds), *Proc. 6th Intl. Conf Aluminium Alloys (ICAA6)*, July 5–10, 1998, Toyahashi, Japan, Japan Institute for Light Metals, Tokyo, Vol. 2, pp. 739–744.
- Chakrabarti D J and Laughlin D E (2004), 'Phase relations and precipitation in Al–Mg–Si alloys with Cu additions', *Prog. Mater. Sci.* 49, 389–410.
- Chester R J and Polmear I J (1983), 'Precipitation in Al–Cu–Mg–Ag alloys', in *The Metallurgy of Light Alloys*, Inst. of Metals, London, pp. 75–81.
- Chopra H D, Liu K J, Muddle B C, and Polmear I J (1995), 'The structure of metastable $\{111\}\alpha$ precipitates in an Al–2.5wt. % Cu–1.5 wt. % Mg –0.5 wt. % Ag alloy', *Philos. Mag. Lett.* 71, 319–325.
- Chopra H D, Muddle B C, and Polmear I J (1996), 'The structure or primary strengthening precipitates in an Al–1.5 wt. % Cu–4.0 wt. % Mg–0.5 wt. % Ag alloy', *Philos. Mag. Lett.* 73, 351–357.
- DeSorbo W, Treafitis H N, and Turnbull D (1958), 'Rate of clustering in Al–Cu alloys at low temperatures', *Acta Metall.* 6, 401–413.
- Edwards G A, Stiller K, Dunlop G L, and Couper M J (1998), 'The precipitation sequence in Al–Mg–Si alloys', *Acta Mater.* 46, 3893–3904.
- Federighi T (1958), 'Quenched-in vacancies and rate of formation in aluminium alloys', *Acta Metall.* 6, 379–389.

- Gable B M, Shiftlet G J, and Starke E A Jr (2004), 'The effect of Si additions on Ω precipitation in Al-Cu-Mg-(Ag) alloys', *Scripta Mater.* 50, 149–153.
- Gjønnes J and Simensen C J (1970), 'An electron microscope investigation of the microstructure in an aluminium-zinc-magnesium alloy', *Acta Metall.* 18, 881–890.
- Guinier A (1938), 'Structure of age hardenable Al-Cu alloys', *Nature* 142, 569.
- Hall O E (1951), 'The deformation and aging of mild steel', *Proc. Phys. Soc.* 747–753 B64, 747.
- Hardy H K (1951–1952), 'The ageing characteristics of ternary aluminium-copper alloys with cadmium, indium or tin', *J. Inst. Met.* 80, 483–492.
- Hono K, Sakurai T, and Pomear I J (1994), 'Pre-precipitate clustering in an Al-Cu-Mg-Ag alloy', *Scripta Metall. Mater.* 30, 695–700.
- Hono K, Satoh T, and Hirano K (1986), 'Evidence of multi-layer GP zones in Al-1.7 at% Cu alloy', *Philos. Mag.* 53A, 495–504.
- Howe J M, Lee J, and Vasudevan A K (1988), 'Structure and deformation behaviour of T_1 precipitate plates in an Al-2Li-1Cu alloy', *Metall. Trans.* 19A, 2911–2926.
- Huang B-P and Wang Z-Q (1998), 'Effects of Li content on precipitation in Al-Cu-(Li)-Mg-Ag-Zr alloys', *Scripta Mater.* 38, 357–362.
- Hyde J M and English C A (2000), 'Microstructural processes in irradiated materials', in R G E Lucas, L Snead, M A J Kirk, and R G Elliman (eds), *MRS 2000 Fall Meeting Symposium*, Boston, MA, pp. 27–29.
- Kanno M, Suzuki H, and Kanoh O (1979), 'Energy dispersive X-ray spectroscopy on so-called tin-rich precipitates in aluminum-copper alloy containing a small amount of tin', *J. Jpn. Inst. Met.* 29, 223–226.
- Kanno M, Suzuki H, and Kanoh O (1980), 'The precipitation of q' phase in an Al-4Cu-0.06In alloy', *J. Jpn. Inst. Met.* 44, 1139–1145.
- Karlik M and Jouffrey B (1997), 'High resolution electron microscopy study of Guinier Preston (GP1) zones in Al-Cu based alloys', *Acta Mater.* 45, 3251–3263.
- Knowles K M and Stobbs W M (1988), 'The structure of $\{111\}$ age-hardening precipitates in Al-Cu-Mg-Cu-Ag alloys', *Acta Crystallogr.* B44, 207–227.
- Lee Y-S, Ringer S P, Polmear I J, and Muddle B C (1994), 'Precipitate stability in alloys based on the Al-Cu system', in T H Sanders, Jr. and E A Starke, Jr. (eds), *4th Intl. Conf. on Aluminium Alloys—Their Physical and Mechanical Properties (ICAA4)*, Georgia Institute of Technology, Atlanta, GA, September 11–16, pp. 582–589.
- Lee Y-S, Muddle B C, and Polmear I J (1995), 'High strength Al-Cu-Mg-Ag alloys with controlled Li additions', in K S Kim, J K Moon, and S J Kim (eds), *Proc. 2nd Pacific Rim Intl. Conf. on Advanced Materials and Processing*, Korean Inst. of Metals and Materials, Vol. 3, pp. 2221–2228, Kyongju.
- Lefebvre W, Danoix F, Costa G Da, Geuser F De, Hallem H, Deschamps A, and Dumont M (2007), '3DAP measurements of Al content in different types of precipitates in aluminium alloys', *Surf. Interface Anal.* 39, 206–212.
- Li X Z, Hansen V, Gjønnes J, and Wallenberg L R (1999), 'HREM study and structure modelling of the h' phase, the hardening precipitates in commercial Al-Zn-Mg alloys', *Acta Mater.* 47, 2651–2659.
- Lumley R N and Polmear I J (2004), 'The effect of long term creep exposure on the microstructure and properties of an underaged Al-Cu-Mg-Ag alloy', *Scripta Mater.* 50, 1227–1231.
- Lynch J P, Brown L M, and Jacobs M H (1982), 'Microanalysis of age-hardening precipitates in aluminium alloys', *Acta Metall.* 30, 1389–1395.

- Maloney S K, Hono K, Polmear I J, and Ringer S P (1999), 'The chemistry of precipitates in an aged Al-2.1Zn-1.7Mg at% alloy', *Scripta Mater.* 41, 1031–1038.
- Marceau R K W, Sha G, Ferragut R, Dupasquier A, and Ringer S P (2009), 'Solute clustering in Al-Cu-Mg alloys during the early stages of elevated temperature ageing', (accepted on 05/05/2010 *Acta Mater.*).
- Marceau R K W, Sha G, and Ringer S P (2008), 'Cluster hardening in Al-Cu-Mg alloys: Analysis of Cu-Mg atomic clustering', in J. Hirsch, B. Strotzki and G. Gottstein (Eds), *Aluminium Alloys: Their Physical and Mechanical Properties*, Vol. 1, Wiley-VCH Verlag GmbH & Co. KGaA, Weinheim, pp. 83–90.
- Marioara C D, Andersen S J, Jansen J, and Zandbergen H W (2001), 'Atomic model for GP-zones in a 6082 Al-Mg-Si system', *Acta Mater.* 49, 321–328.
- Matsuda K, Gamada H, Fujii K, Uetani Y, Sato T, and Kamio A (1998), 'High-resolution electron microscopy on the structure of Guinier-Preston zones in an Al-1.6 mass Pct Mg₂Si alloy', *Metal. Mater. Trans.* 29A 1161–1167.
- Miller M K, Cerezo A, Hetherington M G, and Smith G D W (1996), *Atom Probe Field Ion Microscopy*, Oxford Science, Oxford.
- Moody M P, Stephenson L T, Ceguerra A V, and Ringer S P (2007b), 'Quantitative binomial distribution analyses of nanoscale like-solute atom clustering and segregation in atom probe tomography data', *Microsc. Res. Tech.* 71, 542–550.
- Moody M P, Stephenson L T, Liddicoat P V, and Ringer S P (2007a), 'Contingency table techniques for three dimensional atom probe tomography', *Microsc. Res. Tech.* 70, 258–268.
- Murayama M and Hono K (1998), 'Three dimensional atom probe analysis of pre-precipitate clustering in an Al-Cu-Mg-Ag alloy', *Scripta Mater.* 38, 1315–1319.
- Murayama M and Hono K (1999), 'Pre-precipitate clusters and precipitation processes in Al-Mg-Si alloys', *Acta Mater.* 47, 1537–1548.
- Murayama M, Horita Z, and Hono K (2001), 'Microstructure of two-phase Al-1.7 at% Cu alloy deformed by equal-channel angular pressing', *Acta Mater.* 49, 21–29.
- Murray J L (1985), 'The Al-Cu system', *Int. Met. Rev.* 30, 211–233.
- Nicholson R B, Thoms G, and Nutting J (1958–1959), 'Electron microscopic studies of precipitation in aluminium alloys', *J. Inst. Met.* 87, 429–438.
- Perlitz H and Westgren A (1943), 'The crystal structure of Al₂CuMg', *Arkiv. Kemi. Mineral. Geol.* 16B, 1–5.
- Petch N J (1953), 'The cleavage strength of polycrystals', *J Iron Steel Inst.* 174, 25–28.
- Phillips V A (1973), 'High resolution electron microscope observations on precipitation in Al-3%Cu alloy', *Acta Metall.* 23, 751–767.
- Polmear I J. (1995), *Light alloys: Metallurgy of the light metals*, 3rd ed., Arnold, London.
- Polmear I J and Chester R J (1989), 'Abnormal age hardening in an Al-Cu-Mg alloy containing silver and lithium', *Scripta Metall.* 23, 1213–1217.
- Polmear I J and Hardy H K (1952–1953), 'Some metallographic observations on aged aluminium-copper alloys', *J. Inst. Met.* 81, 427–432.
- Preston G D (1938), 'Structure of age hardenable Al-Cu alloys', *Nature* 142, 570.
- Ravi C and Wolverton C (2004), 'First-principles study of crystal structure and stability of Al-Mg-Si-(Cu) precipitates', *Acta Mater.* 52, 4213–4227.
- Reich L, Murayama M, and Hono K (1998), 'Evolution of Ω phase in an Al-Cu-Mg-Ag alloy – A three dimensional atom probe study', *Acta Mater.* 46, 6053–6062.
- Ringer S P and Hono K (2000), 'Microstructural evolution and age hardening in aluminium alloys: atom probe field-ion microscopy and transmission electron microscopy studies', *Mater. Charact.* 44, 101–131.

- Ringer S P, Hono K, Polmear I J, and Sakurai T (1996), 'Nucleation of precipitates in aged Al-Cu-Mg-(Ag) alloys with high Cu:Mg ratios', *Acta Mater.* 44, 1883–1898.
- Ringer S P, Hono K, Polmear I J, and Sakurai T (1994a), 'Atom probe study of the effects of Ag and Mg additions on precipitation processes in Al-Cu and Al-Cu-Li alloys', in W C Johnson, J M Howe, D E Laughlin, and W A Soffa (eds), *Intl. Conf. on Solid-Solid Phase Transformations in Inorganic Materials*, Pittsburgh, PA, July 17–22, TMS, Warrendale, PA, pp. 165–170.
- Ringer S P, Yeung W, Muddle B C, and Polmear I J (1994b), 'Precipitate stability in Al-Cu-Mg-Ag alloys aged at high temperatures', *Acta Metall. Mater.* 42, 1715–1725.
- Ringer S P, Hono K, and Sakurai T (1995), 'The effect of trace additions of Sn on precipitation in Al-Cu alloys: An atom probe field ion microscopy study', *Metall. Mater. Trans.* 26A, 2207–2217.
- Ringer S P, Sakurai T, and Polmear I J (1997), 'Origins of hardening in aged Al-Cu-Mg-(Ag) alloys', *Acta Mater.* 45, 3731–3744.
- Ringer S P, Prasad K S, and Quan G C (2008), 'Internal co-precipitation in aged Al-1.7Cu-0.3Mg-0.1Ge (at.%) alloy', *Acta Mater.* 56, 1933–1941.
- Rioja R J and Laughlin D E (1977), 'The early stages of GP zone formation in naturally aged Al-4wt. % Cu alloys', *Metall. Trans.* 8A, 1257–1261.
- Sandberg N, Slabanja M, and Holmestad R (2007), 'Ab initio simulations of clustering and precipitation in Al-Mg-Si alloys', *Comput. Mater. Sci.* 40, 309–318.
- Sankaren R and Laird C (1974), 'Effects of trace additions Cd, In and Sn on the interfacial structure and kinetics of growth of q' plates in Al-Cu alloy', *Acta Metall.* 22, 957–969.
- Serizawa A, Hirose S, and Sato T (2008), 'Three-dimensional atom probe characterization of nanoclusters responsible for multistep aging behavior of an Al-Mg-Si alloy', *Metall. Mater. Trans.* A39, 243–251.
- Sha G and Cerezo A (2004a), 'Early-stage precipitation in Al-Zn-Mg-Cu alloy (7050)', *Acta Mater.* 52, 4503–4516.
- Sha G and Cerezo A (2004b), 'Characterization of precipitates in an aged 7xxx series Al alloy', *Surf. Interface Anal.* 36, 564–568.
- Sha G and Cerezo A (2005), 'Kinetic Monte Carlo simulation of clustering in an Al-Zn-Mg-Cu alloy (7050)', *Acta Mater.* 53, 907–917.
- Sha G, Ringer S P, Duan Z C, and Langdon T G (2009a), 'An atom probe characterisation of grain boundaries in an aluminium alloy processed by equal-channel angular pressing', *Int J. Mat. Res.* 12, 1674–1678.
- Sha G, Wang Y B, Liao X Z, Duan Z C, Ringer S P, and Langdon T G (2009b), 'Influence of equal-channel angular pressing on precipitation in an Al-Zn-Mg-Cu alloy', *Acta Mater.* 57, 3123–3132.
- Silcock J M (1960–1961), 'The structural ageing characteristics of Al-Cu-Mg alloys with copper: magnesium weight ratios of 7:1 and 2.2:1', *J. Inst. Met.* 89, 203–210.
- Silcock J M, Heal T J, and Hardy H K (1953–1954), 'Structural ageing characteristics of binary aluminium-copper alloys', *J. Inst. Met.* 82, 239–248.
- Silcock J M, Heal T J, and Hardy H K (1955), 'The structural ageing characteristics of ternary aluminium-copper alloys with cadmium, indium or tin', *J. Inst. Met.* 84, 23–31.
- Sully A H, Hardy H K, and Heal T J (1949–1950), 'The aluminium-tin phase diagram and the characteristics of aluminium alloys containing tin as an alloying element', *J. Inst. Met.* 76, 269–294.
- Suzuki H, Kanno M, and Araki I (1975), 'Precipitation of the intermediate phase in Al-Cu-Sn alloys', *J. Jpn. Inst. Light Met.* 25, 413–421.

- Taylor J A, Parker B A, and Polmear I J (1978), 'Precipitation in Al–Cu–Mg–Ag casting alloy', *Met. Sci.* 12, 478–482.
- Thomas G (1961–1962), 'The aging characteristics of aluminium alloys: Electron transmission studies of Al–Mg–Si alloys', *J. Inst. Met.* 90, 57–62.
- Valiev R Z, Islamgaliev R K, and Alexandrov I V (2000), 'Bulk nanostructured materials from severe plastic deformation', *Prog. Mater. Sci.* 45, 103–189.
- Valiev R Z and Langdon T G (2006), 'Principles of equal-channel angular pressing as a processing tool for grain refinement', *Prog. Mater. Sci.* 51, 881–981.
- van Huis M A, Chen J H, Sluiter M H F, and Zandbergen H W (2008), 'Phase stability and structural features of matrix-embedded hardening precipitates in Al–Mg–Si alloys in the early stages of evolution', *Acta Mater.* 55, 2183–2199.
- Van Nuyten J B M (1967), 'Quenched structures and precipitation in Al–Cu alloys with and without trace additions of Cd', *Acta Metall.* 15, 1765–1770.
- Vaumousse D, Cerezo A, and Warren P J (2003), 'A procedure for quantification of precipitate microstructures from three-dimensional atom probe data', *Ultramicroscopy* 95, 215–221.
- Vietz J T and Polmear I J (1966), 'The influence of small additions of silver on the ageing of aluminium alloys: Observations on Al–Cu–Mg alloys', *J. Inst. Met.* 94, 410–419.
- Wada M, Kita H, and Mori T (1985), 'FIM observation of GP zones in an Al–4Cu alloy', *Acta Metall.* 33, 1631–1635.
- Wolverton C (2001), 'Crystal structure and stability of complex precipitate phases in Al–Cu–Mg–(Si) and Al–Zn–Mg alloys', *Acta Mater.* 49, 3129–3142.
- Xu C, Furukawa M, Horita Z, and Langdon T G (2005), 'Influence of ECAP on precipitate distributions in a spray-cast aluminum alloy', *Acta Mater.* 53, 749–758.
- Zandbergen H W, Andersen S J, and Jansen J (1997), 'Structure determination of Mg_5Si_6 particles in Al by dynamic electron diffraction studies', *Science* 277, 1221–1225.
- Zhao Y H, Liao X Z, Zhou J, Valiev R Z, and Zhu Y T (2004), 'Microstructures and mechanical properties of ultrafine grained 7075 Al alloy processed by ECAP and their evolutions during annealing', *Acta Mater.* 52, 4589–4599.
- Zhilyaev A P and Langdon T G (2008), 'Using high-pressure torsion for metal processing: Fundamentals and applications', *Prog. Mater. Sci.* 53, 893–979.

Solute partitioning to enhance mechanical properties of aged aluminium alloys

I.J. POLMEAR, Monash University, Australia

Abstract: Deliberate partitioning of solute elements between the matrix solid solution and dispersed precipitates in aged aluminium alloys can be facilitated simply by underageing or, less commonly, by adjusting alloy compositions. Although these practices usually result in some reduction in tensile properties, it has been shown that significant improvements may be achieved in creep resistance and fatigue strength. If secondary precipitation is encouraged after underageing, simultaneous increases in tensile properties and fracture toughness are possible.

Key words: solute partitioning, precipitation hardening, secondary ageing, heat treatment.

13.1 Introduction

During the heat treatment of alloys which respond to age hardening, it is usual to seek to maximize the amount of solute that engages in the precipitation process. In this regard, a commonly used ageing cycle for aluminium alloys is the T6 temper in which the alloy is solution treated, quenched and aged to peak strength at a suitable elevated temperature (e.g. 150°C). Whereas such a temper usually allows high levels of tensile properties to be achieved, recent results have shown that other mechanical properties, such as creep and fatigue resistance, may be improved if the solute elements are deliberately encouraged to partition between the matrix solid solution and the fine precipitates that promote strengthening (Polmear, 1959; Arumalla and Polmear, 1985; Lumley et al., 2002; Lumley and Polmear, 2004; Lumley et al., 2005). Two possible ways to achieve such a condition are to create alloy compositions for which there is a surplus of a suitable solute above that normally required for the actual precipitation process or to age existing alloys for shorter times (i.e. underageing).

Another commonly shared belief has been the implicit acceptance that, once an alloy has been aged at an elevated temperature, its mechanical properties remain stable during exposure for an indefinite time at a significantly lower temperature. However, Loeffler et al. (1983) revealed that highly saturated Al-Zn alloys, aged initially at 180°C, continued to age harden by so-called 'secondary precipitation' when they were cooled and held at ambient temperature. Similar behaviour has since been observed for highly saturated lithium-containing alloys aged first at 170°C and then exposed for long periods at 60–130°C (Lynch, 1991; Peel, 1991; Pitcher et al., 1992; Balmuth and Chellman, 1994; Noble et al., 1994; Kerr et al.,

1996). In this case, strength and hardness increase with time but the alloys tend to embrittle (Gao et al., 1998; Itoh et al., 1999; Starink et al., 2000; Noble et al., 2000). Now, it is recognized that secondary precipitation is a more general phenomenon which involves solute that has not participated in the initial precipitation process. Furthermore, it has also been shown that secondary precipitation may be controlled so that it has beneficial effects on certain mechanical properties (Lumley et al., 2003, 2005).

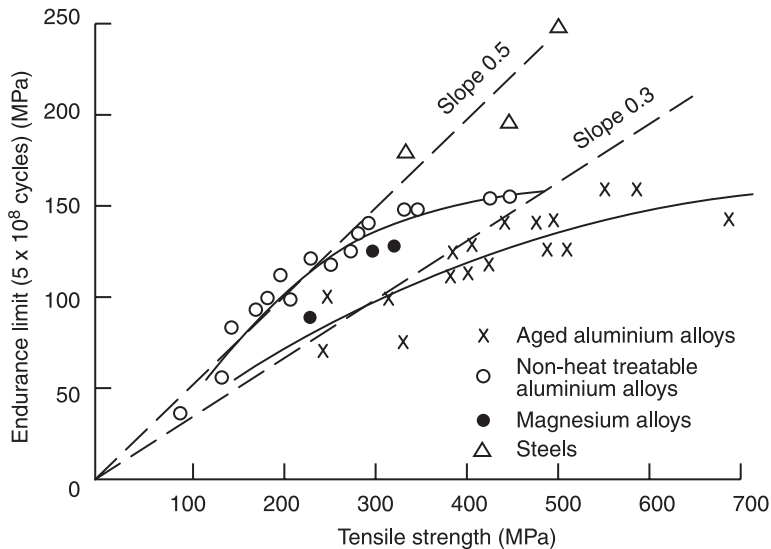
Heat treatments involving underageing, and those that promote secondary precipitation, have recently been studied as means by which the service performance of aged aluminium alloys may be improved. Although deliberate underageing results in some sacrifice of tensile properties, there is evidence that, under conditions involving creep or fatigue stressing, dynamic changes may occur in service which enable the useful lives of components and structures to be extended (Lumley et al., 2002, 2005; Lumley and Polmear, 2004). Such changes appear to take place by processes that help counteract microstructural damage as it develops. Where secondary precipitation occurs, it has been shown that tensile and fracture toughness properties may be raised, in some cases simultaneously (Lumley et al., 2003; Lumley et al., 2005).

The purpose of the present paper is to review the changes in mechanical properties that can be achieved in aged aluminium alloys through the deliberate partitioning of solute between matrix and precipitate, and to examine the mechanisms involved.

13.2 Solute partitioning through compositional change

Contrary to the behaviour of most steels, the steady increases that have been achieved in the tensile properties of age hardened aluminium alloys have not been accompanied by proportionate improvements in fatigue properties. This situation is illustrated in Fig. 13.1 which shows the relationships between fatigue endurance limit (5×10^8 cycles) and tensile strength for different alloys (Varley, 1970). It will be noted that the fatigue endurance:tensile strength ratios are the lowest for the aged aluminium alloys and, as a general rule, the more these alloys depend on precipitation hardening to achieve higher values of tensile strength, the lower this ratio becomes.

General studies of fatigue processes in metals and alloys have shown that cracks normally initiate at the surfaces of components or structures. It is here that the strain becomes progressively more localized due to the presence of pre-existing stress concentrations such as notches or corrosion pits, coarse (persistent) slip bands in which minute extrusions and intrusions can form, or at relatively soft regions, such as precipitate-free zones, that may be present adjacent to grain boundaries in aged aluminium alloys (e.g. Forsyth and Stubbington, 1954–55; Wood, 1956; Forsyth, 1957; Laird, 1979). With such alloys, the concentration of strain in the persistent slip bands can be particularly harmful because precipitate



13.1 Fatigue ratios (endurance limit:tensile strength) for aluminium alloys and steels (Varley, 1970).

particles within the bands may be cut by moving dislocations causing them to re-dissolve once they have become smaller than the critical size for thermodynamic stability (Polmear and Bainbridge, 1959; Calabrese and Laird, 1974). This process promotes softening within the slip bands which, in turn, leads to a further concentration of strain so that crack formation is accelerated. It was therefore apparent that two possible strategies to improve the fatigue properties of age hardened aluminium alloys could be to increase the size and/or stability of precipitates and other finely dispersed particles, or to reduce the mobility of dislocations in these highly strained regions.

Some success has been achieved in delaying the initiation of fatigue cracks through the presence of fine intermetallic compounds that are capable of dispersing dislocations more uniformly throughout the matrix. However, these particles do tend to have the adverse effect of assisting crack propagation (e.g. Lutjering et al., 1973; Albrecht et al., 1976). Another early suggestion (Polmear, 1959) was to adjust the compositions of age hardened alloys so that excess solute not required for the precipitation process is available to partition to the matrix which may serve to reduce dislocation mobility during fatigue stressing. The experiment aimed at achieving this objective is described below.

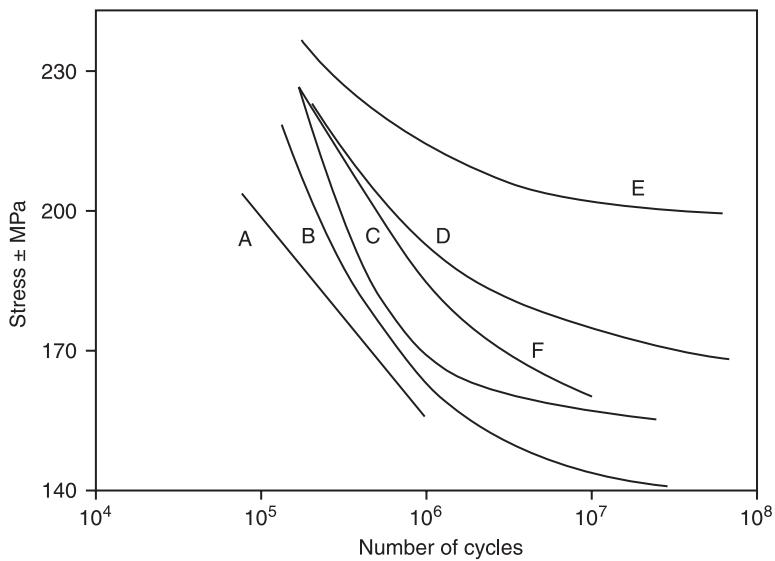
Since the 1940s, compositions based on the Al-Zn-Mg system have served as one of the two classes of high-strength aluminium alloys most widely used for aircraft construction. Early studies of a wide range of ternary compositions suggested that, once the Mg:Zn ratio exceeded a certain value, excess Mg may be available that was not required in the precipitation process and could be retained

Table 13.1 Ternary Al-Zn-Mg alloy compositions and T6 tensile properties

Alloy	Mg wt%	Zn wt%	Mg:Zn ratio	0.1% Proof stress (MPa)	Tensile strength (MPa)	Elongation (%)
A	1.05	8.3	0.13	303	380	14.4
B	2.0	5.8	0.35	328	420	15.5
C	3.0	5.1	0.59	310	407	17.7
D	4.0	4.5	0.89	214	374	30.0
E	5.0	4.1	1.22	219	367	27.7
F	6.0	3.7	1.62	324	386	15.5

in the matrix (Polmear, 1958–59). This observation was thought to be significant because yield point phenomena had been observed during the deformation of binary Al-Mg alloys which was indicative that solute Mg/dislocation interactions do occur (Phillips et al., 1952–1953). For these reasons, a comparative study (Polmear, 1959) was made of the effect of composition on the fatigue properties of a range of high purity, ternary Al-Zn-Mg alloys in which the Mg:Zn ratio was varied from 0.13 to 1.62, and for which it was expected that the same T6 ageing treatment (16 h at 125°C) would result in fairly similar values of tensile strength (Table 13.1; Cook et al., 1951).

Rotating cantilever tests ($R = -1$) were carried out on specimens prepared from forged bars that had recrystallized during heat treatment. Results are shown in Fig. 13.2 and, although complete stress:number of cycles (S-N) curves for each



13.2 Stress-number of cycles (S-N) curves for ternary Al-Zn-Mg alloys (Polmear, 1959).

alloy were not determined, it was clear that the fatigue behaviour varied greatly with composition. Highest fatigue endurance was observed with alloys D, E and F which had the greatest Mg:Zn ratios. Of these alloys, E had the best properties and it should be noted that the Mg:Zn ratio in this case lay between those for D and F. Somewhat lower fatigue properties were obtained for alloys B and C which had Zn and Mg contents closest to many current commercial compositions. Alloy A performed worst and, in this case, crack propagation occurred readily along grain boundaries suggesting that they may have become embrittled during ageing.

Tensile properties also affect fatigue performance, and it is significant to note that good fatigue endurance was generally associated with low ratios of proof stress to tensile strength. In this regard, alloys D and E had proof stress values well below those for the other four alloys. However, this feature can only partly explain the higher fatigue properties since, although they had similar low ratios of proof stress:tensile strength (~ 0.6), the fatigue strength of E was notably higher.

Following these encouraging results, a preliminary assessment was made of the possible commercial potential of alloys based on the ternary composition of E (Al-4Zn-5Mg). Other elements, such as manganese, that are normally present in the relevant commercial alloys were added to control grain structure. Some extruded bars were produced, and it was confirmed that relatively high levels of fatigue properties could be maintained. However, this wider test program revealed that the modified alloys were particularly susceptible to stress-corrosion cracking and the experimental program was therefore abandoned. This result highlighted the difficulty of modifying the composition of an alloy to improve one particular property without adversely affecting its behaviour under other service conditions.

13.3 Studies of underaged alloys

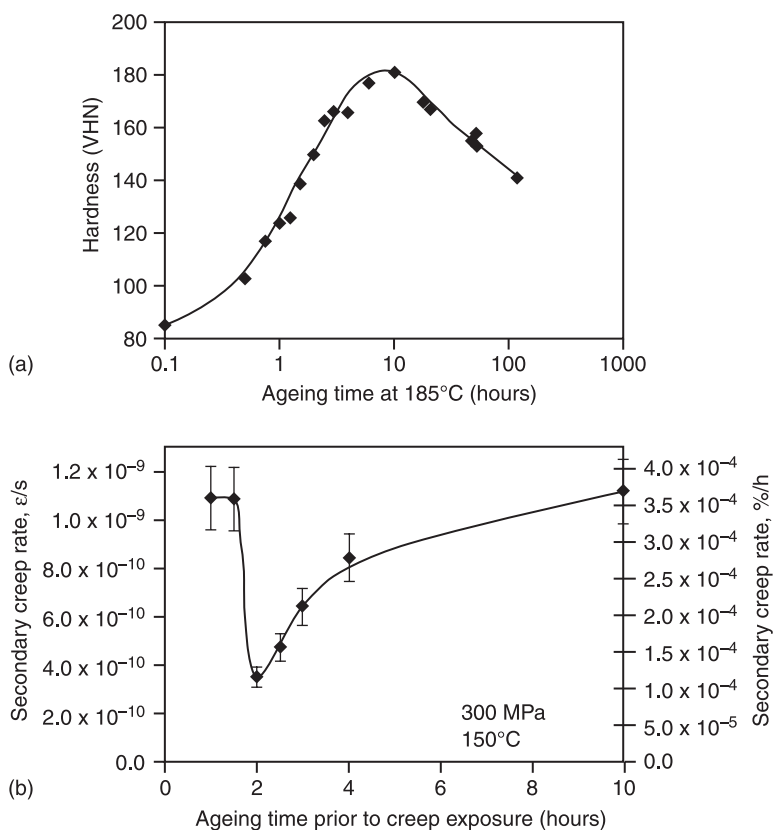
13.3.1 Creep performance

In recent studies of the creep behaviour of aged aluminium alloys, special attention has been given to compositions based on the Al-Cu-Mg-Ag system in which small amounts of stable phase designated Ω (e.g. Auld and Vietz, 1969; Chester and Polmear, 1980). This phase has the same composition as the θ' phase that forms in binary Al-Cu alloys (Reich et al., 1998a), but it precipitates on the $\{111\}_{\alpha}$ rather than the $\{100\}_{\alpha}$ matrix planes. It is generally thought to have an orthorhombic structure (Knowles and Stubbs, 1988; Muddle and Polmear, 1989). Once Ω has formed, the Ag and Mg atoms have been shown to segregate from the precipitate/matrix interfaces and there is evidence that coherency is maintained along the $\{111\}_{\alpha}$ planes (Reich et al., 1998b; Hutchinson et al., 2001).

An early study of the creep behaviour of a high-purity, experimental alloy Al-4%Cu-0.3%Mg-0.4%Ag hardened predominantly by the Ω phase revealed that the secondary creep rate at 125°C was reduced by approximately 65% if the alloy was tested in the underaged (UA) condition (1 h at 170°C) following

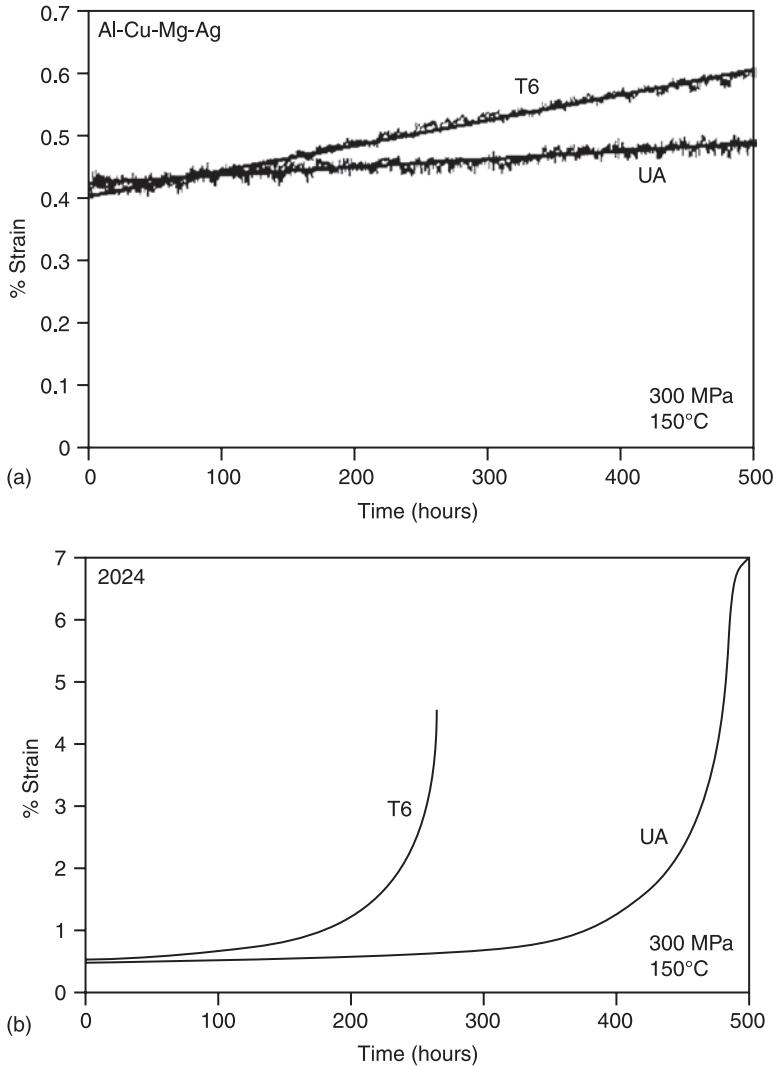
quenching from the solution treatment temperature, rather than in the fully age hardened T6 temper (12 h at 170°C) (Arumalla and Polmear, 1985). This result was unexpected because the UA alloy had a significantly lower value of 0.2% proof stress (313 MPa) when compared with the T6 condition (363 MPa).

Later, this study of the effects of underageing on creep behaviour was expanded using extrusions prepared from the more complex Ag-containing alloy Al-5.6%Cu-0.45%Mg-0.45%Ag-0.3%Mn-0.18%Zr (Lumley et al., 2002). The hardness-time curve of this alloy aged at 185°C is shown in Fig. 13.3(a) and, in the peak aged condition (10 h), it was found to have creep properties superior to those of various commercial alloys such as 2219, 2618 and 2048 (Polmear et al., 1999). Accelerated creep tests at 150°C and a stress of 300 MPa were then conducted on the alloy in the UA condition. In this case, the UA treatment that resulted in the lowest rate of secondary creep rate was 2 h at 185°C (Fig. 13.3b). As shown in Fig.



13.3 (a) Hardness-time curve for the alloy Al-5.6%Cu-0.45%Mg-0.45%Ag-0.3%Mn-0.18%Zr (wt.%) aged at 185°C. (b) Secondary creep rate as a function of prior ageing time at 185°C for tests carried out at 300 MPa and a temperature of 150°C. (Lumley et al. 2002).

13.3(b) and Fig. 13.4(a), the minimum value recorded was $3.5 \times 10^{-10} \text{ s}^{-1}$ which is approximately one-third the creep rate for the same alloy aged to a T6 temper ($1.1 \times 10^{-9} \text{ s}^{-1}$). Respective values of 0.2% proof stress were UA: 435 MPa and T6: 480 MPa. When further creep tests were conducted at the lower temperature of 130°C and stress of 200 MPa, the UA alloy was found to exhibit zero secondary creep after prolonged testing for 20 000 h (Lumley and Polmear, 2004). Improved



13.4 Creep curves for (a) the experimental Al-Cu-Mg-Ag-Mn-Zr alloy, and (b) the commercial alloy 2024 in the UA and fully hardened (T6) conditions. Tests carried out at a stress of 300 MPa and a temperature of 150°C. (Lumley et al., 2002).

creep performance was also recorded for the commercial alloy 2024 (Al-4.4%Cu-1.5%Mg-0.6%Mn) when it was tested in the UA condition (Fig. 13.4b). In this case, tertiary creep was delayed and the time to failure was increased from 269 h in the T6 condition to 480 h by underageing (Lumley, Morton and Polmear, 2002). Results for these two alloys suggest that the beneficial effects of UA on creep properties may apply more generally to aged aluminium alloys.

One general explanation for the enhanced creep properties of UA aluminium alloys could be that residual solute present in the matrix is available to form atmospheres around dislocations thereby impeding or preventing their motion during the creep process. Other possible reasons were sought by making a detailed analysis of the microstructures of the Al-Cu-Mg-Ag-Mn-Zr alloy in the following conditions (Lumley et al., 2002):

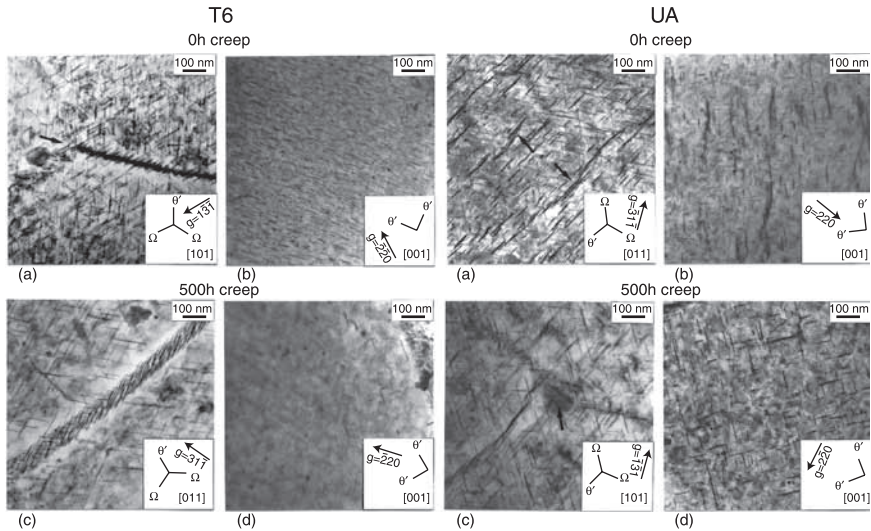
- after the initial UA and T6 ageing treatments;
- at the beginning of creep at 150°C after loading to a stress of 300 MPa; and
- after accelerated creep testing for 500 hours under these conditions.

Specimens for examination by transmission electron microscopy were prepared from within the gauge lengths of the specimens and parallel to the longitudinal direction of the extruded bars. These were produced as thin, 3 mm diameter, discs using an electrical discharge machine to avoid the possibility of mechanical deformation. These discs were then thinned by standard electropolishing methods and examined in a JEOL: 2000EX microscope operating at 200 kV.

The microstructures of the Al-Cu-Mg-Ag alloy in the T6 and UA conditions following creep tests at 150°C are shown in Fig. 13.5. Comparisons suggest that the beneficial effects of UA may also be due to one or more of the following factors:

1. Retention of plates of the θ' precipitate within the matrix during creep rather than their dissolution that was observed when tested in the T6 condition.
2. Additional dynamic precipitation of θ' that has occurred on mobile dislocations throughout the matrix during creep. Such precipitation may be assisted by the release of vacancies into the matrix from the surfaces of the Ω precipitates in the UA alloy (Ferragut et al., 2009).
3. Retention of a finer dispersion of the Ω precipitate within the matrix.
4. Stabilization of subgrain boundaries due to precipitation there of fine arrays plates of the θ' and Ω phases.

The physical origin of the enhanced creep resistance of the UA alloy has also been analysed theoretically by Hutchinson et al. (2006), who considered the motion of a dislocation through a microstructure hardened by the presence of thin plates of the Ω phase on the $\{111\}_\alpha$ planes. For the experimental conditions described above, it was found that the dominant mode of deformation was by dislocation creep. As a first approximation, the steady creep rate $d\varepsilon/dt = \rho\beta v$, where ρ is the dislocation density, v is the dislocation velocity, and β is the Burgers vector.



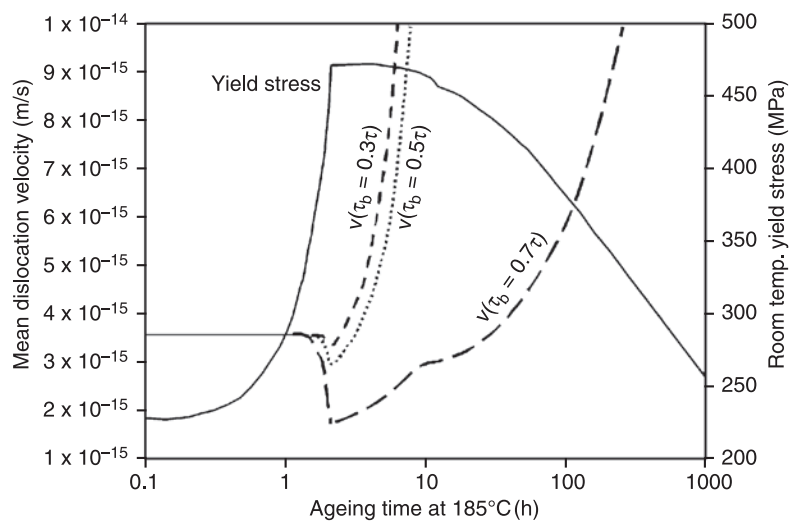
13.5 Microstructures of the Al-Cu-Mg-Ag-Mn-Zr alloy in the T6 and UA conditions following creep tests at 300 MPa and 150°C. Orientations in the $[101]\alpha$ and $[001]\alpha$ directions (Lumley et al., 2002).

In making their study, Hutchinson et al. (2006) assumed that, for a given temperature and stress, the dislocation density ρ of the alloy showed little change during the creep test. They therefore attributed the minimum in the creep rate of the UA alloy shown in Fig. 13.3(b) to a reduction in dislocation velocity v , the mean value of which will depend on the times taken for dislocations to glide between precipitates and to climb over them. Results of their calculations are shown in Fig. 13.6 and confirm that, for three assumed levels of back stress (τ_b) on the climb dislocations, the mean dislocation velocities were expected to have minimum values when the alloy is UA for 2 h at 185°C, as was demonstrated experimentally in Fig. 13.3(b).

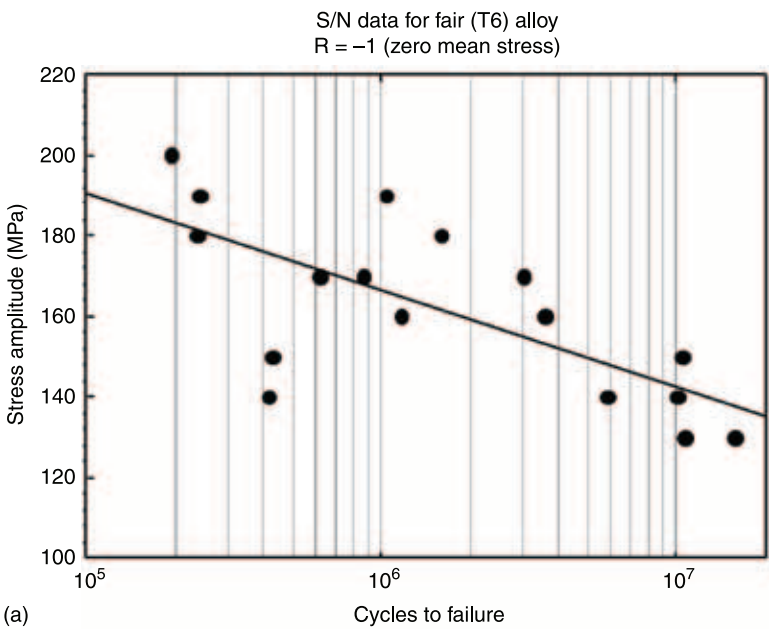
13.3.2 Fatigue studies

Together with the creep study described above, a comparison was made of the fatigue behaviours of the Al-Cu-Mg-Ag-Mn-Zr alloy in the UA and T6 conditions (Lumley et al., 2005). Specimens were again machined with their long axes parallel the longitudinal direction of the heat treated extrusions. Fatigue tests were conducted at room temperature in an axial load machine at a stress ratio of $R = -1$ (zero mean stress). Multiple tests were made at differing stress levels such that failure occurred within 10^5 – 10^7 cycles, and the results are shown in Fig. 13.7.

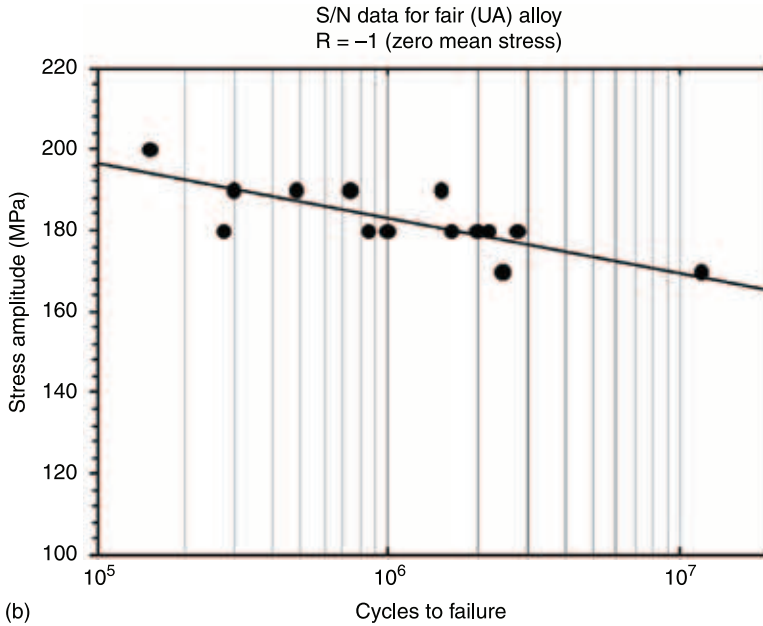
Comparison of the S-N curves indicated that the scatter of individual results is much greater in the T6 than in the UA condition. Furthermore, the best-fitting curves have different slopes with the UA alloy sustaining progressively longer



13.6 Computed mean dislocation velocities (v) under creep conditions as a function of ageing time for the Al-Cu-Mg-Ag-Mn-Zr at 185°C (Hutchinson et al., 2006). v = mean dislocation density, τ_b = back stress on dislocation.



13.7 Stress–number of cycles (S–N) data for the Al-Cu-Mg-Ag-Mn-Zr alloy tested in the (a) T6 and (b) UA conditions (Lumley et al., 2005).



13.7 Continued.

lives and the stress level was reduced. In this regard, the estimated cyclic stresses to cause failure in 10^5 , 10^6 and 10^7 cycles are shown in Table 13.2. In summary, it was found that the UA alloy could sustain a stress some 18% greater than that for the fully hardened alloy for equal failure times of around 10^7 cycles. Alternatively, for a cyclic stress 175 MPa, the UA alloy had a lifetime to failure some 10 times that for the alloy aged to a T6 temper.

Transmission microscopy was used to compare the microstructures of specimens that had been tested at 10^5 , 5×10^5 and 8×10^5 cycles at a cyclic stress of 160 MPa, and thin specimens were prepared in the manner described above. Observations again revealed that, whereas dissolution of the θ' precipitate took place during fatigue testing of the specimens aged to a T6 temper, there was evidence that dynamic precipitation of this phase occurred in the matrix of the UA alloy. In effect, it seems that the microstructural degradation normally caused by

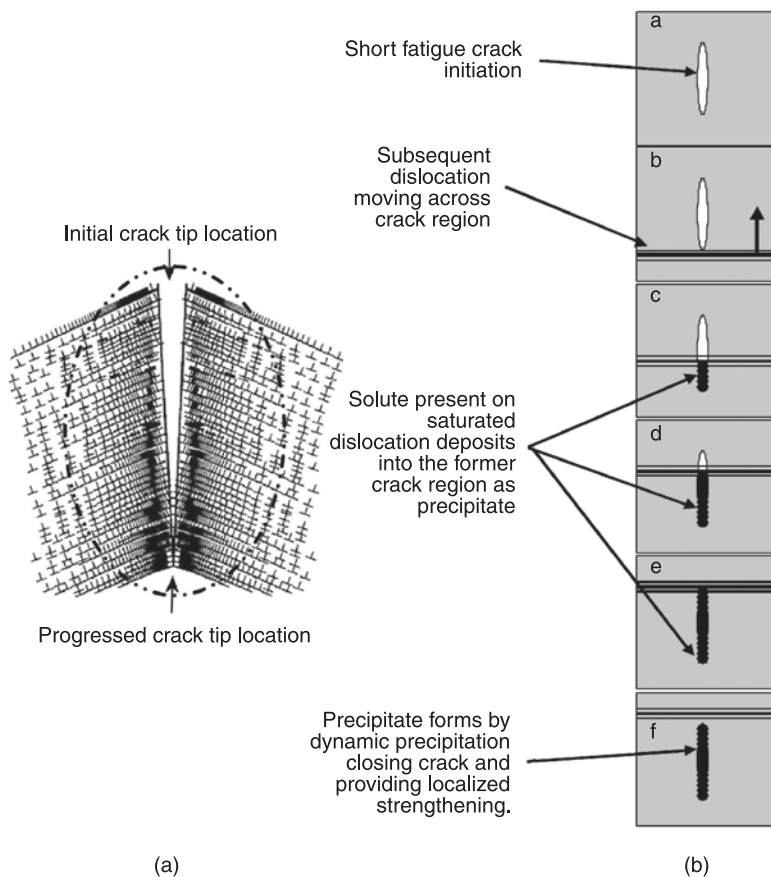
Table 13.2 Cyclic stress failure data

Cycles	10^5	10^6	10^7
T6	190MPa	168MPa	144MPa
UA	196MPa	183MPa	172MPa

Source: Lumley et al. (2005)

dislocations generated by cyclic stressing was nullified because solute atoms retained in the matrix were available to facilitate dynamic precipitation which, in turn, immobilizes these defects.

Another possible explanation is that the dynamic precipitation occurring during cyclic stressing of the UA alloy may facilitate the closure of developing cracks (Lumley et al. 2005). This follows because a crack has a relatively high free energy at its tip, as well as a high density of dislocations within its associated plastic zone, as shown schematically in Fig. 13.8(a) (Riemelmoser and Pippan, 1998). It is to be expected, therefore, that this localized region will serve as a favoured site for the heterogeneous nucleation of precipitates. A possible sequence of events that could lead to crack closure is shown in Fig. 13.8(b) (Lumley et al., 2005). Such a process



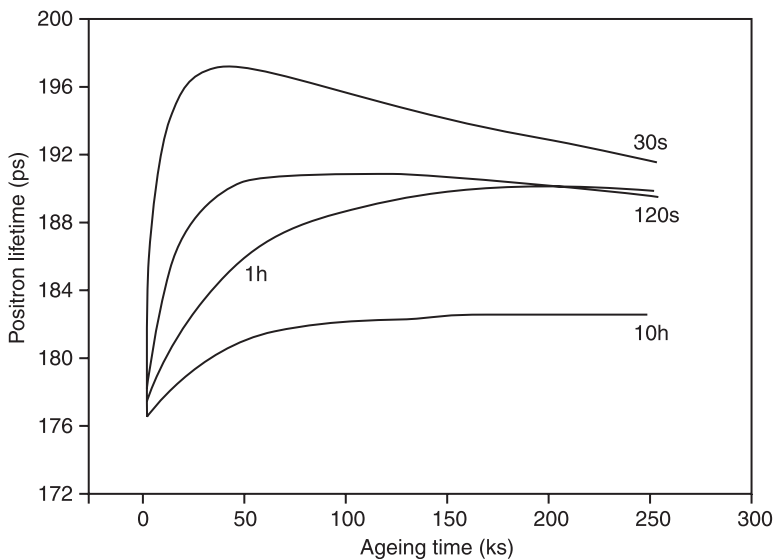
13.8 Schematic figures showing (a) a high density of dislocations in the plastic zone at a crack (Riemelmoser and Pippan 1998), and (b) the proposed sequence of events (a–f) leading to crack closure by a process of dynamic precipitation of solute from impinging dislocations (Lumley et al., 2005).

of crack closure is further enhanced because dense, heterogeneous precipitation of θ' causes a volume expansion that may result in localized compressive forces being generated at the crack tip (Lumley, 2007).

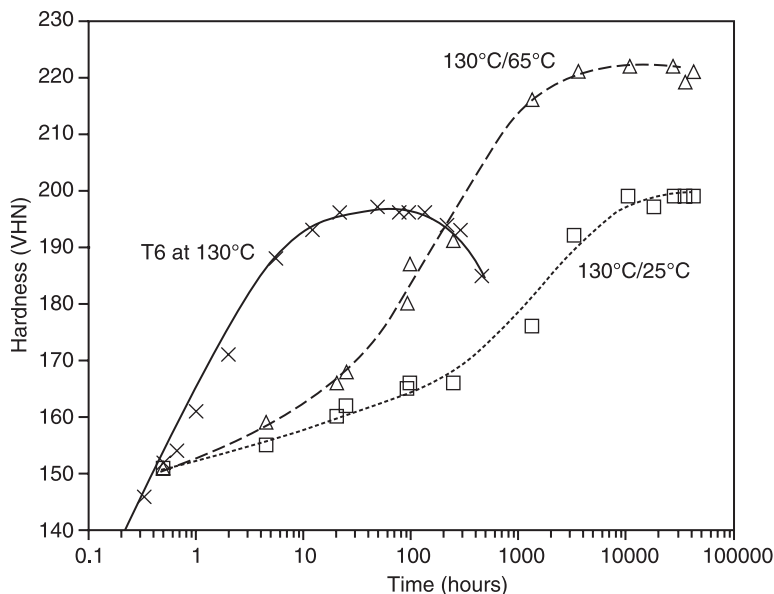
13.4 Secondary precipitation

Studies of a wide range of aluminium alloys have revealed that the levels of residual or 'free' solute that may remain in solid solution until the alloys are in the overaged condition is higher than previously accepted (Majimal et al., 2004; Nairn et al., 2006). Furthermore, positron annihilation spectroscopy has shown that relatively high concentrations of vacancies may also be present that will assist solute diffusion at low ageing temperatures (e.g. 20°C) after first ageing at significantly higher temperature, such as 180°C (Somoza et al., 2000) (Fig. 13.9). The increases in positron lifetimes are taken to indicate that the retained vacancies (and solute atoms) are mobile at 20°C, thereby allowing further (secondary) ageing to occur.

Solute partitioning leading to further precipitation during secondary ageing is particularly favoured if the alloy is first artificially aged for a relatively short time (i.e. UA). This behaviour is illustrated in Fig. 13.10 for the commercial alloy 7075 (Al-5.5%Zn-2.5%Mg-1.5%Cu-0.23%Cr) which normally reaches a peak hardness of around 195 Hv if aged for 24 h at 130°C (Lumley et al., 2005). If this alloy is first



13.9 Positron lifetimes during secondary ageing of the alloy Al-4%Cu-0.3%Mg at 20°C after solution treating at 520°C, quenching at 0°C, and first ageing for 30 s, 120 s, 1 h or 10 h at 180°C (from Somoza et al., 2000).

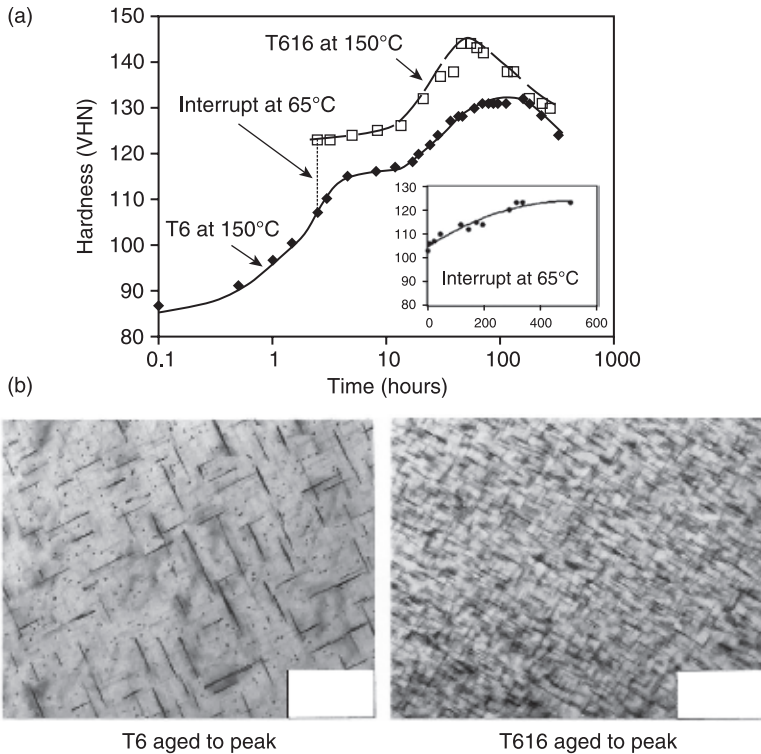


13.10 Hardness-time curves for the aluminium alloy 7075 aged at 130°C (solid line), and UA 0.5 h at 130°C, quenched to 25°C, and held either at this temperature or at 65°C (dashed lines) (from Lumley et al., 2005).

UA for 0.5 h at 130°C, and quenched to 25°C, the hardness is 150 Hv. Prolonged secondary ageing at this temperature will see the hardness increase gradually to 200 Hv. Alternatively, if the UA alloy is given a secondary ageing treatment at the slightly higher temperature of 65°C after quenching from 130°C, the hardness increases more rapidly and reaches a high value of 225 Hv after 1000 h.

During secondary ageing at these lower temperatures, GP zones usually form from the solute retained in solid solution in the matrix (Lumley et al., 2003, 2005, 2006). If, after a suitable dwell period, artificial ageing at or close to the initial elevated temperature is resumed then the microstructure corresponding to peak hardness is refined. As a result, a greater overall level of hardness (and tensile properties) can be achieved than is possible using a single stage T6 ageing treatment. This effect is shown for the alloy Al-4%Cu in Fig. 13.11 in which the multi-stage ageing schedule is given the temper designation T6I6, where 'I' indicates that artificial ageing at the initial elevated temperature has been interrupted. If such a treatment is given to an alloy that is hardened by the presence of two precipitates, the normal proportions of each present in the final microstructure may also be changed.

As shown in Table 13.3, experimental interrupted ageing cycles have been developed that enable simultaneous increases in tensile properties and fracture toughness properties to be achieved for a wide range of aluminium alloys.



13.11 (a) Differences in hardness-time curves for Al-4%Cu aged at 150°C, with and without an interrupted period of secondary ageing at 65°C. The inset plot shows the hardness change during the dwell period at 65°C. (b) Transmission electron micrographs in the [001] α direction showing dispersions of the θ' precipitate plates and minor amounts of the θ'' phase in the two aged conditions [T6 temper: 100 h at 150°C; T616 temper: 3 h at 150°C quench to 20°C, 500 h at 65°C and 50 h at 150°C (from Lumley et al., 2003)].

Normally an undesirable inverse relationship exists between these particular mechanical properties.

13.5 Conclusion

1. Studies involving both experimental and commercial aluminium alloys are revealing that more solute elements remain in solid solution in the matrix during conventional age hardening treatments than would be predicted from a study of the respective equilibrium phase diagrams.
2. Further partitioning of solute to the matrix can be achieved if alloys are deliberately UA. Although such a treatment inevitably results in some

Table 13.3 Effects of interrupted ageing and secondary hardening on the mechanical properties of selected aluminium alloys

Alloy ¹ and temper ²	0.2% proof stress (MPa)	Tensile strength (MPa)	Elongation %	Fracture toughness ³ MPa√m
2014-T6	414	488	5	26.9
2014-T6I6	436	526	10	36.2
6061-T6	267	318	13	36.8
6061-T6I6	299	340	13	58.4
6061-T6I4	302	341	16	43.2
7050-T6	546	621	14	37.6
7050-T6I6	574	639	14	41.1
7050-T6I4	527	626	16	52.0
8090-T6	349	449	4	42.2
8090-T6I6	391	512	5	31.0
357-T6	287	325	7	25.5
357-T6I6	341	375	5	26.0
357-T6I4	280	347	8	35.9

Source: Lumley et al., 2003

Notes:

¹ Wrought alloys except for casting alloy 357.

² Temper designation T6 involves single stage artificial ageing of alloys to peak strength at appropriate temperatures. Temper designation T6I4 indicates that the T6 temper was interrupted by quenching and holding for a long time at 65°C. In this case, artificial ageing is not resumed as it is for the T6I6 temper.

³ Fracture toughness tests on the wrought alloys in the S-L direction. All tests under plane strain conditions except for alloy 6061.

reduction in tensile properties when compared with those for the fully hardened T6 temper, creep and fatigue resistance may both be enhanced.

3. Solute partitioning can be used to promote increased secondary precipitation at low temperatures in alloys that are first artificially aged, and new heat treatment cycles have been developed in which elevated temperature ageing is interrupted by a dwell period at a lower temperature. These interrupted ageing treatments can allow simultaneous increases to be achieved in tensile and fracture toughness properties.
4. Potentially, making compositional changes to alloys to promote solute partitioning is another way to improve particular mechanical properties. However, opportunities to do this appear to be much more limited because other properties may be affected adversely.

13.6 Acknowledgments

The author's thanks are due to Dr Roger Lumley of the Australian Commonwealth Scientific and Industrial Research Organization, Light Metals Flagship, Melbourne, who initiated and conducted much of the experimental work described in this review.

13.7 References

- Albrecht, J, Martin, J.M.R., Lutjering, G. and Martin, J.W. (1976), Influence Of Micromechanisms On Fatigue Crack Propagation Rate Of Al Alloys, *Proc. 4th Inter. Conf. on Strength of Metals and Alloys*, Nancy, France., pp.463-467.
- Arumalla, S.R. and Polmear, I.J. (1985), Fatigue And Creep Behaviour Of Aged Alloys Based On Al-4%Cu-0.3%Mg, *Proc. 7th Inter. Conf. on Strength of Metals and Alloys*, Montreal, Canada, Pergamon Press, Oxford, vol.1, pp.453-458.
- Auld, J.H. and Vietz, J.T.(1969), *The Mechanism of Phase Transformations in Crystalline Solids*, Monograph and Report Series No. 33, Inst. Metals, London, pp.53-57.
- Balmuth, E.S. and Chellman, D.J. (1994), *Proc. 4th Inter. Conf. on Aluminium Alloys*, Atlanta, USA, eds. Sanders, T.H. and Starke, E.A., Georgia Inst. of Technology, vol. 1, pp.282-289.
- Calabrese, C. and Laird, C.(1974), Cyclic stress-strain response of two-phase alloys: part I. Microstructures containing particles penetrable by dislocations, *Mater. Sci. and Eng.*, 13, 2, 141-157.
- Chester, R.J. and Polmear I.J. (1980), TEM Investigations of Precipitation in Al-Cu-Mg-Ag and Al-Cu-Mg Alloys, *Micron*, 11, 311-312.
- Cook, M., Chadwick, R. and Muir N.B. (1951), Observations on Some Wrought Aluminium-Zinc-Magnesium Alloys, *J. Inst. Metals*, 79, 293-304.
- Ferragut, R., Dupasquier, A., Macchi, C.E., Somoza A., Lumley, R.N. and Polmear, I.J. (2009), Vacancy-Solute Interactions During Multiple Step Ageing in Al-Cu-Mg-Ag alloys, *Scripta Mater.*, 60, 137-140.
- Forsyth, P.J.E. and Stubbington, C.A., (1954-55), The Slip-Band Extrusion Effect Observed In Some Aluminium Alloys Subjected To Cyclic Stresses, *J. Inst. Metals*, 83, 395-399.
- Forsyth, P.J.E., (1957), Slip-Band Damage and Extrusion, *Proc. Roy. Soc. A*, 242, 198-202.
- Goa, X., Nie, J-F. and Muddle, B.C.(1998), Secondary Hardening in 2090 (Al-Cu-Li) Alloys, *Proc. 6th Inter. Conf. on Aluminium Alloys*, eds. Satoh, T. et al, Toyohashi, Japan, Japan Inst. Light Metals, Tokyo, vol. 2, 651-656.
- Hutchinson, C.R., Fan, X., Pennycook, S.J. and Shiflet, G.J.(2001), On the Origin of the High Coarsening Resistance of Ω plates in Al-Cu-Mg-Ag Alloys, *Acta Mater.*, 49, 2827-2841.
- Hutchinson, C.R., Cornall, P. and Goune, M. (2006), On the Origin of Enhanced Creep Resistance in Underaged Al-Cu Based Alloys, *Mater. Sci. Forum*, 519-521, 1029-1034.
- Itoh, G., Kanno, M., Hagiwara, T. and Sakamoto, S. (1999), Embrittlement in an Age Hardened 2091 Aluminium Alloy by Exposure at Elevated Temperatures Below the Ageing Temperature, *Acta Mater.* 47, 3799-3809.
- Kerr, M.J., Sweet, E.D., Bennett, C.G. and Muddle, B.C.(1996), Effect of Alkali Impurities on Low Temperature Stability of 2090 Al-Cu-Li-Alloys, *Mater. Sci., Forum*, 217-222, 1079-1084.
- Knowles, K.M. and Stobbs, M.J.(1988), The Structure of { 111 } Age Hardened Precipitates in Al-Cu-Mg-Ag alloys, *Acta Cryst.*, 344, 207-227.
- Laird, C. (1979), Mechanisms and Theories of Fatigue in Fatigue and Microstructure, Amer. Soc. Metals, Metals Park, Ohio, USA, pp.149-203.
- Loeffler, H., Kovacs, I. and Lendvai, J. (1983), Decomposition Processes in Al-Zn-Mg Alloys, *J. Mater. Sci.*, 18, 2215-2240.
- Lumley, R.N., (2007) Self Healing in Aluminium Alloys, in *Self Healing Materials, an Alternative Approach to 20 Centuries of Materials Science*, S. van der Zwaag ed., Springer, Dordrecht, the Netherlands, pp.219-254.

- Lumley, R. N., Buha, J., Polmear I.J., Morton, A.J. and Crosky, A.G. (2006), Secondary Precipitation in Aluminium Alloys and Its Role in Modern Heat Treatment, *Mater. Sci. Forum*, 519-521, 283-290.
- Lumley, R.N., Morton, A.J. and Polmear, I.J.(2002), Enhanced Creep Performance in an Al-Cu-Mg-Ag Alloy Through Underageing, *Acta Mater.*, 50, 3597-3608.
- Lumley, R.N., Polmear, I.J. and Morton, A.J. (2003), Interrupted Ageing and Secondary Precipitation in Aluminium Alloys, *Mater. Sci. Tech.*, 19, 1453-1460.
- Lumley, R.N. and Polmear, I.J.(2004), The Effect of Long Term Creep Exposure on the Microstructure and Properties of an Underaged Al-Cu-Mg-Ag Alloy, *Scripta Mater.*, 50, 1227-1231.
- Lumley, R.N., O'Donnell, R.B., Polmear, I.J. and Griffiths J.R (2005), Enhanced Fatigue Resistance by Underageing an Al-Cu-Mg-Ag Alloy, *Mater. Forum*, 29, 256-261.
- Lumley, R.N., Polmear, I.J. and Morton, A.J. (2005), Development of Mechanical Properties During Secondary Ageing in Aluminium Alloys, *Mater. Sci. Tech.*, 21, 1025-1032.
- Lutjering, G., Döcker, H. and Munz, D. (1973), Microstructure and fatigue behaviour of Al-alloys, *Proc. 3rd Inter. Conf. on Strength of Metals and Alloys*, Cambridge, England, Inst. Metals, pp. 427-432.
- Lynch, S.P. (1991), Fracture of 8090 aluminum-lithium plate I. Short transverse fracture toughness, *Mater. Sci. Eng A*, A136, 25-43.
- Marjinal, J., Molenat, G., Danoix, D., Thuillier, O., Blavette, D., Lapasset, G. and Casanove, M.J. (2004), High-Resolution Electron Microscopy and Tomographic Atom Probe Studies of Hardening Precipitation in an Al-Cu-Mg Alloy, *Phil. Mag.*, 84, 3263-3280.
- Muddle, B.C. and Polmear, I.J. (1989), The Precipitate Ω Phase in Al-Cu-Mg-Ag Alloys, *Acta Metall.*, 37, 777-789.
- Nairn, K.M., Gable, B.M., Stark, R., Ciccoscillo, N., Hill, A.J., Muddle, B.C. and Bastow, T.J. (2006), Monitoring the Evolution of the Matrix Composition in Age Hardenable Al-Cu Alloys, *Mater. Sci. Forum*, 519-521, 591-597.
- Noble, B., Harris, S.J. and Dinsdale, K. (1994), Low Temperature Embrittlement of 8090 in the Damage Tolerant Condition, *Proc. 4th Inter. Conf. on Aluminium Alloys*, Atlanta, USA, eds. Sanders, T.H. and Starke, E.A. Jr., Georgia Inst. of Technology, vol. 1, p.460.
- Noble, B, Harris, S.J. and Dinsdale, K. (2000), Reduction in Toughness in Aluminium-Lithium Alloys Caused by Long Term Exposure at Low Temperatures, *Mater. Sci. Forum*, 331-337, 1353.
- Peel, C.J. (1991), Applications and Developments for Aluminium-Lithium Alloys, in *Aluminium-Lithium Alloys VI*, eds. Peters, M.J. and Winkler, P.J., DGM Informationsgesellschaft, p.1259.
- Phillips, V.A., Swain, A.J. and Eborall, R. (1952-53), Yield Point Phenomena and Stretcher Strain Markings in Aluminium-Magnesium Alloys, *J. Inst. Metals*, 81, 625.
- Phillips, V.A. (1952-53), Effect of Composition and Heat Treatment on Yield Point Phenomena in Aluminium Alloys, *J. Inst. Metals*, 81, 649.
- Pitcher, P.D., Stewart, R.J. and Gupta, S. (1992), A Study Of Reversion Behavior In 8090 Alloys Using Small Angle Neutron Scattering And Transmission Electron Microscopy, *Scripta Metall.*, 26, 511-516.
- Polmear, I.J. (1958-59), The Upper Temperature Limit of Stability of GP Zones in Ternary Aluminium-Zinc-Magnesium Alloys, *J. Inst. Metals*, 87, 24-25.
- Polmear, I.J.(1959), Fatigue Properties of Ternary Aluminium-Zinc-Magnesium Alloys, *Nature*, 183, 1388-1389.

- Polmear, I.J. and Bainbridge, I.F. (1959), Fatigue Deformation in the Interior of Aged Ternary Aluminium-Zinc-Magnesium Alloys, *Phil. Mag.*, 4, no. 48, 1293-1304.
- Polmear I.J., Pons, G., Octor, H., Sanchez, C., Morton, A.J., Borbidge, W. and Rogers, S. (1999), After Concorde : Evaluation of an Al-Cu-Mg-Ag Alloy for Use in the Proposed European Supersonic Transport, *Mater. Sci. Tech.*, 15, 861-868.
- Reich, L., Murayama, M. and Hono, K. (1998a), 3DAP Study of the Effect of Mg and Ag Additions on Precipitation in Al-Cu-Li Alloys, *Proc. 6th Int. Conf. on Aluminium Alloys (ICAA-6)*, Japan Inst. Light Metals, Tokyo, Vol. 2, 645-650.
- Reich L., Murayama, M. and Hono, K. (1998b), Evolution Of Phase In An Al-Cu-Mg-Ag Alloy-A Three-Dimensional Atom Probe Study, *Acta Mater.*, 46, 6053-6062.
- Riemelmoser, F.O., and Pippan, R., (1998), Mechanical Reasons for Plasticity-Induced Crack Closure Under Plane Strain Conditions, *Fatigue Fract. Eng. Mater. Struct.*, 21, 1425-1433.
- Somoza, A, Dupasquier, A., Polmear, I.J., Foligati, P. and Ferragut, R. (2000), Positron Annihilation Study of Ageing in Al-Cu Based Alloys : II Ag Microalloying, *Phys. Rev. B*, 61, 14454-14463.
- Starink, M.J., Hobson, A.J., Sinclair, I. and Gregson, P. (2000), Embrittlement of Al-Cu-Li-Mg Alloys at Slightly Elevated Temperatures: Microstructural Mechanisms of Hardening, *Mater. Sci. Eng.*, A289, 130-142.
- Varley, P.C. (1970), *The Technology of Aluminum Alloys*, Newnes-Buttersworth.
- Wood, W.A. (1956), in *Fatigue of Aircraft Structures*, ed. Freudenthal A.M., Academic Press, pp.1-12.

Vacancies in aluminium and solute-vacancy interactions in aluminium alloys

A. SOMOZA, Universidad Nacional del Centro de la Provincia de Buenos Aires and Comisión de Investigaciones Científicas de la Provincia de Buenos Aires, Argentina
and A. DUPASQUIER, Politecnico di Milano, Italy

Abstract: In the present chapter, different aspects related to vacancies and to processes involving vacancies in pure aluminium and aluminium-based age-hardenable alloys are discussed. Special attention is given to the study of solute-vacancy interactions and the formation of solute-vacancy complexes during ageing. Taking into account the modern scientific approach to the study of the physical mechanisms involved in vacancy formation and migration, solute-vacancy binding, solute aggregation and precipitation, experimental and theoretical studies are presented and discussed. Specifically, experimental results were obtained using conventional (e.g. electrical resistivity, thermal expansion, transmission electron microscopy) and non-conventional experimental techniques (e.g. positron annihilation spectroscopy, nuclear magnetic resonance); while the theoretical ones are by first-principle calculations and Monte Carlo simulations.

Key words: aluminium alloys, age hardening, precipitation sequence, solute-vacancy interaction, solute clustering.

14.1 Introduction

14.1.1 Aim of this chapter

For more than a century, there have been examples presented in literature on the behaviour of dilute solid solutions wherein the association of solute atoms with lattice vacancies is considered to play a major role. For example, almost 50 years ago it was reported that the kinetics of aluminium age hardenable alloys were extremely sensitive to quenching conditions and solute content. Despite no direct evidence, experiments on aluminium-copper alloys suggested this effect was due to the interaction of solute atoms and vacancies.

It is now well accepted that solute-vacancy association is one of the fundamental processes controlling precipitation hardening phenomena in age hardenable alloys. Following high-temperature solution treatment and quenching, ageing treatments are normally carried out at temperatures low enough to avoid significant production of new vacancies and, as a result, non-equilibrium vacancies (i.e., excess vacancies retained after quenching or produced by cold work) are especially important. Vacancies mediate the transport of solute atoms and contribute to the

stability of precipitates by reducing misfit stresses between them and the matrix material. Although the concentration of quenched-in vacancies is very low (normally below 10^{-4} vacancies per atom) in comparison with the concentration of minority elements in an alloy, their action is crucial in determining the decomposition sequence of the supersaturated solid solution (SSSS). However, vacancies are an elusive component of any alloy, not only because of their low concentration but also because they cannot be imaged by any microscopy even at atomic resolution. The most effective way of studying vacancies and related phenomena implies the combined use of complementary experimental techniques as well as of theoretical approaches and modelling.

In the present chapter, different aspects related to vacancies in pure aluminium and Al-based age hardenable alloys are discussed with a focus on solute-vacancy interactions. A description is given of experimental studies on kinetic processes involving vacancies in pure aluminium (i.e., formation and migration), and of solute diffusion and vacancy-solute interactions in aluminium alloys. To this aim, we firstly analyse results obtained using more established conventional techniques such as electrical resistivity and dilatometry, and then draw correlations to modern analytical techniques such as positron annihilation spectroscopy (PAS) and nuclear magnetic resonance (NMR). Some results on diffusion phenomena in selected alloys are also presented. Account of different theoretical methods developed to analyse the processes explored using some of the experimental techniques mentioned above is then given. First-principle calculations are used to obtain vacancy formation energies in pure aluminium. The same kind of theoretical approach is used to calculate solute-vacancy binding energies in multicomponent alloys and precipitation processes in selected Al-based alloys, as well as to support the interpretation of PAS results on vacancy-like formation in pure aluminium. Monte Carlo simulations of solute clustering and vacancy-microalloying elements interactions in alloys are also presented.

A short summary of the main results presented will then be provided along with comments on the benefit of multi-technique (experimental and calculation) approaches to the study of vacancy related phenomena. Potential future trends are then considered and discussed.

14.1.2 Ageing processes in aluminium alloys

Age-hardening in aluminium alloys is a well-known thermal treatment for particular groups of aluminium alloys, described in more detail elsewhere in this book. Essentially this process consists of solution treatment at high temperature to form a saturated solid solution and increase the vacancy content, followed by quenching to freeze in the SSSS. The alloy is then held at a suitable lower temperature for ageing, wherein the decomposition of the SSSS begins by the formation of a fine distribution of nano-sized precipitates. From the technological viewpoint, it is important to control the size, the morphology and the spatial

distribution of these precipitates, in order to achieve an optimum combination of properties.

The decomposition of an alloy, initially prepared in the form of a SSSS, is a complicated phenomenon controlled by thermodynamical factors (phase stability) as well as atomistic processes (solute transport). Ageing normally takes place through a sequence of stages, during which metastable phases are initially formed, and then disappear or are transformed into more complex but more stable phases. Variations in this sequence depend primarily on composition and temperature. The mechanism of precipitate nucleation from the SSSS in effect governs the scale of the precipitate dispersion, which is a very important factor in determining the mechanical properties of the heat treated alloy.

14.1.3 Literature review

The reader may find relevant information on precipitation sequences, clustering phenomena, formation of intermediate precipitates as well as other phenomena involved in the age hardening process, in different Al-based systems in, for instance, Friedel and Guinier, 1963; Kelly and Nicholson, 1963; Martin, 1968; Cahn et al., 1991; Cahn, 2001; Christian, 2002; Balluffi et al., 2005; Polmear, 2006. We do not review here this subject, which is important, but not specific to the scope of the present chapter. However, these topics are discussed elsewhere in this book.

14.2 Experimental studies of vacancies and solute-vacancy interactions

14.2.1 General introduction

Vacancy formation and migration in pure aluminium

The majority of the experimental methods for studying vacancies and vacancy-like defects in metals and alloys involve non-equilibrium conditions. Of the techniques for generating vacancies in excess of the equilibrium concentration, quenching from high temperatures is a well-known procedure to lock in the high temperature vacancy concentration. More specifically, the procedure consists of annealing of metals and alloys at known high temperatures, then quenching to retain the high temperature concentration of vacancies prior to taking measurements. The alternative methodology relies on measurements at thermal equilibrium, which implies dealing with point defect concentrations fixed by thermodynamics. Both lines of attack have been used to determine the characteristic activation energies for vacancy formation and migration, in combination with conventional measurement techniques (thermal expansion, electrical resistivity, internal friction) or with nuclear methods (self-diffusion measurements with radioactive tracers, NMR and PAS). In particular, positron annihilation lifetime

spectroscopy (PALS), which is a variant of PAS, provides a most sensitive and specific tool for vacancy detection and identification. The potential of NMR and PAS for measuring vacancy migration energies in metals is fully recognised in several textbooks of Physical Metallurgy.

The vacancy formation energy is experimentally determined from measurements of the temperature dependence of the total vacancy concentration; specifically, it is obtained from the slope of an Arrhenius plot (logarithm of the concentration vs. the reciprocal of the temperature). In the case of pure aluminium, thermal expansion and electrical resistivity (ER) measurements cover, with reasonable accuracy, the concentration range from 10^{-3} to 10^{-4} vacancies/atomic site and this technique was widely used in the 1960s (Simmons and Baluffi, 1960a, 1960b). ER suffers from the disadvantage that the temperature dependence of the ER due to phonon scattering is not well known because of anharmonic effects. Using an improved variant of NMR, Detemple et al. (1995) obtained reliable values of the actual concentration of the excess vacancies in pure polycrystalline aluminium foils under plastic deformation. A review on vacancy behaviour in metals can be found in Siegel, 1978. It is important to note that whereas ER is particularly useful for the concentration range from 10^{-3} to 10^{-4} vacancies/atomic site, the range explored by PALS is extended from 10^{-7} to 10^{-4} vacancies/atomic site (Schaefer et al., 1987).

As is well known, vacancies in pure aluminium easily migrate at room temperature and the number of quenched-in vacancies is in general below the sensitivity limits of conventional experimental techniques. Nevertheless, residual resistance could be used for determining the vacancy migration energy in aluminium under special circumstances, i.e. where measurements were made in a limited range at high-temperature (Ono and Kino, 1978). In addition, under special experimental conditions, NMR diffusion measurements on pure aluminium allowed a determination of vacancy formation and migration energies (Gullion and Conradi, 1987).

Vacancies and solute-vacancy interactions in aluminium alloys

It is well known that there are strong interactions between the solute atoms and vacancy-like defects that result in structural instabilities. In fact, it is difficult to give a discussion on solute-vacancy interaction independently of a general frame linked to the decomposition sequence of the SSSS.

The current knowledge on the kinetic mechanisms involved in the solute-vacancy interactions during the precipitation sequence is mostly inferred from indirect evidence, gathered from ER (Section 14.2.2) and from TEM observations of the dislocation loops left after the collapse of the clusters (see, for instance, Westmacott et al., 1961). However, since the 1990s PAS has given invaluable information regarding the role of vacancies during the decomposition of the SSSS. The potential of PAS for the study of light alloys was illustrated

recently with special regard to age-hardening, severe plastic deformation, fatigue and fracture in aluminium and magnesium-based alloys (Dupasquier et al., 2004).

Recent studies, leading to the direct determination of composition and of the structure of pre-precipitate and precipitate structures in Al-Cu-X and Al-Zn-X systems [Guinier–Preston (GP) like zones, co-clustering, etc.] and precipitates by different variants of atom probe (AP) and high resolution transmission electron microscopy (HRTEM), are described by, for example, Ringer et al. (1997), Reich et al. (1999), Ferragut et al. (1999), Ringer and Hono (2000), Ringer (2006) and Tolley et al. (2009).

The continuing progress with advanced imaging techniques, however, does not suppress the interest for other well-established experimental methods: small angle X-Ray scattering (SAXS), small angle neutron scattering (SANS), differential scanning calorimetry (DSC) and mechanical properties measurements. Examples regarding Al-Cu-X and Al-Zn-X based alloys can be found in Deschamps et al. (1997, 2006), Sato et al. (2003) and Zahra et al. (2005).

Dumont et al. (2005), Dupasquier et al. (2007) and Esmaeili et al. (2007) present some interesting case studies of precipitation hardening using several of the above-mentioned techniques.

14.2.2 Conventional techniques

Vacancies in pure aluminium

Since the early 1950s very interesting papers dealing with the equilibrium concentration of vacancies in pure metals (aluminium, silver, gold and copper) were published. ER was used as the main experimental technique. In contrast to modern atomic scale characterisation methods, ER does not require any sophisticated equipment or sample preparation methods. This technique provides information on the macroscopic scale and, as discussed below, at the same time is sensitive to atomic-scale phenomena such as solute clustering and solute-vacancy interactions (Federighi, 1965). However, the sensitivity of the technique to different chemical and physical variables has made quantitative analysis a difficult task. From the theoretical point of view, the interpretation of ER results for simple metals and alloys has been considered in terms of a pseudopotential formalism (for details see Rossiter, 1987).

The pioneering work by Simmons and Baluffi (Simmons and Baluffi, 1960a, 1960b) can be considered one of the most important contributions to the experimental study of vacancy formation under thermal equilibrium conditions. These authors combined ER measurements at high temperature with thermal expansion. This technique involves a determination of the differences between the relative change of the specimen length and the relative change of X-ray lattice parameter. It is important to mention that in this case the interpretation of the

experimental results is supported by a strong theoretical basis, that is the formula proposed by Eshelby (1955). The vacancy formation energy reported by Simmons and Baluffi (1960a) from equilibrium vacancy measurements was in the range of 0.74–0.76 eV, which was an excellent determination.

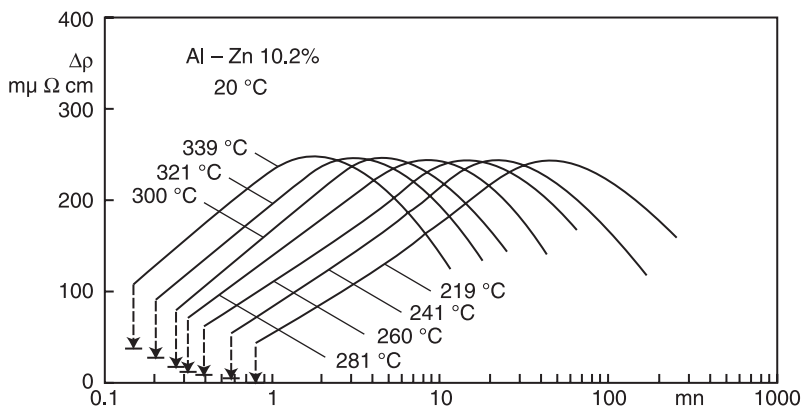
Solute-vacancy interactions in aluminium alloys

Non-equilibrium studies on defects produced by quenching have been performed since the 1950s. Specifically, investigations on solute-vacancy binding were based on measurements of bulk properties such as ER, internal friction and hardness. Indirectly, qualitative results have been supplied by transmission electron microscopy.

Most initial experimental information on solute-vacancy interactions was obtained by means of ER measurements, which were considered at that time to give the most accurate quantitative results. From these measurements, for instance, the disappearance by annealing of quenched-in vacancies in the presence of impurities could be observed (Damask and Dienes, 1960).

Regarding aluminium age-hardenable alloys, the principal effort was focused on the study of the early stages of precipitation. It was already known that in age hardenable alloys the rate of formation of pre-precipitates or ‘zones’ (representing a solute-rich and matrix-coherent cluster), was about 10^7 higher than that expected from the diffusion coefficients of the metals under consideration (Cu, Zn, Ag, Be, etc.). This discrepancy was attributed to the presence of excess quenched-in vacancies, which acted as vehicles for the transport of solute atoms (Seitz, 1952). This hypothesis was supported by Federighi (1958) and other authors using hardness and ER measurements. These pioneering works produced reliable estimates of the order of magnitude of the solute-vacancy binding energy. In the following section, some particular but illustrative examples are given.

Panseri and Federighi (1960) used ER measurements to study the early stages of ageing of Al-10 wt.%Zn. In Fig. 14.1, the ER $\Delta\rho$ as a function of the natural ageing time for different quenching temperatures (from 219°C to 339°C) is shown. It can be seen that the general trend of the resistivity-time curves consists of an initial increase, followed by a decrease. A similar behaviour was reported for other aluminium alloys like Al-Ag (Hashimoto, 1965). The initial resistivity increase was attributed to pre-precipitation phenomena during which small solute clusters are formed. The maximum values of $\Delta\rho$ are reached when the size of the solute clusters is of the same order of magnitude of the wavelength of the conduction electrons. Nowadays, it is clear that for the resolution available in the 1960s, the clusters were too small to be detected by TEM. The maximum of the $\Delta\rho$ values was reported to depend only on the ageing temperatures, and consequently on the number of clusters. In all cases, it was found that the characteristic time necessary to reach the maximum of each resistivity-time curve at room temperature decreases when the quenching temperature increases. This



14.1 Electrical resistivity of the Al-10wt. %Zn alloy as a function of the ageing time at room temperature for different quenching temperatures (after Panseri and Federighi, 1960).

result was attributed to the dependence of the quenched-in vacancy concentration on the quenching temperature. Therefore, an estimate of the vacancy formation energy was derived from the dependence of the different characteristic times to reach the respective resistivity maxima on the quenching temperature. Moreover, from isothermal ageing at different low temperatures, the migration energy of Zn atoms in Al was also determined.

The solute-vacancy interaction in Al-Cu alloys containing 1.7–3.9 wt.%Cu (Kimura et al., 1962) was also studied by ER. In this case, the authors paid attention to very short ageing times; i.e., to the early stages of precipitation, and thus physical information on the kinetics of pre-precipitation processes was obtained from the initial rate of ageing. An apparent vacancy formation energy (E_v^f) of 0.67 ± 0.06 eV and a binding energy (E_{v-Cu}^{Al}) between a copper atom and a vacancy of about 0.20 eV were reported. The E_v^f value estimated for these Al-Cu alloys is almost the same, within the experimental scatter, as that reported by Panseri and Federighi (1960) for Al-10 wt.%Zn (0.70 ± 0.02 eV). On the other hand, the binding energy of vacancies with zinc atoms ($E_{v-Zn}^{Al} \sim 0.06$ eV) reported by these authors is almost three times lower than that reported by Kimura et al. (1962) for Al-Cu alloys.

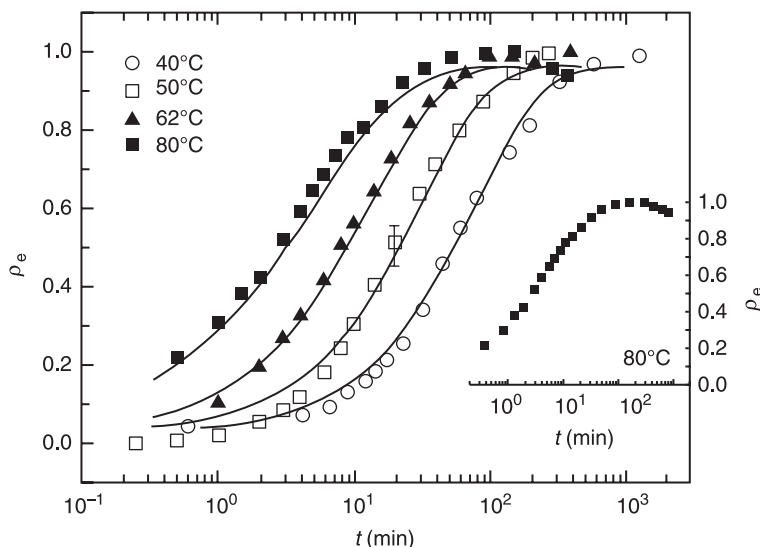
Murty and Vasu (1972), through a systematic resistometric investigation of different aluminium-silver alloys containing 0.2, 0.4, 0.6 and 1.3 wt.%Ag, reported values of the solute-vacancy binding energy (E_{v-Ag}^{Al}). In this work, the vacancy-Ag atom binding energy lay in the range of 0.09 to 0.13 ± 0.02 eV. This energy value is practically one half of that obtained by Hashimoto (1965) from ER, which is 0.25 ± 0.05 eV in binary and ternary Al-Ag-based alloys. The discrepancy in the binding energy values reported by Hashimoto and by Murty and Vasu was solved after a re-analysis of Hashimoto's data. A revised value E_{v-Ag}^{Al} between 0.13 and

0.14 eV was obtained, which is in good agreement with that reported by Murty and Vasu. The influence of a third element of known binding energy (0.01 wt.%Ge, 0.01 wt.%In, 0.1 wt.%Sb) on the ageing kinetics of some binary alloys was also analysed.

The Bangalore group (India) published various and very interesting articles on ER studies of clustering and solute-vacancy interactions in several aluminium alloys. Among these works, the works of Raman et al. (1971) and Das (1972) deserve special attention. In both cases, values of the solute-vacancy binding energy were obtained from the times taken to reach the resistivity peak. In the first paper (Raman et al., 1971), the authors reported values of the solute-vacancy binding energy for Ag, Be, Ce, Dy, Fe, Li, Mn, Nb, Pt, Sb, Si and Yb by measuring the effect of the addition of only 0.01 at.% of these elements on the clustering rate in the binary Al-4.4 at.%Zn alloy. It was very innovative to add to the well-studied Al-Zn system different minor alloying elements of the Periodic Table with particular characteristics. For instance, the atoms of Ag, Li, Nb, Pt and Sb possess similar size but different valency; Ce, Dy, Y and Yb have similar valency and size; and Be, Fe, Mn and Si have similar, but smaller sizes than Al and Zn, and have varying valencies. From the experimental viewpoint, the energy values reported were determined with an accuracy of ± 0.02 eV, which in some cases (Fe, Be, Dy) was not enough to be considered as a good estimation. In the second paper, Das (1972) reported results on the annealing of vacancies during isochronal and isothermal heat treatments in quenched Al-Zn, Al-Zn-Be, Al-Zn-Fe, Al-Zn-Mn and Al-Zn-Si alloys. The binary alloy, on which the ternary alloys were based, was the same as the previous work (Al-4.4 at.% Zn). From the vacancy formation and vacancy migration energies for each alloy, the corresponding solute-vacancy binding energies and information on the decomposition of the SSSS of the binary alloys containing ternary trace additions were obtained.

The development of theoretical models in the 1970s and 1980s (see for instance Rossiter and Wells, 1971; Hillel and Rossiter, 1981; Hillel, 1983) contributed significantly to the understanding of the evolution of ER during ageing and its relation to the formation of the clusters and GP zones in aluminium alloys, and this is discussed further in Section 14.3 (Modelling).

In recent years, ER studies have concentrated on the study of the early stages of ageing at low temperatures. Furthermore, ER measurements are now used jointly with other advanced experimental techniques to gain deeper understanding of precipitation phenomena in commercial aluminium alloys. For instance, Ferragut et al. (2002) used ER and SAXS (synchrotron light was used instead of X-ray tubes as in the classical works of Guinier and of Preston) to follow the early stages of pre-ageing in the Al alloy AA7012 at moderate temperatures. The temperatures of the pre-aging heat treatments were chosen near to room temperature, low enough to avoid the nucleation of incoherent particles. From isothermal measurements (see Fig. 14.2), and assuming that during pre-ageing, in the limit case of small pre-precipitates, the relative resistivity ρ increase could be



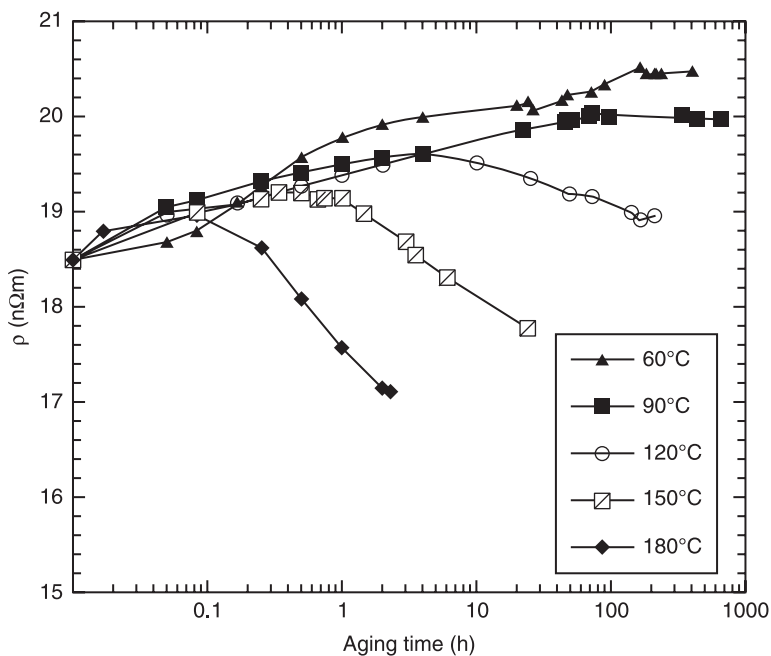
14.2 Isothermal pre-ageing curves of the relative resistivity ρ_e at different temperatures for samples of 7012 alloy quenched from 470°C. The full lines represent fits to the experimental data with the Johnson-Mehl-Avrami function (see text). The evolution of ρ_e during pre-ageing at 80°C is also shown in the inset figure (after Ferragut et al., 2002).

well described by means of the Johnson-Mehl-Avrami function, these authors derived an activation energy for the microstructural mechanism responsible for the formation of pre-precipitate particles. Furthermore, the parallel SAXS data demonstrated that the resistivity changes were correlated to an increase of the volume fractions of the structures formed. This process was associated with the migration of Mg-vacancy pairs in the Al-Zn-Mg-based commercial alloy.

Recently, ER was employed in combination with three-dimensional atom probe (3DAP) analysis to investigate the early stage decomposition of the Al alloy AA6111 (Esmaeili et al., 2007). The investigations were carried out in the temperature range 60–180°C, where ER initially increased with ageing time (see Fig. 14.3). 3DAP measurements provided information on the shape, number density and solute content of the precipitates, as well as the solute concentration of the matrix, for the ageing conditions corresponding to the resistivity maxima. As a conclusion, these authors reported that solute diffusion is not controlled by the formation of new vacancies but is assisted by the presence of excess vacancies associated with solute atoms.

Diffusion processes in aluminium and aluminium alloys

Point defects in metals were first considered in scientific literature to explain diffusional phenomena. These are basic to understand many reactions in metallic



14.3 The evolution of electrical resistivity during ageing in AA6111 in the temperature range 60–180°C (the authors thank Esmaili et al. (2007) and Taylor & Francis Ltd, <http://www.informaworld.com>)

systems, since diffusion limits the rate of phase transformations, solubility, grain growth, recrystallisation, etc.

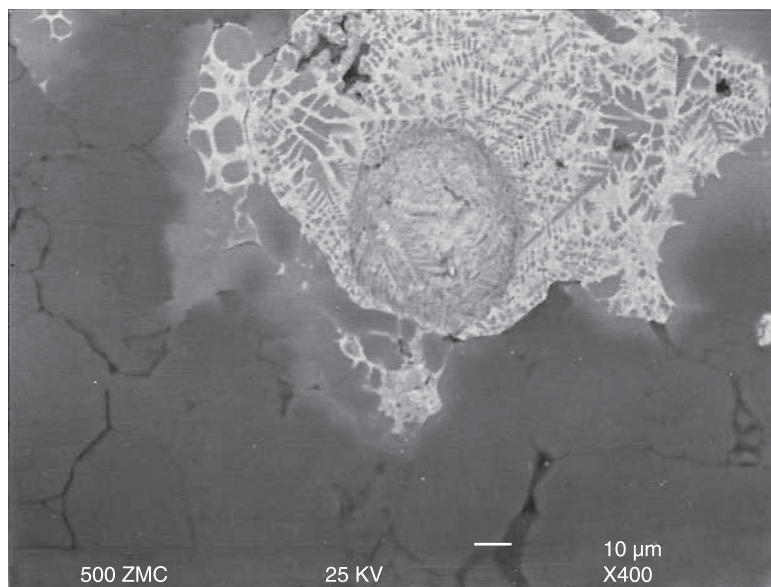
For some time, it has been well known that in aluminium age-hardenable alloys the formation of GP zones at low temperatures (near ambient temperature) following solution treatment and quenching occurs at a rate many orders of magnitude higher than that expected from the extrapolation of high-temperature diffusion data. Basically, the vacancies increase the solute diffusion rates, accelerating the nucleation processes of the precipitates or of their precursors (e.g. solute-vacancy clusters). It is also known that vacancies do not change the size of the stable nucleus, but increase the probability that early structures reach the critical stability size. In aluminium age-hardenable alloys the solute-vacancy binding energy is small enough to allow the vacancies that accompany solute atoms to the clusters to return to the Al matrix. This process is repeated until the vacancies are eliminated at sinks such as grain boundaries or dislocations. An interesting example is the formation of GP zones in Al-Zn-Mg alloys, wherein hardening continues indefinitely at near ambient temperatures. This vacancy behaviour was well described by the vacancy pump model (Girifalco and Herman, 1965) and more details are given in Section 14.3.

Diffusion processes are also critical in other kinds of kinetic metallurgical processes. For instance, very detailed work concerning the relationship between additive particle size and solubility in terms of its effects on transient liquid phase sintering and the development of microstructure in Al-based alloys was published by Lumley (1997) and Lumley and Schaffer (1998). Briefly, liquid phase sintering is an important industrial process in which, during sintering, the liquid phase flows between powder particles favouring the development of microstructural properties. It must be recalled that, when using liquid phase sintering, the liquid comes from the melting of additives or from the incipient melting of eutectics which are formed by diffusion. In non-ideal sintering systems, there is appreciable solid solubility of the additive in the base producing a preferential diffusive flow from the additive to the base element. For instance, Al-Cu alloys have non-ideal solubility conditions, i.e., the diffusivity of Cu into Al at 600°C is 0.63507 cm²/s (Lide, 1995) and Al into Cu is 0.07823 cm²/s (Mehrer, 1990). So, the faster diffusivity of the additive element (Cu) in the base (Al) enhances the homogenisation rate and reduces the amount of Cu available to form a liquid phase. As a result, both additive particle size and heating rate significantly alter the microstructural evolution of transient liquid phase sintered alloys. In particular, sintered alloys based on Al-Zn, Al-Mg and Al-Cu all exhibit this effect, and all have non-ideal sintering characteristics.

For example, an examination of the microstructural development of an Al-8Zn-2.5Mg-1Cu (wt.%) alloy during transient liquid phase sintering at 620°C was conducted using different ranges of (elemental) Zn particle sizes. Two major effects were observed to take place: (1) the temperature at which the maximum volume of liquid phase occurs apparently increases with increasing the average Zn particle size; and (2) coarser additive particles increase the quantity of liquid. As a result, a greater degree of particle and grain mobility is facilitated, causing improved sintering. Where a fine range of Zn powders were used, the sintering liquid acted only in the immediate vicinity of prior additive powders, whereas for the coarse and medium ranges the liquid phase infiltrated throughout the sample. However, the range exhibiting the most effective liquid phase (wide-spreading liquid acting across the whole sample) was developed from a broad particle size range. This size range combines the advantages of having some coarse additive powders with the localised effect of the fine additive powders (Lumley, 1997).

In Fig. 14.4, a typical backscattered SEM micrograph is shown of an Al-Zn-Mg-Cu alloy during sintering as the liquid phase reacts with the base aluminium powders. The microstructure reveals a light grey region around the particles which, in agreement with the literature (e.g. Mehrer, 1990, p. 404) was assigned to the enhanced diffusivity of Zn atoms in the Al matrix. This diffusional process precedes infiltration of the liquid phase throughout the prior particle boundaries.

One disadvantage of this phenomenon is that to achieve a well-sintered microstructure relatively large additive powder particles need to be added to the powder blends, which results in large secondary pore sizes (residual from the



14.4 Microstructure of an Al-8Zn-2.5Mg-1Cu alloy (wt.%) during sintering, obtained by backscattered SEM (after Lumley, 1997).

elemental additive particles) in the alloy. However, a solution to this problem was found to be to use a fine additive particle size combined with a high heating rate (e.g. placing the sample directly into a hot furnace). As a result, diffusion that would normally occur during heating to the sintering temperature was reduced, and the reaction between the additive and the base elements occurred at higher temperatures, meaning greater quantities of liquid phase were formed, improving the sintered microstructure while maintaining a smaller secondary pore size (Lumley and Schaffer, 1998).

14.2.3 Spectroscopic techniques

Microstructural analysis of the precipitation sequence using nuclear magnetic resonance

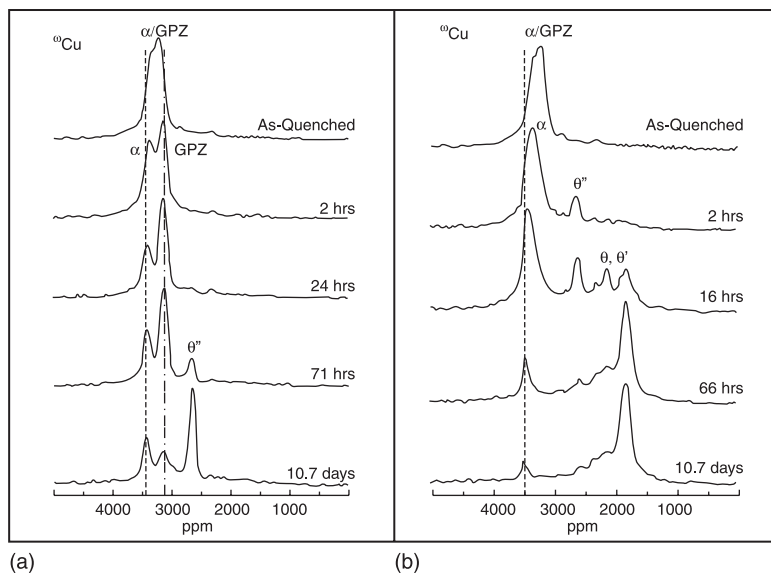
Nuclear spins are very suitable to probe the local distribution of internal magnetic fields and electric-field gradients in the vicinity of a solute atom in alloys systems. NMR is a Zeeman spectroscopy in which the magnetic sublevels m_i of the nucleus with spin I are split by an energy proportional to the magnetic field acting at the nucleus. This energy splitting can be detected by observing the absorption of electromagnetic radiation of an appropriate frequency using a NMR spectrometer in a strong magnetic field. The selected frequencies at which the spectrometer works depend on the nuclei used. Experimentally, spectra with different

characteristic lines are obtained. These lines are associated with different crystallographically distinguishable atoms. Details on this technique are given in Slichter (1990).

Since the 1960s, several works reported systematic investigations on copper alloys using NMR. For instance, Rowland (1960) reported the effects of various solute elements in a copper matrix. The quantitative experimental information was obtained from the ^{63}Cu NMR intensity behaviour. Other nuclei like ^{107}Ag and ^{109}Ag were used by Rowland (1962) to study silver alloys with many solute atoms. Since that time, NMR has been used as a very reliable nuclear experimental technique to study different kinds of alloys, such as those with simple or complex band structure and the ferromagnetic ones. However, the use of this technique is limited to certain alloys, since it is necessary to find a NMR-sensitive nucleus of one of the elements constituting the alloys, i.e., matrix or alloying elements.

In the specific case of aluminium age-hardenable alloys, only the Al-Cu-based systems are easily studied, since ^{63}Cu and ^{27}Al are available as adequate nuclei. Limitations also exist due to the use of powdered samples for analysis. However, NMR may provide an excellent examination of nearest neighbour information of selected atomic species. That is, it can provide information on the immediate environment surrounding atoms of an additive element. Recent studies on the microstructural evolution of Al-Cu-based alloys were performed by Bastow and Celotto (2003) and Bastow (2005) using an analytical method based on ^{63}Cu NMR spectroscopy. In these works, quantitative results on the precipitate phases present at different ageing stages of the SSSS decomposition were reported. A brief account of this study is reported here with the aim of showing the full capability of the NMR technique.

In Fig. 14.5(a) and (b), the ^{63}Cu NMR spectra corresponding to the Al-1.7at.% Cu aged at two different temperatures are represented as a function of the frequency resonance shifts (called Knight shifts), which are proportional to the applied magnetic field (Bastow and Celotto, 2003). The shift axis is given in parts per million (ppm) with respect to the Knight shift zero that is obtained with a well-known reference sample. As highlighted in the respective spectra, different phases of the precipitation sequence of this alloy were observed. The starting point was the as-quenched stage, which consists of a partially resolved doublet with minor intensity variations. The peak at higher shift was attributed to Cu in substitutional sites in the Al fcc α -phase and the peak at lower shift was assigned to GP zones. The selected ageing temperatures allow following the phase transformation at different rates. In Fig. 14.5(b), it should be noted that the higher temperature (190°C) is above the GP zone *solvus*. As can be seen, ^{63}Cu NMR revealed detailed information on the microstructure evolution of the alloy, identifying the different phases that are formed and their respective populations. The authors also used ^{27}Al NMR, but the dominant signal coming from the Al matrix did not reveal a distinguishable signal from the precipitates.



14.5 (a) ^{63}Cu NMR spectra from Al-1.7 at.%Cu aged at 130°C for the times indicated. The dotted lines show the shifts in the α and GPZ line shapes relative to their final positions. (b) ^{63}Cu NMR spectra from Al-1.7 at.%Cu aged at 190°C for the times indicated. The dotted line shows the shift in the α' line shapes relative to their final position (after Bastow and Celotto, 2003).

As mentioned above, the use of NMR is limited by the availability of adequate nuclei. Therefore, this technique cannot at present be easily extended to other Al-based age-hardenable systems of strong technological interest, like those containing Si, Mg or Zn as main alloying elements. As may be appreciated, NMR does not directly provide information on vacancies; rather it is best used as a complementary technique to other methods of analysis.

Studies of vacancy-like defects in pure aluminium using positron annihilation spectroscopy

PAS is a well-established high-sensitivity technique for detecting open volume sites in solids. It has been applied to the study of the defect structure in solids for almost 40 years, and is presently used in many fields of materials science. The physical principles of the study of lattice defects by PAS are discussed in Hautojärvi and Corbel (1995, pp. 491–528).

The PAS technique involves injecting positrons into a sample of alloy and observing the gamma rays that are emitted when a positron is annihilated in an encounter with an electron. The extreme sensitivity of PAS to vacancies, even in concentrations as low as 10^{-6} vacancies/atomic site, comes from the propensity of positrons to become easily trapped by any open volume defect that might

exist in pure metals and in alloys. Examples of open volume defects which may trap positrons include vacancies, vacancy clusters, vacancy-solute clusters, dislocations, stacking faults, incoherent dispersoids, misfit regions between matrix and precipitates, subgrain boundaries and grain boundaries. Trapping at open volume defects has two effects on the annihilation process: (1) it increases the average lifetime of the positrons; and (2) it changes the energy spectrum of the emitted gamma rays. The origin of the lifetime increase is that the probability of positron-electron encounters in empty atomic sites is reduced in comparison to the bulk solid. The effect on the gamma spectrum is related to the difference in the velocity distribution of the electrons that a positron may encounter when in the bulk or in a vacancy. The velocity of the electrons affects the gamma ray spectrum by the Doppler effect: faster electrons produce larger Doppler broadening of the annihilation line in the gamma spectrum, and slower electrons give less Doppler broadening. In the study of defects, PAS is normally used in two variants corresponding to the two different effects described above: PALS and coincidence Doppler broadening (CDB) spectroscopy.

PALS is the experimental technique by which the statistical distribution (spectrum) of positron lifetimes can be determined. The positron lifetime spectrum is a superposition of exponential decays, whose number corresponds to the number of different annihilation routes. An example that demonstrates the sensitivity of this technique to lattice defects and to the chemical composition of the material is shown in Fig. 14.6. The data were taken for well-annealed Al and Cu, also for cold-rolled Al (five per cent thickness reduction).

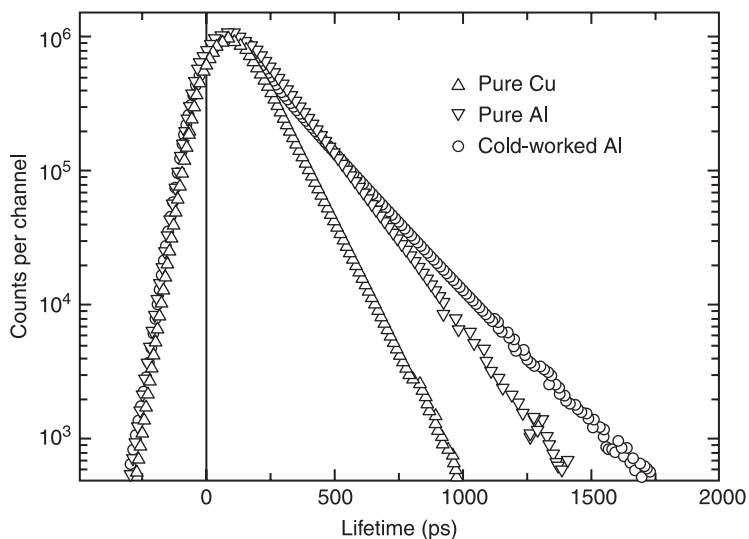
A value of 164 picoseconds (ps) was reported for the positron lifetime in well-annealed pure aluminium (Schaefer et al., 1987) while longer characteristic lifetime τ_{def} for a number of defects in pure Al is given in Table 14.1. Theoretical values of positron lifetimes in vacancy clusters are also included in the table.

PALS has also been used in the determination of the vacancy formation energy in pure Al by equilibrium measurements (Kim et al., 1974; McKee et al., 1972; Hall et al., 1974; Schaefer et al., 1987). The values given by the above authors are 0.71 ± 0.3 , 0.67 ± 0.3 , 0.69 ± 0.3 and 0.68 ± 0.3 eV, respectively.

CDB spectroscopy is the technique by which the shape of line at 511 keV is measured with very high signal-to-noise ratio by using two high-resolution semiconductor gamma spectrometers in coincidence. The annihilation line is broadened by the Doppler effect associated with the centre-of-mass motion of the annihilating electron-positron pair. The energy scale can be converted to momentum by the relationship:

$$P_z = \frac{E - 511 \text{ keV}}{c}$$

where p_z is the momentum component of the electron-positron pair along the axis of the spectrometer and c the velocity of light. The requirement of having low noise, i.e. few accidental background counts, is most important for studies aiming



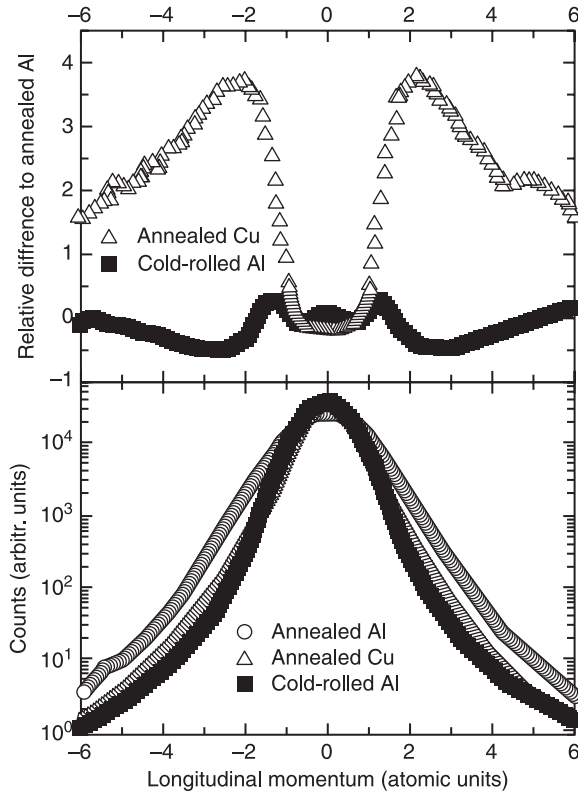
14.6 Comparison of experimental lifetime spectra for positrons annihilated in different metals: well-annealed Cu (up triangles); well-annealed Al (down triangles); cold-rolled Al (circles). The spectra were taken with a resolution of 190 ps (FWHM); background and source components are subtracted (after Dupasquier et al., 2004).

at identifying the chemical nature of the environment probed by the positron, since the most distinctive signal of the different atomic species is in the low count tails of the spectrum at high momentum. The sensitivity of the CDB technique to the presence of defects and to the chemical environment is evident in the data of Fig.14.7, showing a comparison between CDB spectra for well-annealed Cu, well-annealed Al and cold-rolled Al CDB spectra. In the upper frame of this figure, the spectra are reported as relative differences to the well-annealed Al case. This means of presentation, which has the virtue of enhancing the details in the high-momentum tails, is often adopted in CDB studies.

The relative difference curve for cold-rolled Al displays peaks at $p_L = \pm 1.3$ atomic units, which are due to the positron confinement in an atomic-size open

Table 14.1 Trapping coefficients and characteristic lifetimes of positrons trapped at defects in aluminium

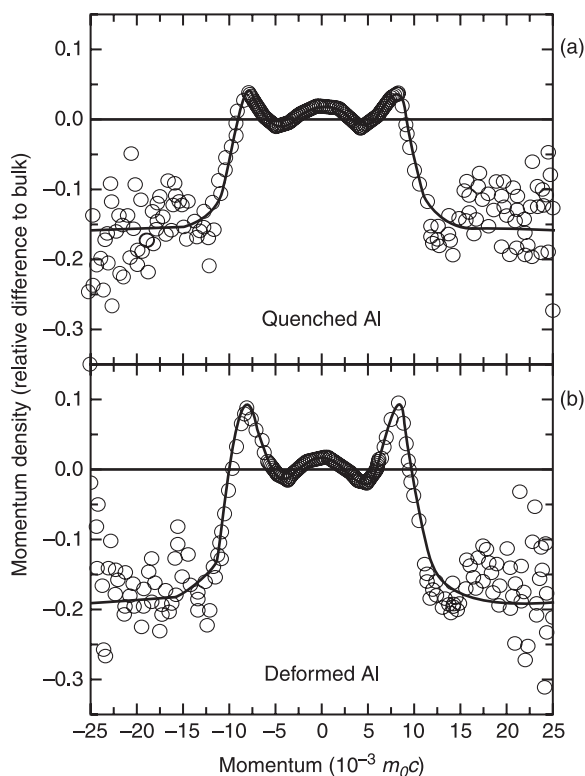
Defect species	τ_{def}	Reference
Vacancies	245–251 ps	(Hakkinen et al., 1990; Dupasquier et al., 1993)
Clusters of 7/16/35 vacancies	380/500/565 ps	(Puska and Nieminen, 1994)
Dislocations single slip/double slip/cold rolled	215/220/240 ps	(Hidalgo et al., 1992)



14.7 Doppler broadening of the positron–electron annihilation line from a CDB experiment. Lower panel: annealed Al (triangles), annealed Cu (circles), cold-rolled Al (solid squares). Upper panel: same data as above for Cu (triangles) and cold-rolled Al (solid squares), shown in terms of the relative difference to annealed Al (after Somoza et al., 2002).

volume (most probably, vacancies associated with dislocations). At high momentum, the curve becomes negative due to the decrease of the high-momentum contribution of Al core electrons. The Cu curve shows a strong structure peaking at $p_L = \pm 2.0$ atomic units, due to 3d and to core electrons; this is the ‘fingerprint’ that indicates the presence of Cu at annihilation sites in an alloy that contains copper.

An illustrative example of the capability of the CDB technique to distinguish different kind of open-volume defects introduced in pure aluminium is given in Fig. 14.8 (see details in Calloni et al., 2005). In this case, the comparison is between two pure Al samples, both containing open volume defects. In one sample (Fig. 14.8a), the defects were vacancies retained by quenching, and in the other



14.8 CDB spectra for defected pure Al (relative differences to well-annealed Al) (after Calloni et al., 2005). The solid lines are the result of a computation procedure (see Section 14.3).

the positron traps were vacancy-like defects associated with dislocations. As can be seen in the figure, the relative difference functions obtained measuring the thermal or mechanically treated samples show elements of similarity but they cannot be scaled to a common master curve. This issue is discussed in detail when dealing with the analysis of CDB data by *ab-initio* calculations in Section 14.3.

Studies of solute-vacancy complexes using positron annihilation spectroscopy

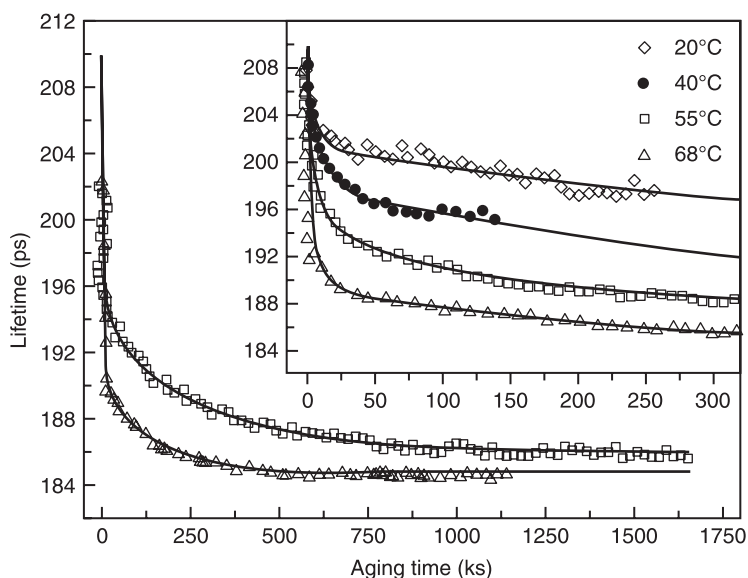
After the discovery of the sensitivity of positron spectra to the formation of GP zones (Dlubek et al., 1979), PAS has been intensively applied to study the role of vacancies and of vacancy-solute interactions in the ageing behaviour of aluminium alloys. In particular, PAS has been used to obtain information on the formation kinetics of vacancy-solute clusters in the early stages of ageing, on the propensity of solute atoms and aggregates to bind vacancies, and on the local chemistry next to open volumes. Critical reviews of this activity can be found in Dupasquier et al. (1998, 2004). A list of some of the most recent papers in this field comprises:

Honma et al. (2004), Čížek et al. (2005b), Bastow and Hill (2006), Melikhova et al. (2006), Staab et al. (2006), Dupasquier et al. (2007), Kaiser et al. (2007), Hautakangas et al. (2008), Staab et al. (2008), Ferragut et al. (2009) and Marceau et al. (2010). Furthermore, the presence of open spaces and solute at grain boundaries has been investigated in nanocrystalline Al-alloys prepared by severe plastic deformation, for example see Čížek et al. (2005b), Lechner et al. (2009) and Ferragut et al. (2009b).

Both PALS and CDB give useful information. PALS is well suited to follow the kinetics of the evolution processes taking place during isochronal or isothermal treatments of an alloy, whereas CDB is normally used for the chemical analysis of the site where the positron actually annihilates. In order to understand the information that can be drawn from PALS and CDB on vacancy-solute interactions in Al-based alloys it is instructive to see a few examples.

Due to the preferential annihilation of the positrons in open-volume defects, the evolution of the microstructure of an alloy may produce changes in the average positron lifetime observed by PALS. It is important to keep in mind, however, that such changes may have different origins, related to the number density of free vacancies and of vacancy-solute clusters, to their spatial distribution, to the chemical environment of the positron annihilation site. Therefore, the interpretation of PALS data in terms of microstructural properties of the alloy should always be guided by wisdom drawn from other analytical techniques. Examples of the combination of PALS with other techniques (CDB, TEM, DSC, SAXS, NMR, AP tomography) can be found in most of the references quoted above.

Fig. 14.9 shows PALS results (Somoza et al., 2000), regarding the decomposition of a SSSS of Al-4Cu-0.3Mg (wt.%). The curves depicted in this figure are positron lifetime isotherms taken in situ at moderate temperatures ($<70^{\circ}\text{C}$). Within these temperature limits, the microstructure of the alloy evolves by progressive formation of coherent solute aggregates (small disordered solute clusters in the early stages and metastable GP zones at later stages). Isolated vacancies migrate easily in Al, thus are not likely to be present after a few minutes at room temperature; however the high initial value of the positron lifetime tells us that in the freshly prepared SSSS a high density of vacancy-solute pairs or small clusters survives. When ageing proceeds and larger aggregates of solute are formed, it is possible that some quenched-in vacancies are annihilated or lost, but the data of the figure show that a large fraction of the initial vacancy population continues to exist after long ageing times as a component of metastable precipitate structures. The proof is that the asymptotic value of the positron lifetime is about 20 ps larger than that expected for an alloy without vacancies and is far too small for vacancies in Al (about 240 ps). On the contrary, it is rather near to the value expected for vacancies in Cu (about 190 ps). This suggests that the residual vacancies are probably in a Cu-rich environment, and is consistent with the hypothesis that they are trapped inside the GP zones. A quantitative determination of the chemical composition in contact with vacancies cannot be obtained from

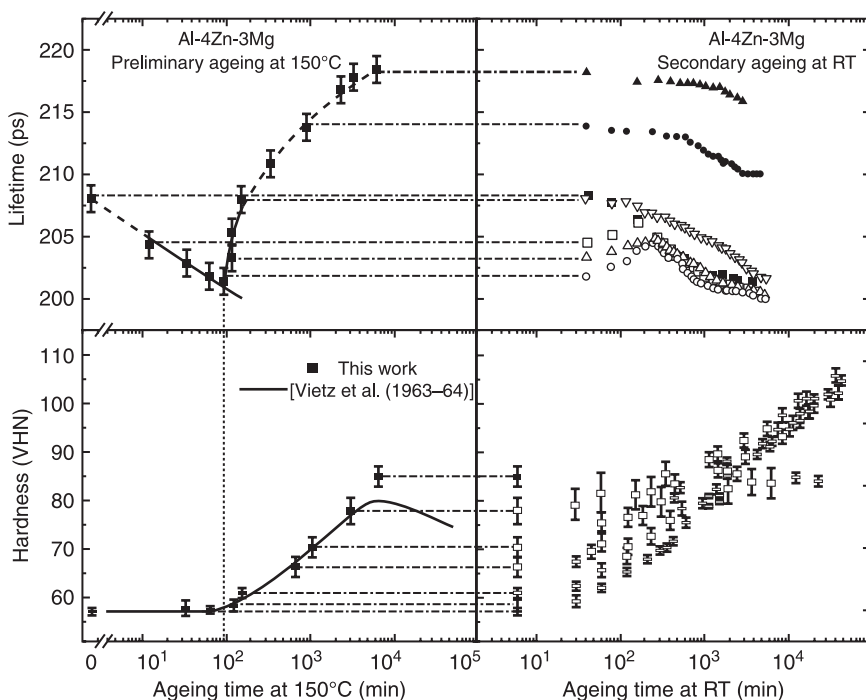


14.9 Positron average lifetime versus ageing time at fixed temperatures for Al-4%Cu-0.3%Mg (wt.%) (after Somoza et al., 2000).

PALS data, but information regarding the kinetics of the decomposition process can be drawn from the temperature dependence of the curves depicted in Fig. 14.9. It is important to note that all these curves can be reduced to a single master curve by proper time scaling. An Arrhenius plot of the scaling factors leads to the determination of the activation energy of the aggregation process, which is controlled by vacancy-assisted solute diffusion in the solid matrix.

Another example of PALS results, regarding a different physical situation and a different alloy (Al-4Zn-3Mg, in wt.%), is given in Fig. 14.10 (see Macchi et al., 2003). The upper left frame of this figure shows positron lifetime isotherms at 150°C. The curve has an initial decreasing branch that corresponds to the formation of coherent solute aggregates, similar to Fig. 14.9. Then a sharp kink is present, concomitant with the onset of hardening (see the lower left frame), which is then followed by the typical rising branch that is always observed when there is precipitation of a semicoherent or an incoherent phase. This latter effect is due to the formation of vacancy-like sites at the misfit interfaces between matrix and precipitates, and is believed to be related to the formation of the equilibrium T phase (see HRTEM results of Maloney et al., 2001). One clear advantage of the PALS technique therefore is that it clearly identifies when incoherent precipitation begins; it also shows that precipitation proceeds in two regimes, corresponding to the different slopes of the rising branch of the lifetime isotherm. It seems reasonable to attribute the steeper slope to nucleation and growth sustained by matrix supersaturation, while the following slower stage indicates dominant

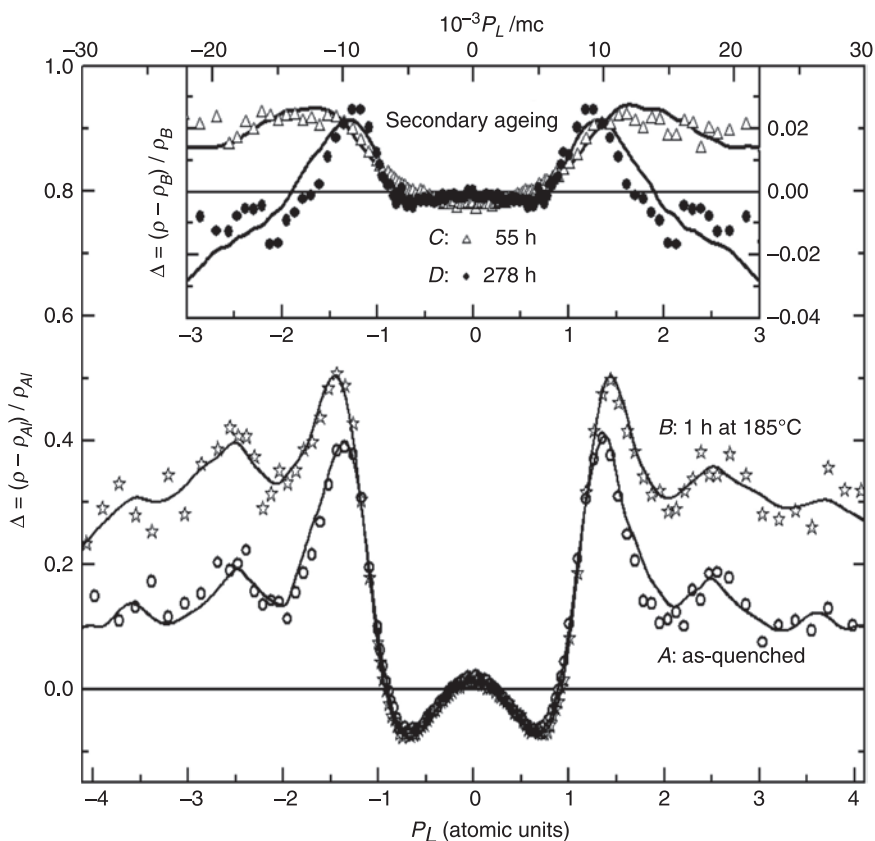
growth by coalescence. This conjecture is supported by the results shown in the upper right frame of Fig. 14.10. Here, the positron lifetime isotherms are taken at room temperature after a preliminary ageing at 150°C, which is interrupted at various times (starting point of the dashed lines connecting left and right frames). When the interruption of the preliminary ageing occurs in the first precipitation stage, the positron lifetime displays a non-monotonic behaviour and the hardness curves show an important secondary ageing effect (see Chapter 13). The initial rise of the room temperature lifetime isotherms indicates an increased probability of positron trapping and/or a change in the chemistry probed by the positron. This occurs because the vacancies released from the precipitates encounter sufficient solute in the matrix to promote the nucleation of small coherent solute aggregates, which are more efficient to trap positrons because they are more finely distributed than the larger, incoherent particles. A loss of vacancies eventually occurring after long ageing times might justify the final positron lifetime reduction. However, when the preliminary ageing is interrupted during the coalescence stage, the vacancies that leave the precipitates do not find enough solute to produce new aggregates and are lost. The lower right frame of Fig. 14.10 shows that no secondary hardening occurs in this case.



14.10 Positron lifetime and Vickers hardness versus ageing time at 150°C (left frames) and at room temperature after preliminary ageing at 150°C (right frames) for Al-4Zn-3Mg (wt.%) (after Macchi et al., 2003).

As shown in the previous section, CDB spectra are clearly sensitive to the chemical environment where the positron is annihilated. When positrons are trapped at vacancies, this environment is essentially given by the 12 nearest neighbours of the vacant lattice site. For a correct interpretation of the CDB data, one has to keep in mind that the chemistry of the local environment next to a vacancy buried in a tridimensional solute aggregate or at the edge of a precipitate does not necessarily reflect the average composition of the particle. Thus, CDB data are complementary to, and in general different from, the results of other analytical tools (e.g. AP tomography, see Chapter 12).

An example of CDB data for one Al alloy is in Fig. 14.11 (see Ferragut et al., 2009a), which displays variations in the momentum spectra of the annihilating electron-positron pairs occurring in Al-5.6Cu-0.45Mg-0.45Ag-0.3Mn-0.18Zr (wt.%) when artificially aged for 1 hour at 185°C, then left at room temperature



14.11 CDB spectra for Al-5.6Cu-0.45Mg-0.45Ag-0.3Mn-0.18Zr (wt.%). The solid lines are linear combinations of CDB spectra measured for pure elements (after Ferragut et al., 2009a).

for long times. The fitting curves through the experimental points are obtained as linear combinations of the CDB spectra obtained for the pure constituents of the alloy. The coefficients of the linear combinations give an approximated evaluation of the fraction of positrons that are trapped by vacancies and of the concentration of each element in contact with the vacancies (Somoza et al., 2002; Folegati et al., 2007). The results of this analysis for the curves shown in Fig. 14.11 are reported in Table 14.2, together with the results of the PALS measurements performed with the same samples.

The concentration values reported in Table 14.2 as ‘expected’ are derived from the hypothesis that the nearest neighbour positions of a vacant atomic site that are not occupied by Al atoms are divided amongst the other elements in proportion to their atomic concentration. A positive difference between a measured concentration value and the corresponding expected value is an indication of preferential binding between the vacancy and the specific element. The data reported in the last column of Table 14.2, for instance, demonstrate a strong preferential binding between vacancies and Ag atoms that makes the contact vacancy-Ag well above the statistical value even when the solute is well dispersed in the matrix. On the contrary, the vacancy-Mg contact is low after quenching, when only isolated vacancy-solute pairs or small clusters are present, consistent with the prediction of a negative vacancy-Mg binding energy (Wolverton, 2007). However, the vacancy-Mg contact becomes high when Mg is included in the larger solute aggregates formed after ageing at elevated temperature.

14.3 Modelling

14.3.1 Introduction

A modern approach to the understanding of the nucleation and precipitation processes requires the use of computer simulations at atomic scale. In the previous section, experimental studies of aluminium and age hardening alloys carried out using conventional and non-conventional techniques were presented. This section is devoted to the discussion of different theoretical approaches to the analysis of various aspects basically linked to the early stages of the precipitation sequence: atom dynamics during nucleation and growth of solute clusters; solute-vacancy binding and formation of solute/microalloying elements/vacancy clusters. It is worth mentioning that aluminium has often been used as a test case for developing the computational methodology in materials science. Therefore, the concepts presented in this section are certainly valid for other metallic systems. As may be appreciated, it is only in a relatively few cases that calculations derived from models would be expected to replace experiments as a major source of information for properties of materials. One example where significant potential does exist is in determination of the phenomenological aspects of solute-vacancy binding in Al. First-principle calculations may also be used to further improve the interpretation of

Table 14.2 Results of PALS and CDB measurements on Al-5.6Cu-0.45Mg-0.45Ag-0.3Mn-0.18Zr (wt.%)

Sample	Sequence of thermal treatments			Positron mean lifetime (ps)	Positron trapping fraction (%)	(b) Fractional atomic concentrations at vacancies (at. %)				
	Solution treatment + quenching	Ageing 185°C (h)	Dwell time at 22°C (h)			Al	Cu	Mg	Ag	
A	Yes	0	0	214	89	74 (74)	19 (21.0)	2 (4.2)	5 (0.8)	←Measured ←Expected
B	Yes	1	0	193	66	45 (45)	29 (44.3)	18 (8.9)	8 (1.8)	←Measured ←Expected
C	Yes	1	55	194	65	43 (43)	30 (46.0)	18 (9.2)	9 (1.8)	←Measured ←Expected
D	Yes	1	278	203	72	49 (49)	26 (41.1)	15 (8.2)	10 (1.7)	←Measured ←Expected
(a) Nominal atomic concentrations (not including Mn and Zr)										

the experimental data obtained measuring positron–electron annihilation momentum distributions.

14.3.2 Vacancies in pure aluminium

The density functional theory is a versatile method used in condensed matter physics to calculate the electronic structure of many-body systems and all the properties that are governed by electron interactions (Hohenberg and Kohn, 1964 and Kohn, 1999). The aluminium properties (lattice constant, bulk modulus and cohesive energy) are almost exactly reproduced by different approximations (local density approximation, LDA, and generalised gradient approximation, GGA) of the density functional theory. The GGA approximation was used by Carling et al. (2000) to calculate the vacancy formation energy in Al, with excellent agreement with the available experimental data (see Table 14.3). Furthermore, they discussed the physical origin of the non-linearity that is observed in the Arrhenius plot of the vacancy concentration, a behaviour that is consistently observed by differential dilatometry measurements at high temperature, as well as by self-diffusion and positron annihilation lifetime techniques. The curvature of the Arrhenius plot had been tentatively explained as being the result of the formation of divacancies. In fact, Carling et al. (2000) showed that divacancies are thermally unstable in Al; thus the non-linear behaviour was attributed to anharmonicities of the atomic vibrations in the vacancy environment. This subject has been re-discussed recently by Koning et al. (2004) and Ramos de Debiaggi et al. (2006) on the basis of molecular static and molecular dynamics calculations using embedded atom interatomic potentials. The non-linearity of the Arrhenius plot was assigned to a joint contribution of vacancies, anharmonics effects and self-interstitials.

Table 14.3 Experimental and theoretical values of the vacancy formation energies E_V^f .

Method	E_V^f (eV)	Reference
Experimental (ER and thermal expansion)	0.74–0.76	(Simmons and Baluffi, 1960a)
Experimental (PAS)	0.71 ± 0.3	(McKee et al., 1972)
Experimental (PAS)	0.67 ± 0.3	(Kim et al., 1972)
Experimental (PAS)	0.69 ± 0.3	(Hall et al., 1974)
Experimental (PAS)	0.68 ± 0.3	(Schaefer et al., 1987)
Experimental (NMR)	0.66 ± 0.3	(Gullion and Conradi, 1987)
Calculation (LDA)	0.76	(Carling et al., 2000)
Calculation (GGA)	0.69	(Carling et al., 2000)

The experimental data were obtained using different techniques as indicated in the table. The theoretical energy values are evaluated using the local-density approximation (LDA) and the generalised gradient approximation.

14.3.3 Solute-vacancy binding energies in alloys

The solute-vacancy binding energy is a key parameter in controlling the diffusion of the solute, thus the formation of precipitates that determine the mechanical properties. In spite of the abundance of experimental data on solute-vacancy binding for several atomic species in Al, an important reason to develop calculations of the same parameter is that there is often disagreement amongst experimental data. It is clear that accurate measurement techniques are not easily developed, and the Mg-vacancy binding energy is a typical case; for a review see Mondolfo (1976).

Wolverton and co-workers [see for instance Ravi and Wolverton (2004), Wolverton and Ozolinš (2006) and Wolverton (2007)] have implemented a method based on first-principle atomistic calculations in the framework of the density functional theory using a well-known software code (Vienna *ab-initio* Simulation Package – VASP) that was developed for different calculations in condensed matter. Detailed information regarding the calculations is given in Wolverton and Ozolinš (2006). The results of the calculations for solutes like Mg, Cu, Ag, Zn and Si are in very good agreement with the data that come from the most accurate experiments. In a second step, binding energies for solute atoms for which experimental data are not available were predicted. The first-principle calculations provide information on physical factors that affect binding, like the effect of the solute atom size. For example, these authors concluded that larger atoms tend to bind more strongly with vacancies, independently if the solutes are in the same row or column in the periodic table. This behaviour is not applicable to transition 3d metals, which require an explanation in terms of the electronic structure band filling effects.

Mantina et al. (2009) also used the density functional theory to predict the impurity diffusion coefficients of Mg, Si and Cu in dilute fcc Al alloys.

14.3.4 Growth of solute clusters

The predictive power of the calculations has been applied not only to the study of formation and binding of vacancies, but also to modelling of solute cluster formation. The ternary cluster expansion description, which is different from the direct first-principle calculations where the structure has to be specified in advance, was used to study the formation of the first precipitates that form from a solid solution, i.e., GP zones in the Al-Mg-Si system (Sandberg et al., 2007). This topic remains contentious in this family of alloys.

In the mid-1960s, Girifalco and Herman (1965) developed a kinetic model for the growth of GP zones in Al-based alloys. Assuming that excess quenched-in vacancies were responsible for the high rates of formation of GP zones, the model proposed the growth of spherical GP zones as a consequence of the diffusion of solute-vacancy complexes to the zones. Briefly, under certain favourable physical conditions the so-called vacancy pump model assumed that, when solute-vacancies complexes reach the GP zone-matrix interface, they release the

vacancies. The new free vacancies contribute to enhance a vacancy gradient which is directed radially outward from the zone-matrix interface. It was considered that this gradient was responsible for driving vacancies away from the zone and back into the matrix where new solute-vacancy complexes are formed. This model was satisfactorily tested with ER measurements on a Zn-rich Al-Zn alloy. Some time later Ipohorski and Bonfiglioli (1970) tried to test the model using SAXS to characterise the GP zones in Al-10%Zn and Al-10%Zn-0.1%Mg (wt.%). Although at that time the SAXS technique did not give accurate results on the early stages of GP zones formation, it was possible to obtain a radius growth law of such zones during ageing. The authors of this paper found that the parameters obtained were in good agreement with those predicted by the vacancy pump model. However, some issues remained unclear such as the importance of adopting an oversimplified image of the solid solution behaviour.

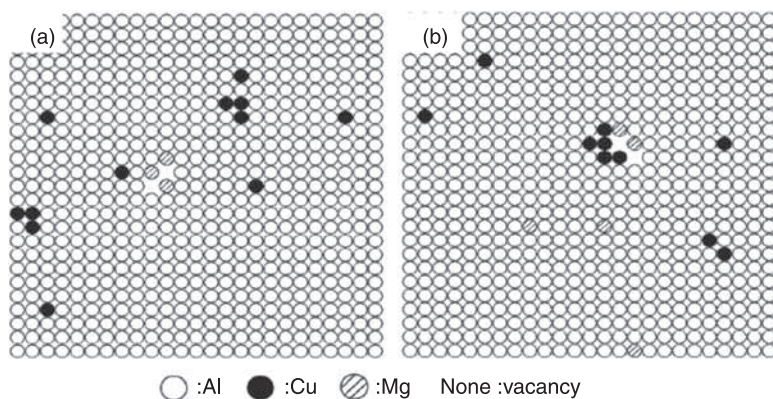
Sha and Cerezo (2005) simulated the early stages of precipitation in a commercial Al-Zn-Mg-Cu alloy using a simple vacancy jump model for atomic diffusion. The computation was carried out using a kinetic Monte Carlo (KMC) technique jointly with high-resolution imaging 3D-AP experimental technique. The results give some responses on how cluster chemistry evolves during the early stage of precipitation and also allow establishment of the link between the early stages of clustering (GP 1 in this alloy) and further precipitation of metastable phases (e.g. η'). Besides, the KMC model presents a reasonably good simulation of the physical processes taking place during the ageing of the alloy. Computations via KMC also permitted a deeper analysis of the decomposition process of the SSSS in the early stages of ageing. As a result, detailed information on the mechanisms of nucleation and growth of solute clusters was determined that could not be obtained experimentally.

14.3.5 Solute-vacancy interaction

Sato and co-workers (see for instance, Sato, 2000; Sato et al., 2003) used Monte Carlo step (MCS) simulation to address the role that microalloying elements play in the microstructural evolution of the alloys submitted to ageing treatments. The computation gives evidence of the interaction of microalloying elements and quenched-in vacancies during the early stages of ageing. Specific information on the simulation procedure is given in the above-mentioned papers, but in brief the MCS computation can be explained as follows. The pair interactions among solute/microalloying element/vacancy are quantified by a set of ordering parameters derived from known thermodynamic quantities and from phase diagrams, which are introduced as input data together with the activation energies for vacancy formation and migration. In the initial configuration, all the lattice sites are occupied at random by the base element (aluminium), solute atoms and vacancies. Then, the solute and the vacancies are left to diffuse and form clusters. The evolution of the structure is followed by evaluating a number of relevant

parameters (e.g. residual concentration of solute in the matrix, degree of short-range order, number density and average diameter of the solute clusters) as a function of the number of steps of the MC computation. The papers by Sato and co-workers cited above report results for Al-Cu, Al-Zn, Al-Li-Cu and Al-Mg-Si alloys, and include experimental data obtained using ER, hardness, DSC, TEM and 3DAP techniques. The case of Al-2.5at.% Cu with 0.3 at.% Mg as a microaddition (Sato et al. 2003) is presented here as an example. The ordering parameter that quantifies the Mg-vacancy interaction was taken about -8 kJ/kmol; the negative value indicates preferential binding of vacancies to Mg atoms, an assumption that perhaps should be revised on account of more recent first-principle calculations (Wolverton 2007). The diffusion of solute was realistically modelled by vacancy migration at 273 K with an initial concentration of free vacancies of 1.5×10^{-4} . Some results of the computation are reported in Fig. 14.12, which shows the two-dimensional atom arrangement on the (100) plane after 1.5×10^6 MC steps. Figure 14.12(a) demonstrates that vacancies are preferentially trapped by Mg atoms with a consequent decrease in the number of free vacancies and a decreased diffusion of Cu atoms. Figure 14.12(b) shows that Cu tends to form co-clusters with Mg-vacancy complexes. From this result, it was concluded that Cu/Mg/vacancy complex clusters act as effective nucleation sites for GP zones and that the formation of Mg-vacancy pairs retards the clustering of Cu atoms through the vacancy trapping mechanism.

In summary, the results of MCS simulations indicate that, in the initial stage of ageing at 273 K, some microalloying elements preferentially trap quenched-in excess vacancies and retard cluster formation. It was also found that the complex clusters of solute/microalloying element/vacancy are formed during the subsequent ageing stage and that they act as effective nucleation sites for clusters and GP zones.



14.12 Examples of atom arrangements on the (001) plane simulated for 5×10^6 MCS at 273 K: (a) vacancy trapping, and (b) Cu/Mg/vacancy complex clusters (after Sato et al., 2003).

14.3.6 First-principle calculations in positron annihilation spectroscopy

The interpretation of the positron annihilation experimental data needs the support of theoretical methods with quantitative predicting power. The density functional theory, applied within the LDA and GGA schemes, allows reliable predictions of positron lifetimes in bulk solids or for positrons trapped in vacancies, agglomerates of vacancies or dislocations (see Table 14.1). A review of this topic was reported by Puska and Nieminen (1994). The experimental detection of divacancies in pure aluminium near the melting point by PALS was a matter of discussion in the mid-1970s. In fact, positron lifetimes for clusters of vacancies ($n > 2$) cannot be experimentally determined. So, first-principle calculation becomes a fundamental tool to predict positron lifetimes in agglomerates.

In the case of Al-based alloys, a first-principle calculation based on the density functional theory has been recently performed for the positron lifetime for vacancy-Cu complexes in an aluminium matrix. While the lifetime measured in Al-Cu was around 210 ps (Marceau et al., 2006), the calculated value reported by Folegati et al. (2007) decreases from 227 to 210 ps when the number of Cu atoms surrounding the vacancy increases from 0 to 8, then rises again up to 236 ps when all the 12 nearest neighbour positions are occupied by Cu. The reason for this non-monotonic dependence is the relaxation of the local atomic structure, which depends not only on the number of the Cu atoms around the vacancy but also on the geometrical configuration of the complex. These results suggest that PALS is not the most adequate positron technique to analyse the fractional concentrations of solute atoms in contact with vacant atomic sites.

The density functional theory has been used to calculate the momentum density of the annihilating positron–electron pairs, which is experimentally accessible via Doppler broadening measurements (see Section 14.2.3). This topic is further developed in a review article by Barbiellini (2001). A comparison between experimental data and theoretical predictions for open volume defects in pure Al was reported by Calloni et al. (2005). In this work, which has already been mentioned in Section 14.2.3, the defects were introduced either by quenching from high temperature or by cold-working. The different distributions obtained in the two cases are shown in Fig. 14.8. The solid lines in this figure are the result of the first-principle calculation (density functional theory with local density approximation). As can be seen, the computation shows a very good agreement with the experimental data. The clear differences between the distributions of the two families of defects come from the extension of the open volume seen by positrons (i.e., quenched-in vacancies or vacancy-like defects associated with dislocations). These results show that the CDB technique is also sensitive to the local geometry of the open-volume defects, which adds to the well-known sensitivity to the local chemistry at the annihilation site.

As mentioned in Section 14.2.3, the electron–positron momentum distributions measured by the CDB can be used to obtain information on the atomic composition

in immediate contact with the vacancy where the positron is trapped (i.e., chemical composition of the vacancy-impurity complexes). Recently, Folegati et al. (2007) reported first results on *ab-initio* electronic structure calculations for vacancy-solute complexes in the same systems experimentally studied by Somoza et al. (2002). The aim of this work was to study the possibility of quantitative analysis of solute-vacancy complexes in metallic alloys. A specific goal was to test the reliability of the concentration values obtained by the linear combination method by Somoza et al. (2002) as revised by Ferragut (unpublished, cited in Folegati et al., 2007), which has been mentioned in Section 14.2.3. Thus, the authors modelled the solute-vacancy complexes in binary Al-Cu, ternary Al-Mg-Cu and quaternary Al-Mg-Cu-Ag alloys. It was found that the linear combination method gives an accurate reproduction of the theoretical spectra and that the coefficient of the linear combination are in fair agreement (typically, better than 10%) for atoms having occupied *d* atom shells, such as Cu and Ag. On the contrary, it was reported that the distinction between the contribution to the CDB spectra of the elements adjacent in the periodic table, such as Mg and Al, could be difficult.

14.4 Conclusion

Different aspects related to vacancies processes in pure aluminium and aluminium-based age-hardenable alloys have been presented. Results obtained using both traditional (e.g. ER, thermal expansion, transmission electron microscopy) and new experimental techniques (e.g. PAS, NMR), together with theoretical approaches (first-principle calculations, Monte Carlo simulations) have been reviewed. As a conclusion, the following points deserve to be highlighted:

- (1) Concerning the formation of vacancies and their migration in pure aluminium: Results obtained from equilibrium and non-equilibrium measurements allow a determination of vacancy formation and vacancy migration energies. Energy values obtained using ER and thermal expansion techniques are about 10% above those reported from the use of more sensitive and specific tools for vacancy detection and identification like PAS.
- (2) Concerning solute-vacancy interactions, solute transport and clustering, and precipitation sequences in alloys: These kinetic processes were analysed following the decomposition of the SSSS in which the quenched-in vacancies play an important role, principally during the early stages of ageing. Advanced imaging techniques offer high-quality experimental information on the different structures formed during ageing. However, they cannot directly give evidence on the role of vacancies in the solute transport during the formation of the different intermediate and final nanostructures. Since the early 1960s, experimental information on phenomena involving vacancies in aged aluminium alloys such as binding energy values has been mainly obtained by ER measurements. Now, qualified information on solute clustering and the

formation of solute-vacancy complexes is mostly obtained using PAS. This technique and NMR give detailed knowledge about the further formation of metastable and stable phases in aluminium age-hardenable alloys. Additionally, positron techniques give unique information on the chemistry of the local environment next to a vacancy.

Modelling deserves special attention. Theoretical approaches to the phenomena mentioned in (1) and (2) give valuable complementary information and guide the interpretation of the experimental results. In some cases, the scarcity of reliable experimental data means models and first-principle calculations become the main source of quantitative information regarding specific mechanisms.

14.5 Acknowledgements

Alberto Somoza wishes to acknowledge Emeritus Professor Ian Polmear (Department of Materials Engineering, Monash University, Melbourne, Australia) and Dr Roger Lumley (CSIRO, Light Metals Flagship, Melbourne, Australia) for many stimulating discussions on different topics presented in this chapter.

14.6 References

- Balluffi R.W., Allen S.M. and Craig Carter W. (2005), *Kinetics of Materials*, Hoboken, Wiley-Interscience.
- Barbiellini B. (2001), *New Directions in Antimatter Chemistry and Physics*, in Surko C.M. and Gianturco F.A. (Eds.), the Netherlands, Kluwer Academic Publishers, pp. 127–150
- Bastow T.J. (2005), ‘ ^{63}Cu NMR analysis of microstructure evolution in Al-Cu-Mg alloys’, *Philosophical Magazine*, 85, 1053–1066.
- Bastow T.J. and Celotto S. (2003), ‘Structure evolution in dilute Al-Cu alloys observed by ^{63}Cu NMR,’ *Acta Materialia*, 51, 4621–4630.
- Bastow T.J. and Hill A. (2006), ‘Early stage hardening in AlCuMg alloy studied by ^{63}Cu nuclear magnetic resonance and positron annihilation’, *Materials Science Forum*, 519–521, 1355–1360.
- Cahn R.W. (2001), *The Coming of Materials Science*, 1st Ed., Oxford, Pergamon Materials Series, Pergamon.
- Cahn R.W., Haasen P. and Kramer E.J. (1991), *Phase Transformation in Materials in Materials Science and Technology: A Comprehensive Treatment* (vol. 5), New York, VCH Publishers.
- Calloni A., Dupasquier A., Ferragut R., Folegati P., Iglesias M.M., Makkonen I. and Puska M.J. (2005), ‘Positron localization effects on the Doppler broadening of the annihilation line: Aluminum as a case study’, *Physical Review B*, 72, 054112.
- Carling K., Wahnström G., Mattson T.R., Mattsson A.E., Sandberg N. and Grimvall G. (2000), ‘Vacancies in Metals: From first principles calculations to experimental data’, *Physical Review Letter*, 85, 3862–3865.
- Čížek J., Prochazka I., Kuriplach J., Stulikova I. and Vostry P. (2005a), ‘Annealing process in quenched Al-Sn alloys: A positron annihilation study’, *Physical Review B*, 71, 064106.

- Čížek J., Procházka I., Smola B., Stulikova I., Kuzel R., Cieslar M., Matej Z., Cherkaska V., Brauer G., Anwand W., Islamgaliev R.K. and Kulyasova G. (2005b), 'Positron annihilation studies of microstructure of ultra fine grained metals prepared by severe plastic deformation', *Materials science forum*, 482, 207–210.
- Damask A.C. and Dienes G.J. (1960), 'Theory of vacancy annealing in impure metals', *Physics Review*, 120, 99–104.
- Das E.S.D. (1972) 'Resistometric studies of clustering and solute-vacancy interactions in aluminium alloys (Al-Zn, Al-Zn-Be, Al-Zn-Fe, Al-Zn-Mn and Al-Zn-Si)', *Scripta materialia*, 6, 187–190.
- Deschamps A., Bréchet Y., Guyot P. and Livet F. (1997), 'On the influence of dislocations on precipitation in an Al-Zn-Mg alloy', *Zeitschrift für Metallkunde*, 88, 601–606.
- Deschamps A., Dumont, M., Lae J. and Bley F. (2006) 'Use of small-angle X-ray scattering for the characterisation of precipitates in aluminium alloys', *Materials science forum*, 519–21, 1349–1354.
- Detemple K., Kanert O., De Hosson J.Th.M. and Murty K.L. (1995), 'In-situ nuclear magnetic resonance investigation of deformation-generated vacancies in aluminium', *Physical Review B*, 52, 125–133.
- Dlubek G., Kabisch O., Brümmer O. and Löffler H. (1979), 'Precipitation and dissolution processes in age-hardenable Al-alloys. A comparison of positron annihilation study and X-ray small-angle scattering investigations', *Physica Status Solidi (a)*, 55, 508–518.
- Dumont M., Lefevre W., Doisneau-Cottignies and Deschamps A. (2005), 'Characterisation of the composition and the volume fraction of η' and η precipitates in an Al-Zn-Mg alloy by a combination of atom probe, small-angle X-ray scattering and transmission electron microscopy', *Acta Materialia*, 53, 2881–2892.
- Dupasquier A., De Diego N., Folegati P., Somoza A. (1998), 'Current positron studies of structural modifications in age-hardenable metallic systems', *Journal of Physics: Condensed Matter*, 10, 10409–10422.
- Dupasquier A., Ferragut R., Iglesias M.M., Massazza M., Riontino G., Mengucci P., Macchi C. and Somoza A. (2007), 'Hardening nanostructures in an AlZnMg alloy', *Philosophical Magazine A*, 87, 3297–3323.
- Dupasquier A., Kögel G. and Somoza A. (2004), 'Studies of light alloys by positron annihilation techniques', *Acta Materialia*, 52 4707–4726.
- Dupasquier A., Romero R. and Somoza A. (1993), 'Positron trapping at grain boundaries', *Physical Review B*, 48, 9235–9245.
- Eshelby J.D. (1955), 'The elastic interaction of point defects', *Acta Metallurgica*, 3, 487–490.
- Esmaili S., Vaumousse D., Zandbergen W., Poole W.J., Cerezo A. and Lloyd D.J. (2007), 'A study on the early-stage decomposition in the Al-Mg-Si-Cu alloy AA6111 by electrical resistivity and three-dimensional atom probe', *Philosophical Magazine*, 87, 3797–3816.
- Federighi T. (1958), 'Quenched-in vacancies and rate of formation of zones in aluminium alloys', *Acta Metallurgica*, 6, 379–380.
- Federighi T. (1965), *Lattice Defects in Quenched Metals*, in Cotterill R.M., Ooyama M., Jackson J.J. and Meshii M. (Eds.), New York, Academic Press.
- Ferragut R., Dupasquier A., Macchi C.E., Somoza A., Lumley R.N. and Polmear I.J. (2009), 'Vacancy-solute interactions during multiple-step ageing of an Al-Cu-Mg-Ag alloy', *Scripta Materialia*, 60, 137–140.
- Ferragut R., Liddicoat P.V., Liao X.Z., Zhao Y.H., Lavernia E.J., Valiev R.Z., Dupesquier A. and Ringer S.P. (2009b), 'Chemistry of grain boundary environment in nanocrystalline Al 7075', *Journal of Alloys and Compounds* (in print – published online doi:10.1016/j.jallcom.2009.10.104)

- Ferragut R., Somoza A. and Tolley A. (1999), 'Microstructural Evolution of the 7012 Alloy During the Early Stages of Artificial Ageing', *Acta Materialia*, 47, 4355–4364.
- Ferragut R., Somoza A. and Torriani I. (2002), 'Pre-precipitation study in the 7012 Al-Zn-Mg-Cu alloy by electrical resistivity', *Materials Science and Engineering A*, 334, 1–5.
- Folegati P., Makkonen I., Ferragut R. and Puska M.J. (2007), 'Analysis of electron-positron momentum spectra of metallic alloys as supported by first-principles calculations', *Physical Review B*, 75, 054201.
- Friedel J. and Guinier A. (1963), *Metallic Solid Solutions*, New York, W. A. Benjamin Inc.
- Girifalco L.A. and Herman H. (1965), 'A model for the growth of Guinier-Preston zones – the vacancy pump', *Acta Metallurgica*, 13, 583–590.
- Gullion T.W. and Conradi M.S. (1987), 'Separate migration and formation energies of vacancies in aluminum measured by NMR', *Physical Review B*, 36, 3880–3883.
- Hakkinen H., Mäkinen S. and Manninen M. (1990), 'Edge dislocations in fcc metals: Microscopic calculations of core structure and positron states in Al and Cu', *Physical Review B*, 41, 12441–12453.
- Hall T.M., Goland A.N. and Snead C.R. jr (1974), 'Applications of positron-lifetime measurements to the study of defects in metals', *Physical Review B*, 10, 3062–3074.
- Hashimoto F. (1965), 'Interaction between a vacancy and an Ag atom in aluminium', *Journal of Physical Society of Japan*, 20, 336–346.
- Hautakangas S., Schut H., van Dijk N.H., Rivera Díaz del Castillo P.E.J. and van der Zwaag S. (2008), 'Self-healing of deformation damage in underaged Al-Cu-Mg alloys', *Scripta materialia*, 58, 719–722.
- Hautojärvi P. and Corbel C. (1995). *Positron Spectroscopy of Solids*, in Dupasquier A, Mills jr A P (Eds.), Amsterdam, IOS Press.
- Hidalgo C., Gonzales-Doncel G., Linderroth S., and San Juan J. (1992), 'Structure of dislocations in Al and Fe as studied by positron-annihilation spectroscopy', *Physical Review B*, 45, 7017–7021.
- Hillel A.J. (1983), 'Electrical resistivity of GP zones–Temperature dependence', *Philosophical Magazine B*, 48, 237–243.
- Hillel A.J. and Rossiter P.L. (1981), 'Resistivity mechanism during clustering in alloys', *Philosophical Magazine B*, 44, 382–388.
- Hohenberg P. and Kohn W. (1964), 'Inhomogeneous electron gas', *Physical Review B*, 136, 864–871.
- Honma T., Yanagita S., Hono K., Nagai Y. and Hasegawa M. (2004), 'Coincidence Doppler broadening and 3DAP study of the pre-precipitation stage of an Al-Li-Cu-Mg-Ag alloy', *Acta Materialia*, 52, 1997–2003.
- Ipohorski M. and Bonfiglioli A.F. (1970), 'Kinetics of growth of GP zones: Experimental verification of the vacancy pump model', *Acta Metallurgica*, 18, 281–285.
- Kaiser M., Nambissan P., Banerjee M., Sachdeva A. and Pujari P. (2007), 'Positron lifetime studies and coincidence Doppler broadening spectroscopy of Al-6Mg-xSc (x = 0 to 0.6 wt.%) alloy', *Journal of Materials Science*, 42, 2618–2629.
- Kelly A. and Nicholson R.B. (1963), In Chalmers, B (1963), 'Precipitation hardening', *Progress in Material Science*, 10, 158–266, New York, McMillan.
- Kim S.M., Buyers W.J.L., Martel P. and Hood G.M. (1974), 'Vacancy-silicon binding energy in aluminium by positron annihilation', *Journal of Physics F: Metal Physics*, 4, 343–350.
- Kimura H., Kimura A. and Hasiguti R.R. (1962), 'A resistometric study on the role of quenched-in vacancies in ageing on Al-Cu alloys', *Acta Metallurgica*, 10, 607–619.
- Kohn W. (1999), 'Electronic structure of matter-wave functions and density functional', *Reviews of Modern Physics*, 71, 1253–1266.

- Koning M., Ramos de Debiaggi S. and Monti A.M. (2004), 'Vacancy-formation thermodynamics in aluminium and nickel: A computational study', *Defect and Diffusion Forum*, 224–225, 59–74.
- Lechner W., Puff W., Mingler B., Zehetbauer M.J., Würschum R. (2009), 'Microstructure and vacancy-type defects in high-pressure torsion deformed Al–Cu–Mg–Mn alloy', *Scripta materialia*, 61, 383–386.
- Lide C. (1995), *Handbook of Chemistry and Physics*, 75th ed. CRC Press, Cleveland.
- Lumley R.N. (1997), 'The transient liquid phase sintering of aluminium based alloys', PhD Dissertation, Department of Mining, Minerals and Materials Engineering, The University of Queensland, Australia.
- Lumley R.N. and Schaffer G.B. (1996), 'The effect of solubility and particle size on liquid phase sintering', *Scripta materialia*, 35, 589–595.
- Lumley R.N. and Schaffer G.B. (1998), 'The effect of additive particle size on the mechanical properties of sintered aluminium-copper alloys', *Scripta materialia*, 39, 1089–1094.
- Macchi C., Somoza A., Dupasquier A. and Polmear I.J. (2003), 'Secondary precipitation in Al–Zn–Mg–(Ag)', *Acta Materialia*, 51, 5151–5158.
- Maloney S.K., Hono K., Polmear I.J. and Ringer S.P. (2001), 'The effect of a trace addition of silver upon elevated temperature ageing of an Al–Zn–Mg alloy', *Micron*, 32 741–747.
- Mantina M., Wang Y., Chen L.Q., Liu Z.K. and Wolverton C. (2009), 'First principles impurity diffusion coefficients', *Acta Materialia*, 57, 4102–4108.
- Marceau R.K.W., Ferragut R., Dupasquier A., Iglesias M.M. and Ringer S.P. (2006), 'Vacancy-Solute Interactions in Al–Cu–Mg', *Materials science forum*, 519–521, 197–202.
- Marceau R.K.W., Sha G., Ferragut R., Dupasquier A. and Ringer S.P. (In press, 2010), 'Evolution of atomic-scale solute clustering in Al–Cu–Mg alloys and their contribution to the rapid hardening phenomenon – I. Elevated temperature ageing', *Acta Materialia*.
- Martin J.W. (1968), *Precipitation Hardening*, Oxford, Pergamon Press.
- McKee B.T.A., Jost A.G.D. and MacKenzie I.K. (1972), 'Positron – vacancy interaction in aluminium', *Canadian Journal of Physics*, 50, 415–420.
- Mehrer H. (1990) In: *Landolt-Börnstein Numerical Data and Functional Relationships in Science and Technology*, Group III: Crystal and Solid State Physics, Vol. 26.
- Melikhova O., Kuriplach J., Čížek J. and Procházka I. (2006), 'Vacancy – solute complexes in aluminium', *Applied Surface Science*, 252, 3285–3289.
- Mondolfo L.F. (1976), *Aluminum Alloys: Structure and Properties*, London, Butterworth.
- Murty K.N. and Vasu K.I. (1972), 'Vacancy-solute interaction energies in aluminium-silver alloys', *Scripta materialia*, 6, 13–16.
- Ono K. and Kino T. (1978), 'Migration energy of mono-vacancy in aluminum at high temperature', *Journal of Physical Society of Japan*, 44, 875–881.
- Panseri C. and Federighi T. (1960), 'A resistometric study of pre-precipitation in Al–10%Zn', *Acta Metallurgica*, 8, 217–238.
- Polmear I.J. (2006), *Light Alloys: From Traditional Alloys to Nanocrystals*, 4th ed. Oxford, Elsevier.
- Puska M.J. and Nieminen R.M. (1994), 'Theory of positrons in solids and on solid surfaces', *Reviews of Modern Physics*, 68, 841–897.
- Raman K.S., Das E.S.D. and Vasu K.I. (1971), 'Clustering and solute-vacancy binding energies in al–4.4%Zn alloy with 0.01% ternary additions', *Journal of Materials Science*, 6, 1367–1378.
- Ramos de Debiaggi S., Koning M. and Monti A.M. (2006), 'Thermodynamics and kinetics of self-interstitials in aluminum and nickel', *Physical Review B*, 73, 1–9.

- Ravi C. and Wolverton C. (2004), 'First-principles study of crystal structure and stability of Al-Mg-Si-(Cu) precipitates', *Acta Materialia*, 52, 4213–4227.
- Reich L., Ringer S.P., and Hono K. (1999), 'Origin of the initial rapid age hardening in an Al-1.7at.%Mg-1.1at.%Cu alloy', *Philosophical Magazine Letters*, 79, 639–648.
- Ringer S.P. (2006), 'Advanced nanostructural analysis of aluminium alloys using atom probe tomography', *Materials science forum*, 519, 25–34.
- Ringer S.P., Hono K., Sakurai T. and Polmear I. J. (1997), 'Cluster hardening in an aged Al-Cu-Mg alloy', *Scripta materialia*, 36, 517–521.
- Ringer S.P. and Hono K. (2000), 'Microstructural evolution and age hardening in aluminium alloys: Atom Probe Field-Ion Microscopy and Transmission Electron Microscopy Studies', *Materials Characterization*, 44, 101–131.
- Rossiter P.L. (1987), *The Electrical Resistivity of Metals and Alloys*, London, Cambridge University Press.
- Rossiter P.L. and Wells P. (1971), 'The dependence of electrical resistivity on short-range order', *Journal of Physics C*, 4, 354–363.
- Rowland T.J. (1962), 'Knight shift in silver base solid solutions', *Physical Review*, 125, 459–467.
- Rowland T.J. (1960), 'Nuclear magnetic resonance in copper alloys. Electron distribution around solute atoms', *Physical Review*, 119, 900–912.
- Sandberg N., Slabjanja M. and Holmestad R. (2007), 'Ab initio simulations of clustering and precipitation in Al-Mg-Si alloys', *Computational Mater. Science*, 40, 309–318.
- Sato T. (2000), 'Early stage phenomena and role of microalloying elements in phase decomposition of aluminum alloys', *Materials science forum*, 331–337, 85–96.
- Sato T., Hirose K., Hirose K. and Maeguchi T. (2003), 'Roles of microalloying elements on the cluster formation in the initial stage of phase decomposition of Al-based alloys', *Metallurgical and Materials Transactions A*, 34, 2745–2755.
- Schaefer H.-E., Gugelmeier R., Schmolz M. and Seeger A. (1987), 'Positron lifetime spectroscopy and trapping at vacancies in aluminium', *Materials science forum*, 15–18, 111–116.
- Seitz F. (1952), *L' état solide*, Inst. Intern. de Physique, Solvay, 401.
- Sha G. and Cerezo A. (2005), 'Kinetic Monte Carlo simulation of clustering in an Al-Zn-Mg-Cu alloy (7050)', *Acta Materialia*, 53, 907–917.
- Siegel R.W. (1978), 'Vacancy concentration in metals', *Journal of Nuclear Materials*, 70, 117–146.
- Simmons R.O. and Baluffi R.W. (1960a), 'Measurements of equilibrium vacancy concentrations in aluminum', *Physical Review*, 117, 52–61.
- Simmons R.O. and Baluffi R.W. (1960b), 'Measurements of the high-temperature electrical resistance of aluminum: Resistivity of lattice vacancies', *Physical Review*, 117, 62–68.
- Slichter C.P. (1990), *Principles of Magnetic Resonance*, 3rd ed. New York, Springer-Verlag.
- Somoza A., Dupasquier A., Polmear I.J., Folegati P. and Ferragut R. (2000), 'Positron annihilation study of the aging kinetics of AlCu-based alloys. Part I: Al-Cu-Mg', *Physical Review B*, 61, 14454–14463.
- Somoza A., Petkov M.P., Lynn K.G. and Dupasquier A. (2002), 'Stability of vacancies during solute clustering in Al-Cu-based alloys', *Physical Review B*, 65, 094107.
- Staab T.E.M., Krause-Rehberg R., Hornauer U. and Zschech E. (2006), 'Study of artificial aging in AlMgSi (6061) and AlMgSiCu (6013) alloys by positron annihilation', *Journal of Materials Science*, 41, 1059–1066.
- Staab T.E.M., Haaks M. and Modrow M. (2008), 'Early precipitation stages of aluminum alloys-The role of quenched-in vacancies', *Applied Surface Science*, 255, 132–135.

- Tolley A., Ferragut R. and Somoza A. (2009), 'Microstructural characterization of a commercial Al-Cu-Mg alloy combining Transmission Electron Microscopy and Positron Annihilation Spectroscopy', *Philosophical Magazine*, 89, 1095–1110.
- Westmacott T.H., .Barness S., Hull D. and Smallman R.E. (1961), 'Vacancy trapping in quenched aluminium alloys', *Philosophical Magazine*, 6, 929–935.
- Wolverton C. and Oznolinš V. (2006), 'First-principles aluminum database', *Physical Review B*, 73, 144104.
- Wolverton C. (2007), 'Solute-vacancy binding in aluminium', *Acta Materialia*, 55, 5867–5872.
- Zahra A.M., Zahra C.Y. and Dumont M., (2005) 'Effects of Ag or Si on precipitation in the alloy Al-2.5 mass% Cu-1.5 mass% Mg', *Philosophical Magazine*, 85, 3735–3754.

Modeling the kinetics of precipitation in aluminium alloys

C.R. HUTCHINSON, Monash University, Australia

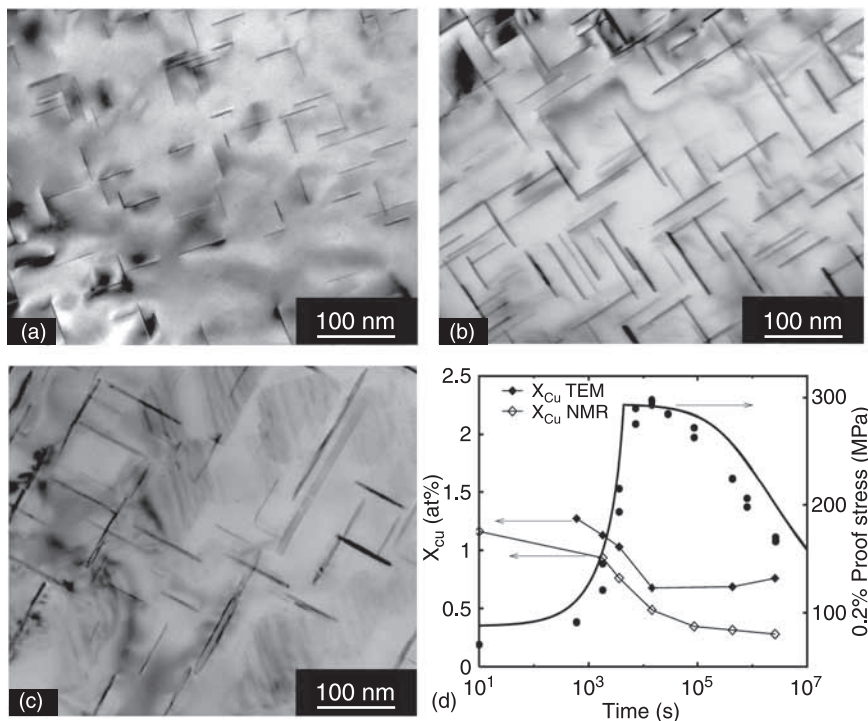
Abstract: The distinguishing feature of the microstructures of 2xxx, 6xxx and 7xxx series aluminium alloys, used extensively by the automotive and aerospace industries, is that they contain a distribution of precipitates. The mechanical properties of these alloys are largely controlled by the nature of the interactions between dislocations and precipitates and therefore tailoring the precipitate distribution is one of the methods to improve the engineering performance. In this chapter, an outline of the current state-of-the-art in describing quantitatively (modeling) precipitation processes in Al alloys is presented. Emphasis is placed on the effects of time and temperature, but the role of alloy chemistry, precipitate shape and the role of plastic deformation are also introduced. The advantages and disadvantages of the different modeling approaches are outlined.

Key words: precipitation modeling, kinetic Monte Carlo, class models, non-spherical precipitates.

15.1 Introduction

The distinguishing feature of microstructures of aluminium (Al) alloys belonging to the 2xxx (Al-Cu-(Mg)), 6xxx (Al-Mg-Si) and 7xxx (Al-Zn-Mg) series is that they contain a distribution of one or more precipitates (Polmear, 1995). Examples of plate-shaped θ' (Al_2Cu) precipitates in a laboratory Al-3Cu (wt. %) alloy are shown in Fig. 15.1(a–c) obtained using transmission electron microscopy (TEM).

These classes of precipitate containing alloys find widespread use in the transportation and aerospace industries because they have excellent combinations of strength, damage tolerance, processability, environmental resistance, density and cost. The mechanical properties of these alloys are largely controlled by the nature of the interactions between dislocations and precipitates and therefore tailoring the precipitate distribution is one of the primary tools available to the manufacturer to improve the engineering performance. Precipitates have chemistries that differ from the Al matrix and therefore their formation requires long-range solute diffusion. As a result we can expect that the kinetics of precipitate formation will depend on both time and temperature. The effect of time is clearly illustrated in Fig. 15.1. Precipitates become larger with increasing time at 200°C. Most precipitates found in important engineering Al alloys also have crystal structures different to the surrounding Al matrix and therefore their formation requires both a change in structure and long-range diffusion. This is the case for the precipitates shown in Fig. 15.1.



15.1 Bright field TEM micrographs taken from an Al-3Cu-0.05Sn (wt. %) alloy aged for various times at 473 K. The electron beam is close to [001]_α. (a) 30 min, (b) 4 h (peak aged) and (c) 5 days. The precipitates are the Al₃Cu θ' phase. (d) Experimental measurements (points) and model calculations (solid lines) of 0.2% proof stress and atomic fraction of Cu in solid solution, as a function of isothermal annealing time at 473 K (adapted from da Costa Teixeira et al., 2008).

This chapter is about describing quantitatively (modeling) the kinetics of formation and evolution of precipitate distributions such as those shown in Fig. 15.1. It is natural to ask: Why is this important? There are two reasons.

The first is that manufacturers use thermal treatments to generate the precipitate structures that give their products the desired mechanical properties. These thermal treatments usually involve a number of stages, contain non-isothermal segments, differ from one alloy composition to another and depend on the final set of mechanical properties required. If the thermal treatments are applied concurrently with plastic deformation, such as during a forming operation, they are then referred to as thermo-mechanical treatments. Although the thermal and thermo-mechanical treatments developed in the past contained a significant degree of experimental trial-and-error or semi-empiricism to develop, increasingly engineers are turning to quantitative descriptions of the precipitation processes to help understand the

changes during a given thermal treatment and as a potential design tool to help optimize the process (for a review relevant to industrial processing see Bratland et al., 1997). Even for one alloy chemistry, the combinations of time and temperature that can be applied in a thermal treatment are infinite. The probability of identifying optimal treatments through experimental trial-and-error is extremely slim and would be prohibitively expensive. Process designers require predictive tools that can be used to 'virtually' investigate the probable effects of different thermal treatments and therefore identify which are worth experimental investigation. The quantitative descriptions of the precipitation process must explicitly include the dependence on time, temperature, alloy chemistry and sometimes also deformation. If these are available and well calibrated they can be used in process design to identify, for example, thermal treatments that minimize the energy consumed by the process, or the total thermal treatment time, or the strengthening increment obtained for a given alloy. Examples of the efficiencies that can be realized by using models of precipitation kinetics as process design tools are shown in the case studies in Section 15.3.

The second reason why it is important to be able to describe quantitatively the precipitation process is that the microstructures of the alloys evolve during service. In terms of the microstructure shown in Fig. 15.1, the average size of the precipitates, or the number of precipitates per unit volume, or the precipitate shape or precipitate type may change during service. These changes may occur because the material is subject to thermal loads during service (such as the aerodynamic heating of the wings of passenger aircraft) or may be subject to thermal loads during a joining operation such as welding. In other cases, the material may be subjected to mechanical loading (such as fatigue or creep loading in internal combustion engine components) which, as will be discussed in Section 15.4, can influence strongly the precipitate state. A consequence of the evolution of the precipitate microstructure during service is that the mechanical properties also evolve. Usually, the mechanical properties deteriorate due to the change in microstructure and in cases such as the use of precipitate containing Al alloys in automotive or aerospace load-bearing applications, an understanding of the evolution of the mechanical properties is essential for safe design and operation. The ideal situation would be to have absolutely stable precipitate microstructures that do not change at all. In practice this is not possible and instead emphasis is placed on designing microstructures that change as little as possible under the operating conditions and on an understanding of the rates at which the changes occur.

Often products made from precipitate containing Al alloys are designed for a lifetime of 20 years or longer. It is usually impractical to perform experiments for this long to determine the degree to which the properties of an alloy will deteriorate due to changes in the precipitate state. Instead, alloy designers can now couple quantitative descriptions of the evolution of precipitate structure, subject to the thermal and thermo-mechanical loadings experienced during service, to models relating the precipitate structure to the mechanical properties to obtain an

indication of the expected variation during service. In this way, the quantitative descriptions of the kinetics of precipitation processes can be used as alloy design tools.

In this chapter, a brief outline of the current state-of-the-art in modeling precipitation processes in Al alloys is presented. Emphasis is placed on the effects of time and temperature, since this is the most developed area, but the effect of alloy chemistry, precipitate shape and the role of plastic deformation will also be introduced. Efforts are made to highlight the advantages and disadvantages of the different modeling approaches and highlight the areas where future work is required. The types of precipitation models that will be discussed here are currently being used by Al alloy and process design teams for the reasons outlined above. No doubt new uses will be found as the approaches gain maturity and more widespread acceptance.

15.2 Physical processes controlling precipitation

Precipitation is a general phenomenon occurring in a wide range of materials in both the solid and liquid states. In Al alloys, it is precipitation in the solid, face-centered cubic (FCC) matrix that is of interest and this can occur when the matrix is supersaturated with respect to one or more solute additions. In general, whenever an alloy system exhibits a decreasing solid solubility with decreasing temperature, a thermodynamic possibility for precipitation exists. Precipitation involves three key processes: nucleation, growth and coarsening (Wagner et al., 2002). All three depend on both thermodynamic (e.g., solid solubility) and kinetic parameters (e.g., diffusivities of the alloying elements) of the alloy system. Nucleation involves the initial formation of the new phase (precipitate) in the matrix and its subsequent increase in size is referred to as growth. Nucleation and growth are both driven by the reduction in chemical supersaturation of the system and therefore once the precipitate volume fraction reaches the (local) equilibrium value, both processes cease. Coarsening [also referred to as Ostwald ripening (Ostwald, 1896)] is driven by the reduction of the excess energy due to the precipitate/matrix interfaces and once this process is complete only a single precipitate will exist, although in practice this may take a very long time (Voorhees, 1992). The driving force for coarsening is much less than that for growth, and therefore coarsening processes are usually much slower.

An important feature of precipitation processes is that nucleation, growth and coarsening are competing processes that overlap significantly (Wagner et al., 2002) and this feature must be captured by models of precipitation if they are expected to quantitatively describe experimental results. Nucleation and growth both reduce the chemical supersaturation and therefore the progress of one process reduces the driving force for the other process. Coarsening may even overlap with the nucleation phase although the driving forces for these two processes are different. Robson (2004) has discussed the conditions under which this may be expected.

Commercial Al alloy microstructures often contain a number of different precipitate types. If these precipitate types contain any of the same solute atoms, e.g.

T_1 (Al_2CuLi) and θ' (Al_2Cu), then not only is there an overlap and competition between the nucleation, growth and coarsening phases of a given precipitate phase but a competition also exists between the two precipitate types. Similarly, if precipitates are formed both in the FCC matrix and at defects such as grain boundaries or dislocations, a competition also exists between these precipitates and may result in the formation of precipitate free zones (PFZs) adjacent to the defects. PFZs have important effects on fracture, fatigue and corrosion properties of alloys.

The precipitates that form in Al alloys have a variety of shapes. They exist in plate-shaped form (such as the θ' (Al_2Cu) precipitates shown in Fig. 15.1 and also as spheres (Fig. 15.2a), rod-like (Fig. 15.2b) and lath-like shapes (Fig. 15.2c; Polmear, 1995)). The important role of precipitate shape in influencing the precipitation kinetics will be highlighted in Section 15.3.2.

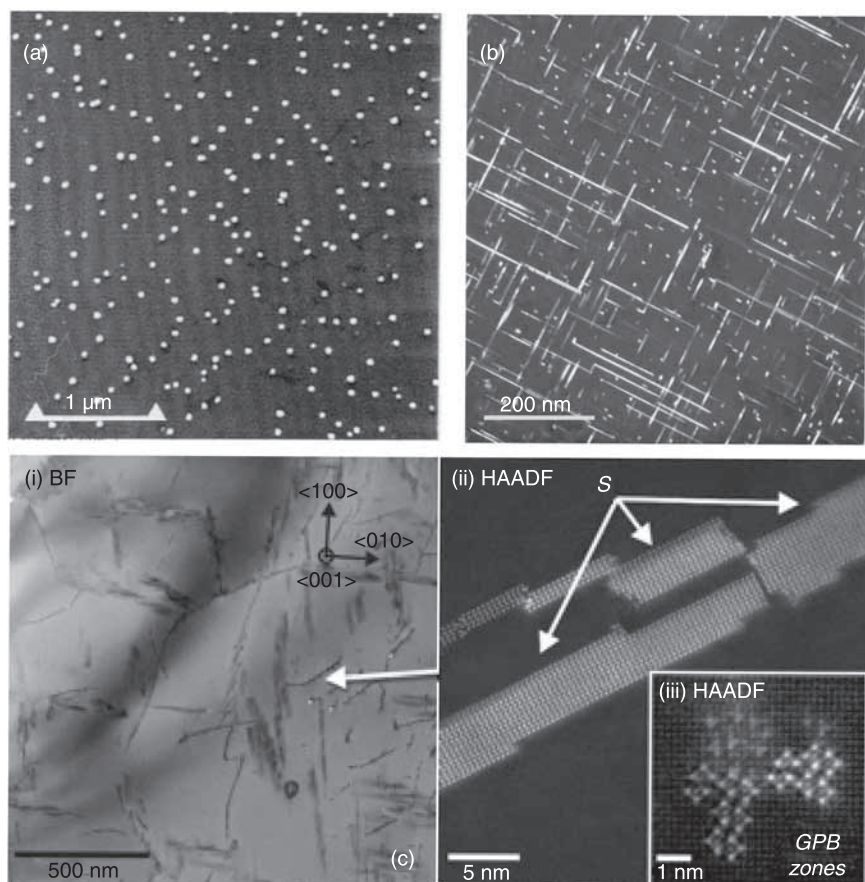
Some precipitates may also form with chemistries deviating significantly from the equilibrium composition (e.g., Moore and Howe, 2000; Moore et al., 2002) and the composition inherited by the growing phase may even evolve during the precipitation process (Clouet et al., 2006). Al alloys in particular also often contain a number of transition phases which may form due to nucleation advantages, but which may later catalyse the nucleation of subsequent phases (Polmear, 1995). If these exist and influence strongly the formation and evolution of the microstructure and the properties which are ultimately of interest then they must be captured quantitatively by the precipitation model.

Finally, precipitate containing microstructures are rarely spatially homogeneous. For reasons of segregation during solidification, the local bulk composition of an Al alloy may vary from one region to another, or different regions of a given Al alloy product may experience slightly different thermal or thermo-mechanical processing histories which may result in spatially heterogeneous precipitate distributions. An obvious example is during welding. The regions around a weld are subjected to different thermal histories and the precipitate state in the different regions of the weld can vary dramatically with a strong effect on the local variation in mechanical properties.

The variety of features and effects that can influence a precipitation process in a material such as Al is large, and this gives richness to the types of precipitate microstructures that can be developed. At the same time, it is neither feasible nor practical to capture every detail of each effect in a physically based model of precipitation and simplifications must be made. Modeling is an art of simplification and the skill is in knowing which level of simplification is appropriate.

15.3 Current approaches to modeling precipitation kinetics

There is a large range of choice in the level of detail that can be built into a model for precipitation. A good rule of thumb is to make the model as simple as possible to retain the physical transparency of the underlying physical processes but



15.2 (a) Dark field TEM micrograph illustrating spherical Al_3Sc precipitates (white) formed by aging an Al-0.18 at.% Sc alloy for 168 h at 350°C , (b) Dark field TEM micrograph illustrating rod-shaped precipitates (the electron beam is closely parallel to $[001]_\alpha$ in a commercial 6111 (Al-Mg-Si alloy) aged for 2 months at 180°C and (c) (i) Bright field and (ii) High angle annular dark field TEM images of laths of S phase precipitates (Al_2CuMg) nucleated on dislocations in an Al-Cu-Mg alloy aged for 9 h at 200°C (adapted from Novotny and Ardell, 2001, Poole et al., 2005; Ralston et al., 2010).

detailed enough to capture the microstructural features that influence most strongly the property of interest. The first question to ask is always: What am I trying to describe or predict?

Consider the evolution of the room temperature yield stress with aging time at 200°C of the Al-3 wt.% Cu alloy shown in Fig. 15.1d. It is clear that the state of the precipitation (Fig. 15.1a–c) strongly affects the yield strength. The simplest

model for the evolution of the precipitate state is to describe it by a single parameter, the volume fraction of precipitates, V_f . A simple Johnson-Mehl-Avrami type approach might be chosen for this. However, the V_f of precipitates in this material is constant from the peak-aged state of 4 h through to very long aging times of 30 days (da Costa Teixeira et al., 2008). Figure 15.1(d) illustrates that the yield strength varies substantially during this period. It is clear that describing (modeling) the precipitate microstructure by only one parameter, V_f , is too simple even for the simplest of the microstructurally dependent mechanical properties, the yield strength.

The next level of complexity is to describe the precipitate microstructure by an average precipitate size, \bar{R} , and number per unit volume, N_v . The volume fraction can be calculated from knowledge of these two parameters and the precipitate shape. In many engineering applications, this level of complexity is sufficient. For other problems, it is necessary to describe the full particle size distribution, $f(R)$ and the presence of multiple, competing precipitate phases. For problems involving fracture and corrosion properties it may be necessary to describe accurately the spatial heterogeneity generated by the competition between precipitates at grain-boundaries and dislocations and within the matrix and the formation of PFZs. The choice of modeling approach is dictated by the problem of interest and the properties deemed important.

A feature of the precipitate microstructure that is particularly important in Al alloys is the precipitate shape. As will be shown in Section 15.3.1, the state-of-the-art in precipitation modeling is very well developed for spherical precipitates. Unfortunately, the situation for non-spherical precipitates is much less so. The majority of the important precipitates in commercial Al alloys are non-spherical; plate-, lath- and rod-shaped (Fig. 15.1 and Fig. 15.2) precipitates play a prominent role in the commercially important Al alloys (Polmear, 1995). A key question is whether these important precipitates can be approximated as spherical for modeling purposes? The answer depends on the problem being treated. In some cases this approximation may be suitable but our current understanding of the effect of microstructure on the mechanical properties of Al alloys suggests that this approximation is usually a poor one.

The current approaches for precipitation modeling assuming spherical and non-spherical precipitate shapes are outlined below and a number of examples are chosen from the literature to illustrate the use of the models for alloy and process design.

Nucleation of new phases involves the formation of an aggregate of atoms with a chemistry and, more often than not, a crystal structure different from the FCC Al matrix. When initially formed these aggregates have sizes of the order of a nanometer or less. For features so small it seems natural to appeal to atomistic modeling approaches to describe the nucleation process. However, examination of typical precipitates in Fig. 15.1 illustrates that precipitates can grow to hundreds of nanometers in size and that thermal treatment times can be many hours or

days. Such sizes and timeframes are usually too long for existing atomistic simulation approaches (e.g., Mishin et al., 2010) and instead continuum (or mesoscale) approaches may seem more appealing. This multi-scale nature of the precipitation problem is one of the challenging aspects. Atomistic and continuum approaches have both been developed to describe precipitation reactions, each with their advantages and disadvantages. These approaches are summarized below.

15.3.1 Spherical precipitates

Continuum (mesoscale) approaches

The continuum approaches to describing precipitation kinetics are based on differential equations for nucleation, growth and coarsening coupled in an appropriate manner to capture the competition and overlap between the processes.

Mean radius approaches

Based on descriptions for the kinetics of the individual processes of nucleation, growth and coarsening developed over many years by the physical metallurgy community, and building on the work of Kampmann and Wagner (1984) and Langer and Schwartz (1980), Deschamps and Bréchet (1999) developed a method of coupling these equations in a simple way that also captures the key features of the competition and overlap of the processes. The Deschamps and Bréchet model monitors only the average precipitate size and number density. It assumes spherical precipitates and a homogeneous spatial distribution.

Precipitation is described in two stages. The first involves concurrent ‘nucleation + growth’. The second involves concurrent ‘growth + coarsening’. This approach assumes no overlap between nucleation and coarsening and this is reasonable for many practical conditions (Robson, 2004).

The nucleation rate, $\frac{dN}{dt}$, is described using classical nucleation theory (CNT) (Volmer and Weber, 1926; Becker and Doring, 1935; Zeldovich, 1943; Russell, 1980).

$$\left. \frac{dN}{dt} \right|_{\text{Nucleation} + \text{Growth}} = N_0 Z \beta^* \exp\left(-\frac{\Delta G^*}{kT}\right) \exp\left(-\frac{\tau}{t}\right) \quad [15.1]$$

N is the number per unit volume of precipitates, t is time, N_0 is the number of potential nucleation sites per unit volume (if all sites in the matrix are potential sites then $N_0 = 1/v_{at}$ where v_{at} is the atomic volume), Z is known as Zeldovich’s factor ($\sim 1/20$), k is Boltzmann’s constant, T is temperature,

$$\beta^* = \frac{4 \pi R^{*2} D_S X_S}{a^4} \quad [15.2]$$

is a parameter describing the attachment kinetics of atoms to the nucleus, D_s is the diffusivity of the solute in the matrix, X_s is the concentration of solute in the matrix, a is the lattice parameter of the matrix and

$$\tau = \frac{1}{2\beta^* Z} \quad [15.3]$$

is an incubation time for nucleation (Turnbull, 1948; Kampmann and Wagner, 1984).

The most important parameter entering Eq. 15.1 is the activation barrier for nucleus formation, ΔG^* . For spherical precipitates forming in a perfect lattice with no strain effects, the nucleation barrier can be written

$$\Delta G^* = \frac{16}{3} \pi \frac{\gamma^3}{\Delta G_V} \quad [15.4]$$

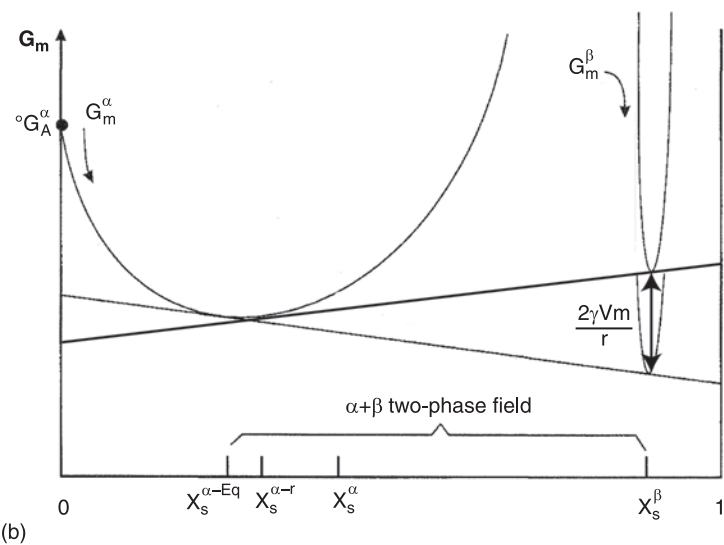
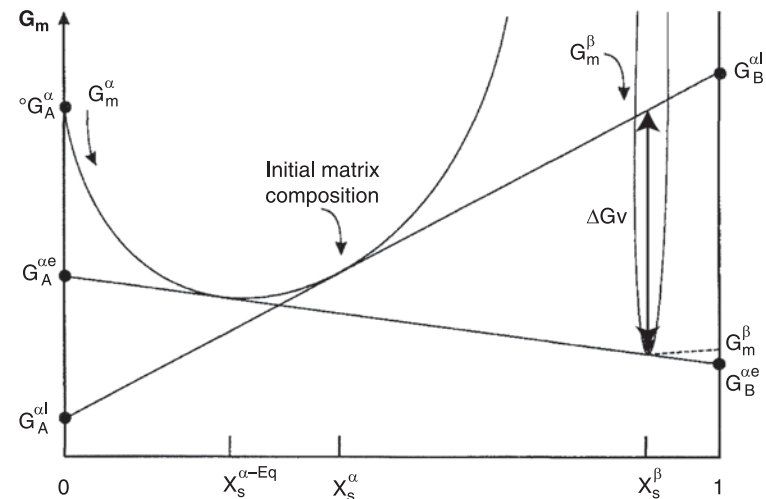
γ is an 'effective' interfacial energy of the hypothetical dividing surface (Gibbs, 1928) separating the nucleus and the matrix and ΔG_V is known as the onset driving force for precipitation.

The size of a precipitate when it nucleates is known as the critical nucleus size and is expressed as

$$R^* = - \frac{2\gamma}{\Delta G_V} \quad [15.5]$$

The onset driving force for nucleation is a thermodynamic quantity. Consider the hypothetical Gibbs free energy curves as a function of composition for a binary system in Fig. 15.3(a).

If a precipitate, β , of composition X_s^β is to nucleate from a supersaturated matrix of α of bulk composition X_s^α , then the onset driving force is defined as the vertical distance, ΔG_V . It is clear that calculations of ΔG_V require descriptions of the Gibbs free energy curves, as a function of composition and temperature, for each of the phases present in the system of interest. In a ternary system, the curves shown in Fig. 15.3 would be surfaces and the tangent allowing calculation of ΔG_V would be a plane. Higher order systems require the higher order geometry. If the Gibbs free energy curves are not known then often assumptions are made about the thermodynamics of the system such as 'ideal solution' behavior. Fortunately, descriptions of the Gibbs free energy curves for several of the important phases present in Al alloys have already been developed by the CALPHAD community (Saunders and Miodownik, 1998) and are available as databases that can be used by thermodynamic programs such as Thermo-Calc (2010), Pandat (2010) and FactSage (2010). Using these programs, which can easily be coupled to user-defined codes, the thermodynamic quantities necessary for calculations of precipitation kinetics, such as the onset driving force (Fig. 15.3a) can be readily calculated. The increased use of these thermodynamic descriptions will drive the refinement and development of the databases further and many Al alloy producers have their own proprietary databases that they have built over many years.



15.3 Schematic Gibbs free energy curves for the α and β phases in the A-B system. (a) The onset driving force for precipitation of β from an α matrix of composition X_s^α is illustrated by ΔG_v . (b) The additional free energy added to the β phase due to interface curvature of radius r ($2\gamma V_m/r$) and the resulting variation in the local equilibrium compositions of B at the matrix, $X_s^{\alpha-r}$ and precipitate, X_s^β , interfaces (adapted from Hillert, 1999).

Classical nucleation theory has a long history and was initially developed for condensation of liquid from a gas phase. Nevertheless, it is used extensively for nucleation from the solid state and the interested reader is referred to the detailed descriptions of the underlying ideas found in Russell (1980) and Aaronson and Lee (1999). The basic physical picture is a competition between the increase in energy resulting from the formation of an interface between a new phase and the matrix and the decrease in energy resulting from the replacement of a volume of matrix of high energy with a volume of precipitate phase of lower energy. Equation 15.1 describes the rate with which this occurs based on thermal fluctuations of the atomic configurations in the matrix phase. Equations 15.1–5, combined with the necessary input thermodynamic and kinetic data, provide a means of calculating the nucleation rate and subsequent integration gives the number of precipitates per unit volume.

There is a feature of Eq. 15.1 that should be highlighted at the outset. A consequence of the mathematical form of Eq. 15.1 is that extremely small changes in γ result in orders of magnitude changes in the nucleation rate. The reality is that γ is not known with sufficient certainty to use Eq. 15.1 in a purely predictive manner. It always requires some calibration and γ is usually fine-tuned based on experimental observations. This is the major disadvantage of precipitation models that use CNT to describe nucleation.

Deschamps and Bréchet describe the evolution of the mean precipitate size, \bar{R} , during the nucleation + growth stage of their model as:

$$\left. \frac{d\bar{R}}{dt} \right|_{\text{Nucleation + Growth}} = \frac{D_S}{\bar{R}} \frac{X_S - X_{Eq}^R}{X_{ppt} - X_{Eq}^R} + \frac{1}{N} \frac{dN}{dt} (\alpha R^* - \bar{R}) \quad [15.6]$$

The first term on the right hand side of Eq. 15.6 is the classical solution for the diffusional growth rate of a spherical precipitate of size \bar{R} (Zener, 1949). X_{ppt} is the composition of the precipitate, X_{Eq}^R is the concentration of solute in the matrix at the matrix/precipitate interface of a precipitate of radius \bar{R} and α is a constant usually taken to be 1.05. The value of X_{Eq}^R captures the fact that the solute concentration in the matrix in equilibrium with another phase depends on the curvature of the interface of the phase. This is the well-known Gibbs-Thomson effect (Gibbs, 1928; Thomson, 1849; Martin et al., 1997; Perez, 2005). Due to curvature, the Gibbs free energy of the phase is increased by an amount $2\gamma/R$. If the Gibbs free energy curves for the phases are known then this energy can simply be added to the precipitate phase and the common tangent construction can be used to calculate the local equilibrium composition of both the matrix and the precipitate when in contact. This is shown in Fig. 15.3(b). Analytical approaches to calculating X_{Eq}^R do exist but they must be used with care and rapidly become complicated in multi-component systems. Since most Al alloys are multi-component it is generally easier to evaluate X_{Eq}^R using the approach shown in Fig. 15.3(b).

The second term of the right hand side of Eq. 15.6 is the effect on the mean precipitate size from the arrival of newly nucleated precipitates of size R^* during

the time increment dt . During the increment dt , existing precipitates will grow and new precipitates will nucleate. The parameter α accounts for the fact that only precipitates slightly larger than R^* can grow. The precise value of α has no effect on the calculation result.

Numerical integration of Eq. 15.1 and Eq. 15.6 allows an evaluation of the time evolution of \bar{R} and N during the nucleation + growth stage. Since a solute balance must also apply, the solute remaining in the matrix, X_s , at each point in time can be evaluated from

$$X_0 = \frac{4}{3} \pi \bar{R}^3 N X_{ppt} + \left(1 - \frac{4}{3} \pi \bar{R}^3 N\right) X_s \quad [15.7]$$

X_0 is the bulk solute content of the alloy. X_s must be evaluated at each point in time because it influences the nucleation rate through changes in the onset driving force for nucleation (Fig.15.3a) and the growth rate (Eq. 15.6).

During a pure growth regime, there is no nucleation of new precipitates (Eq. 15.8) and existing precipitates grow with a rate described by the classical solution (Eq. 15.9)

$$\left. \frac{dN}{dt} \right|_{Growth} = 0 \quad [15.8]$$

$$\left. \frac{d\bar{R}}{dt} \right|_{Growth} = \frac{D_s}{\bar{R}} \frac{X_s - X_{Eq}^R}{X_{ppt} - X_{Eq}^R} \quad [15.9]$$

Once the supersaturation of solute in the matrix has been exhausted by nucleation and growth, i.e. $X_s = X_{Eq}^R$, then a coarsening regime applies. The evolution of the precipitate size and number density during this stage is driven by a reduction in the area of precipitate/matrix interfaces and the solution, in the limit of a zero volume fraction of spherical precipitates, was given by Lifshitz and Slyozov (1961) and Wagner (1961). The relation describing the increase in the average precipitate size during coarsening is known as the LSW law (Eq. 15.10). Deschamps and Bréchet, using the mass balance, also evaluate the evolution of the number density of precipitates during coarsening (Eq. 15.11).

$$\left. \frac{d\bar{R}}{dt} \right|_{Coarsening} = \frac{4}{27} \frac{D_s}{\bar{R}^2} \frac{2\gamma v_{at}}{kT} \frac{X_s}{X_{ppt} - X_s} \quad [15.10]$$

$$\left. \frac{dN}{dt} \right|_{Coarsening} = \frac{4}{27} \frac{D_s}{\bar{R}^3} \frac{2\gamma v_{at}}{kT} \frac{X_s}{X_{ppt} - X_s} \left[\frac{2\gamma v_{at}}{\bar{R} kT} \frac{X_s}{X_{ppt} - X_s} \left(\frac{3}{4\pi \bar{R}^3} - N \right) - 3N \right] \quad [15.11]$$

Deschamps and Bréchet describe the growth + coarsening stage of their precipitation model by:

$$\left. \frac{d\bar{R}}{dt} \right|_{\text{Growth} + \text{Coarsening}} = (1 - f_{\text{Coarse}}) \left. \frac{d\bar{R}}{dt} \right|_{\text{Growth}} + f_{\text{Coarse}} \left. \frac{d\bar{R}}{dt} \right|_{\text{Coarsening}} \quad [15.12]$$

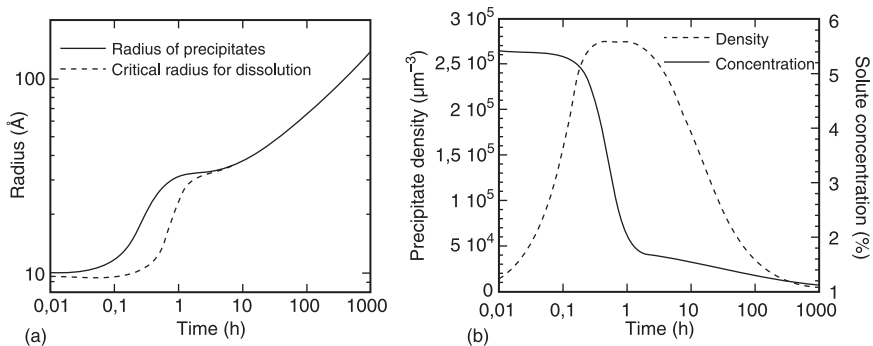
$$\left. \frac{d\bar{N}}{dt} \right|_{\text{Growth} + \text{Coarsening}} = f_{\text{Coarse}} \left. \frac{d\bar{N}}{dt} \right|_{\text{Coarsening}} \quad [15.13]$$

f_{Coarse} is a function having the properties that $f_{\text{Coarse}} = 0$ when $R \gg R^*$ and $f_{\text{Coarse}} = 1$ when $R = R^*$. The choice of the function does not affect the calculations and a number of authors (Deschamps and Bréchet, 1999; Gouné et al., 2004; Perrard et al., 2007) have used different functional forms.

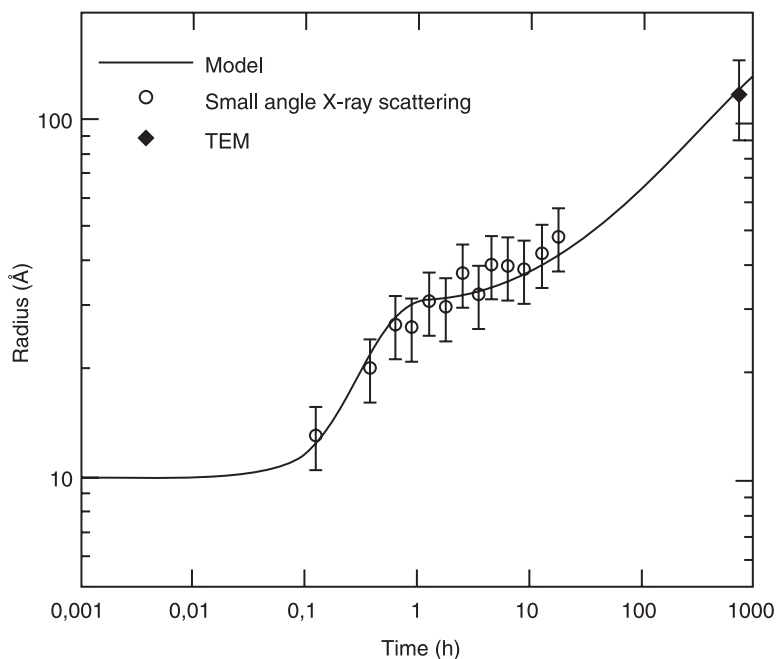
Numerical integration of Eq. 15.12 and 15.13 allows an evaluation of the time evolution of \bar{R} and N during the growth + coarsening stage. The final ingredient of this model is a criterion to know when to stop integrating the equations corresponding to nucleation + growth (Eqs. 15.1 and 15.6) and instead integrate the equations corresponding to the growth + coarsening stage (Eqs. 15.12 and 15.13). A suitable criterion is when the decrease in the number density of precipitates due to coarsening is greater than the increase due to nucleation.

$$-\left. \frac{dN}{dt} \right|_{\text{Growth} + \text{Coarsening}} > \left. \frac{dN}{dt} \right|_{\text{Nucleation} + \text{Growth}} \quad [15.14]$$

Deschamps and Bréchet applied this model to the kinetics of precipitation in an Al-Zn-Mg alloy. An example of the model calculations for the evolution of the mean precipitate size, number density, critical radius and solute in solution, for an isothermal heat treatment at 160°C, is shown in Fig. 15.4. The mean precipitate radius is equal to the critical radius for nucleation at both short and long times as expected. The number density increases initially with time, remains constant for a short period of time (corresponding to a pure growth regime) and then begins to



15.4 Evolution of precipitate parameters during isothermal aging at 160°C for an Al-Zn-Mg alloy using the Deschamps and Bréchet mean radius model for precipitation. (a) Mean precipitate radius and critical radius, and (b) number density of precipitates and matrix solute concentration as a function of aging time. The calculations were performed using an interfacial energy, $\gamma = 0.3 \text{ J/m}^2$ (adapted from Deschamps and Bréchet, 1999).



15.5 Comparison between the predictions of the evolution of the mean precipitate size in an Al-Zn-Mg alloy subjected to isothermal aging at 160°C using the Deschamps and Bréchet mean radius model and experimental measurements of precipitate size using small-angle X-ray scattering (SAXS) and TEM (Deschamps and Bréchet, 1999).

decrease during coarsening. The evolution of mean precipitate radius during aging at 160°C has been experimentally measured using small-angle X-ray scattering (SAXS) and TEM. The measurements are compared with the Deschamps and Bréchet model in Fig. 15.5. The agreement is quite satisfactory.

The Deschamps and Bréchet model considers the uniform precipitation of a single precipitate in the Al matrix of an Al-Zn-Mg alloy. The same model can be used to describe the formation and competition between multiple phases. These may be phases of different types, or the same precipitate phase nucleated in different locations, such as in the matrix and at dislocations or grain boundaries. The only modification needed is that separate equations will exist for the nucleation, growth and coarsening of the different precipitates and they will be coupled through the mass balance for solute (Eq. 15.7). Deschamps and Bréchet (1999) have examined the competition between precipitation in the matrix and on dislocations using this model in the same Al-Zn-Mg alloy. Perez and Deschamps (2003) have examined the competition in precipitation between two different phases in a low carbon steel but this variation has not been applied to this problem in Al alloys at this stage.

Case study: selecting non-isothermal heat treatments for precipitation hardening systems

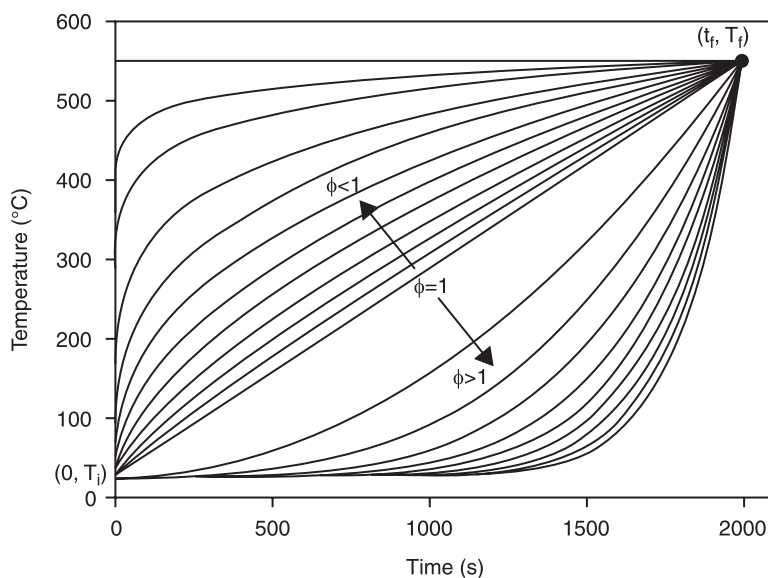
The expressions describing the nucleation, growth and coarsening in the Deschamps and Bréchet model are represented in differential form. They may be integrated according to any thermal treatment profile and their use is not restricted to isothermal heat treatments. Hutchinson et al. (2007) have applied this model to the precipitation of pure Cu in an Fe-2Cu (wt.%) alloy with the goal of optimizing the non-isothermal heat treatment profiles to maximize yield strength and to minimize the energy required by the thermal treatment. This alloy was chosen because the precipitates are spherical, pure Cu, and experimental data on the evolution of precipitate size, number density and yield stress as a function of isothermal aging at a range of temperatures was already available. This data was necessary to tune the selection of the effective interfacial energy parameter, γ , which enters into Eq. 15.1.

These authors considered a family of thermal treatment profiles (T, t) starting at a large range of different initial temperatures ($T_i, 0$) and finishing at (T_f, t_f). The family selected was described by the expression:

$$T(t) = T_i + \frac{(T_f - T_i)t^\phi}{t_f^\phi} \quad [15.15]$$

There is nothing special about this expression. It is simply a convenient way of representing a family of monotonically increasing or decreasing curves, ending at the point (T_f, t_f) by only two parameters, T_i and ϕ . A plot showing example curves is shown in Fig. 15.6, for one choice of T_i , corresponding to room temperature. These authors coupled the Deschamps and Bréchet precipitation model to a model relating the precipitate state to the resulting yield strength and ran the model for all of the thermal treatment profiles represented by Eq. 15.15 to generate 'Processing Maps' illustrating the yield strengths achievable using different non-isothermal heat treatment profiles. The results corresponding to the isothermal treatment, the optimal treatment found by the model and the worst treatment are compared in Fig. 15.7. The predictions of this process model were compared with experiment by performing non-isothermal experiments. The comparisons are shown in Fig. 15.7(d). The optimal thermal treatment allowed an increase in yield strength of ~10%.

This work illustrated that a large number of different thermal treatments exist which can give the same final precipitate state and mechanical properties. Of course not all thermal treatments require the same energy or are as convenient to implement in practice. The model was applied to the question of energy minimization for a given yield strength of material. Assuming that the energy required for a thermal treatment was proportional to $\int T(t)dt$ these authors found that the same yield strength obtained using an isothermal treatment could be obtained using a non-isothermal treatment with 65% of the energy. The non-isothermal

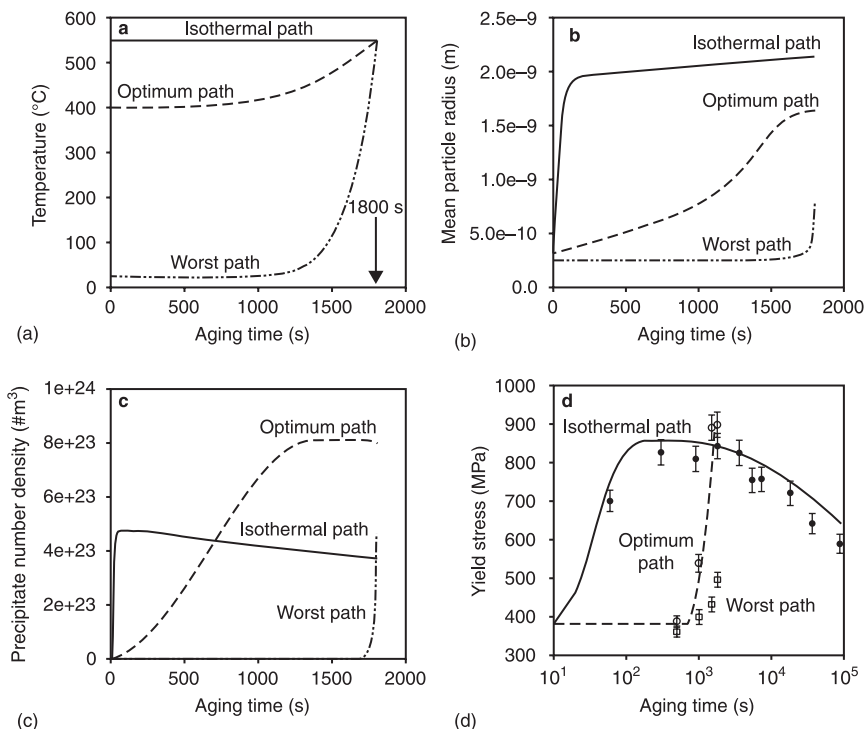


15.6 Examples of monotonic thermal treatment profiles belonging to the family described by Eq. 15.15, between an initial point $(0, T_i)$ and an end-point (t_f, T_f) . A large range of profiles can be described by variations in two parameters, T_i and ϕ (Hutchinson et al., 2007).

heat treatments identified by Hutchinson et al. could not have been discovered without the use of models of the precipitation process and are an example of the types of efficiencies in alloy and process design that can be obtained. It is expected we will see more and more of this type of analysis, especially for applications in Al alloys, given the large efficiencies possible.

Class models

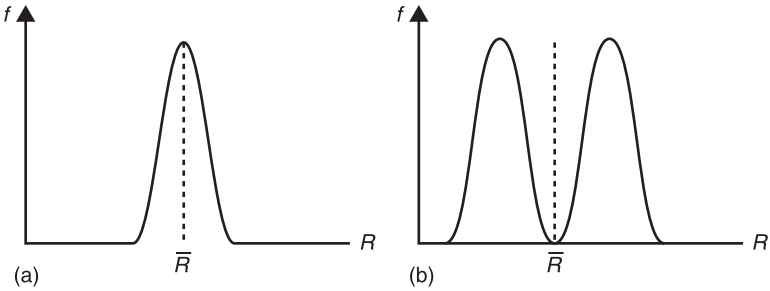
The Deschamps and Bréchet model considers only the mean precipitate size. The suitability of this model depends on how reasonable it is to represent the real precipitate size distribution by an average for the problem being studied. If the real precipitate distribution resembles that shown in Fig. 15.8(a), then the mean is probably a reasonable representation. However, if a microstructure has been subject to a thermal treatment that gives rise to a bimodal precipitate size distribution such as that shown in Fig. 15.8(b), then it is questionable that the mean size is an adequate representation. If the property of interest is yield strength, and the radius representing the transition between dislocation shearing of precipitates and the bypassing mechanisms lies between the large and small precipitates in the bimodal distribution of Fig. 15.8(b), then the average size will result in a very poor calculation of the yield strength. This is an example where the Deschamps and Bréchet model is not sufficient, and the full precipitate size



15.7 (a) Plot of the treatment temperature as a function of time for the isothermal heat treatment, the optimal thermal treatment and a very poor thermal treatment found from the family described by Eq. 15.15 for the maximization of yield strength of an Fe-2Cu (wt. %) alloy for an end-point of the thermal treatment of (1800s, 550°C), (b) The corresponding evolution of calculated mean particle radii, (c) number density, and (d) evolution of the calculated and experimentally measured yield stresses for the thermal treatments shown in (a) (adapted from Hutchinson et al., 2007).

distribution must be considered. Similar situations exist for precipitate distributions subject to high temperature reversion treatments (such as retrogression and re-aging) or large and rapid changes in temperature, such as during welding. Under such situations, a different approach is required and these approaches can be grouped under the title of ‘class models’. The primary difference is that they monitor the full particle size distribution evolution instead of only the mean size.

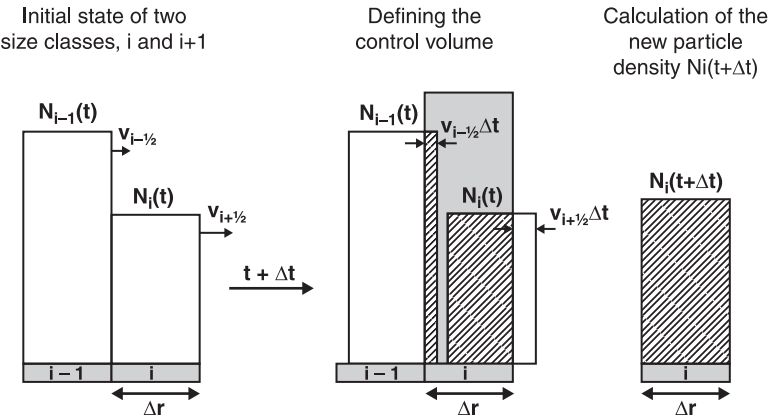
To represent the full precipitate size distribution, the class models discretize the size distribution into classes of size ΔR . An example is shown in Fig. 15.9 for the $i-1$, and i th size classes. The number of precipitates within each size class is monitored and therefore the concentration of solute remaining in solution at any point in time can be calculated by applying a mass balance across the full precipitate size distribution. Nucleation is described using CNT (Eq. 15.1) and



15.8 Schematic illustration of (a) monotonic particle size distribution, $f(R)$ and (b) bimodal particle size distribution, $f(R)$. The mean particle size, \bar{R} , is a reasonable approximation to the real distribution in (a) but it is a poor representation of the bimodal distribution shown in (b).

therefore the disadvantage of the lack of certainty regarding γ applies also to the class models. New precipitates are added to a size class corresponding to R^* .

The change in size of precipitates belonging to each size class at each point in time is described using Eq. 15.9. Whereas in the Deschamps and Bréchet model this was used only to describe the pure growth regime of precipitate evolution, in the class models this single equation describes the full growth and coarsening behavior. Examination of Eq. 15.9 shows that it can describe both growth and dissolution depending on the current values of X_S and X_{Eq}^R (which will be different for the different size classes). Coarsening occurs when the supersaturation is exhausted and this occurs for different size classes of precipitates at different concentrations of X_S . In this way, those precipitates with sizes that fall below R^*



15.9 Calculation of the number density of particles in size class i after a time increment of Δt . In this case the particles in both classes i and $i-1$ have positive growth rates, v . Under these conditions the number density is calculated by: $N_i(t + \Delta t) = N_i(t) - N_i(t)v_{i+1/2} \frac{\Delta t}{\Delta r} + N_{i-1}(t) \frac{\Delta t}{\Delta r}$ (adapted from Nicolas, 2002).

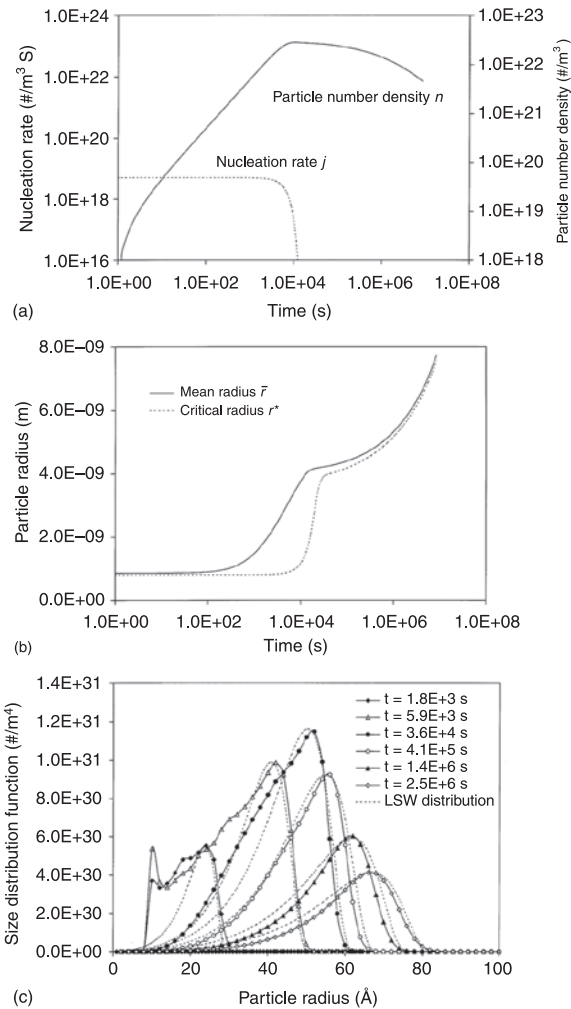
(which evolves as X_s evolves) naturally dissolve as part of the coarsening process. The class models are beautiful in their simplicity and elegance (only Eq. 15.1 and Eq. 15.9 are required). Different authors use different approaches to managing the bookkeeping of the numbers of precipitates in the different size classes (Kampmann and Wagner, 1984; Myhr and Grong, 2000; Maugis and Gouné, 2005). Some authors keep the sizes of each class constant and move the number of precipitates between classes. Others keep the number constant and move the sizes of the classes. This needs to be done with care and with attention to the time step, dt , for integration. The approaches all give the same results. The interested reader is referred to a nice comparison by Perez et al. (2008) of the different approaches to the class models and a comparison with the mean radius approach. The class models, although simple in principle, are computationally more intensive than the mean radius approaches, although with the current advances in computational power this is now not as much of an issue as it once was. As a result, we will see over the coming years a continual shift in favor of the class models instead of the mean radius approach models.

An example of the type of description of precipitation given by the class models is shown in Fig. 15.10. This is an example from the work of Myhr and Grong (2000) who used this model to describe precipitation in the Al-Mg-Si alloy 6082 under isothermal heat treatment conditions at 180°C. The evolution of the size distribution, and a comparison with the LSW distribution (which is *a priori* assumed in the Deschamps and Bréchet model and is necessary to arrive at Eq. 15.10), is clearly seen.

Case study: reversion treatments and welding

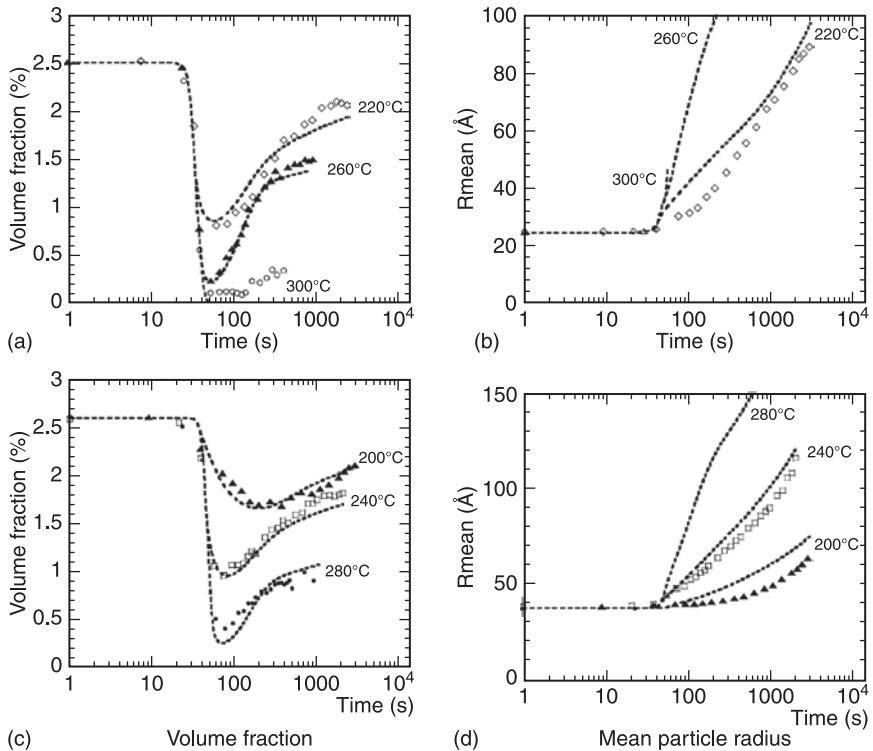
The class models have been applied to a wide range of precipitation problems in Al alloys and their specialty is dealing with highly non-isothermal treatments, such as welding or reversion treatments. Nicolas and Deschamps (2003) used a class model to understand the precipitate evolution in an Al-Zn-Mg alloy 7108 during reversion treatments as a function of initial precipitate state (T6 and T7). Their model results are compared with experimental measurements obtained using SAXS in Fig. 15.11. The agreement is very satisfactory.

A number of authors have applied class models to the problem of welding of Al alloys (Frigaard et al., 2001; Nicolas and Deschamps, 2003; Deschamps et al., 2005; Kamp et al., 2006, 2009; Myhr and Grong, 2009). In these cases the authors couple models or experimental measurements of the time evolution of the temperature at different positions in and around the weld and then use the class model to describe the temporal and spatial evolution of the precipitate state. As an example, Myhr and Grong (2009) considered single pass butt welding of Al-Mg-Si alloys. They coupled models of the heat flow from the welding process to a class model for precipitation and a model for the resulting hardness as a function of precipitate state to describe the variation in hardness



15.10 Examples of the output from the class model for precipitation for an Al-Mg-Si alloy aged isothermally at 180°C. (a) Evolution of the nucleation rate and number density of precipitates per unit volume with aging time, (b) Increase in the mean precipitate radius and the critical radius and (c) Plots of the calculated full particle size distribution as a function of aging time. The LSW distribution is plotted for comparison (Myhr and Grong, 2000).

across the welded region. An example of the comparison between experiment and model is shown in Fig. 15.12 for three different Al-Mg-Si alloys. Myhr and Grong then used their welding process model to optimize the welding parameters to obtain the desired spatial distribution of hardness. This is a nice example of using precipitate kinetics models as a process design tool.

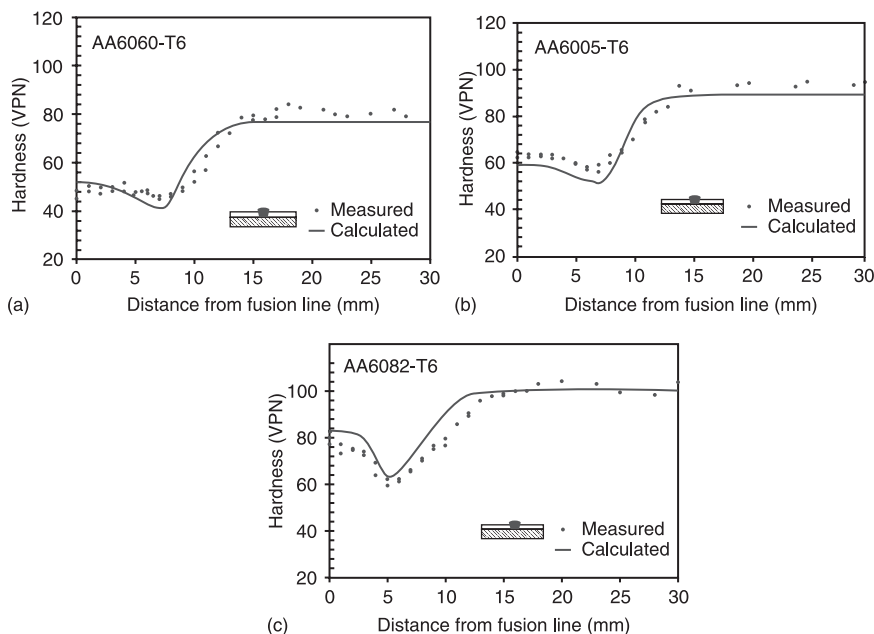


15.11 Modeled precipitation evolution (dashed line) according to a class model compared with the experimental measurements (symbols) made using small angle x-ray scattering measurements during reversion treatments of the T6 temper (a, b) and the T7 temper (c, d) for an Al-Zn-Mg alloy. The evolution of the mean radius and volume fraction of precipitates is shown (Nicolas and Deschamps, 2003).

Atomistic approaches

The continuum models for precipitation are very efficient for describing the growth and coarsening regimes of the evolution of a precipitate distribution. Their biggest weakness is the sensitivity of CNT to variations in γ and our lack of precise knowledge of γ . This means that the continuum models cannot be used in a completely predictive manner. An effective γ must first be fine-tuned and then the models can be used to extrapolate to conditions a little away from those used to tune γ . This limitation resulting from our imperfect knowledge of γ has long been recognized.

To overcome this limitation some authors have applied atomistic approaches to attempt to describe the nucleation and subsequent early stage growth of precipitates in Al alloys. In particular, a number of authors have used Lattice Kinetic Monte Carlo (LKMC) approaches to simulate precipitate nucleation in



15.12 Comparison of experimental measurements and model predictions of the hardness profiles across the heat-affected zone of three different single-pass butt welds [(a) 6060, (b) 6005 and (c) 6082]. The predictions of the hardness evolution are made by coupling a model for the spatial and temporal evolution of the temperature with a class model for precipitation and a model relating the state of precipitation to the hardness (adapted from Myhr and Grong, 2009).

Al (Clouet et al. 2004, 2005a, 2006; Slabanja and Wahnström, 2005). The downsides of this approach are that due to the computational demands it is limited to short aging times and large supersaturations and has so far only been applied to coherent phase precipitation where the crystal structure of the precipitate can be expressed in terms of the underlying lattice of the matrix.

Clouet et al. (2004, 2005a, 2006) have studied the precipitation of Al_3Sc and Al_3Zr in Al using the LKMC approach to contribute to the understanding of the nucleation process in Al alloys. The computer simulation considers a rigid FCC lattice and all of the atoms are constrained to occupy sites on this lattice. Initially, the different atoms species might be distributed at random. The Al-Sc and Al-Zr systems are model systems since the precipitates have an $L1_2$ crystal structure (Al_3Zr only when it is small such as at the nucleation state) which is an ordered FCC lattice and the lattice parameters of the precipitates are very close to those of the Al matrix so constraining the atoms to lie on the rigid FCC is a reasonable approximation (strain energy need not be considered). The thermodynamics of the system is represented by a bond energy summation (E) over the system:

$$E = \frac{1}{2N_S} \sum_{\substack{n,m \\ i,j}} \epsilon_{ij}^{(1)} p_n^i p_m^j + \frac{1}{2N_S} \sum_{\substack{r,s \\ i,j}} \epsilon_{ij}^{(2)} p_r^i p_s^j \quad [15.16]$$

N_S is the total number of lattice sites in the simulation box and p_n^i is an occupation number with $p_n^i = 1$ if site n is occupied by an atom of type i and $p_n^i = 0$ if not. The first and second summations in Eq. 15.16 apply to the first and second nearest neighbors pairs of atomic sites, and $e_{ij}^{(1)}$ and $e_{ij}^{(2)}$ are the effective energies of the pairs of sites. It is clear that all of the thermodynamic properties lie in the first and second nearest neighbor interaction energies, $e_{ij}^{(1)}$ and $e_{ij}^{(2)}$. These must be chosen correctly to properly reproduce the thermodynamic properties of the alloy of interest and Clouet et al. (2004) calculated these quantities so that the energies of formation of Al_3Sc and Al_3Zr as well as the solid solubilities of Sc and Zr in Al are correctly reproduced. In Al alloys diffusion occurs by vacancy exchange with a neighboring atom. In the LKMC approach, the attempt frequency for a vacant site in the simulation lattice to exchange with one of its nearest neighbor atom sites, α , is:

$$\Gamma_{\alpha-V} = V_\alpha \exp\left(-\frac{E_\alpha^{act}}{kT}\right) \quad [15.17]$$

v_α is an attempt frequency and E_α^{act} is energy required to move the α atom from its original position to the saddle point between its site and that of the vacancy. v_α and E_α^{act} are chosen so as to properly reproduce the Al self diffusion coefficient and the impurity diffusion coefficients of Sc and Zr in Al and depend on the bond energies of the atoms surrounding the exchange site.

To run the Kinetic Monte Carlo algorithm a single vacancy is added to the simulation lattice and at each step the vacancy can exchange positions with one of its nearest neighbors. The time increment corresponding to the jump of the vacancy is given by (Clouet et al., 2004):

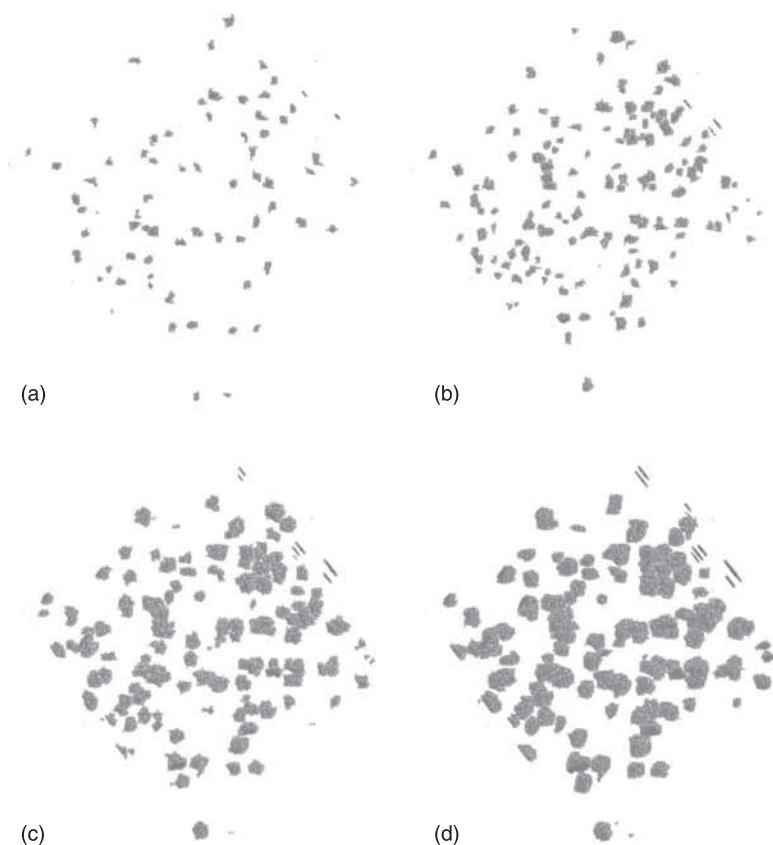
$$\Delta t = \frac{1}{N_S \left(1 - 13 X_{Sc, Zr}^{Bulk}\right) X_V^{Al}} \frac{1}{\sum_{\alpha=1}^{12} \Gamma_{\alpha-V}} \quad [15.18]$$

$X_{Sc, Zr}^{Bulk}$ is the overall concentration of Sc or Zr in the simulation lattice and X_V^{Al} is the real concentration of vacancies in pure Al as predicted by the thermodynamic parameters of the model. The atomic configurations on the rigid lattice evolve by subsequent jumps of the vacancy and the kinetics of the system is monitored by successive summation of Δt . The LKMC approach is simple in principle but care must be taken in correctly identifying the thermodynamic and kinetic input parameters. In particular the interaction energy between the solute atoms such as Sc and Zr and the vacancy must be known with accuracy. Wolverton (2007) has recently presented first principle calculations of these quantities for a range of solute additions in Al and while they generally showed good agreement with the experimental measurements of Hutchinson et al. (2008a) made using positron lifetime annihilation spectroscopy (PALS), the origin of the differences in the

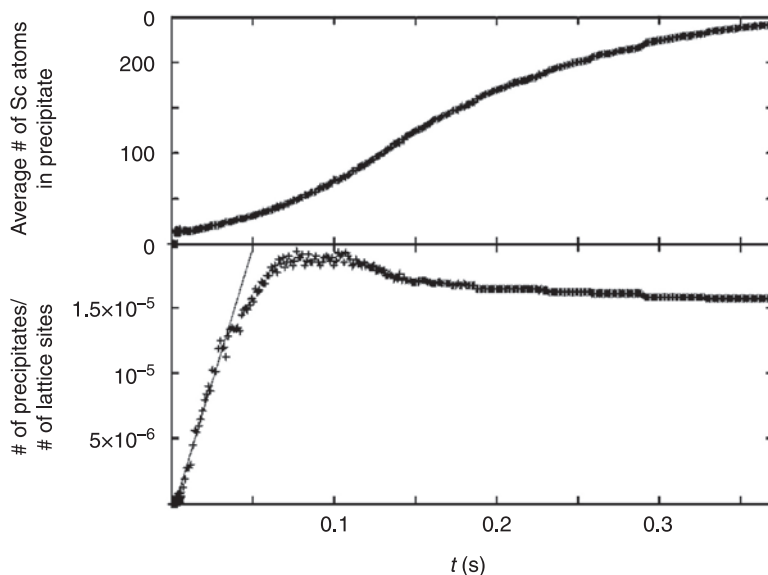
measure for the binding energy between a Mg atom and a vacancy remains unresolved. An example of the predicted temporal evolution of an Al-0.5Sc (at.%) alloy aged at 500°C is shown in Fig. 15.13.

Analysis of the atomic configurations in Fig. 15.13 allows an identification of parameters such as the evolution of the number of precipitates, the precipitate size distribution, the mean precipitate size and the concentration of solute remaining in solid solution that can then be compared with experiment. Analysis of the simulation data in Fig. 15.13 yields the precipitate characteristics shown in Fig. 15.14. A region of linear increase in the number of precipitates can be seen at early stages. This corresponds to steady-state nucleation.

The nucleation of precipitates shown in Fig. 15.13 and summarized in Fig. 15.14 did not require choices of the interfacial energy, γ , which is required by



15.13 Lattice Kinetic Monte Carlo (LKMC) simulation of the kinetics of precipitation of Al_3Sc from an Al-0.5 at.% Sc alloy at 773 K. The simulation box contains 8×10^6 lattice sites. Only those Sc atoms belonging to the L_{12} Al_3Sc phase are shown to illustrate the evolution of the precipitates. (a) 24 ms, (b) 60 ms, (c) 151 ms and (d) 366 ms (adapted from Clouet et al., 2004).

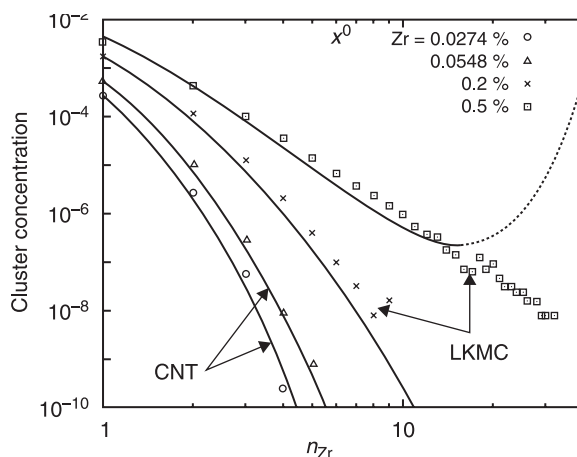


15.14 Evolution of the average number of precipitates, N_{sp} , in the simulation box shown in Figure 15.13 (normalized by the number of lattice sites, N_s) and the average precipitate size measured as the average number of Sc atoms in the precipitates, $\langle n_{sp} \rangle$ as a function of aging time according to the LKMC simulation. The alloy is an Al-0.5 at.% Sc alloy aged at 773 K (adapted from Clouet et al., 2004).

CNT (Eq. 15.1). Such information is already captured in the thermodynamic description of the system, Eq. 15.16. The natural question is then: How do the predictions of the LKMC simulation compare with CNT?

The answer according to Clouet et al. is: very well, so long as the thermodynamic parameters entering into CNT are evaluated correctly. This is often non-trivial and the interested reader is referred to the original articles for details. The predictions of the size distributions of Al_3Zr precipitates in a range of Al-Zr alloys annealed at 500°C are compared with the predictions according to CNT in Fig. 15.15. The agreement is good.

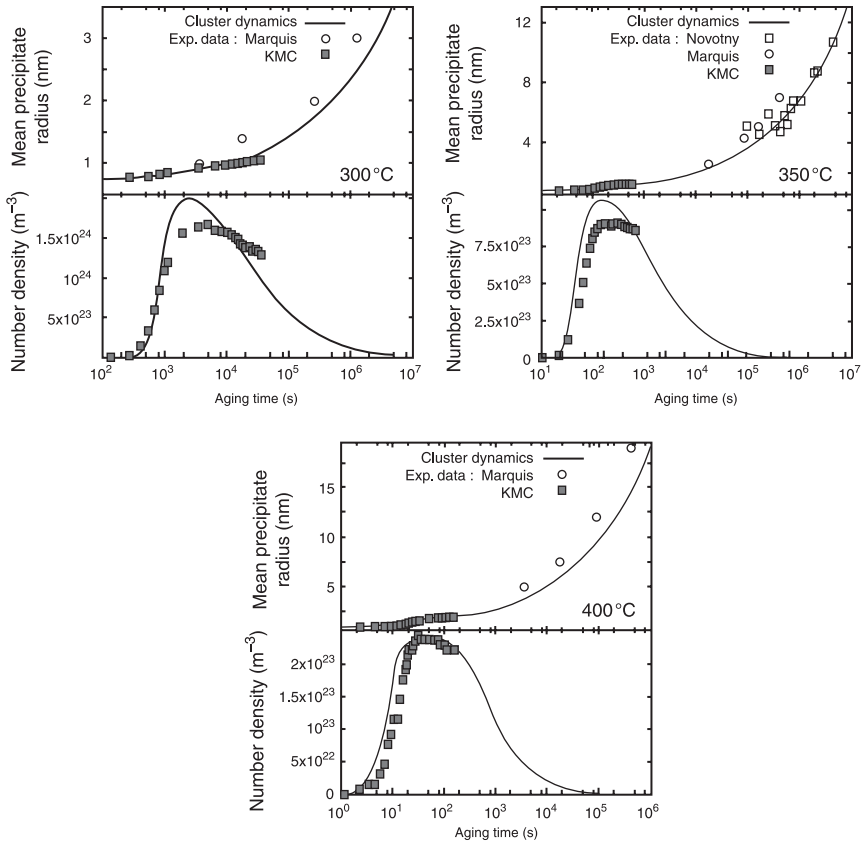
The results of LKMC simulations have also been compared with experimental data. Comparisons between measured and calculated mean precipitate size data for an Al-0.18Sc (at.%) alloy aged at 300°C, 350°C and 400°C is shown in Fig. 15.16. The comparisons for the smallest precipitates at 300°C are reasonable but detailed comparisons are not possible because the LKMC simulation times are too short to reach precipitate sizes that are typically measured using TEM or SAXS. This is one of the major limitations of the LKMC approach; it is restricted to short aging times and to large supersaturations.



15.15 Comparisons of cluster (precipitate) size distributions in four Al-Zr alloys with Zr contents ranging from 0.0274 up to 0.5 at.% calculated using the LKMC approach (symbols) and classical nucleation theory (lines; adapted from Clouet et al., 2004).

The solid lines in Fig. 15.16 refer to the results of a model known as Cluster Dynamics. This approach is well known in the nuclear industry for treating problems of irradiation and precipitation under irradiation but is not commonly applied to problems in Al alloys and for this reason has not been covered in this chapter. However, this is a promising approach that overcomes some of the limitations of both the LKMC approach and the continuum approaches discussed earlier and the interested reader is referred to the following references for applications of cluster dynamic simulations to precipitation in Al alloys (Clouet et al., 2005b; Guyot and Lae, 2006; Barbu and Clouet, 2007; Guyot et al., 2009).

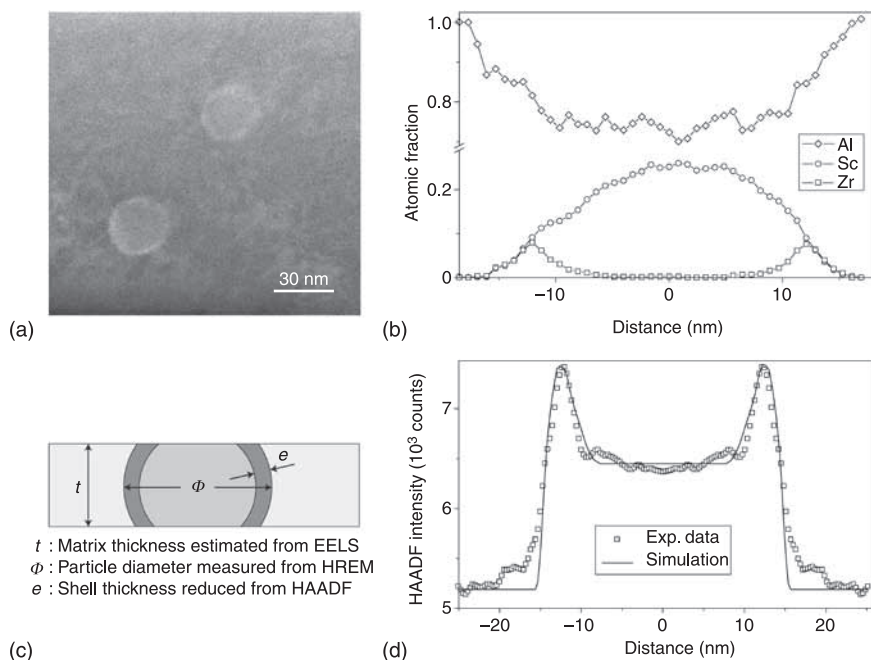
The LKMC approach offers a major advantage over the continuum approaches for questions relating to the kinetic pathways followed by a system as it precipitates. This is important for multi-component systems and has been applied to the problem of the precipitation in Al-Sc-Zr ternary alloys. In these systems the $L1_2$ precipitate phase forms with an inhomogeneous composition (Forbord et al., 2004; Fuller et al., 2005; Tolley et al., 2005; Clouet et al., 2006). The core is rich in Sc and the shell is rich in Zr (Fig. 15.17). These observations cannot be easily explained by the continuum type models discussed earlier (although these approaches do allow the nucleus composition to differ from the composition inherited during growth). The LKMC approach has been used to rationalize the observations shown in Fig. 15.17 and reveals that the inhomogeneous composition is a direct result of the difference in diffusivities between Sc and Zr in the Al lattice. This is an example of a precipitation problem that could only be treated at the atomistic level.



15.16 Calculated precipitate number density and average radius as a function of aging time for an Al-0.18 at.% Sc alloy aged at 300, 350 and 400°C using the lattice kinetic Monte Carlo approach (LKMC) (closed symbols) and the Cluster Dynamics approach (lines). The open symbols correspond to experimental measurements (adapted from Clouet et al., 2005a).

15.3.2 Non-spherical precipitates (plates, rods, laths)

All of the approaches considered so far to describe the precipitation kinetics in Al alloys have assumed the precipitates are spherical or have applied models to precipitation of spherical precipitates. The examples shown in Fig. 15.5 and Fig. 15.11 (7xxx series Al alloy) and Fig. 15.12 (6xxx series alloy) all approximated the precipitates as spherical. The precipitates in these alloys are not spherical. Indeed the precipitates in most important engineering Al alloys are highly non-spherical. The precipitate shape has a strong influence on the mechanical properties and in cases where the shape is far from spherical, such as the plate-shaped precipitates shown in Fig. 15.1, this feature should be captured by the



15.17 (a) High angle annular dark-field (HAADF) image of particles observed in an aluminium solid solution containing 0.09 at.% Sc and 0.03 at.% Zr aged for 32 h at 450°C showing the bright contrast associated with the Zr-enriched shell. (b) The EDX line-scan of the bottom particle. (c) The geometrical model used to simulate the HAADF contrast. (d) The rotationally averaged profile of the HAADF intensity from the bottom particle agrees with the simulated one for precipitates with core and shell compositions equal to Al_3Sc and $\text{Al}_3\text{Zr}_{0.5}\text{Sc}_{0.5}$, respectively (Clouet et al., 2006).

precipitation model. As will be shown, the characteristics of the precipitation kinetics also depend on the precipitate shape and have features that are fundamentally different from the kinetics of precipitation of spherical precipitates.

Despite the importance of precipitate shape in Al alloys there has been much less activity in developing models for the precipitation kinetics that explicitly take into account the non-spherical morphology.

Atomistic approaches

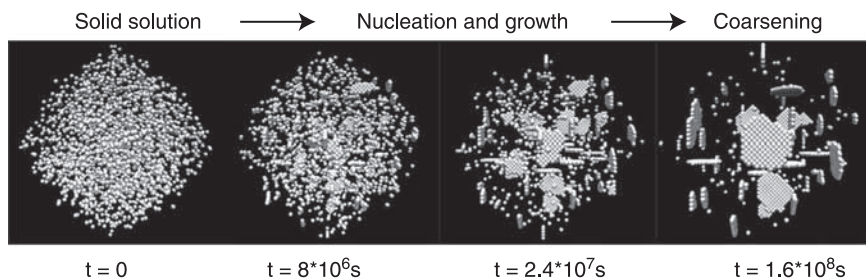
The LKMC approach used by Clouet and co-workers to study the precipitation kinetics of Al_3Sc and Al_3Zr did not make any assumptions about the shape of the precipitates. The LKMC approach only describes diffusion by the vacancy exchange mechanism and the shape of the precipitate is a result of the calculation. In this particular case, diffusion is isotropic in the FCC matrix, and the interaction

parameters, $e_{ij}^{(1)}$ and $e_{ij}^{(2)}$ did not contain anything built into them that would lead to a non-spherical precipitate morphology. However, the approach is capable of treating non-spherical precipitates so long as they can be described by atomic rearrangements on the underlying FCC lattice.

Wang et al. (2005) have used LKMC to describe the precipitation of GP zones in Al-Cu alloys. GP zones are single atomic planes rich in Cu. In the case of the Al_3Sc treated by Clouet et al. (2004), the lattice parameters of the precipitate and matrix phases were very close and therefore constraining the atoms to lie on a fixed FCC lattice was a reasonable approximation. In the case of GP zone precipitation in Al this is not the case. The lattice parameter of FCC Cu is significantly different to that of Al and therefore a FCC Cu rich arrangement of atoms embedded in the FCC Al matrix will result in a spatial variation in lattice parameters. To describe this situation realistically in the LKMC approach, Wang et al. include a strain energy term in their summation of the total energy of the system. This term does not presume a shape for the precipitates but simply accounts for the lattice mismatch arising from the difference in sizes of the Al and Cu atoms.

An example of LKMC calculation for Al-1.0Cu (at.%) annealed at 100°C is shown in Fig. 15.18. The evolution from an initial random solid solution to single atomic layer thick GP zones aligned in $\{100\}_\alpha$ directions can be clearly seen.

The evolution of the atomic arrangements shown in Fig. 15.18 can be analyzed and the nucleation rate and measures and the evolution of average particle size can be extracted. The advantage of such an approach is that it overcomes the difficulties associated with CNT and does not require any assumptions about the shapes of the precipitates forming. The disadvantages are that the LKMC approach can only be applied to short aging times and large supersaturations and that the crystal structure of the precipitate must be described in terms of the underlying FCC Al lattice so that the precipitation process can be described



15.18 Lattice kinetic Monte Carlo (LKMC) simulation of GP zone formation in an Al-1.0 at.% Cu alloy aged at 373 K. Only the Cu atoms are shown and the formation of single planes of Cu on the $\{100\}_\alpha$ planes of the Al matrix is clear. The thermodynamic input for these calculations was made using first principles calculations (Wang et al., 2005).

purely in terms of diffusion via vacancy exchange (i.e., a real crystal structure change is not required).

However, in most commercially relevant Al alloys, the precipitates that form are highly non-spherical and have crystal structures that cannot be described in terms of the underlying FCC lattice. Furthermore, it is usually necessary to describe the long-term evolution of the microstructure when the precipitates become large enough that they cannot be efficiently described by atomistic approaches. In these cases, it is necessary to appeal to the continuum approaches.

Continuum approaches

In Section 15.3.1, both the mean radius approach and the class models were introduced for the modeling of the kinetics of precipitation of spherical precipitates. Unfortunately such simple approaches that couple differential equations for the different stages of precipitate evolution do not generally exist for non-spherical precipitates. There are two formidable difficulties that lead to this situation. The first is that a general approach for calculating the anisotropy in phase interface mobility (as a function of temperature, chemistry and driving force) does not currently exist. The second is that a simple expression to describe the coarsening of a distribution of non-spherical precipitates does not exist and indeed it does not seem possible that a simple expression like the LSW law (Eq. 15.10) could be derived. These difficulties both require some explanation.

Anisotropy in phase interface mobility

It is currently possible to calculate the equilibrium shape of precipitates in Al alloys (e.g., Wolverton, 1999, 2000; Muller et al., 2000). The equilibrium shape depends on two effects: the anisotropy of interfacial energy (which can be calculated using atomistic approaches) and the strain energy that results from differences in the elastic constants and molar volumes between the precipitate and the matrix. The problem is that such shapes correspond to conditions where the phase interfaces are stationary. To describe the precipitation process requires an understanding of how the interfaces move and to describe the evolution of precipitate shape during a precipitation process requires an understanding of the anisotropy in motion of the phase interfaces (e.g., Thornton et al., 2003). This anisotropy in interface motion is controlled by a kinetic parameter of the phase interface known as the mobility. The mobility is inversely proportional to the energy required to accomplish the crystal structure change across the precipitate/matrix interface. A high mobility means that the structural change across the interface occurs easily and does not consume much energy and the interface can migrate comparatively quickly. A low mobility means that the structural rearrangement at the interface is not so easy, requires a non-negligible amount of energy to accomplish and the interface migrates comparatively slowly (the local

equilibrium assumption for the compositions at a migrating phase interface presumes that the mobility is infinite and no energy is required for the structural change). Clearly the mobility depends on the local atomic arrangement at the interfaces and at this stage an easy way to calculate these quantities for phase interfaces does not exist. As a result we cannot calculate, *a priori*, the expected shape evolution of a single precipitate during precipitation in Al. Given the expected dependence of the interface mobility on the local atomic arrangement (geometrical and chemical), calculations of the phase mobility must be made using atomistic approaches and indeed these are currently being made using Molecular Dynamics simulations for grain boundaries (e.g., Janssens et al., 2006). The interested reader is referred to the very nice recent review on atomistic approaches for treating interfaces (Mishin et al., 2010). However, the extension of the MD approach to solid-state phase interfaces is non-trivial and it may be some time before we have access to these mobilities.

One way to circumvent this problem is to assume that the precipitate growth is shape-preserving (they have a constant shape during growth) and then to use classical solutions for the diffusion equations applied to the particular shape of the precipitate. These are available for plate-shaped (Eq. 15.19) and needle-shaped precipitates (e.g., Hillert, 1957; Hillert et al., 2003):

$$\frac{dL_{\text{plate}}}{dt} = \frac{D_S}{2 \cdot R_p} \frac{X_S - X^{\alpha\beta}}{X^\beta - X^{\alpha\beta}} \left(1 - \frac{R_c}{R_p} \right) \quad [15.19]$$

L is the length of the plate. R_p is the radius of the tip of the plate and R_c is a critical radius of the plate tip at which the velocity of growth will decrease to zero because of the effect of capillarity.

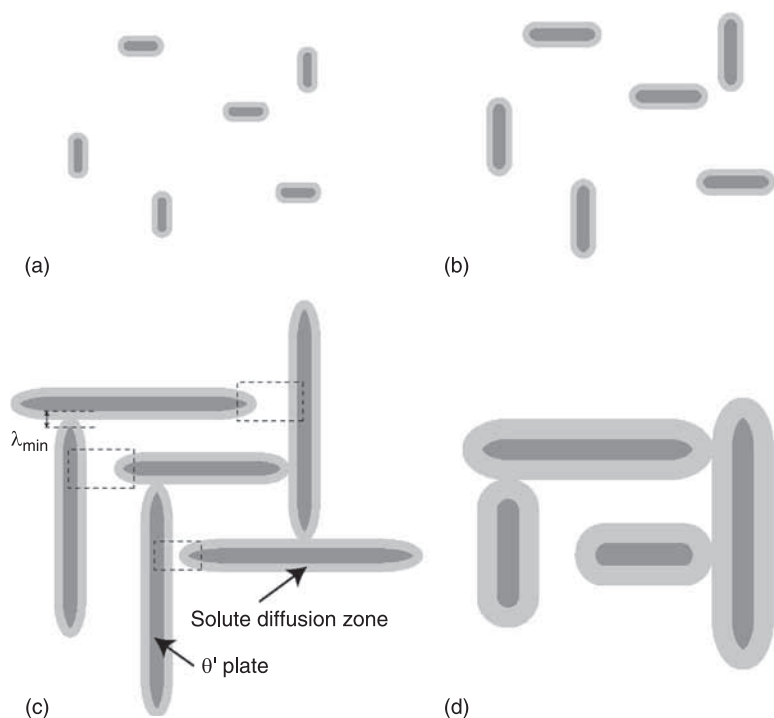
It can clearly be seen that use of Eq. 15.19 requires an estimate of the plate tip radii and the critical radii at which the free energy driving growth is fully consumed by the capillarity effect at the tip. The latter can be estimated if the interfacial energy of the plate tip is known but the radius of the tip is difficult to measure experimentally. Often assumptions are made regarding a relationship between the plate tip radius and the critical radius, such as the Maximum Growth Rate hypothesis (Zener, 1946; Hillert, 1957).

The reasonableness of using Eq. 15.19 depends on the degree to which the shape of a precipitate evolves during precipitation. In some cases this might be a suitable approximation, but in other cases it will not. It is well known, for example, that precipitate plates in Al alloys are often seen to lengthen rapidly with almost no change in thickness due to the high differences in interface mobility and this leads to a large change in precipitate shape evidenced by measures of the aspect ratio (length/thickness; e.g. Laird and Aaronson, 1969; Howe et al., 1985; Rajab and Doherty, 1989; Moore and Howe, 2000). It should be emphasized that such approaches do not predict the shape of the precipitate from first principles. They assume a shape and the differential equations describing the changes in length

(Eq. 15.19) are simply solutions of the diffusion problem for that assumed geometry solved under conditions where shape preservation during growth is assumed.

Coarsening of a distribution of non-spherical precipitates

The second major difficulty for non-spherical precipitates is to describe the coarsening kinetics. For spherical precipitates a relatively simple, classical solution, the LSW law, describes the evolution of the mean precipitate radius during coarsening. Derivation of the LSW required an assumption about the precipitate shape. In reality, the shape of the precipitate should be found as part of the solution to the coarsening problem and that is one of the difficulties (Voorhees, 1992). Furthermore, for general non-spherical precipitates, even if a particular non-spherical shape is assumed, it does not seem possible to arrive at a simple expression such as the LSW law (Eq. 15.10) that could be used in a mean radius approach to describe coarsening. A second major difficulty is that the LSW law strictly applies only in the limit of a zero volume fraction of precipitates. This means that it is derived under the conditions of non-interacting precipitates. This is certainly not true for non-spherical precipitates. Consider the schematic illustration of a distribution of plate-shaped precipitates, precipitating on $\{100\}_\alpha$ planes in Fig. 15.19 viewed along a $\langle 100 \rangle_\alpha$ direction. Since the precipitates are non-spherical so also are the solute diffusion fields surrounding them. It is clear that at some stage during growth the solute diffusion fields of the precipitates will impinge on each other. As a result, a description of the coarsening of such a distribution requires a model that explicitly considers the local neighborhood of each precipitate. The mean field type of approach that led to the derivation of the LSW law will not be sufficient in such cases. Furthermore, there is another difficulty. Those parts of the precipitate plates that impinge on each other are in regions where the local solute supersaturation has been relieved and therefore coarsening will begin in this region. However, other parts of the same precipitate are exposed to regions of the matrix where the supersaturation has not been relieved. Therefore, a single precipitate may be undergoing coarsening in one region (e.g., at the tip) and growth in another. Such situations cannot be rigorously described using the simple approaches that work well for spherical precipitates. Furthermore, it illustrates a feature of non-spherical precipitates that is fundamentally different from that of spherical precipitates. Indeed, it is impossible to avoid a large overlap between growth and coarsening in the cases of non-spherical precipitates such as those shown in Fig. 15.1. In Hutchinson et al.'s (2007) search for optimized non-isothermal heat treatment profiles that maximize the strengthening increment from spherical particles discussed in Section 15.3.1, a key aspect was the identification of thermal treatments that minimize the overlap of growth and coarsening. Such situations are impossible for non-spherical precipitates and therefore the optimized thermal profiles will have fundamentally



15.19 Schematic representation of the diffusional growth and coarsening of a distribution of plate-shaped precipitates on $\{100\}_{\alpha}$ planes of an Al matrix viewed along a $\langle 100 \rangle_{\alpha}$ direction. (a) Rapid nucleation and early growth of the θ' precipitates; (b) diffusional precipitate growth; (c) soft impingement of adjacent plates at different times (dotted rectangles). The white regions represent the untransformed supersaturated matrix; and (d) coarsening during which a decrease in the number density is observed (da Costa Teixeira et al., 2008).

different forms. These have been discussed by da Costa Teixeira et al. (2008) for the case of plate-shaped precipitates that form with a large change in composition.

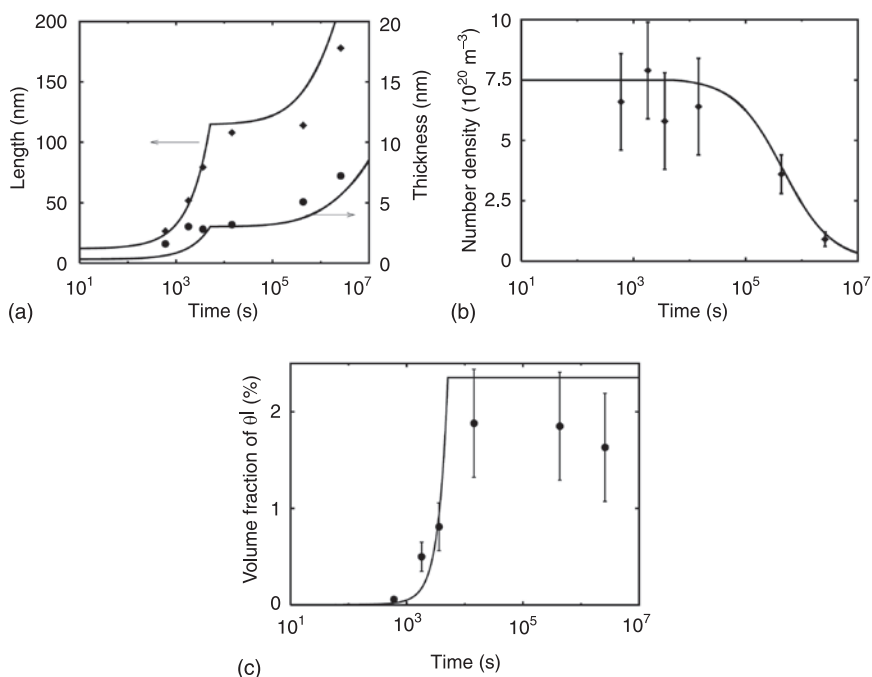
Although the approaches for non-spherical precipitates are much less mature than for spherical precipitates, there are two treatments in the literature that are worth mentioning. They represent, respectively, low and high computational cost approaches to treating the problem of θ' (Al_2Cu) in Al-Cu alloys.

The low cost approach was proposed by da Costa Teixeira et al. (2008) who modeled the precipitation of θ' in an Al-3Cu (wt. %) alloy (Fig. 15.1) at 200°C assuming site saturated nucleation (all nucleation occurred within 10 min under these conditions and therefore the experimental measurement of the initial plate density was a model input), shape preserved precipitate plate lengthening (assuming a constant aspect ratio) until, on average, soft impingement of plates

occurred (Fig. 15.19), followed by coarsening at a constant volume fraction described using the LSW kinetics assuming the plate-shaped precipitates could be represented by spheres of equivalent volume for the purpose of the kinetics. No doubt this approach is very approximate, but for the case of θ' the aspect ratio did not change very greatly during the reaction and these authors were mostly interested in aging times up to the onset of coarsening. A comparison between the predictions of their mean precipitate size model and experimental measurements made using TEM is shown in Fig. 15.20. The agreement is quite reasonable considering the low cost of the model.

However, this approach ignores the important problem of the coarsening of the distribution of plate-shaped precipitates. This is indeed important in many engineering problems, especially for the long-term prediction of the evolution of microstructure.

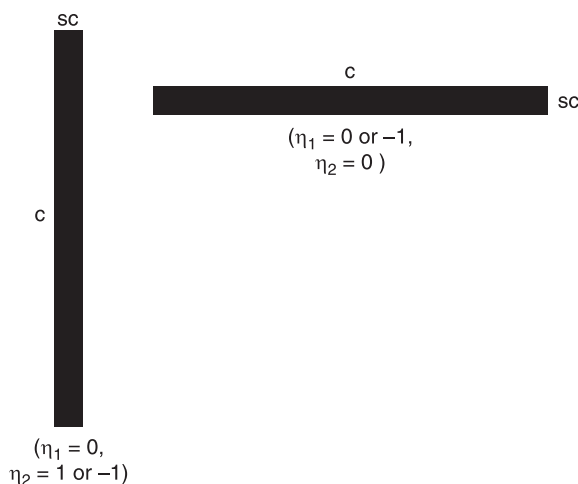
An alternative continuum approach, which is perfectly suited to the difficult topological problem of describing the evolution of a microstructure containing a



15.20 Experimental measurements (points) and model calculations (solid lines) of (a) precipitate length and thickness, (b) number density, and (c) volume fraction as a function of isothermal annealing time of an Al-3Cu-0.05Sn (wt. %) alloy aged isothermally at 473 K. The precipitate microstructures corresponding to these measurements are shown in Figure 15.1 (adapted from da Costa Teixeira et al., 2008).

distribution of interacting non-spherical particles, is the phase field approach (Chen, 2002). In this approach the microstructure is defined by a series of parameters (referred to as order parameters) that describe the long-range compositional field throughout the microstructure (e.g., $X_S(x,y,z,t)$), as well as non-conserved parameters that identify the precipitates and their orientations. These fields vary continuously throughout the microstructure, including across the interfaces separating, for example, the matrix and the precipitates. An example of the order parameters describing the θ' precipitates in two dimensions is shown in Fig. 15.21.

The parameters η_1 and η_2 identify the precipitates and their orientation. The microstructural evolution is described by solving a coupled set of evolution equations for each of the order parameters (one conserved order parameter describing the composition field and the non-conserved order parameter describing the precipitates and their orientation). For a review of this approach the reader is referred to Chen (2002). This approach has the advantages that the sets of evolution equations can be solved relatively easily, any strain effects arising between the matrix and the precipitates can be described naturally in the model, and the approach can describe properly the topological evolution resulting from the interaction between non-spherical particles. The model requires both thermodynamic and kinetic inputs, including the anisotropy of interfacial energy and interface mobility. The anisotropy of interface mobility is not known so

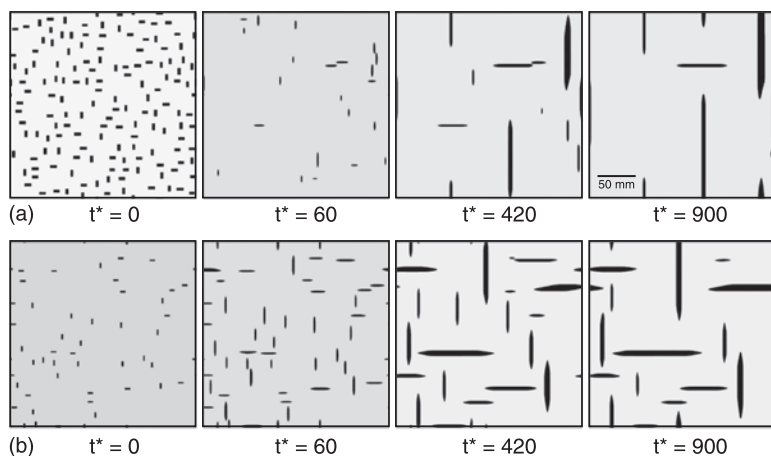


15.21 Schematic representation of the θ' (Al_2Cu) precipitates in two dimensions showing the two variants along with their order parameters (η_1 and η_2) used in the phase field simulation of the microstructural evolution of this Al-Cu binary alloy. The interfaces of the variant are labeled as coherent (c) or semi-coherent (sc) to illustrate the orientation dependence of the interfacial energy (Vaithyanathan et al., 2004).

authors usually consider only the anisotropy of interfacial energy to drive the shape evolution of the precipitates. Of course such an approach will arrive at the correct equilibrium precipitate shape but it should not be expected to give quantitative agreement with the kinetics of shape evolution until the mobility values for the phase interfaces can be calculated with some certainty and this data is used as an input to these types of calculations.

Nevertheless, the results of the phase field approach are impressive. Vaithyanathan et al. (2002, 2004) applied this approach to the precipitation of θ' (Al_2Cu) in two Al-Cu alloys and some results are shown in Fig. 15.22.

The evolution of microstructure shown in Fig. 15.22 shows a striking similarity to that shown in Fig. 15.1, illustrating the potential of this approach. Aside from the unavailability of interface mobility values to be used as inputs into the phase field model, the approach is very computationally intensive when performed in three dimensions with statistically significant volumes and numbers of precipitates, and great care must be taken with the discretization used to solve the sets of coupled evolution equations for the order parameters so that interface thicknesses (which are diffuse in this approach) remain physically reasonable (i.e. 0.2–2nm). There is a further important limitation to consider: the phase field approach cannot describe nucleation. Instead, nucleation must be introduced artificially and then the phase field approach can describe very well the growth and coarsening regimes. CNT can be used but, like other continuum approaches, the lack of sufficient precision in the knowledge of γ is a problem.



15.22 Phase field simulation of the microstructural evolution, as a function of dimensionless time, for an (a) Al-3Cu and (b) Al-4Cu alloy containing only θ' (Al_2Cu) precipitates. $T^* = 900$ corresponds to a real time of ~ 10 and 7.5 h for the three per cent and four per cent alloys aged at 200°C (Vaithyanathan et al., 2004).

15.4 Coupling precipitation and plastic deformation

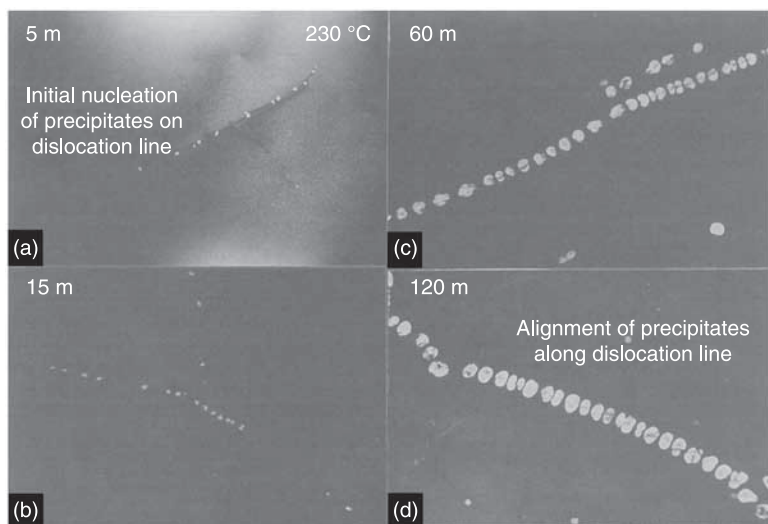
In many industrially relevant Al alloy processing schedules the precipitation process is modified by plastic deformation. This may involve a deformation of the supersaturated material prior to a thermal treatment and therefore a distribution of dislocations is present in the material prior to precipitation. These heterogeneities are known to accelerate all three stages of the precipitation process (nucleation, growth and coarsening), modify the spatial distribution of precipitates and may even influence the identity and shape of the phases that are formed (e.g., Cassada et al., 1991; Wang and Shiflet, 1995, 1996, 1998; Deschamps and Bréchet, 1998; Polmear, 1995). In other cases the deformation may occur in a material with a pre-existing distribution of precipitates. If the precipitates are readily sheared by the dislocations then the deformation can cause precipitate dissolution resulting in changes to the microstructure which are usually associated with softening (Suresh, 1998). In other cases, such as the elevated temperature deformation that may occur during some industrially forming operations, precipitation and deformation may occur simultaneously, and under these conditions the resulting precipitate state is not easily predicted.

Given the technical importance of the effect of dislocations on precipitation, authors have attempted to incorporate their effect into models for the precipitation process. In the final section we shall review very briefly the effects and highlight the most important references for the interested reader.

15.4.1 Precipitation in a pre-existing deformation structure

The nucleation, growth and coarsening stages of a precipitation reaction are all influenced by the presence of a distribution of dislocations. It is well known that dislocations act as preferred nucleation sites for many precipitates; TEM micrographs of δ' (Al_3Li) nucleating heterogeneously on dislocations in an Al-Li alloy are shown in Fig. 15.23 to illustrate the effect (Wang and Shiflet, 1996).

There are a number of potential mechanisms of interaction between the dislocation and precipitates that can lead to accelerated nucleation. The chemistry in the vicinity of the dislocation may be modified by chemical segregation, the strain field of the dislocation may effect locally the diffusion, the strain-field of the dislocation may help partly compensate for the strain-field associated with the nucleus and therefore nucleation at the dislocation is favored or nucleation may even consume part of the dislocation line resulting in the replacement of a volume of material of high Gibbs free energy with one of low free energy. The possible combinations of effects are very rich and all of the details are far from being properly understood. Nevertheless, authors have attempted to describe these effects quantitatively so that they can be incorporated into models of precipitation (Cahn, 1957; Dollins, 1970; Gomez-Ramirez and Pound, 1973; Larché, 1979).



15.23 Dark field TEM micrographs illustrating the heterogeneous nucleation and growth of δ' (Al_3Li) on dislocations during isothermal aging: (a) 5 min, (b) 15 min, (c) 60 min and (d) 120 min at 230°C in an Al-2.27 at.% Li binary alloy. The precipitates appear white and the matrix dark in dark-field imaging of Al (adapted from Wang and Shiflet, 1996).

The dislocation core is also a region of comparative disorder and it is known that diffusion is accelerated within the dislocation core. As a result, precipitate growth and coarsening may be modified for precipitates lying on dislocations and models also exist to describe these possible effects (e.g., Hoyt, 1991; Deschamps and Bréchet, 1998). The interested reader is referred to the summary by Larché (1979) for a review of the approaches. The treatments summarized by Larché apply at the continuum level. Analytical equations similar to those for growth and coarsening described in Section 15.3.1 have been derived and these can be readily substituted into the mean radius and class models for precipitation when needed. However, the models for the effect of dislocations on nucleation of precipitation are usually expressed in terms of CNT with a modified activation barrier for nucleation (and N_0 value (Eq. 15.1)). While these models do appear to qualitatively capture the main effects of dislocations on the nucleation of precipitates, the uncertainty surrounding precise values of γ precludes their quantitative test and, for practical purposes, the catalyzing effect of dislocations on precipitate nucleation is usually treated by tuning an effective γ to experimental data. This problem of CNT is not overcome by the presence of a distribution of heterogeneities.

It would appear prudent to appeal to LKMC simulations to contribute to the understanding of the effect of dislocations on the nucleation of precipitates in Al

alloys, given the contribution they have made to nucleation in the absence of defects (e.g., Clouet et al., 2004, 2005, 2006). The difficulty is that dislocations represent regions of significant local strain and the rigid lattice assumed in LKMC is far from realistic in the vicinity of a dislocation. The atoms are, in places, far from sites of the periodic FCC lattice. Nevertheless, Hin et al. (2008a, 2008b) have applied LKMC to the precipitation of NbC precipitates at dislocation in steels. They incorporated the effect of segregation to the dislocation core by attributing a different energy to the sites of the lattice and described the effect of the strain field by superimposing an additional energy on the periodic lattice sites surrounding the dislocation according to their distance from the dislocation core, in accordance with analytic descriptions of the strain field of the dislocation. Although such approaches are only approximate, these calculations have helped with an understanding of the competition between precipitation on dislocations and in the bulk, the shape evolution of the precipitates on the dislocations and the role of the strain-field and segregation energies on the precipitation process. Such approaches have not yet been applied to Al alloys but could aid greatly in the quantitative understanding of the precipitation process for coherent precipitates such as Al_3Sc , Al_3Zr , Al_3Li on dislocations, including the dependence on the competition with bulk precipitation and the dependence on the processing variables such as temperature and supersaturation.

15.4.2 Deformation of a pre-existing precipitate structure

It is well known that the precipitate state strongly affects the motion of dislocations. This is the reason for the interest in precipitation processes. However, the motion of dislocations can also strongly influence the state of precipitation. In particular, in systems containing shearable precipitates, strain-induced dissolution may occur. This is well known to the fatigue community where cyclic deformation can localize into persistent slip bands and deformation within the slip band can lead to complete dissolution of the precipitates, leading to a comparatively soft regions within the slip band and a precipitate hardened one outside of it. This has been observed extensively in precipitation hardened Al alloys (Vogel et al., 1982; Kohler et al., 1984; Bréchet et al., 1987; Suresh, 1998). Strain-induced precipitate dissolution is an important technological phenomenon and a number of authors have attempted to develop models to describe this process in terms of the deformation parameters and the precipitate state (Bréchet et al., 1987; Bréchet and Estrin, 1994; Hutchinson et al., 2009). The interested reader is referred to the original works for details but the basic physical picture is that the repeated shearing of precipitates raises their energy (by creating anti-phase boundaries in the case of ordered precipitates, and/or creating additional interfacial area) such that the solute is driven back into solution. Such systems should be considered as driven systems (Martin and Bellon, 1997; Bréchet and Hutchinson, 2006) and the variety of steady-state microstructures that can be obtained under deformation

offers a further scope to the Al alloy designer that has not yet been exploited (Hutchinson et al., 2008b).

15.4.3 Simultaneous precipitation and deformation

As a final comment, the separation into precipitation on a pre-existing dislocation structure and deformation of a pre-existing precipitate structure is a little artificial. In many industrial situations both occur simultaneously and a full description of the microstructure evolution requires a coupling of the effects. A first step in this direction has been made by Zhu (1997, 1998) who has modified a class model for precipitation of Al_3Li in Al-Li alloys to take into account the effects of dislocations on precipitate formation and dissolution. The richness in possible behavior is very large and as the modeling approaches outlined in this chapter gain maturity and greater acceptance we should expect to see much more of this type of modeling.

15.5 Future trends and perspectives

The continuum (mesoscale) models for precipitation of spherical precipitates are now relatively well developed and can be easily implemented on a desktop PC. For cases where the precipitates can be approximated as spherical, it can be expected that a significant increase in the use of these models for alloy and process design will occur in the near term. In particular, given the rapid increase in computing power, it is expected that the class models, which give access to the full particle size distribution, will increasingly replace the mean radius approaches. Already the use of these models for questions of process design [Hutchinson et al. (2007) for the choice of non-isothermal heat treatments, Nicolas and Deschamps (2003) for understanding reversion treatments, Myhr and Grong (2009) for optimizing welding conditions] has shown the large efficiencies that can be realized and it is expected that such uses will increase dramatically in the coming decade, particularly as energy costs rise for the Al alloy manufacturers. Furthermore, as the thermodynamic databases containing the expressions for the Gibbs free energy curves of the important phases in Al alloys are expanded and increasingly include descriptions for metastable phases, it is expected that efforts that consider the competition between precipitation of multiple phases (in the spirit of Perez and Deschamps, 2003) will become much more common, and will include the competition between different nucleation sites, such as dislocations and grain boundaries, opening the possibilities for modeling the formation of PFZs (e.g., Robson et al., 2003) and the mechanical properties that depend sensitively on these features.

Increasingly precipitation models will be coupled to models for heat flow, deformation and the mechanical response of Al alloys to create what is referred to as 'through process models'. These are now commonplace in the scientific

literature and it is expected that they will become increasingly important in industry for questions of alloy and process design.

A key problem for the continuum models is the sensitivity of CNT to the uncertainty in the 'effective' γ . Unfortunately, more accurate calculations of γ are not going to help this situation because of the role of heterogeneities in the FCC matrix of Al which normally dominate the nucleation sites. It is accurate calculations of the 'effective' interfacial energy of Gibbs' hypothetical dividing surface that are required, and in the vicinity of defects and chemical heterogeneities, it should not be expected that a full theoretical treatment will arrive soon. In the time being, effective γ 's will remain to be tuned to a subset of experimental information and then the through process models will be used to extrapolate to conditions not studied experimentally. Rather than replacing completely experimentation, the coupling between experiment and modeling will become even closer; such modeling requires experimental input more than ever.

Clearly, the situation for highly non-spherical precipitates requires much work and this is especially necessary for applications to Al alloys where plate and rod-shaped precipitates are so prominent. In many cases it is not acceptable to approximate these precipitates as spherical, even though this is done in the scientific literature. In the next decade, it is expected that interphase boundary mobilities will become available from Molecular Dynamics simulations and this data will provide the necessary inputs to the phase field models that can then be used to help derive simpler expressions for the growth and coarsening behavior of distributions of non-spherical precipitates. These simpler expressions can then be used in through process models that use, for example, the class model.

Quantitatively describing nucleation is one of the great remaining challenges of physical metallurgy and it is not clear if the computational tools or experimental techniques are currently available to solve this problem. This may be a problem that will only become ripe for the next generation. Nevertheless, the LKMC approaches are providing great insight into the nucleation and early growth stages for precipitates that do not require a crystal structure change upon nucleation, but approaches that do consider the structure change are needed and it is hoped these will be developed within the next decade.

Although formidable problems lie ahead, especially for nucleation and for capturing the important features of non-spherical precipitates in Al alloys, progress has been very rapid during the past 20 years and there is much to be optimistic about. The number of examples of using precipitation models for process and alloy design problems in Al alloys is testament to their current usefulness. It is expected that these uses will greatly expand during the coming decade.

15.6 References

Aaronson, H.I. and Lee, J.K. (1999), 'The kinetic equations of solid-solid nucleation theory and comparisons with experimental observations', in *Lectures on the theory of phase*

- transformations*, 2nd ed., Warrendale, PA, The Minerals, Metals and Materials Society (TMS).
- Barbu, A. and Clouet, E. (2007), 'Cluster dynamics modeling of materials, advantage and disadvantages,' *Solid State Phenomena*, 129: 51–58.
- Becker, R. and Doring, W. (1935), 'Kinetische Behandlung der Keimbildung in übersättigten Dämpfen,' *Annalen der Physik*, 416: 719–731.
- Bratland, D.H., Grong, O., Shercliff, H., Myhr, O.R. and Tjøtta, S. (1997), 'Modelling of precipitation reactions in industrial processing,' *Acta Materialia*, 45: 1–22.
- Bréchet, Y. and Estrin, Y. (1994), 'On a pseudo Portevin-Le Chatelier effect,' *Scripta Materialia et Metallurgica*, 31: 185–190.
- Bréchet, Y. and Hutchinson, C.R. (2006), 'Defect-induced solid state patterning in metals and alloys,' *Solid State Physics: Advances in Research and Applications*, 60: 181–287.
- Bréchet, Y., Louchet, F., Marchionni, C., Vergergaugry, J.L. (1987), 'Experimental (TEM and STEM) investigation and theoretical approach to the fatigue-induced dissolution of δ prime precipitates in a 2.5 wt-percent Al-Li alloy,' *Philosophical Magazine A*, 56: 353–366.
- Cahn, J.W. (1957), 'Nucleation on dislocations,' *Acta Metallurgica*, 5: 169–172.
- Cassada, W.A., Shiflet, G.J. and Starke, E.A. (1991), 'The effect of plastic deformation on Al_2CuLi (T1) precipitation,' *Metallurgical and Materials Transactions A*, 22: 299–306.
- Chen, L.Q. (2002), 'Phase-field models for microstructure evolution,' *Annual Review in Materials Science*, 32: 113–140.
- Clouet, E., Barbu, A., Lae, L. and Martin, G. (2005b), 'Precipitation kinetics of Al_3Zr and Al_3Sc in aluminium alloys modeling with cluster dynamics,' *Acta Materialia*, 53: 2513.
- Clouet, E., Nastar, M. and Sigli, C. (2004), 'Nucleation of Al_3Zr and Al_3Sc in aluminium alloys: From kinetic Monte Carlo simulations to classical theory,' *Physical Review B*, 69: 064109.1–064109.14.
- Clouet, E., Nastar, M., Barbu, A., Sigli, C. and Martin, G. (2005a), 'Precipitation in Al-Zr-Sc alloys: A comparison between kinetic Monte Carlo, cluster dynamics and classical nucleation theory,' in Howe, J.M., Laughlin, D.E., Lee, J.K., Dahmen, U. and Soffa, W.A. (Eds), *Solid-Solid Phase Transformations in Organic Materials*, Warrendale, PA: The Minerals, Metals and Materials Society.
- Clouet, E., Lae, L., Epicier, T., Lefebvre, W., Nastar, M. and Deschamps, A. (2006), 'Complex precipitation pathways in multi-component alloys,' *Nature Materials*, 5, 482.
- da Costa Teixeira, J., Cram, D.G., Bourgeois, L., Bastow, T.J., Hill, A.J. and Hutchinson, C.R. (2008), 'On the strengthening response of aluminium alloys containing shear-resistant, plate-shaped precipitates,' *Acta Materialia*, 56: 6109.
- Deschamps, A. and Bréchet, Y. (1999), 'Influence of predeformation and ageing of an Al-Zn-Mg alloy – II: Modeling of precipitation kinetics and yield stress,' *Acta Materialia*, 47: 293.
- Deschamps, A., Genevois, C., Nicolas, M., Perrard, F. and Bley, F. (2005), 'Study of precipitation kinetics: Towards non-isothermal and coupled phenomena,' *Philosophical Magazine*, 26–27: 3091.
- Dollins, C.C. (1970), 'Nucleation on dislocations,' *Acta Metallurgica*, 18: 1209–1215.
- FactSage Software (2010), *FactSage*. Available from: <http://www.factsage.com> [accessed 14 Jan 2010].
- Forbord, B., Lefebvre, W., Danoix, F., Hallem, H. and Marthinsen, K. (2004), 'Three dimensional atom probe investigation of the formation of $\text{Al}_3(\text{Sc}, \text{Zr})$ -dispersoids in aluminium alloys,' *Scripta Materialia*, 51: 333.

- Frigaard, O., Grong, O. and Midling, O.T. (2001), 'A process model for friction stir welding of age hardenable aluminium alloys,' *Metallurgical and Materials Transactions A*, 32A: 1189.
- Fuller, C.B., Murray, J.L. and Seidman, D.N. (2005), 'Temporal evolution of the nanostructure of $\text{Al}_3(\text{Sc,Zr})$ alloys: Part 1 – chemical compositions of $\text{Al}_3(\text{Sc, Zr})$ precipitates,' *Acta Materialia*, 53: 5401.
- Gibbs, J.W. (1928), *The Collected Works of JW Gibbs*, New York, Longmans, Green and Co.
- Gomez-Ramirez, R. and Pound, G.M. (1973), 'Nucleation of a second solid phase along dislocations,' *Metallurgical and Materials Transactions A*, 4: 1563.
- Gouné, M., Maugis, R., Da Costa, E.P. and Bouleau, D. (2004), 'Precipitation of copper in ferrite : Prediction of the strengthening kinetics,' *Revue de Metallurgie – Cahiers D*, 101: 71.
- Guyot, P. and Lae, L. (2006), 'Cluster dynamics modelling of precipitation kinetics in $\text{Al}(\text{Zr,Sc})$ alloys,' *Advanced Engineering Materials*, 8: 1243.
- Guyot, P., Lepinoux, J. and Sigli, C. (2009), 'Application of cluster dynamics modeling to the precipitation in aluminum alloys,' *International Journal of Materials Research*, 100: 1440.
- Hillert, M. (1957), *The role of interfacial energy during solid state phase transformations*, Jernkontorfs Annaler 141, 757.
- Hillert, M. (1999), *Application of Gibbs energy-composition diagrams*, in Lectures on the theory of phase transformations, 2nd ed, Warrendale, PA, The Minerals, Metals and Materials Society (TMS).
- Hillert, M., Hoglund, L. and Agren, J. (2003), 'Diffusion-controlled lengthening of Widmanstätten plates,' *Acta Materialia*, 51: 2089–2095.
- Hin, C., Bréchet, Y., Maugis, P. and Soisson, F. (2008a), 'Kinetics of heterogeneous precipitation of NbC in alpha-iron,' *Acta Materialia*, 56: 5535–5543.
- Hin, C., Bréchet, Y., Maugis, P. and Soisson, F. (2008b), 'Heterogeneous precipitation on dislocations: Effect of the elastic field on precipitate morphology,' *Philosophical Magazine*, 88: 1555–1567.
- Howe, J.M., Aaronson, H.I. and Gronskey, R. (1985), 'Atomic mechanisms of precipitate plate growth in the Al-Ag system – 1: Conventional transmission electron microscopy,' *Acta Metallurgica*, 33: 639–649.
- Hoyt, J.J. (1991), 'On the coarsening of precipitates located on grain boundaries and dislocations,' *Acta Metallurgica et Materialia*, 39: 2091–2098.
- Hutchinson, C.R., da Costa Teixeira, J. and Bourgeois, L. (2008b), 'Dynamically responding microstructures: a means to simultaneously achieve high strength and high elongation in Al alloys?,' in J. Hirsch, B. Skrotzki and G. Gottstein (Eds), *Aluminum Alloys: Their Physical and Mechanical Properties*, Wiley-VCH, Weinheim, pp. 1647–1652.
- Hutchinson, C.R., Gable, B.N., Ciccossillo, N., Loo, P.T., Bastow, T.J. and Hill, A.J. (2008a), 'An experimental determination of solute-vacancy binding energies in high purity dilute Al-X alloys,' in Hirsch, J., Skrotzki, B. and Gottstein, G. (Eds), *Aluminum Alloys: Their Physical and Mechanical Properties*, Wiley-VCH, Weinheim, pp. 788–794.
- Hutchinson, C.R., Goune, M. and Redjaimia, A. (2007), 'Selecting non-isothermal heat treatment schedules for precipitation hardening systems: An example of coupled property-process optimization,' *Acta Materialia*, 55: 213–223.
- Hutchinson, C.R., Loo, P.T., Bastow, T.J., Hill, A.J. and da Costa Teixeira, J. (2009), 'Quantifying the Strain-Induced Dissolution of Precipitates in Al Alloy Microstructures using Nuclear Magnetic Resonance,' *Acta Materialia*, 57: 5645–5653.

- Kamp, N., Reynolds, A.P. and Robson, J.D. (2009), 'Modelling of 7050 aluminium alloy friction stir welding,' *Science and Technology of Welding and Joining*, 14: 589–596.
- Kamp, N., Sullivan, A., Tomasi, R. and Robson, J.D. (2006), 'Modelling of heterogeneous precipitate distribution evolution during friction stir welding process,' *Acta Materialia*, 54: 2003–2014.
- Kampmann, R. and Wagner, R. (1984), 'Kinetics of precipitation in metastable binary alloys – theory and application to Cu-1.9 at. % Ti and Ni-14 at. % Al,' in *Decomposition of Alloys: The Early Stages*, Pergamon Press, Oxford.
- Kohler, E., Bischoff, E., Gerold, V. (1984), 'Chemical analysis of persistent slip bands in an age-hardened aluminium-silver alloy by means of EDS,' *Scripta Metallurgica*, 18: 699–702.
- Laird, C. and Aaronson, H.I. (1969), 'Growth of γ plates in an Al-15%Ag alloy,' *Acta Metallurgica*, 17: 505–519.
- Langer, J.S. and Schwartz, A.J. (1980), 'Kinetics of nucleation in near-critical fluids,' *Physical Review A*, 21: 948–958.
- Larché, F. (1979), 'Nucleation and precipitation on dislocations,' in Nabarro, F.R.N (Ed.), *Dislocation in Solids*, North-Holland, pp. 137–153.
- Lifshitz, I.M. and Slyosov, V.V. (1961), 'The kinetics of precipitation from supersaturated solid solution,' *Journal of Physics and Chemistry of Solids*, 19(1–2): 35–50.
- Martin, G. and Bellon, P. (1997), 'Driven alloys,' *Solid State Physics: Advances in Research and Applications*, 50: 189.
- Martin, J.W., Doherty, R.D. and Cantor, B. (1997), *Stability of Microstructure in Metallic Systems*, Cambridge University Press, Cambridge.
- Maugis, P. and Gouné, M. (2005), 'Kinetics of vanadium carbonitride precipitation in steel: A computer model,' *Acta Materialia*, 53: 3359–3367.
- Mishin, Y., Asta, M. and Li, J. (2010), 'Atomistic modeling of interfaces and their impact on microstructure and properties,' *Acta Materialia*, 58: 1117–1151.
- Moore, K.T. and How, J.M. (2000), 'Characterization of γ plate-shaped precipitates in an Al-4.2 at. % Ag alloy – Growth kinetics, solute field, composition and modeling,' *Acta Materialia*, 48: 4083–4098.
- Moore, K.T., Howe, J.M. and Veblen, D.R. (2002), 'On the solute field of composition of γ plates in an Al-22 at. % Ag alloy,' *Metallurgical and Materials Transactions A*, 33A: 1561–1565.
- Muller, S., Wolverson, C., Wang, L.W. and Zunger, A. (2000), 'Predicting the size- and temperature-dependent shapes of precipitates in Al-Zn alloys,' *Acta Materialia*, 48: 4007–4020.
- Myhr, O.R. and Grong, O. (2000), 'Modelling of non-isothermal transformations in alloys containing a particle distribution,' *Acta Materialia*, 48: 1605–1615.
- Myhr, O.R. and Grong, O. (2009), 'Novel modeling approach to optimization of welding conditions and heat treatment schedules for age hardening Al alloys,' *Science and Technology of Welding and Joining*, 14: 321–332.
- Nicolas, M. (2002), *Evolution de l'état de précipitation dans un alliage Al-Zn-Mg lors de traitements thermiques anisothermes et dans la zone affectée thermiquement de joints soudés*, PhD thesis, Institut National Polytechnique de Grenoble, France.
- Nicolas, M. and Deschamps, A. (2003), 'Characterization and modeling of precipitate evolution in an Al-Zn-Mg alloy during non-isothermal heat treatments,' *Acta Materialia*, 51: 6077.
- Novotny, G.M. and Ardell, A.J. (2001), 'Precipitation of Al_3Sc in binary Al-Sc alloys,' *Materials Science and Engineering A*, A318: 144–154.

- Ostwald, W. (1896), *Lehrbuch der Allgemeinen Chemie*, vol. 2, part 1. Leipzig, Germany.
- Pandat Software (2010), *Compu-Therm LLC, Madison WI, USA*. Available from: <http://www.computherm.com/pandat.html> [accessed 14th Jan 2010].
- Perez, M. (2005), 'Gibbs-Thomson effect in phase transformations,' *Scripta Materialia*, 52: 709.
- Perez, M. and Deschamps, A. (2003), 'Microscopic modeling of simultaneous two-phase precipitation: Application to carbide precipitation in low-carbon steels,' *Materials Science and Engineering A*, A360: 214–219.
- Perez, M., Dumont, M. and Acevedo-Reyes, D. (2008), 'Implementation of classical nucleation and growth theories for precipitation,' *Acta Materialia*, 56: 2119–2132.
- Perrard, F., Deschamps, A. and Maugis, P. (2007), 'Modeling the precipitation of NbC on dislocations in α -Fe,' *Acta Materialia*, 55: 1255–1266.
- Polmear, I.J. (1995), *Light Alloys: Metallurgy of the Light Metals*, 3rd ed., Arnold, London.
- Poole, W.J., Wang, X., Lloyd, D.J. and Embury, J.D. (2005), 'The shearable-non-shearable transition in Al-Mg-Si-Cu precipitation hardening alloys: Implications on the distribution of slip, work hardening and fracture,' *Philosophical Magazine*, 85: 3113–3135.
- Rajab, K.E. and Doherty, R.D. (1989), 'Kinetics of growth and coarsening of faceted hexagonal precipitates in an FCC matrix – 1 Experimental observations,' *Acta Metallurgica*, 37: 2709–2722.
- Ralston, K.D., Birbilis, N., Weyland, M. and Hutchinson, C.R. (2010), 'On the effect of precipitate size on the yield strength-pitting susceptibility correlation in Al-Cu-Mg alloys' in press, *Acta Materialia*.
- Robson, J.D. (2004), 'Modelling the overlap of nucleation, growth and coarsening during precipitation,' *Acta Materialia*, 52: 4669–4676.
- Robson, J.D., Jones, M.J. and Pragnell, P.B. (2003), 'Extension of the N-model to predict competing homogeneous and heterogeneous precipitation in Al-Sc alloys,' *Acta Materialia*, 51: 1453.
- Russell, K.C. (1980), 'Nucleation in solids – the induction and steady-state effects,' *Advances in Colloid and Interface Science*, 13: 205–318.
- Saunders, N. and Miodownik, A.P. (1998), *Calphad (Calculation of Phase Diagrams): A Comprehensive Guide*, New York, Pergamon.
- Slabanja, M. and Wahnström, G. (2005) 'Kinetic Monte Carlo study of Al-Mg precipitation,' *Acta Materialia*, 53: 3721–3728.
- Suresh, S. (1998), *Fatigue of Materials*, Cambridge University Press, Cambridge.
- Thermo-Calc Software (2010), Stockholm, Sweden. Available from: <http://www.thermocalc.com> [accessed 14th Jan 2010].
- Thomson, J. (1849), *Theoretical Considerations of the Effect of Pressure in Lowering the Freezing Point of Water*, Trans. Roy Soc Edin, 16, 575.
- Thornton, K., Agren, J. and Voorhies, P.W. (2003), 'Modelling the evolution of phase boundaries in solids at the meso- and nano-scales,' *Acta Materialia*, 51: 5675–5710.
- Tolley, A., Radmilovic, V. and Dahmen, U. (2005), 'Segregation in Al₃(Sc,Zr) precipitates in Al-Sc-Zr alloys,' *Scripta Materialia*, 52: 621–625.
- Turnbull, D. (1948), *Transient Nucleation*, Transactions AIME, 175, 774.
- Vaithyanathan, V., Wolverson, C., and Chen, L.Q. (2002), 'Multiscale modeling of precipitate microstructure evolution,' *Physical Review Letters*, 88: 125503.1–125503.4.
- Vaithyanathan, V., Wolverson, C., Chen, L.Q. (2004) 'Multiscale modeling of θ' precipitation in Al-Cu binary alloys,' *Acta Materialia*, 52: 2937–2987.

- Vogel, W., Wilhelm, M., Gerold, V. (1982), 'Persistent slip bands in fatigued peak aged Al-Zn-Mg single-crystals. I: Development of dislocation microstructure and change of precipitate distribution,' *Acta Metallurgica*, 30: 21–30.
- Volmer, M. and Weber, A. (1926), 'Keimbildung in übersättigten gebilden,' *Zeitschro Phys Chemie*, 119: 277–301.
- Voorhees, P.W. (1992), 'Ostwald ripening of two-phase mixtures,' *Annual Review in Materials Science*, 22: 197–215.
- Wagner, C. (1961), 'Theorie der altering von niederslagen durch umlosen (Ostwald-reifung),' *Z. Elektrochem*, 65: 581.
- Wagner, R., Kampmann, R. and Voorhees, P.W. (2002), 'Homogeneous second-phase precipitation,' in Kosterz, G. (Ed.), *Phase Transformation in Materials*, Weinheim, Wiley VCH, pp. 309–407.
- Wang, Z.M. and Shiflet, G.J. (1995), ' δ' nucleation and growth on low-angle dislocation boundaries in Al-Li,' *Physica Status Solidi*, 149: 105–122.
- Wang, Z.M. and Shiflet, G.J. (1996), 'Heterogeneous nucleation of δ' on dislocations in a dilute aluminium-lithium alloy,' *Metallurgical and Materials Transactions A*, 27A: 1599–1609.
- Wang, Z.M. and Shiflet, G.J. (1998), 'Growth of δ' on dislocations in a dilute Al-Li alloy,' *Metallurgical and Materials Transactions A*, 29A: 2073–2085.
- Wang, J., Wolverson, C., Muller, S., Liu, Z.K. and Chen, L.Q. (2005), 'First-principles growth kinetics and morphological evolution of Cu nanoscale particles in Al,' *Acta Materialia*, 53: 2759–2764.
- Wolverson, C. (1999), 'First-principles prediction of equilibrium precipitate shapes in Al-Cu alloys,' *Philosophical Magazine Letters*, 79: 683–690.
- Wolverson, C. (2000), 'First-principles theory of 250 000-atom coherent alloy microstructure,' *Modelling and Simulation in Materials Science and Engineering*, 8: 323–333.
- Wolverson, C. (2007), 'Solute-vacancy binding in aluminium,' *Acta Materialia*, 55: 5867–5872.
- Zeldovich, Y.B. (1943), 'On the theory of new phase formation: Cavitation,' *Acta Phisicochim USSR*, 18: 1–22.
- Zener, C. (1946), *Kinetics of the Decomposition of Austenite*, Trans. AIME. 167, 550.
- Zener, C. (1949), 'Theory of growth of spherical precipitates from solid solution,' *Journal of Applied Physics*, 20: 950–953.
- Zhu, A.W. (1997), 'Evolution of size distribution of shearable ordered precipitates under homogeneous deformation: Application to an Al-Li alloy,' *Acta Materialia*, 45: 4213–4223.
- Zhu, A.W. (1998), 'Strain localization and formation of heterogeneous distribution of shearable ordered precipitates: Application to an Al-10 at.% Li single crystal,' *Acta Materialia*, 46: 3211–3220.

Ultrafine-grained aluminium alloys: processes, structural features and properties

Y. ESTRIN, Monash University and CSIRO Process Science and Engineering, Australia and M. MURASHKIN and R. VALIEV, Ufa State Aviation Technical University, Russia

Abstract: This chapter provides a review of the processing techniques based on severe plastic deformation (SPD), namely high pressure torsion and equal channel angular pressing, as applied to age-hardenable and non age-hardenable Al alloys. The unusual mechanical properties of the Al alloys obtained by the various SPD methods considered are presented in terms of the ultrafine-grained microstructure and segregation/precipitation formation in the alloys produced. The outlined ‘portrait’ of the Al alloys whose microstructure has been modified by SPD also includes such features as very high strength, fatigue resistance and tensile ductility. Finally, the potential of SPD processing techniques for developing marketable Al products with improved properties is discussed.

Key words: severe plastic deformation (SPD), high-pressure torsion (HPT), equal channel angular pressing (ECAP), grain refinement, ultrafine-grained (UFG) Al alloy, microstructure, age-hardenable Al alloys, non age-hardenable Al alloys, strength, ductility, fatigue.

16.1 Introduction

One of the principal tools for controlling the mechanical properties of metallic materials is the control of the grain size of a polycrystalline material. Under deformation conditions when resistance to plastic flow is governed by dislocation glide and diffusion-controlled processes are not an issue, a reduction in the grain size leads to strengthening of the material. According to the Hall–Petch relation, strength obeys an inverse square root dependence on the average grain size.^{1,2} In addition, the strain-hardening capacity of the material is also increased, provided it has not been exhausted in the grain refinement process itself. By contrast, for high temperature deformation controlled by diffusion or grain boundary sliding, grain refinement leads to improved formability and often to the occurrence of superplasticity (SP).^{3,4}

Driving this principle to an extreme, i.e. achieving grain refinement down to nanoscale (below 100 nm),⁵ has been a key step in producing bulk materials with exceptional properties. An important breakthrough in modern materials science was the application of *severe plastic deformation (SPD)* techniques for producing ultrafine-grained (UFG) structures with an average grain size in the submicron range.⁶ Starting from the first work in this field⁷ aluminium alloys have advanced to become the most developed UFG materials. A significant advantage of SPD techniques is their applicability to nearly all commercial aluminium alloys.

Nowadays, UFG Al alloys can be obtained by means of powder metallurgy, for example by consolidation of powders obtained by ball milling.⁸ However, from a practical point of view, SPD of bulk billets is the most promising processing route for manufacturing ultrafine-grained metals and alloys for various industrial applications.

This chapter aims at presenting recent developments related to the use of SPD techniques for grain refinement in a wide range of metals and alloys. Special emphasis is placed on the basic principles of SPD processing and suitable regimes for their realisation in order to form UFG structures in commercial aluminium alloys. The chapter also considers structural features and mechanical properties of UFG aluminium alloys, such as strength, ductility, fatigue behaviour and crack growth resistance. It also deals with the effect of post-deformation processing (annealing, ageing, deformation) on microstructure and properties of UFG aluminium alloys. Superplasticity is another property characteristic of Al alloys that is of scientific as well as practical interest. The benefit of SPD is that in the UFG alloys superplasticity tends to occur at relatively low temperatures and/or high strain rates. However, this subject was recently covered in great detail in a number of review papers,^{9–11} so that the present one is focused on the properties of UFG alloys mainly at room temperatures.

16.2 Severe plastic deformation techniques used in processing of Al alloys

SPD represents a group of metal-forming processes through which large shear strains are induced in the material in order to obtain high strength by significant grain refinement. The basic principles of UFG structure development were presented in many works reported in the recent reviews.^{9,11–13} They include the requirement of high strains (with true strain in excess of six to eight) at relatively low temperatures (less than $0.4 T_m$, where T_m is the melting temperature), which is possible only under high imposed hydrostatic pressure. Another feature of SPD is the possibility to process billets whose shape is retained due to the special geometry of the process. This makes it possible to employ repeated cycles of the process.

From the early studies of UFG structure formation onwards,^{7,11} two SPD processing techniques have been developed most intensively: these are high pressure torsion (HPT) and equal channel angular pressing (ECAP). On their basis a number of new SPD processing techniques have been developed during the last 10–15 years. These developments have been recently reviewed in several surveys^{6,9,12} and books.^{13–15}

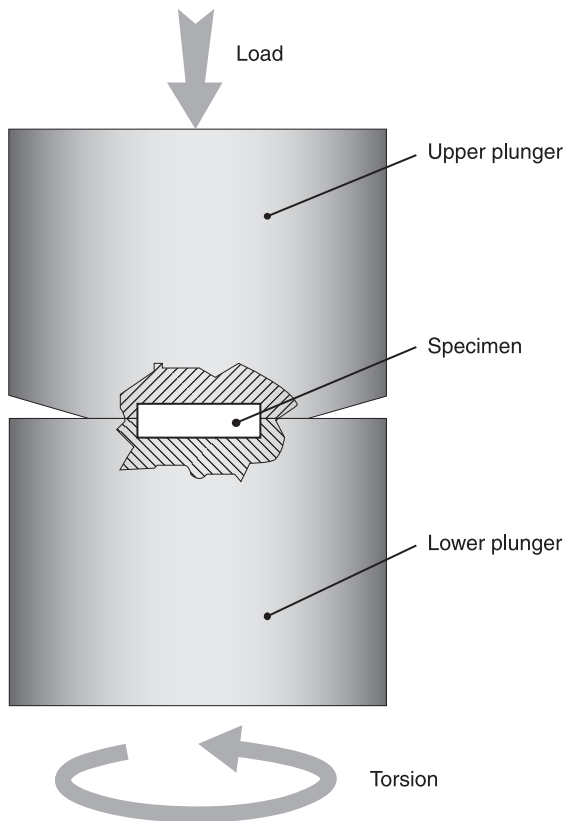
The basic challenges SPD processing is facing include application of these techniques to low ductility and hard-to-deform alloys, process up-scaling (increase in dimensions of UGF billets); fabrication of semi-products in the form of rods, sheets, wires, etc.; increase in the efficiency of the processing techniques; and adaptation of SPD techniques to the existing manufacturing environment.

The basic trends and principal results of SPD processing are briefly considered hereafter.

‘High pressure torsion (HPT)’ refers to SPD processing in which the sample, generally in form of a disc 10–20 mm in diameter and 1 mm thick, is subjected to torsional straining under a high hydrostatic pressure.^{11,12} The disc is located between two anvils, typically within a cavity (Fig. 16.1), a hydrostatic pressure (P) of 1–10 GPa is applied and torsional plastic straining is achieved by rotation of one of the anvils.

Significant grain refinement of the metals and alloys subjected to HPT processing is already observed after deformation by 1/2–1 full rotation. Yet to produce a homogeneous nanostructure with an average grain size of 100 nm and less, several rotations are required. To date, HPT has been applied to various metallic materials resulting in UFG structure development.^{12,16,17}

HPT is usually applied to relatively small discs, but there have been recent attempts to extend this technique to processing of larger billets, for example



16.1 Schematic of HPT.

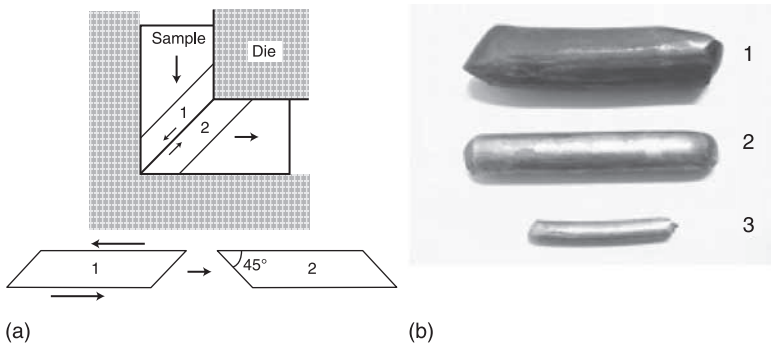
cylindrical samples 2.5–8.0 mm high.¹⁸ In a number of works the possibility of using HPT for ring billets with a diameter of 30–100 mm was explored.¹⁹ Such form of workpieces helps avoiding inhomogeneity of the UFG structure produced. Ring-shaped workpieces can also be used in manufacturing of various items.

‘Equal channel angular pressing (ECAP)’ is a technique in which very large strains can be imparted onto metal billets by simple shear. It was first introduced by V.M. Segal and his co-workers in the early 1980s.²⁰ The simple shear occurs as the sample passes through the section of an angular die where the entry and the exit channels meet (Fig. 16.2a). Since the cross-section area of the billet remains unchanged in this process, the billet can be pressed repeatedly, so that exceptionally high cumulative strains can be achieved.

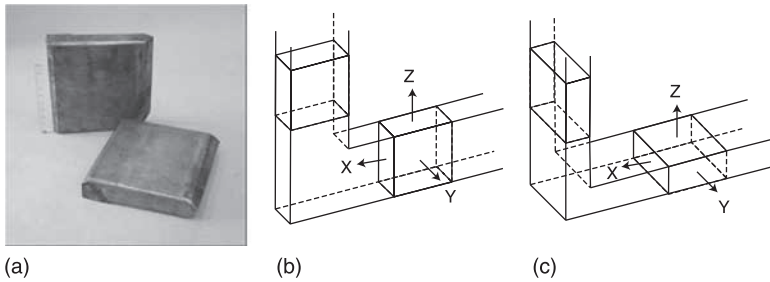
In the early 1990s R.Z. Valiev and co-workers developed ECAP techniques further and applied them for the first time with an express aim of producing UFG structures with the average grain size down to the nanometre range.⁷ Currently, ECAP is the most popular SPD technique⁹ widely applied for rods and bars of various metals and alloys to obtain the UFG structure (Fig. 16.2b).

In addition to rods and bars ECAP processing can also be applied to plate-shaped workpieces.^{20–24} For example, plates with UFG structure have been produced using a special die-set (Fig. 16.3a).^{21,22} There are two distinct configurations in pressing of plates. These configurations are illustrated in Fig. 16.3(b) and (c) where the plate is oriented vertically and horizontally, respectively. In the coordinate system used in Fig. 16.3 these two configurations correspond to plates having their major axes oriented in the X and Z or X and Y directions, respectively.

Research on flat specimens is of great practical importance as plates, along with rods, are widely applied in industry. Further development of ECAP processing



16.2 The principle of ECAP showing the shearing plane within an angular die: (a) the elements denoted 1 and 2 are transposed by shear as indicated in the lower part of the figure; (b) a view of billets of different diameters D after processing by ECAP (1) $D = 60$ mm, (2) $D = 40$ mm and (3) $D = 20$ mm.⁹

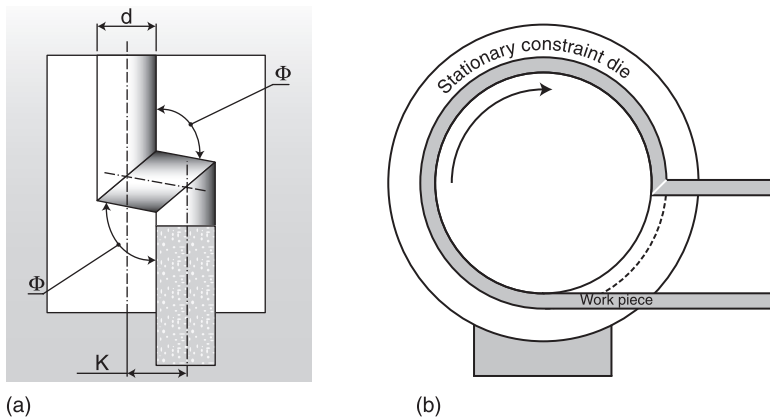


16.3 (a) Plate billets after ECAP processing²² and application of ECAP to plate samples: (b) vertical configuration and (c) horizontal configuration.^{23,24}

for flat products is essential for manufacturing of sheet metals with an UFG structure, which are in great demand.

Among the latest ECAP techniques,⁹ rotary-die ECAP²⁵ and side-extrusion²⁶ should be mentioned, although they are not widely used as yet. New trends in ECAP processing aimed at UFG structured billets are directed towards the development of techniques suitable for their industrial application.⁹ Among such techniques, two are particularly promising: ECAP with parallel channels (Fig. 16.4a) and ECAP-Conform (Fig. 16.4b). Detailed descriptions of these processes, as well as a discussion of their advantages, are provided in the original works.^{27–31}

‘Accumulative roll-bonding (ARB)’ is another interesting technique which was suggested to produce UFG structure in sheet metals.^{32–34} In this technique a



16.4 (a) Sketch of ECAP with parallel channels. Here d denotes the channel diameter, K the distance between the axes of the two channels²⁷ and Φ the angle between the two parts of the channel; (b) Schematic illustration of the ECAP-Conform process.³⁰

sheet is rolled to half of its original thickness. The rolled sheet is then cut into two halves that are stacked together. The sequence of rolling, cutting and stacking operations is repeated a number of times so that a large strain is accumulated in the sheet, while its initial size is kept unchanged until the end of processing. As a result of such multi-pass rolling a consolidated sheet with an UFG microstructure is produced. It was shown²⁸ that for reliable bonding between the sheet layers deformation under isothermal conditions at $0.4\text{--}0.5 T_m$ with thickness reduction of less than 50% per pass is required. To develop a relatively homogeneous UFG structure in metals and alloys with an average grain size measuring $0.4\text{--}0.6\text{ }\mu\text{m}$, seven to ten passes are necessary (which corresponds to a strain of 5.6–8).

Development of SPD techniques for processing aluminium alloys to produce UFG structure requires die-sets of special design (particularly using back-pressure,^{35,36} a suitable choice of lubricants, etc.), optimisation of the processing regimes with regard to the processing route, temperature, applied pressure and the rate of deformation. For example, in ECAP, billet pressing can be carried out using at least four different routes (A, Bc, B and C), and the choice of a route influences the microstructure formation significantly.⁹ That is why development of UFG structure for particular classes of Al alloys requires an individual approach, which considers their chemical and phase composition, age hardenability and other specific properties.

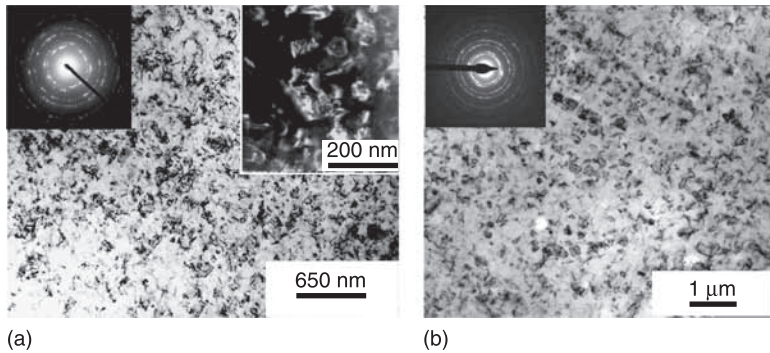
In what follows, an overview of the results of research on UFG aluminium alloys produced by SPD techniques is given. It covers commercial Al alloys of the 2xxx, 3xxx, 5xxx, 6xxx and 7xxx series.

16.3 Producing ultrafine-grained aluminium alloys by means of SPD techniques

Aluminium alloys are traditionally divided into two classes: heat treatable and non-heat treatable. Already in early works^{37–39} it was suggested that in order to achieve the maximum microstructure refinement and strength enhancement Al alloys should be subjected to solid solution treatment prior to SPD processing. For heat treatable alloys, such preliminary treatment leads to the additional benefit of precipitation hardening by nano-sized phases after SPD and subsequent ageing.^{39–44}

This issue was recently studied on several commercial Al alloys subjected to HPT processing.^{45,46} Figure 16.5(a) demonstrates the UFG structure of a non-heat treatable Al alloy 1570 after solid solution treatment and HPT at a pressure of 6 GPa and 10 anvil revolutions.

It is seen that a homogeneous UFG structure with a mean grain size of about 100 nm and predominantly high-angle grain boundaries is formed. The same processing of age-hardenable alloys, such as 6061 (Mg 0.8–1.2, Si 0.4–0.8, Cu 0.15–0.4, Cr 0.15–0.35, Mn 0.15, Fe 0.7, Zn 0.25, Ti 0.15 wt.%) (Fig. 16.5b),

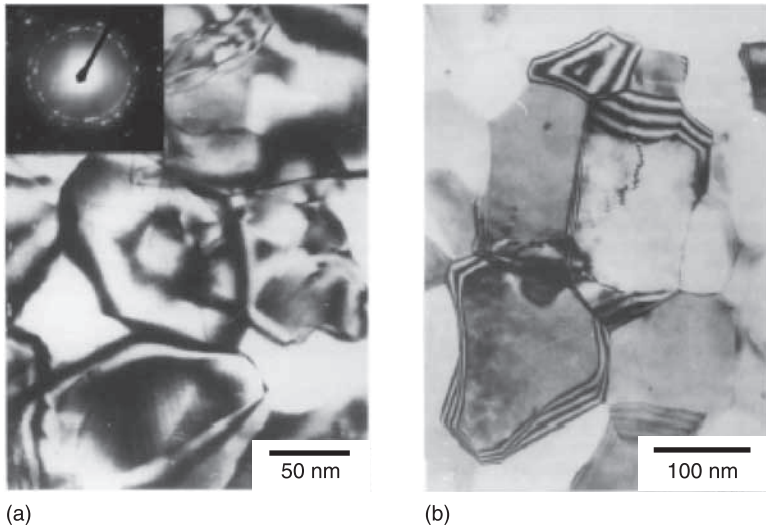


16.5 TEM microphotographs of (a) a non-heat treatable alloy 1570 and (b) a heat treatable alloy 6061 after HPT at room temperature.

1420 (Al-5.5Mg-2.1Li-0.12Zr wt.%)³⁸ and V96Z1 (Al-5.7Zn-2.7Mg-2.3Cu-0.15Zr wt.%)^{39,47} resulted in rather similar UFG structures.

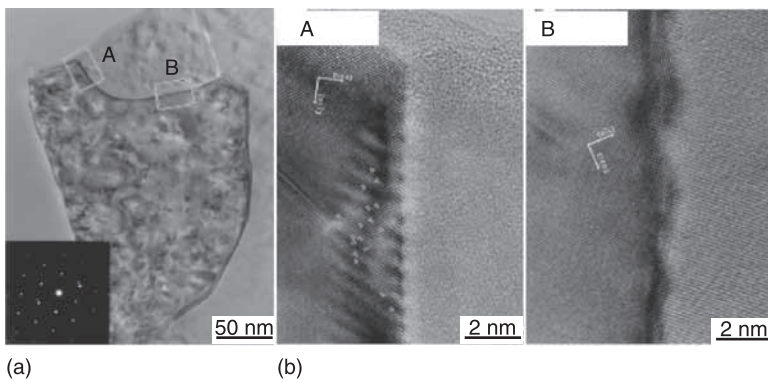
Another important feature of the UFG structures produced by SPD methods is the formation of so-called non-equilibrium grain boundaries with deformation-induced dislocations and disclinations. A theory of such grain boundaries, along with their experimental observations, has been considered in detail.^{11,48} The non-equilibrium grain boundaries exhibit a specific diffraction contrast in the transmission electron microscopy (TEM). A typical example of such diffraction contrast is an image of a nanostructured alloy Al-4%Cu-0.5%Zr³⁷ with a mean grain size of about 0.2 μm produced by HPT (Fig. 16.6a). By comparison, Fig. 16.6(b) demonstrates the microstructure of the same sample subjected to additional annealing at 160°C for one hour. In both cases, grain structures with predominantly high-angle boundaries were observed. Nevertheless, the appearance of the thickness extinction contours at grain boundaries in Fig. 16.6(a) differs from that in Fig. 16.6(b) in that considerable spreading is seen in the latter. The physical nature of such spreading of thickness extinction contours in TEM micrographs of grain boundaries in UFG materials is related to large internal stresses and crystal lattice distortions near non-equilibrium grain boundaries in the alloys subjected to SPD.^{49,50}

Detailed studies of UFG grain boundaries in Al alloys after HPT by means of high-resolution transmission electron microscopy (HRTEM)^{50,51} showed that grain boundaries are usually non-equilibrium and contain periodic steps, facets and/or other grain boundary defects (see areas A and B in Fig. 16.7). Each facet contains about four to five atomic layers and the facet density is very high, about 10^9 m^{-1} . Considerable distortions and deformation of crystal lattice are frequently observed in the images of atomic planes near grain boundaries. Some images of atomic layers break at the locations marked with '⊥', indicating the presence of dislocations (Fig. 16.7, area A).



16.6 TEM micrographs of the Al-4%Cu-0.5%Zr alloy: (a) after severe straining by HPT and (b) after HPT with additional annealing at 160°C for 1 hour.⁴⁹

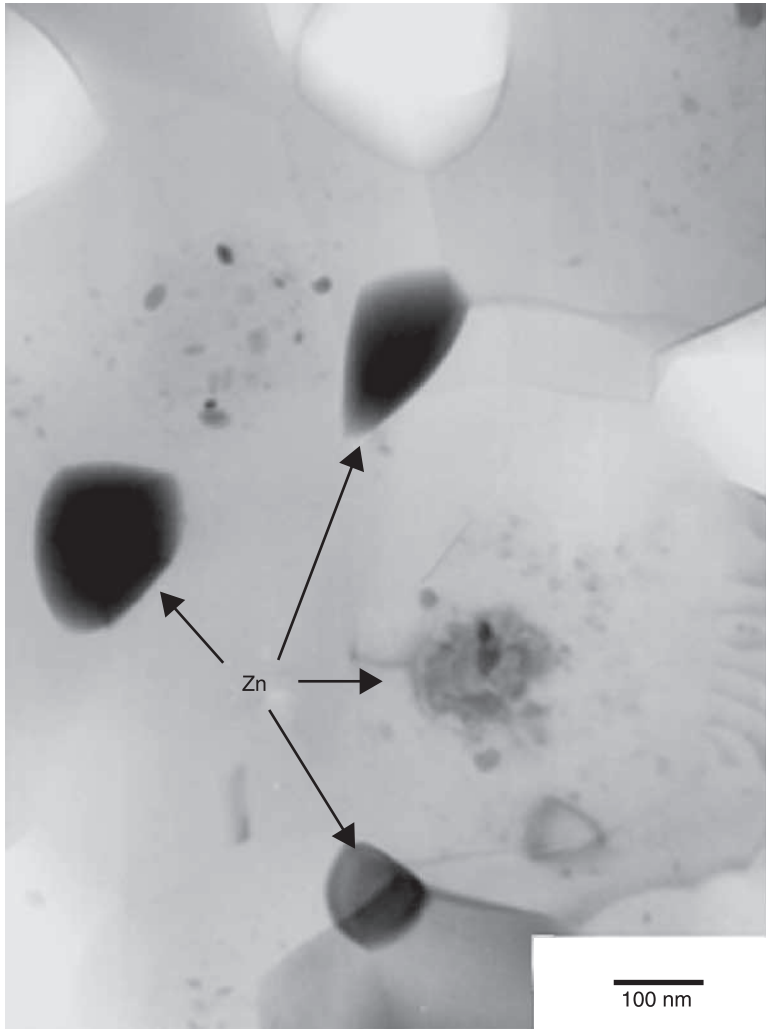
It was also established in the works^{45,46} that in both non age-hardenable and age-hardenable alloys active precipitation of second phases may occur during HPT already at room temperature. The mechanism for that may be associated with the decay of supersaturated solid solution in the process of dynamic strain ageing (DSA). In the process of HPT in the alloys Al-Zn with zinc content up to 30 wt.%, the solid solution decomposes almost completely in the beginning of



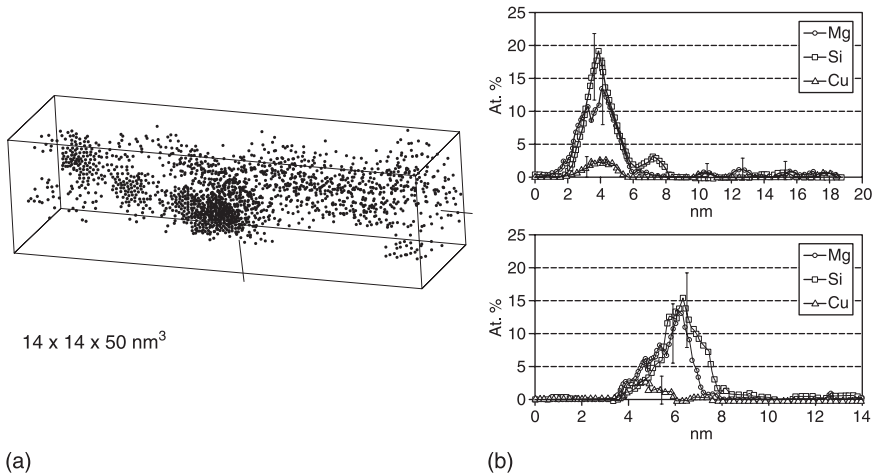
16.7 (a) A TEM micrograph of an Al-3% Mg alloy after processing through seven HPT revolutions; (b) high-resolution images of the two positions labeled A and B. The locations of dislocations at the grain boundary are marked by a symbol '⊥'.⁵⁰

HPT processing. This is followed by the formation of a two-phase UFG structure⁵² that consists of Al grains about 400 nm in size and Zn grains 50–150 nm in size (Fig. 16.8).

HPT processing of commercial Al alloys at room temperature often gives rise to grain boundary segregation. This is demonstrated by the results of three dimensional atom probe (3DAP) microscopy for the case of 6061 (Fig. 16.9).⁴⁶



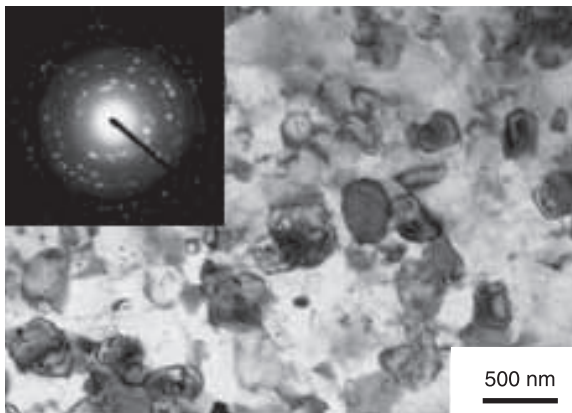
16.8 Microstructure of the Al-30 wt.% Zn alloy formed in the billet processed by HPT at room temperature: Zn-phase precipitation at triple junction and inside the Al grains is evident.



16.9 Distribution of Mg, Cu and Si atoms in a 3D reconstructed volume ($14 \times 14 \times 50 \text{ nm}^3$) for alloy 6061 processed by HPT. (a) Segregation of Si, Mg and Cu along a planar defect is clearly seen; (b) composition profiles computed across the region of segregation.

In order to form an UFG structure that would be closer to equilibrium in Al alloys, the billets were processed by HPT at higher temperatures. Thus, grain refinement of the 1570 alloy achieved by processing at 200°C was about $\sim 210 \text{ nm}$ (Fig. 16.10).⁴⁵ The figure shows that the grain boundary structure produced is, indeed, closer to equilibrium. However, as described below, DSA occurring in Al alloys along with the development of nanometre scale grain structure can affect the achieved properties greatly.

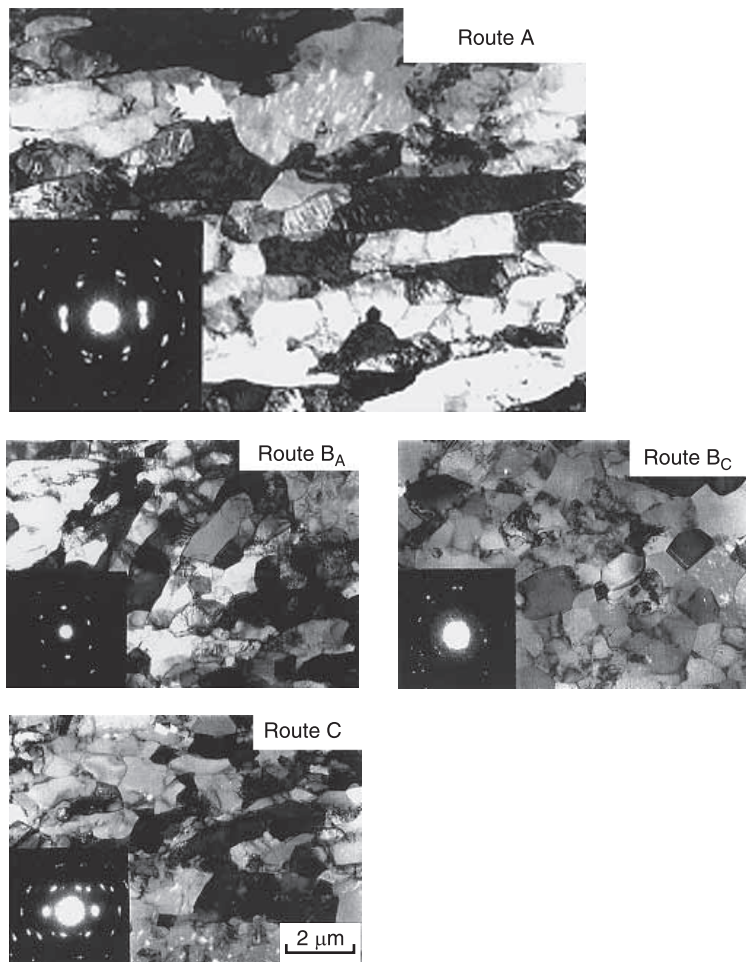
In early works on ECAP processing of Al alloys aiming at producing a UFG structure^{53–55} it was found that one to two passes are usually sufficient for



16.10 TEM micrographs of the 1570 alloy after HPT at 200°C .⁴⁵

considerable grain refinement of initial microstructure. However, the dislocation cell structures formed exhibited low-angle boundaries. Increase in the number of passes to four and more resulted in a UFG structure with mainly high-angle grain boundaries (Fig. 16.11). With the accumulation of strain the dislocation cell and sub-grain boundaries evolve into high-angle grain boundaries. From the figure it is apparent that route Bc contributes to this evolution most efficiently, whereas processing through routes A and C resulted in mainly sub-grain structure.^{9,53,54}

Homogeneous and equiaxed UFG structures with an average grain size of about 200–400 nm were achieved in such commercial alloys as 6061,^{43,56,57} 1421,⁴⁷ 1560⁵⁸ and others after ECAP processing through route Bc in Fig. 16.11.



16.11 Appearance of the microstructures on the X plane for polycrystalline aluminium after four passes of ECAP using routes A, C, B_c and B_A, together with the associated SAED patterns.^{53,54}

It was also reported that a high concentration of alloying elements, in particular Mg,⁵⁹ in Al alloys necessitates an increase of the number of passes of ECAP required to obtain a homogeneous equiaxed structure. The data reported in the work⁵⁹ suggest that this effect is associated with a decrease in the dislocations mobility and the attendant reduction in the recovery rate in Al-Mg alloys.

Formation of homogeneous UFG structure in commercial Al alloys is observed as a rule after eight and more ECAP passes.^{56–59} However, recent research on the Al 6061 alloy²⁹ proved that ECAP-PC processing, described earlier in ‘SPD techniques used in processing of Al alloys’, reduces the number of passes to four, which is two times less when compared to conventional ECAP.

A number of characteristics apart from the routes and number of passes can affect the *producing UFG* of Al alloys obtained by ECAP processing. Among them, however, and worthy of special emphasis, are the angle of intersection of channels, the angle of curvature, pressing speed and temperature as well as internal heating during ECAP.⁹

It has been established⁶⁰ that channel angle of 90° represents an optimum configuration for an ECAP die leading to equiaxed UFG structure. After the same number of passes, angle values in excess of 90° lead to a less homogeneous structure with a high fraction of low-angle boundaries.

The pressing temperature is another key factor in the use of ECAP for UFG structure development in Al alloys. The first detailed investigations of the influence of temperature involved samples of pure Al, Al-3% Mg and Al-3%Mg-0.2%Sc alloys with the pressing conducted in the range from room temperature to 300°C.⁶¹ Experimental results showed an increase in the average grain size with increasing process temperature. At the same time, it was concluded from an examination of SAED patterns that the fraction of low-angle grain boundaries increases with temperature due to faster recovery and the associated decrease in the number of dislocations absorbed into sub-grain walls.

Although it is generally easier to press specimens at elevated temperatures, an optimum UFG structure with the smallest possible grain size and the highest fraction of high-angle grain boundaries will be attained when ECAP is performed at the lowest possible temperature. Dynamic ageing is also possible during ECAP processing at high temperatures,^{29,57,58} which may affect properties of UFG materials.

A further SPD technique for producing UFG structures in metal sheets of Al alloys is ARB, described in ‘SPD techniques used in processing of Al alloys’ above. By this technique UFG structure was established in 1100, 5083, 3003 and 8011 Al alloys.^{32–34,62} A relatively homogeneous UFG structure with the average grain size of 0.4–1.0 mm is achieved after seven to ten passes. The UFG structure developed in Al alloys by ARB technique is characterised by strong anisotropy: the grains are elongated and oriented along rolling direction, unlike in microstructures produced by other SPD techniques based on ECAP processing. This anisotropy may be eliminated by subsequent ageing at 200°C.⁶²

To control the beneficial effect of SPD processing in terms of grain refinement and the attendant enhancement of strength, reliable modelling tools based on the knowledge of the underlying physical mechanisms are needed. A suitable modelling frame was provided in the works,^{63,64} in which large strain deformation in dislocation cell-forming metals was considered. The dislocation cell walls and the cell interiors were treated as two separate ‘phases’, and the variation of stress with plastic strain in these ‘phases’ was related to the evolution of the dislocation densities therein. With certain assumptions,^{63–65} the model is capable of predicting the evolution of the size of the dislocation cells, which for large strains sufficient for accumulation of large misorientations between neighbouring cells can be regarded as grains proper. In addition, a module for predicting the texture evolution during SPD processing was developed.^{63–65} A good predictive capability of the model is demonstrated in Fig. 16.12(a) and (b), where the calculated texture is seen to match the experimental one very well. A comparison between the calculated and the measured pole figures (Fig. 16.12) demonstrates that the description of the texture provided by the model is reasonably adequate.

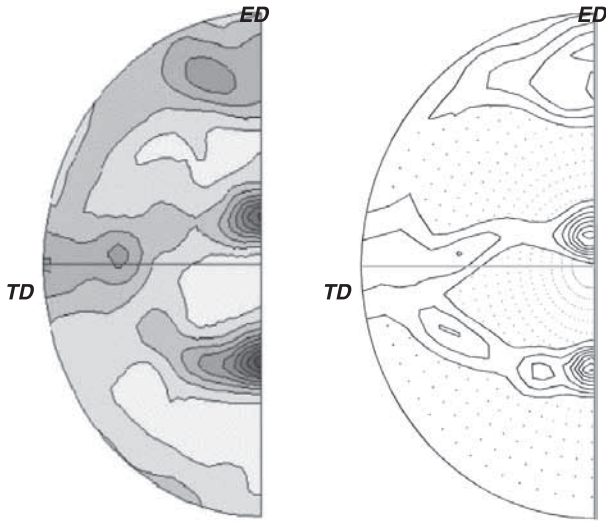
16.4 Mechanical properties of UFG Al alloys at room temperature

Fabrication of UFG Al and Al alloys by various SPD techniques, namely HPT, ECAP, ARB and others, made it possible to conduct systematic experimental investigations on microstructural features and mechanical properties of the materials such as strength, ductility, fatigue and superplasticity. We present some recent results of research on mechanical properties of Al and its alloys below.

16.4.1 Strength and ductility

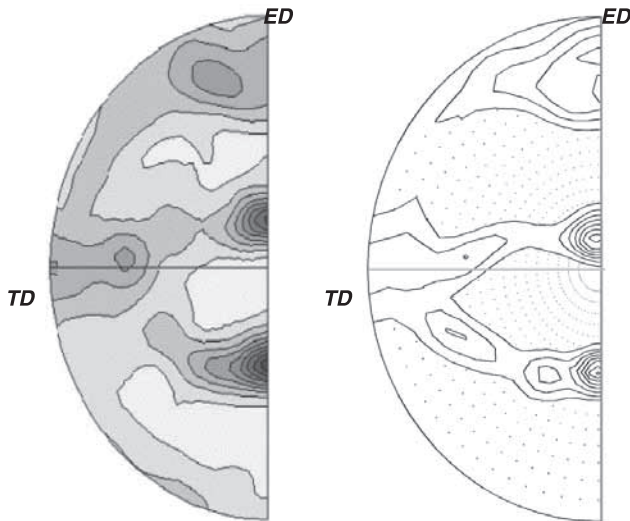
As mentioned in the previous section, the greatest grain refinement in Al and Al alloys can be achieved by HPT processing. Early research has shown that HPT applied to Al alloys results in development of UFG structure with an average grain size of about 100 nm. Compared to conventionally processed alloys, this grain refinement down to the true nanoscale leads to an increase of strength by a factor of 2–2.5. Reports^{66–68} provide examples of Al-Mg alloys with Mg content in the range of 1.5–5.9 wt.%, where microhardness values of 1.5–2.5 GPa were achieved by HPT processing. It was found^{39,69–71} that development of nanostructure by HPT is also effective for enhancement of strength in age-hardenable alloys. Thus, HPT processing of alloys 1421 (Al-5.7Mg–2.1Li–0.2Sc–0.11Zr), V96Z1 (Al-7.5Zn-2.7Mg-2.3Cu-0.15Zr) and 2024 (Al-4.2Cu-1.6Mg-0.6Mn) (all values in wt.%) conducted after quenching at room temperature resulted in Vickers hardness values of 2.6 GPa, 2.8 GPa and 2.4 GPa, respectively.

The importance of quenching before HPT processing was first highlighted in the work.³⁹ Such treatment preserves the capability of the alloy for further



(a) Experimental

(b) Simulated



(a) Experimental

(b) Simulated

16.12 Effect of four ECAP passes on the texture development in Al: (a) measured (111) pole figure; (b) model prediction.⁶⁵

hardening during ageing in the nanostructured state. It was demonstrated that HPT processing of the V96Z1 alloy resulted in an increase of Vickers hardness from 1.26 GPa to 2.24 GPa owing to the average grain size reduction to about 70 nm. The following natural ageing for 20 days led to further rise of the hardness to 2.8 GPa. This extraordinary strength is explained by additional dispersion hardening, which is very effective in the nanostructured state. The authors^{39,70} also noticed an interesting fact: HPT processed nanostructured alloys exhibited softening when HPT was followed by additional ageing at 50–300°C, whereas ageing of the same materials in the coarse-grained state resulted in their hardening.

It should be noted that earlier estimations of mechanical properties in UFG Al alloys formed by HPT technique were restricted to the microhardness measurements. Application of new HPT dies with advanced capacity and the use of equipment for precise mechanical tests of small samples⁷² made it possible to investigate a broader range of mechanical characteristics of UFG Al alloys refined down to nanometre scale.

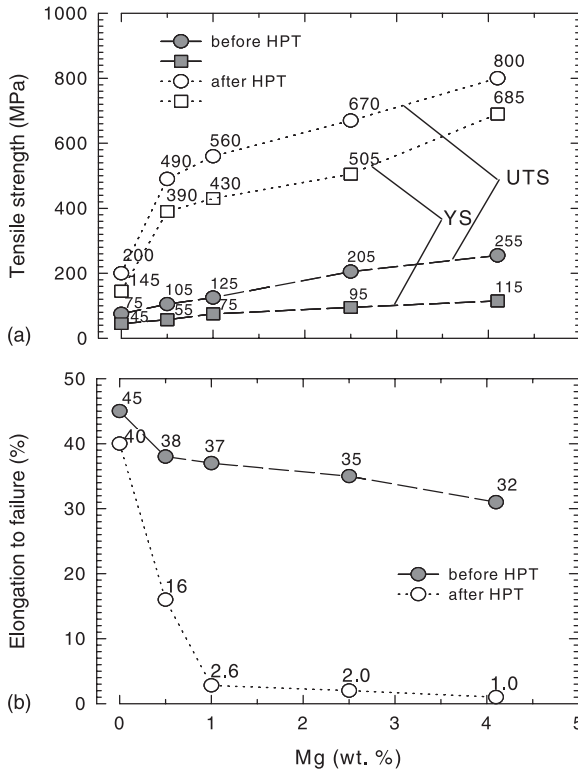
A number of recent publications have been devoted to the tensile properties of Commercial Purity Al, binary Al-Mg alloys with Mg content of 0.5 and 2.5 wt.%,^{51,73} a non age-hardenable 1570 alloy (Al-5.7Mg-0.4Mn-0.32Sc wt.%)⁴⁵ and an age-hardenable 6061 alloy (Mg 0.8–1.2, Si 0.4–0.8, Cu 0.15–0.4, Cr 0.15–0.35, Mn 0.15, Fe 0.7, Zn 0.25, Ti 0.15 wt.%)⁴⁶ The results obtained are discussed below.

Initial samples of all the investigated alloys, measuring 20 mm in diameter and 1 mm in thickness, were processed by HPT with the applied pressure of 6 GPa and more than 10 anvil revolutions. HPT processing of Al and Al alloys was conducted at room temperature, providing the maximum structure refinement. In addition, the 1570 alloy was HPT processed in isothermal conditions at 100°C and 200°C.

In tensile tests on Al alloys processed by room temperature HPT a significant improvement of strength was observed. The effect of HPT was most pronounced in binary Al-Mg alloys where UFG structure development resulted in a spectacular increase of the tensile strength by a factor of four (Fig. 16.13).

From these data it can be concluded that mechanical properties of the alloys studied depend on their Mg content. The reasons for such changes in strength have been addressed in other reports^{59,66,74,75} suggesting that an increase in Mg content results in structure refinement of Al alloys and contributes to an increase in the dislocation density after SPD processing. Both these effects contribute to enhanced strength of the alloys.

A similar strengthening effect was found in HPT processed 1570 alloy with Mg content of 5.7 wt.%. Nanostructuring of this alloy gave rise to a high-strength state (Table 16.1), the magnitude of strength not only exceeding that of high-alloyed age-hardenable alloys of the 7xxx series, but also reaching the levels of strength of some steels and Ti alloys (Table 16.1).



16.13 Effect of HPT on strength (a) and ductility (b) of commercial purity Al and binary Al-Mg alloys with Mg content of 0.5 wt.%, 1.0 wt.%, and 2.5 wt.%, and the commercial alloy AA5182 with Mg content of 4.2 wt.%.

Mechanical properties of 6061 Al alloy processed by HPT processing are also presented in Table 16.1. The strength of the material is twice as high as in the reference coarse-grained material after T6 heat treatment.

Along with high strength, the highest tensile ductility after HPT processing was observed in pure Al (tensile elongation $\delta \sim 40\%$) and binary Al-0.5Mg alloy ($\delta \sim 16\%$). The ductility of UFG 1570 and 6061 alloys was also reasonably good (cf. Table 16.1). Magnesium segregation on grain boundaries in these alloys is believed to lead to smaller grain size (hence strengthening), while promoting intergranular crack propagation thus reducing ductility.

Increased tendency to the formation of solid solutions due to HPT was also observed in the age-hardenable 6061 alloy. Formation of an UFG structure with the smallest grain size produced by HPT was accompanied with formation of nanometre-sized segregations of the principal alloying elements: Mg and Si.⁴⁶ Subsequent ageing of the material at 160°C for 0.5 hour led to more than doubling of its tensile ductility ($\delta \sim 13.5\%$ compared to $\delta \sim 5.5\%$ in the as-deformed state). It should be noted that the occurrence of segregation in UFG 6061 alloy influenced

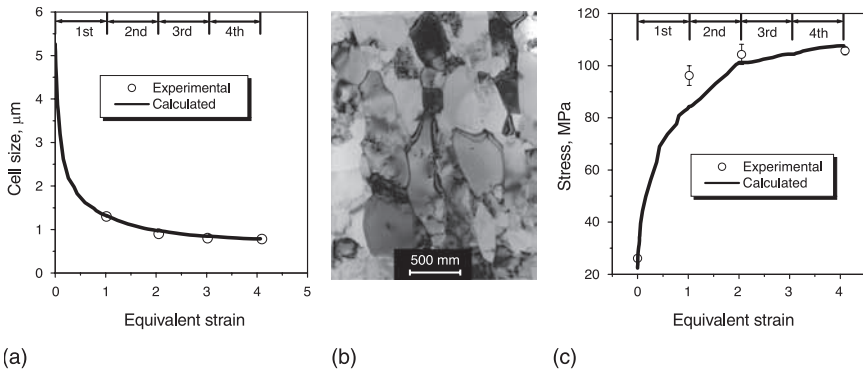
Table 16.1 Mechanical properties of Al alloys 1570 and 6061 at room temperature

Alloys	Treatment	YS (MPa)	UTS (MPa)	El (δ) (%)	Ref.
1570	Solid solution treatment + HPT at room temperature	905 \pm 31	950 \pm 35	4.7 \pm 0.3	45
	HPT at 100°C	865 \pm 25	890 \pm 18	4.0 \pm 0.4	
	HPT at 200°C	845 \pm 33	—	—	
	Conventional treatment (H14)	338	442	6.0	
	Solid solution treatment (annealing at 380°C)	257 \pm 13	394 \pm 11	17.0 \pm 1.0	
6061	Solid solution treatment + HPT at room temperature	660	690	5.5	46
	HPT + ageing at 160°C, 0.5 h	565	585	13.5	
	T6	276	365	14.9	

its properties less than the grain size and the dislocation density did, unlike in the above-mentioned Al-Mg alloys. It can be concluded that age-hardenable Al alloys of the 6xxx series with a UFG structure imparted on them by HPT processing maintain a substantial capacity for ductility improvement by means of additional ageing. As a result of such treatment, ductility of UFG alloys approaches that of the coarse-grained ones after the conventional T6 treatment (Table 16.1). A very favourable combination of strength and ductility can thus be achieved with UFG alloys.

A few words on the validity of the magnitude of strength and tensile ductility of UFG Al alloys obtained from mechanical tests on small-sized samples are due here. Some concerns may arise when ductility is measured on samples with the gauge section less than 3 mm in length. In order to allay these concerns and ensure that proper characteristics of UFG alloys are obtained, all tests were conducted using a rig equipped with a laser extensometer, capable of performing elongation measurements with an accuracy of 0.1 mm. All the above-mentioned tests of UFG Al alloys were compared with tests on similar miniaturised samples of the reference materials in the initial coarse-grained state and/or after conventional age-hardening treatment. The results of tests on miniaturised 1570 alloy samples were verified using standard testing.⁴⁵ The strength and ductility results for small-sized samples differed from the results for standard ones by no more than 15%, which is acceptable. The results reported have set a frame for extensive work on commercial Al alloys aimed at achieving a desired combination of high strength and large ductility.

The possibility for considerable strengthening of Al and Al alloys by ECAP processing was presented in numerous publications.^{9,21,22,40–43,76–80} With this technique significant grain refinement was achieved, but not to the extent HPT can deliver. As was mentioned above, the greatest grain size reduction in Al alloys occurs in the first ECAP step with subsequent passes leading to a gradual



16.14 Effect of ECAP on the grain size (a, b) and the tensile strength (c) of Al. Figures (a) and (c) are from the work of Baik et al.⁷⁷ Fig. (b) showing the grain structure of Al after eight ECAP passes stems from the work of Estrin et al.⁷⁸

decrease in grain size tending to saturation. Accordingly, tensile strength rises precipitously after the first pass and then undergoes incremental growth with subsequent passes – again with a trend to rather rapid saturation. While the magnitude of the strengthening effect for pure aluminium is rather modest (about 100 MPa) in absolute terms, the relative growth of strength – by a factor of five or so – is extreme.⁷⁷

The effect of ECAP processing on room temperature mechanical properties of both non age-hardenable and age-hardenable Al alloys was reported by various groups.^{79,80} The publications addressed a divergence in properties achieved by ECAP processing of non age-hardenable and age-hardenable alloys. Furthermore, data on the influence of additional treatments, such as rolling and ageing, on the properties of UFG materials were provided. The mechanical properties (strength and ductility) of ultrafine-grained Al alloys induced by ECAP processing were compared to those of their coarse-grained analogues, which were subjected to conventional strengthening treatment.

The most interesting results reported in these works and some recent reviews are summarised in Tables 16.2 and 16.3.

According to Table 16.2, the greatest influence of ECAP processing was recorded for commercially pure Al and Al alloys of the 3xxx series.^{80,82} Al-Mg alloys with UFG structure produced by ECAP do exhibit an increase in strength over that achieved by conventional strengthening treatment by cold rolling to maximum strength (H18), but it is not very spectacular. However, it should be mentioned that lack of considerable gain of strength in such alloys as 5056, 5083 and 1560 in the UFG state is a result of the difficulty of ECAP processing at room temperature due to low formability of these materials. In addition, temperature increase during high-cycle ECAP processing^{21,58,79} is not conducive for

Table 16.2 Mechanical properties of non age-hardenable Al alloys at room temperature

Alloy/chemical composition (wt.%)	Processing	YS (MPa)	UTS (MPa)	El (%)	Ref.
1100 (99Al)	Conv. H18 ¹	152	165	5	81
	ECAP at RT, $N = 6$	190	–	25	82
3103 (Al 1.1Mn 0.6Fe)	Conv. H18 ¹	230	250	4	83
	ECAP at RT, $N = 6$	250	270	6	80
5056 (Al 4.8Mg 0.07Mn 0.06Cr)	Conv. H18 ¹	405	435	10	83
	ECAP at RT, $N = 4$	410	440	12	84
5083 (Al 4.4Mg 0.7Mn 0.15Cr)	Conv. H116 ²	235/240 ³	310/325	17/13	21
	ECAP at ~200°C, $N = 12$	370/385 ³	420/435	11/10	79
	ECAP + anneal. 200°C, 2 h	315/325 ³	370/385	20/15	
1560 (Russian grade)	Conv. H18 ¹	423	470	5	85
(Al 6.0Mg 0.6Mn)	ECAP at ~200°C, $N = 12$	375/384 ³	467/478	10/9	79
	ECAP + anneal. 200°C, 8 h	315/325 ³	418/437	18/16	
	ECAP + cold rolling 20%	432	505	6	43
	ECAP + rolling at 120°C, strain: 90%	540	635	4	79

Notes: ¹ H18 – cold-rolled condition with strain of about 75%, in accordance with the work of Archakova et al.⁸⁵

² H116 – cold-rolled and stabilised conditions, for ductility improvement.⁸³

³ Properties in longitudinal/transverse direction with respect to ECAP.

N = number of passes, strain $\varepsilon \sim 1$ for each ECAP pass.

RT = room temperature.

strengthening. A remedy is often provided by using ECAP with back-pressure.⁸⁶ Thus, it was reported for AA5083 that with the aid of back-pressure, it was possible to conduct ECAP of the alloy at room temperature, thus achieving grain refinement down to the average grain size of 250 nm and a UTS of 427 MPa with a tolerable loss of ductility.

An optimum combination of strength and ductility of UFG Al alloys was achieved by applying ECAP with subsequent low temperature pre-recrystallisation annealing.^{21,79} The strength of the alloys subjected to such combined treatment did not exceed the level of strength of a conventional coarse-grained material subjected to a sequence of thermomechanical treatment steps, but a twofold ductility increase was achieved.

In general, cold or hot rolling treatment was found to be highly effective for improvement of strength in non age-hardenable and age-hardenable UFG Al alloys.^{43,79} While rolling as such cannot provide sufficiently severe deformation, further enhancement of strength is achieved due to additional increase in the dislocations density. Table 16.2 shows that the yield strength of 1560 Al alloy was additionally increased by about 40% after post-ECAP rolling treatment.

Age-hardenable alloys display much more prominent increase in strength after ECAP processing^{41,43,57,80,87–89} than non age-hardenable ones. Moreover, the

processing by ECAP with subsequent artificial ageing proved to be most effective for age-hardenable alloys (Table 16.3). Such processing resulted in strength some 40% higher than that of conventionally treated (T6) alloy.^{41,43,80} It should be emphasised that enhancement of strength in UFG materials is achieved with no (or almost no) loss of ductility and, in some cases, even with an increase in ductility. It was shown⁴³ in the instance of the 6061 Al alloy that a further increment of strength in UFG materials after ageing can be achieved by cold rolling. Such three-stage processing contributes to a maximum hardening effect capitalising on a combination of grain size strengthening (Hall–Petch), precipitation hardening and increased density of dislocations.

A significant increase of strength by ECAP processing with subsequent ageing was demonstrated for a number of alloys of the age-hardenable series 2xxx and 7xxx. For example, for the 7050 and 7075 alloys such processing led to an increase of the tensile strength by some 30%,^{88,89} and for the alloy 2024 this figure was about 15%.⁴¹

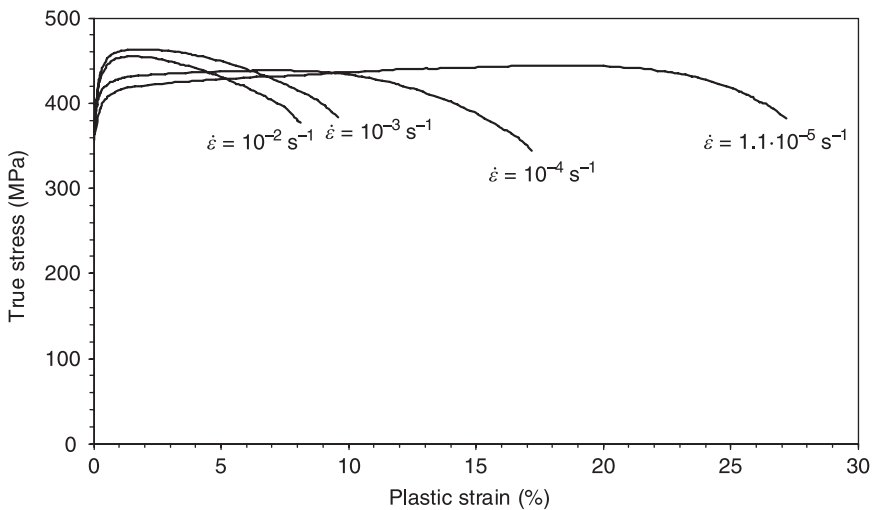
Analysis of various factors that influence strength suggests that the effect of nanoscale precipitates formed during ECAP is significant.⁹⁰ It is suggested that a combination of strengthening by grain refinement (Hall–Petch) and precipitation strengthening produced by ECAP processing is the main factor in the enhanced

Table 16.3 Mechanical properties of age-hardenable Al alloys at room temperature

Alloy/chemical composition (wt.%)	Processing	YS (MPa)	UTS (MPa)	El (%)	Ref.
6061 (Al 0.9Mg 0.7Si)	Conv. T6	268	365	15	43
	ECAP at 100°C, $N = 4$	386	434	11	
	ECAP + ageing at 130°C, 24 h	434	470	10	
	ECAP + ageing + cold rolling 15%	475	500	8	
6082 (Al 0.64Mg 1.0Si 0.52Mn)	Conv. T6	370	385	10	80
	ECAP at RT, $N = 6$ + ageing at 90°C, 192 h	437	447	17	
6060 (Al 0.74Mg 0.6Si 0.13Cr)	Conv. T6	230	250	7	
	ECAP at RT, $N = 9$ + ageing at 110°C, 72 h	310	320	14	
6005 (Al 0.56Mg 0.8Si 0.47Mn)	Conv. T6 ¹	280	310	9	
	ECAP at RT, $N = 7$ + ageing at 110°C, 72 h	380	395	12	
7050 (Al 6.0Zn 1.9Mg 2.1Cu 0.08Zr)	Conv. T6	–	520	14	88
	ECAP at 120°C, $N = 3$ + ageing at 120°C, 16 h	–	677	~14	
7075 (Al 5.6Zn 2.5Mg 1.6Cu 0.3Mn 0.23Cr)	Conv. T6	505	570	11	89
	ECAP at RT, $N = 2$ + natural ageing at RT, 1 month	650	720	8.4	
2024 (Al 4.1Cu 1.2Mg 0.6Mn 0.1 Cr)	Conv. T351	474	602	18	41
	ECAP at 160°C, $N = 1$	566	660	10	
	ECAP + ageing at 100°C, 20 h	628	715	16	

strength of age-hardenable alloys. As was shown in the work⁴³, additional strengthening of alloys of the 6xxx series is possible through increasing the precipitate density by cold rolling. Enhancement of strength of non age-hardenable alloys is achieved through utilising the same mechanisms, except, of course, for precipitation hardening.

Improvement of strength of Al alloys by severe plastic deformation is commonly associated with a loss of tensile ductility. Reduced strain hardening capability of the material processed by SPD leading to premature onset of tensile necking is the main cause. Increased strain rate sensitivity of the flow stress owing to grain refinement is usually insufficient for stabilisation against tensile necking suggested by Hart's necking criterion.⁹¹ Ma⁹² has summarised the various approaches to improving tensile ductility of UFG materials without losing their outstanding strength. These include processing leading to a bimodal grain structure,^{93,94} introducing fine precipitates,⁹⁵ deforming the material at high strain rates and/or low temperatures⁹⁶ and other approaches. An entirely different strategy was proposed in the work⁹⁷ based on a study of ECAP-processed alloy 6082.^{97,98} The effect of strain rate on the tensile properties of the material at room temperature is illustrated in Fig. 16.15. A high strength (in excess of 400 MPa) in combination with large tensile ductility was achieved^{97,98} at a small strain rate (about 10^{-5} s^{-1}). The occurrence of multiple micro-shear bands involving cooperative grain boundary sliding was suggested to 'defuse' the initiation of macro-shear bands thus delaying the onset of macroscopic failure. The diverse strategies for achieving high strength combined with good tensile ductility appear to have resolved a 'paradox' of SPD-processed metals.⁹⁹



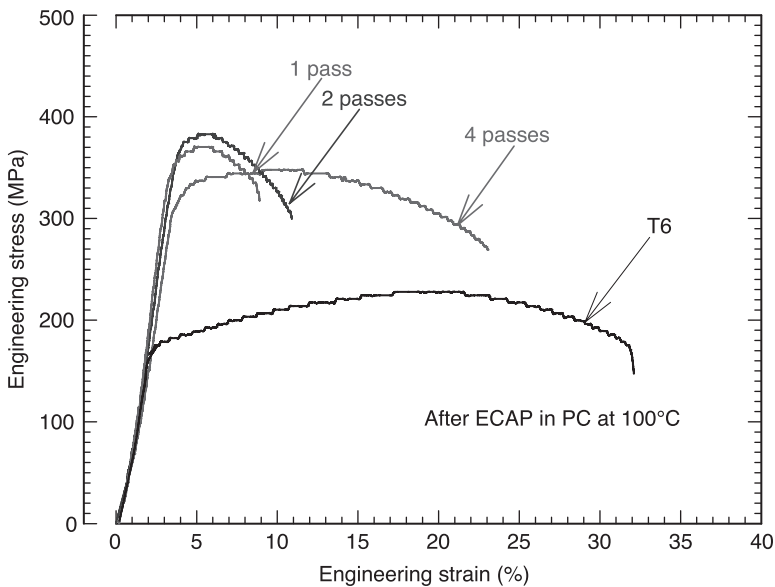
16.15 Strain rate dependence of the deformation behaviour of ECAP processed AA6082 under tension at room temperature.⁹⁸

A similar mechanical behaviour was recently observed for the UFG 6061 alloy formed by a new processing technique,²⁹ in which two ECAP steps are combined in a single process. The process is referred to as equal channel angular pressing in parallel channels (ECAP-PC). An increase in both strength and ductility was recorded after four processing steps using this promising technique (Fig. 16.16).

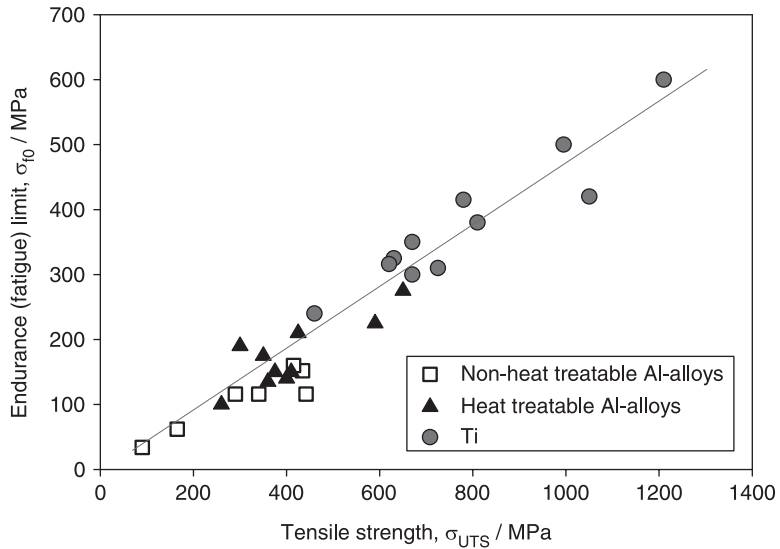
16.4.2 Fatigue behaviour

Fatigue properties are among the most important aspects of mechanical response of materials, and sufficient fatigue resistance is crucial for practical application of structural materials. It is associated with damage accumulation under cyclic loading eventually leading to fracture.

Over the last decade the fatigue properties of Al alloys processed by ECAP (in combination with other thermomechanical treatments) have been studied extensively. Indeed, ECAP processed billets are usually sufficiently big for obtaining samples of UFG metals and alloys required for fatigue tests. A recent overview of the results can be found in the work.¹⁰⁰ As discussed in the previous section, the tensile strength is generally raised by ECAP processing. As it is commonly assumed that the endurance (fatigue) limit correlates with the tensile strength, the fatigue limit can be expected to be improved by ECAP as well. This



16.16 Stress–strain curves of the Al alloy 6061 at room temperature after ECAP-PC processing vis-à-vis a curve for conventionally heat-treated material (T6).²⁹

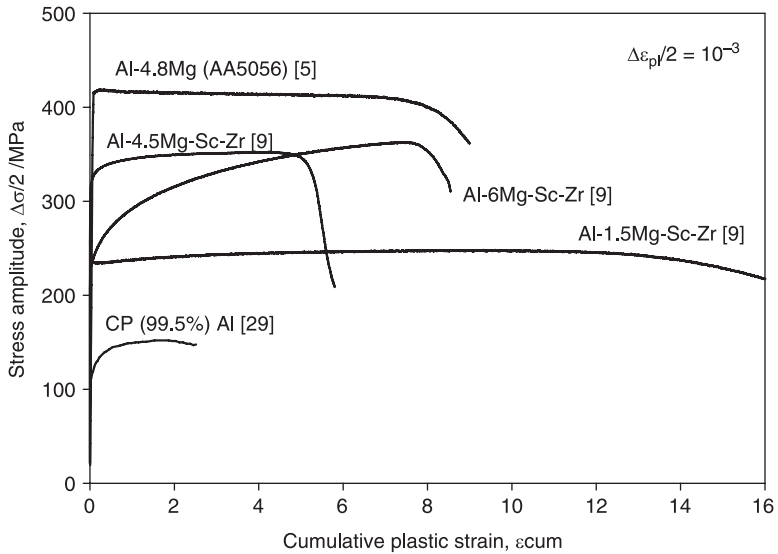


16.17 Correlation between the fatigue limit and the tensile strength for age-hardenable (heat treatable) and non-heat treatable Al alloys¹⁰⁰ (also included are data points for titanium, which support the general trend observed for Al alloys).

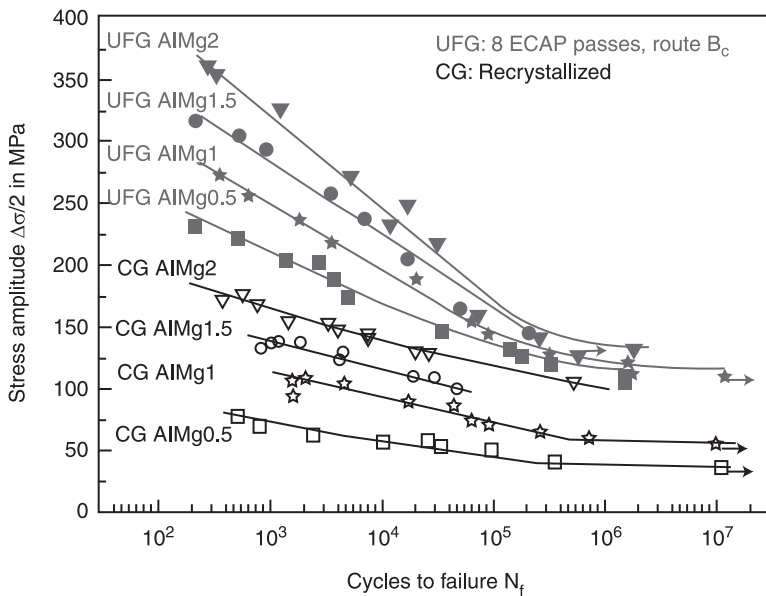
correlation, indeed, appears to be confirmed for ECAP processed Al alloys, as demonstrated in Fig. 16.17. However, the magnitude of the fatigue strength is not increased as significantly as strength under monotonic loading. While the ratio of the endurance limit to the ultimate tensile strength for coarse-grained materials often exceeds 0.5, for UFG Al alloys its magnitude is below 0.5, as seen from the slope of the regression line in Fig. 16.17. For AA5056^{101,102} and some Al-Mg-Sc alloys^{103,104} better results were achieved by conventional processing rather than by ECAP.

The aforementioned enhancement of fatigue resistance by ECAP generally refers to high-cycle fatigue (HCF). The situation is more complicated for low-cycle fatigue (LCF). As a matter of fact, grain refinement by severe plastic deformation deteriorates the ability of Al alloys to sustain cyclic loads under the LCF regime. It was suggested¹⁰⁰ that the reason for that is greater availability of grain boundaries in orientations favourable for intergranular crack propagation in ultrafine-grained materials.

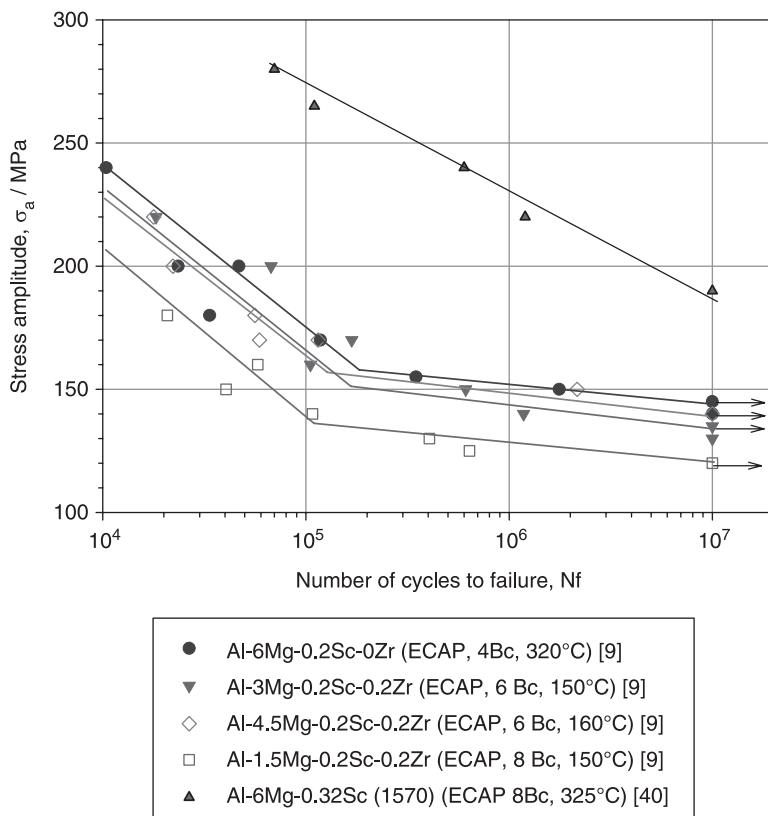
Single phase Al alloys with ultrafine-grain structure exhibit a decrease of stress amplitude (softening) when they are cyclically deformed under constant strain amplitude. This kind of response varies from alloy to alloy, as illustrated in Fig. 16.18 and Fig. 16.19. Hoeppel et al.¹⁰⁵ established that UFG Al-Mg alloys with Mg content in the 0.5–2 wt.% range (Fig. 16.19) possess a lower fatigue resistance for higher Mg content, i.e. for largest degree of microstructure



16.18 Cyclic response of SPD processed commercial purity (CP) Al and Al-Mg¹⁰⁰ at a plastic strain amplitude $\Delta\epsilon_{pl}/2 = 10^{-3}$ (the reference numbers correspond to those in the work of Estrin and Vinogradov¹⁰⁰).



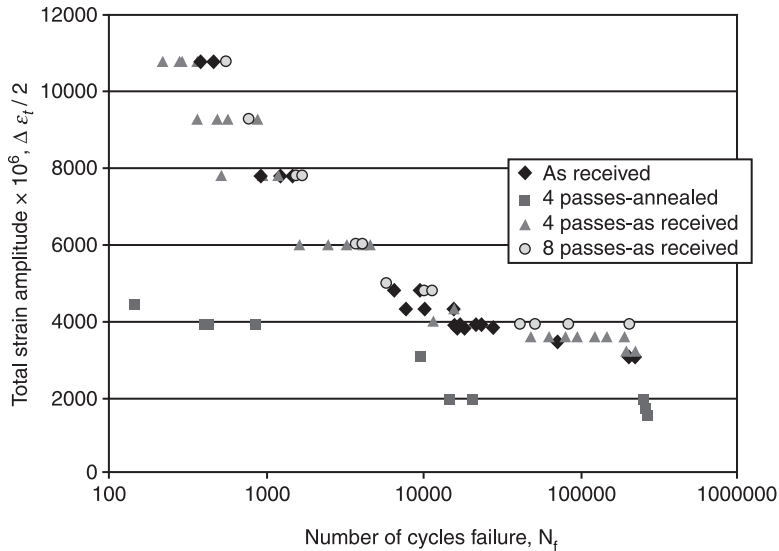
16.19 Woehler (S-N) plot for fatigue of UFG AIMg0.5, AIMg1, AIMg1.5 and AIMg2 and the coarse-grained counterparts of these alloys. The fatigue strength increases with the alloy content, in particular, in LCF range (from the work of Hoppel et al.¹⁰⁵).



16.20 HCF properties of age-hardenable Al-Mg-Sc alloys¹⁰⁰ under stress amplitude control (the reference numbers correspond to those in the work of Estrin and Vinogradov¹⁰⁰).

refinement. Under those conditions the UFG materials exhibited fatigue properties inferior to those of coarse-grained materials in both LCF and HCF regimes. Additions of Sc tend to suppress cyclic softening, or even result in cyclic strengthening, as is the case with Al-6Mg-Sc-Zr. This is reflected in a significantly extended fatigue life of ECAP processed Sc-containing alloys (cf. Fig. 16.20).

The variation of the fatigue properties with the number of ECAP passes was studied for AA2124 under strain amplitude control.¹⁰⁶ Figure 16.21 demonstrates clearly that fatigue life after eight passes is higher than that after four passes, especially in the HCF range. As was reported in the work,¹⁰⁵ fatigue properties of UFG Al-Mg alloys depend on details of ECAP processing. Thus, route Bc ECAP resulted in a significant fatigue strength improvement after 4–12 passes. However, the data reported in the work¹⁰⁷ provide a different picture. It was found that a single ECAP pass gave rise to an increase in fatigue strength of AA6061 by



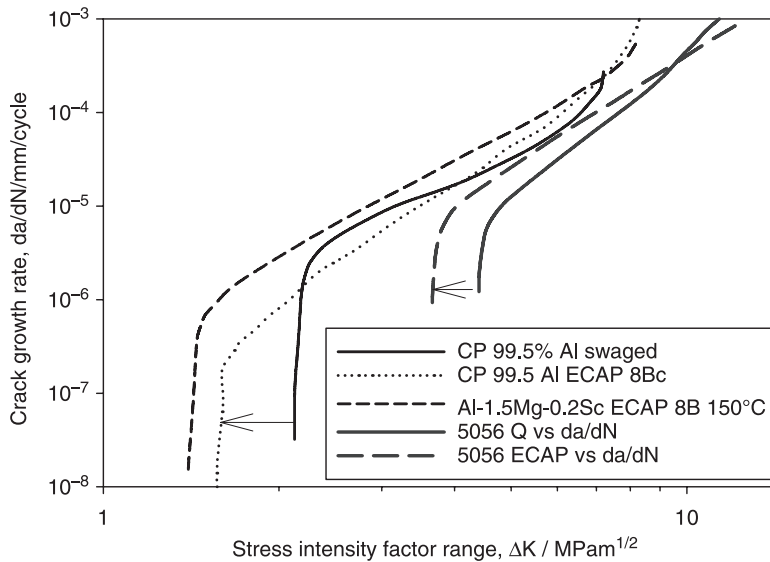
16.21 Effect of ECAP on fatigue properties of AA2124.¹⁰⁶

80 MPa, to be compared with 50 MPa achieved by conventional heat treatment (T6). However, after six ECAP passes the fatigue strength dropped by 60 MPa, in spite of the fact that the tensile strength was still increasing.

The findings presented above are yet another demonstration that one cannot generally expect overall improvement of fatigue properties by SPD processing *per se*, and that a clear understanding of the details of the microstructure produced and its role in fatigue mechanisms is required.

A very important aspect of fatigue resistance of UFG materials in the HCF regime is crack growth. The dependence of the crack growth rate, da/dN (where a is the crack length and N the number of fatigue cycles), on the stress intensity factor range ΔK for commercial purity aluminium and the non age-hardenable AA5056 is shown in Fig. 16.22. It is seen that the crack growth 'threshold' is lowered by ECAP processing, which is extremely undesirable. This drop in the threshold value can be understood in terms of less out-of plane deflections a propagating crack experiences in the ultrafine-grained ECAP-induced structure. Unfortunately, age-hardenable alloys, e.g. AA6061, show similar effects.¹⁰⁸ One may expect¹⁰⁰ that a way to combat this detrimental effect would be to try and produce a more non-uniform, e.g. bi-modal, grain structure. This may enforce a more tortuous crack path, thus leading to higher resistance to crack growth.

An important observation¹⁰⁰ is that the chemical composition of Al alloys appears to play a crucial role in the fatigue resistance, as in some cases the cumulative effect of solid solution strengthening and precipitation strengthening is more significant than the effect of grain refinement by SPD. Age-hardenable



16.22 Reduction of fatigue threshold of CP aluminium and non age-hardenable AA5056 as a result of ECAP processing.¹⁰¹ The arrows indicate a shift of the "threshold" upon ECAP of Al and alloy 5056.

alloys are generally more receptive to improving fatigue properties by ECAP, especially if solute and precipitate pinning of grain boundaries are utilised in a knowledgeable way to suppress grain coarsening during fatigue of an UFG alloy.

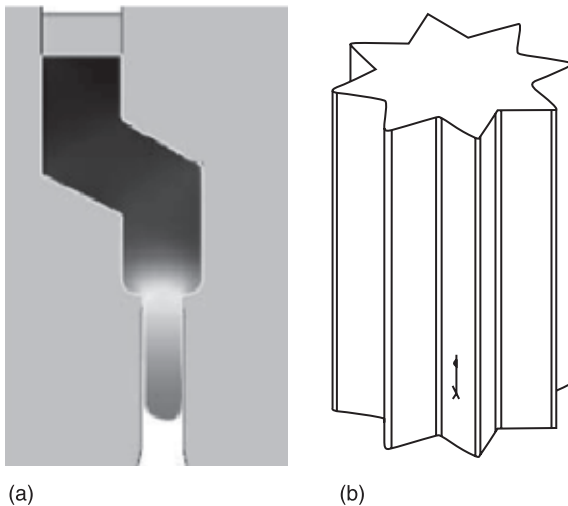
16.5 Innovation potential of UFG Al alloys

Promising markets for the UFG Al alloys produced by means of SPD techniques appear to exist in those product sectors where enhanced mechanical properties, in particular high static and cyclic strength as well as a large strength-to-weight ratio, are critical. In view of the data presented in this review one may state that the application of optimised SPD techniques leads to the formation of UFG microstructures in the Al alloys that provide an increase of strength of 30–200% and more, and/or enhancement of ductility and fatigue characteristics over those of conventional, coarse-grained Al grades. With this evident improvement of properties exhibited by UFG Al alloys one can envisage their versatile use as structural materials for aerospace, automobile, building and defence applications.¹⁰⁹ Therefore, further development and application of SPD-based processing techniques at industry scale can be anticipated.

Already at present, the SPD techniques developed initially for producing experimental specimens for laboratory scale research are targeting technologies for production of semi-products and commercial articles from UFG Al alloys. One of the trends is scaling up to larger dimensions of UFG rod-shaped billets.

Thus, recent work¹¹⁰ looked at the influence on the mechanical properties, microstructure and suitability of the Al alloy 6061 for subsequent pressure shaping when laboratory scale billets (12.5 mm in diameter) are scaled-up to dimensions relevant for commercial applications (e.g. 100 mm diameter). The results confirmed the possibility of scaling-up the most frequently applied SPD technique – ECAP – to production of semi-products with industry-scale dimensions. Conversely, miniaturisation of the die-sets for SPD processing, down to a millimetre scale may, in the authors' opinion,¹¹¹ open up new interesting directions in the fabrication of micro-mechanical devices and MEMS from the UFG Al alloys with new properties. Applications in cables, wire ropes or woven matting are also envisaged.

It was demonstrated²⁹ that application of the ECAP-PC technique may have a great potential in production of Al rods with UFG structure and enhanced mechanical properties. This promising technique developed as a variant of conventional ECAP enables one to use half of the number of strain cycles, thus improving the process efficiency and throughput. Besides, according to the results in the works,^{27,28} this technique makes it possible to increase the utilisation of the material. Another indisputable advantage of the ECAP-PC technique is that it may be customised to the conditions of full-scale production. Researchers at the Ufa State Aviation Technical University are currently engaged in studies aiming to combine direct pressing of Al alloys, which is routinely applied in metal-forming industries for fabrication of semi-products (rods, extruded profiles, etc.),



16.23 Integrated ECAP/extrusion process: (a) die design combining two ECAP passes (channel angle 120°) and a final extrusion step; (b) possible product profile produced in the exit channel of the die.¹¹¹

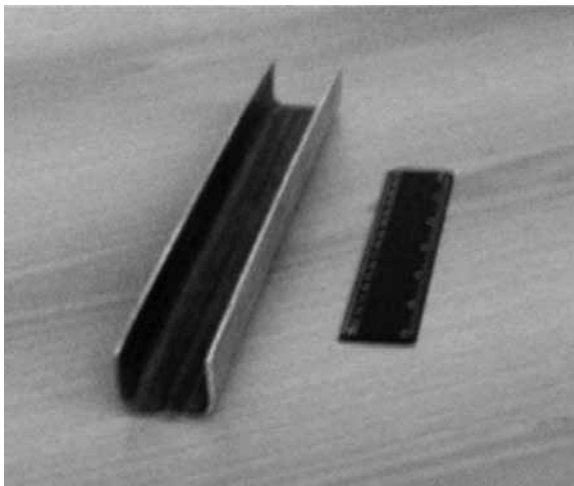
with ECAP-PC. It is planned to integrate the die-sets for such combined processing in commercial equipment, e.g. horizontal hydraulic presses.

Another target of great practical importance is fabrication of SPD-processed UFG Al semi-products in the form of plates (Fig. 16.3),^{21–24} which can be used for further fabrication of sheet products. As was demonstrated in the works,^{22,43} additional cold rolling of plates may result in high-strength sheets from UFG Al alloys, which are in great demand for structural applications in the defence and civil areas.

A further promising development for fabrication of high-strength semi-products from UFG Al alloys was suggested in the work.¹¹² That work demonstrated the feasibility of warm rolling and profiling of the UFG alloy 1421 fabricated by ECAP. It was shown that sheets and profiles with homogeneous UFG structure and high strength can be formed by warm rolling in a regime of low-temperature superplasticity (Fig. 16.24).

Commercial scale fabrication of UFG Al alloys requires designing and building equipment for *continuous* SPD production of semi-products such as rods, plates and sheets with the stock specifications satisfying the potential customer.

The feasibility of such development was highlighted in the works,^{30,113} where the formation of an UFG structure and enhancement of mechanical properties of long Al billets in the form of thin rods and sheets was demonstrated. Continuous processing of such billets is performed by means of the aforementioned technique that combines ECAP with the ‘Conform’ process.¹¹⁴ Pilot-scale production of ECAP-‘Conform’ equipment has already been launched in Ufa, Russia.³⁰ This



16.24 Profile fabricated from the UFG Al alloy 1421 in a regime of low-temperature superplasticity.¹¹²

equipment permits control of process parameters, including the angle between the channels, strain rate, temperature, etc., which makes it suitable for processing of a range of different Al alloys.

Interesting new developments with die-sets for manufacturing HPT billets of relatively large dimensions from Al alloys, which show record-breaking levels of strength, also open up prospects for the production of various new products, e.g. MEMS parts. Recent studies showed that high-strength nanostructured Al workpieces produced by HPT may also be used in structural components of various controllers.

16.6 Conclusion

In this chapter, we presented an overview of the current state of research and development in the area of ultrafine-grained Al alloys produced by severe plastic deformation. The area is growing at a very fast pace, and the level of knowledge of what happens during SPD processing at microstructural scale is impressive. It is also well understood what properties of age-hardenable and non age-hardenable Al alloys are achievable with the SPD techniques available to date. With more and more emerging patent actions following (yet lagging behind) the numerous research publications, there is an expectation that we shall soon witness major breakthroughs leading to novel marketable aluminium products. It is hoped that this review will attract the attention of researchers and technologists to the potential SPD processing of Al alloys offers.

16.7 Acknowledgements

One of the authors (Yuri Estrin) would like to acknowledge partial support from the National Research Foundation of Korea through the World Class University Program at Seoul National University, funded by the Ministry of Education, Science and Technology (R31-2008-000-10075-0). R.Z. Valiev and M.Yu. Murashkin acknowledge the support for this work from the Russian Foundation for Basic Research and the Russian Ministry for Science and Education.

16.8 References

1. Hall E.O. The deformation and ageing of mild steel: 3 discussion of results, *Proc. Phys. Soc. (London)* 64B(381) (1951), pp. 747–753.
2. Petch N.J. The cleavage strength of polycrystals, *J. Iron Steel Inst.* 174(1) (1953), pp. 25–28.
3. Langdon T.G. *Metall. Trans.* 13A (1982), pp. 689–702.
4. Mukherjee A.K. *Mater. Sci. Eng. A* 322(1) (2002), pp. 1–22.
5. Gleiter H. Nanocrystalline materials, *Prog. Mater. Sci.* 33(4) (1989), pp. 223–330.
6. Valiev R.Z., Estrin Y., Horita Z., Langdon T.G., Zehetbauer M.J., and Zhu Y.T. Producing bulk ultrafine-grained materials by severe plastic deformation, *J. Met.* 58(4) (2006), pp. 33–39.

7. Valiev R.Z., Krasilnikov N.A., and Tsenev N.K. Plastic deformation of alloys with submicro-grained structure, *Mater. Sci. Eng. A* 137 (1991), pp. 35–40.
8. Witkin D.B. and Lavernia E.J. Synthesis and mechanical behavior of nanostructured materials via cryomilling, *Prog. Mater. Sci.* 51 (2006), pp. 1–60.
9. Valiev R.Z. and Langdon T.G. (2006) *Prog. Mater. Sci.* 51(2006), pp. 881–981.
10. Kawasaki M. and Langdon T.G. *J. Mater. Sci.* 42 (2007), pp. 1782–1796.
11. Valiev R.Z., Islamgaliev R.K., and Alexandrov I.V. Bulk nanostructured materials from severe plastic deformation, *Prog. Mater. Sci.* 45 (2000), pp. 103–189.
12. Zhilyaev, A.P. and Langdon T.G. Using high-pressure torsion for metal processing: Fundamentals and applications, *Prog. Mat. Sci.* 53 (2008), pp. 893–979.
13. Estrin Y. Ultrafine grained Al alloys by severe plastic deformation: processes and properties, in *Aluminium Alloys*, J. Hirsch, B. Skrotzki, and G. Gottstein, eds, Wiley-VCH, Weinheim, 2008, Vol. 1, pp. 71–82.
14. Kolobov Yu. R., Valiev R.Z. et al. *Grain Boundary Diffusion and Properties of Nanostructured Materials*, Cambridge International Science Publishing (CISP), Cambridge, 2007.
15. Estrin Y. and Maier H.J. (eds) Nanomaterials by severe plastic deformation IV, *Selected peer reviewed papers from the 4th International Conference on Nanomaterials by Severe Plastic Deformation*, August 18–22, Goslar, Germany, 2008.
16. Horita Z., Smith D.J., Furukawa M. et al. An investigation of grain boundaries in submicrometer-grained Al-Mg solid solution alloys using high-resolution electron microscopy, *J. Mater. Res.* 11(8) (1996), pp. 1880–1889.
17. Hebesberger T., Stüwe H.P., Vorhauer A., Wetscher F., and Pippan R. Structure of Cu deformed by high pressure torsion, *Acta Mater.* 53 (2005), pp. 393–402.
18. Horita Z. and Langdon T.G. *Scripta Mater.* 58 (2008), p. 1029.
19. Harai Y., Ito Y., and Horita Z. *Scripta Mater.* 58 (2008), pp. 469–472.
20. Segal V.M., Reznikov V.I., Drobyshevskiy A.E., and Kopylov V.I. Metals shaping by simple shear, *Russian Metall.* 1 (1981), pp. 99–103. (in Russian)
21. Markusev M.V., Bampton C.C., Murashkin M.Yu., and Hardwick D.A. Structure and properties of ultra-fine grained aluminium alloys produced by severe plastic deformation, *Mater. Sci. Eng.* A234/236 (1997), pp. 927–931.
22. Markusev M.V. and Murashkin M.Yu. On fracture of fine and ultra-fine grain aluminium alloys via complex angular pressing, *Proceedings of the Aluminium alloys. Their physical and mechanical properties*, J. Hirsch, B. Skrotzki and G. Gottstein, eds, 2008, Vol. 2, pp. 1518–1524.
23. Ferrasse S., Segal V.M., and Alford F. *Mater. Sci. Eng.* A372 (2004), p. 235.
24. Kamachi M., Furukawa M., Horita Z., and Langdon T.G. *Mater. Trans.* 45 (2004), p. 2521.
25. Ma A., Nishida Y., Suzuki K., Shigematsu I., and Saito N. *Scripta Mater.* 52 (2005), p. 33.
26. Azushima A. and Aoki K. Properties of ultrafine-grained steel by repeated shear deformation of side extrusion process, *J. Mater. Sci. Eng.* A337 (2002), pp. 45–49.
27. Raab G.I. Plastic flow at equal channel angular processing in parallel channels, *Mater. Sci. Eng.* A410/411 (2005), pp. 230–233.
28. Raab G.I. Advanced ECAP techniques with increased strain per pass, *TMS 2006 Annual Meeting on Ultra-Fine Grained Materials IV*, Y.T. Zhu, T.G. Langdon, Z. Horita et al., eds, March 12–16, San Antonio, TX, USA, 2006, pp. 177–181.
29. Valiev R., Murashkin M., Bobruk E., and Raab G. Grain refinement and mechanical behavior of the Al alloy, *Mater. Trans.* 50(1) (2009), pp. 82–86.

30. Raab G.J., Valiev R.Z., Lowe T.C., and Zhu Y.T. Continuous processing of ultrafine grained Al by ECAP-Conform, *Mater. Sci. Eng. A* 382 (2004), pp. 30–34.
31. Raab G.I., Valiev R.Z., Gunderov D.V., Lowe T., Misra A., and Zhu Y.T. Long-length ultrafine-grained titanium rods produced by ECAP-Conform, *Mater. Sci. Forum* 584/586 (2008), pp. 80–83.
32. Saito Y., Utsunomiya H., Tsuji N., and Sakai T. Novel ultra-high straining process for bulk materials – development of the accumulative roll-bonding (ARB) process, *Acta. Mater.* 47 (1999), p. 579.
33. Xing Z.P., Kang S.B., and Kim H.W. Softening behavior of 8011 alloy produced by accumulative roll bonding process, *Scripta Mat.* 45 (2001), pp. 597–604.
34. Xing Z.P., Kang S.B., and Kim H.W. Structure and properties of AA3003 alloy produced by accumulative roll bonding process, *J. Mat. Sci.* 37 (2002), pp. 717–722.
35. Raab G.I., Krasilnikov N.A., and Valiev R.Z. *Fizika i Tekhnika Vysokikh Davleniy* (Physics and Engineering of High Pressures) 10(4) (2000), p. 73.
36. Lapovok, R.Ye. The role of back-pressure in equal channel angular extrusion, *J. Mater. Sci.* 40 (2005), p. 341.
37. Valiev R.Z., Korznikov A.V., and Muliukov R.R. Structure and properties of ultrafine-grained materials produced by severe plastic deformation, *Mat. Sci. Eng. A* 168 (1993), pp. 141–148.
38. Rabinovich M.K., Markushev M.V., and Murashkin M.Yu. Special features of formation of the submicrocrystalline structure in strain-heat treatment of aluminum alloy 1420 in different initial states, *Met. Sci. Heat Treat.* 39(4) (1997), pp. 172–176.
39. Stolyarov V.V., Latush V.V., Shundalov V.A., Salimonenko D.A., Islamgaliev R.K., and Valiev R.Z. Influence of severe plastic deformation on ageing effect of Al-Zn-Mg-Cu-Zr alloy, *Mat. Sci. Eng. A* 234/236 (1997), pp. 339–342.
40. Kim J.K., Jeong H.G., Hong S.I. et al. Effect of aging treatment on heavily deformed microstructure of 6061 aluminum alloy after equal channel angular pressing, *Scripta Mater.* 45 (2001), pp. 901–907.
41. Kim W.J., Chung C.S., Ma D.S. et al. Optimization of strength and ductility of 2024 Al by equal channel angular pressing (ECAP) and post-ECAP aging, *Scripta Mater.* 49 (2003), pp. 333–338.
42. Horita Z., Ohashi K., Fujita T. et al. Achieving high strength and high ductility in precipitation-hardened alloys, *Adv. Mater.* 17 (2005), pp. 1599–1603.
43. Murashkin M.Yu., Markushev M.V., Ivanisenko Yu.V., and Valiev R.Z. Strength of commercial aluminum alloys after equal channel angular pressing (ECAP) and post-ECAP processing, *Sol. State Phenomena.* 114 (2006), pp. 91–96.
44. Chinh N.Q., Gubicza J., Czepe T., Lendvai J., Xu C., Valiev R.Z., and Langdon T.G. Developing a strategy for the processing of age-hardened alloys by ECAP at room temperature, *Mater. Sci. Eng. A* 516 (2009), pp. 248–252.
45. Murashkin M.Yu., Kil'mametov A.R., and Valiev R.Z. Structure and mechanical properties of an aluminum alloy 1570 subjected to severe plastic deformation by high-pressure torsion, *Phys. Metals. Metall.* 106(1) (2008), pp. 90–96.
46. Nurislamova G., Sauvage X., Murashkin M. et al. Nanostructure and related mechanical properties of Al 6061 alloy processed by severe plastic deformation, *Phil. Mag. Lett.* 88(6) (2008), pp. 459–466.
47. Islamgaliev R.K., Yunusova N.F., Sabirov I.N., Sergeeva A.V., and Valiev R.Z. Deformation behavior of nanostructured aluminum alloy processed by severe plastic deformation, *Mat. Sci. Eng. A* 319/321 (2001), pp. 874–878.

48. Nazarov A.A., Romanov A.E., Valiev R.Z. On the structure, stress fields and energy of non-equilibrium grain boundaries, *Acta Metal. Mater.* 41(4) (1993), pp. 1033–1040.
49. Musalimov R.Sh. and Valiev R.Z. Dilatometric analysis of aluminium alloy with submicrometre grained structure, *Scripta Mater.* 27 (1992), pp. 1685.
50. Horita Z., Smith D.J., Furukawa M. et al. An investigation of grain boundaries in submicrometer-grained Al-Mg solid solution alloys using high-resolution electron microscopy, *J. Mater. Res.* 11(8) (1996), pp. 1880–1889.
51. Liu M.P., Roven H.J., Ungar T., Balogh L., Murashkin M., and Valiev R.Z. Grain boundary structure and deformation defects in nanostructured Al–Mg alloys processed by high pressure torsion, *Mat. Sci. Forum* 584/586 (2008), pp. 528–534.
52. Straumal B.B., Baretzky B., Mazilkin A.A., Phillipp F., Kogtenkova O.A., Volkov M.N., and Valiev, R.Z. *Acta Mater.* 52 (2004), pp. 4469.
53. Iwahashi Y., Horita Z., Nemoto M., and Langdon T.G. An investigation of microstructural evolution during equal-channel angular pressing, *Acta Mater.* 45 (1997), pp. 4733–4741.
54. Iwahashi Y., Horita Z., Furukawa M., Nemoto M., and Langdon T.G. *Metal. Trans. A.* 29A (1998), pp. 2011–2013.
55. Furukawa M., Iwahashi Y., Horita Z. et al. The shearing characteristics associated with equal-channel angular pressing, *Mater. Sci. Eng. A* 277 (1998), pp. 328–332.
56. Ferrasse S., Segal V.M., Hartwig K.T., and Goforth R.E. Development of a submicrometer-grained microstructure in aluminum 6061 using equal channel angular extrusion, *J. Mater. Res.* 12(5) (1997), pp. 1253–1261.
57. Kim W.J., Kim J.K., Park T.Y. et al. Enhancement of strength and superplasticity in a 6061 Al alloy processed by equal-channel-angular-pressing, *Metall. Mater. Trans. A* 33A (2002), pp. 3155–3164.
58. Markushev M.V. and Murashkin M.Yu. Structure and mechanical properties of commercial Al–Mg 1560 alloy after equal-channel angular extrusion and annealing, *Mater. Sci. Eng. A* 367 (2004), pp. 234–242.
59. Iwahashi Y., Horita Z., Nemoto M., and Langdon T.G. Factor influencing the equilibrium grain size in equal-channel angular pressing: Role of Mg addition to aluminum, *Metal. Trans. A* 29A (1998), pp. 2503–2510.
60. Nakashima K., Horita Z., Nemoto M., and Langdon T.G. Influence of channel angle on the development of ultrafine grains in equal-channel angular pressing, *Acta. Mater.* 46(5) (1998), pp. 1589–1599.
61. Yamashita A., Yamaguchi D., Horita Z., and Langdon T.G. *Mater. Sci. Eng. A* 287 (2000), p. 100.
62. Tsuji N., Ito Y., Saito Y., and Minamino, Y. Strength and ductility of ultrafine grained aluminum and iron produced by ARB and annealing, *Scripta Mater.* 47 (2002), pp. 893–899.
63. Estrin Y., Toth L., Brechet Y., and Molinari A. *Acta Mater.* 46 (1998), pp. 5509–5522.
64. Toth L., Molinari A., and Estrin Y. *J. Eng. Mat. Tech.* 124 (2002), pp. 71–77.
65. Baik S.C., Estrin Y., Kim H.S., and Hellmig H.J. *Mater. Sci. Eng. A* 351 (2003), pp. 86–97.
66. Furukawa M., Horita Z., Valiev R.Z., and Langdon T.G. Microhardness measurements and the Hall–Petch relationship in an Al–Mg alloy with submicrometer grain size, *Acta Mater.* 44(11) (1996), pp. 4619–4629.
67. Valiev R.Z., Chmelik F., Bordeaux F., Kapelski G., and Baudalet B. *Scripta Metall. Mater.* 27 (1992), pp. 855.
68. Dobatkin S.V., Zakharov V.V., and Valiev R.Z. Nanostructures in Al-based alloys after severe plastic deformation, *Proceedings of the First Joint International Conference*

- on *Recrystallization and Grain Growth*, G. Gottstein and D.A. Molodov, eds, Springer-Verlag, Berlin, 2001, pp. 509–514.
69. Islamgaliev R.K., Salimomenko D., Shestakova L.O., and Valiev R.Z. High-strength conditions of ultrafinegrained Al alloys, *Izvestija vuzov (High schools proceedings) on Nonferrous Metal Industry*, 1997, Vol. 6, pp. 52–57. (in Russian)
 70. Islamgaliev R.K., Yunusova N.F., Sabirov I.N., Sergeeva A.V., and Valiev Deformation behavior of nanostructured aluminum alloy processed by severe plastic deformation, *Mat. Sci. Eng. A* 319/321 (2001), pp. 874–878.
 71. Dobatkin S.V., Zakharov V.V., and Rokhlin L.L. Specific features of the strengthening during severe plastic deformation of supersaturated solid solutions, *Mat. Sci. Forum* 503/504 (2006), pp. 399–406.
 72. Kulyasova O.B., Islamgaliev R.K., and Valiev R.Z. On the specific features of tensile tests of small samples of nanostructured materials, *Phys. Met. Metall.* 100(3) (2005), pp. 277–283.
 73. Roven H. *Grain Refinement and Mechanical Properties in Nanostructured Al and Al–Mg Alloys Subjected to Severe Plastic Deformation*, TMS, 2009.
 74. Dobatkin S.V., Zakharov V.V., Valiev R.Z. et al. Nano- and sub-microcrystalline structure formation during high pressure torsion of Al–Sc and Al–Mg–Sc alloys, *Nanomaterials by Severe Plastic Deformation*, M. Zehetbauer and R.Z. Valiev, eds, J. Wiley VCH, Weinheim, Germany, 2003, pp. 158–164.
 75. Wang J., Iwahashi Y., Horita Z. et al. An investigation of microstructural stability in an Al–Mg alloy with submicrometer grain size, *Acta Mater.* 44(7) (1996), pp. 2973–2982.
 76. Horita Z., Fujinami T., Nemoto M., and Langdon T.G. *J. Mater. Process. Technol.* 117 (2001), pp. 288–292.
 77. Baik S.C., Estrin Y., Kim H.S., and Hellmig H.J. *Mater. Sci. Eng. A* 351 (2003), pp. 86–97.
 78. Estrin Y., Fomenko V., Grigorova T., Isaev N., Pustovalov V., Shumilin S., and Janecek M. *Adv. Eng. Mater.* 11 (2009), pp. 9–15.
 79. Markushev M.V. and Murashkin M.Y. *Proceedings of the Symposium on Ultrafine Grained Materials II*, Y.T. Zhu, T.G. Langdon, R.S. Mishra, S.L. Semiatin, M.J. Saran and T.C. Lowe, eds, TMS, Warrendale, PA, USA, 2002, pp. 371–380.
 80. Roven H.J., Nesboe H., Werenskiold J.C., and Seibert T. *Mater. Sci. Eng. A* 410/411 (2005), pp. 426–429.
 81. Davis J.R., ed., *Aluminium and aluminium alloys*, *ASM Specialty Handbook*, ASM International, Materials Park, OH, 1993, p. 784.
 82. Horita Z., Fujinami T., Nemoto M., and Langdon T.G. Microstructures and mechanical properties of submicrometer grained Al alloys produced by equal-channel angular extrusion, *Proceedings of the ICAA-6 Aluminium Alloys*, 1998, Vol. 1, pp. 449–454.
 83. Hatch J.E., ed., *Aluminium: Properties and physical metallurgy*, ASM International, Materials Park, OH, 1984.
 84. Kawazoe M., Shibata T., Mukai T., and Higashi K. Elevated temperature mechanical properties of 5056 Al–Mg alloy processed by equal-channel-angular-extrusion, *Scripta Mater.* 36 (1997), pp. 699–705.
 85. Archakova Z.N., Balakhonov G.A., and Basova I.G. *Structure and Properties of Al Semi-Products*, Metallurgy Publishers, Moscow, 1984, p. 588.
 86. Stolyarov V.V. and Lapovok R. Effect of backpressure on structure and properties of AA5083 alloy processed by ECAP, *J. Alloys Compd.* 378 (2004), pp. 233–236.

87. Zhao Y.H., Liao X.Z., Jin Z., Valiev R.Z., and Zhu Y.T. *Acta Mater.* 52 (2004), pp. 4589–4599.
88. Zheng L.J., Li H.X., Hashmi M.F., Chen C.Q., Zhang Y., and Zeng M.G. *J. Mater. Process. Technol.* 171 (2006), pp. 100–107.
89. Zhao Y.H., Liao X.Z., Jin Z., Valiev R.Z., and Zhu Y.T. Microstructures and mechanical properties of ultrafine grained 7075 Al alloy processed by ECAP and their evolutions during annealing, *Acta Mater.* 52 (2004), pp. 4589–4599.
90. Gubicza J., Schiller I., Chinh N.Q., Illy J., Horita Z., and Langdon T.G. *Mater. Sci. Eng. A* 460/461 (2007), pp. 77–85.
91. Kim H.S., and Estrin Y. *Appl. Phys. Lett.* 79(25) (2001), pp. 4115–4117.
92. Ma E. *J. Met.* 58(4) (2006), pp. 49–53.
93. Wang Y.M. and Ma E. *Acta Mater.* 52 (2004), pp. 1699–1709.
94. Hayes R.W., Witkin D., Zhou F., and Lavernia E.J. *Acta Mater.* 52 (2004), pp. 4259–4271.
95. Zhao Y.H., Liao X.Z., Cheng S., Ma E., and Zhu Y.T. *J. Adv. Mater.* 18 (2006), pp. 2280–2283.
96. Wang Y. and Ma E. *Acta Mater.* 52 (2004), pp. 1699–1709.
97. Sabirov I., Estrin Y., Barnett M.R., Timokhina I., and Hodgson P.D. *Scripta Mater.* 58, pp. 163–166.
98. Sabirov I., Estrin Y., Barnett M.R., Timokhina I., and Hodgson P.D. *Acta Mater.* 56 (2008), pp. 2223–2230.
99. Valiev R.Z., Alexandrov I.V., Lowe T.C., and Zhu Y.T. *J. Mater. Res.* 17 (2002), pp. 5–8.
100. Estrin Y. and Vinogradov A. *Engineering Fracture Mechanics*, in press.
101. Vinogradov A., Patlan V., Kitagawa K., and Kawazoe M. *Nanostruct. Mater.* 11 (1999), pp. 925–934.
102. Patlan V., Vinogradov A., Higashi K., and Kitagawa K. *Mater. Sci. Eng. A* 300 (2001), pp. 171–182.
103. Vinogradov A., Washikita A., Kitagawa K., and Kopylov, V.I. *Mater. Sci. Eng. A* 349 (2003), pp. 318–326.
104. Washikita A., Kitagawa K., Kopylov V.I., Vinogradov A., *Proceedings of the Symposium on Ultrafine Grained Materials II*, Y.T. Zhu, T.G. Langdon, R.S. Mishra, S.L. Semiatin, M.J. Saran and T.C. Lowe, eds, TMS, Warrendale, PA, USA 2002, pp. 341–345.
105. Hoppel H.W., May J., and Goken M. Fatigue behavior of UFG Al: Influence of the ECAP route and magnesium content, *Proceedings of 6th International Conference on Low Cycle Fatigue (LCF 6)*, P.D. Portella, T. Beck, M. Okazaki, eds, DVM, Berlin, Germany, 2008, pp. 325–332.
106. Lapovok R., Loder C., Dalla Torre, F.H., and Semiatin, S.L. *Mater. Sci. Eng. A* 425 (2006), pp. 36–46.
107. Chung C.S., Kim J.K., Kim H.K., and Kim W.J. Improvement of high-cycle fatigue life in a 6061 Al alloy produced by equal channel angular pressing, *Mater. Sci. Eng. A* 337 (2002), pp. 39–44.
108. Kiessling R., Hübner P., Biermann H., and Vinogradov A. *Int. J. Mater. Res.* 97 (2006), pp. 1566–1570.
109. Lowe T.C. and Zhu Y.T. *Adv. Eng. Mater.* 5 (2003), p. 373.
110. Srinivasan R., Cherukuri B., and Chaudhury P.K. *Mater. Sci. Forum* 503/504, p. 371.

111. Estrin Y., Janecek M., Raab G.I., Valiev R.Z., and Zi A. *Metall. Mater. Trans.* 38A (2007), p. 1906.
112. Islamgaliev R.K., Yunusova N.F., Valiev R.Z., Krasilnikov N.A., Ovidko I.A., and Nurislamova G.V. Fabrication of profiles from ultrafine-grained Al alloy 1421, *Met. Sci. Heat Treat.* 2 (2009), pp. 29–34.
113. Huang Y. and Prangnell P.B. Continuous frictional angular extrusion and its application in the production of ultrafine-grained sheet metals, *Scripta Mater.* 56 (2007), pp. 333–336.
114. Green D. *J. Inst. Met.* 100 (1972), pp. 295–300.

Design for fatigue crack growth resistance in aluminum alloys

D.A. LADOS, Worcester Polytechnic Institute, USA

Abstract: The chapter discusses integration of fundamental knowledge of materials science with fracture mechanics to aid in the optimization of existing aluminum alloys and the development of new alloys for improved fatigue and fatigue crack growth (FCG) resistance in structural applications. The chapter also addresses the importance of experimental, analytical and computational tools for accurate fatigue life predictions and design of fatigue critical structural components. Specifically, issues related to small crack growth and residual stress effects, critical parameters controlling FCG, FCG mechanisms at the microstructure scale of various cast and wrought aluminum alloys, and design considerations will be reviewed and discussed.

Key words: fatigue crack growth, cast and wrought aluminum alloys, microstructure, residual stress, fracture mechanics based design.

17.1 Introduction

In April 2009, U.S. President Obama stated in his address to the National Academy of Sciences: ‘But energy is our great project, this generation’s great project. And that’s why I’ve set a goal for our nation that we will reduce our carbon pollution by more than 80 percent by 2050’. To achieve this crucial worldwide goal, the transition to renewable and clean energy must be combined with higher energy efficiencies in transportation technologies through weight reduction. One way to reduce vehicle weight is to replace ferrous materials in structural components with *well-engineered and novel lighter metals*. In structural components, dynamic properties and fatigue performance of the materials are critical as more than 90% of all mechanical failures are fatigue related.¹ Therefore, a successful transition to lighter metals in such applications needs to be based on a robust understanding and optimization of the dynamic response and fatigue performance of the materials. Another means to reduce weight is to *use accurate life prediction tools to design structural components with a higher degree of confidence*, which requires appropriate fatigue data generation, interpretation and use. This will allow the application of sufficient yet not excessive safety factors, which will result in further weight and cost reductions. This chapter will address both fronts by discussing FCG mechanisms at the microstructure scale of various cast and wrought aluminum alloys, as well as important considerations for improved design for FCG resistance. The discussions in this chapter are relevant to both the materials and processing and design communities.

17.2 Background and current state of knowledge

The use of aluminum alloys has experienced a significant increase in structural applications over the past several decades due to their strength-to-weight and processing advantages, and will continue to rise. Fatigue crack initiation and crack propagation are important considerations in structural design as well as in materials and process development for aerospace, automotive and marine applications. Aluminum components for fatigue critical applications can be designed using either the traditional ‘safe life’ approach (based on stress/strain-life curves) or the ‘fail safe’ approach (a damage tolerant approach based on fracture mechanics). Since even high quality aluminum components, especially in cast conditions, contain defects such as porosity, oxides and other inclusions, crack initiation life can often be a small fraction of the total life. Therefore, materials-process design and selection for fatigue critical applications should consider fatigue crack propagation. Successful materials design and optimization for FCG resistance in structural components must consider factors from two sources. First are material characteristics such as alloy’s composition and its specific micro/nano-structure. While composition dictates the volume fraction of the micro/nano-structural features, their size, shape and distribution are controlled by processing factors and conditions such as grain refiners, phase modifiers, solidification conditions, mechanical working, heat treatment, surface treatment. Second, and equally important for life predictions and materials design, are the generation, interpretation and use of the FCG data themselves.

Damage tolerant designs commonly used for structural components utilize linear elastic fracture mechanics calculations based on the propagation of ‘*long cracks*’ (i.e., da/dN vs. ΔK curve generated from specimens such as the compact tension or C(T) specimen. This curve has three regions: Region I, a transition from no propagation below the threshold value, ΔK_{th} , to a finite and slow crack growth; Region II of stable crack growth characterized by the Paris Law, $da/dN = C \cdot \Delta K^m$; and Region III of fast and unstable crack growth approaching failure at the fracture toughness, ΔK_{FT}). However cracks, especially in early growth stages, are characterized by a ‘*small crack*’ growth behavior, which cannot be replicated by long crack growth data; the first observation of the ‘anomalous’ behavior of small cracks was reported in the 1970s.² At low stress ratios, small cracks propagate at stress intensity ranges below the long crack growth threshold, ΔK_{th} ,^{3–7} and for the same stress intensity, small cracks propagate at significantly faster rates than long cracks. The large differences between long and small crack growth data, especially in the near-threshold regime, can lead to significant over-estimations of the fatigue response and serious design errors, particularly for high cycle fatigue applications when threshold behavior is decisive.

Small cracks have been classified^{4,6–8} as mechanically small (comparable to the scale of the local plasticity; a Linear Elastic Fracture Mechanics (LEFM) limitation – Elastic-Plastic Fracture Mechanics (EPFM) considerations are needed), microstructurally small [comparable to the size of the Microstructural Characteristic Dimension (MCD) of the material; a continuum mechanics

limitation], and physically small (significantly larger than the MCD of the material). Microstructurally small cracks exhibit an oscillating growth rate behavior of acceleration followed by retardation due to a reduction of the crack tip driving force upon interaction with characteristic microstructural features. In wrought alloys, this retardation has been associated with grain boundaries,^{6,7,9,10} while in cast aluminum alloys it has been related to secondary microstructural phases such as eutectic Si particles.^{6,7,11–13} The mechanisms driving physically small cracks are considered to be fundamentally different from those of microstructurally small cracks and less microstructurally sensitive.¹⁴ The differences between long and small cracks have been reasoned through closure arguments^{6,7} even though closure cannot explain crack acceleration/retardation occurring in early stages. Closure, or premature contact of the crack faces during the unloading part of the loading cycle prior to minimum load, was first observed by Christensen under positive loading,¹⁵ and first measured for cyclic tension and established as a concept by Elber.^{16,17} Since then, numerous studies have been conducted to better understand this complex phenomenon and identify ways to measure it. The most commonly used technique to determine crack closure is based on compliance measurements taken from either a front face displacement gage or a back face strain gage. Significant difficulties in analyzing closure results have been encountered mainly due to large scatter observed on similar materials, depending on the measurement technique used, measurement location^{18,19} and specimen geometry.^{20,21}

There are various sources of closure including plasticity, oxide or debris, roughness/microstructure, residual stress, viscous fluid penetration, phase transformation; these are reviewed elsewhere.^{22,23} It must be noted that Elber developed the effective stress intensity factor range, $\Delta K_{\text{eff}} = K_{\text{max}} - K_{\text{op}}$, to compensate for the effects of plasticity induced crack closure. This type of closure is related to plastic deformation and induced residual compressive stress on the sides of the crack faces as a result of being once part of the plastic zone ahead of the crack tip. Other researchers used plasticity induced crack closure to predict crack growth under spectrum loading.^{24,25} At low crack growth rates in the near-threshold regime, this mechanism is limited (unless overloads were applied to the sample), and other closure mechanisms play important roles. Microstructure/roughness can be an important contributor to closure, and this type of closure has been used to explain the near-threshold behavior of aluminum alloys^{6,7,26,27} and aluminum alloy composites.^{28–30} Another important source of closure is residual stress. This mechanism was extensively studied, mostly from the perspective of localized internal stresses at the crack tip, and reviewed by Suresh.³¹(pp. 222–313) Researchers have investigated these internal stress mechanisms as an alternative to closure in an attempt to explain small crack behavior.³² There is another type of residual stress, macro or externally induced during processing such as quenching, which can often be significantly high and override all other closure mechanisms. The significance of macro residual stresses in fatigue crack propagation and methods to correct crack growth data for residual stress have been developed by Lados and Apelian.³³

The need for reinterpretation of the physical significance of crack closure was raised, and theories based on partial closure^{34,35} or no closure^{36–38} were proposed. A single stress intensity factor range (ΔK_{th} , whose interpretation is usually related to crack closure) was found insufficient to explain the effects of stress ratio, and the concept of a dual-parameter threshold (K_{max} and ΔK_{th}) was proposed.^{36–38} Fatigue mechanisms based on microstructural stress singularities and dislocation generation have been some of the most vigorously debated alternatives to closure, although several other mechanisms have also been proposed, many of them being detailed in a recent review.³⁹ Most of the alternatives to closure mechanisms are still inconsistent and somewhat contradictory. To determine a true small crack growth behavior various closure corrections techniques have been proposed^{35,40–47} including the Adjusted Compliance Ratio (ACR) method developed by Donald et al.⁴⁷ Other researchers assessed different methods to generate near-threshold small fatigue crack growth data that do not involve closure such as the Compression Pre-cracking Constant Amplitude (CPCA) method.^{48,49} Despite all pros and cons, crack closure remains a most important near-threshold related concept, and long crack-to-small crack corrections are critical to generate accurate data for life predictions and design.

A well-defined and universally accepted method to evaluate crack closure and correlate it with FCG behavior at the microstructure scale of the material is still lacking. Moreover, closure has only been able to explain the differences between long and physically small cracks.⁶ Closure corrective models are fracture mechanics based and cannot account for differences between physically small and microstructurally small crack growth behavior. Microstructural contributions are critical to provide the correct small crack growth threshold and allow for accurate life predictions and design. *It is important to understand microstructurally small crack growth behavior in the near-threshold regime and develop unique corrective methods that integrate closure corrections (Fracture Mechanics based) with characteristic microstructural elements (Materials Science based).* Closure contributions are also less significant in Regions II and III of crack growth, where crack propagation mechanisms are dictated by microstructural features characteristic to each material/microstructure.^{13,50–57} Understanding crack growth mechanisms at the microstructure scale enables designers to tailor the material's microstructure through processing for optimal performance in applications using FCG resistance as a design goal. *It is important to establish crack growth mechanisms at the microstructure scale of the materials, at all growth stages.* Advancements in these directions will be presented and discussed in subsequent sections.

17.3 Materials, processing, mechanical properties and fatigue crack growth testing

Cast and wrought aluminum alloys with different strengthening mechanisms (i.e., precipitation strengthened and solution strengthened) and different microstructures will be reviewed and discussed in this chapter. The selected materials include two

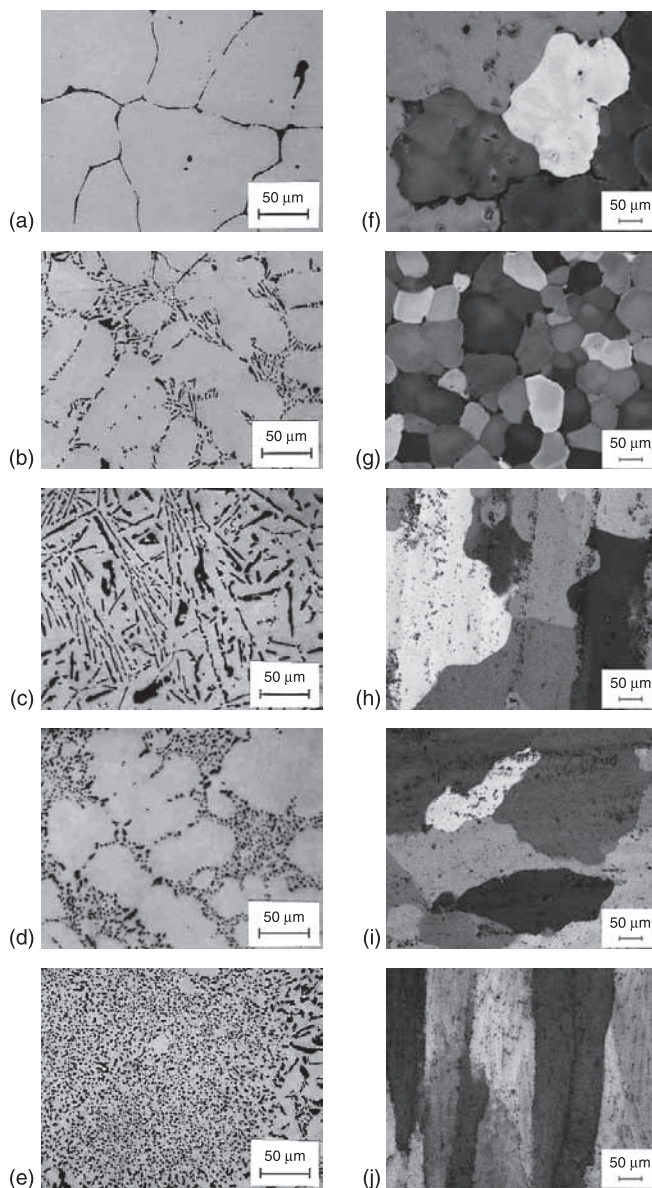
types of cast aluminum alloys, Al-Si-Mg alloys (Mg-Si precipitation hardened alloys, T61 heat treated, similar grain size and SDAS and different Si content and morphology) and Al-Mg alloys (as-cast solution hardened alloys with different grain size), and three 6061 wrought aluminum alloys (Mg-Si precipitation hardened alloys, T61 heat treated, with different grain structure – recrystallized and fibrous). Two T61 heat treatments were applied; one used a room temperature water quench and the other a cryogenic up-hill quench,^{33,58} which provided high and low residual stress conditions in the materials. Mechanical properties of the alloys are given in Table 17.1, and the microstructures are presented in Fig. 17.1(a)–(j). More details on the materials and processing can be found elsewhere.^{6,50,55,56} The selected materials allow exemplification and interpretation of FCG mechanisms across classes of materials, microstructures and multi-scales in different conditions and at different stages of crack growth.

Two specimen geometries were used for the FCG testing. The *long FCG work* was performed on compact tension, C(T), specimens. All C(T) specimens were tested under *K*-control per ASTM E647 at *R* = 0.1, 0.5 and 0.7 in laboratory air at room temperature, 24°C, and relative humidity 20–50%. Threshold data were generated under decreasing *K*, while data for Regions II and III were produced

Table 17.1 Tensile properties of Al-Si-Mg and 6061 alloys in T61 heat treatment conditions and Al-Mg alloys in as-cast conditions

Alloy	UTS		YS*		Total elongation, e
	US (ksi)	SI (MPa)	US (ksi)	SI (MPa)	(%)
Al-1%Si-Mg	40.6	280.2	29.6	204.2	13.93
Al-7%Si-Mg (UM)	45.1	311.3	33.9	233.7	7.34
Al-13%Si-Mg (UM)	51.5	355.0	38.3	264.1	7.47
Al-7%Si-Mg (M)	45.2	312.0	35.0	241.0	6.08
Al-13%Si-Mg (M)	49.7	342.7	39.0	269.1	7.33
Al-7%Mg (large GS)	31.9	219.6	18.6	128.0	6.26
Al-7%Mg (small GS)	36.2	249.5	19.1	131.6	7.88
6061 (0.08%Cr) – recrystallized, tension parallel to deformation direction (Fig. 17.1(h))	46.7	321.7	40.0	275.8	21.66
6061 (0.08%Cr) – recrystallized, tension perpendicular to deformation direction (Fig. 17.1(i))	45.3	312.5	38.6	266.3	20.33
6061 (0.18%Cr) – fibrous, tension parallel to deformation direction (Fig. 17.1(j))	60.6	418.0	54.4	375.3	16.00

Notes: * 0.2% offset yield strength; UM represents unmodified eutectic Si morphology, M modified eutectic Si morphology and GS grain size.



17.1 Materials selected for discussion (same magnification): (a), (b), (c), (d), (e) Cast Al-1,7,13%Si-Mg – unmodified and Sr-modified eutectic Si morphology; GS~280 μm; SDAS~25 μm;^{6,50} (f), (g) Cast Al-7%Mg (A535) alloys – two grain sizes (~275 μm and ~75 μm);^{55,56} (h), (i) wrought 6061 – recrystallized grains (GS~200μm × 400μm) with crack perpendicular (LT) and parallel (TL) to the deformation direction; (j) wrought 6061 – fibrous grains (GS~100 μm × 600 μm) with crack perpendicular (LT) to the deformation direction;⁵⁶ GS = grain size, SDAS = secondary dendrite arm spacing.

under increasing K . In high Region III, the test was continued using a shallower K -gradient to obtain the steeper Region III data. The compliance technique was used to monitor the crack advance, and the frequency was set to 20–25 Hz (except in Region III where it was decreased to capture sufficient data points). The *small FCG work* was done on single corner notched rectangular specimens with starting triangular corner flaws of 300–500 μm for different materials. To monitor the crack advance, a reversing DC potential difference method was used for both active and reference voltage measurements. The pre-cracking was performed at a stress ratio, $R = -1.2$ to -1.7 , with a gradual increase in stress until crack advance was detected. After ~ 0.06 mm of crack extension, the stress ratio was changed to $R = 0.1$, and the stress was gradually increased until crack growth was again detected. The cyclic stress was then maintained constant throughout the entire test. More details on the specimen geometries and FCG testing can be found elsewhere.^{6,50,55,56}

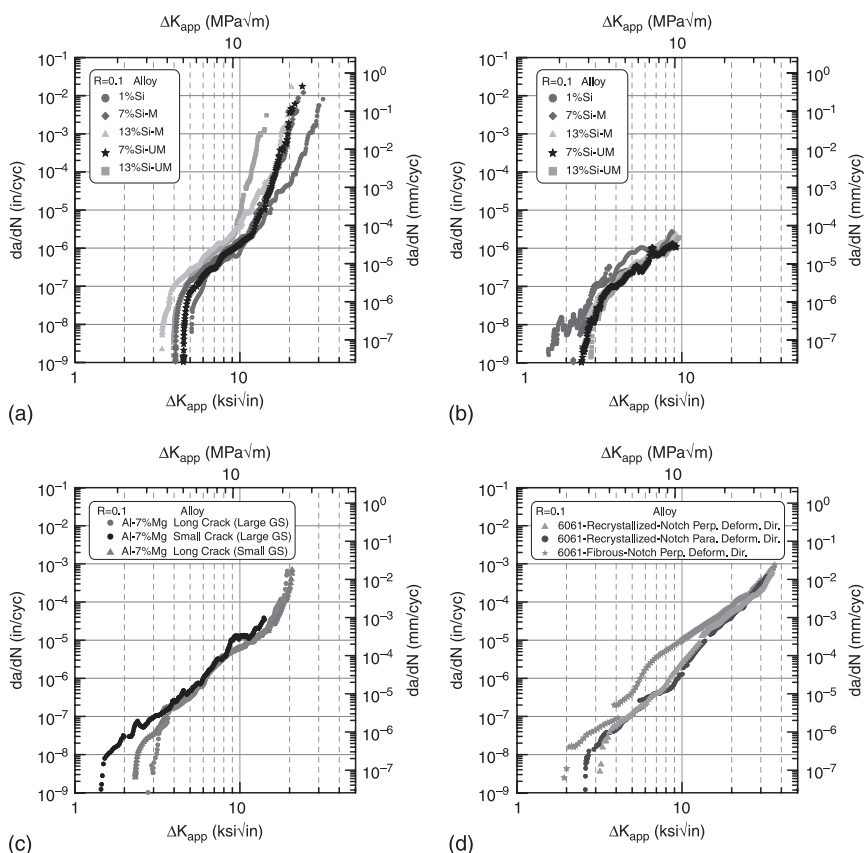
17.4 Fatigue crack propagation in the near-threshold regime

17.4.1 Propagation mechanisms of long cracks

‘Long crack’ data and large safety factors have been used for damage tolerant design in structural applications to prevent premature failure and compensate for the absence of small crack growth data and the lack of understanding of ‘small cracks’. Significant differences between long and small crack growth behavior have been reported for various alloy systems including wrought Al alloys,^{5,59–62} cast Al alloys,^{6,7,11,12,63,64} steels,⁶⁵ Ti alloys,⁶⁶ Cu alloys⁶⁷ and Ni-base superalloys.⁶⁸ As an example, experimentally measured long crack growth thresholds, ΔK_{th} (Fig. 17.2(a) and 17.2(c)-right), are higher than the physically small crack growth thresholds (Fig. 17.2(b) and 17.2(c)-left) for both sets of cast materials. The differences are attributed to crack closure. For long cracks, part of the applied forces are used to reopen the mismatched interfering fracture surfaces; thus, the magnitudes of the applied stress intensity factor ranges are reduced, and less cyclic damage occurs at the crack tip. The dominant source of closure associated with these materials is roughness.^{6,7,15,19} Roughness induced closure, active near the crack tip, is dictated by the alloy’s microstructure and can be quantified by comparing Fig. 17.2(a) and (b), and also in Fig. 17.2(c).

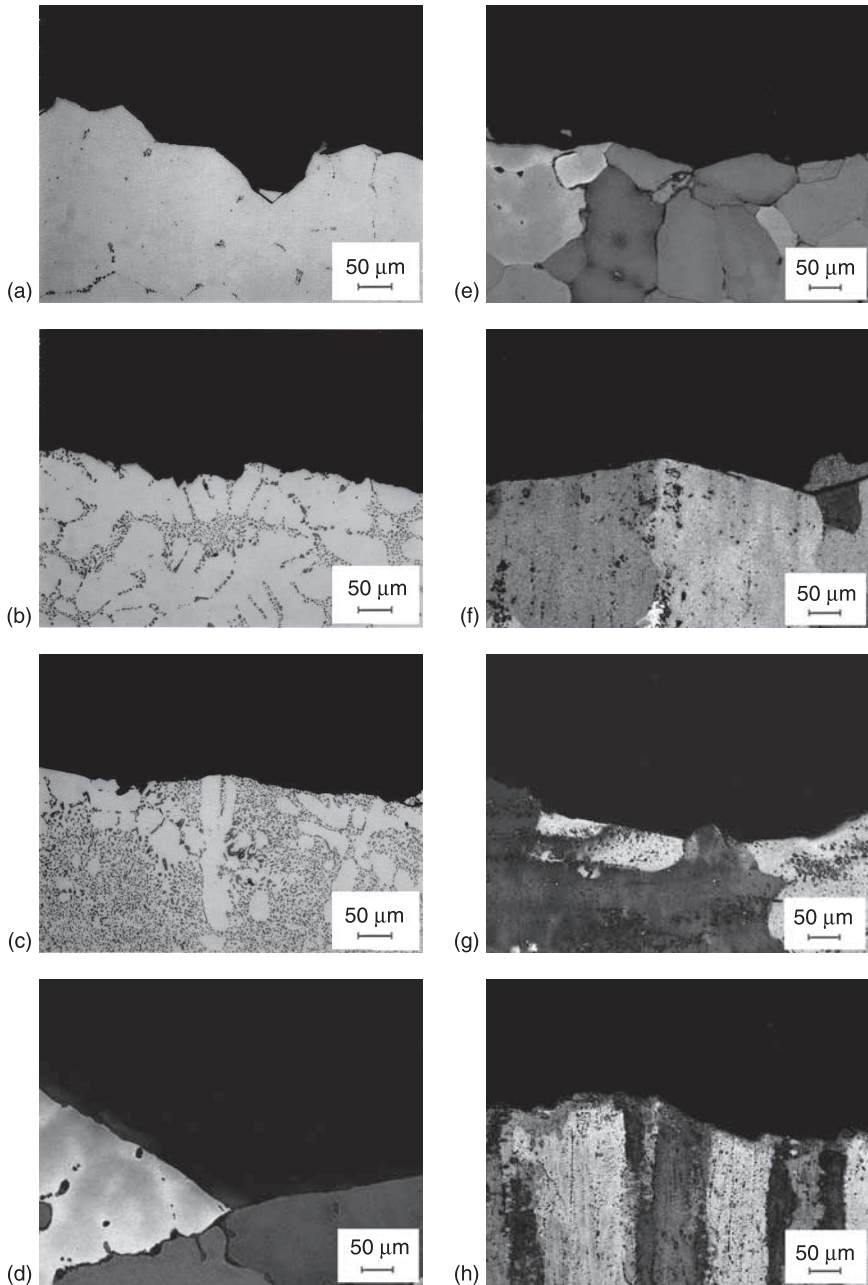
These differences in long crack growth thresholds observed in Fig. 17.2 can be explained through the effects of the alloy’s microstructural features on crack deflection, which dictate the fracture surface roughness and thus the level of roughness induced closure (Fig. 17.3). In Al-1%Si-Mg alloys with no eutectic, Al-Mg alloys and 6061 alloys, the crack advances through the α -Al matrix until obstacles such as grain boundaries cause an orientation change (for 6061 alloys, interactions with secondary Al(CrMnFe)Si particles are observed). In Al-7, 13%Si-Mg alloys, eutectic Si particles deflect the crack, thus creating deflection

distances smaller than the grain size, less roughness and lower ΔK_{th} than that of the Al-1%Si-Mg alloy. Roughness values in the near-threshold regime are consistent with the long crack threshold ranking, and are also in direct correlation with the MCD causing crack deflection in each alloy,^{6,55,56} namely grain size (for Al-1%Si-Mg, Al-Mg and 6061 alloys), SDAS (for Al-7%Si-Mg alloys) and inter-Si particle distance (for Al-13%Si-Mg alloys), as shown in Fig. 17.3. Overall, long crack growth thresholds of cast Al-Mg alloys are similar to those of wrought 6061 alloys, and lower than those of cast Al-Si-Mg alloys, Fig. 17.2(c) and (d) versus (a).



17.2 Fatigue crack propagation behavior of Al-Si-Mg, Al-Mg and 6061 alloys^{6,55,56}: (a) long and (b) small crack growth data for Al-Si-Mg alloys; (c) long and small crack growth data for Al-Mg alloys; and (d) long crack growth data for 6061 alloys.

Figure 17.2(a) shows the effects of Si content and morphology on long ΔK_{th} of cast Al-Si-Mg alloys. Increases in Si content decrease ΔK_{th} , and Si modification further reduces ΔK_{th} , for both the 7 and 13%Si alloys. Unmodified Al-Si-Mg



17.3 Crack path deflection for Al-Si-Mg, Al-Mg, and 6061 alloys at low ΔK : (a), (b), (c) Al-1.7, 13%Si-Mg; (d), (e) Al-7%Mg (large & small GS); (f), (g) 6061-recrystallized (crack perpendicular and parallel to the deformation direction); (h) 6061-fibrous (crack perpendicular to the deformation direction).

alloys have higher long ΔK_{th} than the modified alloys for both 7 and 13%Si. For the same vol.% Si, Si particles are coarser and more distantly spaced in unmodified alloys (especially in the 13%Si alloys); thus, in unmodified alloys, the crack may not always be deflected by Si particles at the edge of the dendrites, and also, when the crack debonds or fractures Si particles, larger deflections are created.^{6,7} Larger deflections generate rougher surfaces hence more roughness induced crack closure, and higher ΔK_{th} . In Al-Mg alloys, the MCD controlling crack deflection is the grain size, just like in the Al-1%Si-Mg and 6061 alloys.^{6,7,55,56} Figure 17.2(c) shows an increase in threshold for the large grained material indicating a higher roughness induced closure level; this is due to more distantly spaced interactions of the crack with grain boundaries,⁵⁵ Fig. 17.3(d) versus (e). Similar mechanisms contribute to the higher thresholds of 6061 alloys when the crack grows perpendicular to the deformation direction compared to those generated when the growth is parallel to the deformation direction, Fig. 17.2(d).⁵⁶ However, for these alloys, the secondary Al(CrMnFe)Si particles also play a role in the roughness induced closure and threshold ranking.

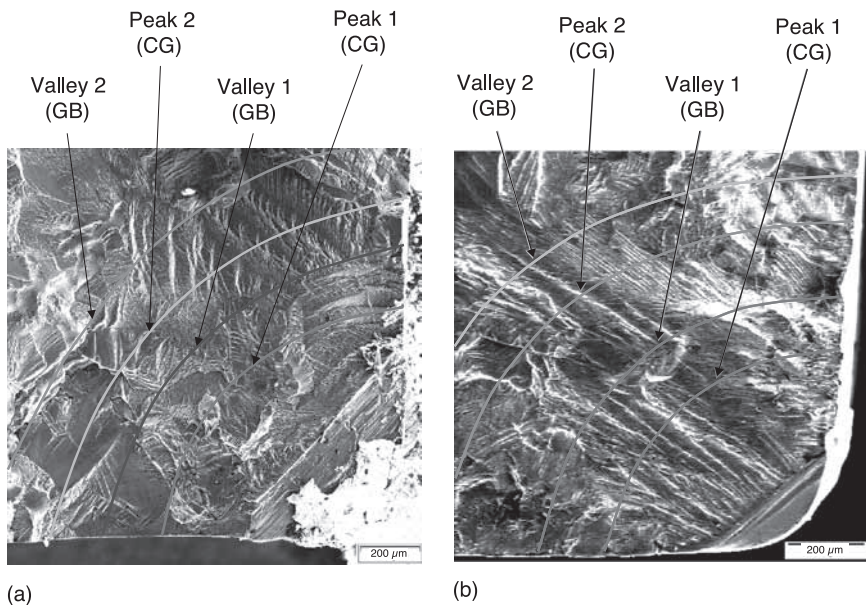
17.4.2 Propagation mechanisms of small cracks – small crack growth effects

Different criteria^{69,70} have been proposed to define small crack sizes (see also the general guidelines in ASTM E647). However, for a correct mechanistic understanding of the crack growth behavior, the general guidelines must be tailored to the alloy's MCD.⁶ A growing crack is considered mechanically small if its length is in the order of the plastic zone size ($a \approx r_p$); microstructurally small if its length is in the order of the MCD [$a \approx (5 \text{ to } 10) \times \text{MCD}$]; physically small when its length is significantly larger than the MCD ($a \gg \text{MCD}$). It has been shown that small cracks have not only much lower thresholds and faster growth rates than long cracks,^{3–7} but also, fundamentally different growth mechanisms.¹⁴ While long crack growth thresholds are mainly controlled by closure,^{6,7} the threshold of microstructurally small cracks is characterized by an acceleration/retardation behavior.^{6,8–13} The growth of physically small cracks is similar to that of long cracks without closure effects.⁶

The initial crack size in the small crack growth tests discussed here was $\sim 500 \mu\text{m}$ for all Al-Si-Mg alloys and $\sim 300 \mu\text{m}$ for the Al-Mg alloy. Due to the differences in microstructural characteristic features and mechanical behavior of the studied alloys, a combined microstructural-mechanical assessment was done to determine the initial crack growth stage for each of the alloys. Since the plastic zone size in the near-threshold regime is roughly $5\text{--}10 \mu\text{m}$ for the Al-Si-Mg alloys and $40\text{--}45 \mu\text{m}$ for the Al-Mg alloys, none of the alloys experienced mechanically small crack growth.

To determine whether or not any of the alloys exhibited microstructurally small crack growth behavior, the MCDs for each alloy were established. For the

Al-Si-Mg and Al-Mg alloys, these were: $MCD_{Al-1\%Si-Mg} = MCD_{Al-7\%Mg} = GS$, $MCD_{Al-7\%Si-Mg} = SDAS$, and $MCD_{Al-13\%Si-Mg} = d_{Si-Si}$ (inter-Si particle spacing). At a grain size of $\sim 275 \mu m$ (i.e., $MCD_{Al-1\%Si-Mg}$ and $MCD_{Al-7\%Mg}$), microstructurally small crack behavior is expected for both Al-1%Si-Mg and Al-7%Mg alloys. The peaks and valleys on the small crack growth curves of these alloys, Fig. 17.2(b) and (c), correspond to retardation/acceleration at the grain-boundaries (GB)/center-of-the-grains (CG) as observed in Fig. 17.4(a) and (b). For the 7%Si alloys, the initial crack size represents $\approx 20 \times MCD_{Al-7\%Si-Mg}$, and thus, a physically small crack growth behavior is expected for these alloys [fact confirmed by the absence of the oscillating behavior of this alloy in Fig. 17.2(b)]. For the 13%Si alloys, the initial crack size is two orders of magnitude larger than the $MCD_{Al-13\%Si-Mg}$, which corresponds to a significant population of Si particles. Therefore, these alloys also show an initial physically small crack growth behavior.



17.4 SEM pictures of the fracture surfaces showing the growth of small cracks for: (a) Al-1%Si-Mg and (b) Al-7%Mg (large GS) alloys;^{6,55} the peaks and valleys in figures correspond to the first two peaks and valleys in Fig. 17.2(b) and (c) (average behavior).

Closure corrections were performed using the ACR method experimentally developed by Donald et al.⁴⁷ and analytically derived from fundamental principles of fracture mechanics by Lados et al.⁷¹ The ACR method is based on load-displacement records and presents the advantage that accounts for partial closure effects below the opening load, which are most relevant at high opening loads, such as in the near-threshold regime. This method estimates ΔK_{eff} in relation to the

ratio of the actual displacement range ($\Delta\delta_{cl}$) to the displacement range that would have occurred in the absence of closure ($\Delta\delta_{nc}$). This method uses remote (front face) displacement measurements as the local crack tip displacement is impractical or impossible to obtain. These displacements are a 'quantitative' measure of the 'qualitative' strain activity of the broken surfaces in the crack wake. Displacement measurements are evaluated relative to the original displacement of the notch at the beginning of the test, and therefore the adjusted compliance ratio is calculated by subtracting the initiation notch displacement from displacements in the presence and absence of closure: $ACR = (\Delta\delta_{cl} - \Delta\delta_i) / (\Delta\delta_{nc} - \Delta\delta_i)$. Converting to compliance, the expression of ACR becomes: $ACR = (C_s - C_i) / (C_o - C_i)$ where $C_s = \Delta\delta_{cl} / \Delta P$ is the secant compliance, $C_o = \Delta\delta_{nc} / \Delta P$ is the compliance above the opening load and $C_i = \Delta\delta_i / \Delta P$ is the compliance of the notch before crack initiation. Once ACR is determined, ΔK_{eff} is calculated using Eq. 17.1 as:

$$\Delta K_{eff} = ACR \cdot \Delta K_{app} = \frac{\Delta\delta_{cl} - \Delta\delta_i}{\Delta\delta_{nc} - \Delta\delta_i} \cdot \Delta K_{app} = \frac{C_s - C_i}{C_o - C_i} \cdot \Delta K_{app} \quad [17.1]$$

Comparing Fig. 17.5(a) and (b) with Fig. 17.2(b) and (c), it can be observed that closure corrected long crack growth data are similar with the physically small crack growth data. This indicates that closure corrective techniques, Eq. 17.2, are able to correct for closure and to provide physically small crack growth behavior from long crack growth testing. However, these methods do not account for microstructure related retardation effects; the retardation/acceleration behavior upon interaction with either grain boundaries or Si particles needs to be addressed independently using non-fracture mechanics techniques (i.e., materials science based tools, where a microstructural adjustment dependent on MCD, microhardness, elastic modulus, interfacial strength, etc. must be incorporated, Eq. 17.3), Fig. 17.6.^{6,55,56} In the cases presented here, only two alloys (Al-1%Si-Mg and Al-7%Mg) showed microstructurally small crack growth behavior. However, if all cracks were started at the microstructurally small stage, a ranking of the materials would be expected; the closer the characteristic microstructural obstacles impeding crack growth the higher the threshold. For the cast alloys, this can lead to an opposite threshold behavior of microstructurally small cracks compared to that of long cracks.

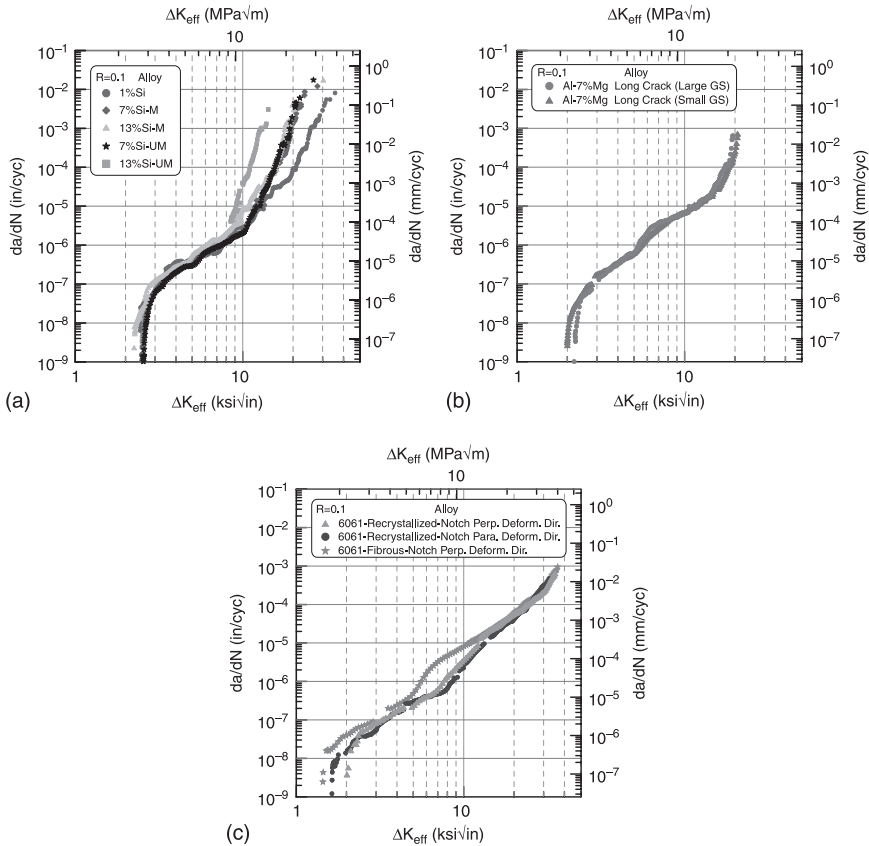
$$\Delta K_{eff-FM} = FMT \cdot \Delta K_{app} \quad [17.2]$$

(Fracture Mechanics Correction: Closure)

$$\Delta K_{eff-Total} = (FMT + MT) \cdot \Delta K_{app} \quad [17.3]$$

(Total Correction: Closure + Microstructure)

where FMT = Fracture Mechanics Term = ACR or other closure corrective parameter; MT = Microstructural Term = $f(\text{MCD, microhardness, elastic modulus, interfacial strength, etc.})$

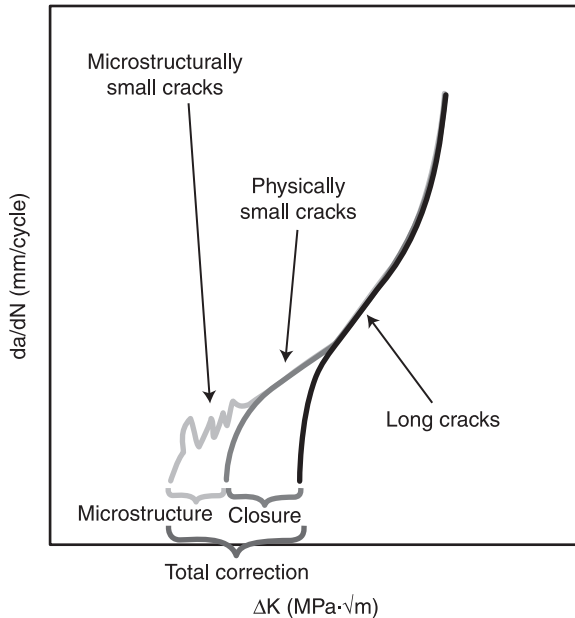


17.5 Fatigue crack growth behavior of (a) Al-Si-Mg, (b) Al-Mg and (c) 6061 alloys after ACR closure correction.^{6,55,56}

These developments are critical in eliminating ‘guess design’ and premature failures as well as extending inspection intervals for aircraft and other fatigue critical components. Unnecessary large safety factors are currently used to compensate for the lack of understanding of these effects and unavailability of accurate FCG design data. Accurate and confident design with appropriate but not excessive safety factors will lead to important *weight reductions in structural applications*. In addition to overall *improved fatigue life predictions and better materials and component design*, the use of such new corrective methods (Fig. 17.6) could further result in *unique insight and original correlations between ΔK_{th} and S-N data for very high cycle fatigue* under appropriate combinations of stress level and crack length.

17.4.3 Processing residual stress effects

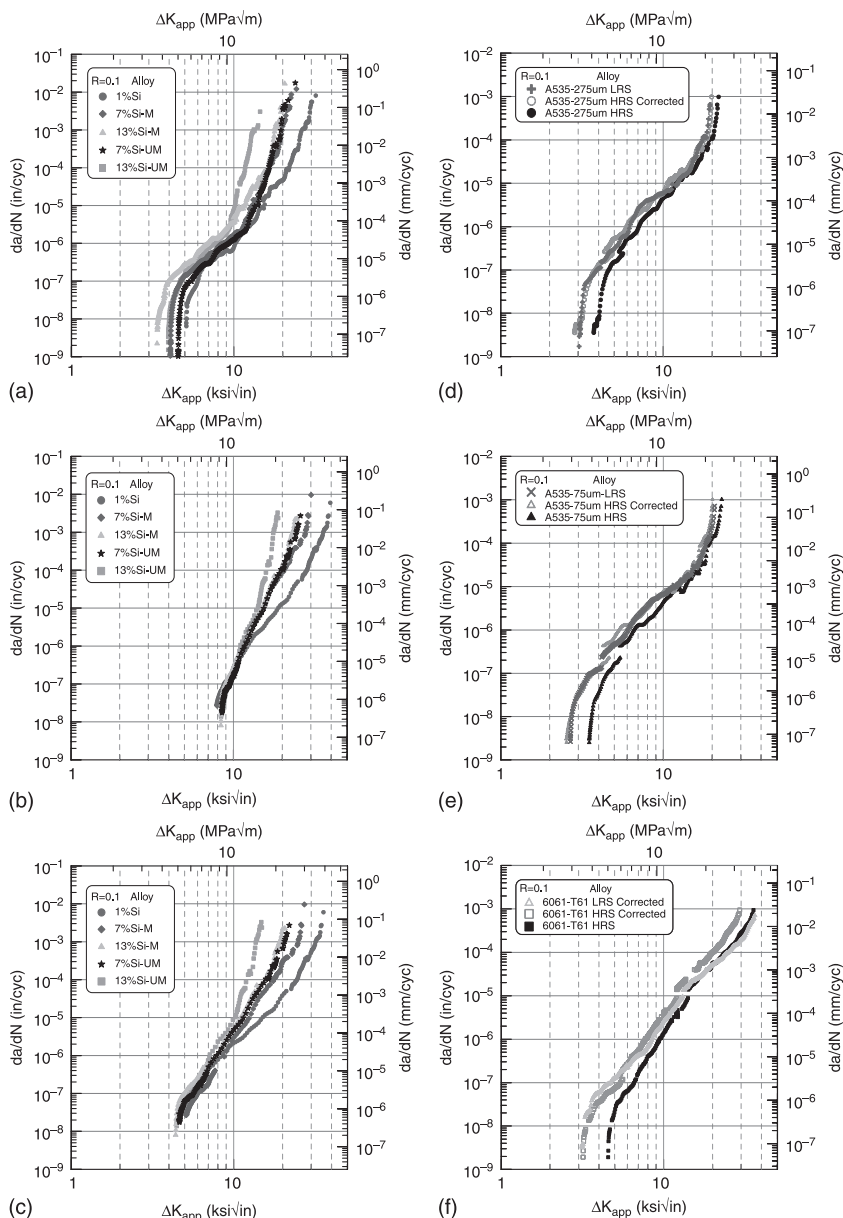
In addition to the small crack growth effects, FCG response of aluminum alloys can also be significantly affected by the presence of bulk residual stresses



17.6 A long-to-small crack corrective model accounting for both closure and microstructural effects.^{6,56}

introduced during manufacturing and post-manufacturing processes such as heat treatment. There is a qualitative understanding of the effects of residual stress on the FCG behavior, but the effects need to be comprehensively quantified and/or accounted for. The difficulty in evaluating residual stress effects is rooted both in the *complexity of measuring residual stresses* and in the *lack of residual stress corrective mathematical models* able to convert experimental data biased by residual stress into residual stress free data for design. For example, in cast Al-Si-Mg alloys, it has been found that the presence of high compressive residual stresses due to quenching increased significantly the threshold values compared to the residual stress free thresholds (a 100% increase),^{6,7,33} Fig. 17.7(a) versus (b). Similar behavior was observed for the Al-Mg and 6061 alloys, Fig. 17.7(d)–(f) for various degrees of residual stress. The significant elevation in thresholds was attributed to enhanced closure levels caused by the presence of high compressive residual stresses, as everything else was kept constant. For tensile residual stresses the opposite behavior was reported,⁷² with a decrease in threshold values and no closure contributions.

When high residual stresses are present, not only are higher thresholds obtained, Fig 17.7(b) and (d)–(f), but often the threshold ranking observed for residual stress free samples is lost, Fig. 17.7(b) versus (a).^{6,7,33} In the presence of residual stresses, there is an increase in the total closure level, and also a change in the closure operating mechanisms. While for low residual stresses, microstructure/roughness



17.7 Fatigue crack growth behavior of cast Al-Si-Mg and Al-Mg alloys and wrought 6061 alloys with low and high residual stresses before and after residual stress corrections^{6,33,73}: (a) Al-Si-Mg alloys with low residual stresses; (b) Al-Si-Mg alloys with high compressive residual stresses; (c) Al-Si-Mg alloys with high compressive residual stresses after residual stress correction; (d), (e) Al-Mg alloys with large and small GS in low, high and high-corrected residual stress conditions; and (f) 6061 alloy in low, high and high-corrected residual stress conditions; LRS represents low residual stress and HRS high residual stress.

induced closure is dominant and active in the vicinity of the crack tip, for high residual stresses, the crack tip remains open, and closure mechanisms become operative near the notch of the C(T) specimen (bulging effect);^{6,33} this was used to explain the loss in threshold ranking.^{6,33} Thus, for high compressive residual stress conditions, the contributions of the alloy's characteristic microstructure/roughness induced closure, even though present, become imperceptible, and thresholds are dominated by residual stress induced closure mechanisms.^{6,33}

Accurate residual stress corrections are critical for *generating true and un-biased material behavior* for aluminum alloys and *preventing large errors in estimating the fatigue crack growth performance* of the material. A corrective model, the Restoring Force Model 1.0 (RFM 1.0), has been proposed to compensate for the presence of compressive residual stress and generate residual stress free FCG data.³³ RFM 1.0 is a fracture mechanics based model, which evaluates K_{res} values by using notch displacements due to residual stress and applied forces that establish residual stress equilibrium at the notch tip. In this approach, K_{res} can be conveniently evaluated before the start of the FCG test, and the residual stress correction of the FCG curve can be subsequently done, for low stress ratio, R , using Eq. 17.4:

$$\Delta K_{\text{corr-RFM}} = \Delta K_{\text{app}} + K_{\text{res}} \quad [17.4]$$

The RFM 1.0 model provides good FCG data corrections for compressive and symmetric residual stress distributions in cast Al-Si-Mg alloys, Fig. 17.7(a) versus (c). Comparing data with high residual stress before and after RFM correction, Fig. 17.7(b) and (c), the effects of residual stress induced closure can be evaluated. The differences between RFM and ACR corrected data, Fig. 17.7(c) and 17.5 (a), indicate roughness induced closure contributions since ACR is a global closure correction, compensating for both residual stress and roughness induced closures, and RFM is a residual stress corrective model. Recently, the second generation of the model, Restoring Force Model 2.0 (RFM 2.0), has been developed⁷³ to incorporate changes in crack length during testing, stress ratio effects, material properties and plasticity contributions. Residual stress corrections for cast and wrought aluminum alloys using RFM 2.0 are presented in Fig. 17.7(d)–(f), indicating the ability of the model to compensate for compressive residual stresses and provide un-biased material property data.

There are other methodologies used for residual stress corrections, such as the crack-compliance method, that evaluates K_{res} in real-time during a FCG test using load-displacement records.^{71,74} It needs to be noted that the effects of residual stress on long crack growth data (i.e., data obtained from specimens such as compact tension) can be significantly amplified compared to the effects on small crack growth data due to reduced applied stresses for given stress intensities; in the case of small cracks, residual stress corrections will not than be necessary.

17.5 Fatigue crack propagation mechanisms in Regions II and III of crack growth

Closure contributions are less significant in Regions II and III of crack growth, where crack propagation mechanisms are dictated by weak material-specific microstructural features found in the plastic zone ahead of the crack tip.⁵⁰ To accommodate the evolution of the FCG process from plane strain to plane stress, an original equation, Eq. 17.5, was developed to calculate the plastic zone size by taking into account weighted contributions from both plane strain and plane stress.⁷⁵ This formulation was further used to evaluate crack propagation mechanisms in Regions II and III of crack growth in materials with both low and high residual stresses;^{50,56,76} K_{res} was incorporated in the equation for the analysis of specimens with high residual stress.

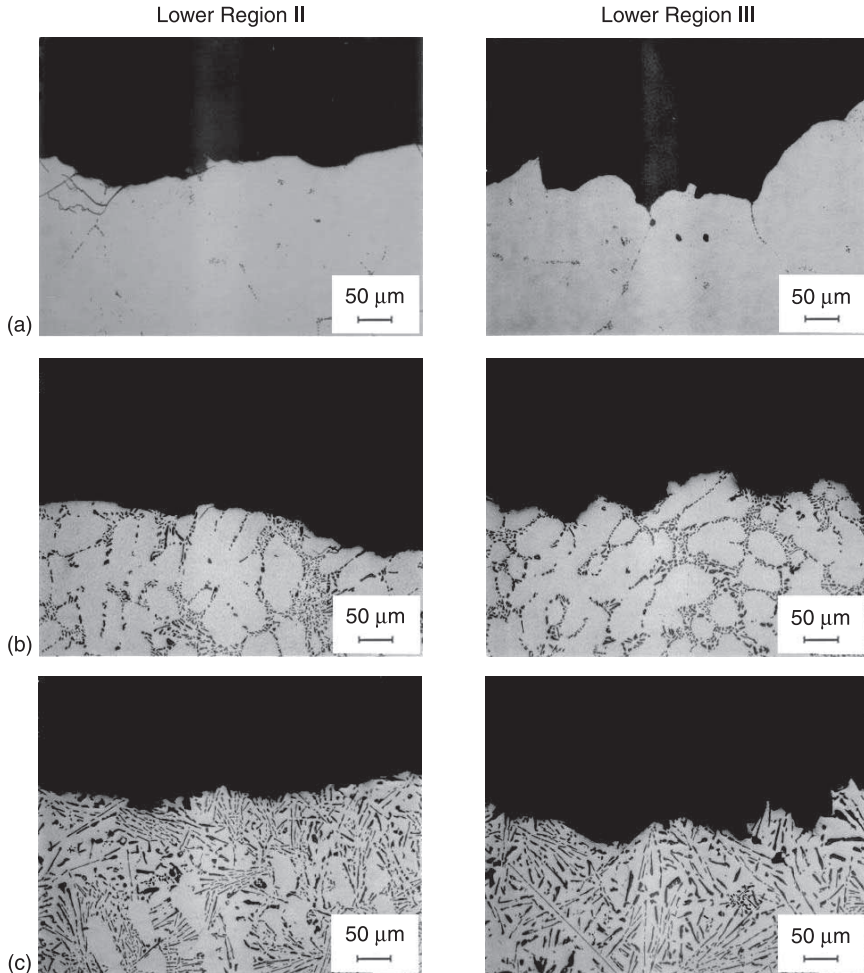
$$r_p \approx \left(\frac{1}{2\pi}\right)^n \left(\frac{1}{6\pi}\right)^{1-n} \frac{(K_{\text{max}} + K_{\text{res}})^2}{\sigma_{\text{YS}}^2} \cos^2 \frac{\theta}{2} \left(1 + 3 \sin^2 \frac{\theta}{2}\right) \quad [17.5]$$

$$\text{where } n = \frac{1.33 \cdot r_{\text{p(plane-stress)}}}{B} \quad 0 < n \leq 1$$

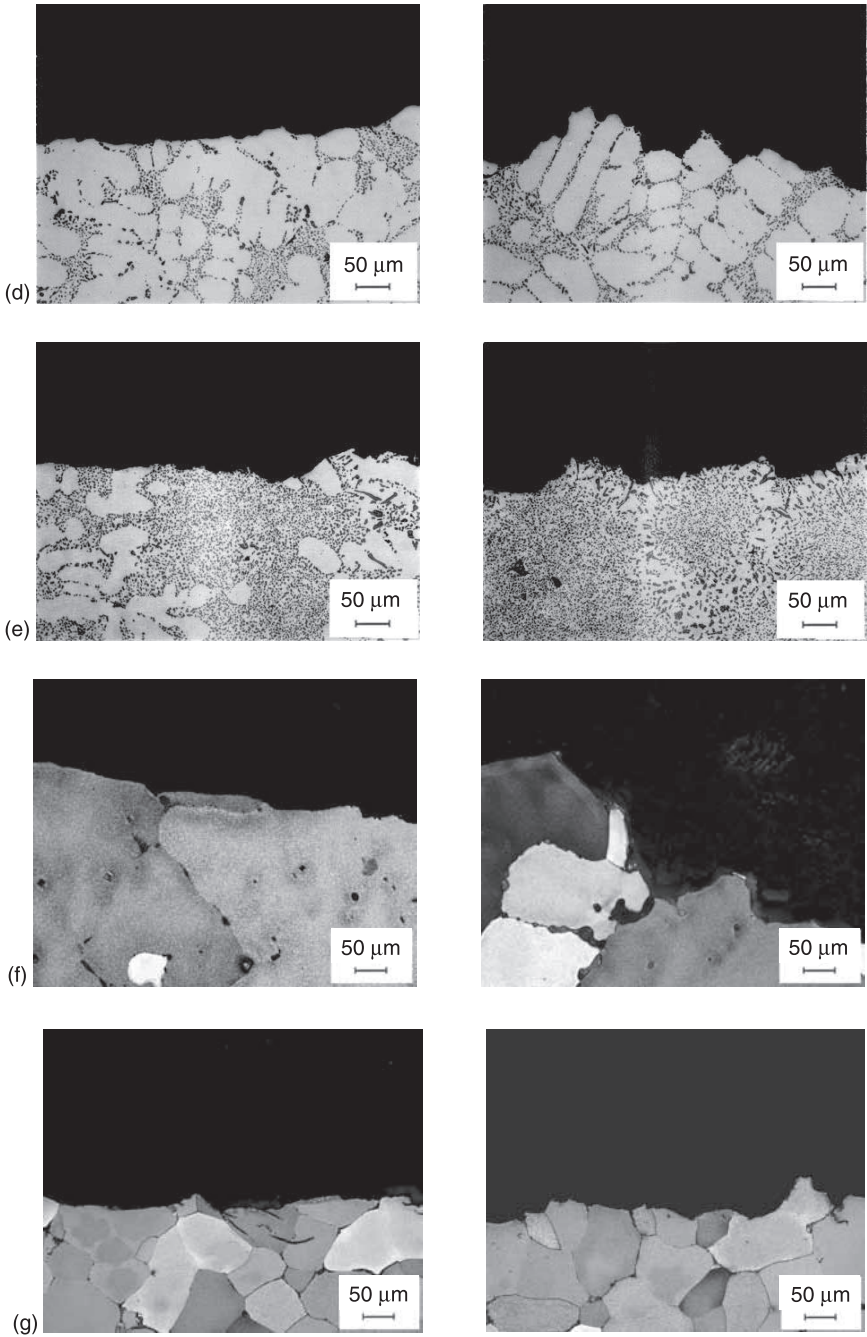
Fracture surface roughness increases as cracks propagate through Region II and into Region III, Fig. 17.8. As an example, for a modified Al-7%Si-Mg alloy, the surface roughness index increased from 1.2 in lower Region II to 1.8 in lower Region III, which corresponds to an increase in crack growth rate from 6.6 to 93 nm/cycle.

Changes in roughness are associated with a gradual change in propagation mechanisms at the microstructure scale. These mechanistic changes can be explained by considering the amount of damaged material ahead of the crack tip at various ΔK levels, which can be approximated by the monotonic plastic zone size.^{50,75} The plastic zone radius needs to be compared with the MCD, which controls the crack advance. In cast Al-Si-Mg alloys, crack growth mechanisms have been correlated to the primary α -Al structure,^{50–56} Si particles (morphology and distribution) and Si particle/matrix interface strength.^{13,50,57} At low ΔK , the crack advances through the damaged microstructural constituent found directly ahead of the crack tip, primarily the dendritic structure, with few interactions with Si when weakened interfaces/particles are conveniently encountered ahead/near the crack tip, Fig. 17.9-left. As ΔK increases, the number of Si particles on the fracture surface increases, reflecting the crack's preference for advancement via Si particles. For the crack to exclusively follow Si particles, a continuous path of debonded or cracked Si particles in the plastic zone ahead of the crack tip is required. In this case, it becomes energetically more favorable for the crack to deviate from the planar advancement and meander through the regions of least resistance. In lower Region II, the crack interacts with individual Si particles, then, at higher ΔK in Region II, it follows a sequence of Si particles primarily

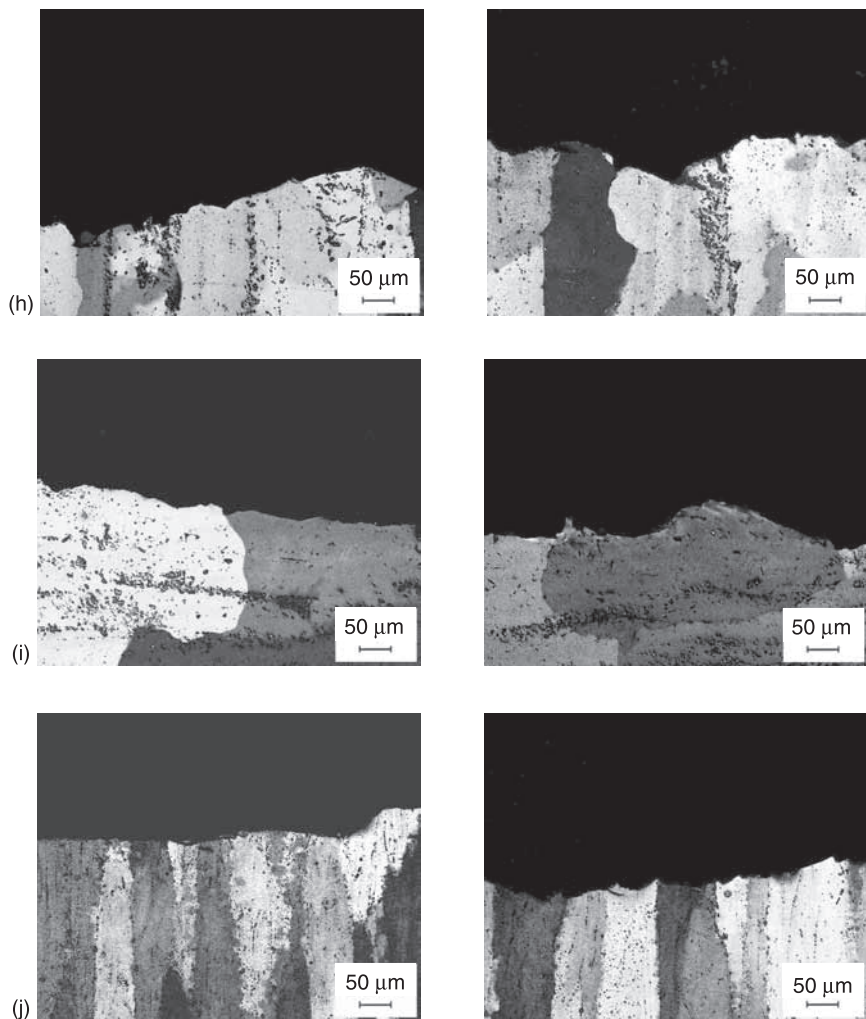
located on the cell boundaries not too far from the main crack direction, Fig. 17.9-middle. As ΔK further increases, the roughness increases, a plastic zone large enough to damage one (or more) complete Al-Si eutectic region(s) is reached, and a continuous network of damaged Al-Si eutectic colonies becomes available to the crack, Fig. 17.9-right. This propagation mode occurs near the transition from Paris regime to Region III.



17.8 Changes in fracture surface roughness for Al-Si-Mg, Al-Mg, and 6061 alloys with increasing ΔK from lower Region II (left) to lower Region III (right)^{50,55,56}: (a) Al-1%Si-Mg; (b) Al-7%Si-Mg-UM; (c) Al-13%Si-Mg-UM; (d) Al-7%Si-Mg-M; (e) Al-13%Si-Mg-M; (f) Al-7%Mg (large GS); (g) Al-7%Mg (small GS); (h) 6061-recrystallized (crack perpendicular to deformation direction); (i) 6061-recrystallized (crack parallel to deformation direction); (j) 6061-fibrous (crack perpendicular to deformation direction).

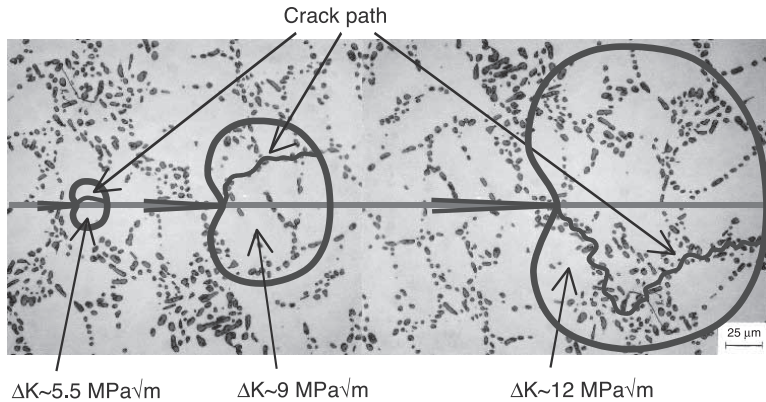


17.8 Continued.



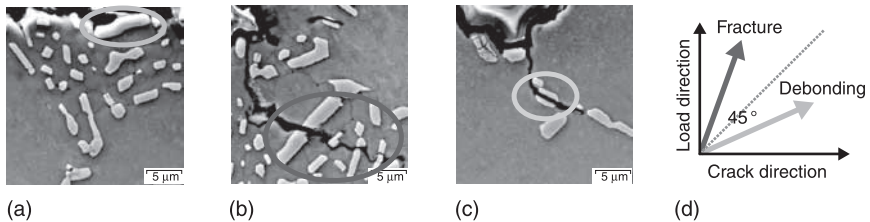
17.8 Continued.

At low ΔK , Si particles tend to decohere from the matrix in the plastic zone^{13,30,50} as there is not enough strain energy in the plastic zone to fracture them, unless they have a high aspect ratio and their principal axis is perpendicular to the crack plane. In such cases, Si particles have high resistance to debonding due to large interface areas parallel to the loading direction, and they are more likely to fracture. It was observed⁵⁰ that high aspect ratio Si particles with an inclination angle to the crack plane $<45^\circ$ or $>135^\circ$ have a tendency to debond, Fig. 17.10(a) and (d), while particles with angles between 45° and 135° are expected to fracture, even at low crack driving forces, Fig. 17.10(b) and (d). However, when a Si



17.9 Plastic zone size and crack path changes at the microstructure scale of Al-7%Si-Mg alloys for different ΔK levels.⁵⁰

twin plane is parallel to the crack front, Si particles can fracture at angles $<45^\circ$ or $>135^\circ$, Fig. 17.10(c). At high ΔK , when the plastic zone is large and the cumulative strain damage is high, the number of fractured Si particles increases even in the modified structures, and cracks propagate via both debonding and fracture mechanisms.



17.10 Failure mechanisms for Si particles with high aspect ratio: (a) debonding; (b) fracture; (c) fracture on twin plane; (d) transition from debonding to fracture as a function of particle orientation with respect to load and crack directions.⁵⁰

Region III is characterized by a fast crack growth through the eutectic regions. The overload fracture in upper Region III occurs almost entirely through ductile static tearing of the large Al-Si eutectic regions. Thus, fracture toughness (highest ΔK value) is mainly dictated by the Si particle morphology; the coarse/irregular Si morphology provides convenient paths for the crack to debond or cut through, while the modified Si morphology is more fracture resistant and exerts more resistance to crack growth. Modified 7%Si alloys show slightly improved behavior in Region III compared to unmodified alloys, but the effect of modification is more pronounced in the case of 13%Si alloys, Fig. 17.2(a).

Thermal modification during heat treatment minimizes the differences in Si morphology between unmodified and modified alloys. However, the large plates in 13%Si alloys require a longer time to fragment and spheroidize, which explains the larger differences between the high ΔK crack growth behavior of unmodified and modified 13%Si alloys. Larger differences in fracture toughness are caused by larger differences in Si morphology, which is a function of Si content, modification, solidification conditions and heat treatment time. The Si morphology ranking is in agreement with the fracture toughness ranking for the Si-containing cast alloys. Results of this study agree with the literature for A356⁵² and Al-12%Si-0.35%Mg⁵⁷ alloys.

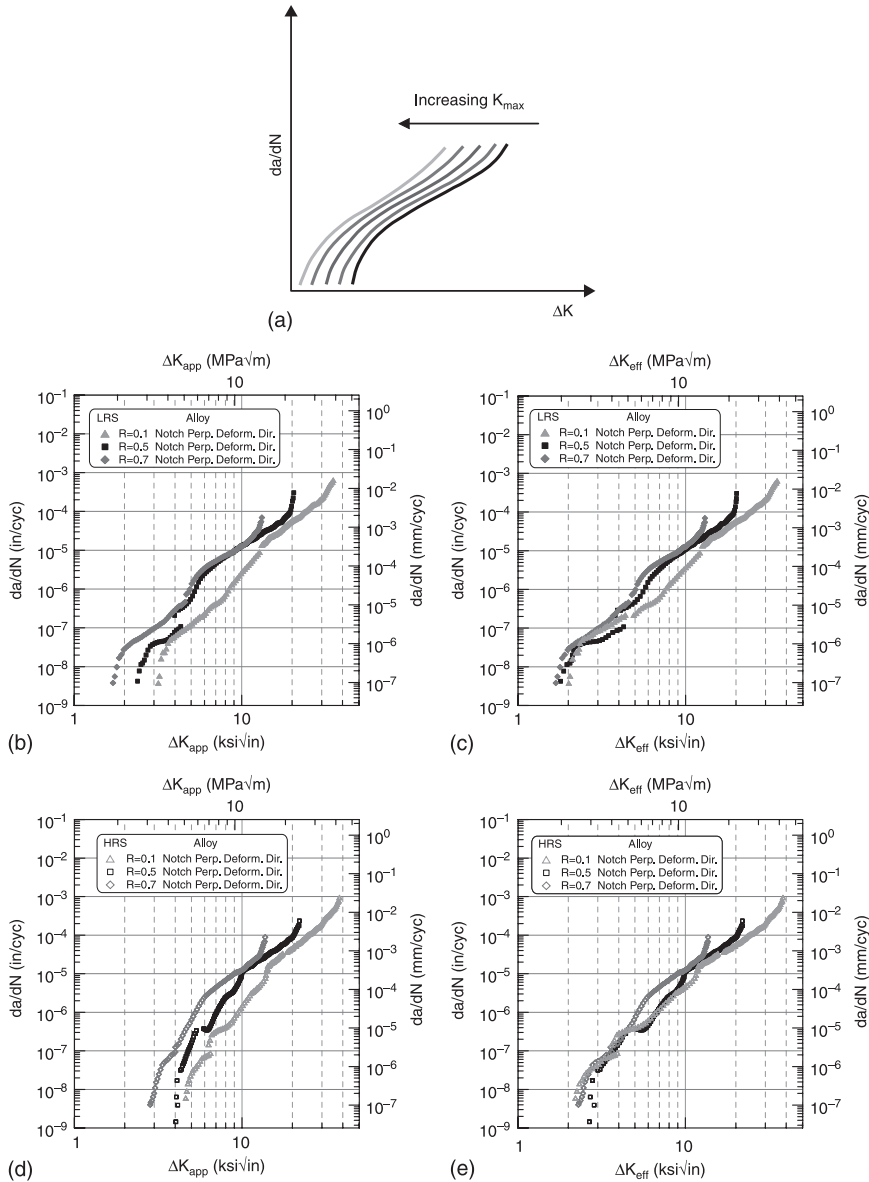
In the Al-Si-Mg alloys, which do not contain eutectic Si (i.e., 1%Si), the crack growth mechanisms change from transgranular to intergranular,⁵⁰ Fig. 17.8(a). In these alloys, the crack shows preference for damaged grain boundaries in the plastic zone. With increasing ΔK , the plastic zone grows until it becomes sufficiently large to facilitate propagation along grain boundaries. For these alloys, grain size becomes the controlling parameter in fatigue crack growth and fracture toughness, similar to wrought alloys. The behavior of Al-Mg cast alloys is also related to the grain size. However, the low and similar yield strength and matrix microhardness in these materials play an important role in crack propagation, and explain the similar crack growth rates and mechanisms in Region II of alloys with different grain size. Crack propagation in Al-Mg alloys is facilitated by both grain boundaries and the weak matrix, which presents another path of least resistance in front of the crack.⁵⁵ Thus, the transition to transgranular propagation only occurs at high ΔK . This behavior is similar to the one of Al-Si-Mg alloys T4 heat treated where the weaker α -Al matrix represents an alternative crack propagation path in addition to damaged Si/Al interfaces and Si particles in eutectic regions.⁵⁰ For the as-cast Al-Mg alloys, Region II is more extended than in the case of Al-Si-Mg T61 alloys indicating a predominantly transgranular crack propagation with a mixed mode in high Region II.⁵⁵ The extended transgranular mode is related to the alternative crack propagation through the Al-matrix. Fracture toughness of the small grained Al-Mg alloy is slightly higher than that of the large grained material due to the ductile monotonic failure at grain boundaries associated with the upper Region III. The crack growth in 6061 materials can be rationalized similarly,⁵⁶ remembering that the higher yield strength, and correspondingly lower plastic zone, as well as the presence of the Al(CrMnFe)Si particles will retard the transition to intergranular propagation mode, Fig. 17.8(h)–(j). Such a transition is even more difficult when the crack advances perpendicular to the deformation direction, which is consistent with the fracture toughness values. In such cases, an intergranular mode is observed only if the grain boundaries are located near the tip of the advancing crack, Fig. 17.8(j).

17.6 K_{max} and stress ratio effects on fatigue crack growth

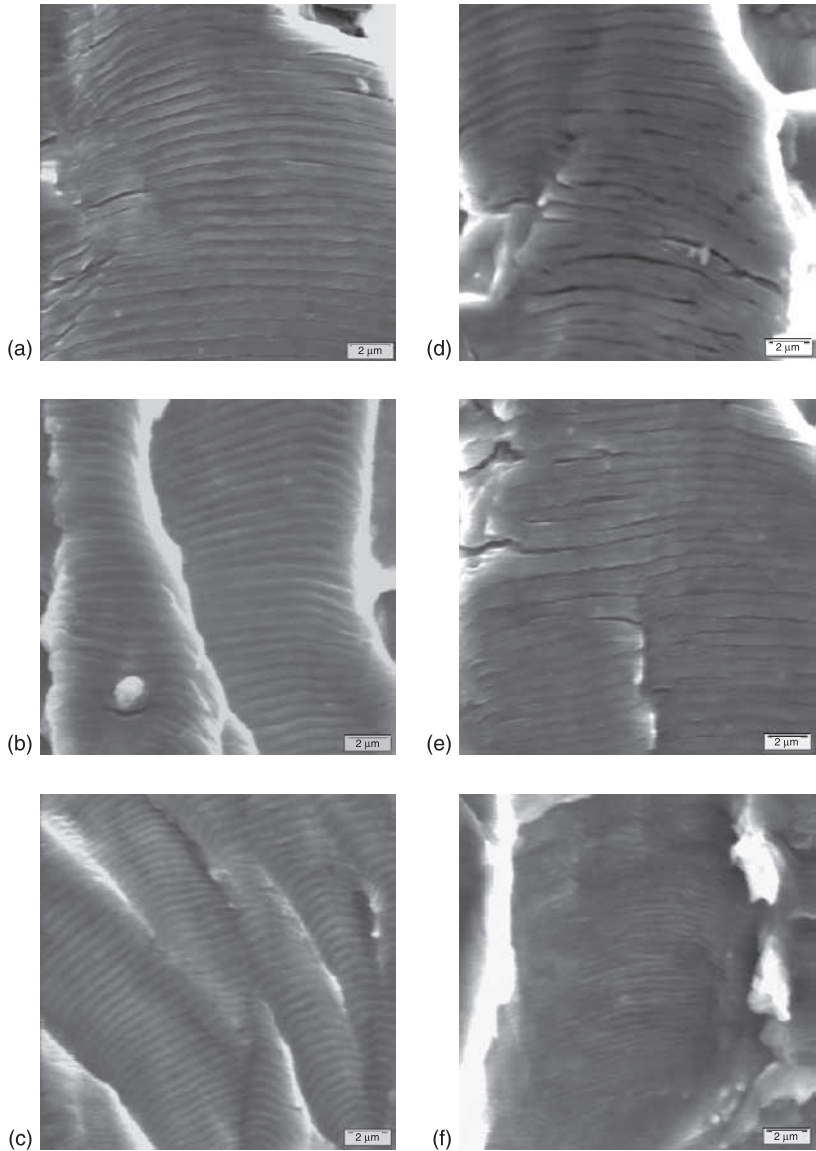
Another approach to generate closure-free data, besides closure corrections, is to perform constant K_{max} tests. In such tests, the stress ratio, R , is often greater than 0.9 near threshold. Due to the fact that K_{max} remains constant, steep K -gradients can be used without the risk of crack growth retardation. Since K_{min} is increased as the crack advances, closure becomes less important and it eventually disappears at low ΔK values near the threshold. A characteristic of this method, however, relates to the fact that it is affected by second order K_{max} effects. Specifically, the crack growth rate is not uniquely determined by ΔK , but it is also a function of K_{max} , and, for the same material, multiple thresholds can be obtained depending on the value of the K_{max} at which the test was conducted. K_{max} effects on the ΔK_{th} value are qualitatively presented in Fig. 17.11(a).

High stress ratio tests can also be conducted to produce data less affected by closure. Figures 17.11(b) and (d) show FCG results for tests conducted on specimens with low and high residual stresses at low, intermediate and high positive stress ratios, $R = 0.1$, $R = 0.5$ and $R = 0.7$ respectively.^{56,76} The low and high stress ratios experienced crack growth in the presence and absence of closure, while the intermediate stress ratio created partial closure conditions. It was observed that for both low and high residual stresses, the higher the stress ratio the lower the threshold due to reduced closure contributions. After closure corrections using ACR, the differences in threshold for both low and high residual stress conditions have been significantly reduced as observed in Fig. 17.11(c) and (e). However, the thresholds of the high residual stress specimens were still slightly higher, and the ranking was lost. It is also important to note that for high residual stress conditions, the applied stress ratio, R_{app} , will not represent accurately the stress ratio at the crack tip due to the presence of residual stresses. Thus, under high residual stress conditions, an effective stress ratio, R_{eff} , needs to be considered, especially at low K_{max} values. Also, for tests conducted at stress ratios higher than $R = 0.7$, it is likely to encounter secondary K_{max} effects, which will not be accounted for by closure corrections (e.g. in Fig. 17.11(c), $R \geq 0.8$ threshold data may not coincide with the closure corrected data from the other stress ratios due to K_{max} effects).

At the microstructure scale, striations observed in Region II of crack growth show decreasing correlation to average growth rates with increasing stress ratio from $R = 0.1$ to $R = 0.5$ to $R = 0.7$, Fig. 17.12. This decrease was related to an increase in static failure and tearing during crack growth at high stress ratio.⁷⁶ At any crack length the average measured growth rate is a combination of dynamic and static failures. At higher stress ratios, when a larger K_{max} is required to produce an equivalent ΔK , higher levels of plasticity will lead to greater levels of static failure and tearing and lower contributions of dynamic failure.



17.11 (a) Schematic representation of FCG rates of a material tested at various constant K_{max} , decreasing ΔK ; (b), (c) low residual stress (LRS) 6061 alloys tested at $R = 0.1, 0.5$ and 0.7 before and after closure corrections; (d), (e) high residual stress (HRS) 6061 alloys tested at $R = 0.1, 0.5$ and 0.7 before and after closure corrections.^{7,56,76}

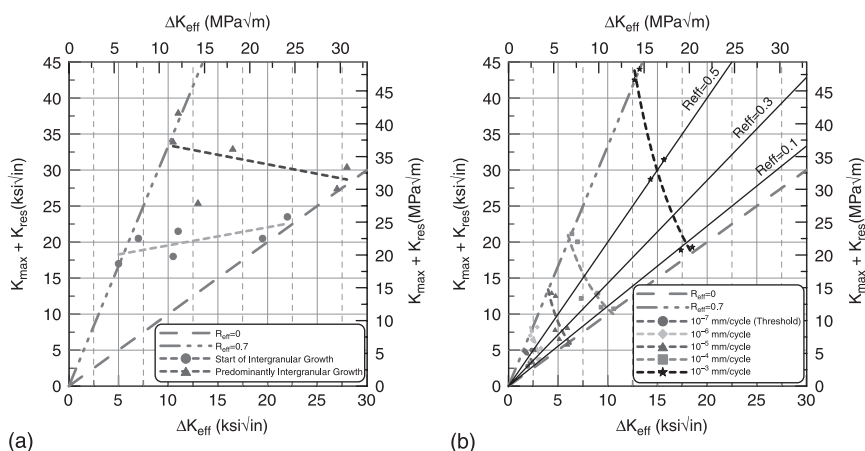


17.12 SEM fractographs of steady state crack growth behavior of 6061 alloys in low and high residual stress conditions for low, intermediate and high applied stress ratios revealing striations⁷⁶: (a), (b), (c) low residual stress, $R = 0.1, 0.5$ and 0.7 ; (d), (e), (f) high residual stress, $R = 0.1, 0.5$ and 0.7 ; average crack growth rate: $\sim 1\ \mu\text{m}/\text{cycle}$.

17.7 A dual parameter ΔK - K_{\max} approach to fatigue crack growth

To aid in the characterization of the fatigue response of materials, a two-parameter approach emphasizing the inter-dependence of ΔK and K_{\max} was proposed by Vasudevan and Sadananda.^{36–38} The approach assumes that crack growth behavior, such as crack threshold, requires a combination of dynamic and monotonic loading conditions in order for a crack to grow. This approach requires the effective stress intensity range, ΔK_{eff} , and thus, small crack growth data have been typically used in such analyses. The approach was recently applied by Lammi and Lados⁷⁶ to long FCG data generated on 6061 alloys, after closure corrections were applied to obtain ΔK_{eff} values. Samples with both low and high residual stresses were investigated, incorporating the residual stress effects in the analysis through the use of $K_{\max} + K_{\text{res}}$ and R_{eff} .

The two parameter methodology was extended to illustrate the transition of crack growth mechanisms at the microstructure scale from transgranular to intergranular as the crack advances from low Region II to high Region II to Region III.⁷⁶ The transition from transgranular to intergranular crack growth does not show dependence on ΔK_{eff} but rather $K_{\max} + K_{\text{res}}$, corresponding to the static damage and radius of the plastic zone ahead of the crack tip. This correlates well with the use of the monotonic plastic zone to explain the FCG mechanisms at different stages of crack growth (see discussion presented in Section 17.5 for various types of cast and wrought aluminum alloys). Various crack growth rates were plotted as a function of ΔK_{eff} and $K_{\max} + K_{\text{res}}$, and interdependence between the two parameters was observed. These results are presented in Fig. 17.13,⁷⁶ and



17.13 ΔK_{eff} versus $K_{\max} + K_{\text{res}}$ phase space for 6061 alloys showing: (a) the relationship between ΔK_{eff} and $K_{\max} + K_{\text{res}}$ that creates domains of transgranular, mixed mode and intergranular crack growth at various stress ratios and (b) the interplay between ΔK_{eff} and $K_{\max} + K_{\text{res}}$ that generates given crack growth rates at various stress ratios.⁷⁶

they serve as a combined tool to predict the crack path characteristics and crack growth rates at any ΔK_{eff} and $K_{\text{max}} + K_{\text{res}}$. This method can be equally applied to physically small and long cracks with quantitative understanding of the effects of closure and residual stress.

17.8 K_{max} sensitivity and data normalization for generating design curves

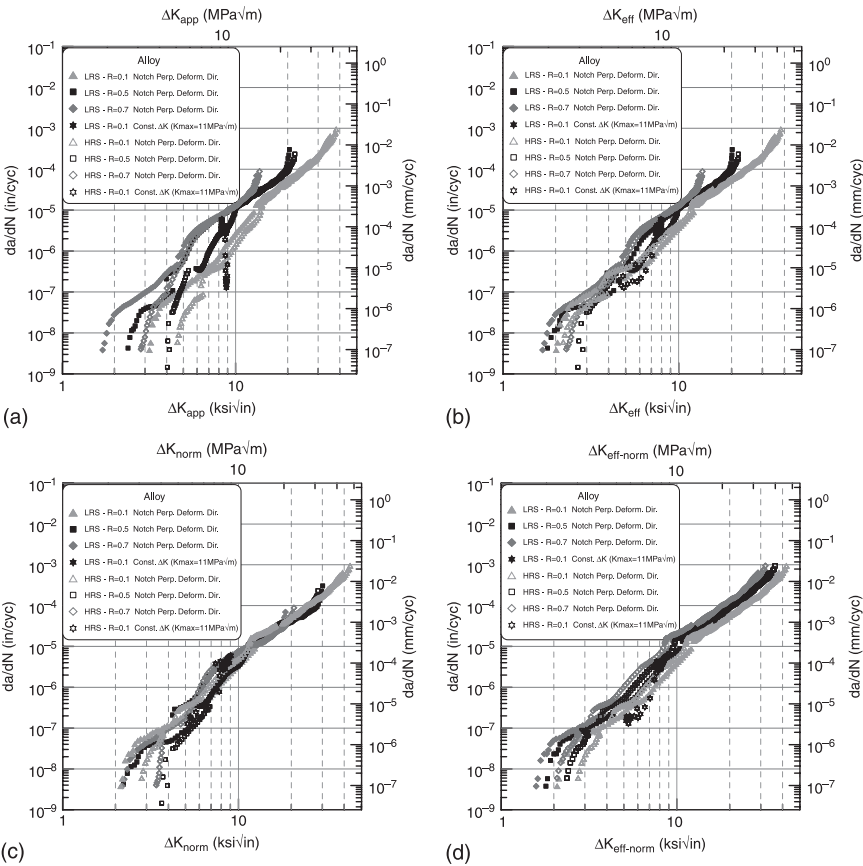
As discussed thus far, FCG data generated from long cracks are often confounded by closure and residual stress effects, and there are various methodologies used in the field to either compensate for these effects or circumvent them during testing. Therefore, it is important to conclude this chapter with a discussion on one such methodology that addresses these issues from the design perspective, and generates accurate design curves for life predictions.⁷⁴ The method is primarily important for cases affected by residual stress, including tensile residual stresses, which cannot be accurately handled by either current residual stress corrective methods or global closure corrective methods such as the ACR method. For low residual stress conditions, the method can be mainly used to generate data for various stress ratios, which may be needed in design applications, but have not all been experimentally determined – the ACR method can be used to determine ΔK_{eff} data, but cannot be used to generate data for various stress ratios from test data at just one stress ratio. The fundamentals of this data reduction method will be discussed next, and an example on the application of the method to 6061 alloys with low and high residual stresses will be provided.

Compressive residual stress has a direct impact on the crack tip driving force, ΔK , especially at low stress ratios and at near-threshold crack growth rates. Tensile residual stress may only affect K_{max} since the crack can remain fully open even at the minimum load. Regardless of whether or not compressive or tensile residual stresses are present, correlating stress ratio effects using the ACR method often results in the observation that the FCG response is determined not only by ΔK_{eff} , but it also depends on K_{max} . It was also observed that this K_{max} dependence takes the form of a power law where the magnitude of the exponent is a measure of K_{max} sensitivity.⁷⁷ In a manner similar to that proposed by Walker,⁷⁸ a unique intrinsic FCG curve (Master Curve) can be obtained by normalizing the stress intensity based on Eq. 17.6. In order to correctly incorporate K_{max} sensitivity in the normalization process, it is necessary to first determine the effective stress intensity using the ACR method. Also, K_{res} needs to be added to the applied K_{max} for data generated on specimens with high residual stress. Thus, the normalization equation becomes:

$$K_{\text{norm}} = \Delta K_{\text{eff}}^{1-n} \cdot (K_{\text{max}} + K_{\text{res}})^n \quad [17.6]$$

The K_{max} sensitivity concept is intended to compensate for the interaction between ΔK and K_{max} under predominantly elastic conditions and does not

apply to upper Region II and Region III behavior. A methodology to correct FCG data for plasticity can be found elsewhere.⁷⁵ The value of the K_{\max} sensitivity exponent n is dependent on the material and environmental conditions. For aluminum alloys, the typical value for n is in the 0.10–0.25 range, which indicates a larger contribution from ΔK than K_{\max} . The steps in determining K_{norm} for 6061 alloys with low and high residual stresses are shown in Fig. 17.14(a)–(c) ($n = 0.25$). The normalization process removes stress ratio, residual stress and remote closure effects establishing the basis for generating residual stress free design curves. The normalized curve is a good indicator of the physically small crack growth behavior of the material, and it is not expected to mask material and environmental effects. Thus, the normalization process allows a direct comparison between the responses of different materials in different environments.



17.14 Fatigue crack growth data for 6061 with low and high residual stress showing: (a) ΔK_{app} data; (b) ΔK_{eff} data using the ACR closure corrective method; (c) ΔK_{norm} data; (d) $\Delta K_{\text{eff-norm}}$ data from a single normalized curve after reintroducing stress ratio effects.⁵⁶

In order to further use the normalized curve into a life prediction routine, it is necessary to reintroduce the stress ratio effect (but not residual stress effects), and solve for $\Delta K_{\text{eff-norm}}$ knowing that:

$$K_{\text{max}} + K_{\text{res}} = \frac{\Delta K_{\text{eff}}}{(1-R)} \quad [17.7]$$

Equation 17.6 can be rearranged to solve for $\Delta K_{\text{eff-norm}}$ as shown in Eq. 17.8:

$$\Delta K_{\text{eff-norm}} = K_{\text{norm}} \cdot (1-R)^n \quad [17.8]$$

Equation 17.8 can be used to construct a curve for each stress ratio of interest from a single normalized curve. In Fig. 17.14(d), stress ratio effects were reintroduced using Eq. 17.8 for the normalized curve tested at a stress ratio $R = 0.1$. After re-processing, Fig. 17.14(d), data initially corresponding to one stress ratio ($R = 0.1$) closely matched the experimental test data for three stress ratios after ACR closure corrections, for both low and high residual stress conditions, Fig. 17.14(b). Determining the proper stress ratio for design also requires knowledge of the applied stress and the residual stress for the structure (R_{app} for low residual stress and R_{eff} for high residual stress conditions). If a given design application requires a long crack growth consideration instead of a small crack, closure effects may also need to be reintroduced into the design curve, which often can be done directly in the life prediction software.

17.9 Conclusion

The integrated knowledge discussed here represents the foundation for *optimizing existing aluminum alloys* for FCG performance based on better initiation life (higher thresholds) and better propagation life (reduced crack propagation rates in Regions II and III and higher fracture toughness) – the higher the threshold the better the high cycle fatigue response, and the higher the toughness the better the low cycle fatigue and impact resistance of the material. The mechanistic understanding also *provides necessary micro/nano-structural guidelines for engineering future cast and wrought aluminum alloys* and tailoring their respective processes. In addition, the combined materials science-fracture mechanics tools discussed here are critical to and provide guidance for *accurate fatigue life predictions and design* of fatigue critical structural components.

17.10 References

1. Dieter GE. Mechanical metallurgy. 3rd ed. Columbus, OH: McGraw-Hill; 1986. pp. 375.
2. Pearson S. Initiation of fatigue cracks in commercial aluminum alloys and the subsequent propagation of very short cracks. Eng Fract Mech. 1975;7:235–47.

3. Miller KJ. Short crack problem. *Fatigue Fract Eng Mater Struct*. 1982;5:223–32.
4. Suresh S, Ritchie RO. Propagation of short fatigue cracks. *Int Met Rev*. 1984;29: 445–76.
5. Lankford J. The growth of small fatigue cracks in 7075-T6 aluminum. *Fatigue Fract Eng Mater Struct*. 1982;5:238–48.
6. Lados DA, Apelian D, Donald JK. Fatigue crack growth mechanisms at the microstructure scale in Al-Si-Mg cast alloys: mechanisms in the near-threshold regime. *Acta Mater*. 2006;54(6):1475–86.
7. Lados DA, Apelian D, Paris PC, Donald JK. Closure mechanisms in cast Al-Si-Mg alloys and long-crack to small-crack corrections. *Int J Fatigue*. 2005;27(10–12): 1463–72.
8. Ritchie RO, Lankford J. Small fatigue cracks: a statement of the problem and potential solutions. *Mater Sci Eng*. 1996;84:11–6.
9. Tanaka K. Modeling of propagation and non-propagation of small fatigue cracks. In: Ritchie RO, Lankford J, editors. *Small fatigue cracks*. Warrendale, PA: The Metallurgical Society of the American Institute of Mining, Metallurgical and Petroleum Engineers; 1986. pp. 343–61.
10. de los Rios ER, Navarro A. Considerations of grain orientation and work hardening on short-fatigue crack modeling. *Phil Mag A: Phys Condens Matter Defects Mech Prop*. 1990;61:435–49.
11. Shiozawa K, Tohda Y, Sun SM. Crack initiation and small fatigue crack growth behavior of squeeze-cast Al-Si aluminium alloys. *Fatigue Fract Eng Mater Struct*. 1997;20(2):237–47.
12. Plumtree A, Schafer S. Initiation and short crack behavior in aluminium alloy castings. In: Miller KJ, de los Rios ER, editors. *The behavior of short fatigue cracks*, EGF Pub 1. London: Mechanical Engineering Publications; 1986, p. 215–27.
13. Gall K, Yang N, Horstemeyer M, McDowell DL, Fan J. The debonding and fracture of Si particles during the fatigue of a cast Al-Si alloy. *Metall Mater Trans A*. 1999;30A(12):3079–88.
14. Lankford J, Davidson DL. In: *Proceedings of the Second International Workshop on Small Fatigue Cracks*. Santa Barbara, CA; 1986.
15. Christensen RH. Fatigue crack growth affected by metal fragments wedged between opening-closing crack surfaces. *Appl Mater Res*. 1963:207–10.
16. Elber W. Fatigue crack closure under cyclic tension. *Eng Fract Mech*. 1970;2:37–45.
17. Elber W. The significance of fatigue crack closure. In: *Damage tolerance in aircraft structures*. ASTM STP 486. Philadelphia: American Society for Testing and Materials, 1971, 230–42.
18. Ohta A, Kosuge M, Sasaki E. Change of fatigue closure level with gauge location along crack line. *Int J Fract*. 1979;15:R53–7.
19. Jones JW, Macha DE, Corbly DM. Observations on fatigue crack opening load determinations. *Int J Fract*. 1978;14:R25–30.
20. Horng JL, Fine ME. Near-threshold fatigue crack propagation rates of dual-phase steels. *Mater Sci Eng*. 1984;67:185–95.
21. Vecchio RS, Crompton JS, Hertzberg RW. The influence of specimen geometry on near threshold fatigue crack growth. *Fatigue Fract Eng Mater Struct*. 1987;10: 333–42.
22. Suresh S, Ritchie RO. Near-threshold fatigue crack propagation: a perspective on the role of crack closure. In: Davidson DL, Suresh S, editors. *Proceedings of the*

- International Symposium on Fatigue Crack Growth Threshold Concepts. Philadelphia: The Metallurgical Society of AIME; 1983.
23. Taylor D. Fatigue thresholds: their applicability to engineering situations. *Int J Fatigue*. 1988;10:67–79.
 24. Newman JC Jr. A crack-closure model for predicting fatigue crack growth under aircraft spectrum loading. In: Chang JB, Hudson CM, editors. *Methods and models for predicting fatigue crack growth under random loading*. ASTM STP 748. Philadelphia: American Society for Testing and Materials; 1981. pp. 53–84.
 25. Newman JC Jr. Fatigue-life prediction methodology using a crack-closure model. *J of Eng Mater Technol*. 1995;117:433–9.
 26. Kubota M, Ochi Y, Ishii A, Shibata R. Crack propagation properties on HIP-treated cast aluminum alloys. *Mater Sci Research Int*. 1998;4(3):193–9.
 27. Kumai S, Sekikawa A, Hu J, Higo Y, Nunomura S. Effects of roughness-induced crack closure on fatigue crack growth in AC4CH cast aluminum alloys (in Japanese). *J Jap Inst Light Metals*. 1995;45(4):204–8.
 28. Kumai S, Hu J, Higo Y, Nunomura S. Effects of dendrite cell size and particle distribution of the near-threshold fatigue crack growth behaviour of cast Al-SiCp composites. *Acta Mater*. 1996;44(6):2249–57.
 29. Shang JK, Yu W, Ritchie RO. Role of silicon carbide particles in fatigue crack growth in SiC-particulate-reinforced aluminum alloy composites. *Mater Sci Eng A*. 1988;A102:181–92.
 30. Sugimura Y, Suresh S. Effects of SiC content on fatigue crack growth in aluminum alloys reinforced with SiC particles. *Metall Mater Trans A*. 1992;23A(8):2231–42.
 31. Suresh S. *Fatigue of materials*. 1st ed. Cambridge: Cambridge University Press; 1991.
 32. Sadananda K, Vasudevan AK. Short crack growth behavior. In: *Fatigue and fracture mechanics 27*. ASTM STP 1290. Philadelphia: American Society for Testing and Materials; 1997. pp. 301–16.
 33. Lados DA, Apelian D. The effect of residual stress on the fatigue crack growth behavior of Al-Si-Mg cast alloys: mechanisms and corrective mathematical models. *Metall Mater Trans A*. 2006;37A(1):133–45.
 34. Donald JK, Paris PC. An evaluation of DK_{eff} estimation procedures on 6061-T6 and 2024-T3 aluminum alloys. *Int J Fatigue*. 1999;21:S47–57.
 35. Paris PC, Tada H, Donald JK. Service load fatigue damage – a historical perspective. *Int J Fatigue*. 1999;21:S35–46.
 36. Vasudevan AK, Sadananda K, Louat N. A review of crack closure, fatigue crack threshold and related phenomena. *Mater Sci Eng A*. 1994;A188:1–22.
 37. Vasudevan AK, Sadananda K, Glinka G. Critical parameters for fatigue damage. *Int J Fatigue*. 2001;23:S39–53.
 38. Vasudevan AK, Sadananda K, Louat N. Two critical stress intensities for threshold crack propagation. *Scripta Metall*. 1993;28:65–70.
 39. Lawson L, Chen EY, Meshii M. Near-threshold fatigue: a review. *Int J Fatigue*. 1999;21:S15–34.
 40. El Haddad MH, Smith KH, Topper TM. Fatigue crack propagation of short cracks. *J of Eng Mater Technol*. 1979;101:42–6.
 41. Donald JK. A procedure for standardizing crack closure levels. In: Newman JC Jr, Elber W, editors. *Mechanics of fatigue crack closure*. ASTM STP 982. Philadelphia: American Society for Testing and Materials; 1988. pp. 222–9.
 42. Couper MJ, Neeson AE, Griffiths JR. Casting defects and the fatigue behavior of an aluminum casting alloy. *Fatigue Fract Eng Mater Struct*. 1990;13:213–27.

43. Skallerud B, Iveland T, Harkegard G. Fatigue life assessment of aluminum alloys with casting defects. *Eng Fract Mech.* 1993;44:857–74.
44. Chen DL, Weiss B, Stickler R. Contribution of the cyclic loading portion below the opening load to fatigue crack growth. *Mater Sci Eng A.* 1996; A208:181–7.
45. Hinkle AJ, Brockenbrough JR, Burg JT. Microstructural material models for fatigue design of castings. In: *Proceedings from developments in aluminum use for vehicle design.* SAE SP-1164. Detroit, MI; 1996. pp. 21–7.
46. Conley JG, Moran B, Gray J. A new paradigm for the design of safety critical castings. In: *Proceedings from SAE International Congress and Exposition.* SAE SP-1350. Detroit, MI; 1998. pp. 25–38.
47. Donald JK, Bray GH, Bush RW. An evaluation of the adjusted compliance ratio technique for determining the effective stress intensity factor. In: Panontin TL, Sheppard SD, editors. *Fatigue and fracture mechanics 29.* ASTM STP 1332. Philadelphia: American Society for Testing and Materials; 1999. pp. 674–95.
48. Newman J, Schneider J, Daniel A, McKnight D. Compression pre-Cracking to generate near threshold fatigue-crack-growth rates in two aluminum alloys. *Int Journal of Fatigue.* 2005;27(10–12):1432–40.
49. Newman JC Jr, Yamada Y. Compression precracking methods to generate near-threshold fatigue-crack-growth-rate data. *Int Journal of Fatigue.* (in press, available online February 2009)
50. Lados DA, Apelian D, Major JF. Fatigue crack growth mechanisms at the microstructure scale in Al-Si-Mg cast alloys: mechanisms in regions II and III. *Metall Mater Trans A.* 2006;37A(8):2405–18.
51. Kumai S, Hu J, Higo Y, Nunomura S. Effects of solidification structure on fatigue crack growth in AC4CH cast aluminum alloys (in Japanese). *J Jap Inst Light Metals.* 1995;45(4):198–203.
52. Kumai S, Aoki S, Han SW, Sato A. Effects of dendrite cell size and eutectic Si particle morphology on fatigue crack growth in cast and HIPed AC4CH alloys. *Mater Trans JIM.* 1999;40(7):685–91.
53. Caton MJ, Jones JW, Boileau JM, Allison JE. The effect of solidification rate on the growth of small fatigue cracks in a cast 319-type aluminum alloy. *Metall Mater Trans A.* 1999;30A(12):3055–68.
54. Chan KS, Jones P, Wang Q. Fatigue crack growth and fracture paths in sand cast B319 and A356 aluminum alloys. *Mater Sci Eng A.* 2003;341A(1–2):18–34.
55. Lados DA. Fatigue crack propagation mechanisms of long and small cracks in Al-Si-Mg and Al-Mg cast alloys. *Proceedings of the 4th International Light Metal Technology Conference 2009, Trans Tech Publications – Materials Science Forum,* 2009. pp. 618–619, 563–74.
56. Gavras AG, Lados DA. Fatigue crack growth mechanisms of long and small cracks in structural materials (internal reports). *Integrative Materials Design Center, Worcester Polytechnic Institute;* 2009.
57. Lee FT, Major JF, Samuel FH. Fatigue crack growth and fracture behavior of Al-12wt%Si-0.35wt%Mg-(0-0.02)wt%Sr casting alloys. *AFS Trans.* 1996;104: 785–95.
58. Lados DA, Apelian D, Wang L. Minimization of residual stress in heat treated cast Al-Si-Mg alloys using uphill quenching: mechanisms and effects on static and dynamic properties. *Mater Sci Eng A.* 2010; A527:3159–65.
59. Morris WL, James MR, Buck O. Growth rate models for short surface cracks in Al 2219-T851. *Metall Trans A.* 1981;A12:57–64.

60. Bolingbroke RK, King JE. A comparison of long and short fatigue crack growth in a high strength aluminum. In: Miller KJ, de los Rios ER, editors. *The behaviour of short fatigue cracks*. London: Mechanical Engineering Publications; 1986. pp. 101–14.
61. Kaynak C, Ankara A. Short fatigue crack growth in Al 2024-T3 and Al 7075-T6. *Eng Fract Mech*. 1992;43:769–78.
62. Halliday MD, Cooper C, Poole P, Bowen P. On predicting small fatigue crack growth and fatigue life from long crack data in 2024 aluminum alloy. *Int J Fatigue*. 2003;25:709–18.
63. Caton MJ, Jones JW, Allison JE. The Influence of heat treatment and solidification time on the behavior of small-fatigue-cracks in a cast aluminum alloy. *Mater Sci Eng A*. 2001;A314:81–5.
64. Fan J, McDowell DL, Horstemeyer MF, Gall K. Computational micromechanics analysis of cyclic crack-tip behavior for microstructurally small cracks in dual-phase Al-Si alloys. *Eng Fract Mech*. 2001;68:1687–1706.
65. Klesnil M, Polak J, Liskutin P. Short crack growth close to the fatigue limit in low carbon steel. *Scripta Metall*. 1984;18:1231–4.
66. Gerdes C, Gysler A, Lutjering G. Propagation of small surface cracks in titanium alloys. In: Davidson DL, Suresh S, editors. *Fatigue Crack Growth Threshold Concepts*. Warrendale, PA: The Metallurgical Society of the American Institute of Mining, Metallurgical and Petroleum Engineers; 1984. pp. 465–78.
67. Neumann P, Tonnessen A. Fatigue crack formation in copper. In: Ritchie RO, Lankford J, editors. *Small fatigue cracks*. Warrendale, PA: The Metallurgical Society of the American Institute of Mining, Metallurgical and Petroleum Engineers; 1986. pp. 41–9.
68. Newman P, Beevers CJ. Growth of short fatigue cracks in high strength Ni-base superalloys. In: Ritchie RO, Lankford J, editors. *Small fatigue cracks*. Warrendale, PA: The Metallurgical Society of the American Institute of Mining, Metallurgical and Petroleum Engineers; 1986. pp. 97–116.
69. Ritchie RO, Lankford J. Overview of the small crack problem. In: Ritchie RO, Lankford J, editors. *Small fatigue cracks*. Warrendale, PA: The Metallurgical Society of the American Institute of Mining, Metallurgical and Petroleum Engineers; 1986. pp. 1–5.
70. Miller KJ, de los Rios ER, editors. *Short fatigue cracks*,ESIS 13. London: Mechanical Engineering Publications; 1992.
71. Lados DA, Apelian D, Donald JK. Fracture mechanics analysis for residual stress and crack closure corrections. *Int J Fatigue*. 2007;29(4): 687–94.
72. Bucci RJ. Effect of residual stress on fatigue crack growth rate measurement. In: Roberts R, editor. *Fracture mechanics: thirteenth conference*. ASTM STP 743. Philadelphia: American Society for Testing and Materials; 1981. pp. 28–47.
73. Lammi CJ, Lados DA. Effects of processing residual stresses on fatigue crack growth behavior of structural materials: mathematical and analytical corrections. *Int J Fatigue*. submitted.
74. Donald JK, Lados DA. An integrated methodology for separating closure and residual stress effects from fatigue crack growth rate data. *Fatigue Fract Eng Mater Struct*. 2007;30(3):223–30.
75. Lados DA, Apelian D. Limitations of elastic definitions in Al-Si-Mg cast alloys with enhanced plasticity: linear elastic fracture mechanics versus elasto-plastic fracture mechanics. *Eng Fract Mech*. 2006;73(4):435–55.

76. Lammi CJ, Lados DA. Effects of processing residual stresses on fatigue crack growth behavior of structural materials: experimental approaches and microstructural mechanisms. *Metall Mater Trans A*. submitted.
77. Donald JK, Bray GH, Bush RW. Introducing the K_{\max} sensitivity concept for correlating fatigue crack growth data. *High Cycle Fatigue of Structural Materials* (Professor Paris PC Symposium), Soboyejo W, Srivatsan TS, editors. The Minerals, Metals and Materials Society; 1997. pp. 123–41.
78. Walker K. The effect of stress ratio during crack propagation and fatigue for 2024-T3 and 7075-T6 aluminum. In: *Effects of environment and complex load history on fatigue life*. ASTM STP 462. Philadelphia: American Society for Testing and Materials; 1970. pp. 1–14.

J.F. KNOTT, The University of Birmingham, UK

Abstract: The chapter treats fracture processes in aluminium and its alloys mainly in two areas: forming processes and components in engineering structures. There is focus on the roles of the strain hardening exponent and the volume fraction and nature of second-phase particles in controlling formability and fracture toughness. Some parallels are drawn between sheet-metal forming and the behaviour of thin-section engineering components. Attention is paid to the effects of defects on ultimate tensile strength values in castings, to the fracture of metal-matrix composites and to the effect on fracture of intense localisation of slip due to dynamic strain-aging.

Key words: strain-hardening, plastic instability, second-phase particles, fracture toughness, strain-aging.

18.1 Introduction

Any treatment of fracture processes in ‘aluminium’ has to take account of the different types of alloys of this versatile metal and the different applications in which these alloys are employed. Pure aluminium and solid solution alloys (1xxx, 3xxx and 5xxx series) are used in kitchen foil, drinks cans and formable sheet products; precipitation-hardened alloys (2xxx, 6xxx, 7xxx and 8xxx series) are employed in rocket motor tubes, in extrusions, struts and panels in land-based transportation vehicles; and in wings, fuselage and undercarriages for aircraft. Wide use is made of as-cast components (4xxx series) and there are some specialised applications for particulate metal-matrix composites (MMCs). There is interest in welded components: recently, in those involving friction-stir welding. Service duty often involves both cyclic loading (fatigue) and effects of environment (corrosion, stress-corrosion). These are treated in other chapters, the present chapter concentrates on fracture in aluminium alloys under monotonic loading at temperatures below the creep range.

There are two main aspects of monotonic fracture in practice:

1. in forming processes;
2. in the subsequent service operation of structural components.

The main differences are that forming processes involve gross shape changes, such that large overall plastic strains are produced: the yield strength is clearly exceeded throughout the whole body. In service operation, design stresses are restricted to a fraction of the yield strength, so that plastic deformation is confined to the local region ahead of a stress concentrator, such as a notch or a crack-like

defect, where steep strain gradients are present. Under severe over-loads, such as those met in earthquake loading or when vehicles collide, the design basis may be grossly exceeded and structural components are subjected to conditions similar to those experienced in forming processes. In the present chapter, attention is focused on fracture in cold-forming operations and in structural components.

Aluminium and primary solid solutions based on aluminium have a face-centred-cubic (fcc) crystallographic structure, and fail by ductile fracture mechanisms. The fracture properties of both cast and wrought alloys are, however, strongly influenced by the presence of second-phase particles. In castings, there may be effects due to shrinkage cavities, pores, oxide bi-films or intermetallics. The presence of iron and silicon in wrought material gives rise to brittle intermetallic particles, which crack at low strain; similar behaviour is often exhibited by reinforcing particles in MMCs. Even in wrought alloys with controlled amounts of Fe and Si, there may still be effects of oxide films that persist from the original cast form. It is also common practice to add elements such as Cr or Zr to affect grain-size control *via* the formation of 'dispersoid' particles, which may serve as sites for micro-void formation. In pure precipitation-hardening alloy systems, it is possible for the ageing particles themselves to affect fracture processes. Under-aged (UA) alloys tend to exhibit concentrated slip-bands; over-aged (OA) alloys are associated with more dispersed slip. Dynamic strain-ageing in Mg-containing alloys promotes intense localisation of slip, which gives rise to shear fractures following macroscopic slip planes.

The ductile fracture mechanisms operative in such a wide range of applications incorporate a number of basic concepts: the onset of plastic instability; external and internal geometry changes; onset of through-thickness localised shear in thin sheet; void coalescence in plane strain stress-states; localisation and fast fracture ahead of pre-existing cracks. These concepts will be treated in the relevant sections, which also contain detailed references to the various micro-structural features summarised above.

18.2 Fracture in uni-axial tension

It is useful to start with the conditions leading to a plastic 'necking' instability in a uni-axial tensile test, since this represents a particularly simple form of 'cold forming': a stretched bar failing well after general yield, when subjected to gross plastic strains. Conventionally, the material is treated as a defect-free continuum, and under load control (as in forming operations) failure is assumed to follow shortly after the criterion for plastic instability has been met. The criterion for the onset of necking of a uni-axial tensile specimen makes use of the fact that the UTS load, in a graph of load versus strain, exhibits a maximum. If the load, $P = \sigma_T A$, where σ_T is the true stress and A is the instantaneous area (both σ_T and A varying with strain), the condition for a maximum is:

$$dP = \sigma_T dA + A d\sigma_T = 0 \quad \text{i.e.} \quad d\sigma_T / \sigma_T = -dA/A \quad [18.1]$$

The second point is that plastic deformation takes place at constant volume ($dV = 0$). For a uniformly deforming bar (up to the onset of necking), the volume, $V = lA$, where l is the instantaneous length. Hence:

$$dV = l dA + A dl = 0 \quad \text{i.e.} \quad -dA/A = dl/l = d\epsilon_T \quad [18.2]$$

where, by definition, $dl/l = d\epsilon_T$ is the true strain. From Eq. 18.1 and Eq. 18.2, the condition for necking (a load maximum) is given by:

$$d\sigma_T/\sigma_T = d\epsilon_T \quad \text{i.e.} \quad d\sigma_T/d\epsilon_T = \sigma_T \quad [18.3]$$

For a material with a true stress/true strain curve conforming to a simple, power-law relationship (with K as a constant):

$$\sigma_T = K \epsilon_T^n \quad [18.4]$$

Equation 18.3 in reverse order, $\sigma_T = d\sigma_T/d\epsilon_T$, becomes

$$K \epsilon_T^n = n K \epsilon_T^{(n-1)} \quad \text{i.e.} \quad \epsilon_T = n \quad [18.5]$$

where n is the strain-hardening exponent.

The association of failure under-load control with the onset of plastic instability highlights: first, the difference between the contributions of uniform strain (up to instability) and non-uniform strain (post-instability) to total ductility; second, the relevance of such ductility to failure under the conditions imposed. Consider the failure of hard-drawn wire under load control. A good example, although not involving aluminium, is the failure of the (steel) 'E'-string of a violin, when it 'snaps', if over-tightened during tuning. Similar behaviour would be observed for the failure of hard-drawn aluminium wire in a simple, load-controlled tensile test. Suppose that the aluminium wire is strain-hardened, during drawing, to a yield strength of 350 MPa; let the 'gauge length' be 1 m, and the diameter 1 mm. After such a large degree of cold work, the hardening exponent, n , is essentially zero, and we see, from Eq. 18.5 that the material necks as soon as it yields ($\epsilon_T = n = 0$). The yield strength is then identical to the ultimate tensile strength (UTS). The 0.2% proof strength cannot be defined because no plastic offset corresponding to 0.2% permanent strain can be obtained.

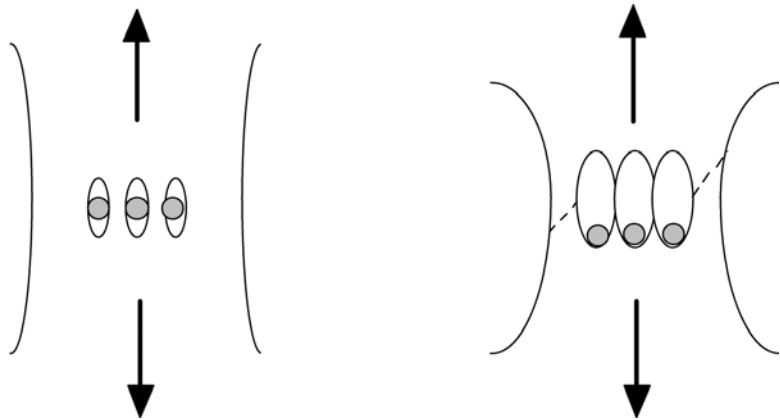
Even if the material necks to a perfect point, i.e. exhibiting 100% reduction in area, the (non-uniform) plastic displacement is only 1 mm, assuming slip on planes orientated at 45° to the tensile stress axis. Over a gauge length of 1 m, this is a strain of 0.1%. The elastic strain, ϵ_{el} at the point of instability is σ_Y/E , where E is Young's modulus, ~70 GPa for aluminium. With $\sigma_Y = 350$ MPa, $\epsilon_{el} = 350/(70 \times 10^3) = 0.5\%$, five times larger than the total non-uniform plastic strain. The stored elastic strain energy at the point of instability is $\sigma_Y^2/2E$ per unit volume, and this is released when instability/'failure' occurs, imparting kinetic energy to the broken halves. The effect is more pronounced for long wires and cables because the stored elastic energy at the point of instability is greater. A point to emphasise is that, even if the reduction in area were only 50%, the sequence of

events and the overall perception of behaviour would not be altered. 'Failure' would still be associated with the onset of instability, and the energy release would not be materially altered.

If the material were softened by annealing and then tested, there would be a substantial uniform plastic strain before the onset of instability. Similarly, uniform strain enables large plastic deformations to be obtained in sheet-forming operations before localisation occurs: hence, from Eq. 18.5, material with high strain-hardening exponents should be used. Under some conditions, as for the hard-drawn wire, there may be rather little relevance of different values of tensile ductility as measured by the percentage reduction-in-area (RA%), but in others, such as the bending of sheet over a former, where failure is associated, not with a plastic instability, but with a limiting strain, values of RA% (reflecting effects of inclusion content) may correlate with the limiting strains that can be obtained without fracture.

Under load control, the onset of plastic instability is associated with a near-instantaneous approach to total failure (separation of the test-piece into two halves), but in a 'hard' displacement-controlled testing machine, it is possible to develop a 'neck' (local reduction of external cross-section) that initially continues to reduce in section in a stable manner (under decreasing load) with increasing applied tensile strain. Instability occurs when the elastic unloading rate of the loading system becomes tangential to the slope of the (decreasing) load-displacement curve. The necked geometry can be developed further, without failure of the sample, by surrounding the test-piece with a stiff 'collar', which deforms elastically in parallel with the necked specimen and does not allow instability to occur. An analogous example is to be found in the use of multi-stranded cable for load-controlled applications. Here, if an imperfection in a single strand were to promote a localised neck, it would not lead to catastrophic failure because the strand is constrained (*via* frictional gripping) by its neighbours, which act similarly as a stiff 'collar'.

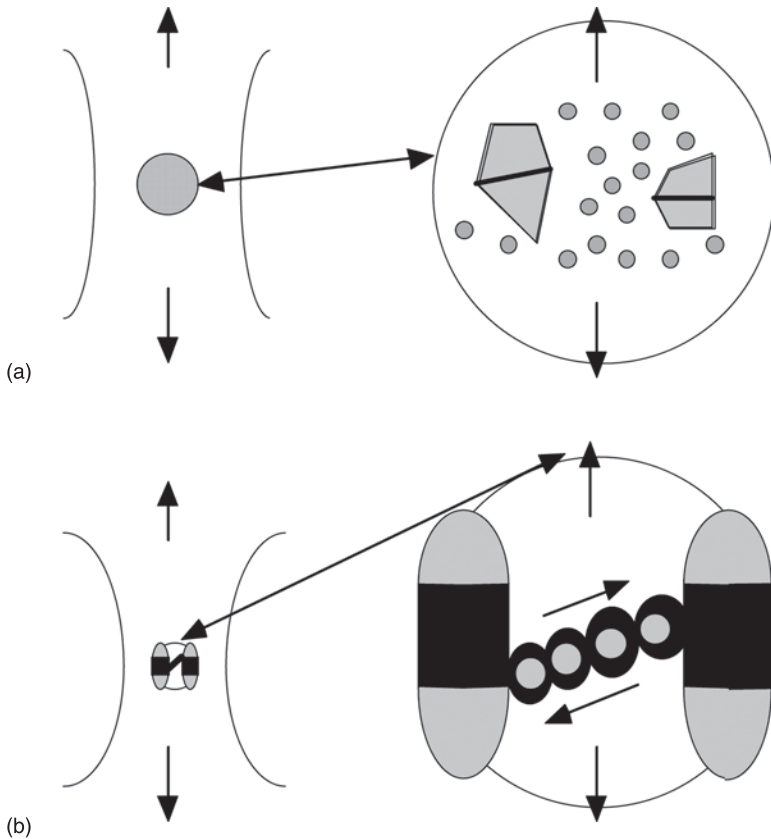
Above, it was assumed that the material necked to a single point, achieved by successive slips on two pairs of slip planes inclined at 45° to the tensile axis: these, in a continuum, are the planes across which the maximum shear stresses act. In commercial engineering materials, however, it is found that second-phase particles promote internal void formation, which leads to 'internal necks' concentrated in the central region of the externally necked test-piece. Following Puttick (1959) the sequence of events in a ductile material, such as copper, containing easily de-bonded non-metallic inclusions, is illustrated in Fig. 18.1. Voids are initiated at rather low plastic strain and initially grow predominantly parallel to the tensile stress axis. As the macroscopic neck develops, an increasingly large hydrostatic stress state is generated in the centre of the necked region and radial tensile stresses, normal to the applied stress, are produced. These encourage lateral growth of the voids, until they eventually coalesce as a series of 'internal necks' to produce a central 'crack', having a disc-like cross-section normal to the



18.1 Ductile fracture in a simple metal, such as copper, containing a distribution of easily de-bonded non-metallic inclusions (e.g. copper oxide in copper). Voids form around the inclusions at low strain and grow initially parallel to the tensile axis. As the neck develops and the hydrostatic component of stress becomes greater, the voids grow in lateral directions and finally coalesce to produce a set of internal necks. This forms the 'cup' of a 'cup-cone' fracture: the 'cone' is formed by shear fracture when the crack-like 'cup' occupies sufficient of the cross-section to induce concentrated shear in the outer annulus.

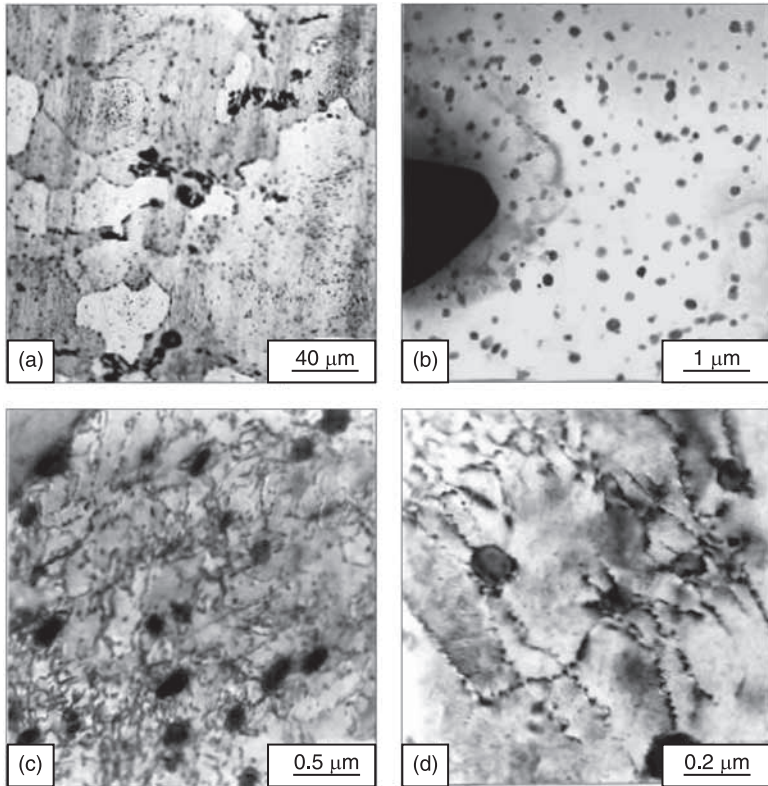
main tensile stress axis, but with steep peaks and troughs in any through-section plane containing that axis. When the central 'crack' occupies sufficient of the cross-section, shear is localised to bands at steep angles to the plane of the 'crack' and final separation takes place by shear. Figure 12 in Puttick (1959) shows a clear example of shear separation in a pure, polycrystalline sample of aluminium. Note that it is not possible to shear consistently on the conical surface implied by the circular cross-sectional geometry, but, in practice, any misalignment in the loading train, or spatial inhomogeneity in the distribution of second-phase particles, allows a single shear plane to predominate. The central void coalescence produces the 'cup' of a 'cup-cone' ductile fracture and the final shear separation produces the 'cone'.

This general sequence is followed in slightly modified form in most commercial wrought aluminium alloys: see Singh and Flemings (1969) and Garrett and Knott (1978). The sequence here is that the large, Fe/Si inclusions fracture at low strain, and as the test-piece is strained further, the cracks open up as voids, see Fig. 18.2. These internal voids allow shear bands to concentrate between the voids. In turn, the dislocations in the shear bands tangle around dispersoids, exerting stress on the dispersoid/matrix interface. Eventually, these interfaces de-cohere, and 'micro-voids' form in the shear band. The fracture surface then exhibits a series of larger voids (from inclusions) and micro-voids (centred on dispersoids). Particularly in OA precipitation-hardening alloys, a third, even finer, set of voids



18.2 Modification of the simple 'internal necking' mechanisms illustrated in Fig. 18.1 for a commercial aluminium alloy. (a) At relatively low strain, the large Fe/Si-containing intermetallics crack: at this stage (as seen in the 'higher magnification' diagram) the dispersoids have not de-cohered, although dislocations may be tangled around them. (b) At higher strain, the cracks in the Fe/Si particles have blunted to form voids. This promotes the formation of shear bands between voids and increasingly large numbers of dislocations tangle around the dispersoids, until the interfaces de-cohere. Resistance to further flow now decreases sharply, and a 'fast shear' linkage is produced between adjacent voids.

may form as a result of dislocations looping around the (OA) precipitates, and causing these to de-cohere from the matrix. The basic features are shown in Fig. 18.3. Often, the failure in tensile tests results from the onset of instability, as described above, and many of the void formation and linkage processes are post-instability. As will be described in Section 18.7, however, similar micro-structural features occur ahead of sharp cracks, where the steep strain gradient leads to progressive crack extension, before global instability. It might be noted that



18.3 Second-phase particles in duralumin (Al 4.5Cu 1Mg): (a) low magnification, showing grains and large, (~50mm) Fe/Si-containing intermetallics; (b) higher magnification, showing edge of large particle and distribution of (~0.2mm diameter) dispersoids; (c) lightly deformed alloy, showing dislocations tangling around dispersoids; (d) as (c) for a heavily overaged alloy, showing dislocations interacting with both dispersoids, and also the ageing precipitates (courtesy Dr G.G. Garrett).

superimposed hydrostatic pressure has a major effect on the growth and coalescence processes, but negligible effect on void nucleation (Liu and Lewandowski, 1993).

18.3 Fracture in thin sheet: stretching and deep-drawing operations

In biaxial plane stress, subjected to principal stresses: σ_1 , σ_2 ($\sigma_3 = 0$), plastic flow is produced by the deviatoric (non-hydrostatic) component of the stress-system, which is often put as the 'equivalent' stress, σ^* , defined (for plane stress) by:

$$\sigma^* = (1/\sqrt{2}) \{ \sigma_1^2 - \sigma_1\sigma_2 + \sigma_2^2 \}^{1/2} \quad [18.6]$$

With a similar definition for ‘equivalent’ strain, ϵ^* in terms of ϵ_1 and ϵ_2 , and the assumption of power-law hardening of the form of Eq. 18.4 a criterion for the onset of necking in thin sheet under biaxial stresses is given by:

$$d\sigma^*/d\epsilon^* = \sigma^*/z \quad [18.7]$$

where z is a function of σ_1 and σ_2 . Johnson and Mellor (1973) consider a material obeying a stress/strain law of the form:

$$\sigma^* = C(B + \epsilon^*)^n \quad [18.8]$$

where C and B are constants, and show that the instability condition is given by:

$$d\sigma^*/d\epsilon^* = n\sigma^*/(B + \epsilon^*) = \sigma^*/z \quad [18.9]$$

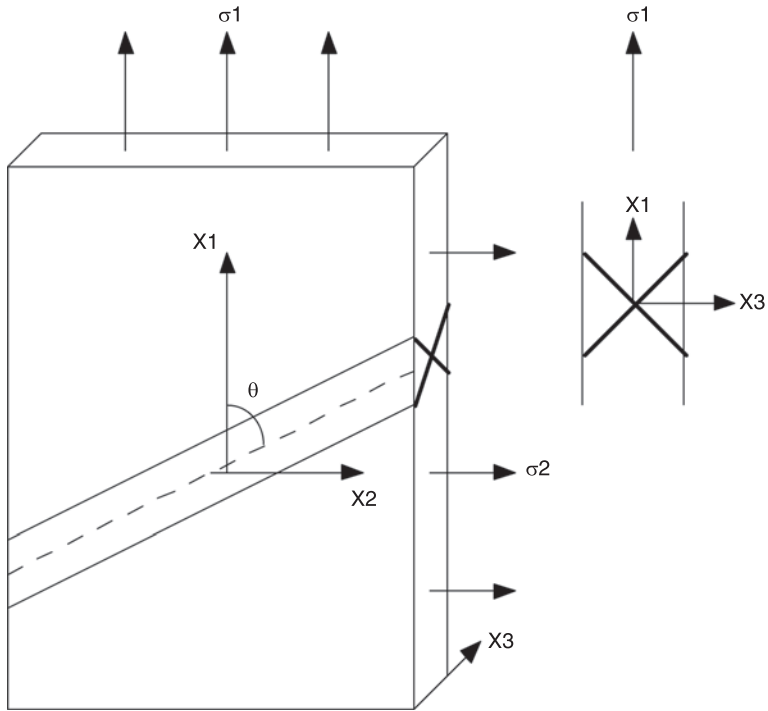
The equivalent stress definition derives from the Mises’ yield criterion. This is written as: $\{(\sigma_1 - \sigma_2)^2 + (\sigma_2 - \sigma_3)^2 + (\sigma_3 - \sigma_1)^2\} = \text{const.}$ In pure shear, $\sigma_1 = -\sigma_2 =$ the shear yield stress, k , and the constant is $6k^2$. In uni-axial tension, $\sigma_2 = \sigma_3 = 0$ and the constant is $2Y^2$, since $\sigma_1 = Y$, the tensile yield strength. Hence, $Y = \sqrt{3}k$. The effective stress, σ^* , is obtained by taking the square-root of the LHS of the Mises’ expression and applying a $(1/\sqrt{2})$ factor, so that, in uni-axial tension, $\sigma^* = Y$. In plane stress biaxial loading, $\sigma_3 = 0$, and the LHS of the Mises’ criterion reduces to $2\{\sigma_1^2 - \sigma_1\sigma_2 + \sigma_2^2\}$. The inclusion of the $(1/\sqrt{2})$ factor in the definition of σ^* in Eq. 18.6 again gives $\sigma^* = Y$ when $\sigma_2 = 0$. The general conclusion is that localisation of flow is postponed to high strains if the material possesses a high value of strain-hardening exponent, n , in Eq. 18.4 and Eq. 18.8. The ability to continue to harden sufficiently at high strain ensures that deformation continues to spread in a quasi-homogeneous manner. Sharp yield points and any Lüder’s strain resulting from the unpinning of dislocations must be prevented. Dislocation pinning and strain-ageing effects can occur in Al-alloys containing Mg, and it has been demonstrated that intense shear localisation can occur in as-quenched Al-Zn-Mg alloys, if these are deformed at very slow strain-rates (see Section 18.8).

The (plane stress) necking of a thin sheet of rigid/perfectly plastic material (i.e. $n = 0$) subjected to biaxial in-plane stresses σ_1 and σ_2 (where $0 < \sigma_2 < 0.5 \sigma_1$) is of interest. Necking (equivalent to yielding in plastic/rigid material) occurs on slip-lines inclined at 45° to the X_1 and X_3 axes, Fig. 18.4. This implies that the traces of these slip lines in the X_1X_2 plane assume an angle such that there is *zero* extension in that plane (yield being through-thickness only). The Levy–Mises’ expressions relate a plastic strain increment, $d\epsilon_{pl}$, to the deviatoric component of the stress field, i.e. to the principal stress minus the hydrostatic stress. For a slip line inclined at an angle θ to X_1 (hence at $(90 - \theta)$ to X_2), the stress in the direction θ is:

$$\sigma_{\theta\theta} = (\sigma_1 \cos^2\theta + \sigma_2 \sin^2\theta) \quad [18.10]$$

The hydrostatic stress is $\sigma_H = (1/3) \Sigma (\sigma_1 + \sigma_2 + \sigma_3)$, which, in plane stress ($\sigma_3 = 0$), is $(1/3)(\sigma_1 + \sigma_2)$. The Levy–Mises’ expressions reduce to:

$$d\epsilon_{pl}/(\sigma_{\theta\theta} - \sigma_H) = m \quad [18.11]$$



18.4 Formation of a neck in thin sheet, subjected to in-plane, orthogonal tensile stresses. The shear planes are at 45° through the thickness, and there is a direction, θ , along which the plastic strain is zero.

where $\dot{\eta}$ is a non-zero constant. If (the numerator) $d\epsilon_{pl}$ in the θ direction is zero, the only way in which Eq. 18.11 can be satisfied is if the denominator is also zero. Hence, $\sigma_{\theta\theta} = \sigma_H$, i.e.

$$(\sigma_1 \cos^2 \theta + \sigma_2 \sin^2 \theta) = (1/3)(\sigma_1 + \sigma_2) \quad [18.12]$$

For $\sigma_2 = 0$, $\theta = 54^\circ 44'$, and it is observed that this is the angle assumed by a slip band when heavily cold-worked strip is subjected to uni-axial tension. For $\sigma_2 = 0.5\sigma_1$, the RHS of Eq. 18.12 becomes $(1/2)\sigma_1$. The LHS is $\sigma_1 \cos^2 \theta + (1/2)\sigma_1 - (1/2)\sigma_1 \cos^2 \theta = (1/2)\sigma_1 \cos^2 \theta + (1/2)\sigma_1$. Hence, $(1/2)\sigma_1 \cos^2 \theta = 0$, $\theta = 90^\circ$. This stress state also applies to that for a (seamless) thin-walled tube subjected to internal pressure loading: here, the hoop stress is twice the longitudinal stress and the analysis suggests that a neck would form normal to the hoop (circumferential) stress. Johnson and Mellor (1973: their fig. 10.12) give the maximum principal strain at instability as functions of n and B , Eq. 18.8. The location of the neck around the circumference in homogeneous material is not definable, but, in practice, there will be some local concentration of inclusions that gives a bias to

the location. In a longitudinally welded tube, the localisation is most probably associated with the weld/heat-affected zone (HAZ).

For $\sigma_2 > 0.5\sigma_1$, the solution to Eq. 18.10 is mathematically indeterminate, since $\cos^2\theta$ is negative. In equi-biaxial tension, it is clear that it would be difficult to define any unique in-plane direction for zero extension, but it is something of a curiosity that definition is not possible over quite a wide range of biaxiality. The indeterminacy is resolved in real material by the presence of small spatial fluctuations: in grain-size distribution (although the grain-size dependence of yield strength in aluminium alloys is weak), in 'meso-scale' crystallographic texture (which gives a bias to the operation of specific slip systems) or in non-metallic inclusion content (producing a local 'soft spot' that might promote the formation of a neck). The treatment of 'diffuse necking' (in the $0.5\sigma_1 < \sigma_2 < \sigma_1$ region) relies on the initial presence of a 'perturbation', which is most commonly identified with a somewhat porous region, resulting from the formation of an array of voids around non-metallic inclusions. Extensions of the Marciniak theory to develop forming-limit diagrams are given in Sowerby and Duncan (1971).

Inclusion control is a factor of major importance in sheet metal deformation, and the issues are highlighted in the production of drinks cans (A consumption in the USA of 10^{11} cans per annum has been quoted.). There are two conflicting requirements. The body of the can must be able to be deep-drawn to an appropriate height/diameter ratio, with very thin walls. This necessitates the use of ultra-clean material. The second requirement is to ensure that the contents are readily, and reliably, available to the consumer. This requires a lid to the can that can be opened by means of a 'ring-pull' or similar device. The 'ripping-open' of such a 'ring-pull' is a (Mode III, 'anti-plane strain') fracture (see Section 18.5), which is facilitated by the presence of inclusions to concentrate fracture in the grooves provided in the can-top. High values of n are preferred for the can body, but are not required for the fracture process. One consequence is that, although the all-aluminium can is re-cyclable, it cannot be fully re-cycled for deep-drawing grades because the lid is not of the cleanliness required.

Another common experience of the fracture of pure aluminium is the tearing of pieces of kitchen foil from a roll. A carefully made strip specimen of such foil subjected to uni-axial tension will, in theory, neck and fail along a slip-band inclined at $54^\circ 44'$ to the tensile axis: see above. In practice, it may be necessary to provide some form of anti-buckling device and/or precise in-plane alignment of the gripping system to guard against twisting out of plane and, as for the 'ring-pull' fracture, fail under the influence of a Mode III component of the applied stress. This mode of separation will be treated in more detail in Section 18.5. In tearing kitchen foil, the movement of one's hands: first, causes a small edge-crack to form by concentrating (Mode III) strain at the edge of the foil; second, propagates the (Mode III) crack, which, at greater length, becomes unstable. Note that a relatively straight, stable separation may be obtained by tearing slowly, with

one half clamped by, e.g., a straight edge. More commonly, a serrated edge is used. This produces a sequence of short Mode III fractures: the serrations act as a slightly more macroscopic version of the inclusions in the ‘ring-pull’.

18.4 Fracture in aluminium alloy castings

In the Introduction, reference was made to the various forms of defects that may exist in cast aluminium alloys, and the effects that these may have on tensile properties and resistance to fracture. The present section describes these in more detail, and demonstrates how a model-based analysis of the UTS may be used to illustrate the significance of such defects. From Eq. 18.5, the criterion for necking is given by $\epsilon_T = n$. By substitution into Eq. 18.4 this gives the true stress at the UTS as Kn^n and the nominal stress ($\sigma_{\text{nom}} = \sigma_T (A/A_0)$), where A is the area at the UTS and A_0 is the original area as:

$$\sigma_{\text{nom}} = Kn^n / (\exp n) \quad [18.13]$$

The UTS is, of course, the nominal stress at the load maximum and what is demonstrated by Eq. 18.13 is that its value is determined entirely by the parameters K and n in Eq. 18.4. The relationship between true stress and true strain is regarded as inherently fixed for uniform, homogeneous material and the parameters K and n are likely to show minimal variability in experimental measurements made on different samples of pure material of constant grain size and identically annealed or cold-worked condition. Similar minimal variability would be expected for the parameters, C , B and n in Eq. 18.8. The prediction of the model is therefore that the UTS is a single-valued parameter.

It is useful to represent any distribution graphically and two forms of presentation may be used. One is the probability density function (PDF) which shows the histogram of the number of occurrences of a particular value as ordinate, plotted versus the range of values on the abscissa. The histogram is fitted to a smooth curve, which may further be given an algebraic form. For a single-valued parameter, the PDF becomes a single ‘spike’ (a delta function) located, for the example given above, at the value of the UTS. A second form is the cumulative distribution function (CDF) which is the integral of the PDF, representing the number of occurrences of the range of values up to a point of interest: it is usually scaled as a fraction or percentage of the total number of values. For the case of the single-valued parameter, the CDF is a step function, having a value of zero up to the (single-valued) UTS, and unity (or 100%) above the UTS. In any set of experimental results, however, there will be some degree of experimental error. Here, these are treated as small and randomly distributed about the mean i.e. as unbiased. The cross-sectional area of the test-piece may not be quite uniform, so that some section may be slightly smaller than that at the original measurement point; there may be small variations in the values of K and n from test-piece to test-piece (depending on grain size variation, texture variation, inclusion

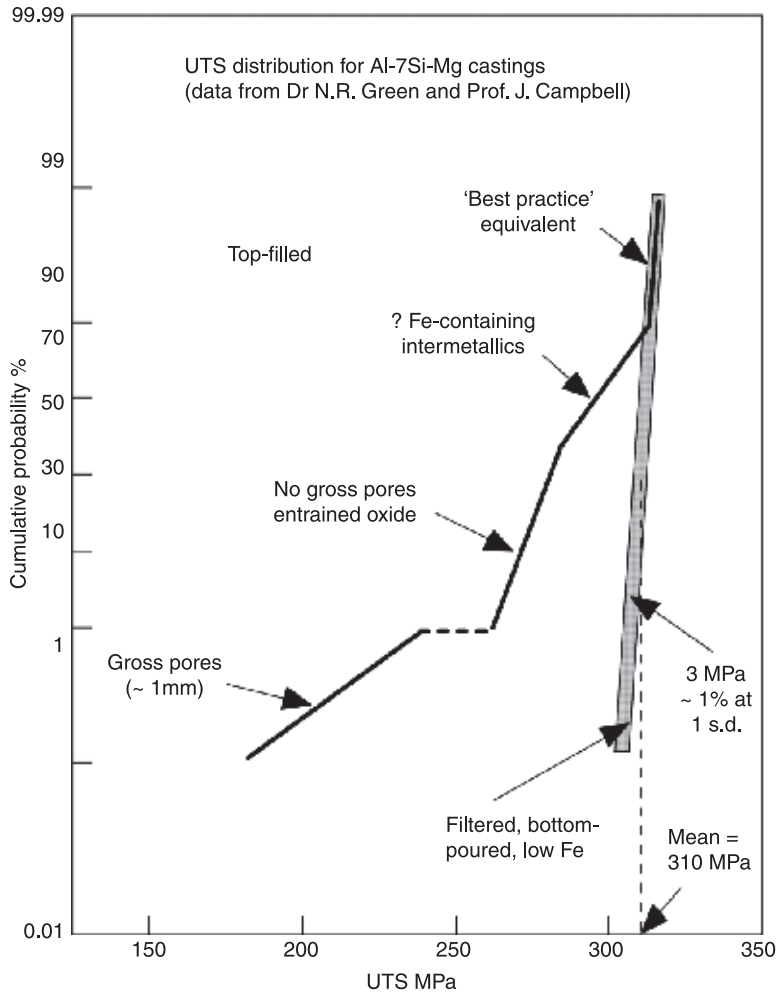
distribution etc.). The central limit theorem (see Sokolnikov and Redheffer 1966) shows that such random errors are distributed in a normal manner about the mean. For an inherently single-valued parameter, the PDF becomes a Gaussian (normal) function (with a standard deviation, SD, reflecting the degree of variation in random variables) and the CDF becomes the error function erf , which is the area under the Gaussian, but scaled by a factor of $2/\pi^{0.5}$ to provide a value of unity for the total range. It is convenient to represent the CDF on normal probability paper, which has its ordinate scaled about 50% (or 0.5) in a manner such that the error function plots as a straight line: ± 1 SD corresponds to frequencies of 16% and 84%.

The use of such a representation is illustrated by the analysis by Knott et al. (2000) of results obtained by Green and Campbell (1993) who measured the values of UTS in a standard aluminium casting alloy, LM 25 (7.5 Si 0.36 Mg), resulting from different casting procedures and different iron contents. Their 'best practice' set of castings is represented by material which contained low iron (0.1% rather than 0.37%) and which was filtered and bottom-poured, with a running and gating system designed to produce quiescent filling of the mould. Twenty-five specimens in this condition were tested to obtain values of the UTS. Green and Campbell plotted the results as a Weibull distribution, but, following the argument above, it is instructive to plot them on normal probability paper to test the prediction of the model for the UTS. Median ranking is employed, with the median rank of order m , F_m , derived from the close approximation: see Bompas-Smith (1973);

$$F_m = (m - 0.3)/(N + 0.4) \quad [18.14]$$

where N is the total number in the set e.g. $F_7 = 6.7/25.4 = 26.4\%$, $F_{13} = 12.7/25.4 = 50\%$. The result is shown in Fig. 18.5. The data are closely distributed about a mean of 310 MPa with a SD of approx. 3 MPa, i.e. 1% of the mean. Results obtained elsewhere for a similar LM 25 alloy with 0.1% iron gave a UTS of 315 MPa, consistent with the overall scatter. These findings support the basic prediction of the model that the UTS is a single-valued function, assuming that the SD of $\pm 1\%$ simply represents random experimental errors.

Figure 18.5. also shows the CDF corresponding to the UTS values for a high (0.37%) iron content alloy poured in a turbulent manner (45 samples). This CDF exhibits a much wider spread of values than that for 'best practice' material. The eye is guided to the differences between the predictions of the model and the experimental results, and this leads to a need to examine the reasons for the differences in behaviour. Following such examination, it is found that the CDF can be regarded as encompassing (three or four) different regions, depending on the nature, size and local volume fraction of different types of defect present in this second set of castings. First, consider the extremes. The bottom 10% of the distribution, having UTS values ranging from only 180 to 240 MPa, was found to contain gross pores, of diameter 1 mm or so. The top 12% had UTS values equal



18.5 Schematic analysis of variability in UTS for Al7Si castings. 'Best practice' castings exhibit a high UTS with small variation. The wide spread of values for other castings reflects the effects of (different types of) defects.

to those for 'best practice' material. A substantial proportion of the population (from 10% to 60%) showed a significant reduction in UTS (260–280 MPa) compared with 'best practice' (always greater than 300 MPa). Here, there were no gross pores, but entrained oxide films of substantial size ($>100\ \mu\text{m}$) were seen on the fracture surface. The final group would initially be classed as that proportion of the population (60–88%) for which the UTS varies from 280 MPa to approximately 310 MPa. The method of plotting tends, however, to mislead: if this proportion were to be plotted as a separate group, the points represented

between 75% and 88% would superpose on the 'best practice' line and only those in the 60%–75% range would lie clearly outside this line. Neither pores nor oxides were observed on the fracture surfaces for this group and it was deduced that those specimens exhibiting UTS values significantly lower than 300 MPa contained particularly large clusters of iron-containing intermetallics. It may be noted that a value obtained elsewhere for the UTS of a die-cast LM 25 alloy, containing 0.37% Fe, was 289 MPa, in agreement with these figures.

Even if the defected population is not so gross that it affects the UTS, defects can still have a strong effect on fatigue life. One particular study (Knott et al., 2000) related to the use of cast nodes in space-frame structures for 4×4 , lightweight, aluminium vehicles. The material studied was a standard, sodium modified, Tibor© grain-refined casting alloy (LM 25) of composition 7.5%Si 0.36%Mg 0.11%Fe. Both sand-cast (UTS 315 MPa) and die-cast conditions (UTS 289 MPa) were fatigued to failure, and the fatigue surfaces were examined fractographically to reveal the types of defect responsible for initiating the main fatigue crack. In as-cast, sand-cast material, the initiators were surface hollows (possibly associated with sand particles in the mould) of widths in the range 200–300 μm and depths in the range 70–100 μm . Although micro-cracks were initiated at other surface defects such as shrinkage pores or gas pores, such cracks did not propagate to failure: the surface hollows were dominant. In polished, sand-cast material, the initiation sites were found to be shrinkage cavities located at, or just below, the surface. These cavities could be 100–200 μm in size, but the dimension intersecting the surface was only some 20–50 μm . In die-cast material, fatigue cracks initiated from oxide films located at or near the surface. The films were usually tangled or folded. Micro-analysis using EDX indicated that the films were not simply aluminium oxide, but the spinel $\text{MgO} \cdot \text{Al}_2\text{O}_3$. Further details on film formation are given in Campbell (2006).

18.5 Fracture in high strength wrought alloys: fracture toughness

The inevitable consequence of developing higher strength in an alloy is that it will be subjected to higher stresses and strains in service. It will experience higher duty. What is important is that the material should be able to withstand the higher duty without failure: it should maintain its integrity. The focus in this section is on applications in engineering structural components and those of most interest are associated with the aerospace industry and other transportation systems, where fuel costs and technical performance rely heavily on weight saving. The incentive to increase loads and reduce cross-sectional areas to save weight is large, but there is a paramount need to ensure integrity, for safety reasons. The tightrope between economic efficiency and safety is one that the design engineer must walk with care. Engineering structures are designed to exhibit overall elastic response. Localised yielding may occur in the vicinity of stress-raisers such as cut-outs,

rivet-holes or bolt-holes, but this local yielding gives rise to work hardening or cyclic hardening, so that, after a few cycles, 'shakedown' occurs and further deformation is quasi-elastic.

Major stress-raisers can be allowed for in design e.g. by thickening a cross-section surrounding a cut-out or penetration. Ameliorative techniques can be applied to reduce the effect of high tensile stresses around holes, e.g. by the use of cold expansion to produce beneficial compressive stresses around bolt-holes or lugs. A more serious cause for concern is the presence of unexpected crack-like defects, which can produce very high stresses at their tips. Such defects can arise during material manufacture, as a result of abuse during assembly and fit-up during routine overhauls' casual scratching as parts slide against each other, or from exposure during service operation (e.g. sharp stones on a runway impacting on an undercarriage). The importance of such defects under monotonic loading can be assessed through the material's fracture toughness, K_{Ic} : see Knott (1973). Precise forms for stress intensity factor, K , vary with crack geometry, but, for a relatively small, surface-breaking, semi-elliptical crack, the simple expression:

$$K = \sigma_{app} (\pi a)^{0.5} \quad [18.15]$$

gives a reasonable, if slightly conservative, form to aid assessment. Here, the crack length is ' a ' and the applied stress is σ_{app} . In test-pieces, the form is more complicated, but the principle is to measure the value of σ_{app} , σ_F , at which the test-piece fails and thence to determine a critical value of K , K_{Ic} . In service application, the value of σ_{app} is the design stress in the region of the crack, and the known value of K_{Ic} is used to deduce the size of defect that is critical with respect to fast fracture. This then gives a specification for the non-destructive testing (NDT) procedures, to ensure that defects of a critical size are not present in the component. It might be noted that crack length scales with the square of σ_{app} . The consequence is that if no improvement in fracture toughness is made, an increase in 0.2% proof strength from just below 500 MPa to just above 700 MPa implies a decrease in defect size by a factor of two. (The design stress is a constant fraction of the yield stress.)

For the tougher alloys, it may not be possible to measure valid values of K_{Ic} in small test-pieces and recourse is then made to non-linear measures of fracture toughness: the crack-tip opening displacement (CTOD), δ , or the J-integral, J . The relationship between these parameters under conditions of small-scale yielding is as follows:

$$K^2 = E'J = ME'\sigma_Y d \quad [18.16]$$

where E' is Young's modulus in plane stress or $E/(1 - \nu^2)$ in plane strain (where ν is Poisson's ratio) and M is a factor, usually taken as two for elastic/plastic material, but varying with hardening exponent for power-law hardening material.

Knott (1992) gives a simple example of the use of fracture toughness as related to the integrity of materials for rocket-motor tubes. These are cylindrical tubes, of

diameter, d , sufficient to accommodate the propellant and length, l , dictated by ballistic and propulsive design. There is incentive to minimise the weight of the tube whilst ensuring that the launch fulfils its purpose, i.e. to maximise the pressure within the tube whilst simultaneously decreasing the weight. The pressure is limited by the need to prevent yielding in the tube wall, so that the material chosen must combine high yield strength and low density. To maximise the pressure/weight ratio, with d and l constant, the materials parameter that must be maximised is (σ_Y/ρ) , the specific strength (here, σ_Y = yield strength, ρ = density). Knott (1992) compared 7075 T651 ($\sigma_Y = 572$ MPa, $\rho = 2.86$ Mgm⁻³) and N707 spray-formed material (Al11Zn2.4Mg1Cu, $\sigma_Y = 705$ MPa, $\rho = 2.88$ Mgm⁻³) with G150 ($\sigma_Y = 2300$ MPa) and G125 ($\sigma_Y = 1900$ MPa) maraging steels, both having a density of 7.9 Mgm⁻³. Relative values of (σ_Y/ρ) for the four materials are 20, 24.5, 24 and 29, respectively, so that it appears that the best technical choice is to use G150 steel. It is, however, necessary also to consider material integrity, which, in this case, equates to the tube being able to remain intact during the launching thrust, rather than bursting as a result of fast crack propagation. Calculation of the critical defect size follows from Eq. 15 by substitution of a value of σ_{app} equal to $0.9\sigma_Y$ (a high design stress, for a simple aerospace component) and values of K_{Ic} for the materials and heat treatments. These were 39, 37, 67 and 33 MPam^{0.5}, leading to critical defect sizes of 1.8, 1.1 0.5 and 0.08 mm. The figures were used to assess: first, the ability of NDT techniques to detect flaws of the critical size; second, the possibility that abuse during handling might introduce flaws of concern. Recognition of the fact that current NDT techniques are not capable of giving highly reliable detection of defects of the size 0.08 mm applicable to G150 steel, added to the rather high likelihood of obtaining a random scratch of this size, led to the conclusion that, from an integrity point of view, it would be unwise to use G150 maraging steel for general rocket tube production. The choice in practice would more likely fall between G125, which has a critical defect size of 0.5 mm but a specific strength of 24, and 7075 with a critical defect size of 1.8 mm and a specific strength of 20. The N707 alloy would appear promising for this application because its specific strength, 24.5, is at least as good as that of G125 maraging steel and the critical defect size is twice as large. The spray process is also compatible with components of cylindrical symmetry: a possible process route might be deposition onto a cylindrical mandrel, followed by pressurised expansion to full tube dimensions.

The above example not only shows how fracture toughness may be used to assist material selection, but also introduces the concept of balancing two failure criteria: one based on plastic collapse of the cross-section; the other based on the onset of fast fracture. These two criteria are embodied in the failure assessment diagram (FAD) embedded in the 'R6' assessment procedure: see Knott and Withey (1993). The FAD has, as ordinate, the ratio $K_r = K_{app}/K_{Ic}$ and, as abscissa, the ratio $L_r = \text{applied load } (L_{app})/\text{collapse load } (L_{GY})$ based on yield strength. The failure locus, derived by elastic/plastic analysis, extends beyond $L_r = 1$, but

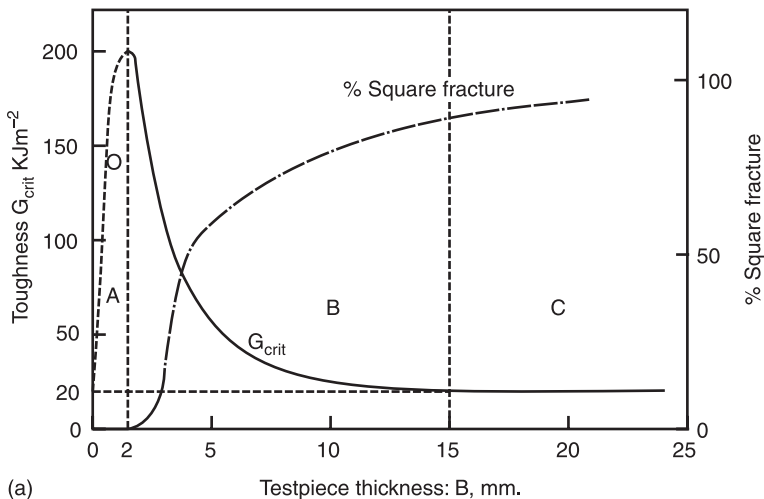
involves ‘cut-offs’ for specific types of steel: these vary with strain-hardening capacity. The FAD approach is widely used to assess steel structures, but is equally applicable, in principle, to structures fabricated in aluminium alloys. An earlier version of the FAD plotted the ratio K_r versus S_r = applied load/collapse load based on a flow stress equal to $(\sigma_Y + \text{UTS})/2$: here, the failure locus did not extend beyond $S_r = 1$. Knott (1989) examined the applicability of this earlier FAD to fracture toughness data obtained by Wiltshire and Knott (1981) for the aluminium alloy 7010, having a range of crack length/test-piece width (a/W) ratios, from the standard 0.45–0.55 down to 0.01. The lower (a/W) ratios correspond to higher fractions of the plastic collapse load, i.e. to higher values of S_r . The match between experimental failure points and the failure locus was encouragingly good, and there is interest in exploring how these and other data might be analysed in terms of the current FAD, and whether, for post-yield failures, it might be appropriate to include ‘cut-offs’ depending on strain-hardening characteristics. One potential application is the treatment of the failure criteria in those aluminium castings (see above) whose UTS values (260–280 MPa) fall well below the value for ‘best practice’ material (310 MPa, SD 3 MPa). A possible cause for this is the presence of oxide (bi-)films acting as cracks: such cracks are ~0.1 mm in size (~40% of the shortest crack tested by Wiltshire and Knott) and the fracture toughness of the matrix is low. Whereas a high volume fraction of pores, associated with even lower values of UTS, may reduce the cross-sectional area to an extent that the UTS is based simply on a smaller area, the films are present at much lower volume fraction and crack propagation is arguably a more likely cause. See Byczynski and Campbell (2002).

The underlying assumptions involved in Eq. 18.15 and Eq. 18.16 are that the stresses are in-plane: either plane stress, with $\sigma_{33} = 0$, or plane strain, with the through-thickness strain $\epsilon_{33} = 0$. The crack is assumed to run on a plane normal to the applied stress. Many aluminium applications, however, utilise thin sheet: cooking foil; aircraft fuselage; body panels in transportation vehicles. As for sheet-metal forming, the shear occurs in the X_1X_3 plane, although the presence of the loaded crack produces a plastic zone predominantly collinear with the crack length, rather than at $54^\circ 44'$ to the tensile axis (X_1). It is possible to derive a full form for the CTOD, δ , in plane stress when the crack is subjected to an applied stress σ_{app} :

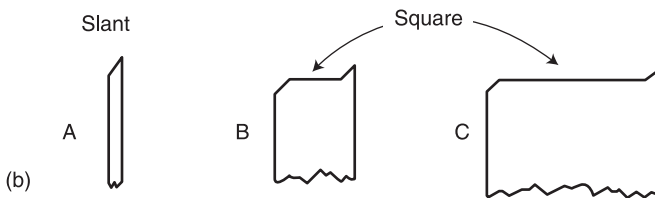
$$\delta = (8\sigma_Y a / \pi E) \ln \{ \sec(\pi \sigma_{\text{app}} / \sigma_Y) \} \quad [18.17]$$

This reduces to the relationship between K^2 and δ in Eq. 18.16 at low applied stress: see Knott and Withey (1993). In practice, however, unless anti-buckling guides are incorporated, it is often observed that a tensile stress applied to a thin sheet containing a crack induces local buckling, and the crack starts to advance by through-thickness sliding: a so-called ‘anti-plane strain’ mode (Mode III) of cracking. In an infinite body, the Mode III crack sliding displacement can be related to the applied shear stress through an equation of the form of Eq. 18.17

(with tensile values replaced by their shear equivalents). In the thin sheet, however, there is a limit to the shear displacement, given by $\sqrt{2}B$, where B is the sheet thickness (sliding-off at 45°). Once this displacement has been achieved, the crack propagates in a catastrophic manner. Knott (1973) re-analysed the effect of test-piece thickness, B , on fracture toughness values, pointing out that, for thin sheet, the value of 'plane stress' fracture toughness would increase in a linear manner with B , to a maximum, when the thickness was sufficient, in its centre, to develop sufficient hydrostatic stress to produce a small amount of 'square' fracture (see Fig. 18.6). Only if the test-piece were sufficiently thick would the onset of 'square' fracture (predominantly 'plane strain' at the required thickness) cause total instability. Intermediate thicknesses are of interest because many aluminium panels or plates may have thicknesses less than that required to produce a plane strain fracture. It is observed that the fracture may initiate in the 'square' mode, over, for example, 40% of the thickness, but that, as the applied load is increased and the plastic zone increases in size, there is more through-thickness stress



(a)

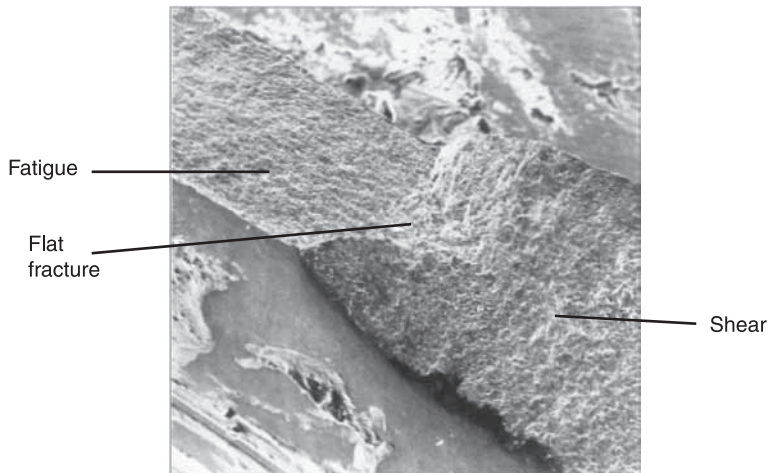


(b)

18.6 Variation of fracture toughness with test-piece thickness. In region C, 'plane strain' fracture toughness requirements are met. In region A, through-thickness sliding prevails. In region B, some square fracture is found in the early part of crack extension, but final failure is 'slant': through-thickness shear.

relaxation, and the 'square' fracture occupies progressively less of the thickness, to a vanishingly small fraction. Final failure then ensues by the 'sliding-off' shear mechanism (see Fig. 18.7). It is of interest (with reference to Withey [1997]) that the thickness of the fuselage of the *Comet* airliners (three of which crashed in the early 1950s) was only 0.71 mm (0.91 mm around the windows), so that it is likely that the final catastrophic fractures were of the 'sliding-off' type. A second factor is that the pressurised cabins of modern aircraft at high altitude can potentially behave in a manner similar to that of a pressurised tube: if a small crack is present, a tube can bulge and promote the through-thickness mode of fracture.

Cottrell (1963) referred to the 'sliding-off' as a 'cumulative' fracture, contrasted with a 'non-cumulative' plane strain crack extension, which he pictured as the progressive increase in crack length and CTOD being accommodated by (in-plane) plastic zones ahead of the crack, of ever-increasing size. His conclusion was that, in plane strain, the zones would completely traverse the un-cracked ligament before any cracking instability could occur. This argues against the possibility of obtaining a 'valid' plane strain fracture toughness value for a ductile fracture mechanism, yet this is what is observed for many high-strength aluminium alloys. The resolution of this paradox rests on the fact that Cottrell was considering



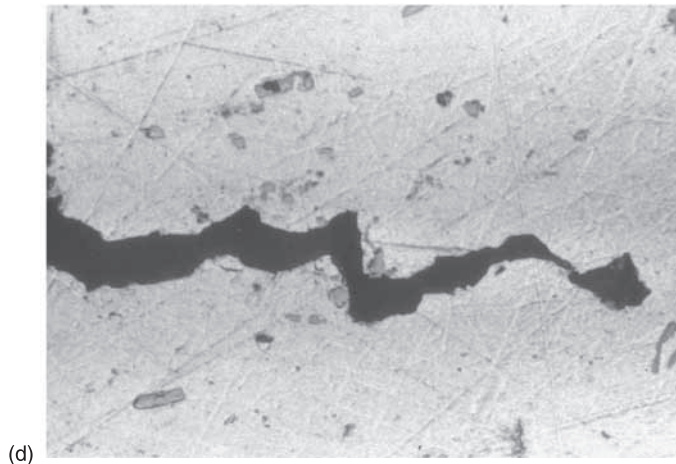
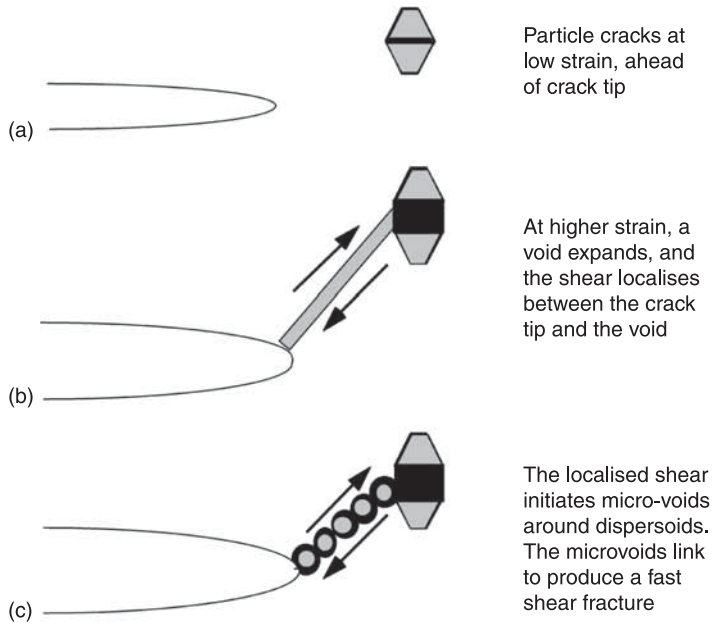
18.7 Example of crack extension in 2 mm thick aluminium alloy plate. The initial fatigue crack has a crack-tip front ~normal to the direction of growth, in the plane normal to the applied stress. The crack initially extends in the centre of the plate as a 'flat' fracture, but, as it grows, the surface plastic zones become larger, more through-thickness yielding occurs, and a smaller fraction of the through-thickness cross-section is able to maintain sufficient constraint to generate 'flat' ('square') fracture. The point of instability is reached when the plastic zones become sufficiently large to allow a through-thickness instability to occur (courtesy Dr G.G. Martin).

the material to be a homogeneous continuum, whereas, as described for tensile tests and again below, the alloys usually contain brittle intermetallics, which crack at low strain, so that the region ahead of a crack tip contains a distribution of voids, between which, shear is concentrated. In the next section, we examine the ways in which the micro-structural features influence fracture toughness.

18.6 The fracture toughness of aluminium alloys: micro-structural aspects

The fracture toughness of a high-strength aluminium alloy reflects a strain-controlled fracture process. The evidence for this is that the fracture path assumes a 'zig-zag' profile, following directions of maximum shear stress (rather than running normal to the maximum tensile stress), see Fig. 18.8; and that, in equiaxed (isotropic) material, the value of K_{Ic} *increases* slightly with decrease in temperature. If the crack-tip displacements at fracture do not vary with temperature, the critical value of J at fracture, $J_{Ic} = M\sigma_Y\delta_f$ (Eq. 18.16) *increases* with decrease in temperature because σ_Y increases: hence, K_{Ic} increases (Eq. 18.16). The general principles controlling fracture toughness in aluminium alloys have been treated by Garrett and Knott (1978) and by Chen and Knott (1981). Fracture behaviour is controlled by the volume fractions and character of second-phase particles in three scales of size range: (1) inclusions; (2) dispersoids; (3) aging precipitates.

1. Inclusions: The main inclusions in aluminium alloys detrimental to fracture toughness are those containing iron and silicon. A variety of inclusions of the form $Fe_xSi_yAl_z$ may be present. These are brittle intermetallics, of size $5\text{ }\mu\text{m}$ and above, and generally form in the melt. They often have angular form and, in the larger sizes, could be polycrystalline. As in tensile tests, they crack or de-cohere at low strain. In a test-piece containing a long pre-crack, this implies that the region around the crack tip rapidly develops into a distribution of voids, possessing free-surface properties and exerting image force attractions on dislocations emerging from the crack tip. (Essentially, the shear modulus in the direction of a void is reduced, so that it is easier for slip to continue along this path.) This causes flow to localise between the crack tip and the inclusion, producing an enhanced strain concentration that facilitates the initiation of fracture at other particles, such as dispersoids, lying in the shear band: see Fig. 18.8(a) and (b). This sequence of events, in which the 'un-cracked ligament' is that between the crack tip and a void, rather than the crack tip and the far boundary of the test-piece helps to resolve the 'Cottrell (1963) paradox' described in the previous section. Hunsicker (1976) has described the sequence of alloy development employed to produce 7xxx series alloys with improved fracture toughness. An important feature is to reduce the iron and silicon contents to less than 0.1% each (or 0.2% in total). These are still rather high levels for inclusion-forming impurities, and it is arguable that yet further



18.8 (a)–(d) Region around the tip of a crack in high-strength aluminium alloy. Note the formation of voids centred on intermetallics, and the linkage between these voids by 'fast shear' (courtesy Dr R.F. Smith).

improvements might be made by reducing iron and silicon contents to even lower levels. This is, of course, a costly venture and there is a technical reason for suspecting that there is a limit below which further improvements in K_{Ic} will not be obtained. The argument follows a model first proposed by Smith, Cook and Rau (1997), and used to consider the analogous case of sulphide

levels in high-strength steel. The effect of the inclusions is that they crack or de-cohere at low strain ahead of a crack tip and that this allows flow to localise, eventually to initiate voids around dispersoids, which link together in the shear band. If then, the inclusion spacing is such that fracture initiates around dispersoids before the plastic zone encompasses the nearest inclusions, any further increase in inclusion spacing (reduction in Fe and Si) will not provide any increase in toughness. The issue has been treated in some detail in Knott (1992).

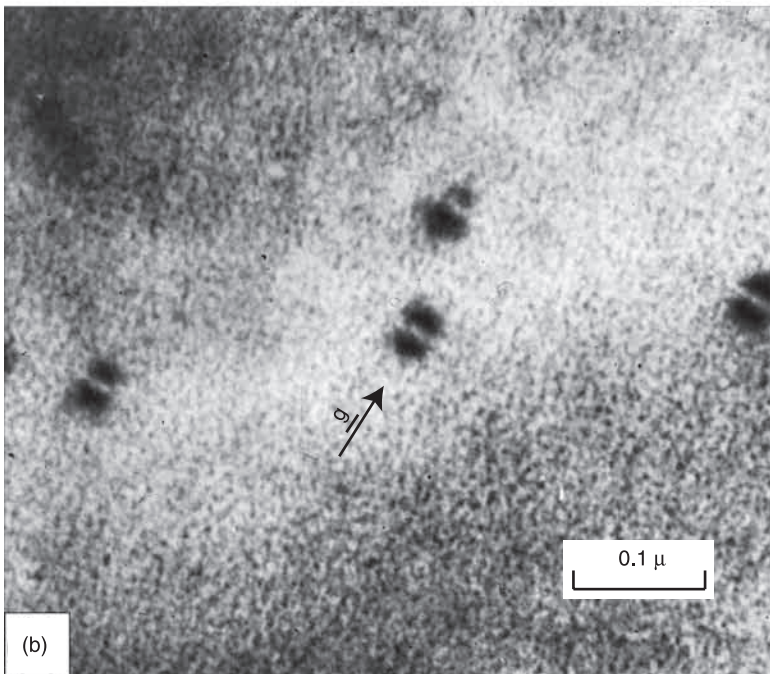
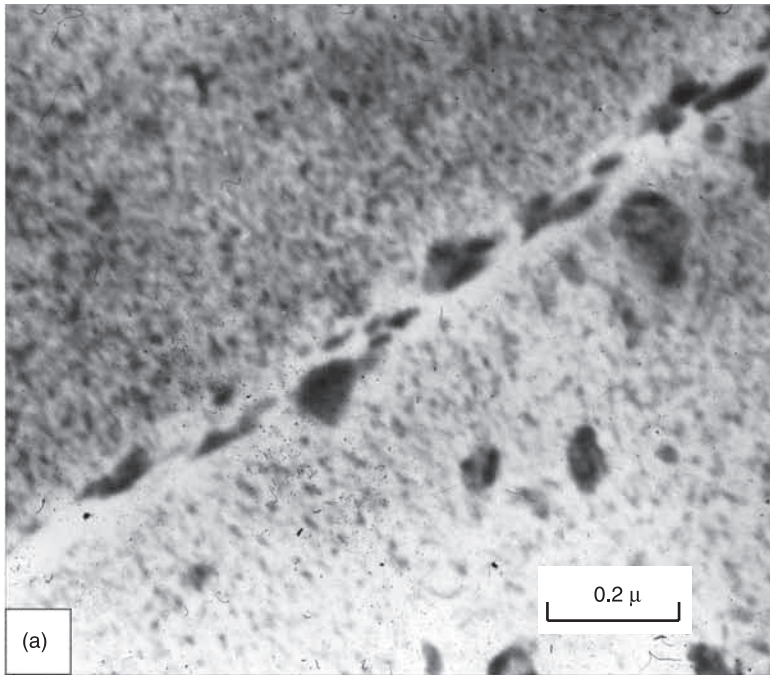
2. Dispersoids: The second type of particle, the dispersoid, is an intermetallic of size typically in the range 0.02–0.5 μm . Dispersoids may be produced deliberately to achieve grain-size control during solution treatment or may arise from the interaction of minor alloying additions or impurities in the solid state. Deliberate additions of Cr, to give grain refinement in 7475, produce E-phase dispersoid ($\text{Al}_{18}\text{Cr}_2\text{Mg}_3$) of typical linear dimension 0.07 μm in size (having an irregular shape): equivalent additions of Zr in 7010 produce ZrAl_3 spheres of <0.03 μm diameter. Examples are shown in Fig. 18.9. The crystal lattice of ZrAl_3 is tetragonal, with an ' a ' lattice parameter of 0.401 nm, close to that for pure aluminium (0.405 nm): the dispersoids are semi-coherent, with large elastic strain fields. The process of fracture occurs by the tangling of slip dislocations around the dispersoid particles and exerting stress until the particle cracks, the interface de-coheres, or the particle shears. Any of these mechanisms causes a marked decrease in the resistance to continuing shear and localisation occurs: further stress is then placed on the next dispersoid in the path of the slip band and in an increasing load test, this fails even more rapidly, so that fracture can become catastrophic. Note that it is necessary for crack- or void-like discontinuities to be present ahead of the crack to allow catastrophic fracture in plane strain. A simple shear mechanism in a continuum would proceed in a 'non-cumulative' manner and general yield (of the un-cracked ligament) would precede final instability. Following Ashby (1966), de-cohesion of a dispersoid/matrix interface will take place when a critical stress, σ_c , is obtained. This is given by:

$$\sigma_c = H\gamma_c d/2b\lambda \quad [18.18]$$

where H is a factor of proportionality having magnitude approximately $(Gb/2\pi)$, γ_c is a critical value of the average shear strain in the slip band, d is the dispersoid diameter, b is the Burgers' vector of the dislocations in the loops (or pile-up) and λ is the dispersoid spacing. Hence:

$$\gamma_c = 2b\sigma_c \lambda/Hd \quad [18.19]$$

It is possible to relate this critical shear strain to the critical CTOD for fracture initiation, δ_i , using a semi-empirical approach due to Hahn and Rosenfield (1975), who related the average strain at the crack tip to the CTOD *via* the



18.9 Dispersoids in 7xxx alloys: (a) E-phase in 7475; (b), ZrAl_3 in 7010. Note evidence of coherency strains in (b) (courtesy Prof C.Q. Chen).

‘width’ of the plastic zone $l_{(n)}$, the suffix denoting that l is a function of the strain-hardening exponent, n . Their expression is:

$$\delta_i = 2\gamma_c l_{(n)} \quad [18.20]$$

and $l_{(n)}$ is related to the hardening exponent, n , through an expression derived empirically from observations on silicon-iron alloys.

$$l_{(n)} \sim 0.0025n^2 \quad [18.21]$$

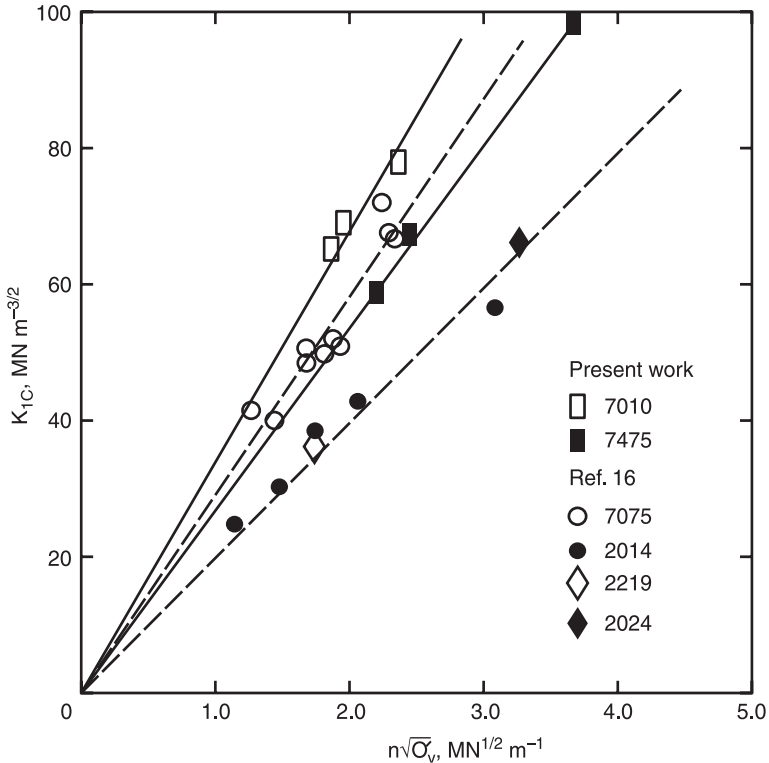
Rearrangement of the equations gives:

$$\delta_i = (b/10H) \sigma_c n^2 \lambda d^{-1} \quad [18.22]$$

and, from Eq. 18.16,

$$K_{Ic} = \{(Mb/10H)E\sigma_c\sigma_Y n^2 \lambda d^{-1}\}^{0.5} \quad [18.23]$$

In experiments made to demonstrate effects of matrix work hardening characteristics without any change in dispersoid distribution, graphs of δ_i versus n^2 or K_{Ic} versus $n\sqrt{\sigma_Y}$ give plausible straight lines (see Fig. 18.10). Differences in slope are obtained for different alloys and these can be attributed



18.10 Dependency of fracture toughness, K_{Ic} , on $n\sqrt{\sigma_Y}$ in high-strength aluminium alloys (courtesy Prof C.Q. Chen).

to different values of dispersoid size, d , and/or of interfacial fracture stress/work-of-fracture, γ_c . For example, 7010 has a higher slope than that for 7475 and this can be attributed to the smaller size and mismatch of ZrAl_3 compared with E-phase.

- 3 Aging precipitates: The aim of precipitation hardening is to increase the strength of an alloy, but the nature of the precipitates affects the distribution of slip and hence the ability to produce high stress concentrations at given levels of applied strain. The main features have been described by Garrett and Knott (1978) so that only a brief account will be given here. In UA conditions, the hardening mechanism is provided initially by elastic strain fields around coherent zones or semi-coherent intermediate precipitates. As the applied stress is increased, dislocations cut the hardening precipitates and work is needed to create new mismatch surface between the particle and the matrix. In Al-Li alloys, the δ' precipitate Al_3Li is ordered in the L1_2 structure. When this is cut by a single dislocation, it creates an anti-phase boundary across the particle. This is a high-energy configuration and it is energetically favourable to pass pairs of dislocations through the particle: the first, disordering the L1_2 lattice; the second, re-ordering it. Once a particle has been sheared, it is easier to pass subsequent dislocations along the same path, so that slip bands in the UA condition tend to be long and sharp. Uni-axial tensile specimens in the UA condition often fail by shearing across the cross-section at 45° to the applied tensile stress. The yield strength in the UA condition continues to rise with aging time because more precipitate comes out of solution and there is some transformation from zones to more stable intermediate precipitates. In the OA condition, all precipitate is out of solution, coherency is lost and particles coarsen by Ostwald ripening. For a fixed volume fraction, increase in particle size implies an increase in interparticle spacing and the yield strength drops because the Orowan bowing stress is inversely proportional to interparticle spacing. During the Orowan bypass process, dislocation loops are left tangled around the ageing precipitate, as shown in Fig. 18.3(d). The precipitate eventually de-coheres to produce a void under the action of the high local stresses. The slip in OA specimens tends to be much more uniformly dispersed than that in UA specimens and uni-axial test-pieces usually fail by a conventional cup-cone fracture. In OA Al-Li single crystals, however, there is evidence of shearing of δ' precipitates at large strains. The peak-aged (PA) condition simply represents the point at which all precipitates are out of solution and coarsening has not commenced. The slip still tends to be of a rather planar nature and uni-axial specimens often fail by shear.

These simple concepts are often modified in commercial alloys as a result of the presence of dispersoids and differences in heat-treatment procedures. A pre-age at temperatures of order 100°C is often given to grow GP zones close to the grain boundary to ensure higher strength when the alloy is aged above the GP solvus (alternatively, a boiling-water quench may be employed, but this may not generate

an ideal GP structure if the alloy is quench sensitive). Often, a slight over-age is given, to obtain dispersed slip because this gives better stress-corrosion resistance. It is also common to stretch material in its as-rolled or as-extruded form by a few percent plastic strain, to remove residual stresses induced by the working processes. The full range of effects of these stretching treatments has not been comprehensively catalogued, but they clearly introduce plastic strain into un-aged alloy and therefore influence the precipitate structure and subsequent slip distribution in the aged alloy. A somewhat related feature is the occurrence of 'quench bands'. If the quench is severe, anisotropy in the thermal expansion of adjacent grains in the polycrystalline mass can lead to mismatch strains which are relieved by dislocation movement in individual grains (often starting from grain boundary triple points) during the quench. On ageing, precipitation in these slip bands tends to have a different form (heterogeneously nucleated, higher temperature products) from that in the grains. Suggestions have been made that these are soft zones, able to serve as sites for fatigue crack initiation. Such bands modify the character of precipitates and slip structure.

The effects of slip character on fracture toughness are not always those that would be predicted. The work of Chen and Knott (1981) ranked 7010 and 7475 in the order UA (highest toughness), OA, PA, in alloys aged to give the same yield strength in UA and OA conditions, but Manaharan and Lewandowski (1990) found negligible difference between the toughness of a SiC particulate reinforced 7Zn2Cu2Mg0.12Zr alloy in the UA and OA conditions (at similar yield strengths). Attention here perhaps needs to be paid to the possibility of brittle fracture mechanisms occurring in the reinforcing particles (see below) *vis-à-vis* those in inclusions and/or dispersoids. Although the general fracture mechanisms in aluminium alloys are strain controlled, they are facilitated by the presence of cracks and voids ahead of the main crack tip and the formation of some of these could result from tensile-stress-controlled processes. It follows that the higher crack-tip stress levels associated with the PA condition could lead to easier cracking of brittle particles and hence a lower overall fracture toughness.

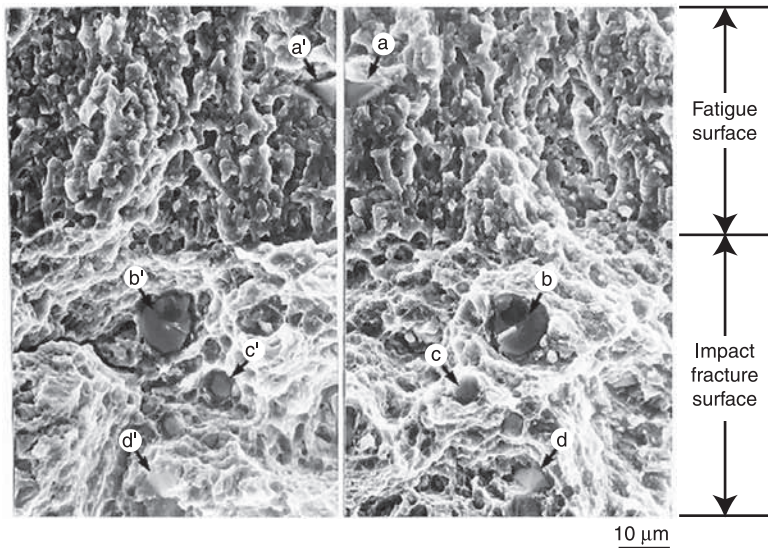
18.7 Fracture in aluminium particulate metal-matrix composites

There has been much interest in recent years with respect to the mechanical properties of aluminium-based MMCs in which the alloy is mixed with ceramic particles by processes such as squeeze-casting into a fibre-mat pre-form (e.g. Saffil alumina fibres), Cospray (SiC grit) or mechanical comminution and mixing (SiC grit). The Saffil fibre MMCs have found applications in automotive piston crowns and piston rings, for which wear resistance is the prime requirement, and stresses are generally compressive. Here, I concentrate on the SiC-containing particulate MMCs for which more general applications have been anticipated. The volume fraction (V_p) of SiC particles is usually in the range 10–20% and the

particle diameter may range from 3 to 20 μm . With such additions, it is possible to increase Young's modulus to approximately 90 GPa (in an Al-Li alloy) with no increase in density. The yield strength tends not to be quite as high as that obtained in the strongest monolithic alloys, but values of order 450 MPa can be obtained.

For such MMCs to be widely accepted for general engineering use, attention must be paid to their integrity under tensile loading if defects are present, and it is found that the plane strain fracture toughness values for MMCs are significantly lower than those of best monolithic alloys (a maximum value of 28 $\text{MPa m}^{0.5}$ has been quoted for an 8090 alloy containing 13% SiC). At a design stress of $0.8 \times 450 \text{ MPa} = 360 \text{ MPa}$, the maximum size of defect that could be tolerated would be $a = (1/\pi) (K_{Ic}/\sigma_Y)^2 = 2 \text{ mm}$. This value is small and places great emphasis on the ability to control, detect and size defects. The figure may be tolerable for components such as the rocket motor tube, but, if stiffness is not the limiting factor, the basic strength level of the MMC (450 MPa) does not make it viable from a stress/weight argument, when compared with competitive alloys. One area for which the MMCs may be of particular interest is that of space structures, as parts of communications satellites, space telescopes etc. Here, it is important to combine stiffness with low weight, but the structures are not necessarily highly stressed. A further advantage of MMCs over monolithic alloys (in addition to that of specific stiffness) is that their global thermal expansion coefficients are much reduced, so that overall thermal distortions, experienced as a part moves from a position experiencing direct solar radiation to one that receives no radiation, will be minimised. This does not, however, obviate the possibility of local expansion mismatches between matrix and particle giving rise to thermal fatigue. In more general applications such as aircraft spars or landing gear, crack extension by mechanical fatigue has also to be assessed.

The sequence of events leading to fracture ahead of a fatigue pre-crack tip in SiC particulate reinforced MMCs bears many similarities to that in monolithic alloys which contain high Fe and Si contents. The SiC particles behave rather like the Al/Fe/Si intermetallics and crack at low strains, allowing flow to localise between the pre-crack tip and the newly created crack or void ahead of the tip; see Lewandowski, Liu and Hunt (1989) and Kumai, King and Knott (1990). This localised flow then initiates micro-voids around dispersoid particles which link by shear or by the formation of an even finer set of voids around ageing particles. The volume fraction of SiC particles is very much larger than that of the intermetallics in tough, monolithic alloys and this is clearly important with respect to the fracture process and the low values of fracture toughness observed. As indicated in the previous section, there is evidence that the fracture of coarse SiC particles (and coarse intermetallics) might occur in response to the level of tensile stress ahead of the crack tip, even though the micro-void linkage depends on strain level. Evidence of such micro-cracking is shown in Fig. 18.11. The fracture toughness might be improved by reducing the size of SiC particles e.g. from 20 to 3 μm

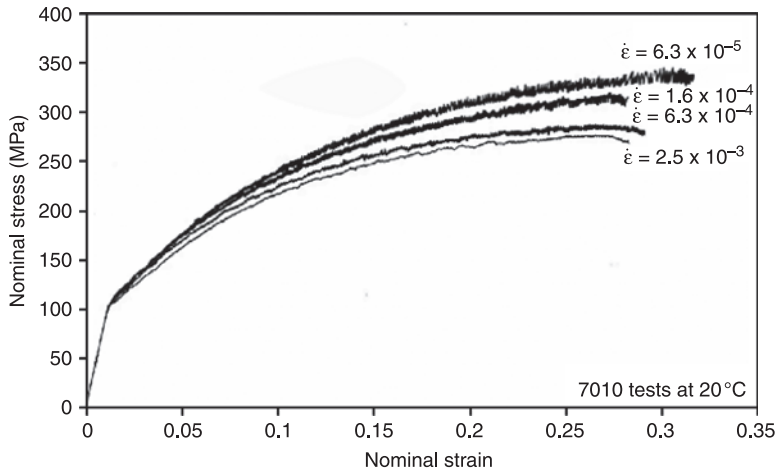


18.11 Fracture in SiC_p – reinforced particulate Al MMC; matching fracture faces. Note fracture of large SiC particle (b) ahead of pre-crack tip; fracture of smaller particle (c); possible de-cohesion of particle (d). Also, fracture of particle (a) as part of ‘fatigue’ crack growth (courtesy Prof S. Kumai).

diameter, but, unless the strain required to cause fracture is such that fracture in SiC occurs after void formation around dispersoids, there will still be detrimental effects on fracture toughness because the volume fraction is so large.

18.8 Effects of serrated yielding (dynamic strain-aging) on fracture

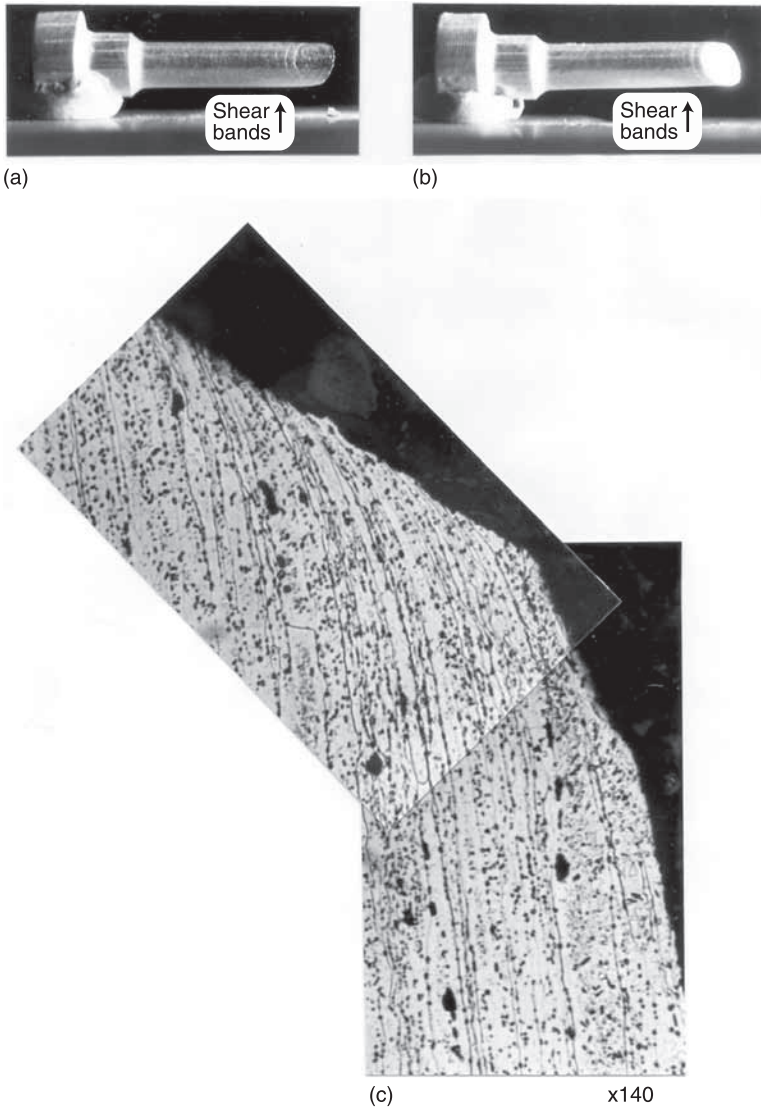
A final point of interest concerning slip character concerns flow localisation in alloys possessing ‘negative’ strain-rate sensitivity. If an alloy, such as 7010, is tested in the as-quenched condition at very low strain-rate it exhibits serrations in the stress-strain curve (see Fig. 18.12). The yield strength increases with decrease in strain-rate, up to a temperature of 100°C , but shows the usual slight increase with an increase in strain-rate at -196°C . These observations are attributed to the strain-ageing of dislocations, pinned by Mg atoms (King, You and Knott 1981). Flow is extremely localised and uni-axial tensile specimens fail by shear on a plane at 45° to the stress axes, almost ignoring microstructure, see Fig. 18.13 and Fig. 18.14. At -196°C , the fracture has more of the appearance of a ‘cup-cone’ fracture. A plausible explanation for these observations is that, if the strain-rate is sufficiently slow, the associated total plastic strain can be achieved by flow within a single slip band. The mobile dislocation density in this band is too high to be



18.12 Serrated yielding in Al-Zn-Mg alloy (courtesy Prof J.E. King, Dr C.P. You).

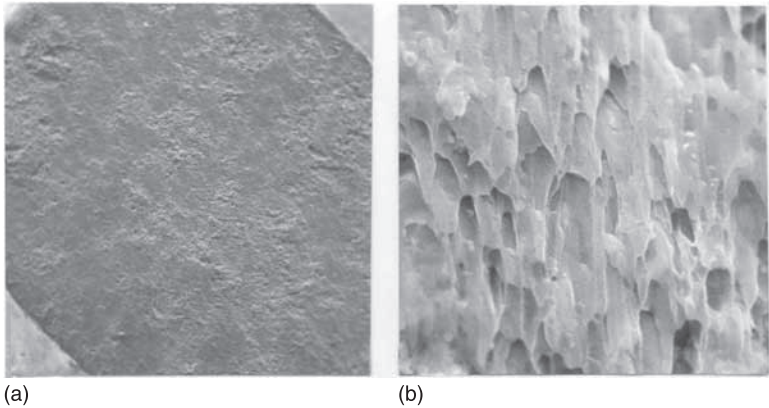
fully pinned by Mg atoms, but dislocations outside the band are strongly pinned and immobile. Any increase in strain-rate (and associated increase in applied stress) forces dislocations to move throughout the pinned grains, so that deformation does not remain localised. The effect is observed not only in tensile specimens, but also in notched specimens and at crack tips. The macroscopic slip-lines ahead of a circular notch assume the form of logarithmic spirals (at 45° to radial and circumferential principal stresses) and it can be seen that these are the paths followed by the shear cracks. In one example, voids have opened under the action of the hydrostatic stress below the notch, in the other (Lewandowski and Knott 1985), in the concentrated shears have opened up a quadrilateral cavity (Fig. 18.15). Complete shear localisation in a steep stress gradient is likely to be more prevalent for tests under strain control. Under load control, an initial crack could accelerate; the local crack-tip strain-rate would then increase and the localisation effect would disappear.

One application in which this localisation phenomenon has been observed is in the cold expansion of Al-Zn-Mg tube (Embury and LeRoy 1977): the geometry here was again of circular geometry and the cracks similarly followed logarithmic spirals. Another area in which it could potentially be of relevance is that of welded alloys. Alloys of composition 4–4.5%Zn–2%Mg have been widely used in welded constructions, such as military bridges and armoured vehicles: with the advent of friction-stir welding, there is substantial interest in welding aerospace alloys with higher Zn and Mg, such as 7xxx series alloys. Fusion welds generate residual stresses on cooling, and part of the HAZ ‘reverts’ during the welding process (i.e. precipitates in the HAZ region are taken into solution) and then cools rapidly. Some components may, as part of service duty, experience temperatures

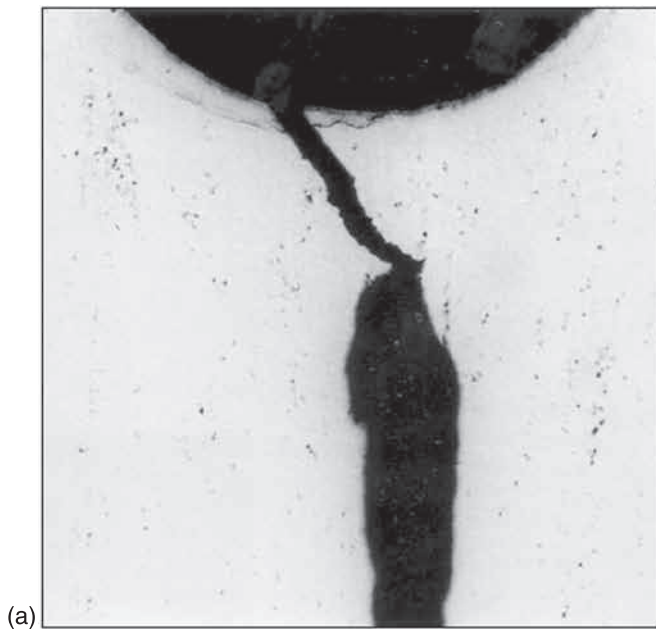


18.13 (a)–(c) Shear fracture in Al-Zn-Mg tensile specimens tested at low strain-rate (courtesy Prof J.E. King, Dr C.P. You).

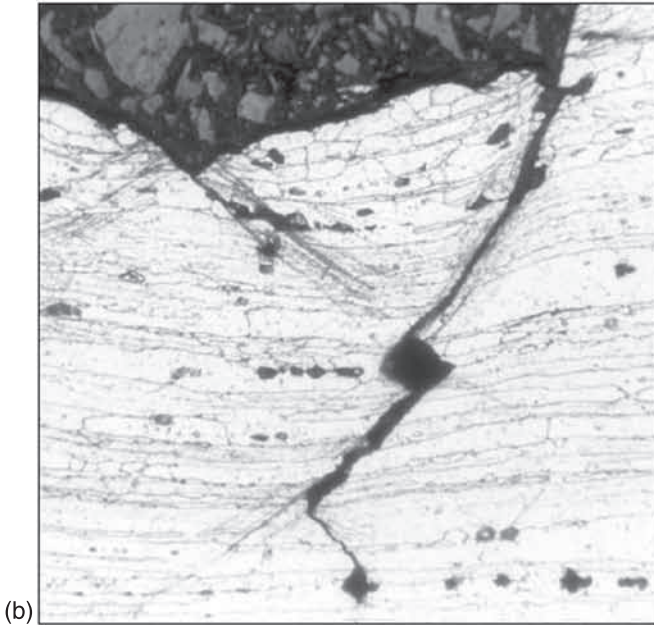
of order 50°C, e.g. on a landing strip or in deserts in hot countries. This may give rise to relaxation of residual stress (at a low strain-rate) so that the conditions leading to shear localisation could be present. It is also possible that the operating environment contains corrosive species, and slip-assisted stress corrosion is promoted by localisation of slip.



18.14 (a) and (b) Nature of fracture surface in tensile specimens. Note heavy shear, bearing almost no relationship to microstructure (courtesy Prof J.E. King, Dr C.P. You). a) $\times 225$ b) $\times 900$



18.15 Alternative behaviour in notched bars: (a) shear on logarithmic spiral plus opening of voids below notch; (b) localised shears generating quadrilateral voids (courtesy Dr R.F. Smith, Prof J.J. Lewandowski). $\times 175$



18.15 Continued.

18.9 Future trends: optimised properties versus 'fitness for purpose'

The sections above have illustrated a number of factors that influence the fracture resistance of aluminium and its alloys. The initial division was into failure in forming processes contrasted with failure in structural engineering components (with some qualification relating to extreme overload events). When the details of these various types of failures are explored, it becomes clear that similar materials properties can improve the resistance to fracture in both areas. Good sheet formability is achieved in alloys with high strain-hardening exponent, n , and low inclusion content. Good fracture toughness similarly requires a high value of n , combined with sufficiently widely dispersed inclusions, and, ideally, dispersoids with high interfacial work of fracture (or resistance to particle shear). The main difference between the two areas is the required (yield) strength level of the alloy. Many of the applications for formed sheet do not necessitate extremely high strengths and so use can be made of pure aluminium or solid-solution hardened alloys. Some extra strain hardening may be induced during the uniform strain component associated with the forming process: a good example of this is found in the walls of deep-drawn drinks cans. In solid solutions, the possibility of fracture around dispersoids or ageing particles does not arise, but the pinning and flow localisation effects associated with Mg-containing alloys need to be

recognised. It is important to differentiate between forming processes for which the limiting failure condition is limited by a plastic instability criterion and those (e.g. bending over a former) for which it is limited by material ductility (in the appropriate stress-state): these factors bear critically on the requirements for specifications on material cleanliness.

The structural alloys have been developed to meet structural engineers' design challenges: usually expressed as specific strength (σ_y/ρ), combined with specific stiffness (E/ρ), although specific stiffness is much the same for both steels and aluminium alloys. Aluminium does much better in bending, where the appropriate parameter is (E/ρ^2). The incentive, particularly for transportation systems, is to develop alloys with high yield strengths, which, for aluminium alloys, requires precipitation-hardening systems. In turn, the development of high strength through precipitation hardening implies a decrease in strain-hardening coefficient, n , and therefore some decrease in fracture toughness: Garrett and Knott, and Chen and Knott indicate that the fracture toughness, K_{Ic} , is proportional to $n\sqrt{\sigma_y}$, which allows an optimisation procedure to be followed. The further factors that affect fracture toughness are the inclusion content, and the density and cohesion of dispersoids.

The importance of control of Fe/Si inclusions was addressed comprehensively by Hunsicker (1976), leading to a recommendation that both Fe and Si should be restricted to 0.1% (combined {Fe + Si} 0.2% max.). In terms of chemical compositional limits on steels, these are not onerous restrictions (in modern line-pipe steels, e.g., both S and P are <0.005%), but, for the aluminium industry, achievement of such levels has significant cost implications. There is a clear difference in philosophy between the 1976 'purist' Hunsicker view and today's 'pragmatic' view that can be stated as 'What can we get away with – safely?' I do not challenge – indeed, I support – this second view because it is one that attempts to define the tightrope along which all responsible design engineers and their materials colleagues have to negotiate their path. I cannot properly address the question in detail in this chapter because the modes of failure of most concern involve initiation and sub-critical growth of cracks by fatigue and/or environmentally assisted cracking mechanisms (including internal embrittlement, e.g., caused by the diffusion of lead to grain boundaries). The present chapter is concerned simply with final fracture. The rocket motor-tube example in Section 18.5 gives a framework for posing, and answering, the question when only monotonic loading is involved, but this is not the general situation. It is, however, of crucial importance to address the question 'What is "fit for purpose"?' Money, effort, energy can be spent to seek perfection, but at enormous cost. The associated cost may be so great that the project is not pursued. This is not an optimum solution. What is important is to use Fracture Mechanics methodologies and other analysis to quantify what is 'fit for purpose' and to use our (quantified) understanding of failure mechanisms to produce alloys of specified resistance to fracture to meet the demands of any particular design and its associated service duty. In this context, there are, I believe, strong reasons for more widespread

adoption of newer forms of the FAD to address both the failure of high-strength aluminium alloys and the relevance of casting defects in Al/Si alloys. Throughout, however, there must be an accepted 'design life' to which the crack-growth and final failure criteria relate. In this respect, the issue of 'ageing (civil) aircraft', as an example, includes not only the design, material selection and 'lifing' calculations as related to the service duty associated with the original airline operator, but also to further duty that may be imposed by any subsequent purchase and operation of the aircraft. Details of this may prove difficult to establish.

As a final point, I return to the failure of thin, and moderately thick (up to, say, 6 mm thick), sheet, since many high-strength aluminium structural alloys are employed in this form. There are close analogies between the failure of sheet components containing quite long cracks ('plane stress' fracture toughness tests) and initially crack-free sheets that subsequently fail in sheet-forming processes. The localisation of flow ('shear fracture') in through-thickness shear is clearly identified in analyses of sheet-forming processes, but appears to be less well recognised in 'standard' Fracture Mechanics test procedures that concentrate on 'plane strain' criteria. The sequence of events in fracture toughness tests is by no means simple, because it involves: first, the development of the (plane stress) plastic zone on the side surfaces; second, the development of through-thickness shear; third, the role of formation of micro-voids on dispersoid or other second-phase particles and the effect that this may have on concentration of (through-thickness) shear. The overall problem needs to be addressed by a multi-disciplinary team, including finite-element modelling specialists, fracture mechanics specialists, and metallurgical specialists. It is a salutary reminder that the *Comet* fuselage was only 0.71 mm thick.

18.10 References

A good reference on fracture in metal forming is the paper by Embury and LeRoy (1977). The article by Campbell (2006) gives a comprehensive description of effects of entrained oxide films on mechanical behaviour. The papers by Garrett and Knott (1978) and Chen and Knott (1981) give the details of the relationship between microstructure and fracture toughness. The paper by King, You and Knott (1981) describes the localisation of flow leading to localised shear fracture and evidence for pinning of dislocations by Mg.

Ashby, M.F. (1966) 'Work hardening of dispersion-hardened crystals', *Phil Mag*, 14: 1157–1165.

Bompas-Smith, J.H. (1973) *Mechanical survival: The use of reliability data*, London, McGraw-Hill.

Byczynski, G.E. and Campbell, J. (2002) *The effects of oxide film defects on the strength and reliability of 319 alloy castings*. In: 2nd International Aluminium Casting Technology Symposium. ASM International, USA, pp. 65–74.

Campbell, J. (2006) 'Entrainment defects', *Mat Sci Tech*, 22: 127–145.

- Chen, C.Q. and Knott, J.F. (1981) 'Effects of dispersoid particles on toughness of high-strength aluminium alloys', *Metal Science*, 15: 357–364.
- Cottrell, A.H. (1963) 'Mechanisms of fracture', *Proc Roy Soc*, A276: 1–14.
- Embury, J.D. and LeRoy, G.H. (1977) 'Failure maps applied to metal deformation processes', 'Fracture '77', Proc. Fourth Intl. Conf. on Fracture ed. D.M.R. Taplin Pergamon/University of Waterloo press, 1, pp. 15–42.
- Garrett, G.G. and Knott, J.F. (1978) 'The influence of compositional and micro-structural variations on the mechanism of static fracture in aluminium alloys', *Met Trans*, 9A: 1187–1201.
- Green N.R. and Campbell J. (1993) 'Statistical distributions of fracture strengths of cast Al-7Si-Mg alloy' *Mat Sci Eng: A*, 173: 261–266.
- Hahn, G.T. and Rosenfield, A.R. (1975) 'Metallurgical Factors Affecting Fracture Toughness of Aluminium Alloys', *Met Trans*, 6A, 653–662.
- Hunsicker, H.Y. (1976) *The Contribution of Physical Metallurgy to Engineering Practice Rosenhain Centenary Conference*, The Royal Society, London, pp. 339–355.
- Johnson, W. and Mellor, P.B. (1973) *Engineering Plasticity*, London, Van Nostrand Reinhold Company,
- King, J.E., You, C.P. and Knott, J.F. (1981) 'Serrated yielding and the localised shear failure mode in aluminium alloys', *Acta Met*, 29: 1553–1565.
- Knott, J.F. (1973) *Fundamentals of fracture mechanics*, London, Butterworths.
- Knott, J.F. (1989) 'Effects of microstructure and stress state on ductile fracture in metallic alloys', *Proc. Seventh Intl. Conf. on Fracture, Houston, 1989*, 'Advances in Fracture Research', ed. K. Salama et al., Pergamon, 1, 125–138.
- Knott, J.F. (1992) 'Micro-Mechanistic Aspects of Crack Growth Resistance in Heat-Treatable Aluminium Alloys', *Proc. Third Intl. Conf. on Aluminium Alloys*, ed. L. Arnberg, O. Lohne, E. Nes and N. Ryum. Norwegian Institute of Tech and Sintef, 3, pp. 215–238.
- Knott, J.F., Bowen, P., Luo, J., Jiang, H. and Sun, H.L. (2000) 'The structural integrity of cast aluminium automotive components subjected to fatigue loads', *Mat Sci Forum*, 331–337: 1401–1412.
- Knott, J.F. and Withey, P.A. (1993) *Fracture mechanics – Worked examples*. Institute of Materials, London.
- Kumai, S., King, J.E. and Knott, J.F. (1990) 'Short and long fatigue crack growth in a SiC reinforced aluminium alloy', *Fat Fract Eng Matls Struct*, 13: 511–524.
- Lewandowski, J.J. and Knott, J.F. (1985) 'Microstructural effects on flow localization in 7000 series aluminium alloys', in *Proc. ICSMA 7 'Strength of Metals and Alloys'*, ed. H.J. McQueen et al., Pergamon, pp. 1305–1313.
- Lewandowski, J.J., Liu, D.S. and Hunt, W.H. (1989) 'Effects of matrix microstructure and particle distribution on fracture of an aluminium metal matrix composite', *Mat Sci Eng: A*, 107: 241–255.
- Liu, D.S. and Lewandowski, J.J. (1993) 'The effects of superimposed hydrostatic pressure on deformation and fracture: Part 1, Monolithic 6061 aluminium' *Met Trans*, A28: 601–608.
- Manoharan, M. and Lewandowski, J.J. (1990) 'Crack initiation and growth toughness of an aluminium metal-matrix composite', *Acta Met*, 38: 489–496.
- Puttick, K.E. (1959) 'Ductile fracture in metals', *Phil Mag*, 4: 964–969.
- Singh, S.N. and Flemings, M.C. (1969) 'Influence of ingot structure and processing on mechanical properties and fracture of a high strength wrought aluminium alloy', *Trans Met Soc AIME*, 245: 1811–1819.

- Smith, E., Cook, T.S. and Rau, C.A. (1977) 'Flow localisation and the fracture toughness of high strength materials', *Fracture 1977, Proc. 4th Intl. Conf. on Fracture*, ed. D.M.R. Taplin, Pergamon/University of Waterloo Press, pp. 215–223.
- Sokolnikov, I.S. and Redheffer, R.M. (1966) *Mathematics of Physics and Modern Engineering*, 2nd ed., New York, McGraw-Hill Book Company, pp. 642–645.
- Sowerby, D. and Duncan, J.L. (1971) 'Failure in sheet metal in biaxial tension', *Int. J. Mech Sci* 13: 217–229.
- Wiltshire, B. and Knott, J.F. (1981) 'The fracture toughness of high-strength engineering alloys containing short cracks', *Proc. 5th Intl. Cong. on Fracture, 'Advances in Fracture Research'*, ed. D Francois et al., Pergamon, pp. 87–95.
- Withey, P.A. (1997) 'Fatigue failure of the De Haviland Comet I', *Eng Failure Anal*, 4: 147–154.

Corrosion and corrosion protection of aluminium

N. BIRBILIS and B. HINTON,
Monash University, Australia

Abstract: This chapter reviews the various forms of corrosion of aluminium and its alloys. It also considers corrosion protection strategies currently in use. The chapter includes a case study based on aerospace applications of aluminium. As well as including many of the principal forms of aluminium alloy corrosion, the case study discusses aspects of corrosion in service, very often associated with occluded and local micro-environments.

Key words: corrosion, stress corrosion cracking, corrosion fatigue, pitting, localised corrosion.

19.1 Introduction

From a corrosion perspective, aluminium has been a successful metal, finding applications ranging from household foil and beverage cans to essential construction material for aircraft and space vehicles. Transportation, largely aerospace applications, has provided the greatest stimulus for both alloy development and corrosion research that continues today (Polmear, 1995).

As covered in prior chapters, aluminium and its alloys offer a diverse range of desirable properties that can be matched closely to the demands of each application by the appropriate choice of composition, temper, fabrication and processing mode (Davies, 1999).

In the past half century, the major topics for corrosion research in relation to aluminium alloys have included localised corrosion of aluminium alloys containing magnesium, the stress corrosion cracking of alloys used in aerospace applications, galvanic corrosion of aluminium in atmospheric and automotive applications, corrosion inhibition and most recently the filiform corrosion of aluminium sheet. Some of the present aluminium corrosion challenges are the ramifications from the elimination of chromates as inhibitors in protection schemes, the tolerance of higher impurity levels due to the increased use of recycled metal, the integration of lithium into alloys while retaining corrosion resistance and the sensitisation of non-heat treatable aluminium-alloys.

This chapter will address the issues related to various forms of corrosion of aluminium and its alloys. Additionally, some attention will be given to corrosion protection strategies currently in use. In an approach unique to this chapter compared to typical corrosion publications, this chapter will culminate in a case

study. The study will focus on an aerospace application, which includes many of the principal forms of aluminium alloy corrosion. Additionally, the aspects of corrosion in service, which is very often associated with occluded and local micro-environments, are emphasised.

19.2 General, galvanic and pitting corrosion

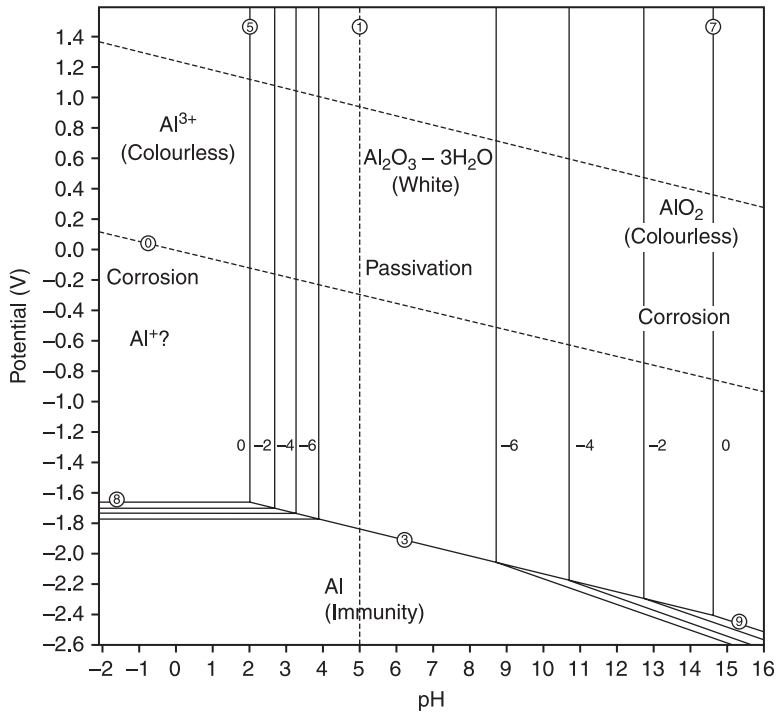
Thermodynamically, aluminium is a highly reactive metal with a high affinity for oxygen, as indicated from its position on the electromotive force series. The metal is however highly resistant to most atmospheres and chemicals. This resistance is due to the inert and protective character of the aluminium oxide film which forms on the metal surface and which rapidly reforms if damaged. In most environments, therefore, the rate of corrosion of aluminium decreases rapidly with time. The protective oxide film on aluminium attains a thickness of about 10 Å on freshly exposed metal in seconds. Oxide growth is modified by impurities and alloying additions and is accelerated by increasing temperature and humidity (or immersion in water). The protective oxide film inhibits corrosion because it is both resistant to dissolution and is a good insulator that restricts electrons produced by oxidation of the metal from participating in any cathodic reaction accompanying the oxidation reaction.

19.2.1 General corrosion

Corrosion of aluminium is an electrochemical process that involves the dissolution of metal atoms. It only occurs once the oxide film has been dissolved or damaged. Aluminium is amphoteric in nature, its oxide film being stable in neutral conditions, but soluble in acidic and alkaline environments. The thermodynamic stability of aluminium oxide films is expressed by the potential versus pH (Pourbaix) diagram (Fig. 19.1; Pourbaix, 1966).

This diagram indicates the theoretical conditions under which aluminium: (1) should corrode (forming Al^{3+} at low pH values and AlO_2^- at high pH values), (2) becomes passive due to the presence of a hydrargillite film, i.e. $\text{Al}_2\text{O}_3 \cdot 3\text{H}_2\text{O}$ (at near-neutral pH values) and (3) is immune to corrosion (at very negative potentials). The nature of the oxide varies according to temperature, and above about 75°C boehmite ($\text{Al}_2\text{O}_3 \cdot \text{H}_2\text{O}$) is the stable form. It should be noted that the potential-pH diagram does not indicate one of the most important properties of aluminium, i.e. its ability to become passive in strongly acid solutions of high redox potential such as concentrated nitric acid.

Given that corrosion is an electrochemical process, the corrosion potentials which develop at the surface of different aluminium alloys are of considerable importance. Also, the difference between the potential of aluminium alloys and other metals is important, as is the relationship between the potential of microstructural constituents of a single alloy. As a general rule, dissolution occurs



19.1 Pourbaix diagram for pure aluminium.

in strongly acid or strongly alkaline solutions (as per the Pourbaix diagram). Even where corrosion may occur, aluminium may be preferred to other metals because its corrosion products are less obvious than, say, typical ferrous ‘rust’.

19.2.2 Bimetallic or galvanic corrosion

Aluminium is anodic to many other metals and when coupled in an electrolyte, the resultant potential difference causes a current to flow and considerable corrosion can result. Corrosion is most severe when the resistance of the electrolyte is low, e.g. seawater. In some cases surface moisture films resulting from aggressive atmospheres can give rise to galvanic corrosion. In practice, copper, brasses and bronzes in marine conditions cause the most galvanic corrosion problems. The corrosion potentials for a range of non-heat treatable (wrought), heat treatable (wrought) and cast aluminium alloys, together with standard corrosion potentials for some other metals based on measurements made according to ASTM G69-97 (2009), are shown in Table 19.1.

Where noble metals contained in intermetallic particles are present in the microstructure of aluminium alloys, they may exhibit different behaviour to aluminium. The surface of copper is particularly efficient at supporting cathodic

Table 19.1 Comparison of measured corrosion potentials in 1M NaCl containing 9 ± 1 g/l H_2O_2

Material	Corrosion potential (V_{SCE})
Al (99.999)	-0.75
Cu (99.999)	+0.00
Fe	-0.55
Mg	-1.64
Zn	-0.99
1100	-0.74
2014-T6	-0.69
2024-T3	-0.60
3003	-0.74
5052	-0.76
5154	-0.77
6061-T4	-0.71
6061-T6	-0.74
6063	-0.74
7039-T6	-0.84
7055-T77	-0.75
7075-T6	-0.74
7075-T7	-0.75
7079-T6	-0.78
8090-T7	-0.75

reactions (e.g. water reduction). Limiting cathodic currents for oxygen reduction measured for pure copper are reported to be in the vicinity of 1.5 mA cm^{-2} , whereas limiting currents on pure aluminium are at least two orders of magnitude lower (Seegmiller et al., 2004). The successful utilisation of noble metals in close proximity to aluminium therefore requires careful design to avoid the potential to establish a micro-galvanic corrosion cell.

Given that the majority of other engineering metals display potentials that are considerably more noble than those of aluminium, bimetallic corrosion of aluminium is a frequent cause of service-related corrosion failure. The rate of such attack can be rapid and corrosion can be severe. Engineering solutions are generally simple and involve providing sufficient protection using combinations of paints and physical barriers to ensure that either electrical or electrolytic continuity is broken.

Contact with steel can accelerate attack on aluminium. Titanium may behave in a similar manner to steel. Stainless steel in contact with aluminium may increase attack on aluminium rather significantly in a moist environment. If passivated, the high electrical resistance of the surface oxide film on stainless steels minimises bimetallic effects in less aggressive environments. Passivation is an acid-based chemical treatment used on stainless steels to increase the thickness and protective capability of the naturally occurring passive film.

19.2.3 Crevice corrosion

If a crevice is formed between two aluminium surfaces, or between the surfaces of aluminium and a non-metallic material (i.e. a polymer) localised corrosion can and most often will occur within the crevice in the presence of electrolyte.

Crevice corrosion is due to the formation of a local cell action, since at the mouth of the crevice, the concentration of oxygen is higher than that within the crevice. The difference in oxygen concentration leads to a difference in local corrosion potentials leading to corrosion in the less noble area, which is the oxygen depleted zone within the crevice. Concomitantly, the oxygen-rich zone (i.e. the mouth) assumes the role of the cathode.

Crevice corrosion can be a very problematic form of corrosion in an engineering sense as the sites for crevice corrosion are often difficult to avoid in 'real' constructions which include welded lap joints, riveting, valve seats or even deposits that arise in service (Roberge, 1999). The general rules for the severity of crevice corrosion are presently under active research for several metal alloy systems, aluminium included (Chen et al., 2008). Typically, in aluminium, tighter crevices lead to more rapid initiation of attack (owing to less electrolyte and a steeper oxygen concentration profile being achieved more rapidly).

19.2.4 Pitting corrosion

Pitting is the most commonly encountered form of corrosion for aluminium alloys. In certain near-neutral aqueous solutions, a pit once initiated will continue to propagate into the metal due to acidification of the solution within the pit. The acidic conditions limit the formation of protective alumina films that usually prevent pit growth (Frankel, 1998).

Pitting arises when localised/aggressive environments break down the nominally passive and corrosion resistant film. Such an environment usually contains halide ions, of which chlorides are the most common. Solutions containing chlorides are very harmful and can create local corrosion potential gradients between the metal surface and occluded regions (i.e. within a pit) where the chloride is concentrated or accumulated.

Pits may form at scratches, mechanical defects, second phase particles or stochastic local discontinuities in the oxide film. The case of pitting arising from the interaction between the matrix and second phase particles is the most common cause of pit initiation, and will be described in detail below.

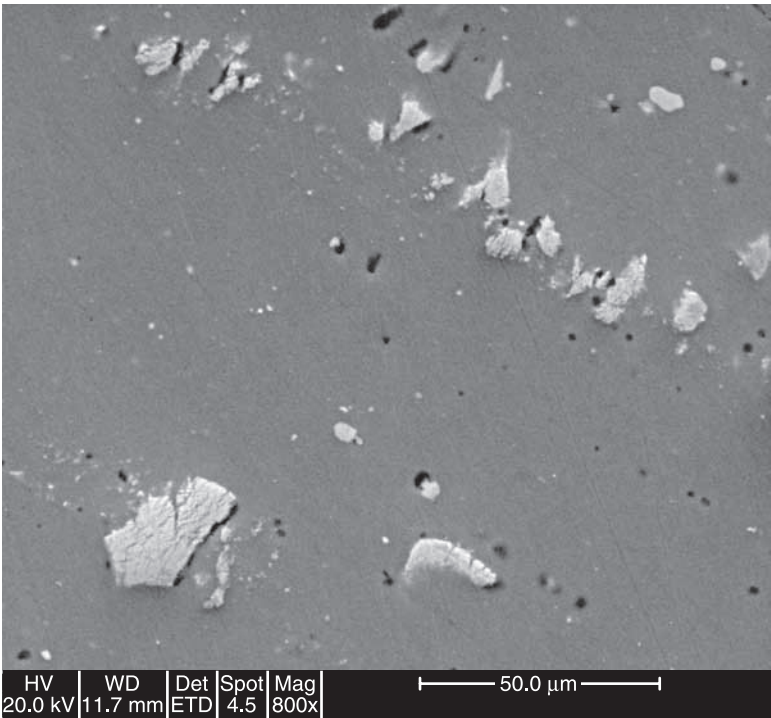
Pitting only occurs in the near neutral pH range since the oxide is unstable in a bulk sense under acidic or alkaline conditions (so by definition, pitting refers to a local loss of passivity). Chlorides facilitate the breakdown of the film by forming AlCl_3 , which is also usually present in the solution with the pits. When aluminium ions migrate away from pits, aluminium hydroxide species precipitate as a membrane, further isolating and intensifying local acidity, and sustained pitting of the metal

results. While the shape of pits can vary rather significantly depending on alloy type and environment, pit cavities are nominally hemispherical. This distinguishes pits as the localised corrosion initiation points from other forms of corrosion which include propagation modes (reliant on there being an initial pit) such as intergranular or exfoliation corrosion (described in the next section). Reviews of certain aspects of pitting corrosion were given recently by Szklarska-Smialowska (1999, 2005). Those reviews highlighted from a detailed mechanistic point of view, the processes (on the atomic level) which lead to break down of the film due to halide interaction were presently not understood in sufficient detail. However, different analytical techniques including Secondary Ion Mass Spectroscopy (SIMS), X-ray Photoelectron Spectroscopy (XPS) and autoradiography have revealed an adsorption of Cl^- upon passive films of aluminium.

The microstructures developed in aluminium alloys are complex and incorporate a combination of equilibrium and non-equilibrium phases. Typically, commercial alloys can have a chemical composition incorporating up to ten alloying additions. It is prudent, from a corrosion point of view, to understand the role that impurity elements have on microstructure. While not of major significance to alloy designers, impurity elements, such as iron, manganese and silicon, can form insoluble compounds. These constituent particles are comparatively large and irregularly shaped with characteristic dimensions ranging from one to approximately ten micrometres. These particles are formed during alloy solidification and are not appreciably dissolved during subsequent thermo-mechanical processing. Rolling and extrusion tend to breakup and align constituent particles within the alloy. Often constituents are found in colonies made up of several different intermetallic compound types. Because these particles are rich in alloying elements, their electrochemical behaviour is often significantly different to the surrounding matrix phase. In most alloys, pitting is associated with specific constituent particles present in the alloy (Buchheit, 1995). A range of alloying elements are found in constituent particles (typical example seen in Fig. 19.2), examples include Al_3Fe , Al_6Mn and $\text{Al}_7\text{Cu}_2\text{Fe}$.

Many studies over the past decade have been carried out in order to assess the effect of intermetallic particles on the corrosion susceptibility of specific aluminium alloys (Zamin, 1981; Mazurkiewicz and Piotrowski, 1983; Pryor and Fister, 1984; Nişancioğlu, 1990; Scully et al., 1993; Seri, 1994; Searles et al., 2001; Afseth et al., 2002; Birbilis and Buchheit, 2005). In the mid-1990s, Buchheit (1995) collected the corrosion potential values for intermetallic phases common to aluminium alloys mainly in chloride containing solutions. More recently the focus has been on the electrochemical properties of iron-containing intermetallics, and copper-containing intermetallics (Birbilis et al., 2006), and this has been expanded into a more comprehensive treatise covering a variety of common intermetallics present in commercial aluminium alloys (both wrought and cast) (Birbilis and Buchheit, 2005). An abridged summary of the results of these studies is shown in Table 19.2.

The identification and structural characterisation of intermetallic particles present in aluminium alloys has to date been quantified by particle extraction



19.2 General microstructure of AA2024-T3, revealing constituent particles (image courtesy Kevin Ralston).

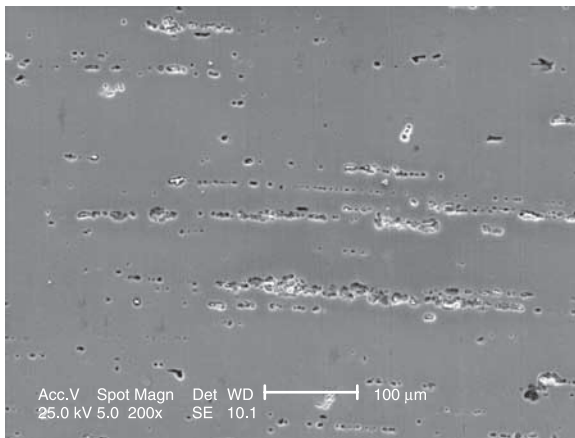
Table 19.2 Summary of corrosion potentials for intermetallic particles common to Al alloys

Phase	Corrosion potential (mV _{SCE}) in 0.1M NaCl
Al ₃ Fe	−539
Al ₂ Cu	−665
Al ₆ Mn	−779
Al ₃ Ti	−603
Al ₃₂ Zn ₄₉	−1004
Mg ₂ Al ₃	−1013
MgZn ₂	−1029
Mg ₂ Si	−1538
Al ₇ Cu ₂ Fe	−551
Al ₂ CuMg	−883
Al ₂₀ Cu ₂ Mn ₃	−565
Al ₁₂ Mn ₃ Si	−810
Al-2%Cu (solid solution)	−672
Al-4%Cu (solid solution)	−602

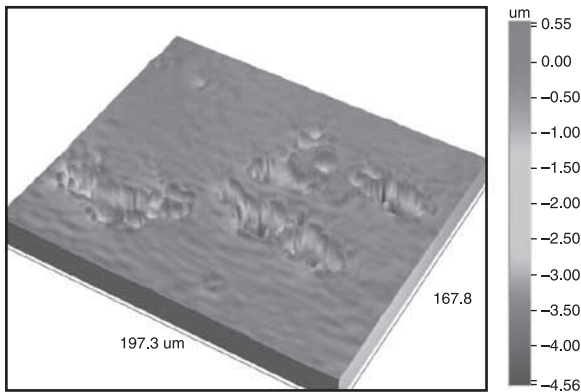
techniques combined with electron probe microanalysis, and by scanning and transmission electron microscopy combined with X-ray microanalysis. Most recently, Electron Backscatter Diffraction (EBSD) has been used.

Intermetallic particles in aluminium alloys may be either anodic or cathodic relative to the matrix. As a result, two main types of pit morphologies are typically observed. Circumferential pits appear as a ring around a more or less intact particle or particle colony, and the corrosion attack is mainly in the matrix phase. This type of morphology arises from localised galvanic attack of the more active matrix promoted by the more noble (cathodic) particle as is shown in Fig. 19.3, which also shows the phenomenon with an image collected via optical profilometry.

The second type of pit morphology is due to the selective dissolution of the constituent particle. Pits of this type are often deep and may have the remaining



(a)



(b)

19.3 (a) Scanning electron micrograph of early stage corrosion development upon AA7075-T651. (b) Optical profilometry image of AA7075-T651 which has suffered from pitting corrosion (images courtesy of Mary K. Cavanaugh).

remnants of the particle in them. This morphology has been interpreted as particle fallout, selective particle dissolution in the case of electrochemically active particles or, in the case of some copper-bearing particles, particle dealloying and non-faradaic liberation of the copper component.

Localised corrosion activity is however a complex phenomenon that is still under active research. Localised corrosion leads to local pH gradients as recently studied in detail by Ilevbare and Schneider (Ilevbare et al., 2004; Schneider et al., 2004). Cathodic sites of enhanced oxygen reduction generate hydroxyl ions promoting local pH increase, which can then modify the subsequent rate and morphology of corrosion propagation. The precise morphology of particle-induced pitting is important for emerging damage accumulation models. For these models to be predictive, it is necessary to develop a comprehensive, self-consistent accounting of this type of pitting. In cases where the electrochemical characteristics of constituent particles have been rigorously characterised, they have been found to have much more complicated behaviour than categorised by simple characterisations such as 'noble' or 'active'.

In addition to the principal modes of attack described above, other forms not dealt with in detail herein include: dealloying (Sieradzki, 1993; Newman and Sieradzki, 1994; Buchheit, 1997; Vukmirovic et al., 2002; Muster et al., 2008) and filiform corrosion (Coleman et al., 2007; McMurray et al., 2007; Schneider et al., 2007).

19.3 Localised corrosion: intergranular and exfoliation

Intergranular corrosion (IGC) is a phenomenon of which the precise mechanisms have been under debate for almost half a century (Hunter et al., 1963). Intergranular corrosion is a special form of microstructurally influenced corrosion, whereby the grain boundary 'region' of the alloy is electrochemically different to the bulk or adjacent alloy microstructure.

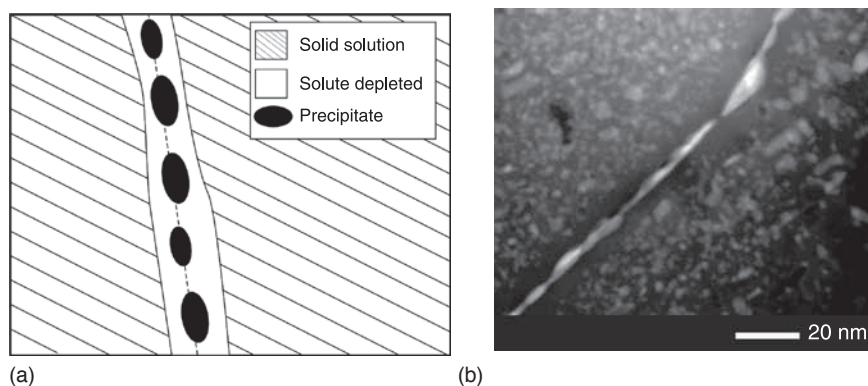
Corrosion activity may develop because of some heterogeneity in the grain boundary structure. In aluminium-copper alloys, precipitation of Al_2Cu particles at the grain boundaries leaves the adjacent solid solution anodic and more prone to corrosion. With aluminium-magnesium alloys the opposite situation occurs, since the precipitated phase Mg_2Al_3 is less noble than the solid solution. Serious intergranular attack in these two alloys may however be avoided, provided that correct manufacturing and heat treatment conditions are observed.

In the case of the aluminium-magnesium system, almost all commercial alloys are supersaturated as the magnesium solubility at ambient temperatures is less than 1 wt%. This effectively means that for alloys with more than 3 wt% magnesium elevated service temperatures can lead to grain boundary precipitation and sensitisation of grain boundaries to an intergranular corrosion susceptibility. The extent of this sensitisation may be approximately deduced from the continuity of Mg_2Al_3 precipitation at the boundaries. Apparently continuous boundaries correspond to high levels of sensitisation to intergranular corrosion.

The level of sensitisation to intergranular corrosion of 5xxx series alloys fabricated sheet, plate or extrusion can be easily determined by measurement of the Mass Loss after exposure to Nitric Acid (NAMLT Test) in accordance with ASTM G67–04. This is a 24 hours exposure to nitric acid and a measurement of weight loss due to intergranular corrosion and loss of grains. An NAMLT value of more than 30 g/cm² of surface is necessary before an alloy has become sensitised to intergranular corrosion or cracking. The test method used to evaluate susceptibility to intergranular corrosion depends on alloy type. For 2xxx and 7xxx series alloys ASTM G110–92 (2009) is most commonly used for assessing susceptibility to intergranular corrosion.

In the case of aluminium-zinc-copper alloys, where the precipitated phase is the very anodic MgZn₂ (η), intergranular corrosion occurs rather readily. Again, however, susceptibility to intergranular corrosion is strongly dependent on the heat treatment condition and its effect on grain boundary solute segregation, the morphology and composition of the grain boundary precipitate and the surrounding alloy matrix (Knight, 2003). The most resistant heat treatments are based on the use of over-ageing to the T7 temper or more complex heat treatments which involve retrogression and reageing to minimise the trade-off between alloy strength and intergranular corrosion resistance (Polmear, 1995; Davies, 1999). Grain boundary density also plays a role in the amount of IGC that occurs, with the short transverse direction more susceptible than the rolling or transverse direction in rolled/wrought products.

The images in Fig. 19.4 help rationalise the metallurgical origins of intergranular corrosion.

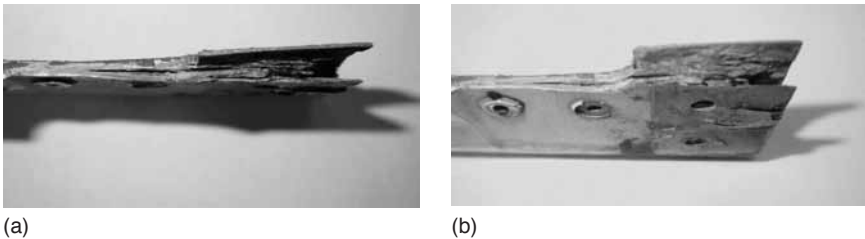


19.4 (a) Schematic of hypothetical grain boundary in an Al-X-Y alloy. This schematic indicates the different chemistry that exists in the grain interior, solute depleted zone (precipitate free zone) and grain boundary precipitates – giving rise to electrochemical heterogeneity localised at the grain boundary region. (b) Dark field STEM image of high angle grain boundary in AA7075-T651, revealing grain boundary precipitates (MgZn₂) and a distinguishable precipitate free zone.

Intergranular corrosion differs from pitting corrosion and while intergranular corrosion may initiate from a pit, it propagates more rapidly than pitting corrosion along susceptible intergranular pathways. Both may have a deleterious effect on fatigue crack initiation, and act as severe stress concentrators which may reduce the number of cycles to failure under cyclic loading. At this stage, a timely comment needs to be made regarding the role of micro-environments. While pitting corrosion can initiate in bulk neutral conditions, once pitting is stable and indeed once corrosion propagation proceeds by mechanisms such as intergranular corrosion (or other forms described below in this chapter), the local environment at the corroding metal is likely to significantly differ to the bulk electrolytic environment. Typically, electrolytes at pit bases or occluded regions (viz. in aircraft lap joints, etc.) can be either acidic or alkaline (under certain conditions), further promoting enhanced rates of localised attack.

Exfoliation corrosion (Davies, 1999; Zhao and Frankel, 2007) of aluminium alloys is the result of intergranular corrosion. It generally occurs where the alloy microstructure has been heavily deformed (i.e. by rolling) and the grain structure has been flattened and extended in the direction of working. Intergranular corrosion attack from transverse edges and pits then runs along grain boundaries parallel to the alloy.

Exfoliation is characterised by the lifting of layers of relatively uncorroded intragranular metal caused by the swelling of corrosion product in the layers of IGC. Exfoliation is observed on aircraft components around rivet or bolt holes where the end grain of the microstructure is exposed. Testing for exfoliation corrosion is carried out in accordance with any of several ASTM tests, including the acidified salt spray test ASTM G85-09, ASTM G66-99 (2005) (ASSET Test) and most commonly the EXCO immersion test ASTM G34-01 (2007). A typical example of exfoliation corrosion is seen in Fig. 19.5.



19.5 (a) and (b) Exfoliation corrosion on an AA2024-T4 aluminium alloy aircraft component. The exfoliation corrosion is a result of corrosion initiating at fastener holes (image courtesy of DSTO).

19.4 Environmentally assisted cracking

More generally, Environmentally Assisted Cracking (EAC) is a term that incorporates stress corrosion cracking (SCC), liquid metal embrittlement (LME), corrosion fatigue (CF) and hydrogen embrittlement (HE).

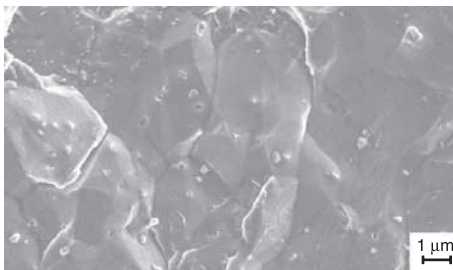
19.4.1 Stress corrosion cracking

SCC is a time dependent intergranular fracture mode (in aluminium alloys) that requires the combined presence of a susceptible alloy, a sustained tensile stress and a corrosive environment. The stresses may be (1) applied, as a result of components operation, (2) residual, from the heat treatment process (quenching) and cold working or (3) assemble as a result of joining.

The minimum tensile stress required to cause SCC in susceptible alloys is usually significantly less than the macroscopic yield stress (Scamans and Holroyd, 1986; Scamans et al., 1987). Susceptibility to SCC has restricted the use of aluminium alloys, particularly 7xxx series alloys, to specific applications. There are several theories postulated for the mechanism of SCC. The main theories are either corrosion dominated where cracking is due to preferential corrosion along the grain boundaries by anodic dissolution (i.e. analogous to intergranular corrosion) or hydrogen dominated where cracking along grain boundaries is enhanced by absorbed atomic hydrogen. The origin of this hydrogen is the result of intergranular corrosion itself (so generated by corrosion in acidified cracks) and it is considered that the presence of absorbed hydrogen weakens grain boundaries. Again, the corroding metal experiences an aggressive micro-environment that is unique and different from the bulk electrolytic environment, making SCC quite an insidious damage mode.

As SCC is a very important phenomenon for aluminium alloys, in order to do the topic justice, the reader is referred to specific monographs on the topic for a more detailed treatise of the SCC theories (Sedriks, 1990; Jones, 1992), along with the mechanical aspects of SCC. An example of a fracture surface showing the intergranular SCC fracture mode for a typical legacy aircraft alloy is shown in Fig. 19.6.

SCC development depends on both the duration and magnitude of applied tensile stress. Crack growth rate data as a function of the stress intensity are commonly used in the evaluation of SCC resistance for aluminium alloys (Jones, 1992). Such tests identify a minimum (threshold) stress intensity below which cracking will not occur.



19.6 High resolution SEM micrograph of a SCC fracture surface taken from an AA7079-T651 DCB specimen exposed to 75% relative humidity (specimen was from the T/6 position from 3-inch thick rolled plate) (image courtesy Steven P. Knight).

Low strength and relatively pure aluminium alloys are not susceptible to SCC. The alloys most prone to SCC are the 7xxx, 2xxx and higher strength 5xxx series alloys (i.e. those that have grain boundaries populated by precipitates). Stress corrosion cracking of 7xxx alloys occurs in water and water vapour in addition to chloride-containing electrolytes. Most other susceptible alloys fail only due to exposure to environments containing chloride ions.

Most service failures involving SCC have occurred in the short transverse direction (Summerson and Sprowls, 1986). The relative resistance of certain aluminium alloys to SCC is tabulated in Table 19.3 (adapted from Davies, 1999). An example of an in-service SCC failure is shown in Fig. 19.7.

19.4.2 Corrosion fatigue

Corrosion fatigue is the interaction of irreversible cyclic plastic deformation with localised corrosion activity. The combination of these mechanisms (combined mechanical and corrosion) and the transition from initiation to propagation is a matter under present research and of considerable technological importance. Corrosion pits have been routinely observed to nucleate crack growth in structures subject to fatigue loading (van der Walde et al., 2005). In fact, a recent paper reveals that in a fatigue study of aerospace alloy 7075-T6, all specimens in that study fractured from cracks associated with pitting (Jones and Hoepfner, 2005). Indeed, the numerous studies referenced within the work of Davies (1999) support the notion that pitting has a critical and detrimental effect on fatigue life. A fatigue crack can initiate from a corrosion pit or surface flaw when the flaw reaches a critical size at which the stress intensity factor is above a threshold for fatigue cracking or conversely when the rate of fatigue crack growth exceeds that of pit

Table 19.3 Qualitative SCC resistance of aluminium alloys (in the rolled plate form)

Alloy and temper	SCC resistance
2014-T3	Poor
2024-T3, T4	Poor
2024-T8	Good
2124-T851	Good
2219-T6, T8	Excellent
6061-T6	Excellent
7049-T73	Good
7 × 75-T6	Poor
7 × 75-T73	Excellent
7 × 75-T76	Intermediate
7079-T6	Poor

Source: Adapted from Davies (1999) (original source: US Air Force Research Laboratory, Wright Patterson Air Force Base, OH)



(a)



(b)



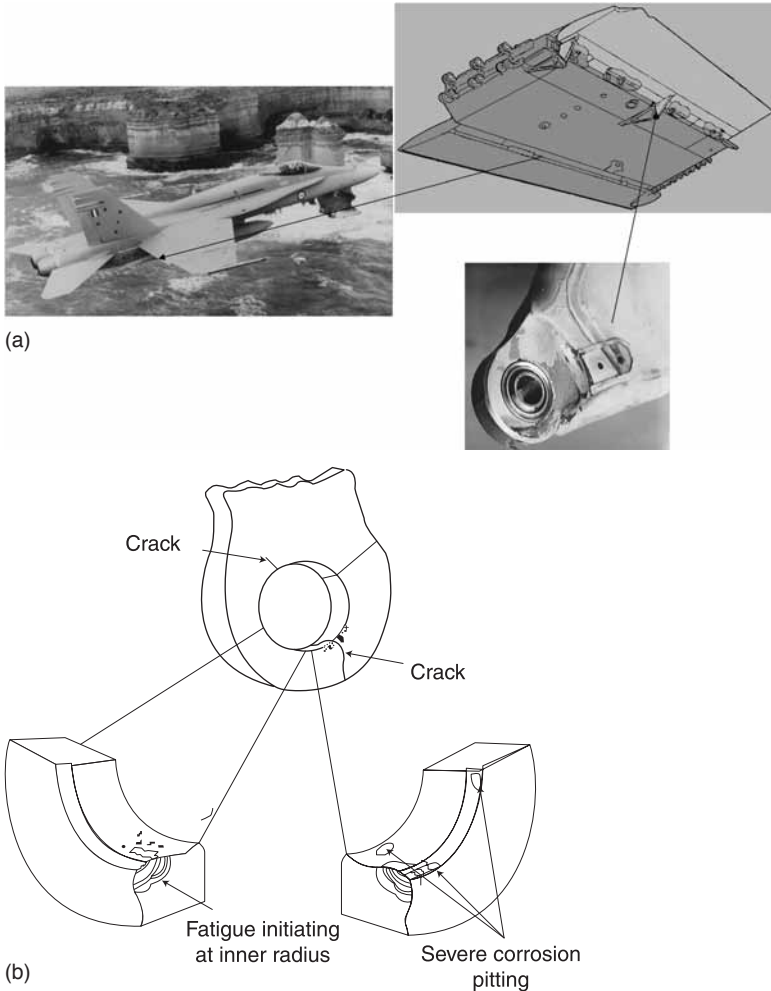
(c)

19.7 Stress corrosion cracking of a Boeing 707 aircraft flap track support bracket (a). Material was an AA7079-T6 alloy forging. Stress corrosion cracking occurred at the forging line (b). Crack growth marks on fracture resulting from cyclic service (c). Failure occurred as a result of susceptible material, combined with a corrosive environment and the presence of stress (residual and applied) (images courtesy DSTO).

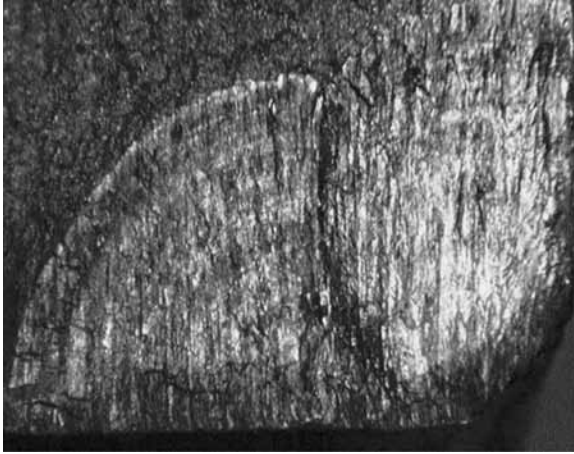
growth (Hoeppe, 1979; Kondo, 1989). Again, since CF is a phenomenon that involves a mechanical component (and not corrosion alone), a significant amount of work exists in the mechanical area, including dedicated monographs (Hertzberg, 1995; Suresh, 1998). CF phenomena are diverse and specific to the environment and particular application at hand, however, the variables which influence CF crack growth propagation are stress intensity, frequency of loading, stress ratio, alloy composition and microstructure (hence electrochemical potential) and the environment composition (and temperature). An example of in-service CF failure is shown in Fig. 19.8.

19.4.3 Hydrogen embrittlement

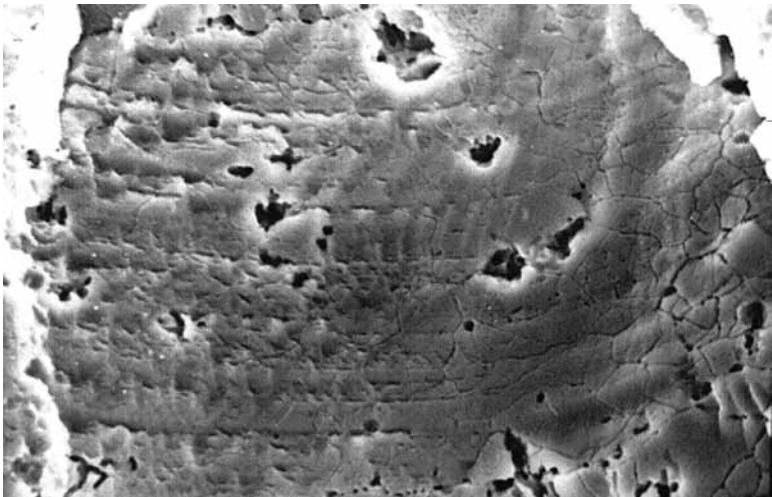
Hydrogen may readily dissolve in aluminium and all of its alloys, both in the molten state and during elevated temperatures close to the alloy melting temperature where the atmosphere may include water vapour or excessive hydrocarbons. Hydrogen from molten aluminium results in porosity in cast products but does not have an influence on corrosion performance or subsequent HE.



19.8 (a) Corrosion fatigue failure of F-18 aircraft wing trailing edge flap. (b) Location of fatigue cracking and region subsequently micro-sectioned for analysis. (c) Optical micrograph of characteristic corrosion fatigue fracture surface. (d) Higher magnification scanning electron micrograph showing the fatigue fracture surface and the corrosion damage on the fracture surface couple with brittle striations (Barter et al., 1994).



(c)



(d)

19.8 Continued.

Recent work, however, is beginning to show there is experimental evidence that hydrogen generated during corrosion can penetrate into grain boundaries and lead to embrittlement (Osaki et al., 2006; Thakur et al., 2007; Lynch et al., 2008). The mechanism by which hydrogen causes this embrittlement is difficult to study and is reported to act either by facilitating enhanced dislocation emission ahead of an advancing crack, or by bond weakening and enhanced plasticity ahead of an advancing crack.

Understanding HE is important in unravelling the mechanism and modes of this failure mode for aluminium alloys. However, so far, this has not been a factor

that has restricted the use of aluminium. No specific tests for assessing HE susceptibility of aluminium alloys currently exist.

19.4.4 Liquid metal embrittlement

LME is not commonly observed in aluminium alloys. It can be defined as a mode of attack that results in a complete loss of alloy ductility of a solid metal, well below the normal yield stress, as a result of the surface being wet by a liquid metal. LME induced fractures are generally intergranular in aluminium alloys. It is well known that gallium in contact with aluminium can result in disintegration of the aluminium (or aluminium alloy) into individual grains; placing serious restrictions on gallium usage and its presence in the vicinity of aircraft. In addition, mercury can also embrittle aluminium and its alloys. Aluminium has also been noted as being embrittled appreciably by indium, sodium, tin-zinc and lead-tin alloys.

19.5 Corrosion protection in the aircraft structure

The natural passive oxide on aluminium alloy aircraft components is insufficient to protect from corrosion in service. Therefore, a range of technologies and multilayered protection schemes are used to prevent degradation of these components in severe operational environments. This section describes the various layers that make up protection schemes commonly used on military aircraft.

A layer which may be used to form part of a protection scheme for aluminium alloys is metallic rather than non-metallic. As discussed in an earlier section, the presence of various microstructural phases in the surfaces of aluminium alloys can affect corrosion resistance. A simple but very effective way of overcoming this problem for components made from sheet is through the use of cladding, known as Alclad. This term was originally a trademark of the Alcoa Company, but is now used as a generic term to describe sheet produced by metallurgically bonding high-purity aluminium surface layers to high-strength aluminium alloy core material by hot rolling. The cladding thickness is typically between two per cent and ten per cent of the sheet thickness. The clad alloy for use on 2xxx series alloys is generally around 99.5% Al, while that for 7xxx series alloys is 99% Al with 1% Zn. Because of the absence of microstructural phases such as intermetallic particles in the clad alloy it has a higher corrosion resistance than the core alloy. Alclad sheet is commonly used by the aircraft industry for external surfaces such as fuselage skins.

The protection scheme used on aircraft generally consists of an inorganic coating which serves largely as a pre-treatment or surface preparation step, and an organic coating consisting of a primer paint and a finishing topcoat paint. The main purpose of the pre-treatment process is to provide some corrosion protection capability, and improved adhesion for the following paint coating.

The pre-treatment process is also important because it includes steps such as an alkaline clean, etching and deoxidising which are all designed to remove the existing oxide film from the aluminium alloy and any organic contaminants. Contamination may affect the adhesion of subsequent paint coatings. The two pre-treatment processes used in the aircraft industry are conversion coatings and anodising. Wernick et al. (2007) and Biestek and Weber (1976) provide detailed descriptions of the characteristics of these coatings and how they are produced.

Chromate conversion coatings have been widely used in the aircraft industry for over 80 years. They are produced by immersion, spraying or swabbing with an acid solution containing the salts of hexavalent chromium ions (chromates). The contact times vary depending on the application and the alloy, but can range up to several minutes. The process produces a film consisting largely of hydrated chromium oxide (Hughes et al., 1997). The film also retains some soluble hexavalent chromate ions. These ions are very powerful corrosion inhibitors. For aluminium alloys, they may inhibit both the cathodic reaction, typically oxygen reduction, and the anodic reaction (Frankel and McCreery, 2001). The chromium oxide film is around 0.5 μm thick, but may be up to 1 μm (Biestek and Weber, 1976). In the aircraft industry the coating thickness is generally quoted in weight as between 430 mg m^{-2} and 650 mg m^{-2} . This film is very adherent, and can provide protection for alloys such as 2xxx and 7xxx series for in excess of 168 hours in the very severe industry standard neutral salt spray test (NSS) (ASTM B117-09). For military applications, the corrosion protection and adhesion performance of chromate conversion coatings are covered by US Military Specification MIL-DTL-5541F (2006) and the properties and formulation are covered by MIL-DTL-81706B (2006).

Anodised coatings are produced by electrochemical polarisation in an electrolyte-containing chromic acid, phosphoric acid or sulphuric acid. Anodising produces a thick oxide film of up to 10 μm depending on the acid anodising bath (Biestek and Weber, 1976) (natural oxide films on aluminium are typically up to 0.05 nm). These films provide better corrosion protection than chromate conversion coatings; however, they can be more brittle. Because of this, conversion coatings or anodised coatings may be used on different parts of an aircraft structure depending on structural and loading considerations. The corrosion protection performance of anodised coatings may be improved by sealing in boiling water, or with solutions of nickel and cobalt salts (Biestek and Weber, 1976). Sealing has the effect of growing the walls of any pores in the oxide film, thus reducing any porosity (Biestek and Weber, 1976). Anodising processes and the properties of films formed are covered by US Military Specification MIL-A-8625F (2003).

Owing to environmental, health and safety concerns there is legislation in various parts of the world to limit and prevent the use of chromates due to their inherent toxicity, and carcinogenicity, and the fact that chromium being a heavy metal causes waste disposal problems. Many alternatives to chromate conversion coatings have been considered (Hinton, 1991), however, as yet most of these do not match the corrosion protection performance of chromate conversion coatings,

especially on corrosion prone alloys such as the 2xxx series and the 7xxx series alloys when subjected to the NSS test.

Concerns about chromates have led to the development of boric-sulphuric acid anodising as a replacement for chromic acid anodising, and this process is being used on some aircraft components (<http://www.boeing.com/companyoffices/doingbiz/environmental/chromic.html>).

Primer paint coatings for aluminium alloy are designed to provide improved adhesion of subsequent topcoats. They contain high levels of corrosion inhibiting pigment, in addition to their being a barrier which prevents access of moisture to the surface. The primer is the primary source of corrosion protection in the protective scheme. The primer most commonly used in aircraft structure is a two part epoxy polyamide. It consists of an epoxy resin binder and a polyamide resin hardener. Titanium dioxide is added for durability and opacity, and extenders such as silica are added to fill out the coating. The corrosion inhibition additive is strontium chromate, which provides the powerful hexavalent chromate inhibitor ions. These ions may leach from the coating particularly at points where the coating is damaged or cracked, and there provide protection.

The primer coating is typically 15–25 μm thick for a single dry coat. For military aircraft, primers must satisfy the requirements of US Military Specification MIL-PRF-2337J (2007). Generally, epoxy polyamide primers have been organic solvent based. However, environmental concerns are forcing the aircraft industry to look for coatings which have very low levels of volatile organic compounds (VOCs) or which use water as the solvent for the polymeric resin binder. US Military Specification MIL-PRF-85582D (2006) covers the properties of water-based primers.

For external aerodynamic surfaces on aircraft, such as fuselages, tails and wings, and in landing wheel bays a polyurethane topcoat is applied over the primer. This topcoat is a two part system consisting of an isocyanate resin and a hydrolated polyester hardener. The function of the topcoat is to protect the primer against ultraviolet radiation, to provide general chemical resistance and to be durable and flexible. Polyurethane topcoats are generally applied to a dry film thickness of around 50 μm . For military aircraft, polyurethane topcoats must satisfy the requirements of US Military Specification MIL-PRF-85285D (2009). Over time, topcoats may degrade due to weather exposure, temperature excursions from high-altitude flight, soil accumulation and stressing. This degradation leads to discolouration, chalking and cracking; the latter particularly in areas of structure where flexing can occur.

Another important part of the aircraft component protective scheme is the use of sealants. All paint coatings harden and crack eventually. The cracks allow moisture to penetrate through to the alloy substrate. As an added layer of protection sealants are used particularly in highly stressed regions such as joints and fastener holes. They are based on organic compounds, such as polysulphides and polythioesters, with properties such as excellent adhesion and high elasticity at

low temperatures. Because of these properties and the fact they are applied to thicknesses of around 200 μm , they provide an additional effective barrier to the ingress of moisture at joints and holes. In those locations they serve to prevent corrosion and to isolate dissimilar metals thus preventing galvanic corrosion. Sealants are applied to the mating surfaces of joints, and to fastener holes of components, and assembly takes place while the sealant is still curing. This approach allows excess sealant to be squeezed from the joints to provide a barrier to the ingress of moisture. This method of construction for corrosion protection is known as wet assembly. All internal and external locations on an aircraft structure which could collect moisture are typically protected using flexible sealants in addition to paint coatings.

Even with a comprehensive protective scheme in place consisting of a conversion coating, primer and topcoat and wet assembly with sealant, coatings will eventually fail given time. A practical example describing how this failure occurs is provided in the case study in the next section. It is now common in some parts of aircraft structures which are prone to corrosion, to apply an additional layer of protection using corrosion inhibiting compounds (CICs). These are organic formulations consisting of carrier solvent containing dissolved oil, wax or resin and some organic-based corrosion inhibitors such as phosphonates and sulphonates. Similar products for domestic use are WD40TM and RP7TM which are multi-purpose lubricating and penetrating sprays. CICs are typically sprayed onto the structure after the full protective system is in place. When the solvent evaporates, a film of oil, wax or resin is left together with the inhibitors. They therefore provide an additional barrier layer for protection, and a source of corrosion inhibitors when moisture is present. Some CICs also have water displacing and repellant properties, which enable them to be used to prevent moisture accessing exposed metal at cracks in paint coatings and sealants within joints and holes, or to remove moisture. Many CICs remain mobile on the surface for some time and can provide protection when cracks form in the underlying paint coating. CICs conform to a range of US Military Specifications (MIL-L-87177A, 1991; MIL-PRF-16173E, 1993; MIL-PRF-81309F, 2005; MIL-DTL-85054C, 2007) and aircraft manufacture specifications. CICs have excellent corrosion prevention properties (Hinton et al., 2000) and they are able to arrest the growth of existing corrosion process including stress corrosion cracking (Hinton et al., 1996). However, it is important to understand that they do have a limited effective life, and are only temporary coatings, and therefore need frequent replacement.

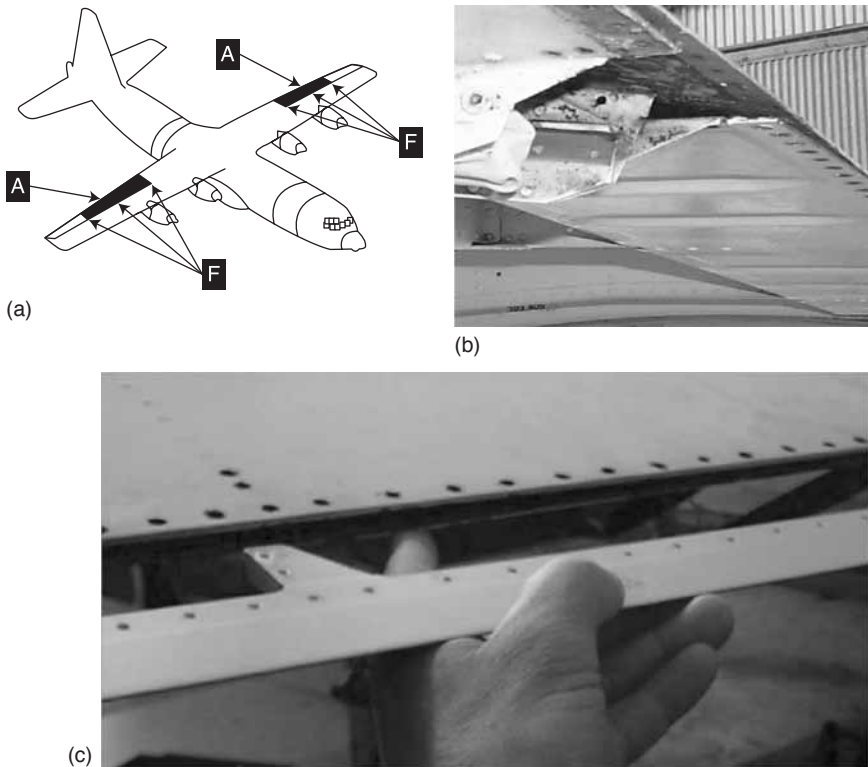
19.6 Summary case study: corrosion of a C-130J Hercules aircraft wing trailing edge strip

The following case study provides examples of some types of corrosion that are commonly observed on aluminium alloy aircraft components. It also

demonstrates the stages in the development of corrosion with a nominally sound comprehensive protective scheme in place. The study highlights the role of alloy microstructure, and the relationship between the macro-environment external to a component, and the micro-environment at the site of corrosion initiation and propagation.

19.6.1 Assembly and component details

Figure 19.9(a)–(c) shows the location of the trailing edge strip in the wing of a large military transport aircraft. This strip was machined from AA2024-T4 aluminium alloy plate. AA2024 is a high-strength (precipitation hardenable) aluminium-copper-magnesium alloy widely used in aircraft construction. The strip contains several changes in section, machined edges and fastener holes. These features expose the end grain of the rolled alloy microstructure (transverse direction), which is susceptible to localised forms of corrosion, including pitting



19.9 (a) Schematic showing location of trailing edge strip (A) at rear of the wing trailing edge (F). (b) The rear of the flap showing the trailing edge without the strip in place. (c) The trailing edge strip removed from the rear edge.

and intergranular corrosion. The role of the strip is to provide a connecting aerodynamic joining piece for the rear ends of the upper and lower surface panels of the wing trailing edge. The strip is joined to the panels through the use of several titanium fasteners. The upper and lower surface panels were made from carbon fibre reinforced epoxy composite with a layer of glass fibre composite on those areas in contact with the aluminium alloy edge strip. The purpose of the glass composite is to prevent galvanic interaction between the carbon fibre and the aluminium alloy.

The strip was protected by a chromate conversion coating, an epoxy polyamide primer pigmented with chromate inhibitor and a polyurethane topcoat. Before assembly, a polysulphide sealant was applied to those surfaces of the strip mating with the upper and lower panel surfaces of the trailing edge. The fasteners were wet installed with a coating of sealant. This is considered a comprehensive corrosion protection scheme.

19.6.2 Operating environment

As previously discussed, the role of the environment is critical in the corrosion of aluminium alloy components. The aircraft from which this component was taken is usually operated from bases up to 50 km from the Australian sea coast where atmospheric salt deposition rates are relatively low. However, the aircraft is also operated from landing strips all over the world, with many of these strips located close to a sea coast. Descent to landing from altitude with over sea approaches, and landing on runways containing dust and soil high in chloride content, ensures that salt contaminants are collected within the aircraft structure including the trailing edge. At many bases during the winter months especially, the temperature over night falls below the dew point and condensation of moisture occurs within cold structural components on aircraft parked on runways. During summer months, the relative humidity at many bases can be high. After landing from high altitude flights during which aircraft surface temperatures may be as low as -50°C , condensation occurs within components such as the trailing edge.

It is clear, therefore, that two essential ingredients for corrosion, moisture and salt, which together form a conducting (and aggressive) electrolyte may readily accumulate in structural components. Furthermore, accumulated dirt and soil will trap and retain condensed moisture. Drying out of a poultice of salty dust and soil collected on component surfaces and within joints will be limited, unless high temperatures and low humidity are experienced by the aircraft while it is on the runway awaiting operations. Sodium chloride adsorbs moisture (deliquescence) or 'wets out' at relative humidities above 73%. However, sea salts 'wet out' at a relative humidity above 35% because they contain magnesium salts. Rain periods either during flight or while an aircraft is in the ground may wash any salt contaminants from the aircraft. However, rain will have no effect within a structure such as the trailing edge. As will be discussed later, it is possible that rain could

solubilise any salt contaminants and allow them to penetrate further into the structure through defects in protective coatings around fastener holes. A seemingly benign macro-environment may have little resemblance to the environment within components where corrosion commonly occurs, highlighting the critical importance of micro-environment in the understanding of aluminium corrosion.

19.6.3 Coating failure

Mechanical failure

Corrosion will not occur until the protective coating system fails. All polymeric coatings will admit moisture by diffusion over time. However, in the relatively complex configuration of the trailing edge, there are many factors that will contribute to the mechanical failure of paint coatings and sealants. All coatings (paints and sealants) will age, harden and crack with time due to constant exposure to extremes of temperature, infra-red and ultraviolet radiation. These environmental factors break down the molecular structure of the coating and under stress they crack. Cracks will admit moisture through the coating and at a faster rate than by normal diffusion. The stresses present, which cause the coatings to crack, are the result of a number of factors. The main one is the operating or working loads on the component. In the case of the trailing edge, the constant aerodynamic buffeting during flight is the source of cyclic stressing at all joints on the trailing edge. In locations such as around fastener heads, at holes and along joint lines, thin films of paint (primer or primer and topcoat) will be subjected to significant stress levels. Within the joints, e.g. inside fastener holes and across the faying surfaces between the upper and lower trailing edge panels and the edge strip, the constant working of the joint due to the operational loads will produce a rubbing and fretting action. The absorption of moisture into the coatings and the freeze/thaw cycle due to time on the ground and at high altitude will also produce an internal source of cyclic stress. All of these stresses, in combination with the environmental degradation of mechanical properties of the thin polymeric layer of coating, will eventually produce many cracks and flaws. It is the combination of years of operation and environmental exposure that will eventually cause the protective coatings to fail mechanically. The network of cracks formed will allow all constituents of the macro-environment described earlier to penetrate through to the substrate metal. There the micro-environment becomes dominated not by the environmental variables associated with the aircraft location and mission type, but by the corrosion process itself.

Chemical failure

Even though all the ingredients may be present for corrosion to occur within cracks that have developed in coatings within the joints and holes in the strip, corrosion will not occur immediately. As mentioned in Section 19.5 the epoxy

polyamide primer not only provides a barrier coating as part of the total protective scheme, but also acts as a source of chromate inhibiting ions. Chromate ions are one of the most effective corrosion inhibitors for Al alloys in a wide range of environments. Small quantities of chromate ions are also available from the chromate conversion coating. Chromate ions leached from the primer and conversion coating at the point of failure migrate to any exposed metal and form a protective film of chromium oxide (Clarke et al., 2002). However this film, while protective, will also break down over time, due to the movement of the joints and fastener through rubbing and fretting. While additional chromate ions from the coating may be available to repair the damaged oxide film; due to the continual ingress of moisture or the continued presence of existing moisture through the processes describe above, gradual depletion of the chromate ions from the primer by leaching occurs. At a point in time when all available chromate ions of sufficient concentration to prevent corrosion are consumed, the protective capability of the coating system will be lost and corrosion will occur. This process of coating mechanical failure and chromate depletion within joints and holes is a continuous process at different stages and at different points within those locations. It may be possible that in one area within a joint bare metal becomes exposed, and chromate ions available from a primer surface nearby within the joint may migrate through any thin layer of moisture to the exposed substrate and provide inhibition.

19.6.4 The corrosion processes

Figure 19.10 shows an edge strip with extensive exfoliation corrosion. The damage in this case is the result of several types of corrosion having occurred, developed to various stages and eventually coalescing.

These different types of corrosion were pitting, intergranular, exfoliation and underfilm/filiform corrosion. Corrosion damage was detected along the machined ridge on the upper surface of the strip and the shallow radius on the lower surface of the strip, at the rear edges of the upper and lower edge panels. An example is shown in Fig. 19.11.

At these locations the sealant and paint coating along the joint line failed and pits developed. Figure 19.11 shows corrosion damage at a machined edge on the upper surface of the strip. This damage would have originated as a result of moisture and salt penetrating a crack in the sealant along the edge of the strip where the upper panel fits. The underlying paint coating may have failed at that point or nearby allowing moisture to penetrate to the metal substrate. At the point of the defect or flaw in the paint coating, a pit would have developed. It is clear from Fig. 19.11 that corrosion has spread laterally from this point beneath the adjacent coating. The spread in corrosion would have been the result of further pitting and intergranular attack, resulting in lifting of the paint coating (known as underfilm corrosion). At the machined edge shown in Fig. 19.11, this damage would have developed into exfoliation similar to that shown in Fig. 19.10.

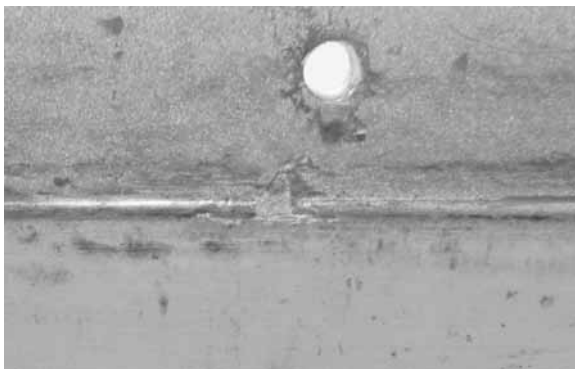


19.10 A general view of widespread exfoliation corrosion on the lower surface of a trailing edge strip.

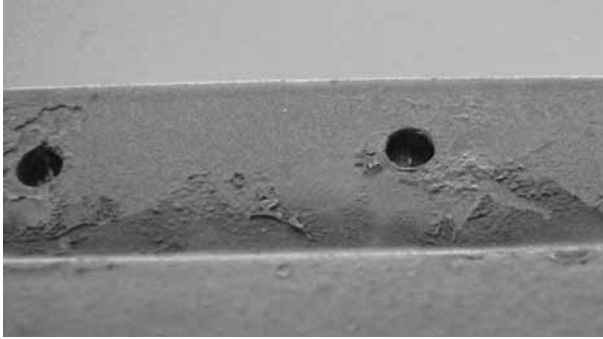
Machining of the strip exposes the end grain of the alloy microstructure, thus providing a highly susceptible pathway along grain boundaries for intergranular attack.

At many sites on the trailing edge strip, corrosion initiated at the holes (Fig. 19.12 and 19.13). This appeared as underfilm or filiform corrosion, and blistering of the paint adjacent to the hole. Blistering was caused by the build-up of corrosion product. Figure 19.14 shows how such corrosion damage progressed, developed into widespread attack and exfoliation corrosion causing lifting of the surface layers of the alloy.

The corrosion on the surfaces of the edge strip beneath the upper and lower panels and within the holes would have been driven by the microclimate associated with the moisture and salt contaminants which had penetrated to there through failure of the paint and sealant coatings.



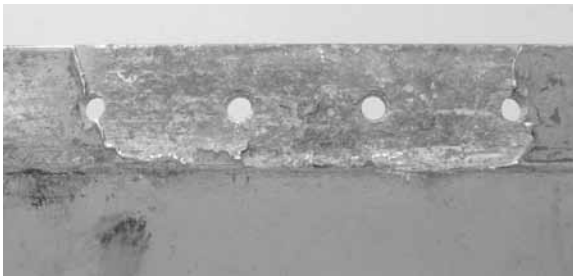
19.11 Corrosion damage at a machined edge on the upper surface of the strip.



19.12 Filiform corrosion associated with a fastener hole on the upper edge of the strip.



19.13 Corrosion around fastener holes with paint removed as a result of blistering due to corrosion product build up.



19.14 Advance exfoliation corrosion damage initiating around fastener holes.

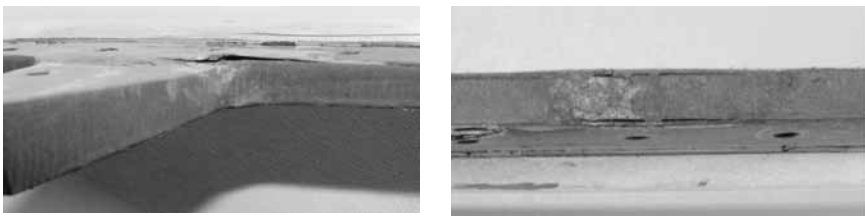
Overall, the component geometry, the occluded spaces, the presence of salt unable to be washed away, the formation of deliquescent aluminium ions and the hydrolysis of aluminium ions to form acid (Baes and Mesmer, 1976), serve to provide a very aggressive environment that may never dry out. In areas of contact between the panels and the edge strip where coatings failed, moisture could penetrate. Any carbon fibres of the composite panel which may have been in contact with the edge strip would have accelerated the corrosion through the galvanic

interaction of carbon and the aluminium alloy. However, the layer of glass-reinforced composite would need to have been damaged for that contact to occur. The titanium fasteners may have had an influence on the corrosion within and around the holes. Titanium is a more noble metal than AA 2024 aluminium alloy. However, the strength of the galvanic corrosion on the aluminium produced by contact with the titanium would have been limited by the small contact area available through any defects which may have been present in the sealant used to wet install the fasteners.

Many examples of corrosion damage were found along the edge of the strip inside the trailing edge between the upper and lower panels (Fig. 19.15). In these cases corrosion was initiated by pitting which had developed at flaws in the paint coating. The pitting developed into intergranular corrosion that subsequently led to exfoliation and the lifting of the layers of alloy microstructure. In these examples, the end grain of the rolled aluminium alloy edge strip would have been exposed to accumulated water within the trailing edge as no drain holes were designed into the lower panels. Indeed, water stains and tide marks were found inside the lower panel. It appears as though moisture eventually penetrated the protective coating along the edge, the chromate inhibitor was exhausted and corrosion developed.

19.6.5 Summary

In this case study, the alloy chosen for the edge strip was most likely based on strength and fatigue resistance considerations. AA2024 is known to be prone to corrosion; however, faith in corrosion prevention was placed in the protective coating. The design of the edge strip was probably chosen for reasons of ease of manufacture and cost. Exposure of the vulnerable end grain of the microstructure due to machining was most likely unavoidable. The moisture which obviously collected inside the flap had in some cases found its way into the joints and holes, which could have been prevented by incorporating drain holes into the lower panel surfaces. This has been done by the aircraft maintainers in order to limit the future occurrence of the problem. Further, possible ways of mitigating the corrosion problem may be via the use of penetrating oily based CICs discussed in Section 19.5. Alternatively, detergent washing solutions containing surfactants which have very active surface penetrating properties, and which have strong



19.15 Corrosion damage on the edge of the strip located inside the trailing edge.

corrosion inhibiting properties, would also provide some protection (Hinton et al., 1984, 1995). With such detergents, both cleaning and a corrosion preventative maintenance would be combined.

19.7 Acknowledgements

Many thanks to DSTO Australia for the material related to the case study, and for the Figures used throughout the chapter. Thanks also to Julie Fraser, for editorial and graphic assistance, and to colleagues who kindly donated relevant images.

19.8 References

- Afseth, A., Nordlien, J.H., Scamans, G.M., and Nişancioğlu, K. (2002) Effect of thermo-mechanical processing on filiform *corrosion* of aluminium alloy AA3005, *Corrosion Science*, 44: 2543.
- ASTM B117-09 Standard Practice for Operating Salt Spray (Fog) Apparatus.
- ASTM G34-01 (2007) Standard Test Method for Exfoliation Corrosion Susceptibility in 2XXX and 7XXX Series Aluminum Alloys.
- ASTM G66-99 (2005) Standard Test Method for Visual Assessment of Exfoliation Corrosion Susceptibility of 5XXX Series Aluminum Alloys.
- ASTM G67-04 Standard Test Method for Determining the Susceptibility to Intergranular Corrosion of 5XXX Series Aluminum Alloys.
- ASTM G69-97 (2009) Standard Test Method for Measurement of Corrosion Potentials of Aluminium Alloys.
- ASTM G85-09 Standard Practice for Modified Salt Spray (Fog) Testing.
- ASTM G110-92 (2009) Standard Practice for Evaluating Intergranular Corrosion Resistance of Heat Treatable Aluminum Alloys by Immersion in Sodium Chloride plus Hydrogen Peroxide Solution.
- Baes, C.F. Jr. and Mesmer, R.E. (1976) *The Hydrolysis of Cations*, John Wiley, Interscience Publication, New York.
- Barter, S., Sharp, O.K., and Clark, G. (1994) The failure of an F-18 trailing edge flap hinge, *Engineering Failure Analysis*, 1(4): pp. 255–266.
- Biestek, T. and Weber, J. (1976) *Electrolytic and Chemical Conversion Coatings: A Concise Survey of their Production, Properties and Testing*, Portcullis Press Ltd., Redhill.
- Birbilis, N. and Buchheit, R.G. (2005) Electrochemical characteristics of intermetallic phases in aluminum alloys: An experimental survey and discussion, *Journal of the Electrochemical Society*, 152(4): B140–B151.
- Birbilis, N., Cavanaugh, M.K., and Buchheit, R.G. (2006) Electrochemical behavior and localized corrosion associated with $\text{Al}_7\text{Cu}_2\text{Fe}$ particles in aluminum alloy 7075-T651, *Corrosion Science*, 48(12): 4202–4215.
- Buchheit, R.G. (1995) *Journal of Electrochemical Society*, 142: 3994.
- Buchheit, R.G., Grant, R.P., Hlava, P.F., McKenzie, B., and Zender, G.L. (1997) *Journal of the Electrochemical Society*, 144: 2621.
- Burleigh, T.D. (1991) The postulated mechanisms for stress corrosion cracking of aluminum alloys: A review of the literature 1980–1989, *Corrosion*, 47(2): 89–98.

- Chen, Z.Y., Cui, F., and Kelly, R.G. (2008) Calculations of the cathodic current delivery capacity and stability of crevice corrosion under atmospheric environments, *Journal of the Electrochemical Society*, 155(7): C360–C368.
- Clarke, W.J., Ramsey, J.D., McCreery, R.L., and Frankel, G.S. (2002) *Journal of the Electrochemical Society*, 149: B179.
- Coleman, A.J., McMurray, H.N., Williams, G., et al. Inhibition of filiform corrosion on AA6111-T4 using in-coating phenylphosphonic acid, *Electrochemical and Solid State Letters*, 10(5): C35–C38.
- Davies, J.R. (ed.) (1999) *Corrosion of Aluminium and Aluminium Alloys*, ASM International, Materials Park, OH.
- Frankel, G.S. (1998) Pitting corrosion of metals: A review of the critical factors, *Journal of the Electrochemical Society*, 145(6): 2186–2198.
- Frankel, G.S. and McCreery, R.L. (2001) Inhibition of Al alloy corrosion by chromates, *The Electrochemical Society Interface (Winter)*, 10(4): 34–38.
- Hertzberg, R.W. (1995) *Deformation and Fracture Mechanics of Engineering Material*, 4th edn., Wiley, New York.
- Hinton, B.R.W. (1991) Corrosion prevention and chromates, the end of an era? Part 2, *Metal Finishing*, 89(10): 15.
- Hinton, B.R.W., Rohan, P., Cosgrove, M., and Luscombe, D. (1995) *Washing detergents and corrosion inhibition, corrosion and prevention 1995*, Conference of Australasian Corrosion Association, Melbourne.
- Hinton, B.R.W., Ryan, N.E., and Trathen, P.N. (1984) Inhibition of corrosion and stress corrosion cracking in high strength aluminium alloys by surface active agents, *Proceedings of the 9th International Congress on Metallic Corrosion*, National Research Council of Canada, Ottawa, pp. 144–150.
- Hinton, B.R.W., Trathen, P.N., Duxbury, E., Salagaras, M., and Bushell, P. (2000) The protection performance of corrosion prevention compounds on aluminium alloys in laboratory and outdoor environments, *The Fourth Joint DoD/FAA/NASA Conference on Aging Aircraft*, Washington, DC.
- Hinton, B.R.W., Trathen, P.N., Haberecht, P., and Bushell, P. (1996) Prevention and control of corrosion on aircraft structure with corrosion prevention compounds, *4th International Aerospace Corrosion Control Symposium*, 26–28 June, Jakarta, Indonesia.
- Hoeppner, D.W. (1979) Model for prediction of fatigue lives based upon a pitting corrosion fatigue process, *Proceedings of ASMT-NBS-NSF Symposium in Fatigue Mechanisms*, J.T. Fong, ed., ASTM STP675, ASTM, West Conshohocken, PA, pp. 841–870.
- Hughes, A.E., Taylor, R.J., and Hinton, B.R.W. (1997) Chromate conversion coatings on 2024 Al alloy, *Surface and Interface Analysis*, 25(4): 223–234.
- Hunter, M.S., Frank, G.R., and Robinson, D.L. (1963) Mechanism of corrosion of 2024 alloy as revealed by electron microscopy, *Proceedings of 2nd International Congress on Metallic Corrosion*, National Association of Corrosion Engineers (NACE), Houston, p. 66 (1963).
- Ilevbare, G.O., Schneider, O., Kelly, R.G., and Scully, J.R. (2004) *Journal of the Electrochemical Society*, 151: 453.
- Jones, K. and Hoeppner, D.W. (2005) Pit-to-crack transition in pre-corroded 7075-T6 aluminum alloy under cyclic loading, *Corrosion Science*, 47(9): 2185–2198.
- Jones, R.H. (ed.) (1992) *Stress-Corrosion Cracking*, ASM International, Materials Park, OH.
- Knight, S.P. (2003) *A Review of Heat Treatments*, Australasian Corrosion Association, Melbourne.

- Kondo, Y. (1989) Prediction of fatigue crack initiation life based on pit growth, *Corrosion*, 45: p. 7.
- Lynch, S.P., Knight, S.P., Birbilis, N., and Muddle, B.C. (2008) Stress corrosion cracking of Al-Zn-Mg-Cu alloys: Effects of composition and heat treatment, *Proceedings of the 2008 International Hydrogen Conference: Effects of hydrogen on materials*, Jackson Hole, WY, USA, pp. 243–250.
- Mazurkiewicz, B. and Piotrowski, A. (1983) *Corrosion Science*, 23: 697.
- McMurray, H.N., Coleman, A.J., Williams, G., et al. Scanning Kelvin probe studies of filiform corrosion on automotive aluminum alloy AA6016, *Journal of the Electrochemical Society*, 154(7): C339–C348.
- MIL-A-8625F US Military Standard Anodic Coatings for Aluminum and Aluminum Alloys, September 2003.
- MIL-DTL-5541F US Military Standard Chemical Conversion Coatings on Aluminium and Aluminium Alloys 1990, July 2006.
- MIL-DTL-81706B, US Military Standard Chemical Conversion Materials for Coating Aluminium and Aluminium Alloys, May 2006.
- MIL-DTL-85054C US Military Specification Corrosion Preventive Compound, Clear (AMLGUARD) February 2007.
- MIL-L-87177A US Military Specification Lubricants, Water Displacing, Synthetic, February 1991.
- MIL-PRF-16173E US Military Specification Corrosion Preventive Compound, Solvent Cutback, Cold-Application, January 1993.
- MIL-PRF-23377J Specification Primer Coatings: Epoxy, High-Solids, April 2007.
- MIL-PRF-81309F US Military Specification Corrosion Preventive Compounds, Water Displacing, Ultra-Thin Film, May 2005.
- MIL-PRF-85285D US Military Specification Coating: Polyurethane, Aircraft and Support Equipment, February 2009.
- MIL-PRF-85582D Specification Primer Coatings: Epoxy, Waterborne, June 2006.
- Muster, T., Hughes, A.E., and Thompson, G.E. (2008) Copper distributions in aluminium alloys, in *Corrosion Research Trends*, I.S. Wang (ed.), Nova Science Publishers. NY, pp. 35–106.
- Newman, R.C. and Sieradzki, K. (1994) Metallic corrosion, *Science*, 263: 1708–1709.
- Nişancioğlu, K. (1990) Electrochemical behavior of aluminum-base intermetallics containing iron, *Journal of the Electrochemical Society*, 137: 69.
- Osaki, S., Kondo, H., and Kinoshita, K. (2006) Contribution of hydrogen embrittlement to SCC process in excess Si type Al-Mg-Si alloys, *Materials Transactions*, 47(4): 1127–1134.
- Polmear, I.J. (1995) *Light Alloys: Metallurgy of the Light Metals*, 3rd edn, Arnold, London.
- Pourbaix (1966) *Atlas of Electrochemical Equilibria in Aqueous Solutions*, NACE International, Houston, TX.
- Pryor, M.J. and Fister, J.C. (1984) *Journal of the Electrochemical Society*, 131: 1230.
- Roberge, P.R. (1999) *Handbook of Corrosion Engineering*, McGraw Hill, New York.
- Scamans, G.M. and Holroyd, N.J.H. (1986) Stress-corrosion of aluminium aerospace alloys, *Journal of the Electrochemical Society*, 133(8): C308–C308.
- Scamans, G.M., Holroyd, N.J.H., and Tuck, C.D.S. (1987) The role of magnesium segregation in the intergranular stress corrosion cracking of aluminium alloys, *Corrosion Science*, 27(4): 329–347.
- Schneider, O., Ilevbare, G.O., Kelly, R.G., et al. (2007) In situ confocal laser scanning microscopy of AA2024-T3 corrosion metrology – III: Underfilm corrosion of epoxy-coated AA2024-T3, *Journal of the Electrochemical Society*, 154(8): C397–C410.

- Schneider, O., Ilevbare, G.O., Kelly, R.G., and Scully, J.R. (2004) *Journal of the Electrochemical Society*, 151: 465.
- Scully, J.R., Knight, T.O., Buchheit, R.G., and Peebles, D.E. (1993) *Electrochemical characteristics of the Al₂Cu, Al₃Ta and Al₃Zr intermetallic phases and their relevancy to the localized corrosion of Al alloys*, *Corrosion Science*, 35: 185–195.
- Searles, J.L., Gouma, P.I., and Buchheit, R.G. (2001) *Metallurgical and Materials Transactions A*, 32A: 2859.
- Sedriks, A.J. (1990) *Stress corrosion cracking: Test methods*, National Association of Corrosion Engineers, Houston, TX.
- Seegmiller, J.C., Bazito, R.C., and Buttry, D.A. (2004) *Journal of Electrochemical Society*, 7(1): B1–B4.
- Seri, O. (1994) The effect of NaCl concentration on the corrosion behavior of aluminum containing iron, *Corrosion Science*, 36(10): 1789.
- Sieradzki, K. (1993) *Journal of the Electrochemical Society*, 140(10): 2868–2872.
- Summerson, T.J. and Sprowls, D.O. (1986) Corrosion behavior of aluminium alloys, *Proceedings of the International Conference of the Hall-Heroult Process*, 15–20 June, University of Virginia, Engineering Materials Advisory Services Ltd., Warley, UK, Vol. III, pp. 1576–1662.
- Suresh, S. (1998) *Fatigue of Materials*, Cambridge University Press, Cambridge, New York.
- Szklarska-Smialowska, Z. (1999) *Corrosion Science*, 41: 1743.
- Szklarska-Smialowska, Z. (2005) *Pitting and Crevice Corrosion*, NACE International, Houston.
- Thakur, A., Raman, R., and Malhotra, S.N. (2007) Hydrogen embrittlement studies of aged and retrogressed-reaged Al-Zn-Mg alloys, *Materials Chemistry and Physics*, 101(2–3): 441–447.
- van der Walde, K., Brockenbrough, J.R., Craig B.A., et al. (2005) Multiple fatigue crack growth in pre-corroded 2024-T3 aluminum, *International Journal of Fatigue*, 27: 1509–1518.
- Vukmirovic, M.B., Dimitrov, N., and Sieradzki, K. (2002) Dealloying and corrosion of Al alloy 2024-T3, *Journal of the Electrochemical Society*, 149(9): B428–439.
- Wernick, S., Pinner, R., and Sheasby, P.G. (2007) *The Surface Treatment and Finishing of Aluminum and its Alloys*, 6th edn., ASM International, Materials. Park, OH.
- Zamin, M. (1981) Role of Mn in the corrosion behavior of al-mn alloys, *Corrosion*, 37(11): 627.
- Zhao, X.Y. and Frankel, G.S. (2007) Quantitative study of exfoliation corrosion: Exfoliation of slices in humidity technique, *Corrosion Science*, 49(2): 920–938.

Joining of aluminium and its alloys

S. LATHABAI, CSIRO Process Science and Engineering, Australia

Abstract: Joining and welding are key enabling technologies for manufacture. The quality and reliability of a manufactured product are often determined by the quality of its joints. This chapter presents an overview of the various processes used for joining aluminium and its alloys. Recent advances which have enabled the joining of these materials, both to themselves and to other materials, more economically, at higher productivity and with excellent quality and reliability, are highlighted.

Key words: mechanical joining, fusion welding, solid state welding, brazing, adhesive bonding.

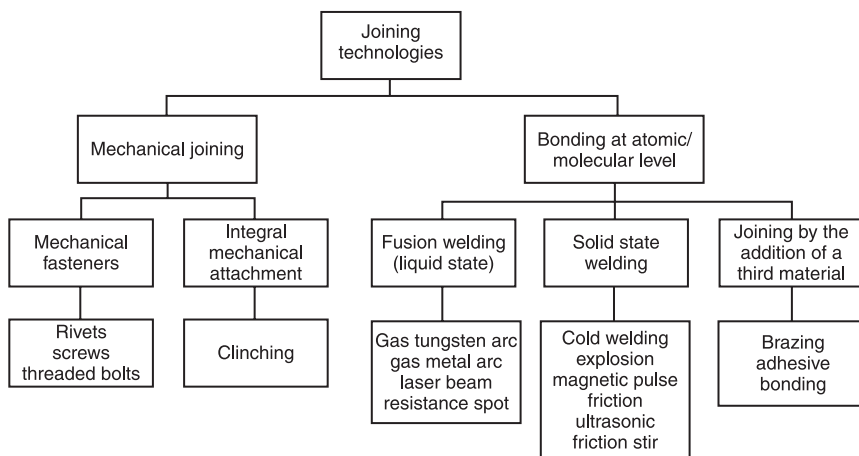
20.1 Introduction

Most manufactured products are assembled from parts or components. As such, joining and welding are key enabling technologies for manufacture. The quality and reliability of a manufactured product are often determined by the quality of its joints. The ideal joint should be indistinguishable from the materials it has joined. In reality, a joining process has not yet been invented which would perform adequately on all materials for all possible geometries. Therefore, the selection of the best process for a particular material in a given application is an important consideration.

As noted in the Introduction to this book, the general use of aluminium worldwide is expected to continue to increase, particularly in the transport sector. Increased use of lightweight materials, including aluminium alloys, in transport applications is well recognised as a strategy to reduce the vehicle mass, thereby reducing fuel consumption and greenhouse emissions. Aluminium alloys also find applications in other areas of the transport sector as well as in the construction and domestic appliance sectors. The high strength-to-weight ratio, excellent formability and corrosion resistance of aluminium alloys make them materials of choice for the aerospace, marine and rail transport industries. It is clearly essential that appropriate joining technologies are available to integrate aluminium alloys into products or structures in an economic, reliable and rapid manner, particularly as new alloys and processes are developed. Furthermore, the emerging trend in the automotive industry is a multi-material design approach, in which the ideal lightweight material, be it a high strength steel, a lightweight alloy of aluminium or magnesium or a fibre-reinforced polymer composite, is selected to produce a component, based on factors such as performance, durability, manufacturability and cost. This means that many of the joints will be between dissimilar materials

which can compound the problems of quality and reliability in the final product or subassembly. To avoid joint failures, developing or selecting the appropriate joining technology is a critical priority, and has to become an integral part of product design.

There are two fundamental approaches to joining a material to another of similar (or dissimilar) composition. The principal difference between the two approaches is in the nature of the bond created, which, in turn, influences the nature of the joint and its strength. In one approach, the parts are held to each other by mechanical means; in the other case, bonding between the materials or parts occurs at the atomic/molecular level. Mechanical joining uses the first approach while fusion welding, solid state welding, brazing and soldering, and adhesive bonding fall under the second category. Based on this distinction, joining processes may be classified as shown in Fig. 20.1. There are two methods to accomplish mechanical joining: by employing additional joining elements called fasteners or by using or forming some geometric features integral to the mating parts that enable joining by mechanical interference or interlocking. In fusion welding processes, the joint is formed in the liquid state, while in solid state welding processes, joining is accomplished without the melting of the workpieces. In both cases, a metallurgical bond is formed. A metallurgical bond is also formed in the case of brazing. However, here the bonds are formed without the melting of the workpieces; a molten filler, which generally melts above $\sim 450^{\circ}\text{C}$, is forced into a close-fitting joint by capillary action. A weaker chemical bond (such as Van der Waals) is formed in adhesive bonding in which a non-metallic adhesive undergoes a physical or chemical hardening reaction causing the parts to join together.



20.1 Classification of joining technologies based on the nature of the bond attained.

During fusion welding, the energy input provided by the process results in melting of the workpieces and also a filler metal (if used), and joining occurs in the liquid state. The high temperatures attained cause changes in the microstructure in the zone adjoining the weld and this in turn can cause local degradation of the properties of the material. The lower temperatures associated with solid state joining processes mean that such degradation is minimised or even avoided when they are used. This is also the case with brazing and adhesive bonding. Mechanical joining processes are the best performers in this regard as they accomplish joining with little or no heating and hence no thermal degradation of the microstructure and properties of the workpiece materials. As a result of the strong metallurgical bonding produced by fusion and solid state welding and brazing, and to a lesser extent, the chemical bonding associated with adhesives, these processes produce joints that are strong and permanent. This means that disassembly of welded and adhesive bonded joints without damage is not possible, should that become necessary, for instance, for portability, repair or recycling at end-of-life of the component. A unique advantage of the mechanical joining processes is that they allow disassembly with no damage to the parts.

Aluminium and its alloys can be joined by all of these different joining technologies, with varying degrees of success. In many instances, processes and equipment originally developed for other metals, particularly steel, have been successfully adapted for joining aluminium. However, there are also examples where the reverse has occurred, i.e., a process which was first used for aluminium joining has since been applied to other materials. There is a large body of literature in the public domain which provides exhaustive information on the various welding and joining processes and their application to aluminium. It would be impractical and impossible to attempt to reproduce all of that information here. Instead, our objective is to present an overview of the various processes used for joining aluminium and its alloys and highlight recent advances which have enabled the joining of these materials, both to themselves and to other materials, more economically, at higher productivity and with excellent quality and reliability.

20.2 Mechanical joining

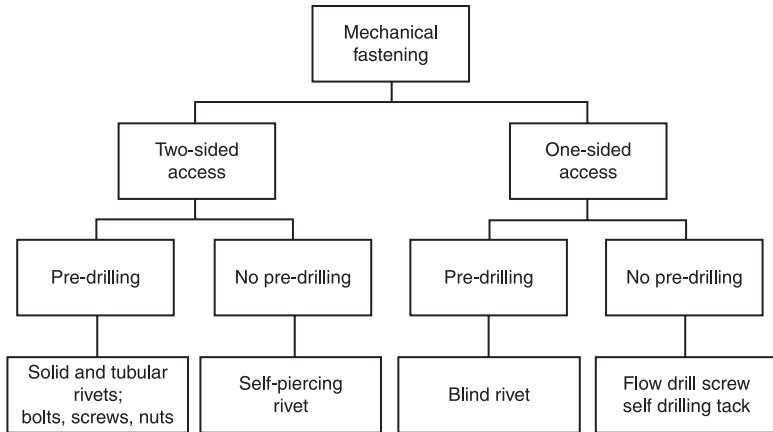
Mechanical joining is accomplished by generating mechanical interference and interlocking between the parts being joined either through the use of an additional joining element, referred to as a fastener, or by introducing a designed or plastically deformed geometrical feature integral to the parts. Processes based on the former method are referred to as mechanical fastening processes, while the term integral mechanical attachment has been used to describe the latter (Messler, 1993, 2004). The earliest instances of application of mechanical joining probably date to pre-historic times when primitive stone tools were produced by attaching a sharp stone to a split straight stick to produce

a spear or axe for more efficient, productive and safer hunting (Messler, 2003). The technology has been used continuously since then and mechanical joining methods have proliferated. By one estimate, mechanical joining constitutes about 50% of all joining accomplished by various options, based on dollar or dollar-equivalent value (Messler, 2003). Although mechanical joining can be used with any material type, the technology is particularly suited for metals which are tolerant to the deformations occurring locally during the joining. As metallurgical bonding is not formed, material intermixing and chemical compatibility are not major concerns. It is therefore not surprising that mechanical joining is extensively used for joining aluminium and its alloys to each other, as well as for dissimilar joining to other materials. In this section, we examine mechanical joining processes that are currently widely used for joining aluminium alloys.

20.2.1 Mechanical fastening

As mentioned earlier, mechanical fastening relies on the use of an additional joining element or fastener which creates interlocking between abutting or overlapping parts, thereby preventing relative motion and physical separation. The applied loading on a fastened joint may produce either shear or tensile forces on the faying surfaces of the joint. In the former case, the fastener resists the load by pinning the joint against motion using bearing forces between the fastener and the parts, or by resisting the shear through the action of friction at the joint faying surfaces. Under tension loading, the fastener resists the load entirely by developing a preload or clamping force (Messler, 1993).

Mechanical fastening processes have been classified in the literature based on whether the fasteners are threaded or not (Messler, 1993, p. 80; Budde, 1994a). Here, we have adopted a different scheme for broadly grouping mechanical fastening processes, based on accessibility requirements for making the joint, i.e., whether or not the process allows installation and setting of the fastener from one side, thus making it ideally suited for applications where access to the blind side is impossible or impractical. As shown in Fig. 20.2, a subclassification is then made for each category, based on whether pre-drilling of the parts being joined is required for installation of the fastener or not. Mechanical fasteners that require accessibility from both sides *and* pre-drilling include solid and tubular rivets, threaded fasteners such as bolts, nuts and screws while self-piercing rivets (SPR) do not require pre-drilling. Blind rivets, as the name indicates, enable joining when access is only available from one side of the joint, but do require pre-drilling for insertion. Self-drilling screws with special tips and flow drilling screws deliver the advantage of one side accessibility while eliminating the need for pre-drilling of the parts. Flow drilling screws cause the material around the hole to extend beyond the normal thickness thus providing enough material for thread engagement.



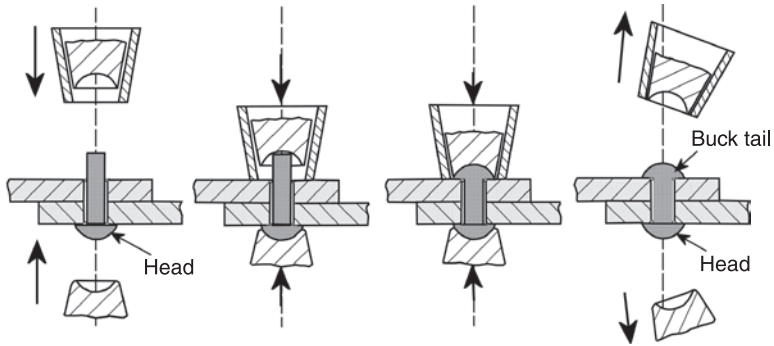
20.2 Classification of mechanical fastening processes.

Threaded fasteners

Bolts, nuts and screws constitute a large category of threaded mechanical fasteners in which threading, external around a cylindrical shaft or internal within the body, enable development of a clamping force on a joint (Messler, 1993, p. 63). In general, threaded fasteners require a prepared hole, so that two-sided access is required, unless self-tapping screws or self-piercing bolts are used. The clamping force is developed either through the friction between the fastener and the material into which the fastener is forced, as in the case of a screw (self-tapping), or through the opposing motion produced by internal threads in a nut (or on one of the parts) and the external threads on a bolt or screw. Threaded fasteners facilitate disassembly without component damage which is particularly advantageous for portability, access for maintenance or servicing, modification or reconfiguration. To avoid galvanic corrosion when joining aluminium parts, aluminium, stainless steel or coated steel fasteners are used; copper and brass fasteners are unsuitable.

Solid and tubular rivets

As shown in Fig. 20.3, a solid rivet typically has a head and a smaller diameter shank which is placed into a pre-drilled hole in workpieces that are properly aligned. A second head is created by plastically deforming or upsetting the projecting shank. Tubular or semi-tubular rivets have a hollow shank. These rivets are widely used for joining aluminium alloys in the aerospace industry. The feature that distinguishes the rivets is their head design, which are many. When used for aerospace applications, the heads can be countersunk or shaved to offer an aerodynamically smooth contour. Rivets can be upset manually, often by hammering the head while bucking the foot, or automatic C-frame machines

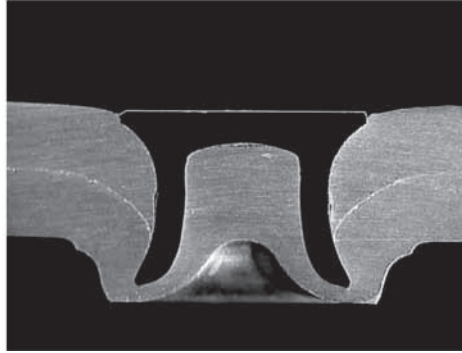
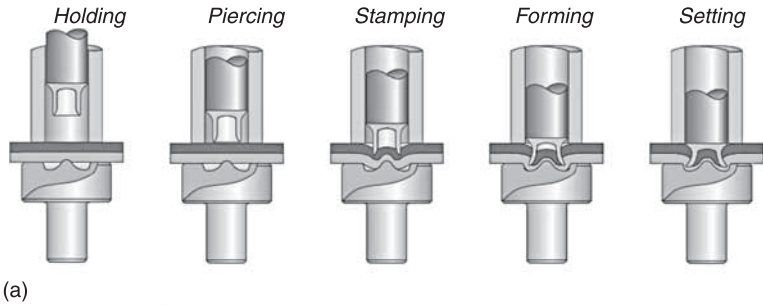


20.3 Setting a solid rivet to form a joint between overlapping sheets (source: LWF, University of Paderborn, Germany).

can be used which apply a squeezing force to both head and tail simultaneously, as shown in Fig. 20.3 (European Aluminium Association, 2009). When used in the aerospace industry, rivets belonging to the 2xxx and 7xxx alloy designations are widely used, and to a lesser extent, 5xxx rivets are also used. The main advantages of the rivets are: (1) low fabrication costs due to their simple geometries and ability to be mass-produced by high-speed machines; (2) low installation cost as insertion and setting are fast and repetitive and require little operator skill and can be easily automated; and (3) the ability to produce permanent joints that can be easily inspected immediately after installation by visual examination (Messler, 1993, p. 80). Disadvantages include greater degree of difficulty for removal for disassembly when compared to threaded fasteners and lower strength in static tension or fatigue than bolts.

Self-piercing rivets

As the name suggests, SPR are designed to both pierce and form a permanent fastening within the parts being joined (Barnes and Pashby, 2000b; He et al., 2008). As shown in Fig. 20.4(a), the SPR process is essentially a cold-forming operation in which two or more sheets of material are joined by driving a semi-tubular rivet through the top sheet(s), piercing the bottom sheet without perforating it and spreading the rivet skirt under the guidance of a suitable die. Exact alignment between the parts being joined and between the parts and the rivet setting machinery is not critical as the process does not require pre-drilled holes. However, the nature of the process is such that quite high setting forces are required, typically 40 kN (He et al., 2008) and a C-frame structure is used to withstand this force. As a result, the process requires access to both sides of the joint. SPR has been used to join aluminium alloy sheets with total joint thickness (stack-up) between 1.8 and 11 mm (Henrob Ltd., 2006; Wilhelm Böllhoff GmbH & Co. KG, 2009a). Figure 20.4(b) displays the cross-sectional view of an SPR joint made between



20.4 (a) Schematic illustration of the various stages of self piercing riveting; (b) cross-sectional view of an SPR joint between 3 mm thick sheets of an aluminium alloy (courtesy Wilhelm Böllhoff GmbH & Co. KG, Germany).

two 3 mm thick aluminium alloy sheets. The rivets can be made of high-strength steel, stainless steel or aluminium and are supplied with various hardness levels and surface finishes to achieve maximum corrosion resistance.

In common with other mechanical joining processes, SPR is particularly suited for joining dissimilar materials and multiple mechanical stacks. As noted, no pre-drilling is required. The process is environmentally friendly, with no fumes, sparks or dust being generated. Fast cycle times, amenability to automation, low energy requirements and relatively low costs are other important advantages. However, disadvantages include the need for two-sided access, the relatively high force required for rivet setting and difficulty in applying to less formable materials than aluminium and steel, such as magnesium alloys. The bulges and indents associated with the process may not be aesthetically appealing in some applications; however the recent development of die-less SPR appears to address this by using a flat anvil instead of a contoured die (Neugebauer et al., 2008).

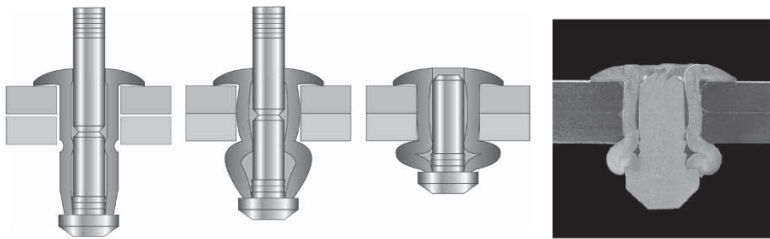
As SPR is considered to be an alternative to resistance spot welding (see Section 20.3.3) particularly for joining aluminium alloy sheets, many research studies have compared the mechanical behaviour of SPR joints with that of resistance spot welded joints. It has been found that SPR joints display comparable

static strength and superior fatigue behaviour compared to spot welded joints (He et al., 2008). It is thus emerging that SPR is a robust, simple and cost-effective technique for joining sheets of various materials, including aluminium alloys, even when the cost of the rivets is taken into consideration. SPR has already found application in aluminium-intensive vehicles from Jaguar and Audi; the Jaguar XJ body shell has approximately 3600 SPRs while the newer XK has about 2500–2600 of these rivets (Mortimer, 2005).

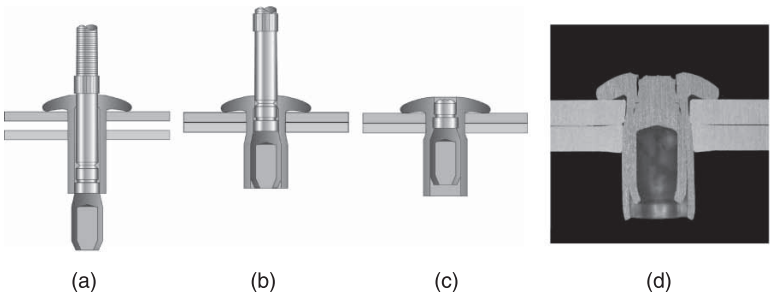
Blind rivets

Blind rivets, also known as breakstem rivets, are the most innovative of the entire group of unthreaded fasteners, as they enable mechanical joining that would otherwise be impossible (Messler, 1993, p. 84). The principal advantage of blind rivets is that their unique design accommodates accessibility from one side of a structure or assembly, making them ideally suited for applications where access to the blind side is impossible or impractical. As shown in Fig. 20.5, blind rivets are

Solid mandrel head rivet



Hollow mandrel head rivet



20.5 Schematic illustration of the stages in the setting of blind rivets: (top row) solid mandrel head rivet; (bottom row) hollow mandrel head rivet. (a) Placing the rivet in a pre-drilled hole; (b) upsetting the rivet; (c) completed joint; (d) cross-sectional view of a blind riveted joint between two 2 mm thick sheets of an aluminium alloy (schematics courtesy Avdel UK Ltd.).

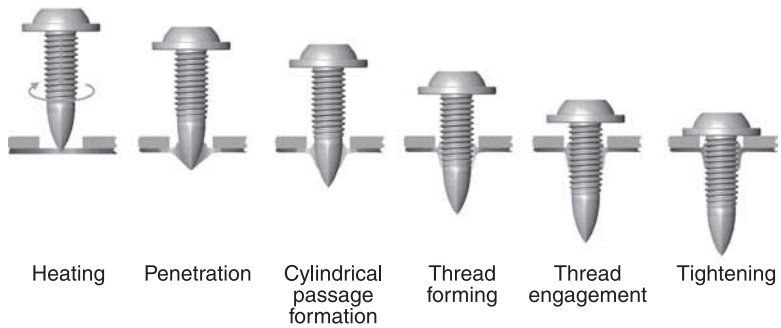
multi-piece assemblies, consisting of a tubular rivet body with a head and coaxially within it, a mandrel. The mandrel consists of a stem and a head with a larger diameter than that of the rivet body. The mandrel head is at the end away from the rivet head, and may be solid or hollow, as shown in Fig. 20.5. The mandrel stem has a weakened section or a notch near the head. During blind riveting, the rivet is placed inside a pre-drilled hole in the sheet stack. The hole diameter is slightly larger than the nominal rivet diameter. Using an appropriate rivet setting tool, the rivet head is pressed flush against the upper workpiece and the mandrel is pulled back. In the process, the larger diameter mandrel head causes the rivet body to flare against the reverse side of the sheets, providing a mechanical interlock between the head and the deformed body. As the load on the mandrel increases and exceeds a predetermined value, it breaks at the notch or the weakened zone and is extracted appropriately. In many designs, the mandrel remains locked in the shear plane for optimum joint strength. Carbon steel, stainless steel and aluminium rivets are available and are selected based on the level of corrosion resistance desired. For additional corrosion resistance, special coatings are used (Avdel UK Ltd., 2008).

Whilst one-sided accessibility is the primary advantage of blind rivets, additional advantages include low cost, fast assembly, lightweight and portable assembly tools, vibration proof assembly and exceptional versatility. However, they do require pre-drilled holes and this could be a disadvantage in some instances. The total thickness of sheets that can be joined ranges from 0.5 mm to more than 20 mm.

Mechanical fastening with one-sided accessibility and no pre-drilling

The new developments in mechanical fastening aim to combine in the one process the advantages offered by some of the processes described above: access from one side of the joint without the requirement of pre-drilling. The common feature in these processes is the use of frictional heating generated between the fastener and the workpieces to soften the material, enabling piercing and forming. In these processes, the fastener itself is driven into the overlapping workpieces at high pressure, while rotating at a high speed. The frictional heat generated plasticises the material adjoining the plunging fastener and dramatically reduces the force required to drive it into the work pieces. The heat generated does not raise the temperature of the workpieces to temperatures that might cause microstructural changes and hence affect the mechanical properties. The processes work well for light alloys of aluminium and magnesium, but have also been used for joining steel sheets.

Flow drilling screws (Fig. 20.6), rotating at speeds up to 5000 rpm, form a female thread on the flash material extruded at the blind side without generating chips or swarf. Once the thread is formed, the rotational speed is reduced and the screw is driven home to engage the threads, and tightened with a preset torque. Aluminium sheets up to 3.5 mm in thickness have been joined without pre-drilling (EJOT GmbH & Co. KG, 2009). Flow drilling screws have already been used in



(a)



(b)

20.6 (a) Schematic illustration of making a joint using flow drill screws; (b) cross-sectional view of a joint between a 1.2 mm thick aluminium sheet and a 3 mm thick die cast aluminium material, made using a flow drill screw (M5 × 20) (courtesy EJOT GmbH, Germany).

some aluminium-intensive cars (Mortimer, 2005; EJOT GmbH & Co. KG, 2009): 48 in Jaguar X150 and 229 in the Audi TT coupe. A recent development is based on the same concept, self-drilling by a fastener, which is referred to as a 'tack'. No threads are formed in the extruded material in this case; instead, the workpiece material adjoining the tack, softened by the frictional heating, is displaced into straight knurlings on the tack shaft, causing mechanical interlocking (Wilhelm Böllhoff GmbH & Co. KG, 2009c). Both these processes are also suitable for dissimilar materials joining, for example, aluminium to steel or a polymer.

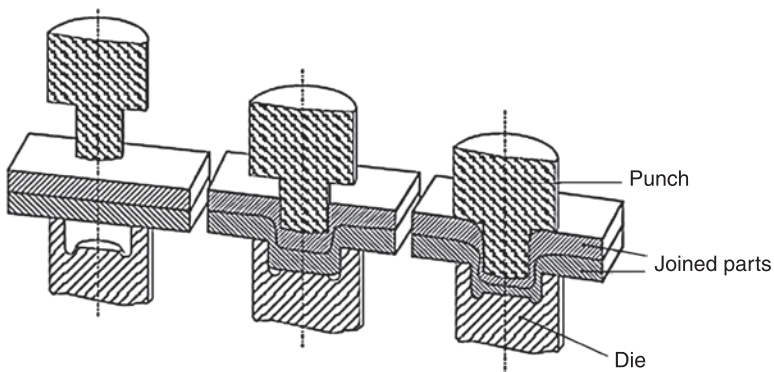
20.2.2 Mechanical interlocking by integral attachment

In this group of mechanical joining processes, a supplementary joining element is not used. Instead a geometrical feature, integral to the parts being joined, introduced either in the design of the parts themselves or by plastic deformation by the joining process, causes mechanical interference and interlocking, thus creating a joint (Messler, 2004, p. 159). As no fasteners are used, this eliminates the need for handling them, pre-drilling the parts to be joined and using tools to

install the fasteners. Dove tails, tongues and grooves, and snap-fits are examples of features designed into the components, causing mechanical interlocking and thus accomplishing joining. Interlocking features can also be created at the interface between overlapping parts by plastically deforming one or both materials to create interlocking protuberances or recesses. Clinching, which relies on the second approach to achieve mechanical joining, has been widely used for joining aluminium alloy sheets and extrusions, particularly in the automotive industry.

During clinching, shown schematically in Fig. 20.7, the materials to be joined are forced into a die by a punch (Budde, 1994b; Wilhelm Böllhoff GmbH & Co. KG, 2009b). As soon as the material at the bottom of the stack makes contact with the die, it starts to flow laterally under the action of the pressure exerted by the punch. The die may be one piece or segmented, and held in place by steel spring. In the latter case, the movable die sections are pushed outwards which allows the flowing of the material to form a button. The local deformation forms an interlocking joint. The punch is then moved back to its starting position either by the operator or by the release of the force by a pneumatic timer. The joined part can now be removed and the side sections of the die are drawn back together by a spring. The tool life is typically dozens of thousands of joints under optimal conditions, with some component manufactures estimating a tool life of 50 000–100 000 joints (Varis, 2006).

In common with SPR, clinching is regarded as an alternative for resistance spot welding of aluminium alloy sheets and hence it is appropriate to consider the advantages offered by clinching over that process (Barnes and Pashby, 2000b; Wilhelm Böllhoff GmbH & Co. KG, 2009b). The investment costs for clinching are considerably lower as there is no need for expensive electrical installations for welding transformers or cooling water, nor is there any need for extraction systems as no fumes are generated. The energy consumption for operation is low and the tools have long service life. There are no post-processing costs as the surfaces of



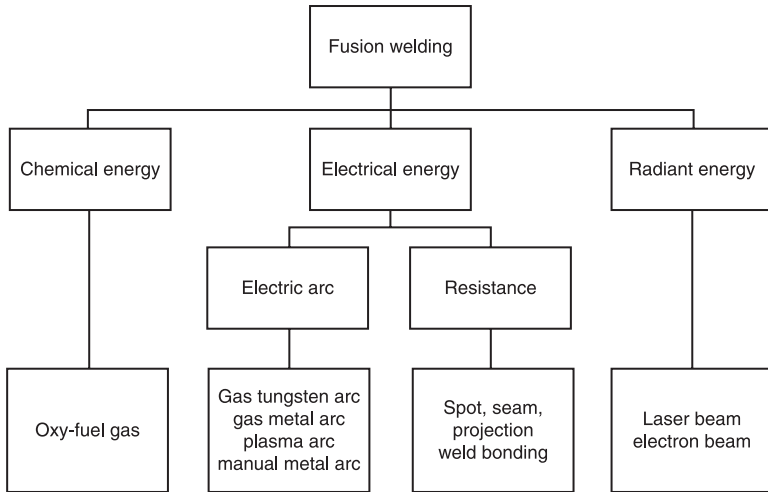
20.7 Schematic illustration of the various stages in clinching (Budde, 1994).

the parts being joined are not damaged. The cycle times are low, of the order of ~ 1 s, and the process is amenable to a high degree of automation. However, there are limitations as well: access is required to both sides of the joint and despite the use of surface coatings, surface irregularities or crevices can occur as a result of the plastic deformation, which could allow corrosion to occur (Barnes and Pashby, 2000b). Bulges and indents associated with both techniques may not be aesthetically desirable. However, as also noted in the case of SPR, new dieless clinching processes have been developed which use a flat anvil, resulting in connections without anvil-side protrusions (Neugebauer et al., 2008).

20.3 Fusion welding

Welding is the joining of two components by creating a metallurgical bonding at the interface by bringing together atoms and molecules composing those materials into intimate contact under the action of heat, pressure or both. When the heat supplied is sufficient to cause melting or fusion of the materials being joined, the processes are called fusion welding processes. The melting of the base materials and a filler material, if added, provides a supply of highly mobile atoms at the interface which form the bond upon solidification of the liquid by epitaxial growth of new grains upon the grains of the unmelted base materials. Thus, the bond formation in fusion welding occurs with the participation of the parent materials. The source of heat in fusion welding processes can be chemical, electrical or a high-energy beam (Messler, 1999, p. 40). Chemical sources of heat include exothermic combustion of a fuel gas by air or oxygen. The heat from an electrical arc or resistance heating are examples where electrical energy is the source while high-energy beams provide heat by the conversion of the kinetic energy of the particles in the beam upon collision with the work.

Whatever the nature of the heat source, all fusion welds exhibit distinctly different microstructural regions, depending upon the temperature to which that region was heated. The region of the welded joint where the solidus temperature of the alloy was exceeded and melting or fusion occurred is called the fusion zone (FZ); the locus of points whose peak temperature is equal to the solidus temperature, marks the fusion line. As one moves away from the fusion line, the peak temperatures progressively decrease below the solidus temperature of the alloy, but are above some critical transformation temperature. Here, observable microstructural changes occur due to phase transformations in the solid state, such as recrystallisation and/or grain growth in cold worked materials, or overaging or dissolution of precipitates in age-hardening materials. This region is referred to as the heat affected zone (HAZ). At a distance farther away from the HAZ, no observable microstructural changes occur because the material therein has not been heated to a temperature above a critical transformation temperature; this region is called the unaffected base material.

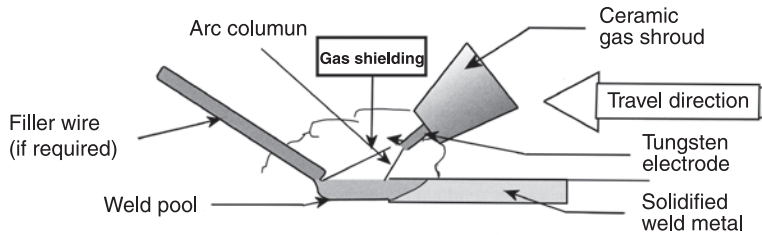


20.8 Classification of fusion welding processes based on energy source.

Figure 20.8 presents the principal fusion welding processes that are used for joining aluminium alloys and the energy sources used by them to bring about fusion. Note that oxy-fuel gas welding and shielded (manual metal) arc welding processes find limited application in the joining of aluminium alloys and will not be discussed here. A brief description of the principal processes that are currently used for fusion welding aluminium and associated recent process developments are discussed in this section. More complete coverage is available in the references at the end of the chapter.

20.3.1 Gas tungsten arc welding

Gas tungsten arc welding (GTAW), shown schematically in Fig. 20.9, uses an electric arc struck between a non-consumable tungsten electrode and the workpiece to generate the heat required for fusion (O'Brien, 1991, p. 70). An inert shielding gas such as argon, helium or a mixture of both is used to shield the tungsten electrode and the weld pool from oxidation. Hence, the process is also referred to as tungsten inert gas welding. The process may be used with or without the addition of filler metal. GTAW may be conducted using either direct current (DC) or alternating current (AC). In the former case, the tungsten electrode may be connected either to the positive or the negative terminal of the power supply resulting in direct current electrode positive (DCEP) and direct current electrode negative (DCEN) modes. With DCEN, 70% of the heat is generated at the anode (workpiece) and 30% at the cathode (electrode); the reverse occurs with DCEP. The higher heat input to the workpiece with DCEN mode results in deeper weld penetration than in the DCEP mode. Conversely, in



20.9 Schematic illustration of gas tungsten arc welding (GTAW) process (source: Mathers, 2002).

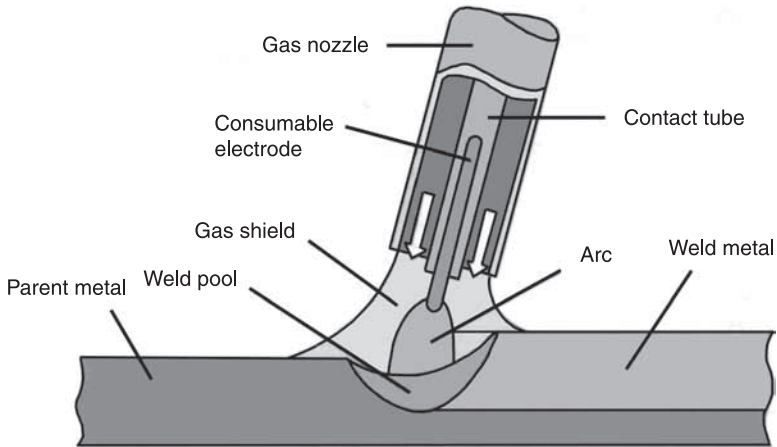
DCEP mode, the higher heat generation at the tungsten electrode means that water cooling of the electrode holder is required. DCEP mode also results in a cathodic cleaning action on the workpiece as a result of the large positive ions that strike the surface, removing the oxide layer present there. This mode is thus important in the joining of aluminium with its ubiquitous oxide layer but the beneficial cleaning action is countermanded by the limited current-carrying ability of the tungsten electrode without overheating it (Oates, 1996, p. 30).

When GTAW is conducted with AC, periodic reversal of the electrode polarity occurs. Thus, AC can combine the cathodic cleaning action of electrode positive with the deep penetration characteristic of electrode negative. When the current decays to zero, different effects occur, depending upon polarity. When the electrode becomes negative, it supplies electrons immediately to reignite the arc; however, when the weld pool becomes negative, it cannot supply electrons until the voltage is raised sufficiently to initiate cold-cathode emission. Without this voltage, the arc becomes unstable. With conventional sinusoidal welding power supplies, some means of arc stabilisation is required during the voltage reversal, such as using a high voltage, high frequency spark in parallel with the arc. Modern welding power supplies designed specifically for GTAW have the capability for square wave AC and for wave balancing, which address this problem with arc instability during AC welding (Oates, 1996, p. 37).

The advantages of GTAW include inherently low-heat input which offers better control of weld filler dilution by the substrate and makes it suitable for welding thin sheets. The excellent shielding offered by argon, helium or their mixtures means that the process is very clean. However, its greatest limitation is its low deposition rate (0.5–1 kg/h; Messler, 1999, p. 55).

20.3.2 Gas metal arc welding

Gas metal arc welding (GMAW), also known as metal inert gas welding (MIG), employs a continuous consumable solid wire as both electrode and filler metal with an inert shielding gas to protect the arc and the weld pool, as shown schematically in Fig. 20.10. The advantages of GMAW include high welding speeds, excellent oxide film removal and capability to weld in all positions. These



20.10 Schematic illustration of gas metal arc welding (GMAW) process (source: Mathers, 2002).

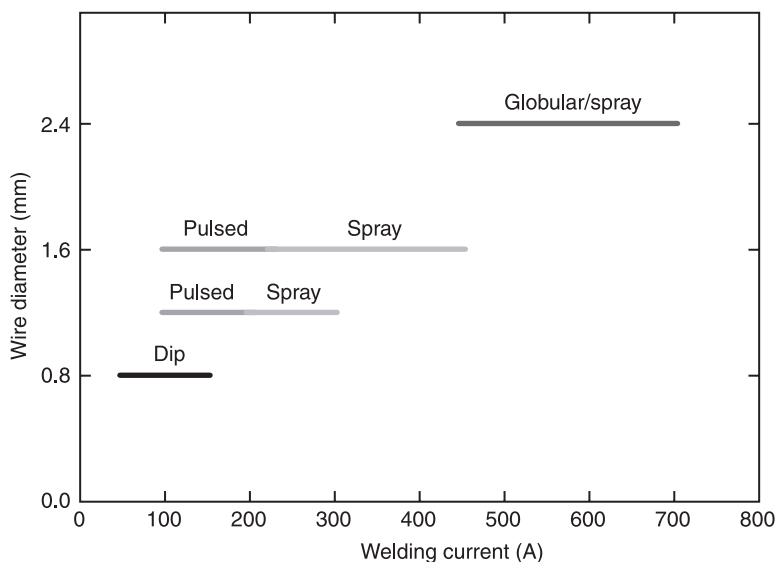
characteristics make it the most widely used manual arc welding process for joining aluminium (Mathers, 2002, p. 116). The shielding gases used are argon, helium or combinations of the two. Argon is most commonly used and produces a smooth, quiet and stable arc. However, argon results in low heat inputs and slow welding speeds. Helium increases the arc voltage by ~20% compared with argon, resulting in a hotter arc, increased penetration and a wider weld bead. The increased heat input also enables faster welding speeds, as much as three times that achieved on a similar joint with argon shielding (Mathers, 2002, p. 130).

Constant voltage DC power sources are used, either with DCEN or DCEP, but the latter mode is more common. In DCEP mode, electrons from the negatively connected workpiece strike the positive wire, give up their kinetic energy in the form of heat and aid the melting of the wire. There is also the added benefit of cathodic cleaning for oxide removal. A distinct advantage of GMAW is the ability to change and control the mode of metal transfer from the consumable metal electrode by using an appropriate combination of shielding gas composition, power source type, arc current and voltage and wire feed rate (Mathers, 2002, p. 118). The three principal metal transfer modes are spraying, globular and short-circuiting (also known as dip-transfer). When welding at low currents, the tip of the continuously fed filler wire may not melt fast enough to maintain the arc, but may dip into the weld pool and short circuit. This causes the wire to melt and the molten metal is drawn into the weld pool by surface tension effects. The arc re-establishes itself and the cycle continues. This is known as the dip-transfer or short-circuiting mode of metal transfer. The low currents required for this mode enable the welding of thin sections without melt-through and out-of-position welding is facilitated by the direct transfer of molten metal through contact. However, excessive spatter may be produced if welding parameters are not

correctly adjusted. At higher currents, the filler metal is melted from the wire tip and transferred across the arc in the form of fine, discrete molten particles or droplets. The metal transfer is very stable, directional and essentially free of spatter. During GMAW of aluminium, spray transfer occurs down to relatively low currents because of its low melting point, resulting in a spatter-free joint.

Rather than using constant currents and dip transfer mode during welding, it is also possible to weld using a pulsed-current process, in which intermittent, high-amplitude pulses are superimposed on a low-level steady current that maintains the arc. The background current is insufficient to melt the filler wire but the pulse of high current melts the wire and projects this as a spray of droplets of a controlled size across the arc giving excellent metal transfer at low average welding currents. Figure 20.11 shows typical welding current ranges for various metal transfer modes for a range of wire diameters.

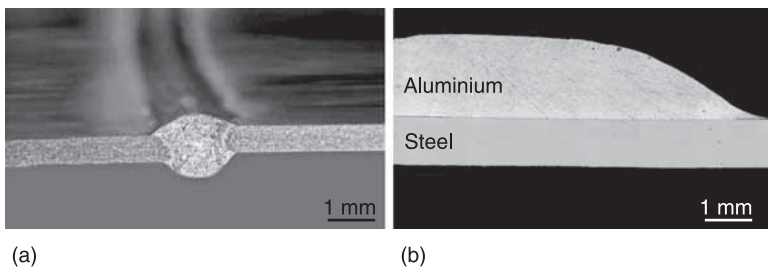
The need for higher productivity, represented by high deposition rates, has resulted in some new developments in GMAW. These include welding with large cross-section wires/strips and tandem welding with twin wires (Trommer, 2009). In principle, high deposition rates are possible by increasing the wire feed rate. However, there is a limit to the highest wire feed rate that can be used, particularly in the case of aluminium alloys. In aluminium welding, a deposition rate of 4 kg/h has been achieved using strips of cross-section 4 mm by 0.6 mm and 5 kg/hr using wires of 3.2 mm in diameter. Welding with these higher cross-section wires/strips has been made possible by the development of a high performance power source that can deliver the desired amperage and/or duty cycle (e.g. 900 A at 60% duty



20.11 Variation in metal transfer mode with welding current for various wire diameters (Source: Mathers, 2002).

cycle); this power source is made up of two single power sources working in a power-sharing mode (Trommer, 2009). In the case of twin wire GMAW, two independent arcs operating in the same weld pool enable major improvements in productivity. Here as well, two inverter-based power sources coupled in series are used, each with its own microprocessor control unit and wire feeder. All the above processes are used in a mechanised or robotic application.

Cold metal transfer (CMT) is a new GMAW technology for automated and robot-assisted applications in which reduced thermal inputs lead to low distortions and higher precision (Fronius International GmbH, 2008; Zhang et al., 2009). The CMT process is based on the dip-transfer arc; however, three striking criteria differentiate the CMT process from the familiar dip-transfer arc-process: the wire motions are incorporated into the process-control; the thermal input is diminished, and the metal transfer takes place without spattering. A precisely controlled oscillating motion with a frequency up to 70 Hz is superimposed on the forward motion of the wire. The associated wire retraction assists droplet detachment during the short circuit and the metal can transfer into the weld pool without the aid of the electromagnetic force. Higher quality joints, free from spatter, can be produced by CMT but the most significant advantages are that thin gauge sheet, down to 0.3 mm thick, can be welded and aluminium-to-steel joining can be achieved. Figure 20.12(a) shows the cross-sectional view of a butt weld between two 0.8 mm thick sheets of AlMg3 (AA 5754), while Fig. 20.12 (b) presents the cross-sectional view of the weld bead in a fillet joint between steel and aluminium (Fronius International GmbH, 2008). It should be noted that the dissimilar joining of aluminium to steel is not straightforward by conventional fusion welding methods, both due to the large disparity in the melting points of these two materials and the formation of brittle Fe-Al intermetallics, which cause weld cracking. During CMT, the aluminium workpiece and filler metal both melt, creating a melt which wets the steel surface, which does not melt. In effect, a welded joint is formed on the aluminium side and a brazed joint on the steel side (Fronius International GmbH, 2008). CMT

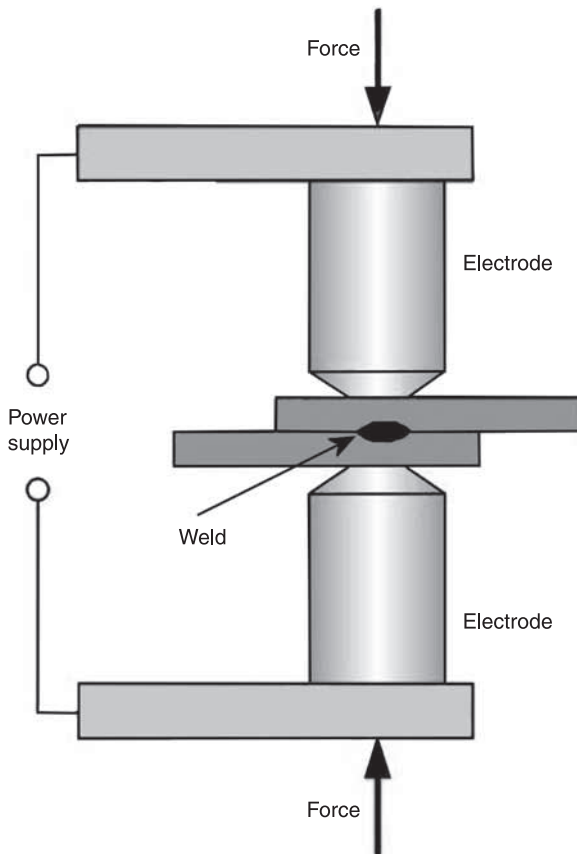


20.12 Macrographs showing the cross-sectional views of joints produced using CMT: (a) Butt weld between two AlMg3 (AA 5754) aluminium sheets, 0.8 mm in thickness; (b) fillet weld between an aluminium alloy and steel (courtesy: Fronius International GmbH, Austria).

technology has already found application in the automotive and allied sector: Audi has recently announced the first use of CMT welding process in the fabrication of the tail lights for the Q5 model's aluminium tailgate (Rügheimer, 2009).

20.3.3 Resistance welding

Resistance welding processes are a group of fusion welding processes in which the heat for fusion is generated by the resistance to the flow of electric current through the parts being joined. As shown in Fig. 20.13, contact resistance at the faying surfaces of the parts heats the area locally by Joules (I^2R) heating, resulting in melting and the formation of a nugget (Oates, 1996, p. 72; Mathers, 2002, p. 166). The processes require the application of both heat and pressure to achieve a sound joint. Pairs of water-cooled electrodes, usually made of copper or copper alloyed with refractory metals, conduct current to the joint, apply



20.13 Schematic illustration of the resistance spot welding process.

pressure by clamping to improve contact and reduce contact resistance at the electrode-workpiece interface and help to contain the molten metal in the nugget. The main process parameters are the currents used which are quite high, of the order of several thousands to tens of thousands of amperes, and the electrode force and shape. A great advantage of the processes is the very low cycle time, of the order of a few milliseconds.

There are a number of variants of the resistance welding process, which include spot, seam, projection and butt welding. Many of these processes (with the exception of butt welding) are used for joining overlapping sheets of material, which may have different thicknesses. The simplest of these, and perhaps the most widely used, particularly in the automotive industry and especially for joining steel sheets, is the spot welding process. The process is economical, easily automated and ideally suited for large volume production. Seam welding is used in the production of thin sheet, leak tight containers such as fuel tanks.

However, application of the process to join aluminium alloys is not as straightforward as with steels. The high electrical conductivity of aluminium alloys ($\sim 35 \text{ m}/\Omega\text{mm}^2$ for pure aluminium and $\sim 15 \text{ m}/\Omega\text{mm}^2$ for aluminium alloys at 20°C versus $\sim 9 \text{ m}/\Omega\text{mm}^2$ for low alloy steels) means that high welding currents, about twice that required for joining steels of equivalent thickness, and large capacity equipment are required (Dorn, 1994b). The thin, tenacious oxide layer on the surface of aluminium and alloys is a non-conductor of electricity and must be removed by mechanical or chemical methods. The direct contact of the oxide layer with the electrode leads to an accumulation of heat at the electrode-workpiece interface, and metal pick up on the electrode, drastically reducing the electrode life unless cleaned often. Another factor that contributes to short electrode life is the fact that the copper from the electrode alloys with the aluminium workpiece, resulting in rapid wear. Despite this, the process has nevertheless been used in the automotive industry in large volume production, for instance, in the fabrication of the lightweight spot welded all-aluminium tail gate of General Motors Yukon (European Aluminium Association, 2009).

Five types of power sources are commonly used for joining aluminium: single phase AC or DC machines; three phase DC machines with either primary or secondary rectification, and inverter units with secondary rectification (Mathers, 2002, p. 167). The choice of equipment is made based on factors such as the primary current available, the output current required, the amount of space required between and around the electrodes, whether portability is required and as always, the cost of the equipment.

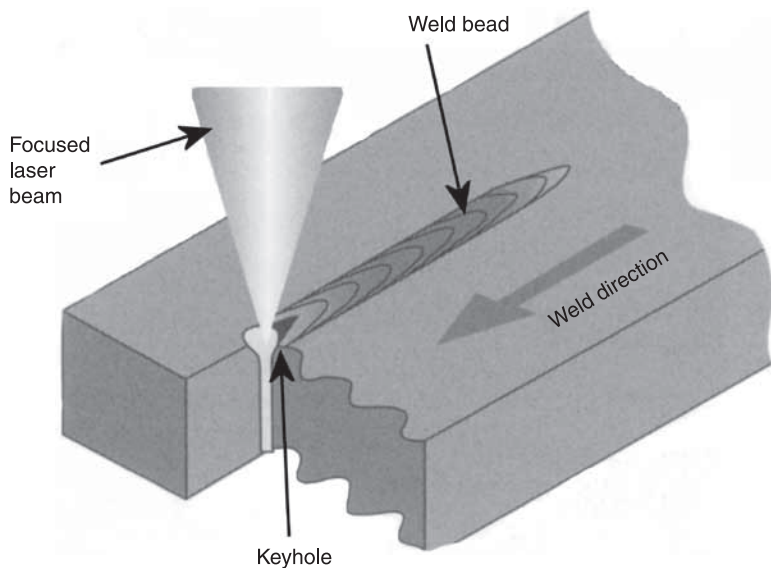
Weldbonding

Weldbonding is a hybrid joining process that combines spot welding with adhesive bonding (see Section 20.6) to take advantage of the benefits of each process: the high joint efficiency, resistance to diverse and complex loading, and temperature

tolerance of welding; the load-spreading, stress concentration-softening and structural damage tolerance of adhesive bonding (Messler, 2002). In this process, the adhesive is placed between the parts to be joined and resistance welds are then made through the adhesive layer. The adhesive is then allowed to cure either at room temperature or in an oven. The spot welds hold the joint together while the adhesive is curing. The electrode force during welding squeezes the adhesive at the spot weld location, creating a current path through the sheets. Weldbonding improves the fatigue life and durability of joints over that obtained by spot welding alone, provides protection from galvanic corrosion, and is used in the aerospace and transportation industries. Disadvantages include additional costs of adhesive, added curing operation, time and labour costs for the adhesive bonding. Premature curing of the adhesive can increase the resistance between the faying surfaces and result in excessive heating and associated problems during spot welding.

20.3.4 Laser welding

Laser welding is a fusion welding process in which the heat generated by a high-energy-density photon (light) beam produces melting (Oates, 1996, p. 71; Mathers, 2002, p. 150). Since the laser beams can be focused very sharply, a smaller volume of metal is melted and less heat energy goes into the workpiece. The concentrated, high-energy-density heat source enables the weld to be made in the keyhole mode (Fig. 20.14), improving the absorption of the laser beam due to reflections within



Molten metal flows around keyhole and recombines to form weld

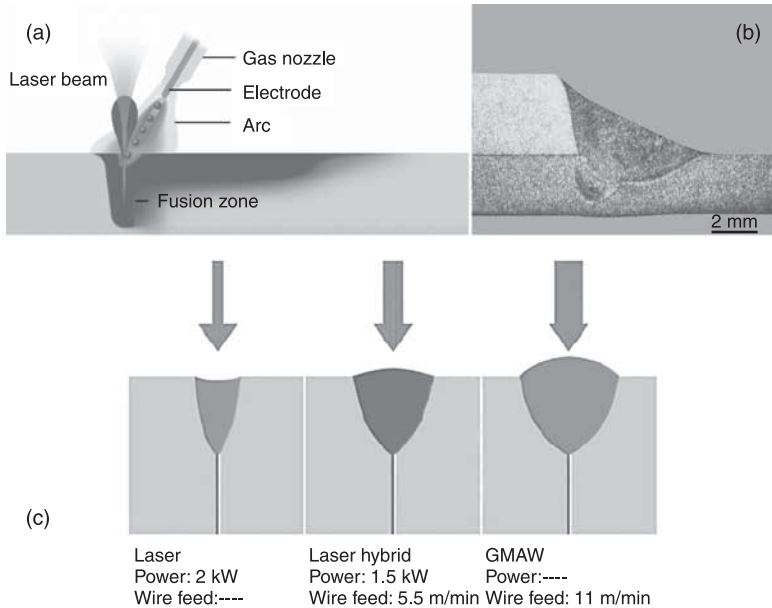
20.14 Schematic of keyhole laser welding (source: Mathers, 2002).

the cavity. The deeply penetrating keyhole weld produces a very narrow weld, and a correspondingly narrow HAZ, as compared to arc welding. This minimises both distortion and the loss of strength observed in the HAZ of both heat treatable and non-heat treatable aluminium alloys (discussed further in Section 20.3.5). A further advantage is the minimisation of the loss of low boiling point alloying elements in aluminium alloys such as Mg and Zn. The high-energy beam also enables very fast welding speeds to be achieved thus improving productivity.

Laser welding is being increasingly used for joining aluminium alloys, both in the aerospace and the automotive industries. The major difficulty in laser welding of aluminium alloys is that aluminium does not couple well with the 1.06 μm wavelength light emitted by the Nd:YAG laser or the 10.6 μm wavelength emitted by the CO_2 laser (Oates, 1996; Mathers, 2002). This means that the laser beam tends to get reflected, rather than being absorbed by the workpiece, thus not contributing to its melting. Furthermore, once a weld pool is established, the reflectivity goes down dramatically, resulting in a power density that is too high. However, development work carried out mostly for and by the automotive industry, has addressed these problems by improved focusing of the beam and by development of control systems which can vary the energy input to compensate for the reflectivity change when the weld pool is established. A recent Audi Press Release describes the extensive use of laser welding in its sports cars, Audi TT and Audi R8, as follows: 'Laser welding allows large sheet panels to be joined perfectly to the body structure because its linear connecting seams are stronger and more rigid than individual weld points. In the TT, laser welding is used for high-precision invisible aluminium joints between the roof and the side panel as well as for the major welds in the sill area. Together they are 5.30 metres long. The Audi A8 sedan has more than 20 meters of such welds' (Rügheimer, 2009). The aerospace industry also has successfully used laser welding for 2xxx and 6xxx alloys in many applications and success has also been reported in the laser welding of the Al-Li alloys 2090 and 2091 (Oates, 1996, p. 71). Clearly, laser welding of aluminium alloys has come a long way.

Laser hybrid welding

The quest for high-performance welding processes has resulted in a number of relatively recent new developments in which the laser has been combined with the arc from a conventional welding power source. Although GMAW, GTAW and plasma-arc processes have been used, GMAW has been the preferred fusion welding process (Staufer et al., 2008). Figure 20.15(a) illustrates the principle of laser hybrid welding and a sectional view of a laser-hybrid joint made between two sheets of AlMgSi (AA 6082) is presented in Fig. 20.15(b). The laser hybrid process combines the advantages of each process, while their respective disadvantages disappear. As we have seen, laser welding is characterised by a very narrow HAZ, a high ratio of weld penetration depth to weld width, and high



20.15 (a) Schematic representation of laser hybrid welding; (b) macrograph showing cross-sectional view of a lap weld between two sheets of AlMgSi1 (AA 6082), 2 mm and 1.5 mm thick, respectively, made using AlSi5 filler wire, 1.6 mm diameter, at deposition rate of 1.7 kg/h; (c) comparison of the weld bead profiles for laser welding, laser hybrid welding and GMAW; weld penetration depth and travel speed were held constant (schematic illustrations and photo courtesy Fronius International GmbH, Austria).

welding speeds; however, it has a low ability to bridge gaps so that tight fit up tolerances are essential. In contrast, the low-energy-density GMAW process produces a distinctly larger weld pool and has much better ability to bridge gaps. Both processes act simultaneously at the same process zone. As shown in Fig. 20.15(c), the laser hybrid process can achieve the same weld penetration using half the wire feed speed used by GMAW when used on its own and a lower power level than that used by the laser welding process, on its own (Staufner et al., 2008). In addition, the laser hybrid process can tolerate greater variations in fit-up.

20.3.5 Metallurgical considerations in fusion welding

The microstructure, mechanical properties and performance of fusion welded joints of aluminium alloys (as indeed of any metal alloy) are influenced by many factors, including the composition, form and temper of the base metals, the filler metal used, the welding process and parameters, joint design, post-weld mechanical or thermal treatments and the service environment (Oates, 1996,

p. 100). As discussed earlier, a fusion-welded joint consists of three distinct zones: the FZ, the HAZ and the unaffected base material, depending upon the thermal history experienced. The properties of the FZ are influenced by the composition of the weld metal and the rate of solidification, which in turn is controlled by the welding process and the parameters used. The weld metal has an as-cast structure consisting of a mixture of the filler metal if added, and the parent metal(s); thus its composition is dependent upon the composition of the parent metal and the filler wire. A higher rate of solidification generally produces a finer microstructure with better mechanical properties.

Porosity is a problem that is confined to the weld metal and arises from the gas dissolved in the molten weld metal becoming trapped as it solidifies. The primary source of porosity in aluminium welds is hydrogen, which has a high solubility in molten aluminium, but negligible solubility in the solid state. As a result, it is extremely difficult to produce a porosity-free weld in aluminium. Hydrogen can be introduced into the weld metal from residual hydrocarbons or hydrated oxides on the surfaces of base and filler metals as well as from faulty welding equipment or improper gas shielding that permits moist atmospheric contamination. To achieve low levels of porosity, it is essential that bare filler wire is properly cleaned and stored in a dry environment until needed for production, and the base metal is thoroughly degreased, followed by mechanical cleaning such as stainless steel wire brushing. The shielding gas used should have a dew point less than -50°C .

Hot cracking is another problem that is often observed in aluminium alloy fusion welds and is a function of how the metal alloy solidifies. Hot cracking occurs at high temperatures, while the weld metal is solidifying and hence it is also known as solidification cracking, hot fissuring or centre line cracking (since the cracking is usually observed along the weld centre line). The addition of alloying elements to aluminium causes it to solidify over a range of temperatures; if the temperature range is large, then a liquid film is still present at the inter-dendritic regions as the weld metal cools and contracts. The shrinkage stresses associated then cause cracking to occur in these regions. All aluminium alloys are susceptible to hot cracking and only differ in their degree of susceptibility. Non-heat treatable aluminium alloys with low-Mg contents (<2.5 wt.%) and most alloys of the 2xxx and 7xxx series show a high susceptibility to cracking which limits their fusion weldability. Various approaches have been developed to eliminate hot-cracking problems in aluminium weld metals. These include the control of the weld pool composition by appropriate choice of a filler metal, addition of grain refiners such as Ti and Zr to the filler to refine the weld metal grain size, using the highest weld speed possible to reduce the time the weld metal is in the hot short temperature range, using welding and assembly sequences that minimise restraint and residual stresses, etc.

We have noted earlier that the HAZ spans the region in a fusion-welded joint between the fusion line (delineated by the locus of points that have been heated to

the solidus temperature of the alloy) and the unaffected base material (delineated by the locus of points that have been heated to a critical temperature where observable microstructural changes occur). Thus, by its very definition, HAZ represents a region in a fusion-welded joint which is expected to display properties radically different from those of the unaffected base material. This is particularly the case for aluminium alloys that have been strengthened by either cold working or precipitation hardening. The cold worked alloys will experience a strength loss in the HAZ due to recrystallisation, which is expected to begin to occur in the region that has been heated to about 200°C and progressively increases, with full annealing being observed at regions that have been heated to 300°C and higher. Grain growth will also occur as one gets closer to the fusion line. A similar but more complex effect is observed in the HAZ of heat treatable alloys. Here, the loss in strength is caused by dissolution of precipitates in 2xxx series alloys and a coarsening or overageing of precipitates in 6xxx and 7xxx alloys.

20.4 Solid state welding

Solid state welding processes are a group of processes that accomplish joining at the faying surfaces of parts, principally but not exclusively, through plastic deformation of the parent material(s) due to the application of pressure, at temperatures below their melting point, without the addition of a filler material that melts (Messler, 1999, p. 94). A metallurgical bond is produced, with assistance from solid state diffusion. Some heat is generated by the process or supplied externally, which enables plastic deformation to occur at lower stresses, without any melting occurring. The energy sources for solid state welding processes are generally mechanical in nature, either directly the pressure applied or derived from frictional forces. Heat and pressure, either individually or in combination, together with time, bring about coalescence at the faying surfaces of the part being joined.

Solid state welding processes offer several advantages over fusion processes (Messler, 1999, p. 95). As no melting occurs generally and the heat input is lower than in fusion processes, there is less disruption to the microstructures of the materials being joined and hence less effect on their properties. Problems of hot cracking and porosity, as well as a cast solidification microstructure at the weld, are avoided. In the absence of fusion, intermixing of the materials involved tends to be minimal on a macroscopic scale in most of these processes, and so materials of dissimilar compositions can often be joined. However, there are process disadvantages as well: most of the processes require stringent cleaning of the joint faying surfaces; elaborate tooling and specialised equipment, rarely portable, are required. Furthermore, most processes are automated which can be both an advantage and a shortcoming. There are also difficulties with quality monitoring and inspection, and repairing of defective joints.

This group of welding processes includes cold welding, hot pressure welding, forge welding, roll welding, explosion welding, friction welding, ultrasonic welding, magnetic pulse welding and diffusion welding. It is interesting to note that some of the oldest welding processes ever used are solid state processes (forge welding) as also some of the newest (friction stir welding). In this section, we examine briefly the solid state welding processes that are commonly used in the joining of aluminium alloys.

20.4.1 Cold welding

As the name suggests, cold welding (CW) is performed without the addition of heat. An external pressure is applied to the two parts being joined, resulting in substantial plastic deformation. Accordingly, a fundamental requirement of CW is that at least one of the materials being joined is ductile and does not display significant work hardening. As such, commercially pure aluminium and some of its alloys are well suited to CW. CW can be conducted in both butt and lap configurations (Iordachescu, 2009; Sahin, 2008). In the butt mode, the metal expelled from the joint during welding has to be removed mechanically. The plastic deformation occurring in the butt mode breaks up the oxides on the surface and these are also expelled with the flash. Thus, pre-cleaning of the faying surfaces is not as critical for butt joints, but in lap joints, surface cleaning is crucial, usually degreasing followed by wire brushing is carried out. It is also important that there is little delay between the cleaning and CW.

While CW does not produce a HAZ, it does produce a mechanically affected zone (MAZ) at the bond region, where the material has been subjected to strain hardening as a result of the imposed plastic deformation (Iordachescu, 2009). Tensile testing of samples from a butt joint of commercially pure aluminium, designed to fail at various regions in the MAZ has shown that the tensile strength of the bond is higher than that of the base material, and that in a standard tensile test, failure occurs away from the bond line, in the unaffected base material (Iordachescu, 2009).

Aluminium alloys of the 2xxx and 7xxx series, which cannot be fusion welded due to their tendency for hot cracking, can be successfully cold welded in the butt configuration. Butt and mitre joints can be made in most aluminium alloy wire, rod, tubing and simple extruded shapes. An upset distance of approximately 1.5 times the material thickness is required for butt joints in soft annealed alloys; higher strength alloys require greater upset distance, about 4–5 times the material thickness (Oates, 1996, p. 80). Welds in lap joints require a thickness reduction of about 70% at the weld location (Sahin, 2008).

20.4.2 Explosion welding

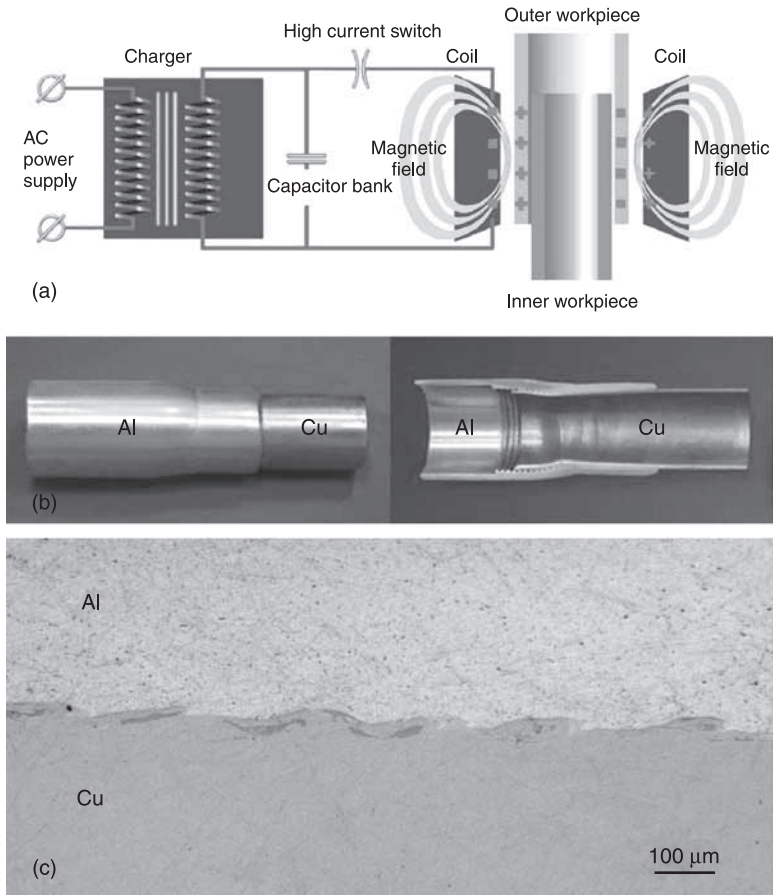
Explosion welding uses energy from the detonation of an explosive to produce a solid state weld (O'Brien, 1991, p. 766; Messler, 1999, p. 103). The controlled

detonation of a properly placed and shaped explosive charge causes the properly aligned workpieces to come together extremely rapidly, at a low contact angle. When this occurs, the air between the workpieces is squeezed out at supersonic velocities. The resulting jet cleans the metal surfaces of oxides and causes highly localised rapid heating to high temperatures. The high strain rate deformation occurring at the immediate vicinity of the impacting parts, caused additional heating. The clean surfaces are compressed together under high pressure from the explosion, which promotes the formation of a metallurgical bond. The bond zone of an explosion weld has a characteristic wavy appearance, reflecting the severe, highly localised plastic deformation occurring in the process. Explosion welding is limited to lap joints and to cladding of parts with a second metal. The process is used for cladding carbon steel, stainless steel, copper or titanium with aluminium. Explosion welded bi-metallic sections are often used as transition segments. Conventional fusion welding is used to weld similar metal on each side of the segment. In effect, aluminium to steel joining is achieved, without the problems associated with joining these two metals directly to each other.

20.4.3 Magnetic pulse welding

Magnetic pulse welding (MPW) is analogous to explosion welding in that the high velocity impact and jet phenomenon occur, but the energy required is produced by magnetic pulses, rather than by controlled explosion (Aizawa et al., 2007; Shribman, 2007; Faes, 2009). A typical MPW system, shown in Fig. 20.16(a), consists of a power supply which contains a bank of capacitors, a fast switching system and a coil. The parts to be joined are inserted into the coil, the capacitor bank is charged, and the low inductance switch is triggered by a pulse trigger system causing the current flows through the coil. When current is applied to the coil, a high-density magnetic flux is created around the coil, and as a result an eddy current is induced in the workpieces. The eddy currents oppose the magnetic field in the coil and a repulsive force is created. This force drives the workpieces together at an extremely high velocity and creates an explosive or impact type of weld. The process is ideally suited for metals with high conductivity, such as aluminium and copper. As a solenoid coil is used, the process is limited to tubular parts, but in a recent development either a double layer H-shaped coil or a single layer E-shaped coil is used for joining flat, overlapping sheets of aluminium and steel (Aizawa et al., 2007).

MPW displays the advantages of a solid state welding process: the ability to join dissimilar materials and no HAZ. The welding speed is very high as the complete weld is made in milliseconds. The power demand is low and the process is claimed to have excellent reproducibility. Potential applications in the automotive industry include welding of aluminium fuel filters, tubular seat components involving both steel and aluminium materials, drive shafts and hydroformed parts (Kochan, 2000).



20.16 (a) Magnetic pulse system layout; (b) a copper tube welded coaxially to an aluminium tube by magnetic pulse welding (courtesy Pulsar Ltd., Israel); (c) cross-sectional view of a copper to aluminium magnetic pulse weld (courtesy Research Centre of the Belgian Welding Institute, 2008).

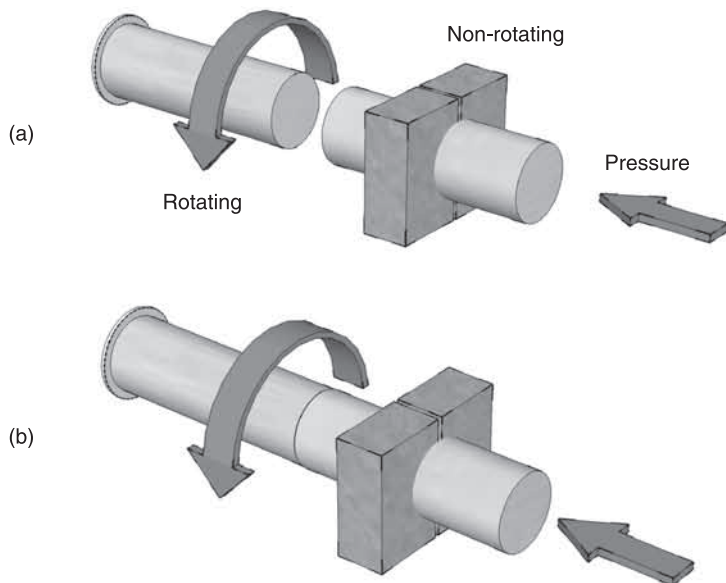
Figure 20.16(b) shows an aluminium tube that has been welded to a copper tube placed coaxially within it, by MPW. As seen in the optical micrograph in Fig. 20.16(c), a wavy, metallurgical bond has been formed between the two dissimilar materials.

20.4.4 Friction welding

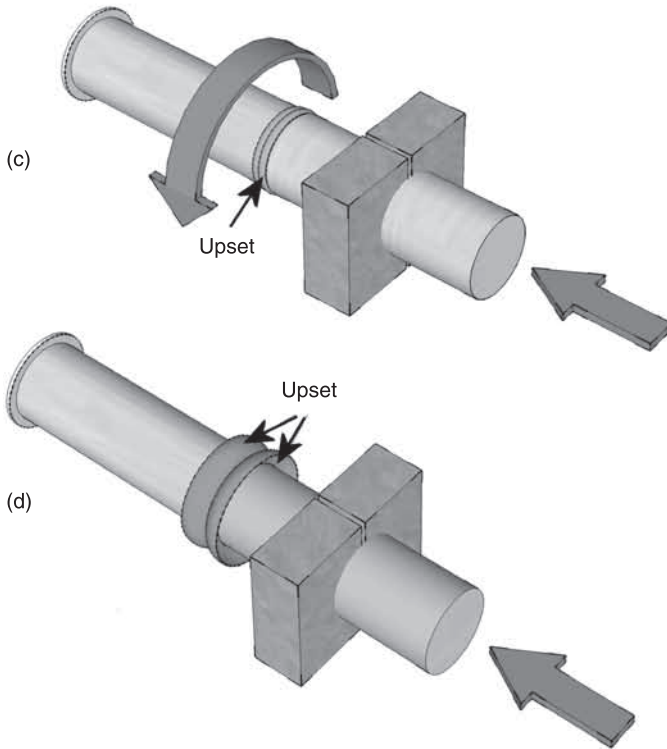
Friction welding is a solid state joining process, which is based on the conversion of mechanical energy into heat at the faying surfaces of the parts being joined by causing relative movement between them while in intimate contact under a

compressive force (O'Brien, 1991, p. 740). The relative movement may be achieved by rotation or by angular or linear reciprocation. Figure 20.17 displays schematically the basic steps involved. The process begins by rotating one workpiece while the other is held stationary (Fig. 20.17a). When the required rotational speed is attained, the two workpieces are brought in contact, as shown in Fig. 20.17(b). Frictional heating occurs at the interface and softens the materials at its vicinity, and upsetting starts, Fig. 20.17(c). A hot forging action occurs under the applied compressive force, forming a metallurgical bond at the interface, as shown in Fig. 20.17(d). The rotation is stopped and the upsetting is completed. The weld produced has a narrow HAZ, a plastically deformed zone adjacent to the bond and no FZ. The plastically displayed material or flash may be removed in a later operation if a smooth surface is required.

The most common form of friction welding uses rotary motion and is best suited for joining circular parts in rod, bar, tube and pipe form (O'Brien, 1991, p. 740). Linear friction welding, based on a linear reciprocating motion has also been successfully used to join aluminium parts without circular symmetry. However, the process is not capable of welding longitudinal seams in a flat plate. Most aluminium alloys can be joined by friction welding, including those belonging to the 7xxx series which are not fusion weldable because of their cracking susceptibility (Oates, 1996, p. 81). Pre-weld cleaning is not as critical as for other welding processes as the rubbing action at the interface breaks up the



20.17 (a)–(d) Schematic of the basic steps involved in friction welding (courtesy FPE & Gatwick Fusion 2009).

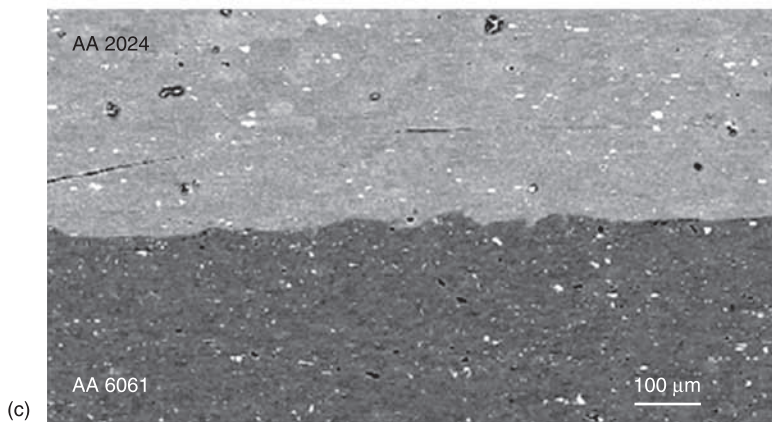
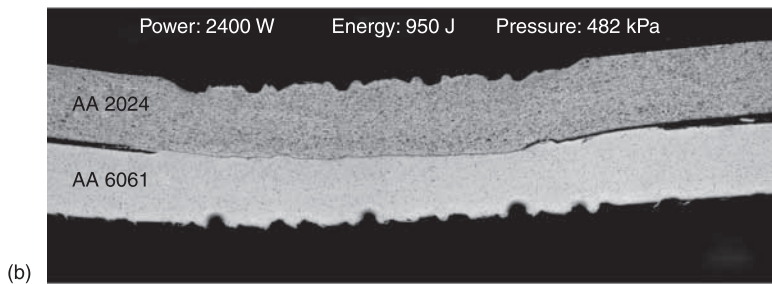
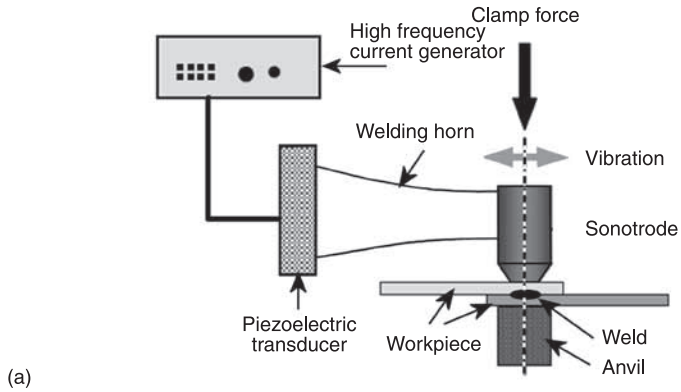


20.17 Continued.

oxide layer and exposes clean metal. Joint strength approaching that of the base material can be obtained, even for these high strength heat treatable alloys. The process also enables joining of aluminium to other metallic materials: two widely used combinations are aluminium to copper alloy joining, used in the electrical industry, and aluminium to stainless steel joining, used for producing transition couplings in piping systems and pressure vessels (Oates, 1996, p. 81).

20.4.5 Ultrasonic welding

Ultrasonic welding (UW) accomplishes joining by the local application of high frequency, low amplitude vibratory motion to the workpieces. The process has been used to join foils and sheet gauges of aluminium alloys, as well as to join thin wires to sheet and foil. Figure 20.18(a) shows the basic process set up for making spot welds in metals (Feng and Diamond, 2004). An electromechanical converter (such as a piezoelectric transducer) converts high-frequency electric current to mechanical vibrations. The mechanical vibration is then modulated and amplified



20.18 (a) Schematic illustration of an ultrasonic welding setup; (b) macrograph showing a low magnification cross-sectional view of an ultrasonic weld made between overlapping sheets of AA 2024 and AA 6061; (c) higher magnification scanning electron micrograph showing the nature of the bond between the two sheets (Feng and Diamond, 2004).

by the booster/horn before it is applied to the workpiece through the sonotrode. A moderate clamping force is applied to ensure that the mechanical vibration is transferred to the sheet-to-sheet interface (the faying surface), where the weld is created. Typically, the mechanical vibration is at 20–40 kHz with an amplitude range of 5–50 μm . The power delivered to the workpiece is in the range of several hundred to several thousand watts, although more powerful UW power sources are being developed (Feng and Diamond, 2004).

UW is essentially a variation of friction welding. The lateral mechanical vibration of the sonotrode causes a small amount of relative motion between the workpieces at the interface, and together with the clamping pressure, breaks the surface oxides and other contaminants. As a result, clean metal surfaces are brought into contact under pressure. Frictional heating at the bond interface promotes both localised deformation and diffusion in the region where the pressure is applied. As in other friction welding processes, metallurgical bonds can be obtained without melting at the bonding interface. The self-cleaning nature of UW and its ability to form metallurgical bonds without melting are both important advantages of the process (Feng and Diamond, 2004; Oates, 1996, p. 80). Figure 20.18(b) shows the cross-sectional view of an ultrasonic weld made between overlapping 1 mm thick sheets of AA 2024 and AA 6061 aluminium alloys. A good metallurgical bond formed over an area slightly larger than the circular impression left by the sonotrode (indicated by the roughening of the upper surface of the AA 2024 sheet by the knurled surface of the sonotrode). The wavy nature of the bond formed is visible in the higher magnification image of the weld interface, shown in Fig. 20.18(c).

The top sheet thickness limit in lap joint UW is 1.5 mm, although spot welds have been made in thicknesses up to 3.2 mm (Oates, 1996, p. 80). The process is not suitable for joining thicker sections. All aluminium alloys can be ultrasonically welded, but the degree of weldability varies with the alloy and temper. In common with other solid state welding processes, dissimilar joining of aluminium to other metals is possible with this process.

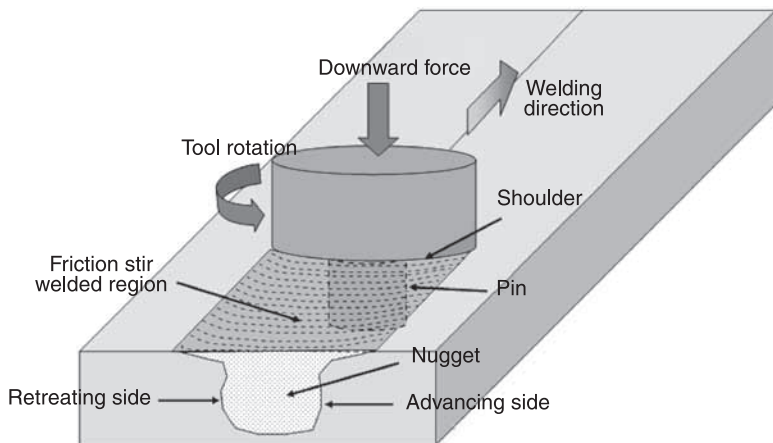
20.4.6 Friction stir welding

Friction stir welding (FSW) is undoubtedly the most significant new development for the joining aluminium and its alloys. This solid state welding process was invented by The Welding Institute (TWI), UK, in 1991 (Thomas et al., 1991). A recent comprehensive review of the FSW of aluminium alloys has referred to it as a ‘radically new joining process’ (Threadgill et al., 2009) and this appears to be an apt description. Research and development in FSW has burgeoned since 1991, as evidenced by the fact that by the end of 2007, TWI had issued 200 licences for use of the process; 1900 patent applications had been filed and the number of research publications has grown exponentially (Threadgill et al., 2009). We commented earlier on the general trend where joining technologies developed for

other materials, in particular steels, were adapted for the joining of aluminium alloys. In contrast, FSW was first applied for joining aluminium alloys, and subsequently developments are ongoing to apply it to other materials such as copper alloys, magnesium alloys, steels, nickel alloys and titanium alloys.

It would be impossible to do justice to the large body of information available on FSW in general, and its application to aluminium alloys in particular, in this chapter. As with other joining processes a brief description of the process and its advantages and disadvantages will be presented. For more detailed information on FSW, the reader is referred to the aforementioned review (Threadgill et al., 2009) as well as to a number of excellent general reviews of FSW (Mishra and Ma, 2005; Mishra and Mahoney, 2007; Nandan et al., 2008).

The basic concept of FSW is remarkably simple. Figure 20.19 illustrates the main features of the process and also defines the terminology used to describe these features. A non-consumable, rotating tool with a cylindrical shoulder and a specially profiled pin is plunged into the joint line between two abutting or overlapping workpieces. The tool serves three primary functions: heating of the workpieces, movement of material to produce the joint and containment of the hot metal beneath the tool shoulder. Heat is generated at the workpieces, both due to the friction between the workpieces and the rotating tool pin, and by the severe plastic deformation of the workpieces. The localised heating softens the material around the pin, without reaching the melting point. The tool rotation and translation along the joint line causes the softened material to move from the front to the back of the pin, thus filling the hole left by the pin and forming a solid state joint. As shown in Fig. 20.19, the side of the weld for which the tool moves in the same direction as the traversing direction is called the ‘advancing side’; the other side where tool rotation opposes the traverse direction is referred to as the ‘retreating side’. The process is thus asymmetrical, as most of the



20.19 Schematic illustration of friction stir welding (Mishra and Ma, 2005).

deformed material is extruded past the retreating side of the tool. Joining is accomplished by the combined action of heat and deformation, but there is no bulk fusion; thermocouple measurements and microstructural evidence indicate that during FSW of aluminium, temperature stays below 500°C (Threadgill et al., 2009). Tool design has a critical effect on the microstructure and mechanical properties of friction stir welds. The main process parameters are the tool rotational speed and the traverse speed.

The main advantages of FSW are summarised in Table 20.1. Some of these advantages can be viewed as shortcomings in certain circumstances, and these

Table 20.1 Advantages and limitations of FSW

Advantages	Disadvantages
<ul style="list-style-type: none"> • FSW, as a solid state process, can be applied to all the major aluminium alloys including hard-to-fusion weld alloys of 2xxx, 7xxx and 8xxx series. • Avoids problems of hot cracking, porosity, etc. common to fusion welding. • Mechanised process, no specialised welding skills required. • No shielding gas or filler wire required. • Remarkably tolerant to poor quality edge preparation: gaps up to 20% of plate thickness can be tolerated. • Absence of fusion leads to significant reduction in distortion. • Welding in any position; both butt and lap geometries. • Excellent mechanical properties. • Workplace friendly: no ultraviolet or electromagnetic radiation hazards, zero spatter, fume. • Energy requirements fall between those for laser welding and GMAW. • High welding speeds and high joint completion rates: single pass welding for a wide range of sheet thickness (0.5–50 mm or more). 	<ul style="list-style-type: none"> • Absence of filler wire means process cannot be easily used for fillet welds. • Lacks flexibility of manual processes when access is difficult or complex weld shape is required. • Presence of a hole at the end of weld may be a disadvantage, but solutions have been devised. • Workpieces need to be restrained in well-designed support tooling to react to the applied forces and to prevent the probe from pushing the workpieces apart. • Efficient power consumption is dependent on matching machine size with the size of the weld, but this is not always practical.

Source: Threadgill et al. (2009)

have also been listed. The process is now mature and robust and is becoming increasingly well established in the fabrication of critical components made from aluminium alloys in the marine, aerospace, rail and automotive industries. The first major application of FSW in the aerospace sector was in the welding of fuel tanks for the Delta II and later Delta IV rockets (Threadgill et al., 2009). The manufacturer, Boeing, reported virtually zero defect incidence and significant cost savings over the previous variable polarity plasma arc process. The process has also been used in the fabrication of the large fuel tank for the space shuttle.

Friction stir spot welding

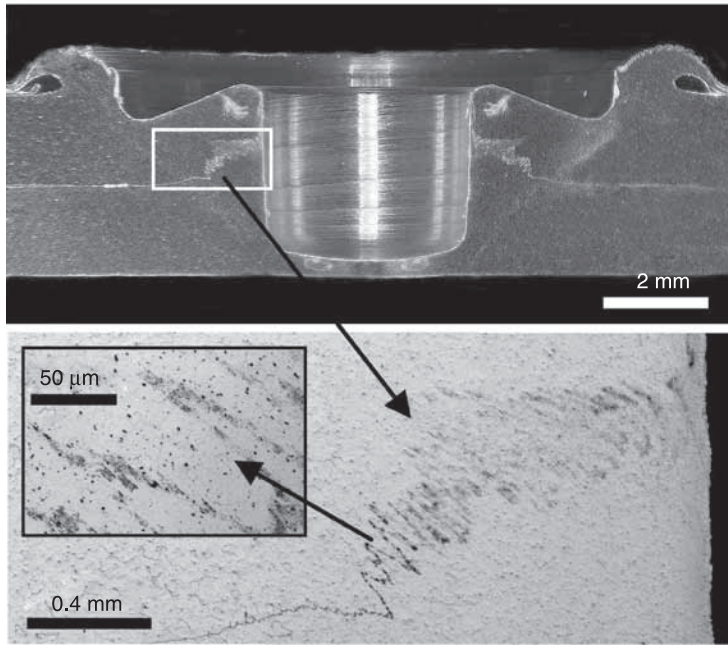
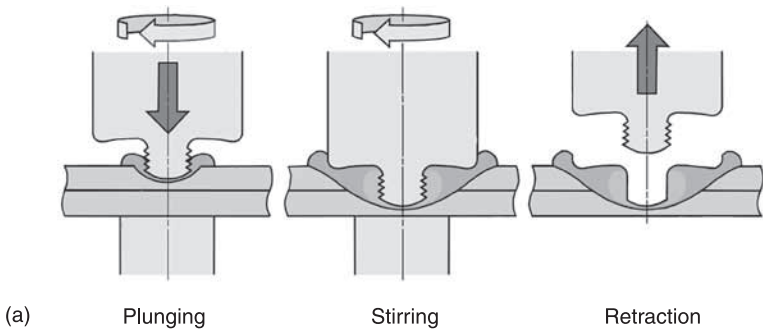
Within recent years, a variant of FSW has emerged as a technology for rivet replacement, primarily in the automotive industry: friction stir spot welding (FSSW), also referred to as friction spot joining (Sakano et al., 2001; Kawasaki Heavy Industries, 2009). The major difference between FSSW and FSW is that there is no translation of the tool in the former process. As shown in Fig. 20.20(a), a rotating tool with a pin at its tip is plunged into the overlapping sheets. The frictional heat generated between the rotating tool and the work piece causes plastic flow of material. A strong compressive forging pressure is generated when the tool shoulder contacts the sheet surface and then moves down further into the overlapping sheets. The tool is retracted after an optional dwell period. At this point, a solid state bond is formed at the interface between the two sheets. Figure 20.20(b) displays the cross-sectional view of a friction stir spot weld made between overlapping sheets of an Al-Mg-Si alloy (AA 6060-T5), 1.7 mm in thickness; the higher magnification images in Fig. 20.20(b) show the nature of the annular solid state bond formed during FSSW (Lathabai et al., 2006).

The process was implemented in the automotive industry on the Mazda RX-8 aluminium rear door in 2003 (Hancock, 2004); in 2005, Mazda went on to use the process for joining the aluminium alloy trunk lid to galvanised steel bolt retainer in its MX5 (Mazda Motor Corporation-News Release, 2005; Gendo et al., 2007).

Microstructural features of friction stir welds

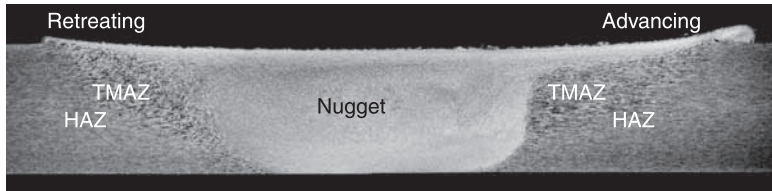
As we have seen, in a fusion weld, the highest temperature experienced by the solid parent material is its melting point and that at the fusion line, the temperature attained is the solidus temperature of the alloy. In contrast, the highest temperature experienced by the material in the joint area of a friction stir weld is significantly lower than the bulk alloy melting temperature. The wide range of strain, strain-rates and thermal cycles to which different regions of a friction stir weld are exposed means that a wide variety of microstructures form at the joint.

A nomenclature has been developed to describe the microstructural features associated with a friction stir weld (see (Threadgill et al., 2009) for a detailed



20.20 (a) Schematic illustration of friction stir spot welding (Kawasaki Heavy Industries, 2009); (b) cross-sectional views at various magnifications of a friction stir spot weld made between overlapping 1.7 mm thick sheets of AA 6060-T5 (Lathabai et al., 2006).

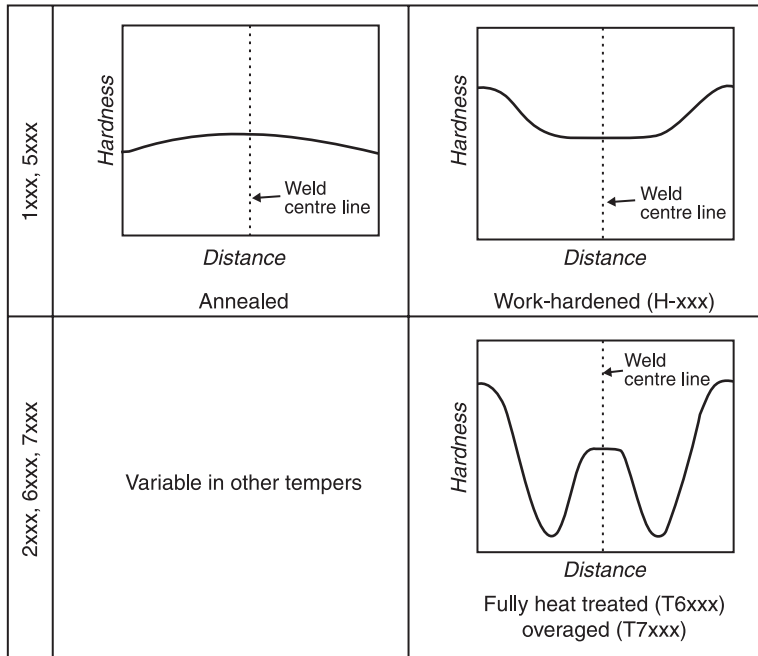
description). Figure 20.21 shows the cross-sectional view of a friction stir weld in which the regions with the different microstructures and the nomenclature used to describe them, are highlighted. As in the case of fusion welds, the material remote from the joint line, which is not deformed or has experienced a thermal cycle that caused detectable changes in the microstructure and mechanical properties, is called the unaffected material, base or parent material.



20.21 Transverse cross-sectional view of a friction stir weld in an aluminium alloy showing different regions of the weld: HAZ, TMAZ and weld nugget.

The region close enough to the weld for thermal cycles to have modified the microstructure and/or properties, but no apparent plastic deformation is detected, is referred to as the HAZ, analogous to the HAZ in fusion welds. The HAZ is detected under an optical microscope by a change in etching response and by a change in hardness. In heat treatable aluminium alloys, it is widely accepted that some coarsening of precipitates occurs here, and possibly, precipitate dissolution. In strain hardened non-heat treatable alloys, dislocation networks may recover, causing low angle grain boundaries to form. As the weld centre is approached, clear evidence of plastic deformation is discernable in the grain structure.

In the thermomechanically affected zone (TMAZ), the material has been plastically deformed by the FSW tool and heat from the processing has also affected the material. In the outer part of the TMAZ, the original grains are identifiable in the deformed structure, but closer to the weld centre line, in the region referred to as the nugget or stirred zone, the strains, temperature and time at elevated temperature are such that dynamic recrystallisation occurs, resulting in a fine, equiaxed grain structure. The processes occurring in the nugget (apart from recrystallisation) differ depending on the type of alloy being considered. For non-heat treatable alloys, annealing is the only process that can occur. If the base metal is in a strain hardened condition, then the nugget displays a substantial decrease in hardness relative to the base metal; if the starting temper is fully annealed (O), then the properties of the nugget is virtually similar to that of the base material, with a small strengthening increment due to microstructural refinement. In heat treatable alloys, the processes occurring within the nugget are more complex; depending upon the alloy and the combination of process parameters used, the nugget may become overaged, partially solution heat treated or a single phase solid solution. Transverse microhardness profiles can provide insights into the effect of these changes occurring within the various regions on of a friction stir weld. Figure 20.22 presents schematic hardness profiles which summarise the effect of the microstructural changes occurring in friction stir welds made in heat treatable and non-heat treatable aluminium alloys (Threadgill et al., 2009).



20.22 Schematic plots showing generic hardness responses across friction stir welds in heat treatable and non-heat treatable alloys of different tempers (Threadgill et al., 2009).

20.5 Brazing

Brazing is a joining process that produces bonding between two parts at the atomic/molecular level with the aid of a third material, referred to as the filler material. The filler material composition is such that it melts at a lower temperature than the materials being joined. The fundamental difference between fusion welding and brazing is that in the latter case, joining is accomplished *without* the melting of the parent materials. By definition, brazing refers to processes where the temperatures involved are above 450°C, and the filler metals used for brazing aluminium alloys are themselves alloys of aluminium, specifically Al-Si binary alloys with Si contents in the range 7–12 wt.% and melting points in the range 560–610°C (Mundt, 1994; Oates, 1996, p. 85).

During brazing, the filler metal melts at the temperature selected, wets the surfaces of the joint and is distributed by capillary action (Messler, 1993, p. 286). A metallurgical bond is formed between the parent materials and the molten filler. Due to rapid diffusion kinetics at the high brazing temperatures, the metallic bond is also characterised by an interchange of atoms between filler and the parent material. The need for capillary flow of the filler metal means that joint spacing

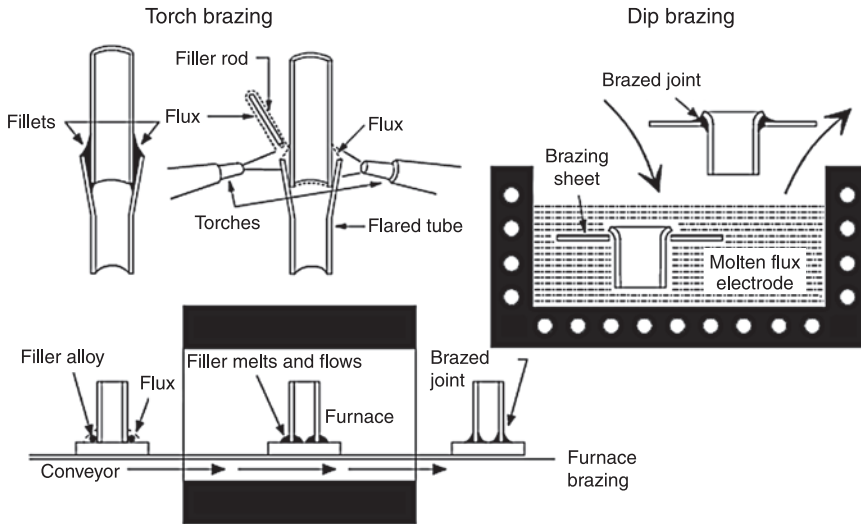
has to be small, of the order of 50–100 μm . As a result, the preferred joint design for brazing is a lap joint.

Non-heat treatable alloys of the 1xxx and 3xxx series are readily brazeable, as also 5xxx series alloys with less than 2 wt.% Mg (Mundt, 1994; Oates, 1996, p. 85). Higher Mg alloys of the 5xxx series are difficult to braze because of poor wetting characteristics and melting points below those of the available filler metals. The most brazeable of the heat-treatable alloys are those of the 6xxx series; the alloys of the 2xxx series and the 7xxx series are not brazeable, as their solidus temperatures are lower than the melting temperatures of the available filler metals. When joining sheet alloys, the brazing filler metal may first be clad or roll bonded to the sheets, in other cases, the filler metal may be applied separately in the form of wire, sheet or powder.

Critical to the achievement of a good brazed joint in aluminium alloys is the removal of the surface oxide film and the protection of the bare surface from oxidation until the joining is completed. This is achieved with the aid of brazing fluxes and appropriate surface preparation. Aluminium brazing fluxes are mixes of alkali and alkaline earth fluoride and chloride inorganic salts. Apart from dissolving the oxide layer and protecting the cleaned surface from oxidation, fluxes also lower the surface tension of the filler metal and improve the wetting characteristics of the base metal. However, the fluxes may leave a corrosive residue, which must be removed by soaking in agitated hot water followed by chemical cleaning to remove final traces. Chloride-free, non-corrosive fluxes are under development and their residues are less harmful.

Surface preparation for brazing has two main functions: removal of any grease, oil and dirt from parent metal and filler surfaces; and thinning of the oxide layer on the surfaces. Vapour degreasing, ultrasonic degreasing, and cleaning with hot detergents and water address the first requirement. Chemical cleaning with caustic or nitric-hydrofluoric acid solution can be effective in removing the heavy surface oxides.

Depending upon the source of heat used, different brazing methods exist. These include torch brazing, dip brazing or flux-bath brazing, furnace brazing (Fig. 20.23), vacuum and controlled atmosphere brazing and laser brazing (Messler, 1993, p.287; Mundt, 1994). Here, we present a brief description of some of the brazing processes used for joining aluminium alloys. Torch brazing uses a fuel gas flame as the heat source for the brazing process. The fuel gas is mixed with air or oxygen to produce a flame, which is applied to the workpiece until the assembly reaches the appropriate brazing temperature. Then the pre-placed filler is melted or handfed wire can be introduced. Dip brazing is one of the oldest brazing processes. The parts to be joined are immersed into molten flux or molten filler metal with a layer of flux to prevent oxidation. The bath is maintained at the appropriate temperature for brazing. The principal advantage of dip brazing is its ability to uniformly heat parts that have a wide range of thicknesses. However, the



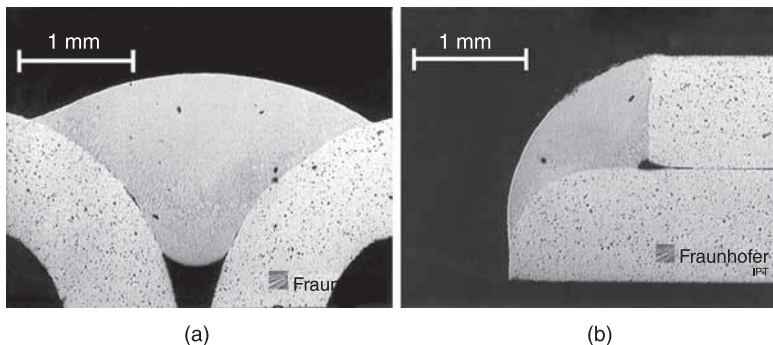
20.23 Typical setups for torch brazing, dip brazing and furnace brazing (Mundt, 1994).

drawback is that unless proper cleaning is carried out, residual flux can give rise to corrosion problems in service.

Furnace brazing is the most popular method for brazing aluminium alloys. In this process, the parts to be brazed are cleaned, the faying surfaces coated with flux, the filler metal positioned and the parts assembled (Messler, 1993, p. 288; Mundt, 1994). Furnace brazing can be conducted as a batch process or in a continuous production line. The furnace temperature is controlled precisely and fast heating rates to brazing temperature are used to prevent Si diffusion from the filler into the parent material. After brazing, the assembly is cooled and quenched if possible. Furnace brazing is carried out either in a controlled dry, inert atmosphere or in vacuum. Generally, no flux is used when brazing in vacuum, which is an advantage as post braze cleaning is not required. Vacuum brazing produces higher quality joints than any other brazing process. During heating in vacuum, the oxide layer cracks as the thermal expansion of the aluminium substrate is significantly higher than that of the oxide. However, in the vacuum of 10^{-4} – 10^{-6} torr, the newly formed aluminium surface does not oxidise again. One requirement is that Mg is present, at least in the filler, in order to disrupt the oxide films, promote wetting in the absence of a flux and to serve as a getter for the oxygen by forming Mg vapour (Mundt, 1994).

Laser brazing is a fairly recent development that is finding increasing application in the automotive industry. Because of the precise nature in which the low energy input can be applied, precise control of the wetting of the base material and melting of the filler metal is possible, enabling complex joint

geometries to be processed and braze properties to be controlled to improve reliability. The high quality is characterised by absence of porosity and cracking and a smooth, barely visible seam. The local melting and rapid thermal cycles minimise distortion and reduce diffusion which can lead to the formation of intermetallics, particularly during the dissimilar joining of aluminium to steel. Laser brazing has been used in the fabrication of steel roof seams, side panel seams, and trunk lid seams by automakers such as Volkswagen, Daimler and Audi (Staufer et al., 2008). Flux free laser brazing of an Al-Mg-Si alloy (AlMgSi1, AA6082) has been accomplished by an adjustment of the local energy flux density distribution in the laser beam focal spot (Donst, 2009). Two different solid lasers were used for this purpose: one laser beam was used for the activation of the surface and thus to improve wetting of the base material with the brazing filler and a second laser beam was used for the input of the necessary energy to achieve a working temperature for the brazing process. Figure 20.24 presents cross-sectional views of two types of joints produced on AlMgSi1 alloy using laser brazing. The advantages of a flux-free process, which also eliminates the need for chemical pre-cleaning, are obvious. The process has also been used for flux-free steel to aluminium joining (Corus Automotive, 2006). We have noted earlier the problems involved in joining aluminium to steel by fusion welding processes. During laser brazing, an aluminium-based filler metal is melted to create a weld on the aluminium side. The molten filler metal then ‘wets’ the steel, creating a ‘brazed joint’ on the steel side of the weld (Corus Automotive, 2006). Importantly, tests have shown that this new technique creates only a very thin Fe-Al intermetallic layer making it possible to create joints that are, in some cases, stronger than the base materials themselves. However, high capital costs are a major disadvantage of the laser brazing process.



20.24 Macrographs showing cross-sectional views laser brazed AlMgSi1 (AA6082) aluminium alloy joints: (a) a seam joint and (b) a fillet joint (courtesy Fraunhofer IPT, Germany).

20.6 Adhesive bonding

Adhesive bonding is a process in which joining between two or more parts is accomplished by the solidification or hardening of a non-metallic adhesive material, placed between the faying surfaces of the parts (O'Brien, 1991, p. 839). The surfaces being joined are not melted, although they may be heated. In this sense, adhesive bonding is similar to brazing and soldering, although the bonding formed is not a metallurgical bond, rather, it is chemical in nature. The hardening of the adhesive may occur by purely physical means or via a chemical reaction. Physically bonding adhesives use either the evaporation or vaporisation of a solvent or the cooling of a liquid to form an inner bond. Chemically reactive adhesives are further classified into cold hardening and heat hardening systems. They are based on thermosetting resins which harden or cure by chemical reactions that occur with the addition of a hardener or catalyst (Dorn, 1994a; O'Brien, 1991, p. 844). Once they cure, these adhesives cannot be remelted and a broken joint cannot be rebonded by heating. Depending upon composition, thermosetting adhesives may soften or weaken at high temperature and ultimately decompose.

Aluminium is an almost ideal candidate for adhesive bonding because it has a high surface energy which enables the organic adhesives to easily wet it (Petrie, 2007). The long term mechanical performance of the adhesive bonded joints is dependent on the chemical nature of the adhesives and the environment in which they are expected to perform. As such, the selection of the adhesive is based on the strength required, the type of stress involved (whether peel or shear, static or dynamic) and the operating environment. Most notable for joining aluminium are the epoxy adhesives, which can be formulated to cure rapidly or slowly at room temperature (O'Brien, 1991, p. 846). The high temperature performance and moisture resistance of these adhesives can be enhanced by curing at elevated temperatures. The cleanliness and preparation of the surface are particularly important for these types of adhesives. Anaerobic acrylic adhesives are gaining wide acceptance for bonding aluminium alloys. These adhesives can provide joint strengths equivalent to those obtained with epoxies, without the need to ensure oil-free and pristine bonding surfaces (O'Brien, 1991, p. 846). These adhesives are capable of dissolving thin films of mill oil into the adhesive layer without adversely affecting joint strength or performance.

Surface preparation is critical in achieving a good initial adhesive bond strength. This generally involves cleaning the surface to remove contaminants that can result in a weak boundary layer. The strength and stability of the bond formed is further enhanced if the naturally formed surface oxide is removed and replaced with a new oxide layer that is continuous and corrosion resistant. The most common surface preparations that have been used for bonding aluminium can be classified into three groups: simple cleaning (solvent wiping and/or vapour degreasing) and mechanical abrading; chemical etching; and primers and conversion coatings (Petrie, 2007). The parameters of the pre-treating process and

their control can be crucial in assuring consistency from joint to joint. For instance, it has been reported that the temperature used for rinsing and drying aluminium should not exceed 70°C, as different oxides are formed above and below this temperature (Petrie, 2007) and the oxide formed below this temperature, bayerite, apparently provides better adhesion. When bonding aluminium to itself or to other materials, the optimal surface preparation should be determined based on the initial strength and durability required. Table 20.2 serves as a guide for selecting an appropriate pre-treatment; as can be seen in this table, chemical etching produces higher initial bond strength and, in turn, produces higher reliability and longer service life in a bonded assembly. Primers are often used when making structural aluminium joints in the aerospace and automotive industries (Petrie, 2007, 2008). Primers have a low viscosity, which allows them to chemically wet a metal surface more effectively than the more viscous adhesives. They are also used to provide corrosion resistance to the etched surface during assembly and to the bonded joint in service.

The most efficient use of adhesives in any manufacturing operation depends on the optimisation of adhesive selection, joint design, and process conditions (Adderley, 1988). It is essential that adhesive bonded joints are designed so that the loading stresses are directed along the lines of the adhesive's greatest strength. If adhesive bonding is replacing mechanical fastening or spot welding some structural redesign will probably be necessary. A bonded joint may be subjected to tensile, compressive, shear, cleavage or peel stresses; in practice a bonded structure often has to sustain a combination of these stresses. Most of the well-established structural adhesives are strongest in tension, compression and shear, and are relatively weak in cleavage and peel because the applied force is then concentrated into a single line of high stress. It follows that for maximum strength, joints should be designed so that cleavage and peel stresses are minimised.

Table 20.2 Effect of substrate treatment on strength of aluminium joints bonded with epoxy adhesives

Surface treatment	Bond strength
<ul style="list-style-type: none"> • Solvent wipe (trichloroethylene) • Abrasion on surface (sand blasting, coarse sand paper, etc.) plus solvent wipe • Hot vapour degrease (trichloroethylene) • Abrasion of surface plus vapour degrease • Alodine treatment (conversion coating) • Anodising • Caustic etch • Chromic acid etch (sodium dichromate + H₂SO₄) 	<ul style="list-style-type: none"> • Low to medium strength • Medium to high strength • Medium strength • Medium to high strength • Low strength • Medium strength • High strength • Maximum strength

Source: Petrie (2007)

As in the case of other joining processes discussed in this chapter, adhesive bonding has many advantages and a few disadvantages. These are summarised in Table 20.3 (Petrie, 2008). Adhesives have always played a significant role in the aircraft/aerospace industry, primarily because they offer a low-weight, fatigue-resistant, and aerodynamically sound method of assembly (Petrie, 2008). For more than half a century, adhesive bonding has been one of the most important joining techniques used in the aerospace industry. The application of adhesive bonding technology provides extremely lightweight designs due to the excellent strength/weight ratio of the adhesive and the consequent use of lightweight metals including aluminium and titanium alloys, polymeric composites, and honeycomb or other sandwich structures that are afforded by adhesive bonding (Petrie, 2008). The benefits offered by adhesive bonding have

Table 20.3 Advantages and disadvantages of adhesive bonding

Advantages	Disadvantages
<ul style="list-style-type: none"> • Provides large stress-bearing area. • Improved joint stiffness due to continuous bond area rather than point contact as in mechanical fastening. • Provides excellent fatigue strength. • Damps vibration and absorbs shock. • Minimizes or prevents galvanic corrosion between dissimilar metals. • Joins all shapes and thicknesses. • Provides smooth contours. • Seals joints. • Joins any combination of dissimilar materials. • Heat, if required, is too low to affect metal parts. • Provides attractive strength-to-weight ratio. • No distortion as in fusion welding. • Often less expensive and faster than mechanical fastening. 	<ul style="list-style-type: none"> • Surface must be carefully cleaned. • Long cure times may be needed. • Limitation on upper continuous operating temperature (generally 175–200°C). • Heat and pressure may be required for cure. • Jigs and fixtures may be required. • Rigid process control usually necessary. • Inspection of finished joint is difficult. • Useful life depends on the service environment. • Environmental, health and safety considerations are necessary. • Special training may be required. • Adhesive joints are inherently weak under peel loading and design of bonded joints need to take this into consideration.

Source: Petrie (2008)

also been recognised by the automotive industry (Barnes and Pashby, 2000a). For example, Jaguar used adhesive bonding together with SPR and flow drilling screws in assembling aluminium bodies of the XK model from extrusions, castings and pressings (Mortimer, 2005). Audi has recently announced that 229 flow drilling screws are used for the aluminium-steel hybrid construction used in Audi TT Coupe and 80% of these are reinforced with structural adhesives which also form a separating layer between aluminium and steel, thus solving the problem of contact galvanic corrosion (Rügheimer, 2009).

20.7 Conclusion

As stated in the introductory chapter of this book, the general use of aluminium worldwide will continue to increase, despite the many major economic challenges facing both the aluminium industry, and the manufacturers who buy the metal. A recent market insight report points out that the increased demand for aluminium in the automotive sector and the increasingly common trend of replacing steel and other metals in the heavy machinery, process and other non-automotive industries means that there will be increased need and opportunities for aluminium joining technologies (Chauhan, 2009). Indeed the aluminium industry technology roadmap, developed by the US Department of Energy, identifies the development of low-cost joining techniques for similar and dissimilar materials as a top priority R&D need (US Department of Energy Industrial Technologies Program, 2003). Clearly, welding and joining are key enabling technologies for the aluminium industry. In this chapter, we have examined the many joining technologies used in aluminium fabrication. We have seen that while there are many non-traditional processes that offer significant advantages in specialised applications, many of the traditional welding processes have unique advantages which will continue to make them the processes of choice in a number of applications. In the fabrication of heavy structures, arc welding will continue to dominate due to the flexibility and economy of this process, but laser beam and FSW processes are becoming increasingly well established in the fabrication of critical components because of their unique capabilities. Progress in these relatively new processes is significant and as further development and improvement occur, they will continue to grow in importance.

20.8 References

- Adderley, C.S. (1988) 'Adhesive bonding', *Materials & Design*, 9(5): 287–293.
- Aizawa, T., Kashani, M. and Okagawa, K. (2007) 'Application of magnetic pulse welding for aluminium alloys and SPCC steel sheets', *Welding Journal*, 86: 119s–124s.
- Avdel UK Ltd. (2008) *Breakstem systems*. Available from: http://www.avdel-global.com/fileadmin/user_upload/Data/PDF/Brochures/EN/Avdel_BreakstemSystems_EN.pdf [Accessed 9 October 2009].

- Barnes, T.A. and Pashby, I.R. (2000a) 'Joining techniques for aluminium spaceframes used in automobiles: Part I – solid and liquid phase welding', *Journal of Materials Processing Technology*, 99: 62–71.
- Barnes, T.A. and Pashby, I.R. (2000b) 'Joining techniques for aluminium spaceframes used in automobiles: Part II – adhesive bonding and mechanical fasteners', *Journal of Materials Processing Technology*, 99: 72–79.
- Budde, L. (1994a) Definition and classification of mechanical fastening methods, *Training in Aluminium Application Technologies (TALAT)*, European Aluminium Association (EAA). Available from: <http://www.eaa.net/eea/education/TALAT/lectures/4103.pdf> [Accessed 9 October 2009].
- Budde, L. (1994b) Clinching, *Training in Aluminium Application Technologies (TALAT)*, European Aluminium Association (EAA). Available from <http://www.eaa.net/eea/education/TALAT/lectures/4102.pdf> [Accessed 9 October 2009].
- Chauhan, A. (2009) 'Aluminium welding is here to stay and is the key to future growth, notes Frost & Sullivan', *Frost and Sullivan market insight*. Available from: <http://www.frost.com/prod/servlet/market-insight-print.pag?docid=175952415> [Accessed 29 October 2009].
- Corus Automotive (2006) *Corus develops new steel to aluminium welding technique*. Available from: http://www.corusautomotive.com/en/news/press_releases/2006_laser_brazing [Accessed 23 October 2009].
- Donst, D. (2009) *Laser beam brazing of aluminium materials*. Available from: <http://www.ipt.fraunhofer.de/EN/businessactivities/Prozesstechnologie/Laserstrahlenwendungen/Forschungsthemen/LaserBeamBrazingofAluminiumMaterials.jsp> [Accessed 28 October 2009].
- Dorn, L. (1994a) 'Adhesive bonding of aluminium', *Training in Aluminium Application Technologies (TALAT)*, European Aluminium Association (EAA). Available from: <http://www.eaa.net/eea/education/TALAT/4000/4700.htm> [Accessed 9 October 2009].
- Dorn, L. (1994b) 'Resistance welding', *Training in Aluminium Application Technologies (TALAT)*, European Aluminium Association (EAA). Available from: <http://www.eaa.net/eea/education/TALAT/lectures/4500.pdf> [Accessed 9 October 2009].
- EJOT GmbH & Co. KG (2009) 'EJOT FDS® in the "body in white" of the Audi TT'. Available from: http://www.ejot.com/ejot.de/Verbindungstechnik—195,websiteLang_en.htm [Accessed 9 October 2009].
- European Aluminium Association (2009) *aluMATTER*. Available from: <http://aluminium.matter.org.uk/content/html/eng/default.asp?catid=47&pageid=2144416963> [Accessed 9 October 2009].
- Faes, K. (2009) *Innovative electromagnetic high-velocity welding (magnetic pulse welding)*, Belgian Welding Institute, Gent, Belgium. Available from: http://www.bil-ibs.be/eng/Research/research_2008_MPW.htm [Accessed 26 October 2009].
- Feng, Z. and Diamond, D. (2004) 'Basic studies of ultrasonic welding for advanced transportation systems', *Progress Report for High Strength Weight Reduction Materials FY 2003*, US Department of Energy, Washington DC. Available from: http://www.ms.ornl.gov/programs/energyeff/hswrm/pdf/hswrm_2003ProgReport.pdf [Accessed 9 October 2009].
- FPE & Gatwick Fusion (2009) *Friction welding*. Available from: <http://www.fpe.co.uk/processes/friction-welding> [Accessed 26 October 2009].
- Fronius International GmbH (2008) *The new revolution in digital GMA welding – CMT: Three letters – one new technology – innumerable benefits*. Available from: <http://>

- www.fronius.com/cps/rde/xbcr/SID-E4F87D46-8E14734C/fronius_international/22_cmt_the_new_revolution_in_digital_gma_welding_gb.pdf [Accessed 9 October 2009].
- Gendo, T., Nishiguchi, K., Asakawa, and Tanioka, S. (2007) *Spot friction welding of aluminium to steel*, SAE Technical Paper 2007-01-1703, SAE World Congress and Exhibition, Detroit, MI, SAE International.
- Hancock, R. (2004) 'Friction welding of aluminium cuts energy cost by 99%', *Welding Journal*, 83(2): 40–42.
- He, X., Pearson, I. and Young, K. (2008) 'Self-pierce riveting for sheet materials: State of the art', *Journal of Materials Processing Technology*, 199: 27–36.
- Henrob Ltd. (2006) *Self pierce riveting productions*. Available from: <http://www.henrob.co.uk/languages/english/pdf/Introduction%20to%20SPR.pdf> [Accessed 9 October 2009].
- Iordachescu, M., Iordachescu, D., Planas, J., Scutelnicu, E., Ocăna, J.L. (2009) 'Material flow and hardening at butt cold welding of aluminium', *Journal of Materials Processing Technology*, 209: 4255–4263.
- Kawasaki Heavy Industries (2009) 'Friction spot joining – A new method for light alloy joining'. Available from: www.kawasakirobot.co.uk/fsj_e.pdf [Accessed 26 October 2009].
- Kochan, A. (2000) 'Magnetic pulse welding shows potential for automotive applications', *Assembly Automation*, 20(2): 129–131.
- Lathabai, S., Painter, M.J., Cantin, G.M.D. and Tyagi, V.K. (2006) 'Friction spot joining of an extruded Al-Mg-Si alloy', *Scripta Materialia*, 55: 899–902.
- Mathers, G. (2002) *The welding of aluminium alloys*, Cambridge, Woodhead.
- Mazda Motor Corporation-News Release (2005) *Mazda develops world's first steel and aluminum joining technology using friction heat*. Available from: <http://www.mazda.com/publicity/release/2005/200506/050602.html> [Accessed 28 October 2009].
- Messler, R.W., Jr. (1993) *Joining of advanced materials*, Stoneham, MA, Butterworth-Heinemann.
- Messler, R.W., Jr. (1999) *Principles of welding*, New York, John Wiley & Sons.
- Messler, R.W., Jr. (2002) 'Weld-bonding: the best or worst of two processes?', *Industrial Robot*, 29(2): 138–148.
- Messler, R.W., Jr. (2003) 'Joining comes of age: from pragmatic process to enabling technology', *Assembly Automation*, 23: 130–143.
- Messler, R.W., Jr. (2004) *Joining of Materials and Structures: From Pragmatic Process to Enabling Technology*, Oxford, Elsevier Butterworth-Heinemann.
- Mishra, R.S. and Ma, Z.Y. (2005) 'Friction stir welding and processing', *Materials Science and Engineering*, 50:, 1–78.
- Mishra, R.S. and Mahoney, M.W. (Eds) (2007) *Friction Stir Welding and Processing*, Materials Park, OH, USA, ASM International.
- Mortimer, J. (2005) 'Jaguar "Roadmap" rethinks self-piercing technology', *Industrial Robot*, 32(3): 209–213.
- Mundt, R. (1994) 'Introduction to brazing of aluminium alloys', *Training in Aluminium Application Technologies (TALAT)*, European Aluminium Association (EAA). Available from <http://www.eaa.net/ea/education/TALAT/lectures/4601.pdf> [Accessed 9 October 2009].
- Nandan, R., DebRoy, T. and Bhadeshia, H.K.D.H. (2008) 'Recent advances in friction stir welding – process, weldment, structure and properties', *Progress in Materials Science*, 53: 980–1023.

- Neugebauer, R., Todtermushke, M., Mauermann, R. and Riedel, F. (2008) 'Overview on the state of development and the application potential of dieless mechanical joining processes', *Journal of Architectural Engineering*, 8(4): 51–60.
- Oates, W.R. (Ed) (1996) *Welding Handbook, Vol.3: Materials and Applications – Part 1*, 8th ed., American Welding Society, Miami, FL.
- O'Brien, R.L. (Ed.) (1991) *Welding Handbook, Vol.2: Welding Processes*, 8th ed., American Welding Society, Miami, FL.
- Petrie, E.M. (2007) 'Adhesive bonding of aluminium alloys', *Metal Finishing*, 105(9): 49–56.
- Petrie, E.M. (2008) 'Adhesives for the assembly of aircraft structures and components', *Metal Finishing*, 106(9): 26–31.
- Research Centre of the Belgian Welding Institute (2008) *Innovative electromagnetic high-velocity welding techniques (magnetic pulse welding)*. Available from: http://www.bil-ibs.be/eng/Research/research_2008_MPW.htm [Accessed 26 October 2009].
- Rügheimer, U. (2009) *Bundled expertise – lightweight design in series production*, Audi Press Release. Available from: <http://www.audiusanews.com/newsrelease.do?id=1513&mid=69> [Accessed 25 October 2009].
- Sahin, M. (2008) 'Effect of surface roughness on weldability in aluminium sheets joined by cold pressure welding', *Industrial Lubrication and Tribology*, 60(5): 249–254.
- Sakano, R., Murakami, K., Yamashita, K., Hyoe, T., Fujimoto, M., Inuzuka, M., Nagao, Y. and Kashiki, H. (2001) 'Development of spot FSW robot system for automobile body members'. *Proceedings of the 3rd International Symposium of Friction Stir Welding*, Kobe, Japan, TWI.
- Shribman, V. (2007) *White paper: magnetic pulse welding of automotive HVAC parts*. Available from <http://www.pulsar.co.il/technology/?aid=9898fe13d7202ed96076342e0d4f6318&did=20> [Accessed 26 October 2009].
- Staufer, H., Rührnößl, M. and Miessbacher, G. (2008) *LaserHybrid welding and laserBrazing: state of the art in technology and practice by the examples of the Audi A8 and VW-Phaeton*. Available from: http://www.fronius.com/cps/rde/xbcr/SID-E4F87D46_8E14734C/fronius_international/12_laserhybrid_laserloeten_gb.pdf [Accessed 9 October 2009].
- Thomas, W.M., Nicholas, E.D., Needham, J.C., Murch, M.G., Temple-Smith, P., Dawes, C.J. (1991) *Improvements related to friction welding*, US 5460317; EPS 0616490 (Patent).
- Threadgill, P.L., Leonard, A.J., Shercliff, H.R. and Withers, P.J. (2009) 'Friction stir welding of aluminium alloys', *International Materials Reviews*, 54(2): 49–93.
- Trommer, G. (2009) *High-performance welding: One catchphrase, four alternatives*. Available from: http://www.fronius.com/cps/rde/xbcr/SID-E4F87D46-8E14734C/fronius_international/09_hochleistungsschweissen_gb.pdf [Accessed 9 October 2009].
- US Department of Energy Industrial Technologies Program (2003) *Aluminium industry technology roadmap*. Available from: http://www1.eere.energy.gov/industry/aluminum/pdfs/al_roadmap.pdf [Accessed 29 October 2009].
- Varis, J. (2006) 'Economics of clinched joint compared to riveted joint and example of applying calculations to a volume product', *Journal of Materials Processing Technology*, 172: 130–138.
- Wilhelm Böllhoff GmbH & Co. KG (2009a) *Rivset: general principles*. Available from: [http://www2.boellhoff.com/web/centres.nsf/Files/RIVSET_GB_6701/\\$FILE/RIVSET_GB_6701.pdf](http://www2.boellhoff.com/web/centres.nsf/Files/RIVSET_GB_6701/$FILE/RIVSET_GB_6701.pdf) [Accessed 9 October 2009].

- Wilhelm Böllhoff GmbH & Co. KG (2009b) *Rivclinch: general principles*. Available from: http://www.boellhoff.com/en/de/assembly_systems/rivclinch_clinching.php [Accessed 9 October 2009].
- Wilhelm Böllhoff GmbH & Co. KG (2009c) *Rivtac: High speed joining with pneumatic hand tool*. Available from: [http://www2.boellhoff.com/web/centres.nsf/Files/RIVTAC_GB_6810/\\$FILE/RIVTAC_GB_6810.pdf](http://www2.boellhoff.com/web/centres.nsf/Files/RIVTAC_GB_6810/$FILE/RIVTAC_GB_6810.pdf) [Accessed 9 October 2009].
- Zhang, H.T., Feng, J.C., Heb, P., Zhang, B.B., Chen, J.M. and Wang, L. (2009) 'The arc characteristics and metal transfer behaviour of cold metal transfer and its use in joining aluminium to zinc-coated steel', *Materials Science and Engineering A*, 499: 111–113.

S.H. HUO, M. QIAN and G.B. SCHAFFER, The University of Queensland, Australia and E. CROSSIN, The University of Queensland, Australia and RMIT University, Australia

Abstract: Conventional press and sinter aluminium powder metallurgy is a well-developed, cost-effective process for net-shaped fabrication of complex parts via die compaction and sintering. This chapter provides an overview of the PM process in general and sintering in particular. Key issues in the PM processing of aluminium are considered, including the roles of magnesium and the atmosphere on sintering and how these factors affect densification and the microstructure.

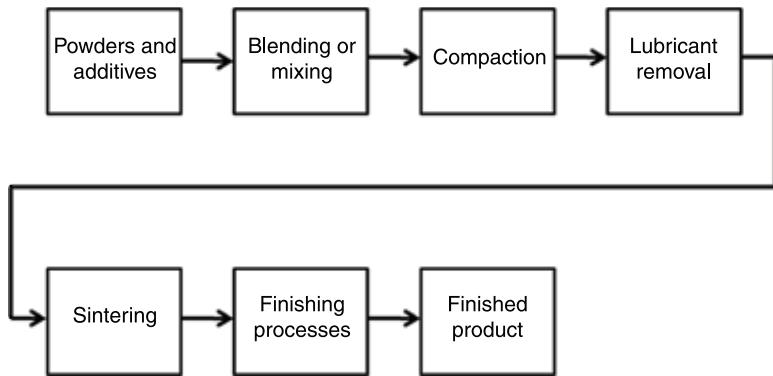
Key words: sintering, powder metallurgy, densification, aluminium.

21.1 Introduction

This chapter is about the sintering of aluminium powder materials. The scope is restricted to the conventional press and sinter powder metallurgy (PM) route, and to where aluminium differs from other sintering systems. An overview of the PM process is presented in Section 21.2. Sintering fundamentals relating to the essential mechanisms for densification and microstructure evolution, with a particular focus on liquid-phase sintering (LPS), are presented in Section 21.3. Sintering aluminium is considered in Section 21.4, including a review of surface oxide characteristics of air-atomised aluminium in Section 21.4.1, which constitutes a basis for understanding the complexity of sintering aluminium; this is followed by the role of magnesium in disruption of the oxide film in sintering in Section 21.4.2; the role of atmosphere in Section 21.4.3; and the activated sintering induced by trace element additions in Section 21.4.4. A summary of the development of commercial grade aluminium PM alloys and their applications are detailed in Section 21.5. Finally, potential avenues for future research are discussed in Section 21.6.

21.2 The press and sinter powder metallurgy process

The typical press and sinter powder metallurgy process is represented schematically in Fig. 21.1. It consists of the mixing of elemental and/or alloy powders, compaction of the powder mixture to a near-net shaped part, the removal of lubricant from the part, sintering, and optional finishing processes. The un-sintered part is commonly referred to as a 'green' compact. Sintering is given further consideration in Sections 21.3 and 21.4.



21.1 A schematic of the press and sinter powder metallurgy route.

Gas atomisation is the principal technique used to produce powders for powder metallurgy and the majority of aluminium powders are air-atomised (Schaffer, 1996). SEM images of typical air-atomised and argon-atomised aluminium powders are shown in Fig. 21.2. The powder production technique directly influences the powder characteristics, such as particle shape, size and composition, which in turn influence the compaction and sintering processes (German, 1997) and ultimately the properties of the final part. The surface characteristics of air-atomised aluminium powder and the oxidation behaviour of aluminium powder are given detailed consideration in Section 21.4.1.

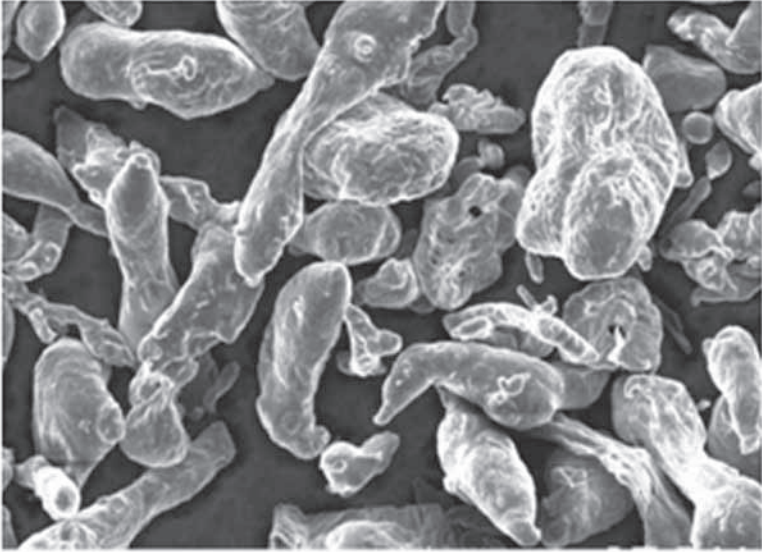
The intermingling of powder is termed blending if the powder is of the same nominal composition, or mixing if the powder is produced from multiple components (Dotter, 1993). Powder mixtures offer advantages over blended powders in terms of material cost, sintering times and compaction behaviour (Dotter, 1993; Schaffer, 1996). Uni-axial pressing is the standard compaction technique in press and sinter powder metallurgy (German, 1997). Typically, loose powder is fed into the die cavity, the upper and lower punches apply pressure to the powder, forming a green compact, which is then ejected.

Non-uniform compaction pressures, die wall friction and/or internal stresses during pressing can result in green density variations through the compact, leading to dimensional and mechanical property variations in the sintered part (German, 1996; Schaffer 1996). These green density gradients can be minimised through part and die design or by the addition of lubricants. Four overlapping stages occur during compaction (German, 1989):

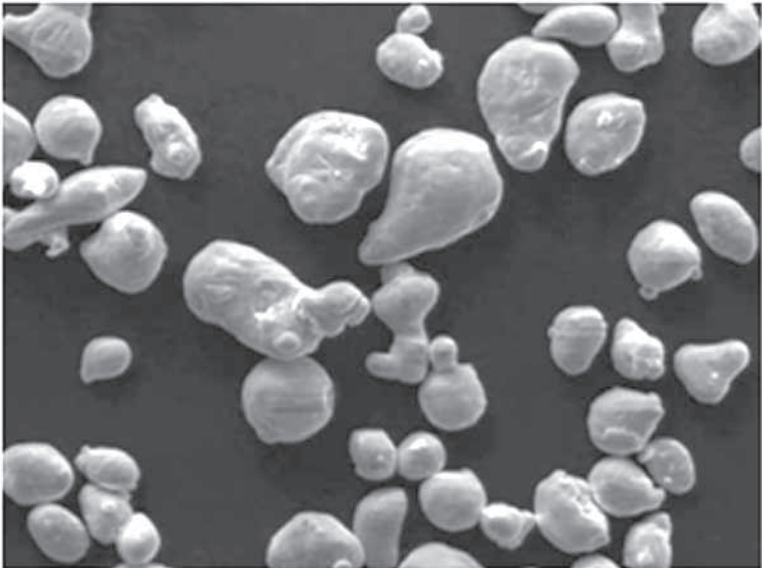
- particle rearrangement
- localised plastic deformation
- homogenous plastic deformation and
- bulk compression

The plastic deformation stages result in the flattening of the particle contacts and the filling of voids adjacent to the contact points (German, 1989; Simchi and Veltl, 2006).

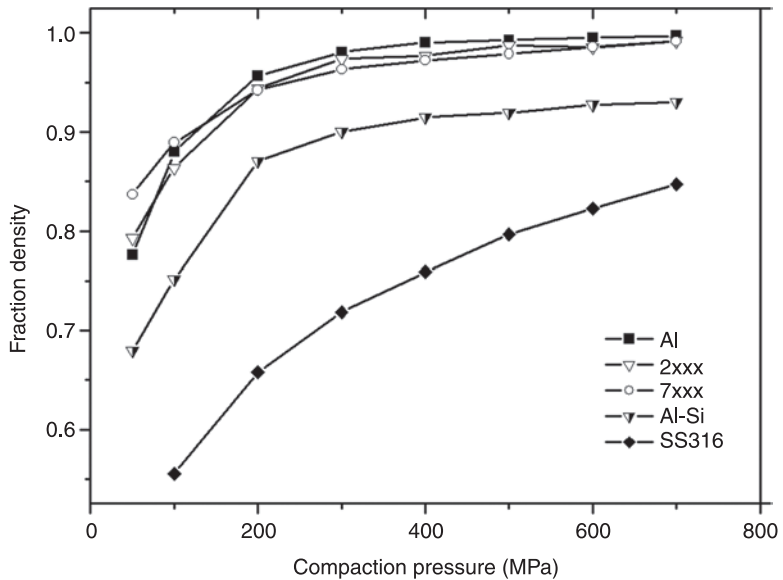
(a)



(b)



21.2 (a) and (b) SEM secondary electron images showing the typical morphology of air-atomised Al-powders that have irregular shapes in contrast to more spherical shapes atomised by an inert gas such as argon or nitrogen gases. The amount of oxygen present in the atomising gas has a strong influence on the morphology of the atomised aluminium powders, which is attributed to the pinning effect of oxide nuclei that form on the droplets before they have solidified (Özbilen et al., 1989).



21.3 Comparison of the compressibility between Al-Zn (7xx) and Al-Si pure aluminium, Al-Cu (2xxx), and 316 stainless steel powders.

An outstanding characteristic of aluminium powder is its excellent compressibility, as shown in Fig. 21.3. Air-atomised aluminium powder can be compacted to over 90% theoretical density at 165 MPa while pressures exceeding 700 MPa are required to attain similar density for iron-based powder (Dudas and Dean, 1969a; 1969b). This allows for the use of smaller presses, fragile tool design (such as thin-walled punches or small core rods for intricate designs) and assists in minimising die and punch wear (Generous, 1980). These characteristics are vital to the net shape capability of aluminium PM. Aluminium is well known for its severe seizing and galling characteristics against steel. Lubrication, therefore, has to be introduced to reduce the friction between the pressed compact and tool components (Thompson, 1993), thereby reducing tool wear and ejection pressures (German, 1997). Lubricants used are typically stearic acid-based and are admixed with the powder to a level of between 0.5 and 1.5 wt%. The lubricant is then removed prior to sintering in a pre-heat operation. This process is often referred to as burn-off, de-lubrication or de-waxing. Finishing processes, or post-sintering operations, are used to meet specific property requirements and include sizing, heat-treatment, machining and surface treatments (Schaffer, 1996; German, 1997). The finishing processes used for PM parts are essentially the same as those used for cast and forged components.

21.3 Sintering fundamentals

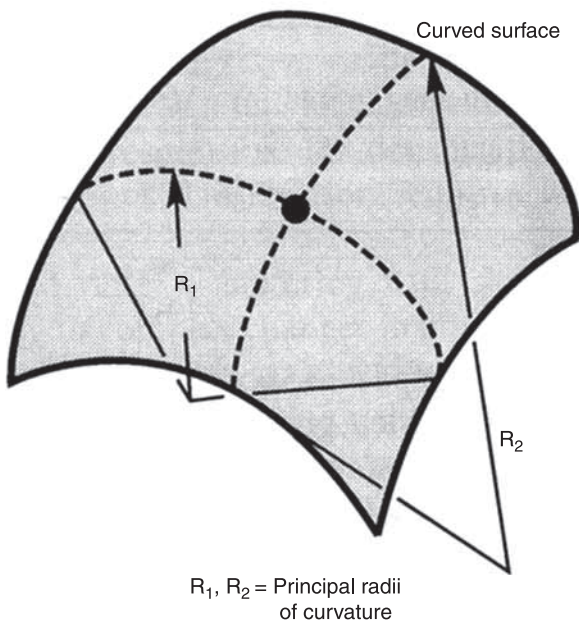
Sintering is the thermally activated bonding of particles, which occurs at temperatures below the melting point of the major constituent, but can involve a

liquid phase (German, 1997). Sintering results in the particles bonding together and allows interdiffusion of alloying additives that are usually blended with the powder. The size and structure of pores surrounding particles may change during sintering, resulting in increased density. An external pressure can be applied to enhance the elimination of pores during sintering (German, 1996). The driving force for sintering is the decrease in the total interfacial energy. A reduction in the total interfacial energy can be achieved by (a) the substitution of high surface energy interfaces by lower surface energy interfaces such as the substitution of solid-vapour interfaces with grain boundaries or by (b) reducing the total surface area per unit volume (Kang, 2005).

The stress associated with a curved surface, often termed the sintering stress, σ , is given by the Laplace equation:

$$\sigma = \gamma \left(\frac{1}{R_1} + \frac{1}{R_2} \right) \quad [21.1]$$

where γ is the surface tension and R_1 and R_2 are the principal radii of curvature, as illustrated in Fig. 21.4. During sintering, curved particle surfaces will flatten over time to reduce the sintering stress (German, 1996). Mass transport mechanisms facilitate the reduction in sintering stress through the movement of matter away from regions of high energy to regions of low energy.

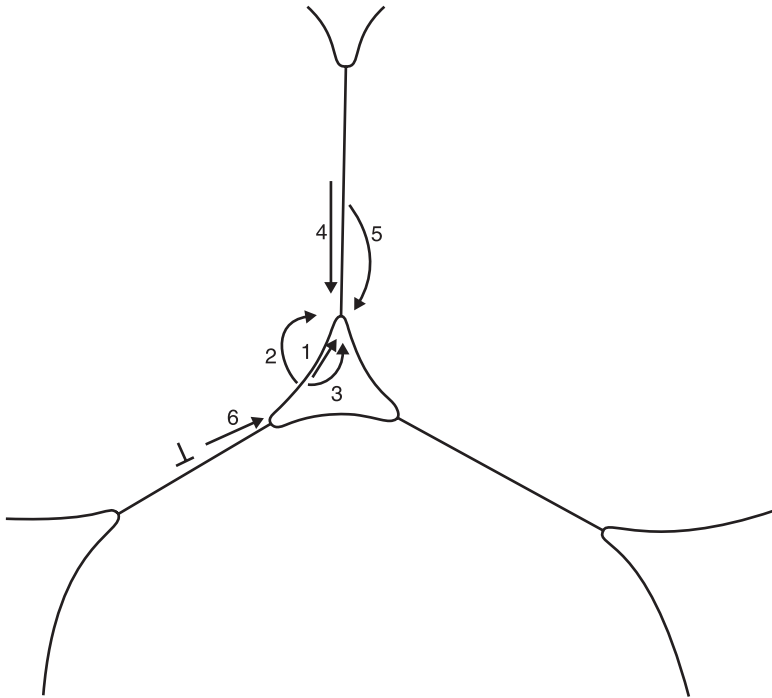


21.4 The stress associated with a curved surface is related to the two principal radii of curvature through the Laplace equation, Eq. 21.1 (German, 1997).

Sintering mechanisms are divided into two categories: (i) solid-state sintering and (ii) LPS. The sintering of aluminium is typically carried out in the presence of a liquid phase in order to achieve higher densities in a shorter time. As such, this section has a particular focus on LPS mechanisms.

21.3.1 Solid-state sintering

In solid-state sintering, mass-transport mechanisms are limited to the diffusion of solid and vapour phases. There are at least six diffusion mechanisms which lead to the growth of contacts between solid particles, termed necks, Fig. 21.5 and Table 21.1. Only the diffusion of matter from the grain boundaries and dislocations to the necks leads to vacancy annihilation, a reduction in the centre-to-centre distance of the particles and densification (Lenel, 1980). Densification is also possible in amorphous material through viscous flow.



21.5 A schematic of the transport mechanisms in solid-state sintering. Matter is transported to the particle necks via diffusion along grain boundaries, through the bulk, and through the vapour phase (Rahaman, 1995).

Table 21.1 Transport mechanisms during solid-state sintering

Mechanism	Source	Diffusion pathway	Shrinkage (Yes/No)
1	Surface	Surface	N
2	Surface	Vapour	N
3	Surface	Bulk	N
4	Grain boundary	Boundary	Y
5	Grain boundary	Bulk	Y
6	Dislocations	Bulk	Y

Source: Kang (2005), Rahaman (1995)

Solid-state densification rates increase with:

- sintering temperature, due to enhanced diffusivity;
- decreased particle size, due to an increase in the total surface energy prior to sintering;
- activated sintering, where chemical additions or the application of energy (e.g. due to phase changes or the application of electrical energy) are used to lower the thermal energy required for sintering (German, 1997).

21.3.2 Liquid phase sintering

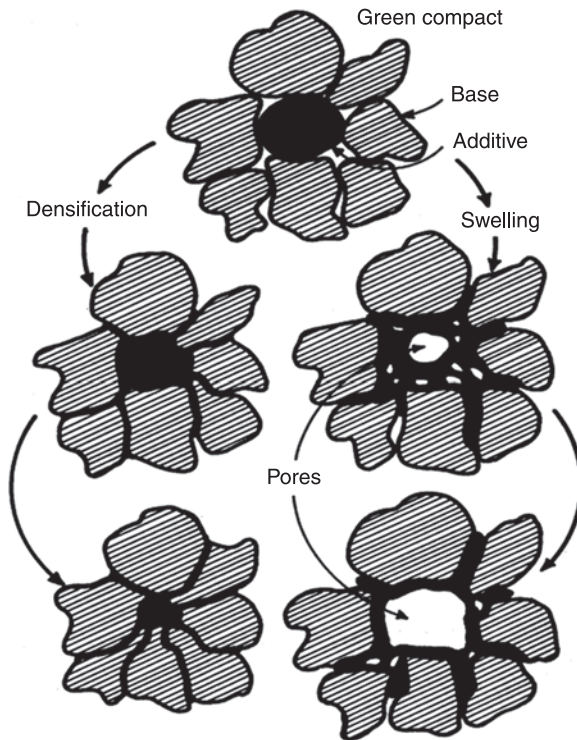
Liquid phase sintering (LPS) is defined as sintering involving a coexisting liquid and solid during part or whole of the sintering cycle. The presence of a liquid phase between particles leads to capillary forces that can result in densification and allows for the dissolution of solid away from regions of high surface energy and their subsequent re-precipitation. As such, densification rates can be greatly enhanced by the presence of a liquid. LPS allows for densification at lower temperatures than that of solid-state sintering. The potential disadvantages of liquid phase sintering include high distortion, deterioration of mechanical properties due to the solidification of brittle phases along grain boundaries and/or grain growth during sintering, the limitation of the final part in high-temperature applications, and thermodynamic factors, which can limit the choice of alloying elements.

LPS systems can be categorised by the way the liquid forms or by the amount of liquid present. In super-solidus liquid phase sintering (SLPS), the liquid phase forms when pre-alloyed powder is heated above its solidus. In reactive sintering, liquid can form due to exothermic reaction(s) of dissimilar powders. Persistent, transient and partially transient liquid phase sintering systems rely on additives to form the liquid. The additives are either elemental or master alloy powders. The liquid forms when the additive powders melt, or react with each other or the base powders to form a liquid.

In transient LPS, the additive is fully soluble in the solid base at the sintering temperature and the liquid content reduces to zero during sintering. The amount of

liquid formed in transient systems is heavily dependent on processing conditions, including the heating rate and powder particle size (Lumley and Schaffer, 1996). In persistent liquid phase sintering, the liquid is present throughout sintering. The requirements for favourable LPS are (German, 1986; Schaffer et al., 2001):

- The liquid should wet the solid. Wetting is given further consideration in Section 21.3.3.
- The additive should have a low solubility in the solid base so that it remains segregated to particle boundaries and maximises the liquid content, thus enabling shrinkage mechanisms based on solution re-precipitation. Conversely, if the additive has a high solubility in the base, swelling can occur, Fig. 21.6.
- The base should have high solubility in the liquid (formed by the additive) and the base should have a high diffusivity through the liquid to ensure mass transport.
- Liquids should be completely miscible and intermediate solid compounds should not form, to ensure mass transport and liquid spreading is not

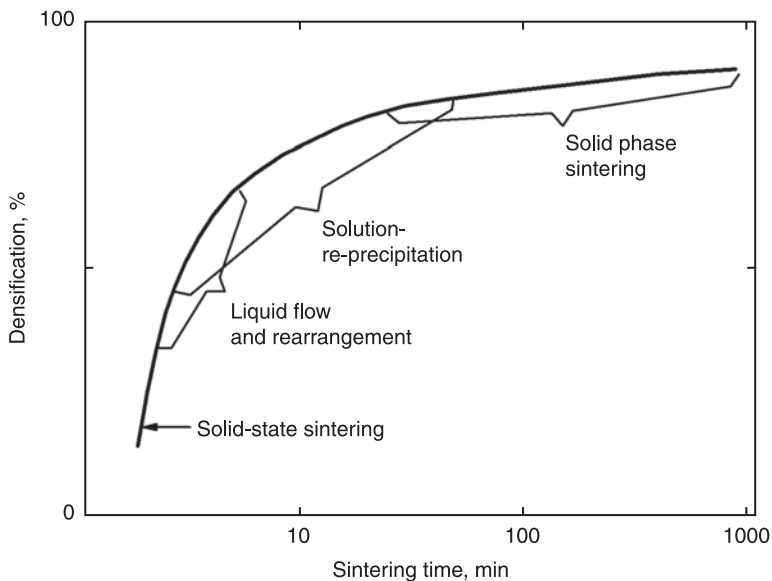


21.6 Shrinkage (left) or swelling (right) as a result of solubility differences between the base and the additive phases (German, 1996).

constrained during sintering. The prevention of shrinkage by the presence of a solid-phase surrounding the liquid-phase has been reported for LPS of Fe-Ti (German and Dunlap, 1986).

In Kingery's classical theory (Kingery, 1959), liquid phase sintering occurs by three concurrent mechanisms, as shown in Fig. 21.7, including: (1) particle rearrangement, resulting in rapid densification; (2) contact flattening by solution re-precipitation, leading to a reduction in the centre-to-centre distance of the particles; and (3) the coalescence of solid particles, where densification is limited by solid-state sintering mechanisms. The dominant mechanism changes as sintering progresses.

Kingery's classical LPS theory has been criticised for a number of reasons. The rate of particle rearrangement presented by Kingery is an assumption with little experimental evidence (Kang, 2005) and the relative movement of individual particles was not considered (Huppmann et al., 1979). In addition, grain-growth via Ostwald ripening, which occurs by solution re-precipitation, was overlooked (Mortensen, 1997). Finally, the coalescence of solid particles by grain boundary elimination assumes that no liquid is present between any of the particles in the later stages of sintering. Despite these criticisms, Kingery's theory is used extensively as the foundation for developing the understanding of LPS mechanisms.



21.7 The classical approach to the mechanisms occurring during liquid phase sintering (German, 1996).

21.3.3 Wetting

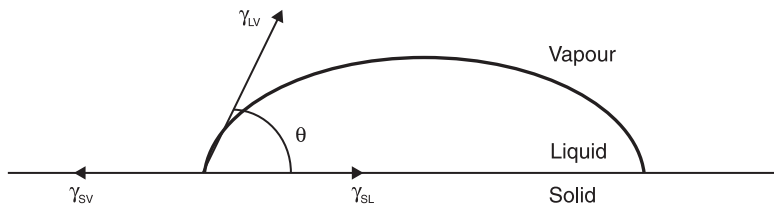
Wetting is not a sintering mechanism but its role is critical in liquid phase sintering. Wetting describes the interaction of solid, liquid and vapour phases. Good wetting enhances liquid phase sintering mechanisms via strong capillary forces between the liquid and solid substrate and by increasing the solid–liquid interface area. Wetting is influenced by the surface tension of the liquid and the strength of the solid–liquid interaction at the interface (Delannay et al., 1987) but are slightly different. The terms ‘surface tension’ and ‘surface energy’ are often used interchangeably (Saiz et al., 1998). The surface energy is the work necessary to form new surface area (Eustathopoulos et al., 1999), whereas the surface tension is the tangential stress (force per unit length) in the surface layer. The surface tension, γ , is related to the surface energy, σ :

$$\gamma = \sigma + \frac{d\sigma}{d\varepsilon} \quad [21.2]$$

where ε is the lattice strain. For liquids, the liquid–vapour surface tension, γ_{LV} , is equal to the liquid–vapour surface energy, σ_{LV} . The solid–vapour and solid–liquid interface tensions are γ_{SV} and γ_{SL} , respectively. An indication of the wetting characteristics of a liquid on a solid is the contact angle (also referred to as the wetting angle), θ , given at equilibrium by Young’s equation, Fig. 21.8 and Eq. 21.3.

$$\cos \theta = \frac{(\gamma_{SV} - \gamma_{SL})}{\gamma_{LV}} \quad [21.3]$$

A system is said to be non-wetting when the solid–liquid surface energy is greater than the solid–vapour surface energy resulting in a contact angle of greater than 90° . Conversely, a system is said to be wetting when the solid–liquid surface energy is less than the solid–vapour surface energy; the contact angle is then less than 90° . A decrease in the liquid–vapour surface energy either decreases the contact angle, in the wetting case, or increases the contact angle, in the non-wetting case. A decrease in the γ_{SL} or both γ_{LV} and γ_{SL} can decrease the contact angle, causing a transition from non-wetting to wetting (Eustathopoulos et al., 2001). A transition from non-wetting to wetting can occur by the formation of a



21.8 Schematic of the equilibrium wetting angle of a liquid in contact with a solid substrate (Liu and German, 1996).

more wettable substrate (Warren and Andersson, 1984; Protsenko et al., 2007). On the other hand, the formation of a less wettable substrate can lead to a transition from wetting to non-wetting (Eustathopoulos et al., 1999).

The measurement of the contact angle between aluminium and a substrate is hindered by the high affinity of aluminium for oxygen. The formation of an oxide skin on liquid aluminium can give obtuse contact angles. An example of this behaviour is the wetting of aluminium on its oxide. When an oxide skin is present on liquid aluminium, the liquid does not wet aluminium oxide. When the oxide skin surrounding the liquid decomposes, at high temperature or at low oxygen partial pressures (Laurent et al., 1988), or is disrupted mechanically (Nizhenko, 2001), the liquid exhibits an acute contact angle on aluminium oxide. The variation in measured contact angles of liquid aluminium on various substrates in the literature can largely be attributed to atmosphere effects rather than measurement error (Eustathopoulos et al., 1999).

The wetting characteristics depend on the substrate, atmosphere, composition of the liquid and temperature. The wetting conditions in aluminium powder metallurgy are not readily characterised for several reasons:

- The nature of the interface between the aluminium substrate and the liquid is unknown.
- The oxygen partial pressure deep within a porous compact is many orders of magnitude lower (2.6×10^{-32} Pa) (Schaffer and Hall, 2002) than that which can be obtained in conventional wetting experiments, which is typically between 10^{-15} and 10^{-5} Pa (Eustathopoulos et al., 1999).
- There is no published data of the contact angles at the usual sintering temperatures (between 550°C and 620°C).
- There is limited data for the effect of specific liquid compositions on the wettability of any given substrate.

Although the wetting behaviour of the aluminium liquid deep within a powder compact cannot be easily characterised, certain wetting conditions can be inferred from experimental observations. During the sintering of aluminium with magnesium, there are a number of possible solid substrates which could co-exist deep within the compact, including aluminium, magnesia-aluminate spinel and aluminium oxide. In the presence of nitrogen, aluminium nitride and magnesium nitride could also be expected. The contact angle of liquid aluminium on its own solid, an fcc metal with little surface anisotropy, is expected to be close to zero (Eustathopoulos et al., 1999). The reported contact angles of liquid aluminium on Al_2O_3 are between 77° and 120° (Champion et al., 1969; Laurent et al., 1988; Jung et al., 1996; Levi and Kaplan, 2002; Rocha-Rangel et al., 2003). The wetting of aluminium on aluminium nitride is better than on aluminium oxide, with reported contact angles of between 39° (Naidich and Taranets, 1998) and 60° (Eustathopoulos et al., 1999). It was suggested that the wetting of aluminium on aluminium nitride is strongly influenced by the segregation of oxygen, which

forms Al_2O_3 or an oxy-nitride, to the detriment of wetting (Eustathopoulos et al., 1999). There are no reported contact angles of liquid aluminium on magnesia-aluminate spinel nor on magnesium nitride.

A decrease in the solid–liquid interface tension, γ_{SL} , can cause a transition from non-wetting to wetting. A reduction in γ_{SL} can occur by the segregation of surface active elements to the solid–liquid interface or by the formation of more wettable solids at the interface (Eustathopoulos and Drevet, 1998). For the wetting of liquid metals on oxides, elements in the liquid that have a high affinity for oxygen segregate to the solid liquid and reduce the interface tension (Delannay et al., 1987). For example, if a liquid containing aluminium and magnesium is in contact with alumina, the magnesium because it has a higher affinity for oxygen than aluminium will segregate to the solid–liquid interface, enhancing wetting (Miller, 2004). In addition, magnesium is expected to disrupt the aluminium oxide to expose the underlying aluminium, further enhancing wetting. It has been suggested that the segregation of magnesium to the solid–liquid interface can enhance wetting of aluminium-magnesium liquid on TiCN (Levi et al., 1999). There are no known reports on the influence of magnesium on the wetting of liquid aluminium on aluminium nitride. However, magnesium may be beneficial because it can help eliminate any oxides, which are detrimental to the wetting of aluminium on aluminium nitride (Eustathopoulos et al., 1999). The Gibb's free energy of the reaction between magnesium liquid and aluminium nitride is positive. The formation of a more wettable compound is thus unlikely if magnesium liquid is in contact with aluminium nitride. The wetting angle can be further reduced by decreasing the liquid–vapour surface tension. The liquid–vapour surface tension can be decreased by the segregation of surface active components to the liquid–vapour interface (Mills and Su, 2006). Elements most likely to be surface active in metals are those with limited solubility in the liquid metal (Iida and Guthrie, 1988) or those with a low surface tension.

The decrease in the liquid–vapour surface tension of aluminium with oxygen is well documented (Mills and Su, 2006), but there are few publications which report the effects of nitrogen. The surface tension of pure aluminium in a nitrogen atmosphere is lower than that in argon at temperatures greater than 850°C (Saravanan et al., 2001), but at lower temperature there is little difference between the surface tensions under argon or nitrogen. It was suggested that the reduction in surface tension was due to disruption of the oxide surrounding the liquid aluminium, leading to the reaction of the exposed aluminium to the nitrogen atmosphere allowing for the formation of aluminium nitride (Saravanan et al., 2001).

The liquid–vapour surface tensions of elements common in the liquid phase sintering of aluminium are shown in Table 21.2. Tin and magnesium have a lower liquid–vapour surface tension than that of aluminium and are likely to segregate to the liquid–vapour interface, improving acute wetting angles.

Table 21.2 The minimum and maximum reported liquid–vapour surface tensions of pure elements at their melting points

Element	Surface tension ($\times 10^{-3}$, N.m $^{-1}$)
Al	1009–1100
Mg	577
Si	859
Cu	1255–1374
Sn	546–586
Zn	789–817

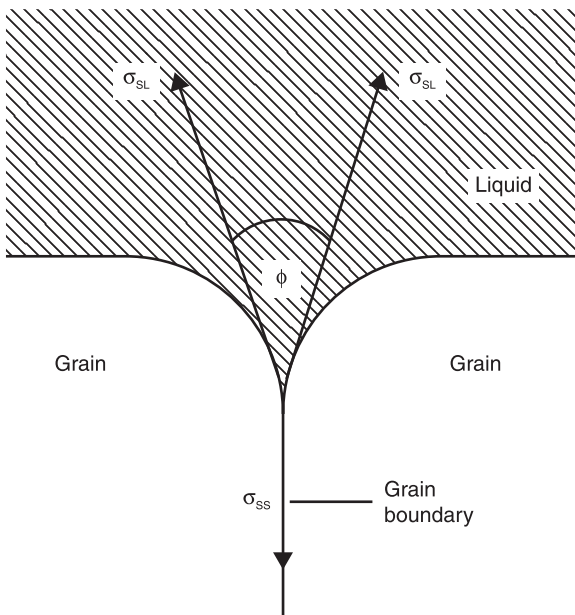
Source: Mills and Su (2006)

21.3.4 Dihedral angle

The dihedral angle is similar to the contact angle in that it involves the balance of interface energies. The dihedral angle, ϕ , forms where a grain boundary intersects the liquid and is a measure of grain boundary penetration by a liquid, Fig. 21.9.

The relationship between the dihedral angle, the solid–solid interface energy, σ_{SS} , and the solid–liquid interface energy σ_{SL} , is given by:

$$2\sigma_{SL} \cos \frac{\phi}{2} = \sigma_{SS} \quad [21.4]$$



21.9 Dihedral angle for liquid in contact with grains (Rahaman, 1995).

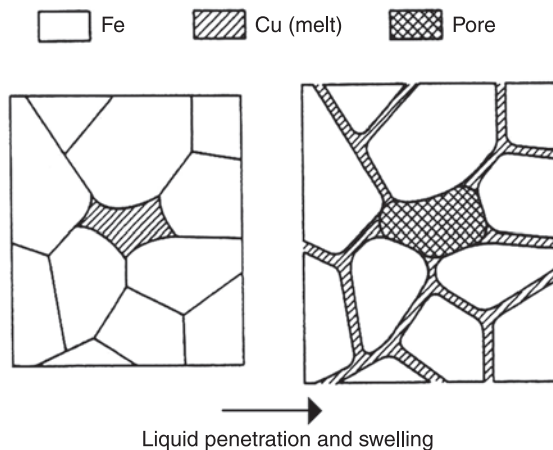
When the energy associated with two solid–liquid interfaces, $2\sigma_{\text{SL}}$, is less than the solid–solid interface energy, σ_{SS} , liquid will penetrate along the grain boundary. As the dihedral angle increases, the penetration of the liquid phase along grain boundaries is reduced and the number of solid/solid contacts increase. Excessive penetration of grain boundaries by liquid can lead to macroscopic swelling (Kaysser et al., 1980; Tabeshfar and Chadwick, 1984; Wanibe et al., 1990; Danninger, 1992), as illustrated in Fig. 21.10. This type of swelling can be alleviated by reducing the $\sigma_{\text{SS}}/\sigma_{\text{SL}}$ ratio through alloying additions (Jamil and Chadwick, 1985).

21.3.5 Rearrangement

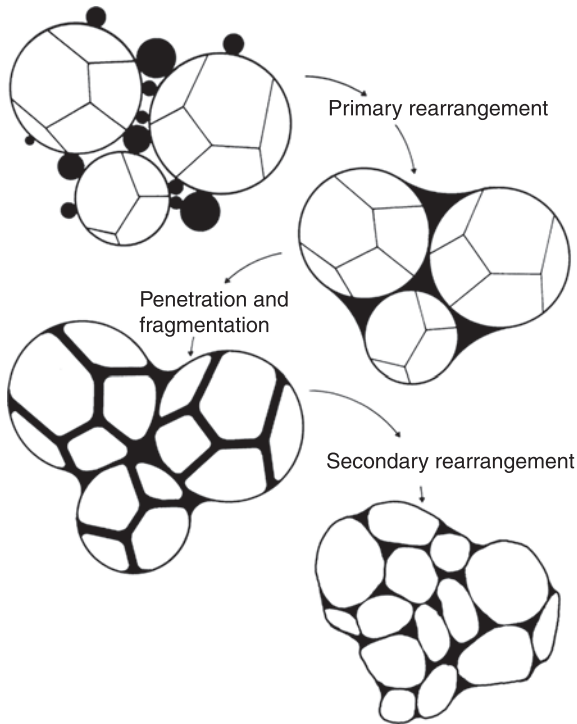
Primary rearrangement is the relative movement of particles in contact with a liquid phase under the action of surface tension forces, leading to a change in the packing density. Secondary rearrangement occurs when liquid penetrates grain boundaries, leading to particle fragmentation and repacking of the fragments to higher packing densities (Liu and German, 1999). These two processes are represented schematically in Fig. 21.11. This section will consider primary rearrangement only.

The capillary forces during rearrangement in LPS have been modelled by several authors using a liquid-bridge model of spherical particles, Fig. 21.12 (Huppmann and Riegger, 1975; Shaw, 1986; Svoboda et al., 1996; Xu and Mehrabadi, 1997; Liu and German, 2001; Nikolic, 2004).

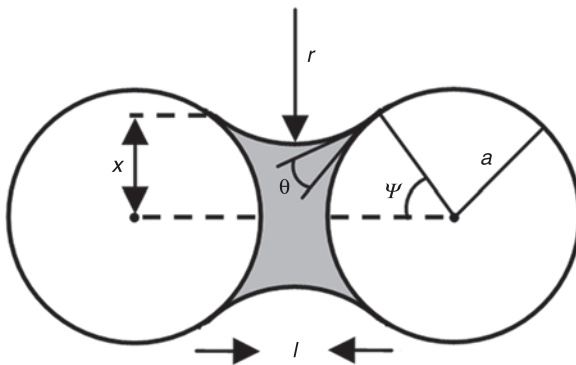
The liquid–vapour surface tension and the capillary pressure exert a force between the particles. The force, F , is given by (Kang, 2005):



21.10 The penetration of liquid copper down iron grain boundaries causing swelling (adapted from Kaysser et al. [1980]).



21.11 The formation of liquid leading to primary rearrangement or secondary rearrangement in polycrystalline particles (German, 1996).



21.12 Schematic of two spherical particles connected by a liquid bridge (Kang, 2005). The interparticle distance is given by l , a is the particle radius, θ is the wetting angle and ψ is the contact angle. The shape of the liquid is defined by the principal radii of curvature, x and r .

$$F = \gamma_{LV} \left[\pi a^2 \sin^2 \Psi \left(\frac{1}{r} - \frac{1}{x} \right) 2\pi + 2\pi a \sin \Psi \sin(\Psi + \theta) \right] \quad [21.5]$$

where γ_{LV} is the liquid–vapour surface tension, a is the particle radius, θ is the wetting angle and Ψ is the contact angle. The shape of the liquid is defined by the parameters x and r , and is estimated by the circle approximation (Cahn and Heady, 1970; Kang, 2005), using the following two relationships:

$$x = a \sin \Psi - \left[a(1 - \cos \Psi) + \frac{l}{2} \right] \frac{1 - \sin(\Psi + \theta)}{\cos(\Psi + \theta)} \quad [21.6]$$

$$r = \frac{a(1 - \cos \Psi) + \frac{l}{2}}{\cos(\Psi + \theta)} \quad [21.7]$$

where l is the separation distance. Whether or not the interparticle force is repulsive or attractive, and the magnitude of the force, is dependent on the geometry of the liquid and solid and the wetting angle. The important outcomes of the relationship between geometry, wetting and the forces acting on the particles are:

- The force is attractive for low wetting angles and increases with reduced wetting angle. The interparticle distance decreases until the particles touch. The net result is shrinkage (Huppmann and Riegger, 1975; Nikolic, 2004).
- The force can be repulsive for wetting angles slightly below 90° and is repulsive for wetting angles greater than 90° . The interparticle distance increases until the force is zero. The net result is swelling (Huppmann and Riegger, 1975; German, 1996).
- The attractive force increases when the particle size decreases (Kingery, 1959; Mortensen, 1997; Liu et al., 2001).
- At low wetting angles, increasing the liquid content can decrease the attractive force between the particles (Huppmann and Riegger, 1975; Nikolic, 2004).

An apparent anomaly in the liquid-bridge model is that an increase in liquid content can reduce the attractive force between particles, despite the commonly held belief that increasing the liquid content enhances rearrangement. Two factors overlooked in the liquid-bridge models can explain this apparent anomaly. First, the presence of solid–solid contacts in an array of particles impedes densification by rearrangement (Liu and German, 1999; Liu and German, 2001). Rearrangement occurs when the mean capillary pressure is greater than the mean bonding strength per grain (Liu and German, 1999). As the liquid content increases, the number of dissolved solid bonds increases which in turn decreases the strength of the compact and enhances densification by rearrangement (Liu and German, 1999). Secondly, the liquid-bridge model does not take into account the number of liquid-bridges formed throughout the compact. If increasing the liquid volume increases the number of liquid-bridge contacts throughout an array of particles, primary rearrangement will be enhanced. Thus, the homogenous distribution of liquid through the compact is important (Huppmann et al., 1979; Xu and Mehrabadi, 1997).

A criticism of the liquid-bridge model is that it does not account for particle sliding. The sliding of grains is accompanied by shearing of the liquid film between adjacent particles (Liu and German, 1999). For Newtonian fluids, the stress associated with shear of the liquid increases with the liquid viscosity (Dryden and Watt, 1981; Fox and McDonald, 1994; Liu and German, 1999). It follows that the resistance against sliding of the particles should increase with the liquid viscosity. Therefore, the densification rate due to rearrangement decreases with increasing liquid viscosity (Svoboda et al., 1996). German (German, 1996) includes the influence of viscosity in an estimation of the shrinkage rate due to rearrangement, given by:

$$\frac{d(\Delta L/L_0)}{dt} = \frac{\Delta P w}{D \eta} \quad [21.8]$$

where ΔP is the capillary pressure, w is the liquid thickness, D is the particle size and η is the liquid viscosity. Equation 21.8 overestimates observed shrinkage rates because it does not take into account rate limiting steps, including heat transfer and the spreading and penetration of liquid throughout the microstructure (German, 1985).

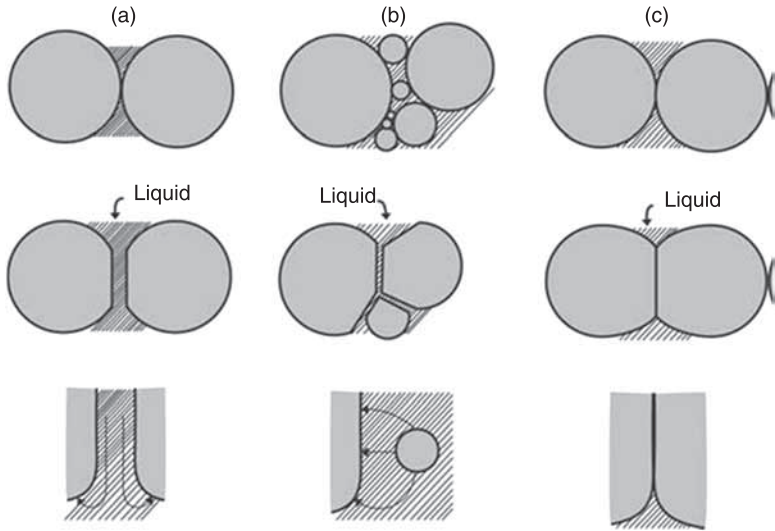
Rearrangement stops when the solid particles are packed to the maximum obtainable density without deformation (Mortensen, 1997). It follows then that rearrangement is enhanced when the initial packing density is low. During rearrangement the particles can become tightly packed and a solid skeleton can form which can isolate interconnected pores (Lee and Kang, 1998). Further densification relies on the elimination of these isolated pores. Two mechanisms have been proposed for the elimination of isolated pores; solution re-precipitation and pore-filling (Johnson and German, 1996; Lee and Kang, 1998).

21.3.6 Solution re-precipitation

Solution re-precipitation involves the dissolution of solid at solid/liquid interfaces, transport of the solute through the liquid, and re-precipitation of the solute at sites of lower chemical potential (Petzow and Kaysser, 1984). Solution re-precipitation mechanisms have been collectively termed 'secondary rearrangement' because they can lead to further shrinkage after primary rearrangement (Petzow and Kaysser, 1984). This form of secondary rearrangement should not be confused with secondary rearrangement resulting from the penetration of liquid down grain boundaries, as presented in Section 21.3.5. The solution re-precipitation phenomena which can lead to shrinkage are Ostwald ripening, contact flattening and solid state bonding.

Ostwald ripening

Ostwald ripening occurs via the dissolution of matter at regions with a small radius of curvature and re-precipitation at regions with a large radius of curvature, Fig. 21.13(b). Ostwald ripening leads to the dissolution of smaller solid grains,



21.13 The three mechanisms of grain shape accommodation and neck growth during solution re-precipitation controlled LPS densification: (a) contact flattening, (b) dissolution of small grains (Ostwald-ripening) and (c) solid-state bonding (German et al., 2009).

diffusion of the solute through the liquid and the re-precipitation of the solid onto large grains. The net result is grain growth.

Grain growth does not necessarily result in densification, but can facilitate liquid redistribution (German, 1996). Grain growth follows a kinetic law:

$$G^n = G_0^n + Kt \quad [21.9]$$

where G is the grain size after time t , G_0 is the initial grain size, n is an exponent depending on the growth mechanism ($n = 3$ for diffusion-controlled growth) and K is the rate constant. There are conflicting views on the influence of liquid content on grain growth. Experiments by several authors have found that increasing the liquid content decreases the grain growth rate constant (Kang and Yoon, 1982; Kwon and Messing, 1990; German, 1995; German, 1996; Lee and Kang, 1998; German and Olevsky, 1998). On the contrary, it has been suggested that increasing the amount of liquid does not significantly affect the rate of densification due to grain growth (Mortensen, 1997), but rather it promotes rearrangement (Kwon and Messing, 1990). A consistent, accepted explanation on the influence of liquid content on grain growth during liquid phase sintering is lacking (German, 1995).

Contact flattening

Contact flattening relies on the presence of a liquid film between two solid grains. The curvature of the liquid menisci between the solid particles, and the

liquid–vapour surface tension exerts a compressive stress in the solid–liquid contact region (Kaysser and Petzow, 1985; Kaysser, 1991). The solubility of solid atoms within the contact region is high and there is a net diffusion of solid through the liquid to regions of lower chemical potential at the contact peripheries. The result of this mass transport is a flattening of the grains at the solid/liquid interfaces, which results in a reduction in the centre-to-centre distance of the particles and thus shrinkage. The process of contact flattening is presented schematically in Fig. 22.13(a).

The densification rates due to contact flattening are limited by the dissolution of matter at the contact zone or by the diffusion of mass away from the contact zone (German, 1996). It was estimated that the shrinkage due to contact flattening for the diffusion-limited case was (Kingery, 1959):

$$\frac{\Delta L}{L_0} = \left(\frac{6k_2 \delta D C_0 \gamma_{LV} V_0}{k_1 R T} \right) r^{-\frac{4}{3}} t^{\frac{1}{3}} \quad [21.10]$$

where k_1 and k_2 are constants of proportionality, δ is the liquid boundary thickness, D is the diffusivity of the solid in the liquid, C_0 is the initial concentration of the solid in the liquid, γ_{LV} is the surface tension, V_0 is the initial volume, R is Boltzmann's constant, T is the temperature. A similar expression exists for dissolution-limited contact flattening:

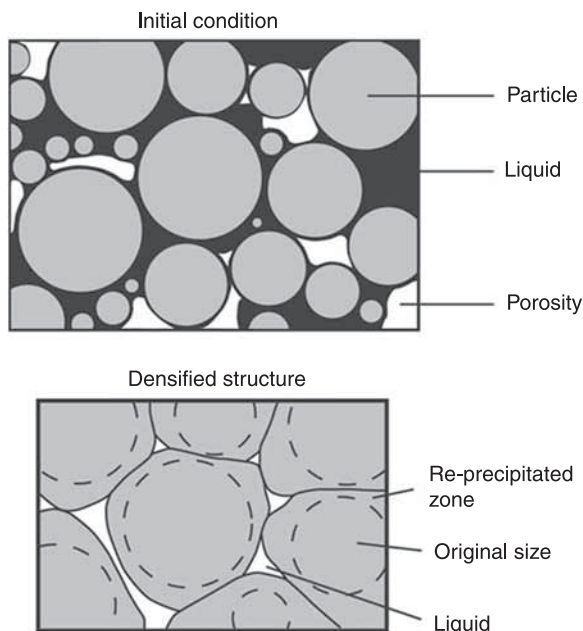
$$\frac{\Delta L}{L_0} = \left(\frac{2k_4 k_2 \delta D C_0 \gamma_{LV} V_0}{k_1 R T} \right) r^{-1} t^{\frac{1}{2}} \quad [21.11]$$

where k_4 is a constant of proportionality. There is little consensus on the effect of the liquid volume on contact flattening. Based on a two-particle model with a particle separation distance approaching zero (i.e. after rearrangement) and low contact angle, increasing the liquid content decreases the stress associated with the liquid menisci and the liquid–vapour surface tension (Kang, 2005). In addition, the diffusion distance from the centre of the contact zone to the edge of the liquid neck increases with the liquid content. These two factors suggest that contact flattening is inhibited by increased liquid contents. Conversely, if the number of solid–solid contacts in an array of particles decreases with increased liquid content, the average effective stress at the liquid–solid contacts increases, thus increasing the liquid content can be beneficial to contact flattening (Kwon and Messing, 1990; Kwon and Messing, 1991). It was suggested that the liquid volume has a negligible influence on the densification rate due to contact flattening (Svoboda et al., 1996; Mortensen, 1997).

A quantitative understanding of the effect of temperature on contact flattening has not been well established because the temperature changes the geometrical parameters, which influence the pressure at the solid–liquid interface, as well as the difference in solubility between the centre of the solid–liquid contact region and its peripheries. Low green densities are associated with a larger volume of larger pores (Svoboda et al., 1996; Mortensen, 1997). The large pore radius means that the pressure in the solid/liquid contact zone is reduced, which, in turn,

decreases the contact flattening shrinkage rate (Mortensen, 1997). Increasing the pressure difference between the external atmosphere and the isolated pores enhances contact flattening. This increase in the pressure difference can be achieved by applying an external pressure, which increases the average force at the solid/liquid interface (Mortensen, 1997) or by decreasing the pressure in isolated pores (Mortensen, 1997).

Kingery's early contact flattening theory does not include the possibility of Ostwald ripening during sintering. Later models incorporated the effects of particle coarsening (Kaysser and Petzow, 1985; Svoboda et al., 1996; Mortensen, 1997), however a comparison of one of these models to experimental evidence suggests that contact flattening is not a major shrinkage mechanism during liquid phase sintering (Kaysser and Petzow, 1985). Rather, shape accommodation during grain growth was proposed as a more important shrinkage mechanism (Petzow and Kaysser, 1984; Kang et al., 1985; Kaysser and Petzow, 1985) and can lead to the appearance of flattened contacts, as shown schematically in Fig. 21.14. An additional criticism of the contact flattening mechanism is that there has been no unambiguous microstructural evidence of its occurrence during sintering (Kaysser, 1991). Indeed, some authors suggest that contact flattening is unlikely and that grain growth induces the filling of pores by liquid.



21.14 A conceptual outline of the changes associated with solution re-precipitation densification where both grain growth and grain shape accommodation act to release liquid to fill residual pores (German et al., 2009).

Solid state bonding

The third mechanism involves growth of the intergrain contact by diffusion along the liquid wetted grain boundary, as indicated in Fig. 21.13(c) (German et al., 2009). The contact zone enlarges to change the grain shape with simultaneous shrinkage of the grains. This does not involve grain coarsening, but it requires a cooperative redistribution process of the mass deposited where the grain boundary intersects the liquid (German, et al., 2009).

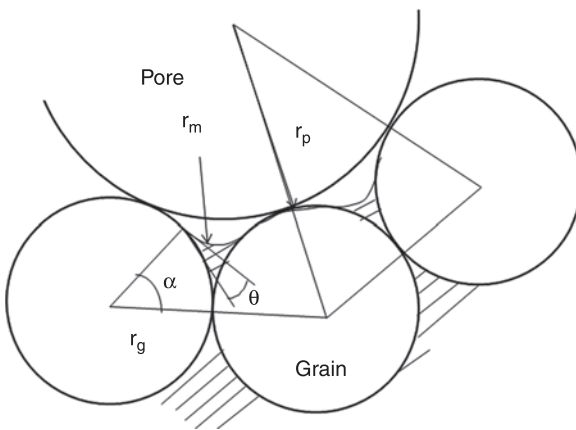
21.3.7 Pore-filling

Densification can occur by the filling of pores with liquid during grain growth (Kang et al., 1991). A schematic of the geometry of the liquid surrounding multiple grains and a pore is shown in Fig. 21.15. The liquid meniscus radius, r_m , at the pore surface is related to the grain size, r_g , wetting angle, θ , and the position of the menisci between the grains, α , by (Park et al. 1984):

$$r_m = r_g \frac{(1 - \cos \alpha)}{\cos(\alpha + \theta)} \quad [21.12]$$

During sintering, the grains coarsen and the liquid meniscus radii increase. The liquid menisci coalesce to form a spherical pore when the liquid meniscus radius equals the pore radius, r_p ; the pore surface is then completely wetted by liquid (Park et al., 1984). This condition is the critical point for pore filling (Park et al., 1986). The liquid pressure, P_l , is related to the liquid–vapour surface tension, γ_{LV} , and the liquid meniscus radius by (Park et al., 1984):

$$P_l = \frac{-\gamma_{LV}}{r_m} \quad [21.13]$$

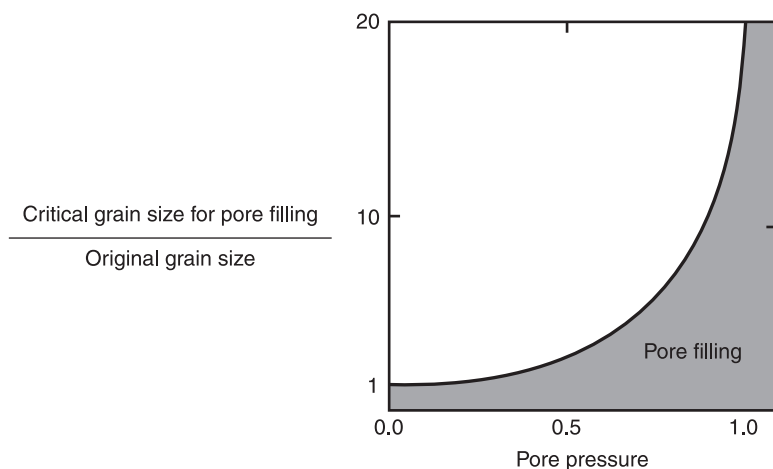


21.15 The liquid meniscus radius, r_m , at the pore surface is related to the grain size, r_g , wetting angle, θ , and the position of the menisci between the grains, α (Park et al., 1984).

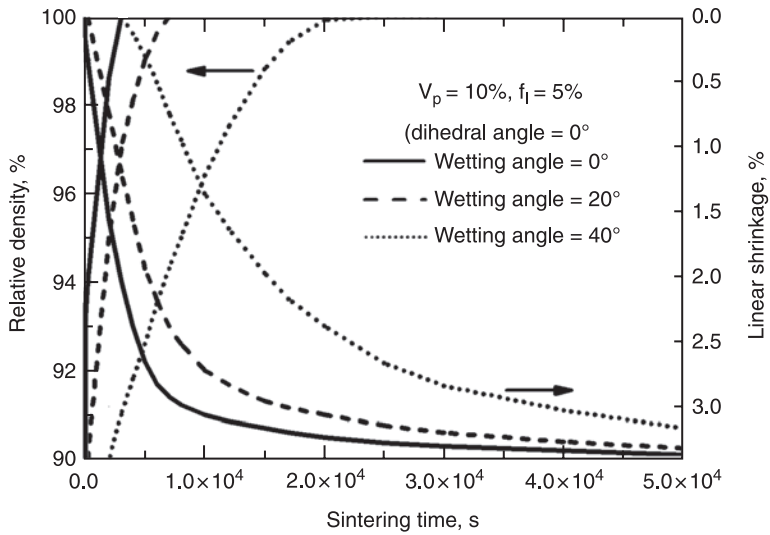
As the grains continue to grow, the liquid menisci at the specimen surface increase, whereas the pore radius is limited by the pore size. The pressure of the liquid at the pore surface is therefore lower than at the sample surface, which induces flow of liquid into the pores. The flow of liquid into isolated pores depends on the pressure of the entrapped gas, P_p , and the external atmosphere (Cho et al., 1986). Gas trapped within pores delays the critical condition for pore filling (Park et al., 1984). It follows then that reducing the pressure of gas within a pore will decrease the critical grain size for pore filling (Fig. 21.16).

For compacts with a limited volume of liquid, the liquid menisci at the pore surface will have a small radius of curvature, which induces a compressive stress between the grains, making pore filling difficult to achieve (Kang et al., 1991). Thus, densification by other mechanisms is important when the volume fraction of liquid is low (Kang et al., 1991). Likewise, the liquid meniscus radius increases with liquid content, which promotes pore filling (Lee and Kang, 1998; Lee and Kang, 2005). For a given liquid volume, the densification rates due to pore-filling decrease when the pore volume fraction increases (Lee and Kang, 1998). Increasing the grain growth rate will reduce the time at which the critical grain size is reached and the rate of densification due to pore filling (Lee and Kang, 2005). Because the pore must be covered by the liquid prior to pore filling, increasing the wetting angle retards pore-filling kinetics (Lee and Kang, 2005), Fig. 21.17, and the critical grain size increases with the wetting angle, Fig. 21.18.

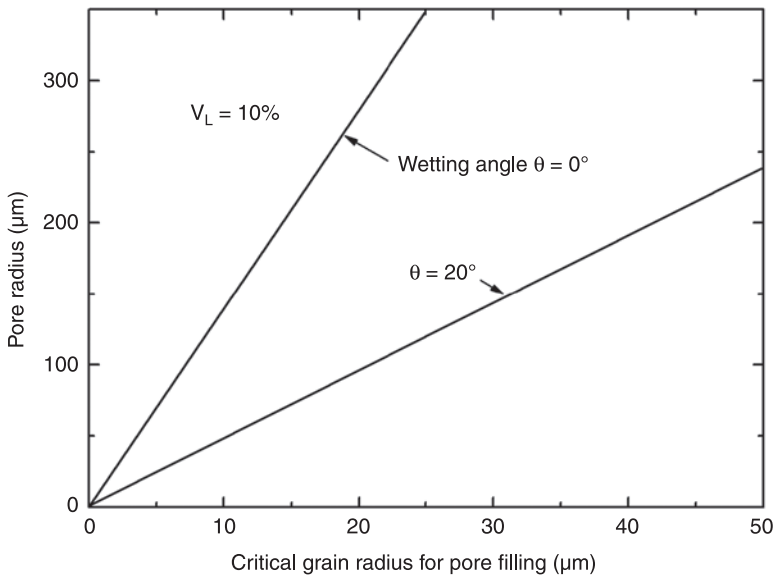
Shaw (1986) suggested an alternative model to the pore-filling model described above. Shaw modelled the changes in free energy resulting from the filling of pores with liquid in a two-dimensional array of circular particles. The model predicts that liquid will fill pores in order of increasing co-ordination number;



21.16 The ratio of the critical grain size for pore filling to the original grain size increases with the internal pore pressure (Cho et al., 1986).



21.17 Calculated curves of relative density and shrinkage with sintering times showing the effect of the wetting angle for a given liquid content, dihedral angle and porosity content (Lee and Kang, 1998).



21.18 The effect of the wetting angle for the critical grain size for pore filling (Park et al., 1986).

i.e. small pores fill before larger ones. In addition, the filling of large pores only occurs if there is a sufficient liquid volume or that a certain amount of shrinkage occurs. Shaw suggests that the pore-filling theory based on grain growth can be misleading because it considers the pores in isolation and does not consider the effect of grain coarsening on the pore size distribution.

21.4 Sintering of aluminium

Sintering of aluminium is typically carried out at a temperature between 570°C and 620°C. Liquid phases can then result from melting of the low-melting additive powders and from interdiffusion, Table 21.3. In general, high liquid fraction leads to fast densification (German, 1997), but it also makes dimensional control more difficult (Schaffer and Huo, 2000). Sintering occurs in a series of overlapping but balanced stages via various densification mechanisms (refer to Section 21.2), all of which depend on temperature, time and the atmospheric conditions. Furnaces used for sintering typically are muffle type three zone conveyor furnaces, similar to protective atmosphere furnaces used for sintering copper and iron based powder materials. The characteristic that distinguishes the sintering of aluminium from that of copper and iron is that sintering of aluminium requires strict dew point control (-60°C or lower) and temperature control (approx. $\pm 3^{\circ}\text{C}$), which are essential to ensure the development of quality sintered microstructures, mechanical properties and dimension consistency. The sintering atmosphere has a critical influence on the sintering processes. This is further discussed in detail in Section 21.4.3.

21.4.1 Surface oxide

Because of its extreme high affinity for oxygen, aluminium is always covered by an oxide. The thickness of the oxide is dependent on the temperature at which it formed and the atmosphere in which it is stored, particularly the humidity. Aluminium powders produced by air-atomisation have typical oxygen contents of about 0.3 wt.% (Schatt and Wieters, 1997) or 0.3–0.6 wt.% (Daver et al., 1989). Fresh oxide on bulk aluminium at room temperature is widely reported as being 10–20 nm thick (Olefjord and Karlsson, 1986; Olefjord and Nylund, 1994). The thickness on atomised powder can vary from 50 to 150 nm (Ozbilen et al., 1989; Nielsen et al., 1993; Anderson et al., 1998). The variation in the thickness is partially attributed to the method used for the measurement. For example, the oxide thickness was reported to be about 40–60 nm according to the depth profiles of Al and O collected from an Auger analysis of air-atomised Al-4Fe-4Ni-1.1Si-(0–1.0)Mg powders (Kondoh et al., 2001). The thickness determined by other means was reported to be in the range of 5–15 nm (Schaffer, 2000). Binary aluminium powders produced by inert gas-atomisation, such as argon, however, have a much thinner oxide film, 0.7–2.04 nm (Upadhyaya, 2000). The oxide on aluminium is usually amorphous (Anderson et al., 1998; Jeurgens et al., 2000) and

Table 21.3 Calculated equilibrium liquid mass fraction of some press and sinter PM aluminium alloys

Temperature (°C)	Liquid mass fraction (%)			
	Al-0.25Cu- 1Mg-0.7Si (6xxx)	Al-3.8Cu- 1Mg- 0.7Si (2xxx)	Al-6.5Zn- 2.5Mg- 1.5Cu (7xxx)	Al-14Si- 0.5Mg-1.5Cu (Al-Si)
550	0	4.8	0.8	19.7
560	0	6.1	2.8	51.2
570	0	9.0	6.1	98.1
580	0	11.6	9.7	99.2
590	0.4	15.4	16.1	100
600	2.2	19.7	24.2	100
610	4.8	26.3	38.1	100
620	9.1	34.2	56.5	100

hydrated (Arbuzova, 1976; Nylund and Olefjord, 1994) with an adsorbed water layer (Flumerfelt and Anderson, 1998). The crystalline structure of the oxide film is dependent on the crystallographic face on which the oxide has nucleated and also on the thickness of the oxide film (Shinohara et al., 1982; Eldridge et al., 1988; Jeurgens et al., 2000). Thermodynamic analyses showed that the energy of the Al-Al₂O₃ interface stabilizes the amorphous Al₂O₃ only up to a few nanometres, e.g., 4 nm on {110} Al and 2 nm on {100} Al at room temperature; and 7 nm on {110} Al and 3 nm on {100} Al at 600°C (Jeurgens et al., 2000). As a consequence, inert gas-atomised aluminium powder is thus more likely than air-atomised powder to be covered by an amorphous oxide layer.

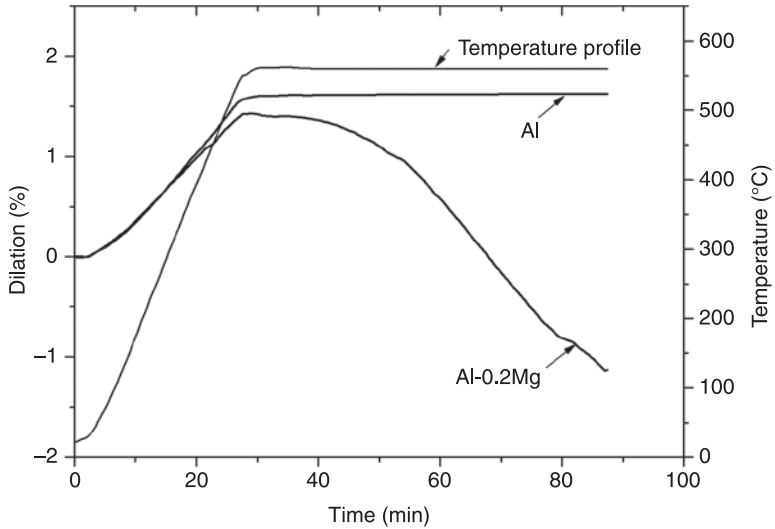
Because of hygroscopic characteristics of the oxide film, the surface of air-atomised powder normally consists of a system of the Al-Al₂O₃·nH₂O type (Arbuzova, 1976), which includes both hydrated aluminium oxide, Al(OH)₃, and physically adsorbed water. Air-atomised aluminium powders pre-alloyed with magnesium, lithium and zinc are more hygroscopic than pure aluminium powders (Plakhotnikova, 1988). Hydration can accelerate further oxidation of the powder, as the remaining oxide layer becomes thinner (Olefjord and Nylund, 1994). On heating, dehydration usually starts from approximately 150°C and is complete at a temperature slightly above 500°C, leaving crystalline γ -Al₂O₃ (Estrada et al., 1991).

21.4.2 The role of magnesium

The surface oxide films on metal powder hinder sintering. Conventional metal powders, such as iron- and copper-based powders, are sintered in a reducing atmosphere to reduce these oxides to facilitate sintering and to prevent further oxidation (German, 1996). In this respect, aluminium is unique because its oxide

is thermodynamically very stable and the reduction of Al_2O_3 requires extremely low oxygen partial pressures (e.g. 10^{-43} Pa) at the melting point of aluminium (Eustathopoulos et al., 1999) which cannot be achieved by conventional means. The LPS of aluminium is further inhibited by the poor wetting of liquid aluminium on Al_2O_3 . In order to facilitate sintering, the oxide surrounding the aluminium must be reduced or disrupted to allow for diffusion and for the wetting of the underlying metal by the sintering liquid (Lumley et al., 1999; Kondoh et al., 2001). A number of mechanisms for aluminium oxide disruption or reduction have been proposed including: (i) partial disruption via plastic deformation of the aluminium powder during compaction (Esper and Leuze, 1971; Daver et al., 1989; Simchi and Veltl, 2003); however, the mechanical disruption caused by conventional die consolidation is insufficient to enable extensive sintering (Daver et al., 1989); (ii) partial disruption via the formation of liquid between the oxide and the underlying metal (Kehl and Fischmeister, 1980; Kehl and Fischmeister, 1982); (iii) disruption of the oxide via cracking during heating (Hall et al., 2003); (iv) partial disruption via reaction of the aluminium oxide with magnesium, forming MgAl_2O_4 (Lumley et al., 1999) or MgO (Kimura et al., 1997); and (v) reducing the oxygen partial pressure via the reaction of oxygen with magnesium (Sercombe and Schaffer, 2004) or the oxidation of aluminium in the outer regions of PM compacts, termed self- or autogenous gettering (Schaffer and Hall, 2002).

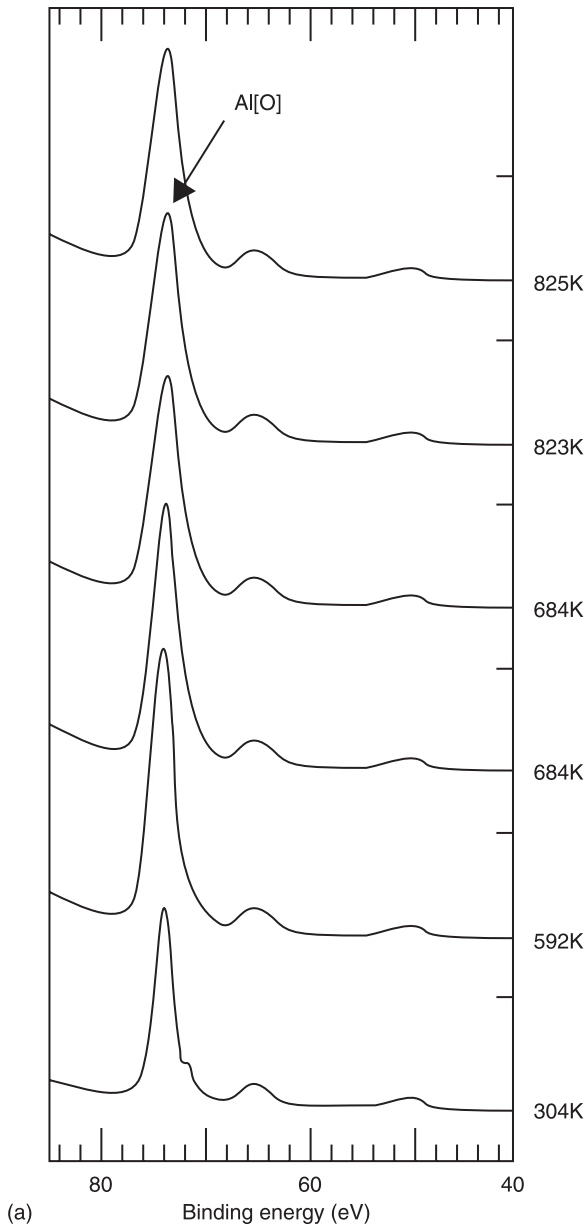
Magnesium plays a critical role in disrupting the oxide film chemically, enabling quality sintering for PM aluminium alloys (Lumley et al., 1999; Kondoh et al., 2000). It serves a similar purpose in aluminium powder metallurgy to conventional reducing atmospheres in ferrous and cuprous powder metallurgy – it removes the oxide as a barrier to sintering. Figure 21.19 demonstrates the beneficial effect of magnesium. As one of the major ingredients, magnesium was used in the early attempts to make useful aluminium PM materials (Kempf, 1940). The first two commercial aluminium PM alloys, 601 AB (Al-1.0Mg-0.6Si-0.25Cu) and 201 AB (Al-4.4Cu-0.5Mg-0.8Si), both contained magnesium (Dudas and Dean, 1969a, 1969b). The optimum amount of magnesium required to facilitate the sintering of aluminium is dependent on the volume of the oxide and is therefore dependent on the particle size and the thickness of the oxide on the aluminium particles (Sercombe, 1998; Lumley et al., 1999). One report (Lawrence and Foerster, 1971) suggests that the beneficial influence of magnesium on the sintering response decays as the powder blends are kept in storage for long times. Excessive use of magnesium is unnecessary; the optimum range is 0.1–1.0 wt.% for the sintering of binary Al-Mg alloys depending on the Al particle size (Lumley et al., 1999). The densification reduces when the magnesium concentration is greater than the critical amount (Sercombe, 1998; Lumley et al., 1999). The reduction in density at higher magnesium contents has been attributed to the diffusion of magnesium into aluminium (Savitskii, 1993; Sercombe, 1998).



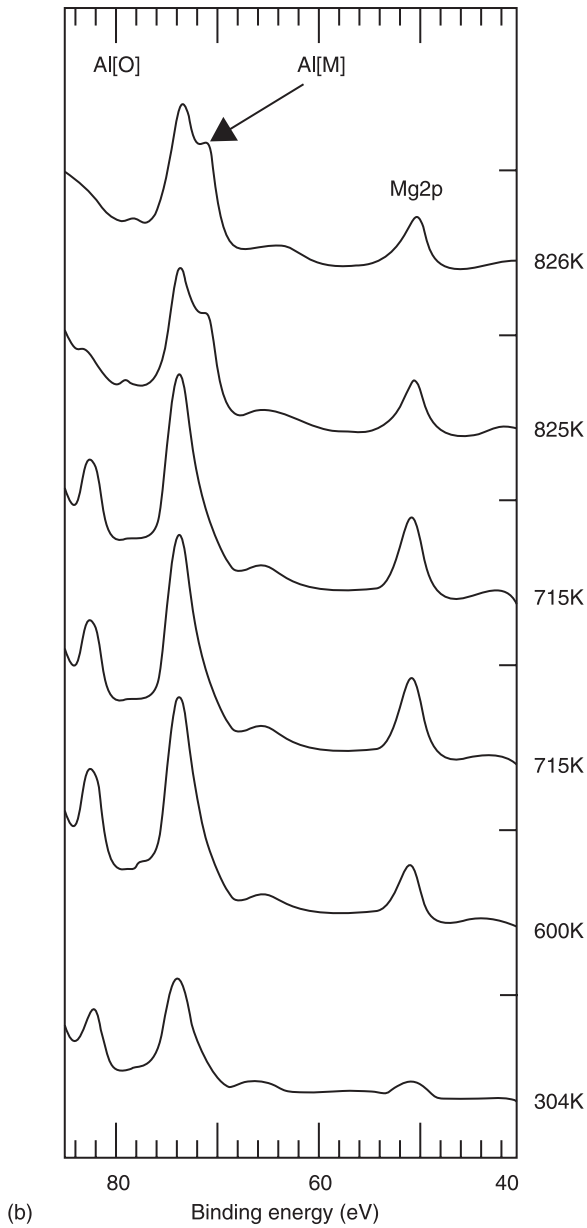
21.19 Dilatometer curves for samples of Al and Al-0.2Mg in nitrogen, showing that the addition of 0.2 wt.%Mg enables the sintering of aluminium in nitrogen. Air-atomised Al powder ($d_{50} = 77 \mu\text{m}$) and elemental Mg with a particle size of $<45 \mu\text{m}$ were used. The powder was compacted at 100 MPa.

The critical role of magnesium in sintering aluminium was not fully understood until magnesium was found to act as both a reducing agent to disrupt the oxide film and a getter to reduce the oxygen content in the local sintering atmosphere in the late 1990s (Kondoh et al., 1995; Kimura et al., 1997; Lumley et al., 1999; Kondoh et al., 2001). The disruption of the oxide via reaction with the magnesium occurs at temperatures above 500°C (Kimura et al., 1997). The in-situ X-ray photoelectron spectroscopy (XPS) results obtained from heating air-atomised Al powder and an Al-1Mg powder blend to 553°C in a vacuum of 10^{-7} Pa (Kondoh et al., 2001) are shown in Fig. 21.20. A single peak at 74.7 eV that corresponds to the spectrum of Al2p in an oxidised state (Al[O]) was detected throughout the heating of pure aluminium powder, Fig. 21.20(a). In contrast, an additional peak at 72.5 eV that corresponds to metallic aluminium, Al[M], emerged at 552°C during the heating for the Al-1Mg blend, Fig. 21.20(b). This indicates an effective disruption of the Al_2O_3 film by Mg. The disruption of the Al_2O_3 is most likely to occur through the reaction: $3\text{Mg} + 4\text{Al}_2\text{O}_3 \rightarrow 3\text{MgAl}_2\text{O}_4 + 2\text{Al}$, where formation of magnesia aluminate spinel, MgAl_2O_4 , was detected in a sintered Al-2.5Mg alloy (Lumley et al., 1999).

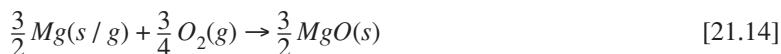
To enable Al to remain metallic at 560°C in vacuum, an oxygen partial pressure of $P_{\text{O}_2} < 9.01 \times 10^{-55}$ Pa is required (Qian and Schaffer, 2010). The preservation of metallic Al suggests an oxygen free environment in the local sintering atmosphere. The Gibbs free energy of reaction, ΔG_{MgO} , for the oxidation of magnesium as solid (s) or vapour (g) is similar,



21.20 In-situ XPS analyses during heating to 553°C in a vacuum of 10^{-7} Pa: (a) pure Al powder; (b) Al-1Mg blend. Metallic Al, Al[M], was detected in the Al-1Mg sample at 552°C. Heating rate from 397°C to 560°C was 0.026 K/s. Air-atomised powder with a mean particle size of 45 μm was used (reprinted with permission from Kondoh et al. [2001]).



21.20 Continued.



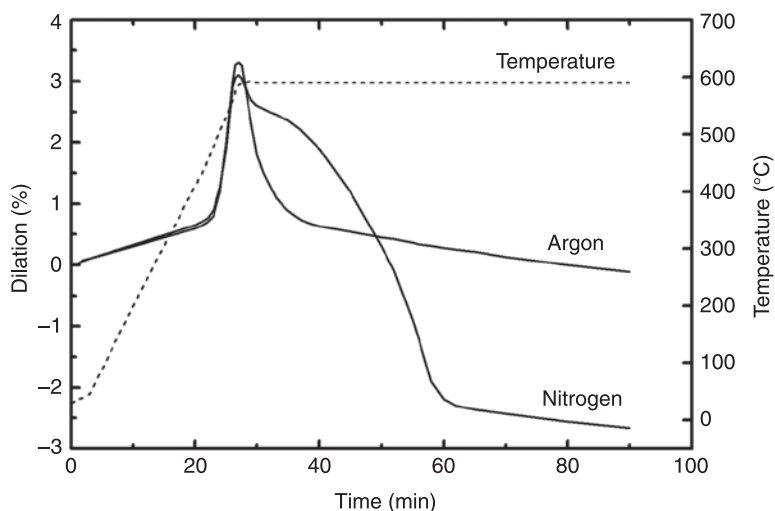
Similarly, the established thermodynamic data (Knacke et al., 1991) gives

$$\Delta G_{\text{MgO}} = -767.3 - \frac{3}{4} \times 6.922 \times \ln \frac{P_{\text{O}_2}}{P^0} \text{ kJ / mol} \quad [21.15]$$

Assuming the supply of Mg suffices to lead to, and also maintain, equilibrium with oxygen in the sintering atmosphere, an equilibrium oxygen partial pressure, $P_{\text{O}_2}^{\text{eq}}$, can be defined from Eq. 21.15 by setting $\Delta G_{\text{MgO}} = 0$. For sintering at 560°C, $P_{\text{O}_2}^{\text{eq}} = 2.91 \times 10^{-59}$ Pa, when $\Delta G_{\text{Al}_2\text{O}_3} > 0$ at $P_{\text{O}_2}^{\text{eq}} = 2.91 \times 10^{-59}$ Pa, means that Al_2O_3 is no longer thermodynamically stable and will then decompose into Al and O_2 . The effective disruption of the Al_2O_3 oxide film by magnesium assists the initiation of sintering while the oxygen free local sintering atmosphere created by magnesium enables sintering to fully develop. Both roles of magnesium are crucial for the effective sintering of aluminium.

21.4.3 The role of atmosphere

Atmosphere plays a critical role in LPS of aluminium alloys. Early work indicates that the sintering of aluminium is enhanced under a nitrogen atmosphere (Daver et al., 1989). Dilatometer curves of Al-3.8Cu-1Mg-0.7Si under argon and nitrogen, shown in Fig. 21.21, demonstrate that the total shrinkage is substantially greater



21.21 Dilatometer curves of Al-3.8Cu-1Mg-0.7Si under argon and nitrogen, showing that the expansion and initial shrinkage is similar, but the total shrinkage is substantially greater under nitrogen (Schaffer et al., 2008).

under nitrogen than in argon, though the initial expansion is similar (Schaffer et al., 2008). Nitrogen was found to facilitate the formation of aluminium nitride (Schaffer and Hall, 2002; Schaffer et al., 2006). It was first suggested that the heat released during reaction of aluminium with nitrogen to form aluminium nitride induces local melting, which in turn improved sintering (Schaffer and Hall, 2002). Later, it was suggested that the formation of aluminium nitride within closed pores reduced the pressure therein, which has two effects on shrinkage. First, the reduction in pore pressure unbalances the meniscus forces and induces pore-filling (Schaffer et al., 2006). Secondly, the reduced pore pressure increases the sintering stress which increases the densification rate due to solution re-precipitation (Schaffer et al., 2008). Although sintering in nitrogen is advantageous, nitrogen has been shown to slow the shrinkage response in the early stages of Al-Cu-Mg-Si alloys (Schaffer et al., 2008). This slow shrinkage may be due to the formation of aluminium nitride on the liquid surface, which may be detrimental to wetting and therefore the sintering response (Schaffer et al., 2008).

Magnesium plays a key role in the formation of aluminium nitride. It facilitates the disruption or reduction of the stable oxide surrounding the aluminium, which allows for the underlying aluminium to react with nitrogen. The formation of magnesium nitride has been regarded as a precursor for the formation of aluminium nitride (Hou et al., 1995). At low green densities, magnesium is not required because the autogenous oxygen gettering of aluminium in the outer regions of the compact allows for the formation of aluminium nitride deep within the compact (Schaffer and Hall, 2002). The sintered density of Ecka 321, an Al-Mg-Si master alloy, is higher in nitrogen than in argon (Martín and Castro, 2003), suggesting that nitrogen is also beneficial to the sintering of Al-Mg-Si alloys. The nature of the nitride in press and sinter aluminium has not been well characterised. The presence of small nodules rich in nitrogen has been found on particle and on internal pore surfaces for aluminium compacts sintered in a nitrogen atmosphere (MacAskill et al., 2006; Pieczonka et al., 2008).

Assuming sintering takes place under nitrogen at atmospheric pressure, the basic reactions are:



The Gibbs free energy of reaction, ΔG , for each reaction is given by:

$$\Delta G = \Delta G^0 + RT \ln Q_r \quad [21.18]$$

where ΔG^0 is the standard free energy of reaction, R is the gas constant ($8.31 \text{ JK}^{-1}\text{mol}^{-1}$), T is the reaction temperature, and Q_r is the reaction quotient. For reactions in Eq. 21.16 and 21.17,

$$Q_r^{Al_2O_3} = \left(\frac{P_{O_2}}{P^0} \right)^{-3/4} \quad [21.19]$$

$$Q_r^{AlN} = \left(\frac{P_{N_2}}{P^0} \right)^{-1/2} \quad [21.20]$$

where P_{N_2} and P_{O_2} are the nitrogen and oxygen partial pressures in the sintering atmosphere, and P^0 is the atmospheric pressure.

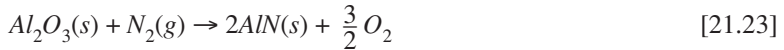
The established thermodynamic data at 560°C (Knacke et al., 1991) gives $\Delta G_{AlN}^0 = -220.8$ kJ/mol and $\Delta G_{Al_2O_3}^0 = -705.9$ kJ/mol. For sintering in high purity nitrogen, $P_{N_2} / P^0 \approx 1$. Accordingly,

$$\Delta G_{AlN} = -220.8 \text{ kJ/mol} \quad [21.21]$$

$$\Delta G_{Al_2O_3} = -705.9 - \frac{3}{4} \times 6.922 \times \ln \frac{P_{O_2}}{P^0} \text{ kJ/mol} \quad [21.22]$$

ΔG_{AlN} is thus constant at a given sintering temperature in nitrogen while $\Delta G_{Al_2O_3}$ depends on P_{O_2} in the nitrogen atmosphere.

By plotting ΔG_{AlN} and $\Delta G_{Al_2O_3}$ as a function of $RT \ln P_{O_2}$, where $RT = 6.922$ kJ/mol at 560°C, the intersection of ΔG_{AlN} and $\Delta G_{Al_2O_3}$ at $P_{O_2} = 2.66 \times 10^{-36}$ Pa defines the threshold oxygen partial pressure for the stability of Al_{2O_3} in nitrogen at 560°C. AlN is more stable than Al_2O_3 when $P_{O_2} < 2.66 \times 10^{-36}$ Pa in nitrogen. Consequently,

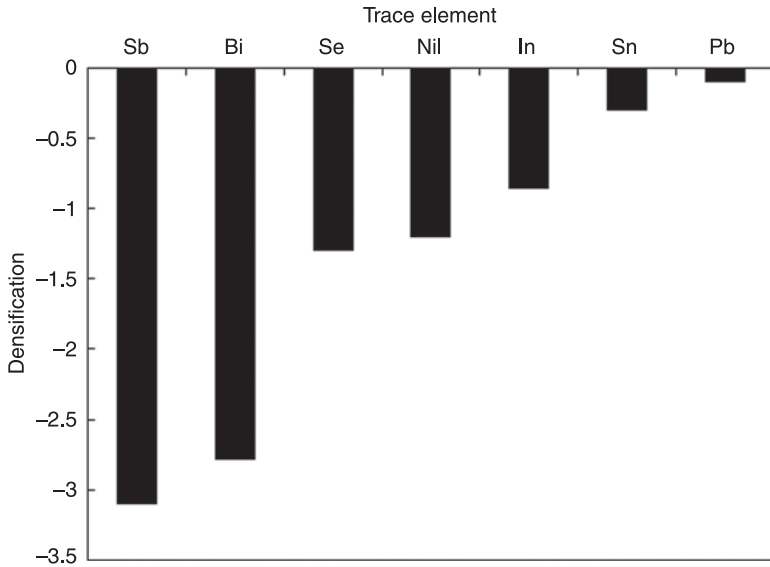


which means effective disruption of the oxide film as the reaction proceeds and sintering will be enabled.

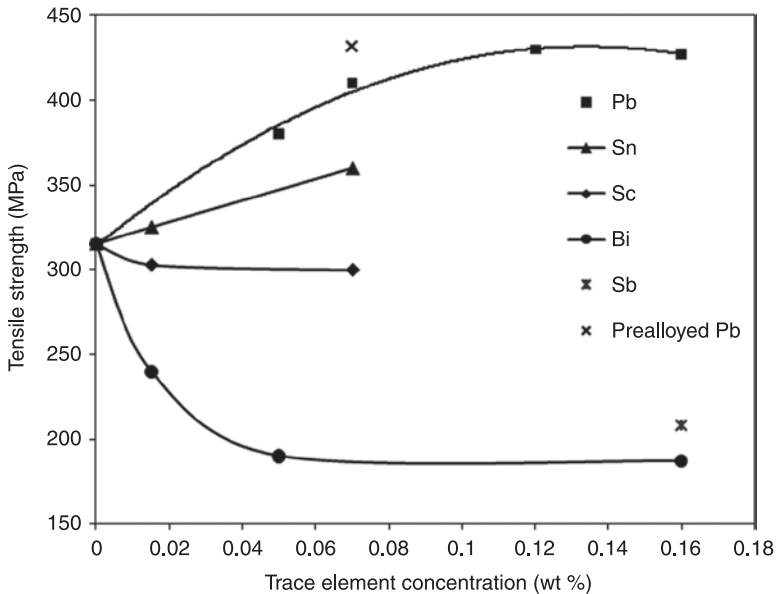
However, even ultra high purity nitrogen still contains a minimum of about 1 ppm oxygen, equivalent to $P_{O_2} \approx 10^{-1}$ Pa. By further purification, the oxygen content may be reduced to 1 ppb or 10^{-4} Pa, compared to the threshold $P_{O_2} = 2.66 \times 10^{-36}$ Pa required for disrupting Al_2O_3 . It is obvious that the threshold is unachievable under conventional sintering environment.

21.4.4 Trace element induced activated sintering

Trace additions of certain elements have a disproportionate effect on the LPS of aluminium alloys. For example, the addition of between 0.05 wt% and 0.5 wt% Pb or Sn activates sintering in the Al-Zn-Mg-Cu system (Schaffer and Huo, 1999). Of the beneficial elements, Pb has the greatest effect on sintering of the Al-Zn-Mg-Cu system, followed by Sn and then In; while Se has no effect and Bi and Sb are detrimental to sintering, Fig. 21.22 and 21.23. Significant difference in the distribution of liquid was observed between the Pb-containing alloys, where continuous intergranular liquid seams were developed and the liquid is evenly distributed throughout the matrix, and Pb-free alloys, where liquid pools remain



21.22 Densification of Al-8Zn-2.5Mg-1Cu-0.07X, where X = Sb, Bi, Se, In, Sn and Pb; nil represents the alloy without a trace element addition (Schaffer and Huo, 1999).



21.23 Effect of trace element concentration on fully heat treated (T6) tensile strength of Al-8Zn-2.5Mg-1Cu-X alloy where trace element was added as separate, elemental addition to alloy: superimposed on curves is a value for alloy made using prealloyed Zn-0.9Pb master alloy powder (Schaffer and Huo, 1999).

(Schaffer and Huo, 1999). Quantitative microstructural analysis showed that the volume of liquid did not differ between the two systems.

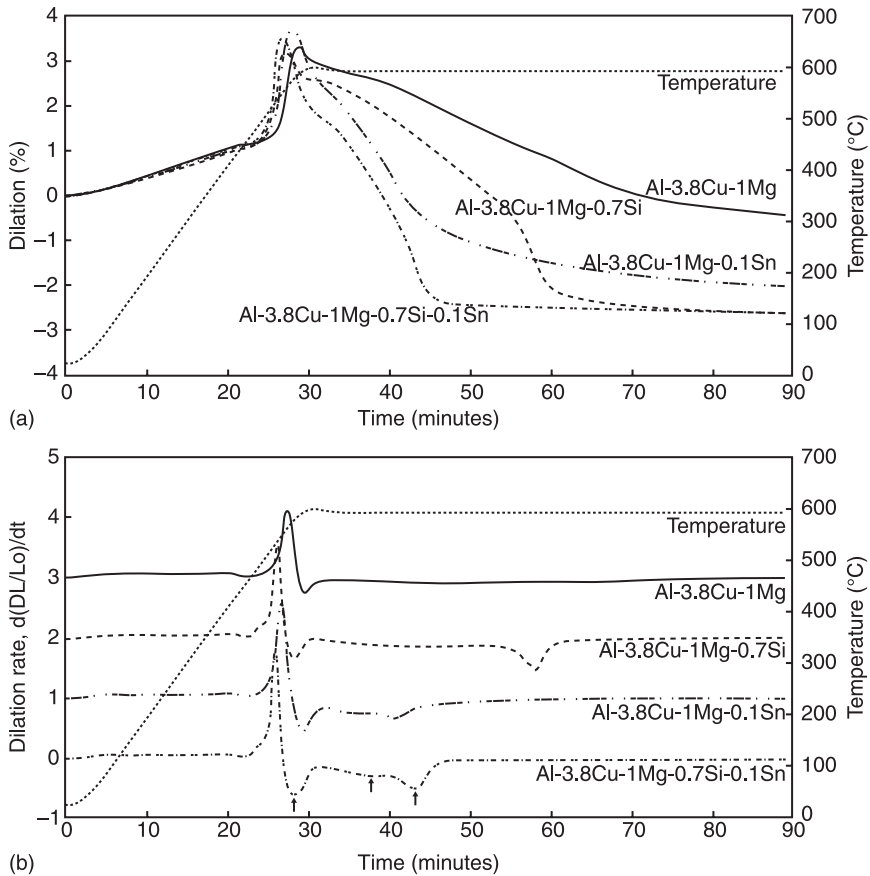
The activation effect is not limited to the Al-Zn-Mg-Cu system. Trace elements, in particular Sn, have a beneficial effect on the sintering of Al-Cu-Mg and Al-Cu-Mg-Si alloys (Sercombe and Schaffer, 1999; Schaffer et al., 2008). It was first suggested that the trace elements diffuse into the Al ahead of the Cu, where they preferentially bind with vacancies in the Al, reducing the subsequent rate of Cu diffusion into the matrix, allowing more liquid to persist for longer times (Sercombe and Schaffer, 1999). Later, positron annihilation spectroscopy indicated that the presence of Sn may not actually alter the vacancy concentration in the sintered alloys, suggesting that Sn may not bind preferentially to vacancies in the aluminium matrix in these Al-Cu-Mg-Si alloys. Rather, it appears that tin may limit the formation of aluminium nitride on specific surfaces (Schaffer et al., 2008).

The role of Sn is unique. A trace amount of Sn was reported to aid the LPS of aluminium under nitrogen but hinder LPS under argon (Schaffer et al., 2008). Under argon, shrinkage occurs in a single stage and the shrinkage rate decays monotonically over time. Sintering shrinkage under nitrogen occurs in three distinct stages and the rate increases over time, Fig. 21.24, corresponding to shrinkage induced by (i) a change in wetting characteristics between the liquid and the surface of the Al particles, leading to primary rearrangement; (ii) an increase in sintering stress during solution re-precipitation, as a result of the consumption of the nitrogen within closed pores due to formation of AlN (Lee and Kang, 1998); and (iii) pore filling induced by the formation of the AlN (Schaffer and Hall, 2002).

The surface tensions of the trace elements are significantly lower than that of aluminium, and therefore might be expected to segregate to the liquid–gas interface and lower the surface tension of the liquid. It has been shown experimentally that < 1 at.% Pb can almost halve the surface tension of zinc and aluminium (Thresh et al., 1964; Goumiri et al., 1979). An analytical transmission electron microscopy examination of the Al-Zn-Mg-Cu-trace system indicated that the trace elements were confined to the interparticle and grain-boundary regions, not in solution in the aluminium matrix (Schaffer et al., 2001). Hence, tin or the other trace elements can effectively decrease the surface tension of the system. The change in surface tension will be beneficial to sintering if it transforms the liquid from non-wetting to wetting. These results suggested that the elements favourable to sintering segregate to the liquid–vapour interface and thereby lower the surface tension of the liquid, which reduces the wetting angle, enhances wetting, improves liquid spreading and therefore improves sintering (Schaffer et al., 2001).

21.5 PM aluminium alloys and their applications

The earliest known attempt to make a PM aluminium alloy was that by Sauerwald and Elsner in 1925, followed by Kikuchi in 1937 (Bickerdike, 1947). More



21.24 Dilatometer curves (a) and the time derivatives (b) of the four alloys under nitrogen at 590°C. There are three distinct shrinkage events in all cases, arrowed in the Al-3.8Cu-1Mg-0.7Si-0.1Sn alloy (Shaffer et al., 2008).

systematic trials were made to sinter aluminium and its alloys in air, vacuum and ammonia in the 1940s (Kempf, 1940; Bickerdike, 1947; Goetzel, 1950), where ten different binary Al-X systems ($X = \text{Mg, Zn, Cu, Fe, Ni, Si, Pb, Sn, Ti}$ and C) and a variety of their combinations were tested. Factors that affect the attendant mechanical properties of the sintered aluminium alloys were identified. These include (i) the compaction pressure; (ii) alloy composition; (iii) heating rates and atmosphere; and (iv) sintering temperature in relation to the solidus of the alloy (Kempf, 1940; Bickerdike, 1947; Goetzel, 1950).

Efforts to develop press-and-sinter aluminium PM continued in the 1950s and 1960s. Self-lubricating aluminium PM bearings containing 18–20% porosity were developed in the 1960s (Storchheim, 1962; Kobrin, 1964; Lyle, 1967). The production process included cold pressing at 70–140 MPa and sintering at 600°C

for 10–30 min, followed by oil impregnating and sizing (Lyle, 1967). The sintered density was in the range $1.89\text{--}2.11\text{ g cm}^{-3}$ (Lyle, 1967). The oxide film on the aluminium powder particle was considered to be a prime advantage in this application, as it resists smearing action by the shaft so that most pores can be kept open for self-lubrication (Kobria, 1964).

Significant progress in understanding the sintering of binary Al-Cu alloys was achieved in 1968 (Matthews, 1968; Wantanabe and Yamada, 1968). A sintered density of 2.60 g cm^{-3} and tensile strength of 172 MPa were achieved for an Al-2Cu (wt.%) alloy on laboratory trials at US Bronze Powders, Inc (AMPAL) (Matthews, 1968). These values are comparable to wrought-annealed Al-Cu alloys with similar composition. However, the production of aluminium PM parts was hindered by a range of technical problems, including (i) the severe seizing and galling characteristics of aluminium powder against die compaction; (ii) absence of a proper internal lubricant; (iii) lack of sintering procedures to provide consistent properties; and (iv) inferior flow characteristics of aluminium powder (Storchheim, 1962; Dudas and Dean, 1969a, 1969b; Blakeslee, 1971). The turning point emerged in 1969 when two American companies, The Aluminum Company of America, Inc (Alcoa) and Chrysler's Amplex Division, both announced breakthroughs in aluminium PM (Anon., 1969). Suitable internal lubricants were identified; the processing difficulties were addressed; and commercially viable sintering processes were developed (Dudas and Dean, 1969a; 1969b). Three primary aluminium powder materials were supplied by Alcoa for the production of sintered aluminium PM parts from 1969: gas atomised 1202 powder (0.15Fe, 0.10Si, 0.30 Al₂O₃, balance Al) and two press-ready alloy blends – 601AB and 201AB (Anon., 1969). Alloy blend 601AB (Al-0.25Cu-1Mg-0.6Si) was similar to 6061 wrought aluminium alloy while 201AB (Al-4.4Cu-0.5Mg-0.8Si) was similar to 2014. Tensile strengths ranging from 110 to 248 MPa were attained for 601AB depending on density and heat treatment, whereas 201 AB exhibited tensile strengths up to 330 MPa in the fully heat treated T6 temper (Dudas and Dean, 1969a, 1969b).

The compositions of current aluminium PM alloys, Table 21.4, are largely based on wrought or cast alloys and as such, many of the alloys are difficult to process and offer poor mechanical properties. The poor mechanical properties limit the use of aluminium PM alloys to low-stress applications, such as automotive cam-shaft bearing caps (Aronson, 2002). The Al-Mg-Si-Cu alloys, AMB 6711 and Alumix 321, are all based on the composition of wrought aluminium alloy 6061. The composition of Alumix 231, high in silicon, is close to that of cast 336.0 alloy. The processing window of these high-silicon alloys is narrow because small temperature variations can lead to large fluctuations in the liquid content. Although the Al-Zn-Mg-Cu based alloys offer high strength, the transient nature of the liquid in this system means that they are very sensitive to processing conditions, including powder particle size and heating rate (Schaffer and Huo, 1999).

Table 21.4 Compositions and properties of selected commercial wrought, cast and PM aluminium alloys (ASM, 1990; Kearney, 1990; ECKA Granulate GmbH & Co. KG, 2008; Ampal Inc., 2005; Huo and Schaffer, 2002; Huo, 2003). The temper designations are given next to the mechanical properties

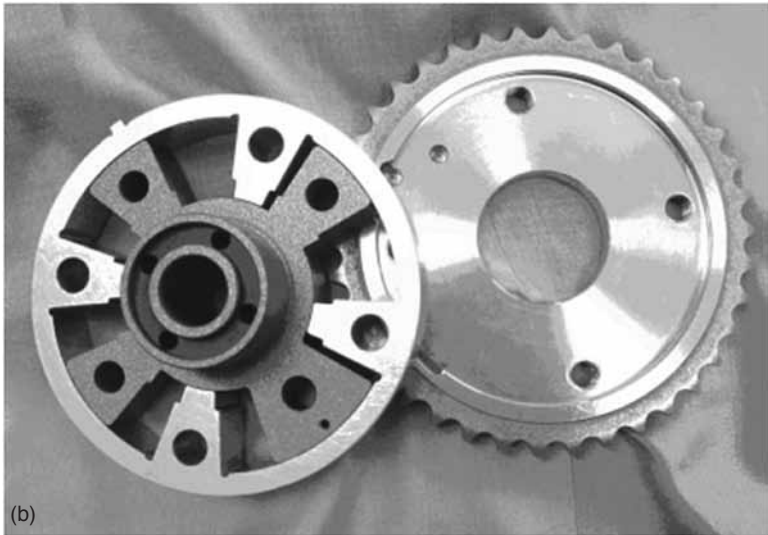
System	Manufacture method and designation	Composition (wt%)	Tensile strength (MPa)	Yield strength (MPa)	Elongation (%)
Al-Cu-Mg-(Si)-(Mn)-(Sn)	PM AMB 2712	3.8 Cu			
		1.0 Mg	278 (T4)	199 (T4)	4.9 (T4)
		0.7 Si	355 (T6)	335 (T6)	0.9 (T6)
	PM Alumix 123	4.5 Cu			
		0.7 Si	190	Not specified	4.0
	PM Alumix 13	0.5 Mg			
		4.5 Cu	160	Not specified	5.0
	Wrought 2014	0.5 Mg			
		4.4 Cu	186 (0)	97 (0)	18 (0)
		0.8 Si	427 (T4)	290 (T4)	20 (T4)
		0.8 Mn	483 (T6)	414 (T6)	13 (T6)
Al-Mg-Si-Cu-(Cr)-(Sn)	PM AMB 6711	0.5 Mg			
		1.0 Mg	155 (0)	88 (0)	10 (0)
		0.8 Si	230 (T4)	203 (T4)	2.0 (T4)
	PM Alumix 321	0.25 Cu			
		1.0 Mg	120	Not specified	5.0
	Wrought 6061	0.2 Cu			
		1.0 Mg	124 (0)	55 (0)	25 (0)
		0.6 Si	241 (T4)	145 (T4)	22 (T4)
Al-Si-Mg-Cu-(Ni)	PM Alumix 231	0.3 Cu			
		0.2 Cr	310 (T6)	276 (T6)	12 (T6)
		14 Si			
	Cast 336.0	2.5 Cu	240	Not specified	1.0–2.0
		0.5 Mg			
		12 Si	248 (T551)	193 (T551)	0.5
	PM Alumix 431	2.5 Ni	324 (T651)	296 (T651)	0.5
		1.0 Mg			
Al-Zn-Mg-Cu-(Cr)	Wrought 7075	1.0 Cu			
		5.5 Zn	400	Not specified	2.0
		2.5 Mg			
	PM Alumix 431	1.5 Cu			
		5.6 Zn	228 (0)	103 (0)	17 (0)
		2.5 Mg	503 (T6)	434 (T6)	11 (T6)
		1.6 Cu			
		0.23 Cr			

The application of 201 AB and 601 AB press and sinter PM parts (drive pulleys) in business machines (Generous, 1980) was materialised in the 1970s. Alcoa introduced aluminium PM parts at American Powdered Metals in 1972 (Pease and West, 2002). By the late 1970s, more than 30 different aluminium PM parts were used by Xerox in their copying machines (Generous, 1980). The business machine application was the largest user of aluminium PM parts (Generous, 1980; ASM, 1998). Fasteners made of sintered aluminium were commercially produced from 1981 to 1984 by Deutsch Fastener Corporation, ElSegundo, CA (Pease and West, 2002). Significant commercial application of the PM aluminium materials were not realised until Metal Powder Products (MPP) began manufacturing PM aluminium camshaft bearing caps for General Motor's Northstar dual overhead cam engine in 1992 (Foss and Defranco, 1994; Capus, 2005). Today, automotive cam caps production is by far the largest application for PM aluminium. MPP has produced more than 45 million aluminium PM cam caps since 1992 using the Alcoa 201AB type of alloy (Lall and Heath, 2000; MPP, 2009).

The cam caps were first used in the dual-overhead cams of the GM Northstar engines in 1993 and subsequently introduced in GM's Ecotec V-6 engines and Chrysler's 2.7 litre V6 and Saturn four cylinder engines due to their satisfactory performance (Lall and Heath, 2000; Anon., 2003). Figure 21.25(a) shows an end cam shaft bearing cap produced by MPP with powder supplied by AMPAL Inc. The caps are produced to a minimum density of 2.5 g cm^{-3} and have typical tensile strength, yield strength and hardness of 217 MPa, 183 MPa, and 55 HRE, respectively (Pease and West, 2002). The PM approach eliminates expensive machining required by die-cast bearing caps, and offers tolerances of $\pm 0.04 \text{ mm}$. In addition, all intricate oil tunnels are produced to net shape using the press and sinter PM process (MPP, 2009), which leads to a 35% cost savings over the extensively machined die-cast caps (Pease and West, 2002). The automotive application has been gradually expanded from cam shaft bearing caps to other more demanding parts, such as chain sprockets for BMW (Pohl, 2006, MPR special feature, 2006; Huo et al., 2008) and stator rings (Anon., 2006), see Fig. 21.25(b).

21.6 Future trends

Up to 30 countries in the world are known to have production facilities for aluminium powder. The total aluminium powder shipments are estimated to be around 45 500 tons from 2001 to 2007 (White, 2002; Schaefer et al., 2004; 2005; Paullin, 2008), but declined 15% in 2008 (Paullin, 2009). Despite its abundant supply, aluminium PM remains a minor participant in the overall aluminium powder market. The future of aluminium PM, therefore, will depend on more value-added innovative designs and products, which requires innovation in research and development.



21.25 PM aluminium automotive components: (a) automotive cam cap (Metal Powder Products, 2009); (b) rotor and sprocket parts for aluminium cam phaser system (Pohl, 2006).

Currently, the uses of PM aluminium parts are restricted to low-stress applications, where the net shape capability is critical for cost reduction. The primary reason for the limited use of aluminium PM alloys is that there are limited commercial grade aluminium PM alloys available. As a result, design engineers

find it is difficult to specify PM parts for new applications. Furthermore, the mechanical properties of existing PM alloys, especially modulus, wear resistance or elevated temperature property retention, do not meet the needs for an expanded range of applications (Hunt, 2000).

Although these limitations were well recognised a decade ago, there has been little progress in this regard. Innovative and cross-disciplinary initiatives are needed from a research perspective for the development of a wide range of high-performance aluminium PM alloys that could be used for medium to high stress applications, including those subject to cyclic stresses. The aluminium alloys will have to be reinforced to enable significant improvement in properties. Future composites will exhibit more uniform microstructure, better interfacial bonds and finer and evenly distributed reinforcement particles. In addition to the usual tensile strength data, a significant improvement in the stiffness of aluminium PM parts, e.g. >100 GPa, could open new markets for aluminium PM, if they are also cost effective. Aluminium PM composites thus still represent an important research direction.

Fatigue is an important design consideration for PM parts subject to cyclic stresses. In general, the fatigue strength of press-and-sinter aluminium PM parts is about half that of wrought alloys with similar composition (ASM, 1998). This low fatigue may not be a problem for low-stress non-dynamic applications, but it requires much improved fatigue strengths in order for the aluminium PM parts to penetrate into high-load applications in automotive drivetrains. Because of the involvement of pores, the fatigue of a sintered aluminium alloy may differ appreciably from that of a cast or wrought alloy. At present experimental data on the fatigue of sintered aluminium alloys are still very limited (Grayson et al., 2006). Post-sintering heat treatment should be fully exploited. Innovative alloy design for high-strength aluminium PM alloys should be directed to using PM as a means of net shape forming.

21.7 Acknowledgements

The authors would like to thank Mr Stephen Bonner for his assistance in conducting the dilatometer work. Thanks are also due to Dr Yu Peng for providing the SEM image of argon atomised aluminium powder, Fig. 21.2. This work has been supported in part by the CAST-CRC and AMPAL Inc.

21.8 References

- Ampal Inc. (2005) *Ampalloy AMB 6711 product information sheets*. Received February 16, 2005 (cited 2005 9/2/2005).
- Anderson, I.E., Foley, J.C. and Flumerfelt, J.F. (1998) 'Simplified aluminium powder metallurgy processing routes for automotive applications', in Jandeska, W.F. and Chernenkoff, R.A. (Eds): *Powder Metallurgy Aluminum and Light Alloys for Automotive Applications*, MPIF, Dearbon, MI.

- Arbuzova, L.A., Danilkin, V.A. and Kunin, L.L. (1976) 'Amount of H_2O on the surface of an aluminum powder', *Powder Metallurgy and Metal Ceramics*, 15: 663–665.
- Aronson R.B. (2002) 'Have you considered P/M parts?' *Manufacturing Engineering*, 128(2): 59–71.
- ASM (1990) 'Properties of wrought aluminum and aluminum alloys', in *ASM Handbook Volume 2: Properties and Selection: Nonferrous Alloys and Special-Purpose Materials*, 10th ed., Materials International, Materials Park, 62–122.
- Cahn, J.W. and Heady, R.B. (1970) 'An analysis of the capillary forces in liquid-phase sintering of spherical particles', *Metallurgical Transactions*, 1(1): 185–189.
- Champion, J.A., Keene, B.J. and Sillwood, J.M. (1969) 'Wetting of aluminium oxide by molten aluminium and other metals', *Journal of Materials Science*, 4(1): 39–49.
- Cho, S.J., Kang, S.J.L. and Yoon, D.N. (1986) 'Effect of entrapped inert gas on pore filling during liquid phase sintering', *Metallurgical Transactions A*, 17: 2175–2182.
- Danninger, H. (1992) 'Sintering of Mo alloyed P/M steels prepared from elemental powders, II: Mo homogenization and dimensional behaviour', *Powder Metallurgy International*, 24(3): 163–168.
- Daver, E.M., Ullrich, W.J. and Patel, K.B. (1989) 'Aluminium P/M parts – materials, production and properties', *Key Engineering Materials*, 29–31: 401–428.
- Delannay, F., Froyen, L. and Deruytère, A. (1987) 'Review – The wetting of solids by molten metals and its relation to the preparation of metal-matrix composites', *Journal of Materials Science*, 22: 1–16.
- Dotter, R.T. (1993) 'Blending and Premixing of Metal Powders', in *ASM Handbook: Volume 7 – Powder Metallurgy*, 9th ed., Materials International, Materials Park, pp. 186–189.
- Dryden, J.R. and Watt, D.F. (1981) 'Redistribution of stresses during creep-bending of grain boundary sliding materials', *Materials Science Research*, 14: 261–270.
- Dudas, J.H. and Dean, W.A. (1969a) 'The production of precision aluminium powder metallurgy parts', *Light Metal Age*, 27(6): 18–24.
- Dudas, J.H. and Dean, W.A. (1969b) 'The production of precision aluminium P/M parts', *International Journal of Powder Metallurgy*, 5(2): 21–36.
- ECKA Granulate GmbH & Co. KG (2008). *Ecka Alumix Product Information*. Available from <http://www.ecka-granules.com/> (accessed 17 August 2008).
- Eldridge, J.I., Hussey, R.J., Mitchell, D.F. and Graham, M.J. (1988) 'Thermal oxidation of single-crystal aluminum at 550°C', *Oxidation of Metals*, 30: 301–328.
- Esper, F.J. and Leuze, G (1971) 'The influence of the powder particle size on the properties of aluminum P/M parts', *Powder Metallurgy International*, 3(3): 123–126.
- Estrada, J.L., Duszczak, J. and Korevaar, B.M. (1991) 'Gas entrapment and evolution in prealloyed aluminium powder', *Journal of Materials Science*, 26: 1431–1442.
- Eustathopoulos, N. and Drevet, B. (1998) 'Determination of the nature of metal-oxide interfacial interactions from sessile drop data', *Materials Science and Engineering A*, 249(1–2): 176–183.
- Eustathopoulos, N., Nicholas, M.G. and Drevet, B. (1999) *Wettability at High Temperatures: Pergamon Materials Series*, ed. Cahn R W, Vol. 3, Amsterdam, Pergamon.
- Eustathopoulos, N., Drevet, B. and Muolo, M.L. (2001) 'The oxygen-wetting transition in metal/oxide systems', *Materials Science and Engineering A*, 300(1–2): 34–40.
- Flumerfelt, J.F. and Anderson, I.E. (1998) 'The surface chemistry of pure aluminium powders as measured with quadrupole mass spectrometry', in: *International Conference on Powder Metallurgy and Particulate Materials*, MPIF, Las Vegas, NV.

- Fox, R.W. and McDonald, A.T. (1994) *Introduction to Fluid Mechanics*, John Wiley & Sons, New York.
- Generous, J.D. (1980) 'Aluminium P/M applications in business machines', in Hausner, H.H., Antes, H.W. and Smith, G.D. (Eds): *Modern Developments in Powder Metallurgy Vol. 13: Ferrous and Nonferrous Materials*, Princeton, NJ, Metal Powder Industries Association, pp. 501–510.
- German, R.M. (1985) *Liquid Phase Sintering*, Plenum Press, New York.
- German, R.M. (1986) 'Phase diagrams in liquid phase sintering treatments', *Journal of Metals*, 38(8): 26–29.
- German, R.M. (1989) *Particle Packing Characteristics*, Metal Powder Industries Federation, Princeton.
- German, R.M. (1995) 'Microstructure of the gravitationally settled region in a liquid-phase sintered dilute tungsten heavy alloy', *Metallurgical and Materials Transactions A*, 26(2): 279–288.
- German, R.M. (1996) *Sintering theory and practice*, John Wiley & Sons, New York.
- German, R.M. (1997) *Powder Metallurgy Science*, 2nd ed., Metal Powder Industries Federation, Princeton.
- German, R.M. and Dunlap, J.W. (1986) 'Processing of iron-titanium powder mixtures by transient liquid phase sintering', *Metallurgical and Materials Transactions A*, 17: 205–213.
- German, R.M. and Olevsky, E. (1998) 'Modeling grain growth dependence on the liquid content in liquid-phase-sintered materials', *Metallurgical and Materials Transactions A*, 29(12): 3057–3067.
- German, R.M., Pavan, S. and Park, S.J. (2009) 'Review: liquid phase sintering', *Journal of Materials Science*, 44: 1–39.
- Grayson, G.N., Schaffer, G.B., Griffiths, J.R. (2006) 'Fatigue crack propagation in a sintering 2xxx series aluminium alloy', *Materials Science and Engineering A*, 434(1–2): 1–6.
- Hall, B.J. and Schaffer, G.B. (2002) 'Statistical experimental design of Al-Cu-Mg-Si P/M alloys', *Journal of Light Metals*, 2(4): 229–238.
- Hall, B.J., Schaffer, G.B., Ning, Z., McPhee, W.A.G., Miller, D.N., Drennan, J. and Cumming, D.J. (2003) 'Al/AlN layered composites by direct nitridation of aluminium', *Journal of Materials Science Letters*, 22(22): 1627–1630.
- Hou, Q., Mutharasan, R. and Koczek, M. (1995) 'Feasibility of aluminium nitride formation in aluminum alloys', *Materials Science and Engineering A*, 195: 121–129.
- Huo, S.H. (2003) *Report to Ampal*, October–November 2003, The University of Queensland.
- Huo, S.H., Heath, W. and Lall, C. (2006) 'The market development of PM aluminum', in *Powder Metallurgy World Congress*, September 2006, Busan, Korea.
- Huo, S.H. and Schaffer, G.B. (2002) *Report to Ampal*, July 2002, The University of Queensland.
- Huppmann, W.J. and Riegger, H. (1975) 'Modelling of rearrangement processes in liquid phase sintering', *Acta Metallurgica*, 23(8): 965–971.
- Huppmann, W.J., Riegger, H., Kaysser, W.A., Smolej, V. and Pejovnik, S. (1979) 'The elementary mechanisms of liquid phase sintering, I: rearrangement', *Zeitschrift für Metallkunde*, 70: 707–713.
- Iida, T. and Guthrie, R.I.L. (1988) *The Physical Properties of Liquid Metals*, Clarendon Press, Oxford.

- Jamil, S.J. and Chadwick G.A. (1985) 'Investigation and analysis of liquid phase sintering of Fe-Cu and Fe-Cu-C compacts', *Powder Metallurgy*, 28(2): 65–71.
- Johnson, J. and German, R.M. (1996) 'Solid-state contributions to densification during liquid-phase sintering', *Metallurgical and Materials Transactions B*, 27(6): 901–909.
- Jung, W., Kim, D.Y., Song, H. and Park, S.W. (1996) 'Variation of contact angles with temperature and time in the Al-Al₂O₃ system', *Metallurgical Transactions*, 27(1): 51–55.
- Kang, S.J.L. (2005) *Sintering: Densification, Grain Growth and Microstructure*, Elsevier, Oxford.
- Kang, S. and Yoon, D.N. (1982) 'Kinetics of grain coarsening during sintering of Co-Cu and Fe-Cu Alloys with low liquid contents', *Metallurgical and Materials Transactions A*, 13(8): 1405–1411.
- Kang, S.J.L. and Yoon, D.N. (1991) 'Densification and Shrinkage During Liquid-Phase Sintering', *Journal of the American Ceramic Society*, 74(2): 425–427.
- Kang, S.J.L., Kaysser, W.A., Petzow, G. and Yoon, D.N. (1985) 'Growth of Mo grains around Al₂O₃ particles during liquid phase sintering', *Acta Metallurgica*, 33(10): 1919–1926.
- Kaysser, W.A. (1991) 'Liquid phase sintering', in Jenkins, I. and Wood, J.V. (Eds): *Powder Metallurgy: An Overview*, The Institute of Metals, London, pp. 183–197.
- Kaysser, W.A., Huppmann, W.J. and Petzow, G. (1980) 'Analysis of dimensional changes during sintering of Fe-Cu', *Powder Metallurgy*, 23(2): 86–91.
- Kaysser, W.A. and Petzow, G. (1985) 'Ostwald-ripening and shrinkage during liquid-phase sintering', *Zeitschrift für Metallkunde*, 76(10): 687–692.
- Kearney, A.L. (1990) 'Properties of cast aluminum alloys', in *ASM Handbook Volume 2: Properties and Selection: Nonferrous Alloys and Special-Purpose Materials*, 10th ed., Materials International, Materials Park, pp. 152–177.
- Kehl, W. and Fischmeister, H.F. (1980) 'Liquid phase sintering of Al-Cu compacts', *Powder Metallurgy*, 3: 113–119.
- Kehl, W. and Fischmeister, H.F. (1982) 'Observations on dimensional changes during sintering of Al-Cu compacts', *Material Science Monographs*, 14: 269–274.
- Kempf, L.W. (1940) 'Properties of compressed and heated aluminium alloy powder mixtures', in Wulff, J. (1942) *Powder Metallurgy*, Cleveland, The American Society for Metals, pp. 314–316.
- Kimura, A., Shibata, M., Kondoh, K., Takeda, Y., Katayama, M., Kanie, T. and Takada, H. (1997) 'Reduction mechanism of surface oxide in aluminum alloy powders containing magnesium studied by x-ray photoelectron spectroscopy using synchrotron radiation', *Applied Physics Letters*, 70(26): 3615–3617.
- Kingery, W.D. (1959) 'Densification During Sintering in the Presence of a Liquid Phase, I. Theory', *Journal of Applied Physics*, 30(3): 301–306.
- Kondoh, K. and Takeda, Y. (2000) 'Tribological property of in situ directly nitrided and sintered Al/AlN composite', *Powder Metallurgy*, 43: 69–75.
- Kondoh, K., Kimura, A., and Watanabe, R. (2001a), 'Effect of Mg on sintering phenomenon of aluminium alloy powder particle', *Powder Metallurgy*, 44(2): 161–164.
- Kondoh, K., Kimura, A. and Watanabe, R. (2001b), 'Analysis of tin behaviour on surface of rapidly solidified aluminium alloy powder particles during heating', *Powder Metallurgy*, 44(3): 253–258.
- Kondoh, K., Yamagata, S., Hayashi, T., Takano, Y. and Takeda, Y. (1995) *Proceedings of the 88th Conference of Japan Institute of Light Metals*, Sapporo, Japan Institute of Light Metals, pp. 85–86.

- Kwon, O.H. and Messing, G.L. (1990) 'Kinetic analysis of solution-precipitation during liquid-phase sintering of alumina', *Journal of the American Ceramic Society*, 73(2): 275–281.
- Kwon, O.H. and Messing, G.L. (1991), 'A theoretical analysis of solution-precipitation controlled densification during liquid-phase sintering', *Acta Metallurgica et Materialia*, 39(9): 2059–2068.
- Laurent, V., Chatain, D., Chatillon, C. and Eustathopoulos, N. (1988), 'Wettability of Monocrystalline Alumina by Aluminium Between Its Melting Point and 1273K', *Acta Metallurgica*, 36(7): 1797–1803.
- Lawrence, G.D. and Foerster, G.S. (1971) 'Pressureless sintering of aluminum powder', *Metals Engineering Quarterly*, pp. 25–30.
- Lee, S. and Kang, S.L. (1998) 'Theoretical analysis of liquid-phase sintering: pore filling theory', *Acta Materialia*, 46(9): 3191–3202.
- Lee, S.M. and Kang, S.J.L. (2005) 'Microstructure development during liquid-phase sintering', *Zeitschrift für Metallkunde*, 96(2): 141–147.
- Lenel, F.V. (1980) *Powder Metallurgy – Principles and Applications*, Metal Powder Industries Federation, Princeton.
- Levi, G., Bamberger, M. and Kaplan, W.D. (1999) 'Wetting of porous titanium carbonitride by Al-Mg-Si alloys', *Acta Materialia*, 47(14): 3927–3934.
- Levi, G. and Kaplan, W.D. (2002) 'Oxygen induced interfacial phenomena during wetting of alumina by liquid aluminium', *Acta Materialia*, 50: 75–88.
- Liu, J., Cardamone, A.L. and German, R.M. (2001) 'Estimation of capillary pressure in liquid phase sintering', *Powder Metallurgy*, 44(4): 317–324.
- Liu, Y. and German, R.M. (1996) 'Contact angle and solid-liquid vapour equilibrium', *Acta Materialia*, 44(4): 1657–1663.
- Liu, J. and German, R.M. (1999) 'Densification and shape distortion in liquid-phase sintering', *Metallurgical and Materials Transactions A*, 30(12): 3211–3217.
- Liu, J. and German, R.M. (2001) 'Rearrangement densification in liquid-phase sintering', *Metallurgical and Materials Transactions A*, 32(12): 3125–3131.
- Liu, Y., German, R.M. and Iacocca, R.G. (1999) 'Microstructure quantification procedures in liquid-phase sintered materials', *Acta Materialia*, 47(3): 915–926.
- Liu, J., Lal, A. and German, R.M. (1999) 'Densification and shape retention in supersolidus liquid phase sintering', *Acta Materialia*, 47(18): 4615–4626.
- Lumley, R.N. and Schaffer, G.B. (1996) 'The effect of solubility and particle size on liquid phase sintering', *Scripta Materialia*, 35(5): 589–595.
- Lumley, R.N., Sercombe, T.B. and Schaffer, G.B. (1999) 'Surface oxide and the role of magnesium during the sintering of aluminium', *Metallurgical and Materials Transactions A*, 30(2): 457–463.
- MacAskill, I.A., Donaldson, I.W. and Bishop, D.P. (2006) 'On development of press and sinter Al-Ni-Mg powder metallurgy alloys', *Powder Metallurgy*, 49(4): 314–322.
- Martín, J.M. and Castro, F. (2003) 'Liquid phase sintering of P/M aluminium alloys: effect of processing conditions', *Journal of Materials Processing Technology*, 143–144: 814–821.
- Miller, D.N. (2004) *The Sintering of α -Alumina Reinforced Aluminium Alloy Matrix Composites*, in School of Engineering, The University of Queensland, Brisbane.
- Mills, K.C. and Su, Y.C. (2006) 'Review of surface tension data for metallic elements and alloys: Part 1 – pure metals', *International Materials Reviews*, 51(6): 329–351.

- Mortensen, A. (1997) 'Kinetics of densification by solution-precipitation', *Acta Materialia*, 45(2): 749–758.
- Naidich, Y.V. and Taranets, N.Y. (1998) 'Wettability of aluminium nitride by tin–aluminium melts', *Journal of Materials Science*, 33(15): 3993–3997.
- Nielsen, P., Liu, Y.L. and Hansen, N. (1993) 'Manufacturing of aluminium composites with high purity matrix', in: *Powder Metallurgy World Congress*, Japan Society of Powder and Powder Metallurgy, Japan.
- Nikolic, Z.S. (2004) 'A model for 3-D study of rearrangement in liquid phase sintering', *Zeitschrift fur Metallkunde*, 95(11): 993–1000.
- Nizhenko, V.I. (2001) 'Wetting of Al₂O₃-Based Oxide Ceramics by Molten Aluminum', *Powder Metallurgy and Metal Ceramics*, 40(5): 271–276.
- Nylund, A. and Olefjord, I. (1994) 'Surface analysis of oxidized aluminium – Part I', *Surface and Interface Analysis*, 21: 283–289.
- Olefjord, I. and Karlsson, A. (1986) 'Surface analysis of aluminium foil', in Sheppard, T. (Ed.): *Aluminium Technology '86*, The Institute of Metals, London, pp. 24–27.
- Olefjord, I. and Nylund, A. (1994) 'Surface analysis of oxidized aluminium – Part II', *Surface and Interface Analysis*, 21: 290–297.
- Ozbilen, A., Unal, A. and Sheppard, T. (1989) 'Influence of oxygen on morphology and oxide content of gas atomised aluminium powders', in Small, W.M. (Ed.): *Physical Chemistry of Powder Metals – Production and Processing*, The Minerals, Metals and Materials Society, 1989.
- Park, H.H., Cho, S.J. and Yoon, D.N. (1984) 'Pore filling process in liquid phase sintering', *Metallurgical and Materials Transactions A*, 15(6): 1075–1080.
- Park, H.H., Kwon, O.J. and Yoon, D. (1986) 'The critical grain size for liquid flow into pores during liquid phase sintering', *Metallurgical and Materials Transactions A*, 17(11): 1915–1919.
- Petzow, G. and Kaysser, W.A. (1984) 'Basic mechanisms of liquid phase sintering', in *Sintered Metal-Ceramic Composites*, Elsevier, New Delhi.
- Pieczonka, T., Schubert, T., Baunack, S. and Kieback, B. (2008) 'Dimensional behaviour of aluminium sintered in different atmospheres', *Materials Science and Engineering A*, 478(1–2): 251–256.
- Plakhotnikova, N.A., Gopienko, V.G., Kolpachev, A.A. and Reznikova, G.A. (1988) 'Chemical reaction of aluminium alloy powders with water', *Powder Metallurgy and Metal Ceramics*, 27: 605–608.
- Protsenko, P., Terlain, A. and Eustathopoulos, N., (2007) 'Wetting of W by liquid Pb and PbLi alloys and surface interactions', *Journal of Nuclear Materials*, 360(3): 265–271.
- Qian, M. and Schaffer, G.B. (2010) 'Sintering of aluminium and its alloys', in Fang Z.K. (Ed.): *Sintering of Advanced Materials*, Woodhead, Cambridge, UK.
- Rahaman, M.N. (1995) *Ceramic Processing and Sintering*. Marcel Dekker, New York.
- Rocha-Rangel, E., Becher, P.F. and Lara-Curzio, E. (2003) Influence of carbon on the interfacial contact angle between alumina and liquid aluminium, *Surface and Interface Analysis*, 35(2): 151–155.
- Saiz, E., Tomsia, A.P. and Cannon, R.M. (1998) 'Ridging effects on wetting and spreading of liquids and solids', *Acta Materialia*, 46(7): 2349–2361.
- Saravanan, R.A., Molina, J.M., Garcia-Cordovilla, J. and Louis, E. (2001) 'Effects of nitrogen on the surface tension of pure aluminum at high temperatures', *Scripta Materialia*, 44: 965–970.

- Savitskii, A.P. (1993) *Liquid Phase Sintering of the Systems with Interacting Components*, Russian Academy of Sciences, Tomsk.
- Schaffer, G.B. (1996) 'Powder metallurgy as a net shape processing technology', *Materials Forum*, 20: 131–143.
- Schaffer, G.B. (2000) 'Net shape powder processing of aluminium', *Materials Forum*, 24: 109–124.
- Schaffer, G.B. and Hall, B.J. (2002) 'The influence of the atmosphere on the sintering of aluminium', *Metallurgical and Materials Transactions A*, 33A(10): 3279–3284.
- Schaffer, G.B., Hall, B.J., Bonner, S.J., Huo, S.H. and Sercombe, T.B. (2006) 'The effect of the atmosphere and the role of pore filling on the sintering of aluminium', *Acta Materialia*, 54(1): 131–138.
- Schaffer, G.B., Huo, S.H., Drennan, J. and Auchterlonie, G.J. (2001) 'The effect of trace elements on the sintering of an Al-Zn-Mg-Cu alloy', *Acta Materialia*, 49: 2671–2678.
- Schaffer, G.B., Sercombe, T.B. and Lumley, R.N. (2001) 'Liquid phase sintering of aluminium alloys', *Materials Chemistry and Physics*, 67(1): 85–91.
- Schaffer, G.B., Yao, J.Y., Bonner, S.J., Crossin, E., Pas, S.J. and Hill, A.J. (2008) 'The effect of tin and nitrogen on liquid phase sintering of Al-Cu-Mg-Si alloys', *Acta Materialia*, 56(11): 2615–2624.
- Schatt, W. and Wieters, K.P. (1997) *Powder Metallurgy: Processing and Materials*, European Powder Metallurgy Association, Shrewsbury, pp. 247–248.
- Sercombe, T.B. (1998) *Non-Conventional Sintered Aluminium Powder Alloys*, Department of Mining, Minerals and Materials Engineering, The University of Queensland, Brisbane.
- Sercombe, T.B. and Schaffer, G.B. (1999a) 'On the use of trace additions of Sn to enhance sintered 2xxx series Al powder alloys', *Materials Science and Engineering A*, 268(1): 32–39.
- Sercombe, T.B. and Schaffer, G.B. (1999b) 'The effect of trace elements on the sintering of Al-Cu alloys', *Acta Materialia*, 47(2): 689–697.
- Sercombe, T.B. and Schaffer, G.B. (2003) 'Rapid manufacturing of aluminum components', *Science*, 301: 1225–1227.
- Sercombe, T.B. and Schaffer, G.B. (2004) 'On the role of magnesium and nitrogen in the infiltration of aluminium by aluminium for rapid prototyping applications', *Acta Materialia*, 52(10): 3019–3025.
- Shaw, T.M. (1986) 'Liquid redistribution during liquid-phase sintering', *Journal of the American Ceramic Society*, 69(1): 27–34.
- Shinohara, K., Seo, T. and Kyogoku, H. (1982) 'Transmission electron microscopy studies on the oxidation of aluminium', *Z. Metallkunde*, 73: 774–780.
- Simchi, A. and Veltl, G. (2003) 'Investigation of warm compaction and sintering behaviour of aluminium alloys', *Powder Metallurgy*, 46: 159–164.
- Simchi, A. and Veltl, G. (2006) 'Behaviour of metal powders during cold and warm compaction', *Powder Metallurgy*, 49(3): 281–287.
- Svoboda, J., Riedel, H. and Gaebel, R. (1996) 'A model for liquid phase sintering', *Acta Materialia*, 44(8): 3215–3226.
- Tabeshfar, K. and Chadwick, G.A. (1984) 'Dimensional changes during liquid phase sintering of Fe-Cu compacts', *Powder Metallurgy*, 27(1): 19–24.
- Thompson, C.B. (1993) 'Lubrication of Metal Powders', in *ASM Handbook: Volume 7. Powder Metallurgy*, 9th ed., Materials International, Materials Park, pp. 190–193.

- Upadhyaya, G.S. (2000) *Sintered Metallic and Ceramic Materials*, John Wiley, Chichester, pp. 248–334.
- Wanibe, Y., Yokoyama, H. and Itoh, T. (1990) ‘Expansion during liquid phase sintering of iron-copper compacts’, *Powder Metallurgy*, 33(1): 65–69.
- Warren, R. and Andersson, C.H. (1984) ‘Silicon carbide fibres and their potential for use in composite materials, Part II’, *Composites*, 15: 101–111.
- Xu, K. and Mehrabadi M.M. (1997) ‘A micromechanical model for the initial rearrangement stage of liquid phase sintering’, *Mechanics of Materials*, 25: 137–157.

Laser sintering and rapid prototyping of aluminium

T.B. SERCOMBE, The University of Western Australia, Australia

Abstract: This chapter describes the development of an infiltrated aluminium system that can be used to make complex components directly from computer models. The chapter first examines the formation of an aluminium nitride skeleton, which is central to the success of the system. Next, the infiltration of aluminium into the preform is discussed, followed by an analysis of the dimensional changes that occur during the process.

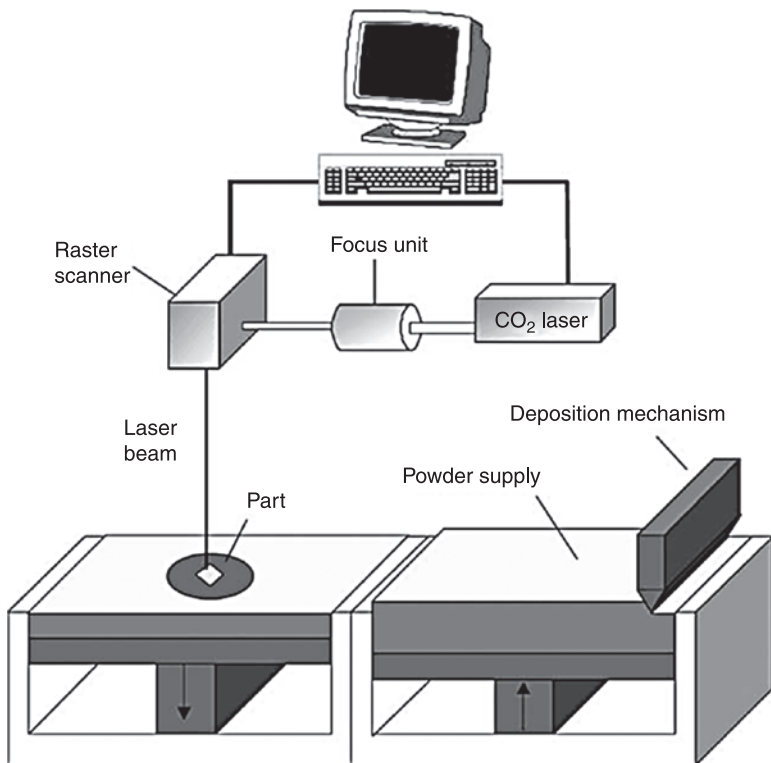
Key words: rapid manufacturing, aluminium, infiltration, aluminium nitride.

22.1 Introduction

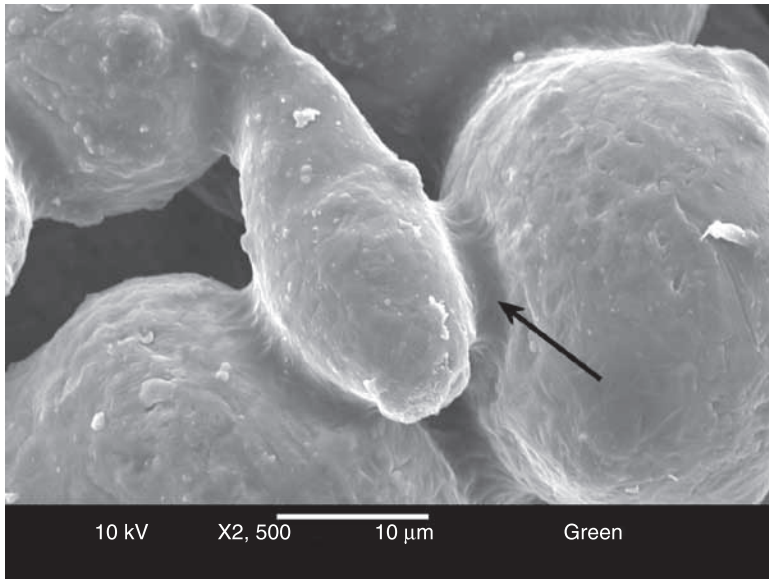
Rapid prototyping (RP) is the fabrication of prototype parts directly from a computer solid model without the need for an expensive tool or die set. There are a number of different technologies that are collectively grouped under this banner, all of which produce parts in a layer-wise manner. In essence, the computer model is sliced into thin layers (typically $<100\text{ }\mu\text{m}$ thick) and the three dimensional part created by the sequential production of these two-dimensional (2D) sections. While there are a number of different approaches to produce these 2D cross-sections, in all cases energy and/or material is delivered to a point to produce a solid. A series of lines are then traced out to make a layer and a series of layers formed to make a three dimensional part. Rapid manufacturing (RM) is a new concept which has been derived from RP. Instead of making prototypes, which are generally used for form and fit only, RM is concerned with the manufacture of functional parts directly from a computer solid model using a layer-wise RP device. The key advantage of the RM paradigm is the massive reduction it provides in product development time and associated costs. This is achieved through the rapid realisation of mechanical designs and the ease and speed with which these can be modified. Because there are negligible geometrical restrictions, RM may also create major changes in the way designers work. Indeed, random changes of product geometry will lead to entirely new product forms. This will take us beyond what is currently considered to be manufacturable.

One method to manufacture metallic components using RM is to initially produce a resin-bonded metal powder preform using selective laser sintering. This technology uses a feedstock of either resin coated metal powder or metal powder with $\sim 10\text{ vol}\%$ admixed resin. A relatively low power CO_2 laser scans across the surface of the powder, melting the resin and bonding the metal powder

particles together to form a layer. The build platform then descends $\sim 100\ \mu\text{m}$ and a new layer of powder is deposited on top and the process continues. A schematic of the process is shown in Fig. 22.1 (Simchi and Pohl, 2003). At the completion of the build, the powder that has not been exposed to the laser beam can be easily brushed away and the sintered parts removed. At this stage, the part is $\sim 50\%$ dense and only strong enough to handle gently, as the powder particles are held together only by polymer necks, as shown in Fig. 22.2. Densification can be achieved by first thermally removing the polymer, followed by sintering to high temperature (Sercombe, 2001, 2003a, 2003c; Souvignier et al., 2001). However, due to the large amount of shrinkage that the parts undergo (15–20%), it is difficult to maintain dimensional accuracy and therefore the size of the part is limited to $\sim 1\ \text{cm}^3$ (Iacocca and Myers, 2000; Sercombe, 2001). The dimensional problem is essentially eliminated if the part is infiltrated instead of sintered. During this process, a lightly sintered porous body is infiltrated with a liquid. As little sintering occurs, there is a negligible dimensional change from the preform to the final part.



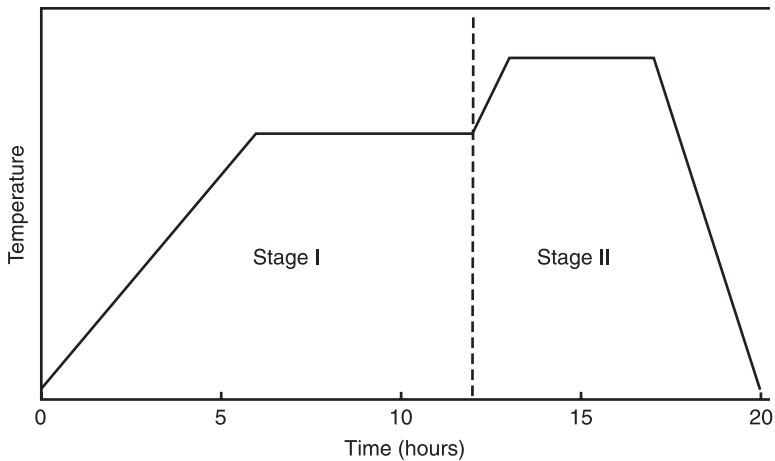
22.1 Schematic of the selective laser sintering apparatus (reprinted from Simchi and Pohl [2003] with permission from Elsevier).



22.2 Scanning electron image of laser sintered aluminium containing 10 vol% nylon. The laser beam has melted the nylon, which has formed necks between the powder particles (arrowed).

The following discussion outlines the development of an infiltrated aluminium system that can be used to produce functional parts using selective laser sintering. It is divided into three main areas: the formation of the skeleton, infiltration of the preform and the dimensional changes that occur during the process. In general, the aluminium powder used was a pre-alloyed Al6061 (nominally Al – 1 wt%Mg-0.6 wt%Si), while the resin binder was a fine nylon powder which constituted approximately 10% by volume. At times, commercially pure (99.7%) Al powder was used in order to study the role of powder chemistry on the process, while additions of elemental Mg and Sn (at ~1 wt% level) were added to remove the oxygen from the nitrogen atmosphere and control the nitride growth rate, respectively. This is discussed in detail below.

A typical furnace cycle is shown in Fig. 22.3. Stage I involves a slow heating rate to an intermediate temperature, followed by an isothermal hold. During heating, the resin thermally decomposes and is removed from the preform, while the isothermal hold partially converts the aluminium to an interconnected A/N skeleton. During Stage II, the temperature is increased to above the melting point of the infiltrant and infiltration of the skeleton occurs.



22.3 Overall furnace cycle for the infiltration of the aluminium preforms. During the heating in Stage I the resin is decomposed and removed. The first isothermal hold partially converts the aluminium into an interconnected AlN skeleton. The temperature is then raised to above the melting point of the infiltrant, where infiltration of the preform occurs.

22.2 The skeleton

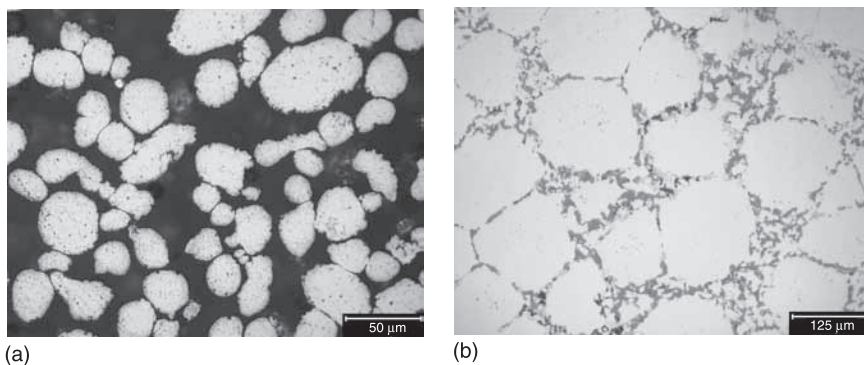
In order to maintain geometrical accuracy during infiltration, there is a requirement that a percolating solid skeleton not only forms, but is not attacked by the infiltrant. In most infiltration systems, the formation of this skeleton is created through solid state sintering of the powder particles, and can be performed in either a separate thermal process or during heating to the infiltration temperature. The former approach is necessary when the infiltrant melts at a temperature below where sintering can be affected. Where a high melting temperature infiltrant is used, sufficient skeleton can be formed during slow heating to the infiltration temperature, although care needs to be taken to ensure that excessive densification does not occur.

The use of an aluminium powder preform poses several unique challenges. Firstly, aluminium is covered by a thermodynamically stable oxide layer, the thickness of which is dependent on the temperature at which it formed and the atmosphere under which it is stored. Typically, the oxide layer on bulk aluminium at room temperature is 10–20 Å (Nylund and Olefjord, 1993, 1994; Olefjord and Nylund, 1994; Mizuno et al., 1996; Nylund et al., 1998), while the layer can vary between 50 and 150 Å on powder (Ozbilen et al., 1989; Kim et al., 1985; Nielsen et al., 1993; Anderson et al., 1998). This layer acts as a barrier to solid state sintering, and therefore creation of the skeleton. However, additions of Mg have been shown to be effective in disrupting the oxide layer and facilitating the solid state sintering of aluminium (Lumley et al., 1999). It is therefore possible to form a traditional sintered skeleton.

It is also crucial that the skeleton is not attacked or dissolved by the infiltrant. If this occurs, then the preform loses structural integrity and loss of dimensional accuracy results. For this reason, a dissimilar metal is usually used for the infiltrant. Common examples of infiltration systems that have been used with preforms made from RP technologies include bronze into stainless steel (Uzunsoy et al., 2002; Uzunsoy and Chang, 2005), aluminium into mullite (Soundararajan et al., 2001), copper into ZrB_2 (Bradley et al., 1997) and magnesium into SiC (Wohlert et al., 1996). For aluminium preforms, the infiltrant's melting point needs to be below the temperature at which appreciable sintering will occur (typically 600°C). This means that the choice of metal is limited to the low melting point alloys such as zinc, tin and lead. However, all these metals have very high density and since the infiltrant constitutes approximately 40–50% of the volume of the component, the lightweight advantage of aluminium is lost. Hence, there was a need to consider low melting point aluminium-based infiltrants (such as the ternary eutectic Al-14.7Si-4.5Mg), which melts at 560°C (ASM, 1992). This creates another problem. Although it is possible to create a conventional aluminium skeleton through solid state sintering, the use of Al-based infiltrants causes dissolution of the sintered necks between the powder particles, effectively destroying the skeleton. This results in loss of accuracy, large grain growth and essentially a sintered microstructure, as shown in Fig. 22.4. It therefore became necessary to develop a non-traditional skeleton. This was achieved by the partial conversion of the aluminium to an interconnecting aluminium nitride skeleton.

22.2.1 Formation of aluminium nitride

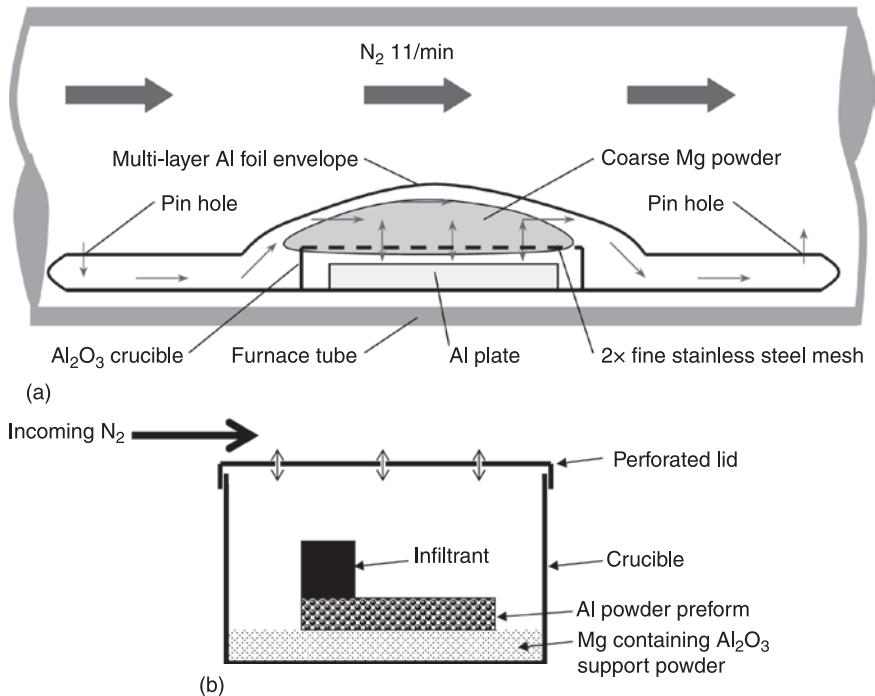
High-temperature direct nitriding of molten aluminium has been performed to produce powders and whiskers (see e.g. Komeya et al., 1993a; Weimer et al., 1994; Baik and Drew, 1996; Weimer, 1997; Radwan and Bahgat, 2006, 2007;



22.4 Laser sintered powder preform after (a) removal of the binder and (b) infiltration. Note the change of scale. Without an inert skeleton forming, the aluminium (grey particles) has undergone a large amount of grain growth.

Radwan et al., 2006) and usually involves reacting of fine molten Al droplets at high temperatures (1000–1500°C). Various additions, such as lithium and calcium (Komeya et al., 1993a, 1993b) or NH_4Cl (Radwan and Bahgat, 2007), have been used to reduce the temperatures required for the conversion. In addition, the formation of surface coatings on aluminium has been attempted using various direct nitriding techniques such as plasma assisted nitriding. However, only relatively thin layers ($<15\text{ }\mu\text{m}$) have been able to be produced to date (Meletis and Yan, 1991; Chen et al., 1994; Renevier et al., 1999; Ebisawa and Saikudo, 1996; Richter et al., 2000; Telbizova et al., 2001; Gredelj et al., 2002). Thicker layers ($\sim 1\text{ mm}$) have been reported when ion nitriding was used in combination with a fluidised bed and barrel nitriding (Okumiya et al., 2001, 2005).

The processes outlined above are not suitable for the in situ production of an AlN skeleton prior to infiltration. A low-temperature method is required in order to incorporate the nitridation into the infiltration cycle. It has recently been reported that the conversion of Al to AlN can be achieved at low temperatures ($\sim 540^\circ\text{C}$) both on powder (Sercombe and Schaffer, 2003, 2004a) and on Al plate (Kent et al., 2006). In order to make the formation of AlN possible, the oxidation reaction must be completely suppressed. This required strict atmosphere control in order to maintain the very low oxygen partial pressures required (Scholz and Greil, 1991) and was achieved using three complementary methods. First, the furnace is evacuated to remove the majority of the air (i.e. oxygen) and then back filled with high purity (Sercombe and Schaffer, 2004a) or ultra high purity (Kent et al., 2006) nitrogen. Secondly, since the incoming gas contains a small (ppm level) amount of oxygen which is sufficient to suppress the nitridation reaction, it was necessary to isolate the aluminium from direct contact with the gas, as shown in Fig. 22.5. The perforated cover allows only a small amount of the incoming gas to come in close contact with the preform. Finally, magnesium is used to preferentially react with any oxygen in the atmosphere. The preforms contained approximately 2wt% elemental Mg and there was a similar amount added to the Al_2O_3 support powder. Magnesium is an effective getter as it has a very strong affinity for oxygen and a relatively high vapour pressure ($\sim 100\text{ Pa}$ at 600°C ; Lide, 2007). Hence, at the processing temperature, appreciable Mg vapour will surround the sample. The nearly sealed crucible also acts to contain the Mg vapour to the atmosphere surrounding the preform. It has also been suggested (Hou et al., 1995; Lee et al., 2001) that the Mg is acting as a catalyst for the formation of AlN by forming an intermediary Mg_3N_2 which then reacts with Al to form AlN. The presence of a yellow residue at the end of the furnace cycle and the presence of an ammonia smell tended to support the fact that Mg_3N_2 was forming as this compound is not stable in the presence of water vapour and decomposes to form MgO and NH_3 . Whether or not the formation of Mg_3N_2 is important to the formation of AlN is unclear. However, the fact that it does form is a further indication that the oxygen partial pressure is extremely low within the crucible.

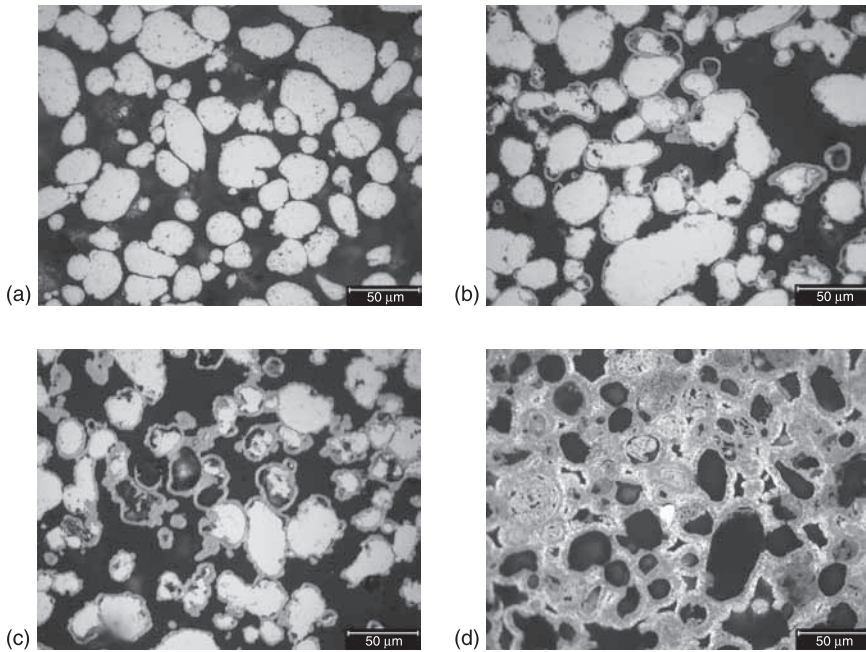


22.5 Schematic of the crucible layout used to nitride (a) plates (reproduced with permission from Kent [2008]) and (b) powder.

22.2.2 Growth of aluminium nitride

In order for the nitride to form an interconnecting skeleton, it must grow outwards from the powder particle surface. This implies that the diffusion of the aluminium through the nitride needs to be greater than the diffusion of nitrogen. Fortunately, the nitride layer does grow outwards, and is shown forming over time on 6061 powder in Fig. 22.6. As the ring of nitride grows, it consumes the aluminium from within the particles. The mechanism of growth has been studied in some detail on aluminium plate (Kent, 2008). Initially discrete nodules are present on the surface which consist of randomly oriented particles within an aluminium matrix (Kent, 2008). Over time, these nodules grow and coalesce to form a continuous layer. As the layer thickens, the AlN forms columnar grains aligned in the direction of growth. Metallic Al was also detected in the AlN layer, which is assumed to be diffusing to the surface to continue the growth.

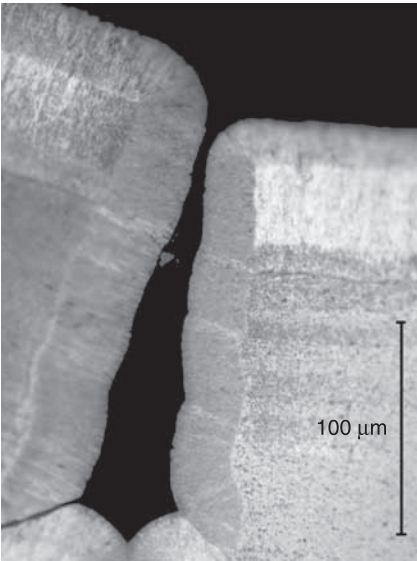
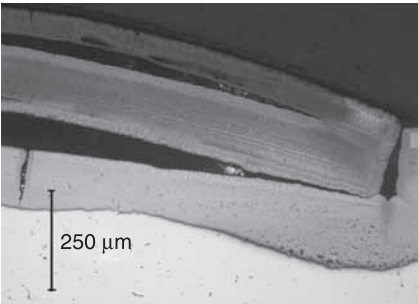
When growing on pure aluminium, the nitride also grows inwards (Kent, 2008). For this to occur, diffusion of the nitrogen through the layer must become possible. One mechanism, whereby this could occur, is if the layer becomes cracked. There is some evidence of cracking on both powder and plate, as can



22.6 The growth of the nitride layer on 6061-2Mg preforms at 540°C after (a) 0 h, (b) 4 h, (c) 6 h and (d) 10 h. The outwards growing layer is the AlN, which forms an interconnected skeleton (a–c reprinted from Sercombe and Schaffer (2004) with permission of Elsevier).

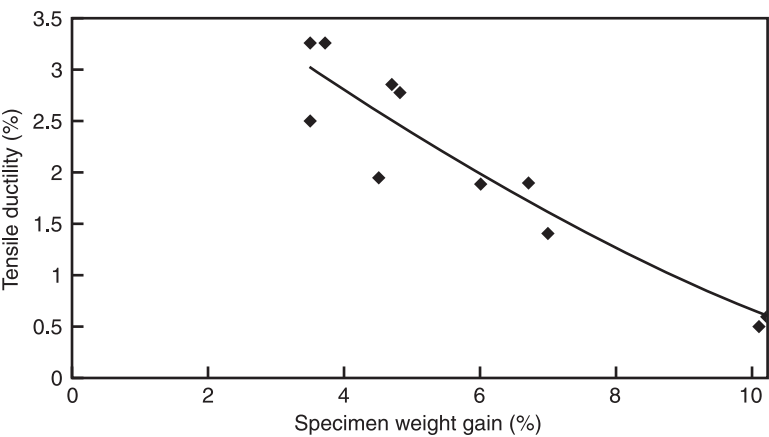
be seen in Fig. 22.7. The nitride layer has continued to grow on the surfaces of the crack, acting to close them. On plate, the inward forming nitride was found to be a combination of Al and hexagonal AlN. However, on powder, it is presumed that once the reaction goes to completion, the structure is completely AlN. The microstructural features observed on the nitride formed on plate are similar to that on powder and therefore it appears reasonable to assume that the same growth mechanisms are active on both.

The thickness of the nitride layer has a large influence on the properties of the infiltrated parts. Ductility is especially affected, as shown in Fig. 22.8. Hence, there is a need to be able to control the nitride growth rate such that an optimised thickness can be easily achieved. The growth rate is dependent on many factors including the temperature, composition of the powder, the amount of elemental Mg added and whether or not other elemental additions have been made (Sercombe and Schaffer, 2004a, 2004b). For the transformation of pure Al, there is an initial incubation period where no nitride forms, which is likely to be the time required to remove the oxygen from the atmosphere. Once the nitride begins to grow, complete conversion occurs over a



22.7 Cracked nitride layer formed on plate. It is apparent that the layer has grown into the area exposed to the nitrogen [from Kent (2008)].

very short period (<10 minutes). In contrast, the alloy powder 6061 nitrides more slowly, but there is still a relatively rapid transition of about one hour from un-nitrided to fully nitrided. Additions of low melting point elements, such as Sn, reduce the growth rate of the nitride significantly (Kondoh et al., 1999, Kondoh et al., 2000; Sercombe and Schaffer, 2004b). Whether the Sn is added as a separate alloying addition or pre-alloyed in to the powder has no effect on



22.8 The relationship between the amount of weight gain (due to nitridation) and the resultant ductility for 6061-2Mg-1Sn preforms infiltrated with Al-5Mg. Clearly less nitride is beneficial.

its efficiency (Sercombe and Schaffer, 2004b). One mechanism where the Sn may be controlling the nitride growth rate is by slowing the diffusion of the Al through the nitride layer. Although the exact mechanism by which the aluminium diffuses through the nitride is not known, it has been postulated (Kent, 2008) that it may occur by solid state self-diffusion. It has also been widely reported (Kimura and Hasiguti, 1961; Hashimoto, 1965; Ohta and Hashimoto, 1965; van den Beukel, 1967) that Sn reduces the diffusivity of aluminium through a vacancy binding mechanism. That is, the Sn is effectively removing vacancies from the system, preventing the solid state diffusion of the aluminium, thus controlling the nitride growth. Another mechanism that was proposed by Kondoh (Kondoh et al., 1999) is that the Sn acts as a physical barrier between the aluminium and atmosphere. However, the thickness of the layer is constant and SEM analysis of the powder (Sercombe and Schaffer, 2004b) has revealed that the Sn is present in isolated areas between the aluminium particle and nitride. Hence, it appears that this mechanism of control is unlikely.

It is clear that the addition of both Mg and Sn is crucial to the formation and control of the nitride layer and is therefore vital to the overall success of the system.

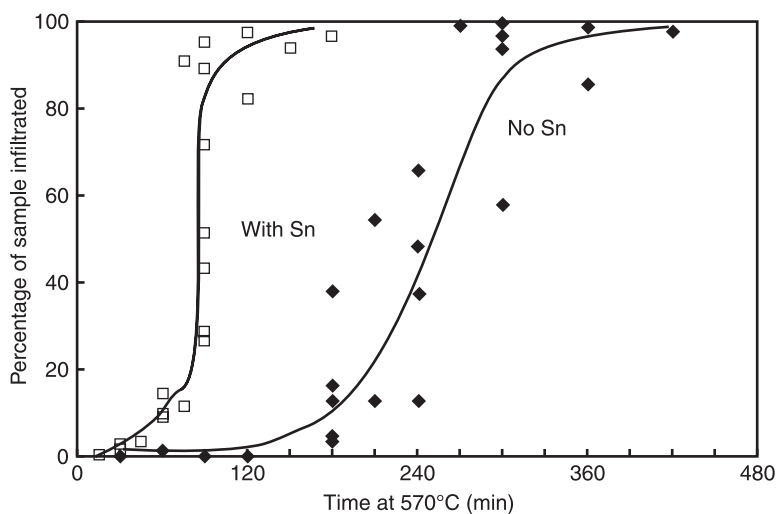
22.3 Infiltration

Conventional infiltration systems use an infiltrant with a lower melting point than the skeleton (e.g. Cu infiltrated in to steel). In the current examples, the preform was usually pre-alloyed 6061 powder (solidus temperature of 580°C [ASM, 1991]). In order to satisfy the relative melting point requirements, highly alloyed infiltrants such as the ternary Al-14.7wt%Si-4.3wt%Mg eutectic (~560°C [ASM, 1992]) or Al-33wt%Cu eutectic (548°C [ASM, 1992]) were required. These infiltrants allowed nitridation to occur at 540°C and then infiltration at 570°C without melting of the powder or excessive nitridation occurring. Although these alloys proved successful, they have very low ductility, causing the resultant part to be brittle (tensile ductility <1%).

Unlike conventional infiltration systems, the skeleton is an interconnected AlN nitride layer. Since AlN has a melting point of ~2800°C (Moffat, 1984), it is possible to retain a rigid preform, even after the preform powder has completely melted. This relaxes the temperature limits on the infiltrant, and allows any aluminium alloy to be used. The infiltrant used was usually 6061, as this was readily available and is heat treatable to produce acceptable properties. Since the liquidus temperature of this alloy is ~650°C, infiltration was usually performed at ~700°C. The high infiltration temperature meant that the atmosphere needed to be changed from nitrogen to either vacuum or argon at the end of the nitridation step, to prevent excessive nitridation from occurring during infiltration. Other infiltrants that have been successfully used include pure Al, Al-5Mg and Al-4.4Cu-1.6Mg-0.5Si.

When the low melting point eutectic alloys were used and infiltration could occur at low temperature (570°C), the infiltration front tended to be relatively flat (Sercombe and Schaffer, 2004b), which is characteristic of slug flow (Preziosi et al., 1996). The addition of Sn to the preform not only controlled the rate at which the nitride layer grew, but also influenced the rate of infiltration. As shown in Fig. 22.9, the presence of Sn in the preform increased the infiltration rate, thus decreasing the time needed to achieve full infiltration. Microstructural analysis of partially infiltrated bars (Sercombe and Schaffer, 2004b) revealed that the infiltrated region was depleted in Sn, which was concentrated at the advancing liquid front. Tin has a low surface tension (Smithells et al., 1992) and will therefore segregate to the molten aluminium vapour interface, reducing the effective surface tension of the aluminium (Goumiri et al., 1979). This has been shown to improve the sintering response of aluminium (Schaffer et al., 2001), including parts fabricated by selective laser sintering (Sercombe, 2001, 2003b). By a similar mechanism, Sn can be expected to increase the infiltration rate and it is therefore not surprising that it is observed at high concentrations at the head of the advancing interface.

Low alloy content infiltrants necessitated the use of elevated infiltration temperatures and for these alloys, a different infiltration route was observed (Yu and Schaffer, 2009). The distance that the infiltrant penetrated did not appear to be dependent on either time or temperature. Liquid appeared to flow instantaneously along the whole sample, partially filling the porosity. This meant



22.9 The effect of hold time on the infiltration of 6061-2Mg preforms with and without 1%Sn. The presence of Sn decreases the time it takes for infiltration to occur. The infiltrant was 14.7wt%Si-4.3wt%Mg and infiltration temperature 570°C. The preforms had been partially nitrified before infiltration.

that the density of the sample was uniform along its whole length. Over time, there was a gradual filling of the preform, until the sample was fully infiltrated. Whether infiltration occurred in nitrogen, argon or vacuum, affected the pathway though which the infiltrant penetrated the preform. Under vacuum, the areas near the surface tended to fill first, followed by the interior. This is different to what was observed in both Ar and N₂ atmospheres, where the central region infiltrated first, followed by the surface. In all three atmospheres, the terminal density was approximately the same.

22.4 Dimensional changes

One of the important driving forces for the development of an infiltrated system is the small amount of dimensional change that occurs during infiltration compared with sintering. There are several stages in the process where deviation in dimensions can occur including during the building of the laser sintered part (i.e. the difference between the computer model and resin-bonded part), upon thermal decomposition of the resin, formation of the AlN skeleton and its subsequent infiltration.

To a large extent, the accuracy of the green (laser sintered) part can be controlled by the correct use of scale and laser offset values to account for the inherent shrinkage, diameter of the laser beam and diffusion of heat into the surrounding powder that occurs during laser sintering. Since the actual dimensions of the part are dependent on its position in the part bed (Sercombe and Hopkinson, 2008), improved accuracy can be achieved by deriving the scale and offset values from a scale part as close to the same position as possible. During the removal of the binder, the collapse of the powder particles onto each other causes a net shrinkage, with the change in the Z dimension (by convention the direction in which the part is being built) being greater due to gravity (Sercombe and Hopkinson, 2006). The formation of the nitride does not have a significant effect on the dimensions of the part, and at the completion of the nitridation hold, the overall shrinkage is ~0.3–0.5% (depending on the direction). The greatest dimensional change occurs during infiltration, which results in a net shrinkage of ~1%, uniformly in all directions (Sercombe and Hopkinson, 2006, 2008). Therefore, although the original premise was to form a rigid skeleton, it appears that this is not completely the case as significant shrinkage does occur during infiltration. However, it is not clear whether this shrinkage occurs during the infiltration of the porous preform or during solidification of the infiltrated part. The overall shrinkage for the whole infiltration process is ~1.5%, which is approximately an order of magnitude lower than if the preform were sintered.

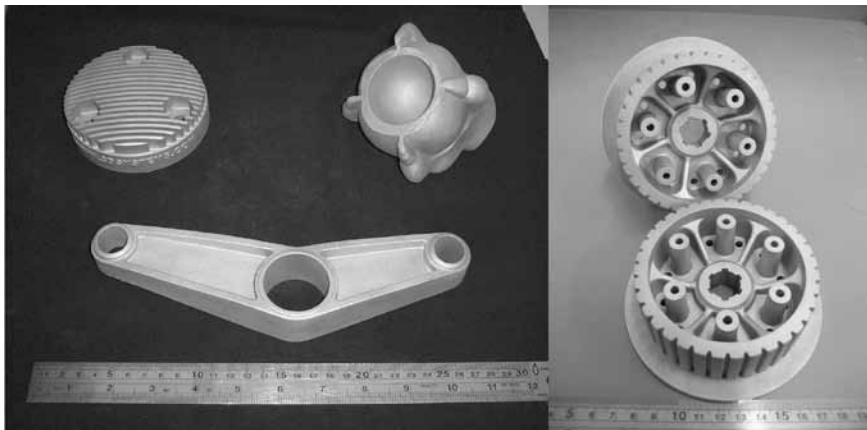
The absolute accuracy of the infiltrated parts has been measured to be within 0.1 mm of the nominal value in the X and Y direction, with the Z direction slightly worse, but still < 0.2 mm (Sercombe and Hopkinson, 2006). These errors

compare favourably with sand casting (± 0.8 mm for dimensions between 25 and 175 mm) and investment casting (± 0.4 mm for 75 mm sections), and are similar to that achievable with die castings (± 0.25 mm) (ASM, 1990).

22.5 Conclusion

The process to produce complex infiltrated aluminium components first requires the production of a resin bonded aluminium powder preform using selective laser sintering. In a single furnace cycle, the resin is thermally decomposed and removed from the preform, the aluminium partially converted into a percolating AlN skeleton which is then infiltrated with a second aluminium alloy. Examples of parts made using this approach are shown in Fig. 22.10. To date, parts in excess of 1 kg have been manufactured, with feature sizes as small as 0.6 mm possible.

The success of the system relies on being able to maintain an extremely low oxygen partial pressure in the atmosphere in order to suppress the ubiquitous oxidation reaction. This is achieved through a combination of a high purity nitrogen supply, effective isolation of the part from the incoming gas flow and Mg to gather any remaining oxygen. The rate of growth of the nitride skeleton can be controlled through the addition of Sn to the preform. Hence, it was possible to accurately control the thickness of the nitride layer. This was necessary as too little nitridation compromised the dimensional stability during infiltration and too much resulted in low ductility. The formation of the AlN skeleton relaxed the normal temperature limitations on the selection of the infiltrant and it is possible to use any Al-based alloy as the infiltrant, as the preform remains



22.10 Examples of aluminium parts made by infiltrating laser sintered aluminium preforms. Clockwise from top left: heat exchanger from a lawnmower engine, artistic sculpture, transmission components and structural bracket.

dimensionally stable even after the powder has melted. Hence, it became possible to select the infiltrant based on property requirements rather than melting point.

Using this technology, it is possible to manufacture complex aluminium components directly from a computer model without the need for machining or the production of any tooling. Since it is just as easy to make two sequential parts with tailored differences as it is to make them identical, we have now gone beyond what is currently considered economically viable manufacturing. Parts customised to the end user can be made for the same cost and in the same time as identical items. However, this technology is best suited for parts of high geometric complexity, where a relatively small number of parts are needed. For large production runs, the process cannot compete with traditional mass production techniques, except where the geometry makes traditional manufacturing impossible. For the first time, there is no longer a geometric constraint for the manufacture of aluminium components, with designers no longer needing to compromise their design for ease of manufacture.

22.6 Acknowledgements

Aspects of this work were supported by 3D Systems Inc, The Aluminium Powder Co Ltd and The Australian Research Council. The author would also like to acknowledge Professor Graham Schaffer at The University of Queensland, who was a vital part of this work.

22.7 References

- Anderson, I.E., Foley, J.C. & Flumerfelt, J.F. (1998) *In* W.F. Jandeska, R.A. Chernenkoff, eds. *Powder Metallurgy Aluminum and Light Alloys for Automotive Applications*. 10–11 November 1998. Dearborn, MI: MPIF.
- ASM (1990) *ASM Handbook Volume 15: Casting*, Materials Park, OH, ASM International.
- ASM (1991) *ASM Handbook Volume 2: Properties and Selection: Nonferrous Alloys and Special-Purpose Materials*, Materials Park, OH, ASM International.
- ASM (1992) *ASM Handbook Volume 3, Alloy Phase Diagrams*, Materials Park, OH, ASM International.
- Baik, Y. & Drew, R.A.L. (1996) 'Aluminium Nitride: processing and applications', *Key Engineering Materials*, 122–124: 553–560.
- Bradley, W., Stucker, B., Eubank, P.J., Norasethekul, S., Kim, E. & Bozkurt, B. (1997) 'Rapid prototyping of EDM electrodes of zirconium-diboride/copper', *Rapid Prototyping/Laser Applications in the Automotive Industries*, Florence, Italy, Automotive Automation Limited, Croydon, England.
- Chen, H.Y., Stock, H.R. & Mayr, P. (1994) 'Plasma-assisted nitriding of aluminum', *Surface and Coatings Technology*, 64: 139–147.
- Ebisawa, T. & Saikudo, R. (1996) 'Formation of aluminum nitride on aluminum surfaces by ECR nitrogen plasmas', *Surface and Coatings Technology*, 86–87: 622–627.

- Goumiri, L., Joud, J.C. & Desre, P. (1979) 'Estimation de la tension superficielle d'alliages liquides binaires présentant un effet de taille important', *Surface Science*, 88: 461–473.
- Gredelj, S., Gerson, A.R., Kumar, S. & Cavallaro, G.P. (2002) 'Inductively coupled plasma nitriding of aluminium', *Applied Surface Science*, 199: 183–194.
- Hashimoto, F. (1965) 'Interaction between a vacancy and an Ag atom in aluminium', *Journal of the Physical Society of Japan*, 20: 336–346.
- Hou, Q., Mutharasan, R. & Koczak, M. (1995) 'Feasibility of aluminium nitride formation in aluminum alloys' *Materials Science and Engineering A*, 195: 121–129.
- Iacocca, R.G. & Myers, N. (2000) 'The development of an aluminum alloy for selective laser sintering applications', *PM2TEC 2000: 2000 International Conference on Powder Metallurgy & Particulate Materials*, 30 May–3 June 2000, New York, USA.
- Kent, D. (2008) 'Synthesis and characterisation of aluminium nitride formed on aluminium at low temperature', PhD Thesis, The University of Queensland.
- Kent, D., Schaffer, G.B., Sercombe, T.B. & Drennan, J. (2006) 'A novel method for the production of aluminium nitride', *Scripta Materialia*, 54: 2125–2129.
- Kim, Y.W., Griffith, W.M. & Froes, F.H. (1985) 'Surface oxides in P/M aluminum-alloys', *Journal of Metals*, 37: 27–33.
- Kimura, H. & Hasiguti, R. (1961) 'Interaction of vacancies with Sn atoms and the rate of GP zone formation in Al-Cu-Sn Alloys', *Acta Metallurgica*, 6: 1076.
- Komeya, K., Matsukaze, N. & Meguro, T. (1993a) 'Synthesis of AlN by direct nitridation of al-alloys', *Nippon Seramikkusu Kyokai Gakujutsu Ronbunshi-Journal of the Ceramic Society of Japan*, 101: 1319–1323.
- Komeya, K., Mitsuhashi, E. & Meguro, T. (1993b) 'Synthesis of AlN powder by carbothermal reduction-nitridation method – effect of additives on reaction-rate', *Nippon Seramikkusu Kyokai Gakujutsu Ronbunshi-Journal of the Ceramic Society of Japan*, 101: 377–382.
- Kondoh, K., Kimura, A. & Watanabe, R. (1999) 'Analysis on behaviour of tin on aluminium alloy powder surface during heating', *Journal of the Japan Society of Powder and Powder Metallurgy*, 46: 1141–1147.
- Kondoh, K., Kimura, A. & Watanabe, R. (2000) 'Effect of tin on directly nitriding reaction of rapidly solidified aluminum alloy powder', *Journal of the Japan Society of Powder and Powder Metallurgy*, 47: 42–46.
- Lee, K.B., Sim, H.S., Kim, S.H., Han, K.H. & Kwon, H. (2001) 'Fabrication and characteristics of AA6061/SiCp composites by pressureless infiltration technique', *Journal of Materials Science*, 36: 3179–3188.
- Lide, D.R. (2007) *CRC Handbook of Chemistry and Physics*, 88th ed., Cleveland, OH, CRC Press.
- Lumley, R.N., Sercombe, T.B. & Schaffer, G.B. (1999) 'Surface oxide and the role of magnesium during the sintering of aluminum', *Metallurgical and Materials Transactions A*, 30: 457–463.
- Meletis, E.I. & Yan, S. (1991) 'Formation of aluminum nitride by intensified plasma ion nitriding', *Journal of Vacuum Science & Technology a-Vacuum Surfaces and Films*, 9: 2279–2284.
- Mizuno, K., Nylund, A. & Olefjord, I. (1996) 'Surface analysis of oxide formed during heat treatment of Al-Mg-Si alloys', *Materials Science and Technology*, 12: 306–314.
- Moffat, W.G. (1984) *The Handbook of Binary Phase Diagrams*, New York, Genium.

- Nielsen, P., Liu, Y.L. & Hansen, N. (1993) 'Manufacturing of aluminium composites with high purity matrix', *Powder Metallurgy World Congress*, Kyoto, Japan, Japan Society of Powder and Powder Metallurgy.
- Nylund, A. & Olefjord, I. (1993) 'Surface-analysis of air exposed rapidly solidified aluminum powder', *Powder Metallurgy*, 36: 193–197.
- Nylund, A. & Olefjord, I. (1994) 'Surface-analysis of oxidized aluminum, 1: Hydration of Al_2O_3 and decomposition of $Al(OH)_3$ in a vacuum as studied by ESCA', *Surface and Interface Analysis*, 21: 283–289.
- Nylund, A., Mizuno, K. & Olefjord, I. (1998) 'Influence of Mg and Si on the oxidation of aluminum', *Oxidation of Metals*, 50: 309–325.
- Ohta, M. & Hashimoto, F. (1965) 'Binding energy between a vacancy and an atom of third element and their effect on the initial ageing of Al-10wt%Zn alloys', *Transactions of the Japan Institute of Metals*, 6: 9–14.
- Okumiya, M., Tsunekawa, Y. & Murayama, T. (2001) 'Surface modification of aluminum using ion nitriding and fluidized bed', *Surface & Coatings Technology*, 142: 235–240.
- Okumiya, M., Tsunekawa, Y., Sugiyama, H., Tanaka, Y., Takano, N. & Tomimoto, M. (2005) 'Surface modification of aluminum using ion nitriding and barrel nitriding', *Surface and Coatings Technology*, 200: 35–39.
- Olefjord, I. & Nylund, A. (1994) 'Surface-analysis of oxidized aluminum, 2: oxidation of aluminum in dry and humid atmosphere studied by ESCA, sem, sam and EDX', *Surface and Interface Analysis*, 21: 290–297.
- Ozbilen, A., Unal, A. & Sheppard, T. (1989) Influence of oxygen on morphology and oxide content of gas atomised aluminium powders, in Small, M. (Ed.): *Physical Chemistry of Powder Metals-Production and Processing*, St. Mary's, PA, Minerals, Metals and Materials Society.
- Preziosi, L., Joseph, D.D. & Beavers, G.S. (1996) 'Infiltration of initially dry, deformable porous media', *International Journal of Multiphase Flow*, 22: 1205–1222.
- Radwan, M. & Bahgat, M. (2006) 'Novel growth of aluminium nitride nanowires', *Journal of Nanoscience and Nanotechnology*, 6: 558–561.
- Radwan, M., Bahgat, M. & El-Geassy, A.A. (2006) 'Formation of aluminium nitride whiskers by direct nitridation', *Journal of the European Ceramic Society*, 26: 2485–2488.
- Radwan, A. & Bahgat, M. (2007) 'A modified direct nitridation method for formation of nano-AIN whiskers', *Journal of Materials Processing Technology*, 181: 99–105.
- Renevier, N., Czerwec, T., Billard, A., Von Stebut, J. & Michel, H. (1999) 'A way to decrease the nitriding temperature of aluminium: the low-pressure arc-assisted nitriding process', *Surface & Coatings Technology*, 116–119: 380–385.
- Richter, E., Gunzel, R., Parasacandola, S., Telbizova, T., Kruse, O. & Moller, W. (2000) 'Nitriding of stainless steel and aluminium alloys by plasma immersion ion implantation', *Surface & Coatings Technology*, 128: 21–27.
- Schaffer, G.B., Huo, S.H., Drennan, J. & Auchterlonie, G.J. (2001) 'The effect of trace elements on the sintering of an Al-Zn-Mg-Cu ALLOY', *Acta Materialia*, 49: 2671–2678.
- Scholz, H. & Greil, P. (1991) 'Nitridation reactions of molten AL-(MG, SI) alloys', *Journal of Materials Science*, 26: 669–677.
- Sercombe, T.B. (2001) 'The production of functional al prototypes using selective laser sintering', *P/M Science and Technology Briefs*, 3: 22–25.
- Sercombe, T.B. (2003a) 'The effect of resin type on the sintering of maraging steel', *Materials Science and Engineering A*, 344: 312–317.

- Sercombe, T.B. (2003b) 'On the sintering of uncompacted, pre-alloyed Al powder alloys', *Materials Science and Engineering A*, 341: 163–168.
- Sercombe, T.B. (2003c) 'Sintering of freeformed maraging steel with boron additions', *Materials Science and Engineering A*, 363: 242–252.
- Sercombe, T.B. & Schaffer, G.B. (2003) 'Rapid manufacturing of aluminum components', *Science*, 301: 1225–1227.
- Sercombe, T.B. & Schaffer, G.B. (2004a) 'On the role of magnesium and nitrogen in the infiltration of aluminium by aluminium for rapid prototyping applications', *Acta Materialia*, 52: 3019–3025.
- Sercombe, T.B. & Schaffer, G.B. (2004b) 'On the role of tin in the infiltration of aluminium by aluminium for rapid prototyping applications', *Scripta Materialia*, 51: 905–908.
- Sercombe, T.B. & Hopkinson, N. (2006) 'Process shrinkage and accuracy during indirect laser sintering of aluminium', *Advanced Engineering Materials*, 8: 260–264.
- Sercombe, T.B. & Hopkinson, N. (2008) 'Process repeatability and sources of error in indirect SLS of aluminium', *Rapid Prototyping Journal*, 14: 108–113.
- Simchi, A. & Pohl, H. (2003) 'Effects of laser sintering processing parameters on the microstructure and densification of iron powder', *Materials Science and Engineering A*, 359: 119–128.
- Smithells, C.J., Brandes, E.A. & Brook, G.B. (1992) *Smithells' metals reference book*, Oxford, Butterworth-Heinemann.
- Soundararajan, R., Kuhn, G., Atisivan, R., Bose, S. & Bandyopadhyay, A. (2001) 'Processing of mullite-aluminum composites. American Ceramic Society', *Journal of the American Ceramic Society*, 84: 509–513.
- Souvignier, C.W., Sercombe, T.B., Huo, S.H., Calvert, P. & Schaffer, G.B. (2001) 'Freeform fabrication of aluminum metal-matrix composites', *Journal of Materials Research*, 16: 2613–2618.
- Telbizova, T., Parascandola, S., Prokert, F., Barradas, N.P., Richter, E. & Moller, W. (2001) 'Ion nitriding of Al: growth kinetics and characterisation of the nitride layer', *Surface & Coatings Technology*, 12: 1028–1033.
- Uzunsoy, D., Chang, I.T.H. & Bowen, P. (2002) 'Microstructural evolution and mechanical properties of RapidSteel 2.0', *Powder Metallurgy*, 45: 251–254.
- Uzunsoy, D. & Chang, I.T.H. (2005) 'The effect of infiltrant choice on the microstructure and mechanical properties of Rapidsteel 2.0', *Materials Letters*, 59: 2812–2817.
- van den Beukel, A. (1967) 'On the relationship between self-diffusion, melting, and vacancy-impurity binding in dilute alloys', *Physica Status Solidi*, 23: 165–170.
- Weimer, A.W. (1997) *Carbide, nitride, and boride materials synthesis and processing*, London, Chapman & Hall.
- Weimer, A.W., Cochran, G.A., Eisman, G.A., Henley, J.P., Hook, B.D., Mills, L.K., Guiton, T.A., Knudsen, A.K., Nicholas, N.R., Volmering, J.E. & Moore, W.G. (1994) 'Rapid process for manufacturing aluminum nitride powder', *Journal of the American Ceramic Society*, 77: 3–18.
- Wohlert, M., Bourell, D., Lee, G. & Beaman, J. (1996) In T.S. Srivatsan and J.J. Moore, E. (Ed.) *Processing and Fabrication of Advanced Materials V*, Cincinnati, OH.
- Yu, P. & Schaffer, G.B. (2009) 'Microstructural evolution during pressureless infiltration of aluminium alloy parts fabricated by selective laser sintering', *Acta Materialia*, 57: 163–170.

J. HIRSCH, Hydro Aluminium Deutschland GmbH, Germany

Abstract: The principles of aluminium alloy sheet processing, the main configurations and process parameters and the metallurgical effects involved are presented for industrial sheet manufacturing, from DC sheet ingot or twin-roll thin slab casting, homogenisation, hot and cold rolling as well as annealing. The main process conditions and thermo-mechanical parameters are described along with their effects on microstructure evolution during deformation, recovery and recrystallisation. Grain structure and texture as well as the resulting properties strength, formability, anisotropy are predicted and integrated into process models to improve through process control and material optimization strategies for rolled sheet.

Key words: sheet alloy specification, DC casting, twin-roll casting, homogenisation, microstructure evolution, annealing, rolling (hot and cold), rolling mill design, integrated simulation, through-process modelling (TPM).

23.1 Introduction

Aluminium is a light metal that is easy to melt, cast and then process in a large variety of fabrication and forming processes. Rolling it to sheet is one of the major ‘downstream’ fabrication processes for semi-finished products used in numerous applications. Rolled products, i.e. sheet, plate and foil, constitute almost 50% of all aluminium used. Unalloyed aluminium (i.e. technically pure), Al99.5 (AA1xxx), is a relatively soft material, due to its atomic structure (a closed-packed FCC lattice with high stacking fault energy) and few alloy elements (impurities). It does not strain harden heavily during deformation, therefore exhibiting an almost infinite formability, as required for extremely thin foil rolling. However, with specific alloying elements aluminium can also achieve relatively high strength, so it is used in structural applications (architecture, engineering, machinery, etc.) and light-weight vehicles (aerospace, planes, cars, trucks, busses, ships, trains, trams, etc.). With its specific properties superior to many other materials aluminium sheet is also found in many products like heat exchangers, lithographic printing plates, condenser foil, etc.

Aluminium is a relatively young material – compared to classical steel – and its main alloys have been discovered and developed within the past 100 years. In the early 20th century, aluminium began to play a major industrial role, for example in airplanes, however, after the 2nd world war a strong growth and new applications emerged, especially for aluminium sheet. Large rolling capacities were built and volumes in commercial (civil) sheet products were introduced to the market only 50 years ago. With this development more specially designed alloys and more

advanced processing routes (e.g. TRC, belt- or strip-casting, high-capacity tandem rolling lines and foil rolling) have been invented.

Aluminium sheet fabrication, in general, starts with one of the following casting processes, having quite different volume capacities (Karhausen and Korhonen, 2003). The conventional DC casting process runs very efficiently in high-volume plants (CRU, 2008), where in a coupled breakdown and subsequent multi-stand 'tandem' hot rolling process strip is produced from large ingots. The major deformation steps involved generate relatively fine microstructures with optimum mechanical properties and excellent surface qualities. For many aluminium alloy products and modern sheet applications such high quality is mandatory.

After DC casting the ingots go through the typical sequence of processing steps:

- 1 surface scalping removes the as-cast surface structures, oxides and segregations
- 2 pre-heating (homogenisation) heats up the ingots and modifies its microchemistry
- 3 hot and cold rolling flattens the material and generates specific properties and qualities
- 4 final (or inter-) annealing softens the material and generates a specific grain structure.

Each of these process steps affects microstructure evolution – and thus final sheet properties – in quite specific ways (Hirsch, 2006a, 2006b). Sheet rolling, in particular, refines the grain structure, crushes the large constituent particles (10–50 μm) and reduces porosity. During hot rolling the metal recrystallises, mostly in-between the rolling passes. It remains in a relatively soft condition and low rolling forces allow large deformation steps without major energy input. During cold rolling, however, extreme work hardening takes place in aluminium alloys, raising the sheet strength significantly (e.g. in Al-Mg-Mn can-body or end stock).

Cold rolling also provides tight tolerances and allows a special surface finish. However, it limits formability and processability, so inter- or final annealing steps are usually applied.

For high strength and quality specific aluminium alloys are used, containing typical elements like Mg, Mn, Si and Fe (i.e. non-heat treatable) and Cu, Zn, Mg and Si (heat treatable) often in combination for aluminium sheet alloys (Hirsch et al., 2006).

For the latter additional special continuous annealing lines are required as the last sheet fabrication process step, to freeze in the precipitating elements in solid solution and ensure the typical (strong) age-hardening characteristics in final 'bake hardening' processes such as used for Al-Mg-Si (AA6xxx) automobile body sheet (Brünger et al., 2006). Bake hardening further hardens

the sheet parts at the customer's facility after part forming in the soft and solution annealed 'T4' stage.

The main aluminium alloys and their sheet fabrication methods are now well established. However, there is still intensive research and development for further improvement of some sheet alloy variants and specific designed properties. For example, varying alloy and sheet processing routes are important to meet some special and ever growing customer requirements and quality demands. As aluminium competes with other (sheet) materials and needs to gain or maintain its position in the highly competitive global market, new high-quality aluminium alloys and (sheet) products are still being developed in many – at first sight quite unspectacular – applications and products for our daily life. This requires continuous optimisation and improvement by adapting alloys and process parameters to changing (i.e. more efficient) plant configurations and property requirements of established or new customer specifications (Kaestner and Hirsch, 2008).

In order to run most efficiently aluminium sheet rolling plants have been established within large international 'Integrated Aluminium Companies'. The different configurations are analysed in their competitiveness (CRU, 2008), based on data of metal and energy price, cast house details, furnaces, slab dimensions, mill details and various other indices. To survive in the global competition these companies have developed the necessary expertise and key competencies in sheet fabrication and application, combining basic material/alloy and specific processing know-how. This is now used in sophisticated simulation tools being integrated into TPM 'Through-Process Models' (Hirsch, 2006a, 2006b) combining metallurgical parameters (alloy composition, thermo-mechanical and microstructural effects) with sheet processing parameters (like temperature, strain and strain rate) affecting final sheet properties (strength, formability, anisotropy, etc.) and other important quality aspects (sheet profiles and flatness, surfaces, etc.). These simulation tools are capable of predicting the complex (combined) effects of variations in alloy compositions and processing routes on the evolution of microstructure and properties in any combination. They are used successfully for further alloy development, special process optimisations, new innovation strategies and also for customer-specific processes and important business aspects, like cost reduction, capacity optimisation and product and process flexibility.

23.2 Aluminium alloys and specifications

23.2.1 Aluminium alloy classes and elements

Technically pure '99.5' aluminium has a low strength (20–50 MPa) and limited strain hardening (up to about 170 MPa) – and even more so high-purity aluminium, which stays soft by dynamic recovery and recrystallisation even at

room temperature forming. For commercial use high strength is achieved by the addition of specific alloy elements. The established alloy elements and the associated alloy groups are listed in the introduction to this book, and discussed further in the following section.

Non-heat treatable Al alloys

Achieve a higher strength by solid solution hardening – often coupled with strain hardening. – The strength of this alloy group is generated by the hardening effect of elements in solid solution (e.g. manganese, silicon, iron, magnesium, chromium and others, also in their combinations). Furthermore, these alloys are mostly work hardenable, i.e. further strengthening occurs by cold working, e.g. during cold rolling (H1x-temper) and/or part forming, sometimes a high temperature treatment is applied to reduce the strain hardening effect and regain the lost formability (H2x-temper); furthermore, certain temperature treatments have a stabilising effect (H3x-temper) to ensure stable properties.

Heat treatable Al alloys

Achieve a higher strength by precipitation ‘age’ hardening. Here strength is enhanced by the addition of alloying elements such as copper, zinc and magnesium in combination with silicon. Such alloy additions generate fine precipitates and create the ‘age hardening’ effect in combination with appropriate heat treatments that include

- 1 solution annealing and quenching (T4 temper, i.e. after some time at room temperature)
- 2 precipitation or age hardening (T6 temper, i.e. after additional age-hardening heat treatment).

(see ‘Main tempers (i.e. fabrication stages) of aluminium alloys’ and Chapter 1 of this book).

23.2.2 Alloying elements

Aluminium alloys are traditionally listed in the ‘AA’ alloy classes, a four digit number with the first digit defining the main alloy element:

1xxx series

Pure aluminium of 99% or higher purity (A1 99.5, with iron and silicon as the major impurities) has many applications, for example in packaging and electronics. These alloys have good formability and corrosion resistance, high thermal and electrical conductivity, low mechanical properties and excellent

workability. Some increases in strength may also be obtained by strain hardening.

2xxx series

Copper is the principal alloying element in this group, often with some magnesium as a secondary addition. These alloys require solution heat treatment and artificial aging to obtain optimum yield strength values, but often with attendant loss in elongation. The alloys in this series have limited corrosion resistance, e.g. to inter-granular corrosion.

3xxx series

Manganese is the major alloying element of alloys in this group, which are generally non-heat treatable. However, only a limited percentage of manganese, up to about one per cent, can be effectively added to aluminium.

4xxx series

Silicon is the major alloying element of this group, which can be added in sufficient quantities (up to 12%) to cause substantial lowering of the melting point without producing brittleness in the resulting alloys. For these reasons aluminium-silicon alloys are used in welding wire and as brazing alloys where a lower melting point than that of the parent metal is required.

5xxx series

Magnesium is one of the most effective and widely used alloying elements, and is often used in combination with manganese, as a moderate to high strength non-heat treatable alloy with good welding and corrosion resistance characteristics. Under unfavourable conditions alloys with less than three per cent Mg become susceptible to inter-crystalline corrosion.

6xxx series

Al-Mg-Si alloys in this group contain silicon and magnesium in approximate proportions to form Mg_2Si precipitates, thus making them heat treatable. They are typically not as strong as most of the 2xxx or 7xxx alloys, but have good formability, weldability and corrosion resistance and find numerous applications.

7xxx series

Zinc additions coupled with magnesium (and copper, as well as other elements such as manganese and chromium in small quantities) result in heat treatable alloys of very high strength. Some outstanding members of this group are 7075,

7050 and 7049, which are among the highest strength alloys available and are used in air-frame structures and for highly stressed (automotive) parts.

8xxx series

Other elements (e.g. Fe, Li, etc.). Alloys contain excess Fe to achieve higher strength materials (e.g. foil applications). Li additions generate new age-hardening alloys for lightweight, high strength and high elastic modulus air-space applications.

23.2.3 Main tempers (i.e. fabrication stages) of aluminium alloys

Besides alloys the specific process effects on properties are defined as tempers and wrought alloys (e.g. plate and sheet) are delivered in the following conditions:

- F – as-fabricated (no specific temper)
- O – annealed (soft temper)
- H – strain hardened (e.g. cold rolled)
- W – solution heat treated (age-hardening alloys)
- T – thermally treated to stable tempers (age-hardening alloys).

Non-heat treatable alloys are normally delivered either as-fabricated (temper ‘F’) or fully annealed (temper ‘O’), so they are (relatively) soft and formability is high. Any storage or exposure to elevated temperature does not affect their room temperature strength. If, however, the alloy is worked or delivered in a cold deformed (e.g. rolled) ‘Hxy temper’ the material is strain hardened and therefore significantly harder. Heating a deformed material at medium or high temperatures will lose some of the (deformation) strength due to recovery. At sufficiently high temperature, (primary) recrystallisation takes place, which fully replaces the deformed structure by newly formed grains, reducing strength and re-establishing ductility (i.e. formability). Even higher temperatures and/or long exposure times can result in further grain growth.

After cold working (e.g. rolling) and annealing the following ‘Hxy temper’ designations are typical for non-heat treatable alloys:

- H1y – strain-hardened only (e.g. cold rolled)
- H2y – strain-hardened and partially annealed
- H3y – strain-hardened and stabilised (e.g. for corrosion)
- H4y – strain-hardened and lacquered or painted.

The first digit (x) after H indicates the type of thermal processing and the second digit (y) after H indicates the degree of strain hardening (9 = max.).

In contrast to the above the heat treatable alloys are hardened by precipitation hardening after high temperature (solution) annealing and quenching. In

combination with cold working and artificial aging very high-strength levels are obtained. The frequently used tempers here are:

T4 = solution annealed, naturally aged

T3 = solution annealed, naturally aged, cold formed

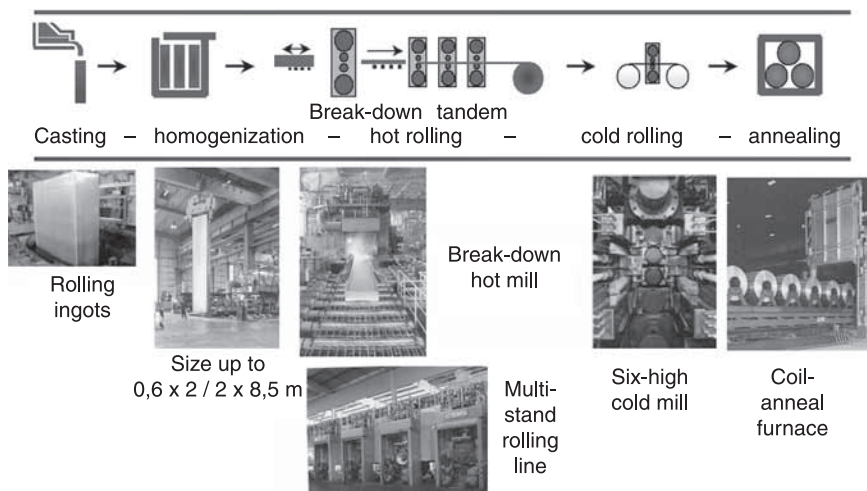
T6 = solution annealed, artificially aged

T8 = solution annealed, deformed, artificially aged.

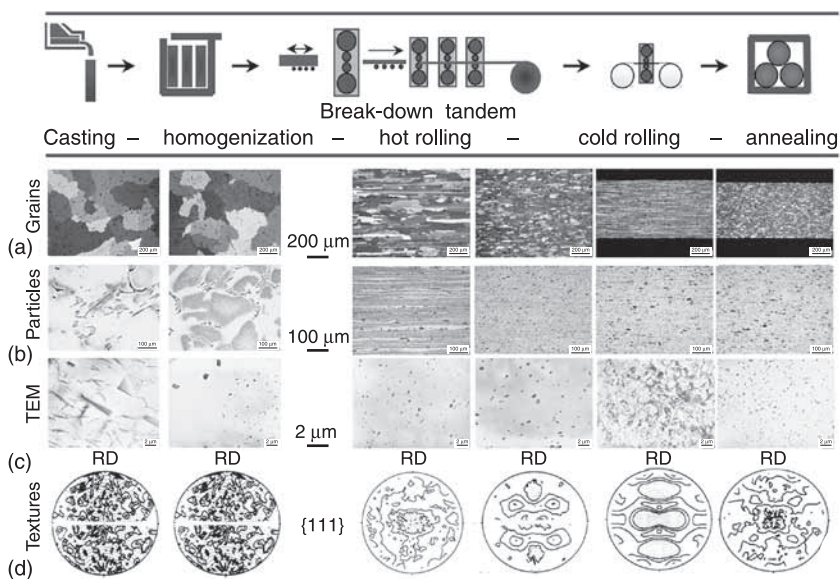
For more details see J.G. Kaufmann (2001), J. Datta (2003) and AA-Teal Sheets (2009) and the introduction to this book.

23.3 The aluminium sheet fabrication processing route and microstructure evolution

The established processing route for the production of Al alloy sheet is schematically depicted in Fig. 23.1, showing the typical stages and equipment used in modern (multi-stand) hot rolling lines, starting with DC casting, ingot pre-heating (homogenisation), hot and cold rolling and intermediate or final (coil) annealing. Figure 23.2 shows the corresponding microstructures: (a) grains, (b) and (c) particles (surface-etched and in TEM) and (d) textures of a typical non-heat treatable Al-Mg-Mn alloy. The alloy begins with a relatively coarse and random as-cast structure/texture and ends with a much finer cold rolled and/or annealed microstructure with crushed and mixed up particles, and a specific pronounced texture. These will be discussed in more detail in the following sections.



23.1 Process chain and industrial equipment of aluminium sheet production.



23.2 Evolution of typical microstructures in industrial aluminium sheet production: (a) grain structure; (b) precipitation structure; (c) TEM; (d) Textures as {111} pole figures.

23.3.1 Casting (DC – direct chill casting)

As the first step in the fabrication process of high-quality aluminium sheet ‘direct chill’ (DC) casting has been the established process since being invented in 1936. For common alloys it generates characteristic effects on grain size and/or cell size (dendrite arm spacing ‘DAS’), macroscopic/microscopic distribution, size, type, number and volume of intermetallics (constituent phases) or secondary phases (dispersoids), elements in supersaturation, surface segregation or shell zone thickness, fir-tree zones, etc. Other important microstructural aspects in DC casting are non-metallic impurities, hydrogen content and porosity. The formation of these structural parameters is determined through the relevant casting and solidification processes. A more detailed description of how these parameters are defined and what part of the casting and solidification processes influences their development is given in (Schneider and Grün, 2006).

During early solidification of the ingot’s surface area the ‘shell’ zone is formed on contact with the water-cooled mould wall. The solidified surface subsequently shrinks back from the mould wall and forms the typical DC cast surface. The shell can be divided into a fine cell region that solidifies immediately and a coarse cell region due to an air-gap formation between the shell and the mould wall. Here specific segregation regions occur with an

above-average concentration of alloying elements due to inter-dendritic liquid transported to the surface.

The overall efficiency of the processing route is to a large degree determined by batch size. Large ingots are produced (e.g. >30 tons) that can be processed in corresponding hot mills. The grain structure (Fig. 23.2a) shows a coarse cell size and large constituent particles of eutectic precipitates of Al-Mn-Fe-Si phases, due to low cooling rates involved. The typical DC cast grain structure consists of columnar and/or equi-axed crystals, depending on purity, grain refinement and location. A close to random texture is usually observed when grain refinement is applied. Depending on the concentration of alloying elements and the existing solidification conditions the cast grains solidify with a smooth, cellular or dendritic solidification front. Wrought aluminium alloys solidify with a cellular solidification front into varying cell fineness within a grain, depending on the local solidification time between liquidus and solidus temperature. In the centre the cells have time to grow and become larger.

During solidification the solubility of alloying elements in solid solution (Al) changes with decreasing temperature. This causes some shift in alloy concentration in both the liquid and solid state, leaving some compositional variation in the solidified crystal, i.e. 'micro-' (on cell size scale) and/or 'macro-segregation' (over the full ingot solidification width), unless equilibrium is always maintained, usually only by extremely slow cooling. In DC casting high cooling rates tend to concentrate the alloy elements at the solidification front, leading to solid solution concentration differences. The extent of segregation is determined by the rate of solidification, the amount of convection in the melt during solidification and by the tendency of the respective alloying elements to segregate (known as the 'k-factor'). In contrast to micro-segregations, macro-segregations cannot be reduced by diffusion processes during ingot pre-annealing or homogenisation (see next section).

In general, DC cast ingots are characterised by a grain size of about 1 mm (if grain refiner is applied) similar to the cell DAS, with large (10–20 μm) constituent particles of eutectic precipitates (e.g. Al-Mn-Fe-Si phases, Fig. 23.2a). Random texture is also typical. Local variations in the distribution of alloying elements and their constitution caused by micro- and macro-segregation effects can impose some local microstructural variations in the as-cast slab.

An important advantage of DC casting ingot processing is the surface scalping to fully remove the as-cast surface, detrimental for further processing and many surface quality-related products.

23.3.2 Aluminium strip casting and twin-roll casting

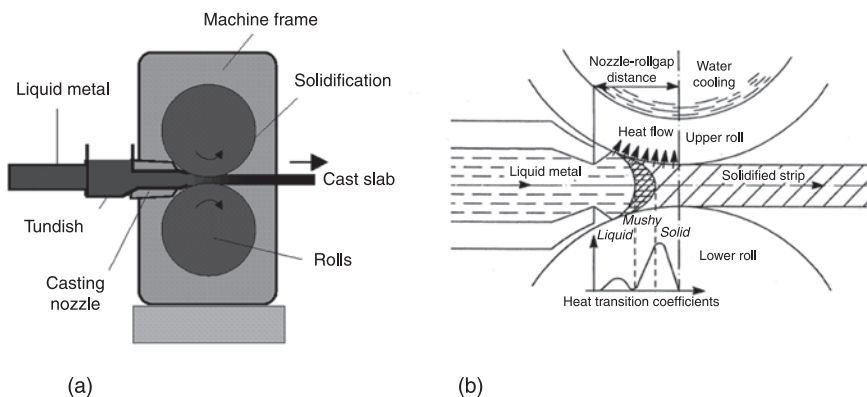
DC casting as a discontinuous process requires large ingot sizes and corresponding large process equipment (and investment) to be most efficient. For smaller quantities

the technical development of a continuous casting process of smaller size strip was pursued for many years. Twin-roll casting 'TRC' of relative thin (2–12 mm) sheet has become a well-established process, competing with conventional casting and hot rolling routes (Karhausen and Korhonen, 2003). The aluminium solidifies between two rotating rolls being (hot) rolled immediately to some extent, depending on the process parameters. Figure 23.3 shows the TRC process and illustrates the principal solidification range and process (solidification/rolling) parameters. Figure 23.4 shows a typical microstructure of TRC A199.5 strip.

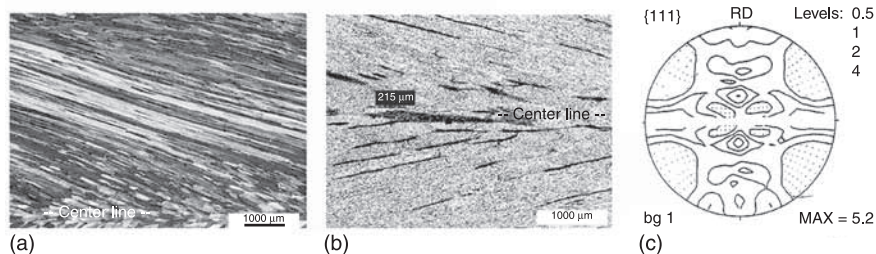
The capacity of TRC is determined by the extraction of the heat from the liquid aluminium, so large rolls are used, providing a relatively – although only a few mm – long solidification length. Also if highly thermal conductive roll material (e.g. copper) is used, the (rolling, i.e. solidification) speed is limited. Only a few metres per minute are possible, with highest speed and productivity for thinner as-cast sheet gauges, due to the smaller heat volume. In classical twin-roll casters one to two tons per hour can be achieved with 10 to 2 mm final strip gauge, respectively.

The aluminium surface solidifies quickly when in direct contact with the TRC rolls. Although some 'release agent' (e.g. graphite) is used, some oxide on the specific TRC surface formation cannot be avoided. It cannot be removed easily either – as in DC casting by scalping – so surface effects might occur which limit the sheet quality for aluminium products with special applications like litho-printing or outer body automotive panels, where a high surface quality is mandatory.

As solidification is much faster than in conventional DC casting, many of the elements stay in solid solution. They start to precipitate during subsequent



23.3 'TRC' twin roll casting of aluminium strip: (a) TRC equipment; (b) sketch of solidification section.



23.4 Microstructure of twin roll casting of 6 mm Al 99.5 TRC strip:
(a) grain structure; (b) precipitation structure; (c) texture.

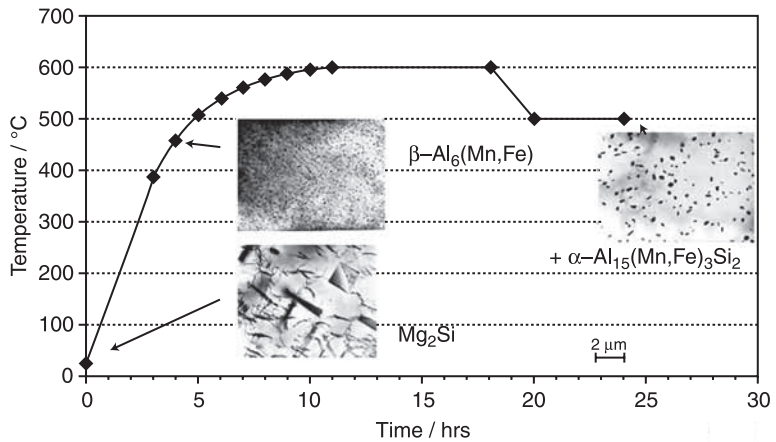
annealing processes and there might significantly affect the microstructure (i.e. recrystallised grain size and texture) formation. In cases where this results in an unfavourable, coarse recrystallisation structure, a TRC strip homogenisation and/or inter-annealing is applied to improve final (e.g. forming) properties. Since supersaturated alloy elements (like Fe) strongly suppress recovery and recrystallisation, cold rolled TRC strip has a high thermal stability, suitable for maintaining strength in a final thermal treatment of cold rolled sheet/foil at certain customer applications (e.g. lacquering).

However, some insoluble 'constituent' particles may also form in the TRC process (Fig. 23.4b). These have a much finer size and form than in DC casting (Fig. 23.2b). A specific segregation effect of insoluble elements (e.g. Al-Fe-X particles, Fig. 23.4b) is often observed as 'centre line segregation' of TRC sheet, where the fast moving solidification fronts meet in the TRC process.

23.3.3 Sheet ingot pre-annealing 'homogenisation'

After DC casting the ingots are cooled down and scalped to remove the critical (uneven and highly segregated) surface. They are then re-heated to relieve internal stresses (from the inhomogeneous cooling during DC casting) and to achieve the best forming behaviour for subsequent hot rolling. This process is called pre-heating or 'homogenisation'. If a certain temperature schedule is conducted, specific metallurgical changes occur in the microstructure, controlled by the temperature/time schedule applied, due to diffusion processes of the elements either as precipitated phases and/or in (supersaturated) solid solution. These changes may be summarised as:

- Elements in (supersaturated) solid solution (e.g. Mn, Fe, Cr) precipitate and coarsen at sufficiently high temperatures and time.
- Present (precipitated but unstable) phases (e.g. Mg_2Si) dissolve.
- Some micro-segregation effects are reduced.

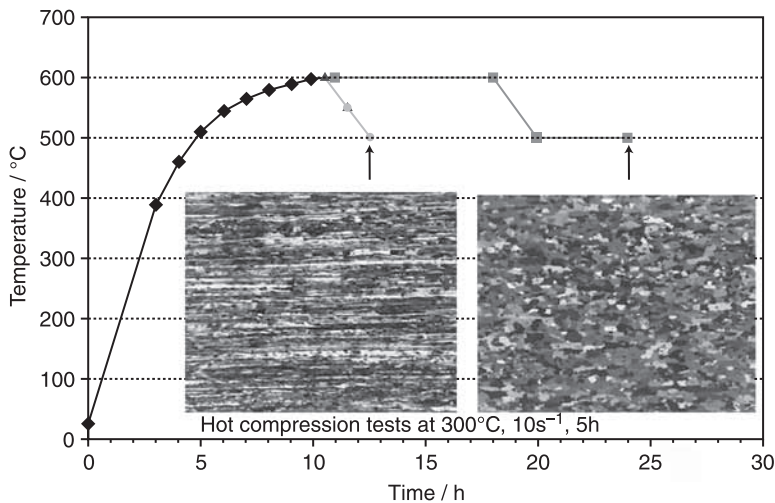


23.5 Typical temperature/time evolution during homogenisation of DC-cast Al-Mg1Mn1 ingots and evolution of dispersoids phases.

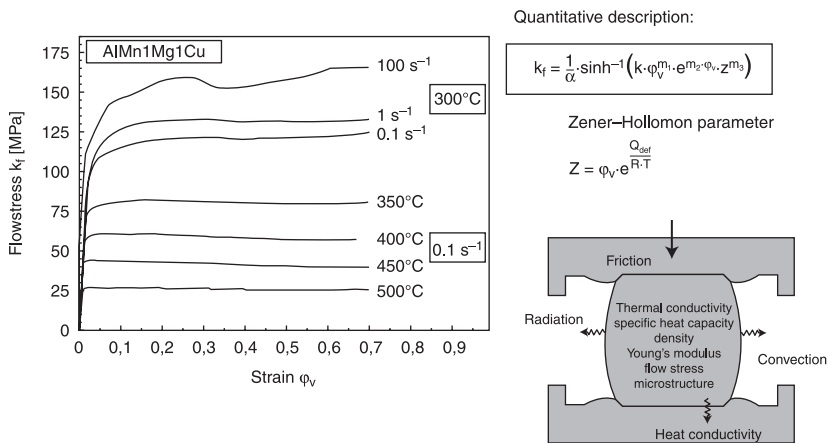
- Coarse (eutectic) primary phases are split off due to surface tension.
- Highly spread-out 'Chinese Script' constituents are refined or dissolved.
- Second phase particles can be transformed in their constitution.

Figure 23.5 shows an example of a typical temperature cycle for the homogenisation of DC cast Al-Mg1Mn1 rolling ingots and the evolution of dispersoid size, density and corresponding phases. Micro-segregation is reduced to some extent, at least for fast diffusing elements. The sharp eutectic 'primary' phases are present in a somewhat rounded form (Fig. 23.2b – second column) and their constitution is transformed during the process. Those elements in supersaturated solid solution (e.g. Mn) precipitate and coarsen at high temperatures and with increased time.

In plants with separate casting and hot rolling processes the slab is cooled down from homogenisation temperature and later re-heated to hot rolling temperature. In a more efficient combined process, cooling is just to the hot rolling temperature. In any case the related variations in solid solution and dispersed particle distribution and size need to be controlled by optimum heat treatment conditions since they affect subsequent microstructure development and final properties. The optimum heat treatment conditions control the dissolved elements and/or newly formed, fine precipitated second phase particles (dispersoids) as well as their specific size and distribution. These significantly affect the subsequent microstructure evolution (e.g. strain hardening, recrystallisation, texture formation) in the hot rolling process and so may also influence final material properties. Figure 23.6 illustrates the effect of variation in homogenisation parameters on recrystallisation after hot deformation in a laboratory compression test simulating hot rolling (see Fig. 23.7).



23.6 Effect of homogenisation variation on recrystallisation after hot deformation.



23.7 Flow stress curves at varying temperatures and strain rates in hot compression tests of AlMg1Mn1, and the quantitative description of the (steady state) flow stress level.

23.3.4 Hot rolling

Hot rolling is performed either on a single stand reversing mill or on a roughing reversing mill (Fig. 23.1 and 23.2 – third column) followed by a multi (two to four) – stand tandem finishing mill (fourth column). The pre-heated ingot is rolled

at the highest possible temperatures in order to reduce flow stress (Fig. 23.7), which allows heavy deformation steps and the most efficient processing. The upper temperature limits are determined by melting effects – which can cause ingot fracture (e.g. crocodiling), when deformation is inhomogeneous – and/or hot strip surface deterioration. The contact of the hot rolled aluminium with the steel mills is lubricated by a water/oil emulsion, specifically designed to optimise lubrication and cooling. The direct contact, however, involves some friction and sticking effect and builds up a specific metal/oxide layer, affecting lubrication and the (hot) rolled ingot surface.

During tandem hot rolling sheet thicknesses of less than 3 mm can be achieved. These are coiled for customer delivery or further cold rolling. The main hot mill process configurations meet different production requirements, product qualities and applications (Karhausen and Korhonen, 2003).

In the order of increasing capacity (kilo-tons per year ‘ktpy’) these are:

- 1 ~10 ktpy: thin strip production (6–10 mm) by continuous twin-roll casting ‘TRC’
- 2 >100 ktpy: thin slab casting (around 20 mm) by continuously twin-belt casting, followed by hot rolling on a multi-stand tandem line/strip casting
- 3 >150 ktpy: direct chill ‘DC’ casting (discontinuously) of large ingots (~600 mm thick, >2 m wide and 4–9 m long), followed by hot rolling, usually in two steps, on a breakdown roughing mill and on a single stand reversing (Steckel) mill
- 4 >500 ktpy: direct chill ‘DC’ casting followed by hot rolling on a breakdown roughing mill and a multi-stand tandem line (Woodward, 1999).

For most sheet products the fabrication process ends with cold rolling to finish gauge (pure aluminium 99.5 eventually down to foil thickness ~6–10 µm), described in ‘Cold rolling’.

Hot rolling mill design

The main features incorporated into modern hot rolling mill design include the following aspects:

- Large coil weights (>20 tons) to increase productivity, yield and mill uptime.
- Capability to roll strip and plate in widths of >2000 mm.
- Flexibility to operate across the range of soft, medium and hard alloys.
- Powerful mills (2 × 3700 kW plus) with work rolls driven directly.
- Capability to finish and coil material 2–18 mm in thickness.
- Hydraulic gap controls, with mill steer and roll eccentricity compensation.
- Work roll chock mounted scratch brushes.
- Fast work roll change.
- Adaptive and predictive process control technology using temperature sensors and profile and thickness gauges.

- Efficient spray control systems providing high-resolution thermal control of work rolls.
- Intelligent process models for the metallurgical requirements of high-quality products.
- Efficient roll brushing to control friction, material pick-up and surface quality.

Microstructure evolution during hot rolling

Hot rolling transforms the as-cast microstructure into a much finer (hot) deformed – and often recrystallised – fine grained structure (Fig. 23.2a), often with a typical cube texture (Fig. 23.2d). Furthermore, the hard coarse constituent particles and eutectic phases are crushed and aligned and more evenly distributed – together with the very fine dispersoids (Fig. 23.2b). The decreasing temperatures during rolling may trigger some precipitation reactions of specific phases in over-saturated aluminium alloys (e.g. in age-hardenable Al-Mg-Si alloys), that may hinder recrystallisation.

The relatively thick ingots allow some lateral material flow during hot rolling. In some hot mills ingot broadening is controlled by special side rolls. In general, hot rolling:

- 1 determines the profile of the strip, that is maintained – and must be controlled accordingly – in any subsequent cold rolling pass and
- 2 has a significant effect on finished material quality for many aluminium alloys.

The evolution of microstructure in hot rolling of aluminium alloys depends on the interaction of the main process parameters: temperature, strain, strain rate and inter-stand time (Hirsch, 2006a, 2006b). The hot strip geometry and microstructure also affects the final sheet geometry and properties, also after final cold rolling, so special attention must be paid to the hot mill process configuration and parameters.

Due to the increased speed and decreased inter-pass time at the final passes multi-stand tandem mills are also capable of keeping sufficiently high rolling temperature to ensure hot band recrystallisation (self annealing) for most conventional aluminium alloys. Furthermore, process parameters can be kept relatively constant over the length of the hot band (>1000 m in a modern hot line). So for can-body sheet (CBS) consistent high quality is best produced on tandem hot rolling lines, since recrystallisation and the important evolution of cube texture (required for good formability of the finished sheet, described below) is enhanced (Hirsch, 2006a).

For small mill configurations with single stand reversing hot rolling mills it is difficult to maintain a consistent temperature over the strip length so additional hot band annealing practices might be required. The control of critical thermo-mechanical and metallurgical effects is achieved by precise control of hot mill parameters, including simulation of metallurgical effects like

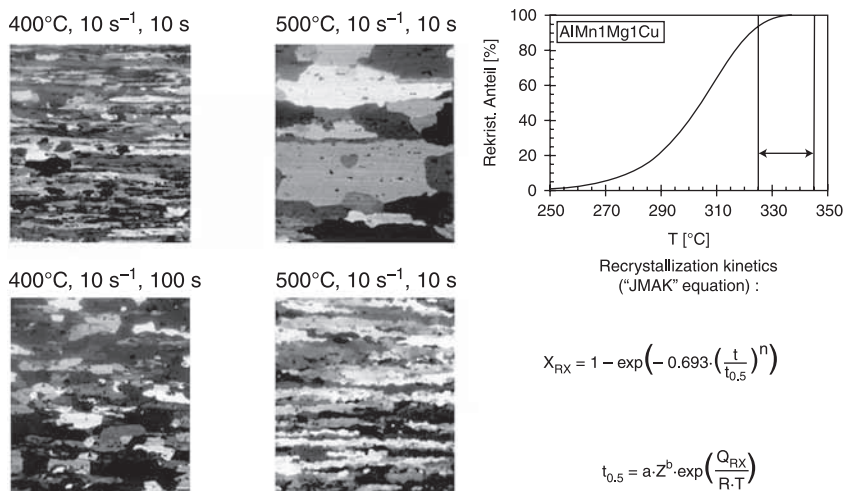
recrystallisation and microstructure/texture formation. A high rolling and coiling temperature can avoid a hot band annealing treatment, but too high temperatures lead to frequent inter-stand recrystallisation. On the other hand, too low temperatures might hinder recrystallisation, and hot strip annealing might cause unfavourable recrystallisation nucleation mechanisms (like particle stimulated nucleation 'PSN'). Both of these effects strongly affect the critical (cube) texture formation (Engler et al., 2007).

In aluminium alloys, strain hardening significantly decreases at elevated temperatures due to dynamic recovery and recrystallisation effects, i.e. dislocation multiplication is immediately compensated. This allows easy deformation at a relatively low and constant flow stress and generating a highly recovered sub-grain microstructure with a low dislocation density ($\sim 10^{10}$ l/m²). Aluminium shows dynamic recrystallisation (i.e. recrystallisation during deformation) only in high-purity Al, while genuine recrystallisation occurs (sometimes immediately) after hot rolling, depending on alloy additions (like Mg or Mn). Deformation stress/strain curves can be measured in tensile test to limited strains and accuracy. Up to true strains of $\varphi \approx 1$ compression (upsetting) tests are used, analysed locally by FEM modelling to consider hot temperature frictional effects (Karhausen, 1995). Hot flow stress curves quickly reach a steady state, i.e. they are independent of strain, but strongly depend on temperature and strain rate (Fig. 23.7). Holding the test samples at temperature before quenching allows an analysis of the corresponding microstructure evolution (Fig. 23.6), as a function of temperature, strain rate and time. The observed variety of microstructures in (hot) deformed and fully (or partly) recrystallised samples has been investigated and quantitatively described (Hirsch et al., 2004).

Recrystallisation rate is commonly described by the Johnson–Mehl–Avrami–Kolmogorow 'JMAK' equation, with $t_{0.5}$ given as a function of the Zener–Holomon parameter 'Z' (see Fig. 23.7). In Al–Mg–Mn alloys, recrystallisation after high temperature exposure can occur within a few seconds or minutes – depending on temperature, strain, strain rate and alloy content. The resulting grain structure also varies significantly with these parameters, as shown in Fig. 23.8 for an Al–Mg alloy.

Partial inter-stand recrystallisation (for reference see Fig. 23.1) may be predicted during multi-stand hot rolling. Full recrystallisation after exiting the hot mill at high temperatures may also occur. Both significantly affect the actual finished gauge properties. Since samples cannot be taken easily in a multi-stand hot rolling line for an investigation of microstructural evolution, the process is simulated in laboratory 'plane strain compression' tests and integrated into sophisticated computer process simulations, thereby providing information regarding the required process parameters.

In tandem hot rolling (in contrast to single reversing 'Steckel' mill hot rolling) high strain accumulation due to reduced recovery and recrystallisation in-between



23.8 Varying recrystallisation microstructures after high temperature deformation of Al-Mg-Mn alloys and the quantitative description of recrystallisation kinetics by the 'JMAK' Johnson-Mehl-Avrami-Kolmogorow equation.

stands generates faster (more complete) recrystallisation after coiling, a finer recrystallised final grain size and a sharper (cube) recrystallisation texture. This prominent recrystallisation texture is generated from preferentially growing (cube) orientations nucleating from long, quasi-stable (hot) deformation bands (i.e. deformed grains). At lower temperature, however, when deformation is inhomogeneous (e.g. in shear bands or near coarse large second phase particles) other orientations (e.g. from PSN) can compete in the (local) texture formation process, generating mostly randomly oriented new grains.

23.3.5 Cold rolling

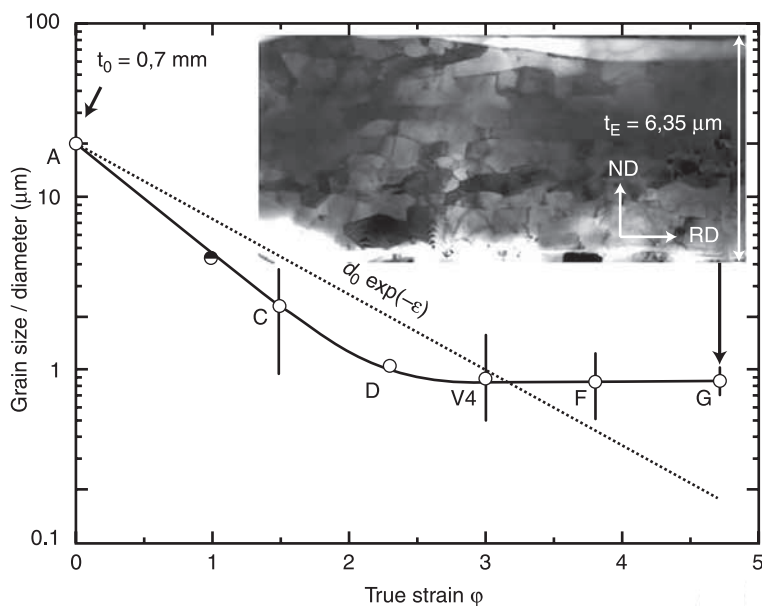
The same design principles described above for hot rolling are also valid for cold rolling and the related mill configurations. The cold rolling process runs at room temperature and usually under oil lubrication. In a few cases an oil/water emulsion is used, which enhances cooling but requires careful water removal before coiling. With the lubrication also used for local cooling, cold rolling allows a good control of shape, flatness and surface of the finish gauge sheet.

Microstructure evolution during cold rolling

The bulk deformation flattens the (mostly equi-axed and recrystallised) grains (Fig. 23.2a), further aligns the constituent and dispersed particles (Fig. 23.2b), and generates the typical FCC rolling texture (Fig. 23.2d). Cold rolling

significantly strain hardens the material, as it generates a high dislocation density present in a stable and fine sub-grain structure (about $0.5\ \mu\text{m}$ sub-grain diameter). Figure 23.9 shows the measured evolution of grain size during cold rolling of Al 99.5 which is continuously reduced with strain. In foil rolling, however, special conditions apply (Barten, 2002). Here after extremely high deformation ($>90\%$ reduction) the grain size also stays constant (near $1\ \mu\text{m}$ thickness). As a result, the finish gauge foil is composed of layers of about six grains, highly flattened, each with about 12 sub-grains in the normal direction (see e.g. the microstructure of a longitudinal foil section; Kaestner and Hirsch, 2008) shown in Fig. 23.9.

The straight line in the logarithmic plot of grain thickness evolution with strain in Fig. 23.9 indicates the expected grain size due to pure plane strain deformation during cold rolling. After a strain of $\varphi = 3$ (corresponding to 95% reduction) it does not decrease further as described above. Furthermore, it shrinks faster than expected in the early cold rolling stages ($\varphi < 3$), which can be explained by an initial grain fragmentation due to local variations in slip patterns. Owing to the variation in boundary conditions, some areas of the initial uniform grain activate different slip systems, and so follow different orientation changes towards their stable (β -fibre) orientation. This effect is important for subsequent nucleation effects during recrystallisation. Here the cube orientation is assumed to survive



23.9 Technical pure aluminium cold rolled to the extreme. Measured grain size reduction with cold rolling strain of Al 99.5 and sub-grain structure in a longitudinal section of a $6.35\ \mu\text{m}$ thin foil.

even heavy rolling as a ‘metastable’ rolling texture component, surrounded by divergent orientation zones (i.e. split off grains). As a result, it can act as a preferred recrystallisation nucleation orientation in any subsequent annealing process – or during self annealing in hot rolling (see Hot rolling).

Cold rolling deformation geometry generates the typical FCC plane strain ‘rolling’ texture (Fig. 23.2d). It consists of a set of stable ‘ β ’ fibre which can be described by a $\pm 35^\circ$ rotation around a $\langle 110 \rangle$ axis, tilted 60° from the normal direction, ND, towards the rolling direction, RD (Hirsch and Lücke, 1988), revealing the three main orientations: Cu $\{112\}\langle 111 \rangle$, S $\{123\}\langle 523 \rangle$ and Bs $\{011\}\langle 211 \rangle$. These have a strong influence on specific (anisotropic) properties like strength, formability and etching behaviour, to name a few examples. The crystallographic texture evolution during deformation is due to the selection of specific slip systems and can be predicted (Hirsch, 2006a). This includes both:

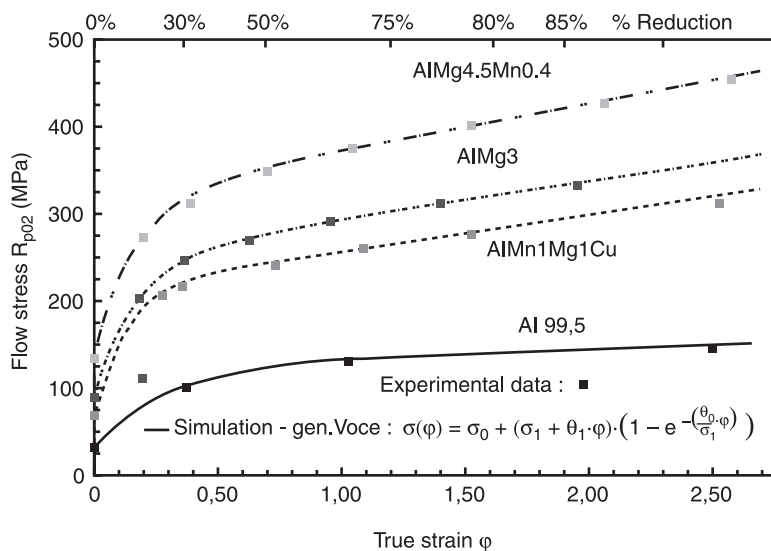
- 1 the impact on flow stress evolution during rolling (considered by assessing the changes in ‘Taylor factor’ M) and
- 2 the impact on sheet anisotropy, like earing in deep drawing (Engler et al., 2007).

In aluminium the hot strip (recrystallisation) ‘cube’ texture is able to balance the 45° ears formed by the cold rolling β -fibre orientations due to the opposing ($0^\circ/90^\circ$) earing characteristics and a relatively slow (roll) rotation rate. This is extremely important in obtaining a low earing behaviour in heavily cold rolled CBS (Hirsch, 2006a).

Strength evolution during cold rolling

For cold rolling the strain hardening of aluminium alloys is an important aspect in processing control and sheet properties (see Chapter 11 of this book). For (technically) pure aluminium and some typical non-heat treatable Al-Mg-Mn sheet alloys, the flow stress evolution (i.e. strain hardening) is shown in Fig. 23.10 as function of cold rolling strain up to high rolling strains (90% reduction). Pure ‘99.5’ aluminium shows a limited strain hardening response and an almost constant flow stress of about 150 MPa. This is due to the stable dislocation density and sub-grain structure and explains the almost infinite formability. Al 99.5 can be cold rolled to extremely thin gauges of $6\ \mu\text{m}$ (Fig. 23.9) in large scale industrial foil rolling processes. Super-thin foil is produced by cold (foil) rolling in a very efficient way (coils of >2000 mm width, cold rolled at very high speed of >1500 m/min) with quite sophisticated equipment and under strictly controlled surface and lubrication conditions (Hirsch et al., 1997). Thin foil is used for food protection and conservation in foil/paper/plastic laminates (Kaestner and Hirsch, 2008).

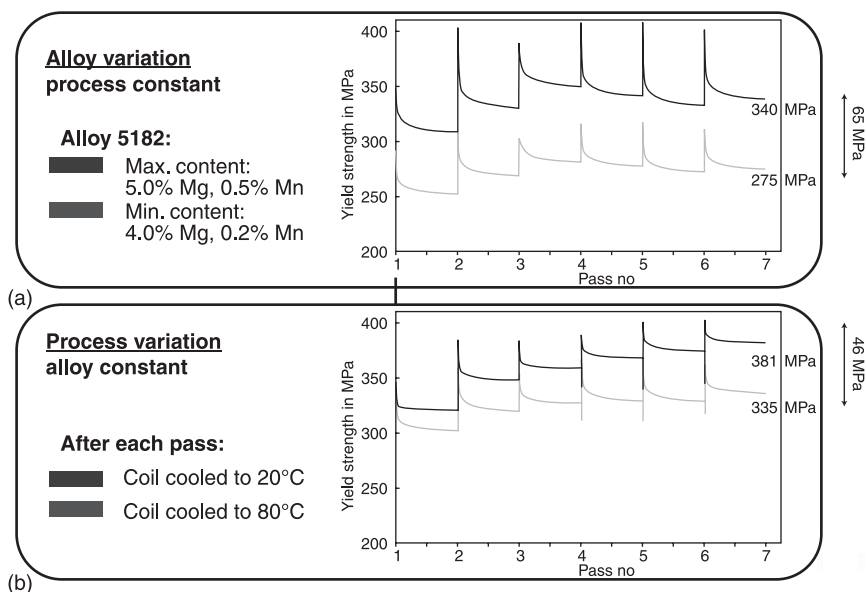
With some additions of certain alloy elements (e.g. Mg and/or Mn) significantly higher strain hardening rates are achieved (Fig. 23.10), which require different cold rolling equipment. The non-heat treatable Al-Mg-Mn ‘AA-5xxx’ alloys



23.10 Strain hardening curves during cold deformation of technical pure Al and some Al-Mg-Mn alloys and their quantitative description by the 'generalised Voce equation'. (Voce 1947)

are a specific example and are cold rolled accordingly to criteria for specific 'medium' to 'high strength' sheet alloys, used for many structural and packaging applications. As a comparison, the (AlMg1Mn1 'AA3104') CBS is highly formable in the can-making process, while AlMg4.5Mn 'AA5182' achieves very high strength (>400 MPa) and retains some formability, showing characteristic shear-band formation and seamless fracture behaviour, well suited for the 'easy open' can lid.

At high rolling speed the deformation energy – dissipated as heat – cannot be extracted fast enough by the cooling oil or emulsion, so that a significant temperature increase (>100°C) can occur, especially for the highly strain hardened alloys and for coiling of thick gauges. This leads to relatively high temperatures of such coiled sheets, so that considerable softening may take place due to recovery. This effect can be measured and predicted in integrated simulation models, used to determine the correct strain hardening behaviour of these alloys under various industrial 'cold' rolling conditions, as shown in Fig. 23.11, for the high strength alloy AlMg4.5Mn 'AA5182' (Karhausen et al., 2006). After each cold rolling step the strength increases, but the increase in temperature leads to a certain drop in strength with (coil cooling) time. This depends on the alloy composition, i.e. Mg and Mn contents (in Fig. 23.11a their variation within the official alloy limits are chosen). While Mg enhances strain hardening – and temperature rises – Mn mainly reduces recovery, thus both alloy elements are often used in combination. If, however, in-between cold rolling steps the coil temperature is not completely set



23.11 Simulated strength evolution during industrial cold rolling, with variations in: (a) alloy composition (within the AA limits) and (b) industrial rolling parameters 'back-to-back processing' (Karhausen and Kopp 2002).

to room temperature (e.g. by back-to-back processing of the coils) the recovery effect is enhanced, and a strength variation – similar to the one achieved by alloy composition – is observed.

23.3.6 Annealing

Non-heat treatable alloys

In elevated temperature processing, recovery and recrystallisation are microstructural features, reducing the effect of strain hardening, for example during hot rolling. Annealing of a cold rolled sheet generates a new microstructure and soft material condition, suitable for subsequent forming process. While recovery gradually softens the strain hardened sheet, recrystallisation as a discontinuous process eventually generates a completely new grain structure and texture, depending on temperature, time and preceding strain. Recovery occurs at relatively low temperatures and exponentially decreases the material strength accumulated during cold rolling by reducing the dislocation density with annihilation and/or re-arranging the (accumulated) dislocation density and substructure. Recrystallisation – in contrast – occurs at relatively high temperatures (>300°C in technical Al alloys) and leads to a complete reorganisation of the microstructure by the effect of a specific nucleation event that triggers large angle

grain boundaries to move, whipping out the (high) dislocation densities of the deformed microstructure. Thus new (mostly equi-axed) grains are formed with sizes and textures depending on the rolling strain and specific microstructural features (e.g. particles and/or supersaturated alloy elements).

These effects are controlled by the microstructure generated by the preceding (hot or cold) rolling conditions. Depending on these, the preceding rolling and final annealing conditions (temperature/time) usually produce a fine grain size (Fig. 23.2a) and softer material with a typical FCC recrystallisation (e.g. cube) texture is generated (Fig. 23.2d). The specific recrystallisation texture evolution is based on oriented nucleation and growth effects and can be simulated by sophisticated models, predicting the spectrum of potential (local) orientations (e.g. at grain boundaries and deformation or transition bands) and selecting the specific nucleation orientations by subsequent growth mechanisms. In this way the range of typical recrystallisation textures observed in different Al alloys under varying conditions can be predicted (Engler and Hirsch, 2009).

Annealing therefore creates a new (usually fine grained) structure and texture, and is particularly useful for intermediate annealing treatments which may be necessary in-between rolling passes to reduce strain hardening especially of highly alloyed sheets.

Heat treatable alloys

For the second important ‘highest strength’ Al alloy group the final annealing is applied to force the main elements – responsible for the age-hardening effect of the final sheet – back into solid solution, as they are mostly precipitated during the earlier, usually slow, coil cooling from the hot rolling temperature. To freeze them in a high quenching rate is required, so a continuous annealing process is used, where the sheet is conducted on a hot air cushion through a long annealing furnace from the unwound coil, and at the outlet it is quenched (by forced air and/or water) before re-coiling. It is in this way the Al-Mg-Si automotive sheet alloys are processed, generating the ‘bake hardening’ mechanism to significantly enhance sheet strength after part forming, assembly and final lacquering treatments. With specifically designed alloys and thermo-mechanical processes (annealing and quenching) the main sheet properties (formability, strength, fast baking response) for automotive parts can be designed in great detail, providing high formability or good age-hardening sheet qualities (Brünger et al., 2006).

Such a continuous annealing process, however, is more elaborate and costly than conventional coil annealing. However, it sometimes may also be applied to conventional (inter-) annealing of non-heat treatable alloys (e.g. Al-Mg-Mn), in order to achieve a finer grain size and/or a better ‘thermal stability’ of the further cold rolled finish gauge sheet due to supersaturated (quenched-in) alloys elements.

23.4 Parameters and metallurgical effects in Al alloy sheet processing

Besides alloy composition (aluminium alloys and specifications) the microstructural features, i.e. grains (size and texture) and particles (constituents and dispersoids) which are controlled by the (interacting) thermo-mechanical sheet fabrication processes, determine sheet properties and significantly affect final material performance. This includes further (customer) processing (e.g. forming) as well as that required for the final application. Table 23.1 lists the main processing steps in the production of aluminium sheet, along with the main process parameters that are controlled and how these then affect the principal metallurgical parameters determining sheet material properties.

Strength is a principal quality of materials needed for structural design and similar applications, where the material must sustain certain loads. Formability is the other important quality parameter that must be present in many subsequent forming operations for specific sheet applications. The variables of state which describe the condition of a material volume element at any stage of the process chain are:

- dislocation density ρ including their type (edge, screw) and their spatial distribution (cell walls and interior)
- sub-grain size δ and sub-boundary misorientation
- solute content and precipitation state (constituents, dispersoids)
- grain size and texture (Taylor factor M).

Table 23.1 Process parameters (1st row) and metallurgical effects (2nd row) in Al sheet production

Process step:	DC cast	Pre-annealing	Hot rolling	Cold rolling	Coil annealing
Process parameters	Alloy – elements ingot size, casting speed and temperature	Time and temperature	Schedule: rolling steps and speed, temperature, inter-stand time	Rolling reduction, speed and temperature	Time and temperature
Metallurgical parameters/ related properties	Alloy distribution, constituent particles, solid solution	Solid solution reforming of constituents, precipitating dispersoids/ thermal stability	Hot deformed recrystallised structure and texture/ strength, formability, anisotropy	Deformation structure/ strength, formability, anisotropy (earing), surface	Recrystallised structure and texture/ strength, formability, anisotropy

The process variables which describe the workpiece geometry and the process are:

- global geometry of workpiece (ingot, slab, sheet, extrusion)
- a spatial discretisation of the workpiece (e.g. in an FEM net)
- local temperature of the volume elements.

In recent years, sophisticated ‘physical-based’ integrated models have been developed used in the Through-Process Models (TPM) (Hirsch, 2006b), which make use of the basic data to trace material characteristics and predict properties at any processing stage. The inter-dependencies of the process and state variables for the process chain of aluminium sheet production, including final application, are considered in a complete TPM simulation to consider certain variations, for example in:

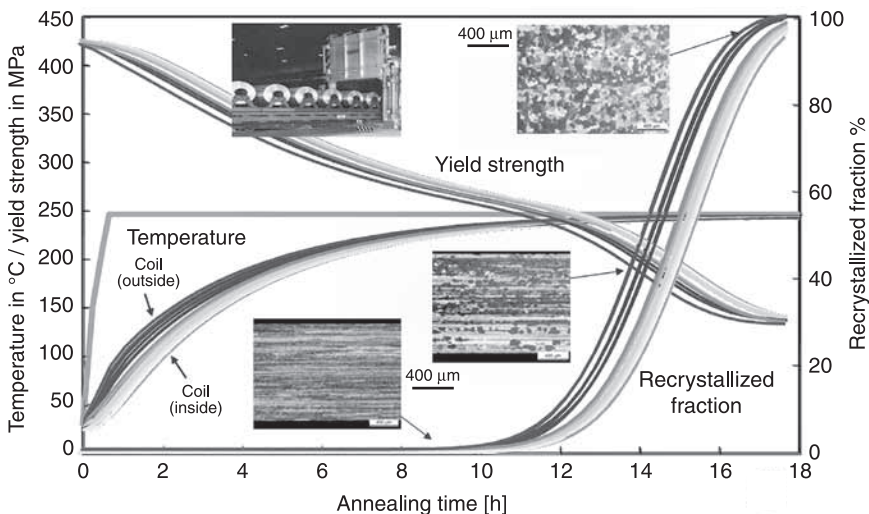
- 1 the casting microstructure (e.g. micro- or macro-segregation effects of elements)
- 2 the dispersoids size/distribution due to homogenisation variations
- 3 thermo-mechanical processing (extrusion, hot/cold rolling and annealing) effects on:
 - i strain hardening behaviour (alloy content, particle effects)
 - ii recrystallisation kinetics (nucleation and growth)
 - iii texture formation (deformation and recrystallisation)
- 4 the final microstructure finally affecting, for example:
 - i forming behaviour of the finish gauge sheet (strain hardening, softening, anisotropy)
 - ii surface appearance of profiles (e.g. texture streaking).

All models and corresponding sub-models are scaled down to the state variables, and microstructure models will interact when simultaneous reactions occur. An offline coupling might be sufficient for some effects like recrystallisation during annealing which has no significant reaction with the thermal model. Specific microstructural features like precipitation effects, however, need to be coupled with a microchemistry model to include critical precipitation reactions that affect any subsequent recrystallisation process. When physical parameters and variables of state are applied that describe alloy effects, any fitting to single alloys or alloy systems is no longer necessary. This allows full TPM capability, i.e. to trace the material condition through the different process stages and finally to derive the resulting material properties and linked alloy and process development properly. However, when reliable numbers on process variations and physical mechanisms are missing, only limited accuracy of the models can be achieved. Through-process models help to improve material quality as well as enhance manufacturing capability and productivity which are all important prerequisites to meet the ever increasing economic requirements for more process efficiency and product quality. With these R&D tools now able to combine a fundamental understanding of the underlying physical mechanisms, their quantitative description and extrapolation allows for their easy use in integrated through process models.

23.5 Integrated material and through-process modelling

(See Chapter 11 of this book.) In recent years, convincing successes of integrated material and through-process modelling 'TPM' have been described and discussed for the conventional mass production and processing of aluminium sheet, including all aspects of DC casting, pre-heating and homogenisation, hot and cold rolling, as well as final annealing (Hirsch, 2006a). Simulation may be applied for specific material properties like flow stress and final strength, as well as for the related microstructure and texture evolution. This includes the evolution during rolling (Fig. 23.10) and annealing (Fig. 23.12) with different alloys, including material constitution and process variations (e.g. Fig. 23.11) required to achieve accurate results of the final properties.

The new 'TPM' methods are now being further developed and implemented and they affect current and future scientific research and its application and influence the aluminium producing industries, in their research and development strategies for enhanced time and efficiency, know-how development and exploitation, in-house education and training, manufacturing flexibility, equipment design and process and quality control. They progressively replace conventional empirical methods and help to link the complete production chain of various alloys and coupled fabrication processes with final behaviour during product forming and application. Their implementation and in-line application will help plant engineers to analyse and



23.12 Simulation of temperature, microstructure (recrystallised, fraction) and yield strength evolution during annealing of a highly cold rolled Al-Mg sheet. Line width indicates temperature variation due to different positions in the coil.

solve practical problems, to increase industrial process variability and material quality and significantly decrease development time and cost.

23.6 Conclusion

Besides alloy composition the microstructural features of grains (size, substructure and texture) and particles (constituents and dispersoids) are the main factors controlling finish gauge material properties and product performance both in use and during secondary (e.g. forming) operations.

The main sheet production processes and control parameters are the following:

- Ingot DC/strip casting
The as-cast microstructure: Grain and cell size (DAS), size and distribution of constituent (eutectic) particles, dispersoids, solid solution content, micro/macro segregation, pores, etc.
- Pre-heating/homogenisation: Variation of the as-cast microstructure and micro-chemistry:
 - Solid solution of elements
 - constituent particles (size, form, constitution)
 - formation of dispersoids.
- Hot and cold rolling: Drastic changes of the as-cast microstructure by specific deformation effects:
 - Crushed and aligned constituent particles and dispersoids
 - High dislocation densities and alloy-specific substructure
 - Modified by recovery (and recrystallisation) in hot and warm rolling.
- Annealing: Restoration of the ‘undeformed’ soft conditions:
 - Recovery changes dislocation densities and substructure (sub-grain size)
 - Recrystallisation creates new grains and (cube) texture, (depending on rolling reduction)
 - Dissolution of age-hardening particles and other elements in solid solution.
- Effect on downstream processes and material properties:
Further sheet processing: Coating (thermal stability)
Customer application: formability (mechanical strength, anisotropy, surface, thermal stability, forming, (crash worthiness, bending, folding); age-hardening behaviour.

The main sheet properties, characterized for specific customer applications are:

- 1 Strength: Tensile properties ($R_{p0.2}$, R_m), hardness
Flow stress descriptions (e.g. Voce).
- 2 Formability: Fracture strain
Erickson depth IE
Drawing ratio β
Forming limit diagram ‘FLD’ (including anisotropy) % Earing Z Yield locus (bi-axial flow stress data).

- 3 Profile/flatness: % thickness variation, I-Units.
- 4 Surface: roughness, streaking, gloss.

23.7 Acknowledgements

Thanks to my colleagues in Hydro R&D Bonn who worked with me on the topic for the last 18 years.

23.8 References

- AA-Teal Sheets (2009) *International Alloy Designations and Chemical Composition Limits for Wrought Aluminum and Wrought Aluminum Alloys*, 1525 Wilson Boulevard, Arlington, VA, USA. Available from: www.aluminum.org
- Barten, A.E. (2002) *Aluminum Rolling Mill Technology: Future Concepts in Thin-Strip and Foil Rolling*, Vol. 233, Verlag Moderne Industrie – Die Bibliothek der Technik.
- Brünger, E., Engler, O., and Hirsch, J. (2006) ‘Al-Mg-Si sheet for autobody application’, in *Virtual Fabrication of Aluminium Products*, Wiley-VCH Verlag, Weinheim, pp. 51–61.
- CRU (2008) *International report on Aluminium Rolling Cost Service*, London, UK. Available from: www.crugroup.com
- Datta, J. (2003) *Aluminium Schlüssel/Key to Aluminium Alloys*, Aluminium-Verlag Marketing & Kommunikation GmbH.
- Engler, O., and Hirsch, J. (2009) ‘Control of recrystallisation texture and texture-related properties in industrial production of aluminium sheet’, *International Journal of Materials Research* 1862–5282, Vol. 100, No. 4, pp. 564–575.
- Engler, O., Löchte, L., and Hirsch, J. (2007) ‘Through-process simulation of texture and properties during the thermo-mechanical processing of aluminium sheets’, *Acta Materialia*, Vol. 55, pp. 5449–5463.
- Hirsch, J. (ed.) (2006a) *Virtual Fabrication of Aluminium Products*, Wiley-VCH Verlag, Weinheim.
- Hirsch, J. (2006b) ‘Through process modelling’, *ICAA10 Materials Science Forum*, W.J. Poole, M.A. Wells, and D.J. Lloyd (eds), Transtec Publications, Switzerland, Vols. 519–521, Part 1, pp. 15–24.
- Hirsch, J., and Grenz, R. (1998) ‘Microstructure control on an aluminium hot reversing finishing mill’, *Hot Deformation of Al Alloys II*, T. Bieler et al. (eds), TMS symposium, Illinois, USA, pp. 305–316.
- Hirsch, J., Häfele, P., Draese, S., and Pawelski, O. (1997) ‘Tribological and surface effects during rolling of aluminium foil’, *Proceedings of the Aluminium Surface: Science and Technology 1 – International Symposium*, H. Terryn (ed.), Elzenveld/Antwerpen, Belgium, pp. 5–12.
- Hirsch, J., Karhausen, K., and Engler, O. (2004) ‘Property control in the production of aluminium sheet by use of simulation’, in *Continuum Scale Simulation of Engineering Materials, Fundamentals-Microstructures-Process Applications*, D. Raabe et al. (eds), Wiley-VCH, Weinheim, p. 705.
- Hirsch, J., Leroy, C., and Green, A. (2006) ‘AluMATTER, an initiative of the European aluminium industry’, *Materials Science Forum*, W.J. Poole, M.A. Wells, and D.J. Lloyd (eds), Transtec Publications, Switzerland, Vols. 519–521, pp. 1209–1214. Available from: www.alumatter.info

- Hirsch, J., and Lücke, K. (1988) 'Mechanism of deformation and development of rolling textures in polycrystalline FCC metals', *Acta Metallurgica*, Vol. 36, No. 11, pp. 2863–2927.
- Kaestner, S., and Hirsch, J. (2008) 'Innovation in established aluminium sheet products (industrial research and development in the aluminium value chain)', *Aluminium Alloys, their Physical and Mechanical Properties*, J. Hirsch et al. (eds), Hydro Aluminium Deutschland GmbH, Koln/Bonn, Germany, pp. 14–23.
- Karhausen, K. (1995) *Integrierte Prozeß- und Gefügesimulation bei der Warmumformung, Umformtechnische Schriften Bd.52*, Verlag Stahleisen GmbH, Düsseldorf.
- Karhausen, K., Crumbach, M., Neumann, L., Hirsch, J., Goerdeler, M., Gottstein, G., and Kopp, R. (2006) 'Through-Process simulation of EN AW-5182 sheet production', in *Virtual Fabrication of Aluminium Products*, J. Hirsch (ed.), Wiley-VCH Verlag, Weinheim, pp. 323–341.
- Karhausen, K., and Kopp, R. (2002) 'Design of an integrated through-process model for rolling of aluminium', 78. Jahrbang 2002, 10, S. 880–885.
- Karhausen, K., and Korhonen, A. (2003) 'Rolling of aluminium', in *Handbook of Aluminum: Physical Metallurgy and Processes*, G.E. Totten, and D. Scott MacKenzie (eds), Marcel Dekker Inc., USA, pp. 351–384.
- Kaufmann, J.G. (2001) *Introduction to Aluminum Alloys and Tempers*, ASM International, Materials Park, OH.
- Schneider, W., and Grün, G.U. (2006) DC casting – Microstructure and specifications', in *Virtual Fabrication of Aluminium Products*, Wiley-VCH Verlag, Weinheim, pp. 7–12.
- Voce, E., (1947) *Journal Institute of Metals*, 74, (1947–1948) p. 537.
- Woodward, R. (1999) *TALAT lecture 1301, TALAT CD-ROM 2.0*, European Aluminium Association. Available from: <http://www.eaa.net/eea/education/TALAT/>

Application of modern aluminium alloys to aircraft

E.A. STARKE, Jr and J.T. STALEY, Consultant,
University of Virginia, USA

Abstract: Aluminum alloys have been the primary material of choice for structural components of aircraft since about 1930. Although polymer matrix composites are being used extensively in high-performance military aircraft and are being specified for the major structural weight of the new Boeing 787 and Airbus A350, aluminum alloys will continue to be used for many commercial and military applications. Well-known performance characteristics, known fabrication costs, design experience and established manufacturing methods and facilities, and their use in hybrid structures are just a few of the reasons for the continued confidence in aluminum alloys that will ensure their use in significant quantities for many years. There have been major advances in aluminum aircraft alloys that continue to keep them in a competitive position. In the early years aluminum alloys were developed by trial and error, but over the past 40 years there have been significant advances in our understanding of the relationships among composition, processing, microstructural characteristics and properties. This knowledge base has led to improvements in properties that are important to aircraft applications. This chapter covers the factors that drive development of new aircraft materials, performance and property requirements for airframe components, and describes aluminum alloys and product forms which meet these requirements. It also discusses the structure–property relationships of aluminum aircraft alloys. Finally, technologies under development for future aircraft are discussed.

Key words: aerospace alloys, structural alloys, performance, manufacturing, structure–property relationships.

24.1 Introduction

Since the first days of powered flight, aircraft designers have striven to achieve minimum weight. From 1903 to about 1930 absolute minimum weight was necessary for practical flight. Consequently, the strength/weight ratio (specific strength) was the prime driver for materials selection and continues to be of major importance to this day. For the first 25 years the airframe was a wooden structure braced by wire and covered with fabric treated with varnishes (Smith, 1991). Sitka spruce was the most favored structural material due to its fine, straight-grained wood with a minimum of knots. The fabric was usually tightly woven wool or cotton covered with a varnish referred to as ‘dope’. With the exception of the engine, fasteners and wires, the early airplane had very little metal in its structure. The Wright brothers did use an aluminum-copper casting

alloy for the crankcase of their self-designed internal combustion engine because of the alloy's strength and the weight requirements of the aircraft (Gayle and Goodway, 1994). However, aluminum was not used for airframes until some years later after precipitation hardening was discovered by Alfred Wilm (Starke and Hornbogen, 2008).

In the 1920s some designers, e.g. Dr Hugo Junkers, Claudius Dornier and Adolph Rohrbach, experimented with aluminum aircraft. The low specific gravity of aluminum (2.7) leads to high specific properties, which, in turn, favor the selection of aluminum alloys in weight-critical applications. Junkers selected 'duralumin', an age-hardenable aluminum alloy which contained additions of copper, magnesium and manganese. Duralumin was the age-hardenable alloy discovered in 1906 by Alfred Wilm, a German chemist, who was seeking a lightweight alloy to replace brass for cartridge casings (Starke and Hornbogen, 2008). Although duralumin was used in dirigibles, it suffered from exfoliation corrosion when exposed to air and, prior to the Junkers design, was not used in load-bearing components of aircraft. However, in 1927, metallurgists at Alcoa developed a method to clad aluminum alloys with pure aluminum, which was not susceptible to exfoliation corrosion, and thereby offered protection in an aggressive environment. At about the same time anodizing, a method for producing a very thick, protective oxide film on the surface of aluminum was developed in England. The anodized film usually contains chemical compounds such as chromates, which are collected from the anodizing bath and render the film more corrosion resistant than films that form naturally in air (Polmear, 1989). The protection given by cladding and anodizing served to establish a dramatically new baseline for aerostructures and after 1927 aluminum alloys became commonplace in airframes (Smith, 1991). The percentage of aluminum in the airframes of commercial jet liners has dropped from about 80% to 20% because of the inroads of polymer matrix composites (PMCs, see Table 24.1). Despite this loss, the market will continue to be large for some time because derivatives

Table 24.1 Structural material usage in large commercial aircraft

Aircraft	Aluminum	Steel	Titanium	PMCs	Other
Boeing 747	81 wt.%	13 wt.%	4 wt.%	1 wt.%	1 wt.%
Boeing 757	78 wt.%	12 wt.%	6 wt.%	3 wt.%	1 wt.%
Boeing 767	80 wt.%	14 wt.%	2 wt.%	3 wt.%	1 wt.%
Boeing 777	70 wt.%	11 wt.%	7 wt.%	11 wt.%	1 wt.%
Boeing 787	20 wt.%	10 wt.%	15 wt.%	50 wt.%	5 wt.%
DC-10	78 wt.%	14 wt.%	5 wt.%	1 wt.%	2 wt.%
MD-11	76 wt.%	9 wt.%	5 wt.%	8 wt.%	2 wt.%
MD-12	70 wt.%	8 wt.%	4 wt.%	16 wt.%	2 wt.%
Airbus A380	61 wt.%	10 wt.%		22 wt.%	7 wt.%
Airbus A350	20 wt.%	7 wt.%	14 wt.%	52 wt.%	7 wt.%

of planes designed before the 2000s will continue to be built. Military planes, even high-speed fighters, continue to use large amounts as supporting structure.

24.2 Drivers for materials selection and aluminum alloy product development for aircraft

There are many drivers and parameters involved in the development and selection of materials for aircraft. They include, but are not limited to, low structural weight, safety factors, cost, availability, manufacturability, reliability and maintainability. The drivers for materials selection and alloy development for aircraft have changed considerably during the more than 100 years of aluminum in aircraft.

24.2.1 The 1930s–1960s

As mentioned previously, from 1903 to 1930 minimum weight was the major criteria for materials selection for aircraft and all other considerations were secondary. From about 1930 through the 1960s, corrosion resistance was also found to be important although the desire for improved performance called for reduced weight. Materials development for aircraft continued to focus on aluminum and there was considerable improvement in the strength/weight ratios of sheet metal alloys as well as the development of other product forms, e.g. extrusions, forgings and thick plate.

Damage tolerance became an important issue in 1954 when three Comet jet airplanes, manufactured with 7075-type aluminum, crashed (Smith, 1991). The cause of the crashes was attributed to premature fatigue failure of the pressurized fuselage associated with stress concentrations at windows and hatches. As thicker structures began to be used as planes grew larger, thick products of 2024-T3, 7075-T6 and particularly 7079-T6 were found to be susceptible to stress corrosion cracking when stressed in the short-transverse direction. In addition, medium gage plate and extrusions developed exfoliation.

Associated with the ‘improved performance’ quest in the 1960s was the drive to fly faster and two major programs (Soviet and English-French) were initiated in 1962 to develop supersonic commercial aircraft designed to fly at Mach 2 +. The aircraft developed by the English-French (the Concorde) was designed to last for 500,000 service hours of which at least 20,000 would be spent at the maximum cruising speed of Mach 2 (Harpur, 1968). Because the combination of moderate temperature and stress affects long term aging (loss of strength) and creep, Mach 2 is the maximum speed at which age-hardenable aluminum alloys can be used as primary structural materials.

24.2.2 The 1970s

The growth of linear elastic fracture mechanics analyses in the 1960s revealed the need for improvements in the combination of strength and fracture toughness of aluminum alloys. In 1978, certification of new aircraft required that manufacturers demonstrate that fatigue cracks would be detected prior to their reaching the critical length associated with catastrophic failure (Dermarkar et al., 1994). The critical crack length and fatigue crack growth characteristics of 2024-T3 provided adequate safety and economical inspection intervals, but the low yield strength caused a weight penalty. In contrast, its low fracture toughness and inferior fatigue crack growth resistance prevented the high strength of 7075-T6 from being considered for fracture critical applications where loads were tension dominated. The desired improvements in aluminum alloys that drove materials development during the 1970s included: an alloy that would develop strength and short-transverse ductility as high as that of 7079-T6 in thick section products along with adequate stress corrosion resistance in the short-transverse direction; an alloy that would develop the strength of 7075-T6 with the resistance to exfoliation corrosion of 7075-T76; and, an alloy that would develop strength approaching that of 7075-T6, fracture toughness approaching that of 2024-T3, fatigue crack growth characteristics sufficient to provide economical inspection intervals, and adequate resistance to exfoliation corrosion.

Boeing provided another driver. They were designing the 757 and 767 at this time, and they expressed a desire for materials that would develop higher strength than 7075-T6 for upper wing skins, materials that would develop higher strength than 2024-T3 for lower wing skins and a material that would provide higher fracture toughness and resistance to the growth of fatigue cracks than 2024-T3 for fuselage skin sheet.

24.2.3 The 1980s

In the 1980s, fuel costs, the market value associated with increased range and landing weight fees resulted in a technical focus on weight reduction. Trade-off studies were made to determine which property improvement had the greatest impact on weight savings. These studies showed that reductions in density were most advantageous and lithium additions would have the greatest influence on reducing the density of aluminum. Aluminum-lithium alloy development programs were initiated in Great Britain, the United States, France, Russia and Japan. The United States and Western Europe focused on higher strength alloys, which contained copper in addition to lithium and magnesium. The objective was to develop gauge-for-gauge substitutes for the standard alloys with similar properties while maintaining manufacturability.

Boeing was designing the 777 at this time, and expressed a desire for materials superior to those in use on the 757 and 767 wings and fuselage in the areas of strength and fracture toughness, and resistance to the growth of fatigue cracks.

24.2.4 The 1990s to the present

In the early 1990s the reality associated with an aging aircraft fleet resulted in a technical focus on improved damage tolerance and improved corrosion resistance. Later in the 1990s and into the twenty-first century there has also been a major focus on the cost of doing business, i.e. acquisition cost, which includes the cost of manufacturing and having environmentally compliant processes, and maintenance cost, which is impacted by material variations, defects, etc. In addition to having high specific strength, damage tolerance and corrosion resistance, new materials must be amenable to new manufacturing methods and be cost effective. Consequently, the current challenge is to develop materials with improvements in both structural performance and life cycle cost. This requires close cooperation between material producers and the airframe's design, analysis, manufacturing and cost experts, so that the material properties can be tailored to the intended application (Liu, 2006).

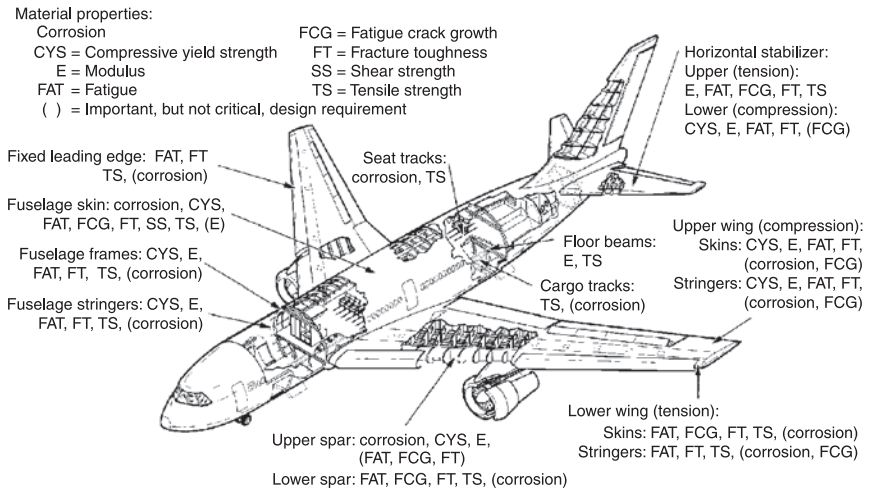
Airbus provided another driver in the 1990s when they decided to proceed with design of the A380. The large size of this plane demanded materials with high strength, fracture toughness and corrosion resistance in massive sections.

24.3 Performance criteria and property requirements for primary structure of subsonic aircraft

If failure of a structural component endangers the aircraft, the component is referred to as primary structure. Other structural components are referred to as secondary structure. Current requirements (Staley and Lege, 1993) for materials for primary structural applications in subsonic aircraft are summarized in Fig. 24.1. The major structural components are the fuselage, the wing, the empennage and supporting structure.

24.3.1 Property requirements for fuselage

The fuselage is a semi-monocoque structure made up of skin to carry cabin pressure (tension) and shear loads, longitudinal stringers or longerons to carry the longitudinal tension and compression loads, circumferential frames to maintain the fuselage shape and redistribute loads into the skin, and bulkheads to carry concentrated loads. In high-performance military aircraft, thick bulkheads are used rather than frames. The fuselage can be divided into three areas: crown, sides and bottom. Predominant loads during flight are tension in the crown, shear in the sides and compression in the bottom. These loads are caused by bending of the fuselage due to loading of the wings during flight and by cabin pressure. Taxiing causes compression in the top and tension in the bottom, however these stresses are less than the in-flight stresses. Strength, Young's modulus, fatigue initiation, fatigue crack growth, fracture toughness



24.1 Property requirements for jetliner and military transport applications (Staley and Lege, 1993).

and corrosion are all important, but fracture toughness is often the limiting design consideration.

24.3.2 Property requirements for wings

A wing is essentially a beam that transmits the entire applied air load to the central attachment to the fuselage. Additional loads are internal fuel pressure, landing gear loads and wing leading and trailing edge loads. The wing box, the part of the wing that carries the loads, consists of top and bottom covers (each cover is composed of a skin and stringers that stiffen the skin and run lengthwise), spars that create the sides of the wing box and run lengthwise (some of the larger airplanes may have three spars) and ribs; the covers take the bending loads. The front and rear spars, as well as the covers, take torsion loads as the wing tries to twist during flight. The ribs keep the covers in shape and keep buckling of the covers and stringers to a minimum.

The wing covers primarily carry the wing box bending moments. The upper skin-stringer is primarily in compression during flight and in tension while taxiing. As for the fuselage, the taxiing loads are usually less than in-flight loads. Compressive yield strength and modulus of elasticity in compression are the static material properties that influence the design of the top skin-stringer. The lower skin-stringer is primarily in tension during flight and in compression during taxiing. Tensile strength, tensile yield strength and tensile modulus are the static material properties that influence the design of the lower skin-stringer. In addition,

the wing is subjected to alternating loads caused during flight and while taxiing. Thus, fatigue resistance is important and can be enhanced by using specialized manufacturing techniques, such as interference fastening, cold expansion of fastener holes and shot peening. It is important that the fatigue life of the stringers be greater than that of the skin material because it is easier to find cracks in the skin than in the stringer. Damage tolerance is also important. In summary, bottom cover materials should exhibit slow crack growth, long critical crack length and high residual strength. Corrosion resistance is also important, as is stress corrosion cracking (SCC) resistance of thick sections.

Ideally, the top of the spars should have the same material property requirements as those of the upper wing skin-stringer, while the bottom should have the same material property requirements as those of the lower wing skin-stringer. The spars act as webs of a beam and must resist shear loads transmitted by the covers and ribs. Material properties that are important are shear yield strength and compressive modulus for the spar web and compressive yield strength and modulus for the web stiffeners. Fatigue, damage tolerance and corrosion resistance are also important. Integrally machined spars are used by some to save weight and finished cost, but additional design detail is needed to stop propagation of cracks.

Ribs transfer loads from the covers to the spars and also resist inertia loads from fuel stored in the wing. These loads require relatively light internal ribs. The ribs are in compression during bending of the wing and transfer concentrated loads from the nacelle and landing gear to the wing spars and covers. Thus, for ribs, static strength properties are important (tensile strength, compressive yield, modulus). Corrosion resistance is also important, and fatigue and damage tolerance could be important.

Aerodynamically contoured leading and trailing edges are used to increase the performance of the airplane and reduce the take-off and landing speed. These elements of the wing are not primary load carrying parts. Fatigue, bending and torsional stiffness and resistance to hail damage are some of the items considered in their design.

24.3.3 Property requirements for empennage

The empennage is the tail of the airplane and consists of a horizontal stabilizer, a vertical stabilizer, elevators and rudders. The horizontal stabilizer is like an upside down wing whose span is roughly 50% that of the wing. Structural design of both the horizontal and vertical stabilizers is essentially the same as for the wing. Both upper and lower surfaces of the horizontal stabilizer are often critical in compression due to bending. Consequently, the modulus of elasticity in compression is the most important property. Supporting structures such as attachments of the wings to the fuselage and attachments of the landing gear to the wings or fuselage are designed for strength, fatigue and fracture toughness.

24.4 Structure–property relationships

The paradigm for alloy development for alloys such as 2024 and 7075 was strictly to determine effects of chemical composition on chiefly tensile properties and resistance to corrosion and stress corrosion cracking. Beginning with the 1960s, developments of aluminum alloys for aerospace applications have been aided by an improved understanding of the relationships among composition, processing, microstructure and many properties. The knowledge base comes from scientific literature, which gives guidelines for these relationships, and industrial experiments. Combining the information obtained from both sources has replaced the ‘trial and error’ approach to alloy development and reduced the time required to obtain the desired result.

24.4.1 Microstructural features

Chemical composition and processing control the microstructure and thus the physical, mechanical and corrosion properties of aluminum alloy products. The chemical compositions of the alloys discussed in this chapter are given in Table 24.2.

In general, microstructural features of importance for property control of the aircraft alloy products include precipitates, dispersoids, degree of recrystallization, grain size and shape, crystallographic texture and intermetallic constituent particles:

- 1 **Precipitates:** The composition, coherency, volume fraction, size, and distribution of precipitates determine their effect. Precipitates form intentionally during aging treatments and unintentionally during quenching. The precipitates that form during aging treatments normally range in size from 1 to 10 nm. The aging or precipitation heat treatments for aircraft alloy products produce three types of matrix precipitates: Guinier-Preston (G-P) zones, metastable precipitates and equilibrium precipitates. G-P zones are fine, completely coherent clusters of aluminum and solute elements and have the same crystal structure as the matrix. The G-P zones are usually, but not always, the precursors of metastable precipitates. The shape and habit plane of the metastable precipitates (the matrix plane on which they precipitate) depend on the balance between strain energy and interfacial free energy. They nucleate primarily in the matrix either homogeneously or heterogeneously at vacancy clusters and less frequently at dislocations. Metastable precipitates normally have a crystal structure that is different from that of the matrix and are completely coherent with the matrix on at least one interface. They have misfit dislocations along interfaces, which are not completely coherent. They are larger than G-P zones, and often, but not always, form by transformation of a G-P zone. They may also nucleate at dislocations, and in Al-Cu-X systems they prefer to nucleate at these sites. Equilibrium precipitates are larger and

Table 24.2 Nominal compositions of aluminum aircraft alloys

Alloy	Weight percentages									
	Zn	Mg	Cu	Mn	Cr	Zr	Fe	Si	Li	Other
1420@	—	5.2	—	—	—	0.1	—	—	2.0	—
2014	—	0.5	4.4	0.8	—	—	0.7*	0.8	—	—
2017	—	0.6	4.0	0.7	—	—	0.7*	0.5	—	—
2020	—	—	4.5	0.55	—	—	0.4*	0.4*	1.3	0.25 Cd
2024	—	1.5	4.35	0.6	—	—	0.5*	0.5*	—	—
2024A	—	1.35	4.1	0.43	—	—	0.15*	0.15*	—	—
2124	—	1.5	4.15	0.6	—	—	0.20*	0.20*	—	—
2224	—	1.5	4.1	0.6	—	—	0.12*	0.12*	—	—
2324	—	1.5	4.1	0.6	—	—	0.12*	0.10*	—	—
2424	—	1.4	4.1	0.6	—	—	0.12*	0.10*	—	—
2524	—	1.4	4.25	0.57	—	—	0.12*	0.08*	—	—
2040	—	0.8	5	0.6	—	0.12	—	—	—	0.2 Ag
2090	—	—	2.7	0.3	—	0.1	0.12*	0.10*	2.25	—
2091	—	1.5	2.1	0.3	0.3	0.1	0.30*	0.20*	2.0	—
2099	—	0.3	2.7	0.3	—	0.085	0.07	0.05	1.8	—
2199	—	0.225	2.6	0.3	—	0.085	0.07	0.05	1.6	—
6013	—	1.0	0.8	0.35	—	—	0.30*	0.8	—	—
7010	6.2	2.35	1.7	—	—	0.1	0.15*	0.12*	—	—
7049	7.7	2.45	1.6	—	0.15	—	0.35*	0.25*	—	—
7050	6.2	2.25	2.3	—	—	0.1	0.15*	0.12*	—	—
7150	6.4	2.35	2.2	—	—	0.1	0.15*	0.12*	—	—
7055	8.0	2.05	2.3	—	—	0.1	0.15*	0.1*	—	—
7075	5.6	2.5	1.6	—	0.23	—	0.4*	0.4*	—	—
7475	5.7	2.25	1.6	—	0.21	—	0.12*	0.10*	—	—
7079	4.3	3.2	0.6	.2	0.15	—	0.4*	0.3*	—	—
7085	7.5	1.5	1.65	0.04	0.04	0.115	0.08	0.06	—	—
7178	6.8	2.8	2.0	—	0.23	—	0.5*	0.4*	—	—
8090	—	0.9	1.3	—	—	0.1	0.30*	0.20*	2.4	—

Notes: * maximum.

Most ingot metallurgy aluminum alloys contain about 0.05–0.1% Ti to refine the ingot grain size.

@ not an Aluminum Association Designation

more widely spaced. They may form by transformation of metastable precipitates. They can also nucleate at dislocations and at interfaces such as grain boundaries and subgrain boundaries, and at the interface between other particles and the matrix. As their size increases, more misfit dislocations must be introduced at certain interfaces to maintain a degree of coherency. The matrix-strengthening precipitates in several aircraft alloy products are presented in Table 24.3.

Precipitates that form unintentionally during quenching are nucleated either at other particles or at grain boundaries. Precipitate-free zones near particles

Table 24.3 Major precipitates in aircraft aluminum alloy products

Alloy-temper	Major precipitate(s)
2X24-T3, T4	G-P zones
2X24-T6, T8	S' = precursor to S, Al_2CuMg
2X19-T8	θ' = precursor to θ , Al_2Cu
6013-T6	Q = $\text{Al}_5\text{Cu}_2\text{Mg}_8\text{Si}_6$
7X75-T6	η' = precursor to η , MgZn_2 or $\text{Mg}(\text{Zn,Cu,Al})_2$
7X75-T76	η' ; η
7X75-T73	η
7050-T76	η'
7050-T74	η
7150-T6	η'
7150-T77	η' ; η
7055-T77	η' ; η
2090-T8	$T_1 = \text{Al}_2\text{CuLi}$; θ' ; $\delta' = \text{Al}_3\text{Li}$
2095-T6, T8	T_1 ; θ'
2091-T3	δ' ; T_1
8090-T8,T7	δ' ; S'

and grain boundaries may be generated during subsequent aging because of both loss of vacancies and solute during the quench.

- 2 Dispersoid particles: The size, distribution and coherency of these particles determine their effect. Dispersoids form during the ingot preheating by precipitation of the transition elements chromium, manganese or zirconium as $\text{Al}_{12}\text{Mg}_2\text{Cr}$, $\text{Al}_{20}\text{Cu}_2\text{Mn}_3$ or $\text{Al}_{12}\text{Mn}_3\text{Si}$ and Al_3Zr particles, respectively. Manganese and chromium were included as early alloying additions before the dispersoids were identified. Once effects of dispersoids containing these elements on controlling grain structure and degree of recrystallization were discovered, they began to be added by design. Zirconium was added intentionally to modern alloys because the smaller size and coherency of Al_3Zr particles make it more attractive with respect to controlling quench sensitivity and recrystallization. Dispersoids normally range in size from 10 to 200 nm. Because they form from a solid-solid reaction, at least one of their interfaces with the matrix is coherent. The Al_3Zr particles precipitate in a metastable L_{12} structure, which has a lattice parameter close to that of aluminum, and are fully coherent with the matrix. Although the tetragonal form of Al_3Zr is the equilibrium phase, the L_{12} structure is remarkably resistant to transformation in the high-strength alloys. Moreover, because of the low diffusion coefficient of zirconium in aluminum, the Al_3Zr dispersoids are highly resistant to coarsening. Crystal structures of the other dispersoids are non-cubic and they are larger. However, their size remains stable after ingot preheating unless subsequent thermal treatments are performed much above the conventional solution treatment temperature. Dispersoids found in some high-strength alloy products are presented in Table 24.4.

Table 24.4 Dispersoids in aircraft aluminum alloy products

Alloy	Dispersoid
2X24	$\text{Al}_{20}\text{Cu}_2\text{Mn}_3$
6013	$\text{Al}_{12}\text{Mn}_3\text{Si}$
7X75	$\text{Al}_{12}\text{Mg}_2\text{Cr}$
7X50	Al_3Zr
7055	Al_3Zr
2090	Al_3Zr
2091	Al_3Zr
2095	Al_3Zr
8090	Al_3Zr

- 3 Degree of recrystallization: The thermomechanical history and the type of dispersoid determine the degree of recrystallization. During bulk metal deformation processing at elevated temperatures, the dislocations in aluminum alloy products arrange themselves into a structure of subgrains by the process known as dynamic recovery. As the temperature decreases and strain rate increases, the stored energy increases. The increase in stored energy is manifested by an increase in the number of dislocations and consequent decrease in size of the subgrains, with an associated increase in the dislocation density in the cell walls. During solution heat treatment, the stored energy of deformation is given an opportunity to decrease by static recovery and/or recrystallization.

Particles have a large influence on the tendency of an alloy to recrystallize. When particles greater than about $3\text{ }\mu\text{m}$ are present during deformation, a high density of dislocations accumulate at particle-matrix interfaces. These high-energy sites serve to nucleate recrystallization during subsequent exposure at elevated temperatures. These particles may be either precipitates formed during processing or constituents formed during ingot solidification. The tendency for recrystallization is opposed by the Zener drag that is imposed by the dispersoid particles on migrating boundaries (1948). Zener suggested that a grain would cease to grow when its radius, R , would approximately be equal to the ratio of the particle radius, r , divided by the particle volume fraction, f , i.e.:

$$R_{\text{crit}} = (3\beta/4)(r/f) \quad [24.1]$$

where β is a constant approximately equal to one.

Thick plate, most forgings and thick extrusions of high-strength alloys are usually fabricated at high temperatures to minimize flow stress. Therefore, they have a low driving force for recrystallization during solution heat treatment. In general, the degree of recrystallization in plate and forgings

increases as thickness decreases because the deformation temperature decreases during hot working. The degree of recrystallization of extruded products also tends to increase with decreasing thickness. In sheet, which is cold worked prior to solution heat treatment, and in plate and extrusions, which are worked in the lower portion of the usual hot working temperature range, the stored energy of deformation is usually sufficient to overcome the pinning effect of the dispersoids on grain boundaries even away from constituent particles (present due to the presence of impurities, e.g., iron and silicon). Consequently, such products usually recrystallize completely during solution heat treatment.

- 4 Grain size and shape: The grain size and shape are also controlled by thermomechanical history and may be influenced by ingot grain refining practice. During hot working, the equiaxed ingot grains deform. Their shape depends on the deformation process employed. The shape of recrystallized grains depends also on composition as well as fabricating practice. Because of segregation during solidification and the nature of most deformation processes, dispersoids are layered in the deformed grains rather than being homogeneously dispersed. Consequently, the morphology of the deformed grains may be retained in the final recrystallized product.
- 5 Crystallographic texture: The deformation process used to produce the product and the thermomechanical history determines the crystallographic texture. The crystallographic texture of rolled plate is customarily described by the Miller indices of the crystal planes and directions parallel to the rolling direction. The texture of rolled plate is characterized largely by the $\{110\}\langle 112\rangle$, $\{112\}\langle 111\rangle$ and $\{123\}\langle 634\rangle$ components (the symbols $\{ \}$ are used to designate crystallographic planes and $\langle \rangle$ are used to designate crystallographic directions). In extruded products, which have a low aspect ratio of width to height, the texture is a dual fiber texture in which the $\langle 111\rangle$ and $\langle 100\rangle$ directions are aligned in the extrusion direction. As the aspect ratio increases, the texture more closely approaches that of rolled plate, but some grains keep their $\langle 100\rangle$ directions parallel to the extrusion direction. Forgings made directly from ingot generally have a random texture because of the multidirectional deformation. In cases where either extrusion or plate is used as forging stock, and the degree of work during forging is not extensive, the extrusion or plate texture may survive in the forged products.
- 6 Intermetallic constituent particles: Intermetallic constituent particles form by a liquid–solid eutectic reaction during solidification. They can be classified into two types, insoluble and sparsely soluble. Insoluble constituents are formed primarily from iron and silicon impurities. Because the low solubility of iron in pure aluminum is reduced by alloying elements, constituent particles containing iron are insoluble. Although silicon has appreciable solubility in aluminum, alloying elements, particularly magnesium, decrease its solubility.

Consequently, while soluble in some alloys, Mg_2Si is virtually insoluble in alloys such as 7075. The size and size distribution of insoluble constituent particles are controlled by the rate of ingot solidification, the chemical composition and the extent and nature of bulk deformation. Particle size decreases as solidification rate increases, as iron and/or silicon content decreases and as the amount of deformation increases.

Generally, the insoluble constituent particles are coarsest and most heterogeneously distributed in thick plate and are finer and more homogeneously distributed in thin sheet. Because deformation processing of forgings usually involves working in several directions, the particles in forgings are usually distributed more homogeneously than those in plate of the same thickness. Constituents generally range in size from 1 to 30 μm . The phase Al_2CuMg is the sparsely soluble phase found in aircraft alloys. Phases that have been observed to be insoluble and sparsely soluble constituent particles in products of some of the aerospace alloys are presented in Table 24.5. Higher purity versions may not have all of the insoluble constituents present.

- 7 Porosity: This is a factor in thick plate and, particularly, in castings. Individual pores can range up to and beyond 200 μm .

24.4.2 Strength

Primary design criteria always involve ultimate tensile and yield strengths. Quantitative relationships exist between strength and precipitate particles, subgrain and grain size and texture (Hornbogen and Starke, 1993). For age-hardenable alloys, strength is primarily controlled by the volume fraction, size and spacing of the matrix precipitates. The upper limit of this strengthening mechanism is described by the modified Orowan equation:

$$\Delta\sigma_p \approx Gb\sqrt{f}/d \quad [24.2]$$

Table 24.5 Usual constituent phases in aircraft aluminum alloy products

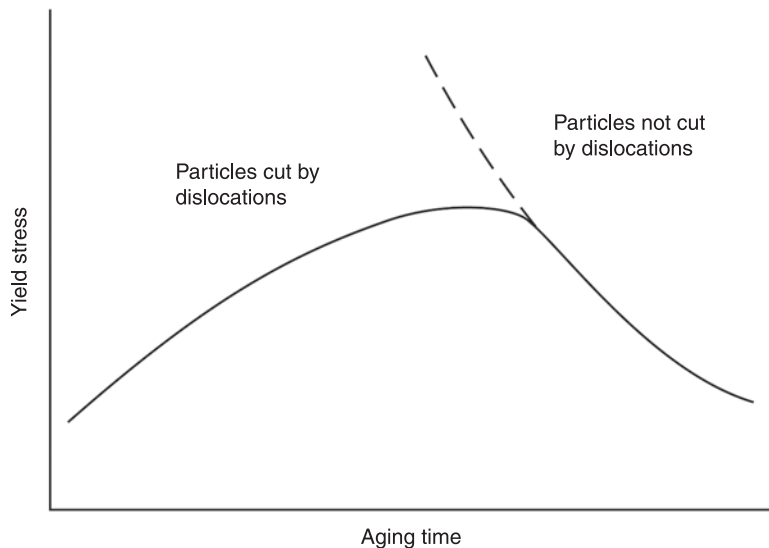
Alloy	Observed constituent phase(s)
2X24	$\text{Al}_7\text{Cu}_2\text{Fe}$, $\text{Al}_{12}(\text{Fe,Mn})_3\text{Si}$, Al_2CuMg , Al_2Cu , $\text{Al}_6(\text{Fe,Cu})$
2X19	$\text{Al}_7\text{Cu}_2\text{Fe}$, $\text{Al}_{12}(\text{Fe,Mn})_3\text{Si}$, Al_2Cu
6013	$\text{Al}_{12}(\text{Fe,Mn})_3\text{Si}$
7X75	$\text{Al}_7\text{Cu}_2\text{Fe}$, $\text{Al}_6(\text{Fe,Mn})$, $\text{Al}_{12}(\text{Fe,Mn})_3\text{Si}$, Mg_2Si
7X50	$\text{Al}_7\text{Cu}_2\text{Fe}$, Mg_2Si , Al_2CuMg
7055	$\text{Al}_7\text{Cu}_2\text{Fe}$, Mg_2Si
2090	$\text{Al}_7\text{Cu}_2\text{Fe}$
2091	$\text{Al}_7\text{Cu}_2\text{Fe}$, Al_3Fe , $\text{Al}_{12}\text{Fe}_3\text{Si}$
2095	$\text{Al}_7\text{Cu}_2\text{Fe}$, Al_2CuLi , Al_6CuLi_3
8090	Al_3Fe

where $\Delta\sigma_p$ is the contribution of the particles to the yield strength of the alloy, G is the shear modulus, b is the Burgers vector of the matrix dislocations, f is the volume fraction of particles and d is the particle diameter. A high volume fraction of very small hard particles is desired but this is difficult to obtain in age-hardening systems. Usually, in age-hardenable aluminum alloys precipitation of the equilibrium phase is preceded by the formation of clusters of solute atoms (G-P zones) and/or intermediate precipitates that may be sheared by dislocations. When shearing occurs the strength associated with the particles can be described by an equation of the form:

$$\Delta\sigma_p \approx cf^m d^n \quad [24.3]$$

where c is an alloy constant that depends on the properties of the particles, m and n are positive exponents so, unlike the case described by the Orowan equation, strength increases with particle size. During aging, the G-P clusters and/or intermediate precipitates grow and strength increases. At some point the deformation mode changes from shearing of particles to the Orowan (looping and bypassing) mechanism and the strength then decreases as the particles grow, i.e. 'overaging' occurs. This phenomenon is illustrated in Fig. 24.2.

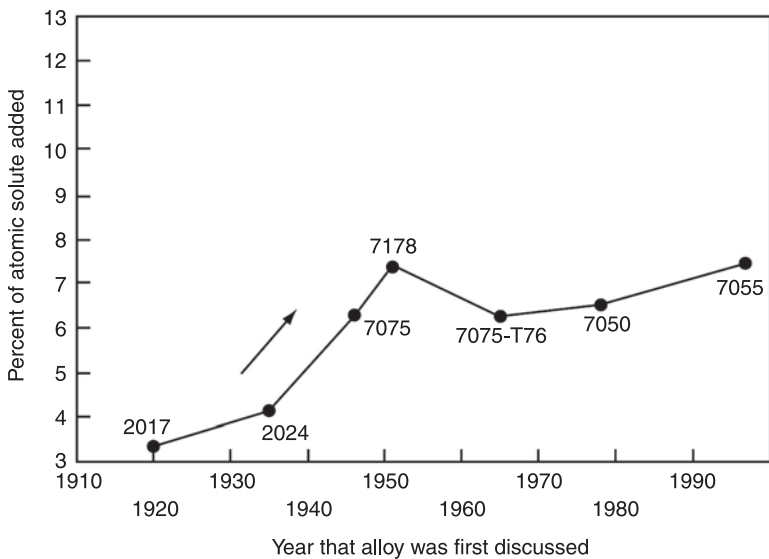
The magnitude of precipitation strengthening relative to that of solid solution strengthening is large. For example, the maximum yield strength of freshly quenched 7XXX-W sheet increases from about 70 MPa to about 200 MPa as total solute content is increased from about 4.5 to 12.5%. In contrast, strength of the same materials in the T6 temper increases from 230 MPa at the lower solute level to over 600 MPa at the higher solute level (Staley, 1992).



24.2 Schematic showing yield strength as a function of aging time for age-hardenable aluminum alloys.

The strength of a particular age-hardenable alloy can be optimized by maximizing those elements that participate in the aging sequence and can be put in solid solution at the solution heat-treatment temperature (Starke, 1977). Solubility should not be exceeded at the solution temperature since all excesses form coarse particles, which do not add significantly to the strength and have an adverse effect on fracture toughness and fatigue properties. The chronology of the increase in atomic per cent solute to some 2XXX and 7XXX aircraft alloys is presented in Fig. 24.3. Alloy 7178-T6 developed very high strength, and plate and extrusions were used for both lower and upper wing skins of several jetliners. Experience showed, however, that 7178-T6 products developed cracks in service sooner than 7075-T6, so it was phased out of use as more damage tolerant materials became available. Alloy 7001 products developed even higher strength, but they were never used for any major structural component because of concerns about damage tolerance. Recent technology has led to the development of a high strength alloy, 7055 that does not have the fracture problems associated with either 7178 or 7001 (Lukasak and Hart, 1991).

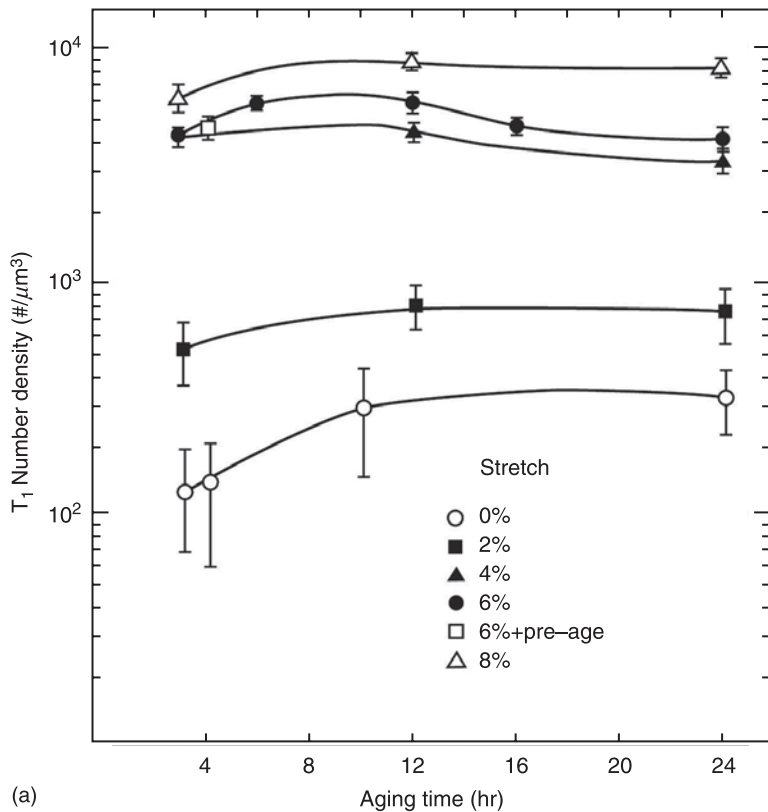
The distribution and size of the strengthening precipitates significantly affect the attainable strength and can be controlled by the aging temperature and time, and in some cases by the amount of deformation prior to aging. Theory tells us that when precipitates have large coherency strains or interfacial energies, defects such as dislocations and subgrain and grain boundaries can be sites for nucleation of precipitates and many 2XXX and 8XXX alloys utilize this



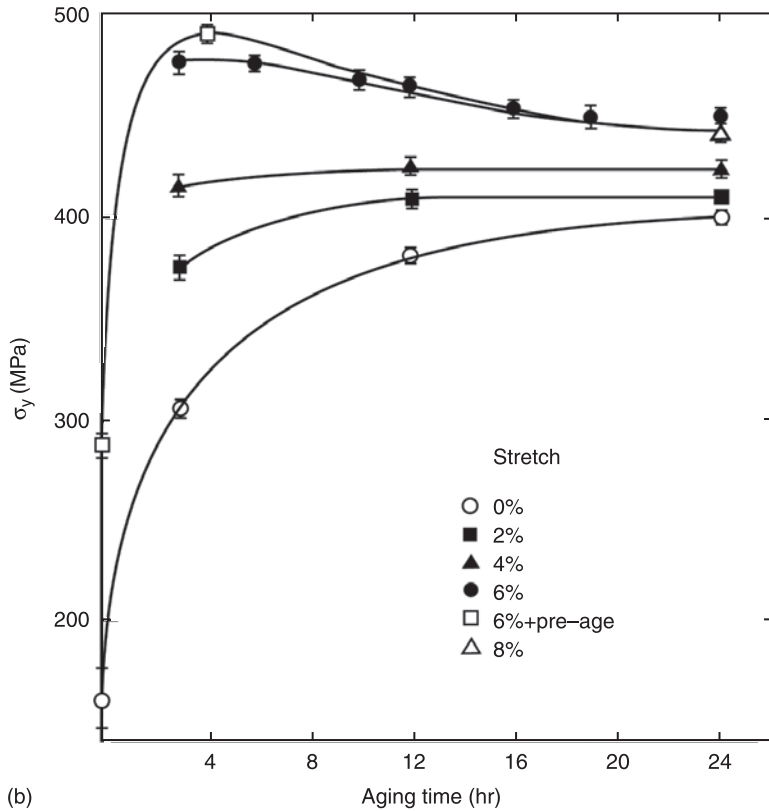
24.3 Solute content of various aircraft aluminum alloys and the year that the alloys were first discussed.

concept. Figure 24.4(a) shows how the number density of T_1 precipitates in 2090 is increased with stretch prior to aging and Fig. 24.4(b) shows how this relates to an increase in strength (Cassada et al., 1991).

Because interactions between dislocations and precipitates are on a much finer scale than interactions between dislocations and grain and subgrain boundaries, degree of recrystallization per se and recrystallized grain size, have little effect on strength of aircraft aluminum alloy products. However, the degree of recrystallization normally affects the crystallographic texture, which does affect strength and anisotropy of properties of aluminum alloy products. This can be explained as follows: Yielding in a polycrystalline material requires that the critical resolved shear stress is reached on a number of slip systems (usually five) in order to maintain compatibility across grain boundaries. It is supposed that every grain undergoes the same deformation as the aggregate. This requires an external stress, which depends on its direction and the crystallographic texture of



24.4 (a) Number density of Al_2CuLi (T_1) precipitates as a function of stretch and aging time at 463°C . (b) Strength in 2090 as a function of stretch and aging time at 463°C .



(b)

24.4 Continued.

the material. Most treatments of this problem are based on the theory of Taylor (1938) and Bishop and Hill (1951) and relate to single-phase materials. Taylor derived a factor, M , which relates the stress necessary for plastic flow to the critical resolved shear stress of a crystal. It predicts whether the slip is easy or difficult and is a function of the crystal orientation, i.e. the texture of the material. The Taylor-factor

$$M = \delta\gamma T / \delta\epsilon \quad [24.4]$$

is the smallest total shear strain, $\delta\gamma T$, necessary to give total macroscopic strain, $\delta\epsilon$. For face-centered-cubic aluminum there are 384 combinations of the five independent slip systems. When the texture is random, M is equal to 3.06 using the Taylor method. Compared to random textured material, strength can be increased by 20% or decreased by 25% if a strong (111) or (100) fiber texture is present (Chin and Mammel, 1969). For sheet and plate materials having a strong texture, the mechanical properties can be considerably anisotropic.

Yield strength anisotropy is observed in thick plates, forgings and extrusions and in thin sheets. In thick products anisotropy is normally observed through the thickness and in thin products in the plane of the sheet. Although strengthening in one direction by crystallographic texture must necessarily be accompanied by weakening in another, designers can often use a material with enhanced strength in one direction. For example, designers take advantage of the approximately 70 MPa higher strength of extruded products used as wing stringers and spars relative to that of rolled plate used for wing covers.

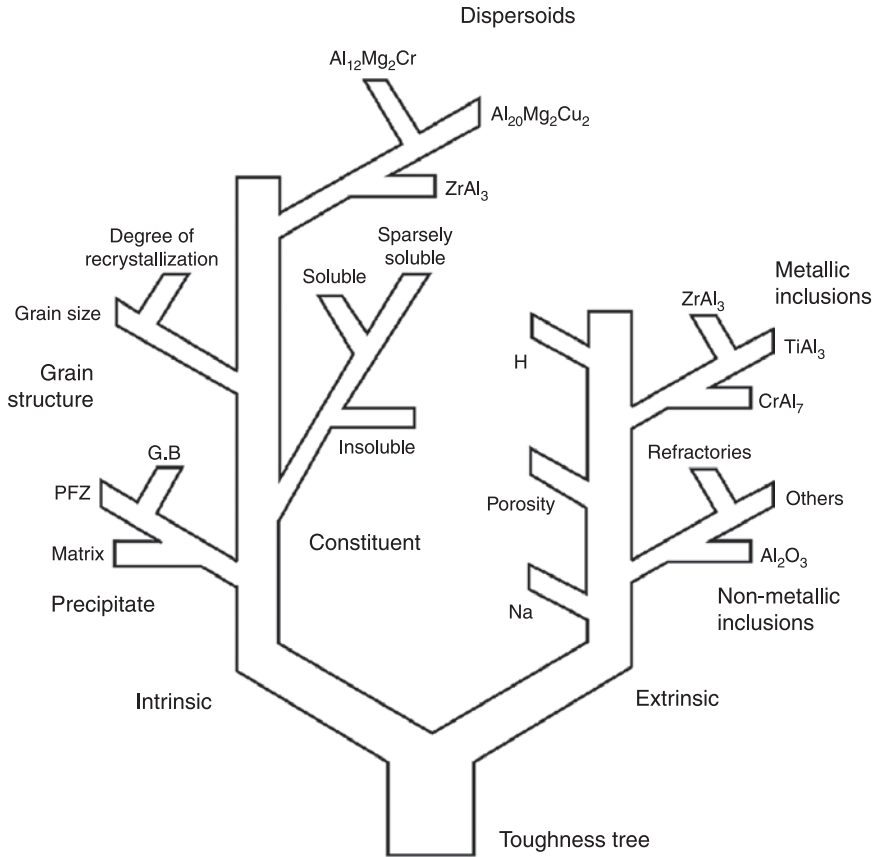
The strength anisotropy in a precipitation-hardened aluminum alloy product depends not only on the crystallographic texture, but on the morphology and habit plane of the precipitates as well (Hosford and Zeisloft, 1972; Bate et al., 1982). The precipitates in these alloys may superimpose an additional anisotropy, which may either reinforce or moderate that imposed by the crystallographic texture. Planar slip appears to be an essential condition for precipitate-enhanced anisotropy.

24.4.3 Fracture toughness

Transgranular fracture is a necessary, but not sufficient condition for high fracture toughness. The 'toughness tree', presented in Fig. 24.5 is an effective tool for classifying the contribution of microstructural features to both intergranular and transgranular fracture. The metallic and non-metallic inclusions on the right-hand side of the tree are treated as extrinsic effects because they are controlled more by defects due to processing than by composition. Metallic and non-metallic inclusion content is minimized by controlling composition, melt temperature, filtering or direct-chill processing. Hydrogen levels are kept low by minimizing exposure to moisture, and deformation processing often closes porosity. The features on the left of the 'toughness tree' are termed intrinsic because they are characteristic of the composition and microstructure of the alloy. These features also depend on the response of the material to deformation processing and heat treatment.

The detrimental effect of large constituent phases on the fracture toughness of aluminum alloys was first identified in 1961 (Quist, 1963) and has been documented by many investigators (Anderson and Quist, 1966; Smith, 1991). Constituent particles participate in the fracture process through void formation at particle/matrix interfaces or by fracturing during primary processing. Minimizing impurity elements, e.g. iron and silicon, and excess solute, can eliminate their volume fraction. Figure 24.6 shows the trend of the amount of Fe + Si on the toughness of 7075 sheet. The same trend holds for 2024 (Thompson and Levy, 1970) and Al-Li alloys (Ashton, Thompson, Gayle, 1986).

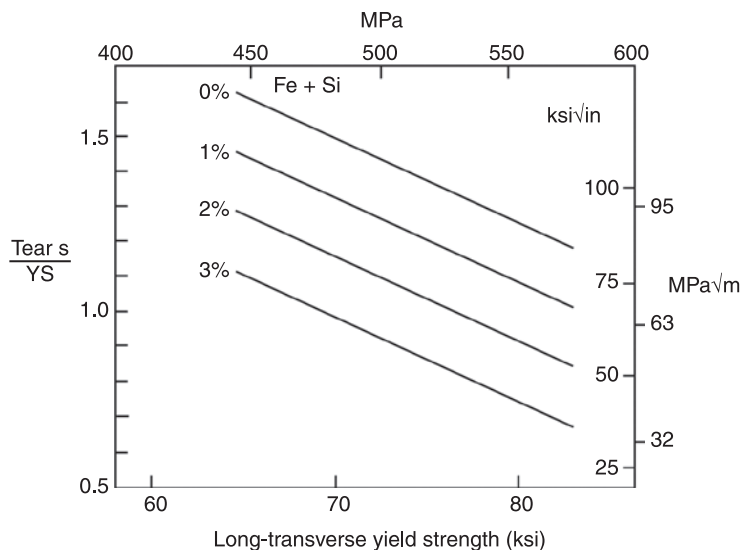
Depending on their size and details of their interface with the matrix, dispersoids may also play an unfavorable role in the fracture process. Specifically, void coalescence between constituent particles may occur by the formation of void sheets associated with the nucleation of fine voids at dispersoids (Van Stone and



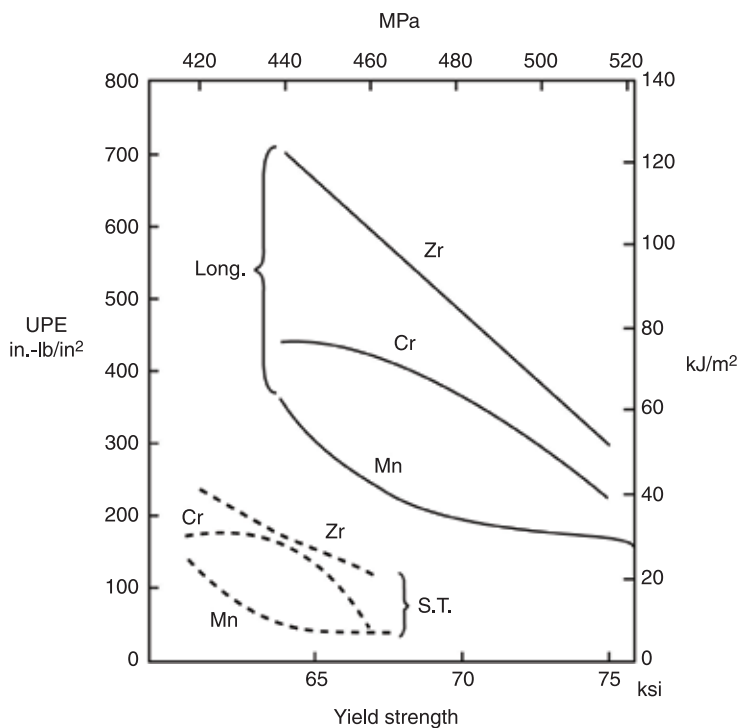
24.5 'Toughness tree' representation of microstructural features that affect toughness in age-hardenable aluminum alloys.

Psioda, 1975). The strength–toughness relationships in Fig. 24.7 were determined for 7075 variants containing different dispersoid forming elements. Since Al₃Zr particles are small and coherent with the matrix (strong interface), they are usually not involved in the fracture process.

Strengthening precipitates are listed explicitly on the toughness tree, but aging effects actually encompass precipitate size and distribution (matrix and grain boundary), precipitate free zone (PFZ) width and deformation mode. Strengthening precipitates increase resistance to plastic deformation and, therefore, reduce the crack opening displacement, which, by itself would increase fracture toughness. However, they may promote strain localization, which leads to premature crack nucleation and low fracture toughness. During aging, heterogeneous precipitation occurs at grain and subgrain boundaries resulting in soft, solute-denuded PFZs in the matrix adjacent to the boundaries (Starke, 1970). The combination of these soft zones, that can localize strain, and grain boundary



24.6 Effects of total Fe + Si on toughness of alloy 7050 sheet.

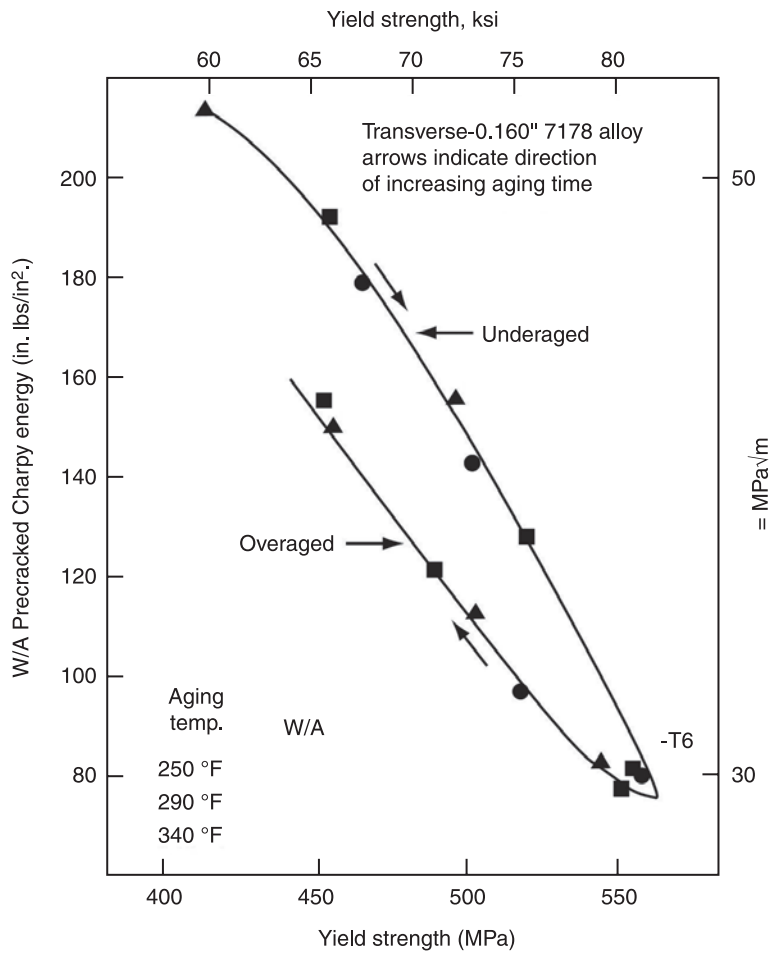


24.7 Plot of propagation energy (a measure of toughness) versus yield strength, illustrating the effect of dispersoid type on toughness of 7075 plate.

precipitates, that can aid in microvoid nucleation, has an adverse effect on fracture toughness by promoting intergranular fracture. Alloy design since the 1960s has focused on reducing the volume fraction of void nucleating particles, by minimizing Fe and Si contents, optimizing solute content to prevent the formation of sparsely soluble constituent particles, and using Zr, when practical, as the dispersoid forming addition, to control the grain size and degree of recrystallization. Experimental observations have shown that for these modified alloys, the fracture behavior is controlled by strain localization in the matrix and PFZs, and void formation at grain boundary precipitates (Staley, 1975; Ashton, Thompson, Starke et al., 1986; Sugamata et al., 1993). More recent alloy design for high fracture toughness has focused on composition and processing controls to minimize grain boundary precipitates and to develop matrix precipitates which homogenize deformation, i.e., precipitates which are not sheared by dislocations.

As strength increases, ductility and fracture toughness usually decrease. To develop high toughness the microstructure must accommodate significant plastic deformation, and yet a microstructure that resists plastic deformation is needed for high strength. Figure 24.8 shows the typical relationship of decreasing toughness with increasing strength that occurs during aging for 7XXX series alloys (Staley, 1975). The balance between strength and toughness is greatly affected by a variety of processing parameters. Quenching efficiency is an important processing parameter, which can now be modeled for complex alloys (Staley, 1987). Quenching affects both the microstructure and properties by determining the amount of solute that precipitates during cooling and that which is available for subsequent age hardening. It also affects the level of residual stresses. Application of modern aluminum alloys to aircraft which, as mentioned previously, can influence manufacturing costs, fatigue and corrosion behavior. Methods to obtain a balance of properties after quenching include cold working before aging, when practical, for 2XXX alloys (Starke, 1989) and selecting aging times and temperatures to minimize grain boundary precipitates and PFZs (Ashton, Thompson, Starke et al., 1986). Figure 24.9 illustrates these effects for 2090. The deformation prior to aging aids in the nucleation and growth of the matrix precipitates which decreases the time to reach peak strength. This, along with low temperature aging, minimizes the amount of grain boundary precipitates and PFZs (which adversely affect fracture toughness) at the desired strength level. Selection of the proper dispersoid for grain structure control, and controlling the chemical composition to minimize coarse constituent phases, is also important.

Grain size and degree of recrystallization can have a significant effect on fracture toughness by influencing the tendency for intergranular fracture. The desired degree of recrystallization depends on product thickness, i.e., whether the part is under plane stress or plane strain. In thin products under plane stress, fracture is controlled by plasticity and a small-recrystallized grain size is

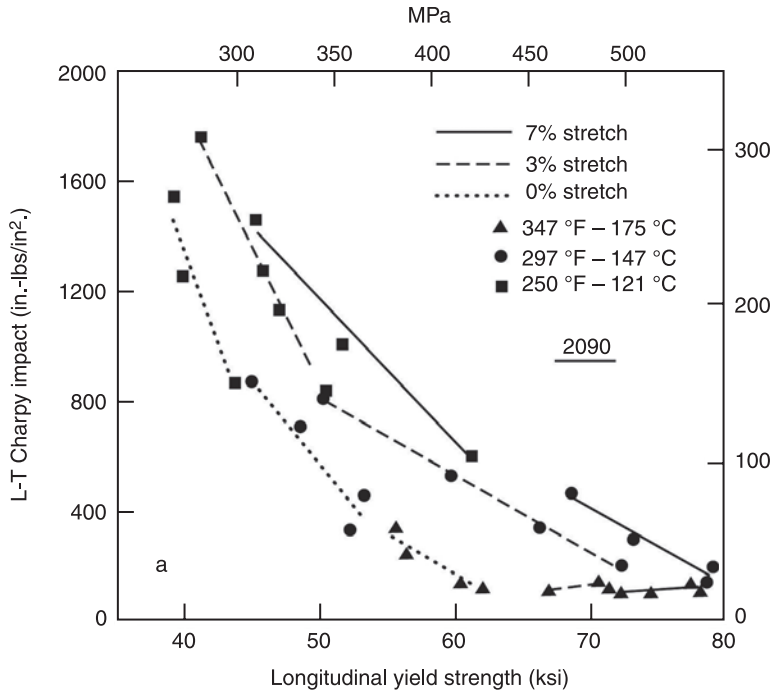


24.8 Strength-toughness relationship for alloy 7178.

preferable. If the grain size is small enough, plasticity will be enhanced without detrimental, low energy, intergranular fracture. However, for thick products under plane strain, fracture is usually controlled by coarse particles and an unrecrystallized grain structure is preferable.

24.4.4 Fatigue crack initiation

Fatigue cracks may initiate on the surface or at internal sites. The initiation event may be associated with surface flaws, defects, slip steps, etc., which concentrate stress. Any microstructural feature, e.g. constituent particles, PFZs, porosity that either concentrate the stress or localize the strain will have an adverse affect on fatigue crack initiation resistance. The major microstructural feature affecting



24.9 Effect of stretch and aging time on the strength-toughness relationship for alloy 2090.

fatigue crack initiation in thick products is porosity (Magnusen et al., 1995). Forgings are often chosen over thick plate when fatigue initiation is a major concern because the compression introduced during forging closes pores, while the light rolling passes necessitated by load restrictions during the initial stages of hot rolling can actually open pores (Bucci et al., 1998). Consequently, a microstructure strengthened by hard, nonshearable particles, free from constituent phases and porosity, and having a small recrystallized or unrecrystallized grain structure, is usually preferable for fatigue crack initiation resistance (Starke and Lütjering, 1979).

24.4.5 Fatigue crack propagation

Microstructure is the principal independent variable that can be used to control the fatigue crack growth rate (FCGR) once loading conditions and environment are established. The principal factors that affect intrinsic FCGR are slip character, slip length and slip reversibility (Starke and Williams, 1989). Each of these factors is affected by both alloy composition and microstructure. Strain localization typically reduces FCGR and increases the threshold stress intensity factor, ΔK_{th} by enhancing crack path tortuosity and crack closure. Wavy (homogeneous) slip

usually corresponds to higher FCGR. Increasing slip length, by having shearable precipitates and a large grain size, tends to reduce FCGR. Planar slip associated with shearable precipitates also decreases FCGR by enhancing slip reversibility which results in less damage in the crack tip plastic zone. The alloy 2024-T3 with shearable G-P zones has better FCGR than 2024 overaged to the same yield strength. However, environmentally related acceleration of FCGR is usually greater in the presence of strain localization.

24.4.6 Stress corrosion cracking

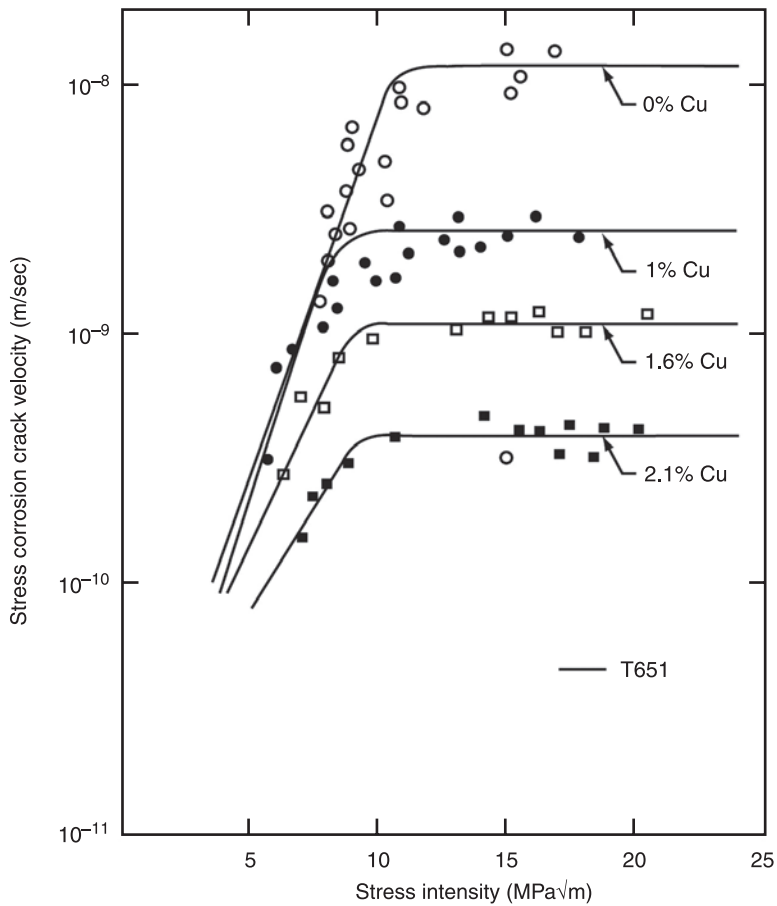
Aluminum alloy structures loaded below the yield strength, σ_y , or the plane strain fracture toughness, K_{IC} may still experience catastrophic failure, even if the load is not cyclic in nature. Cracks may initiate and propagate in the presence of tensile stresses and an aggressive environment. Humid air qualifies as an aggressive environment for some aluminum alloys. This stress corrosion cracking (SCC) failure mode is common in certain microstructural conditions of 2XXX and 7XXX alloy products. The specific aluminum alloy/temper combinations, 7079-T6 (now obsolete), 7075-T6 and 2024-T3, have contributed to over 90% of SCC service failures of aluminum alloy products. Almost all of the failures have been in components loaded in the short-transverse direction (perpendicular to the shortest grain dimension). Because stresses in this direction are generated mainly by residual quenching stresses and fit-up stresses, the components are usually those fabricated from relatively thick products. The T73 temper for alloy 7075 products was developed to solve this problem, but strength was below that of 7075-T6 and 7079-T6 products. Alloy 7050-T74 plate and forgings were developed to provide both strength and resistance to SCC. No known instances of SCC failures of 7075-T73 or 7050-T74 products have been reported, although SCC can be induced in test specimens under extremely severe laboratory conditions.

The exact mechanisms responsible for SCC of a susceptible aluminum alloy in a particular environment remain controversial. However, most proposed mechanisms are variations of two basic theories: crack advance by anodic dissolution or hydrogen embrittlement. The controlling factors in these two SCC models are given in Table 24.6. An important fact to remember is that pure aluminum does not stress corrode, and for any given system, susceptibility usually increases with solute content. This fact, coupled with data and the controlling factors of the two models, suggests that microstructural alterations may influence SCC behavior for a given composition. The reader is referred to reviews on environment-induced cracking of high-strength aluminum alloys (Holroyd, 1989) and on corrosion fatigue crack propagation (Gangloff, 1989) for more details.

Although SCC eludes a complete mechanistic interpretation, it is clear that it is a stress-activated process. Usually, susceptibility, as measured by stress corrosion crack velocity, increases with stress intensity up to some value, Region I, and then remains constant, Region II, as shown in Fig. 24.10 for a series of 7XXX alloys

Table 24.6 Controlling factors in SCC models

Anodic dissolution	Hydrogen embrittlement
Grain boundary precipitate size, spacing and/or volume fraction	Hydrogen absorption leading to grain boundary or transgranular decohesion
Grain boundary PFZ width, solute profile or deformation mode	Internal void formation via gas pressurization
Matrix precipitate size/distribution and deformation mode	Enhanced plasticity (adsorption and absorption arguments exist)
Oxide rupture and repassivation kinetics	



24.10 Stress corrosion crack velocity vs. stress intensity for modified 7050 alloys with various copper contents.

having different copper contents (Sarkar et al., 1981). Therefore, in Region I, factors that control the effective local stress at the crack tip control the crack growth velocity. Since SCC in aluminum alloys is intergranular, the critical local stress, τ_c , necessary for a certain crack growth velocity in region I, is most likely due in part to the dislocations piled up at the grain boundary, i.e. $\tau_c = N\tau_{\text{rss}}$ where τ_{rss} is the resolved shear stress and N is the number of dislocations in the pile-up. When deformation is heterogeneous and planar, i.e. shearable precipitates are present, N can be very high (depending on the grain size or slip length). Consequently, one would prefer the alloy to have hard, non-shearable particles to reduce the stress concentration across the grain boundary for high SCC resistance. In Region II, the required stress is present and susceptibility is most likely associated with the electrochemical difference between the matrix and the grain boundary precipitates. Therefore, controlling the chemical composition of the matrix and the precipitates is important in controlling stress corrosion susceptibility.

24.4.7 Corrosion resistance

All structural materials are susceptible to degradation to some extent from the environment, and aluminum alloy products for aircraft are no exception. Unlike the case with mechanical properties or stress-corrosion cracking, the designer has no means of handling corrosion in the design process except for ensuring that dissimilar materials are insulated so that galvanic corrosion does not occur. Coatings provide some degree of protection, but designers must rely primarily on the inherent corrosion resistance of the material.

Aluminum alloy products corrode in a localized manner either by pitting, intergranular attack or exfoliation. Pitting is the removal of metal at localized sites, resulting in the formation of cavities. Pits can initiate at intermetallic constituent particles, so their size, quantity, location, continuity and corrosion potential relative to that of the adjacent aluminum alloy matrix can influence pitting corrosion behavior (Piascik and Willard, 1994). Intergranular corrosion is selective attack of the grain boundary region with no appreciable attack of the matrix. Electrochemical cells are formed between precipitates on the boundaries and the depleted solid solution. Exfoliation corrosion initiates at a surface but is primarily a subsurface attack that proceeds along multiple narrow paths parallel to the fabricated surface of the product. The attack is usually along grain boundaries (intergranular corrosion), but it has occasionally been observed along striations of intermetallic particles. Exfoliation corrosion is characterized by leafing of thin layers of uncorroded metal between layers of corrosion product that are more bulky (up to 20 times) than the metal from which they came. Products having an equiaxed grain structure, such as in sheet less than about 2 mm thick, do not exfoliate although they may be susceptible to intergranular corrosion.

Of the three types of localized corrosion, pitting is the least damaging and most easily controlled. It can be minimized by alcladding or by surface treatments, and

when it occurs, it is easily detected. Intergranular corrosion can also be minimized by the same procedures, but is much more difficult to detect. Moreover, intergranular corrosion generally causes more severe damage to the structure. Alcladding and surface treatments also improve resistance to exfoliation corrosion. However, not all products are alclad, and newer chromium-free surface treatments are not as effective as the chromium bearing ones used in the past. Consequently, airframe designers are demanding more inherent resistance in the material. Overaging to T76, T74 and T73 tempers can markedly increase resistance to exfoliation of 7XXX products, and such materials are widely used. Until recently, these tempers provided a compromise; strength was sacrificed from 5% to 20% to provide adequate resistance. The T77 temper, however, provides resistance to exfoliation with no sacrifice in strength, and resistance to SCC superior to that of 7075-T6 and 7150-T6. The highest strength aluminum alloy products 7055 plate and extrusions are supplied primarily in the T77 temper. Alloy 2024 products are also resistant to intergranular corrosion in the T8 temper, but fracture toughness and resistance to the growth of fatigue cracks suffer relative to 2024-T3.

Aluminum alloy products of 2024-T3 and 7075-T6 corrode by the preferable pitting mode when they are quenched above a critical rate, which is alloy dependent. With decreasing quench rate, some susceptibility to intergranular corrosion is observed, and as cooling rate decreases further, the mode becomes entirely intergranular. With even lower quench rates, the corrosion mode reverts to pitting; strength is so low, however, that slow quenching is an impractical way to prevent intergranular corrosion. Corrosion depth of 2024-T3 products is constant as long as the mode is pitting, then increases with decreasing quench rate when the mode is mixed or intergranular. In contrast, corrosion depth of 7075-T6 is constant with decreasing quench rate, regardless of corrosion mode (Hatch, 1984). Damage of 7075-T6 sheet as measured by loss in tensile strength of corroded specimens, however, is sensitive to quench rate. Loss in strength is most severe when quenching rate is between 15 and 30 K/s.

Although alloy 7050 and 7150 products in T7 tempers are resistant to exfoliation corrosion, they can be highly susceptible to intergranular corrosion in the W temper depending on the quenching conditions (Staley et al., 1996). When quenched in a manner, which allows sufficient grain boundary precipitation, the rate of attack of 7X50-W products is such that they may suffer intergranular corrosion during the time in the plant between quenching and aging to the final temper. Products that are quenched at a thickness above about 10 mm may require that the user perform 100% surface metal removal (by machining or chem. milling) to insure that any intergranular corrosion is removed.

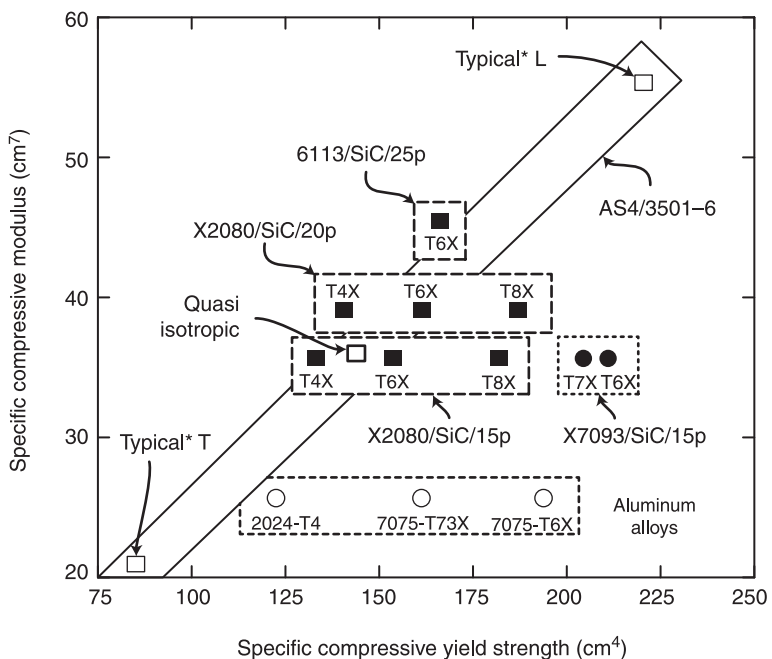
24.4.8 Elastic modulus

The material property that influences the stiffness of a structure is Young's modulus. It is usually not altered significantly by changes in microstructure of an

alloy with a fixed composition. Alloying elements, whether present in solid solution or have precipitated as particles of varying size and distribution seem to have little or no affect on Young's modulus of age-hardenable aluminum alloys. One notable exception is the addition of lithium which can increase the modulus six per cent for every weight percent added, at least up to three weight percent (Starke, 1983). Young's modulus can be increased by more than 50%, however, by the addition of an appreciable volume fraction of hard particles or whiskers such as SiC. The specific modulus of such materials, known as discontinuously reinforced aluminum (DRA), is similar to that of graphite-epoxy composites in typical aircraft structure lay-ups as shown in Fig. 24.11 (Hunt, 1994). DRA (Al 6092/SiC/17.5p) sheet is being used to retrofit the ventral fins and fuel access covers on the F-16 fighter aircraft due to its high modulus and its excellent mechanical properties. DRA is also being used on fan exit guide vanes on all Boeing 777s with Pratt & Whitney engines (Maruyama et al., 1999).

24.4.9 Summary of structure-property relationships

An aluminum alloy product is usually selected based on its ability to provide the lightest and least costly structure. Specific strength is an important consideration as well as durability and damage tolerance in a number of forms. Resistance to



24.11 Specific stiffness–specific strength combinations for DRA materials in comparison to conventional aluminum alloys and graphite/epoxy composite laminates (Hunt, 1994).

catastrophic failure due to the presence of flaws (toughness), sub critical crack growth from cyclic loading (fatigue crack propagation) or environmental interactions (stress corrosion), among others, is important in the design of aircraft structures. Some of the microstructural features desired for a particular property are summarized in Table 24.7.

24.5 New products and recent manufacturing technologies

The majority of recent aluminum alloy developments have been associated, in one way or another, with cost; i.e. reducing the total cost of doing business. Fortunately, the new and improved alloys have also improved the performance of aircraft.

24.5.1 The cost of new materials and products

As mentioned previously, there have been a number of issues that have led to materials development for aircraft: the cost of fuel, value of increased range and landing weight fees have resulted in a focus to reduce weight. Problems associated

Table 24.7 Property–microstructure relationships in aluminum alloys

Property	Microstructural feature	Function of feature(s)
Strength	Uniform dispersion of small, hard particles, fine grain size	Inhibit dislocation motion
Ductility and toughness	No large particles, clean grain boundaries, fine structure, no shearable particles	Encourage plasticity, inhibit void formation and growth, work harden
Fatigue crack initiation resistance	No shearable particles, fine grain size, no surface defects	Prevent strain localization and slip steps on surface, prevent stress concentration
Fatigue crack propagation resistance	Shearable particles, no anodic phases or hydrogen traps, large grain size	Encourage crack closure, branching, deflection and slip reversibility
Pitting	No anodic phases	Prevent preferential dissolution of second phase particles
Stress corrosion cracking hydrogen embrittlement (HE)	No anodic phases, or interconnected hydrogen traps, hard particles	Prevent crack propagation due to anodic dissolution or HE, homogenize slip
Creep	Thermally stable particles on grain boundaries, large grain size	Inhibit grain boundary sliding

with an aging aircraft fleet, i.e. corrosion, fatigue cracks, etc. have resulted in a focus to improve corrosion resistance and damage tolerance. Loss of revenue and the cost of doing business have resulted in a focus to reduce production costs and therefore lower the cost of acquisition. Cost is currently a main driver and all new materials must 'buy' their way onto a new airplane.

The cost of materials for weight reduction should not exceed the costs saved from reduced fuel burn, maintenance and landing fees (Hyatt et al., 1989). Consequently, aerospace companies conduct a cost/benefit analysis for new candidate alloys. The total life-cycle cost consists of acquisition, operation and support costs. Acquisition costs consist of both recurring and non-recurring costs. The non-recurring development costs for design allowables are typically divided by the number of airplanes to be built using the candidate material, and thus add a fixed amount to the cost per pound saved (Hyatt and Axter, 1991). Boeing has developed a formula that is useful when evaluating projected weight savings for recurring materials costs (Hyatt and Axter, 1991):

$$\Delta Q = \frac{1}{u} \left[\frac{\Delta P}{\left(\frac{W_o}{W_c} - 1 \right)} - P_o \right] \quad [24.5]$$

where ΔQ is the cost difference per pound of weight saved, P_o is the price per pound of baseline material, ΔP is the difference in price per pound between the candidate and the baseline material, W_o is the weight of the baseline part, W_c is the weight of the candidate part, and u is the material utilization, i.e., the ratio between the weight of the part and the weight of the purchased material associated with the part.

There are a number of steps necessary before a new or improved material can buy its way onto a new airplane: These include: initial alloy design, development of design allowables, damage tolerance and durability testing, corrosion evaluation and testing, structural testing, electrical and thermal effects analysis, assembly processes and fastening, surface treatments, cost analysis, material/structural certification and manufacturing development.

24.5.2 New 7XXX alloy for the Airbus A380

In response to the need for a material that would develop high strength in thick sections required for the Airbus A380, Alcoa developed alloy 7085. This material has even lower quench sensitivity than 7050 and an improved combination of strength and toughness. The improvement is attributed to the elimination of coarse particles of Al_2CuMg on grain boundaries. The supporting structure of the F22 aircraft is made from forgings of 7085 (Fridez and Liu, 2004).

24.5.3 New Al-Li and AlMgSc aerospace alloys

New aluminum-lithium alloys have shown great potential for saving weight due to their low density, high modulus and mechanical properties that are competitive with other materials (Giummarra et al., 2008). Although there were a number of issues associated with the first and second generation of aluminum-lithium alloys, they were solved in the 1990s when the third generation of Al-Li alloys, beginning with the Weldalite® family, were developed (Lequeu et al., 2008). Some of the improvements were obtained by lowering the lithium content (<2%), controlling the texture and degree of recrystallization, and the addition of zinc to improve the stress corrosion cracking and exfoliation resistance, etc. (Giummarra et al., 2008). Isotropy in tensile and fracture properties have been enhanced through thermomechanical processing which incorporates intermediate recrystallization and optimization of Al_3Zr and $\text{Al}_{20}\text{Cu}_2\text{Mn}_3$ dispersoids (Liu, 2006). Alloys such as 2195, 2x96, 2x97, 2x98 and 2x99 have received significant commercial success in the United States on programs like the External Super Light Weight Tank of the Space Shuttle and the F16 fighter aircraft (Lequeu et al., 2008). Alloys 2196 and 2099 extrusions are being used for cross beams and seat tracks in the fuselage floor structure of the A380 (Tempus, 2009). One of the new alloys, 2198, is being evaluated for possible use for the fuselage skin for the Airbus A350 twin-engine aircraft (Knuewer et al., 2006; Tempus, 2009). 2198 in the T8X temper is being considered due to its combination of high static strength and high damage tolerance and high thermal stability. In addition, it can be laser-beam and friction-stir welded (Knuewer et al., 2006).

The demand for lighter structures and advanced manufacturing technologies has led to the development of AlMgSc alloys, which have a density similar to the latest aluminum-lithium alloys. They offer excellent fatigue and damage tolerance properties, good corrosion resistance and very good weld ability (Buerger et al., 2007). A basic patent for AlSc alloys was filed by ALCOA in 1971 (Willey, 1971) and since that time significant advances have been made in understanding the metallurgical principles and processing requirements for their development. Process technologies like melt spinning can produce a very stable microstructure in AlMgSc alloys compared to other aerospace aluminum alloys. One such alloy, ScaLA®, has been developed through a cooperative program of seven Austrian and two German companies (Gradinger et al., 2008). Strength properties of this second generation AlMgSc alloys are adjustable by the amount of Sc added to the alloy. Appropriate processing generates a very dense network of nano-scaled Al_3ScZr precipitates responsible for high strength (up to 600 MPa) and good notch toughness (Gradinger et al., 2008). Aleris has developed two high performance 5XXX AlMgSc alloys, which they designate as KO8242/KO8542, that are age creep formable, have low density, mid range strength and excellent fatigue crack growth resistance and good toughness (Miermeister et al., 2008). As with other AlMgSc alloys, these alloys

are amenable to laser-beam and friction-stir welding. Currently AlMgSc alloys are being considered by Airbus for use in future fuselage shells and high lift components (Gradinger et al., 2008).

24.5.4 Alloy 2040-T6 for aircraft wheels

Aluminum aircraft wheels are subjected to harsh and demanding operating conditions during service such as heat, carbon dust, runway and aircraft fluids and high-energy braking events. Consequently, strength at ambient and elevated temperatures, corrosion resistance, density, fatigue behavior and fracture resistance are primary material property drivers for an aircraft wheel alloy. The combination of these desired material properties drives the structural design of an aluminum aircraft wheel. Unlike automotive wheels, aircraft wheels are made of two parts: an inboard wheel half and an outboard wheel. The brakes are applied to the inner wheel, so it needs strength at elevated temperatures. Typically, alloy 2014 is used on the inboard wheel half and 7050 on the outboard. As planes got heavier, demands on wheels increased, so stronger alloys were evaluated in an attempt to save weight. The last test hurdle is a 'roll on rim test' designed to simulate the forces on a tireless wheel during a landing. Over decades, several candidate alloys passed tensile, fatigue, corrosion and fracture toughness criteria but failed this test up until 2040-T6. This material is expected to replace both 7050 and 2014-T6.

24.5.5 Manufacturing technology: friction-stir welding and laser welding

New joining methods have led to both a reduction in manufacturing cost and often weight savings in aircraft structures. These include both friction stir welding and laser-beam welding. Aluminum alloys were the first to be friction-stir welded. The process is solid state using a non-consumable rotating tool that creates a plastic layer between two materials and welds them together. The rotating tool, the pin, is plunged into the parts to be joined and stirs the material at the joint interface creating a bond (Stotler and Bernath, 2009). Friction stir welding offers many advantages over other solid-state welding processes, including little distortion, little if any weld shrinkage and a significant reduction in consumable costs (Stotler and Bernath, 2009). Eclipse Aviation first used friction stir welding in aircraft structures on the Eclipse 500 after they received FAA approval in 2002. Stotler and Bernath noted that at 20 inches per minute, friction stir welding is approximately 10 times faster than manual riveting and provides a continuous joint for improved structural rigidity. An extensive review of the application of friction stir welding to aluminum was recently published in *International Materials Reviews* (Threadgill et al., 2009).

Laser-beam welding can be used to join all of the light metals (Schubert et al., 2001). The technology for welding of aircraft structures was pioneered by Airbus (Hasler, 2008). Laser-beam welding is used for joining large metal fuselage parts with stringers, such as those in the Airbus A380 (Anon, 2005). Laser-beam welding is much faster (six meters per minute) than the speed of riveting (200–400 mm per minute) and has many advantages even though it requires a greater amount of inspection. Wide rivet straps in the aircraft skin and at the butt ends of the stringer are no longer required and the method eliminates the need for filler metal between the riveted parts, which reduce weight (Anon, 2005). In addition, the elimination of the rivets makes the structure less susceptible to corrosion.

25.5.6 Manufacturing technology: asymmetric rolling

Asymmetric rolling, in which the circumferential velocities of working rolls are different, imposes extensive shear deformation and can have a significant effect on the resulting microstructure and texture of aluminum and its alloys (Kim and Lee, 2001; Jin and Lloyd, 2005, 2007). Depending on the difference in velocities, roll diameter, temperature etc., textures can be modified and the grain structure refined (Jiang et al., 2009). Aleris has used this technology to develop what they refer to as ‘Snake Rolling’ to reduce porosity and refine the grain structure of 7050-T7451 (Miermeister et al., 2008). Miermeister et al. show that using snake-rolling on a 7050 alloy they can produce a significant reduction in crack growth and, therefore, reduce the inspection intervals on a metallic spar. In addition, the reduction in porosity can have a positive effect on fracture toughness.

24.5.7 Manufacturing technology: crystallographic texture

Rioja has discussed the relationship between processing, composition, texture and properties of aerospace aluminum alloys (1998). He noted that the ‘Brass’ texture component in unrecrystallized plate results in anisotropy in mechanical properties both in-plane and through thickness. Reducing the intensity of crystallographic texture can usually reduce the observed anisotropy. This may be accomplished by recrystallization during solution heat treatment or during an intermediate step when processing wrought alloys, reducing the amount of deformation, replacing coherent dispersoids with semi-coherent/incoherent dispersoids, i.e. by composition control and thermo-mechanical processing (Rioja et al., 2008). Rioja et al. also noted that the dependence of properties on texture is different for T3 and T8 type tempers in 2XXX alloys. The ‘Goss’ texture seems to improve the strength/toughness relationship in recrystallized fuselage sheet in the T-3 tempers and the ‘Brass’ texture improves the fatigue crack growth resistance of plate products in T3 tempers for lower wing applications.

24.6 Conclusion

The combination of specific properties, cost, predictable behavior and reliability, coupled with years of experience in manufacturing, recyclability and a minimal environmental impact, plus the continued development of improved alloys and processes will ensure that aluminum will continue to be widely used for subsonic aircraft in the foreseeable future.

24.7 References

- A. Anon (2005) 'Laser-beam welding makes aircraft lighter', *Fraunhofer Magazine*, 1: 36–37.
- Anderson, W.E. and Quist, W.E. (1966) Aluminum Alloy, United States Patent Number 3, 284, 193.
- Ashton, R.F., Thompson, D.S. and Gayle, F.W. (1986) 'The effect of processing on the properties of Al-Li alloys', in Starke, E.A., Jr and Sanders, T.H., Jr (Eds): *Aluminum Alloys: Their Physical and Mechanical Properties*, EMAS, West Midlands, pp. 403–417.
- Ashton, R.F., Thompson, D.S., Starke, E.A., Jr and Lin, F.S. (1986) 'Processing Al-Li-Cu-(Mg) alloys', in Baker, C., Gregson, P.J. Harris, S.J. and Peel, C.J. (Eds): *Aluminum-Lithium Alloys III*, The Institute of Metals, London, pp. 66–77.
- Bate, P., Roberts, W.T. and Wilson, D.V. (1982) 'The plastic anisotropy of two-phase aluminum alloys-II: anisotropic behavior', *Acta Metallica*, 30: 725–737.
- Bishop, J.F.W. and Hill, R. (1951) 'A theory of the plastic distortion of a polycrystalline aggregate under combined stresses', *Philosophical Magazine*, 42: 414–427.
- Bucci, R.J., Bush, R.W., Hinkle, A.J., Konish, H.J., Kulak, M., Wygonik, R.H. and Kuhlman, G.W. (1998) *Aluminum Alloy Forgings: Property/Performance Attributes, Focus Fatigue and Durability Service Capabilities*, AGARD Advisory Report 353, Advisory Group for Aerospace Research and Development, North Atlantic Treaty Organization.
- Cassada, W.A., Shiflet, G.J. and Starke, E.A., Jr. (1991) 'The effect of plastic deformation on Al₂CuLi precipitation', *Metallurgical Transactions A*, 22: 299–306.
- Chin, G.Y. and Mammel, W.L. (1969) 'Generalization and equivalence of the minimum work', *Transactions of the Metallurgical Society of AIME*, 245, 1211–1214.
- Dermarck, S., Mace, R., Lassince, P., Fertou, D. and Sainfort, P. (1994) 'New developments of aluminum products for aerospace applications', in Hognat, J., Pinzelli, R. and Gillard, E. (Eds): *50 Years of Advanced Materials or Back to the Future*, Proceedings of the 15th International European Chapter Conference of the Society for the Advance of Material and Process Engineering, Toulouse, France, pp. 139–148.
- Fridez, J.D., Liu, John (2004) 'New Aluminum Alloy Products for the Airbus A380', Paper presented at *Aluminum 2004*, 30 August, Essen, Germany.
- Gangloff, R.P. (1989) 'Corrosion fatigue crack propagation in metals', in Gangloff, R.P. and Ires, M.B. (Eds): *Proceedings of the First International Conference on the Environment-Induced Cracking of Metals*, NACE, Houston, Texas, pp. 55–109.
- Gayle, F.W. and Goodway, M. (1994) 'Precipitation hardening in the first aerospace aluminum alloy: the Wright flyer crankcase', *Science*, 266: 1015–1017.

- Giummarra, C., Rioja, R.J., Bray, G.H., Magnusen, P.E. and Moran, J.P. (2008) 'Development of corrosion resistance, high toughness aluminum-lithium aerospace alloys', in Hirsch, J., Skrotzki, B. and Gottstein, G. (Eds): *Aluminum Alloys: Their Physical and Mechanical Properties, ICAAI*, Wiley-VCH GmbH & Co, pp. 176–194.
- Gradinger, R., Schneider, R., Palm, F. (2008) '2nd Generation of AlMgSc materials dedicated for short manufacturing chains in the aerospace industry', *1st EUCOMAS Conference*, Berlin, pp. 63–76.
- Harpur, N.F. (1968) 'Concord structural development', *Journal of Aircraft*, 5: 176–183.
- Hasler, A. (2008) 'Technical challenges and solutions for aluminium in the transportation market', in Hirsch, J., Skrotzki, B. and Gottstein, G. (Eds): *Aluminum Alloys: Their Physical and Mechanical Properties*, Wiley-VCH GmbH & Co, Weinheim, Germany, pp. 24–34.
- Hatch, J. (1984) 'Metallurgy of heat treatment', *Aluminum: Properties and Physical Metallurgy*, pp. 134–199.
- Holroyd, N.J.H. (1989) 'Environment-induced cracking of high-strength aluminum alloys', in R.P. Gangloff and M.B. Ives (Eds): *Environment-Induced Cracking of Metals, Proceedings of the First International Conference*, NACE, Houston, TX, pp. 311–345.
- Hornbogen, E. and Starke, E.A., Jr (1993) 'Theory assisted design of high strength low alloy aluminium', *Acta Metallurgica et Materialia*, 41: 1–16.
- Hosford, W.F. and Zeisloft, R.H. (1972) 'The anisotropy of age-hardened Al-4%Cu single crystals during plane-strain compression', *Metallurgical and Materials Transactions B*, 3: 113–121.
- Hunt, W.A., Jr (1994) 'Discontinuously reinforced aluminum – the second generation', in Ravi, V.A., Srivatsan, T.S. and More, J.J. (Eds): *Processing and Fabrication of Advanced Materials III*, The Minerals, Metals and Materials Society, London, pp. 663–681.
- Hyatt, M.V., and Axter, S.E. (1991) 'Aluminium alloy development for subsonic and supersonic aircraft, in Proceedings of the International Conference of Recent Advances in Science and Engineering of Light Metals, pp. 273–280 (Herano, K., Oikawa, H. and Ikeda, K. (Eds).) Institute of Light Metals, Tokyo.
- Hyatt, M.V., Caton, R. and Lovell, D. (1989) 'Advanced materials development in commercial aircraft', Paper presented at the *AIAA/AHS/ASEE Aircraft Design, Systems and Operations Conference*, Seattle, WA, American Institute of Aeronautics and Astronautics, Washington, DC.
- Jiang, J., Ding, Y., Zuo, F. and Shan, A. (2009) 'Mechanical properties and microstructures of ultrafine-grained pure aluminum', *Scripta Materialia*, 60(10): 905–908.
- Jin, H. and Lloyd, D.J. (2005) 'The reduction of planar anisotropy by texture modification through asymmetric rolling and annealing of AA5754', *Materials Science and Engineering: A*, 399(1–2): 358–367.
- Jin, H. and Lloyd, D.J. (2007) 'Evolution of texture in AA6111 aluminum alloy after asymmetric rolling with various velocity ratios between top and bottom rolls', *Materials Science and Engineering: A*, 465(1–2): 267–273.
- Kim, K.H. and Lee, D.N. (2001) 'Analysis of deformation textures of asymmetrically rolled aluminum sheets', *Acta Materialia*, 49(13): 2583–2595.
- Knuever, M., Schumacher, J., Ribes, H., Eberl, F. and Bes, B. (2006) '2198 – Advanced aluminium-lithium alloy for A350 fuselage skin sheet', Paper presented at the *17th AeroMat Conference & Exposition*, Seattle, Washington.

- Lequeu, P., Eberl, F., Warner, T., Danielou, A. and Bes, B. (2008) 'Latest generation of Al-Li alloys developed by Alcan Aerospace', *1st EUCOMAS Conference*, Berlin, pp. 77–83.
- Liu, John (2006) 'Advanced aluminum and hybrid aerostructures for future aircraft', *Material Science Forum*, 519–521: 1233–1238.
- Lukasak, D. and Hart, R. (1991) 'Aluminum alloy development efforts for compression dominated structure of aircraft'. Paper No. 1985, Society of Allied Weight Engineers.
- Magnusen, P.E., Bucci, R.J., Hinkle, A.J., Brockenbrough, J.R., Konish, H.J. and Miyasato, S.M. (1995) *The Role of Microstructure on the Fatigue Durability of Aluminum Aircraft Alloys*, Final Report ONR Contract N00014-91-C-0128, Office of Naval Research.
- Maruyama, B. and Hunt, W.H., Jr. (1999), 'Discontinuously reinforced aluminum: Current status and future direction', *Journal of the Minerals*, 51(11): 59–61.
- Miermeister, M., Bürger, A., Spangel, S., Kröpfel, I. and Heinz, A. (2008) 'Aleris' advanced aluminium sheet and plate products for high-performance aircraft applications', Paper presented at the *1st EUCOMAS Conference*, Berlin, pp. 85–100.
- Piascik, R.S. and Willard, S.A. (1994) 'The growth of small corrosion fatigue cracks in alloy 2024', *Fatigue and Fracture of Engineering Materials and Structures*, 17: 1247–1259.
- Polmear, I.J. (1989) *Light Alloys, Metallurgy of the Light Metals*, p. 31, Edward Arnold, London.
- Quist, W.E. (1963) *Effect of Composition on the Fracture Properties of Aluminum Alloy 7178*, MSc Thesis. University of Washington, Seattle.
- Rioja, R.J. (1998) 'Fabrication methods to manufacture isotropic Al-Li alloys and products for space and aerospace applications', *Materials Science and Engineering: A*, 257: 100–107.
- Rioja, R.J., Giummarra, C. and Cheong, S. (2008) 'The roll of crystallographic texture on the performance of flat rolled aluminum products for aerospace applications', *TMS Light Metals* (ed. David H. DeYoung), pp. 1065–1069.
- Sarkar, B., Marek, M. and Starke, E.A., Jr (1981) 'The effect of copper content and heat treatment on the SCC characteristics of Al-6Zn-2Mg-XCu alloys', *Metallurgical and Materials Transactions A*, 12: 1939–1943.
- Schubert, E., Klassen, M., Zerner, I., Walz, C. and Sepold, G. (2001) 'Light-weight structures produced by laser-beam joining for future applications in the automotive and aerospace industry', *Journal of Materials Processing Technology*, 115(1): 2–8.
- Smith, R.K. (1991) 'The quest for excellence', in Greenwood, J.T. (Ed.): *Milestones of Aviation*, Crescent Books, New York, pp. 222–296.
- Staley, J.T. (1975) 'Microstructure and toughness of high strength alloys', Presented at the *ASTM Symposium on Properties Related to Toughness*, 22–27 June, Montreal, Canada.
- Staley, J.T. (1987) 'Quench factor analysis of aluminum alloys', *Materials Science and Technology*, 3: 923–935.
- Staley, J.T. (1992) 'Metallurgical aspects affecting strength of heat-treatable alloy products used in the aerospace industry', in Arnberg, L., Lohne, O., Nes, E. and Ryum, N. (Eds): *The 3rd International Conference on Aluminum Alloys, Their Physical and Mechanical Properties*, Vol. III, The Norwegian Institute of Technology anti SINTEF Metallurgy, Trondheim, Norway, pp. 107–143.
- Staley, J.T. and Lege, D.J. (1993) 'Advances in aluminum alloy products for structural applications in transportation', *Journal De Physique IV, Colloque C7*, 3: 179–190.
- Staley, J.T., Byrne, S.C., Colvin, E.L. and Kinnear, K.P. (1996) 'Corrosion and stress-corrosion of 7XXX-W products', *Materials Science Forum*, 217–222: 1587–1592.

- Starke, E.A., Jr (1970) 'The causes and effects of denuded or precipitate free zones at grain boundaries in aluminium-base alloys', *Journal of Metals*, January 1970, vol. 22, pp. 54–63.
- Starke, E.A., Jr (1977) 'Aluminum alloys of the 70's: scientific solutions to engineering problems', *Materials Science and Engineering: A*, 29: 99–115.
- Starke, E.A., Jr (1983) 'The application of the fundamentals of strengthening to the design of new aluminum alloys', in Grifkins, R.C. (Ed.): *Strength of Metals and Alloys*, ICSMA, 6, Pergamon Press, Oxford, pp. 1025–1044.
- Starke, E.A., Jr and Lütjering, G. (1979) 'Cyclic plastic deformation and microstructure', in Meshii, M. (Ed.): *Fatigue and Microstructure*, American Society of Metals, Metals Park, OH, pp. 205–243.
- Starke, E.A., Jr and Williams, J.C. (1989) 'Microstructure and the fracture mechanics of fatigue crack propagation', in Wei, R.P. and Gangloff, R.P. (Eds): *Fracture Mechanics: Perspectives and Directions*, STP 1020, ASTM, Philadelphia, pp. 184–205.
- Starke, E.A., Jr (1989) 'Heat treatable aluminum alloys', in Vasudevan, A.K. and Doherty, R.D. (Eds): *Aluminum Alloys-Contemporary Research and Applications*, Academic Press, San Diego, CA, pp. 35–63.
- Starke, E.A., Jr and Hornbogen, E. (2008) 'Precipitation hardening: from Alfred Wilm to the present', in Hirsch, J., Skrotzki, B. and Gottstein, G. (Eds): *Aluminium Alloys: Their Physical and Mechanical Properties*, ICAAI1, Wiley-VCH GmbH, pp. 3–13.
- Stotler, T. and Bernath, J. (2009) 'Friction stir welding advances', *Advanced Materials & Processes*, 167(3): 35–37.
- Sugamata, M., Blankenship, C.P., Jr and Starke, E.A., Jr (1993) 'Predicting plane strain fracture toughness of Al-Li-Cu-Mg alloys', *Materials Science and Engineering: A*, 163: 1–10.
- Taylor, G.I. (1938) 'Plastic strain in metals', *Journal of the Japan Institute of Metals*, 62: 307–324.
- Tempus, G. (2009) Airbus Deutschland GmbH, Bremen, Germany, private communication with E.A. Starke, Jr.
- Thompson, D.S. and Levy, S.A. (1970) AFML-TR-70-171, Wright-Patterson Air Force Base, OH.
- Threadgill, P.L., Leonard, A.J., Shercliff, H.R. and Withers, P.J. (2009) 'Friction stir welding of aluminium alloys', *International Materials Reviews*, 54(2): 49–93.
- Van Stone, R.H. and Psioda, J.A. (1975) 'Discussion of metallurgical factors affecting fracture toughness of aluminum alloys', *Metallurgical and Materials Transactions A*, 6(4): 668–670.
- Wiley, L.A. (1971) U.S. Patent 3619181.
- Zener, C., private communication to C.S. Smith (1948) 'Grains, phases and interfaces: An interpretation of microstructures', *Transactions of the Metallurgical Society of AIME*, 175: 15.

Materials selection and substitution using aluminium alloys

M. LEARY, RMIT University, Australia

Abstract: This chapter presents a systematic material selection methodology for comparing candidate materials for a specified design scenario. Procedures appropriate for simple geometries and single objectives are presented initially; these procedures are expanded to accommodate sophisticated analyses, including design for a finite lifetime, compromise between multiple objectives defined in non-commensurate units, analysis of non-trivial geometries and topographic optimisation using numeric methods. These procedures are applied with reference to pertinent aluminium substitution scenarios. A specific focus of the chapter is the environmental consequence of material selection. The chapter concludes with a summary of the design scenarios which provide opportunities to achieve competitive advantage by the application of aluminium alloys.

Key words: material selection, fatigue-limited design, non-stationary applications, environmental impact, value functions.

25.1 Introduction

The intended outcome of the material selection process is the identification of one or more materials with properties that satisfy the functional requirements of a product, such as strength or stiffness. Furthermore, it is desirable, although not mandatory, that the materials optimise performance objectives, for example the minimisation of cost or environmental impact. Material selection is a multidisciplinary task which requires the interaction of numerous stakeholders, including product designers, material scientists, test engineers and end-users. Consequently, material selection problems are typically open-ended, with the preferred solution being subject to an ongoing trade-off between numerous constraints and objectives.

Material selection is subject to numerous uncertainties, including those associated with the design specification and material properties. Robust material selection requires a design specification which comprehensively defines the functional requirements and objectives of a product; however, the design specification is often incomplete or poorly defined. Furthermore, the dominant failure mode is a function of the materials used, and a design specification which is valid for one material type may not be valid for another material. Those involved in material substitution must be cautious that the use of novel materials does not reveal a latent failure mode not identified in the initial design specification.

Material selection problems are typically subject to multiple constraints and objectives. These may be measured in non-commensurate units, for example cost and mass, making direct comparison difficult. Material properties are another source of uncertainty. Material property data may be sparse, or measured by experimental methods which are not directly comparable. The associated properties may display significant statistical scatter or may be highly dependant on specific processing attributes.

Owing to these significant uncertainties, material selection problems are often highly complex and material selection decisions are often based on intuition or precedent. This approach is problematic as material selection outcomes are often counterintuitive and cannot be intuitively resolved, and precedent-based design is not appropriate in the face of changing design specifications, for example the increasingly stringent restrictions associated with environmental impact and fuel consumption.

To avoid these pitfalls, this chapter presents systematic material selection procedures to impartially evaluate the feasibility and optimality of candidate materials. These procedures can be applied by either design engineers to evaluate materials for a specific scenario or by material suppliers to identify the scenarios which are best suited to a specific material of interest. Material selection procedures are presented for a range of important design scenarios, including compromise between non-commensurate objectives, common structural elements, analysis of non-trivial geometries and topographic optimisation using numeric methods. The chapter provides novel procedures for fatigue-limited design and new insight into the environmental consequence of material selection. These procedures are applied to characterise the performance of aluminium alloys relative to other candidate materials of interest. Scenarios for which aluminium alloys provide opportunities to achieve competitive advantage are identified.

25.2 Fundamental material selection strategies

25.2.1 Material selection methods

Based on Prof Mike Ashby's significant contribution to the field of material selection (Ashby, 1997a, 1997b; Ashby, 2000; Ashby, 2005; Ashby and Bréchet, 2002; Ashby and Cebon, 2001; Ashby and Johnson, 2003; Ashby and Jones, 1993a, 1993b; Esawi and Ashby, 2003; Sirisalee et al., 2003; Weaver and Ashby, 1997; Wegst and Ashby, 2000), the feasibility and performance of a material for a specific design scenario may be directly evaluated from the constraints and objectives associated with the design specification. Design constraints lead to *material property limits* that screen feasible materials according to the associated material properties. Design objectives lead to ratios of material properties, known as *material selection indices*, that rank the

performance of a material for a given objective. Screening a group of candidate materials by the associated material property limits, and ranking the feasible materials by the material selection indices, allows identification of the optimal material(s) for a specific design scenario (Ashby, 2000).

Material property limits

Design constraints restrict the range of acceptable material properties, thereby defining the associated solution space and providing a screening mechanism that allows identification of materials that are feasible for the design specification. Material property limits may be designated as hard or soft depending on whether the associated constraint is absolute or open to some negotiation, respectively. Constraints of importance are typically associated with maximum cost, minimum design-life, available spatial envelope and allowable deflection.

Material selection indices

A metric of component performance, P , may be fully defined by its functional requirements, F , geometric attributes, G , and associated material properties, M (Ashby, 2005). If these variables are independent, performance may be expressed as a separable function:

$$P = f_1(F)f_2(G)f_3(M) \quad [25.1]$$

For a given functional requirement and geometry, $f_1(F)f_2(G)$, performance is proportional to a specific combination of material properties, defined as the *material index*, M . This representation is applied in the following material property charts (Section 25.2.2). An alternate representation is also used in this work. M^* is the reciprocal of M , and performance is optimised by minimising M^* (Table 25.1). This representation may be more logical for scenarios where the performance measure should be minimised, for example mass or cost, and is compatible with the value function methods of Section 25.6.1. For relevant material properties, α and β , the general form of the material index is:

$$M^* = \left(\frac{\alpha}{\beta^{1/k}} \right) = C \quad [25.2]$$

Material selection indices provide a powerful design tool for guiding material selection for a given design scenario, allowing:

- identification of the material properties relevant to performance
- definition of the relative importance of the relevant material properties
- comparison of the performance of specific materials

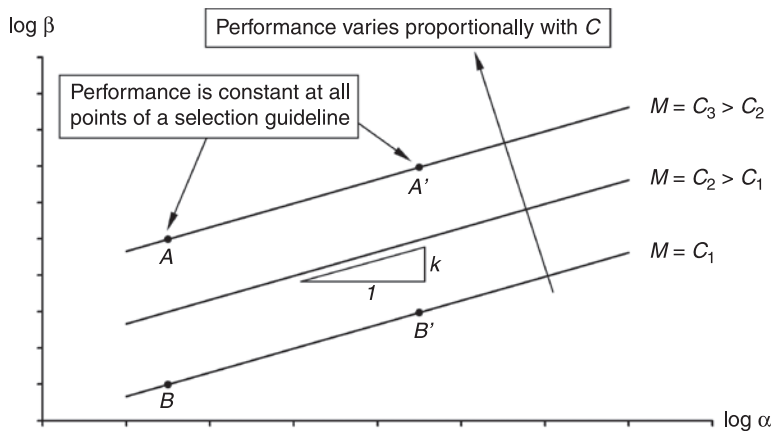
Table 25.1 Material selection indices including the associated free variable and guideline gradient k for strength limited design of beam, tie and plate elements subject to a range of important design objectives

Design objective						
Free variable		k	Minimal mass	Minimal cost	Minimal embodied energy	Minimal CO ₂ emissions
Structural element	Tie	1	$M_{1m}^* = \left(\frac{\rho}{S}\right)$	$M_{1c}^* = \left(\frac{C_m \rho}{S}\right) = C_m M_{1m}^*$	$M_{1e}^* = \left(\frac{E_e \rho}{S}\right) = E_e M_{1m}^*$	$M_{1CO_2}^* = \left(\frac{C_c \rho}{S}\right) = E_c M_{1m}^*$
	w					
	Beam	A (w = d)	3/2	$M_{3/2m}^* = \left(\frac{\rho}{S^{2/3}}\right)$	$M_{3/2c}^* = C_m M_{3/2m}^*$	$M_{3/2e}^* = E_e M_{3/2m}^*$
Plate	d	2	$M_{2m}^* = \left(\frac{\rho}{S^{1/2}}\right)$	$M_{2c}^* = \left(\frac{C_m \rho}{S^{1/2}}\right) = C_m M_{2m}^*$	$M_{2e}^* = \left(\frac{E_e \rho}{S^{1/2}}\right) = E_e M_{2m}^*$	$M_{2CO_2}^* = \left(\frac{E_c \rho}{S^{1/2}}\right) = E_c M_{2m}^*$
	d					

Notes: Nomenclature: material density (ρ), material cost per unit mass (C_m), strength parameter (S), Area (A), width (w), depth (d), material index (M^*_{en}). The first suffix of a material index is the guideline gradient (k), the second suffix refers to the design objective: mass (m), cost (c), embodied energy (e) or CO₂ emissions (CO₂).

25.2.2 Material property charts

When plotted on a log-log chart of the relevant material properties, known as a *material property chart*, the locus of constant performance forms a linear *selection guideline*, with *guideline gradient*, k . The selection guideline is a powerful tool for robust and systematic material selection. For a family of selection guidelines, performance is constant at any point along a selection guideline and is proportional to the constant, C , i.e. the performance at point A is equal to that of point A' (Fig. 25.1). For this work, the physical difference is that the volume of a component made with material A will be greater than that associated with material A' . This outcome is of importance to low density materials such as aluminium. When applying the selection guidelines relevant to this work, performance is maximised towards the upper left hand side of the material property chart. Each combination of structural element and associated free variable has a specific guideline gradient, k (Table 25.1). The guideline gradient defines the relative contribution of the relevant material properties to performance.

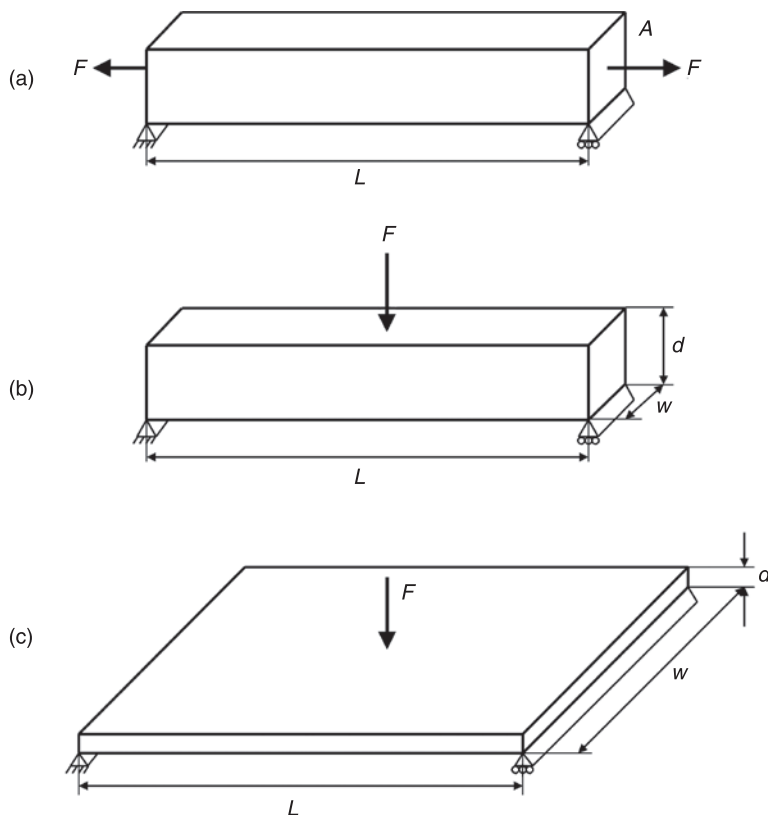


25.1 A generic material property chart, or Ashby map, indicating a family of selection guidelines for relevant material properties α and β .

25.2.3 Material selection indices

Structural components comprise many distinct structural elements, including ties, beams and plates (Fig. 25.2). To simplify analysis, the pertinent geometry of each structural element may be represented by an associated *free variable*. Material selection indices for the identified structural elements have been derived for a series of relevant design objectives (Table 25.1). In summary, these material selection indices are:

- a function of the associated density, ρ , material cost per unit mass, C_m , and the relevant strength parameter, S , which can be yield, ultimate or fatigue-strength



25.2 Simplified structural elements: tie (a), beam (b) and plate (c). Nomenclature: Force (F), Area (A), Length (L), width (w), depth (d).

- independent of the associated boundary conditions, for example the material selection index is independent of whether a structural element has built-in or pin jointed supports
- equal for a tie with area as the free variable and a beam with width as the free variable. This scenario results in the lowest guideline gradient for the material selection indices of interest, i.e. $k = 1$
- equal for a plate with depth as the free variable and a beam with depth as the free variable. This scenario results in the largest guideline gradient for the material selection indices of interest, i.e. $k = 2$.

25.2.4 Potential limitations of material data and selection procedures

When engaging in material selection based on reported material properties, it is important to consider that reported values are typically subject to considerable

uncertainty. The magnitude of this uncertainty is a function of the physical phenomena responsible for the identified failure mode, the testing method applied and the associated sample size. Material selection methods typically focus on design for static properties; however, fatigue-limited structures present an underutilised opportunity for aluminium alloy application and are an important focus of this work. The fatigue failure mode introduces significant design uncertainties:

- Fatigue failure is the consequence of highly localised phenomena, resulting in significant stochastic uncertainties. Extensive sampling is required to characterise these uncertainties, due to the ‘terribly bad representation of a population by a sample’ (Jahn and Maennig, 1997).
- Production imperatives and available budgets typically do not allow for a statistically robust sample size (e.g. Svensson, 2004; Veers, 1996).
- The availability of fatigue test data is limited by the time and cost of data acquisition, which is significantly greater than for static tensile data.
- Fatigue data such as the stress-life (S–N) curves applied in this work are typically presented for a 50% survival probability only, with no explicit estimate of the associated distribution (Maennig, 1996).
- Fatigue analysis is typically based on data obtained from the public domain. Unfortunately, reported fatigue data often have limited applicability due to insufficient documentation of the associated testing conditions. A set of core requirements have been developed to quantify the applicability of reported fatigue test data (Leary and Burvill, 2009). This limitation is especially problematic for magnesium alloys, for which relatively little data are available in the public domain. The data reported in this work for magnesium are based on the most appropriate in the available literature; however, it may be based on higher than average properties which overestimate performance in comparison with aluminium (which is reported for typical values).
- Uncertainty is introduced when mismatch exists between the loading mode and ambient conditions of the test specimen and the conditions of the component under consideration (e.g. Dowling, 1993; Rothbart, 1996).
- A series of disparate test modes are applied for the generation of explicit S–N curves, i.e. rotating bending, alternating bending and uniaxial tension. For a given maximum stress, these modes result in an appreciable variation in the reported fatigue strength (Esin, 1980). The level of variation between test modes decreases with increasing fatigue life, and modification factors have been proposed to accommodate this discordance.
- Material selection indices may provide a non-conservative approximation of the total component mass, as additional mass is not explicitly accounted for, such as the mass associated with end-connectors.

Material property charts are based on nominal values and the associated stochastic variation is not indicated. Of the presented data, Young’s Modulus and material density are subject to very low variation and the results can be applied

with high certainty. By comparison, fatigue strength is subject to significant variation and the associated conclusions should be treated conservatively and confirmed experimentally.

Environmental impact is an increasingly important design consideration, however, there is little consensus on measurement strategies and the associated metrics include uncertainties due to the imprecise nature of the available data and associated estimates. For example (ISO, 1998):

- The definition of an acceptable system boundary is highly complex and difficult to document.
- Emissions vary significantly due to differences in manufacturing methods, power sources and transport distances.

Generic estimates of environmental impact are useful for preliminary analysis, before design effort is expended on a customised life-cycle analysis. However, to acknowledge the identified uncertainties, the reported estimates should include a tolerance bound where possible (Table 25.2).

Despite the associated stochastic uncertainties, physical test data for a given composition will remain constant with time. Material costs are subject to continuous fluctuation (Fig. 25.3), and vary significantly between suppliers and geographic regions. The data included in this work are based on price estimates from commercial software and local and international suppliers. In addition, material comparisons are based on raw material cost only, i.e. production costs associated with each material class are assumed equal. This assumption is valid for initial analysis or when considering material selection for a specific manufacturing process (an example of additional material costs is identified in Section 25.5.2). Environmental consequences of material selection are also subject to time-based variation, as the associated energy consumption and pollution is highly dependant on the specific processing methods applied, which may vary as new manufacturing processes are introduced. Material comparisons based on generic estimates of cost and environmental impact are useful for preliminary analysis rather than the identification of absolute values.

25.3 Material selection for specific scenarios

25.3.1 Material classification

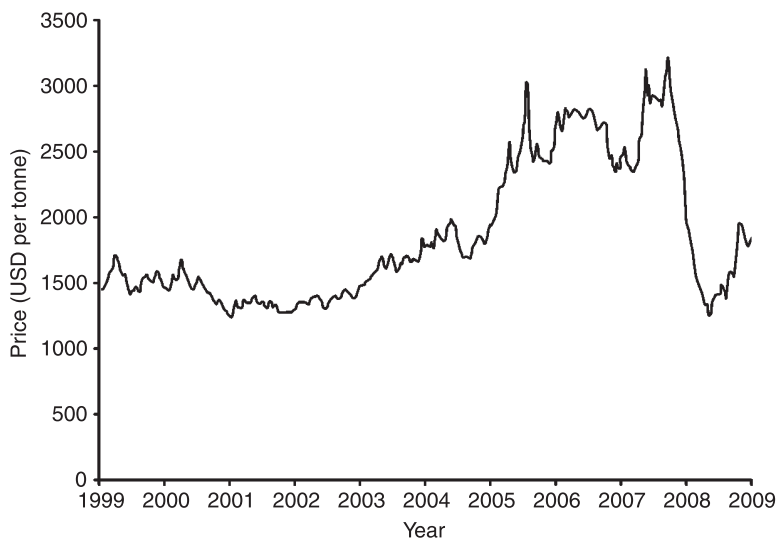
Systematic material selection requires access to a comprehensive database of material properties and feasible processing methods. For example, the Cambridge Engineering Selector (CES EduPack, 2005) includes several thousand entries from a comprehensive spectrum of material types (Ashby and Cebon, 2001; 2002). These materials may be combined to generate custom material property charts for a range of design scenarios, such as:

- yield-strength limited design
- tensile-strength limited design

Table 25.2 Material properties of the candidate light alloy substitute materials and a reference ferrous

Material specification	Sub-class	Common applications	Yield strength, S_y [MPa]	Tensile strength, S_{ut} [MPa]	Fatigue limit, S_∞ [MPa]	Endurance limit, S_e [MPa]	Density, ρ [kg/m ³]	Embodied energy, E_e (MJ/kg)	CO ₂ emissions, E_c (kg/kg)	Material cost, C_m [\$US/kg]
2024-T4	Aluminium	Aerospace, transport	330	460	–	122	2770	184–203	11.6–12.8	2.64
6061-T6	Aluminium	Architectural, transport	276	310	–	81	2710	184–203	11.6–12.8	2.37
7075-T6	Aluminium	Weight critical applications	496	565	–	141	2800	184–203	11.6–12.8	2.77
AZ31B-F	Magnesium	Aerospace, racing vehicles	132	234	–	130	1770	356–394	22.4–24.8	8.25
ZK60A-T5	Magnesium	Aerospace, transport	180	289	–	125	1824	356–394	22.4–24.8	22.7
Ti-6-4	Titanium	Weight critical applications	1070	1025	623	–	4430	855–945	53.8–59.5	35.3
AISI 1040	Steel	Automotive suspension	365	550	296	–	7845	22.4–24.8	1.9–2.1	0.35

Source: Material properties obtained for from a range of sources (Battelle, 1998; Boyer, 1986; CES, 2005; Lampman, 1995). Material cost based on estimates for raw material offered by international and domestic suppliers.



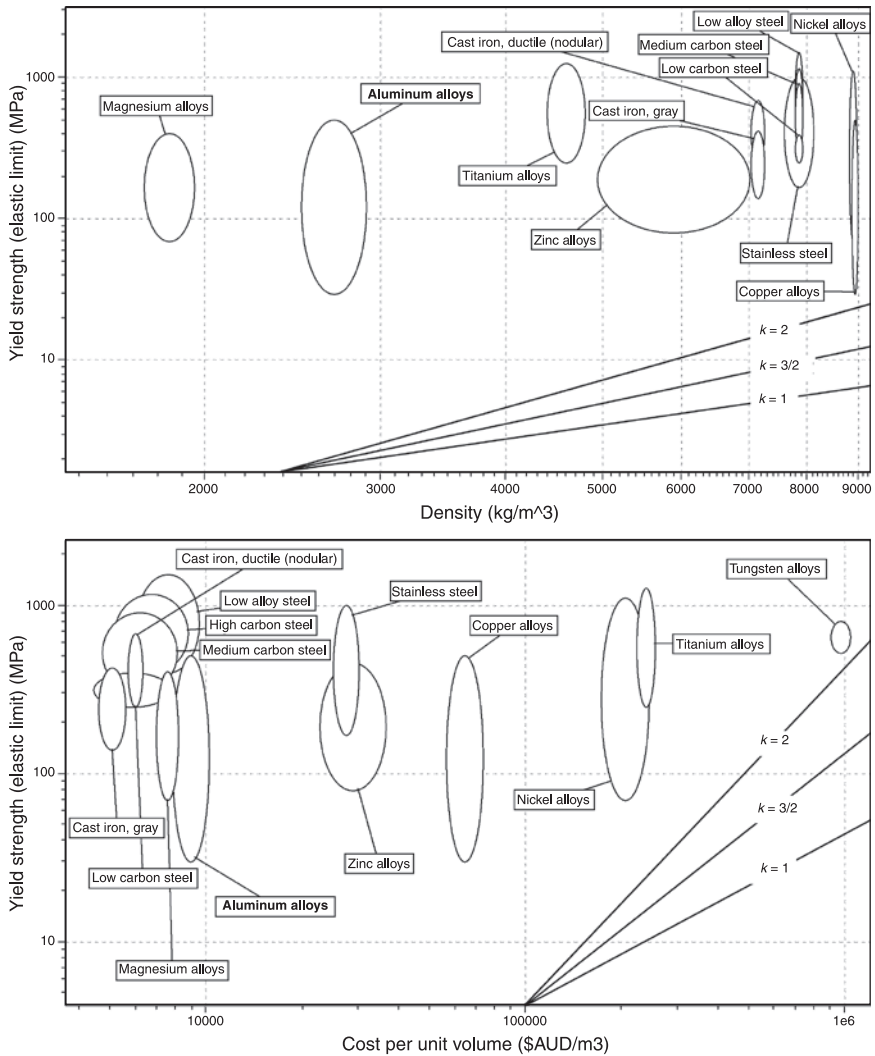
25.3 Variation of aluminium cash-buyer price for the decade ending 2009 (source: London Metal Exchange).

- stiffness-limited design
- fatigue-limited design

Material property charts are presented for yield and fatigue-limited design (presented for infinite life, Section 25.3.3) for the objectives of minimal mass and minimal cost (Fig. 25.4 and 25.5).

25.3.2 General material property chart outcomes

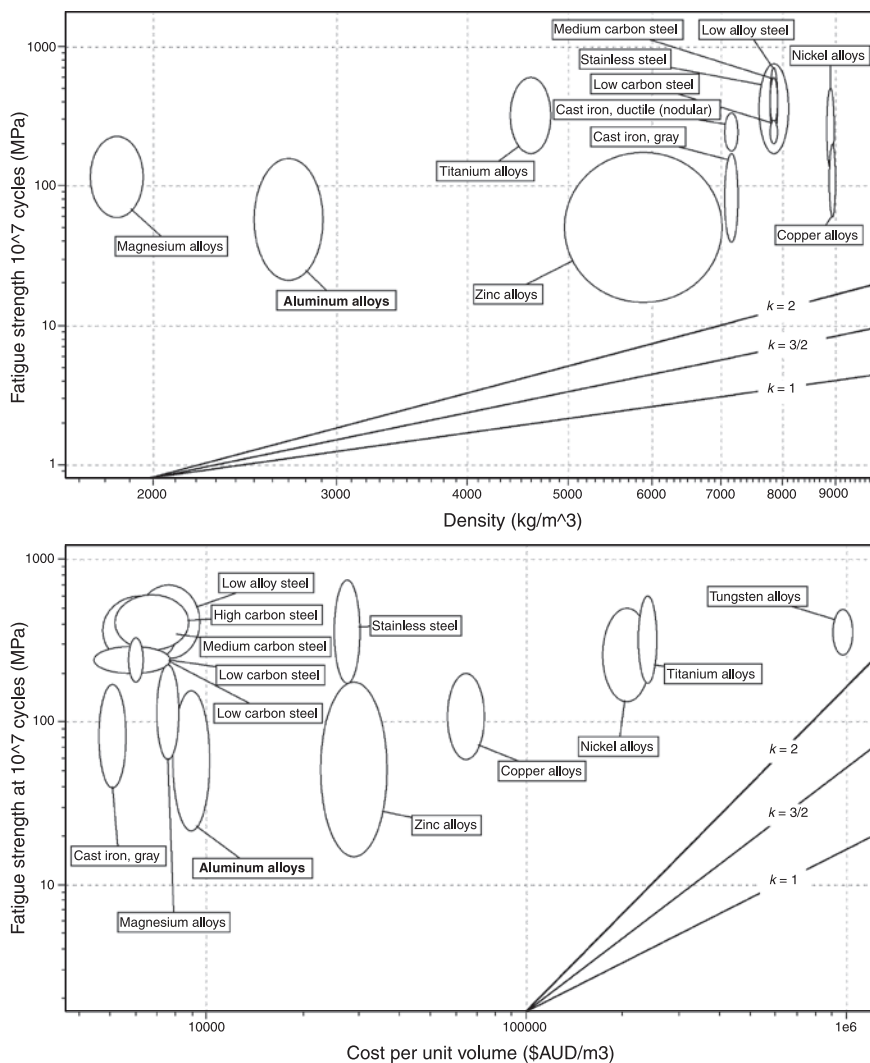
Each combination of structural element and associated free variable has a specific guideline gradient, k (Table 25.1). The guideline gradient defines the importance of the relevant material properties (Fig. 25.4 and 25.5). For low values of k , such as for a tensile element, the selection guideline tends towards the horizontal axis of the material property chart. Consequently, performance scales with the vertical-axis; i.e. the mechanical property term. These material selection scenarios benefit from high strength in preference to low density. These scenarios are not optimal for light alloy application, for example yield-limited minimal mass design (Fig. 25.4). For large values of k , such as for a plate element or variable depth beam, the selection guideline tends towards the vertical, and performance scales with the horizontal-axis; i.e. the material density, ρ , for minimal mass design and the cost per unit volume, $C_m\rho$, for minimal cost design. Design scenarios with high values of k benefit from a low density (or cost per unit volume for minimal cost design) in preference to high mechanical properties. Consequently, scenarios with high values of k provide the best opportunity for the application of aluminium alloys.



25.4 Material property charts for yield strength limited design, including selection guidelines relevant to this work. Upper: minimal mass design. Lower: minimal cost design (charts from the CES EduPack, 2005).

25.3.3 Non-trivial geometries

The material property charts provide a robust mechanism to select optimal materials for single objective design scenarios. Extension of these outcomes to complex (non-trivial) product geometries may result in mismatch between the theoretical and actual outcomes. Non-trivial product geometries can often be simulated by combining the basic structural elements with appropriate stress concentration factors



25.5 Material property charts for fatigue strength limited design, with selection guidelines relevant to this work. Upper: minimal mass design. Lower: minimal cost design (charts from the CES EduPack, 2005).

(e.g. Peterson, 1953; Pilkey, 1997), thereby increasing the scope of material selection scenarios for which the material selection curves may be applied. For complex geometries that cannot be accommodated by these methods, a practical compromise is to apply material property charts to refine the quantity of material selection choices and apply numeric optimisation methods to these candidates (Section 25.5.1).

The application of stress concentration factors is appropriate for light alloys and most ferrous metals which are not subject to dynamic loading. An important

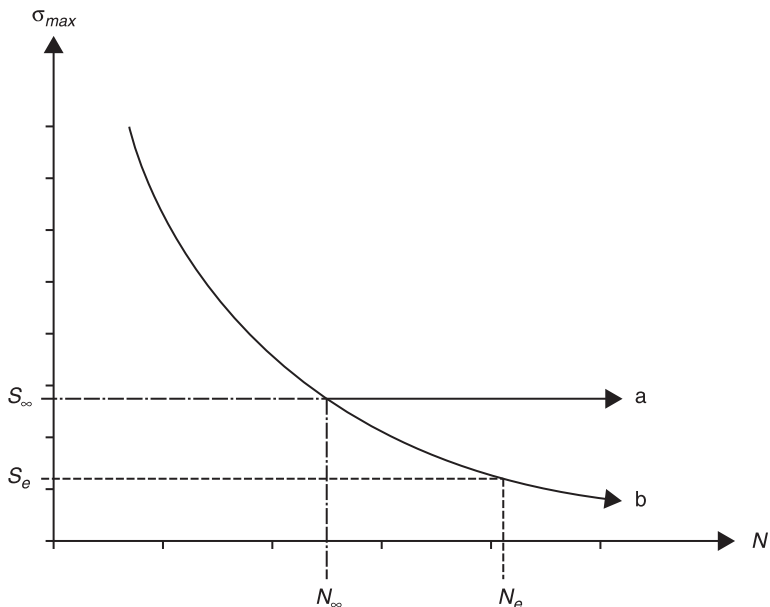
exception occurs for dynamically loaded structures, which display a varying response to stress concentration effects according to the notch sensitivity, q . Notch sensitivity is sparsely documented, as for all fatigue data. For fatigue-limited design, recourse should be made to notched specimens (e.g. Battelle, 1998), or the conservative assumption of full-notch sensitivity should be made.

25.3.4 Material selection for fatigue-limited scenarios

Infinite-life design

The traditional approach to material selection for fatigue-limited scenarios is the infinite-life design (ILD) criterion. The ILD criterion requires that peak component stress, σ_{max} , is always below the fatigue-limit, S_∞ , resulting in a component that will theoretically survive dynamic loading indefinitely (Fig. 25.6). The ILD criterion provides a logical starting point for fatigue-limited design as:

- The fatigue limit is the most extensively available measure of material fatigue response (e.g. Ashby and Bréchet, 2002).



25.6 Schematic S–N curve for an idealised material with a fatigue-limit (a) and a material with no fatigue-limit (b). The performance of these hypothetical materials is identical for $\sigma_{max} > S_\infty$. Nomenclature: maximum stress (σ_{max}), fatigue limit (S_∞), endurance limit (S_e), number of cycles at which the fatigue limit occurs (N_∞), number of cycles at which the endurance limit is defined (N_e).

- The ILD criterion provides a conservative design that is independent of the service-life of the actual component.

However, the ILD criterion precludes the application of materials that do not display a fatigue limit, for example aluminium. For such materials, the associated endurance limit, S_e , can provide an initial basis for estimating the performance of a candidate material, however, there is opportunity for flawed design outcomes depending on the relative magnitude of the required design-life,¹ N , and the number of cycles associated with the fatigue limit, N_∞ , or endurance limit, N_e (Fig. 25.6).

- If the design-life is less than the number of cycles associated with the endurance limit (or fatigue limit) of the material under consideration, the ILD criterion results in modelling uncertainties due to the mismatch between the predicted and actual fatigue strength. These uncertainties are conservative, but result in component overdesign.
- If the required design-life exceeds the number of cycles associated with the endurance limit ($N_e \leq N$), the design is non-conservative, and there exists a risk of in-service failure.²

The ILD criterion is useful to provide an initial estimate of the mass reduction opportunities and costs associated with proposed aluminium substitution programmes. However, it does not engage with the unique properties of aluminium and can result in component overdesign, or risk of in-service failure.

Finite-life design

Automotive component design has been traditionally based on ILD, however, demand for mass optimisation has led to an increased application of the finite-life design (FLD) criteria for automotive component design (e.g. Tsybaney and Ponomarev, 2001). FLD criteria require that a component safely withstand the design-life, including an appropriate design safety factor, and may fail if the associated design-life is exceeded. FLD for complex and uncertain loading conditions, as are observed in suspension components for example, requires significantly higher design effort to safely implement than ILD, but has the potential to provide mass reduction by:

- allowing safer application of materials that do not have a well-defined fatigue limit, such as aluminium, and
- reducing the modelling uncertainties that occur when the design-life is less than the number of cycles associated with the fatigue limit or endurance limit of the material under consideration.

Traditional fatigue-limited material selection procedures do not engage with the unique requirements of FLD, particularly the dependence of material performance on the required design-life. In response to this deficiency, a design tool has been

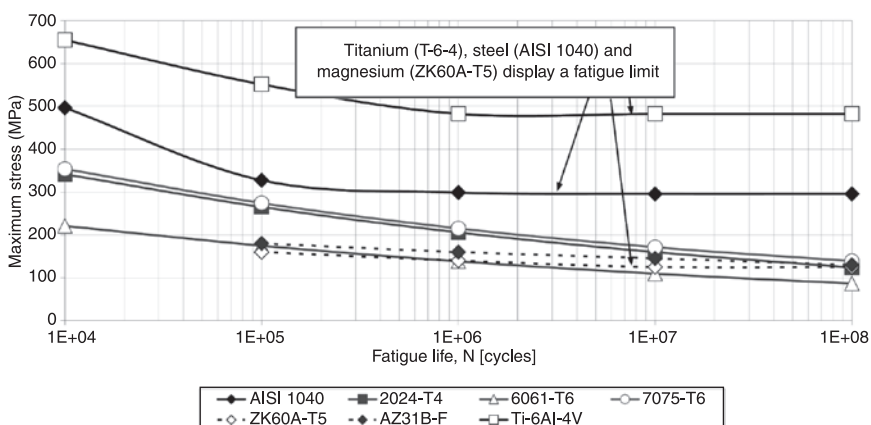
developed to systematically assess material performance for FLD (Leary and Burvill, 2001). By systematically evaluating the material indices at a range of design-lives, a *material selection curve* may be generated to assist material selection for FLD. Given that the material index, M^* , tends to zero as performance increases, the lowest material selection curve is optimal for a given design-life. The design tool allows performance to be graphically presented versus the required design-life. These material selection curves:

- provide a basis for assessing the relative performance of candidate materials
- guide material selection for finite-life design applications and
- provide a reverse engineering tool for identifying the envelope of conditions for which light alloys are optimal for finite-life design applications.

Although the material selection curves are applicable for any design scenario, candidate materials have been considered in this chapter which are compatible with the forging method of manufacture, including grades of aluminium, magnesium and titanium. A ferrous metal with a precedent for application in forged automotive applications provides a performance baseline for assessing the relative performance of the light alloy alternatives (Table 25.2, Fig. 25.7). The endurance limit is reported for materials that do not display a well-defined fatigue limit, for example most of the candidate light alloys.

25.3.5 Material selection curves

A systematic approach has been developed to compare the performance of candidate materials for fatigue-limited applications for the structural elements of interest (Section 25.2.1). Material performance will be compared for a range of design-life requirements, and the design objectives of minimal mass, minimal



25.7 Candidate material S–N curves (material properties for fully reversed data obtained from a range of sources, Table 25.2).

cost and a compromise between mass and cost, resulting in a family of material selection curves for each combination of structural element and design objective (Fig. 25.1):

- Tie, or beam, with width as the free variable, i.e. $k = 1$.
- Beam with width and depth equal and area as the free variable, i.e. $k = 3/2$.
- Beam or plate with depth as the free variable, i.e. $k = 2$.

Material selection curves for $k = 1$: M_{1m}^ , M_{1c}^**

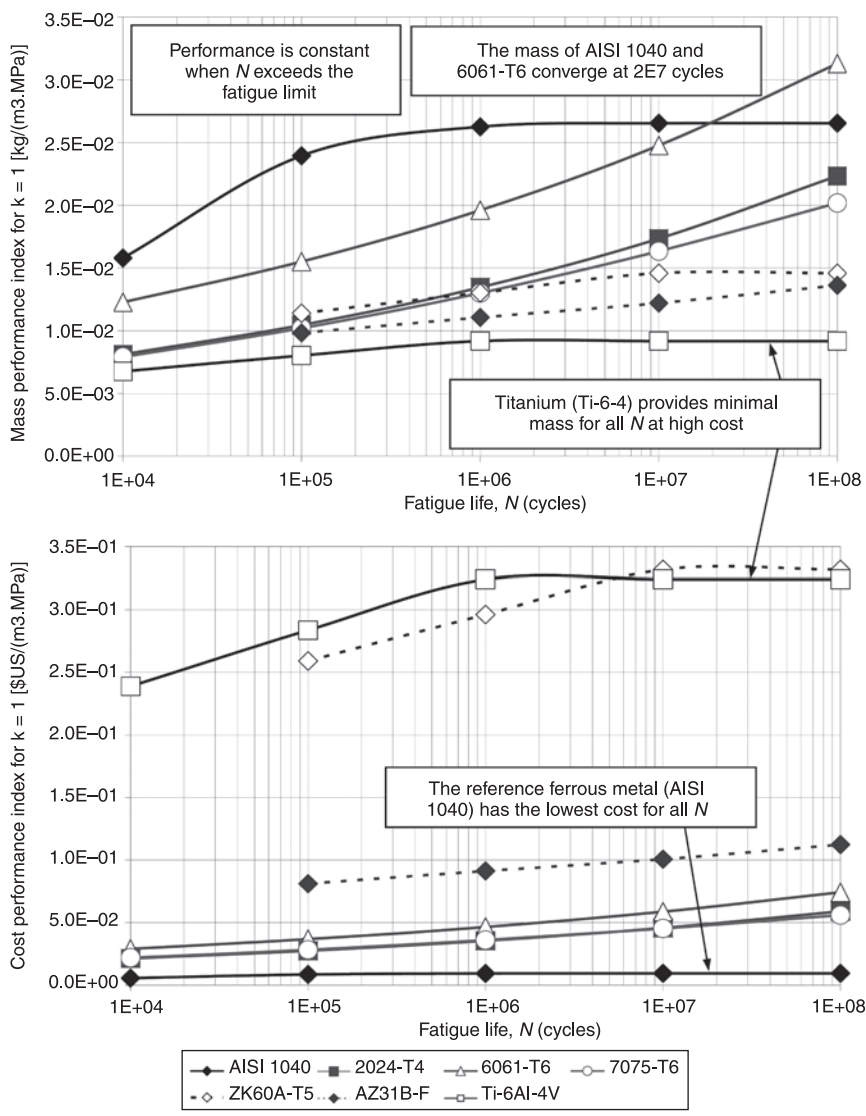
A tie, or a beam, with width as the free variable has the lowest guideline gradient of the scenarios investigated (i.e. $k = 1$) and, as such, performance correlates with fatigue strength more than for the other scenarios (Section 25.3.2). Of the candidate metals, for $k = 1$, titanium (Ti-6-4) is optimal for minimal mass, but has a high associated cost (Fig. 25.8). These attributes suit weight critical applications, such as aeronautics and astronautics. Magnesium (AZ31B-F) provides the second lightest option at significantly lower cost than titanium (Ti-6-4). Of the light alloys, aluminium provides a compromise between mass and cost, allowing more general application. Steel (AISI 1040) is the optimal material for cost-critical applications when $k = 1$; however, it is typically the least effective in terms of mass (Fig. 25.8). An important quality of ferrous metals (such as AISI 1040) is the existence of a fatigue limit, above which the material displays constant fatigue strength, and hence constant performance. This phenomena favours ferrous metals for very high-cycle fatigue applications when compared to aluminium alloys.

Material selection curves for $k = 3/2$: $M_{3/2m}^$, $M_{3/2c}^*$*

The material selection guideline for $k = 3/2$, e.g. a square cross-section beam with the sectional area as the free variable, is more sensitive to low material density than for $k = 1$. For $M_{3/2m}^*$, the reference steel (AISI 1040) minimises cost for all N , but is the least effective candidate in terms of potential mass reduction (Fig. 25.9). Magnesium (AZ31B-F) minimises mass for the fatigue lives considered, but the mass of titanium and magnesium converge as N exceeds $1E8$ cycles. Aluminium alloys have the lowest cost of the light alloys and provides an opportunity for mass reduction over the reference steel for all N .

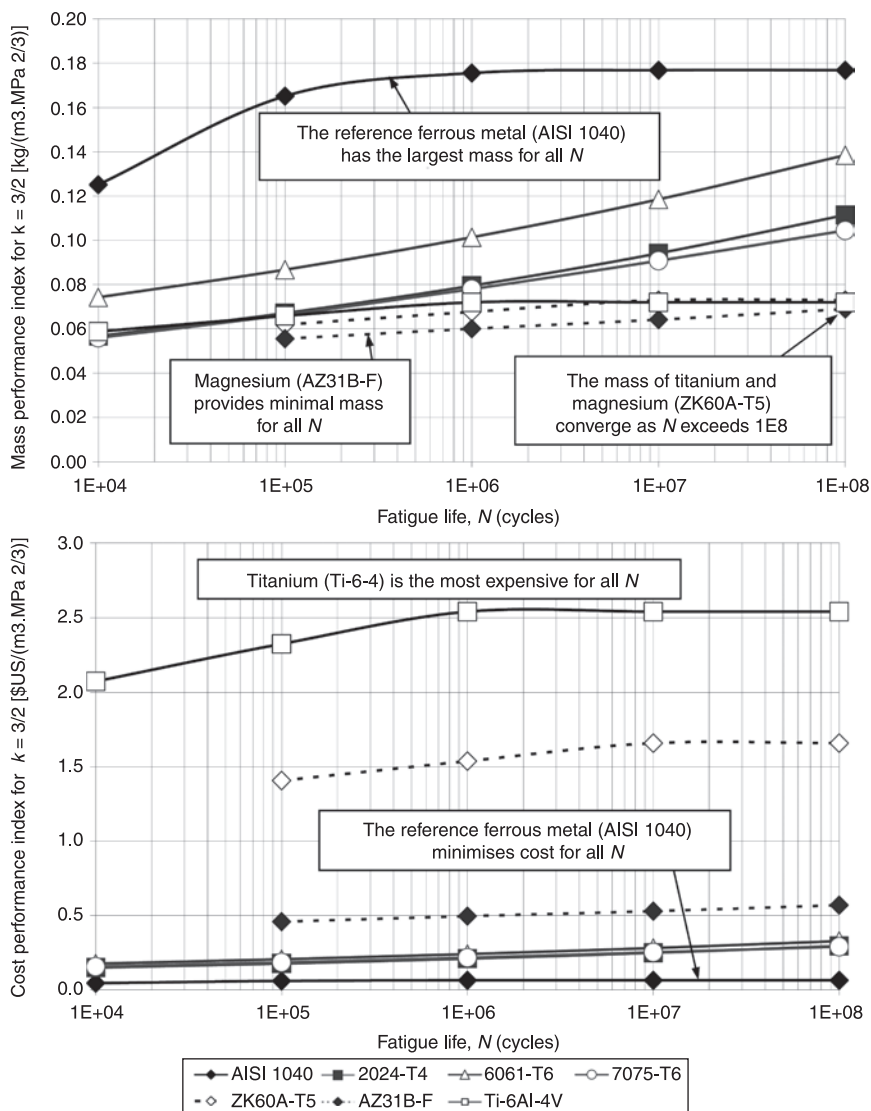
Material selection curves for $k = 2$: M_{2m}^ , M_{2c}^**

The material selection guideline for $k = 2$, e.g. a beam or plate element with depth as the free variable, is the largest guideline gradient investigated in this work. Consequently, the mass, M_{2m}^* , and cost, M_{2c}^* , performance metrics correlate more closely with material density and specific cost, respectively, than for the other relevant selection guidelines (Section 25.3.2). The associated performance



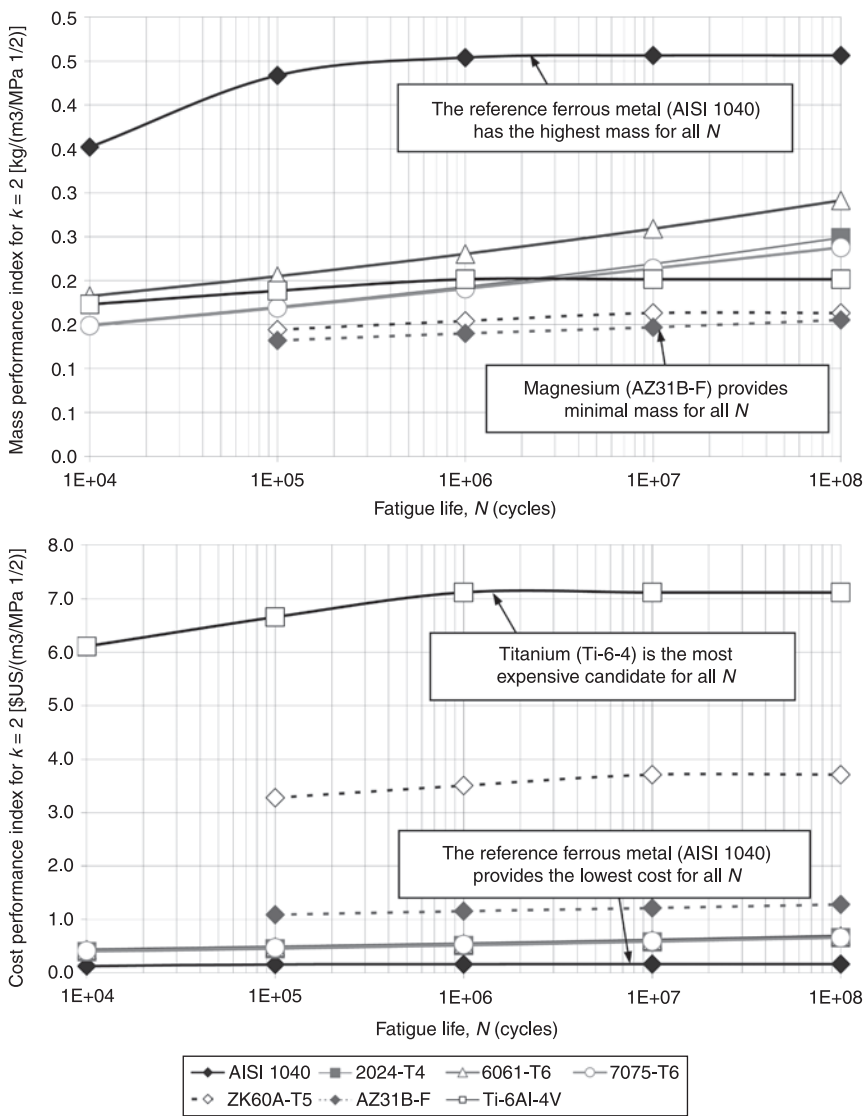
25.8 Material selection curves for fatigue-limited design of minimal mass and minimal cost for $k = 1$. Upper: mass performance index (M^*_{1m}). Lower: cost performance index (M^*_{1c}).

differential between ferrous metals and the candidate light alloys is the greatest of the scenarios investigated (Fig. 25.10). For M^*_{2m} , the optimal material for minimal mass is magnesium (AZ31B-F followed by ZK60-T5). The mass of a titanium component (Ti-6-4) is greater than for the 2024-T4 and 7075-T6 aluminium alloys for fatigue lives in excess of approximately 3E6 cycles. Titanium is the most



25.9 Material selection curves for fatigue-limited design of minimal mass and minimal cost for $k = 3/2$. Upper: mass performance index ($M^*_{3/2m}$). Lower: cost performance index ($M^*_{3/2c}$).

expensive candidate material for any fatigue life. The candidate ferrous metal (AISI 1040) has the lowest associated cost and highest mass of the candidate metals for all N . Aluminium alloys provide an opportunity for significant mass reduction over the candidate ferrous metal without the cost penalty of the other light alloy materials.



25.10 Material selection curves for fatigue-limited design of minimal mass and minimal cost for $k = 2$. Upper: mass performance index (M^*_{2m}). Lower: cost performance index (M^*_{2c}).

25.3.6 Performance summary

The optimal material selection is a function of the required fatigue life, the design objective (e.g. minimal mass or minimal cost) and the associated guideline gradient, k . For low values of k , fatigue strength dominates performance. As k increases, the influence of low density, or specific cost for the case of cost-limited design, dominates

performance. In general, the opportunities for mass reduction by aluminium substitution are maximised if the design focus is on scenarios with large guideline gradient, e.g. a plate or a beam element with free depth, and the design objectives allows for some increase in component cost in exchange for mass reduction.

Of the candidate light alloys, titanium (Ti-6-4) has the largest fatigue strength, by a significant margin, and the highest density. This combination is well suited to scenarios with low values of k which are principally mass limited, e.g. high performance vehicles, aircraft and space vehicles. Magnesium has a relatively low fatigue-strength, but has the lowest density of the light alloys suitable for structural applications. This combination of properties is suited to design scenarios with moderate to high values of k for which mass reduction is the primary design objective; however, the cost of magnesium alloys may be prohibitive for general application (additional complications are identified in Sections 25.2.4 and 25.5.2). Of the candidate light alloys, aluminium provides the minimal cost option and thereby enables cost effective mass reduction. As for all light alloys, aluminium has a relatively low performance when the guideline gradient is low. The greatest opportunity to achieve affordable mass reduction by aluminium substitution is in applications that have a high guideline gradient.

As N exceeds the associated fatigue limit N_∞ , the performance differential between materials that display a fatigue limit and those that do not display a fatigue limit increases monotonically. Consequently, the primary opportunities for aluminium alloy application occur when the required fatigue life does not exceed N_∞ as the associated mass reduction potential is highest.

As identified in Section 25.2.4, these comparisons assume production costs of each material to be equal. An important consideration for the aluminium alloys investigated is that the 2024-T4 and 7075-T6 classes may require surface protection (e.g. Sankaran et al., 2001). The additional cost incurred is dependant on component size, and is often acceptable for premium aerospace products. 6061-T6 is less susceptible to surface corrosion and is more often applied in general applications such as automotive.

25.4 Non-stationary fatigue-limited application

25.4.1 Non-stationary applications

Previous work has identified that aluminium mass reduction programmes require some financial or legislative motivation for mass reduction to be feasible. Non-stationary applications result in economic and environmental consequences that are directly related to the component mass which must be transported during the design-life.

Hubbert's curve and peak oil

Production vehicles are almost exclusively powered by petroleum-based fuels. The available reserves of this non-renewable resource are continuously decreasing;

concurrently, global demand for petroleum is steadily increasing. In the 1950s, Hubbert (1956) proposed that crude oil production follows a normal distribution, now known as *Hubbert's curve*. Hubbert's curve provides a mechanism to predict future oil production rates, in particular, the inflection point, known as *Peak Oil*, at which global oil production rates begin to decrease and enter terminal decline. After Peak Oil, significant divergence occurs between petroleum supply and demand, resulting in a rapidly escalating cost of the diminishing petroleum resource. Although it is only possible to accurately identify Peak Oil retrospectively, current estimates predict either that it has already occurred or is imminent (Campbell and Laherrère, 1998). Independently of the exact date of Peak Oil, the resulting increase in the cost of petroleum significantly increases the importance of reducing component mass in modern vehicle design.

Environmental motivation

The combustion of petroleum fuels results in a series of undesirable emissions, including hydrocarbons (HC) and nitrous oxides (NO_x), that contribute to atmospheric smog; carbon monoxide (CO), a toxic gas that reduces the blood's ability to transport oxygen; and carbon dioxide (CO_2), a significant greenhouse gas that contributes to global warming. Government regulatory bodies are actively regulating transport emissions to mitigate these environmental consequences. The magnitude of undesirable emissions is the product of fuel consumption and the associated emission rates. Emission rates are influenced by technology innovations, such as catalytic converters and low emission fuels. Vehicle mass is the design variable of greatest significance to fuel consumption (e.g. Stone, 1989). Reduced vehicle mass results in lower fuel consumption by simultaneously reducing the tractive effort required to achieve a desired acceleration, and reducing the associated rolling resistance. In addition to these direct benefits, mass reduction offers reduced dead loads and inertial forces, and can enable a secondary weight reduction in the associated structural elements. Alternately, vehicle mass reduction facilitates additional payload with an unchanged vehicle performance. Additional payload may include safety features (e.g. electronic braking systems, airbags and all-wheel drive technologies) and luxury items (e.g. additional glass and auditory insulation materials).

Strategies for accommodating the fuel consumption and environmental impact of non-stationary applications are provided in Sections 25.6 and 25.7.

25.5 Multi-objective problems and numeric optimisation

The material selection indices presented in this work provide a robust mechanism to systematically identify the performance of aluminium alloys for a specific application. However, these methods are subject to several limitations, including the accommodation of multiple concurrent objectives and the applicability of simplified structural elements. Simplified structural elements provide insight into

the relative merit of candidate materials, but may introduce uncertainty if the design scenario under examination is mismatched with the associated structural element. This limitation can be mitigated by the application of stress concentration factors (Section 25.3.3). If acceptable stress concentration factors are not available, recourse may be made to numeric methods. These methods are also highly useful in enabling compromise between multiple design objectives.

25.5.1 Numeric optimisation

Many engineering optimisation problems contain multiple optimum solutions, i.e. the objective function contains multiple minima or maxima. Among these multiple optima there may be one (in the case of a single objective problem) or more (multiple objective problem) absolute minima or maxima. Absolute optimal solutions are known as *global optima* and other optimal solutions are known as *local optima*. Designers are ideally interested in finding global optima; however, the incremental changes required to iterate from an initial solution to the optimum solution(s) can be highly complex and counterintuitive. Numeric optimisation involves the application of numeric algorithms to aid the identification of optima within the feasible design space.

Optimisation algorithms can be classified as either deterministic or stochastic (Collard, 2007). Deterministic algorithms iterate between solutions in the search space according to transition rules based on previous solutions. For example, deterministic algorithms commonly use hill climbing procedures based on the local gradient of the objective function. Deterministic algorithms are typically faster to converge at an optimal solution, however, the solution is not guaranteed to be a global optima. Stochastic algorithms explore the design space based on probabilistic transition rules; introducing randomness into the transition rules provides an effective method of preventing the search from stagnating at local optima. As such, stochastic methods have a better global perspective of the solution space when compared to deterministic optimisation methods (Coley, 1999).

The genetic algorithm (GA) is an important stochastic optimisation algorithm (Deb, 2006). The GA initiates with a random population that is evaluated according to how well the objectives are satisfied. The initial population is altered through manipulations that mimic the processes of evolutionary biology. Multiple iterations of the process are carried out to identify a superior combination of variables that better satisfies the problem objectives.

Optimisation methodology

A typical design optimisation process integrates the strengths of the available algorithms as follows:

1. Initial design space exploration provides an overview of the available design space.

2. Coarse optimisation using stochastic algorithms identifies regions of global optima.
3. Refinement using deterministic algorithms optimises the preferred optimal region.

Numeric optimisation algorithms are compatible with numeric methods such as FEA and CFD. These methods can overcome the limitations of simplified geometric solutions and accommodate highly discontinuous geometries for which stress concentration factors are unlikely to be available. By combining numeric solution methods and optimisation algorithms, it is theoretically possible to achieve autonomous optimisation; the problem is formally defined in terms of the constraints and objectives, and based on extensive materials database and expert systems, an optimal solution is identified in an automated fashion. Despite the attraction of such a method, limitations such as data availability, implementation schedule and available technical resources may stymie the application of automated methods in a production environment (e.g. Fermer and Svensson, 2001).

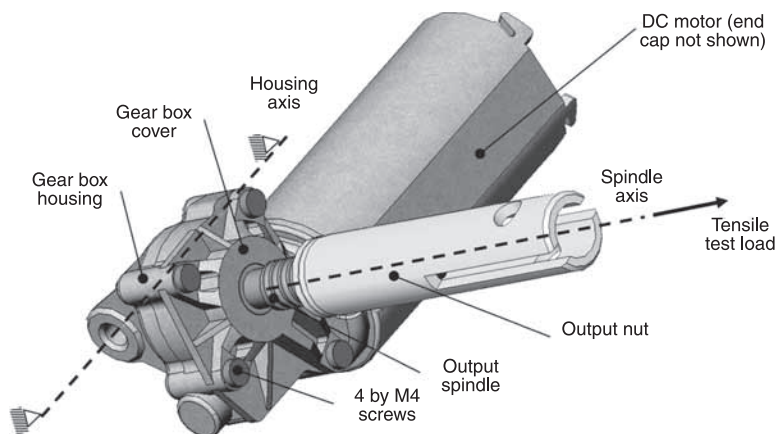
A practical compromise is achieved by the integration of algebraic material selection approaches and numeric methods (e.g. Leary et al., 2009b). Traditional material selection methods engage with a large number of candidate materials, but provide little design guidance for the optimisation of a specific scenario. Conversely, numeric optimisation provides insight into specific scenarios, but incurs significant computational resources. A case study is presented to illustrate the potential integration of both methods, i.e. algebraic material selection procedures are used to screen a broad range of potential components and materials to quantify their relative merit; further assessment by numerical methods identifies opportunities for topological optimisation of the preferred component and material.

25.5.2 Case study – safety-critical actuator

A linear actuator used in automotive applications was identified for mass reduction (Leary et al., 2009a). The component consists of a DC motor, gear box, lead screw and integral housing (Fig. 25.11). The component provides linear actuation in a range of automotive applications. The actuator is safety-critical, and any opportunity to enhance performance (such as initial cost and mass) can only be considered if there is no compromise to structural integrity. The following case study assesses the possibilities of enhanced performance by identifying alternate material selection and structural shape optimisation.

Material selection

The linear actuator is subject to tensile loading along the spindle axis (Fig. 25.11). When subject to this loading, the associated sub-components act as various structural elements:



25.11 Linear actuator assembly.

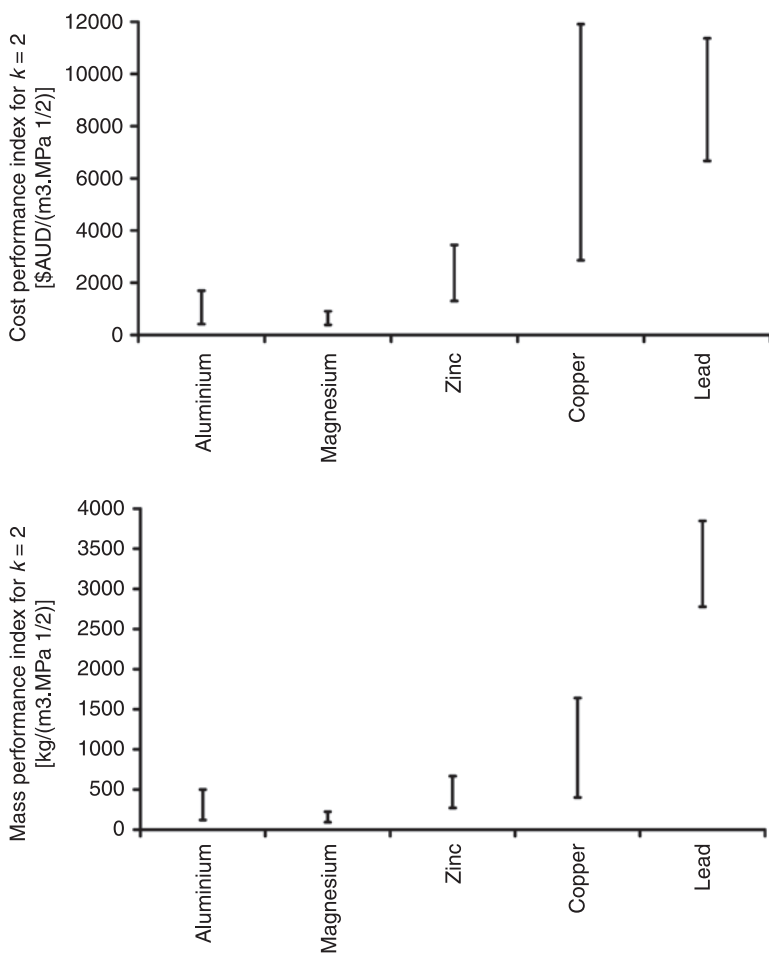
- The mild steel output spindle is nominally subject to uniaxial loading, shear occurs at the thread root and internal support.
- The gearbox housing is a Zn-Al High Pressure Die Casting (HPDC) subject to multi-axial tensile and shear loading.
- The gearbox cover is manufactured as for the housing and acts as a centrally loaded plate with perimeter support.
- The DC motor is independent of the load path and does not contribute to structural integrity.

Of these sub-components, the gearbox cover presents the most probable opportunity for conversion to light alloys due to the high k value of the associated structural element. To formally assess the opportunity for mass reduction, algebraic material selection procedures have been applied, with the following attributes:

- The candidate materials were restricted to materials compatible with the HPDC process, which is the intended method of manufacture. Of the materials available, zinc, lead, copper, magnesium and aluminium are feasible with this constraint.
- The manufacturer specified tensile yield as the failure criteria.
- The gearbox cover was represented by a centrally loaded plate with perimeter supports, i.e. $k = 2$ (Table 25.1).

Material property charts were applied to assist material selection for this test case (Fig. 25.12). In summary:

- Magnesium provides the lowest mass; however, its use in traditional HPDC incurs an additional cost penalty due to high scrap rates and recycling difficulties (Section 25.2.4). Custom processing technologies are under development which may resolve this cost penalty (e.g. Nguyen et al., 2006).
- Although feasible with the intended manufacturing method, lead and copper are non-optimal for the material selection indices of interest. It may have been



25.12 Whisker-plots indicating the potential range of material selection indices, M^* , versus for $k = 2$ for material classes compatible with HPDC (data obtained from Fig. 25.4 and 25.5).

tempting to eliminate these candidate materials earlier in the exercise as intuitively non-optimal. However, this disobeys the fundamental requirement that material selection strategies be systematic rather than intuitive.

- Zinc minimises cost but has non-optimal mass.
- Aluminium provides a compromise between mass and cost.

Optimisation

Based on the initial material selection, aluminium alloy was identified as an opportunity to provide competitive advantage. Concurrently, a novel aluminium

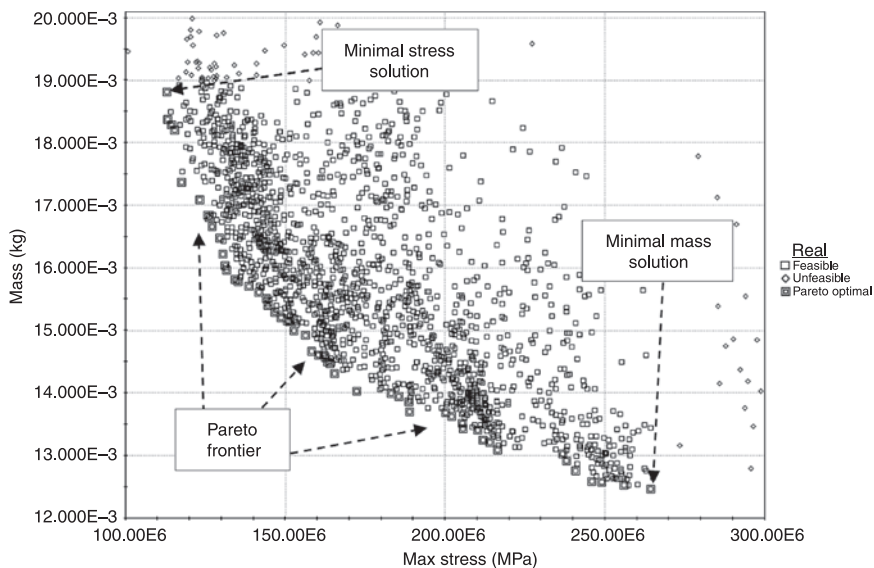
alloy heat treatment was identified that was compatible with the HPDC method. HPDC aluminium alloys are not usually heat treated because the castings are relatively porous and contain entrapped gases. These pores expand during conventional heat treatment resulting in damage which compromises mechanical properties. Recent work has identified a truncated solution treatment that avoids these problems, allowing the yield stress to be approximately doubled while retaining the cost advantage of HPDC (Lumley et al., 2007). The novel material (A380-T64) was prescribed as the preferred candidate for the material substitution programme.

The candidate material offers higher performance than the alloy currently used and permits a more efficient housing cover topology. To identify an optimised topology, a finite element (FE) model of the housing cover was constructed. The FE model consists of parametric geometry, and simulated loading conditions (Fig. 25.14). Initial FE analysis indicated unreasonably high peak stresses in the region of geometric stress concentrations. These spurious results are due to CAD simplifications and poor quality FE mesh, which could be rejected by an experienced FE analyst, but are not compatible with automated numeric analysis, for which the peak stress values are reported as the design measure for a given scenario. CAD geometry was modified to eliminate spurious results and improve parameterisation of the model for the optimisation process, resulting in a robust model that is a close analogue of the stress distribution in the actual part.

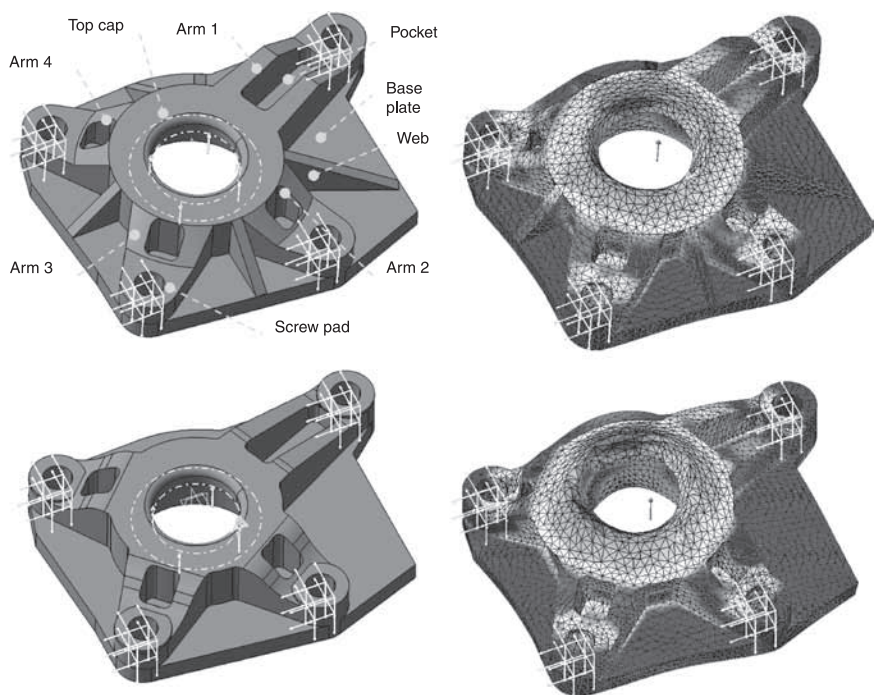
A multi-objective optimisation problem was formulated by interfacing the parametric FE model with commercial optimisation software with the objectives of minimal mass and minimal peak stress. The design parameters were initialised with a randomly generated sequence and subjected to a GA, resulting in a total of 3500 design evaluations. The associated solution space (Fig. 25.13) identifies the performance of all feasible evaluated designs, and displays a typical *Pareto Frontier*, a curve that indicates the optimal solution for some fixed value of a performance objective. Only solutions on the Pareto Frontier should be considered, the preferred solution may be determined by some cost-benefit analysis between competing objectives, for example initial cost versus future fuel savings, for example Section 25.6.2. Based on the design constraints, a global optimum was identified which minimises the housing cover mass without violating stress constraints, reducing component mass from 47 g to 18.5 g (Fig. 25.13).

25.5.3 Opportunities for non-trivial and multi-objective design problems

A significant opportunity exists to develop commercial advantage by the substitution of aluminium alloys in non-trivial components. The concurrent implementation of graphic and numeric methods provides a practical opportunity to respond to these scenarios. Graphical methods enable preferred sub-components and materials to be rapidly identified and compared; numeric methods enable the



25.13 Solution space associated with gearbox cover.



25.14 Original cover geometry and stress distribution (upper) and optimised geometry (lower).

automated analysis of a vast range of feasible geometries for the identified sub-component and materials.

Those engaged in material substitution programmes can take advantage of several opportunities:

- Existing commercial components may not have been subject to a robust optimisation process and may be fundamentally overdesigned.
- Mass reduction strategies have traditionally addressed non safety-critical applications; hence there are many opportunities for aluminium alloy application in safety-critical applications such as automotive suspensions.
- Novel materials, such as the truncated solution heat treated HPDC, provide opportunity for highly complex geometries with highly cost effective materials.
- Increasing fuel costs and environmental legislation are driving an increase in the acceptable cost premium for mass reduction – resulting in a larger number of feasible applications.

25.6 Multiple objective material selection

Previous sections have defined material selection techniques suitable for the optimisation of a single objective, including material selection curves that provide non-subjective design guidance for single objective design, but are subjective when applied to material selection for multiple objectives. Material selection in real-world applications requires compromise between multiple constraints and multiple objectives (e.g. Landru and Brechet, 2000). Material selection procedures are further complicated when the objectives are measured in non-commensurate units (e.g. mass and cost) as this precludes direct comparison. The value function (also known as a utility function) provides a robust tool for multiple objective material selection.

25.6.1 The value function

Value functions are the most commonly used method for resolving multiple simultaneous objectives (Keeney and Raiffa, 1993; Vincke, 1992). A value function, V , is an additive model that defines the net value associated with a specific material according to a series of design objectives (Sirisalee et al., 2003). Cost-benefit analysis is used to define exchange constants, $E^{\$}$, that identify the rate of change of V with respect to performance, P , of each objective (Eq. 25.3). The associated value function then defines the net value of a candidate material in terms of the associated exchange constants and performance variables (Eq. 25.4). As performance is proportional to the associated material selection indices (Section 25.2.1), the value function may be expressed in terms of the associated material selection indices (Eq. 25.5).

$$E^{\$} = \left(\frac{\partial V}{\partial P} \right) \quad [25.3]$$

$$V = E_1^{\$} P_1 + E_2^{\$} P_2 + \dots + E_n^{\$} P_n = \sum_{x=1}^{x=n} E_x^{\$} P_x \quad [25.4]$$

$$V \propto E_1^{\$} M_1^* + E_2^{\$} M_2^* + \dots + E_n^{\$} M_n^* = \sum_{x=1}^{x=n} E_x^{\$} M_x^* \quad [25.5]$$

For the scenarios of interest to this work, V is a function of the exchange constants associated with component mass $E_m^{\$}$, and component cost $E_c^{\$}$ (Eq. 25.6). For consistency with earlier definitions, the performance of a particular material selection increases as V tends to zero. A unit increase in component cost results in a unit increase in V , i.e. $E_c^{\$} = 1$ (Eq. 25.7).

$$V \propto E_c^{\$} M_c^* + E_m^{\$} M_m^* \quad [25.6]$$

$$V \propto M_c^* + E_m^{\$} M_m^* \quad [25.7]$$

The value function represents a compromise between the design objectives of minimal component mass and minimal component cost. The relative importance of component mass and cost is dependent on the associated design scenario, as defined by the exchange constant for component mass $E_m^{\$}$ (Eq. 25.7):

- For $E_m^{\$} \ll 1$, the value function, V , is dominated by the material index for cost, M_c^* , and the relative performance of candidate materials tends to that of the material selection curves for cost-limited design (Section 25.3.4).
- For $E_m^{\$} \gg 1$, V is dominated by the material index for mass, M_m^* , and the relative performance of candidate materials tends to that of the material selection curves for mass-limited design (Section 25.3.4).

A range of value functions are relevant for non-stationary design scenarios (Leary, 2006):

- The *present value function* defines the performance of a material selection based on the Acceptable Cost Premium (ACP) for mass-reduction at the present time.
- The *convergent value function* identifies the ACP for which a potential substitute material such as aluminium will perform equally with a reference ferrous metal at the required design-life.
- The *holistic value function* defines material performance based on the total financial costs, including raw materials and the contribution of component mass to fuel costs over the vehicle design-life. The holistic value function is examined further in this work.

Holistic value function

The holistic value function includes the total financial cost associated with a material selection throughout the vehicle life-cycle, including raw material cost and the contribution of component mass to fuel costs. The costs associated with decommissioning are not explicitly included here. However, decommissioning costs are compatible with the value function method, and can be included as

required (e.g. Council of the European Parliament, 2000). The holistic value of mass reduction is highly sensitive to the design scenario investigated, in particular, the relative magnitude of interest rates, which tend to increase the value of money with time, and inflation rates, which tend to increase the cost of fuel with time (e.g. Hollick, 1993). Peak Oil suggests that inflation of fuel costs will increase more rapidly than interest rates. However, in the absence of more objective data, interest rates and inflation are assumed to be of equal magnitude, and the net present value the total petrol costs accrued over the vehicle design-life is:

$$C_{Total} = FC_{AVE} \cdot D_{Annual} \cdot N_d \cdot C_{Petrol} \quad [\text{\$US}] \quad [25.8]$$

$$C_{Total} = \text{total petrol cost} \quad [\text{\$US}]$$

$$FC_{AVE} = \text{average fuel consumption} \quad [\text{L}/100\text{km}]$$

$$D_{Annual} = \text{annual distance travelled} \quad [100\text{km}/\text{year}]$$

$$N_d = \text{vehicle design-life} \quad [\text{years}]$$

$$C_{Petrol} = \text{petrol cost} \quad [\text{\$US}/\text{L}]$$

The holistic exchange constant for mass reduction, $E_h^{\$}$, also known as the fuel reduction value (FRV), is defined by the partial derivative of C_{Total} with respect to vehicle mass:

$$E_h^{\$} = \frac{\partial C_{Total}}{\partial m} \quad [\text{\$US}/\text{kg}] \quad [25.9]$$

$$E_h^{\$} = \frac{\partial}{\partial m} (FC_{AVE} \cdot D_{Annual} \cdot N_d \cdot C_{Petrol}) \quad [\text{\$US}/\text{kg}] \quad [25.10]$$

$$E_h^{\$} = D_{Annual} \cdot N_d \cdot C_{Petrol} \frac{\partial FC_{AVE}}{\partial m} \quad [\text{\$US}/\text{kg}] \quad [25.11]$$

25.6.2 Case study – light alloy suspension component

A formal appraisal was initiated to quantify the requisite life-cycle parameters to allow evaluation of the holistic exchange constant $E_h^{\$}$, for an Australian-based 2001 model year vehicle (Leary, 2006). Although the outcomes of this specific appraisal are not directly applicable to other design scenarios, the fundamental assessment modes used to generate this data are universally applicable. Furthermore, the method illustrates reasonable assumptions that can be made to overcome limitations in available data.

Requisite life-cycle parameters

To evaluate the holistic exchange constant $E_h^{\$}$, a series of life-cycle parameters are required (Eq. 25.11). As a consequence of limited data availability, these parameters have been obtained by a combination of assessment modes:

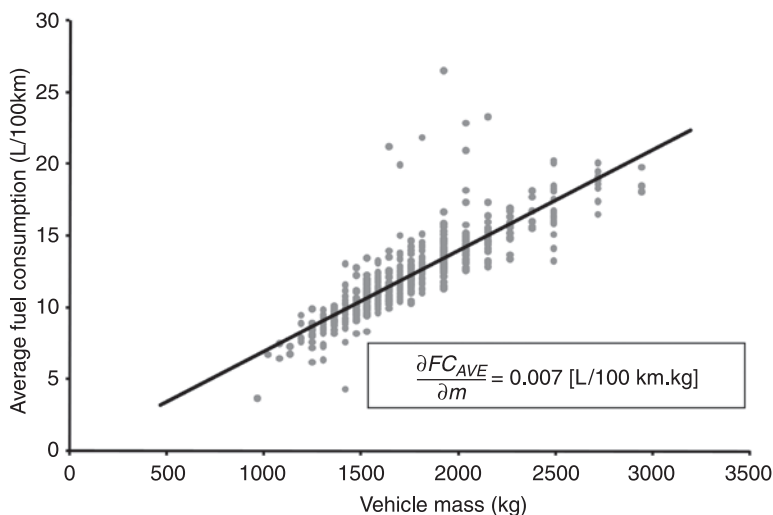
- reference to publicly available Australian vehicle use data
- inference from publicly available international vehicle use data and
- acquisition and statistical analysis of novel data.

Mass-specific fuel consumption

The United States Environmental Protection Agency (US-EPA) has a historically comprehensive and readily obtainable database of vehicle fuel consumption under simulated highway and city driving conditions. The strategies applied to assess fuel consumption and emissions of Australian vehicles are derived from the US-EPA protocols (Standards Australia, 1986), allowing US-EPA test data to be used as a basis for estimating the fuel consumption of Australian vehicles in the absence of more robust data. Although simulated city and highway results may be combined to provide an estimate of average fuel consumption, the robustness of this measure has been debated (e.g. Hellman and Murrell, 1984). An adjustment factor based on the city fuel consumption, FC_{city} , has been reported as being representative of average Australian driving conditions (DPIE, 1996). This basis has been applied in this work to estimate the average vehicle fuel consumption FC_{AVE} , measured in litres per hundred kilometres (Eq. 25.12).

$$FC_{AVE} = 1.06FC_{city} \quad [\text{L} / 100 \text{ km}] \quad [25.12]$$

Based on publicly available US-EPA fuel efficiency data, the relationship between vehicle mass and average fuel consumption, and the associated rate of change have been quantified (Fig. 25.15).



25.15 Average fuel consumption FC_{AVE} , versus vehicle mass.

Annual distance travelled

Research by the Australian Bureau of Statistics (2000) indicates that the average Australian passenger vehicle travels an average of 14 400 km per year. No data on the associated statistical distribution was reported.

Vehicle design-life

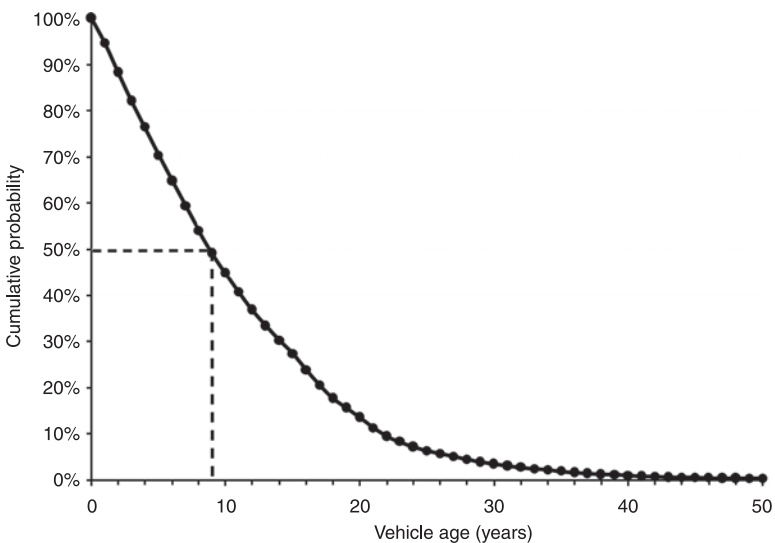
Extensive literature review identified no robust data on an appropriate design-life for Australian vehicles. To overcome this impediment, vehicle registration data were obtained to provide a cumulative probability distribution of the age of vehicles currently registered for use (Subic et al., 2009). The associated vehicle age for a cumulative probability of 50% is 8.8 years (Fig. 25.16).

Petrol cost

Based on International Energy Agency estimates and associated exchange rates, Australian petrol prices per litre, C_{Petrol} , are \$US 0.43.

The outcomes of this appraisal, summarised in Table 25.3, provide a basis for the evaluation of the holistic exchange constant $E_h^{\$}$, and holistic value function ($V_{1h}, V_{3/2h}, V_{2h}$) associated with the design scenario.

$$E_h^{\$} = D_{Annual} \cdot N_s \cdot C_{Petrol} \frac{\partial}{\partial m} \{FC_{AVE}\} \quad [\text{\$/kg}] \quad [25.13]$$



25.16 Cumulative probability distribution of vehicles registered in the Australian state of Victoria in February 2006. Dashed lines indicated the vehicle age for a cumulative probability of 50%.

Table 25.3 Requisite life-cycle parameter summary

Variable	Average value	
$\frac{\partial FC_{AVE}}{\partial m}$	0.007	[L/100 km kg]
D_{Annual}	144	[100 km/year]
N_d	8.8	[years]
C_{Petrol}	0.43	[\$US/L]

$$E_h^{\$} = (144)(8.8)(0.43)(0.007) \quad [\$US/kg] \quad [25.14]$$

$$E_h^{\$} = 3.81 \quad [\$US/kg] \quad [25.15]$$

$$V_{1h} = M_{1c}^* + E_h^{\$} M_{1m}^* \quad [\$US/(m^3 \text{ MPa})] \quad [25.16]$$

$$V_{1h} = M_{1c}^* + 3.81 M_{1m}^* \quad [\$US/(m^3 \text{ MPa})] \quad [25.17]$$

$$V_{3/2h} = M_{3/2c}^* + E_h^{\$} M_{3/2m}^* \quad [\$US/(m^3 \text{ MPa}^{2/3})] \quad [25.18]$$

$$V_{3/2h} = M_{3/2c}^* + 3.81 M_{3/2m}^* \quad [\$US/(m^3 \text{ MPa}^{2/3})] \quad [25.19]$$

$$V_{2h} = M_{2c}^* + E_h^{\$} M_{2m}^* \quad [\$US/(m^3 \text{ MPa}^{1/2})] \quad [25.20]$$

$$V_{2h} = M_{2c}^* + 3.81 M_{2m}^* \quad [\$US/(m^3 \text{ MPa}^{1/2})] \quad [25.21]$$

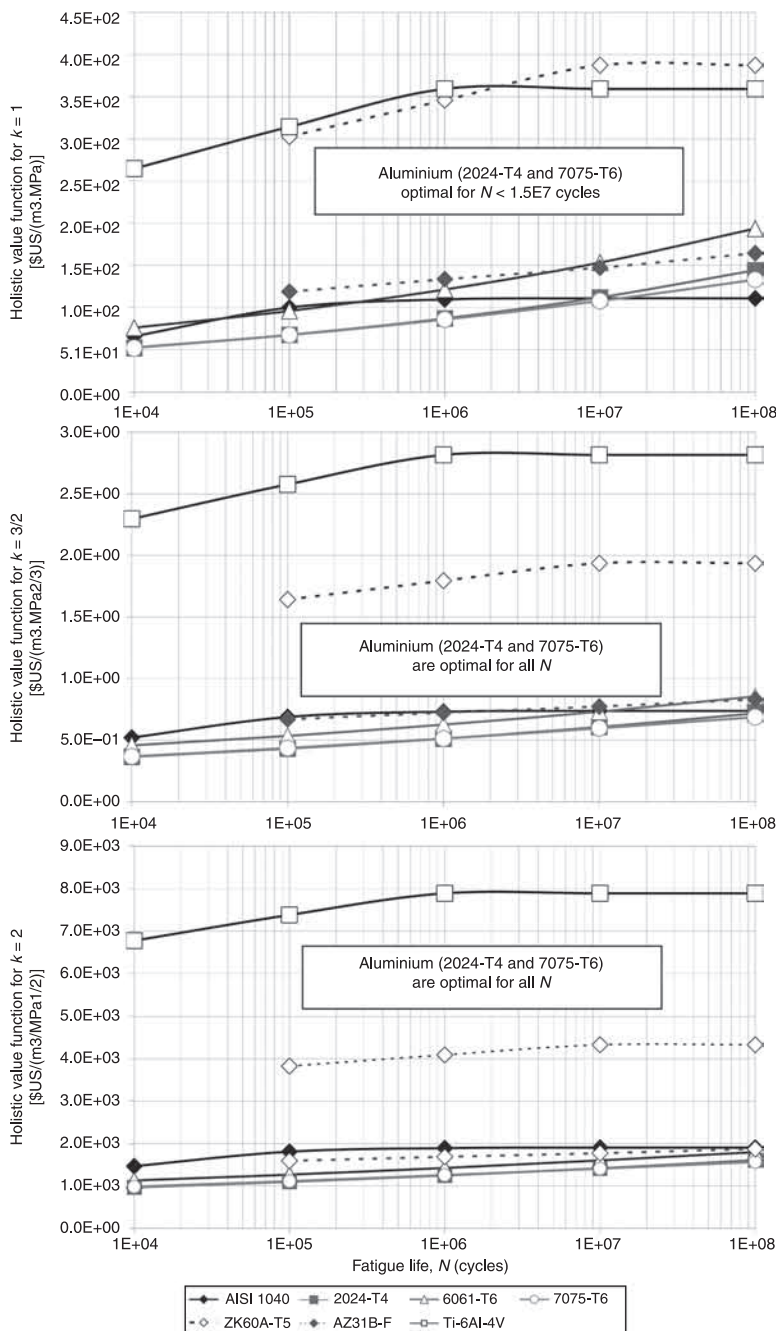
For the average scenario investigated, the holistic exchange constant indicates that each kilogram of vehicle mass contributes approximately \$US 3.81 (Eq. 25.15) to the holistic vehicle cost. The holistic value function has been evaluated for the candidate materials and scenarios of interest (Fig. 25.17).

Of the candidate light alloys, the aluminium alloys (2024-T4 and 7075-T6) are optimal. The holistic value function of these aluminium alloys is nominally equal:

- For $k = 1$ 2024-T4 and 7075-T6 are optimal for $N < 1.5E7$ cycles
- For $k = 3/2$ 2024-T4 and 7075-T6 are optimal for all N
- For $k = 2$ 2024-T4 and 7075-T6 are optimal for all N .

25.7 Environmental consequence of material selection

Environmental impact is an increasingly important consideration for material selection decisions; however, the requisite analysis is complex, and many design metrics have been proposed (e.g. Schmidt and Taylor, 2006). Of these metrics, the method presented in this work will focus on the *embodied energy* and *CO₂ footprint*; however, the method is compatible with other metrics of interest. The system boundary applied in this work will not include the retirement phase as it is considered to have a negligibly small contribution to the holistic life-cycle costs (Gibson, 2000). The following procedures will identify the environmental impact for the manufacturing phase. Methods for use-phase evaluation were discussed in Section 25.6.1.



25.17 Holistic value function versus fatigue life. Upper: V_{1h} , $k = 1$; middle: $V_{3/2h}$, $k = 3/2$; lower: V_{2h} , $k = 2$.

25.7.1 Embodied energy

Embodied energy, E_e , is an estimate of the total energy required to produce one unit-mass of a particular material, including mining of raw materials, transportation and primary processing (Eq. 25.22).

$$E_e = \frac{\sum \text{Estimated energy required for primary production}}{\text{Mass of primary material production}} \quad [25.22]$$

25.7.2 CO₂ emissions

Of the proposed environmental impact metrics, CO₂ emissions are of significant importance due to their contribution to climate change. The CO₂ emission estimate applied in this work is based on the emissions associated with primary production, transport and feedstock manufacture (Eq. 25.23).

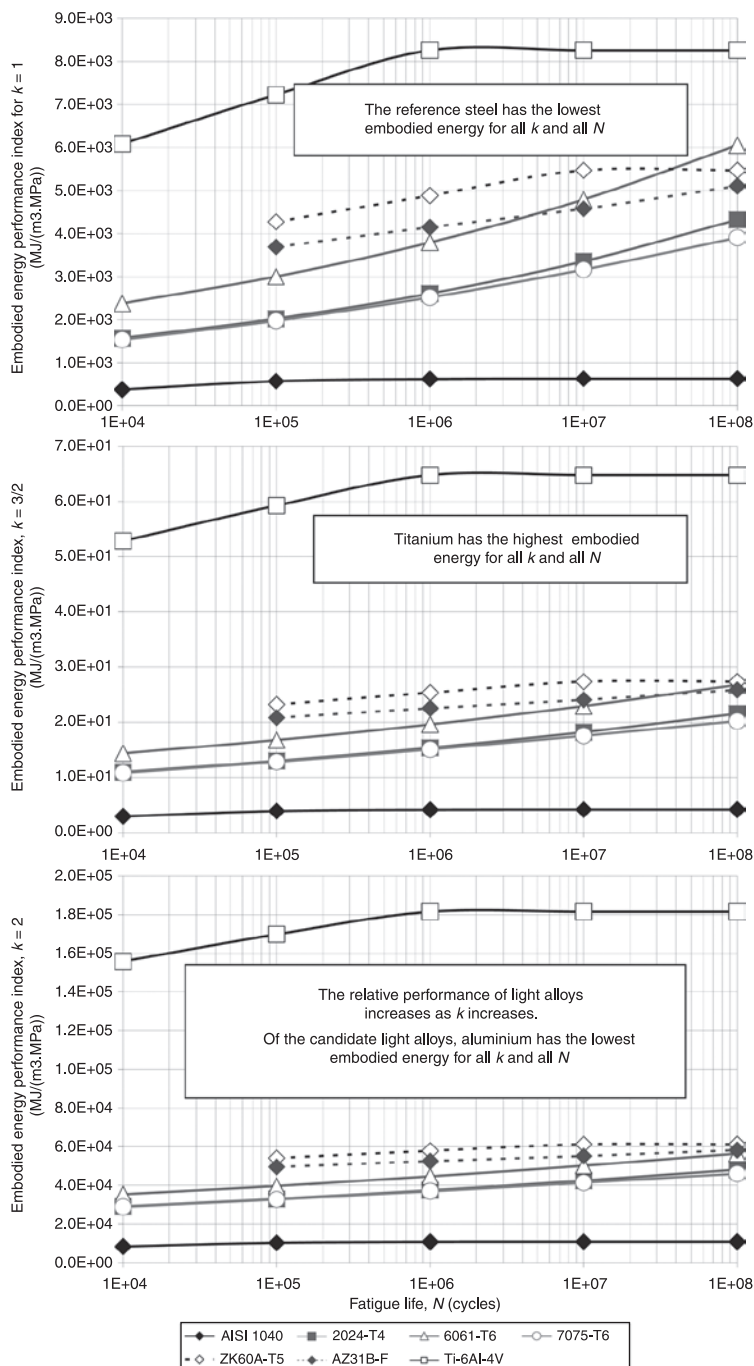
$$E_c = \frac{\sum \text{Mass of CO}_2 \text{ arising from production}}{\text{Mass of material produced}} \quad [25.23]$$

25.7.3 Environmental material selection curves

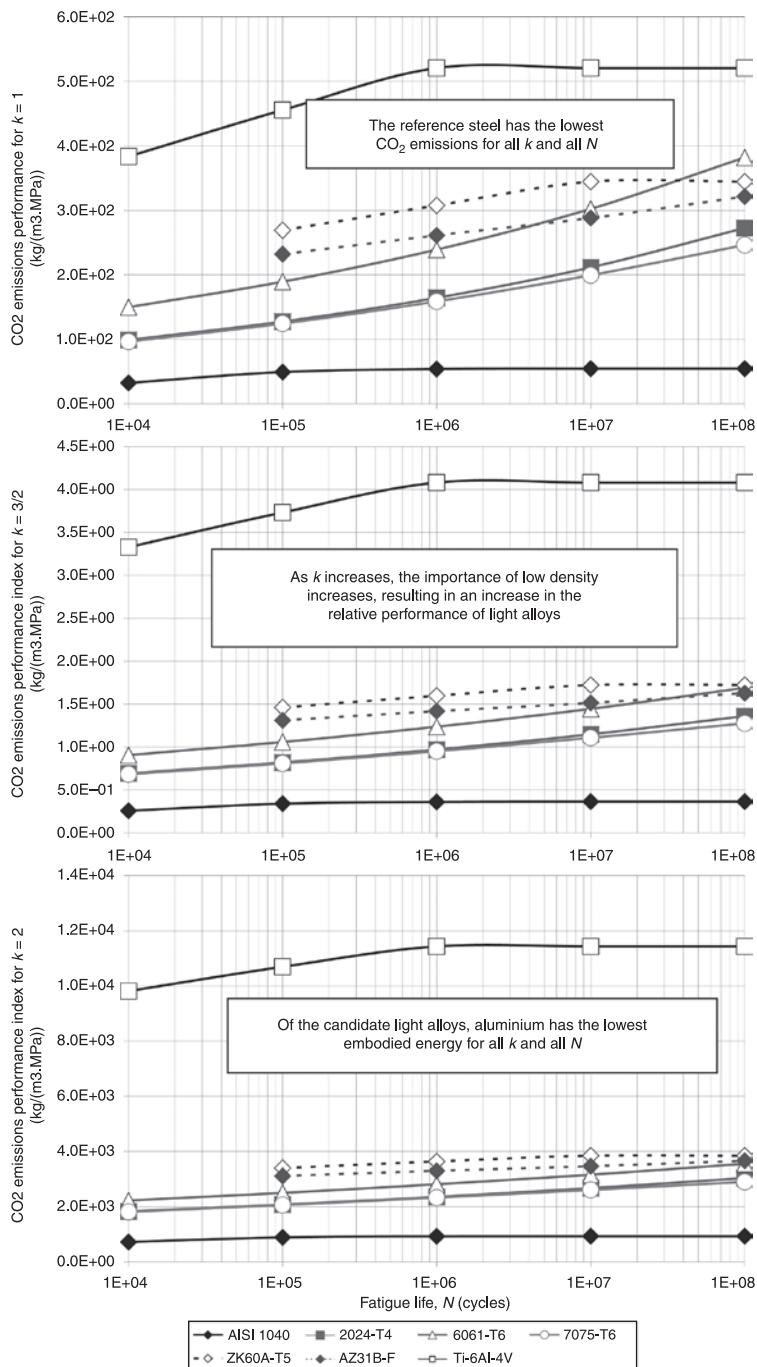
The material selection indices can be modified to accommodate environmental objectives such as minimal embodied energy and minimal CO₂ emissions (Burvill et al., 2009) (Table 25.1). Based on these material selection indices, a series of material selection curves have been plotted for the identified materials (Fig. 25.18 and 25.19). Estimates of embodied energy and CO₂ emission are obtained from industry average estimates obtained from the CES material selection system (Table 25.2). These measures are subject to significant uncertainties and are consequently reported for material types rather than specific alloys. To acknowledge these uncertainties, the reported environmental metrics include a tolerance bound; however, specific metrics in this work are calculated for mean values only for visual clarity.

25.7.4 Secondary aluminium

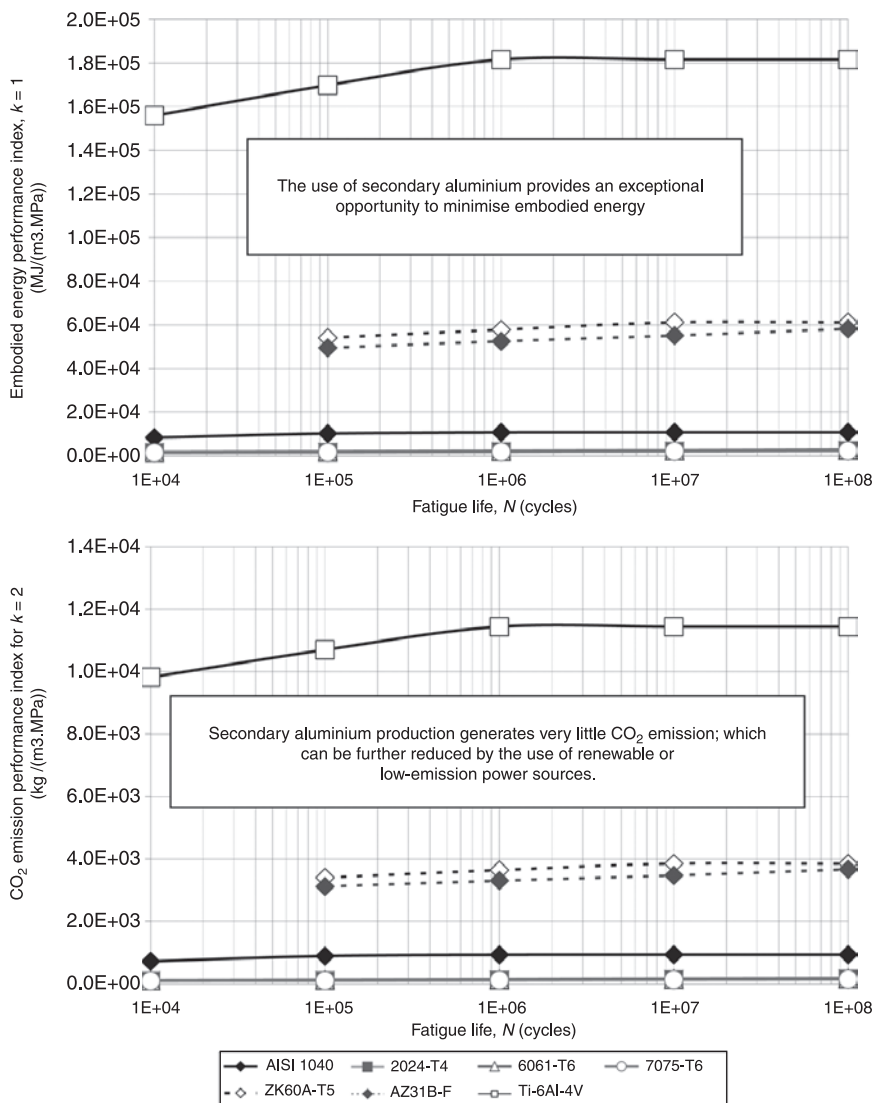
The previous analyses presume the use of primary materials. Primary aluminium processing is energy intensive and results in significant environmental impact. These consequences can be mitigated by utilising renewable or low-emission power sources, and by the application of secondary (recycled) aluminium. Secondary aluminium processing requires only five per cent of the energy consumption associated with primary aluminium (Section 3.2). Furthermore, aluminium is eminently recyclable and secondary and primary aluminium are structurally indistinguishable. To provide insight into the associated environmental merit, the CO₂ emissions and embodied energy associated with secondary aluminium use are indicated in Fig. 25.20.



25.18 Embodied energy for: tie (upper), beam (middle) and plate (lower) structural elements.



25.19 CO₂ emissions for: tie (upper), beam (middle) and plate (lower) structural elements.



25.20 Embodied energy (upper) and CO_2 emissions (lower) associated with secondary aluminium use. Note that all other materials are based on primary production attributes, as in Fig. 25.18 and 25.19.

25.7.5 Summary of environmental material selection outcomes

The material selection curves aid decision-making through increased quantitative certainty of the environmental impact for a range of design scenarios. For the scenarios assessed in this work:

- The environmental consequences associated with primary aluminium production are relatively high (Table 25.2). Consequently, the reference steel provides lower embodied energy and CO₂ emissions for all k and N .
- As k increases, the relative mass of the light alloy solution decreases; however, E_e and E_c remain constant. Consequently, scenarios with large k , for example plates and beams, minimise the environmental consequence of light alloy application.
- Of the investigated light alloys, aluminium provides optimal environmental performance for all k and N .
- Although aluminium provides the optimal environmental performance of the light alloys assessed, this analysis indicates that primary aluminium is not optimal for fatigue limited scenarios that attempt to minimise environmental impact. However, this outcome is highly dependant on the assumption of non-stationary applications, non-renewable energy sources and the use of primary material.
- The use of secondary aluminium provides an opportunity to enhance environmental performance by virtue of the reduction in processing energy. For the scenarios investigated, secondary aluminium provides a significantly lower environmental impact than primary steel (Fig. 25.20).
- Another opportunity to enhance environmental impact is the use of renewable or low-emission power sources, such as solar, tidal and wind energy. Low polluting technologies provide an opportunity to reduce the CO₂ emissions associated with both primary and secondary processing.

It is apparent that aluminium provides a significant opportunity to achieve mass reduction over traditional materials (especially for high k values) but may incur an increased environmental impact. However, secondary aluminium incurs only five per cent of the environmental impact associated with primary processing, with no degradation of mechanical properties, and provides an opportunity to significantly enhance environmental performance. If scenarios are non-stationary, the environmental benefit of reduced mass acts to reduce use-phase emissions, which further offsets the impact associated with aluminium processing. The use of green energy provides another opportunity to reduce CO₂ emissions. These factors result in many scenarios for which aluminium alloys provide a robust opportunity for environmentally optimal material selection.

25.8 Conclusion

Material selection is typically complex and subject to significant uncertainty. Consequently, the designer may be tempted to apply methods based on precedent or intuition. These subjective methods incur a high risk of failing to satisfy the functional requirements and are unlikely to result in optimal outcomes. The application of systematic and objective material selection procedures results in

robust and transparent design decisions which enable significant commercial opportunities for material suppliers and design engineers. This chapter provides a comprehensive review of the pertinent material selection procedures, including:

- Single objective and constraint problems for simple geometries, for example a strength-limited beam of minimal mass.
- Accommodation of non-commensurate units, e.g. minimisation of the holistic cost associated with initial purchase and fuel consumption.
- Compromise between conflicting objectives such as mass, cost and environmental impact.
- Graphical methods for comparing the fundamental performance of candidate materials for common structural elements.
- Numeric methods for the optimisation of non-trivial geometries.
- Methods which accommodate the finite-life design criteria.
- Evaluation of the environmental impact of material selection.

Aluminium alloys display a unique profile of attributes, resulting in an increasing range of scenarios which favour their application. Excellent opportunities for aluminium substitution exist when:

- components are subject to bending or torsion
- the design-life is finite
- recycled material is used, or the product is intended to be recycled, and
- products are non-stationary and consider the holistic costs of material selection.

Material performance is highly dependent on the associated guideline gradient, k . As k increases, the relative importance of low material density, or specific cost for the case of cost-limited design, dominates performance. In general, the opportunities for mass reduction by aluminium substitution are maximised if the design focus is on scenarios with large guideline gradient, such as components subject to bending or torsion.

Fatigue-limited component design is traditionally based on the infinite-life criteria as the resulting design is independent of the associated service-life. Mass reduction imperatives have resulted in an increased use of finite-life criteria, particularly, in non-stationary applications. This change in design philosophy provides new opportunities for the application of aluminium, which does not have a well-defined fatigue-limit. The material selection curves presented in this chapter (Section 25.3.4) provide an opportunity to enable aluminium substitution for finite-life design scenarios.

Although primary production is energy intensive, aluminium is eminently recyclable and as a result, the environmental performance of secondary aluminium is excellent. When applied in non-stationary applications, the associated mass reduction acts to offset environmental impact. Environmental impact can be further reduced by the use of green energy for material processing. As a

consequence of these factors, there exist a range of scenarios for which aluminium alloys are environmentally optimal.

Of the materials investigated, aluminium is optimal for most design scenarios that consider the holistic costs associated with vehicle mass. The imperative for mass reduction in transport applications is continuously increasing due to the decreasing availability of fossil fuels and requirements for reduced vehicle emissions; consequently, the opportunities for mass reduction by the substitution of ferrous metals with aluminium will continue to increase.

25.9 Acknowledgements

The author is indebted to the significant contribution of the following colleagues in the preparation of this manuscript:

Dr Colin Burvill (University of Melbourne, Department of Mechanical Engineering), as supervisor and collaborator in the development of the fatigue-limited material selection curves presented in this work.

Dr Roger Lumley (CSIRO Light Metals Flagship), for collaboration in the safety-critical actuator case study and for providing robust editorial guidance in the preparation of this chapter and this book.

Prof Aleksandar Subic (RMIT University, School of Aerospace, Mechanical and Manufacturing Engineering), for directly supporting this work and for providing guidance in life-cycle analysis and optimisation studies.

Prof Mike Ashby (Cambridge University, Engineering Design Centre), for assistance with the initial fatigue-limited material selection work, and to acknowledge my debt to his contribution to the field.

Maciej Mazur (RMIT University, School of Aerospace, Mechanical and Manufacturing Engineering), for collaboration in the optimisation elements of this work and assistance in preparation of this chapter.

25.10 Notes

1. The design-life is typically based on an estimate of the worst-case loading that may be reasonably expected to occur, combined with an appropriate design safety factor. The service-life is often ill-defined and consequently the design-life includes uncertainties (Leary, 2006).
2. To reduce this risk, the endurance limit is defined at a very high number of cycles, for example $N_e = 5E8$ cycles for aluminium alloys (Lampman, 1995). The fatigue limit for ferrous metals typically occurs at approximately $N_\infty = 1E6$ cycles.

25.11 References

- Ashby, M. F. (1997a). Material property charts. *ASM Handbook, Vol. 20: Materials Selection and Design*. Materials Park, OH: ASM International, pp. 266–280.

- Ashby, M. F. (1997b). Performance indices. *ASM Handbook, Vol. 20: Materials Selection and Design*, pp. 281–290. Materials Park, OH: ASM International.
- Ashby, M. F. (2000). Multi-objective optimization in material design and selection. *Acta Materialia* 48(1): 359–371.
- Ashby, M. F. (2005). *Material Selection in Mechanical Design*, Vol. III. Oxford: Butterworth-Heinemann.
- Ashby, M. F. and Bréchet, Y. (2002). Materials selection for a finite life time. *Advanced Engineering Materials* 4(6): 335–341.
- Ashby, M. F. and Cebon, D. (2001). *Case Studies in Material Selection*. Cambridge: Granta Design Limited.
- Ashby, M. F. and Cebon, D. (2002). *New Approaches to Materials Education* (Report). Cambridge: Cambridge University.
- Ashby, M. F. and Johnson, K. (2003). *Materials and Design: The Art and Science of Material Selection in Product Design*. Oxford: Butterworth-Heinemann.
- Ashby, M. F. and Jones, D. (1993a). *Engineering Materials 1*. Oxford: Pergamon Press.
- Ashby, M. F. and Jones, D. (1993b). *Engineering Materials 2*. Oxford: Pergamon Press.
- Australian Bureau of Statistics. (2000). *Survey of Motor Vehicle Use* (Report 9208.0). Canberra: Australian Bureau of Statistics.
- Battelle. (1998). *Military Handbook Metallic Materials and Elements for Aerospace Vehicle Structures*. Columbus: Battelle.
- Boyer, H., (Ed.) (1986). *Atlas of Fatigue Curves*. Materials Park, OH: ASM International.
- Burvill, C., Leary, M., and Sciafone, F. (2009). *Material selection strategies for environmental-based fatigue design*. International Conference on Engineering Design (ICED 09), 27 August, Design Society, Stanford, CA.
- Cambridge Engineering Selector EduPack. (2005) *Charts*. Cambridge: Granta Design Limited.
- Campbell, C. J. and Laherrère, J. H. (1998). The end of cheap oil. *Scientific American*, March, pp. 60–65.
- Coley, D. (1999). *Genetic Algorithms: An Introduction for Scientists and Engineers*. Singapore: World Scientific.
- Collard, J. (2007) *Geometrical and Kinematic Optimization of Closed-Loop Multibody Systems*. PhD Dissertation, Université Catholique de Louvain, Belgium.
- Council of the European Parliament. (2000). Directive 2000/53/EC of the European Parliament and of the Council of 18 September 2000 on end-of life vehicles. *Official Journal of the European Communities* (L) 269: 34–42.
- Deb, K. (2006). *Optimization for Engineering Design*. New Delhi: Prentice-Hall.
- Department of Primary Industries and Energy. (1996). *Fuel Consumption Project* (Report). Australia: Department of Primary Industries and Energy.
- Dowling, N. E. (1993). *Mechanical Behaviour of Metals*. Englewood Cliffs, NJ: Prentice-Hall.
- Esawi, A. M. K. and Ashby, M. F. (2003). Cost estimates to guide pre-selection of processes. *Materials and Design* 24(8): 605–616.
- Esin, A. (1980). A method for correlating different types of fatigue curve. *International Journal of Fatigue* 2(4): 153–158.
- Fermer, M. and Svensson, H. (2001). Industrial experiences of FE-based fatigue life predictions of welded structures. *Fatigue and Fracture of Engineering Materials and Structures* 24(7): 489–500.
- Gibson, T. (2000). *Life Cycle Assessment of Advanced Materials for Automotive Applications*. SAE Technical Paper – 2000-01-1486.

- Hellman, K. N. and Murell, J. D. (1984). *Development of Adjustment Factors for the EPA City and Highway MPG Values* (Report #840496), Detroit, SAE.
- Hollick, M. (1993). *An Introduction to Project Evaluation*. Melbourne: Longman Cheshire.
- Hubbert, M. K. (1956). *Nuclear Energy and the Fossil Fuels*. Spring meeting of the Southern District, American Petroleum Institute, San Antonio, TX.
- ISO. (1998) *ISO 14040 Environmental Management – Life Cycle Assessment – Principles and Framework*. Geneva: ISO.
- Jahn, J. and Maennig, W.-W. (1997). Safe evaluation of fatigue data in the range of finite endurance. *International Journal of Fatigue* 19(4): 335–344.
- Keeney, R. L. and Raiffa, H. (1993). *Decisions with Multiple Objectives: Preferences and Value Trade-Offs*. Cambridge: Cambridge University Press.
- Lampman, S., (Ed.) (1995). *Fatigue Data Book: Light Structural Alloys*. Materials Park, OH: ASM International.
- Landru, D. and Brechet, Y. (2000). Durability and optimization of structural materials – Troisième Partie – modelisation – new design tools for material and process selection. *Matériaux et Techniques* 88(9–10): 31.
- Leary, M. (2006). *Mass Reduction of Fatigue-Limited, Safety-Critical (FLSC), Ferrous Metal Automotive Components by Forged Light Alloy Substitution*. PhD Thesis, University of Melbourne, Australia.
- Leary, M. and Burvill, C. (2001). *Optimal material selection for finite life automotive suspension applications*. 2nd International Conference on Light Materials for Transportation Systems, pp. 287–294, Pusan, Korea.
- Leary, M. and Burvill, C. (2009). Applicability of published data for fatigue-limited design. *Quality and Reliability Engineering International* 25: 921–932.
- Leary, M., Mazur, M., Lumley, R., and Subic, A. (2009a). *An integrated case study of material selection, testing and optimization*. International Conference on Engineering Design (ICED 09), Stanford, USA, p. 12.
- Leary, M., Mazur, M., and Subic, A. (2009b). The integration of algebraic material selection and numeric optimisation. *Machine Design*, pp. 1–12. Novi Sad, Serbia: Faculty of Technical Services.
- Lumley, R. N., O'Donnell, R. G., Gunasegaram, D. R., and Givord, M. (2007). Heat treatment of high pressure die castings. *Metallurgical and Materials Transactions A* 38A: 2564–2574.
- Maennig, W.-W. (1996). Planning and evaluation of fatigue tests. *ASM Handbook, Vol. 19: Fatigue and Fracture*, pp. 303–313. Materials Park, OH: ASM International.
- Nguyen, T. T., de Looze, G., Carrig, J. F., Nguyen, V., and Cowley, B. (2006) A new high-yield, high-integrity magnesium permanent mold casting process. *AFS Transactions* 114: 695–706.
- Peterson, R. E. (1953). *Stress Concentration Design Factors: Charts and Relations Useful in Making Strength Calculations for Machine Parts and Structural Elements*. New York: Wiley.
- Pilkey, W. D., (Ed.) (1997). *Peterson's Stress Concentration Factors*. New York: John Wiley and Sons.
- Rothbart, H. A. (1996). *Mechanical Design Handbook*. New York: McGraw-Hill.
- Sankaran, K. K., Perez, R., and Jata, K. V. (2001). Effects of pitting corrosion on the fatigue behavior of aluminum alloy 7075-T6: Modeling and experimental studies. *Materials Science and Engineering A* 297(1–2): 223–229.

- Schmidt, W. and Taylor, A. (2006). *Ford of Europe's product sustainability index*. 13th CIRP International Conference on Life Cycle Engineering May 31–June 2, Leuven, Belgium.
- Sirisalee, P., Parks, G. T., Clarkson, P. J., and Ashby, M. F. (2003). *A new approach to multi-criteria material selection in engineering design*. 14th International Conference in Engineering Design (ICED '03), 19–21 August, pp. 451–452, Stockholm, Sweden.
- Standards Australia. (1986). *Methods of Test for Fuel Consumption of Motor Vehicles Designed to Comply with Australian Design Rules 37 and 40*. Sydney: Standards Australia.
- Stone, R. (1989). *Motor Vehicle Fuel Economy*. Basingstoke: Macmillan.
- Subic, A., Schiavone, F., Leary, M., and Manning, J. (2009). Comparative life cycle assessment (LCA) of passenger seats and their effects on different vehicle models. *International Journal of Vehicle Design* vol. 53, number 1–2/2010, pp. 89–109.
- Svensson, T. (2004). Model complexity versus scatter in fatigue. *Fatigue and Fracture of Engineering Materials and Structures* 27(11): 981–990.
- Tsybanev, G. V. and Ponomarev, S. L. (2001). Fatigue of low-carbon and low-alloyed steels for the automotive industry. Part 1: The influence of stress concentration and fretting on fatigue-life of full-scale automobile wheels and specimens. *Strength of Materials* 33(1): 8–14.
- Veers, P. S. (1996). Statistical considerations in fatigue. *ASM Handbook, Vol. 19: Fatigue and Fracture*. Materials Park, OH: ASM International.
- Vincke, P. (1992). *Multicriteria Decision-Aid*. New York: John Wiley & Sons.
- Weaver, P. M. and M. F. Ashby (1997). Material limits for shape efficiency. *Progress in Materials Science* 41(1–2): 61–128.
- Wegst, U. G. K. and Ashby, M. F. (2000). Environmentally conscious materials selection and design of sports equipment. *The Engineering of Sport-Research Development and Innovation*, pp. 521–531. Oxford: Blackwell Science.

- A355 alloy, 194
- A356 alloy, 164, 186
 - chemistry of base alloy, 159
 - elongation to fracture, 188
 - fracture surface, 171
 - mechanical properties, 162
 - pore nucleating on a folded oxide film, 176
 - tapered region in casting, 199–200
- A360 alloy
 - hardening responses, 267
 - surfaces and internal microstructures, 266
- A380 alloy, 186
 - aged to a T6 temper, 268
 - as-cast, 264
 - heat treatment effects on tensile and fracture properties, 293
 - laminar defect leading to blistering, 275
- A356-T6 alloy
 - tensile properties, 159
 - Aluminium Association mould, 160
 - Aluminium Association test casting, 160
 - tensile strength and quality of castings, 163
- A356-T62 alloy, 157
 - average tensile properties, 158
 - minimum/maximum values, 158
- A357-T6 alloy
 - tensile strength and quality of castings, 163
- accumulative roll-bonding, 472
- ACR method *see* adjusted compliance ratio method
- ADC10M, 290, 291
- adhesive bonding, 647–50
 - advantages and disadvantages, 649
 - substrate treatment effect, 648
- adjusted compliance ratio method, 507
- advanced thixotropic metallurgy, 149
- aerospace alloy 7075-T6, 586
- aerospace alloys, 777–8
- AFIM characterisation, 352
- age hardening, 268, 345
 - role of alloying elements, 279–91
- aged aluminium alloys
 - compositional change
 - fatigue ratios, 369
 - creep performance, 371–5
 - alloy hardness-time curve and secondary creep rate, 372
 - alloy microstructures in T6 and UA conditions, 375
 - creep curves for commercial and experimental alloy, 373
 - mean dislocation velocities, 376
- fatigue studies, 375–9
 - cyclic stress failure data, 377
 - dislocations in plastic zone, 378
 - stress-number of cycles data, 376–7
- secondary precipitation, 379–81
 - Al alloy hardness-time curves, 380
 - alloy hardness level using T6 ageing treatment, 381
 - interrupted ageing and secondary hardening effects, 382
 - positron lifetimes during secondary ageing, 379
- solute partitioning
 - mechanical properties enhancement, 367–82
 - through compositional change, 368–71
 - studies of underaged alloys, 371–9
- ageing precipitates, 562
- air set sand casting, 152
- Airbus, 751
- Airbus A350, 777
- Airbus A380, 776, 779
- aircraft
 - aluminium alloys
 - chronology of increase in atomic percent solute, 761
 - dispersoids, 757
 - major precipitates, 756
 - nominal compositions, 755
 - property-microstructure relationships, 775
 - usual constituent phases, 759
 - drivers for materials selection and aluminium alloy product development, 749–51
 - 1970s, 750
 - 1980s, 750
 - 1930s–1960s, 749
 - 1990s to present, 751
 - microstructural features, 754–9
 - crystallographic texture, 758
 - degree of recrystallisation, 757–8
 - dispersoid particles, 756
 - grain size and shape, 758
 - intermetallic constituent particles, 758–9

- porosity, 759
- precipitates, 754–6
- toughness tree representation, 765
- modern aluminium alloys application, 747–80
- new products and recent manufacturing technologies, 775–9
 - Al-Li and AlMgSc aerospace alloys, 777–8
 - alloy 2040-T6 for aircraft wheels, 778
 - asymmetric rolling, 779
 - crystallographic texture, 779
 - friction-stir welding and laser welding, 778–9
 - new materials and products cost, 775–6
 - 7XXX alloy for Airbus A380, 776
- primary structure performance criteria and property requirements, 751–3
 - empennage property requirements, 753
 - fuselage property requirements, 751–2
 - property requirements for jetliner and military transport applications, 752
 - wings property requirements, 752–3
- strength, 759–64
 - propagation energy vs yield strength, 766
 - yield strength vs function of ageing time for age-hardenable aluminium alloys, 760
- stretch and ageing time
 - Al₃CuLi precipitates number density, 762
 - alloy 2090 strength-toughness relationship, 769
 - strength in alloy 2090, 763
- structural material usage in large commercial aircraft, 748
- structure property relationships, 754–75
 - alloy 7178 strength-toughness relationship, 768
 - controlling factors in SCC models, 771
 - corrosion resistance, 772–3
 - elastic modulus, 773–4
 - fatigue crack initiation, 768–9
 - fatigue crack propagation, 769–70
 - fracture toughness, 764–8
 - specific modulus for DRA materials, 774
 - stress corrosion crack velocity vs stress intensity, 771
 - stress corrosion cracking, 770–2
 - total Fe + Si effect on alloy 7050 sheet toughness, 766
- Al alloy 6061, 479, 489, 704
- Al alloy 7085, 776
- Al-8Cu, 2
- Al-Cu alloys, 392
- Al-4.4Cu-1.6Mg-0.5Si, 711
- Al-5Mg, 713
- Al-Si, 142
- Al-9Si, 232
- Al-12Si, 232
- Al-Si-8Cu-Fe, 144
- Al-Si-10Cu-2Fe, 144
- Al-14.7Si-4.5Mg, 708
- Al-Zn-Mg alloy, 369
 - compositions and T6 tensile properties, 370
 - stress-number of cycles curves, 370
- Alcan Compact Degasser, 116
- Alclad, 591
- Alcoa 201AB type, 694
- Al₃CuMg, 759, 776
- alloying, 80–1
- alloying elements
 - role in age hardening, 279–91
 - role in solution treatment, 271–8
- AlMgSc alloy, 777
- alpha alumina, 26, 38, 42, 43
- Alpur, 116
- Alscan, 113
- ALSPEK, 113
- alumina
 - aluminium minerals mining and processing, 24–7
 - Eh-pH diagram, 25
 - Bayer alumina refinery
 - agglomerated gibbsite particles from precipitation, 33
 - agglomerated smelter grade alumina particles, 35
 - calcination, 35–8
 - clarification, 32
 - fluid bed calcined smelter alumina pore size distribution, 37
 - particle size distribution, 34
 - precipitation, 32–4
 - temperature for bauxite digestion, 30
 - impurities, 40–2
 - properties and analyses, 41
 - microstructure, 38–40
 - Al MAS NMR spectra at two magnetic field strengths, 40
 - Rietveld refinement from X-ray diffraction, 39
 - phases or forms relationship, 24
 - production, 23–44, 49
 - speciality aluminas, 42–3
 - trends, 43–4
 - production processes, 27–9
 - Bayer process, 28
 - Petersen process, 29
 - sintering of nepheline, 29
- alumina feeding, 62–3
- aluminium, 1, 23, 24, 51, 70, 647
 - see also* primary aluminium; secondary aluminium
 - alloy development, 2–3
 - aluminium association alloy designation system, 3
 - registered temper designations, 4
 - cast aluminium alloys, 5–6
 - corrosion and corrosion protection, 574–601
 - cost from 1900–2007, 11
 - engineering material, 1
 - fracture resistance, 538–71
 - Al alloy casting, 548–51
 - fracture toughness, 557–63
 - future trends, 569–71
 - high strength wrought alloys, 551–7
 - particulate metal matrix composites, 563–5
 - serrated yielding effects on fracture, 565–7
 - thin sheet, 544–8
 - uni-axial tension, 539–44
 - global usage 1950–2008, 71
 - high pressure die casting, 217–58
 - ingot casting and casthouse metallurgy, 83–123
 - joining technologies, 607–50

- laser sintering and rapid prototyping, 702–15
 - dimensional changes, 713–14
 - infiltration, 711–13
 - skeleton, 705–11
- metallurgy, 1–17
- production, 8, 49–50
 - 2007 bauxite mine production and bauxite reserve base, 9
 - 2007 primary aluminium production by country, 10
 - aluminium cost from 1900–2007, 11
 - US production from 1900–2007, 11
 - world-wide production from 1900–2007, 10
- uses, 8, 13–16
 - 2002–2007 kg per capita usage, 17
 - characteristics and relative importance in different products, 12
 - lifecycles by end use and recycling rates, 13
 - shipments by market in North America, 1960–2007, 14
- wrought aluminium alloys, 7–8
- aluminium age-hardenable alloys
 - ageing processes, 387–88
 - conventional techniques, 391–4
 - electrical resistivity, 392
 - electrical resistivity evolution, 395
 - isothermal pre-ageing curves, 394
 - diffusion processes, 394–7
 - alloy microstructure, 397
 - modelling, 408, 410–15, 411–15
 - atom arrangements, 413
 - first-principle calculations in positron annihilation spectroscopy, 414–15
 - solute clusters growth, 411–12
 - solute-vacancy binding energies, 411
 - solute-vacancy interactions, 386–416
 - experimental studies, 389–90
 - spectroscopic techniques, 403–8
 - CDB spectra, 407
 - Cu NMR spectra from Al-1.7 at. % Cu, 399
 - PALS and CDB measurements, 409
 - positron lifetime and Vickers hardness vs ageing time, 406
 - positron lifetime vs ageing time, 405
 - precipitation sequence microstructural analysis using NMR, 397–9
 - vacancies and solute-vacancy interactions
 - experimental studies, 388–408
- aluminium alloys, 3, 4
 - Al-Cu based alloys, 347–9
 - crystal structure and orientation relationship with matrix, 348
 - 1DAP analysis observed in He FIM image, 350
 - hardness time plot, 349
 - Al-Cu-Mg based alloys, 349–54
 - hardness time plots, 351
 - lath-shaped Mg₂Si precipitates, 353
 - Al-Mg-Si based alloys, 354–6
 - Mg, Si and Cu atom maps, 354
 - Al-Zn-Mg-(Cu) based alloys, 356–9
 - hardness time plots, 357
 - peak hardness microstructures, 359
 - alloying elements, 722–4
 - 1xxx series, 722–3
 - 2xxx series, 723
 - 3xxx series, 723
 - 4xxx series, 723
 - 5xxx series, 723
 - 6xxx series, 723
 - 7xxx series, 723–4
 - 8xxx series, 724
- aluminium casting alloys, 141–2
 - Aluminium Association designation system, 142
- application to aircraft, 747–80
 - drivers for materials selection and product development, 749–51
 - new products and recent manufacturing, 775–80
 - performance criteria and property requirements, 751–3
 - structure property relationships, 754–75
- cast aluminium alloys, 5–6
 - cast aluminium products distribution, 6
 - part size, production rate and casting process, 5
- casting, 141–53
 - feeding and porosity, 144
 - filling the casting, 143–4
- casting processes, 144–53
 - Cosworth process, 153
 - high pressure die casting, 144–50
 - low-pressure die casting, 150–1
 - permanent mould casting, 151
 - sand casting, 151–3
- classes and elements, 721–2
 - heat treatable Al alloys, 722
 - non-heat treatable Al alloys, 722
- coupling precipitation and plastic deformation, 458–61
 - δ' (Al₃Li) heterogeneous nucleation and growth, 459
 - pre-existing precipitate structure deformation, 460–1
 - precipitation in a pre-existing deformation structure, 458–60
 - simultaneous precipitation and deformation, 461
- design for fatigue crack growth resistance, 504–32
 - background and current state of knowledge, 505–7
 - crack growth Regions II and III, 520–5
 - design curves from K_{max} sensitivity and data normalisation, 530–2
 - dual parameter $\Delta K-K_{max}$ approach, 529–30
 - K_{max} and stress ratio effects, 526
 - materials, processing, mechanical properties and testing, 507–8
 - propagation in near-threshold regime, 510–19
- development, 2–3
- high pressure die casting, 217–58
- ingot casting and casthouse metallurgy, 83–123
- joining technologies, 607–50
 - adhesive bonding, 647–50
 - brazing, 643–6
 - classification, 608
 - fusion welding, 618–30

- mechanical fastening, 610–16
- mechanical joining, 609–18
- solid state welding, 630–42
- main tempers, 724–5
- materials selection and substitution, 784–824
 - environmental consequence of material selection, 816, 818–22
 - fundamental material selection strategies, 785–91
 - material selection for specific scenarios, 791–803
 - multi-objective problems and numeric optimisation, 804–11
 - multiple objective material selection, 811–16
 - non-stationary fatigue-limited application, 803–4
- microstructure control in foundry alloys, 142–3
 - eutectic modification, 143–4
 - grain refinement, 143
- non-isothermal heat treatments, 436–40
 - class models, 437–40
 - monotonic thermal treatments profiles, 437
 - particle size distribution, 439
 - particles number density calculations, 439
 - precipitation description, 441
 - treatment temperature, 438
- non-spherical precipitates, 448–57
 - anisotropy in phase interface mobility, 451–3
 - atomistic approaches, 449–51
 - continuum approaches, 451
 - distribution coarsening, 453–7
 - LKMC simulation of GP zone formation, 450
 - mean precipitate size model vs experimental measurements, 455
 - microstructural evolution phase field simulation, 457
 - order parameters describing q' precipitates, 456
 - plate-shaped diffusional growth, 454
- precipitation kinetics modelling, 422–62
 - Al-3Cu alloy plate-shaped precipitates, 423
 - current approaches, 426–57
 - future trends, 461–2
 - physical processes controlling precipitation, 425–6
 - spheres, rod-like and lath-like shapes of precipitates, 427
- precipitation under severe plastic deformation, 359–61
 - SPD vs conventional ageing treatment precipitation, 360
- qualitative SCC resistance, 585
- reversion treatments and welding, 440–7
 - atomistic approaches, 442–7
 - cluster size distributions comparison, 447
 - experimental measurement vs model predictions, 443
 - Lattice Kinetic Monte Carlo simulation, 445
 - LKMC approach, 449
 - modelled precipitation evolution, 442
 - precipitate number density and average radius calculation, 448
 - precipitates average number evolution, 446
- solute clustering and precipitation, 345–62
- specifications, 721–5
- spherical precipitates, 429–35
 - continuum approaches, 429
 - Deschamps and Bréchet model vs experimental measurements of precipitate size, 435
 - Gibbs free energy curves, 431
 - mean radius approaches, 429–35
 - precipitate parameters evolution, 434
- work hardening, 307–38
 - commercial aspects, 332–8
 - fundamentals, 308–12
 - future trends, 338
 - model applications to industrial alloys, 325–32
 - models, 312–25
- wrought aluminium alloys, 7–8
 - aluminium mill products distribution, 7
- Aluminium Association mould, 156–7
- aluminium casting alloys, 141–2
 - case studies, 185–214
 - effect of excess titanium on foundry alloys, 202–4
 - Al-7Si-0.3Mg alloys compositions, 203
 - grain size plotted against Ti:B ratio, 204
 - rod-shaped particles in 0.12Ti-containing A356 alloy, 206
 - variation in yield strength and elongation to fracture, 205
- grain refinement on defect formation, 195–202
 - defects observed in experimental castings, 201
 - grain sizes, 199
 - interconnected macro-porosity at spoke-rim junction, 196
 - mould design schematics, 197–8
 - tapered region in A356 casting, 199–200
- impurity that reduces castability and increases casting defects, 190–5
 - Al-Fe-Si ternary phase diagram liquidus projection, 194
 - defect prone region of cylinder head, 192
 - selecting the right master alloy for eutectic modification, 208–14
 - Al-Sr master alloys microstructures, 210–11
 - strontium content variation, 212–13
- selecting the right master alloy for grain refinement, 207–8
 - calculated potential savings plotted against Q value, 208
 - Q values for wrought alloy compositions, 207
- specification range effect on microstructure and properties, 186–90, 188
 - A356 alloy elongation to fracture, 188
 - mean tensile yield stress vs Mg content of A356/357 alloy, 187
 - predicted values of yield stress and fracture points, 188
 - primary sourced alloys, 186–9
 - pseudo-quality index chart, 191
 - secondary sourced alloys, 189–90
 - tensile flow curves, 190

- aluminium castings
 - fatigue failure, 169–73
 - A356 alloy fracture surface, 171
 - crack, 170
 - pore sizes in solidified Al-7Si-0.3Mg alloy castings, 172
 - W319 alloy measured fatigue life, 173
 - inclusions and porosity on quality, 167–9
 - defect concentration in fracture surface, 169
 - loss of elongation associated with defects, 168
 - quality issues, 155–82
 - effect of metal treatment and transfer on quality, 177–80
 - possible improvements in fatigue life, 180
 - solidification time effect, 162–4
 - A356-T6 and A357-T6 alloy castings
 - tensile strength and quality, 163
 - sources of defects, 174–6
 - pore nucleating on folded oxide film, 176
 - volume fraction porosity, 175
 - standard moulds, 156–62
 - Aluminium Association casting, 156–61
 - Aluminium Association permanent mould test casting, 156–7
 - ASTM B108 test bar, 161–2
 - ASTM B108 test bar mould, 161
 - theoretical basis for quality index, 164–7
 - Al-7%Si-0.4%Mg alloy true stress-true strain curves, 165
 - quality index map, 166
 - Weibull plot
 - 356 alloy castings fatigue life, 181
 - normalised tensile data, 179
 - Sr-modified A356 alloy fatigue life, 181
- aluminium-copper casting alloy, 747–8
- aluminium electrolysis cell, 58
- aluminium fluoride, 54–5, 55, 63
- aluminium oxides *see* alumina
- aluminium powder metallurgy, 655–94
 - aluminium sintering, 678–88
 - applications, 688–92
 - aluminium alloys compositions and properties, 691
 - automotive components, 693
 - future trends, 692–4
 - press and sinter powder metallurgy process, 655–8
 - air and argon-atomised Al powders, 657
 - Al vs stainless steel powder compressibility, 658
 - route schematic, 656
- sintering fundamentals, 658–78
 - curved surface associated stress, 659
 - dihedral angle, 667–8
 - liquid phase sintering, 661–3
 - pore-filling, 675–8
 - rearrangement, 668–71
 - solid reprecipitation, 671–5
 - solid-state sintering, 660–1
 - wetting, 664–7
- aluminium sheet
 - aluminium alloys and specifications, 721–5
 - alloying elements, 722–4
 - classes and elements, 721–2
 - main tempers, 724–5
 - fabrication and processing, 719–45
 - fabrication processing route and microstructure evolution, 725–40
 - aluminium strip casting and twin-roll casting, 727–9
 - annealing, 739–40
 - casting, 726–7
 - cold rolling, 735–9
 - hot rolling, 731–5
 - laser sintered aluminium with nylon, 726
 - sheet ingot pre-annealing homogenisation, 729–30
 - integrated material and through-process modelling, 743–4
 - temperature, microstructure and yield strength simulation, 743
 - parameters and metallurgical effects in Al alloy sheet processing, 741–2
 - main processing steps in aluminium sheet production, 741
- aluminium sintering, 678–88
 - equilibrium liquid mass fraction, 679
 - role of atmosphere, 684–6
 - Al-3.8Cu-1Mg-0.7Si dilatometer curves, 684
 - role of magnesium, 679–84
 - beneficial effect, 681
 - in-situ X-ray photoelectron spectroscopy analyses, 682–3
 - surface oxide, 678–9
 - trace element induced activated sintering, 686
 - Al-8Zn-2.5Mg-1Cu-0.07X densification, 687
 - sintering shrinkage events under nitrogen, 689
 - trace element concentration effect on tensile strength, 687
- aluminium strip casting, 727–9
 - laser sintered powder preforms, 729
 - overall furnace cycle for aluminium preforms infiltration, 728
- Al₃Zr, 756
- anaerobic acrylic adhesives, 647
- annealing, 541, 642, 739–40
 - heat treatable alloys, 740
 - non-heat treatable alloys, 741–2
- anode beam raising, 63
- anode changing, 63
- anode effect, 50
- anodised coatings, 591
- anthracite, 56–7
- anti-plain strain, 555
- argon, 112, 623
- Arrhenius plot, 389, 405, 410
- Ashby map, 790
- ASTM B108, 161
- ASTM B871, 291
- ASTM B117-09, 591
- ASTM G34-01, 584
- ASTM G66-99, 584
- ASTM G85-09, 584
- asymmetric rolling, 779
- atomistic kinetic Monte Carlo simulation, 346, 358
- Audi, 614
- Audi TT coupe, 616
- Auld model, 357

- bake hardening process, 354, 720
- Bauschinger tests, 318, 322
- bauxite, 8, 9, 24, 25, 30, 49, 51
- Bayer process, 30–8, 40–1, 43, 49
 - calcination, 35–8
 - clarification, 32
 - digestion, 30–2
 - flowsheet for alumina production, 28
 - particle size distribution, 34
 - precipitation, 32–4
- bendability, 336–7
- bi-films, 176
- Biot number, 88
- blending, 656
- blind rivets, 610, 614–15
 - riveting stages, 614
- blistering, 598
- boehmite, 26
- Boeing, 750
- Boeing 777, 774
- Boltzmann's constant, 429, 673
- boric-sulphuric acid anodising, 592
- Brass texture, 779
- brazing, 643–6
 - defined, 643
 - laser brazed AlMgSi, 646
 - torch, dip and furnace brazing set-ups, 645
- breakstem rivets, 614
- Burgers vector, 313
- burnt-off, 658

- calcium, 41, 110
- calcium fluoride, 55
- calcium zirconate, 113
- Cambridge Engineering Selector, 791
- can-body test, 733
- carbon, 110
- carbon anodes, 52–4
- cast aluminium alloys, 5–6
 - cast aluminium products distribution, 6
 - part size, production rate and casting process, 5
- casthouse metallurgy, 83–123
- casting, 5–6, 728–9
 - aluminium alloys, 141–53
 - aluminium casting alloys, 141–2
 - feeding and porosity, 144
 - filling the casting, 142–3, 143–4
 - microstructure control in aluminium foundry alloys, 142–3
 - processes, 144–53
 - Cosworth process, 153
 - high pressure die casting, 144–50
 - low-pressure die casting, 150–1
 - permanent mould casting, 151
 - sand casting, 151–3
- cathode, 56–63
- cathodic reactions, 576–7
- CDB *see* coincidence Doppler broadening spectroscopy
- cell lines, 61–2
- central limit theorem, 549
- centre line segregation, 729
- ceramic, 66
- ceramic foam filter, 120–3
- cermet, 66
- chain conveyor casting, 108–10
- chemically reactive adhesives, 647
- Chevron defect, 102
- chlorides, 110, 579
- chlorine, 113–14
- chromate conversion coatings, 591, 595
- chromates, 591, 597
- chromium, 289–91
- chromium oxide film, 591
- Chrysler's 2.7 litre V6, 692
- cladding, 590
- classical nucleation theory, 429, 432
- Claus process, 43
- closure corrective techniques, 515
- Clouland's model, 357
- Cluster dynamics, 447
- coarsening, 425, 433
- coating failure, 596–7
 - chemical, 596–7
 - mechanical, 596
- coincidence Doppler broadening spectroscopy, 400, 403, 407, 409
- cold chamber die casting machine, 219
- cold cracking, 104
- cold folding, 99
- cold metal transfer, 623
- cold rolling treatment, 337, 486, 720, 735–9
 - aluminium parts made by infiltrating laser sintered aluminium preforms, 738
 - hold time effect on 6061–2Mg preforms infiltration, 736
 - simulated strength evolution, 739
 - strength evolution, 737–9
- cold welding, 631
- Comet jet aeroplanes, 556, 749
- compression pre-cracking constant amplitude method, 506
- Considère criterion, 166, 335
- conventional fusion welding, 632
- convergent value function, 812
- copper, 232, 272, 277, 280–1, 284
- copper alloys, 398
- corrosion, 574–601
 - aircraft structure protection, 590–3
 - C-130J Hercules aircraft wing trailing edge strip, 593–600
 - advanced exfoliation corrosion damage, 599
 - assembly and component details, 594–5
 - coating failure, 596–7
 - corrosion around fastener holes, 599
 - corrosion damage along strip edge, 600
 - corrosion processes, 597–600
 - filiform corrosion, 599
 - machine edge corrosion damage, 598
 - operating environment, 595–6
 - trailing edge strip location, 594
 - widespread exfoliation corrosion, 598
 - environmentally assisted cracking, 584–90
 - aircraft stress corrosion cracking, 587
 - corrosion fatigue, 586–7
 - hydrogen embrittlement, 588–90
 - in-service corrosion fatigue failure, 588–9
 - liquid metal embrittlement, 590
 - SSC fracture surface, 585
 - stress corrosion cracking, 585–6
 - general, galvanic and pitting corrosion, 575–82

- AA2024-T3 microstructure, 580
- bimetallic or galvanic corrosion, 576–7
- corrosion potentials summary, 580
- crevice corrosion, 578
- early stage corrosion development, 581
- general corrosion, 575–6
- measured corrosion potentials, 577
- pitting corrosion, 578–82
- Pourbaix diagram, 577
- localised corrosion, 582–4
 - AA2024-T4 exfoliation corrosion, 584
 - intergranular corrosion origins, 583
- corrosion inhibiting compounds, 593
- Cosworth low-pressure sand casting process, 177–8
- Cosworth process, 153
- Coulter counter, 112
- crack closure, 506
- crack compliance method, 519
- cracking, 102–5
- crucible treatment, 117–18
- cryolite, 54, 55, 56
- cumulative distribution function, 548
- cumulative fracture, 556
- current efficiency, 57–9
- DC potential difference method, 509
- de-lubrication, 658
- de-waxing, 658
- deep bed filters, 122–3
- deformation, 458
- Delta II rockets, 640
- Delta IV rockets, 640
- dendrite arm spacing, 157, 163, 726
- density functional theory, 410, 414
- Deschamps and Bréchet model, 429, 435
- deterministic algorithms, 805
- diaspore, 26
- diffuse necking, 334, 547
- dip brazing, 644
- dip-transfer, 621
- direct chill casting, 83–6, 726–7
 - heat flow and solidification, 86–97
 - alloy type on heat flow, stresses and microstructures, 91–3
 - boiling curve and boiling modes, 95
 - direct chill water spray, 96
 - mould cooling, 93–5
 - pool depth measured by dip rod, 90
 - pool shape in 6063 alloy billet casting, 87
 - shell formation in open top mould, 87
 - variation in alloy thermal conductivity, 92
 - water cooling, 95–7
 - safety, 108
 - schematic, 84
 - special variants, 108
 - surface defects, 98–105
 - cracking, 102–5
- direct squeeze casting, 149
- discontinuously reinforced aluminium, 774
- dislocation core, 459
- dislocations, 458
- dispersoids, 559–62
- Doppler effect, 400
- DRA *see* discontinuously reinforced aluminium
- dross, 77–8, 78
- dry scrubbing, 50
- Duralumin, 2, 3, 748
- dynamic strain ageing, 475
- ECAP *see* equal channel angular pressing
- ECAP-Conform, 472, 496
- Eclipse Aviation, 778
- Eddy current separation, 79
- Elasto Plastic Fracture Mechanics, 505
- electric power, 51–2
- electrical resistivity, 389
- electromagnetic casting, 107
- electromechanical process, 575
- Electron Backscatter Diffraction, 581
- elongation to fracture, 167, 169
- energy consumption, 59
- energy efficiency, 59
- epoxy, 647
- equal channel angular pressing, 359, 469, 471
- equilibrium precipitates, 754–5
- exfoliation corrosion, 582–4, 772
- explosion welding, 631–2
- External Super Light Weight Tank, 777
- externally solidified crystals, 149
- FactSage, 430
- failure assessment diagram, 553
- Faraday's first law, 57–8
- fasteners, 608
- fatigue crack growth
 - aluminium alloys design, 504–32
 - background and current state of knowledge, 505–7
 - crack growth Regions II and III, 520–5
 - fracture surface roughness changes, 521–3
 - plastic zone size and crack path changes, 524
 - Si particles failure mechanisms, 524
 - design curves from K_{\max} sensitivity and data normalisation, 530–2
 - design curves K_{\max} sensitivity and data normalisation
 - fatigue crack growth data, 531
 - dual parameter ΔK - K_{\max} approach, 530
 - crack growth rates, 529
 - K_{\max} and stress ratio effects, 526
 - alloy steady crack growth behaviour, 528
 - fatigue crack growth rates, 531
 - materials, processing, mechanical properties and testing, 507–10
 - alloys microstructures, 507–8
 - alloys tensile properties, 508
 - propagation in near-threshold regime, 510–19
 - alloys behaviour after ACR closure correction, 515
 - alloys fatigue crack propagation behaviour, 511
 - crack path deflection, 513
 - fracture surfaces, 514
 - long cracks propagation mechanisms, 510–12
 - long-to-small crack corrective model, 517
 - processing residual stress effects, 516–19
 - small cracks propagation mechanisms, 512–16
 - wrought alloys behaviour, 518
 - fatigue crack growth rate, 769
 - fatigue crack initiation, 768–9

- fatigue crack propagation, 769–70
- fatigue failure, 169–73
- fatigue life, 171, 180, 182
- film boiling, 97
- filtration, 120–3
- finite-life design, 797–8
- first-principle calculations, 411, 414–15
- flotation, 120
- flow drilling screws, 610, 616
- flow stress addition laws, 323–5
- Fondarex vacuum valve, 256
- forming limit diagram, 332, 333
- Fourier transform infrared continuous emissions monitor, 114
- fracture
 - Al alloy casting
 - ultimate tensile strength variability analysis, 550
 - aluminium alloy casting, 548–51
 - aluminium alloys fracture toughness, 557–63
 - crack tip in high-strength Al alloy, 558
 - fracture toughness dependency, 561
 - 7xxx alloy dispersoids, 560
 - future trends, 569–71
 - high strength wrought alloys, 551–7
 - crack extension, 556
 - fracture toughness variation, 555
 - particulate metal matrix composites, 563–5
 - SiC_p-reinforced particulate Al MMC fracture, 565
 - resistance in aluminium and its alloys, 538–71
 - serrated yielding effects, 565–7
 - Al-Zn-Mg alloy, 566
 - alternative behaviour in notched bars, 568–9
 - fracture surface nature in tensile specimens, 568
 - shear fracture, 567
 - thin sheet, 544–8
 - neck formation, 546
 - uni-axial tension, 539–44
 - copper ductile fracture, 542
 - Duralumin second-phase particles, 544
 - internal necking mechanisms modification, 543
- Fracture Mechanics methodologies, 570
- fracture toughness, 764–8
- friction, 101
- friction stir spot welding, 640
 - schematic representation, 641
- friction stir welding, 637–42, 778–9
- friction welding, 633–5
- fuel reduction value, 813
- furnace brazing, 645
- FUSION, 338
- fusion welding, 618–30
 - gas metal arc welding, 620–4
 - butt weld and weld bead cross-sectional view, 623
 - metal transfer mode variation, 622
 - process, 621
 - gas tungsten arc welding, 619–20
 - process, 620
 - laser welding, 626–8
 - keyhole laser welding, 626
 - metallurgical considerations, 628–30
 - processes classification, 619
 - resistance welding, 624–6
 - spot welding process, 624
 - fusion welds, 566
 - fusion zone, 618
- gallium, 590
- gas atomisation, 656
- gas injection, 116
- gas metal arc welding, 620–4
- gas porosity, 250–6
- gas pressurised extrusion belt casting, 105–6
- gas tungsten arc welding, 619–20
- Gaussian distribution, 179
- genetic algorithms, 805
- Gibb's free energy, 666, 681, 685
- gibbsite, 26, 27, 28, 30–8
- global optima, 805
- GM's Ecotec V-6 engines, 692
- Goss texture, 779
- GPB zones, 350
- GPI zones, 356
- GPII zones, 356
- grain-boundaries, 513
- grain boundary density, 583
- grain refinement, 143
 - effect on defect formation, 195–202
 - selecting the right master alloy, 207–8
- grain size, 316–18
- green compact, 655
- growth, 425
- Guinier-Preston zones, 450, 754
- Hall-Héroult process, 1, 49, 50, 53, 67
 - cell technology parameters, 67
 - flowsheet, 51
- Hall-Petch relation, 360, 468, 487
- Hall-Petch slope, 317
- Hart's necking criterion, 488
- health, environment and safety, 63–5
- heat affected zone, 618
- heat balance, 60
- heat treatable alloys, 329–32
- helium, 621
- hexavalent chromate ions, 591
- high-cycle fatigue, 490
- high pressure die casting, 141, 144–50, 807
 - A356 microstructures, 148
 - alloying elements during age hardening, 279–91
 - 380-type alloys, 285
 - A380 and ADC10M microstructures, 290
 - age-hardening responses, 281
 - alloys within Q-forming regions of the phase diagram, 282
 - aluminium grains solute content quantitative analysis, 280
 - copper, 280–1, 284
 - copper progressive increases for as-cast, 283
 - high ductility HPDC compositions, 285
 - HPDC Al-Si-Cu-(Fe) alloy fractography, 289
 - isotherm of quaternary phase diagram for Al-Si-Cu-Mg, 279
 - magnesium, 284–8

- magnesium content effect on 383/A383
 - alloys, 286
 - silicon, 279–80
 - tin, 288–9
 - transition metal elements, 289–91
 - zinc, 288
- zinc in Al-Si-Cu alloys overageing, 288
- alloying elements during solution treatment, 271–8
 - A380 alloy laminar defect leading to blistering, 275
 - as-cast and solution treated and T6 aged alloy, 278
 - blister formation progression, 277
 - copper, 272, 277
 - magnesium, 277–8
 - quantification of changes to silicon particle size, 274
 - regions of variable density, 276
 - silicon, 271–2
 - silicon particles refinement during heating, 273
 - T7 treated HPDC alloy, 271
 - zinc, 278
- aluminium alloys used, 232–5
 - A380/LM24 alloy microstructure, 234
 - defining alloys, 232–3
 - microstructure, 233–5
 - pore fraction with changes in gate velocity, 235
 - sludge factor, 233
- aluminium and its alloys, 217–58
 - complex high pressure die castings, 221
 - early aluminium die casting machine, 220
 - early die casting machine, 218
 - hydraulic systems, 220
 - pneumatic machine, 219
 - Sturges die casting machine patent, 218
- application to industrially produced parts and commercial heat treatment facilities, 291–9
 - A380 and ADC10M heat treated to a T6 temper, 292
 - as-cast and heat treated HPDCs hardness and tensile properties, 297
 - experiments using industrial heat treatment facility, 296
 - fluidised bed basket, 295
 - heat treatment on A380 alloy tensile and fracture properties, 293
 - heat treatment procedures development, 291–5
 - heating rates to solution treatment temperature, 298
 - internal porosity, 297
 - parts sourced for heat treatment procedures development, 294
 - solution treatment temperatures and hardness, 296
 - statistical analysis of heat treated parts, 295–6
 - T6 ageing treated HPDCs statistical analysis, 298
- cold chamber HPDC machine schematic, 145
- defects, 235–56
- flow and cold flow defects, 235–42
 - cold flow marks, 237
 - cold flow region, 241
 - defect problem and some causes, 242
 - differences in metal temperature, 243
 - oil marks on plated surface, 238
 - sheared metals as they freeze, 238, 240–2
 - short shots showing filling of door handle, 244
 - two fronts meeting, 235–7, 236
 - viscosity with solid fraction, 240
- gas porosity, 250–6
 - casting evident in a radiograph, 255
 - changes in wave with plunger speed, 252
 - flow fragmentation due to runner changes, 253
 - flow in the cavity, 252, 254
 - Fondarex vacuum valve, 256
 - level of vacuum in cavity using chill vent, 258
 - minimum radius of curvature for bends, 254
 - radiograph of porosity in casting, 254
 - runner, 251–2
 - runners in a two-cavity die, 253
 - shot sleeve, 251
 - vacuum application to a cavity, 257
 - venting the gas in the cavity, 254–6
 - vents machined into the die, 255
 - wave motion in shot sleeve, 251
- high integrity process, 146
- history, 217–21
- implications for redesign, 299–300
 - design properties in automotive applications and weight reduction implications, 301
 - hardness summary of test samples, 299
- indirect squeeze casting, 149
- melt flow technique, 149–50
- micro vortices, 237–8
 - impacting counter flows, 236
 - long, narrow bosses, 239
 - trapped air, 239
- process, 221–30
 - bimodal grain size, 231
 - changes in grain size, 227
 - conditions, 222–3
 - definition, 221–2
 - effect of hydrogen on reject rate, 232
 - flakes in shot sleeve, 229
 - gas porosity in die castings, 225
 - hydrogen in die casting, 229–30
 - hydrogen solubility, 231
 - metal flow from gate to die surface, 224
 - molten aluminium behaviour, 223–5
 - partial solidification, 228–9
 - pressure on metal and heat transfer, 226
 - role of die and pressure in heat transfer, 225–8
 - soldering layer over the tool steel, 228
 - steps, 222
 - strength of cast aluminium alloys with temperature, 224
 - temperature profile simulation in melt, 230
 - thin steel section of die surrounded by molten metal, 227
 - typical set made of high strength tool steel, 223

- progress on heat treatment, 262–302
 - A380 alloy aged to a T6 temper, 268
 - A380 alloy as-cast, 264
 - A360 alloy hardening responses, 267
 - A360 alloy surface and internal microstructures, 266
 - Al-Cu alloy vs HPDC alloy
 - properties, 269
 - alloys compositions, 269
 - HPDC alloy in the as-cast condition, 265
 - HPDC alloys from different world regions, 263
 - HPDC alloys mechanical properties, 270
 - solution treatment temperature on HPDC alloy C380 tensile properties, 267
- semisolid metal processing, 147–8
- shrinkage porosity, 243, 245–8
 - cooling experiment, 248
 - die showing hot regions, 247
 - elemental additions control, 248
 - gas and shrinkage pore combined, 246
 - gas pore expanding during solidification, 246
 - pressure control, 247–8
 - segregation band due to pressure, 250
 - squeeze pressure on density, 249
 - Sr and Na on porosity level, 250
 - thermal control, 245, 247
 - variation in reject rate, 249
- vacuum assisted die casting principle, 147
- vacuum-assisted techniques, 146–7
- high pressure torsion, 359, 469, 470, 482
- High-Q-Cast method, 147
- high stress ratio tests, 526
- hole drilling strain gauge method, 91
- holistic value function, 812–13
- homogenisation, 729–30
 - crucible layout used to nitride plates and powder, 730
 - nitride layer growth on 6061–2Mg preforms, 731
- horizontal direct chill casting, 99
- hot cracking, 631
- hot isostatic pressure treatment, 173
- hot rolling treatment, 486, 731–5
 - 6061–2Mg–1Sn preforms weight gain and resultant ductility, 735
 - cracked nitride layer formed on plate, 731
 - microstructure evaluation, 733–4
 - mill design, 732–3
- hot tearing, 103
- HPDC *see* high pressure die casting
- Hubbert's curve, 803–4
- hydrogen, 110, 144, 176, 629
 - high pressure die casting, 229–30
 - effect on reject rate, 232
 - solubility in aluminium metal, 231
 - removal, 114–17
- hydrogen embrittlement, 588–90
- hydrogen porosity, 229
- impurity, 112–13
- inclusions, 557–59
 - effect on quality, 167–9
 - removal, 120–3
- indirect squeeze casting, 149
- inert anodes, 65–7
- advantages in developing cell technology, 65–6
- cost reduction, 65
- environmental friendliness, 65–6
- improved occupational health issues, 66
- challenges in development
 - impurity metal content in aluminium, 66
 - wear rate, 66
- infinite-life design, 796–7
- ingot casting
 - aluminium and its alloys, 83–123
 - chain conveyor casting, 108–10
 - direct chill casting, 83–6
 - direct chill casting special variants, 108
 - gas pressurised extrusion billet casting, 105–6
 - heat flow and solidification, 86–97
 - macrosegregation, 97–8
 - melt treatment, 110–23
 - rolling slab technology, 107–8
 - surface defects, 98–105
- intergranular corrosion, 582–4, 599, 772
- origins, 583
- iron, 187, 191, 232, 289–91
- isothermal heat treatments, 436
- isotropic hardening, 308
- Jaguar, 614
- Jaguar 229, 616
- Jaguar X150, 616
- Jaguar XJ, 614
- JOEL: 2000EX microscope, 374
- Johnson–Mehl–Avrami–Kolmogorow equation, 394, 428, 734
- k-factor, 727
- kinematic hardening, 308
- Kinetic Monte Carlo algorithm, 412, 444
- Kingery's classical theory, 663
- Knight shifts, 398
- Kocks-Mecking model, 313, 314, 316, 318
- Kocks-Mecking plot, 308
- La Jamais Contente*, 2
- Lais, 112
- laser-beam welding, 779
- laser brazing, 645–6
- laser hybrid welding, 627–8
 - schematic representation, 628
- laser sintering, 702–15
 - aluminium
 - dimensional changes, 713–14
 - effect of hold time on infiltration, 712
 - infiltration, 711–13
 - parts made by infiltrating laser sintered aluminium preforms, 714
 - laser sintered aluminium with nylon, 704
 - overall furnace cycle, 705
 - selective laser sintering apparatus, 703
 - skeleton, 705–11
 - aluminium nitride formation, 706
 - aluminium nitride growth, 708–11
 - cracked nitride layer formed on plate, 710
 - crucible layout used to nitride plates and powder, 708
 - nitride layer growth on 6061–2Mg preforms, 709

- nitride layer thickness and ductility, 710
- powder preform after binder removal and infiltration, 706
- laser welding, 626–8, 778–9
- Lattice Kinetic Monte Carlo, 442
- LECO, 113
- Levy-Mises' expressions, 545
- LiMCA, 112
- linear addition laws, 323
- Linear Elastic Fracture Mechanics, 504
- linear friction welding, 634
- liquid-bridge models, 670
- liquid metal forging *see* direct squeeze casting
- liquid phase sintering, 396, 661–3
- liquid-vapour surface tensions, 666
- lithium, 774
- lithium fluoride, 55
- LKMC *see* Lattice Kinetic Monte Carlo
- local density approximation, 410
- local necking, 334
- local optima, 805
- low-cycle fatigue, 490
- low pressure die casting, 150–1, 191
 - schematic, 150
 - vacuum permanent mould casting, 151
- LSW law, 433, 451
- lubrication, 101, 658
- Ludwik/Holloman equation, 312
- macrosegregation, 97–8
- MAGMASOFT, 195, 198
- magnesium, 114, 187, 232, 277–8, 284–8, 685, 707, 709, 758–9
- magnesium chloride, 119
- magnesium fluoride, 55
- magnesium silicide, 204
- magnetic pulse welding, 632–3
- magneto hydrodynamics, 60–1
- manganese, 289–91, 371
- Mass Loss after exposure to Nitric Acid, 583
- master alloy, 207–14
- Master Curve, 530
- material property charts, 788
 - fatigue strength limited design, 795
 - yield strength limited design, 794
- materials selection
 - environmental consequence, 816, 818–22
 - CO₂ emissions, 818
 - embodied energy, 818
 - environmental material selection curves, 818
 - environmental material selection outcomes, 821–2
 - secondary aluminium, 818
- fatigue-limited scenarios, 796–8
 - candidate materials S-N curves, 798
 - finite-life design, 797–8
 - infinite-life design, 796–7
 - S-N curve for idealised material with fatigue-limit, 796
- fundamental strategies, 785–91
 - aluminium cash-buyer price variation, 793
 - generic material property chart, 788
 - material data and selection procedures
 - potential limitations, 789–91
 - material property charts, 788
 - material selection indices, 788–9
 - simplified structural elements, 789
- light alloy substitute materials and reference ferrous properties, 792
- light alloy suspension component, 813–16
 - annual distance travelled, 815
 - associated vehicle age for cumulative probability, 815
 - average fuel consumption vs vehicle mass, 814
 - holistic value function vs fatigue life, 817
 - mass-specific fuel consumption, 814
 - petrol cost, 815–16
 - requisite life-cycle parameter, 816
 - requisite life-cycle parameters, 813–14
 - vehicle design-life, 815
- material selection curves, 798–801
 - $k = 1: M^*1m, M^*1c, 799, 800$
 - $k = 2: M^*2m, M^*2c, 799–801, 802$
 - $k = 3/2: M^*3/2m, M^*3/2c, 799, 801$
- methods, 785–7
 - indices including the associated free variable and guideline gradient, 787
 - material property limits, 786
 - material selection indices, 786
- multi-objective material selection, 811–16
 - case study, 813–16
 - value function, 811–13
- multi-objective problems and numeric optimisation, 804–11
 - numeric optimisation, 805–6
 - opportunities for nontrivial and multi-objective design problems, 809, 811
- non-stationary fatigue-limited application, 803–4
 - environmental motivation, 804
 - Hubbert's curve and peak oil, 803–4
- safety-critical actuator, 806–9
 - linear actuator assembly, 807
 - material selection, 806–8
 - optimisation, 808–9
 - parametric geometry and simulated loading conditions, 810
 - potential range of material selection indices, 808
 - solution space associated with gearbox cover, 810
- specific scenarios, 791–803
 - general material property chart outcomes, 793
 - material classification, 791, 793
 - nontrivial geometries, 794–6
 - performance summary, 802–3
- tie, beam, and plate structural elements
 - CO₂ emissions, 820
 - embodied energy, 819
 - embodied energy and CO₂ emissions associated with secondary aluminium use, 821
 - using aluminium alloys, 784–824
- Maximum Growth Rate hypothesis, 452
- mean precipitates radius, 453
- mechanical fastening, 610–16
 - blind rivets, 614–15
 - stages, 614
 - flow drilling screws, 616
 - one-sided accessibility and no-drilling, 615–16

- self-piercing rivets, 612–14
 - process, 613
- solid and tubular rivets, 611–12
- solid rivet setting, 612
- threaded fasteners, 611
- mechanical joining, 609–18
 - clinching stages, 617
 - interlocking by integral attachment, 616–18
 - process classification, 611
- mechanically affected zone, 631
- melt pre-conditioner, 149
- melt refining, 112
- melt spinning, 777
- melt treatment, 110–23
 - hydrogen removal, 114–17
 - Alcan Compact Degasser, 116
 - impurity measurement, 112–13
 - inclusion removal, 120–3
 - ceramic foam filter tile, 121
 - deep bed filter box for inline filtration of inclusions, 122
 - melt processing steps, changes in impurities and possible interventions, 111
 - sodium removal, 117–19
 - rotary flux injector furnace treatment system, 119
 - TAC crucible treatment system, 118
 - use of chlorine, 113–14
 - fluxing with argon containing chloride gas, 113
- melt velocity, 266
- metal anodes, 66
- metal inert gas welding *see* gas metal arc welding
- metastable precipitates, 754
- Mg₃N₂, 707
- Mg₂Si, 759
- micro vortices, 237–8, 239
- microstructural characteristic dimension, 505
- microstructure metal plasticity model, 315
- MIL-DTL-81706B, 591
- Miller indices, 758
- Mises' yield criterion, 545
- Molecular Dynamics simulations, 452
- Moltech, 66
- monolithic alloys, 564
- Monte Carlo step simulation, 412
- mould cooling, 93–5
- mould design, 109–10
- multiple parameter models, 314–15
- NADCA guidelines, 295
- NAMLT test *see* Mass Loss after exposure to Nitric Acid
- necking, 335, 545
- nepheline, 26, 28, 29
- net-shaped castings, 164, 177, 182
- nitric-hydrofluoric acid, 644
- nitrogen, 685
- nitrogen carrier fusion method, 113
- no bake mould casting, 152
- non-destructive testing procedures, 552
- non-heat treatable alloys, 325–8
- non-ideal sintering systems, 396
- non-isothermal heat treatments, 436–40
 - class models, 436–40
 - particle size distribution, 439
 - particles density calculations, 439
 - precipitation description, 441
 - monotonic thermal treatments profiles, 437
 - treatment temperature, 438
- non-shearable precipitates, 320–3
- non-spherical precipitates, 448–57
 - anisotropy in phase interface mobility, 451–3
 - atomistic approaches, 449–51
 - Lattice kinetic Monte Carlo simulation, 450
 - continuum approaches, 451
 - distribution coarsening, 453–7
 - mean precipitate size model vs experimental measurements, 455
 - microstructural evolution phase field simulation, 457
 - order parameters describing q' precipitates, 456
 - plate-shaped diffusional growth, 454
- non-wetting system, 664
- Notorp, 113
- nucleate boiling, 97
- nucleation, 425, 426, 438–9
- order parameters, 456
- Orowan bypass process, 563
- Orowan equation, 759–60
- Ostwald ripening, 272, 663, 671–2
 - see also* coarsening
- oxide (bi-)films, 554
- oxide films, 174, 176, 574, 690
- oxide growth, 575
- oxide layer, 665
- Pandat, 430
- Pareto Frontier, 809
- Paris equation, 170
- partinium, 2
- PAS *see* positron annihilation spectroscopy
- passivation, 577
- peak oil, 803–4, 813
- Peclet number, 88
- Pedersen process, 28, 29
- perfluorocarbon, 50, 64
- permanent mould casting, 151
- petroleum coke, 52, 53
- phosphorus, 41, 53
- physically bonding adhesives, 647
- piezoelectric transducer, 635
- pits, 578
- pitting, 578, 772
- planar slip, 764
- plane strain compression tests, 734
- plastic deformation, 458
- plastic flow, 544
- plunger, 221
- PodFa, 112
- Poisson's ratio, 552
- polyurethane topcoat, 593
- porosity, 174, 631
 - effect on quality, 167–9
- Portevin LeChâtelier effect, 319
- positron annihilation spectroscopy, 351, 379, 399–408, 688
 - first-principle calculations, 414–15
 - solute-vacancy complexes studies, 403–8
 - CDB spectra, 407

- PALS and CDB measurements, 409
- positron lifetime and Vickers hardness vs ageing time, 406
- positron lifetime vs ageing time, 405
- vacancy-like defects studies in pure aluminium, 399–403
- CDB spectra for defecting pure AL, 403
- lifetime spectra for positrons annihilated in different metals, 401
- positron–electron annihilation line Doppler broadening, 402
- trapping coefficients and characteristic lifetimes of positrons in aluminium defects, 401
- positron lifetime annihilation spectroscopy, 444
- potline *see* cell lines
- Pourbaix diagram, 576
- powder metallurgy *see* aluminium powder metallurgy
- Power law, 335
- Power law hardening equation, 312
- Pratt & Whitney engines, 774
- prebaked anodes, 52–3
- precipitate free zone, 765
- precipitates, 319–23
- precipitates free zone, 426
- precipitation, 425
- premature curing, 626
- present value function, 812
- primary aluminium, 16, 110
 - cathode and cathode materials, 56–63
 - aluminium electrolysis cell, 58
 - cell amperage increase, 60
 - cell lines, 61–2
 - cell operation, 62–3
 - current efficiency, 57–9
 - energy consumption and energy efficiency, 59
 - heat balance, 60
 - magneto hydrodynamics, 60–1
 - modern cell lines with pre-bake cells, 61–2
 - concentration ranges of impurity elements, 111
 - electrolyte materials, 54–6
 - cryolite with fluoride additives, 56
 - ionic structure of melt, 55–6
 - past, present and future, 67–8
 - Hall–Héroult cell technology parameters, 67
 - production, 49–68
 - alumina, 49
 - aluminium, 49–50
 - carbon anodes, 52–4
 - energy efficiency in carbon anodes utilisation, 52
 - Hall–Héroult process flow sheet, 51
 - health, environment and safety, 63–5
 - inert anodes, 65–7
 - production by country for 2007, 10
 - raw materials used in production process, 51–2
 - bauxite, 51
 - electric power, 51–2
 - US production from 1900–2007, 11
 - world-wide production from 1900–2007, 10
- primary rearrangement, 668
- primer paint coatings, 592
- probability density function, 548
- processing maps, 436
- pseudo-quality index chart, 191
- pulsed-current process, 622
- pure aluminium, 711
 - conventional techniques, 390–1
 - different aspects related to vacancies, 386–416
 - diffusion processes, 394–7
 - alloy microstructure, 397
 - modelling, 408, 410–15
 - first-principle calculations in positron annihilation spectroscopy, 414–15
 - vacancies, 410
 - vacancy formation energies experimental and theoretical values, 410
 - spectroscopic techniques, 397–408, 399–403
 - CDB spectra for defecting pure AL, 403
 - lifetime spectra for positrons annihilated in different metals, 401
 - positron–electron annihilation line Doppler broadening, 402
 - precipitation sequence microstructural analysis using NMR, 397–9
 - trapping coefficients and characteristic lifetimes of positrons in aluminium defects, 401
 - vacancy-like defects study using positron annihilation spectroscopy, 399–403
 - vacancies and solute-vacancy interactions
 - experimental studies, 388–408
 - vacancy formation and migration, 388–9
- Pythagorean addition law, 323, 324
- quality index, 159, 164, 189
 - map, 166
 - theoretical basis, 164–7
- quantitative microstructural analysis, 688
- quench bands, 563
- quenching, 507
- quenching efficiency, 767
- rack raising, 63
- RAM, 117
- rapid hardening, 350
- rapid manufacturing, 702
- rapid prototyping, 702–15
- recycling, 81–2
- refiners, 71, 72
- remelters, 71
- residual resistance, 389
- residual stress, 505, 530
- resistance welding, 624–6
- Restoring Force Model 1.0, 519
- Restoring Force Model 2.0, 519
- reverberatory furnaces, 80
- rheocasting, 148
- ring pull, 547
- rivets *see* specific rivet
- rolling slab technology, 107–8
- rotary-die ECAP, 472
- rotary flux injector, 119
- rotary furnaces, 80
- rotating cantilever tests, 370
- Saffil fibre MMCs, 563
- salt fluxes, 118–19

- sand casting, 151–3, 178
 - schematic, 152
- sandy alumina, 32
- Saturn four cylinder engines, 692
- ScaLA, 777
- scaling stress, 314
- scrap, 72
- sealants, 592–3
- seam welding, 625
- second-phase particles, 557–63
 - ageing precipitates, 562
 - dispersoids, 559–62
 - inclusions, 557–9
- secondary aluminium, 8, 11, 16, 70
 - history, 70–2
 - global aluminium usage 1950–2008, 71
 - global recycled scrap by market, 72
 - new production off-cuts, 73–4
 - mixed aluminium alloy clippings and solids, 74
 - new production aluminium extrusions, 74
 - post consumer scrap, 74–6
 - baled aluminium UBC scrap, 75–6
 - clean mixed old alloy sheet aluminium, 75
 - mixed aluminium castings, 75
 - processing, 78–81
 - baling and shearing, 79
 - drying and de-coating, 79–80
 - melting and alloying, 80–1
 - milling and screening, 80
 - shredding, 79
 - sorting, 78–9
 - production, 70–82
 - cost drivers, 81
 - future trends, 81–2
 - sources of raw materials, 73–8
 - dross, 77–8, 78
 - swarf, 76–7
 - Taint-tabor, 75
 - Taldon, 77
 - Tense, 76
- secondary dendrite arm spacing, 187, 188
- secondary precipitation, 367
- secondary rearrangement, 668, 671
- selective laser sintering apparatus, 703, 725
- self-drilling screws, 610
- self-piercing rivets, 610, 612–14
 - riveting stages, 613
- semisolid metal casting, 171
- semisolid metal processing, 147–8
- serration, 548
- 7xxxx series Al alloys, 358–9
- severe plastic deformation, 359–61
- severe plastic deformation techniques, 469–73
- shearable precipitates, 319–20
- short-circuiting mode, 621
- short shots, 242, 244
- shot sleeve, 221, 251
- Showa Aluminium, 106
- shrinkage porosity, 243, 245–8
- SICO, 112
- side-extrusion, 472
- silicon, 174, 232, 271–2, 279–80, 758–9
- silver alloys, 398
- single parameter models, 313–14
- single reversing Steckel mill hot rolling, 734–6
- sintering, 658–78
 - curved surface associated stress, 659
 - dihedral angle, 667–8
 - grain boundaries penetration, 668
 - liquid in contact with grains, 667
 - liquid phase sintering, 661–3
 - mechanisms classical approach, 663
 - shrinkage or swelling result of solubility differences, 662
 - pore-filling, 675–8
 - grain size ratio, 676
 - liquid meniscus radius, 675
 - relative density and shrinkage, 677
 - wetting angle effect on critical grain size, 677
 - rearrangement, 668–71
 - liquid formation leading to primary rearrangement, 669
 - spherical particles connected by liquid bridge, 669
 - solid reprecipitation, 672–5
 - contact flattening, 672–4
 - grain shape accommodation and neck growth mechanisms, 672
 - Ostwald ripening, 671–2
 - solid state bonding, 675
 - solution reprecipitation densification, 674
 - solid-state sintering, 660–1
 - transport mechanisms, 661
 - transport mechanisms schematic, 660
 - wetting, 664–7
 - liquid equilibrium wetting angle, 664
 - liquid-vapour surface tensions, 667
- 6xxxx series Al alloys, 354
- sludge, 271
- sludging factor, 232–3
- slumping, 200
- Snake Rolling, 779
- SNIF, 116
- Söderberg anode, 53
- sodium, 41, 58, 110, 112
 - removal, 117–19
- soldering, 228
- solid state sintering, 660–1
- solid state welding, 630–42
 - cold welding, 631
 - explosion welding, 631–2
 - friction stir welding, 637–42
 - advantages and limitations, 639
 - generic hardness response, 643
 - microstructural features, 640–2
 - process main features, 638
 - transverse cross-sectional view, 642
 - friction welding, 633–5
 - basic steps, 634–5
 - magnetic pulse welding, 632–3
 - system layout, 633
 - ultrasonic welding, 635–7
 - set-up, 636
- solidification, 262
- solidification cracking, 629
- solute partitioning, 367–82
- solute-vacancy interactions
 - aluminium alloys, 386–416
 - conventional techniques, 391–4
 - electrical resistivity, 392
 - electrical resistivity evolution, 395
 - isothermal pre-ageing curves, 394

- diffusion processes
 - alloy microstructure, 397
 - experimental studies, 388–408
 - vacancies and solute-vacancy interactions, 389–90
- modelling, 408, 410–15, 411–15
 - atom arrangements, 413
 - first-principle calculations in positron annihilation spectroscopy, 414–15
 - solute clusters growth, 411–12
 - solute-vacancy binding energies, 411
 - solute-vacancy interaction, 412–13
- spectroscopic techniques, 397–408, 403–8
 - CDB spectra, 407
 - Cu NMR spectra from Al-1.7 at. % Cu, 399
 - PALS and CDB measurements, 409
 - positron lifetime and Vickers hardness vs ageing time, 406
 - positron lifetime vs ageing time, 405
 - precipitation sequence microstructural analysis using NMR, 397–9
- SPD techniques *see* severe plastic deformation techniques
- spherical precipitates, 453
- SPR *see* self-piercing rivets
- spray degassing, 117
- spray process, 553
- squeeze casting, 149, 171
- standard moulds, 156–62
- stochastic algorithms, 805
- strain hardening coefficient, 165
- strain-induced precipitate dissolution, 460
- stress corrosion cracking, 356, 585–6, 770–2
- stress intensity, 169
- strontium, 208–9
- strontium chromate, 592
- structural alloys, 570
- super-solidus liquid phase sintering, 661
- superplasticity, 468
- supersaturated solid solution, 349, 387
- surface defects, 98–105
- surface energy, 664
- surface tension, 664
- swarf, 76–7, 79
- sweat furnaces, 80–1
- T-Bar, 108
- TAC, 117
- tack, 616
- Taint-tabor, 75
- Taldon, 75–6, 77
- tandem hot rolling, 734–5
- tapping, 63
- Tata, 74
- Taylor equation, 313
- Taylor factor, 737, 763
- Telegas, 113
- Telic, 77
- Tense, 75, 76
- tensile necking, 488
- tensile properties, 371
- tensile residual stress, 530
- ternary cluster expansion, 411
- test casting, 155, 156
- thermal expansion, 389
- thermal modification, 524
- Thermo-Calc, 430
- thermomechanical treatments, 423
- thermomechanically affected zone, 642
- thixocasting, 148
- thixomoulding, 148
- threaded fasteners, 613
- through process models, 461–2, 721, 742, 743–4
- Ti:B ratio, 203
- Tibor grain-refined casting alloy, 551
- tin, 288–9, 710–11, 712
- titanium, 202–4
- titanium diboride, 92
- titanium dioxide, 593
- torch brazing, 644
- Toshiba, 291
- Tough, 75
- transgranular fracture, 764
- transition metal, 289–91
- trihydrate, 26, 36
- tungsten inert gas welding, 619
- twin roll casting, 83, 727–9
- ultimate tensile strength, 540
- ultrafine grained aluminium alloys, 468–97
 - fatigue behaviour, 489–94
 - age-hardenable alloys high-cycle fatigue properties, 492
 - ECAP effect on AA2124 fatigue properties, 493
 - fatigue limit and tensile strength correlation, 490
 - fatigue threshold reduction, 494
 - severe plastic deformation cyclic response, 491
 - Woehler plot, 491
- innovation potential, 494–7
 - integrated ECAP/extrusion process, 495
 - UFG alloy 1421 fabricated by ECAP, 496
- mechanical properties at room temperature, 480–94
- production using SPD techniques, 473–80
 - 1570 alloy micrographs, 477
 - Al-Cu-Zr alloy micrograph, 475
 - Al-Mg alloy micrograph, 475
 - Al-Zn alloy microstructure, 476
 - ECAP passes effect on texture development, 481
 - heat and non-heat treatable alloy, 474
 - Mg, Cu, and Si atoms distributions, 477
 - polycrystalline aluminium microstructures, 478
- SPD techniques in Al alloys processing, 469–73
 - ECAP-Conform process, 472
 - ECAP principle, 471
 - ECAP processing and application, 472
 - high pressure torsion schematics, 470
 - strength and ductility, 480, 482–9
 - 1570 and 6061 alloys mechanical properties, 484
 - age-hardenable mechanical properties, 487
 - ECAP effect on grain size and tensile strength, 485
 - high-pressure torsion effect, 483
 - non age-hardenable mechanical properties, 486

- strain rate effect on tensile properties, 488
- stress-strain curves, 489
- ultrasonic welding, 635–7
- underfilm corrosion, 597
- uni-axial pressing, 656
- upstream conduction distance, 86
- US Military Specification MIL-A-8625F, 591
- US Military Specification MIL-DTL-5541F, 591
- US Military Specification MIL-PRF-85285D, 592
- US Military Specification MIL-PRF-85582D, 592
- US Military Specification MIL-PRF-2337J, 592
- utility function *see* value function
- vacancy pump model, 395, 411
- vacancy-rich clusters, 356
- Vacural method, 146–7
- vacuum brazing, 645
- vacuum degassing, 116
- vacuum permanent mould casting, 151
- value function, 811–13
- Van der Waals, 608
- vanadium, 53
- vertical direct chill casting, 84, 99
- Vienna *ab-initio* simulation package, 411
- Voce equation, 314
- Voce law, 316, 324
- volatile organic compounds, 592
- V96Z1 alloy, 482
- water cooling, 95–7
- water quenching, 345
- Weibull distribution, 549
- Weibull modulus, 178, 179
- Weldalite family, 777
- Weldbonding, 625–6
- welding, 426, 618, 619–28
 - see also* specific type of welding
- wet assembly, 593
- wetting, 664–7
- wetting angle, 664
- work hardening
 - aluminium alloys, 307–38
 - future trends, 338
 - commercial aspects, 332–8
 - flow stress as a function of rolling strain, 337
 - formability, 332–7
 - forming limit diagrams, 333
 - necking instability plots in strain space, 334
 - necking instability plots in stress space, 335
 - strain hardened tempers, 337–8
 - work hardening exponent
 - variation, 336
 - yield stress and ultimate tensile strength to
 - yield stress ratios, 336
- dislocation-based models, 313–16
 - additional considerations, 316
 - multiple parameter models, 314–15
 - single parameter models, 313–14
 - stage IV behaviour, 315–16
- fundamentals, 308–12
 - high-purity aluminium tensile response, 309
 - phenomenology in high-purity aluminium, 308–11
 - physical basis, 311–12
 - stages and elastic plastic transition, 311
- macroscopic work hardening rate for
 - different flow stress addition laws, 324
- microstructure effects, 316–25
 - Bauschinger tests, 322
 - flow stress addition laws, 323–5
 - grain size effects, 316–18
 - other cases, 325
 - precipitate effects, 319–23
 - solid solution effects, 318–19
- model applications to industrial alloys, 325–32
 - heat treatable alloys, 329–32
 - maximum work hardening rate after
 - elastic-plastic transition, 331
 - non-heat treatable alloys, 325–8
 - rate of dynamic recovery as a function of
 - Mg content, 328
 - stress-strain response and work hardening
 - behaviour, 326, 329–30
- models, 312–25
 - empirical, 312
- work hardening index, 335
- work hardening rate, 313–14, 314
- Wright Flyer 1, 2
- wrought aluminium alloys, 7–8
 - aluminium mill products distribution, 7
- Young's equation, 664
- Young's modulus, 552, 564, 773–4
- Zeeman spectroscopy, 397
- Zeldovich's factor, 429
- Zener drag, 757
- Zener–Holomon parameter, 734
- zinc, 278, 288
- zircon sand, 153
- zirconium, 756
- Zorba, 78–9